

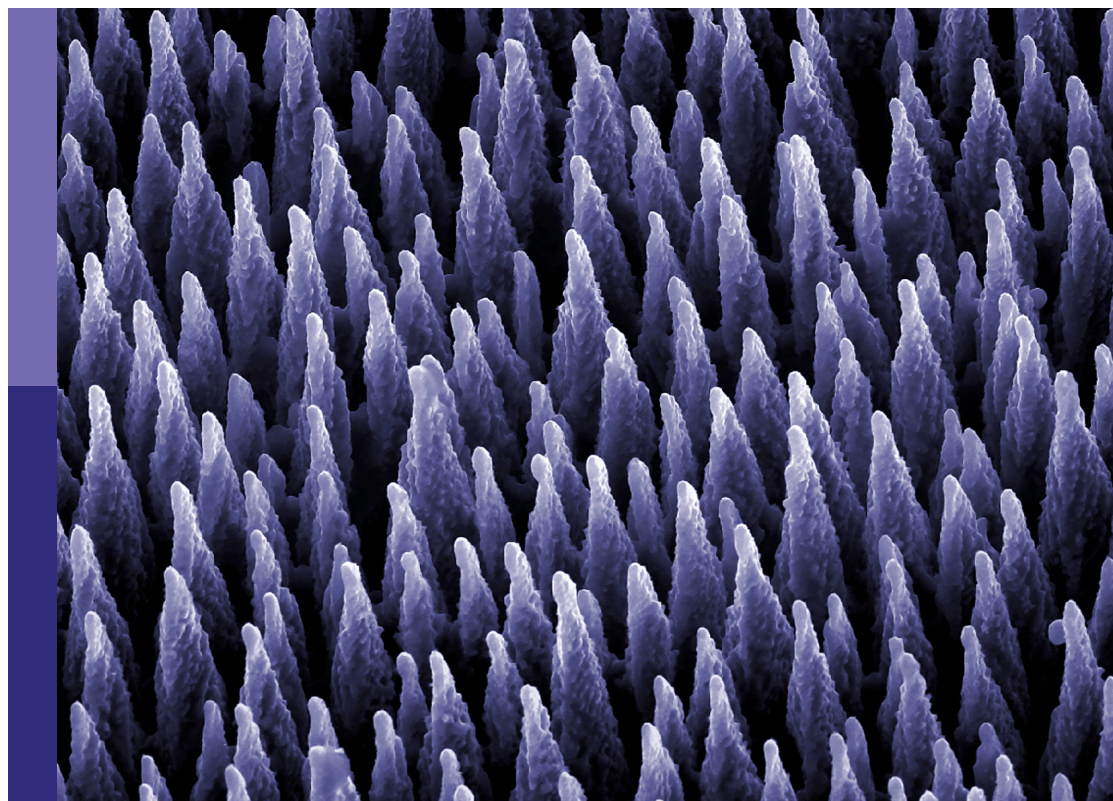
# Celebrating 20 years of CICECO – Aveiro Institute of Materials - Current and future perspectives in the use of material sciences, chemistry, and photonics for a more sustainable future

## **Edited by**

Rute A. S. Ferreira, Verónica de Zea Bermudez,  
Vadim G. Kessler and Sidney J. L. Ribeiro

## **Published in**

Frontiers in Materials  
Frontiers in Photonics  
Frontiers in Chemistry  
Frontiers in Bioengineering and Biotechnology



## FRONTIERS EBOOK COPYRIGHT STATEMENT

The copyright in the text of individual articles in this ebook is the property of their respective authors or their respective institutions or funders. The copyright in graphics and images within each article may be subject to copyright of other parties. In both cases this is subject to a license granted to Frontiers.

The compilation of articles constituting this ebook is the property of Frontiers.

Each article within this ebook, and the ebook itself, are published under the most recent version of the Creative Commons CC-BY licence. The version current at the date of publication of this ebook is CC-BY 4.0. If the CC-BY licence is updated, the licence granted by Frontiers is automatically updated to the new version.

When exercising any right under the CC-BY licence, Frontiers must be attributed as the original publisher of the article or ebook, as applicable.

Authors have the responsibility of ensuring that any graphics or other materials which are the property of others may be included in the CC-BY licence, but this should be checked before relying on the CC-BY licence to reproduce those materials. Any copyright notices relating to those materials must be complied with.

Copyright and source acknowledgement notices may not be removed and must be displayed in any copy, derivative work or partial copy which includes the elements in question.

All copyright, and all rights therein, are protected by national and international copyright laws. The above represents a summary only. For further information please read Frontiers' Conditions for Website Use and Copyright Statement, and the applicable CC-BY licence.

ISSN 1664-8714  
ISBN 978-2-8325-3927-9  
DOI 10.3389/978-2-8325-3927-9

## About Frontiers

Frontiers is more than just an open access publisher of scholarly articles: it is a pioneering approach to the world of academia, radically improving the way scholarly research is managed. The grand vision of Frontiers is a world where all people have an equal opportunity to seek, share and generate knowledge. Frontiers provides immediate and permanent online open access to all its publications, but this alone is not enough to realize our grand goals.

## Frontiers journal series

The Frontiers journal series is a multi-tier and interdisciplinary set of open-access, online journals, promising a paradigm shift from the current review, selection and dissemination processes in academic publishing. All Frontiers journals are driven by researchers for researchers; therefore, they constitute a service to the scholarly community. At the same time, the *Frontiers journal series* operates on a revolutionary invention, the tiered publishing system, initially addressing specific communities of scholars, and gradually climbing up to broader public understanding, thus serving the interests of the lay society, too.

## Dedication to quality

Each Frontiers article is a landmark of the highest quality, thanks to genuinely collaborative interactions between authors and review editors, who include some of the world's best academicians. Research must be certified by peers before entering a stream of knowledge that may eventually reach the public - and shape society; therefore, Frontiers only applies the most rigorous and unbiased reviews. Frontiers revolutionizes research publishing by freely delivering the most outstanding research, evaluated with no bias from both the academic and social point of view. By applying the most advanced information technologies, Frontiers is catapulting scholarly publishing into a new generation.

## What are Frontiers Research Topics?

Frontiers Research Topics are very popular trademarks of the *Frontiers journals series*: they are collections of at least ten articles, all centered on a particular subject. With their unique mix of varied contributions from Original Research to Review Articles, Frontiers Research Topics unify the most influential researchers, the latest key findings and historical advances in a hot research area.

Find out more on how to host your own Frontiers Research Topic or contribute to one as an author by contacting the Frontiers editorial office: [frontiersin.org/about/contact](https://frontiersin.org/about/contact)



# Celebrating 20 years of CICECO – Aveiro Institute of Materials - Current and future perspectives in the use of material sciences, chemistry, and photonics for a more sustainable future

## Topic editors

Rute A. S. Ferreira — University of Aveiro, Portugal

Verónica de Zea Bermudez — University of Trás-os-Montes and Alto Douro, Portugal

Vadim G. Kessler — Swedish University of Agricultural Sciences, Sweden

Sidney J. L. Ribeiro — São Paulo State University, Brazil

## Citation

Ferreira, R. A. S., de Zea Bermudez, V., Kessler, V. G., Ribeiro, S. J. L., eds. (2023). *Celebrating 20 years of CICECO – Aveiro Institute of Materials - Current and future perspectives in the use of material sciences, chemistry, and photonics for a more sustainable future*. Lausanne: Frontiers Media SA. doi: 10.3389/978-2-8325-3927-9

## Table of contents

- 05 **Ferroelectricity in glycine: A mini-review**  
Pavel S. Zelenovskii, Daria S. Vasileva, Semen G. Vasilev, Svitlana Kopyl and Andrei Kholkin
- 13 **Liprobe, a vital dye for lipid aggregates detection in imaging and high-content screens**  
Sandra I. Vieira, Raquel Nunes da Silva, Mariana Alves, Roberto A. Dias, Ana M. Meireles Sousa, Fatima Camões, André Maia, Mónica Almeida, João Rocha, Artur M. Silva and Samuel Guieu
- 24 **Colloidal nanomaterials for water quality improvement and monitoring**  
Ana C. Estrada, Ana L. Daniel-da-Silva, Cátia Leal, Cátia Monteiro, Cláudia B. Lopes, Helena I. S. Nogueira, Isabel Lopes, Maria J. Martins, Natércia C. T. Martins, Nuno P. F. Gonçalves, Sara Fateixa and Tito Trindade
- 45 **Prospects and challenges of the electrochemical reduction of iron oxides in alkaline media for steel production**  
Daniela V. Lopes, Margarida J. Quina, Jorge R. Frade and Andrei V. Kovalevsky
- 53 **Role of salts on the electrical performance of ceria-based electrolytes: An overview**  
João PF Grilo, Atul Jamale, Maksim Starykevich, Filipe ML Figueiredo and Fernando MB Marques
- 70 **Designing  $\text{Ln}^{3+}$ -doped  $\text{BiF}_3$  particles for luminescent primary thermometry and molecular logic**  
Sofia Zanella, Enrico Trave, Elisa Moretti, Aldo Talon, Michele Back, Luís D. Carlos, Rute A. S. Ferreira and Carlos D. S. Brites
- 81 **Micro/mesoporous LTL derived materials for catalytic transfer hydrogenation and acid reactions of bio-based levulinic acid and furanics**  
Margarida M. Antunes, Andreia F. Silva, Auguste Fernandes, Filipa Ribeiro, Patrícia Neves, Martyn Pillinger and Anabela A. Valente
- 102 **Enhanced thermal and photo-stability of a *para*-substituted dicumyl ketone intercalated in a layered double hydroxide**  
Ana L. Costa, Rodrigo P. Monteiro, Paulo D. Nunes Barradas, Simone C. R. Ferreira, Carla Cunha, Ana C. Gomes, Isabel S. Gonçalves, J. Sérgio Seixas de Melo and Martyn Pillinger
- 117 **Tuning the ionic character of sodium dodecyl sulphate via counter-ion binding: An experimental and computational study**  
Germán Pérez-Sánchez, Nicolas Schaeffer, Tamar L. Greaves, Jorge F. B. Pereira and João A. P. Coutinho
- 130 **Review of recycling alternatives for paper pulp wastes**  
Inês Silveirinha Vilarinho, Tânia Gameiro, Marinélia N. Capela, João Carvalheiras, Ana P. F. Caetano, Catarina Novo, Rui M. Novais, Maria Paula Seabra and João António Labrincha

- 150 **Upconverting nanoparticles as primary thermometers and power sensors**  
Joana Costa Martins, Artiom Skripka, Carlos D. S. Brites, Antonio Benayas, Rute A. S. Ferreira, Fiorenzo Vetrone and Luís D. Carlos
- 160 **Layered double hydroxides for corrosion-related applications—Main developments from 20 years of research at CICECO**  
João Tedim, Tiago L. P. Galvão, Kiryl A. Yasakau, Alexandre Bastos, José R. B. Gomes and Mario G. S. Ferreira
- 190 **New liquid supports in the development of integrated platforms for the reuse of oxidative enzymes and polydopamine production**  
Flávia F. Magalhães, Ana F. Pereira, Mara G. Freire and Ana P. M. Tavares
- 202 **Different methods of synthesizing poly(glycerol sebacate) (PGS): A review**  
Bruno Godinho, Nuno Gama and Artur Ferreira
- 229 **Extraction and purification of phycobiliproteins from algae and their applications**  
Gabriela Kovaleski, Mariam Kholany, Lília M. S. Dias, Sandra F. H. Correia, Rute A. S. Ferreira, João A. P. Coutinho and Sónia P. M. Ventura
- 248 **From PEF to PBF: What difference does the longer alkyl chain make a computational spectroscopy study of poly(butylene 2,5-furandicarboxylate)**  
Mariela M. Nolasco, Leonor C. Rodrigues, Catarina F. Araújo, Mariana M. Coimbra, Paulo Ribeiro-Claro, Pedro D. Vaz, Svemir Rudić, Armando J. D. Silvestre, Chaima Bouyahya, Mustapha Majdoub and Andreia F. Sousa
- 260 **Cellulose and protein nanofibrils: Singular biobased nanostructures for the design of sustainable advanced materials**  
Ana C. Q. Silva, Armando J. D. Silvestre, Carla Vilela and Carmen S. R. Freire
- 281 **Simulating the giant magnetocaloric effect—from mean-field theory to microscopic models**  
J. S. Amaral and V. S. Amaral
- 288 **Ionic-liquid-based approaches to improve biopharmaceuticals downstream processing and formulation**  
Catarina Almeida, Augusto Q. Pedro, Ana P. M. Tavares, Márcia C. Neves and Mara G. Freire
- 308 **In-house vs. commercial boron-doped diamond electrodes for electrochemical degradation of water pollutants: A critical review**  
Priscilla Brosler, Ana Violeta Girão, Rui F. Silva, João Tedim and Filipe J. Oliveira





## OPEN ACCESS

## EDITED BY

Vadim G. Kessler,  
Swedish University of Agricultural  
Sciences, Sweden

## REVIEWED BY

Dhiren Kumar Pradhan,  
Geophysical Laboratory (CIS),  
United States

## \*CORRESPONDENCE

Pavel S. Zelenovskii,  
zelenovskii@ua.pt  
Andrei Kholkin,  
kholkin@ua.pt

## SPECIALTY SECTION

This article was submitted to  
Biomaterials,  
a section of the journal  
Frontiers in Materials

RECEIVED 12 April 2022

ACCEPTED 28 June 2022

PUBLISHED 22 July 2022

## CITATION

Zelenovskii PS, Vasileva DS, Vasilev SG,  
Kopyl S and Kholkin A (2022),  
Ferroelectricity in glycine: A mini-  
review.  
*Front. Mater.* 9:918890.  
doi: 10.3389/fmats.2022.918890

## COPYRIGHT

© 2022 Zelenovskii, Vasileva, Vasilev,  
Kopyl and Kholkin. This is an open-  
access article distributed under the  
terms of the [Creative Commons  
Attribution License \(CC BY\)](#). The use,  
distribution or reproduction in other  
forums is permitted, provided the  
original author(s) and the copyright  
owner(s) are credited and that the  
original publication in this journal is  
cited, in accordance with accepted  
academic practice. No use, distribution  
or reproduction is permitted which does  
not comply with these terms.

# Ferroelectricity in glycine: A mini-review

Pavel S. Zelenovskii<sup>1\*</sup>, Daria S. Vasileva<sup>2</sup>, Semen G. Vasilev<sup>3</sup>,  
Svitlana Kopyl<sup>4</sup> and Andrei Kholkin<sup>4\*</sup>

<sup>1</sup>Department of Chemistry & CICECO–Aveiro Institute of Materials, University of Aveiro, Aveiro, Portugal, <sup>2</sup>Department of Physics, Bernal Institute, University of Limerick, Limerick, Ireland,

<sup>3</sup>Department of Chemical Sciences, Bernal Institute, University of Limerick, Limerick, Ireland,

<sup>4</sup>Department of Physics & CICECO–Aveiro Institute of Materials, University of Aveiro, Aveiro, Portugal

Glycine is the simplest natural amino acid, a basic building block for various biomaterials. Supramolecular packing of glycine molecules into three main crystalline polymorphs allows controlling their functional properties, such as piezoelectricity and ferroelectricity. Though piezoelectricity in glycine is well studied and reviewed, its ferroelectric properties were not summarized and analyzed until now. In this mini-review, we briefly discuss glycine polymorphs, their functional properties, and phase transitions, review recent findings on domain structure and polarization switching in  $\beta$ - and  $\gamma$ -glycine, and consider their possible applications in biocompatible photonic and piezoelectric devices.

## KEYWORDS

organic piezoelectrics, ferroelectrics, domain structure, amino acids, glycine

## Introduction

Amino acid glycine is the simplest building block of various biomaterials and is often considered a symbol of life on our planet. Therefore, it has attracted considerable attention in different research fields, mainly in materials science, pharmacology, and medicine. Glycine plays a key role in many physiological processes, e.g., in cancer cell metabolism, (Jain et al., 2012) and is used to treat various diseases, including ischemic stroke, anxiety, insomnia, schizophrenia, benign prostatic hyperplasia, etc (Gusev et al., 2000; Babić and Babić, 2009). It also serves as a bulking agent in pharmaceutical protein formulations (Horn et al., 2018). On a completely different scale, glycine has been found in the interstellar medium (Kuan et al., 2003; Ioppolo et al., 2021) and in the comas of comets and meteorites, (Elsila et al., 2009; Altwegg et al., 2016) thus providing evidence of the panspermia hypothesis (Wesson, 2010). As for the functional physical properties of crystalline glycine, they largely depend on the supramolecular packing of its molecules into three main polymorphs ( $\alpha$ ,  $\beta$ , and  $\gamma$ ), resulting in different crystallographic structures (Heredia et al., 2012; Guerin et al., 2017; Gleeson et al., 2020; Boldyreva, 2021). It has been a long time established that the  $\alpha$ -phase is centrosymmetric (space group  $P2_1/n$ ), in which only surface piezoelectricity and pyroelectricity may exist *via* doping or water incorporation (Piperno et al., 2013; Meirzadeh et al., 2018; Dishon et al., 2020). On the contrary,  $\beta$  and  $\gamma$  phases of glycine are non-centrosymmetric (space groups  $P2_1$  and  $P3_1$ , respectively) (Iitaka, 1960; Iitaka, 1961) and exhibit technologically significant piezoelectric responses, as has been shown by Lemanov in 2000 (Lemanov, 2000).

It was like that until 2012, when another important functional property, ferroelectricity, was reported by Heredia et al. (2012). Using a novel Piezoresponse Force Microscopy (PFM) tool and molecular modeling, it has been shown, that switchable polarization domains exist in  $\gamma$ -glycine microcrystals grown from the solution. Polarization switching was performed by applying DC voltage to the PFM tip at the nanoscale and switchable domains were shown to persist for a long time. That work attracted a wide interest of the research community in different fields and has launched a new round of experimental and theoretical studies of glycine (Bystrov et al., 2014; Bystrov et al., 2015; Bystrov et al., 2016; Guerin et al., 2017; Seyedhosseini et al., 2017; Bai et al., 2018; Tasnim et al., 2018; Hu et al., 2019; Slabov et al., 2019; Bishara et al., 2020; Dishon et al., 2020; Gleeson et al., 2020; Hosseini et al., 2020; Kholkin et al., 2021). Several reviews reported piezoelectric properties of glycine (Tayi et al., 2015; Tofail and Bauer, 2016; Guerin et al., 2017; Maiti et al., 2019; Kim et al., 2020; Li et al., 2020; Boldyreva, 2021; Xu et al., 2021). However, until now, its ferroelectric properties have not been summarized and analyzed.

In this mini-review, we summarize 10 years of rigorous research on ferroelectricity and polarization switching in  $\beta$ -glycine, discuss undesirable phase transitions between polymorphs influencing the ferroelectricity, ways of stabilization of ferroelectric  $\beta$ -phase, and its possible applications in biocompatible photonic and piezoelectric devices.

## Polymorphic phases and ferroelectricity

Ferroelectricity is observed for a specific polymorphic state of the glycine— $\beta$ -phase. Actually, glycine is a model material for studying polymorphism because crystalline glycine can be easily grown from the aqueous solution that, in principle, results in a mixture of different polymorphs— $\alpha$ ,  $\beta$ , and  $\gamma$ . That is due to the Ostwald rule of stages, meaning that the less stable  $\beta$ -phase is formed first, (Seyedhosseini et al., 2014) and then more stable  $\gamma$ - and  $\alpha$ -phases appear. Several papers discussed various possibilities to grow predominantly one phase or another (Boldyreva et al., 2003a; Lee et al., 2008; Poornachary et al., 2008). For instance, selective growth of single-phase piezoelectric  $\gamma$ -glycine can be achieved by the modification of the solution's pH (Boldyreva et al., 2003a; Lee et al., 2008) or addition of trace amounts of chiral impurities into the aqueous solution, (Poornachary et al., 2008) whereas less stable  $\beta$ -phase can be preferentially grown from the solution in the presence of acetic acid (Drebushchak et al., 2002) or glucose (Gerasimov et al., 2022).

In general, polymorphic crystalline phases can be distinguished by various analytical techniques such as differential scanning calorimetry (DSC), thermogravimetric analysis (TGA), infrared, Raman, and solid-state nuclear

magnetic resonance (NMR) spectroscopies, and powder X-ray diffraction (Brog et al., 2013). These integral methods allow detecting the presence of tiny amounts of phases in a mixture. However, for local polarization switching experiments by PFM, the polymorphic phase of an individual microcrystal should be determined. In this case, the choice of the methods is quite limited. Roughly, a phase of an individual crystal can be identified by observation of crystals' habits by optical microscopy. Evaporation of the glycine aqueous solution droplet on a substrate leads to the formation of rhombohedral plate-like  $\alpha$ -glycine crystals (Figure 1A),  $\beta$ -glycine forms elongated rectangular (needle-like) crystals (Figure 1B), and  $\gamma$ -glycine forms trigonal prisms (Figure 1C) (Iitaka, 1961; Bai et al., 2018). However, this is true for as-grown phases only. Due to polymorphic phase transitions, the crystal's phase may change under various external factors (temperature, gases, mechanical treatment, etc.) (Boldyreva et al., 2003b) without habit modification (Isakov et al., 2014). Therefore, special methods for the phase determination of individual microcrystals should be applied prior to studies of ferroelectricity.

This problem can be partially resolved by PFM, which allows distinguishing the centrosymmetric  $\alpha$ -phase (which does not possess any piezoelectric activity) from non-centrosymmetric  $\beta$ - and  $\gamma$ - phases (*a priori* piezoelectric). But the distinction between  $\beta$ - and  $\gamma$ - phases is more difficult. PFM measurements in combination with crystal habit observation were used in (Heredia et al., 2012); however, they have led to an erroneous attribution of ferroelectricity to the  $\gamma$ -phase. Further studies (Isakov et al., 2014; Seyedhosseini et al., 2014; Seyedhosseini et al., 2015; Bystrov et al., 2016; Seyedhosseini et al., 2017; Slabov et al., 2019; Vasileva et al., 2019) showed that experimental results reported in (Heredia et al., 2012) could be actually done on  $\beta$ -phase.

The discrimination between  $\beta$ - and  $\gamma$ -phases by PFM can be done based on the determination of the components of the piezoelectric matrix, which are different for  $\beta$ - and  $\gamma$ -phases (Guerin et al., 2017). However, this method requires precise measurements at different crystal faces, which are not always accessible. Therefore, a more convenient method for the determination of the polymorphic phase of an individual microcrystal is confocal Raman microscopy (CRM). Application of this fast and non-destructible method just before the PFM measurements allows excluding possible artifacts with phase determination. CRM is based on the analysis of spectral fingerprints of each phase (Lee et al., 2008; Surovtsev et al., 2011; Seyedhosseini et al., 2014) and was successfully used for distinguishing phases in micro- and nanocrystals of glycine (Seyedhosseini et al., 2014; Zelenovskii et al., 2016; Seyedhosseini et al., 2017; Slabov et al., 2019) and *in situ* studying an unusual solid-state phase transition (Isakov et al., 2014).

What is especially important is that CRM demonstrated preferable nucleation and stabilization of individual

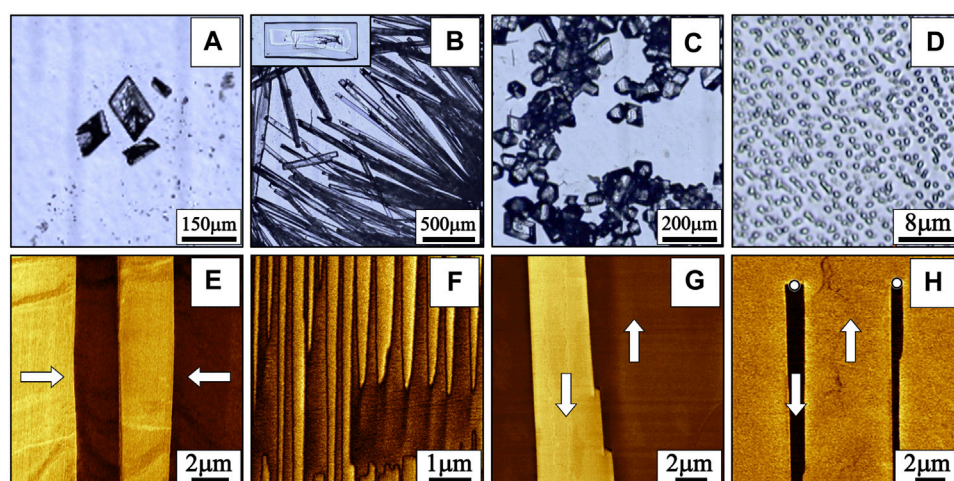


**FIGURE 1**

Morphology of the glycine microcrystals of different polymorphs: (A)  $\alpha$ -phase, (B)  $\beta$ -phase, (C)  $\gamma$ -phase, and (D) microislands of  $\beta$ -glycine. The inset in (B) shows another common morphology of  $\beta$ -glycine crystals well suitable for studies of ferroelectricity. Types of as-grown domains in  $\beta$ -glycine (Vasileva et al., 2019): (E) stripe domains with charged domain walls, (F) quasi-periodic ensembles of needle-like domains, and (G) irregular shaped domains with segmental step-like domain walls. White arrows show the direction of spontaneous polarization. (H) Artificial domains created by the application of an external electric field to the PFM tip.

microcrystals of  $\beta$ -glycine and its quasi-regular arrays of nanocrystals formed *via* evaporative dewetting on a Pt substrate (Figure 1D) (Seyedhosseini et al., 2014; Seyedhosseini et al., 2017). This fact opens the way for studying ferroelectricity in  $\beta$ -glycine and its applications. Preferable  $\beta$ -phase crystallization can be also achieved in nanopores (Hamilton et al., 2008), microfluidic channels (Bhamidi et al., 2015), or under the action of standing surface acoustic waves (Bai et al., 2018). These are promising but more complicated and less studied ways for the ferroelectricity stabilization in glycine.

In 2005, the low-temperature calorimetric measurements on  $\beta$ -glycine revealed an anomaly of heat capacity at 252 K (Drebushchak et al., 2005), which was then confirmed by incoherent inelastic neutron scattering (Bordallo et al., 2008; Aree et al., 2013). Other polymorphs did not show such anomaly. The calculations of enthalpy, entropy, and Gibbs energy for all three polymorphs showed that their thermodynamic properties (and thus macroscopic physical properties) are affected by the arrangement of  $\text{NH}_3^+$  tails of zwitterions rather than by the crystal structure (Drebushchak et al., 2005). Indeed, though, in the gas phase, the zwitterionic form of glycine molecule is less stable than the neutral one (Palla et al., 1980), it can be stabilized in a solution through the hydrogen bonds formation with water molecules (Basch and Stevens, 1990). In a solid phase, the zwitterionic structure of glycine molecules is also preserved and provides an additional interaction between the molecules (Drebushchak et al., 2005). Therefore, the anomaly in the heat capacity observed in  $\beta$ -

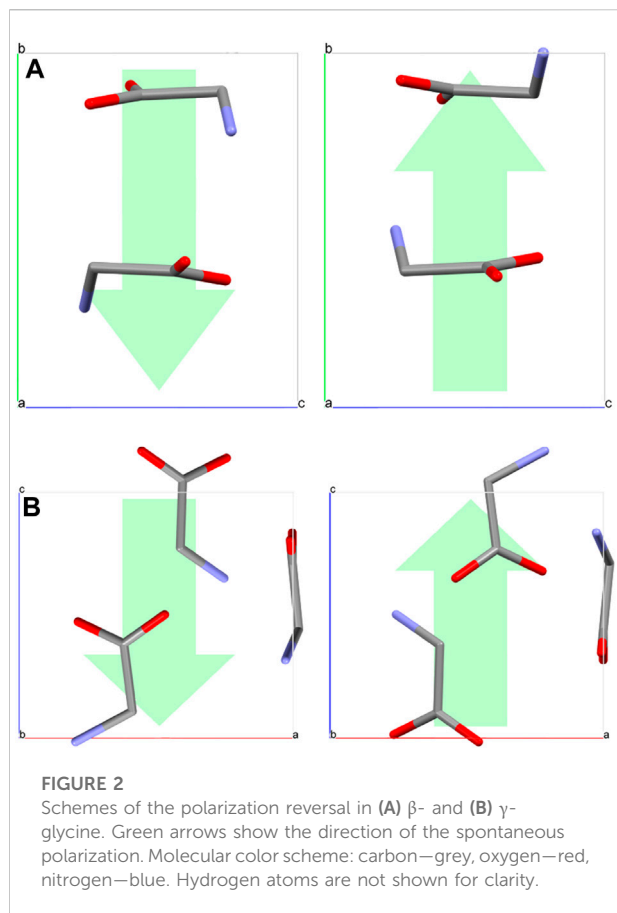
glycine was attributed to a second-order ferroelectric-paraelectric phase transition (Drebushchak et al., 2005).

The detailed phenomenological analysis of this anomaly in terms of the compressible Ising model (Kiraci, 2021) confirmed that conclusion and also demonstrated that the critical exponents in “ferroelectric” ( $T < 252$  K) and “paraelectric” ( $T > 252$  K) phases are consistent with those predicted from the 3D Ising model and the 2D Potts model, respectively. However, as is shown in detail in the following section, the main features of ferroelectricity, such as domain structures and the ability to switch the polarization by an electric field, well persist in  $\beta$ -glycine at room temperature. Therefore, the observed anomaly at 252 K may be related not to the ferroelectric-paraelectric phase transition but, highly likely, to the transition between two ferroelectric phases. This question requires additional studies.

## Domain structures and polarization switching

While piezoelectricity in  $\gamma$ - and  $\beta$ -phases originates from their non-centrosymmetric space groups, its attribution to the class of ferroelectrics can be done only experimentally (Lines and Glass, 1977). PFM can serve as a perfect tool to distinguish not only piezoelectric but also ferroelectric phases due to the domain structure visualization and the polarization switching in a point (Shvartsman et al., 2002; Kalinin et al., 2010; Soergel, 2011). A multitude of recent reports (Isakov et al., 2014;





Seyedhosseini et al., 2014; Seyedhosseini et al., 2015; Bystrov et al., 2016; Hu et al., 2019; Vasileva et al., 2019) have proven that  $\beta$ -glycine is indeed ferroelectric with switchable polarization and diverse domain structures. The as-grown domain structure at nonpolar surfaces of  $\beta$ -glycine crystals, which are usually available for PFM study, consists of three types of domains (Vasileva et al., 2019): 1) stripe-like domains with flat charged domain walls (Figure 1E) appeared due to the variations of defects during the crystal growth; 2) quasi-periodic ensembles of needle-like domains (Figure 1F) appeared under the action of pyroelectric field occurred due to the cooling down of the evaporating droplet; and 3) irregular shaped domains with segmental step-like domain walls (Figure 1G).

Domains can also be created in  $\beta$ -glycine crystals by the application of an external electric field by the PFM tip (Figure 1H). Computer modeling based on density functional theory and molecular-dynamic simulations showed for  $\beta$ -glycine an average coercive field of about 1 V/nm ( $10^3$  kV/mm) (Bystrov et al., 2015; Bystrov et al., 2016), which corresponds to 60 V applied to the PFM tip (Seyedhosseini et al., 2015). In principle, polarization switching in  $\gamma$ -glycine may also be possible, but it requires 4–8 times bigger electric fields (Heredia et al., 2012; Bystrov

et al., 2015). Moreover, the maximum value of the electric field near the apex of the PFM tip with the applied voltage of 100 V is about 3 V/nm only (Seyedhosseini et al., 2015). Higher voltages lead to the electric breakdown of the crystal. Therefore, a single molecule switching in  $\gamma$ -glycine remains a theoretical possibility. Such a big difference in threshold fields for  $\beta$ - and  $\gamma$ -glycine is due to the mechanism of the polarization reversal. As computer modeling demonstrated, (Hu et al., 2019) the spontaneous polarization of  $\beta$ -glycine oriented along the polar crystallographic axis  $b$  stems from an ordered arrangement of the  $-\text{NH}_3^+$  groups, whereas the polarization switching occurs *via* the change of a dihedral angle between the  $-\text{NH}_3^+$  groups and the plane of the carboxyl ( $-\text{COO}^-$ ) groups (Figure 2A). At the same time, polarization reversal of  $\gamma$ -glycine requires the rotation of glycine molecules by  $180^\circ$  around an axis perpendicular to the polar  $c$ -axis (Hu et al., 2019) (Figure 2B), which makes the polarization reversal of  $\gamma$ -glycine much more difficult than that of  $\beta$ -phase.

The artificial needle-like domains created by the PFM tip propagate far outside the field area due to the kinks interaction (Vasileva et al., 2019), and their length depends on the applied voltage and pulse duration (Seyedhosseini et al., 2015). PFM tip movement during the voltage application allows the creation of tailored domain structures with different types of domain walls: neutral and charged head-to-head and tail-to-tail (Vasileva et al., 2019). Usually, tail-to-tail domain walls are flat and oriented normally to the polar axis, whereas head-to-head ones are rough and inclined (Vasileva et al., 2019). That allows suggesting that tail-to-tail domain walls possess higher conductivity, accelerating the screening of the depolarization fields created by the bound charges (Schröder et al., 2012; Schröder et al., 2014; Lu et al., 2015). This assumption is supported by the quantum chemical calculations that showed tail-to-tail walls are around seven times more stable than head-to-head ones (Bystrov et al., 2016).

## Applications and perspectives

As recently demonstrated (Seyedhosseini et al., 2015; Vasileva et al., 2019), the polarization switching and the evolution of the domain structures in  $\beta$ -glycine crystals are qualitatively similar to those found in uniaxial inorganic ferroelectrics. This observation opens up the possibility of applying the methods of domain engineering developed earlier for the creation of tailored micro- and nanodomain structures in inorganic ferroelectrics (Shur and Ye, 2008) for organic ones, which are highly demanded elements of biocompatible photonic devices. It is known that organic nonlinear optical materials have an advantage over their inorganic counterparts due to their big molecular

polarizability and the ability to tune their properties by chemical modifications (Humar et al., 2017). In the case of crystalline organic ferroelectrics, such as  $\beta$ -glycine, the nonlinear optical properties can be additionally improved by the methods of domain engineering (Shur and Ye, 2008) by the creation of a periodical domain structure. Periodically poled  $\beta$ -glycine crystal can significantly enhance the effectiveness of the second harmonic generation and optical parametric oscillation, (Scrymgeour et al., 2014) thus allowing the usage of glycine in biocompatible photonic devices for quantitative tissue imaging and diseases diagnosis (Campagnola, 2011).

Stabilization of  $\beta$ -glycine crystals by Pt substrate (Seyedhosseini et al., 2014), strong piezoelectric activity exceeding that of classical perovskite piezoelectric ceramics (Heredia et al., 2012; Guerin et al., 2017), and nonlinear susceptibility much higher than that of  $\gamma$ -glycine (Gleeson et al., 2020), make  $\beta$ -glycine a promising functional material for various biomedical applications such as wearable and implantable sensors (Bishara et al., 2020; Hosseini et al., 2020; Li et al., 2020), energy harvesting, (Guerin et al., 2017) and nonlinear optical devices (Seyedhosseini et al., 2014; Gleeson et al., 2020). Recently, the combination of chitosan fibers with  $\beta$ -glycine allowed the creation of a new biodegradable sensor for sub-bandage pressure monitoring with quite high sensitivity in the range from 5 to 60 kPa (Hosseini et al., 2020). However, obtained spherulite-like  $\beta$ -glycine crystal structures demonstrate mainly shear piezoresponse that limits the applicability and sensitivity of the sensor. Another configuration of a sensor with  $\beta$ -glycine crystals confined in the cylindrical nanopores with the polar axis oriented along the pores provided pressure sensitivity as low as 1 Pa (Bishara et al., 2020). The application of inkjet printing suggests additional ways of designing the next-generation biosensors (Buanz and Gaisford, 2017; Slabov et al., 2019).

Though ferroelectricity in  $\gamma$ -glycine still remains a theoretical possibility, it also could be interesting for developing wearable and implantable bioelectronic devices even regardless of its slightly weaker piezoelectric response (Guerin et al., 2017). That is due to its phase stability and the pronounced positive therapeutic effect on cognitive functions and neural activity, as compared with  $\alpha$ -glycine (Markel et al., 2011; Malakhin et al., 2012). As far as we know, the biological activity of the  $\beta$ -glycine was not studied yet. The combination of outstanding functional properties, inherent biocompatibility, stability, and direct therapeutic effect can endow  $\gamma$ -glycine-based sensors with additional multi-aspect functions. Recently, they have been grown as wafer-scale films in combination with PVDF (Yang et al., 2021) and demonstrated much higher sensitivity than PVDF polymer patches (Okosun et al., 2021).

Moreover, we suppose that humidity-controlled phase transitions (Isakov et al., 2014) allow, in principle, the

creation of  $\beta$ - $\gamma$  and  $\beta$ - $\alpha$  “chimera” crystals with the combination of two or even three polymorphic phases in one crystal. Such a combination of phases and thus functional properties may additionally expand possible applications of glycine and other amino acid crystals. At the same time, such devices would be able to disintegrate and resorb after completing their work cycle without any adverse long-term effects (Hosseini et al., 2021).

The idea of the control of functional properties *via* supramolecular packing (Guerin et al., 2017) can probably be also extended to  $\beta'$ ,  $\delta$ ,  $\varepsilon$ , and  $\zeta$  phases of glycine existing at high pressures (Boldyreva et al., 2005; Dawson et al., 2005; Goryainov et al., 2005; Goryainov et al., 2006). Thus,  $\varepsilon$ -glycine at about 4.3 GPa belongs to piezoelectric space group  $Pn$ , (Dawson et al., 2005) whereas  $\delta$ -glycine belongs to the centrosymmetric space group  $P2_1/a$  (Dawson et al., 2005). Recent computer modeling (Guerra et al., 2020) revealed three more potentially piezoelectric phases of glycine:  $m$ ,  $t$ , and  $o$  (space groups  $P2_1$ ,  $P4_3$ , and  $P2_12_12_1$ , respectively) that were not observed experimentally yet. These exotic glycine polymorphs are not stable under ambient conditions. However, the possibility of finding ways for their stabilization in further research (as it happened with metastable  $\beta$ -glycine) cannot be ruled out. The authors foresee that such a simple molecule as glycine will bring many more surprises in the future.

## Conclusion

In this mini-review, we summarized the recent findings on ferroelectric properties and polarization switching of  $\beta$ - and  $\gamma$ -phases of glycine. We demonstrated that due to the transitions between polymorphic phases, the crystal habit is not a reliable method for choosing the appropriate crystals for the research, and additional phase confirmation by confocal or micro-Raman spectroscopy is highly recommended. Recent experimental and computer simulation studies of domain structures and polarization switching undoubtedly confirmed ferroelectricity in  $\beta$ -glycine, whereas a single molecule switching in  $\gamma$ -glycine still remains a theoretical possibility. Regardless of the metastability of the  $\beta$ -phase, its stabilization inside nanopores or microfluidic channels, as well as at the Pt substrates, allows considering its usage in various applications, whereas the outstanding nonlinear optical properties and the ability to create stable periodical domain structures make  $\beta$ -glycine a promising material for biocompatible photonic devices. We suppose that the combination of two or three polymorphic phases in one crystal is potentially achievable due to the humidity-controlled phase transitions, and searching the ways for effective stabilization of high-pressure polymorphic phases can open new ways for applications of crystals of this remarkable amino acid.

## Author contributions

Conceptualization, AK; literature review, PZ, DV, and SV; writing—original draft preparation, PZ; writing—review and editing, SK and AK.

## Funding

Portuguese Foundation for Science and Technology (UIDB/50011/2020, UIDP/50011/2020, LA/P/0006/2020, PTDC/CTM-CTM/4044/2020). This work was developed within the scope of the project CICECO-Aveiro Institute of Materials, UIDB/50011/2020, UIDP/50011/2020 and LA/P/0006/2020, financed by national funds through the FCT/MEC (PIDDAC). Part of this work was funded by national funds (OE), through FCT—Fundação para a Ciência e a Tecnologia, I.P., in the scope of the framework contract foreseen in the numbers 4, 5, and 6 of the article 23, of the Decree-Law 57/2016, of August 29, changed by Law 57/2017, of July 19. PZ and AK were supported by FCT through the project “Photomultiferro”- PTDC/CTM-CTM/4044/2020. SV was supported by Career-FIT received funding from the European Union’s Horizon 2020 research and innovation program under the Marie Skłodowska-Curie grant (agreement no. 713654).

## References

- Altwegg, K., Balsiger, H., Bar-Nun, A., Bertheliet, J. J., Bieler, A., Bochsler, P., et al. (2016). Prebiotic chemicals—Amino acid and phosphorus—In the coma of comet 67P/Churyumov-Gerasimenko. *Sci. Adv.* 2, e1600285. doi:10.1126/sciadv.1600285
- Aree, T., Bürgi, H. B., Minkov, V. S., Boldyreva, E. V., Chernyshov, D., Törnroos, K. W., et al. (2013). Dynamics and thermodynamics of crystalline polymorphs. 2.  $\beta$ -Glycine, analysis of variable-temperature atomic displacement parameters. *J. Phys. Chem. A* 117, 8001–8009. doi:10.1021/jp404408h
- Babić, D., and Babić, R. (2009). Complementary and alternative medicine in the treatment of schizophrenia. *Psychiatr. Danub.* 21, 376–381.
- Bai, C., Wang, C., Zheng, T., and Hu, Q. (2018). Growth of  $\beta$ -glycine crystals promoted by standing surface acoustic waves (SSAWs). *CrystEngComm* 20, 1245–1251. doi:10.1039/C7CE02038D
- Basch, H., and Stevens, W. J. (1990). The structure of glycine-water H-bonded complexes. *Chem. Phys. Lett.* 169, 275–280. doi:10.1016/0009-2614(90)85201-M
- Bhamidi, V., Lee, S. H., He, G., Chow, P. S., Tan, R. B. H., Zukoski, C. F., et al. (2015). Antisolvent crystallization and polymorph screening of glycine in microfluidic channels using hydrodynamic focusing. *Cryst. Growth Des.* 15, 3299–3306. doi:10.1021/acs.cgd.5b00420
- Bishara, H., Nagel, A., Levanon, M., and Berger, S. (2020). Amino acids nanocrystals for piezoelectric detection of ultra-low mechanical pressure. *Mater. Sci. Eng. C* 108, 110468. doi:10.1016/j.msec.2019.110468
- Boldyreva, E. (2021). Glycine: The gift that keeps on giving. *Isr. J. Chem.* 61, 828–850. doi:10.1002/ijch.202100103
- Boldyreva, E. V., Drebuschak, V. A., Drebuschak, T. N., Paukov, I. E., Kovalevskaya, Y. A., Shutova, E. S., et al. (2003). Polymorphism of glycine: Thermodynamic aspects. Part II. Polymorphic transitions. *J. Therm. Anal. Calorim.* 73, 419–428. doi:10.1023/A:1025457524874
- Boldyreva, E. V., Drebuschak, V. A., Drebuschak, T. N., Paukov, I. E., Kovalevskaya, Y. A., Shutova, E. S., et al. (2003). Polymorphism of glycine: Thermodynamic aspects. Part I. Relative stability of the polymorphs. *J. Therm. Anal. Calorim.* 73, 409–418. doi:10.1023/A:1025405508035
- Boldyreva, E. V., Ivashevskaya, S. N., Sowa, H., Ahsbahs, H., and Weber, H. P. (2005). Effect of hydrostatic pressure on the  $\gamma$ -polymorph of glycine. 1. A

## Conflict of interest

The authors declare that the research was conducted in the absence of any commercial or financial relationships that could be construed as a potential conflict of interest.

## Publisher’s note

All claims expressed in this article are solely those of the authors and do not necessarily represent those of their affiliated organizations, or those of the publisher, the editors and the reviewers. Any product that may be evaluated in this article, or claim that may be made by its manufacturer, is not guaranteed or endorsed by the publisher.

## Acknowledgments

The authors are grateful for Alla S. Slautina and Vladimir Ya. Shur for their help in the manuscript preparation and fruitful discussions.

polymorphic transition into a new  $\delta$ -form. *Z. Krist.* 220, 50–57. doi:10.1524/zkri.220.1.50.58886

Bordallo, H. N., Boldyreva, E. V., Buchsteiner, A., Koza, M. M., and Landsgesell, S. (2008). Structure-property relationships in the crystals of the smallest amino acid: An incoherent inelastic neutron scattering study of the glycine polymorphs. *J. Phys. Chem. B* 112, 8748–8759. doi:10.1021/jp8014723

Brog, J. P., Chanez, C. L., Crochet, A., and Fromm, K. M. (2013). Polymorphism, what it is and how to identify it: A systematic review. *RSC Adv.* 3, 16905. doi:10.1039/C3RA41559G

Buanz, A. B. M., and Gaisford, S. (2017). Formation of highly metastable  $\beta$  glycine by confinement in inkjet printed droplets. *Cryst. Growth Des.* 17, 1245–1250. doi:10.1021/acs.cgd.6b01633

Bystrov, V. S., Seyedhosseini, E., Bdiqin, I., Kopyl, S., Neumayer, S. M., Coutinho, J., et al. (2015). Bioferroelectricity in nanostructured glycine and thymine: Molecular modeling and ferroelectric properties at the nanoscale. *Ferroelectrics* 475, 107–126. doi:10.1080/00150193.2015.995574

Bystrov, V. S., Seyedhosseini, E., Bdiqin, I. K., Kopyl, S., Kholkin, A. L., Vasilev, S. G., et al. (2016). Glycine nanostructures and domains in beta-glycine: Computational modeling and PFM observations. *Ferroelectrics* 496, 28–45. doi:10.1080/00150193.2016.1157435

Bystrov, V. S., Seyedhosseini, E., Kopyl, S., Bdiqin, I. K., and Kholkin, A. L. (2014). Piezoelectricity and ferroelectricity in biomaterials: Molecular modeling and piezoresponse force microscopy measurements. *J. Appl. Phys.* 116, 066803. doi:10.1063/1.4891443

Campagnola, P. (2011). Second harmonic generation imaging microscopy: Applications to diseases diagnostics. *Anal. Chem.* 83, 3224–3231. doi:10.1021/ac1032325

Dawson, A., Allan, D. R., Belmonte, S. A., Clark, S. J., David, W. I. F., McGregor, P. A., et al. (2005). Effect of high pressure on the crystal structures of polymorphs of glycine. *Cryst. Growth Des.* 5, 1415–1427. doi:10.1021/cg049716m

Dishon, S., Ushakov, A., Nuraeva, A., Ehre, D., Lahav, M., Shur, V., et al. (2020). Surface piezoelectricity and pyroelectricity in centrosymmetric materials: A case of  $\alpha$ -glycine. *Materials* 13, 4663. doi:10.3390/ma13204663

Drebuschak, T. N., Boldyreva, E. V., and Shutova, E. S. (2002).  $\beta$ -Glycine. *Acta Crystallogr. Sect. E Struct. Rep. Online* E58, o634–o636. doi:10.1107/S160053680200836X



- Drebushchak, V. A., Boldyreva, E. V., Kovalevskaya, Y. A., Paukov, I. E., and Drebushchak, T. N. (2005). Low-temperature heat capacity of  $\beta$ -glycine and a phase transition at 252 K. *J. Therm. Anal. Calorim.* 79, 65–70. doi:10.1007/s10973-004-0563-8
- Elsila, J. E., Glavin, D. P., and Dworkin, J. P. (2009). Cometary glycine detected in samples returned by Stardust. *Meteorit. Planet. Sci.* 44, 1323–1330. doi:10.1111/j.1945-5100.2009.tb01224.x
- Gerasimov, A. V., Zubaidullina, L. S., Safiullina, A. S., Nagrimanov, R. N., Ziganshin, M. A., Boldyrev, A. E., et al. (2022). Stabilization of metastable polymorphic form of glycine by glucose. *AIP Conf. Proc.* 2390, 030020. doi:10.1063/5.0069199
- Gleeson, M., O'Dwyer, K., Guerin, S., Rice, D., Thompson, D., Tofail, S. A. M., et al. (2020). Quantitative polarization-resolved second-harmonic-generation microscopy of glycine microneedles. *Adv. Mat.* 32, 2002873. doi:10.1002/adma.202002873
- Goryainov, S. V., Boldyreva, E. V., and Kolesnik, E. N. (2006). Raman observation of a new ( $\zeta$ ) polymorph of glycine? *Chem. Phys. Lett.* 419, 496–500. doi:10.1016/j.cplett.2005.11.123
- Goryainov, S. V., Kolesnik, E. N., and Boldyreva, E. V. (2005). A reversible pressure-induced phase transition in  $\beta$ -glycine at 0.76 GPa. *Phys. B Condens. Matter* 357, 340–347. doi:10.1016/j.physb.2004.11.089
- Guerin, S., Stapleton, A., Chovan, D., Mouras, R., Gleeson, M., McKeown, C., et al. (2017). Control of piezoelectricity in amino acids by supramolecular packing. *Nat. Mat.* 17, 180–186. doi:10.1038/nmat5045
- Guerra, D., Gómez, L. A., Restrepo, A., and David, J. (2020). New stable phases of glycine crystals. *Chem. Phys.* 530, 110645. doi:10.1016/j.chemphys.2019.110645
- Gusev, E. I., Skvortsova, V. I., Dambinova, S. A., Raevskiy, K. S., Alekseev, A. A., Bashkatova, V. G., et al. (2000). Neuroprotective effects of glycine for therapy of acute ischaemic stroke. *Cerebrovasc. Dis.* 10, 49–60. doi:10.1159/000016025
- Hamilton, B. D., Hillmyer, M. A., and Ward, M. D. (2008). Glycine polymorphism in nanoscale crystallization chambers. *Cryst. Growth Des.* 8, 3368–3375. doi:10.1021/cg800326a
- Heredia, A., Meunier, V., Bdiqin, I. K., Gracio, J., Balke, N., Jesse, S., et al. (2012). Nanoscale ferroelectricity in crystalline  $\gamma$ -glycine. *Adv. Funct. Mat.* 22, 2996–3003. doi:10.1002/adfm.201103011
- Horn, J., Tolardo, E., Fissore, D., and Friess, W. (2018). Crystallizing amino acids as bulking agents in freeze-drying. *Eur. J. Pharm. Biopharm.* 132, 70–82. doi:10.1016/j.ejpb.2018.09.004
- Hosseini, E. S., Dervin, S., Ganguly, P., and Dahiya, R. (2021). Biodegradable materials for sustainable health monitoring devices. *ACS Appl. Bio Mat.* 4, 163–194. doi:10.1021/acsabm.0c01139
- Hosseini, E. S., Manjakkal, L., Shakhiveli, D., and Dahiya, R. (2020). Glycine-chitosan-based flexible biodegradable piezoelectric pressure sensor. *ACS Appl. Mat. Interfaces* 12, 9008–9016. doi:10.1021/acsami.9b21052
- Hu, P., Hu, S., Huang, Y., Reimers, J. R., Rappe, A. M., Li, Y., et al. (2019). Bioferroelectric properties of glycine crystals. *J. Phys. Chem. Lett.* 10, 1319–1324. doi:10.1021/acs.jpclett.8b03837
- Humar, M., Kwok, S. J. J., Choi, M., Yetisen, A. K., Cho, S., Yun, S. H., et al. (2017). Toward biomaterial-based implantable photonic devices. *Nanophotonics* 6, 414–434. doi:10.1515/nanoph-2016-0003
- Iitaka, Y. (1960). The crystal structure of  $\beta$ -glycine. *Acta Cryst.* 13, 35–45. doi:10.1107/S0365110X60000066
- Iitaka, Y. (1961). The crystal structure of  $\gamma$ -glycine. *Acta Crystallogr.* 14, 1–10. doi:10.1107/S0365110X61000012
- Ioppolo, S., Fedoseev, G., Chuang, K. J., Cuppen, H. M., Clements, A. R., Jin, M., et al. (2021). A non-energetic mechanism for glycine formation in the interstellar medium. *Nat. Astron.* 5, 197–205. doi:10.1038/s41550-020-01249-0
- Isakov, D., Petukhova, D., Vasilev, S., Nuraeva, A., Khazamov, T., Seyedhosseini, E., et al. (2014). *In situ* observation of the humidity controlled polymorphic phase transformation in glycine microcrystals. *Cryst. Growth Des.* 14, 4138–4142. doi:10.1021/cg500747x
- Jain, M., Nilsson, R., Sharma, S., Madhusudhan, N., Kitami, T., Souza, A. L., et al. (2012). Metabolite profiling identifies a key role for glycine in rapid cancer cell proliferation. *Science* 336, 1040–1044. doi:10.1126/science.1218595
- Kalinin, S. V., Morozovska, A. N., Chen, L. Q., and Rodriguez, B. J. (2010). Local polarization dynamics in ferroelectric materials. *Rep. Prog. Phys.* 73, 056502. doi:10.1088/0034-4885/73/5/056502
- Kholkin, A., Alikin, D., Shur, V., Dishon, S., Ehre, D., Lubomirsky, I., et al. (2021). Local piezoelectric properties of doped biomolecular crystals. *Materials* 14, 4922. doi:10.3390/ma14174922
- Kim, D., Han, S. A., Kim, J. H., Lee, J. H., Kim, S. W., Lee, S. W., et al. (2020). Biomolecular piezoelectric materials: From amino acids to living tissues. *Adv. Mat.* 32, 1906989. doi:10.1002/adma.201906989
- Kiraci, A. (2021). A phenomenological study on ferroelectric  $\beta$ -glycine. *Ferroelectrics* 572, 277–286. doi:10.1080/00150193.2020.1868888
- Kuan, Y. J., Charnley, S. B., Huang, H. C., Tseng, W. L., and Kiesel, Z. (2003). Interstellar glycine. *Astrophys. J.* 593, 848–867. doi:10.1086/375637
- Lee, I. S., Kim, K. T., Lee, A. Y., and Myerson, A. S. (2008). Concomitant crystallization of glycine on patterned substrates: The effect of pH on the polymorphic outcome. *Cryst. Growth Des.* 8, 108–113. doi:10.1021/cg700890m
- Lemanov, V. V. (2000). Piezoelectric and pyroelectric properties of protein amino acids as basic materials of Soft State Physics. *Ferroelectrics* 238, 211–218. doi:10.1080/00150190008008786
- Li, J., Long, Y., Yang, F., and Wang, X. (2020). Degradable piezoelectric biomaterials for wearable and implantable bioelectronics. *Curr. Opin. Solid State Mat. Sci.* 24, 100806. doi:10.1016/j.cossms.2020.100806
- Lines, M. E., and Glass, A. M. (1977). *Principles and applications of ferroelectrics and related materials*. Oxford, UK: Clarendon Press, 680.
- Lu, H., Li, T., Poddar, S., Goit, O., Lipatov, A., Sinitskii, A., et al. (2015). Statics and dynamics of ferroelectric domains in diisopropylammonium bromide. *Adv. Mat.* 27, 7832–7838. doi:10.1002/adma.201504019
- Maiti, S., Karan, S. K., Kim, J. K., and Khatua, B. B. (2019). Nature driven bio-piezoelectric/triboelectric nanogenerator as next-generation green energy harvester for smart and pollution free society. *Adv. Energy Mat.* 9, 1803027. doi:10.1002/aenm.201803027
- Malakhin, I. A., Achkasov, A. F., Ratushnyak, A. S., Zapara, T. A., Markel, A. L., Boldyreva, E. V., et al. (2012). Different effects of  $\alpha$ - and  $\gamma$ -glycine on the aberrant activity of pyramidal neurons of hippocampal slices. *Dokl. Biol. Sci.* 444, 157–161. doi:10.1134/s0012496612030179
- Markel, A. L., Achkasov, A. F., Alekhina, T. A., Prokudina, O. I., Ryazanova, M. A., Ukolova, T. N., et al. (2011). Effects of the  $\alpha$ - and  $\gamma$ -polymorphs of glycine on the behavior of catalepsy prone rats. *Pharmacol. Biochem. Behav.* 98, 234–240. doi:10.1016/j.pbb.2010.12.025
- Meirzadeh, E., Weissbuch, I., Ehre, D., Lahav, M., and Lubomirsky, I. (2018). Polar imperfections in amino acid crystals: design, structure, and emerging functionalities. *Acc. Chem. Res.* 51, 1238–1248. doi:10.1021/acs.accounts.8b00054
- Okosun, F., Guerin, S., Celikin, M., and Pakrashi, V. (2021). Flexible amino acid-based energy harvesting for structural health monitoring of water pipes. *Cell Rep. Phys. Sci.* 2, 100434. doi:10.1016/j.xcrp.2021.100434
- Palla, P., Petrongolo, C., and Tomasi, J. (1980). Internal rotation potential energy for the glycine molecule in its zwitterionic and neutral forms: a comparison among several methods. *J. Phys. Chem.* 84, 435–442. doi:10.1021/j100441a019
- Piperno, S., Mirzadeh, E., Mishuk, E., Ehre, D., Cohen, S., Eisenstein, M., et al. (2013). Water-induced pyroelectricity from nonpolar crystals of amino acids. *Angew. Chem. Int. Ed.* 52, 6513–6516. doi:10.1002/anie.201301836
- Poornachary, S. K., Chow, P. S., and Tan, R. B. H. (2008). Influence of solution speciation of impurities on polymorphic nucleation in glycine. *Cryst. Growth Des.* 8, 179–185. doi:10.1021/cg060570w
- Schröder, M., Chen, X., Haußmann, A., Thiessen, A., Poppe, J., Bonnell, D. A., et al. (2014). Nanoscale and macroscopic electrical ac transport along conductive domain walls in lithium niobate single crystals. *Mat. Res. Express* 1, 035012. doi:10.1088/2053-1591/1/3/035012
- Schröder, M., Haußmann, A., Thiessen, A., Soergel, E., Woike, T., Eng, L. M., et al. (2012). Conducting domain walls in lithium niobate single crystals. *Adv. Funct. Mat.* 22, 3936–3944. doi:10.1002/adfm.201201174
- Scrymgeour, D. A. (2014). “Applications of domain engineering in ferroelectrics for photonic applications,” in *Ferroelectric crystals for photonic applications*. Editors P. Ferraro, S. Grilli, and P. De Natale (Berlin, Heidelberg: Springer), 91, 385–399. Springer Series in Materials Science. doi:10.1007/978-3-642-41086-4\_14
- Syedhosseini, E., Bdiqin, I., Ivanov, M., Vasileva, D., Kudryavtsev, A., Rodriguez, B. J., et al. (2015). Tip-induced domain structures and polarization switching in ferroelectric amino acid glycine. *J. Appl. Phys.* 118, 072008. doi:10.1063/1.4927807
- Syedhosseini, E., Ivanov, M., Bystrov, V., Bdiqin, I., Zelenovskiy, P., VYa, Shur, et al. (2014). Growth and nonlinear optical properties of  $\beta$ -glycine crystals grown on Pt substrates. *Cryst. Growth Des.* 14, 2831–2837. doi:10.1021/cg500111a
- Syedhosseini, E., Romanyuk, K., Vasileva, D., Vasilev, S., Nuraeva, A., Zelenovskiy, P., et al. (2017). Self-assembly of organic ferroelectrics by evaporative dewetting: a case of  $\beta$ -glycine. *ACS Appl. Mat. Interfaces* 9, 20029–20037. doi:10.1021/acsami.7b02952

- Shur, V. Y. (2008). "21 - Nano- and micro-domain engineering in normal and relaxor ferroelectrics," in *Handbook of advanced dielectric, piezoelectric and ferroelectric materials –synthesis, properties and applications*. Editor Z. G. Ye (Cambridge, UK: Woodhead Publishing Ltd), 622–669. doi:10.1533/9781845694005.5.622
- Shvartsman, V. V., AYU, Emelyanov, Kholkin, A. L., and Safari, A. (2002). Local hysteresis and grain size effect in  $\text{Pb}(\text{Mg}_{1/3}\text{Nb}_{2/3})\text{O}_3$ - $\text{PbTiO}_3$  thin films. *Appl. Phys. Lett.* 81, 117–119. doi:10.1063/1.1490150
- Slabov, V., Vasileva, D., Keller, K., Vasilev, S., Zelenovskiy, P., Kopyl, S., et al. (2019). Controlled growth of stable  $\beta$ -glycine via inkjet printing. *Cryst. Growth Des.* 19, 3869–3875. doi:10.1021/acs.cgd.9b00308
- Soergel, E. (2011). Piezoresponse force microscopy (PFM). *J. Phys. D: Appl. Phys.* 44, 464003. doi:10.1088/0022-3727/44/46/464003
- Surovtsev, N. V., Malinovsky, V. K., and Boldyreva, E. V. (2011). Raman study of low-frequency modes in three glycine polymorphs. *J. Chem. Phys.* 134, 045102. doi:10.1063/1.3524342
- Tasnim, T., Goh, A., Gawayed, O., Hu, C. T., Chen, T. Y., Aber, J. E., et al. (2018). Dendritic growth of glycine from nonphotochemical laser-induced nucleation of supersaturated aqueous solutions in agarose gels. *Cryst. Growth Des.* 18, 5927–5933. doi:10.1021/acs.cgd.8b00688
- Tayi, A. S., Kaeser, A., Matsumoto, M., Aida, T., and Stupp, S. I. (2015). Supramolecular ferroelectrics. *Nat. Chem.* 7, 281–294. doi:10.1038/nchem.2206
- Tofail, S. A. M., and Bauer, J. (2016). Electrically polarized biomaterials. *Adv. Mat.* 28, 5470–5484. doi:10.1002/adma.201505403
- Vasileva, D., Vasilev, S., Kholkin, A. L., and VYa, Shur (2019). Domain diversity and polarization switching in amino acid  $\beta$ -glycine. *Materials* 12, 1223. doi:10.3390/ma12081223
- Wesson, P. S. (2010). Panspermia, past and present: astrophysical and biophysical conditions for the dissemination of life in space. *Space Sci. Rev.* 156, 239–252. doi:10.1007/s11214-010-9671-x
- Xu, Q., Gao, X., Zhao, S., Liu, Y. N., Zhang, D., Zhou, K., et al. (2021). Construction of bio-piezoelectric platforms: From structures and synthesis to applications. *Adv. Mat.* 33, 2008452. doi:10.1002/adma.202008452
- Yang, F., Li, J., Long, Y., Zhang, Z., Wang, L., Sui, J., et al. (2021). Wafer-scale heterostructured piezoelectric bio-organic thin films. *Science* 373, 337–342. doi:10.1126/science.abf2155
- Zelenovskiy, P., Vasileva, D., Nuraeva, A., Vasilev, S., Khazamov, T., Dikushina, E., et al. (2016). Spin coating formation of self-assembled ferroelectric  $\beta$ -glycine films. *Ferroelectrics* 496, 10–19. doi:10.1080/00150193.2016.1157434



## OPEN ACCESS

## EDITED BY

Sidney J. L. Ribeiro,  
São Paulo State University, Brazil

## REVIEWED BY

Nirmal Mazumder,  
Manipal Academy of Higher Education, India  
Aniruddha Ray,  
University of Toledo, United States

## \*CORRESPONDENCE

Sandra I. Vieira,  
sivieira@ua.pt  
João Rocha,  
rocha@ua.pt  
Samuel Guieu,  
sguieu@ua.pt

## †PRESENT ADDRESS

Roberto A. Dias,  
VIB-KU Leuven Center for Brain and  
Disease Research, Campus  
Gasthuisberg, Leuven, Belgium

†These authors have contributed equally  
to this work and share first authorship

## SPECIALTY SECTION

This article was submitted  
to Light Sources and Luminescent  
Materials,  
a section of the journal  
Frontiers in Photonics

RECEIVED 07 June 2022

ACCEPTED 05 July 2022

PUBLISHED 15 August 2022

## CITATION

Vieira SI, Nunes da Silva R, Alves M,  
Dias RA, Meireles Sousa AM, Camões F,  
Maia A, Almeida M, Rocha J, Silva AM  
and Guieu S (2022). Liprobe, a vital dye  
for lipid aggregates detection in imaging  
and high-content screens.  
*Front. Photonics* 3:963778.  
doi: 10.3389/fphot.2022.963778

## COPYRIGHT

© 2022 Vieira, Nunes da Silva, Alves,  
Dias, Meireles Sousa, Camões, Maia,  
Almeida, Rocha, Silva and Guieu. This is  
an open-access article distributed  
under the terms of the [Creative  
Commons Attribution License \(CC BY\)](#).  
The use, distribution or reproduction in  
other forums is permitted, provided the  
original author(s) and the copyright  
owner(s) are credited and that the  
original publication in this journal is  
cited, in accordance with accepted  
academic practice. No use, distribution  
or reproduction is permitted which does  
not comply with these terms.

# Liprobe, a vital dye for lipid aggregates detection in imaging and high-content screens

Sandra I. Vieira<sup>1†\*</sup>, Raquel Nunes da Silva<sup>1,2†</sup>, Mariana Alves<sup>1</sup>,  
Roberto A. Dias<sup>1†</sup>, Ana M. Meireles Sousa<sup>3</sup>, Fatima Camões<sup>1</sup>,  
André Maia<sup>4</sup>, Mónica Almeida<sup>5</sup>, João Rocha<sup>6\*</sup>, Artur M. Silva<sup>2</sup>  
and Samuel Guieu<sup>2,6\*</sup>

<sup>1</sup>Institute of Biomedicine iBIMED, Department of Medical Sciences, University of Aveiro, Aveiro, Portugal, <sup>2</sup>LAQV-REQUIMTE, Department of Chemistry, University of Aveiro, Aveiro, Portugal, <sup>3</sup>Department of Developmental Biology, Stanford University School of Medicine, Stanford, CA, United States, <sup>4</sup>i3S—Instituto de Investigação e Inovação em Saúde, Universidade do Porto, IBMC—Instituto de Biologia Molecular e Celular, Universidade do Porto, Porto, Portugal, <sup>5</sup>CESAM, Department of Biology, University of Aveiro, Aveiro, Portugal, <sup>6</sup>CICECO, Department of Chemistry, University of Aveiro, Aveiro, Portugal

Pathological lipid accumulation is a hallmark of several metabolic disorders, and detection of lipid aggregates is an essential step for initial diagnosis and drug screening purposes. However, low-cost, simple, and reliable detection fluorescent probes are not widely available. Here, six push-pull-push dyes were studied, and proved to be highly sensitive to the polarity of the medium, presenting potential to distinguish structures with different hydrophobic indexes. Importantly, in the presence of lipid aggregates their staining specificity highly increased and the fluorescence wavelength blue shifted. One of the compounds, named Liprobe, was physiologically inert in cells, as witnessed by mass-spectrometry and metabolic assays. Liprobe was not toxic to living zebrafish embryos, and differentially stained the muscle and bone tissues. In triglyceride solutions, a high correlation was observed between Liprobe's 558 and 592 nm emissions and the 0–2.5 mg dl<sup>-1</sup> triglyceride range. Confocal and cell-based high content screens revealed that this fluorophore was able to selectively detect lipid droplets and ceramide loads in normal and Farber's disease human fibroblasts, respectively. Our results demonstrate that Liprobe is a suitable fluorescing probe for vital staining of lipid aggregates, compatible with a rapid and cheap high content screening assays for preliminary diagnosis of Farber's disease and, potentially, of other lipidosis.

## KEYWORDS

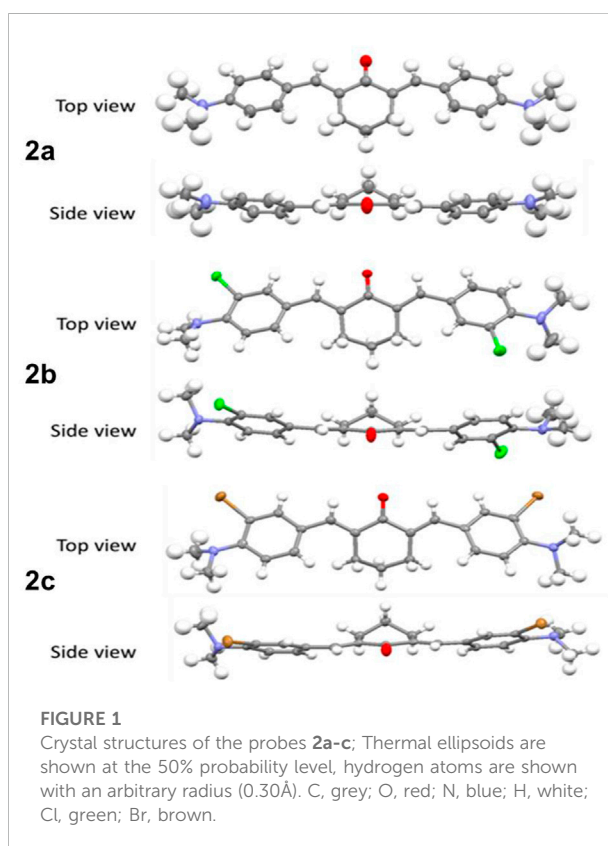
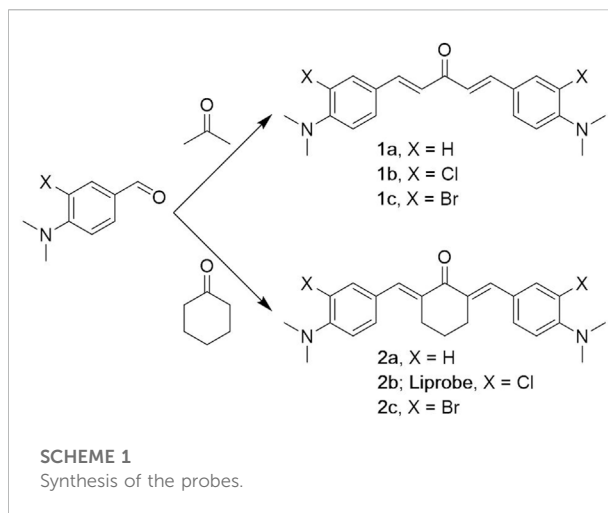
fluorophore, lipid aggregates, live imaging, high-content screening, farber's disease

## Introduction

Lipids comprise a large and important class of biomolecules highly relevant in metabolism and signaling (Hannun and Obeid, 2018). They integrate multiple biochemical functions, such as energy production, cell membranes generation, and act as chemical signals for cell and organ communication. Thus, they are important for all tissues, (Gross and Silver, 2014), (Walther and Farese, 2012) and alterations in the lipid homeostasis may greatly impact the whole organism. Lipid-based disorders (or lipidosis) encompass a wide range of lipid metabolic diseases with harmful accumulation of lipids in various cells and tissues. Most lipid disorders are related to diet and lifestyle (80%) and result in dyslipidaemia, particularly hyperlipidaemia, a well-established risk factor for atherosclerosis and cardiovascular disease that lead to more than 17.9 million deaths per year. (WHO, 2002), (Pischon et al., 2008), (Adams et al., 2006) The other 20% are mostly familial lipid disorders, including inherited lipid storage diseases such as Gaucher, Tay-Sachs, Fabry, and Farber's diseases (Elias et al., 2008). The detection of lipid loads in cells and tissues *via*, e.g., high-content screening (HCS), is important for lipidosis diagnosis and therapeutic drugs screening, and may also assist identifying individuals for risk prevention (Galema-Boers and Van Lennep, 2015).

Cell- or plasma-based HCS diagnosis and drug development must be fast and affordable, benefiting from the implementation of user-friendly probes for lipid aggregates' detection. Fluorescent probes fitting these criteria would be ideal, since fluorescence-based detection techniques are amongst the most sensitive. Fluorescence labelling is highly employed in biology and medicine for therapeutic means (Serra et al., 2009) or to image tissues, cells or specific subcellular structures (Nunes da Silva et al., 2019). Although several fluorescent probes have been developed for lipid droplets staining, (Fam et al., 2018) (Tatenaka et al., 2019) the commercial probes have drawbacks that limit their use, such as poor solubility hindering the staining process, high prices, and a limited range of absorption and emission wavelengths. Hence, it is of interest to develop user friendly and affordable fluorescent probes for lipid load detection, compatible with HCS.

Push-pull fluorophores have been successfully used for imaging living cells, (Didier et al., 2009), (Dang et al., 2018) in particular because of their large Stokes' shifts. For example, certain substituted chalcone derivatives exhibit high quantum yields in solution and are efficient probes for *ex vivo* imaging (Lee et al., 2012). Here, we report a series of six push-pull-push fluorophores, decorated with halogen atoms. All the compounds exhibit good molar extinction coefficients and fair quantum yields. Importantly, the compounds present a large Stokes' shift and their emission maximum is much influenced by the polarity of the surrounding environment, and they are biocompatible. Moreover, they are highly selective for intracellular lipid aggregates, making them intriguing vital dyes for cellular imaging, in particular, for the detection of lipidic aggregates in fundamental and pharmaceutical studies.



## Results and discussion

### Synthesis and photophysical properties of the new push-pull-push chromophores

The chromophores **1a-c** (linear) and **2a-c** (cyclic), decorated with halogen atoms, were synthesized following a common strategy.

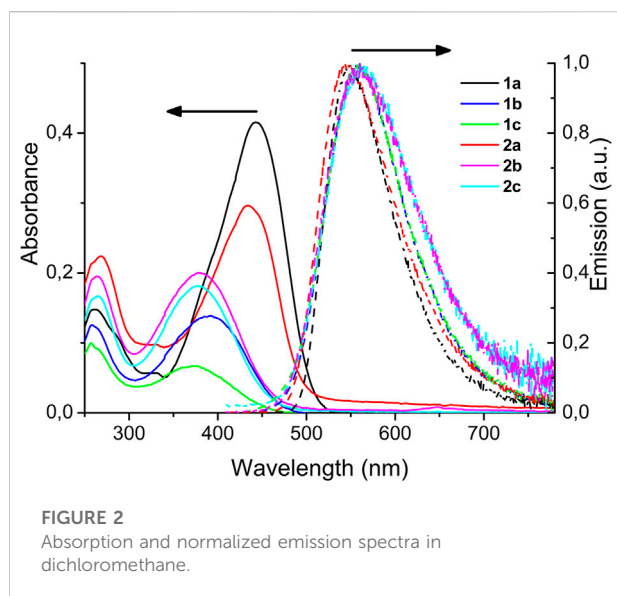


**FIGURE 2**  
Absorption and normalized emission spectra in dichloromethane.

The building blocks were obtained by chlorination or bromination of 4-dimethylaminobenzaldehyde using *n*-chlorosuccinimide or *n*-bromosuccinimide (Guieu et al., 2013), (Vaz et al., 2016). The double condensation of the appropriate benzaldehyde with acetone or cyclohexanone gave the linear and cyclic chromophores, respectively, in fair to good yields (Scheme 1). The structures of the linear (**1a-c**) and cyclic (**2a-c**) fluorophores were confirmed by NMR, MS and HRMS or elemental analysis. Synthesis details and NMR spectra are given in the [Supplementary Materials](#).

The compounds **1a-c** were obtained as oils or amorphous solids, while the cyclic equivalents **2a-c** were crystalline solids. Single crystals suitable for X-ray diffraction were obtained by slow evaporation of a saturated solution in dichloromethane (Cambridge Crystallographic Data Centre). The crystal structure of **2a** has been published, (Yakimanski et al., 1997), and it is described here for comparison with the halogenated analogues. Although in **2a** the asymmetric unit is half of the molecule

(Figure 1), for the halogenated derivatives **2b-c** the asymmetric unit consists of two different molecules, mirror images of each other (only one of the molecules is shown in Figure 1, for clarity).

All bonds and angles are in the normal ranges (Allen et al., 1987). The crystal structures confirmed the formation of the double bonds and their (*E*)- configuration. In the crystals, the two phenyl rings are coplanar and rotated in the same direction relatively to the central cyclohexanone. No halogen bonds are present, the molecules being held together solely by a network of weak hydrogen bonds.

UV-vis absorption experiments were carried out in dichloromethane (DCM) solutions. The main band is ascribed to the  $S_0-S_1$  ( $n-\pi^*$ ) transition, observed at *ca.* 440 nm for **1a** and **2a** (Figure 2, full lines). Substitution of the phenyl rings with a halogen atom shifts this absorption maximum to shorter wavelengths (*ca.* 380 nm). The molar extinction coefficient does not seem to be influenced by the presence of halogens on the phenyl rings (Table 1). The weaker band at 270 nm is similar for all compounds and attributed to the  $S_0-S_2$  ( $p-p^*$ ) transition.

The emission spectra were recorded at low concentration in DCM solutions (Figure 2, dotted lines). All compounds emit at similar wavelength, between 500 and 700 nm, as a broad band centered around 560 nm. The quantum yields are modest, ranging from 0.01 to 0.14 and, in the linear series, the presence of the halogen on the phenyl rings is detrimental to the emission efficiency. In the cyclic series (compounds **2a-c**), the quantum yields are probably too small to allow seeing an influence of the halogen atoms. The large Stokes' shift observed for all chromophores, ranging from 110 to 197 nm, is characteristic of a transition with charge transfer character, occurring from the dimethylamino groups to the ketone via the two butadiene bridges.

## Biocompatibility and imaging in mammalian cultured cells

The choice of a fluorophore for cellular imaging should not rely solely on its *in vitro* properties, such as the quantum yield measured in dichloromethane, but also take in consideration its

**TABLE 1** Photophysical data in dichloromethane.

Compound	$\lambda_{\text{abs}}$ (nm) <sup>a</sup>	$\epsilon$ (M <sup>-1</sup> cm <sup>-1</sup> ) <sup>a</sup>	$\lambda_{\text{em}}$ (nm) <sup>b</sup>	$\phi$ <sup>c</sup>	Stokes' shift (nm)
<b>1a</b>	442	41,000	552	0.14	110
<b>1b</b>	390	14,000	560	0.10	170
<b>1c</b>	370	7 500	562	0.05	192
<b>2a</b>	433	20,000	550	0.01	117
<b>2b</b>	381	20,500	578	0.01	197
<b>2c</b>	378	24,500	572	0.01	194

<sup>a</sup> $\epsilon$  is determined by linear regression of 4 measurements in the range  $10^{-4}$  M to  $10^{-6}$  M in dichloromethane.

<sup>b</sup>Excitation at 400 nm.

<sup>c</sup>Quantum yields are determined with excitation at 400 nm, by linear regression of 4 measurements in the range of absorption 0 to 0.2, by comparison with fluorescein (quantum yield 0.91 at excitation 470 nm in a solution of NaOH 0.01 M in water). (Brouwer, 2011).



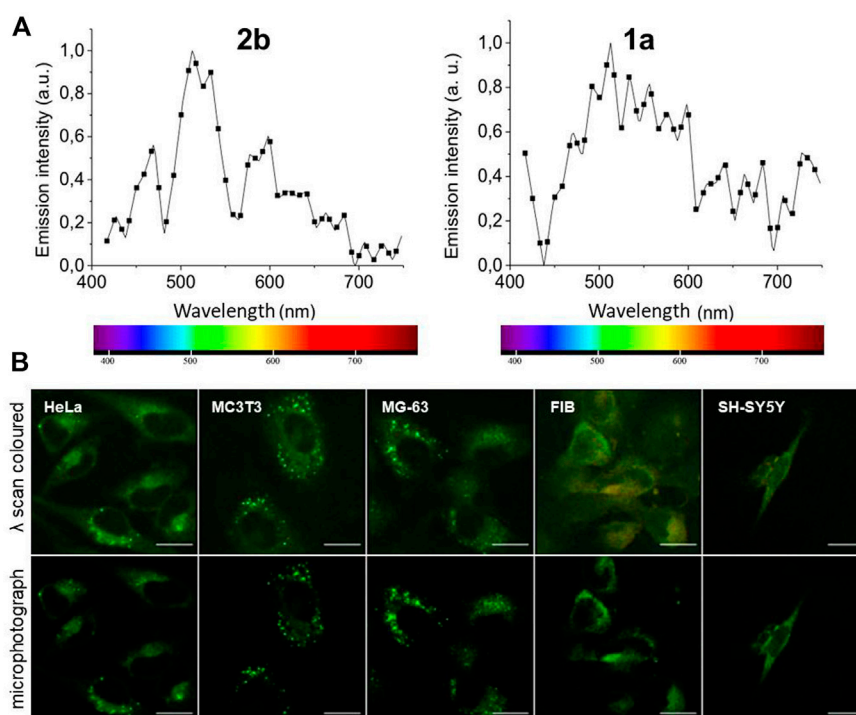


**FIGURE 3**

(A) Lambda scans of fluorophores **2b** (20 μM, left graph) and **1a** (100 μM, right graph) in HeLa cells. (B) Microphotographs of cell lines of human (cervix tumor HeLa, skin Fibroblasts 'FIB', neuroblastoma SH-SY5Y, pre-osteoblast MG63) and rat (pre-osteoblast MC3T3) origins, incubated live with 20 μM of **2b** for 2 h. Upper panel: lambda scans (exc. 405 nm; em. 411–754) and resulting pseudocolors. Lower panel: corresponding microphotographs taken in the 475–625 nm channel, colored green. Bar, 20 μm. Negative controls are shown in [Supplementary Figure S3C](#).

properties in cells. The compounds' capacity to be internalized by living cells, their fluorescence distribution and relative intensity, were first analyzed in HeLa cells (here exemplified for cyclic **2a-c**). As expected, due to their absorption maximum ([Figure 2](#)), the fluorophores could be excited with confocal microscope's 405 and 458 nm laser lines. Given that the optimum concentration to maximize the emission of fluorophores is between 10 and 100 μM (more concentrated the fluorescence is quenched, more diluted the fluorescence decreases linearly), further assays were performed in that concentration range.

All compounds were taken up within 1 h by living HeLa cells ([Supplementary Figure S1](#)). Surprisingly, although the quantum yield of **2b** is 10 times lower than its linear analogue **1b**, the former appeared inside cells with high emission when excited with equal laser power at 405 nm ([Table 1](#) and SI). Nevertheless, a general tendency of brighter emission for fluorophores with chloride for hydrogen substitution could not be found.

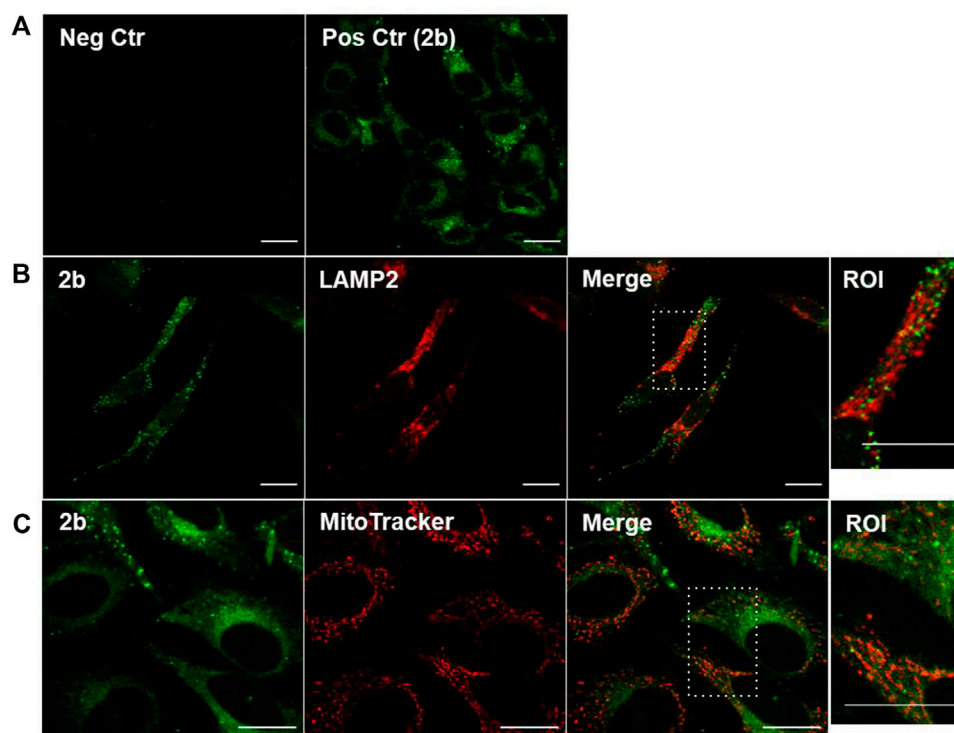
Cells were not affected by 1 h incubation with the fluorophores and, to confirm their biocompatibility, two cell lines (HeLa and MC3T3) were incubated with 1 μM of the compounds for 24 h ([Supplementary Figure S2](#)) and cells viability monitored. Only **1c** and **2a** rendered significantly decreased viabilities, and only in HeLa cells (*ca.* 30 and 20%,

respectively, [Supplementary Figure S2](#)). The fluorophores were still visible in cells following 24 h, here exemplified for **2b** ([Supplementary Figure S3A](#)). Depending on their localization, the fluorophores emitted in the green, yellow, or red regions ([Supplementary Figure S3B](#)).

Importantly, the powdered fluorophores were stable for more than 1 year and their intensities in fixed cells stored in PBS were stable for at least 1 month.

Next, the emission lambda scans of the compounds were recorded on a 510-META confocal microscope upon excitation with the 405 nm diode laser. [Figure 3A](#) shows the emission spectra of **1a** and **2b**, the brightest fluorophores in cells. Spectra of **1b**, **1c**, **2a** and **2c** ([Supplementary Figure S4](#)) were very similar to the spectrum of **2b** ([Figure 3A](#), left graph), with a characteristic narrow peak. Spectrum of compound **1a** displays a wider band ([Figure 3A](#), right graph).

Given its photophysical characteristics in cells, the cyclic compound **2b** was selected as the best-performing fluorophore for live and fixed cells staining. The characteristics of **2b** live imaging in several cell lines, mainly human, were analyzed upon 2 h incubation with 20 μM **2b** ([Figure 3B](#)). Compound **2b** emitted mostly in the green region (lambda-colored), and its emission was

**FIGURE 4**

Co-localization studies of the fluorophore **2b** with endolysosomal and mitochondrial markers in HeLa cells. **(A)** Negative control ('Neg Ctr'), cells not stained; positive control ('Pos Ctr'), living cells incubated for 2 h with 20  $\mu$ M **2b**. Cells were **(B)** co-stained with the endolysosomal marker LAMP2 (in red) after fixation or **(C)** with the viable mitochondrial marker MitoTracker Deep Red FM 633 nm (in red), in living cells. Compound **2b**: exc. at 405 nm, em. 475–625 nm, colored green. LAMP2 and MitoTracker: exc. at 633 nm; em. 650–750 nm. Bar, 20  $\mu$ m.

predominantly detected in cytoplasmic vesicles, where it emitted at higher intensity. Some faint staining of the aqueous cytoplasm could also be observed, while no nuclear staining was usually detected (Figure 3B; negative controls in Supplementary Figure S3C). Cells fluoresced primarily in bright green, occasionally in yellow/orange with red spots, but very rarely in blue (tested with various filter sets and various conditions) (Figure 3B and Supplementary Figure S3B).

The observed **2b** subcellular spotted pattern may indicate lysosomal or mitochondrial staining, and this was further pursued. Co-staining of **2b** with the lysosomal marker LAMP2 and the MitoTracker® vital dye for active mitochondria, revealed some co-localization with fluorophore **2b** (Figures 4B,C, respectively). Although the Mander's coefficients were of  $26.3 \pm 4.6$  and  $29.3 \pm 4.4$  for co-localization with LAMP2 or MitoTracker®, respectively, some of the apparent co-labeled structures were not morphologically equal. Hence, a high percentage of the Liprobe population stained other cytoplasmic structures and we hypothesized that **2b** could differentially stain organelles with different polarities.

## Solvatochromism effect and imaging cellular lipid aggregates

The observed differences between the compounds' emission spectra in DCM and inside cells (Figures 2, 3A; Supplementary Figure S3) prompted us to investigate in more detail their optoelectronic properties, particularly solvatochromism. In a push-pull chromophore, the first excited state is highly polar, in the present chromophores with a negative charge on the oxygen and a positive one on the nitrogen atoms. Therefore, the polarity of the solvent or surrounding structures is crucial for the stabilization or destabilization of this excited state. A polar solvent stabilizes the excited state without influencing much the energy of the ground state, resulting in a decrease in the transition energy (higher emission wavelengths). The opposite occurs with a less polar solvent (lower emission wavelengths).

The influence of the solvent polarity on the emission spectrum was studied for all compounds; given the similarity of the obtained results, only the spectra of compound **2b** are presented here as an example. As expected, in a mixture of THF and hexane (Figure 5A, left graph), when the percentage of hexane increased the polarity of the solvent decreased, and the

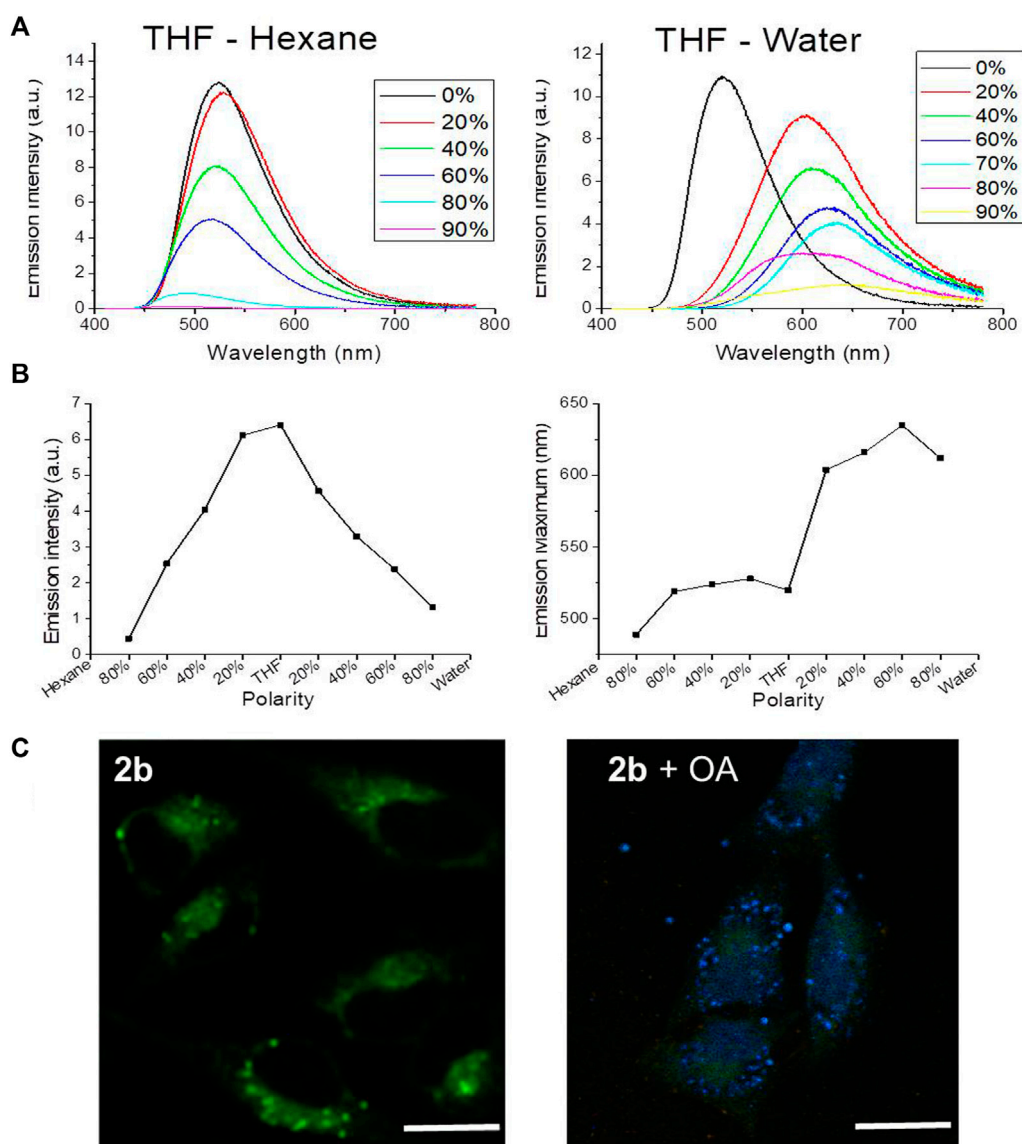


FIGURE 5

(A) Fluorescence of compound **2b** ( $10^{-4}$  M;  $\lambda_{\text{ex}} = 400$  nm) in a THF/Hexane mixture with different percentages of hexane (left), or in a THF/Water mixture with different percentages of water (right). (B) Variation of compound **2b** emission intensity (left) and its maximum emission wavelength (right), versus solvent polarity. (C) Lambda scan colored microphotographs of live HeLa cells incubated with compound **2b** (20  $\mu$ M) for 1h and previously incubated or not with oleic acid ("OA") (exc. 405 nm). Bar, 20  $\mu$ m.

emission maximum blue-shifted. In contrast, when the polarity of the solvent increased in a mixture of THF and water (Figure 5A, right graph), a red shift was observed in the emission maximum. The intensity of the emission was also investigated as a function of the solvent polarity (Figure 5B). The emission was maximal in solvents with medium polarity such as DCM or THF and decreased in more polar (water) or less polar (hexane) solvents. An interesting consequence is that the emission of polar and apolar solutions can be separated. A simple experiment was further conducted: water (2 ml) and hexane

(2 ml) were added to a solution of **2b** in THF; two phases were separated, and the fluorescence was only visible in the hexane phase, confirmed by recording the emission spectra of each phase (not shown). Hence, **2b** is more soluble in pure hexane than in pure water and/or the emission is much stronger in pure hexane than in pure water. The same can be said for the other fluorophores.

Given that the fluorophores' color shifts with the polarity of the environment *in vitro*, (Lakowicz, 2006), we further investigated whether they shift with the hydrophobicity of the subcellular

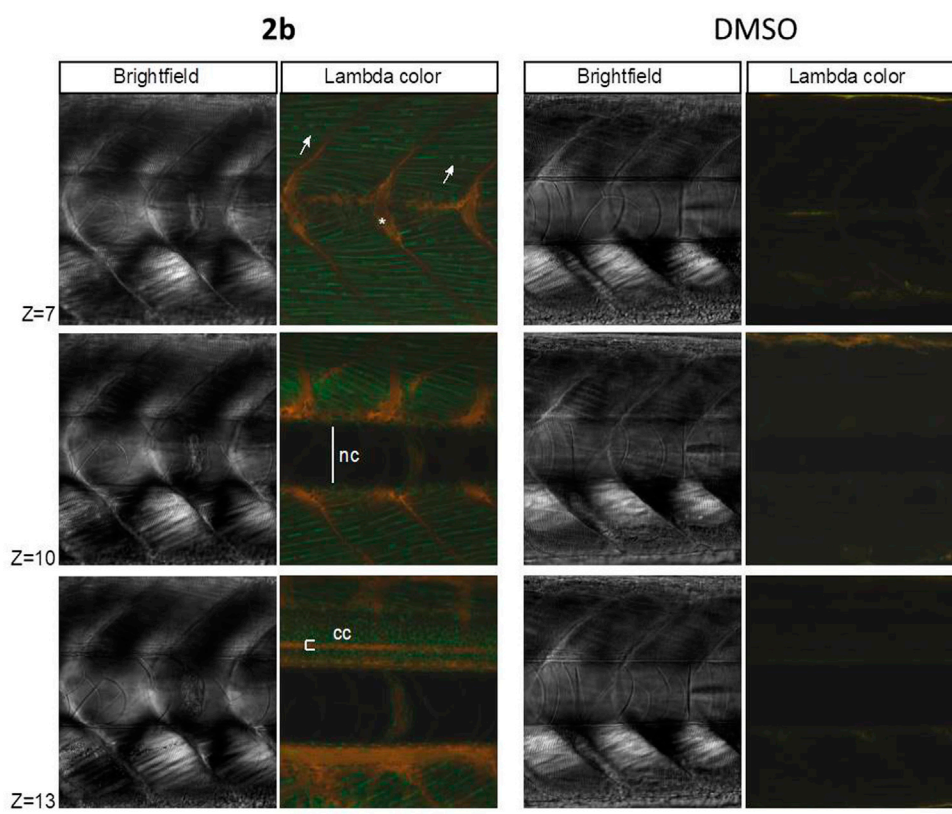


FIGURE 6

Zebrafish embryos at 4.5 dpf were incubated for 16 h with 50  $\mu$ M compound **2b** in DMSO. Confocal lambda scans (exc. 405 nm) of the trunk were taken at the level of the urogenital pore, at different focal planes ("z"). A DMSO alone condition was performed in parallel, as negative control. "nc", notochord canal; "cc", central canal; arrows: muscle cells/fibers—green fluorescing; asterisk: bone/cartilaginous tissue - orange fluorescing. Bar, 100  $\mu$ m.

organelles and are able to selectively mark cells and organelles with higher lipidic load. This was first explored in human cells where the lipid droplets content was increased by cells incubation with an oleic acid solution (Camões et al., 2015) (Figure 5C). Lipid droplets are dynamic cytoplasmic organelles found in most eukaryotic cells, where they participate in lipid storage for energy generation and membrane synthesis, among others (Walther and Farese, 2012).

In the presence of abundant lipid droplets, the fluorophores staining was more defined, revealing its selectivity for lipid aggregates. This also suggests that, in basal conditions, the fluorophores locate in cytoplasmic vesicles with more hydrophobic content. Furthermore, in conditions of lipid droplets abundance a blue-shift of the emission maximum was detected in cells (Figure 5C), with the fluorophores signaling in the blue range. As stated before, the ability of the fluorophores to selectively stain lipids is highly relevant, since they account for nearly half of the mass of cell membranes (Holthuis and Menon, 2014). The most widely used lipid droplet markers (Dang et al., 2018; Tatenaka et al., 2019) (Collot et al., 2018) are lipophilic fluorescent probes such as BODIPY 493/503 and Nile Red (9-diethylamino-5H-benzo [a]

phenoxazine-5-one) (Listenberger et al., 2016). The compounds here presented share cellular staining properties with Nile Red, which is also highly membrane-permeant, not acutely toxic, and its emission shifts from red to yellow according to the level of hydrophobicity of the solvent (Diaz et al., 2008).

## Differential staining of zebrafish embryos' structures

To determine if **2b** was able to penetrate and differentially counterstain small organisms in a physiologically innocuous manner, its solvatochromic staining properties were tested in zebrafish embryos (Figure 6). Vital dyes are extremely valuable to provide contextual information in these embryos that, due to their optical transparency and rapid development, are ideal systems to study numerous biological processes such as development and tissue regeneration (Cooper et al., 2005).

To first test for lethality, embryos were treated at 4 days post-fertilization (dpf) with different concentrations of **2b** (10–50  $\mu$ M)



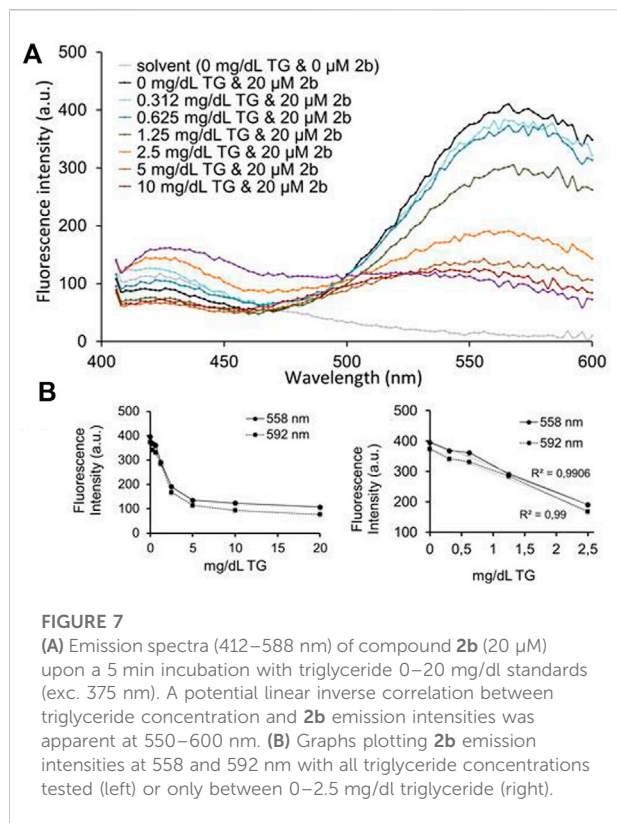


FIGURE 7

(A) Emission spectra (412–588 nm) of compound **2b** (20  $\mu$ M) upon a 5 min incubation with triglyceride 0–20 mg/dL standards (exc. 375 nm). A potential linear inverse correlation between triglyceride concentration and **2b** emission intensities was apparent at 550–600 nm. (B) Graphs plotting **2b** emission intensities at 558 and 592 nm with all triglyceride concentrations tested (left) or only between 0–2.5 mg/dL triglyceride (right).

for increasing time (4–16 h) ( $n \geq 30$  fish/treatment,  $N = 5$ ). No cellular or whole organism toxicity was observed for any **2b** treatment, with 100% viability being obtained at 6 dpf, even with the higher dose tested (50  $\mu$ M).

Lambda scans of embryos treated with **2b** showed that the fluorophore penetrated deeply into the embryonic tissues (40  $\mu$ m) and differentially stained its cells (Figure 6), as previously observed for the mammalian cell cultures (Figures 3–5).

Muscle cells were easily distinguished in **2b** counterstained embryos, with the fluorophore emitting in the green spectral region (Figure 6, arrows). Another easily identifiable structure was the central canal (Figure 6, “cc”), with the fluorophore emitting in the yellow/red -spectral region. Compound **2b** also stained in yellow/red the bone/cartilaginous tissue and was excluded from the notochord region (Figure 6, “nc”). At the single cell level, the fluorophore signal was absent or much reduced in the nuclei, allowing for the quick identification of tissues, such as muscle with clearly visible multinuclear cells (Figure 6, arrows).

## Compound **2b** application to triglyceride quantification

Given the fluorophores’ preference to stain hydrophobic structures and lipids, we explored other applications for **2b**,

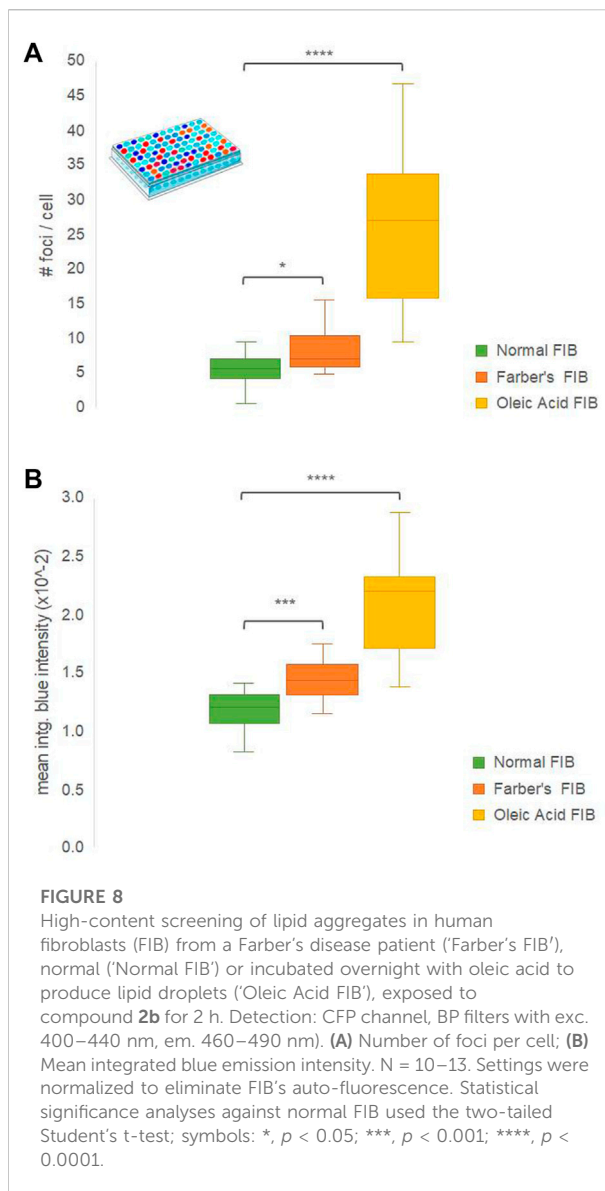


FIGURE 8

High-content screening of lipid aggregates in human fibroblasts (FIB) from a Farber's disease patient ('Farber's FIB'), normal ('Normal FIB') or incubated overnight with oleic acid to produce lipid droplets ('Oleic Acid FIB'), exposed to compound **2b** for 2 h. Detection: CFP channel, BP filters with exc. 400–440 nm, em. 460–490 nm). (A) Number of foci per cell; (B) Mean integrated blue emission intensity.  $N = 10$ –13. Settings were normalized to eliminate FIB's auto-fluorescence. Statistical significance analyses against normal FIB used the two-tailed Student's t-test; symbols: \*,  $p < 0.05$ ; \*\*\*,  $p < 0.001$ ; \*\*\*\*,  $p < 0.0001$ .

namely in the detection and quantification of triglycerides in liquid samples (Figure 7).

A triglyceride standard curve was established, to which compound **2b** was added for 5 min. The fluorophore was excited at 375 nm and the 412–600 nm emission recorded in a microplate reader. Figure 7A shows **2b** emission spectra in the presence of increasing triglyceride concentrations. In the blue region of the spectra, **2b** emission intensities varied, but not linearly increased with triglycerides concentration. However, in the green-yellow region of the spectrum a decrease in the **2b** emission intensity occurred with increasing triglycerides concentration. A zone of inverse correlation was visible between 0 and 2.5–5.0 mg  $\text{dl}^{-1}$  triglyceride, for the 550–600 nm emission interval. Emissions at 558 and 592 nm were plotted against triglyceride concentrations (Figure 7B),



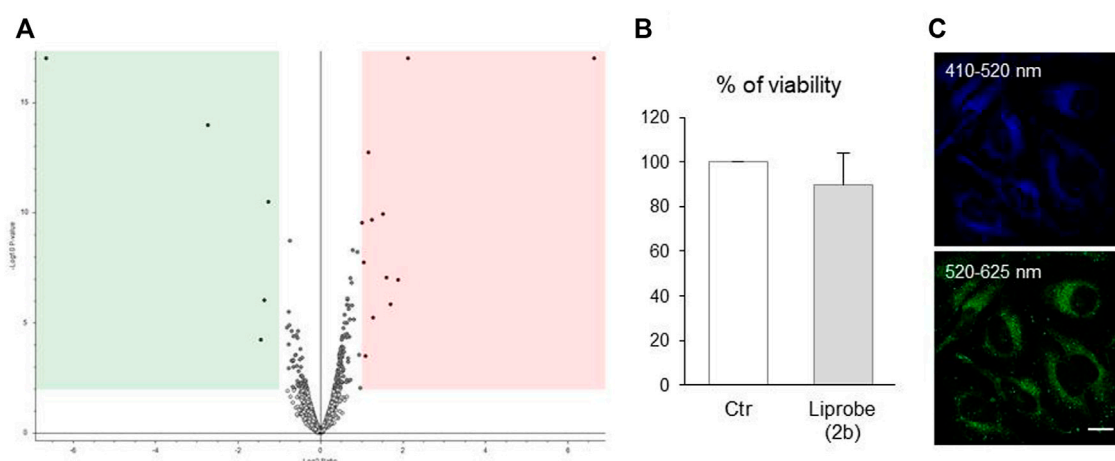


**FIGURE 9**

Compound 2b is inert for living cells and stays in culture for up to 3 days **(A)** Volcano plot with the distribution of proteins detected by mass spectrometry analysis in human fibroblasts, exposed or not to 2b for 24 h, exhibits few differences between the cells' proteomes. After an initial 2 h incubation of HeLa cells with 20  $\mu\text{M}$  2b, **(B)** the fluorophore had no significant effects on the cells' viability (resazurin metabolic assay,  $N = 3$ ), and was still visible in cells after 3 days (confocal microphotographs; exc. 405 nm; em. indicated on the photographs; bar, 10  $\mu\text{m}$ ).

particularly the 0–2.5  $\text{mg dl}^{-1}$  triglyceride range. An inverse correlation was visible for both 558 and 592 nm emission wavelengths, with a correlation ( $R^2$ ) of 0.99. Correlations were of 0.92 (for 558 nm) and 0.93 (for 592 nm) in the 0–5.0  $\text{mg dl}^{-1}$  triglyceride interval (not shown).

These data confirm that, within this linearity range, compound 2b is as a highly sensitive probe to quantify the concentration of triglycerides in liquid samples. Unfortunately, no correlation between the emission of 2b and the triglyceride content of human plasma samples was apparent, due to interferences of undetermined plasma structures in the recorded emission interval (data not shown).

## Compound 2b in cell-based high-content screens for lipidosis pre-diagnosis

Early detection of lipid-based disorders is highly important, as well as the study of new therapeutic approaches for these diseases is. To assess the adequacy of 2b as a probe for pre-diagnosis of lipidosis, Farber's disease was used as example. Inherited Farber's lipogranulomatosis (MIM 228000) is an autosomal recessive neurodegenerative lysosomal disease caused by mutations in the *ASAHI* gene that lead to a deficient acid ceramidase. As a result, ceramide accumulates in lysosomes of several cell types (Yu et al., 2018). The most common method for Farber's disease definitive diagnosis is the determination of acid ceramidase activity using cultured patient fibroblasts. A fluorescent non-molecular screening of the lipidic load of these patient fibroblasts, based on cellular high content screening assays, would be an important add on as a fast and low-

cost pre-diagnostic tool for Farber's disease and other lipid-based disorders.

High content screening assays were performed, testing the capacity of 2b to differentially stain fibroblasts in three conditions: normal fibroblasts (negative control), Farber's fibroblasts (tested condition) and fibroblasts pre-incubated with oleic acid (positive control). All three conditions were randomly distributed over a 96-well plate and the 2b fluorescence in the different wells was recorded in the blue-region. Results are depicted in Figure 8, where the number of lipid aggregates blue-stained foci per cell (Figure 8A) and their mean integrated blue intensity (Figure 8B) are plotted for the three conditions.

A consistent tendency was found for the three conditions in both graphs, where the number of 2b blue foci and their mean integrated blue intensity was significantly increased for Farber's fibroblasts when compared to control ones, and even more increased in normal fibroblasts incubated overnight with oleic acid. This is expected, since oleic acid is more hydrophobic than ceramide, and 2b emits with higher intensity in the blue region in more apolar environments. Compound 2b was also able to blue stain ceramide breakdown products (Supplementary Figure S6 micrographs).

These data confirmed that fluorophore 2b is a reliable option for a fast and cheap pre-diagnostic of Farber's disease by high content screening since the emission blue-shift was sufficient to detect the increase in ceramide load, demonstrating the ability to discern between normal and Farber's disease human fibroblasts (Figure 8). Furthermore, the remarkable results with the oleic acid lipid droplets suggest that 2b value in high content screening cell-based pre-diagnostics or drug screening even increases for other metabolic diseases related to the accumulation of lipids with hydrophobicity indexes higher than ceramide.

## Compound 2b (“Liprobe”) as an inert vital dye for long-term cellular imaging

Since a vital dye should stay in the cell for a long time without hindering the cellular metabolism or impacting other important cellular processes, the biological inertia of **2b** (named “Liprobe”) was studied using proteomic, viability and imaging assays (Figure 9).

Human fibroblasts were incubated with **2b** for 24 h, and its effect on the cellular pathways evaluated by mass spectrometry (nano LC-MS/MS). The proteome of stained and non-stained cells was compared, with the resulting volcano plot graph (Figure 9A) showing the distribution of the detected proteins and their relative abundance in **2b** stained cells. Out of the more than 3,000 proteins identified, only 17 proteins (*ca.* 0.5% of the cellular proteome) were found de-regulated: 5 proteins down-regulated (Figure 9A green area) and 12 proteins up-regulated (pink area). Only one of these proteins (sphingomyelin phosphodiesterase 4) relates to lipid metabolism, and its high values are based on the quantification of only two unique peptides. Hence, **2b** did not alter significantly any cellular pathway.

The long-term maintenance and fluorescence of **2b** in cells, and its long-term effects on the cells’ viability, were also assessed. Confirming its innocuous character, after an initial 2 h incubation of HeLa cells with 20  $\mu$ M Liprobe, the cells’ metabolism was not significantly altered 3 days later (Figure 9B). The fluorophore was still visible in cells after 3 days, emitting in the green and blue (Figure 9C). The value of Liprobe as a vital dye for long-term cellular imaging was thus established.

## Conclusion

A family of new fluorophores relevant for live imaging has been reported and thoroughly characterized. Their synthesis is straightforward and scalable, and further modifications may easily be introduced. In the molecules bearing a cyclic core, the fluorophore with chloride substituents is the best for a variety of biological and biomedical staining procedures. It is permeable to the live cell membrane and not toxic to cells or zebrafish embryos. Furthermore, it does not affect the cell metabolism or proteome and, thus, can be used as a vital dye.

In cells, the cyclic-core fluorophore (“Liprobe”) preferentially localizes in the lipidic structures, such as lipid droplets and pathological lipid aggregates. Liprobe can be used in high content screening, for fast and cheap pre-diagnosis of lipidosis, such as Farber’s disease, discriminating between normal and Farber disease human fibroblasts. It has potential to be used in the pre-diagnosis and drug screening of other metabolic disorders of increased lipid load, particularly

those pertaining the accumulation of highly hydrophobic lipids. Liprobe is, thus, a valuable alternative to commercially available molecular probes for live cell imaging and lipid aggregates’ detection. We are currently working on introducing peripheral modifications to increase its brightness, tune its emission color and modify its selectivity.

## Data availability statement

The original contributions presented in the study are included in the article/Supplementary Material, further inquiries can be directed to the corresponding authors.

## Ethics statement

The animal study was reviewed and approved by Stanford University Institutional Animal Care and Use Committee.

## Author contributions

SG, JR, and AS designed the structures of the molecules, SG synthesized and characterized them. SV designed and coordinated the biological experiments, with the help of RN, MA, RD, FC, and SG. RN, MA, RD, FC, and SV performed the cell biology experiments and AM designed and performed the zebrafish experiments. MA and AM helped to perform the oleic acid and the HCS assays, respectively. SV, RNS, and SG analyzed all the data, compiled the figures and wrote the manuscript. All authors reviewed the manuscript.

## Funding

This work was supported by Portuguese Fundação para a Ciência e a Tecnologia (FCT) via the CICECO-Aveiro Institute of Materials (UID/CTM/50011/2013, UIDB/50011/2020 and UIDP/50011/2020), QOPNA (UID/QUI/00062/2019), LAQV-REQUIMTE (UIDB/50006/2020), Institute for Biomedicine iBiMED (UID/BIM/04501/2013, UID/BIM/04501/2019 - POCI-01-0145-FEDER-007628), by Centro 2020 and Portugal 2020, and by the European Union (FEDER program) via R. Nunes da Silva post-Doctoral fellow grant (BPD/UI98/6327/2018) from the pAGE project (CENTRO-01-0145-FEDER-000003). SG is supported by national funds (OE), through FCT, I.P., in the scope of the framework contract foreseen in the numbers 4, 5, and 6 of the article 23, of the Decree-Law 57/2016, of August 29, changed by Law 57/2017, of July 19. AM was supported by the NMSS grant RG-1707-28694 attributed to William S. Talbot.

## Conflict of interest

The authors declare that the research was conducted in the absence of any commercial or financial relationships that could be construed as a potential conflict of interest.

## Publisher's note

All claims expressed in this article are solely those of the authors and do not necessarily represent those of their affiliated

organizations, or those of the publisher, the editors and the reviewers. Any product that may be evaluated in this article, or claim that may be made by its manufacturer, is not guaranteed or endorsed by the publisher.

## Supplementary material

The Supplementary Material for this article can be found online at: <https://www.frontiersin.org/articles/10.3389/fphot.2022.963778/full#supplementary-material>

## References

- Adams, K. F., Schatzkin, A., Harris, T. B., Kipnis, V., Mouw, T., Ballard-Barbash, R., et al. (2006). Overweight, obesity, and mortality in a large prospective cohort of persons 50 to 71 Years old. *N. Engl. J. Med. Overseas. Ed.* 355, 763–778. doi:10.1056/nejmoa055643
- Allen, F. H., Kennard, O., Watson, D. G., Brammer, L., Orpen, A. G., Taylor, R., et al. (1987). Tables of bond lengths determined by X-ray and neutron diffraction. Part 1. Bond lengths in organic compounds. *J. Chem. Soc. Perkin Trans. 2*, 1. doi:10.1039/p2987000001
- Brouwer, A. M. (2011). Standards for photoluminescence quantum yield measurements in solution (IUPAC Technical Report). *Pure Appl. Chem.* 83, 2213–2228. doi:10.1351/pac-rep-10-09-31
- Cambridge Crystallographic Data Centre. Crystallographic data (excluding structure factors) for the structures here reported have been deposited with the Cambridge Crystallographic Data Centre as supplementary publication No. CCDC 1042558-1042559. Data can be obtained free of charge at [www.ccdc.cam.ac.uk/conts/retrieving.html](http://www.ccdc.cam.ac.uk/conts/retrieving.html) (or from the Cambridge Crystallographic Data Centre, e-mail: deposit@ccdc.cam.ac.uk).
- Camões, F., Islinger, M., Guimarães, S. C., Kilaru, S., Schuster, M., Godinho, L. F., et al. (2015). New insights into the peroxisomal protein inventory: Acyl-CoA oxidases and -dehydrogenases are an ancient feature of peroxisomes. *Biochimica Biophysica Acta - Mol. Cell Res.* 1853, 111–125. doi:10.1016/j.bbamcr.2014.10.005
- Collot, M., Fam, T. K., Ashokkumar, P., Faklaris, O., Galli, T., Danglot, L., et al. (2018). Ultrabright and fluorogenic probes for multicolor imaging and tracking of lipid droplets in cells and tissues. *J. Am. Chem. Soc.* 140, 5401–5411. doi:10.1021/jacs.7b12817
- Cooper, M. S., Szeto, D. P., Sommers-Herivel, G., Topczewski, J., Solnica-Krezel, L., Kang, H. C., et al. (2005). *Dev. Dyn.* 232, 359–368.
- Dang, D., Liu, H., Wang, J., Chen, M., Liu, Y., Sung, H. H. Y., et al. (2018). Highly emissive AIEgens with multiple functions: Facile synthesis, chromism, specific lipid droplet imaging, apoptosis monitoring, and *in vivo* imaging. *Chem. Mat.* 30, 7892–7901. doi:10.1021/acs.chemmater.8b03495
- Diaz, G., Melis, M., Batetta, B., Angius, F., and Falchi, A. M. (2008). Hydrophobic characterization of intracellular lipids *in situ* by Nile Red red/yellow emission ratio. *Micron* 39, 819–824. doi:10.1016/j.micron.2008.01.001
- Didier, P., Ulrich, G., Mély, Y., and Ziessel, R. (2009). Improved push-pull-push E-Bodipy fluorophores for two-photon cell-imaging. *Org. Biomol. Chem.* 7, 3639. doi:10.1039/b911587k
- Elias, P. M., Williams, M. L., Holleran, W. M., Jiang, Y. J., and Schmuth, M. J. (2008). Thematic review series: Skin lipids. Pathogenesis of permeability barrier abnormalities in the ichthyoses: Inherited disorders of lipid metabolism. *J. Lipid Res.* 49, 697–714. doi:10.1194/jlr.r800002-jlr200
- Fam, T. K., Klymchenko, A. S., and Collot, M. (2018). Recent advances in fluorescent probes for lipid droplets. *Mater. (Basel)* 11, 1768. doi:10.3390/ma11091768
- Galema-Boers, J. M. H., and Van Lennep, J. E. R. (2015). Dyslipidemia testing: Why, for whom and when. *Maturitas* 81, 442–445. doi:10.1016/j.maturitas.2015.05.012
- Gross, D. A., and Silver, D. L. (2014). Cytosolic lipid droplets: From mechanisms of fat storage to disease. *Crit. Rev. Biochem. Mol. Biol.* 49, 304–326. doi:10.3109/10409238.2014.931337
- Guieu, S., Rocha, J., and Silva, A. M. S. (2013). Supramolecular organization of bis(3-halo-4-dimethylaminobenzylidene)hydrazines. *J. Mol. Struct.* 1035, 1–5. doi:10.1016/j.molstruc.2012.09.012
- Hannun, Y. A., and Obeid, L. M. (2018). Sphingolipids and their metabolism in physiology and disease. *Nat. Rev. Mol. Cell Biol.* 19, 175–191. doi:10.1038/nrm.2017.107
- Holthuis, J. C. M., and Menon, A. K. (2014). Lipid landscapes and pipelines in membrane homeostasis. *Nature* 510, 48–57. doi:10.1038/nature13474
- J. R. Lakowicz (Editor) (2006). *Principles of fluorescence spectroscopy* (Boston, MA: Springer).
- Lee, S. C., Kang, N. Y., Park, S. J., Yun, S. W., Chandran, Y., Chang, Y. T., et al. (2012). Development of a fluorescent chalcone library and its application in the discovery of a mouse embryonic stem cell probe. *Chem. Commun.* 48, 6681. doi:10.1039/c2cc31662e
- Listenberger, L. L., Studer, A. M., Brown, D. A., and Wolins, N. E. (2016). *Current protocols in cell biology*, 71. Hoboken, NJ, USA: John Wiley & Sons, 4.31.1–4.31.14.
- Nunes da Silva, R., Costa, C. C., Santos, M. J. G., Alves, M. Q., Braga, S. S., Vieira, S. I., et al. (2019). Fluorescent light-up probe for the detection of protein aggregates. *Chem. Asian J.* 14, 859–863. doi:10.1002/asia.201801606
- Pischon, T., Nöthlings, U., and Boeing, H. (2008). Obesity and cancer. *Proc. Nutr. Soc.* 67, 128–145. doi:10.1017/s0029665108006976
- Serra, V. V., Camo, F., Vieira, S. I., Faustino, M. A. F., Tomé, J. P. C., Pinto, D. C. G. A., et al. (2009). *Acta Chim. Slov.* 56, 603–611.
- Tatenaka, Y., Kato, H., Ishiyama, M., Sasamoto, K., Shiga, M., Nishitoh, H., et al. (2019). Monitoring lipid droplet dynamics in living cells by using fluorescent probes. *Biochemistry* 58, 499–503. doi:10.1021/acs.biochem.8b01071
- Vaz, P. A. A. M., Rocha, J., Silva, A. M. S., and Guieu, S. (2016). Aggregation-induced emission enhancement in haloalchalcones. *New J. Chem.* 40, 8198–8201. doi:10.1039/c6nj01387b
- Walther, T. C., and Farese, R. V., Jr. (2012). Lipid droplets and cellular lipid metabolism. *Annu. Rev. Biochem.* 81, 687–714. doi:10.1146/annurev-biochem-061009-102430
- WHO (2002). “Quantifying selected major risks to health,” in *The world health report 2002 - reducing risks, promoting healthy life* (Geneva: WHO). Chapter 4.
- Yakimanski, A. V., Kolb, U., Matveeva, G. N., Voigt-Martin, I. G., and Tenkovtsev, A. V. (1997). The use of structure analysis methods in combination with semi-empirical quantum-chemical calculations for the estimation of quadratic nonlinear optical coefficients of organic crystals. *Acta Crystallogr. A* 53, 603–614. doi:10.1107/s010876739601570x
- Yu, F. P. S., Amintas, S., Levade, T., and Medin, J. A. (2018). Acid ceramidase deficiency: Farber disease and SMA-PME. *Orphanet J. Rare Dis.* 13, 121. doi:10.1186/s13023-018-0845-z



## OPEN ACCESS

## EDITED BY

Verónica de Zea Bermudez,  
University of Trás-os-Montes and Alto  
Douro, Portugal

## REVIEWED BY

Thibaud Coradin,  
UMR7574 Laboratoire de Chimie de la  
Matière Condensée de Paris (LCMCP),  
France  
Rajapandiyar Panneerselvam,  
SRM University, India

## \*CORRESPONDENCE

Tito Trindade,  
tito@ua.pt

## SPECIALTY SECTION

This article was submitted to Inorganic  
Chemistry,  
a section of the journal  
Frontiers in Chemistry

RECEIVED 03 August 2022

ACCEPTED 06 September 2022

PUBLISHED 27 September 2022

## CITATION

Estrada AC, Daniel-da-Silva AL, Leal C,  
Monteiro C, Lopes CB, Nogueira HS,  
Lopes I, Martins MJ, Martins NCT,  
Gonçalves NPF, Fateixa S and Trindade T  
(2022), Colloidal nanomaterials for  
water quality improvement  
and monitoring.  
*Front. Chem.* 10:1011186.  
doi: 10.3389/fchem.2022.1011186

## COPYRIGHT

© 2022 Estrada, Daniel-da-Silva, Leal,  
Monteiro, Lopes, Nogueira, Lopes,  
Martins, Martins, Gonçalves, Fateixa and  
Trindade. This is an open-access article  
distributed under the terms of the  
[Creative Commons Attribution License](#)  
(CC BY). The use, distribution or  
reproduction in other forums is  
permitted, provided the original  
author(s) and the copyright owner(s) are  
credited and that the original  
publication in this journal is cited, in  
accordance with accepted academic  
practice. No use, distribution or  
reproduction is permitted which does  
not comply with these terms.

# Colloidal nanomaterials for water quality improvement and monitoring

Ana C. Estrada<sup>1</sup>, Ana L. Daniel-da-Silva<sup>1</sup>, Cátia Leal<sup>1</sup>,  
Cátia Monteiro<sup>2</sup>, Cláudia B. Lopes<sup>1</sup>, Helena I. S. Nogueira<sup>1</sup>,  
Isabel Lopes<sup>2</sup>, Maria J. Martins<sup>1</sup>, Natércia C. T. Martins<sup>1</sup>,  
Nuno P. F. Gonçalves<sup>1</sup>, Sara Fateixa<sup>1</sup> and Tito Trindade<sup>1\*</sup>

<sup>1</sup>Department of Chemistry and CICECO-Aveiro Institute of Materials, University of Aveiro, Aveiro, Portugal, <sup>2</sup>Department of Biology and CESAM-Centre of Environmental and Marine Studies, University of Aveiro, Aveiro, Portugal

Water is the most important resource for all kind forms of live. It is a vital resource distributed unequally across different regions of the globe, with populations already living with water scarcity, a situation that is spreading due to the impact of climate change. The reversal of this tendency and the mitigation of its disastrous consequences is a global challenge posed to Humanity, with the scientific community assuming a major obligation for providing solutions based on scientific knowledge. This article reviews literature concerning the development of nanomaterials for water purification technologies, including collaborative scientific research carried out in our laboratory (nanoLAB@UA) framed by the general activities carried out at the CICECO-Aveiro Institute of Materials. Our research carried out in this specific context has been mainly focused on the synthesis and surface chemical modification of nanomaterials, typically of a colloidal nature, as well as on the evaluation of the relevant properties that arise from the envisaged applications of the materials. As such, the research reviewed here has been guided along three thematic lines: 1) magnetic nanosorbents for water treatment technologies, namely by using biocomposites and graphite-like nanoplatelets; 2) nanocomposites for photocatalysis (e.g., TiO<sub>2</sub>/Fe<sub>3</sub>O<sub>4</sub> and POM supported graphene oxide photocatalysts; photoactive membranes) and 3) nanostructured substrates for contaminant detection using surface enhanced Raman scattering (SERS), namely polymers loaded with Ag/Au colloids and magneto-plasmonic nanostructures. This research is motivated by the firm believe that these nanomaterials have potential for contributing to the solution of environmental problems and, conversely, will not be part of the problem. Therefore, assessment of the impact of nanoengineered materials on

**Abbreviations:** AOX, adsorbable organic halides; CEC, contaminant of emerging concern; GNP, graphite-like nanoplatelets; GO, graphene oxide; ICPTES, 3-isocyanatopropyl triethoxysilane; LCP, liquid crystal polymer; MF, microfiltration; NF, nanofiltration; NP, nanoparticle; PA, polyamide; PANI, polyaniline; POM, polyoxometalate; PS, poly(styrene); PTFE, poly(tetrafluoroethylene); PVDF, poly(vinyl fluoride); rGO, reduced graphene oxide; RhB, Rhodamine B; SDG, Sustainable Development Goal; SEM, Scanning electron microscopy; SERS, surface enhanced Raman scattering; UN, United Nations; SWCNT, single-walled carbon nanotube; TCE, technology-critical element; TEM, Transmission electron microscopy; TEOS, tetraethylorthosilicate; UF, ultrafiltration.

eco-systems is important and research in this area has also been developed by collaborative projects involving experts in nanotoxicity. The above topics are reviewed here by presenting a brief conceptual framework together with illustrative case studies, in some cases with original research results, mainly focusing on the chemistry of the nanomaterials investigated for target applications. Finally, near-future developments in this research area are put in perspective, forecasting realistic solutions for the application of colloidal nanoparticles in water cleaning technologies.

#### KEYWORDS

colloids, nanomaterials, surface chemistry, inorganic nanoparticles, water quality

## 1 Introduction

Research on colloidal inorganic nanomaterials has developed considerably in the last decades. Taking the last century transition period as a yearly timeline reference, it is possible to trace to about that period the development of important chemical methods for the synthesis of quantum dots, magnetic metal oxides and metals, just to mention a few relevant classes of nanomaterials (Brus, 1984; Ekimov et al., 1985; Bawendi et al., 1990; Steigerwald and Brus, 1990; Schmid, 1992; Weller, 1993; Alivisatos, 1996; Leslie-Pelecky and Rieke, 1996; López-Quintela and Rivas, 1996; Trindade and O'Brien, 1996; Weller, 1998; Manna et al., 2000; Peng and Peng, 2001; Trindade et al., 2001; Esteves and Trindade, 2002; Frey et al., 2009; Teitelboim et al., 2016). Associated to the development of synthetic methods of nanosized colloids has emerged a new paradigm in inorganic synthesis concerning the control of size and shape-dependent intrinsic properties of colloidal particles (Jun et al., 2006; Grzelczak et al., 2008; Tao et al., 2008; Xia et al., 2009; Guerrero-Martínez et al., 2011; Lim and Xia, 2011; Watt et al., 2013; Zhang et al., 2013). Indeed, it is at the nanoscale that several crystalline solids show the transition of the bulk-type behaviour to a cluster-like behaviour as particle size decreases, which scales with a critical dimension identified for that type of solid. Hence, it is now routine to employ chemical methods for preparing semiconductor nanocrystals, whose band gap can be tuned by adjusting the particle size distribution below a certain threshold defined as the Bohr radius of that semiconductor or to synthesise superparamagnetic iron oxides whose dimensions are below the size of Weiss-domain. The control of the optical, electronic and magnetic properties of materials using size (and shape) as additional parameters of chemically controlled characteristics of particles has important consequences in advancing the frontiers of knowledge and on new applications of materials, which is one of the reasons, among others, for which Chemistry is regarded as a central science also in Nanotechnology (Whitesides, 2005; Yina and Talapin, 2013). Furthermore, the properties, manipulation, processing and applications of colloidal inorganic nanoparticles are markedly dependent on their surface chemistry, which has been an active

research topic in the last 2 decades, including in our laboratory (Yin and Alivisatos, 2005; Boles et al., 2016; Daniel-da-Silva and Trindade, 2021).

The unique properties of inorganic nanoparticles make them suitable for applications in diverse areas, which include nanomedicine (e.g., drug delivery, bioimaging, phototherapies) (Lin et al., 2007; Sokolova and Epple, 2008; Trindade and Daniel da Silva, 2011; Vega-Vásquez et al., 2020; Wang and Mattoussi, 2020; Ray and Bandyopadhyay, 2021), energy (e.g., solar cells, lightning) (Kamat, 2008; Cheng et al., 2016; Kumar et al., 2017; Chen et al., 2018; Choe et al., 2021), environment (e.g., water and air purification (Theron et al., 2008; Kumari et al., 2019; Weon et al., 2019; Wadhawan et al., 2020; Li et al., 2021), greenhouse gases capture (Kumar et al., 2020; Cheng et al., 2021), sustainable technologies (e.g., catalysis, biological synthesis) (Polshettiwar and Varma, 2010; Dutta et al., 2015; Kumari et al., 2020; Jeevanandam et al., 2022; Liu et al., 2022; Wani and Suresh, 2022), among many others. These endeavours require transdisciplinary approaches, among which the synthesis and surface modification of the materials are usually regarded at the upstream in the supply chain of functional materials for such devices and processes. A main aspect of our late research has been the exploration of chemical methods for modifying the surface of inorganic nanoparticles, as shown below with distinct systems. Mostly of these methods rely on colloid chemistry of inorganic particles establishing important bridges to other scientific domains, such as polymer chemistry and coordination chemistry. In this context, a series of functional inorganic nanoparticles have been investigated, depending on the target application.

Several water cleaning technologies have been developed, including adsorption, photocatalysis and membrane filtration. Adsorption is an efficient method, very attractive due to the affordable cost and easy operation. Photocatalysis enables water treatment in an eco-friendly manner because solar radiation can be used as an energy source. However, complete mineralization of the pollutants is challenging and may result in oxidation by products formation. The interest in membrane filtration technologies has grown significantly in the last years, but it still faces challenges in membrane fouling, concentrate



disposal and high energy consumption. Together with remediation technologies, preventing measures should be also implemented namely by developing water quality monitoring protocols, that can be easily accessed in different regions of the globe. As an example of this approach, several sensors have been investigated, namely envisaging the optical detection of water contaminants using low-cost and disposable substrates. In this work, we focus on the research of colloidal inorganic nanomaterials and their composites, aiming at nanotechnologies for water cleaning and quality monitoring, which has been a common ground for some of the research carried out in our laboratory during the past years.

## 2 Nanomaterials for water cleaning nanotechnologies

### 2.1 General framework

Water and wastewater management is a major global concern considering an ever-increasing population, Human-driven water pollution and the scarcity of freshwater resources. Specifically, water pollution is critical since it may cause negative impacts on ecosystems and Human health, and it can as well adversely impact economic growth and the social perspectives of societies. Considering this framework, the Organization of United Nations (UN) acknowledged that the availability of good water quality is vital for all living creatures and must be considered a worldwide challenge for this century. The preface of the last edition of the “Guidelines for drinking-water quality” published by the World Health Organization begins with the undisputable sentence: “Access to safe drinking-water is essential to health, a basic human right and a component of effective policy for health protection” (WHO, 2022). Among the seventeen Sustainable Development Goals agreed by world leaders, the Goal 6 (SDG 6) aims to ensure access and sustainable use of water for everyone, while SDG 15 aims to protect, restore and promote sustainable use of ecosystems. Water contamination is a global problem affecting populations and ecosystems, putting at risk such goals, namely by limiting the access to safe drinking-water of large populations worldwide. The prioritisation of this issue has increased in the past decades due to several factors, which includes accentuated water scarcity due to climate changes and increasing levels of water contaminants of emerging concern (CEC). The complexity of this global problem requires actions and decisions at very diverse levels, engaging different actors, from the ordinary citizen to policy decision makers and, with obvious social responsibility, the scientific community.

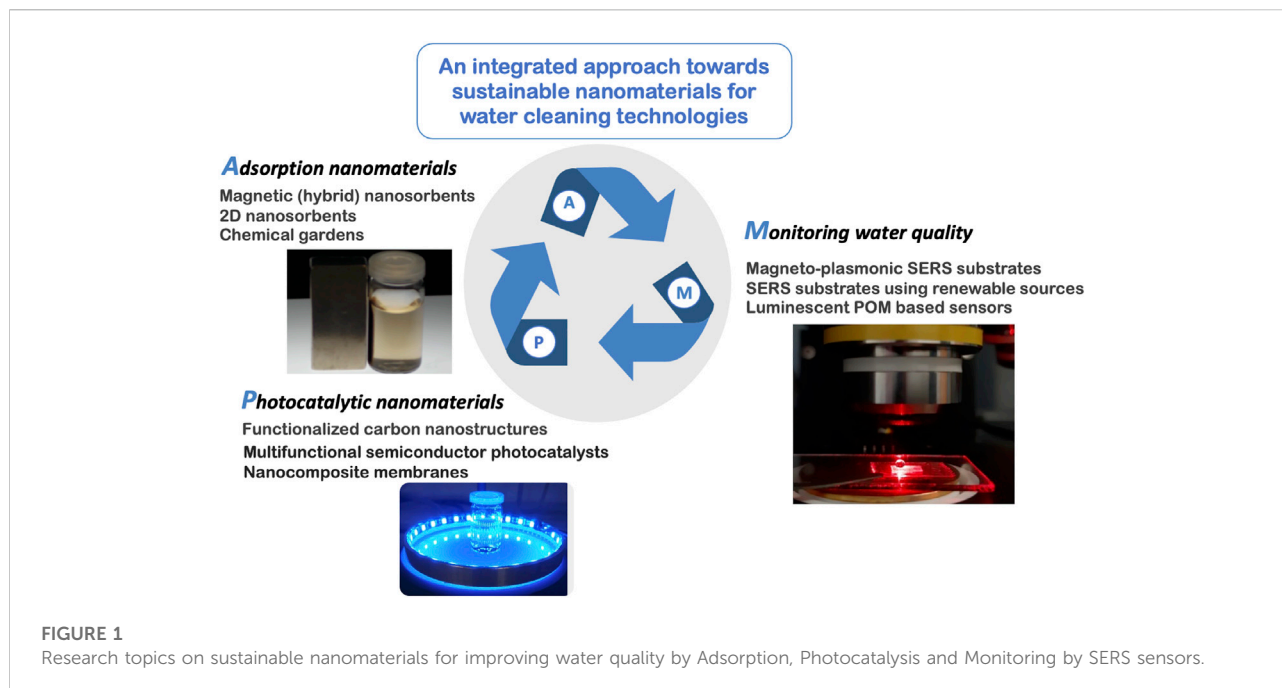
In this context, several nanotechnologies have been developed with potential for implementation and contribute for water remediation and quality improvement. Most of these procedures rely on the use of nanoengineered materials, which have been surface modified accordingly to the envisaged application and the target contaminants to be eliminated.

Probably future developments in this area should be better considered as complementary to conventional water cleaning technologies, which for several purposes are quite effective but less so for the elimination of CEC in certain aqueous environments. Also, water quality monitoring technologies that are easily implemented and communicated in different parts of the globe, including in remote regions, are regarded as important advancements, namely because they value prevention behaviour in relation to remediation practices.

The following article sections are built upon research lines that converge in providing colloidal nanomaterials for water quality improvement and monitoring. Figure 1 illustrates these thematic lines, which have been investigated in our research activity during the past years, as well as new research lines. Rather than providing an exhaustive literature survey on each topic, we favour the communication of our own perspectives on nanomaterials developments that have a great deal to contribute for water cleaning nanotechnologies as identified in illustrative cases of study. Ideally, clean water for all should be supported in sustainable and clean technologies, favouring water contamination prevention rather than remediation measures, but in fact contaminated water is a real problem and purification nanotechnologies can contribute for its solution. The next paragraph provides a summary of topics approaching both general strategies, by following Figure 1 as an illustrative guide.

Adsorption techniques applied to water purification are well-established and carbon activated sorbents are ubiquitous in several procedures. However, the removal of certain water pollutants can be ineffective by using such processes, which requires non-conventional approaches. Surface modified nanosorbents for magnetic separation technologies and multifunctional nanostructures for photocatalysis are examples of nanomaterials that might have impact on new technologies for CEC removal or its prevention. Under this scope, chemical gardens have also attracted our attention. These are self-organizing structures created by nonequilibrium processes and have been known since the discoveries made by Johann Glauber (1646). Still, chemical gardens hide new possibilities for technological applications, including selective adsorption-desorption processes. It is known that these micro- or nanotubules have internal reactive surfaces whose chemistry can be explored to develop sorbents for CEC.

Contexts of applications are diverse but typically might include water treatment stations of industries, hospitals, and municipalities. These applications are clearly dependent on the functionality and associated efficacy of the nanoengineered materials, for which surface chemistry plays a major role. The presence of CEC in water, even in vestigial amounts, poses serious threats to human health and jeopardizes the access of populations to safe drinking-water. Thus, not only water purification methods effective for pollutants' diminutive amounts are required, but accessible and sensitive sensors for water quality monitoring would be a step forward for



management of water supplies. Nanotechnology provides a myriad of possibilities for fabricating reliable sensors, which ideally should also be low-cost and user friendly. Together with technologies based on the internet of things, these sensors might offer on-time answers for water contamination events which might occur in remote zones. As it happens for water remediation and purification technologies, the nanosensors' performance depends on the materials used, namely on their selectivity and nanoscale properties that can be explored for achieving lower detection limits in the field analysis. Optical sensors based on low-cost and versatile SERS substrates are among the most promising for several applications in this context. The risk-benefit balance of these nanomaterials in water cleaning technologies is crucial to decide on their practical use in real contexts. Studies on the assessment of the impact on health and environment of these materials have been carried out, providing a wealth of data that requires a critical and thoroughly analysis. Our research in this area has been mostly collaborative, in providing nanomaterials that have been found as promising for experts on nano- and eco-toxicology to assess, as is also illustrated in this work as an important part of research in this area.

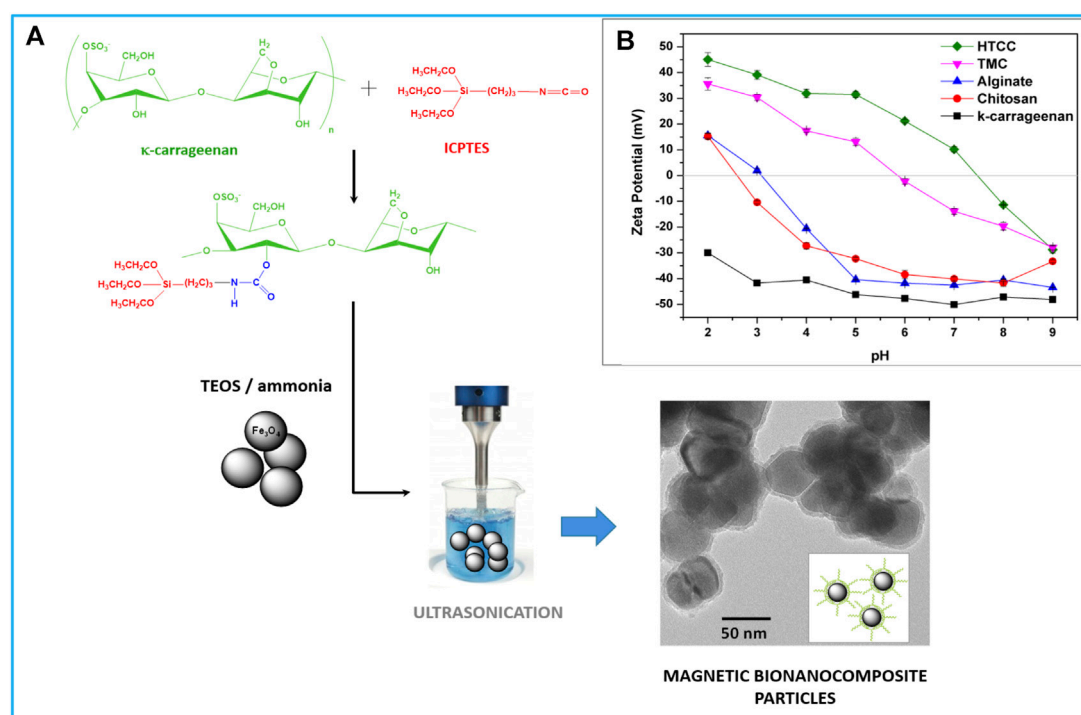
## 2.1 Functionalized magnetic nanosorbents

### 2.2.1 Biocomposite particles

Biopolymers, i.e., natural polymers produced by living organisms, are sustainable materials with low toxicity, abundant and available, whose structure contains functional

groups with an affinity towards diverse pollutants. The properties of biopolymers and their composites have prompted a focus on water treatment applications, namely as adsorbents for water decontamination (Nasrollahzadeh et al., 2021; Yaashikaa et al., 2022). One of the major issues with the adsorption-treatment process is the recovery of spent sorbents, which should be easy and cost-effective (Baskar et al., 2022). Combining biopolymers with magnetic iron oxide nanocrystals results in composites that are easily recovered using magnetic separation, making them very appealing for water treatment through adsorption (Abdel Maksoud et al., 2020; Soares et al., 2020). A rational modification of the surface of the magnetic nanocrystals with the biopolymer is necessary to attain pollutant specificity, high adsorption capacity and reusability. For example, covalent immobilization of the biopolymer onto the surface of the particles is critical to ensure the successful recycling and reuse of the biosorbents.

Our group has developed a method for preparing magnetic biosorbents that took in consideration the context above. The biopolymer is grafted onto a siliceous network that acts as a surface coating of  $\text{Fe}_3\text{O}_4$  nanoparticles during the encapsulation process, yielding an organic-inorganic hybrid shell enriched in the biopolymer component. The encapsulation encompasses the hydrolysis and condensation of a mixture of tetraethyl orthosilicate (TEOS), as the  $\text{SiO}_2$  precursor, and a silicon alkoxide derivative of the biopolymer, in the presence of colloidal magnetic particles. Figure 2A illustrates the preparation of the magnetic biosorbents using the polysaccharide  $\kappa$ -carrageenan, encompassing the derivatization of the biopolymer with a silane coupling agent functionalized

**FIGURE 2**

(A) Scheme illustrating the chemical route to prepare the silicon alkoxide derivative of the biopolymer *k*-carrageenan and the preparation of the magnetic biosorbents through coating the  $\text{Fe}_3\text{O}_4$  nanoparticles with the bio-hybrid siliceous shell; (B) Potential zeta values of magnetic biosorbents prepared using distinct biopolymers (HTCC -N-(2-hydroxypropyl)-3-trimethylammonium chitosan; TMC- trimethylchitosan).

with isocyanate groups (3-isocyanatopropyl triethoxysilane-ICPTES) and the subsequent coating of the  $\text{Fe}_3\text{O}_4$  nanoparticles. This method originates more robust coatings and with a higher degree of functionalization when compared to the conventional techniques of non-covalent coating and surface-grafting approach, which is desirable to obtain reusable sorbents with improved adsorption capabilities. A series of magnetic biosorbents have been prepared by using this route, from polysaccharides with distinct ionic character and variable chemical functionalities, which were efficient in the uptake of target pharmaceuticals (Soares et al., 2016; Soares et al., 2019a; Soares et al., 2019b; Soares et al., 2019c; Soares et al., 2021b; Soares et al., 2022), pesticides (Fernandes et al., 2017; Soares et al., 2021a), organic dyes (Soares et al., 2017b), and non-polar organic solvents from water (Soares et al., 2017a). The biopolymer selected allows the preparation of magnetic nanosorbents with various chemical functionalities and tunable surface charge (Figure 2B). This is a crucial step to attain high adsorption capacity because electrostatic interactions between oppositely charged groups of the biopolymer and the pollutant species play an essential role in their adsorption. Nevertheless, other interactions, such as H-bonding and hydrophobic interactions, may also contribute to the adsorption process (Crini et al., 2019; Badsha et al., 2021).

Assessing the adsorptive performance in conditions closest to the final application is of utmost importance in developing effective treatments. This assessment frequently involves testing the removal of the pollutant in trace concentrations in aqueous matrices of complex nature. In this context, magnetic biosorbents prepared from trimethyl chitosan-based decreased environmentally realistic concentrations of the pesticide glyphosate in spiked effluents of wastewater treatment plants up to 80%, demonstrating their potential application in real conditions (Soares et al., 2021a).

## 2.2.2 Carbon-based 2D materials

Carbon is one of the most abundant elements in the environment and human body (Rao et al., 2021), with the particularity of having an extraordinary ability to bind to other elements. Carbon has extensive allotropy but, until the eighties, few carbon allotropic forms were known, namely, diamond, graphite and fullerene (Kallumottakkal et al., 2021). Since then, many other allotropes have been discovered and produced, including ball shapes such as buckminsterfullerene and sheets such as graphene, opening a research window for a variety of carbon nanomaterials of distinct structural dimensionality.

Two-dimensional nanomaterials are considered the thinnest nanostructures among the different dimensional groups, and

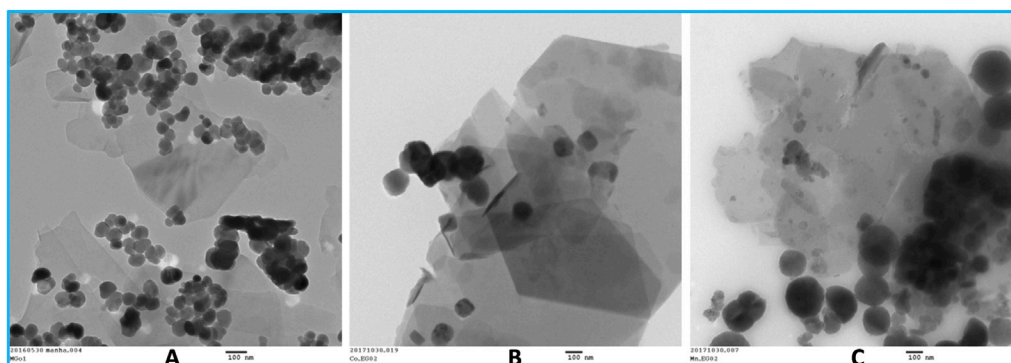


FIGURE 3

TEM images of nanocomposites: (A)  $\text{Fe}_3\text{O}_4/\text{GNPs}$ ; (B)  $\text{CoFe}_2\text{O}_4/\text{GNPs}$  and (C)  $\text{MnFe}_2\text{O}_4/\text{GNPs}$ .

contrary to bulk materials, have a high surface-area-to-volume ratio (Kallumottakkal et al., 2021). In the 2D nanostructures, the relative number of external to internal atoms is higher, and their different functions lead to a change in the behavior of 2D nanomaterials, in comparison to the other dimensional groups, conferring them a variety of unique physical, chemical, and electrical properties (Rafei-Sarmazdeh et al., 2019). Graphene is a 2D material with a hexagonal structure composed of  $\text{sp}^2$ -hybridized C atoms, where each carbon atom is covalently bound with each other in the same plane (Kallumottakkal et al., 2021). For water compatible applications, pristine graphene faces some problems such as poor solubility and agglomeration tendency (Joseph et al., 2021). To overcome these limitations, researchers have come up with a handful of techniques to synthesize structurally similar compounds, like graphene oxide (GO) and graphite-like nanoplatelets (GNP), which can be produced from carbon sources by simple top-down methods (Rao et al., 2021).

Our research group has been interested in exploring GNP for their adsorption capability and ability to enhance the adsorption capacity of various composites, with the aim of removing toxic metal ions from water and/or recovering valuable elements, such as technology critical elements. There has been great interest in this topic (Cardoso et al., 2019) because emerging key technologies are intrinsically dependent of a limited number of elements often termed by technology critical elements (TCE), which includes all lanthanoids and the platinum group elements (Pinto et al., 2021). GNP are a viable and inexpensive materials that can be used as stable substrates for preparing magnetic nanocomposites for water adsorption treatment, thus allowing their use in magnetic separation technologies, as already discussed in the previous section. The GNP are decorated with nanoparticles of spinel ferrites ( $\text{MFe}_2\text{O}_4$ ,  $\text{M} = \text{Fe, Mn, Co}$ ), thereby conferring ability for magnetic separation of the sorbents when exposed to an external magnetic gradient.

The magnetic nanostructures have been prepared by *in situ* alkaline hydrolysis or electrostatic assembly of particulates previously

synthesized. Figure 3 shows TEM images of spinel ferrites, with average sizes below 100 nm, attached onto GNP substrates. All materials quickly approach saturation in the presence of an external magnetic field, and the estimated saturation magnetization, at 300 K, is about 45 emu/g for  $\text{Fe}_3\text{O}_4/\text{GNP}$  and 29 emu/g for the  $\text{CoFe}_2\text{O}_4/\text{GNP}$  and  $\text{MnFe}_2\text{O}_4/\text{GNP}$  composites. As expected, these estimated saturation magnetization values are lower than the values of the respective spinel ferrites at room temperature ( $\text{Fe}_3\text{O}_4$  92 emu/g,  $\text{CoFe}_2\text{O}_4$  55 emu/g and  $\text{MnFe}_2\text{O}_4$  48 emu/g).

The  $\text{Fe}_3\text{O}_4/\text{GNP}$  nanocomposites were investigated to capture selected lanthanoids (La, Eu, and Tb), from unary and ternary solutions, and their performance was compared with the one observed for the isolated components ( $\text{Fe}_3\text{O}_4$  and GNPs) (Afonso et al., 2019). After a 24 h period of exposition of equal amounts of GNP,  $\text{Fe}_3\text{O}_4$  NPs and  $\text{Fe}_3\text{O}_4/\text{GNPs}$  to a ternary solution of La(III), Eu(III) and Tb(III), with an elemental concentration of 100  $\mu\text{g/L}$ , the results show distinct affinity between materials and elements, with the  $\text{Fe}_3\text{O}_4/\text{GNPs}$  composite showing better capability to remove the target elements from water than any of its counterparts (La: 4.7% (GNPs), 3.1% ( $\text{Fe}_3\text{O}_4$  NPs), and 15% ( $\text{Fe}_3\text{O}_4/\text{GNPs}$ ); Eu: 1.2% (GNPs), 0.2% ( $\text{Fe}_3\text{O}_4$  NPs) and 37.6% ( $\text{Fe}_3\text{O}_4/\text{GNPs}$ ); Tb: 0.2% (GNPs), 0.1% ( $\text{Fe}_3\text{O}_4$  NPs) and 35.0% ( $\text{Fe}_3\text{O}_4/\text{GNPs}$ )). The better performance of the nanocomposites can be explained by an increase of active sorption sites due to the introduction of oxygen moieties into the carbon lattice. Trivalent lanthanides are hard Lewis acids with strong chemical affinity for oxygen donors. More, the sorption process showed to be very dependent from solution pH, and only feasible for pH values higher than 5.2, which is the experimental isoelectric point of the composite (Afonso et al., 2019). Consecutive sorption and desorption cycles were also applied to ternary solutions of TCE (100  $\mu\text{g/L}$ ) and for the best experimental conditions studied (pH 7.5, 250 mg/L of  $\text{Fe}_3\text{O}_4/\text{GNPs}$ ) and using 0.1 M  $\text{HNO}_3$  as eluent solution. During the consecutive cycles, the recovery efficiency of the target elements ranged from 82 to 92% for La (III), 88–104%



for Eu (III) and 82–97% for Tb (III). These data elucidate that dilute nitric acid solution (0.1 mol/L  $\text{HNO}_3$ ) is an efficient eluent for the recovery of these elements from the magnetic composite. More, the capability of this nanostructure to remove the selected TCE from water was rarely affected since the values of the removal efficiency remained nearly constant during all cycles, also confirming the stability of the magnetic composite.

In other study,  $\text{Fe}_3\text{O}_4/\text{GNPs}$ ,  $\text{CoFe}_2\text{O}_4/\text{GNPs}$  and  $\text{MnFe}_2\text{O}_4/\text{GNPs}$  composites were investigated to capture mercury and arsenic, from unary and binary solutions. Among the toxic substances of anthropogenic and natural origin, these elements pose greatest threat to the environment, due to their non-degradable nature, severe toxicity and bioaccumulative character (Lopes et al., 2008; Tavares et al., 2020). Arsenic and Hg occupy the 1st and 3rd positions, respectively, on the list of priority hazardous substances of 2019 provided by the Agency for Substances and Toxic Diseases, and so their effective removal from water is a priority to achieve the SDG6 of United Nations. The pH dependency, of the sorption process using these magnetic nanostructures was assessed for the range 4–9. After a 24 h period of exposition of equal amounts of  $\text{MFe}_2\text{O}_4/\text{GNPs}$ , to unary solutions of As(III) (1000  $\mu\text{g/L}$ ) and Hg(II) (50  $\mu\text{g/L}$ ), the results showed that 1)  $\text{Fe}_3\text{O}_4/\text{GNPs}$  were the least effective for removing As(III) or Hg(II) and, 2) As(III) removal was higher for the  $\text{CoFe}_2\text{O}_4/\text{GNPs}$  at pH 7 (90.4%), while  $\text{MnFe}_2\text{O}_4/\text{GNPs}$  displayed higher efficiency to remove Hg(II) at pH 6 (90.6%). In binary solutions,  $\text{CoFe}_2\text{O}_4/\text{GNPs}$  showed more efficiency to As(III) with removal percentages near 90% in ultra-pure water and around 80% in tap water, while  $\text{MnFe}_2\text{O}_4/\text{GNPs}$  removed preferably Hg(II) (85%) in both matrices. Although the above nanocomposites were prepared by similar methods, those containing Co and Mn ferrites performed better than the  $\text{Fe}_3\text{O}_4/\text{GNPs}$  but on the other hand show more potential for metal leaching (Tavares et al., 2020). Indeed, the ferrites nanoparticles display different metal leaching (20–50% of Co, 20–30% of Mn, and <8% of Fe). The free Mn, Co, or Fe sites located at the surfaces of the respective ferrites could exchange with ions in solution, working as active sorption sites, and the different degree of leaching could also explain the different affinity toward the ions.

These studies highlight that magnetic graphite-like nanoplatelets composites can be explored as effective sorbents for different elements. The nanocomposites are prepared using a simple and environmentally friendly procedure, with potential for future application in the removal of toxic elements and/or in the recovery of valuable elements, such as TCE, from industrial or other water systems.

## 2.3 Nanocomposites for photocatalysis

### 2.3.1 Metal oxide nanophotocatalysts

$\text{TiO}_2$  has been the most used semiconductor photocatalyst for effluent treatment because it is relatively inexpensive, photostable over a wide range of pH and the photo-generated

hole-electron pairs are efficient in producing highly reactive oxygen species (Kubacka et al., 2012). In particular,  $\text{TiO}_2$  colloidal nanoparticles have several advantages because of their high surface-to-volume ratio, increased number of delocalized charge carriers over the surface, improved charge transport and lifetime afforded by their dimensional anisotropy, and efficient contribution to the separation of photo-generated holes and electrons (Wang et al., 2014). Previous studies have shown that adsorbable organic halides (AOX) produced in the bleaching treatment stage in pulp and paper mills, can be photodegraded under UV radiation by using  $\text{TiO}_2$  or  $\text{ZnO}$  photocatalysts (Yeber et al., 2000; Ugurlu and Karaoglu, 2009; Kumar et al., 2011). Typically, the metal oxides are dispersed in the effluent as colloids and, at the end of the treatment, the separation and recovery of the photocatalysts are required, which in practice is a costly task and also poses raises issues concerning their effective separation. As discussed below, the immobilization of the catalyst in active supports is a promising strategy, but for conventional immobilized systems there is usually less efficiency in photodegradation due to a reduction in the specific surface area of the catalyst (Li et al., 2009). Alternative strategies have been investigated, such as coupling  $\text{TiO}_2$  semiconducting phases to magnetic nanostructures, enabling magnetic separation of the hybrid photocatalysts without need additional downstream treatment processes. However, these strategies have been mostly tested in degrading dye pollutants in synthetic solutions (Li et al., 2009; Abbas et al., 2014; Gómez-Pastora et al., 2017). There is a lack of studies regarding the applicability of magnetic  $\text{TiO}_2$  hybrids in the treatment of real effluents, namely regarding photodegradation of AOX in samples from pulp and paper mills. The following paragraphs in this subsection describe our research on this scientific problem by using real effluents provided by an industrial unit localized in the Aveiro (Portugal) region.

First, the  $\text{TiO}_2$  photocatalysts were designed for their magnetic properties through the co-precipitation of magnetite ( $\text{Fe}_3\text{O}_4$ ) in the presence of P25  $\text{TiO}_2$ . Magnetic water-dispersible  $\text{TiO}_2$  nanostructures, with a magnetite content of 86 wt% (hybrid A) and 67 wt% (hybrid B), have been prepared by varying the reactants ratio. The ensuing hybrid nanostructures were composed of spheroidal magnetite  $12 \pm 2$  nm in diameter and a  $\text{TiO}_2$  nanoparticles ( $24 \pm 9$  nm), in a ratio 80/20 wt% of anatase/rutile phases. The  $\text{Fe}_3\text{O}_4/\text{TiO}_2$  hybrids were characterized by an absorption edge in the visible region, which is dominated by the  $\text{Fe}_3\text{O}_4$  adsorption whose direct band-gap energy is 2.27 eV. The magnetic  $\text{TiO}_2$  hybrids were then tested for degrading AOX compounds present in the effluent of the bleaching stage from Kraft pulp mills (pH = 2), under UV light irradiation in the presence of  $\text{H}_2\text{O}_2$  as the co-catalyst.

AOX photodegradation was observed regardless the amount of  $\text{TiO}_2$  content in the hybrid photocatalyst. Although the highest AOX removal was observed when using non-magnetic  $\text{TiO}_2$ , the



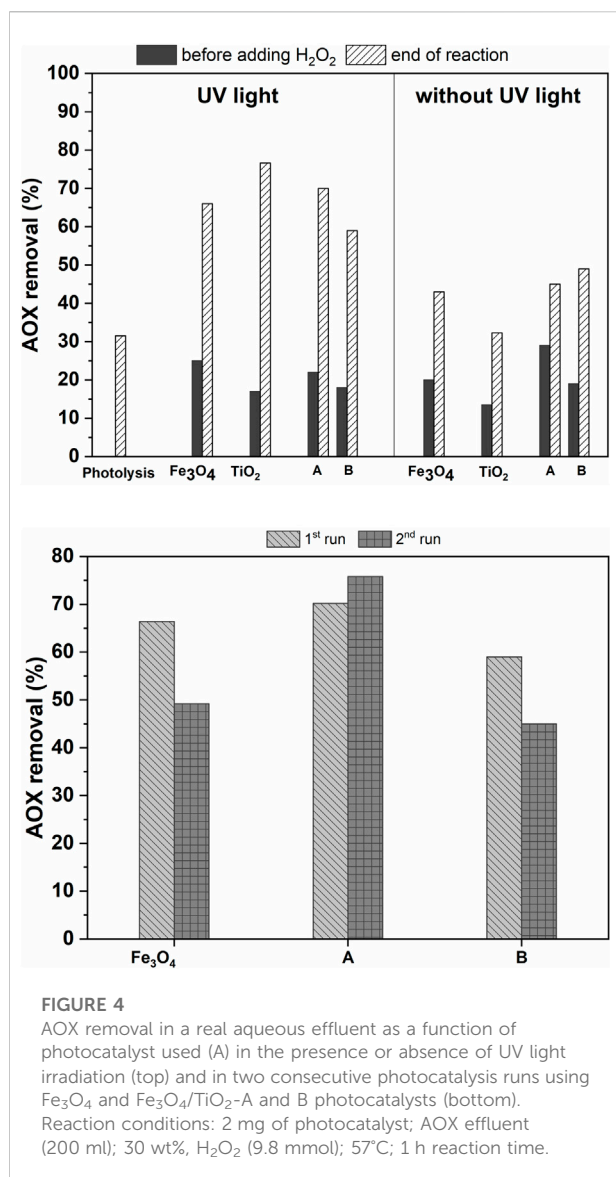
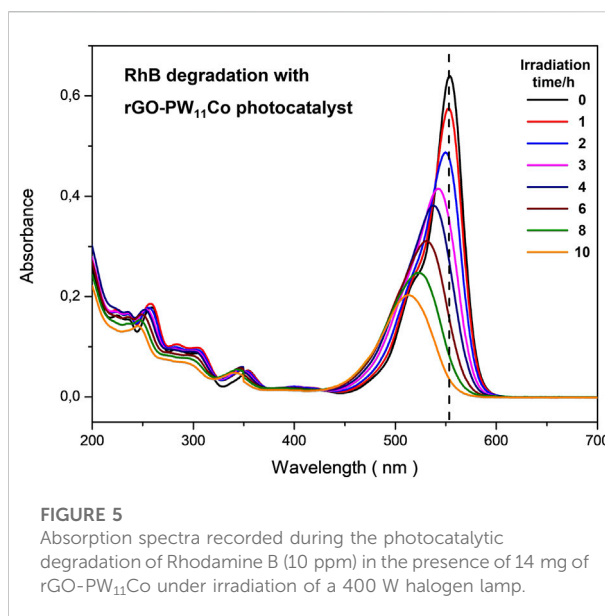


**FIGURE 4**  
AOX removal in a real aqueous effluent as a function of photocatalyst used (A) in the presence or absence of UV light irradiation (top) and in two consecutive photocatalysis runs using Fe<sub>3</sub>O<sub>4</sub> and Fe<sub>3</sub>O<sub>4</sub>/TiO<sub>2</sub>-A and B photocatalysts (bottom). Reaction conditions: 2 mg of photocatalyst; AOX effluent (200 ml); 30 wt%, H<sub>2</sub>O<sub>2</sub> (9.8 mmol); 57°C; 1 h reaction time.

magnetic hybrids enabled 59–73% AOX removal after 60 min under UV irradiation (Figure 4), with the great advantage that could be separated from the treated effluent by magnetic separation and subsequently reused. The identity of the hybrids was intact after two photocatalytic cycles, even though a slight loss of photocatalytic activity and mass loss was observed.

### 2.3.2 POM supported photocatalysts

Polyoxometalates (POMs) show multi-advantages for application as photocatalysts (Walsh et al., 2016), namely their switch-ability by visible light, the possibility of multi-electronic photoreduction, followed by reversible electron exchange with a substrate, the possibility of heterogenization and finally a low cost. The possibility of heterogenization without

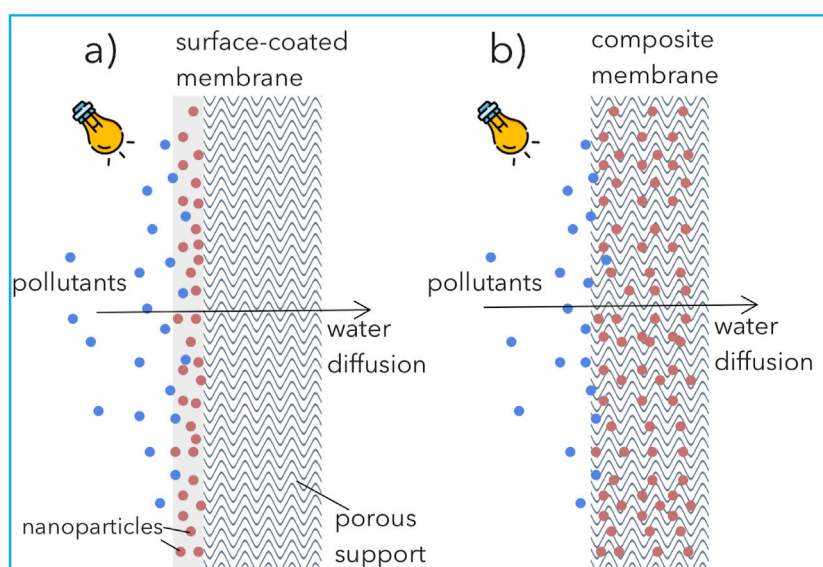


**FIGURE 5**  
Absorption spectra recorded during the photocatalytic degradation of Rhodamine B (10 ppm) in the presence of 14 mg of rGO-PW<sub>11</sub>Co under irradiation of a 400 W halogen lamp.

loss of POM properties is very important for the application of POM based nanomaterials in photocatalysis.

In this work we have been developing new nanostructured hybrid materials based on polyoxometalate clusters supported in graphene (Granadeiro et al., 2012). Graphene supports were obtained by graphene oxide reduction (rGO, reduced graphene oxide). These materials have been optimized for application in the photocatalytic degradation of water pollutants of pharmaceutical origin, one of the most important classes of emergent environmental contaminants (Lopes et al., 2021). The new electron transfer features resulting from the synergetic combination of POMs and rGO have been explored in photocatalysis.

To evaluate the photocatalytic activity in the visible of the polyoxometalate [PW<sub>11</sub>CoO<sub>39</sub>]<sup>5-</sup> supported in rGO (rGO-PW<sub>11</sub>Co), the photodegradation of Rhodamine B (RhB) under visible-light irradiation was conducted at room temperature. RhB was selected as an organic dye model because it shows strong absorption in the visible region (maximum at 554 nm, Figures 5, 0 h) and is photostable in the absence of photocatalyst. As control, identical experiments in the dark were also carried out. The results for a blank experiment, without catalyst, demonstrate that RhB concentration was practically unchanged, suggesting that RhB is stable under visible-light irradiation. Comparative photocatalytic studies using as catalyst the supported rGO-PW<sub>11</sub>Co material and the pure solid K<sub>5</sub> [PW<sub>11</sub>CoO<sub>39</sub>], respectively, under the same experimental conditions, demonstrate that rGO-PW<sub>11</sub>Co shows higher photocatalytic activity than the polyoxometalate by itself. The photodegradation of RhB is closed to 95% after 600 min in the presence of rGO-PW<sub>11</sub>Co catalyst, under visible-light irradiation. The degradation of RhB is followed by the

**FIGURE 6**

Schematic representation of nanoparticles immobilized in/on composite membranes: (A) surface-coated membrane; (B) nanoparticles matrix-blended membrane.

decrease in the characteristic absorbance at 554 nm as well as the maximum absorption shift over time (Figure 5).

The later example presents a POM based heterogeneous photocatalyst (rGO-PW<sub>11</sub>Co) that shows activity under promising conditions, in particular the use of visible-light for irradiation and room temperature.

### 2.3.3 Nanoparticles immobilized in/on membranes

Although photoactive nanoparticles have demonstrated effectiveness for the removal of CEC in wastewater, their direct application as free nanoparticles in suspension mode has also limitations. Nanoparticles tend to aggregate with time, due to Van der Waals interactions, which decrease their performance (Lofrano et al., 2016). Most importantly it requires a complex post-treatment step for the recovery/separation of the solid slurry, with a substantial impact on the overall process cost (Loeb et al., 2019). Thus, more effective strategies have been explored based on the immobilization of nanoparticles in/on membranes (Shen et al., 2020). Besides the fundamental economic advantage, coupling nanoparticles with membranes allow easy scaling and reusability with fewer environmental risks, thus contributing to their real application in wastewater treatments. In these systems, the membrane has the simultaneous role of catalyst support while acting as a barrier for the pollutants to be degraded (Iglesias et al., 2016). Retained molecules during filtration, depending on their physical and chemical properties, are forced towards the membrane increasing their concentration near the liquid/catalyst

interface, thus boosting the degradation rate (Presumido et al., 2021). Moreover, nanocomposite membranes are of interest as it also reduces the membrane fouling effect, which remains the notorious drawback of micro- (MF), ultra- (UF) and nanofiltration (NF) (Xu et al., 2020).

The introduction of nanoparticles promotes changes in morphology and enhances membrane hydrophilicity due to their polarity. Following the solution-diffusion theory, an increase in the nature of the membrane benefits water diffusion and controls the transport process through the membrane, improving its permeability. Conversely, immobilized nanoparticles have reduced active surface area, which entails the maximization of crucial parameters such as light irradiation and mass transfer (Alipour Atmianlu et al., 2021). Different oxides nanoparticles (photocatalysts) have been explored, such as TiO<sub>2</sub> (Martins et al., 2016), ZnO (Shen et al., 2020), ZrO<sub>2</sub> (Huang et al., 2021), WO<sub>3</sub> (Gondal et al., 2017), as well as carbon-based nanomaterials such as GO (Kusworo et al., 2021), g-C<sub>3</sub>N<sub>4</sub> (Li et al., 2019) or SWCNTs (Jue et al., 2020).

Due to high thermal, chemical and mechanical stability, the most used membrane matrix materials are ceramic (Zhang et al., 2020) and polymeric, such as polyvinyl fluoride (PVDF) (Cui et al., 2019), polytetrafluoroethylene (PTFE) (Feng et al., 2018) and polyaniline (PANI) (Vijayakumar and Khastgir, 2018). Nanocomposite membranes can be prepared by nanoparticles surface coating (Figure 6A) or entrapping nanoparticles through blending with the membrane substrate during the manufacturing process (Figure 6B), or even as a free-standing catalyst (Homocianu and Pascariu, 2022).

Surface-coated membranes can be obtained by dip-coating, electrospraying, sputter deposition or gas-phase deposition which generates a nanoparticles layer on its surface (Lakhotia et al., 2018; Alipour Atmianlu et al., 2021). Horovitz et al. (2016) reported the dip-coating of a commercial alumina membrane with N-doped TiO<sub>2</sub> by the sol-gel method. Substantial gain in the carbamazepine removal was observed, however, with a loss in the permeability. Recently (Barati et al., 2021), observed that the *in-situ* growth of hydrophilic iron oxides nanoparticles (<4 nm) did not modify the morphology, porosity or the intrinsic hydraulic resistance of ceramic membranes, however, it significantly increased the rejection of humic acid. Higher loading of iron oxides promoted a porous obstruction, thus a drop in permeability.

Matrix-blended membranes obtained by blending nanoparticles in the membrane matrix allow to minimize the possible catalyst leaching. For fabrication, nanoparticles are dispersed by mixing in the polymer-solvent solution before phase inversion. Martins et al. (2016) immobilized 3–8 wt% TiO<sub>2</sub> nanoparticles in porous PVDF/NaY-based membrane via solvent casting method. Interestingly, the authors reported a minor loss (~3%) in pollutant removal efficiency compared to the nanoparticle suspension assays. Following a similar strategy, Luo et al. (2021) immobilized NCQDs/BiOBr/TiO<sub>2</sub> in PVDF membranes with strong antifouling properties under visible light irradiation. The use of blended nanoparticles promoted the degradation of the pollutant while enhancing the filtration performance due to lower membrane fouling. Yet, the membrane permeability can be compromised due to porous hindrance when high nanoparticle loading is used.

In summary, nanoparticles immobilized in membranes is an effective strategy to overcome the disadvantages associated with conventional slurry-type systems. Surface-coated membranes can improve hydrophilicity and provide antifouling properties; however, the strategy can be ineffective in preventing catalyst leaching. Nanoparticles blended in the membrane matrix are more successful in retaining the catalyst, but the antifouling capacity can be inferior. Deeper optimization to assure porosity, surface dispersion, high photocatalytic activity and improve mass transfer is required to enlarge the broad market commercialization of self-cleaning nanocomposite membranes for environmental application.

## 2.4 Nanostructured platforms for SERS detection

Fleischmann and co-workers noticed the SERS effect for the first time in 1974 (Fleischmann et al., 1974), with its interpretation and deep understanding of underlying mechanisms developed in the subsequent years (Albrecht and Creighton, 1977; Jeanmaire and Van Duyne, 1977; Jensen et al., 2008; Stiles et al., 2008; Valley et al., 2013). However, it was

mainly during the last decades that SERS has been regarded as an essential method for water quality monitoring, offering new possibilities for practical implementation and, in certain cases, lowering analytical detection limits in established analytical protocols (Pinheiro et al., 2018; Tang et al., 2018; Bodelón and Pastoriza-Santos, 2020; Ong et al., 2020). The increasing interest in the application of SERS to water quality monitoring is inseparable from last developments in terms of instrumentation (e.g., detection sensitivity and portability) and also on the nanofabrication methods of analytical substrates, in which surface chemistry plays a determinant role (Li et al., 2014; Yilmaz et al., 2022). In fact, our interest in this research topic has been mainly driven by exploring chemical routes to produce a variety of nanostructured materials with specific features for SERS analysis (Fateixa et al., 2011; Fateixa et al., 2013; Fateixa et al., 2015; Fateixa et al., 2016; Pinheiro et al., 2019b).

### 2.4.1 Nanometal assemblies in polymeric substrates

The fabrication of flexible, low-cost and sensitive SERS substrates has gained great attention in environmental monitoring (Yu and White, 2012; Gao et al., 2016; Fateixa et al., 2018b; Guo et al., 2019; Sun et al., 2021). Polymer-based filter membranes show important features for these purposes, namely robust mechanical resistance and tuneable pore size. These membranes are available in various materials that allow sample concentration by large-volume filtration, promoting the target analyte uptake and, consequently, easier detection by SERS (Xu et al., 2021b). The lightweight and flexibility of membrane SERS substrates can also be combined with portable Raman spectrometers and smartphones, providing on-site detection (Gao et al., 2016; Guo et al., 2019; Sun et al., 2021). Several filtering membranes have been used as SERS substrates, such as cellulose (paper) (Lee et al., 2010; Moram et al., 2018; Wu et al., 2018; Jiao et al., 2022), polyamide (PA) (Yu and White, 2012; Shi et al., 2014; Fateixa et al., 2018a; Yu et al., 2021), PVDF (Yu and White, 2012; Gao et al., 2016; Guo et al., 2019; Sun et al., 2021), and derived polymer-based composites (Fateixa et al., 2018b; Ankudze et al., 2019; Ye et al., 2020). Polymer-based membranes offer flexibility, porosity and extensive fibrillar networks for surface chemical functionalization, which are important features for substrates fabrication, but they are not SERS active themselves. In this regard, plasmonic nanoparticles such as Ag or Au NPs are often used as the SERS active phases present in the filter membranes. The attachment of metal NPs onto the filter membranes can be performed by different approaches, such as 1) filtering colloidal NPs through the membrane (Yu and White, 2012; Shi et al., 2014; Fateixa et al., 2018a); 2) blending or *in situ* growth of NPs within the filter membrane (Lee et al., 2010; Moram et al., 2018; Wu et al., 2018; Yu et al., 2021); 3) coating the filter membrane with Au/Ag assembled structures (Guo et al., 2016); 4) modification of the fibres with NPs prior the membrane fabrication (Guo et al., 2016; Fateixa et al., 2018b; Ankudze et al., 2019).

A straightforward method for SERS substrates based on filter membranes involves syringe filtration of metal sols, as demonstrated by the early work of Yu and White. (2012) on Ag colloidal NPs supported on PA and PVDF membranes. They have demonstrated that this simple, economic and fast method provides efficient SERS substrates, which not only pre-concentrate the target analyte but also decrease the analysis detection time, with improvements in the Raman signal reproducibility of the molecular probe used. This topic was further explored in other laboratories using distinct filter membranes and plasmonic NPs with diverse morphologies, such as spherical Ag and Au NPs (Guo et al., 2016; Fateixa et al., 2018b; Sun et al., 2021; Yu et al., 2021), nanorods and nanowires (Lee et al., 2010; Shi et al., 2014; Wu et al., 2018; Ankudze et al., 2019), nanostars and nanourchins (Mehn et al., 2013; Xu et al., 2021a), and Au/Ag alloys or core-shell (Moram et al., 2018; Sha et al., 2020; Khan et al., 2022). Yu et al. (2021) have investigated Au/PA filter membranes for pesticide detection by comparing distinct fabrication methods, including *in situ* reduction, immersion-adsorption, and filtration. The latter method provided the SERS substrates with the best stability, reproducibility, and the lowest detection limit for the selected pesticides, compared with those prepared using other methods. Gao and co-workers have developed a rapid and sensitive methodology to detect the fungicide ferbam in aqueous samples using a portable Raman spectrometer (Gao et al., 2016). In this way, Ag colloids were previously aggregated by electrolyte addition (NaCl) and then filtered through a PVDF filter membrane. The Ag-loaded PVDF membranes allowed the SERS detection of ferbam dissolved in distilled, tap, and pond water samples at a low concentration of 2.5 µg/L.

Our interest in this topic led us to explore the fabrication of filter membranes using PA and liquid crystal polymer (LCP) for water CEC monitoring (Fateixa et al., 2018a; Fateixa et al., 2018b; Fateixa et al., 2019). A simple strategy was reported to fabricate filter membranes based on composites containing plasmonic NPs and Vectran™, a manufactured aromatic poly (ester) that shows properties useful for filtering membranes (Fateixa et al., 2018b; Fateixa et al., 2019). In fact, Vectran™ is a thermotropic LCP fiber with high Young modulus and high strength, superior heat resistance and excellent chemical stability in comparison to other conventional polymers. Hence, Au and Ag NPs with different morphology (spheres and rods) have been prepared by wet chemical procedures and successfully attached to the LCP fibres previously modified with polyelectrolytes. In this strategy, the optical properties are fine-tuned through judicious selection of the metallic NPs which have been prepared previous the composite fabrication. The metal-loaded nanocomposites were then submitted to hydraulic pressing to fabricate the filter membranes. These SERS substrates were investigated to uptake and detect thiram and paraquat dissolved in water samples using SERS coupled with Raman imaging (Figure 7A).

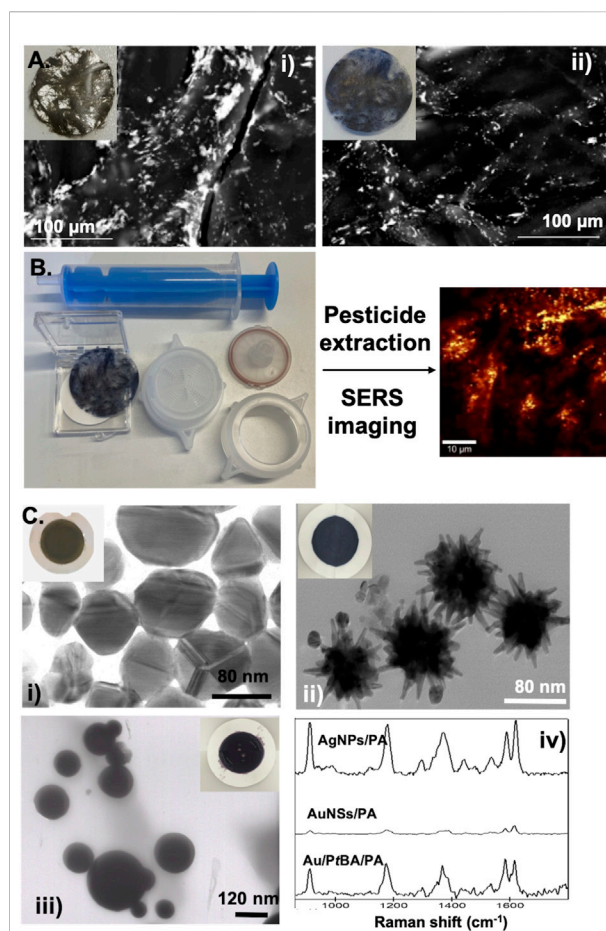


FIGURE 7

(A) SEM images of Ag/LCP (i) and Au/LCP (ii) composites prepared by layer-by-layer approach. Inset: digital photograph of the MNPs/LCP fibres after pressed by hydraulic pressing (B) Schematic illustration of MNPs/LCP filter membrane preparation for SERS detection of pesticides dissolved in water. (C) TEM images of Ag NPs (i), Au nanostars (ii), and Au NPs coated with PtBA (iii) deposited on commercial PA filter membranes and used as SERS substrates for the detection of crystal violet (iv). Insets: digital photographs of PA filter membranes loaded with Ag NPs (i), AuNSs (ii) and Au/PtBA beads (iii).

Alternatively, the *in situ* citrate reduction method applied to Ag(I) dissolved in LCP aqueous suspensions resulted in Ag/LCP fibres, which were then pressed into filter membranes. As a proof of concept, the Ag/LCP filter membranes were supported on polyamide filters, which combine the SERS technique and share similarities with solid phase extraction due to the rapid collection of the molecular analyte for *in situ* detection (Figure 7B). These SERS substrates have shown better SERS response and selectivity for thiram molecules dissolved in water samples than other pesticides (e.g., paraquat). The SERS map shows a strong SERS signal of the thiram molecules, indicating not only the pesticide's spatial distribution but also the active Raman regions (so-called hotspots) due to the presence of the Ag NPs (Fateixa



et al., 2018b). These membranes applied to real aqueous matrices laboratorial spiked with thiram led to SERS signals with enhancement factors of  $1.67 \times 10^7$  and  $3.86 \times 10^5$ , respectively, for Aveiro estuary water and fruit juices samples. The latter value was lower than the maximal residue limit of 5 ppm in fruit, as prescribed by European regulations (EU) 2016/1.

Other studies involved metal-loaded PA filter membranes fabricated by filtration under reduced pressure to detect crystal violet, a synthetic basic cationic dye used in veterinary medicine to treat fungal infections in aquacultures (Fateixa et al., 2018a; Fateixa et al., 2019). Commercial PA filter membranes with a porous size of 200 nm are suitable platforms to load metallic NPs. We have succeeded in depositing Ag and Au particles with different particle sizes and shapes (spheres and stars), and polymeric coated Au NPs (Au/poly (*tert*-butyl acrylate)) and used them as SERS substrates (Figure 7C). Using these metal-loaded PA filter membranes, we have reported, for the first time, the use of Raman imaging combined with SERS spectroscopy not only to optimize the fabrication process of such SERS substrates but also to achieve low detection limits. In more detail, SERS imaging was used to adjust operational parameters, namely the amount of NPs in the filter membrane surface and sample preparation method, and to monitor the active SERS sites' formation in distinct areas of the PA membrane. The Ag/PA filter membranes led to the higher SERS response in the CV analysis with detection limits of 10 fM for Aveiro Estuary water (Fateixa et al., 2018a). This fabrication process can be easily scaled up, and large amounts of contaminated water can be used for in field measurements.

#### 2.4.2 Inkjet printing of SERS substrates

Several methods for fabricating SERS substrates rely on the adaptation of available technologies for routine applications. Among such methods, inkjet printing has also been explored to produce substrates for SERS detection of water pollutants (Yu and White, 2010; Dai et al., 2014; Restaino et al., 2017; Godoy et al., 2020; Martins et al., 2021). This technique has several advantages such as simplicity, low-cost and suitability for large-scale production of substrates. Furthermore, it offers the possibility to adjust the SERS sensor to target applications by employing ink formulations of distinct chemical composition (Yorov et al., 2016; Martins et al., 2021; Fernandes et al., 2022). Another important feature of inkjet printing is that allows the fabrication of SERS sensors on diverse materials with different substrate shapes (e.g., cellulose paper, glass surfaces or silicon wafers) (Hoppmann et al., 2013; Yang et al., 2015; Micciché et al., 2018). In particular, paper is a flexible, biodegradable, lightweight and low-cost material, therefore is highly attractive to develop disposable analytical platforms. Furthermore, paper-based SERS substrates can be employed in point-of-use applications in conjunction with handheld Raman instruments and smartphones (Sun et al., 2019; Zeng et al., 2019). Thus, the

inkjet printing of colloidal metal NPs on paper is gaining considerable attention as a widely accessible method for SERS substrates fabrication (Dai et al., 2014; Godoy et al., 2020; Martins et al., 2021; Fernandes et al., 2022).

Earlier reports on the use of cellulose substrates demonstrated their potential for SERS detection using both vegetable cellulose and bacterial cellulose (Marques et al., 2008). The latter has some advantages, because the cellulose can be used either as dry substrates (paper sheets) or aqueous sponges, both with high level of metal loaded cellulosic nanofibrils. However, the demonstration of the inkjet printing method for fabricating SERS paper-based substrates was only reported later by Yu and White. (2010). These authors have used a commercial inkjet printer to pattern Ag NPs with microscale precision on paper to obtain SERS substrates. In this way, they could detect rhodamine 6G (R6G) dissolved in water in a concentration as low as 10 fmol/μL. Later, White et al. have shown that inkjet printed paper substrates are also sensitive for the detection of antibiotics (e.g., sulfapyridine, ciprofloxacin) (Restaino et al., 2017). Many other reports followed that apply the inkjet printing method using chemical and morphological distinct colloids as the inks, such as Au nanospheres (Godoy et al., 2020), Au nanorods (Dai et al., 2014), and Ag anisotropic NPs (Yorov et al., 2016). In fact, it is not an overstatement to consider the chemistry of nanoinks for printing materials a research topic on its own, such as in the fabrication of paper-based SERS substrates, considering the many possibilities to adjust the sensing properties by applying chemical reasoning to the ink composition.

We have been particularly interested in ink formulations for the preparation of paper-based SERS substrates that offers control of the surface hydrophobicity (Martins et al., 2021). In fact, it has been demonstrated that hydrophobic paper can improve the sensitivity of SERS sensors by preventing the spreading of aqueous droplets employed in the analysis (Lee et al., 2018; Godoy et al., 2020). As consequence, this strategy can be used for increasing the amount of plasmonic NPs in a small area of the substrate by using the respective hydrosols and also allows the concentration of the aqueous analyte in the sensing region. Figure 8A shows paper-based SERS substrates obtained through inkjet printing of aqueous emulsions containing Ag NPs (Figure 8D), as the SERS active phase, and polystyrene (PS) beads that confers hydrophobic properties to the coated paper. Substrates with different levels of hydrophobicity were obtained by varying the weight percentage of PS in the ink formulations and then evaluated using several aqueous samples. The best SERS performance of the Ag/PS coated papers was observed for substrates showing the highest hydrophobicity. It should be noted that this approach is not limited to common office paper; other substrates can be coated either varying the emulsion composition or the metal colloids used in the inkjet printing process, as illustrated in Figures 8A–C. The applicability of these substrates using different aqueous



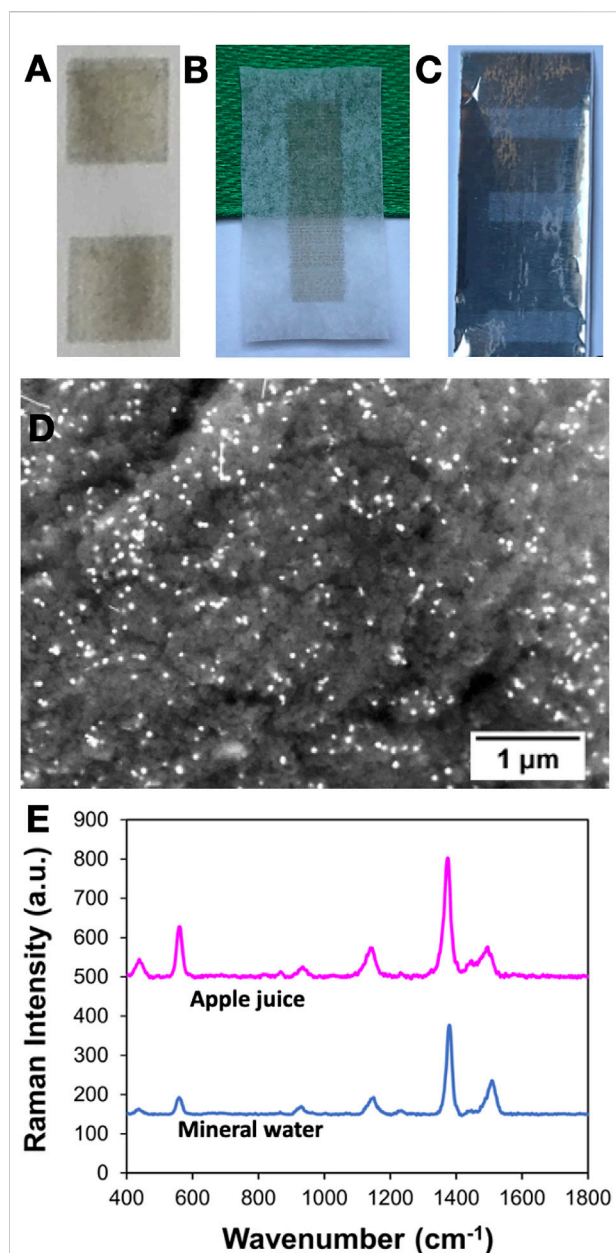


FIGURE 8

SERS substrates prepared by inkjet printing of metal colloids on different types of paper: (A) Ag/PS on office paper; (B) Ag on parchment paper (C) Au/PS on aluminium foil paper; (D) SEM image of office paper printed with Ag/PS ink, showing the metal NPs as white spots on a polymeric background.; (E) SERS spectra of thiram (10<sup>-6</sup> M) spiked in apple juice and mineral water using Ag/PS as the substrate.

matrices was evaluated, such as in the SERS detection of thiram (LOD 0.024 μM) in spiked samples of mineral water and apple juice (Figure 8E) (Martins et al., 2021).

More recently, we have reported the use of dendrimer-stabilized Au:Ag nanoalloys of variable molar ratios for the inkjet printing of SERS substrates on office paper (Fernandes

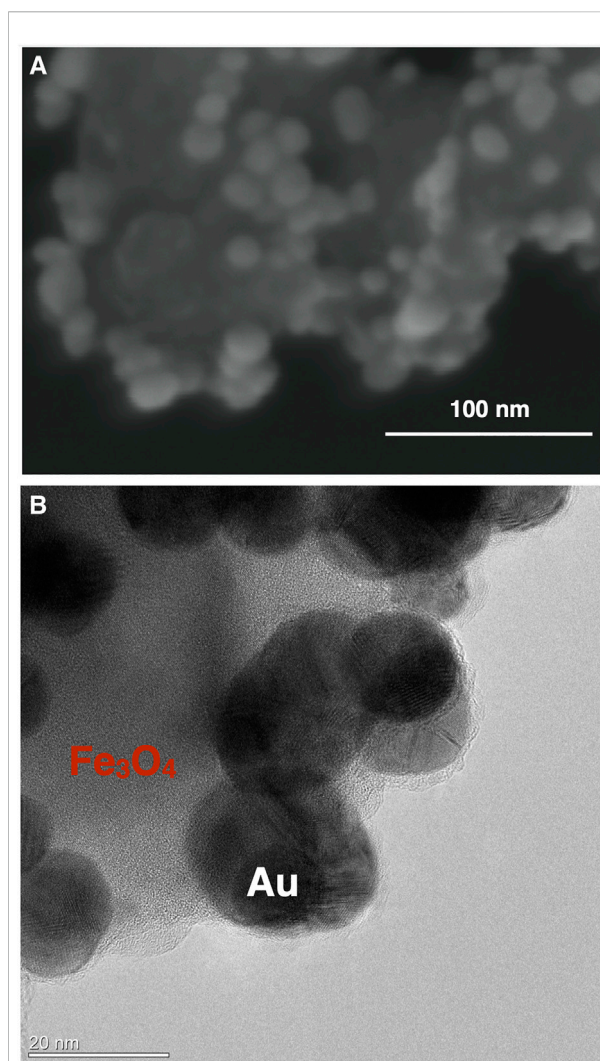


FIGURE 9

Electron microscopy images of multifunctional magneto-plasmonic nanosorbents: SEM (A) and TEM (B) images. The magnetic drivers are Fe<sub>3</sub>O<sub>4</sub> particles decorated with SERS active Au nanoparticles.

et al., 2022). Firstly, Au:Ag alloys were prepared in the presence of poly (amidoamine) dendrimer (PAMAM), resulting in nanoassemblies with plasmonic properties that depend on the chemical composition of the final materials (Fernandes et al., 2021; Fernandes et al., 2022). The dendrimer acts as a “molecular glue” for the clustering of Au and Ag nanocrystals, and also as a reducing and colloidal stabilizer. The dendrimer-stabilized Au:Ag nanoalloys were then used as colloidal inks for the inkjet printing of SERS substrates on paper. To further improve the SERS performance of the substrates, the paper surface was pre-treated with a hydrophobic coating of PS before the deposition of the nanoassemblies. The resulting substrates displayed good SERS sensitivity for the detection of the pesticide thiram in

aqueous solutions, namely by using a portable Raman equipment.

### 2.4.3 Magneto-plasmonic substrates

Owing to their multifunctionality, there has been great interest in magneto-plasmonic systems where two distinct inorganic phases coexist in the same nanostructure, such as in a composite particle of a plasmonic metal and a magnetic iron oxide. These nanostructures can be produced by a variety of methods, leading to a wide assortment of magneto-plasmonic systems. In this regard, we have been interested in colloidal procedures because they can be easily implemented by adaptation of synthesis protocols developed for the single-component counterparts. Hence, two main synthetic approaches have been investigated: 1) the assembly of colloids of both phases and 2) the *in situ* chemical reduction of metal salts in the presence of the colloidal magnetic phase; the latter are typically ferrimagnetic  $\text{Fe}_3\text{O}_4$  NPs. Although featuring distinct characteristics, both methods result in magneto-plasmonic nanosorbents whose basic configuration is observed in the electron microscopy images shown in Figure 9 (Lopes et al., 2016; Pinheiro et al., 2018). In Figures 9B, a detailed TEM image of  $\text{Fe}_3\text{O}_4$ -Au nanosorbents show Au spheroidal NPs (ca. 15 nm) assembled onto surface modified  $\text{Fe}_3\text{O}_4$  NPs (ca. 80 nm); the Au NPs are responsible for SERS activity while  $\text{Fe}_3\text{O}_4$  allows the separation of the multifunctional particles by applying an external magnetic gradient. The attachment of the Au NPs followed previous surface modification of the  $\text{Fe}_3\text{O}_4$  particles with silica shells enriched in dithiocarbamate moieties by using a single-step route (Tavares et al., 2013). Hence, the modification of the nanosorbents' surfaces is a practical consequence of the concept of soft acid (Au)-soft base (S ligand) affinity, which can be extended to the attachment of other noble metal NPs onto dithiocarbamate functionalized magnetites (Lopes et al., 2016).

There are few reports in the literature on the development of colloidal magneto-plasmonic nanomaterials applied to environmental applications, though their multifunctionality have been explored in other areas such as in bioapplications (Hao et al., 2010; Hou et al., 2017; Nguyen et al., 2018; Ovejero et al., 2018; Scaramuzza et al., 2019; Archana et al., 2021; Mukha et al., 2021). However, nanostructures like those shown in Figure 9 can be also explored as a new class of multifunctional nanosorbents for analytical purposes. While the magnetic iron oxide NPs confer the ability for magnetic separation from the aqueous medium, the plasmonic metal NPs allow the SERS monitoring of the target analyte. In this context, we have reported the application of  $\text{Fe}_3\text{O}_4$ -Au nanosorbents in the uptake and SERS detection of water contaminants of emergent concern, such as vestigial pharmaceuticals (Pinheiro et al., 2019a; Pinheiro et al., 2019b). These multifunctional nanosorbents have great potential in analytical kits envisaging water quality monitoring protocols to be applied both in laboratory and on-site analysis. A great advantage in using

magneto-plasmonic nanosorbents for trace analysis is the possibility of successive pre-concentration steps to facilitate the detection of the analyte. Nevertheless, research on this topic has been scarce and the potential of magneto-plasmonic materials is far from being well explored.

## 2.5 Environmental impact of nanomaterials

To overcome the global problem of water pollution, nanomaterials emerged as promising tools for monitoring water quality and for the remediation of wastewaters (Vikesland, 2018; Yaqoob et al., 2020; Davarazar et al., 2021). This is because some of their properties like nano size, large specific surface area, high reactivity, porosity, among others, can be explored for more effective processes. But, despite the beneficial potentials conferred by these properties for water and wastewater monitoring and remediation, these same properties may render them toxic to the biota (Nogueira et al., 2016; Monteiro et al., 2019; Costa et al., 2020; Ghadimi et al., 2020). Considering that it is inevitable that some of the nanoparticles used in water and wastewater treatments will be released into the aquatic ecosystem, concerns arise on their ecotoxicity to the environment. Therefore, targeting the safe use of nanomaterials in the remediation of water and wastewaters and promote the development of sustainable remediation nanotechnologies, in parallel to the study of its chemical efficiency (i.e., removal and/or monitoring of contaminants in water), it is important to address if the nanoparticles per se may constitute a risk to the environment. We have carried out this type of studies as exemplified by the case of study presented below.

We have characterized the ecotoxicity of three systems, mentioned previously in this manuscript, to the freshwater microalgae *Raphidocelis subcapitata*. The selected systems comprised colloidal gold nanostars (Au-NS) and biocomposite magnetic nanosorbents. The latter samples have distinct surface chemistry, one sample comprise coatings of k-carrageenan hybrid siliceous shells ( $\text{Fe}_3\text{O}_4@ \text{SiO}_2/\text{SiCRG}$ ) and the other contains chitosan hybrid siliceous thin shells ( $\text{Fe}_3\text{O}_4@ \text{SiO}_2/\text{SiCHT}$ ). In particular, the selected biocomposite sorbents are of particular interest because they have shown capacity to remove CEC from aqueous media as discussed above (Soares et al., 2016; Soares et al., 2017a). The *R. subcapitata* was used here as the model species because it is one of the recommended by REACH legislation to be tested when characterizing the ecotoxicity of new chemicals during the process for authorization to be placed in the market. Therefore, 72-h growth inhibition assays were performed by exposing *R. subcapitata* to several concentrations of Au-NS (125–200 mg/L),  $\text{Fe}_3\text{O}_4@ \text{SiO}_2/\text{SiCRG}$  (52.4–2000 mg/L) and

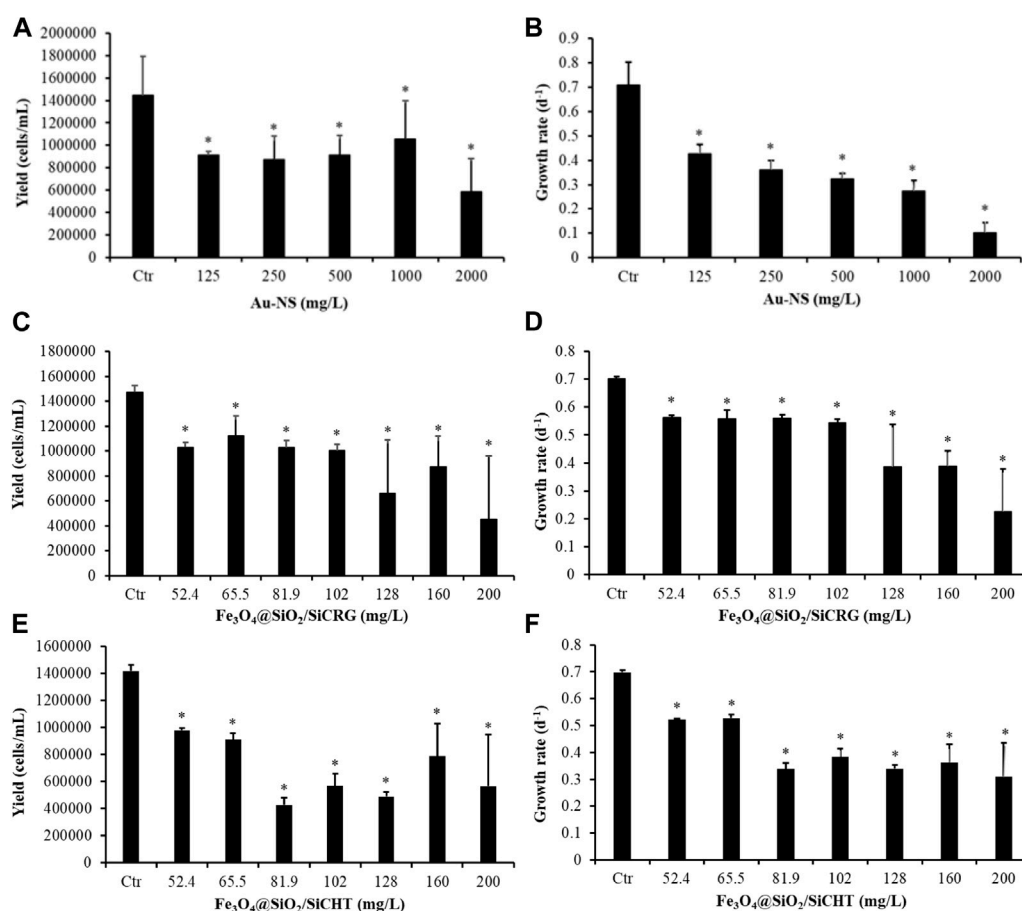


FIGURE 10

Average yield and growth rate of *Raphidocelis subcapitata* after being exposed, for 72 h, to several concentrations of gold nano-spheres ((A) and (B) Au-NS) and of Fe<sub>3</sub>O<sub>4</sub> nanoparticles coated with κ-carrageenan hybrid siliceous shells ((C) and (D) Fe<sub>3</sub>O<sub>4</sub>@SiO<sub>2</sub>/SiCRG) and Fe<sub>3</sub>O<sub>4</sub> nanoparticles coated with chitosan hybrid siliceous thin shells ((E) and (F) Fe<sub>3</sub>O<sub>4</sub>@SiO<sub>2</sub>/SiCHT). \* Indicates significant differences from the respective control ( $p < 0.05$ ).

Fe<sub>3</sub>O<sub>4</sub>@SiO<sub>2</sub>/SiCHT (52.4–2000 mg/L). Figure 10 presents the results obtained in these assays. All the tested concentrations of the three selected nanomaterials induced a significant decrease in the yield and growth rate of *R. subcapitata* ( $p < 0.05$ ). Regarding Au-NS, the concentration causing 20% (EC<sub>20</sub>, considered as the threshold for significant effects) and 50% (EC<sub>50</sub>) of reduction in the growth rate were 32.3 (95% confidence limits-95%CL: 8.84–7.4) and 294.8 (95% CL: 134.4–455.1 mg/L), respectively. Considering these ecotoxicity results, the safe use of Au NS depends on the amount employed for water quality monitoring applications. For example, in a study on magnetite decorated with Au-NS for SERS detection of tetracycline, only 0.250 mg/L of Au-NS were necessary (Pinheiro et al., 2019b), thus it is foreseen a safe use of these Au-NS in this context.

The two samples of magnetic biosorbents exhibited similar toxicity to the microalgae (Figure 10), with EC<sub>20</sub> and EC<sub>50</sub> of

84.8 (95% CL: 50.4–1119) mg/L and 164 (95% CL: 131–198) mg/L for Fe<sub>3</sub>O<sub>4</sub>@SiO<sub>2</sub>/SiCRG and of 29.7 (95% CL: 7.55–51.9) and 139 (93.8–183) mg/L for Fe<sub>3</sub>O<sub>4</sub>@SiO<sub>2</sub>/SiCHT, respectively. The EC<sub>x</sub> values computed for Fe<sub>3</sub>O<sub>4</sub>@SiO<sub>2</sub>/SiCRG were lower than the concentrations used by (Soares et al., 2016) to remove metoprolol from water. These authors used a concentration of 500 mg/L of Fe<sub>3</sub>O<sub>4</sub>@SiO<sub>2</sub>/SiCRG (by adding 10 mg of the sorbent to 2 ml of a metoprolol solution) to remove metoprolol from water and reported a removal higher than 30% after 2 h contact time. This removal efficiency occurred at concentrations of sorbent that may induce toxicity to freshwater biota, since it is higher than the concentration that impairs in 20 and 50% the growth rate of *R. subcapitata*. Given that microalgae are at the base of the trophic level, cascade effects at upper trophic levels may be expected to occur. A direct comparison of the EC<sub>x</sub> here computed for Fe<sub>3</sub>O<sub>4</sub>@SiO<sub>2</sub>/SiCHT could not be done with the amount

needed to remove the non-polar compounds (Soares et al., 2017a) because different units were used in the two studies.

The preliminary results on the ecotoxicity of these three systems, suggest the potential for the safe use of Au-NS in the monitoring of water quality. For  $\text{Fe}_3\text{O}_4@\text{SiO}_2/\text{SiCRG}$  it is expected that the amounts needed for an efficient remediation of contaminated waters will cause an ecological risk to microalgae, suggesting the need to remove these nanosorbents from the treated water before being released into the natural aquatic systems. In this regard, the ability for magnetic separation offered by these nanosorbents constitutes a good asset but that still require further research. In fact, it must be emphasized that these experiments were performed under controlled laboratory conditions and natural waters are much more complex systems than the aqueous media used in laboratory, which may alter the toxicity observed under laboratory conditions. Therefore, these types of studies should also be carried out under more realistic scenarios (e.g., test in media that are relevant/similar to the ones aimed to be remediated) to better understand how the nanosorbents will behave in natural freshwaters. Moreover, scientific evidence exists reporting how environmental characteristics may affect the fate and behaviour of nanoparticles, which, in turn, influences their toxicity to biota [e.g., (Ren et al., 2016; Arvidsson et al., 2020) and references therein]. Furthermore, the toxicity of these nanoparticles after being aged in the environmental matrices must be also explored since published works have reported a reduction in their ecotoxicity after ageing in water and soil matrices (Lehutso et al., 2020).

### 3 Conclusions and outlook

This review focused on recent research on nanomaterials of colloidal nature, to be used in this form or as starting components for other types of materials, envisaging applications that aim to prevent contamination of water sources and/or their treatment, mainly when CEC are involved. The revision of scientific work presented here was also framed by the research topics that our own group has developed on this subject. The several examples presented demonstrate the enormous potential of colloidal nanomaterials in applications aimed at water quality improvement. However, they are in distinct stages of potential application and, in certain cases, mainly regarded as interesting systems for acquiring new scientific knowledge. This is due not only to the nature of nanomaterials and their differentiated complexity, but also to the requirements that apply to each of the technologies in which nanomaterials are used. As an example, it should be noted that the scale at which nanomaterials are used differs between an application as nanosorbent in a water treatment

plant and an analytical kit for laboratorial monitoring a target contaminant.

Although research on nanomaterials as addressed in this work is in different stages of maturation, it is possible to highlight some challenges and possible lines of investigation aimed at their solution. Nanosorbents have clear advantages over conventional materials, however aspects related to selectivity for CEC molecules and subsequent regeneration, if necessary, remain important challenges. The application of colloidal materials in photocatalysis has focused mainly on the use of the UV region of the electromagnetic spectrum, thus complementary and innovative strategies are needed aimed at extending the photocatalytic activity to the visible region. The study of chemical speciation of solutions submitted to photocatalytic treatment is of increasing importance, because total mineralization of pollutant molecules has not been always demonstrated. The use of nanomaterials as adsorbents and in photocatalysis, in a real context of water cleaning technology, must be preceded by environmental impact studies. The strategy of associating magnetic phases either to adsorbents or photocatalysts, is a possible solution to ensure the development of safe and more sustainable processes based on magnetic separation technologies. Another alternative strategy could be the immobilisation of nanomaterials in membranes using new processing technologies that take advantage of the properties of colloidal nanoparticles. With regard to the development of SERS sensors for CEC detection, in addition to the detection limit and selectivity for target analytes, there is a need for quantitative analytical data for specific scenarios. This aspect requires even more fundamental research that integrates, in addition to the aspects of synthesis of plasmonic nanomaterials, the mechanisms associated to their interaction with the analyte molecules, namely by taking into account the nanoscale characterization of the substrate, which impacts on the uniformity and reproducibility of the SERS signal.

In addition, there is a need for pilot projects aimed at water improvement applications for the most promising colloidal nanomaterials, in a realistic context, by selecting specific situations in which these materials can be part of the solution, in whole or in part. This type of approach also requires further ecotoxicity studies, also under realistic conditions, that allow the safe use of nanomaterials for the specific application for which they are intended and, in the required quantities. Finally, it should be noted that the unique properties observed in some of the nanomaterials reviewed here, can also be explored in other research contexts and innovative applications.

### Author contributions

All authors have contributed to the manuscript. TT designed and coordinated the project.



## Funding

This work was financed by Portugal 2020 through European Regional Development Fund (ERDF) in the frame of CENTRO2020 in the scope of the project BIOMAG, CENTRO-01-0145-FEDER-181268 and in the scope of the project CICECO–Aveiro Institute of Materials, UIDB/50011/2020 & UIDP/50011/2020 & LA/P/0006/2020, and CESAM-UIDB/50017/2020 + UIDP/50017/2020 + LA/P/0094/2020, financed by national funds through the FCT/MEC (PIDDAC). The work was also partially funded by Portugal 2020 through the European Regional Development Fund (ERDF) in the frame of Operational Competitiveness and Internationalization Program (POCI) in the scope of the project PROTEUS-POCI-01-0247-FEDER-017729. CM and MM thank the Fundação para a Ciência e Tecnologia (FCT) for the PhD grants PD/BD/150568/2020 and SFRH/BD/131433/2017, respectively. NG acknowledge the funding from the European Union's Horizon 2020 research and innovation programme under the Marie Skłodowska-Curie grant agreement No 101065059. AE, NM, and SF acknowledge the costs of their research contracts (REF-078-88-ARH/2018;

REF-069-88-ARH/2018) resulting from the FCT hiring funded by national funds (OE), through FCT, I. P, in the scope of the framework contract foreseen in 4, 5, and 6 of article 23 of the Decree-Law 57/2016, of 29 August, changed by the law 57/2017, of 19 July. CL acknowledges the funding by FCT through CEECIND/03739/2021.

## Conflict of interest

The authors declare that the research was conducted in the absence of any commercial or financial relationships that could be construed as a potential conflict of interest.

## Publisher's note

All claims expressed in this article are solely those of the authors and do not necessarily represent those of their affiliated organizations, or those of the publisher, the editors and the reviewers. Any product that may be evaluated in this article, or claim that may be made by its manufacturer, is not guaranteed or endorsed by the publisher.

## References

- Abbas, M., Parvatheeswara Rao, B., Reddy, V., and Kim, C. (2014). Fe<sub>3</sub>O<sub>4</sub>/TiO<sub>2</sub> core/shell nanocubes: Single-batch surfactantless synthesis, characterization and efficient catalysts for methylene blue degradation. *Ceram. Int.* 40, 11177–11186. doi:10.1016/j.ceramint.2014.03.148
- Abdel Maksoud, M. I. A., Elgarahy, A. M., Farrell, C., Al-Muhtaseb, A. H., Rooney, D. W., and Osman, A. I. (2020). Insight on water remediation application using magnetic nanomaterials and biosorbents. *Coord. Chem. Rev.* 403, 213096. doi:10.1016/j.ccr.2019.213096
- Afonso, E. L., Carvalho, L., Fateixa, S., Amorim, C. O., Amaral, V. S., Vale, C., et al. (2019). Can contaminated waters or wastewater be alternative sources for technology-critical elements? The case of removal and recovery of lanthanides. *J. Hazard. Mat.* 380, 120845. doi:10.1016/j.jhazmat.2019.120845
- Albrecht, M. G., and Creighton, J. A. (1977). Anomalous intense Raman spectra of pyridine at a silver electrode. *J. Am. Chem. Soc.* 99, 5215–5217. doi:10.1021/ja00457a071
- Alipour Atmianlu, P., Badpa, R., Aghabalaie, V., and Baghdadi, M. (2021). A review on the various beds used for immobilization of nanoparticles: Overcoming the barrier to nanoparticle applications in water and wastewater treatment. *J. Environ. Chem. Eng.* 9, 106514. doi:10.1016/j.jece.2021.106514
- Alivisatos, A. P. (1996). Semiconductor clusters, nanocrystals, and quantum dots. *Science* 271, 933–937. doi:10.1126/science.271.5251.933
- Ankudze, B., Asare, B., Goffart, S., Koistinen, A., Nuutinen, T., Matikainen, A., et al. (2019). Hydraulically pressed silver nanowire-cotton fibers as an active platform for filtering and surface-enhanced Raman scattering detection of bacteria from fluid. *Appl. Surf. Sci.* 479, 663–668. doi:10.1016/j.apsusc.2019.02.067
- Archana, V. N., Sam, S. A., Puthirath Balan, A., and Anantharaman, M. R. (2021). Magneto-optical properties of a magneto-plasmonic nanofluid based on superparamagnetic iron oxide and gold nanoparticles. *J. Magn. Magn. Mat.* 536, 168092. doi:10.1016/j.jmmm.2021.168092
- Arvidsson, R., Hansen, S. F., and Baun, A. (2020). Influence of natural organic matter on the aquatic ecotoxicity of engineered nanoparticles: Recommendations for environmental risk assessment. *NanoImpact* 20, 100263. doi:10.1016/j.nimpact.2020.100263
- Badsha, M. A. H., Khan, M., Wu, B., Kumar, A., and Lo, I. M. C. (2021). Role of surface functional groups of hydrogels in metal adsorption: From performance to mechanism. *J. Hazard. Mat.* 408, 124463. doi:10.1016/j.jhazmat.2020.124463
- Barati, N., Husein, M. M., and Azaiez, J. (2021). Modifying ceramic membranes with *in situ* grown iron oxide nanoparticles and their use for oily water treatment. *J. Memb. Sci.* 617, 118641. doi:10.1016/j.memsci.2020.118641
- Baskar, A. V., Bolan, N., Hoang, S. A., Sooriyakumar, P., Kumar, M., Singh, L., et al. (2022). Recovery, regeneration and sustainable management of spent adsorbents from wastewater treatment streams: A review. *Sci. Total Environ.* 822, 153555. doi:10.1016/j.scitotenv.2022.153555
- Bawendi, M. G., Steigerwald, M. L., and Brus, L. E. (1990). The quantum mechanics of larger semiconductor clusters ("Quantum dots"). *Annu. Rev. Phys. Chem.* 41, 477–496. doi:10.1146/annurev.pc.41.100190.002401
- Bodelón, G., and Pastoriza-Santos, I. (2020). Recent progress in surface-enhanced Raman scattering for the detection of chemical contaminants in water. *Front. Chem.* 8, 478. doi:10.3389/fchem.2020.00478
- Boles, M. A., Ling, D., Hyeon, T., and Talapin, D. V. (2016). The surface science of nanocrystals. *Nat. Mat.* 15, 141–153. doi:10.1038/nmat4526
- Brus, L. E. (1984). Electron-electron and electron-hole interactions in small semiconductor crystallites: The size dependence of the lowest excited electronic state. *J. Chem. Phys.* 80, 4403–4409. doi:10.1063/1.447218
- Cardoso, C. E. D., Almeida, J. C., Lopes, C. B., Trindade, T., Vale, C., and Pereira, E. (2019). Recovery of rare earth elements by carbon-based nanomaterials—a review. *Nanomater. (Basel)* 9, 814. doi:10.3390/NANO9060814
- Chen, F., Guan, Z., and Tang, A. (2018). Nanostructure and device architecture engineering for high-performance quantum-dot light-emitting diodes. *J. Mat. Chem. C* 6, 10958–10981. doi:10.1039/C8TC04028A
- Cheng, Y., Arinze, E. S., Palmquist, N., and Thon, S. M. (2016). Advancing colloidal quantum dot photovoltaic technology. *Nanophotonics* 5, 31–54. doi:10.1515/nanoph-2016-0017
- Cheng, Z., Xu, H., Wang, S., Liu, W., Li, Y., Jiang, L., et al. (2021). Effect of nanoparticles as a substitute for kinetic additives on the hydrate-based CO<sub>2</sub> capture. *Chem. Eng. J.* 424, 130329. doi:10.1016/j.cej.2021.130329



- Choe, H., Jeon, D., Lee, S. J., and Cho, J. (2021). Mixed or segregated: Toward efficient and stable mixed halide perovskite-based devices. *ACS Omega* 6, 24304–24315. doi:10.1021/acsomega.1c03714
- Costa, B., Quintaneiro, C., Daniel-da-Silva, A. L., Trindade, T., Soares, A. M. V. M., and Lopes, I. (2020). An integrated approach to assess the sublethal effects of colloidal gold nanorods in tadpoles of *Xenopus laevis*. *J. Hazard. Mat.* 400, 123237. doi:10.1016/j.jhazmat.2020.123237
- Crini, G., Lichtfouse, E., Wilson, L. D., and Morin-Crini, N. (2019). Conventional and non-conventional adsorbents for wastewater treatment. *Environ. Chem. Lett.* 17, 195–213. doi:10.1007/s10311-018-0786-8
- Cui, Z., Li, W., Zeng, H., Tang, X., Zhang, J., Qin, S., et al. (2019). Fabricating PVDF hollow fiber microfiltration membrane with a tenon-connection structure via the thermally induced phase separation process to enhance strength and permeability. *Eur. Polym. J.* 111, 49–62. doi:10.1016/j.eurpolymj.2018.12.009
- Dai, Z., Xiao, X., Wu, W., Liao, L., Mei, F., Yu, X., et al. (2014). Side-to-side alignment of gold nanorods with polarization-free characteristic for highly reproducible surface enhanced Raman scattering. *Appl. Phys. Lett.* 105, N° 211902. doi:10.1063/1.4902812
- Daniel-da-Silva, A. L., and Trindade, T. (2021). *Surface chemistry of colloidal nanocrystals*. Cambridge: Royal Society of Chemistry. doi:10.1039/9781788016568
- Davarazar, M., Kamali, M., and Lopes, I. (2021). Engineered nanomaterials for (waste)water treatment - a scientometric assessment and sustainability aspects. *NanoImpact* 22, 100316. doi:10.1016/j.impact.2021.100316
- Dutta, D. K., Borah, B. J., and Sarmah, P. P. (2015). Recent advances in metal nanoparticles stabilization into nanopores of montmorillonite and their catalytic applications for fine chemicals synthesis. *Catal. Rev.* 57, 257–305. doi:10.1080/01614940.2014.1003504
- Ekimov, A. I., Efros, A. L., and Onushchenko, A. A. (1985). Quantum size effect in semiconductor microcrystals. *Solid State Commun.* 56, 921–924. doi:10.1016/S0038-1098(85)80025-9
- Esteves, A. C. C., and Trindade, T. (2002). Synthetic studies on II/VI semiconductor quantum dots. *Curr. Opin. Solid State Mat. Sci.* 6, 347–353. doi:10.1016/S1359-0286(02)00079-7
- Fateixa, S., Girão, A. V., Nogueira, H. I. S., and Trindade, T. (2011). Polymer based silver nanocomposites as versatile solid film and aqueous emulsion SERS substrates. *J. Mat. Chem.* 21, 15629–15636. doi:10.1039/c1jm12444g
- Fateixa, S., Correia, M. R., and Trindade, T. (2013). Resizing of colloidal gold nanorods and morphological probing by SERS. *J. Phys. Chem. C* 117, 20343–20350. doi:10.1021/jp407216c
- Fateixa, S., Soares, S. F., Daniel-Da-Silva, A. L., Nogueira, H. I. S., and Trindade, T. (2015). Silver-gelatin bionanocomposites for qualitative detection of a pesticide by SERS. *Analyst* 140, 1693–1701. doi:10.1039/c4an02105c
- Fateixa, S., Wilhelm, M., Nogueira, H. I. S., and Trindade, T. (2016). SERS and Raman imaging as a new tool to monitor dyeing on textile fibres. *J. Raman Spectrosc.* 47, 1239–1246. doi:10.1002/jrs.4947
- Fateixa, S., Nogueira, H. I. S., and Trindade, T. (2018a). Surface-enhanced Raman scattering spectral imaging for the attomolar range detection of crystal violet in contaminated water. *ACS Omega* 3, 4331–4341. doi:10.1021/acsomega.7b01983
- Fateixa, S., Raposo, M., Nogueira, H. I. S., and Trindade, T. (2018b). A general strategy to prepare SERS active filter membranes for extraction and detection of pesticides in water. *Talanta* 182, 558–566. doi:10.1016/j.talanta.2018.02.014
- Fateixa, S., Pinheiro, P. C., Nogueira, H. I. S., and Trindade, T. (2019). Gold loaded textile fibres as substrates for SERS detection. *J. Mol. Struct.* 1185, 333–340. doi:10.1016/j.molstruc.2019.03.001
- Feng, S., Zhong, Z., Wang, Y., Xing, W., and Drioli, E. (2018). Progress and perspectives in PTFE membrane: Preparation, modification, and applications. *J. Memb. Sci.* 549, 332–349. doi:10.1016/j.memsci.2017.12.032
- Fernandes, T., Soares, S., Trindade, T., and Daniel-da-Silva, A. (2017). Magnetic hybrid nanosorbents for the uptake of paraquat from water. *Nanomaterials* 7, 68. doi:10.3390/nano7030068
- Fernandes, T., Fateixa, S., Ferro, M., Nogueira, H. I. S., Daniel-da-Silva, A. L., and Trindade, T. (2021). Colloidal dendritic nanostructures of gold and silver for SERS analysis of water pollutants. *J. Mol. Liq.* 337, 116608. doi:10.1016/j.molliq.2021.116608
- Fernandes, T., Martins, N. C. T., Fateixa, S., Nogueira, H. I. S., Daniel-da-Silva, A. L., and Trindade, T. (2022). Dendrimer stabilized nanoalloys for inkjet printing of surface-enhanced Raman scattering substrates. *J. Colloid Interface Sci.* 612, 342–354. doi:10.1016/j.jcis.2021.12.167
- Fleischmann, M., Hendra, P. J., and McQuillan, A. J. (1974). Raman spectra of pyridine adsorbed at a silver electrode. *Chem. Phys. Lett.* 26, 163–166. doi:10.1016/0009-2614(74)85388-1
- Frey, N. A., Peng, S., Cheng, K., and Sun, S. (2009). Magnetic nanoparticles: Synthesis, functionalization, and applications in bioimaging and magnetic energy storage. *Chem. Soc. Rev.* 38, 2532–2542. doi:10.1039/b815548h
- Gao, S., Zhang, Z., and He, L. (2016). Filter-based surface-enhanced Raman spectroscopy for rapid and sensitive detection of the fungicide ferbam in water. *Int. J. Environ. Anal. Chem.* 96, 1495–1506. doi:10.1080/03067319.2016.1272677
- Ghadimi, M., Zangenehtabar, S., and Homaeigohar, S. (2020). An overview of the water remediation potential of nanomaterials and their ecotoxicological impacts. *WaterSwitzerl.* 12, 1150. doi:10.3390/W12041150
- Godoy, N. V., García-Lojo, D., Sigoli, F. A., Pérez-Juste, J., Pastoriza-Santos, I., and Mazali, I. O. (2020). Ultrasensitive inkjet-printed based SERS sensor combining a high-performance gold nanosphere ink and hydrophobic paper. *Sensors Actuators B Chem.* 320, 128412. doi:10.1016/j.snb.2020.128412
- Gómez-Pastora, J., Dominguez, S., Bringas, E., Rivero, M. J., Ortiz, I., and Dionysiou, D. D. (2017). Review and perspectives on the use of magnetic nanophotocatalysts (MNPCs) in water treatment. *Chem. Eng. J.* 310, 407–427. doi:10.1016/j.cej.2016.04.140
- Gondal, M. A., Sadullah, M. S., Qahtan, T. F., Dastageer, M. A., Baig, U., and McKinley, G. H. (2017). Fabrication and wettability study of WO<sub>3</sub> coated photocatalytic membrane for oil-water separation: A comparative study with ZnO coated membrane. *Sci. Rep.* 7, 1686–1710. doi:10.1038/s41598-017-01959-y
- Granadeiro, C., Cruz, S., Goncalves, G., Marques, P., Costa, P., Ferreira, R., et al. (2012). Photoluminescent bimetallic-3-hydroxypicolinate/graphene oxide nanocomposite. *RSC Adv.* 2, 9443–9447. doi:10.1039/C2RA21388E
- Grzelczak, M., Pérez-Juste, J., Mulvaney, P., and Liz-Marzán, L. M. (2008). Shape control in gold nanoparticle synthesis. *Chem. Soc. Rev.* 37, 1783–1791. doi:10.1039/b711490g
- Guerrero-Martínez, A., Barbosa, S., Pastoriza-Santos, I., and Liz-Marzán, L. M. (2011). Nanostars shine bright for you. Colloidal synthesis, properties and applications of branched metallic nanoparticles. *Curr. Opin. Colloid Interface Sci.* 16, 118–127. doi:10.1016/j.cocis.2010.12.007
- Guo, H., Xing, B., and He, L. (2016). Development of a filter-based method for detecting silver nanoparticles and their heteroaggregation in aqueous environments by surface-enhanced Raman spectroscopy. *Environ. Pollut.* 211, 198–205. doi:10.1016/j.envpol.2015.12.049
- Guo, H., Hamlet, L. C., He, L., and Xing, B. (2019). A field-deployable surface-enhanced Raman scattering (SERS) method for sensitive analysis of silver nanoparticles in environmental waters. *Sci. Total Environ.* 653, 1034–1041. doi:10.1016/j.scitotenv.2018.10.435
- Hao, R., Xing, R., Xu, Z., Hou, Y., Gao, S., and Sun, S. (2010). Synthesis, functionalization, and biomedical applications of multifunctional magnetic nanoparticles. *Adv. Mat.* 22, 2729–2742. doi:10.1002/adma.201000260
- Homocianu, M., and Pascariu, P. (2022). High-performance photocatalytic membranes for water purification in relation to environmental and operational parameters. *J. Environ. Manage.* 311, 114817. doi:10.1016/j.jenvman.2022.114817
- Hoppmann, E. P., Yu, W. W., and White, I. M. (2013). Highly sensitive and flexible inkjet printed SERS sensors on paper. *Methods* 63, 219–224. doi:10.1016/j.ymeth.2013.07.010
- Horovitz, I., Avisar, D., Baker, M. A., Grilli, R., Lozzi, L., Di Camillo, D., et al. (2016). Carbamazepine degradation using a N-doped TiO<sub>2</sub> coated photocatalytic membrane reactor: Influence of physical parameters. *J. Hazard. Mat.* 310, 98–107. doi:10.1016/j.jhazmat.2016.02.008
- Hou, X., Wang, X., Liu, R., Zhang, H., Liu, X., and Zhang, Y. (2017). Facile synthesis of multifunctional Fe<sub>3</sub>O<sub>4</sub>@SiO<sub>2</sub>@Au magneto-plasmonic nanoparticles for MR/CT dual imaging and photothermal therapy. *RSC Adv.* 7, 18844–18850. doi:10.1039/c7ra00925a
- Huang, X., Tian, F., Chen, G., Wang, F., Weng, R., and Xi, B. (2021). Preparation and characterization of regenerated cellulose membrane blended with ZrO<sub>2</sub> nanoparticles. *Membr. (Basel)* 12, 42. doi:10.3390/MEMBRANES12010042
- Iglesias, O., Rivero, M. J., Urtiaga, A. M., and Ortiz, I. (2016). Membrane-based photocatalytic systems for process intensification. *Chem. Eng. J.* 305, 136–148. doi:10.1016/j.cej.2016.01.047
- Jeanmaire, D. L., and Van Duyne, R. P. (1977). Surface Raman spectroelectrochemistry. *J. Electroanal. Chem. Interfacial Electrochem.* 84, 1–20. doi:10.1016/S0022-0728(77)80224-6
- Jeevanandam, J., Kiew, S. F., Boakye-Ansah, S., Lau, S. Y., Barhoum, A., Danquah, M. K., et al. (2022). Green approaches for the synthesis of metal and metal oxide nanoparticles using microbial and plant extracts. *Nanoscale* 14, 2534–2571. doi:10.1039/d1nr08144f

- Jensen, L., Aikens, C. M., and Schatz, G. C. (2008). Electronic structure methods for studying surface-enhanced Raman scattering. *Chem. Soc. Rev.* 37, 1061–1073. doi:10.1039/b706023h
- Jiao, S., Liu, Y., Wang, S., Wang, S., Ma, F., Yuan, H., et al. (2022). Face-to-Face assembly of Ag nanoplates on filter papers for pesticide detection by surface-enhanced Raman spectroscopy. *Nanomaterials* 12, 1398. doi:10.3390/nano12091398
- Joseph, A., Sajith, V., and Sarathchandran, C. (2021). Graphene: The magic material. *Handb. Carbon-Based Nanomater.*, 517–549. doi:10.1016/B978-0-12-821996-6.00001-4
- Jue, M. L., Buchsbaum, S. F., Chen, C., Park, S. J., Meshot, E. R., Wu, K. J. J., et al. (2020). Ultra-permeable single-walled carbon nanotube membranes with exceptional performance at scale. *Adv. Sci. (Weinh.)* 7, 2001670. doi:10.1002/ADVS.2001670
- Jun, Y., Choi, J., and Cheon, J. (2006). Shape control of semiconductor and metal oxide nanocrystals through nonhydrolytic colloidal routes. *Angew. Chem. Int. Ed.* 45, 3414–3439. doi:10.1002/anie.200503821
- Kallumottakkal, M., Hussein, M. I., and Iqbal, M. Z. (2021). Recent progress of 2D nanomaterials for application on microwave absorption: A comprehensive study. *Front. Mat.* 8, 34. doi:10.3389/fmats.2021.633079
- Kamat, P. V. (2008). Quantum dot solar cells. Semiconductor nanocrystals as light harvesters. *J. Phys. Chem. C* 112, 18737–18753. doi:10.1021/jp806791s
- Khan, G. A., Demirtaş, O. Ö., Bek, A., Bhatti, A. S., and Ahmed, W. (2022). Facile fabrication of Au-Ag alloy nanoparticles on filter paper: Application in SERS based swab detection and multiplexing. *Vib. Spectrosc.* 120, 103359. doi:10.1016/j.vibspec.2022.103359
- Kubacka, A., Fernández-García, M., and Colón, G. (2012). Advanced nanoarchitectures for solar photocatalytic applications. *Chem. Rev.* 112, 1555–1614. doi:10.1021/cr100454n
- Kumar, P., Kumar, S., Bhardwaj, N. K., and Choudhary, A. K. (2011). Optimization of process parameters for the photocatalytic treatment of paper mill wastewater. *Environ. Eng. Manag. J.* 10, 595–601. doi:10.30638/eemj.2011.082
- Kumar, S., Nehra, M., Deep, A., Kedia, D., Dilbaghi, N., and Kim, K. H. (2017). Quantum-sized nanomaterials for solar cell applications. *Renew. Sustain. Energy Rev.* 73, 821–839. doi:10.1016/j.rser.2017.01.172
- Kumar, R., Mangalapur, R., Ahmadi, M. H., Vo, D.-V. N., Solanki, R., and Kumar, P. (2020). The role of nanotechnology on post-combustion CO<sub>2</sub> absorption in process industries. *Int. J. Low-Carbon Technol.* 15, 361–367. doi:10.1093/ijlct/ctaa002
- Kumari, S., Tyagi, M., and Jagadevan, S. (2019). Mechanistic removal of environmental contaminants using biogenic nano-materials. *Int. J. Environ. Sci. Technol.* 16, 7591–7606. doi:10.1007/s13762-019-02468-3
- Kumari, P., Singh, P., Singhal, A., and Alka (2020). Cyclodextrin-based nanostructured materials for sustainable water remediation applications. *Environ. Sci. Pollut. Res.* 27, 32432–32448. doi:10.1007/s11356-020-09519-0
- Kusworo, T., Nugraheni, R. E., and Aryanti, N. (2021). The effect of membrane modification using TiO<sub>2</sub>, ZnO, and GO nanoparticles: Challenges and future direction in wastewater treatment. *IOP Conf. Ser. Mat. Sci. Eng.* 1053, 012135. doi:10.1088/1757-899x/1053/1/012135
- Lakhotia, S. R., Mukhopadhyay, M., and Kumari, P. (2018). Surface-modified nanocomposite membranes. *Sep. Purif. Rev.* 47, 288–305. doi:10.1080/15422119.2017.1386681
- Lee, C. H., Tian, L., and Singamaneni, S. (2010). Paper-based SERS swab for rapid trace detection on real-world surfaces. *ACS Appl. Mat. Interfaces* 2, 3429–3435. doi:10.1021/am1009875
- Lee, M., Oh, K., Choi, H.-K., Lee, S. G., Youn, H. J., Lee, H. L., et al. (2018). Subnanomolar sensitivity of filter paper-based SERS sensor for pesticide detection by hydrophobicity change of paper surface. *ACS Sens.* 3, 151–159. doi:10.1021/acsensors.7b00782
- Lehutso, R. F., Tancu, Y., Maity, A., and Thwala, M. (2020). Aquatic toxicity of transformed and product-released engineered nanomaterials: An overview of the current state of knowledge. *Process Saf. Environ. Prot.* 138, 39–56. doi:10.1016/j.psep.2020.03.002
- Leslie-Pelecky, D. L., and Rieke, R. D. (1996). Magnetic properties of nanostructured materials. *Chem. Mat.* 8, 1770–1783. doi:10.1021/cm960077f
- Li, H., Zhang, Y., Wang, S., Wu, Q., and Liu, C. (2009). Study on nanomagnets supported TiO<sub>2</sub> photocatalysts prepared by a sol-gel process in reverse microemulsion combining with solvent-thermal technique. *J. Hazard. Mat.* 169, 1045–1053. doi:10.1016/j.jhazmat.2009.04.040
- Li, Z., Deen, M., Kumar, S., and Selvanapathy, P. (2014). Raman spectroscopy for in-line water quality monitoring—instrumentation and potential. *Sensors* 14, 17275–17303. doi:10.3390/s140917275
- Li, R., Ren, Y., Zhao, P., Wang, J., Liu, J., and Zhang, Y. (2019). Graphitic carbon nitride (g-C<sub>3</sub>N<sub>4</sub>) nanosheets functionalized composite membrane with self-cleaning and antibacterial performance. *J. Hazard. Mat.* 365, 606–614. doi:10.1016/j.jhazmat.2018.11.033
- Li, R., Cui, L., Chen, M., and Huang, Y. (2021). Nanomaterials for airborne virus inactivation: A short review. *Aerosol Sci. Eng.* 5, 1–11. doi:10.1007/s41810-020-00080-4
- Lim, B., and Xia, Y. (2011). Metal nanocrystals with highly branched morphologies. *Angew. Chem. Int. Ed.* 50, 76–85. doi:10.1002/anie.201002024
- Lin, C. A. J., Liedl, T., Sperling, R. A., Fernández-Argüelles, M. T., Costa-Fernández, J. M., Pereiro, R., et al. (2007). Bioanalytics and biolabeling with semiconductor nanoparticles (quantum dots). *J. Mat. Chem.* 17, 1343–1346. doi:10.1039/b618902d
- Liu, Z., McClements, D. J., Shi, A., Zhi, L., Tian, Y., Jiao, B., et al. (2022). Janus particles: A review of their applications in food and medicine. *Crit. Rev. Food Sci. Nutr.*, 1–12. doi:10.1080/10408398.2022.2067831
- Loeb, S. K., Alvarez, P. J. J., Brame, J. A., Cates, E. L., Choi, W., Crittenden, J., et al. (2019). The technology Horizon for photocatalytic water treatment: Sunrise or sunset? *Environ. Sci. Technol.* 53, 2937–2947. doi:10.1021/acs.est.8b05041
- Lofrano, G., Carotenuto, M., Libralato, G., Domingos, R. F., Markus, A., Dini, L., et al. (2016). Polymer functionalized nanocomposites for metals removal from water and wastewater: An overview. *Water Res.* 92, 22–37. doi:10.1016/j.watres.2016.01.033
- Lopes, C. B., Coimbra, J., Otero, M., Pereira, E., Duarte, A. C., Lin, Z., et al. (2008). Uptake of Hg<sup>2+</sup> from aqueous solutions by microporous titano- and zirconosilicates. *Quim. Nova* 31, 321–325. doi:10.1590/S0100-40422008000200025
- Lopes, J. L., Marques, K. L., Girão, A. V., Pereira, E., and Trindade, T. (2016). Functionalized magnetite particles for adsorption of colloidal noble metal nanoparticles. *J. Colloid Interface Sci.* 475, 96–103. doi:10.1016/j.jcis.2016.04.046
- Lopes, J. L., Martins, M. J., Nogueira, H. I. S., Estrada, A. C., and Trindade, T. (2021). Carbon-based heterogeneous photocatalysts for water cleaning technologies: A review. *Environ. Chem. Lett.* 19, 643–668. doi:10.1007/s10311-020-01092-9
- López-Quintela, M. A., and Rivas, J. (1996). Nanoscale magnetic particles: Synthesis, structure and dynamics. *Curr. Opin. Colloid Interface Sci.* 1, 806–819. doi:10.1016/s1359-0294(96)80085-9
- Luo, H., Yan, M., Wu, Y., Lin, X., and Yan, Y. (2021). Facile synthesis of PVDF photocatalytic membrane based on NCQDs/BiOBr/TiO<sub>2</sub> heterojunction for effective removal of tetracycline. *Mater. Sci. Eng. B* 265, 114996. doi:10.1016/j.mseb.2020.114996
- Manna, L., Scher, E. R., and Alivisatos, A. P. (2000). Synthesis of soluble and processable rod-arrow-teardrop and tetrapod-shaped CdSe nanocrystals. *J. Am. Chem. Soc.* 122, 12700–12706. doi:10.1021/JA003055+
- Marques, P. A. A. P., Nogueira, H. I. S., Pinto, R. J. B., Neto, C. P., and Trindade, T. (2008). Silver-bacterial cellulosic sponges as active SERS substrates. *J. Raman Spectrosc.* 39, 439–443. doi:10.1002/jrs.1853
- Martins, P. M., Miranda, R., Marques, J., Tavares, C. J., Botelho, G., and Lanceros-Mendez, S. (2016). Comparative efficiency of TiO<sub>2</sub> nanoparticles in suspension vs. immobilization into P(VDF-TrFE) porous membranes. *RSC Adv.* 6, 12708–12716. doi:10.1039/c5ra25385c
- Martins, N. C. T., Fateixa, S., Fernandes, T., Nogueira, H. I. S., and Trindade, T. (2021). Inkjet printing of Ag and polystyrene nanoparticle emulsions for the one-step fabrication of hydrophobic paper-based surface-enhanced Raman scattering substrates. *ACS Appl. Nano Mat.* 4, 4484–4495. doi:10.1021/acsanm.1c00112
- Mehn, D., Morasso, C., Vanna, R., Bedoni, M., Prosperi, D., and Gramatica, F. (2013). Immobilised gold nanostars in a paper-based test system for surface-enhanced Raman spectroscopy. *Vib. Spectrosc.* 68, 45–50. doi:10.1016/j.vibspec.2013.05.010
- Micciché, C., Arrabito, G., Amato, F., Buscarino, G., Agnello, S., and Pignataro, B. (2018). Inkjet printing Ag nanoparticles for SERS hot spots. *Anal. Methods* 10, 3215–3223. Available at: <http://xlink.rsc.org/?DOI=C8AY00624E>.
- Monteiro, C., Daniel-da-Silva, A. L., Venâncio, C., Soares, S. F., Soares, A. M. V. M., Trindade, T., et al. (2019). Effects of long-term exposure to colloidal gold nanorods on freshwater microalgae. *Sci. Total Environ.* 682, 70–79. doi:10.1016/j.scitotenv.2019.05.052
- Moram, S. S. B., Byram, C., Shibu, S. N., Chilukamarri, B. M., and Soma, V. R. (2018). Ag/Au nanoparticle-loaded paper-based versatile surface-enhanced Raman spectroscopy substrates for multiple explosives detection. *ACS Omega* 3, 8190–8201. doi:10.1021/acsomega.8b01318
- Mukha, I., Chepurna, O., Vityuk, N., Khodko, A., Storozhuk, L., Dzhanagan, V., et al. (2021). Multifunctional magneto-plasmonic Fe<sub>3</sub>O<sub>4</sub>/Au nanocomposites:

Approaching magnetophoretically-enhanced photothermal therapy. *Nanomaterials* 11, 1113. doi:10.3390/nano11051113

Nasrollahzadeh, M., Sajjadi, M., Iravani, S., and Varma, R. S. (2021). Starch, cellulose, pectin, gum, alginate, chitin and chitosan derived (nano)materials for sustainable water treatment: A review. *Carbohydr. Polym.* 251, 116986. doi:10.1016/j.carbpol.2020.116986

Nguyen, T. T., Mammeri, F., and Ammar, S. (2018). Iron oxide and gold based magneto-plasmonic nanostructures for medical applications: A review. *Nanomaterials* 8, 149. doi:10.3390/nano8030149

Nogueira, V. I. J. O., Gavina, A., Bouguerra, S., Andreani, T., Lopes, I., Rocha-Santos, T., et al. (2016). "Ecotoxicity and toxicity of nanomaterials with potential for wastewater treatment applications," in *Applying Nanotechnology for environmental sustainability*, 294–329. doi:10.4018/978-1-5225-0585-3.ch013

Ong, T. T. X., Blanch, E. W., and Jones, O. A. H. (2020). Surface Enhanced Raman Spectroscopy in environmental analysis, monitoring and assessment. *Sci. Total Environ.* 720, 137601. doi:10.1016/j.scitotenv.2020.137601

Ovejero, J. G., Yoon, S. J., Li, J., Mayoral, A., Gao, X., O'Donnell, M., et al. (2018). Synthesis of hybrid magneto-plasmonic nanoparticles with potential use in photoacoustic detection of circulating tumor cells. *Microchim. Acta* 185, 130–138. doi:10.1007/s00604-017-2637-x

Peng, Z. A., and Peng, X. (2001). Formation of high-quality CdTe, CdSe, and CdS nanocrystals using CdO as precursor. *J. Am. Chem. Soc.* 123, 183–184. doi:10.1021/ja003633m

Pinheiro, P. C., Daniel-da-Silva, A. L., Nogueira, H. I. S., and Trindade, T. (2018). Functionalized inorganic nanoparticles for magnetic separation and SERS detection of water pollutants. *Eur. J. Inorg. Chem.* 2018, 3440. doi:10.1002/ejic.201800808

Pinheiro, P. C., Fateixa, S., Daniel-da-Silva, A. L., and Trindade, T. (2019a). An integrated approach for trace detection of pollutants in water using polyelectrolyte functionalized magneto-plasmonic nanosorbents. *Sci. Rep.* 9, 19647. doi:10.1038/s41598-019-56168-6

Pinheiro, P. C., Fateixa, S., Nogueira, H. I. S., and Trindade, T. (2019b). Magnetite-supported gold nanostars for the uptake and SERS detection of tetracycline. *Nanomaterials* 9, 31. doi:10.3390/nano9010031

Pinto, J., Lopes, C. B., Henriques, B., Couto, A. F., Ferreira, N., Carvalho, L., et al. (2021). Platinum-group elements sorption by living macroalgae under different contamination scenarios. *J. Environ. Chem. Eng.* 9, 105100. doi:10.1016/j.jece.2021.105100

Polshettiwar, V., and Varma, R. S. (2010). Green chemistry by nano-catalysis. *Green Chem.* 12, 743–775. doi:10.1039/b921171c

Presumido, P. H., Santos, L. F. dos, Neuparth, T., Santos, M. M., Feliciano, M., Primo, A., et al. (2021). A novel ceramic tubular membrane coated with a continuous graphene-TiO<sub>2</sub> nanocomposite thin-film for CECs mitigation. *Chem. Eng. J.* 430, 132639. doi:10.1016/j.ccej.2021.132639

Rafiei-Sarmazdeh, Z., Zahedi-Dizaji, S. M., and Kang, A. K. (2019). "Two-Dimensional Nanomaterials," in *Nanostructures*. Editors S. Ameen, M. S. Akhtar, and H. Shin (IntechOpen). doi:10.5772/intechopen.85263

Rao, N., Singh, R., and Bashambu, L. (2021). Carbon-based nanomaterials: Synthesis and prospective applications. *Mater. Today Proc.* 44, 608–614. doi:10.1016/j.MATPR.2020.10.593

Ray, S. S., and Bandyopadhyay, J. (2021). Nanotechnology-enabled biomedical engineering: Current trends, future scopes, and perspectives. *Nanotechnol. Rev.* 10, 728–743. doi:10.1515/ntrev-2021-0052

Ren, C., Hu, X., and Zhou, Q. (2016). Influence of environmental factors on nanotoxicity and knowledge gaps thereof. *NanoImpact* 2, 82–92. doi:10.1016/j.impact.2016.07.002

Restaino, S. M., Berger, A., and White, I. M. (2017). Inkjet-printed paper fluidic devices for onsite detection of antibiotics using surface-enhanced Raman spectroscopy. *Methods Mol. Biol.* 2, 525–540. doi:10.1007/978-1-4939-6911-1\_33

Scaramuzza, S., Polizzi, S., and Amendola, V. (2019). Magnetic tuning of SERS hot spots in polymer-coated magnetic-plasmonic iron-silver nanoparticles. *Nanoscale Adv.* 1, 2681–2689. doi:10.1039/c9na00143c

Schmid, G. (1992). Large clusters and colloids. Metals in the embryonic state. *Chem. Rev.* 92, 1709–1727. doi:10.1021/cr00016a002

Sha, X., Han, S. Q., Gao, W., Zhao, H., Li, N., Zhang, C., et al. (2020). A rapid detection method for on-site screening of estazolam in beverages with Au@Ag core-shell nanoparticles paper-based SERS substrate. *Anal. Sci.* 36, 667–674. doi:10.2116/ANALSCI.19P361

Shen, L., Huang, Z., Liu, Y., Li, R., Xu, Y., Jakaj, G., et al. (2020). Polymeric membranes incorporated with ZnO nanoparticles for membrane fouling mitigation: A brief review. *Front. Chem.* 8, 224. doi:10.3389/fchem.2020.00224

Shi, Y. E., Li, L., Yang, M., Jiang, X., Zhao, Q., and Zhan, J. (2014). A disordered silver nanowires membrane for extraction and surface-enhanced Raman spectroscopy detection. *Analyst* 139, 2525–2530. doi:10.1039/c4an00163j

Soares, S. F., Simões, T. R., António, M., Trindade, T., and Daniel-da-Silva, A. L. (2016). Hybrid nano-adsorbents for the magnetically assisted removal of metoprolol from water. *Chem. Eng. J.* 302, 560–569. doi:10.1016/j.ccej.2016.05.079

Soares, S. F., Rodrigues, M. I., Trindade, T., and Daniel-da-Silva, A. L. (2017a). Chitosan-silica hybrid nanosorbents for oil removal from water. *Colloids Surfaces A Physicochem. Eng. Aspects* 532, 305–313. doi:10.1016/j.colsurfa.2017.04.076

Soares, S. F., Simões, T. R., Trindade, T., and Daniel-da-Silva, A. L. (2017b). Highly efficient removal of dye from water using magnetic carrageenan/silica hybrid nano-adsorbents. *Water Air Soil Pollut.* 228, 87. doi:10.1007/s11270-017-3281-0

Soares, S. F., Daniel-da-Silva, A. L., and Trindade, T. (2019a). Trimethyl chitosan/siloxane-hybrid coated Fe<sub>3</sub>O<sub>4</sub> nanoparticles for the uptake of sulfamethoxazole from water. *Molecules* 24, 1958. doi:10.3390/molecules24101958

Soares, S. F., Fernandes, T., Sacramento, M., Trindade, T., and Daniel-da-Silva, A. L. (2019b). Magnetic quaternary chitosan hybrid nanoparticles for the efficient uptake of diclofenac from water. *Carbohydr. Polym.* 203, 35–44. doi:10.1016/j.carbpol.2018.09.030

Soares, S. F., Rocha, M. J., Ferro, M., Amorim, C. O., Amaral, J. S., Trindade, T., et al. (2019c). Magnetic nanosorbents with siliceous hybrid shells of alginate acid and carrageenan for removal of ciprofloxacin. *Int. J. Biol. Macromol.* 139, 827–841. doi:10.1016/j.ijbiomac.2019.08.030

Soares, S. F., Fernandes, T., Trindade, T., and Daniel-da-Silva, A. L. (2020). Recent advances on magnetic biosorbents and their applications for water treatment. *Environ. Chem. Lett.* 18, 151–164. doi:10.1007/s10311-019-00931-8

Soares, S. F., Amorim, C. O., Amaral, J. S., Trindade, T., and Daniel-Da-Silva, A. L. (2021a). On the efficient removal, regeneration and reuse of quaternary chitosan magnetite nanosorbents for glyphosate herbicide in water. *J. Environ. Chem. Eng.* 9, 105189. doi:10.1016/j.jece.2021.105189

Soares, S. F., Trindade, T., and Daniel-Da-Silva, A. L. (2021b). Enhanced removal of non-steroidal inflammatory drugs from water by quaternary chitosan-based magnetic nanosorbents. *Coatings* 11, 964. doi:10.3390/coatings11080964

Soares, S. F., Nogueira, J., Trindade, T., and Daniel-da-Silva, A. L. (2022). Towards efficient ciprofloxacin adsorption using magnetic hybrid nanoparticles prepared with  $\kappa$ -i and  $\lambda$ -carrageenan. *J. Nanostructure Chem.*, 1–20. doi:10.1007/s40097-022-00498-x

Sokolova, V., and Eppel, M. (2008). Inorganic nanoparticles as carriers of nucleic acids into cells. *Angew. Chem. Int. Ed.* 47, 1382–1395. doi:10.1002/anie.200703039

Steigerwald, M. L., and Brus, L. E. (1990). Semiconductor crystallites: A class of large molecules. *Acc. Chem. Res.* 23, 183–188. doi:10.1021/ar00174a003

Stiles, P. L., Dieringer, J. A., Shah, N. C., and Van Duyne, R. P. (2008). Surface-enhanced Raman spectroscopy. *Annu. Rev. Anal. Chem. Palo. Alto. Calif.* 1, 601–626. doi:10.1146/annurev.anchem.1.031207.112814

Sun, M., Li, B., Liu, X., Chen, J., Mu, T., Zhu, L., et al. (2019). Performance enhancement of paper-based SERS chips by shell-isolated nanoparticle-enhanced Raman spectroscopy. *J. Mat. Sci. Technol.* 35, 2207–2212. doi:10.1016/j.jmst.2019.05.055

Sun, J., Zhang, Z., Liu, C., Dai, X., Zhou, W., Jiang, K., et al. (2021). Continuous *in situ* portable SERS analysis of pollutants in water and air by a highly sensitive gold nanoparticle-decorated PVDF substrate. *Anal. Bioanal. Chem.* 413, 5469–5482. doi:10.1007/s00216-021-03531-0

Tang, H., Zhu, C., Meng, G., and Wu, N. (2018). Review—surface-enhanced Raman scattering sensors for food safety and environmental monitoring. *J. Electrochem. Soc.* 165, B3098–B3118. doi:10.1149/2.0161808jes

Tao, A. R., Habas, S., and Yang, P. (2008). Shape control of colloidal metal nanocrystals. *Small* 4, 310–325. doi:10.1002/sml.200701295

Tavares, D. S., Daniel-Da-Silva, A. L., Lopes, C. B., Silva, N. J. O., Amaral, V. S., Rocha, J., et al. (2013). Efficient sorbents based on magnetite coated with siliceous hybrid shells for removal of mercury ions. *J. Mat. Chem. A* 1, 8134–8143. doi:10.1039/c3ta10914c

Tavares, D. S., Lopes, C. B., Almeida, J. C., Vale, C., Pereira, E., and Trindade, T. (2020). Spinel-type ferrite nanoparticles for removal of arsenic(V) from water. *Environ. Sci. Pollut. Res.* 27, 22523–22534. doi:10.1007/s11356-020-08673-9

Teitelboim, A., Meir, N., Kazes, M., and Oron, D. (2016). Colloidal double quantum dots. *Acc. Chem. Res.* 49, 902–910. doi:10.1021/acs.accounts.5b00554

Theron, J., Walker, J. A., and Cloete, T. E. (2008). Nanotechnology and water treatment: Applications and emerging opportunities. *Crit. Rev. Microbiol.* 34, 43–69. doi:10.1080/10408410701710442



- Trindade, T., and Daniel da Silva, A. L. (2011). Nanocomposite particles for bio-applications: Materials and bio-interfaces. doi:10.4032/9789814267816
- Trindade, T., and O'Brien, P. (1996). A single source approach to the synthesis of CdSe nanocrystallites. *Adv. Mat.* 8, 161–163. doi:10.1002/adma.19960080214
- Trindade, T., O'Brien, P., and Pickett, N. L. (2001). Nanocrystalline semiconductors: Synthesis, properties, and perspectives. *Chem. Mat.* 13, 3843–3858. doi:10.1021/cm000843p
- Ugurlu, M., and Karaoglu, M. H. (2009). Removal of AOX, total nitrogen and chlorinated lignin from bleached Kraft mill effluents by UV oxidation in the presence of hydrogen peroxide utilizing TiO<sub>2</sub> as photocatalyst. *Environ. Sci. Pollut. Res.* 16, 265–273. doi:10.1007/s11356-008-0044-x
- Valley, N., Greeneltch, N., Van Duyne, R. P., and Schatz, G. C. (2013). A look at the origin and magnitude of the chemical contribution to the enhancement mechanism of surface-enhanced Raman spectroscopy (SERS): Theory and experiment. *J. Phys. Chem. Lett.* 4, 2599–2604. doi:10.1021/jz4012383
- Vega-Vázquez, P., Mosier, N. S., and Irudayaraj, J. (2020). Nanoscale drug delivery systems: From medicine to agriculture. *Front. Bioeng. Biotechnol.* 8, 79. doi:10.3389/fbioe.2020.00079
- Vijayakumar, V., and Khashtgir, D. (2018). Hybrid composite membranes of chitosan/sulfonated polyaniline/silica as polymer electrolyte membrane for fuel cells. *Carbohydr. Polym.* 179, 152–163. doi:10.1016/j.carbpol.2017.09.083
- Vikesland, P. J. (2018). Nanosensors for water quality monitoring. *Nat. Nanotechnol.* 13, 651–660. doi:10.1038/s41565-018-0209-9
- Wadhawan, S., Jain, A., Nayyar, J., and Mehta, S. K. (2020). Role of nanomaterials as adsorbents in heavy metal ion removal from waste water: A review. *J. Water Process Eng.* 33, 101038. doi:10.1016/j.jwpe.2019.101038
- Walsh, J., Bond, A., Forster, R., and Keyes, T. (2016). Hybrid polyoxometalate materials for photo(electro-) chemical applications. *Coord. Chem. Rev.* 306, 217–234. doi:10.1016/j.ccr.2015.06.016
- Wang, W., and Mattoussi, H. (2020). Engineering the bio-nano interface using a multifunctional coordinating polymer coating. *Acc. Chem. Res.* 53, 1124–1138. doi:10.1021/acs.accounts.9b00641
- Wang, Y., He, Y., Lai, Q., and Fan, M. (2014). Review of the progress in preparing nano TiO<sub>2</sub>: An important environmental engineering material. *J. Environ. Sci.* 26, 2139–2177. doi:10.1016/j.jes.2014.09.023
- Wani, T. A., and Suresh, G. (2022). Plant-mediated green synthesis of magnetic spinel ferrite nanoparticles: A sustainable trend in nanotechnology. *Adv. Sustain. Syst.* 6, 2200035. doi:10.1002/adsu.202200035
- Watt, J., Cheong, S., and Tilley, R. D. (2013). How to control the shape of metal nanostructures in organic solution phase synthesis for plasmonics and catalysis. *Nano Today* 8, 198–215. doi:10.1016/j.nantod.2013.03.001
- Weller, H. (1993). Colloidal semiconductor Q-particles: Chemistry in the transition region between solid state and molecules. *Angew. Chem. Int. Ed. Engl.* 32, 41–53. doi:10.1002/anie.199300411
- Weller, H. (1998). Quantum size colloids: From size-dependent properties of discrete particles to self-organized superstructures. *Curr. Opin. Colloid Interface Sci.* 3, 194–199. doi:10.1016/S1359-0294(98)80013-7
- Weon, S., He, F., and Choi, W. (2019). Status and challenges in photocatalytic nanotechnology for cleaning air polluted with volatile organic compounds: Visible light utilization and catalyst deactivation. *Environ. Sci. Nano* 6, 3185–3214. doi:10.1039/c9en00891h
- Whitesides, G. (2005). Nanoscience, nanotechnology, and chemistry. *Small* 1, 172–179. doi:10.1002/sml.200400130
- WHO (2022). Guidelines for drinking-water quality: Fourth edition incorporating the first and second addenda. *World Heal. Organ.* 4, 1–614. Available at: <https://www.who.int/publications/i/item/9789240045064> (Accessed July 28, 2022).
- Wu, M., Li, P., Zhu, Q., Wu, M., Li, H., and Lu, F. (2018). Functional paper-based SERS substrate for rapid and sensitive detection of Sudan dyes in herbal medicine. *Spectrochimica Acta Part A Mol. Biomol. Spectrosc.* 196, 110–116. doi:10.1016/j.saa.2018.02.014
- Xia, Y., Xiong, Y., Lim, B., and Skrabalak, S. E. (2009). Shape-controlled synthesis of metal nanocrystals: Simple chemistry meets complex physics? *Angew. Chem. Int. Ed.* 48, 60–103. doi:10.1002/anie.200802248
- Xu, H., Xiao, K., Wang, X., Liang, S., Wei, C., Wen, X., et al. (2020). Outlining the roles of membrane-foulant and foulant-foulant interactions in organic fouling during microfiltration and ultrafiltration: A mini-review. *Front. Chem.* 8, 417. doi:10.3389/fchem.2020.00417
- Xu, F., Shang, W., Ma, G., Zhu, Y., and Wu, M. (2021a). Metal organic framework wrapped gold nanourchin assembled on filter membrane for fast and sensitive SERS analysis. *Sensors Actuators B Chem.* 326, 128968. doi:10.1016/j.snb.2020.128968
- Xu, F., Xuan, M., Ben, Z., Shang, W., and Ma, G. (2021b). Surface enhanced Raman scattering analysis with filter-based enhancement substrates: A mini review. *Rev. Anal. Chem.* 40, 75–92. doi:10.1515/revac-2021-0126
- Yaashikaa, P. R., Senthil Kumar, P., and Karishma, S. (2022). Review on biopolymers and composites – evolving material as adsorbents in removal of environmental pollutants. *Environ. Res.* 212, 113114. doi:10.1016/j.envres.2022.113114
- Yang, Q., Deng, M., Li, H., Li, M., Zhang, C., Shen, W., et al. (2015). Highly reproducible SERS arrays directly written by inkjet printing. *Nanoscale* 7, 421–425. Available at: <http://xlink.rsc.org/?DOI=C4NR04656K>.
- Yaqoob, A. A., Parveen, T., Umar, K., and Ibrahim, M. N. M. (2020). Role of nanomaterials in the treatment of wastewater: A review. *WaterSwitzerl.* 12, 495. doi:10.3390/w12020495
- Ye, T., Huang, Z., Zhu, Z., Deng, D., Zhang, R., Chen, H., et al. (2020). Surface-enhanced Raman scattering detection of dibenzothiophene and its derivatives without  $\pi$  acceptor compound using multilayer Ag NPs modified glass fiber paper. *Talanta* 220, 121357. doi:10.1016/j.talanta.2020.121357
- Yeber, C. M., Rodríguez, J., Freer, J., Durán, N., and Mansilla, D. H. (2000). Photocatalytic degradation of cellulose bleaching effluent by supported TiO<sub>2</sub> and ZnO. *Chemosphere* 41, 1193–1197. doi:10.1016/S0045-6535(99)00551-2
- Yilmaz, D., Günaydin, B. N., and Yüce, M. (2022). Nanotechnology in food and water security: On-site detection of agricultural pollutants through surface-enhanced Raman spectroscopy. *emergent Mat.* 5, 105–132. doi:10.1007/s42247-022-00376-w
- Yin, Y., and Alivisatos, A. P. (2005). Colloidal nanocrystal synthesis and the organic-inorganic interface. *Nature* 437, 664–670. doi:10.1038/nature04165
- Yina, Y., and Talapin, D. (2013). The chemistry of functional nanomaterials. *Chem. Soc. Rev.* 42, 2484–2487. doi:10.1039/c3cs90011h
- Yorov, K. E., Grigorieva, A. V., Sidorov, A. V., Polyakov, A. Y., Sukhorukova, I. V., Shtansky, D. V., et al. (2016). Inkjet printing of silver rainbow colloids for SERS chips with polychromatic sensitivity. *RSC Adv.* 6, 15535–15540. doi:10.1039/C5RA25907j
- Yu, H., Lyu, Q., Chen, X., Guo, D., He, D., Jia, X., et al. (2021). Nylon membranes modified by gold nanoparticles as surface-enhanced Raman spectroscopy substrates for several pesticides detection. *RSC Adv.* 11, 24183–24189. doi:10.1039/d1ra03490a
- Yu, W. W., and White, I. M. (2012). A simple filter-based approach to surface enhanced Raman spectroscopy for trace chemical detection. *Analyst* 137, 1168–1173. doi:10.1039/c2an15947c
- Yu, W. W., and White, I. M. (2010). Inkjet printed surface enhanced Raman spectroscopy array on cellulose paper. *Anal. Chem.* 82, 9626–9630. doi:10.1021/ac102475k
- Zeng, F., Mou, T., Zhang, C., Huang, X., Wang, B., Ma, X., et al. (2019). Paper-based SERS analysis with smartphones as Raman spectral analyzers. *Analyst* 144, 137–142. Available at: <http://xlink.rsc.org/?DOI=C8AN01901K>.
- Zhang, H., Jin, M., Xiong, Y., Lim, B., and Xia, Y. (2013). Shape-controlled synthesis of Pd nanocrystals and their catalytic applications. *Acc. Chem. Res.* 46, 1783–1794. doi:10.1021/ar300209w
- Zhang, D., Zhao, J., Yang, P., Chen, Y., and Fan, Y. (2020). Preparation of high stability Pd/ceramic/Ti-Al alloy composite membranes by electroless plating. *Front. Chem.* 8, 202. doi:10.3389/fchem.2020.00202





## OPEN ACCESS

## EDITED BY

Vadim G. Kessler,  
Swedish University of Agricultural  
Sciences, Sweden

## REVIEWED BY

Bo Wang,  
Hebei University of Science and  
Technology, China

## \*CORRESPONDENCE

Daniela V. Lopes,  
daniela.rosendo.lopes@ua.pt  
Andrei V. Kovalevsky,  
akavaleuski@ua.pt

## SPECIALTY SECTION

This article was submitted to Ceramics  
and Glass,  
a section of the journal  
Frontiers in Materials

RECEIVED 02 August 2022

ACCEPTED 13 September 2022

PUBLISHED 28 September 2022

## CITATION

Lopes DV, Quina MJ, Frade JR and  
Kovalevsky AV (2022), Prospects and  
challenges of the electrochemical  
reduction of iron oxides in alkaline  
media for steel production.  
*Front. Mater.* 9:1010156.  
doi: 10.3389/fmats.2022.1010156

## COPYRIGHT

© 2022 Lopes, Quina, Frade and  
Kovalevsky. This is an open-access  
article distributed under the terms of the  
[Creative Commons Attribution License](https://creativecommons.org/licenses/by/4.0/)  
(CC BY). The use, distribution or  
reproduction in other forums is  
permitted, provided the original  
author(s) and the copyright owner(s) are  
credited and that the original  
publication in this journal is cited, in  
accordance with accepted academic  
practice. No use, distribution or  
reproduction is permitted which does  
not comply with these terms.

# Prospects and challenges of the electrochemical reduction of iron oxides in alkaline media for steel production

Daniela V. Lopes<sup>1\*</sup>, Margarida J. Quina<sup>2</sup>, Jorge R. Frade<sup>1</sup> and  
Andrei V. Kovalevsky<sup>1\*</sup>

<sup>1</sup>Department of Materials and Ceramic Engineering, CICECO—Aveiro Institute of Materials, University of Aveiro, Aveiro, Portugal, <sup>2</sup>CIEPQPF, Department of Chemical Engineering, Pólo II—Pinhal de Marrocos, University of Coimbra, Coimbra, Portugal

Steelmaking industries have been facing strict decarbonization guidelines. With a net zero carbon emissions target, European policies are expected to be accomplished before 2050. Traditional steelmaking industry still operates by the carbothermic reduction of iron ores for steel production. Consequently, the steel sector is responsible for a large amount of CO<sub>2</sub> emissions, accounting for up to 9% of the CO<sub>2</sub> worldwide emissions. In this scope, the electrochemical reduction or electrolysis of iron oxides into metallic iron in alkaline media arises as a promising alternative technology for ironmaking. Significant advantages of this technology include the absence of CO<sub>2</sub> emissions, non-polluting by-products such as hydrogen and oxygen gases, lower temperature against the conventional approach (~100°C versus 2000°C) and lower electric energy consumption, where around 6 GJ per ton of iron manufactured can be spared. The present minireview discusses the progress on the electrochemical reduction of iron oxides in alkaline media as a green steelmaking route. A historical overview of the global steelmaking against recent developments and challenges of the novel technology is presented, and the fundamental mechanisms of iron oxide reduction to iron and alternative iron feedstocks are discussed. Factors affecting the Faradaic efficiencies of the alkaline electroreduction of iron oxide suspensions or iron oxide bulk ceramics are also explored, focusing on the concurrent hydrogen evolution reaction. Overall, if scrutinized, this technology may become a breaking point for the steel industry sector.

## KEYWORDS

electrowinning, steelmaking, iron ore, green steel, carbon free technology

## Introduction

The Sustainable Development Goals proposed by the United Nations General Assembly and the European Green Deal provide an integrated roadmap for making the World and EU's economy more sustainable, emphasizing the role of transition to clean and renewable energy sources and carbon-neutral technologies. Large industries, like steel, face strong pressure to lower greenhouse gas emissions (Elavarasan et al., 2022). Thus, high investments in developing alternative technologies, preferably relying on renewable energy, are required. About 1951 million tonnes of crude steel were produced worldwide in 2021, with expected growth in the upcoming years (World Steel Association, 2022). The Blast Furnace coupled with a Basic Oxygen Furnace (BF-BOF) is responsible for 71% of the total steel production during the conventional carbothermic reduction of iron ores with coke to "pig iron" at high temperatures (1,500°C and 1,650 °C when considering BOF). The remaining 29% are related to non-coke-based technologies such as the Electric Arc Furnace (EAF) and the Direct Reduced Iron (DRI). Despite the associated CO<sub>2</sub> emissions, the BF-BOF is expected to continue to be the primary route for steelmaking in the upcoming years due to the high mass production capacity and cost-effectiveness (HORIZON 2020, 2020; Fan and Friedmann, 2021). The resulting emissions account for about 7–9% of the global CO<sub>2</sub> emissions. Due to the demanding steel production rate, 3.0 billion tonnes of CO<sub>2</sub> emissions are estimated for 2050 (Mousa, 2019). Thus, the steelmaking industry is under great strain to improve its technology regarding the use of less raw materials, less energy consumption, lower emissions of particles and gas, and opening new routes for CO<sub>2</sub>-lean steelmaking.

Electrolysis of metal oxides for metal production arises as a greener approach to conventional extraction methods, offering advantages such as the absence of CO<sub>2</sub> emissions, non-polluting by-products such as hydrogen and oxygen gases, and lower electric energy consumption (13 GJ/ton of Fe against 19 GJ/ton (Beer et al., 2000; Allanore et al., 2010b). Electrolysis is a conventional technology nowadays for producing aluminium (Mandin et al., 2019), zinc (Monhemius, 1980), and other metals. Several potentially positive impacts of electrolytic iron production were identified in SIDERWIN project (SIDERWIN, 2022), including 87% reduction in direct CO<sub>2</sub> emissions, 31% reduction in energy use, the ability to involve iron oxide-containing residues like red mud, and potential compatibility with renewable energies.

## A brief historical perspective

Attempts toward electrolytic iron production undertaken in the last century have identified several challenges. It was firstly reported in patents considering alkaline solutions (Estelle, 1915; Angel, 1952), followed by electroplating in acidic baths (Shafer

and Harr, 1958; Izaki, 2010; Gamburg and Zangari, 2011) for iron strips and electrotypes manufacturing in the early 30s. Electrolyte ferrous solutions (FeSO<sub>4</sub> or FeCl<sub>2</sub> at pH ranges of 0.5–5.5) were electrolyzed at temperatures below 100°C. However, light grey and brittle deposits were frequently obtained, even with the addition of Al-Mg-Na sulphates, Fe(BF<sub>4</sub>)<sub>2</sub> or Fe(H<sub>2</sub>NO<sub>3</sub>S)<sub>2</sub>. The pitted iron deposits were observed under acidic conditions, since Fe<sup>2+</sup> and Fe<sup>3+</sup> co-exist in the acidic electrolytic bath, forming a redox cycle loop between the iron species, lowering the overall Faradaic efficiency (Pourbaix, 1974; Allanore et al., 2010c; Izaki, 2010). Few studies have been performed in recent years, except for a few efforts with fluoroborate (Su et al., 2009) and sulphate (Díaz et al., 2008) acidic media. The electrolytic iron production was then mainly investigated considering the alkaline conditions. However, little attention has been paid to this process mostly due to the doubtful mechanism of reduction to Fe (Gorbunova and Liamina, 1966). Until now, questions about the relatively low electrolysis temperature (≈100 °C), insulating properties of Fe<sub>2</sub>O<sub>3</sub> (Morin, 1951; Lee et al., 2012), 10<sup>−14</sup> S/cm, the low solubility of the iron oxides, and presumably single reduction step (Fe<sub>2</sub>O<sub>3</sub> + 3H<sub>2</sub>O + 6e<sup>−</sup> → 2Fe<sup>0</sup> + 6OH<sup>−</sup>), have been the reasons to doubt the prospects of this electrolytic process (Cornell and Schwertmann, 2003; Allanore et al., 2007, 2008).

Significant advances have been made in the last two decades. Iron oxide electrolysis in alkaline aqueous solutions is now considered one of the most promising technologies for iron production (Monteiro et al., 2016; Müller et al., 2016; Ivanova et al., 2017; Cavaliere, 2019). Several large R&D projects have been approved during the last decade seeking alternative CO<sub>2</sub>-free technologies with low energy consumption, such as IERO, ULCOS, LowCarbonFuture, GREENSTEEL, among many others (U.S. Department of Energy, 2014; Lavelaine et al., 2016; Quader et al., 2016; Draxler et al., 2020). The ongoing project on low-temperature electrolysis for steel production, SIDERWIN (SIDERWIN, 2022), has been strongly encouraged by the European Commission under the Horizon 2020, where the first pilot-scale plant for iron production by electrolysis of iron oxide-containing suspensions is being developed.

## Fundamental mechanisms and current research trends

Experimentally, there are two approaches for electroreduction (Figure 1): the electrodeposition of Fe on a working electrode (WE, e.g., Ni (Figure 1A) from iron oxide-based suspensions; or the electroreduction of a bulk iron oxide-based cathode (porous or dense, Figure 1B). Cathodes morphologies before and after reduction are also represented in Figure 1, attending to each type of electroreduction. The iron formation mechanisms and corresponding microstructural evolution are discussed below.

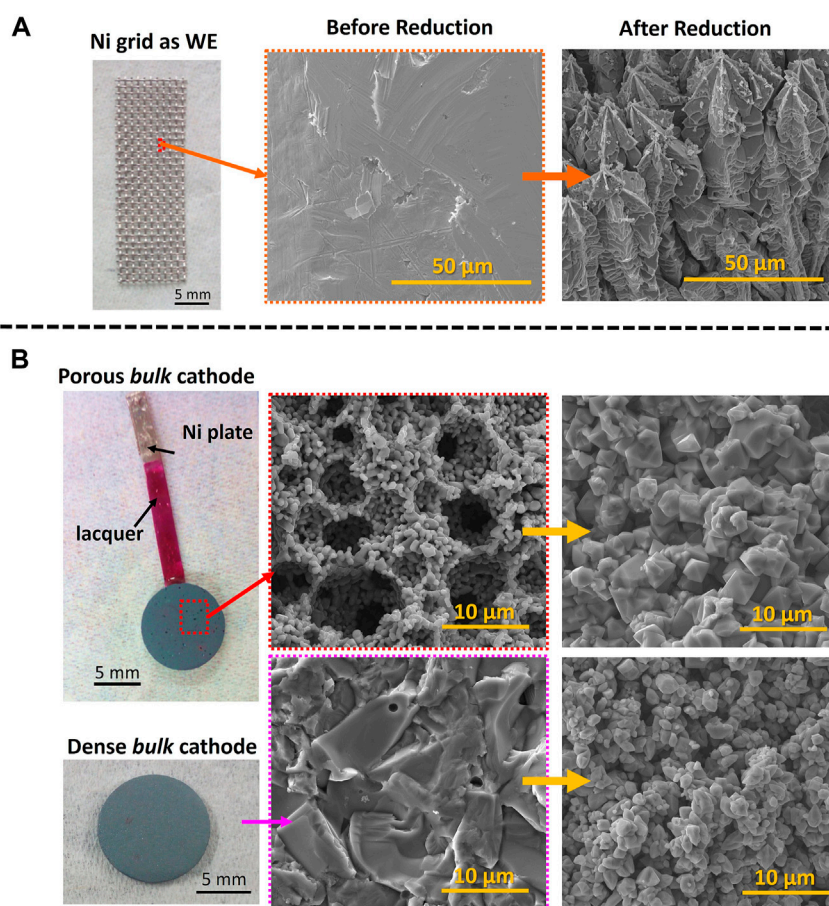


FIGURE 1

Microstructural evolution of the Working Electrode (WE) during the electrochemical reduction to Fe in 10 M NaOH and at 90°C in a (A)  $\text{Fe}_2\text{O}_3$  ceramic suspension and as a (B)  $\text{Fe}_2\text{O}_3$  ceramic bulk cathode.

## Electroreduction from iron oxide-based suspensions

The overall electroreduction mechanism involves two stages: reduction of Fe(III) to Fe(II) species followed by further reduction and cathodic deposition of iron (Gorbunova and Liamina, 1966; Armstrong and Baurhoo, 1972). Thermodynamic studies (Diakonov et al., 1999) proposed the hydrolysis of  $\text{Fe}_2\text{O}_3$  in alkaline solutions to  $\text{Fe}(\text{OH})_4^-$ . However, the low solubility of  $\text{Fe}_2\text{O}_3$  in alkaline conditions ( $\sim 2 \times 10^{-3}$  M at 18 M NaOH, 100°C (Picard et al., 1980b)) raised concerns regarding this mechanism. Since then, significant advances in understanding this process have been made. Today the main emphasis is given to a dissolution/redeposition route and solid-state mechanism. Thus, the preliminary dissolution of  $\text{Fe}_2\text{O}_3$  and formation of  $\text{Fe}(\text{OH})_4^-$  is considered (Picard et al., 1980a; Le and Ghali, 1993; Beverskog and Puigdomenech, 1996; Diakonov et al., 1999; Allanore et al., 2007; Yuan et al., 2009; Yuan and Haarberg, 2009), as  $\text{Fe}_2\text{O}_3 + 3\text{H}_2\text{O} + 2\text{OH}^- \rightleftharpoons 2\text{Fe}(\text{OH})_4^-$ . The

second step consists of the reduction of the  $\text{Fe}(\text{OH})_4^-$  to  $\text{Fe}(\text{OH})_3^-$  in solution,  $\text{Fe}(\text{OH})_4^- + e^- \rightarrow \text{Fe}(\text{OH})_3^- + \text{OH}^-$ , followed by complete reduction and cathodic deposition of Fe,  $\text{Fe}(\text{OH})_3^- + 2e^- \rightarrow \text{Fe}^0 + 3\text{OH}^-$  (Le and Ghali, 1993; Beverskog and Puigdomenech, 1996; Allanore et al., 2007).

A second proposed reduction mechanism involves the adsorption of  $\text{Fe}_2\text{O}_3$  particles at the WE's surface. Around 3 min of the WE immersion in a  $\text{Fe}_2\text{O}_3$  suspension was enough to form Fe deposits after a potentiostatic electroreduction ( $-1.2$  V vs.  $\text{Hg}|\text{HgO}$ ) in a separate particle-free cell (Allanore et al., 2010a). The adsorption effect is caused by electrostatic forces, since the  $\text{Fe}_2\text{O}_3$  particles have a slightly positive zeta potential in strong alkaline media, in contrast with the negatively charged WE (Siebentritt et al., 2014). This second route is expected to occur simultaneously with the first route, despite not being mentioned very often. Alkali concentration, cell operating temperature, and iron oxide load are the main factors determining the contribution of each mechanism to the overall process. Working electrodes (WE) as

graphite (Allanore et al., 2007; Yuan et al., 2009; Tokushige et al., 2013; Feynerol et al., 2017; Maihatchi et al., 2020), Cu rod (Zou et al., 2015a), Fe rod (Ivanova et al., 2015), stainless steel plates (Koutsoupa et al., 2021a; 2021b) or Ni grids (Lopes et al., 2020, 2021, 2022) are usually used. Dendritic/star-like shape Fe deposits are often obtained after the electrochemical reduction of iron oxides in alkaline suspensions (Figure 1A).

## Bulk electroreduction

The bulk electroreduction refers to *in situ* conversion of iron ore pieces or lumps, acting as a cathode (or WE), to Fe. The microstructure of such cathodes is often decisive for electroreduction. The low electrical conductivity of Fe<sub>2</sub>O<sub>3</sub> (10<sup>-14</sup> S/cm (Morin, 1951; Lee et al., 2012)) requires a mechanical connection between the iron oxide piece and the electrochemical cell. A three-phase interlines (3PIs) model is often used for explaining the electrochemical reduction of typical solid insulators (Deng et al., 2005; Xiao et al., 2007; Zou et al., 2015b). Thus, the insulating Fe<sub>2</sub>O<sub>3</sub> can only be reduced after establishing an interface with an electrical conductor (e.g. metal attached to the pellet acting as a current collector) and simultaneously with an electrolyte. Electrically conductive metals such as Ni (Ivanova et al., 2017; Lopes et al., 2018) or steel (Allanore et al., 2008) are frequently used as current collectors.

Chronoamperometry studies of iron electroreduction allow understanding of the bulk shrinking behaviour of iron oxide-based cathodes during Fe formation, where three well-defined regions are visible in the current density vs. time plot (Allanore et al., 2010c; Zou et al., 2015b). Corresponding steps include: i) electrolyte entrance to the external layer of the cathode and expansion of the 3PIs model along the surface; ii) cathode surface reduction to form metallic Fe; iii) the unreduced core is finally reduced to Fe leading to a shrinking of the cathode. The current density is then stabilized, resulting in the “shrinking-core reaction process” proposed by Zou and his co-workers.

Magnetite Fe<sub>3</sub>O<sub>4</sub> phase (10<sup>3</sup> S/cm (Cornell and Schwertmann, 2003; Lee et al., 2012)) is often observed as an intermediate phase during Fe<sub>2</sub>O<sub>3</sub> electroreduction. It is responsible for boosting the current density in the second step of the shrinking-core process. Most authors consider the dissolution-electrodeposition route even in the case of bulk electroreduction (Sato et al., 1970; Schmuki et al., 1996; Allanore et al., 2010c; Zou et al., 2015b, 2015a; Ivanova et al., 2017), where Fe<sub>3</sub>O<sub>4</sub> phase undergoes a reductive dissolution to Fe(II) aqueous species as Fe(OH)<sub>3</sub><sup>-</sup> (Allen et al., 1980). The Fe(II) species react with the neighbouring bulk Fe<sub>2</sub>O<sub>3</sub> promoting new Fe<sub>3</sub>O<sub>4</sub> phase formation. However, other authors (He et al., 2011; Haarberg and Yuan, 2014) consider a solid-state Fe<sub>3</sub>O<sub>4</sub> reduction to Fe. Zou and his co-workers do not completely exclude this route but strongly highlight the main reduction pathway as the

dissolution-electrodeposition (Zou et al., 2015b; 2015a). Other Fe(II) species forming during Fe<sub>3</sub>O<sub>4</sub> reduction (HFeO<sub>2</sub><sup>-</sup>, etc) are also considered and predicted by Pourbaix diagrams (Pourbaix, 1974; Le and Ghali, 1993). On the other hand, Fe(OH)<sub>2</sub> is mostly present at working temperatures below 65°C (Schrebler Guzmán et al., 1979; Le and Ghali, 1993; Zhang and Park, 1994).

Another relevant aspect of the electrochemical reduction of bulk cathodes refers to the porosity increase of around 30–50% when Fe is formed (Allanore et al., 2008; 2010c), promoted by significant density change from Fe<sub>2</sub>O<sub>3</sub> phase (5.26 g/cm<sup>3</sup>) to Fe (7.86 g/cm<sup>3</sup>). The space between the Fe particles becomes wider with the growth of these Fe microstructures in a dendrite shape, increasing the porosity of the metal (Zou et al., 2015a). The electrolyte presence was found between the metal iron oxide layer interface (Allanore et al., 2010c), which can also be crucial when considering the initial porosity of the bulk cathodes. Thus, the processing conditions should ideally provide some connectivity between even residual pores to ensure the percolation of the electrolyte and ionic species inside the cathode towards the current collector (Zou et al., 2015b). When cellular iron oxide-based designed cathodes with open porosities higher than 37 vol% are used (Ivanova et al., 2017; Lopes et al., 2019, 2021, 2022), the electroreduction is facilitated, and the forming Fe crystals preserve the original cellular-based ceramics microstructure, suggesting that the reductive dissolution to Fe(II) occurs in sub-micrometer distances. The porosity of 37 vol% was found to ensure the best performance towards electroreduction, while maintaining suitable mechanical properties of the ceramic cathodes, leading to complete conversion of the ceramic cathode to metallic Fe (Lopes et al., 2019). The Fe microstructure evolution when considering dense or porous bulk ceramic cathodes is demonstrated in Figure 1B.

## Factors affecting the faradaic efficiency of the electroreduction

Hydrogen evolution reaction (HER; 2H<sub>2</sub>O + 2e<sup>-</sup> → H<sub>2</sub> + 2OH<sup>-</sup>) has a parasitic effect on iron electroreduction due to the superimposed cathodic potential region with the reduction to Fe. In fact, the first couple of hours of a cathodic polarization are ascribed to hydrogen adsorption at the cathode, leading to a higher overvoltage (Brossard and Huot, 1991; Allanore et al., 2007). HER is the main factor responsible for the loss of Faradaic efficiency, lowering the quality of Fe deposits. Although it is not possible to eliminate, minimizing HER until a certain level is feasible. The choice of the cathode is of great relevance when considering the electrodeposition from suspensions. Noble metals (Pt, Pd, or Au) have low HER activity, while Fe, Ni, Co, Cu, and Ag have moderate activity. On the other hand, Zn, Ti, Zn, Pb, or Sn have high overpotentials (Ivanova et al., 2015; Rashid et al., 2015). The use of rotation disk electrodes (RDE) (up to



TABLE 1 Comparison of the Faradaic Efficiencies between traditional and alternative iron oxide feedstocks.

	Iron feedstock	Type of electroreduction	WE	Experimental conditions	Faradaic efficiency	Ref
Traditional feedstock	Fe <sub>2</sub> O <sub>3</sub>	Suspension	Graphite rotating disk	18 M NaOH; T = 114°C; 1,000 rpm; j = 4000 A/m <sup>2</sup> ; 33 wt% Fe <sub>2</sub> O <sub>3</sub>	95%	Yuan et al. (2009)
	Fe <sub>2</sub> O <sub>3</sub> iron ore lumps	Bulk	Ore lump + Ni	18 M NaOH; T = 100°C; E = -1.20 V (vs SHE)	53–100%	Allanore et al. (2010c)
	Fe <sub>2</sub> O <sub>3</sub>	Suspension	Graphite rotating disk	18 M NaOH; T = 110°C; 1,000 rpm; j = 1,000–6000 A/m <sup>2</sup> ; 33 and 40 wt% Fe <sub>2</sub> O <sub>3</sub>	95% (40 wt% Fe <sub>2</sub> O <sub>3</sub> + 3000 A/m <sup>2</sup> )	Tokushige et al. (2013)
	Fe <sub>3</sub> O <sub>4</sub>	Bulk	Fe <sub>3</sub> O <sub>4</sub> pellets sintered at 1,100–1,400°C + Ni foil	10 M NaOH; T = 90°C; E = -1.15 V (vs Hg HgO)	85% (pellets with 22% of open porosity)	Monteiro et al. (2016)
	Fe <sub>2</sub> O <sub>3</sub>	Suspension	Graphite rod	18 M NaOH; T = 110°C; 600 rpm; E = -1.66 V; 10 wt% of iron oxides	86% (Fe <sub>2</sub> O <sub>3</sub> )	Feynerol et al. (2017)
	Fe <sub>3</sub> O <sub>4</sub>				5% (Fe <sub>3</sub> O <sub>4</sub> )	
	α-FeOOH				66% (α-FeOOH)	
Alternative feedstock	Fe <sub>2</sub> O <sub>3</sub>	Bulk	Fe <sub>2</sub> O <sub>3</sub> porous pellets fired at 1,100–1,200°C + Ni foil	10 M NaOH; T = 90°C; E = -1.15 V and -1.50 V (vs Hg HgO)	39% (E = -1.15 V) 21% (E = -1.50 V)	Ivanova et al. (2017)
	Red Mud	Suspension	Graphite rod with Ti/Pt grid	12.5 M NaOH; T = 110°C; 600 rpm; j = 45 A/m <sup>2</sup> ; 333.3 g/L of red mud	71% for red mud (45 A/m <sup>2</sup> ) ~80% for Fe <sub>2</sub> O <sub>3</sub> (200–1000 A/m <sup>2</sup> )	Maihatchi et al. (2020)
	Titanomagnetite from iron sands	Bulk	Iron sand + stainless steel	18 M NaOH; T = 110°C; j = 1 A/cm <sup>2</sup>	Very low	Bjareborn et al. (2020)
	Red Mud	Suspension	Stainless steel plate	18 M NaOH; T = 70–130°C; 500 rpm; j = 138 and 1100 A/m <sup>2</sup> ; 10 wt% of red mud or Fe <sub>2</sub> O <sub>3</sub>	~80% for Fe <sub>2</sub> O <sub>3</sub> regardless the temperature (138 A/m <sup>2</sup> ); ~10% (70°C) to 70% (130°C) for red mud (138 A/m <sup>2</sup> )	Koutsoupa et al. (2021a)
	Pseudobrookite	Bulk	Fe <sub>2</sub> TiO <sub>5</sub> + Ni plate	10 M NaOH; T = 80°C; E = -1.30 V (vs Hg HgO)	Very low	Lopes et al. (2022)
	Pseudobrookite	Suspension	Steel rod	10 M NaOH; T = 80°C; 100 rpm; E = -1.15 V (vs Hg HgO); 100 g/L of iron oxide	25%	
	Iron oxide residues from Zn production	Suspension	Graphite rotating disk and silver rod	18 M NaOH; T = 110°C; 500 rpm for rotating disk +100 rpm for magnetic stirrer; E = -1.6 V	-	Haarberg et al. (2022)
	Iron oxide residues from Ni production	Suspension	Graphite rotating disk and silver rod	18 M NaOH; T = 110°C; 500 rpm for rotating disk +100 rpm for magnetic stirring; j = 0.6 A/cm <sup>2</sup> ; 1: 90 g/L of residue	7%	

3,000 rpm) lowers the Faradaic efficiencies from 96% (<1,000 rpm) to 76% (3,000 rpm) due to the combined effect of air and H<sub>2</sub> bubbles at its surfaces (Yuan et al., 2009). RDE also restrict the transport of the suspended particles around the WE (Allanore et al., 2010b). Stirring conditions below 2000 rpm allow to maintain high current efficiency, according to Yuan et al. Moreover, the bubbles can also have a negative impact on the electroreduction by dropping the current density due to the vibration of the ceramic cathodes (Allanore et al., 2010c). However, increasing the porosity of the cathode for the bulk electroreduction allowed the bubbles to escape through the pores, representing one alternative way to minimize this effect (Ivanova et al., 2017).

HER potentials tend to increase for higher cathodic values when the alkaline electrolyte concentrations increase (Nickell et al., 2006). Some authors have been employing 18 M NaOH electrolyte solutions (Allanore et al., 2008, 2010c; Yuan et al., 2009; Tokushige et al., 2013) to minimize the HER effect. Although increasing the concentration of the electrolyte seems to decrease the HER impact and, consequently, the Faradaic efficiency increase, it does not guarantee itself a high efficiency level as, for example, ~70% of efficiency was obtained at 18 M NaOH (Allanore et al., 2007) and ~80% at 10 M NaOH (Ivanova et al., 2015). On the other hand, current efficiency drop from 39% to 21% when potentiostatic cathodic polarizations of -1.15 V and -1.50 V (vs Hg|HgO) are used, respectively, in 10 M NaOH

solutions (Ivanova et al., 2017). This aspect clearly demonstrates the increased HER contribution at higher polarizations for the same electrolyte concentration. The efficiency also increases for higher iron oxide concentration in the alkaline suspension (Allanore et al., 2007). In general, the Faradaic efficiency is a complex parameter affected by the cell configuration, type of electrodes, iron oxide load, current densities or cathodic polarizations applied, and temperature.

## Alternative iron feedstocks and their suitability

An overview analysis of potential feedstocks for electrolytic iron production is given in Table 1. Hematite is a reference iron oxide feedstock for the electrochemical reduction studies in alkaline media showing high efficiencies (>85%), except at high cathodic polarizations (e.g. 39% at  $-1.15$  V) due to HER contribution. Iron (hydroxy-) oxides such as  $\text{Fe}_3\text{O}_4$  and  $\alpha$ - $\text{FeOOH}$  (goethite) also can be used as raw material in suspensions (Feynerol et al., 2017), with consequently lower current efficiencies due to the magnetic behaviour of the particles and high viscosity that restricts the evolution of  $\text{O}_2$  bubbles, respectively. Latest studies on alternative feedstocks include the use of industrial iron-rich waste as red mud from the Bayer process (Maihatchi et al., 2020; Koutsoupa et al., 2021a, 2021b) and iron-rich residues from the Zn and Ni electrowinning industrial production (Haarberg et al., 2022). The use of iron-rich waste is of high interest due to the possibility of waste valorisation, which is strongly supported by the European Commission and contributes to the circular economy. Faradaic efficiencies of red mud reach about 70%, but only when low current density is applied ( $45\text{--}138\text{ A/m}^2$ ) in concentrated electrolytes (>12.5 M). On the other hand, titanomagnetite from natural ironsands (Bjareborn et al., 2020) showed low efficiencies. In fact, significant challenges are imposed when considering various alternative feedstocks. The presence of non-conductive phases suppresses the electroreduction to metallic iron. Ni and Zn residues from industrial production show low efficiencies (<7%) even when considering pre-treatments of both wastes. Several iron-oxide based compositions have been the research aim under the SIDERWIN European project for electrolytic iron production in alkaline media. The impact of Al- (Lopes et al., 2019, 2020), Mg- (Lopes et al., 2021), and Ti- (Lopes et al., 2022) additions to iron-oxide ceramic cathodes and/or suspensions have been investigated. The dissolution of the mentioned species to the electrolyte leads to the partial blocking of the cathode surface, restricting further reduction to Fe. The Ti- blocking effect strongly affects the conversion of the synthetic pseudobrookite mineral ( $\text{Fe}_2\text{TiO}_5$ ), where simply  $\text{Fe}_3\text{O}_4$  phase (intermediary phase) was found at  $-1.15$  V (Lopes et al., 2022). Strong cathodic polarizations were required for producing Fe from

$\text{Fe}_2\text{TiO}_5$  suspensions with consequent impact on the faradaic efficiencies (<25%) due to HER.

## Concluding remarks

Fast implementation of clean energy technologies in steelmaking requires developing cost-effective approaches. Although the recent research results and trends show that metallic iron production by electrolysis is a feasible approach, many experimental challenges still need to be resolved. Up to now, high and reproducible Faradaic efficiencies have been achieved mostly when using pure iron oxides as a feedstock. The presence of impurities harms the current yield, and the detailed relevant mechanisms and corresponding mitigation strategies are still to be discovered. At the same time, the possibility of achieving high Faradaic efficiency while using red mud as an iron feedstock was recently demonstrated, confirming the potential sustainability of the proposed technology and its contribution to the circular economy. It must be noticed that, in commonly used alkaline conditions, the efficiency of iron electroreduction is compromised only by the cathodic evolution of hydrogen gas, which may be considered the fuel of the future, with no carbon footprint, highest enthalpy of combustion, and releasing water as a by-product during energy release. Thus, even if the current efficiency of iron production is still relatively low, the electrolysis process can be potentially adapted to the intermittency of renewable energies and optimized towards iron electroreduction or green hydrogen production, depending on the actual power conditions. This opens new prospects for this approach as a green alternative to traditional steelmaking, where breakthrough technologies are urgent and necessary. The electrolytic iron production arises as a competitive technology against the conventional technology by saving 6 GJ/ton of Fe produced, representing a turning point in the metallurgical industry in the near future. de Beer, 2000.

## Author contributions

DVL and AVK contributed to the design and conceptualization of the minireview. DVL and AVK wrote the draft of the manuscript. MJQ and JRF improved specific sections of the minireview. All authors contributed to the minireview revision and approved the submitted version.

## Funding

This work was developed within the scope of the European SIDERWIN project (SIDERWIN- DLV-768788 - Horizon 2020/ SPIRE10), and CICECO-Aveiro Institute of Materials, UIDB/

50011/2020 and UIDP/50011/2020, and LA/P/0006/2020, financed by national funds through the FCT/MEC (PIDDAC).

## Conflict of interest

The authors declare that the research was conducted in the absence of any commercial or financial relationships that could be construed as a potential conflict of interest.

## References

- Allanore, A., Feng, J., Lavelaine, H., and Ogle, K. (2010a). The adsorption of hematite particles on steel in strongly alkaline electrolyte. *J. Electrochem. Soc.* 157, E24–E30. doi:10.1149/1.3273198
- Allanore, A., Lavelaine, H., Birat, J. P., Valentin, G., and Lapicque, F. (2010b). Experimental investigation of cell design for the electrolysis of iron oxide suspensions in alkaline electrolyte. *J. Appl. Electrochem.* 40, 1957–1966. doi:10.1007/s10800-010-0172-0
- Allanore, A., Lavelaine, H., Valentin, G., Birat, J. P., Delcroix, P., and Lapicque, F. (2010c). Observation and modeling of the reduction of hematite particles to metal in alkaline solution by electrolysis. *Electrochim. Acta* 55, 4007–4013. doi:10.1016/j.electacta.2010.02.040
- Allanore, A., Lavelaine, H., Valentin, G., Birat, J. P., and Lapicque, F. (2007). Electrodeposition of metal iron from dissolved species in alkaline media. *J. Electrochem. Soc.* 154, E187–E193. doi:10.1149/1.2790285
- Allanore, A., Lavelaine, H., Valentin, G., Birat, J. P., and Lapicque, F. (2008). Iron metal production by bulk electrolysis of iron ore particles in aqueous media. *J. Electrochem. Soc.* 155, E125–E129. doi:10.1149/1.2952547
- Allen, P. D., Bignold, G. J., and Hampson, N. A. (1980). The electrodisolution of magnetite: Part III. Iron nucleation processes on magnetite electrodes. *J. Electroanal. Chem. Interfacial Electrochem.* 112, 239–246. doi:10.1016/S0022-0728(80)80405-0
- Angel, E. (1952). *US Patent No 2,622,063, Electrolytic production of iron and iron alloys*. Washington, D.C.: United States Patent Office.
- Armstrong, R., and Baurhoo, I. (1972). The dissolution of iron in concentrated alkali. *J. Electroanal. Chem. Interfacial Electrochem.* 40, 325–338. doi:10.1016/S0022-0728(72)80377-2
- Beer, J. (2000). *Eco-efficiency in industry and science*. Dordrecht, Utrecht, Netherlands: Springer. doi:10.1007/978-94-017-2728-0
- Beverkog, B., and Puigdomenech, I. (1996). Revised Pourbaix diagrams for iron at 25–300 °C. *Corros. Sci.* 38, 2121–2135. doi:10.1016/S0010-938X(96)00067-4
- Bjareborn, O., Arif, T., Monaghan, B., and Bumby, C. W. (2020). Fate of titanium in alkaline electro-reduction of sintered titanomagnetite. *Mat. Res. Express* 7, 106508. doi:10.1088/2053-1591/abb24
- Brossard, L., and Huot, J. Y. (1991). *In situ* activation of cathodes during alkaline water electrolysis by dissolved iron and molybdenum species. *J. Appl. Electrochem.* 21, 508–515. doi:10.1007/BF01018603
- Cavaliere, P. (2019). *Clean ironmaking and steelmaking processes*. Italy: LecceSpringer International Publishing. doi:10.1007/978-3-030-21209-4
- Cornell, R. M., and Schwertmann, U. (2003). *The iron oxides: Structures, properties, reactions, occurrences and uses*. Second Edi. Weinheim: Wiley VCH. doi:10.1002/3527602097
- de Beer, J. (2000). Potential for industrial energy-efficiency improvement in the long term. *Eco Effi. Ind. and Sci.* 5. doi:10.1007/978-94-017-2728-0
- Deng, Y., Wang, D., Xiao, W., Jin, X., Hu, X., and Chen, G. Z. (2005). Electrochemistry at conductor/insulator/electrolyte three-phase interlines: A thin layer model. *J. Phys. Chem. B* 109, 14043–14051. doi:10.1021/jp044604r
- Diakonov, I. I., Schott, J., Martin, F., Harrichourry, J. C., and Escalier, J. (1999). Iron(III) solubility and speciation in aqueous solutions. Experimental study and modelling: Part 1. Hematite solubility from 60 to 300°C in NaOH–NaCl solutions and thermodynamic properties of Fe(OH)<sub>4</sub>(aq). *Geochim. Cosmochim. Acta* 63, 2247–2261. doi:10.1016/S0016-7037(99)00070-8
- Díaz, S. L., Calderón, J. A., Barcia, O. E., and Mattos, O. R. (2008). Electrodeposition of iron in sulphate solutions. *Electrochim. Acta* 53, 7426–7435. doi:10.1016/j.electacta.2008.01.015
- Draxler, M., Schenk, J., Bürgler, T., and Sormann, A. (2020). The steel industry in the European union on the crossroad to carbon lean production—status, initiatives and challenges. *Berg. Huettenmaenn. Monatsh.* 165, 221–226. doi:10.1007/s00501-020-00975-2
- Elavarasan, R. M., Pugazhendhi, R., Irfan, M., Mihet-Popa, L., Khan, I. A., and Campana, P. E. (2022). State-of-the-art sustainable approaches for deeper decarbonization in Europe – an endowment to climate neutral vision. *Renew. Sustain. Energy Rev.* 159, 112204. doi:10.1016/j.rser.2022.112204
- Estelle, A. (1915). *Swedish Patent No 42,849, Förfarande för framställning av järn genom elektrolytisk reduktion i lösning av kaustiskt alkali*. Stockholm: Kungl. Patent och Registreringsverket.
- Fan, Z., and Friedmann, S. J. (2021). Low-carbon production of iron and steel: Technology options, economic assessment, and policy. *Joule* 5, 829–862. doi:10.1016/j.joule.2021.02.018
- Feynerol, V., Lavelaine, H., Marlier, P., Pons, M. N., and Lapicque, F. (2017). Reactivity of suspended iron oxide particles in low temperature alkaline electrolysis. *J. Appl. Electrochem.* 47, 1339–1350. doi:10.1007/s10800-017-1127-5
- Gamburg, Y., and Zangari, G. (2011). *Theory and practice of metal electrodeposition*. London: Springer Science+Business Media, LLC. doi:10.1017/CBO9781107415324.004
- Gorbunova, K. M., and Liamina, L. I. (1966). On the mechanism of iron reduction from alkaline solutions. *Electrochim. Acta* 11, 457–467. doi:10.1016/0013-4686(66)80023-3
- Haarberg, G. M., Qin, B., and Khalaghi, B. (2022). “Electrochemical reduction of iron oxides in aqueous NaOH electrolyte including iron residue from nickel and zinc electrowinning processes,” in *Rare metal technology 2022. The minerals, metals & materials series* (Cham: Springer), 341–347. doi:10.1007/978-3-030-92662-5\_33
- Haarberg, G. M., and Yuan, B. (2014). Direct electrochemical reduction of hematite pellets in alkaline solutions. *ECS Trans.* 58, 19–28. doi:10.1149/05820.0019ecst
- He, Z., Gudavarthy, R. V., Koza, J. A., and Switzer, J. A. (2011). Room-temperature electrochemical reduction of epitaxial magnetite films to epitaxial iron films. *J. Am. Chem. Soc.* 133, 12358–12361. doi:10.1021/ja203975z
- HORIZON2020 (2020). EU coordinated methods and procedures based on real cases for the effective implementation of policies and measures supporting energy efficiency in the Industry. *Technical analysis – iron and steel sector*. NACE C24.1-24.2-24-5, 18.
- Ivanova, Y., Monteiro, J., Horovistiz, A., Ivanou, D., Mata, D., Silva, R., et al. (2015). Electrochemical deposition of Fe and Fe/CNTs composites from strongly alkaline hematite suspensions. *J. Appl. Electrochem.* 45, 515–522. doi:10.1007/s10800-015-0803-6
- Ivanova, Y., Monteiro, J., Teixeira, L., Vitorino, N., Kovalevsky, A., and Frade, J. (2017). Designed porous microstructures for electrochemical reduction of bulk hematite ceramics. *Mat. Des.* 122, 307–314. doi:10.1016/j.matdes.2017.03.031
- Izaki, M. (2010). “Electrodeposition of iron and iron alloys,” in *Modern electroplating*. Editors M. Schlesinger and M. Paunovic (John Wiley & Sons), 309–326. doi:10.1007/BF01022244
- Koutsoupa, S., Koutalidi, S., Balomenos, E., and Panias, D. (2021a). Siderwin — a new route for iron production. *Mat. Proc.* 5, 58. doi:10.3390/materproc2021005058
- Koutsoupa, S., Koutalidi, S., Bourbos, E., Balomenos, E., and Panias, D. (2021b). Electrolytic iron production from alkaline bauxite residue slurries at low temperatures : Carbon-free electrochemical process for the production of

## Publisher's note

All claims expressed in this article are solely those of the authors and do not necessarily represent those of their affiliated organizations, or those of the publisher, the editors and the reviewers. Any product that may be evaluated in this article, or claim that may be made by its manufacturer, is not guaranteed or endorsed by the publisher.

- metallic iron. *Johns. Matthey Technol. Rev.* 65, 366–374. doi:10.1595/205651320X15918757312944
- Lavelaine, H., Van der Laan, S., Hita, A., Olsen, K., Serna, M., Haarberg, G., et al. (2016). *Iron production by electrochemical reduction of its oxide for high CO<sub>2</sub> mitigation (IERO)*. Brussels: European Commission.
- Le, H., and Ghali, E. (1993). Interpretation des diagrammes E-pH du système Fe-H<sub>2</sub>O en relation avec la fragilisation caustique des aciers. *J. Appl. Electrochem.* 23, 72–77. doi:10.1007/BF00241579
- Lee, K. K., Deng, S., Fan, H. M., Mhaisalkar, S., Tan, H. R., Tok, E. S., et al. (2012).  $\alpha$ -Fe<sub>2</sub>O<sub>3</sub> nanotubes-reduced graphene oxide composites as synergistic electrochemical capacitor materials. *Nanoscale* 4, 2958–2961. doi:10.1039/c2nr11902a
- Lopes, D. V., Ivanova, Y. A., Kovalevsky, A. V., Sarabando, A. R., Frade, J. R., and Quina, M. J. (2019). Electrochemical reduction of hematite-based ceramics in alkaline medium: Challenges in electrode design. *Electrochim. Acta* 327, 135060. doi:10.1016/j.electacta.2019.135060
- Lopes, D. V., Kovalevsky, A., Quina, M., and Frade, J. (2020). Electrochemical deposition of zero-valent iron from alkaline ceramic suspensions of Fe<sub>2</sub>-xAl<sub>x</sub>O<sub>3</sub> for iron valorisation. *J. Electrochem. Soc.* 167, 102508. doi:10.1149/1945-7111/ab9a2b
- Lopes, D. V., Kovalevsky, A. V., Quina, M. J., and Frade, J. R. (2018). Processing of highly-porous cellular iron oxide-based ceramics by emulsification of ceramic suspensions. *Ceram. Int.* 44, 20354–20360. doi:10.1016/j.ceramint.2018.08.024
- Lopes, D. V., Lisenkov, A. D., Ruivo, L. C. M., Yaremchenko, A. A., Frade, J. R., and Kovalevsky, A. V. (2022). Prospects of using pseudobrookite as an iron-bearing mineral for the alkaline electrolytic production of iron. *Mater. (Basel)* 15, 1440. doi:10.3390/ma15041440
- Lopes, D. V., Lisenkov, A. D., Sergienko, S. A., Constantinescu, G., Sarabando, A., Quina, M. J., et al. (2021). Alkaline electrochemical reduction of a magnesium ferrosin into metallic iron for the valorisation of magnetite-based metallurgical waste. *J. Electrochem. Soc.* 168, 073504. doi:10.1149/1945-7111/ac1490
- Maihatchi, A., Pons, M.-N., Ricoux, Q., Goettmann, F., and Lapique, F. (2020). Electrolytic iron production from alkaline suspensions of solid oxides: Compared cases of hematite, iron ore and iron-rich bayer process residues. *J. Electrochem. Sci. Eng.* 10, 95–102. doi:10.5599/jese.751
- Mandin, P., Wüthrich, R., and Roustan, H. (2019). Industrial aluminium production: The Hall-heroult process modelling. *ECS Trans.* 19, 1–10. doi:10.1149/1.3247986
- Monhemius, A. J. (1980). “The electrolytic production of chlorates,” in *Topics in non-ferrous extractive metallurgy*. Editor A. R. Burkin (Oxford, UK: Blackwell Scientific Publications), 104–130. doi:10.1038/scientificamerican08021902-22233asupp
- Monteiro, J., Ivanova, Y., Kovalevsky, A., Ivanou, D., and Frade, J. (2016). Reduction of magnetite to metallic iron in strong alkaline medium. *Electrochim. Acta* 193, 284–292. doi:10.1016/j.electacta.2016.02.058
- Morin, F. (1951). Electrical properties of Fe<sub>2</sub>O<sub>3</sub> and Fe<sub>2</sub>O<sub>3</sub> containing titanium. *Phys. Rev.* 83, 1005–1010. doi:10.1103/PhysRev.83.1005
- Mousa, E. A. (2019). Modern blast furnace ironmaking technology: Potentials to meet the demand of high hot metal production and lower energy consumption. *Metall. Mat. Eng.* 25, 69–104. doi:10.30544/414
- Müller, C. I., Sellschopp, K., Tegel, M., Rauscher, T., Kieback, B., and Röntzsch, L. (2016). The activity of nanocrystalline Fe-based alloys as electrode materials for the hydrogen evolution reaction. *J. Power Sources* 304, 196–206. doi:10.1016/j.jpowsour.2015.11.008
- Nickell, R. A., Zhu, W. H., Payne, R. U., Cahela, D. R., and Tatarchuk, B. J. (2006). Hg/HgO electrode and hydrogen evolution potentials in aqueous sodium hydroxide. *J. Power Sources* 161, 1217–1224. doi:10.1016/j.jpowsour.2006.05.028
- Picard, G., Oster, D., and Tremillon, B. (1980a). Electrochemical reduction of iron oxides in suspension in water-sodium hydroxide mixtures between 25 and 140 °C. I: Theoretical study. *J. Chem. Res.* 8, 250–251.
- Picard, G., Oster, D., and Tremillon, B. (1980b). Electrochemical reduction of iron oxides in suspension in water-sodium hydroxide mixtures between 25 and 140 °C. II: Experimental study. *J. Chem. Res.* 8, 252–253.
- Pourbaix, M. (1974). *Atlas of electrochemical equilibria in aqueous solutions*. 2nd Edition. Brussels: Cebalcor Brussels.
- Quader, M. A., Ahmed, S., Dawal, S. Z., and Nukman, Y. (2016). Present needs, recent progress and future trends of energy-efficient Ultra-Low Carbon Dioxide (CO<sub>2</sub>) Steelmaking (ULCOS) program. *Renew. Sustain. Energy Rev.* 55, 537–549. doi:10.1016/j.rser.2015.10.101
- Rashid, M. M., Al Mesfer, M. K., Naseem, H., and Danish, M. (2015). Hydrogen production by water electrolysis: A review of alkaline water electrolysis, PEM water electrolysis and high temperature water electrolysis. *Int. J. Eng. Adv. Technol.*, 2249–8958.
- Sato, N., Kudo, K., and Noda, T. (1970). Single layer of the passive film on Fe. *Corros. Sci.* 10, 785–794. doi:10.1016/S0010-938X(70)80002-6
- Schmuki, P., Virtanen, S., Davenport, A., and Vitus, C. (1996). *In situ* X-ray absorption near-edge spectroscopic study of the cathodic reduction of artificial iron oxide passive films. *J. Electrochem. Soc.* 143, 574–582. doi:10.1149/1.1836483
- Schrebler Guzmán, R. S., Vilche, J. R., and Arvia, A. J. (1979). The potentiodynamic behaviour of iron in alkaline solutions. *Electrochim. Acta* 24, 395–403. doi:10.1016/0013-4686(79)87026-7
- Shafer, W., and Harr, C. (1958). Electrolytic iron powders-production and properties. *J. Electrochem. Soc.* 105, 413–417. doi:10.1149/1.2428876
- SIDERWIN (2022). SIDERWIN. Available at: <https://www.siderwin-spire.eu/>.
- Siebert, M., Volovitch, P., Ogle, K., and Lefèvre, G. (2014). Adsorption and electroreduction of hematite particles on steel in strong alkaline media. *Colloids Surfaces A Physicochem. Eng. Aspects* 440, 197–201. doi:10.1016/j.colsurfa.2012.09.002
- Su, C.-w., He, F.-j., Ju, H., Zhang, Y.-b., and Wang, E.-l. (2009). Electrodeposition of Ni, Fe and Ni-Fe alloys on a 316 stainless steel surface in a fluoroborate bath. *Electrochim. Acta* 54, 6257–6263. doi:10.1016/j.electacta.2009.05.076
- Tokushige, M., Kongstein, O. E., and Haarberg, G. M. (2013). Crystal orientation of iron produced by electrodeoxidation of hematite particles. *ECS Trans.* 50, 103–114. doi:10.1149/05052.0103ecst
- U.S. Department of Energy (2014). *Advanced manufacturing office (AMO)*. Washington, D.C.: U.S. Department of Energy.
- World Steel Association (2022). *World steel in figures*. Brussels: Worldsteel Association.
- Xiao, W., Jin, X., Deng, Y., Wang, D., and Chen, G. Z. (2007). Three-phase interlines electrochemically driven into insulator compounds: A penetration model and its verification by electroreduction of solid AgCl. *Chem. Eur. J.* 13, 604–612. doi:10.1002/chem.200600172
- Yuan, B., and Haarberg, G. (2009). Electrodeposition of iron in aqueous alkaline solution: An alternative to carbothermic reduction. *ECS Trans.* 16, 31–37. doi:10.1149/1.3114006
- Yuan, B., Kongstein, O. E., and Haarberg, G. M. (2009). Electrowinning of iron in aqueous alkaline solution using a rotating cathode. *J. Electrochem. Soc.* 156, D64–D69. doi:10.1149/1.3039998
- Zhang, H., and Park, S. M. (1994). Rotating ring-disk electrode and spectroelectrochemical studies on the oxidation of iron in alkaline solutions. *J. Electrochem. Soc.* 141, 718–724. doi:10.1149/1.2054798
- Zou, X., Gu, S., Cheng, H., Lu, X., Zhou, Z., Li, C., et al. (2015a). Facile electrodeposition of iron films from NaFeO<sub>2</sub> and Fe<sub>2</sub>O<sub>3</sub> in alkaline solutions. *J. Electrochem. Soc.* 162, D49–D55. doi:10.1149/2.0751501jes
- Zou, X., Gu, S., Lu, X., Xie, X., Lu, C., Zhou, Z., et al. (2015b). Electroreduction of iron (III) oxide pellets to iron in alkaline media: A typical shrinking-core reaction process. *Metall. Mater. Trans. B* 46B, 1262–1274. doi:10.1007/s11663-015-0336-8





## OPEN ACCESS

## EDITED BY

Verónica de Zea Bermudez,  
University of Trás-os-Montes and Alto  
Douro, Portugal

## REVIEWED BY

Rodrigo Moreno,  
Spanish National Research Council  
(CSIC), Spain  
Yuqing Meng,  
Idaho National Laboratory (DOE),  
United States

## \*CORRESPONDENCE

Filipe ML Figueiredo,  
lebre@ua.pt  
Fernando MB Marques,  
fmarques@ua.pt

## SPECIALTY SECTION

This article was submitted to Energy  
Materials,  
a section of the journal  
Frontiers in Materials

RECEIVED 13 July 2022

ACCEPTED 01 September 2022

PUBLISHED 28 September 2022

## CITATION

Grilo JPF, Jamale A, Sarykevich M,  
Figueiredo FML and Marques FMB  
(2022), Role of salts on the electrical  
performance of ceria-based  
electrolytes: An overview.  
*Front. Mater.* 9:993583.  
doi: 10.3389/fmats.2022.993583

## COPYRIGHT

© 2022 Grilo, Jamale, Sarykevich,  
Figueiredo and Marques. This is an  
open-access article distributed under  
the terms of the [Creative Commons  
Attribution License \(CC BY\)](#). The use,  
distribution or reproduction in other  
forums is permitted, provided the  
original author(s) and the copyright  
owner(s) are credited and that the  
original publication in this journal is  
cited, in accordance with accepted  
academic practice. No use, distribution  
or reproduction is permitted which does  
not comply with these terms.

# Role of salts on the electrical performance of ceria-based electrolytes: An overview

João PF Grilo<sup>1</sup>, Atul Jamale<sup>1</sup>, Maksim Sarykevich<sup>1</sup>,  
Filipe ML Figueiredo<sup>2\*</sup> and Fernando MB Marques<sup>1,3\*</sup>

<sup>1</sup>Department of Materials and Ceramic Engineering, CICECO – Aveiro Institute of Materials, University of Aveiro, Aveiro, Portugal, <sup>2</sup>Department of Physics, CICECO – Aveiro Institute of Materials, University of Aveiro, Aveiro, Portugal, <sup>3</sup>Department of Materials Engineering, Federal University of Paraíba, João Pessoa, Brazil

This work provides an overview on established achievements and debatable findings involving Ca, Gd or Sm-doped ceria-based electrolytes, using  $\text{Li}_2\text{CO}_3$ ,  $\text{LiNO}_3$  and  $\text{Na}_2\text{CO}_3$  as sintering aid or as second phase. The performance of these materials is discussed considering the characteristics of the oxides and of the salts or derived second(ary) phases (e.g., alkali metal oxides and hydroxides, eutectic mixtures), extensively surveyed to identify influential parameters with respect to processing and electrical performance (e.g., melting and boiling points, thermal decomposition, hydrolysis). The analysis of published data highlights the possible contribution of additional charge carriers to the total conductivity, besides oxide-ion vacancies. Claimed bulk and grain boundary conductivity enhancements are deeply discussed, as well as advantages and limitations of impedance spectroscopy as characterization tool. Irrespective of controversial reasons, reports on unusual improvements of grain boundary conductivity sustain the possibility of advanced grain boundary engineering to enhance the performance of these materials.

## KEYWORDS

ceria, alkali metal salt, solid electrolyte, bulk conductivity, grain boundary conductivity, impedance spectroscopy, microstructure

## Introduction

Solid oxide fuel cells (SOFCs) are devices able to convert chemical into electrical energy *via* electrochemical reactions, where electrolyte and electrodes play a key role. Lower processing and operating temperatures are desirable targets to decrease cost and improve long term performance. Ceria-based ceramics are promising electrolyte materials due to their high ionic conductivity with respect to conventional zirconia-based electrolytes, enabling lower operating temperatures (Mogensen et al., 2000; Kharton et al., 2004). Drawbacks include the partial reduction of  $\text{Ce}^{4+}$  to  $\text{Ce}^{3+}$  under reducing conditions, also the high sintering temperatures ( $>1500^\circ\text{C}$ ) needed to achieve almost full densification (Inaba and Tagawa, 1996; Kharton et al., 2001).

Chemical routes, yielding reactive ceria-based powders, were exploited to lower sintering temperatures (Herle et al., 1997; Chinarro et al., 2007; Ding et al., 2008;

Moure et al., 2009; Cela et al., 2011; Teoh and Chiang, 2012). Large attention was also given to sintering aids, including transition metal oxides (Kleinlogel and Gauckler, 2000; Fagg et al., 2002; Avila-Paredes and Kim, 2006; Pérez-Coll et al., 2006; Pikalova et al., 2007; Gao et al., 2010; Ge et al., 2011; Xu et al., 2011; Villas-boas et al., 2014; Taub et al., 2015; Neuhaus et al., 2018a, 2018b; Santos et al., 2018), and alkali metal salts (Nicholas and De Jonghe, 2007; Li et al., 2012; Le et al., 2013; Zhu et al., 2014; Maheshwari and Wiemhöfer, 2016). Sintering temperatures around 1000°C are easily reached using these admixtures, providing high densifications (in the 95–99% range), and regular grain size distributions.

This work exploits alternative explanations to claimed conductivity enhancements of selected materials using salts as sintering aids or second phases. Bulk conductivity augmentation is hardly explained by conventional effects involving dopant concentration and/or mobility of ionic defects (Figueiredo and Marques, 2013). Thus, emphasis is dedicated to grain boundary effects, large in most reports. Own expertise in similar materials provides a sound background for this purpose (Grilo et al., 2019, 2020; 2021a; 2021b).

Selected examples used in this work might be described as typical of debatable findings, deviating from a conventional review where extensive sets of data on similar oxides are collected and discussed. Here, emphasis is on data on distinct salt-derived phases that might coexist under specific conditions, yielding unusual performance effects. Proper consideration of second(ary) phase effects is almost absent from previous analyses in the literature. While new hypotheses are introduced to explain some findings, there is no intention to disregard previous explanations. The complexity of studied systems cannot be ignored. The presence of minor salt-derived phases is a clear source of uncertainty. Molten phases easily originate quasi steady state rather than true equilibrium conditions. Even in solid state systems, due to slow equilibration kinetics, exact phase boundaries are often uncertain (e.g., see (Duwez et al., 1952; Grain, 1967; Stubican, 1986; Duran et al., 1991)).

This work has a clear focus on ceria-based solid electrolytes, in contrast to composites involving one oxide and one molten phase (e.g., see (Benamira et al., 2007; Ferreira et al., 2011b; Rondão et al., 2013)). The borderline between these families of materials is established by the fully dominant solid-state condition. In oxide+molten salt composites, the molten phase corresponds to more than 10 vol%, and is conceived as provider of specific functionalities, like additional ionic pathway in fuel cells or CO<sub>2</sub> gas separation membranes (Li et al., 2009; Patrício et al., 2014).

The electrical characterization of single-phase solid electrolytes is often based on impedance spectroscopy measurements. This technique provides information on contributions within the bulk grains, across grain boundaries and even on the electrolyte/electrode interfacial processes of a

TABLE 1 List of acronyms and selected physical properties of single-phase electrolytes (Duran et al., 1990; Zha et al., 2003; Maheshwari and Wiemhöfer, 2016).

Compound	Acronym	$d_{th}^a$	MP <sup>b</sup> (°C)
Ce <sub>0.95</sub> Ca <sub>0.05</sub> O <sub>2-δ</sub>	5CDC	6.96	2445
Ce <sub>0.90</sub> Gd <sub>0.10</sub> O <sub>2-δ</sub>	GDC	7.23	
Ce <sub>0.80</sub> Sm <sub>0.20</sub> O <sub>2-δ</sub>	SDC	7.13	

<sup>a</sup> $d_{th}$ , theoretical density.

<sup>b</sup>MP, melting point for pure CeO<sub>2</sub>.

polycrystalline ceramic electrolyte (Van Dijk and Burggraaf, 1981; Maier, 1986; Guo et al., 2002, 2003).

The presence of a second phase, even in minor amounts, can be the source of disturbance of impedance arcs. Porous electrolytes are one of the best studied examples, showing that pore size distribution and volume fraction influence the so-called bulk and grain boundary arcs (Roberts and Schwartz, 1985; Kleitz and Steil, 1997; Pérez-Coll et al., 2010; Marrero-López et al., 2014; El Khal et al., 2017; Cordier et al., 2019). For dispersed insulating phases within a conducting phase, the effective medium theory offers proper background for data analysis (Maxwell, 1904; Kleitz and Steil, 1997). The often-disregarded complexity of analysis in electrolytes with two potential conducting phases is hereby addressed, including a survey of impedance spectra characteristics and corresponding equivalent circuits.

## Materials overview

### Oxides

Materials considered in this work are based on ceria, with Ca, Gd or Sm as dopants. The first composition is interesting with respect to (low) cost, the remaining compositions are electrolytes with premium ionic conductivity. This selection is enough to cover a variety of situations where interaction between oxide and salt (or derived phases) might reveal distinct characteristics. Table 1 shows the acronyms and basic properties of these high-density ceramic refractory materials.

### Salts

Salts are often used only as sintering aids (Nicholas and De Jonghe, 2007), as those listed in Table 2. Carbonates or nitrates, the most common admixtures, might end up as oxides or hydroxides, after thermal processing or exposure to specific environmental species. Comparison with data from Table 1 shows the sharp difference in density and melting point between these compounds and previous oxides.

TABLE 2 List of acronyms and selected physical properties of salts, derived compounds and eutectic mixtures.

Compound	Acronym	$d_{th}^a$	MP <sup>b</sup> (°C)	BP <sup>b</sup> (°C)	Ref
Na <sub>2</sub> CO <sub>3</sub>	NaC	2.53	851	1600 (d*)	Haynes, (2005)
NaOH	—	2.13	318	1390 (d*)	
Na <sub>2</sub> O	—	2.27	1132	1950	
LiNO <sub>3</sub>	LiN	2.38	264	600 (d*)	
Li <sub>2</sub> CO <sub>3</sub>	LiC	2.11	723	1310 (d*)	
LiOH	—	1.46	450	924 (d*)	Ortman and Larsen, (1983)
Li <sub>2</sub> O	—	2.01	1438	2600	
Mixture	Acronym			ET <sup>c</sup> (°C)	Ref
LiNO <sub>3</sub> + 40 mol% LiOH	LiN+LiOH			180	Janz and Tomkins, (1983)
Na <sub>2</sub> CO <sub>3</sub> + 90 wt% NaOH	NaC+NaOH			283	
Li <sub>2</sub> CO <sub>3</sub> + 84 mol% LiOH	LiC+LiOH			433	Bale et al. (2016)
Na <sub>2</sub> CO <sub>3</sub> + 52 mol% Li <sub>2</sub> CO <sub>3</sub>	NLC			498	Jiang et al. (2017)
Li <sub>2</sub> CO <sub>3</sub> + 13 wt% Li <sub>2</sub> O	LiC+LiO			705	Kaplan et al. (2011)

<sup>a</sup> $d_{th}$ , theoretical density.<sup>b</sup>MP and BP, melting and boiling points, respectively.<sup>c</sup>ET, eutectic temperature; d\*, decomposes, see Table 4.

TABLE 3 List of ceria-based solid electrolytes (from top to bottom: Maheshwari and Wiemhöfer, 2016; Zhu et al., 2014; Li et al., 2012; Grilo et al., 2020).

Material			Firing stages and temperatures (°C)		Grain size (μm)	Secondary phase		
						Nominal composition	vol%	
Oxide	Salt	Acronym	1st	2nd		Mass	vol%	
5CDC	NaC	5CCC4:1	400	600 (20 h)	<1	20 wt% NaC	40.7	≤40.7 (NaC)
GDC	LiN	5LiGDC	600	1000	<1	5 cat% (Li <sup>+</sup> )	6.0	≤1.6 <sup>a</sup> (Li <sub>2</sub> O)
SDC	LiC	SDC15Li	700	900	~5	15 cat% (Li <sup>+</sup> )	11.3	≤5.1 <sup>a</sup> (Li <sub>2</sub> O)
GDC	—	GDC	1500		2.6	—	—	nd
	NLC <sup>b</sup>	GDC-5M <sup>c</sup>	1100		1.9	5 mol% NLC	7.8	nd
		GDC-5S <sup>c</sup>			2.6			

<sup>a</sup>Assuming only thermal decomposition of LiN and LiC, and no porosity.<sup>b</sup>NLC, NaC+ 52 mol% LiC.<sup>c</sup>M, mechanical (ceramic) route.<sup>d</sup>S, chemical synthesis route; nd, not detected.

## Oxide electrolytes with salt addition

Table 3 shows the exact compositions and firing conditions experienced by electrolytes considered in this work, grouped according to data sources rather than composition. The first three rows correspond to materials prepared by authors from distinct

institutions. The last row includes three materials prepared in one single institution (own work). These materials will be used as reference.

Materials acronyms in Table 3 were partly introduced in Tables 1, 2. These follow closely those adopted in the source references. However, the range of combinations is wide, and a few

TABLE 4 Selected reactions involving alkali metal-based materials.

Reaction	T (°C)	Remarks	Ref
$\text{Na}_2\text{CO}_3 \text{ (l)} \rightarrow \text{Na}_2\text{O (s)} + \text{CO}_2 \text{ (g)}$	>1200	In Argon, weight loss $w = 9.66 \times 10^2 \exp(-58600/RT)$ (g/cm <sup>2</sup> )	Nakamura et al. (1980)
	>950	In Argon, very slow rate	Kim and Lee, (2001)
	650–700	Sharp weight loss (TGA)	Mareshwari and Wiemhöfer, (2016)
$2\text{NaOH} \rightarrow \text{Na}_2\text{O} + \text{H}_2\text{O}$	475–750	Decomposition rate $r = 50.5 \times \exp(-30230/T)$ (gh <sup>-1</sup> ), vacuum = 13.3 Pa	Yurinskii et al. (2005)
$\text{LiNO}_3 \rightarrow \text{Li}_2\text{O (Li}_2\text{O}_2) + \text{NO}_x$	(500 <sub>start</sub> )-700 <sub>peak</sub>	Based on TGA-DTA data	Sweeney, (1975)
	(485 <sub>start</sub> )-650 <sub>peak</sub>	Based on TGA-DSC data (air: 40 vol%, He:60 vol%)	Ruiz et al. (2010)
$\text{Li}_2\text{CO}_3 \rightarrow \text{Li}_2\text{O} + \text{CO}_2$	>800	Under Argon	Kim and Lee, (2001)
	>710	Under Argon, complete at 900°C	Li et al. (2012)
	825–975	$P_{\text{CO}_2} = 2.33 \times 10^9 \times \frac{1-X_{\text{Li}_2\text{O}}}{X_{\text{Li}_2\text{O}}} \exp(-32500/T)$	Kaplan et al. (2011)
$2\text{LiOH (s)} \rightarrow \text{Li}_2\text{O (s)} + \text{H}_2\text{O (g)}$	290–405	Fraction of released water $x = 1 - k_1 \times \exp(-k_2 \cdot t)$ , vacuum = $4 \times 10^{-4}$ Pa	Kudo, (1979)

examples are used to assist in the capture of the meaning of acronyms. 5CCC4:1 means a Ceria (5CDC) - Carbonate (NaC) - Composite with a 4:1 weight ratio. 5LiGDC means GDC with 5 cat% Li<sup>+</sup>. GDC-5S corresponds to GDC with 5 mol% NLC, prepared by a chemical synthesis (S) route. The extension (M) in GDC-5M designates a ceramic route, starting with mechanical milling. SDC15Li is SDC with 15 cat% Li<sup>+</sup>. When needed, the material acronym also includes a reference to the highest firing temperature (e.g., SDC15Li-900 means SDC15Li sintered at 900°C). Table 3 also provides information on grain size and vol% of distinct phases, with impact on electrical performance.

The first obvious conclusion from these data is that processing temperatures are below salt melting (5CCC4:1), exceed the salt melting and boiling points (5LiGDC), or surpass only the melting point of precursor salts (SDC15Li-900).

## Salt phase changes

Salts are also likely to suffer total or partial decomposition during thermal processing. Table 4 lists typical examples of known reactions, conversion levels and conditions. NaC (used in 5CCC4:1) is expected to be preserved after firing at 600°C. Melting is only at 851°C, and thermal decomposition is significant only above the sintering temperature (600°C). LiN (used in 5LiGDC) might easily boil but also partly decompose, being converted into Li<sub>2</sub>O. LiC (used in SDC15Li) is expected to be partly converted to Li<sub>2</sub>O. NLC (used in GDC-5S and GDC-5M), the eutectic mixture of NaC and LiC, melts at around 500°C. The stability of this phase is high at moderate temperatures (e.g., 650°C), but volatilization and even decomposition to oxides are likely at higher temperatures. These comments explain the values

listed in the last column of Table 3, on predictable higher limits of oxides, from thermal decomposition of salts.

Standard “lab working conditions,” involving ambient air during measurements (with moisture and CO<sub>2</sub>), and unknown/diverse storage conditions of samples, are additional sources of considerable uncertainty. As example, an investigation on the hydrolysis of lithium oxide showed that the starting material (nominally pure Li<sub>2</sub>O) consists of particles with a Li<sub>2</sub>O core covered by a LiOH protective shell (Weber et al., 2018). Furthermore, the loss of water from alkali hydroxides is not fast or easy, requiring high temperatures and long periods of time (see Table 4).

5CDC with NaC should have a considerable volume fraction of this phase (30–40 vol%), the most stable with respect to the adopted thermal processing (600°C). SDC with LiC should have a moderate volume fraction of Li<sub>2</sub>O and/or LiOH (up to 5.1 vol%). The oxide is the most stable phase with respect to the thermal processing steps (up to 900°C), but the hydroxide should form easily from exposure to moisture. GDC with LiN should have a residual volume fraction of Li<sub>2</sub>O (up to 1.6 vol%) and/or LiOH, since LiN starts decomposing before boiling and the oxide and hydroxide are the most stable after the adopted processing temperature (1000°C). GDC-5S and GDC-5M might have residual amounts of alkali-metal carbonates, oxides and/or hydroxides.

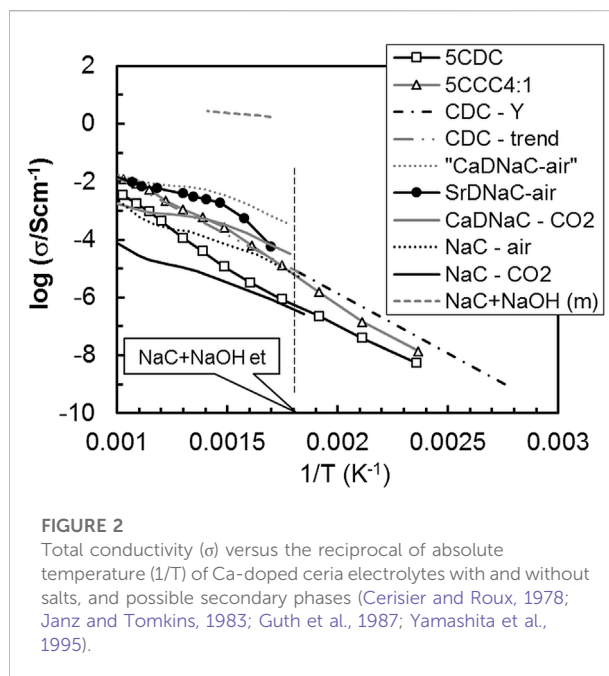
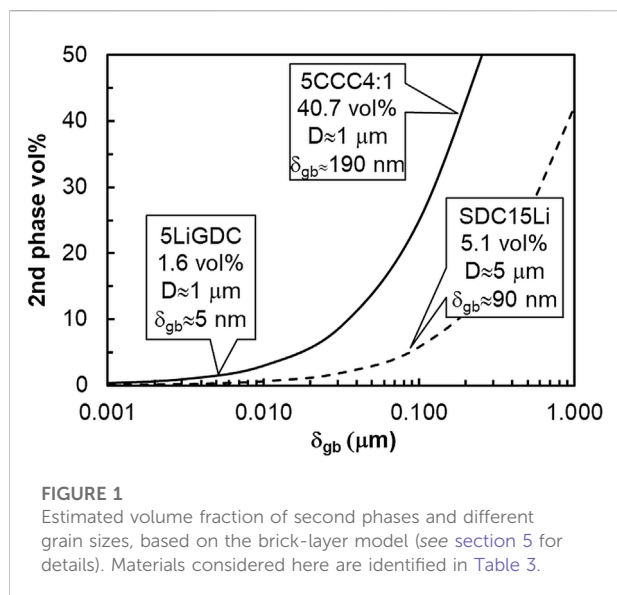
The likely presence of alkali oxides and/or hydroxides in these materials is source of additional phase interactions. Table 2 lists eutectic compositions involving these compounds. The corresponding eutectic temperatures, starting below 200°C, are commonly used in electrical measurements. Partial decomposition of carbonates and nitrates, besides melting and boiling, were considered in the literature only as part of the



TABLE 5 Literature data on bulk ( $\sigma_b$ ), grain boundary ( $\sigma_{gb}$ ) and total conductivity ( $\sigma_t$ ) of electrolytes without and with salt additions (Li et al., 2012; Chen et al., 2014; Maheshwari and Wiemhöfer, 2016). Conductivity ratios ( $\sigma_{ad}$  - material with admixture;  $\sigma_f$  - admixture free) highlight conductivity enhancements (see Tables 1–3 for acronyms).

Material <sup>a</sup>	T (°C)	$\sigma_b$ (S/cm)	$\sigma_{ad}/\sigma_f$	$\sigma_{gb}$ (S/cm)	$\sigma_{ad}/\sigma_f$	T (°C)	$\sigma_t$ (S/cm)	$\sigma_{ad}/\sigma_f$
5CDC	350	$7.4 \times 10^{-5}$	—	$3.5 \times 10^{-6}$	—	350	$3.3 \times 10^{-6}$	19
5CCC4:1		—		—			$6.4 \times 10^{-5}$	
GDC	450	$5.0 \times 10^{-3}$	3.0	$7.0 \times 10^{-3}$	143	550	$1.0 \times 10^{-2}$	4.0
5LiGDC		$1.5 \times 10^{-2}$		1.0			$4.0 \times 10^{-2}$	
SDC	370	$7.0 \times 10^{-4}$	1.7	$3.5 \times 10^{-4}$	1.7	370	$2.3 \times 10^{-4}$	1.7
SDC15Li		$1.2 \times 10^{-3}$		$5.8 \times 10^{-4}$			$3.9 \times 10^{-4}$	

<sup>a</sup>Published data (figures and tables) treated to provide a reasonable basis for comparison. Minor inaccuracy in values estimated from curves in plots might be present (few %).



processing route (Stern and Weise, 1969; Nakamura et al., 1980; Kim and Lee, 2001; Singh and Singh, 2007; Ruiz et al., 2010; Olivares, 2012; Lee et al., 2013). The presence of hydroxides, confirmed in different situations (Lapa et al., 2010; Ferreira et al., 2011a; Xing et al., 2015), is mostly disregarded.

As summary, in ceria-based solid electrolytes with salts, the nominal and actual phase compositions can be quite distinct because of the effects of multiple processing parameters (e.g., gas phase composition, weight losses during firing, weight gain during storage or measurements). Since the kinetics of some reactions is also slow, studied materials include metastable phases, with their proportions changing during measurements under diverse conditions. As example, conductivity hysteresis was found only during a first heating/cooling cycle in Na-doped ceria (Pearce and Thangadurai, 2009).

The presence of Li and/or amorphous phases in these electrolytes decreases the efficacy of energy-dispersive X-ray spectroscopy (EDS) to properly map chemical compositions, or X-ray diffraction (XRD) for complete phase identification. These limitations should be understood only as background information on potential scenarios behind published reports.

## Electrical performance

### Materials overview

Table 5 includes data obtained with  $\text{Na}_2\text{CO}_3$ ,  $\text{Li}_2\text{CO}_3$  and  $\text{LiNO}_3$  salt additions, and ceria-based electrolytes (CDC, GDC

and SDC) (Li et al., 2012; Zhu et al., 2014; Maheshwari and Wiemhöfer, 2016).

These data show impressive, claimed conductivity enhancements for salt containing materials with respect to pure (salt free) oxides, reaching factors of 3 in bulk conductivity, 143 in grain boundary conductivity, and 19 in total conductivity. While all microstructures are slightly distinct, grain size is between 1 and 5  $\mu\text{m}$  (Table 3), and densifications exceed 95%. Sintering temperature, duration, and sintering aids, originate distinct grain size and densification effects, preventing fully comparable sets of sintering parameters and final microstructures.

The microstructural characteristics of these materials can be obtained from a combination of information on grain size (in the order of 1  $\mu\text{m}$  for 5CCC4:1 and 5LiGDC and 5  $\mu\text{m}$  for SDC15Li (Li et al., 2012; Chen et al., 2014; Maheshwari and Wiemhöfer, 2016)) and of volume percentage of the likely residual second phase, after sintering ( $\text{NaC}$  or  $\text{Li}_2\text{O}$ , see Table 3). Assuming a conventional brick-layer model (see Section 5 for details), volume fractions can be used to relate grain size ( $D$ ) and grain boundary thickness ( $\delta_{\text{gb}}$ ), as depicted in Figure 1.

Typical values of  $\delta_{\text{gb}}$  in ionic conductors range between a few nm and a few dozens of nm (Kingery, 1974b, 1974a; Christie and Van Berkel, 1996). Increasing the grain boundary thickness, the volume fraction of this region easily slides to values in excess of 10 vol%, which is already composite territory. With more than 30 vol% of a second phase, percolation is almost inevitable (Jiang and Wagner, 1995). Materials under consideration here include thin grain boundaries (5LiGDC,  $\delta_{\text{gb}} \approx 5$  nm), moderately thick grain boundaries (SDC15Li,  $\delta_{\text{gb}} \approx 90$  nm), and others clearly seating in the composites category (5CCC4:1), with a “nominal grain boundary thickness” around 190 nm.

## Ca-doped ceria (CDC)

For CDC-based electrolytes, NaC is present in large quantity (about 40 vol%), percolating throughout the material. Figure 2 shows the electrical conductivity of 5CDC, 5CCC4:1, and likely secondary phases. Irrespective of this overpopulated plot, naked eye analysis immediately shows that several secondary phases exceed the conductivity of 5CDC ( $\square$ ) or even 5CCC4:1 ( $\Delta$ ).

With respect to salts, pure NaC (in  $\text{CO}_2$  and air) and Sr or Ca-doped NaC are all considered. The trends are for higher conductivity of NaC in air with respect to  $\text{CO}_2$  (see NaC curves), also higher conductivity of Ca-doped NaC with respect to pure NaC (see CaDNaC curve in Figure 2). 5CCC4:1 shows conductivity levels within the range of values reported for pure NaC in air or CaDNaC in  $\text{CO}_2$ .

The consideration of Ca or Sr-doped NaC deserves a short comment. Doped NaC has a conductivity higher than pure NaC. This is a consequence of the formation of mobile and negatively charged  $\text{Na}^+$  vacancies ( $V_{\text{Na}}'$ , in Kröger-Vink notation) to

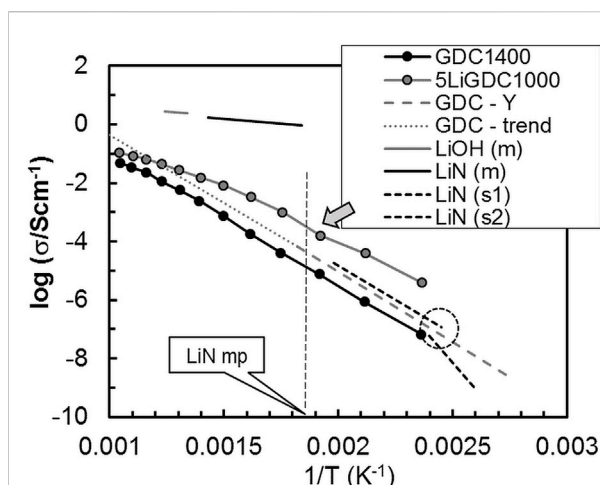


FIGURE 3

Total conductivity ( $\sigma$ ) versus the reciprocal of absolute temperature ( $1/T$ ) of GDC without and with LiN and possible secondary phases (Claes and Glibert, 1985; Yamashita et al., 1995; Skobelev et al., 1996; Zhu et al., 2014). See text for details.

compensate the presence of positively charged  $M^{2+}$  ions ( $M = \text{Ca}^{2+}$  or  $\text{Sr}^{2+}$ ) in normal  $\text{Na}^+$  lattice positions ( $M_{\text{Na}}^\bullet$ ). The simplified electroneutrality condition can be expressed as:

$$[M_{\text{Na}}^\bullet] = [V_{\text{Na}}'] \quad (1)$$

The  $\text{Na}^+$  vacancies are the dominant charge carriers in Ca-doped NaC, and the effect of Ca-doping was demonstrated measuring the electrical conductivity of materials with dopant concentrations increasing up to 0.093 mol% (Figure 2 (Cerisier and Roux, 1978)). The 5CDC electrolyte could easily be the source of minor amounts of Ca as dopant of NaC, where only 0.1 mol% is a meaningful level.

The “fictional” curve suggested for CaDNaC in air exceeds the values in  $\text{CO}_2$  by one order of magnitude, taking into consideration that these relative magnitudes were observed for pure NaC in air and in  $\text{CO}_2$ . To corroborate this approach, data for  $\text{SrCO}_3$  (1 mol%)-doped NaC, in air, is also plotted (Guth et al., 1987). These results are impressively close or even exceed those observed for 5CCC4:1. Overall, the high-volume fraction (about 40 vol%) of NaC in these composites would justify the consideration of the exact role of this phase in the composite material.

If, irrespective of cautious thermal processing, some NaC partly decomposed to  $\text{Na}_2\text{O}$ , and converted into NaOH, the presence of liquid phase (acronym extension “m” for molten) could be expected at temperatures as low as 283°C. Alkali salts or hydroxides show extremely high values of electrical conductivity above melting, in the range 0.1–1  $\text{Scm}^{-1}$  (Li et al., 2007). The electrical conductivity of the NaC+NaOH eutectic composition is also plotted in Figure 2 to highlight this fact. The presence of a

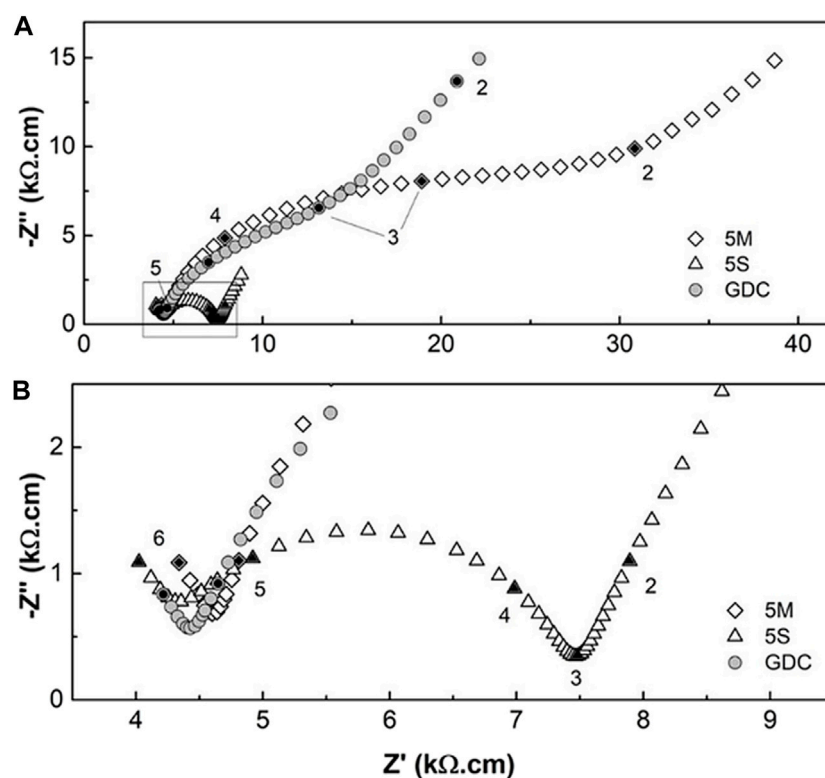


FIGURE 4

(A) Impedance spectra of GDC materials without and with NLC as sintering aid; (B) zoomed area from (A). Numbers close to data points correspond to the  $\log_{10}$  of the frequency (Hz). Adapted from (Grilo et al., 2020). See text for details.

molten phase (NaC+NaOH (m)), even a few vol%, could explain or contribute to the observed high conductivity. Molten phases easily spread and percolate in between grains.

If present in significant amounts, a solid to liquid transition often appears as a sharp change in conductivity with temperature (elongated z-shape in Arrhenius plots). The observed conductivity trend for 5CCC4:1 indeed shows a slight upwards bending close to the NaC+NaOH eutectic temperature (NaC+NaOH et), highlighted in Figure 2 (vertical dashed line). This is the opposite of the downwards bending observed at high temperature in ceramic oxide-ion conductors. This is not a demonstration of the presence of a molten phase but justifies due consideration of this possibility.

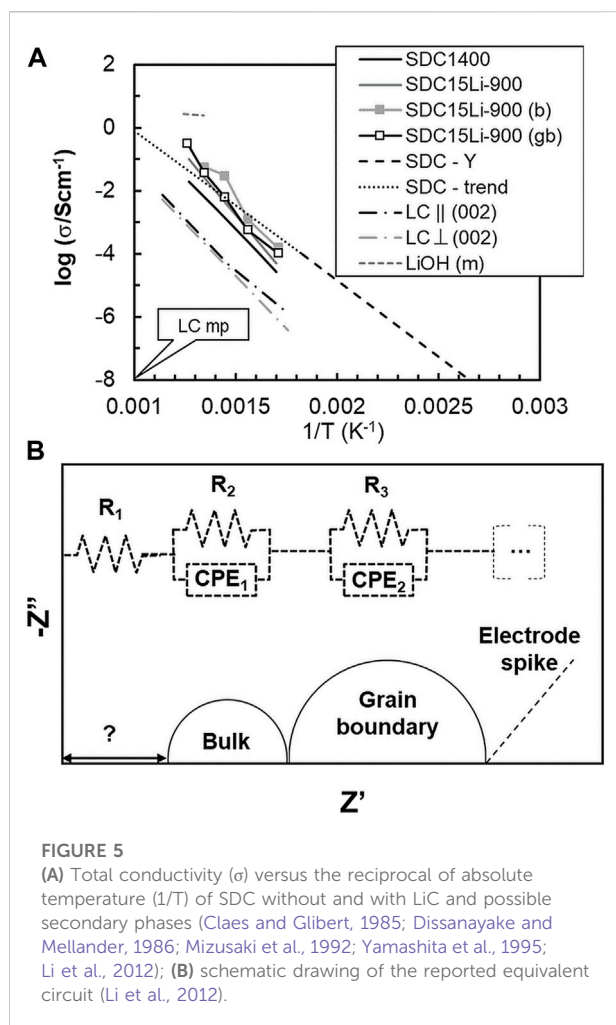
## Gd-doped ceria (GDC)

LiN was added in a small quantity (5 cat% Li<sup>+</sup>) to GDC, sintered at a temperature (1000°C) where melting, boiling and partial salt thermal decomposition are expected. If either LiN, or Li<sub>2</sub>O, or LiOH were present, molten phases could be found starting at temperatures as low as 264°C (melting of LiN), 480°C (melting of LiOH) or even 180°C

(LiN+LiOH eutectic temperature). However, the total equivalent amount of Li<sub>2</sub>O is below 1.6 vol% in the studied electrolyte. From a microstructural point of view, the material has the features of a polycrystalline ceramic with a thin grain boundary.

Figure 3 shows multiple sets of data on the electrical conductivity of distinct materials. Unlike the previous case of NaC+CDC, the reported solid LiN conductivity values are all below the conductivity of 5LiGDC1000. Pure LiN has a phase change with some hysteresis on heating/cooling, with the breaking region shown within a dashed circle (Figure 3), separating data for the two solid LiN phases (s1 and s2, (Claes and Glibert, 1985; Yamashita et al., 1995; Skobelev et al., 1996; Zhu et al., 2014)).

The electrical conductivity of molten LiN and molten LiOH (acronyms with extension “m”) highlights the enormous impact that minor amounts of these phases would have on conductivity. Again, a small upwards bending in the conductivity curve of 5LiGDC1000 (see arrow in Figure 3) coincides with the melting point (mp) of LiN (signaled with a vertical dashed line). Accordingly, the potential presence of molten LiN could be considered as a possible source of unusual conductivity contributions.



Recently, the addition of NaC+LiC (NLC) to GDC, was assessed in own work, to decrease the GDC sintering temperature to 1100°C (Grilo et al., 2020). This is above the eutectic point of NLC (500°C). We recall that materials with a small amount of NLC (5 mol%) were prepared using a ceramic route starting with mechanical milling (M) or a wet chemical synthesis route (S). There was no evidence for localized spots of Na in any sample, and lattice parameters also did not show evidence for solubility of alkali-metal ions in the ceria lattice. Figure 4 depicts low temperature impedance spectra for these materials in air. An introduction to this type of plots is skipped here since these are rather standard in the literature on solid electrolytes.

Figure 4 shows that the same sintering admixture might affect the performance of these materials in distinct manners, depending on the exact processing route. We invoke these materials here since we can fully compare couples of materials versus performance (e.g., “S” versus “M” routes, or pure GDC versus “M” route). All materials were prepared using the same chemicals and shaping routes, and final grain size (around

2–2.5  $\mu\text{m}$ ) and densifications (close to 100%) are comparable. Fluctuations often found in data obtained in distinct labs, are ruled out here.

The impedance spectra in Figure 4 include two arcs at high and intermediate frequency usually attributed to the contributions of bulk (higher frequency range) and grain boundary (intermediate frequency range). An incipient third arc, in the low frequency range, indicates the contribution of electrode processes. Figure 4B shows that there is no meaningful bulk impedance effect, only a slight data scatter. However, when obtained by wet chemistry (GDC-5S), materials present a much lower grain boundary resistivity (Figure 4A). We could add extra evidence to show that materials with high densification, show slight changes in bulk conductivity, but grain boundary conductivity is highly sensitive to contact with salts (e.g., see (Grilo et al., 2021b)).

## Sm-doped ceria (SDC)

LiC was added in considerable amounts (15 cat%  $\text{Li}^+$ ) to SDC. Sintering of these samples was performed at temperatures where melting and even thermal decomposition of LiC would be expected. The upper value of about 5 vol% of a secondary phase after sintering (as  $\text{Li}_2\text{O}$ ) shows that this material is in the transition from a typical polycrystalline ceramic to a composite. If LiC,  $\text{Li}_2\text{O}$ , or LiOH, were present, molten phases could be found starting at temperatures as low as 723°C (melting of LiC), 480°C (melting of LiOH) or 705°C ( $\text{LiC} + \text{Li}_2\text{O}$  eutectic temperature). Figure 5 shows multiple sets of data on the electrical conductivity of SDC and likely secondary phases. The reported pure solid salt (LiC) conductivity is anisotropic (parallel or perpendicular to plane (002)), with distinct values depending on direction. In all cases, the performance of solid LiC is below the performance of SDC15Li-900.

The electrical conductivity of molten LiOH is also shown in Figure 5 to highlight again the enormous impact that minor amounts of a molten phase may have on conductivity. The most controversial aspect in this case is related to the claimed temperature dependence of bulk and grain boundary conductivity, which deviates considerably from common trends for SDC1400 and SDC15Li-900. Activation energies for electrical conductivity in clear excess of 1 eV are unusual in ceria-based electrolytes (see SDC-Y and SDC trend lines, Yamashita et al., 1995). Deeper analysis of source data might explain these findings.

Impedance spectra reported at temperatures below 400°C show two arcs and a spike at low frequency, schematically reproduced in Figure 5, together with the adopted equivalent circuit. The lower frequency arc is interpreted as typical of grain boundary performance and the higher frequency arc is related to the bulk performance (Li et al., 2012). The high frequency intercept of this arc with the  $Z'$  axis (real part of impedance)



is distant from the origin. To account for this situation the authors introduced a resistor ( $R_1 > 100 \text{ ohm}$ ) in series with bulk ( $R_2||\text{CPE}_1$ ) and grain boundary ( $R_3||\text{CPE}_2$ ) standard parallel  $R||\text{CPE}$  circuits (resistance||constant phase element). However, no physical meaning was provided for  $R_1$ . Standard setups (external electrical cables and cell wiring/electrodes) hardly show a resistance compatible with the reported value of  $R_1$ . The analysis of these data is halted here. Additional comments on impedance spectroscopy measurements are provided in the last section of this work.

## Considerations on conductivity enhancement

### Bulk effects

Ceria-based electrolytes are oxide-ion conductors where the prevailing defects are acceptor dopants (e.g., Ca, Gd or Sm, negative defects as substitutional dopants) and oxide-ion vacancies (positive defects). Enhanced bulk conductivity must rely on enhanced concentration and/or mobility of oxide-ion vacancies.

The presence of alkali metal ions ( $\text{Na}^+$ ,  $\text{Li}^+$ ) in solid solution could imply an enhanced concentration of oxide-ion vacancies to balance the total concentration of dopants. The dimensions of these ions for 8-fold coordination (1.18, 0.92 and 0.97 Å for  $\text{Na}^+$ ,  $\text{Li}^+$  and  $\text{Ce}^{4+}$ , respectively (Shannon, 1976)), seem consistent with the possibility of partial replacement. The solubility of up to 7 cat%  $\text{Na}^+$  in ceria was assumed from XRD patterns (Pearce and Thangadurai, 2009), but without consensus (Grilo et al., 2020). The solubility of  $\text{Li}^+$  in ceria also seems controversial. This possibility was raised due to variable lattice parameter of GDC after distinct firing conditions (Zhu et al., 2014). However, in the case of SDC, the XRD patterns showed no changes and this was interpreted as sign of no solubility of  $\text{Li}^+$  in the lattice (Li et al., 2012). In any case, Li was lost from the SDC15Li samples with increasingly high sintering temperatures, with only 1.5 cat% remaining in SDCLi15 fired at 800°C (Li et al., 2012).

The plausible simplified electroneutrality conditions, assuming that alkali metal ions are dissolved in ceria, should be:

$$2[\text{Ca}_{\text{Ce}}''] + 3[\text{Na}_{\text{Ce}}'''] = 2[\text{V}_{\text{O}}^{\bullet\bullet}] \quad (2)$$

for  $\text{Na}^+$

as additional dopant in calcia-doped ceria, and

$$[\text{RE}_{\text{Ce}}'] + 3[\text{Li}_{\text{Ce}}'''] = 2[\text{V}_{\text{O}}^{\bullet\bullet}] \quad (3)$$

for  $\text{Li}^+$  as additional dopant in rare earth (RE)-doped ceria, with  $\text{RE} = \text{Gd}^{3+}$  or  $\text{Sm}^{3+}$ . The total concentration of oxide-ion vacancies ( $[\text{V}_{\text{O}}^{\bullet\bullet}]$ ) should depend on the concentrations of

alkali metal dopants ( $[\text{Na}_{\text{Ce}}''']$  or  $[\text{Li}_{\text{Ce}}''']$ ) besides the alkaline-earth or rare-earth (RE) concentrations ( $[\text{Ca}_{\text{Ce}}'']$  and  $[\text{RE}_{\text{Ce}}']$ , respectively).

Dissolved  $\text{Na}^+$  would imply an enhanced concentration of oxide-ion vacancies but impedance spectroscopy showed an extremely poor electrical conductivity for 7 cat%  $\text{Na}^+$ , about two orders of magnitude lower than reported for pure SDC (Pearce and Thangadurai, 2009). From simple charge balance effects, 7 cat%  $\text{Na}^+$  as dopant should be identical to 21 cat%  $\text{Gd}^{3+}$  or  $\text{Sm}^{3+}$ . A conductivity two orders of magnitude lower with respect to SDC must imply vestigial solubility of  $\text{Na}^+$  or deep trapping of oxide-ion vacancies due to strong defect association. The latter effect would be expected for heavily (triply) charged acceptor dopant defects ( $\text{Na}_{\text{Ce}}'''$ ) with strong tendency to associate with positively (double) charged oxide-ion vacancies. Bulk oxide-ion conductivity enhancements, without substantial increase in the activation energy of ionic conduction, are inconsistent with this picture.

Following a similar reasoning, in the case of  $\text{Li}^+$  as dopant, the reported low solubility (negligible?) cannot justify substantially higher concentration of oxide-ion vacancies. A negative impact on the mobility of oxide-ion vacancies should also be considered since dopants smaller than the host cation originate local lattice strain effects (Mogensen et al., 2000; Skinner and Kilner, 2003). There is no apparent rationale for a reported bulk conductivity enhancement (up to three times higher, see Table 5) when salts with Li are used as sintering admixtures. Both, concentration and mobility of oxide-ion vacancies, are unable to explain this claim. Enhanced bulk conductivity effects exceed what might be considered the state-of-the-art knowledge on the defect chemistry of these systems.

### Grain boundary effects

Unlike for bulk conductivity, grain boundary effects may easily surpass one order of magnitude (Table 5). However, significant grain boundary improvements are claimed in situations ranging from 1 to about 40 vol% of secondary phases. This diversity of situations justifies distinct attempts to explain grain boundary effects.

Early work in the field of ceramic electrolytes identified clear correlations between total conductivity and temperature. In Arrhenius-type plots of  $\ln(\sigma_t)$  versus  $1/T$ , the low temperature activation energy often exceeds the high temperature activation energy, and the effect is enhanced in materials with low purity or small grain size. With the adoption of impedance spectroscopy as characterization tool, two distinct contributions could be clearly identified, corresponding to the bulk and grain boundary (Bauerle, 1969). Defect association is also noticed in the low temperature range (Mogensen et al., 2000; Skinner and Kilner, 2003), but this will be ignored here.

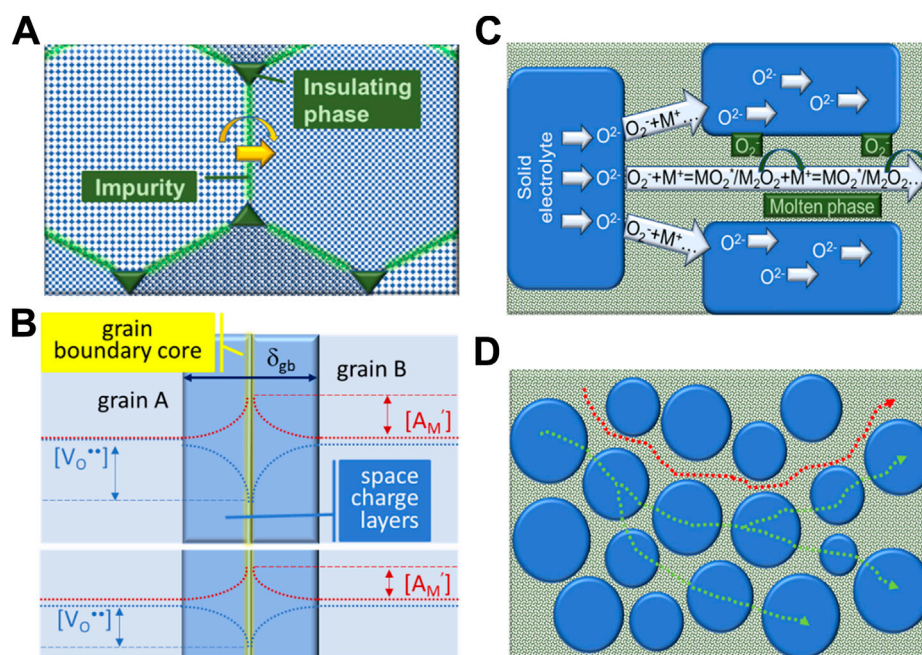


FIGURE 6

Grain boundary schemes: (A) traditional description, including crystallographic orientation mismatch between grains, impurities in the grain boundary region and insulating particles in triple contact points (Bauerle, 1969); (B) electrical grain boundary, with core, space charge layers and concentration profiles of acceptor dopant ( $[A_M]$ ) and oxide-ion vacancies ( $[V_O^{\bullet\bullet}]$ ) (Guo et al., 2003; Guo and Waser, 2006). In the lower insert, levelling of concentration profiles due to an extrinsic species acting as local scavenger (Zhu et al., 2014); (C) combined oxide-ion transport mechanisms, where several species might assist  $O^{2-}$  transport in between grains or along the salt phase; (D) single (salt) phase and dual phase  $O^{2-}$  pathways (Maheshwari and Wiemhöfer, 2016). See text for details.

The classical description used to explain grain boundary effects is shown as scheme in Figure 6A). Grain boundaries are understood as a crystallographic feature, where crystal misorientation and presence of impurities implies excess energy requirements for ionic migration, and interfacial polarization effects.

Secondary phases, namely impurities, might be wetting and covering the entire grain boundary region (blocking ion transport), or might be non-wetting, forming isolated particles in triple joints between multiple grains. The discovery of grain boundary “scavenging” agents, able to combine chemically with impurities/glassy phases, forming isolated particles in joints between grains, like addition of alumina to zirconia-based electrolytes, is a good example of this process. This description, even if more than 40 years old, is still used in many cases to explain grain boundary conductivity improvements (Beekmans and Heyne, 1976; Butler and Drennan, 1982; Guo et al., 1995; Zhang et al., 2004; Sudarsan and Krishnamoorthy, 2018).

Several authors introduced a distinct grain boundary concept, often named as electrical grain boundary (Guo et al., 2003; Guo and Waser, 2006). In acceptor doped oxide-ion conductors, the defect concentrations in the grain boundary

region deviate from bulk values due to segregation of dopant. Their negative charge equalizes a positively charged grain boundary core, which in turn implies the depletion of oxide-ion vacancies in the same region. The overall consequence is the formation of space charge layers around the grain boundary core, decreasing locally the oxide-ion conductivity due to an enhanced electrical potential barrier and depletion of mobile defects. This model is able to explain why ions are partly blocked in high purity materials. The physical scheme used to describe these situations is shown in Figure 6B.

The presence of salts in considerable amounts introduced the need to consider the role of this phase in such materials. As first remark, the concept of grain boundary conductivity seems inaccurate in this case. In the presence of large concentrations of both phases, the oxide grains are fully covered by the salt phase. This means that the often measured “grain boundary” conductivity corresponds to a designation “freely” adopted from the field of polycrystalline solid electrolytes, where impedance spectra can be deconvoluted into bulk, grain boundary and electrode contributions, as introduced earlier.

Having in mind this remark, an enhanced “grain boundary” performance was explained in 5CCC4:1 composites by the presence of a highly conductive phase in the inter-grain

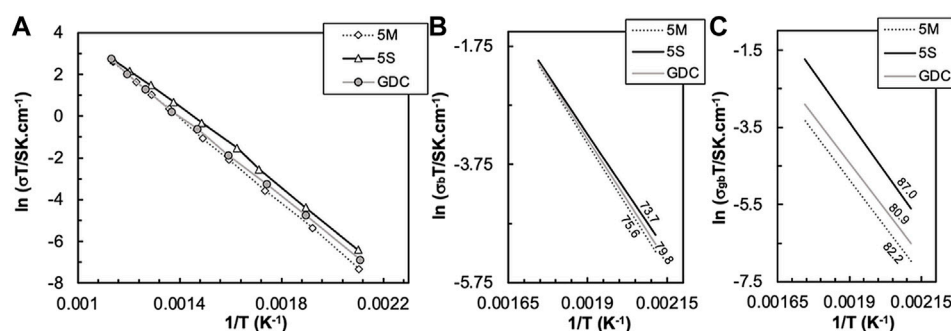


FIGURE 7

Arrhenius-type plots of total (A), bulk (B) and grain boundary conductivity (C) of GDC-based materials sintered without and with NLC (Grilo et al., 2020). In (B,C), lines correspond to data linear trends used to estimate  $E_a$  (kJ.mol<sup>-1</sup>).

region, where several species provide net transport of oxide ions (Maheshwari and Wiemhöfer, 2016). The firstly suggested cooperating mechanism involved the net transport of  $O_2^-$  (superoxide), *via*  $NaO_2^*$  (intermediate species) and  $Na_2O_2$  (peroxide), as drafted in Figures 6C,D.

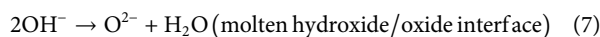
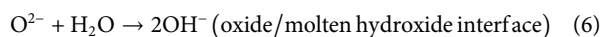
The idea was revised after consideration of the possible role of  $CO_2$ , involving several elementary reactions:



and



inside  $Na_2CO_3$ , where  $CO_2$  moves *via* pores of  $Na_2CO_3$ . Other mechanisms can be envisaged, involving water molecules and  $OH^-$  ions:



Water vapor is present in ambient air and water molecules are known to easily combine with  $Na_2O$  or  $Li_2O$ . Fast transport of  $OH^-$  and fast diffusion of water molecules is expected in molten phases. In fact, the diffusion coefficient of water molecules in molten hydroxides (or salts) is one order of magnitude higher than for most ions (Janz and Bansa, 1982). Also, water molecules are smaller than  $CO_2$  molecules and should diffuse faster (Bergmann et al., 2007; Talesh et al., 2010). In this case, no porosity is required, unlike when  $CO_2$  is considered.

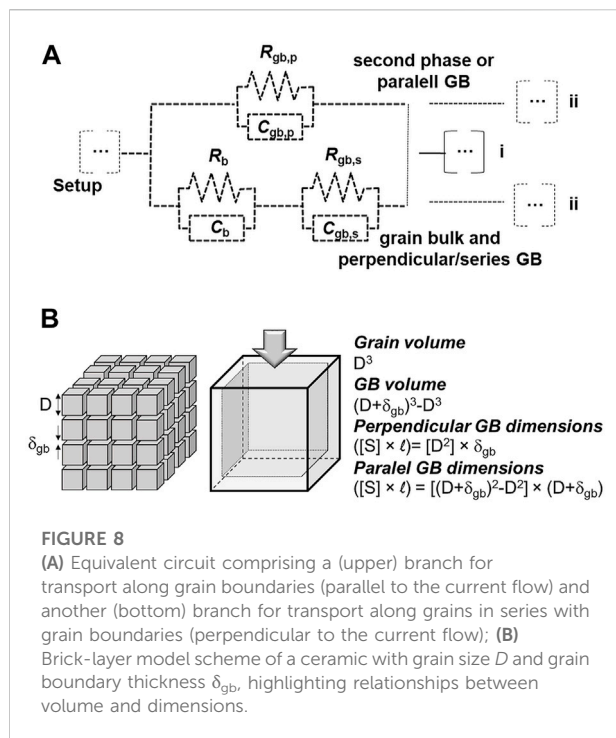
For materials with minor concentrations of sintering aids, a distinct line of reasoning was introduced, invoking modified electrical characteristics of the grain boundary region, with leveling of acceptor dopant and oxide-ion vacancy concentrations nearby the grain boundary core, (Figure 6B, lower insert). This possibility relies on experimental evidence of changes in acceptor dopant profiles close to the grain boundary core (Zhu et al., 2014). This might be named

advanced grain boundary engineering. Own experiments, designed to confine the interaction between oxide and salt exclusively to the grain boundary region of sintered GDC ceramics, found consistent grain boundary conductivity improvements (Grilo et al., 2021b).

Figure 7 shows Arrhenius-type plots in the 200–300°C temperature range, where deconvolution of impedance spectra into bulk and grain boundary arcs is quite accurate, for total ( $\sigma_t$ ), bulk ( $\sigma_b$ ), and grain boundary conductivity ( $\sigma_{gb}$ ) of pure GDC sintered at 1500°C/4 h, and GDC+NLC ceramics prepared using (M) and (S) processing routes. The corresponding activation energies ( $E_a$ ) are depicted in the  $\sigma_b$  and  $\sigma_{gb}$  plots.

The total conductivity of all materials is within a small range of values (Figure 7A). There is no evidence for any impact of molten phases as possible contributors to the total conductivity. Bulk conductivities of all samples showed in Figure 7B are nearly identical, confirming that bulk transport is poorly sensitive to the effect of NLC additions. On the contrary,  $\sigma_{gb}$  values are somewhat distinct, with samples prepared using chemical synthesis showing higher conductivity, even higher than observed for standard GDC (Figure 7C).

For materials prepared using chemical synthesis, dense ceramics were obtained at 1100°C. The presence of NLC changes the local chemical environment. At 1100°C, migration of  $Gd^{3+}$  cations to the grain boundaries is restrained, unlike in pure GDC on cooling from high sintering temperatures. With lower concentration of acceptor cations, the grain boundary potential barrier decreases, and the oxide-ion vacancy concentration profile in the space charge layers are smoother (Lei et al., 2002; Guo and Waser, 2006). A specific mechanism might be considered, where  $Gd^{3+}$  cations combine with  $Li^+$  to form  $GdLiO_2$ , scavenging selectively the concentration of the acceptor dopant. The chemical reaction is known to occur at moderate temperatures (Yamauchi et al., 2008), but there is no report yet on a conclusive observation of  $GdLiO_2$  in GDC+NLC grain boundaries.



In the case of materials prepared using mechanical milling, the effect seems the opposite, with  $\sigma_{gb}$  values lower than for all other materials. While the chemical synthesis route is expected to originate homogeneous materials at ionic level during wet chemistry steps, in the ceramic route, with low processing temperatures, heterogeneities are more likely. Any residual salt particles, with dimensions below the analytical capability of SEM/EDS, may act as potential oxide-ion blocking phases present in the grain boundary region (Cho et al., 2007, 2008; Lin et al., 2015).

The wide range of effects previously introduced is able to explain reports from enhanced to decreasing grain boundary conductivity. Previous comments also indicate that likely phenomena are local, within the few nm distance with respect to the grain boundary core. Only characterization tools with high spatial and chemical resolution (for light elements) can disclose the exact grain boundary characteristics. Such reports are scarce, and most analyses are based on indirect signs. In any case, experimental evidence opens the possibility of advanced grain boundary engineering solutions to circumvent drawbacks observed in conventional ceramics.

## Impedance spectroscopy

Typical impedance spectra obtained at low temperature for solid electrolytes consist of two arcs, associated to bulk and grain boundary contributions (see examples in Figure 4). The grain

boundary may represent a secondary phase distributed along intergranular regions, namely low melting point phases. The reported tendencies of the bulk and intergranular contributions are based on fitting of impedance spectroscopy data using a common equivalent circuit with a series association of resistors to account for the bulk ( $R_b$ ) and grain boundary ( $R_{gb,s}$ ) resistances, each having constant phase elements ( $CPE_b$  and  $CPE_{gb,s}$ ) in parallel, as schematized by the bottom branch in Figure 8A. For simplicity, CPEs are replaced by simple capacitors ( $C_b$ ,  $C_{gb}$ ).

The so-called brick-layer model describes a material with cross-sectional area  $A$  and thickness  $L$ , composed of cubic grains with average grain size  $D$ , surrounded by grain boundaries of thickness  $\delta_{gb}$  (Figure 8B) (Guo and Waser, 2006; Gomes et al., 2009). Considering only the bottom branch of the equivalent circuit to describe a polycrystalline ceramic with large average grain size, thus neglecting transport along parallel grain boundaries with huge electrical resistance due to obvious geometric reasons, the specific grain boundary conductivity ( $\sigma_{sp}$ ) depends on the microscopic geometric factor of the grain boundaries  $\delta_{gb}D^{-1}$ . The latter is given by  $\delta_{gb}D^{-1} = C_bC_{gb}^{-1}$ , assuming equivalent dielectric constants for bulk and grain boundaries ( $\epsilon_b \approx \epsilon_{gb}$ ). Therefore,  $\delta_{gb}$  can be estimated from:

$$\delta_{gb} = DC_bC_{gb}^{-1} \quad (8)$$

and  $\sigma_{sp}$  from:

$$\sigma_{sp} = LC_b(AR_{gb}C_{gb})^{-1} \quad (9)$$

All values needed for Eqs 8, 9 are easily obtained from microstructures ( $D$ ), impedance plots ( $C_b$  and  $C_{gb}$ ), and macroscopic sample dimensions. Often, authors try to correlate the reduction of the amplitude of the grain boundary arc with enhanced grain boundary conductivity, resulting from changes of the core potential or localized effects of sodium or lithium salts (see e.g. (Zhu et al., 2014)). This is a reasonable approach if the grain boundary thickness is small (typically of few nm), or the amount of second phases corresponds to that of an additive (1–2 vol% maximum), and not typical of composites (well above 10 vol%).

The possibility of a parallel branch to this series association was never considered in the analysis of impedance spectra of this kind of electrolytes. However, in a classical brick-layer model, grain boundaries offer two distinct pathways with respect to electrical transport. In between consecutive grains along the current direction the grain boundary is perpendicular to the ionic flow. In between sides of grains, the grain boundary offers a parallel pathway (Figure 8A). The usually assumed high grain boundary resistivity (with respect to the bulk grain) explains the tendency to discard the second branch of the equivalent circuit.

In the following discussion the full circuit with two parallel branches is considered (Figure 8A). The parallel, upper branch (circuit elements with subscript p) might correspond to a secondary phase or a parallel grain boundary. In the latter



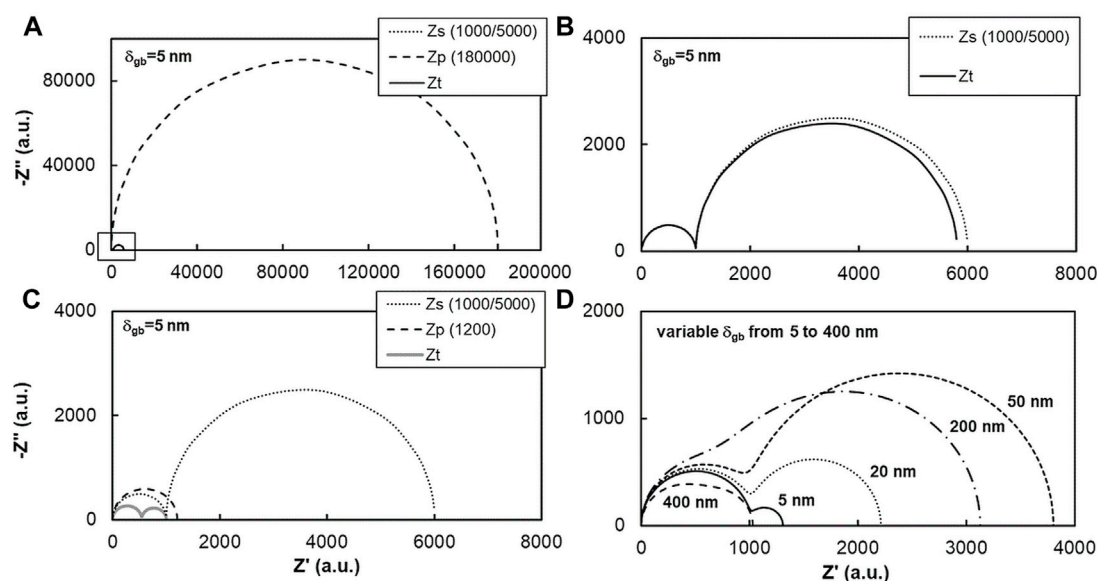


FIGURE 9

Simulated impedance spectra based on the equivalent circuit of Figure 8A, where  $Z_s$  is the impedance of the series (bottom) circuit,  $Z_p$  is the impedance of the parallel (upper) branch and  $Z_t$  is the total impedance of the circuit. The spectra in Figures (A–C) were simulated with  $R_b$ ,  $R_{gb,s}$  and  $R_{gb,p}$  values given in the legend, and  $D = 1 \mu\text{m}$  and  $\delta_{gb} = 5 \text{ nm}$ . Spectra in (D) obtained assuming a constraint on the electrical properties that scale with a variable  $\delta_{gb}$  (see text for details).

case, the electrical properties of the perpendicular and parallel grain boundaries are interlinked (same conductivity and dielectric constant). In the former case they can be manipulated independently.

Other circuit elements besides these are neglected. This includes possible contact/electrical setup impedances and electrode impedances. A remark is needed to emphasize that if the upper branch involves the transport of the same ionic species the electrode impedance should be common to both branches (Figure 8A), case i). However, if a distinct ionic species is involved, a distinct electrode branch should thus be included (Figure 8A), case ii).

Figure 9 shows a set of model impedance spectra where the circuit (s) series and (p) parallel branches are both considered. The order of magnitude of resistances and capacitances is selected to generate spectra with the graphical features commonly observed in published data (clear bulk and grain boundary arcs), but there is no attempt to reproduce exact sets of published data. Arbitrary units are assumed in all examples discussed below.

In Figure 9A the bulk resistance ( $R_b = 1000$ , in the bottom series branch) is only one fifth of the perpendicular/series grain boundary resistance ( $R_{gb,s} = 5000$ ), and both much smaller than the upper parallel resistance ( $R_{gb,p} = 180,000$ ). The much larger impedance of the parallel grain boundary branch ( $Z_p$ ) prevents the observation in this plot of the impedance of the series branch ( $Z_s$ ) and of the total circuit impedance ( $Z_t$ ), both detailed in

Figure 9B. The spectra for  $Z_s$  and  $Z_t$  are almost identical because of the large  $Z_p$ . In this case, the upper parallel branch is almost electrically inactive.

Figure 9C shows the result of a much lower  $Z_p$  ( $R_p = 1200$ ), while the remaining circuit parameters were preserved.  $Z_t$  now is completely different from  $Z_s$ , due to the role of the low parallel resistance. Simple naked eye analysis of these spectra suggests that the (perpendicular) grain boundary impedance is only about 1/10 of the original value while the bulk impedance shrank to about 1/2 of the original value. In fact, they were fully preserved but they appear as if the corresponding conductivities increased. The situation just described fits quite well with previous reports on enormous enhancement of grain boundary conductivity and moderate bulk conductivity improvement. Migration from spectra in Figures 9B,C was obtained with simple consideration of a fast-ionic parallel pathway. This can be easily done assuming distinct phases and properties for the parallel and perpendicular grain boundaries.

Figure 9D repeats the previous exercise but with a constraint on the electrical properties of parallel and perpendicular grain boundaries, by assuming the same specific conductivity ( $\sigma_{sp}$ , see Eq. 9) and dielectric constant ( $\epsilon_r$ ) for the series and the parallel grain boundaries. The initial values of  $R_b = 1000$ ,  $R_{gb,s} = 300$ ,  $C_b = 10^{-9}$  and  $C_{gb,s} = 2 \times 10^{-7}$  corresponding to  $\delta_{gb} = 5 \text{ nm}$  and  $D = 1 \mu\text{m}$ , determine the other relevant parameters, which scale with  $\delta_{gb}$  according to

$$R_{gb,p} = R_{gb,s} D^2 (D + \delta_{gb}) \cdot [\delta_{gb}^2 (2D + \delta_{gb})]^{-1} \quad (10)$$

$$R_b = [\sigma_b (D - \delta_{gb})]^{-1} \quad (11)$$

$$R_{gb,s} = \sigma_{sp}^{-1} D^{-2} \delta_{gb} \quad (12)$$

$$C_{gb,s} = C_b D \delta_{gb}^{-1} \quad (13)$$

$$C_{gb,p} = C_{gb,s} R_b R_{gb,p}^{-1} \quad (14)$$

The spectra in Figure 9D show the impact of increasing  $\delta_{gb}$  on the total impedance. Starting from the initial geometry corresponding to  $\delta_{gb} = 5$  nm, one observes a significant increase of the total impedance up to  $\delta_{gb} = 50$  nm, which is essentially determined by the increase of  $R_{gb,s}$  (Eq. 12). The other parameter in the series branch,  $R_b$ , also increases with increasing  $\delta_{gb}$  (Eq. 11), but much less. Comparison of the two spectra for  $\delta_{gb} = 5$  nm and  $\delta_{gb} = 50$  nm visually confirms this trend since the high frequency arc (on the left, for low impedance) remains nearly unchanged, whereas the low frequency contribution is much larger for  $\delta_{gb} = 50$  nm. Further increase of  $\delta_{gb}$  reverses the trend (the impedance for  $\delta_{gb} = 200$  nm is already smaller than for  $\delta_{gb} = 50$  nm), and the two arcs lose some of their distinctive features and start to overlap.

At  $\delta_{gb} = 400$  nm one observes that the total impedance is already (slightly) smaller than the initial condition ( $\delta_{gb} = 5$  nm), and the spectrum appears as a single, highly depressed arc. This behavior is explained by the accentuated decrease of the parallel branch resistance  $R_{gb,p}$ , which, as shown by Eq. 10, scales down with  $\delta_{gb}$  to the power of  $-3$ , whereas  $R_{gb,s}$  scales up with a simple unity exponent. Therefore, significant changes in the total impedance are only observed for an exorbitant  $\delta_{gb}$  of 400 nm, requiring a large volume fraction of a secondary phase. This condition is typical of a composite but not of a ceramic with a minor secondary phase (partly) in the grain boundary region.

Overall, Figure 9 shows that the usually reported enormous enhancement of the grain boundary conductivity and moderate improvement of the bulk conductivity are not compatible with a simply enhanced grain boundary conductivity, even with due consideration of the so-called parallel pathway. On the contrary, consideration of a secondary phase with high conductivity (Figure 9C) can easily generate the reported changes in the spectra with sintering admixtures. From known properties of solid and molten ionic conductors, the latter are closer to fulfil the high conductivity requirements. From a microstructural point of view, even minor amounts of molten phases can easily percolate throughout contacts between grains, still bonded *via* common grain boundaries.

The presence of a secondary charge transport pathway and carrier (e.g., alkali metal ions) should show up under direct current (dc) conditions (and long tests), since typical electrodes cannot act as sink and source of alkali metal ions. However, this situation is not necessarily detected under alternate current (ac) analysis, as with impedance spectroscopy. A report on dc experiments (Hebb-Wagner method (Neuhaus et al., 2018b)) suggests peculiar constraints while testing Ca-doped ceria with

$\text{Na}_2\text{CO}_3$  as second phase, namely with respect to the (limited) range of allowed applied voltages, with respect to the situation observed with pure Ca-doped ceria. Whether or not this is a confirmation of the presence of multiple species is obviously unclear.

## Conclusion

The assumption of exclusive oxide-ion conductivity in ceria-based electrolytes prepared with salts of alkali metals neglects the possible contribution of other species and compounds with significant conductivity, situation aggravated when even minor amounts of molten phases might be present. A small fraction of a fast-ionic conductor can easily explain claimed trends in (moderate) bulk and (enormous) grain boundary conductivity enhancements.

With (ac) impedance spectroscopy all mobile species can contribute to the total conductivity, preventing the identification of separate contributions. Tests performed under dc conditions and complementary techniques able to detect alternative molten/amorphous phases (e.g., FTIR to detect hydroxides) are needed to fully discard alternative explanations for reported conductivity enhancements. Furthermore, confirmation of exact mechanisms behind grain boundary conductivity enhancements, require advanced analytical tools to confirm most hypotheses under discussion. Advanced grain boundary engineering is feasible using admixtures, opening possibilities up to now rarely exploited. This involves manipulation of the local concentration of species at low temperature, preventing the accumulation of dopants, often observed after high temperature processing. This solution is of particular interest in materials like ceria-based electrolytes. Long term stability of these materials under typical operating conditions also needs proper assessment.

## Author contributions

JG: writing—original draft, formal analysis; AJ and MS: writing—review; FF: conceptualization, writing—review and editing, supervision; FM: conceptualization, writing—review and editing, funding acquisition, supervision.

## Funding

This work was developed within the scope of the project CICECO-Aveiro Institute of Materials, UIDB/50011/2020, UIDP/50011/2020 and LA/P/0006/2020, financed by national funds through the FCT/MEC (PIDDAC). Specific support (AJ) provided by national funds (OE), through FCT, IP, in the scope of the framework contract foreseen in the numbers 4, 5, and 6 of the article 23, of the Decree-Law 57/2016, of August 29, changed

by Law 57/2017, of July 19. MS acknowledges the support of the FCT–2020.00625.CEECIND grant.

## Conflict of interest

The authors declare that the research was conducted in the absence of any commercial or financial relationships that could be construed as a potential conflict of interest.

## References

- Avila-Paredes, H. J., and Kim, S. (2006). The effect of segregated transition metal ions on the grain boundary resistivity of gadolinium doped ceria: Alteration of the space charge potential. *Solid State Ionics* 177, 3075–3080. doi:10.1016/j.ssi.2006.08.017
- Bale, C. W., Bélisle, E., Chartrand, P., Decterov, S. A., Eriksson, G., Gheribi, A. E., et al. (2016). FactSage thermochemical software and databases, 2010–2016. *Calphad* 54, 35–53. doi:10.1016/j.calphad.2016.05.002
- Bauerle, J. E. (1969). Study of solid electrolyte polarization by a complex admittance method. *J. Phys. Chem. Solids* 30, 2657–2670. doi:10.1016/0022-3697(69)90039-0
- Beekmans, N. M., and Heyne, L. (1976). Correlation between impedance, microstructure and composition of calcia-stabilized zirconia. *Electrochim. Acta* 21, 303–310. doi:10.1016/0013-4686(76)80024-2
- Benamira, M., Albin, V., Ringuedé, A., Vannier, R.-N., Bodén, A., Lagergren, C., et al. (2007). Structural and electrical properties of gadolinia-doped ceria mixed with alkali earth carbonates for SOFC applications. *ECS Trans.* 7, 2261–2268. doi:10.1149/1.2729343
- Bergmann, U., Di Cicco, A., Wernet, P., Principi, E., Glatzel, P., and Nilsson, A. (2007). Nearest-neighbor oxygen distances in liquid water and ice observed by x-ray Raman based extended x-ray absorption fine structure. *J. Chem. Phys.* 127, 174504. doi:10.1063/1.2784123
- Butler, E. P., and Drennan, J. (1982). Microstructural analysis of sintered high-conductivity zirconia with Al<sub>2</sub>O<sub>3</sub> additions. *J. Am. Ceram. Soc.* 65, 474–478. doi:10.1111/j.1151-2916.1982.tb10336.x
- Cela, B., de Macedo, D. A., de Souza, G. L., Martinelli, A. E., do Nascimento, R. M., and Paskocimas, C. A. (2011). NiO–CGO *in situ* nanocomposite attainment: One step synthesis. *J. Power Sources* 196, 2539–2544. doi:10.1016/j.jpowsour.2010.11.026
- Cerisier, P., and Roux, F. (1978). A study of the electrical conductivity and transition points of potassium carbonate. *Solid State Commun.* 26, 661–663. doi:10.1016/0038-1098(78)90102-3
- Chen, M., Zhang, H., Fan, L., Wang, C., and Zhu, B. (2014). Ceria-carbonate composite for low temperature solid oxide fuel cell: Sintering aid and composite effect. *Int. J. Hydrogen Energy* 39, 12309–12316. doi:10.1016/j.ijhydene.2014.04.004
- Chinarro, E., Jurado, J. R., and Colomer, M. T. (2007). Synthesis of ceria-based electrolyte nanometric powders by urea-combustion technique. *J. Eur. Ceram. Soc.* 27, 3619–3623. doi:10.1016/j.jeurceramsoc.2007.02.007
- Cho, P.-S., Lee, S. B., Cho, Y. H., Kim, D.-Y., Park, H.-M., and Lee, J.-H. (2008). Effect of CaO concentration on enhancement of grain-boundary conduction in gadolinia-doped ceria. *J. Power Sources* 183, 518–523. doi:10.1016/j.jpowsour.2008.05.041
- Cho, Y. H., Cho, P.-S., Auchterlonie, G., Kim, D. K., Lee, J.-H., Kim, D.-Y., et al. (2007). Enhancement of grain-boundary conduction in gadolinia-doped ceria by the scavenging of highly resistive siliceous phase. *Acta Mat.* 55, 4807–4815. doi:10.1016/j.actamat.2007.05.001
- Christie, G. M., and Van Berkel, F. P. F. (1996). Microstructure - ionic conductivity relationships in ceria-gadolinia electrolytes. *Solid State Ionics* 83, 17–27. doi:10.1016/0167-2738(95)00155-7
- Claes, P., and Glibert, J. (1985). Electrical conductivity and specific mass of the molten LiOH–LiNO<sub>3</sub>, NaOH–NaNO<sub>3</sub>, and KOH–KNO<sub>3</sub> Mixtures. *J. Electrochem. Soc.* 132, 857–862. doi:10.1149/1.2113973
- Cordier, A., El Khal, H., Siebert, E., and Steil, M. C. (2019). On the role of the pore morphology on the electrical conductivity of porous yttria-stabilized zirconia. *J. Eur. Ceram. Soc.* 39, 2518–2525. doi:10.1016/j.jeurceramsoc.2019.02.027
- Ding, D., Liu, B., Zhu, Z., Zhou, S., and Xia, C. (2008). High reactive Ce<sub>0.8</sub>Sm<sub>0.2</sub>O<sub>1.9</sub> powders via a carbonate co-precipitation method as electrolytes for low-temperature solid oxide fuel cells. *Solid State Ionics* 179, 896–899. doi:10.1016/j.ssi.2007.11.015
- Dissanayake, M. A. K. L., and Mellander, B.-E. (1986). Phase diagram and electrical conductivity of the Li<sub>2</sub>SO<sub>4</sub>–Li<sub>2</sub>OC<sub>3</sub> system. *Solid State Ion.* 21, 279–285. doi:10.1016/0167-2738(86)90190-6
- Duran, P., Gonzalez, M., Moure, C., Jurado, J. R., and Pascual, C. (1990). A new tentative phase equilibrium diagram for the ZrO<sub>2</sub>–CeO<sub>2</sub> system in air. *J. Mat. Sci.* 25, 5001–5006. doi:10.1007/bf00580121
- Duran, P., Rodriguez, J. M., and Recio, P. (1991). The ZrO<sub>2</sub>-rich region of the ZrO<sub>2</sub>–MgO system. *J. Mat. Sci.* 26, 467–472. doi:10.1007/bf00576544
- Duwe, P., Odell, F., and Brown, F. H. (1952). Stabilization of zirconia with calcia and magnesia. *J. Am. Ceram. Soc.* 35, 107–113. doi:10.1111/j.1151-2916.1952.tb13081.x
- El Khal, H., Cordier, A., Batis, N., Siebert, E., Georges, S., and Steil, M. C. (2017). Effect of porosity on the electrical conductivity of LAMOX materials. *Solid State Ionics* 304, 75–84. doi:10.1016/j.ssi.2017.03.028
- Fagg, D. P., Kharton, V. V., and Frade, J. R. (2002). P-type electronic transport in Ce<sub>0.8</sub>Gd<sub>0.2</sub>O<sub>2-δ</sub>: The effect of transition metal oxide sintering aids. *J. Electroceram.* 9, 199–207. doi:10.1023/a:1023269326651
- Ferreira, A. S. V., Soares, M. C., Figueiredo, F. M. H. L. R., and Marques, F. M. B. (2011b). Intrinsic and extrinsic compositional effects in ceria/carbonate composite electrolytes for fuel cells. *Int. J. Hydrogen Energy* 36, 3704–3711. doi:10.1016/j.ijhydene.2010.12.025
- Ferreira, A. S. V., Saradha, T., Figueiredo, F. L., and Marques, F. M. B. (2011a). Compositional and microstructural effects in composite electrolytes for fuel cells. *Int. J. Energy Res.* 35, 1090–1099. doi:10.1002/er.1843
- Figueiredo, F. M. L., and Marques, F. M. B. (2013). Electrolytes for solid oxide fuel cells. *WIREs Energy Env.* 2, 52–72. doi:10.1002/wene.23
- Gao, L., Zhou, M., Zheng, Y., Gu, H., Chen, H., and Guo, L. (2010). Effect of zinc oxide on yttria doped ceria. *J. Power Sources* 195, 3130–3134. doi:10.1016/j.jpowsour.2009.11.117
- Ge, L., Li, S., Zheng, Y., Zhou, M., Chen, H., and Guo, L. (2011). Effect of zinc oxide doping on the grain boundary conductivity of Ce<sub>0.8</sub>Gd<sub>0.2</sub>O<sub>1.9</sub> ceramics (Ln = Y, Sm, Gd). *J. Power Sources* 196, 6131–6137. doi:10.1016/j.jpowsour.2011.03.032
- Gomes, E., Mather, G. C., Figueiredo, F. M., and Marques, F. M. B. (2009). Microstructure and electrical properties of aluminium-substituted La(Sr)Ga(Mg)O<sub>3-δ</sub>-based solid electrolytes. *Monatsh. Chem.* 140, 1041–1052. doi:10.1007/s00706-009-0139-1
- Grain, C. F. (1967). Phase relations in the ZrO<sub>2</sub>–MgO system. *J. Am. Ceram. Soc.* 50, 288–290. doi:10.1111/j.1151-2916.1967.tb15111.x
- Grilo, J. P. F., Macedo, D. A., Nascimento, R. M., and Marques, F. M. B. (2021a). Assessment of processing route on the performance of ceria-based composites. *Int. J. Energy Res.* 45, 9069–9082. doi:10.1002/er.6438
- Grilo, J. P. F., Macedo, D. A., Nascimento, R. M., and Marques, F. M. B. (2019). Electronic conductivity in Gd-doped ceria with salt additions. *Electrochim. Acta* 318, 977–988. doi:10.1016/j.electacta.2019.06.148
- Grilo, J. P. F., Macedo, D. A., Nascimento, R. M., and Marques, F. M. B. (2021b). Innovative improvement of sintered ceramic electrolytes by salt infiltration. *Ceram. Int.* 47, 5079–5090. doi:10.1016/j.ceramint.2020.10.086
- Grilo, J. P. F., Macedo, D. A., Nascimento, R. M., and Marques, F. M. B. (2020). Performance of GDC with alkali metal carbonates as sintering aids. *Solid State Ionics* 346, 115221. doi:10.1016/j.ssi.2020.115221

## Publisher's note

All claims expressed in this article are solely those of the authors and do not necessarily represent those of their affiliated organizations, or those of the publisher, the editors and the reviewers. Any product that may be evaluated in this article, or claim that may be made by its manufacturer, is not guaranteed or endorsed by the publisher.

- Guo, X., Sigle, W., Fleig, J. U., and Maier, J. (2002). Role of space charge in the grain boundary blocking effect in doped zirconia. *Solid State Ionics* 154 (155), 555–561. doi:10.1016/s0167-2738(02)00491-5
- Guo, X., Sigle, W., and Maier, J. (2003). Blocking grain boundaries in yttria-doped and undoped ceria ceramics of high purity. *J. Am. Ceram. Soc.* 86, 77–87. doi:10.1111/j.1151-2916.2003.tb03281.x
- Guo, X., Tang, C. Q., and Yuan, R. Z. (1995). Grain boundary ionic conduction in zirconia-based solid electrolyte with alumina addition. *J. Eur. Ceram. Soc.* 15, 25–32. doi:10.1016/0955-2219(95)91296-z
- Guo, X., and Waser, R. (2006). Electrical properties of the grain boundaries of oxygen ion conductors: Acceptor-doped zirconia and ceria. *Prog. Mat. Sci.* 51, 151–210. doi:10.1016/j.pmatsci.2005.07.001
- Guth, U., Babwisch, F., Wulff, H., Möbius, H.-H., and Möbius, H. H. (1987). Electrical conductivity and crystal structure of pure and SrCO<sub>3</sub>-doped Na<sub>2</sub>CO<sub>3</sub>. *Cryst. Res. Technol.* 22, 141–145. doi:10.1002/crat.2170220127
- Haynes, W. M. (2005). *CRC handbook of chemistry and physics*. 91th Edition.
- Herle, J. Van, Horita, T., Kawada, T., Sakai, N., Yokokawa, H., and Dokiya, M. (1997). Fabrication and sintering of fine yttria-doped ceria powder. *J. Am. Ceram. Soc.* 80, 933–940. doi:10.1111/j.1151-2916.1997.tb02924.x
- Inaba, H., and Tagawa, H. (1996). Ceria-based solid electrolytes. *Solid State Ionics* 83, 1–16. doi:10.1016/0167-2738(95)00229-4
- Janz, G. J., and Bansa, N. P. (1982). Molten salts data: Diffusion coefficients in single and multi-component salt systems. *J. Phys. Chem. Ref. Data* 11, 505–693. doi:10.1063/1.555665
- Janz, G. J., and Tomkins, R. P. T. (1983). Molten salts: Volume 5, Part 2. Additional single and multi component salt systems. Electrical conductance, density, viscosity and surface tension data. *J. Phys. Chem. Ref. Data* 12, 591–815. doi:10.1063/1.555693
- Jiang, S., and Wagner, J. B. (1995). A theoretical model for composite electrolytes—II. Percolation model for ionic conductivity enhancement. *J. Phys. Chem. Solids* 56, 1113–1124. doi:10.1016/0022-3697(95)00026-7
- Jiang, Y., Sun, Y., Bruno, F., and Li, S. (2017). Thermal stability of Na<sub>2</sub>CO<sub>3</sub>-Li<sub>2</sub>CO<sub>3</sub> as a high temperature phase change material for thermal energy storage. *Thermochim. Acta* 650, 88–94. doi:10.1016/j.tca.2017.01.002
- Kaplan, V., Wachtel, E., and Lubomirsky, I. (2011). Conditions of stability for (Li<sub>2</sub>CO<sub>3</sub> + Li<sub>2</sub>O) melts in air. *J. Chem. Thermodyn.* 43, 1623–1627. doi:10.1016/j.jct.2011.05.020
- Kharton, V. V., Marques, F. M. B., and Atkinson, A. (2004). Transport properties of solid oxide electrolyte ceramics: A brief review. *Solid State Ion.* 174, 135–149. doi:10.1016/j.ssi.2004.06.015
- Kharton, V. V., Figueiredo, F. M., Navarro, L., Naumovich, E. N., Kovalevsky, A. V., Yaremchenko, A. A., et al. (2001). Ceria-based materials for solid oxide fuel cells. *J. Mat. Sci.* 36, 1105–1117. doi:10.1023/a:1004817506146
- Kim, J. W., and Lee, H. G. (2001). Thermal and carbothermic decomposition of Na<sub>2</sub>CO<sub>3</sub> and Li<sub>2</sub>CO<sub>3</sub>. *Metall. Materi. Trans. B* 32, 17–24. doi:10.1007/s11663-001-0003-0
- Kingery, W. D. (1974a). Plausible concepts necessary and sufficient for interpretation of ceramic grain-boundary phenomena: I, grain-boundary characteristics, structure, and electrostatic potential. *J. Am. Ceram. Soc.* 57, 1–8. doi:10.1111/j.1151-2916.1974.tb11350.x
- Kingery, W. D. (1974b). Plausible concepts necessary and sufficient for interpretation of ceramic grain-boundary phenomena: II, solute segregation, grain-boundary diffusion, and general discussion. *J. Am. Ceram. Soc.* 57, 74–83. doi:10.1111/j.1151-2916.1974.tb10818.x
- Kleinlogel, C. M., and Gauckler, L. J. (2000). Mixed electronic-ionic conductivity of cobalt doped cerium gadolinium oxide. *J. Electroceram.* 5, 231–243. doi:10.1023/a:1026583629995
- Kleitz, M., and Steil, M. C. (1997). Microstructure blocking effects versus effective medium theories in YSZ. *J. Eur. Ceram. Soc.* 17, 819–829. doi:10.1016/s0955-2219(97)89966-9
- Kudo, H. (1979). The rates of thermal decomposition of LiOH(s), LiOD(s) and LiOT(s). *J. Nucl. Mater.* 87, 185–188. doi:10.1016/0022-3115(79)90137-5
- Lapa, C. M., Figueiredo, F. M. L., de Souza, D. P. F., Song, L., Zhu, B., and Marques, F. M. B. (2010). Synthesis and characterization of composite electrolytes based on samaria-doped ceria and Na/Li carbonates. *Int. J. Hydrogen Energy* 35, 2953–2957. doi:10.1016/j.ijhydene.2009.05.036
- Le, S., Zhu, S., Zhu, X., and Sun, K. (2013). Densification of Sm<sub>0.2</sub>Ce<sub>0.8</sub>O<sub>1.9</sub> with the addition of lithium oxide as sintering aid. *J. Power Sources* 222, 367–372. doi:10.1016/j.jpowsour.2012.08.020
- Lee, S., Kim, M., Hwang, M., Kim, K., Jeon, C., and Song, J. (2013). Thermal stability and viscosity behaviors of hot molten carbonate mixtures. *Exp. Therm. Fluid Sci.* 49, 94–104. doi:10.1016/j.expthermflusci.2013.04.006
- Lei, Y., Ito, Y., Browning, N. D., and Mazanec, T. J. (2002). Segregation effects at grain boundaries in fluorite-structured ceramics. *J. Am. Ceram. Soc.* 85, 2359–2363. doi:10.1111/j.1151-2916.2002.tb00460.x
- Li, S., Wang, X., and Zhu, B. (2007). Novel ceramic fuel cell using non-ceria-based composites as electrolyte. *Electrochem. Commun.* 9, 2863–2866. doi:10.1016/j.elecom.2007.10.010
- Li, S., Xian, C., Yang, K., Sun, C., Wang, Z., and Chen, L. (2012). Feasibility and mechanism of lithium oxide as sintering aid for Ce<sub>0.8</sub>Sm<sub>0.2</sub>O<sub>8</sub> electrolyte. *J. Power Sources* 205, 57–62. doi:10.1016/j.jpowsour.2012.01.010
- Li, Y., Rui, Z., Xia, C., Anderson, M., and Lin, Y. S. (2009). Performance of ionic-conducting ceramic/carbonate composite material as solid oxide fuel cell electrolyte and CO<sub>2</sub> permeation membrane. *Catal. Today* 148, 303–309. doi:10.1016/j.cattod.2009.08.009
- Lin, Y., Fang, S., Su, D., Brinkman, K. S., and Chen, F. (2015). Enhancing grain boundary ionic conductivity in mixed ionic-electronic conductors. *Nat. Commun.* 6, 6824–6829. doi:10.1038/ncomms7824
- Maheshwari, A., and Wiemhöfer, H. (2016). Augmentation of grain boundary conductivity in Ca<sup>2+</sup> doped ceria-carbonate-composite. *Acta Mat.* 103, 361–369. doi:10.1016/j.actamat.2015.10.024
- Maier, J. (1986). On the conductivity of polycrystalline materials. *Berichte Bunsenges. fur Phys. Chem.* 90, 26–33. doi:10.1002/bbpc.19860900105
- Marrero-López, D., Dos Santos-Gómez, L., León-Reina, L., Canales-Vázquez, J., and Losilla, E. R. (2014). Influence of the microstructure on the bulk and grain boundary conductivity in apatite-type electrolytes. *J. Power Sources* 245, 107–118. doi:10.1016/j.jpowsour.2013.06.111
- Maxwell, J. C. (1904). *A treatise on electricity and magnetism*, II. Oxford: At The Clarendon Press.
- Mizusaki, J., Tagawa, H., Saito, K., Uchida, K., and Tezuka, M. (1992). Lithium carbonate as a solid electrolyte. *Solid State Ionics* 53 (56), 791–797. doi:10.1016/0167-2738(92)90256-o
- Mogensen, M., Sammes, N. M., and Tompsett, G. A. (2000). Physical, chemical and electrochemical properties of pure and doped ceria. *Solid State Ionics* 129, 63–94. doi:10.1016/s0167-2738(99)00318-5
- Moure, A., Tartaj, J., and Moure, C. (2009). Synthesis and low-temperature sintering of Gd-doped CeO<sub>2</sub> ceramic materials obtained by a coprecipitation process. *J. Am. Ceram. Soc.* 92, 2197–2203. doi:10.1111/j.1551-2916.2009.03215.x
- Nakamura, Y., Harashima, K., Hukuda, Y., Tokumitsu, N., and Yamamoto, S. (1980). Decomposition of sodium carbonate and its mixture with silica by heating and carbon-reduction. *Tetsu-to-Hagane* 66, 2023–2031. doi:10.2355/tetsutohagane1955.66.14\_2023
- Neuhaus, K., Baumann, S., Dolle, R., and Wiemhöfer, H.-D. (2018a). Effect of MnO<sub>2</sub> concentration on the conductivity of Ce<sub>0.9</sub>Gd<sub>0.1</sub>Mn<sub>x</sub>O<sub>2-δ</sub>. *Crystals* 8, 40. doi:10.3390/cryst8010040
- Neuhaus, K., Dolle, R., and Wiemhöfer, H.-D. (2018b). Assessment of the effect of transition metal oxide addition on the conductivity of commercial Gd-doped ceria. *J. Electrochem. Soc.* 165, F533–F542. doi:10.1149/2.1111807jes
- Nicholas, J. D., and De Jonghe, L. C. (2007). Prediction and evaluation of sintering aids for cerium gadolinium oxide. *Solid State Ionics* 178, 1187–1194. doi:10.1016/j.ssi.2007.05.019
- Olivares, R. I. (2012). The thermal stability of molten nitrite/nitrates salt for solar thermal energy storage in different atmospheres. *Sol. Energy* 86, 2576–2583. doi:10.1016/j.solener.2012.05.025
- Ortman, M. S., and Larsen, E. M. (1983). Preparation, characterization, and melting point of high-purity lithium oxide. *J. Am. Ceram. Soc.* 66, 645–648. doi:10.1111/j.1151-2916.1983.tb10614.x
- Patricio, S. G., Papaioannou, E., Zhang, G., Metcalfe, I. S., and Marques, F. M. B. (2014). High performance composite CO<sub>2</sub> separation membranes. *J. Memb. Sci.* 471, 211–218.
- Pearce, M. C., and Thangadurai, V. (2009). Electrical transport properties of aliovalent cation-doped CeO<sub>2</sub>. *Asia. Pac. J. Chem. Eng.* 4, 33–44. doi:10.1002/apj.185
- Pérez-Coll, D., Marrero-López, D., Núñez, P., Piñol, S., and Frade, J. R. (2006). Grain boundary conductivity of Ce<sub>0.9</sub>Ln<sub>0.1</sub>O<sub>2-δ</sub> ceramics (Ln = Y, La, Gd, Sm) with and without Co-doping. *Electrochim. Acta* 51, 6463–6469.
- Pérez-Coll, D., Sánchez-López, E., and Mather, G. C. (2010). Influence of porosity on the bulk and grain-boundary electrical properties of Gd-doped ceria. *Solid State Ionics* 181, 1033–1042. doi:10.1016/j.ssi.2010.06.006
- Pikalova, E. Y., Demina, A. N., Demin, A. k., Murashkina, A. A., Sopernikov, V. E., and Esina, N. O. (2007). Effect of doping with Co<sub>2</sub>O<sub>3</sub>, TiO<sub>2</sub>, Fe<sub>2</sub>O<sub>3</sub>, and Mn<sub>2</sub>O<sub>3</sub> on the properties of Ce<sub>0.8</sub>Gd<sub>0.2</sub>O<sub>2-δ</sub>. *Inorg. Mat.* 43, 830–837.
- Roberts, J. N., and Schwartz, L. M. (1985). Grain consolidation and electrical conductivity in porous media. *Phys. Rev. B* 31, 5990–5997. doi:10.1103/physrevb.31.5990



- Rondão, A. I. B., Patrício, S. G., Figueiredo, F. M. L., and Marques, F. M. B. (2013). Impact of ceramic matrix functionality on composite electrolytes performance. *Electrochim. Acta* 109, 701–709. doi:10.1016/j.electacta.2013.07.229
- Ruiz, M. L., Lick, I. D., Ponzi, M. I., Castellón, E. R., Jiménez-López, A., and Ponzi, E. N. (2010). Thermal decomposition of supported lithium nitrate catalysts. *Thermochim. Acta* 499, 21–26. doi:10.1016/j.tca.2009.10.016
- Santos, T. H., Grilo, J. P. F., Loureiro, F. J. A., Fagg, D. P., Fonseca, F. C., and Macedo, D. A. (2018). Structure, densification and electrical properties of  $Gd^{3+}$  and  $Cu^{2+}$  co-doped ceria solid electrolytes for SOFC applications: Effects of  $Gd_2O_3$  content. *Ceram. Int.* 44, 2745–2751. doi:10.1016/j.ceramint.2017.11.009
- Shannon, R. D. (1976). Revised effective ionic radii and systematic studies of interatomic distances in halides and chalcogenides. *Acta Cryst. Sect. A* A32, 751–767. doi:10.1107/s0567739476001551
- Singh, N. B., and Singh, N. P. (2007). Formation of CaO from thermal decomposition of calcium carbonate in the presence of carboxylic acids. *J. Therm. Anal. Calorim.* 89, 159–162. doi:10.1007/s10973-006-7565-7
- Skinner, S. J., and Kilner, J. A. (2003). Oxygen ion conductors. *Mat. Today* 6, 30–37. doi:10.1016/s1369-7021(03)00332-8
- Skobelev, I., Uvarov, N., and Hairetdinov, E. (1996). Composite solid electrolytes  $MeNO_3-Al_2O_3$  ( $me = Li, Na, K$ ). *Solid State Ionics* 88, 577–580. doi:10.1016/0167-2738(96)00208-1
- Stern, K. H., and Weise, E. L. (1969). High temperature properties and decomposition of inorganic salts. *Natl. Bur. Stand.*, 1–27.
- Stubican, V. S. (1986). Phase equilibria and metastabilities in the systems  $ZrO_2-MgO$ ,  $ZrO_2-CaO$  and  $ZrO_2-Y_2O_3$ . *Adv. Ceram.* 24, 71–82.
- Sudarsan, P., and Krishnamoorthy, S. B. (2018). Grain boundary scavenging through reactive sintering of strontium and iron in samarium doped ceria electrolyte for ITSOFC applications. *Mat. Res. Bull.* 100, 446–457. doi:10.1016/j.materresbull.2017.12.047
- Sweeney, M. (1975). Thermal stabilities of isoelectronic, isostructural nitrates, carbonates and borates. *Thermochim. Acta* 11, 409–424. doi:10.1016/0040-6031(75)80007-4
- Talesh, A., Siamak, S., and Jalal, S. (2010). Comparative study of carbon dioxide and methane adsorption by synthesized fine particles of SAPO-34 molecular sieve. *J. Chem. Chem. Eng.* 29.
- Taub, S., Neuhaus, K., Wiemhöfer, H.-D., Ni, N., Kilner, J. A., and Atkinson, A. (2015). The effects of Co and Cr on the electrical conductivity of cerium gadolinium oxide. *Solid State Ionics* 282, 54–62. doi:10.1016/j.ssi.2015.09.024
- Teoh, L. G., and Chiang, G. W. (2012). Preparation and characterization of nanocrystalline Ca-doped  $CeO_2$  by sol-gel process. *J. Sol-Gel Sci. Technol.* 64, 530–533. doi:10.1007/s10971-012-2885-5
- Van Dijk, T., and Burggraaf, A. J. (1981). Grain boundary effects on ionic conductivity in ceramic  $Gd_xZr_{(1-x)}O_{2-(x/2)}$  solid solutions. *Phys. Stat. Sol.* 63, 229–240. doi:10.1002/pssa.2210630131
- Villas-boas, L. A., Figueiredo, F. M. L., Souza, D. P. F. De, and Marques, F. M. B. (2014). Zn as sintering aid for ceria-based electrolytes. *Solid State Ionics* 262, 522–525. doi:10.1016/j.ssi.2013.11.002
- Weber, G., Sciora, E., Guichard, J., Bouyer, F., Bezverkhyy, I., Marcos Salazar, J., et al. (2018). Investigation of hydrolysis of lithium oxide by thermogravimetry, calorimetry and *in situ* FTIR spectroscopy. *J. Therm. Anal. Calorim.* 132, 1055–1064. doi:10.1007/s10973-017-6943-7
- Xing, W., Peters, T., Fontaine, M. L., Evans, A., Henriksen, P. P., Norby, T., et al. (2015). Steam-promoted  $CO_2$  flux in dual-phase  $CO_2$  separation membranes. *J. Memb. Sci.* 482, 115–119. doi:10.1016/j.memsci.2015.02.029
- Xu, D., Liu, X., Xu, S., Yan, D., Pei, L., Zhu, C., et al. (2011). Fabrication and performance of  $Ce_{0.85}Gd_{0.15}O_{1.925}-Fe_2O_3$  electrolytes in IT-SOFCs. *Solid State Ionics* 192, 510–514. doi:10.1016/j.ssi.2010.03.026
- Yamashita, K., Ramanujachary, K. V., and Greenblatt, M. (1995). Hydrothermal synthesis and low temperature conduction properties of substituted ceria ceramics. *Solid State Ionics* 81, 53–60. doi:10.1016/0167-2738(95)99031-h
- Yamauchi, M., Itagaki, Y., Aono, H., and Sadaoka, Y. (2008). Reactivity and stability of rare Earth oxide- $Li_2CO_3$  mixtures. *J. Eur. Ceram. Soc.* 28, 27–34. doi:10.1016/j.jeurceramsoc.2007.06.013
- Yurkinskii, V. P., Firsova, E. G., and Proskura, S. A. (2005). Thermal dissociation of sodium hydroxide upon evacuation. *Russ. J. Appl. Chem.* 78, 360–362. doi:10.1007/s11167-005-0296-x
- Zha, S., Xia, C., and Meng, G. (2003). Effect of Gd (Sm) doping on properties of ceria electrolyte for solid oxide fuel cells. *J. Power Sources* 115, 44–48. doi:10.1016/s0378-7753(02)00625-0
- Zhang, T. S., Ma, J., Kong, L. B., Chan, S. H., Hing, P., and Kilner, J. A. (2004). Iron oxide as an effective sintering aid and a grain boundary scavenger for ceria-based electrolytes. *Solid State Ionics* 167, 203–207. doi:10.1016/j.ssi.2004.01.006
- Zhu, T., Lin, Y., Yang, Z., Su, D., Ma, S., Han, M., et al. (2014). Evaluation of  $Li_2O$  as an efficient sintering aid for gadolinia-doped ceria electrolyte for solid oxide fuel cells. *J. Power Sources* 261, 255–263. doi:10.1016/j.jpowsour.2014.03.010



## OPEN ACCESS

EDITED BY  
Wenqin Luo,  
Huzhou University, China

REVIEWED BY  
Renren Deng,  
Zhejiang University, China  
Wei Zheng,  
Fujian Institute of Research on the  
Structure of Matter, Chinese Academy  
of Sciences (CAS), China

## \*CORRESPONDENCE

Rute A. S. Ferreira,  
rferreira@ua.pt  
Carlos D. S. Brites,  
carlos.brites@ua.pt

## SPECIALTY SECTION

This article was submitted to Light  
Sources and Luminescent Materials,  
a section of the journal  
Frontiers in Photonics

RECEIVED 03 August 2022

ACCEPTED 14 September 2022

PUBLISHED 29 September 2022

## CITATION

Zanella S, Trave E, Moretti E, Talon A,  
Back M, Carlos LD, Ferreira RAS and  
Brites CDS (2022), Designing Ln<sup>3+</sup>-  
doped BiF<sub>3</sub> particles for luminescent  
primary thermometry and  
molecular logic.  
*Front. Photonics* 3:1010958.  
doi: 10.3389/fphot.2022.1010958

## COPYRIGHT

© 2022 Zanella, Trave, Moretti, Talon,  
Back, Carlos, Ferreira and Brites. This is  
an open-access article distributed  
under the terms of the [Creative  
Commons Attribution License \(CC BY\)](#).  
The use, distribution or reproduction in  
other forums is permitted, provided the  
original author(s) and the copyright  
owner(s) are credited and that the  
original publication in this journal is  
cited, in accordance with accepted  
academic practice. No use, distribution  
or reproduction is permitted which does  
not comply with these terms.

# Designing Ln<sup>3+</sup>-doped BiF<sub>3</sub> particles for luminescent primary thermometry and molecular logic

Sofia Zanella<sup>1</sup>, Enrico Trave<sup>2</sup>, Elisa Moretti<sup>2</sup>, Aldo Talon<sup>2</sup>,  
Michele Back<sup>2</sup>, Luís D. Carlos<sup>1</sup>, Rute A. S. Ferreira<sup>1\*</sup> and  
Carlos D. S. Brites<sup>1\*</sup>

<sup>1</sup>Phantom-g, CICECO-Aveiro Institute of Materials, Physics Department, University of Aveiro, Aveiro, Portugal, <sup>2</sup>Department of Molecular Sciences and Nanosystems, Ca' Foscari University of Venice, Venice, Italy

The design of molecular materials suitable for disparate fields could lead to new advances in engineering applications. In this work, a series of Ln<sup>3+</sup>-doped BiF<sub>3</sub> sub-microparticles were synthesized through microwave-assisted synthesis. The effects of doping are evaluated from the structural and morphological viewpoint. In general, increasing the Ln<sup>3+</sup> concentration the octahedral habitus is distorted to a spheric one, and some aggregates are visible without any differences in the crystalline phase. The optical response of the samples confirms that the BiF<sub>3</sub> materials are suitable hosts for the luminescence of the tested trivalent lanthanide (Ln<sup>3+</sup>) ions (Ln = Eu, Tb, Tm, Ho, Er, Yb). A Yb<sup>3+</sup>/Er<sup>3+</sup> co-doped sample is presented as an illustrative example of all-photonic molecular logic operations and primary luminescent thermometry.

## KEYWORDS

trivalent lanthanide, bismuth fluoride, luminescence, primary thermometry, molecular logic

## Introduction

The development of synthesis routes allowing the design of materials with virtually on-demand properties (*e.g.*, size, shape, functionality) is pivotal for cutting-edge applications in disparate research areas. It is well known that the morphology and size of the materials can impact their physical and chemical properties (Piana *et al.*, 2005; Alivisatos, 1996; Xia *et al.*, 2003), making engineered materials suitable for a wide range of applications. Trivalent lanthanide (Ln<sup>3+</sup>)-bearing materials have been widely investigated due to their distinctive high quantum yield (>50% in the visible spectral range, when incorporated in complexes), long-lived excited states (>1 ms), narrow emission bands (<10 nm), rendering versatility, and photostability, when incorporated in inorganic or organic-inorganic hosts (Bünzli, 2015). Ln<sup>3+</sup>-based materials attracted huge scientific scrutiny during the last 25 years for many optical applications from the development of solid-state lasers (Kuriki *et al.*, 2002), lightning (Bai *et al.*, 2014), displays (Chen *et al.*,

2013), and, in the last 10–15 years to luminescence nanothermometry (Jaue and Vetrone, 2012; Brites et al., 2019).

A relatively recent and sagacious application for  $\text{Ln}^{3+}$ -doped materials is molecular logic, which aims at developing molecular counterparts for current electronic logic systems (De Silva et al., 1993). Any physical and/or chemical change caused by an external stimulus (logic inputs) leading to a physical and/or chemical alteration of the material (logic output), may be interpreted as a transfer function connecting the logic inputs and outputs. Several materials have been designed to mimic the operation of conventional Boolean logic gates, demonstrating basic arithmetic functions and memory units (Erbas-Cakmak et al., 2018; Andréasson and Pischel, 2021; Nicoli et al., 2021). Converting the response of the luminescent material to the logical values 0 and 1, diverse logic gates can be defined. Molecular logic operations comprising chemical species as logic inputs and modifications on the photophysical properties (e.g., emission intensity, absorbance) as the output are those reported most often. Nevertheless, physical stimuli (e.g., light, temperature, pressure, magnetic field) may play the role of logic inputs, with many advantages such as no-contamination, reuse of the device, easy reconfiguration, and reprogramming (Andréasson et al., 2011; Brites et al., 2019; Zanella et al., 2022).

Irrespective of the foreseen applications, to render tailorable photoluminescence response of the  $\text{Ln}^{3+}$ -doped materials, the host material should be precisely designed. Ideally, the host material would not interfere with the luminescence processes, therefore, host materials with low phonon energy are desirable. To date, fluorides, such as  $\text{NaYF}_4$  based materials have been widely investigated as luminescent host materials and remarkable results have been reported.  $\text{NaYF}_4$  has been used as a host in different contexts such as solar cells (Kumar et al., 2020), biodetection (Yi et al., 2004), detecting fingerprints (Xie et al., 2015), and display (Deng et al., 2015). As an alternative to the well-known  $\text{NaYF}_4$ , Bi-based matrices are an appealing candidate to host  $\text{Ln}^{3+}$  ions. In particular, bismuth-based fluoride nanoparticles have been proposed for multi-imaging and phosphor applications (Back et al., 2019), while bismuth oxyhalides of general formula  $\text{BiOX}$  ( $X = \text{F}, \text{Cl}, \text{Br}, \text{I}$ ) have been studied due to their chemical stability, high refractive index and photocatalytic properties (Wang et al., 2020b). Furthermore, bismuth-based compounds have been exploited in different fields such as luminescent thermometry (Back et al., 2020b; Casagrande et al., 2020), water splitting (Kato et al., 2017), fuel cells (Sanna et al., 2015), UV filtering (Zaccariello et al., 2019) and cosmetics production (Zaccariello et al., 2017). There are several synthetic routes to obtain sub-microparticles and nanoparticles of Bi-based systems with different shapes and morphology. One of these is the microwave-assisted synthesis, developed in the 80's (Gedye et al., 1986), that exploits microwave radiation with frequencies between 0.3 and 300 GHz as the heating source (Nüchter et al., 2004). As the microwave energy is not enough to break the chemical bonds, it increases the Brownian motion and consequently the temperature. During the reaction, the heat is

produced by the collisions of the particles, or by the electric dipole of molecules. Several advantages are ascribed to this synthetic method such as the high chemical yield, reproducibility and homogeneity of the synthesis, possible application in green chemistry, and contactless with the heating source (Dąbrowska et al., 2018). Therefore, sub-micro Bi-based fluoride and oxyfluoride particles can be easily synthesized through the microwave approach, with the possibility to obtain a high yield in powder (Escudero et al., 2014).

Here, we present the synthesis, structural and photophysical characterization of  $\text{Ln}^{3+}$ -doped ( $\text{Ln} = \text{Yb}, \text{Er}, \text{Tm}, \text{Eu}, \text{Tb}$ ) bismuth fluoride ( $\text{BiF}_3$ ) sub-micro particles prepared through a microwave-assisted synthesis, demonstrating that several  $\text{Ln}^{3+}$  ions can be efficiently hosted. The  $\text{Er}^{3+}$ - $\text{Yb}^{3+}$  co-doped sample was further explored for molecular logics and luminescent thermometry applications as it presents different emission profiles depending on the power density of the excitation laser. These results open a new path for all-photonics reprogrammable materials that are simultaneously primary thermometers, dismissing the need for recurrent thermal calibrations, and thus enabling the *in-situ* real-time monitoring of the temperature.

## Experimental details

### Chemical and materials

Bismuth nitrate pentahydrate ( $\text{Bi}(\text{NO}_3)_3 \cdot 5\text{H}_2\text{O}$ , Sigma  $\geq 99.99\%$ ), sodium tetrafluoroborate ( $\text{NaBF}_4$ , Across Organic,  $>97\%$ ) were used as bismuth and fluoride sources, respectively. Europium (III) nitrate pentahydrate ( $\text{Eu}(\text{NO}_3)_3 \cdot 5\text{H}_2\text{O}$ , Sigma Aldrich, 99.9%), terbium (III) nitrate pentahydrate ( $\text{Tb}(\text{NO}_3)_3 \cdot 5\text{H}_2\text{O}$ , Sigma Aldrich,  $\geq 99.9\%$ ), ytterbium (III) nitrate pentahydrate ( $\text{Yb}(\text{NO}_3)_3 \cdot 5\text{H}_2\text{O}$ , Sigma Aldrich,  $\geq 99.9\%$ ), erbium (III) nitrate pentahydrate ( $\text{Er}(\text{NO}_3)_3 \cdot 5\text{H}_2\text{O}$ , Sigma Aldrich,  $\geq 99.9\%$ ), thulium (III) nitrate pentahydrate ( $\text{Tm}(\text{NO}_3)_3 \cdot 5\text{H}_2\text{O}$ , Sigma Aldrich,  $\geq 99.9\%$ ), terbium (III) nitrate pentahydrate ( $\text{Tb}(\text{NO}_3)_3 \cdot 5\text{H}_2\text{O}$ , Sigma Aldrich,  $\geq 99.9\%$ ), holmium (III) nitrate pentahydrate ( $\text{Ho}(\text{NO}_3)_3 \cdot 5\text{H}_2\text{O}$ , Sigma Aldrich,  $\geq 99.9\%$ ) were used as  $\text{Ln}^{3+}$  precursors. Diethylene glycol (DEG, Sigma Aldrich,  $\geq 99.0\%$ ), and MilliQ water were used as solvents. Ethanol ( $\text{C}_2\text{H}_5\text{OH}$ , VWR Chemicals 100%) was used in the washing process.

### Synthesis of the sub-micro particles

The experimental protocol already reported elsewhere (Escudero et al., 2014) was adopted to produce oxyfluoride and fluoride bismuth materials. In short, pentahydrate bismuth nitrate,  $\text{Bi}(\text{NO}_3)_3 \cdot 5\text{H}_2\text{O}$ , is dissolved in 24 ml of

diethylene glycol at 348 K for 10 minutes under stirring and then the solution is cooled to room temperature. In the doping procedure,  $\text{Ln}^{3+}$  cations are dissolved in diethylene glycol together with the Bi precursor, with sodium tetrafluoroborate,  $\text{NaBF}_4$  in 6 ml of MilliQ water. These two solutions are then mixed under stirring and the resulting solution is placed in a Teflon-lined autoclave. The reaction occurs in a microwave digestion system (Ethos Plus Microwave, Milestone) at 393 K for 30 s, at 1000 W power. Afterward, the autoclave is quenched in an ice bath for 15 min. The opalescent solution obtained is separated by centrifugation (6,000 rpm) and the white precipitate is washed twice in ethanol and once in MilliQ water. The sample is dried overnight at room temperature and then characterized. The stoichiometry among reagents, temperature, and reaction time have been previously arranged to obtain octahedral sub-micro particles, as detailed in [Supplementary Table S1](#).

## Characterization

**Structural and morphological characterization:** X-ray powder diffraction (XRPD) measurements were performed on a diffractometer (Philips X'Pert) with a goniometer in the Bragg–Brentano geometry (PW 1319), connected to a highly stabilized X-ray source (Nickel-filtered  $\text{Cu-K}_\alpha$  radiation), a focusing graphite monochromator, and a proportional counter with a pulse height discriminator. A step-by-step technique with collection times of 10 s per step (steps of  $0.05^\circ$  in  $2\theta$  units) was employed.

The size, morphology, and EDX analysis of the sub-micro particles were carried out by a field emission scanning electron microscope (FE-SEM, Carl Zeiss Sigma VP) equipped with a microanalysis detector (Bruker Quantax 200). The EDX spectra were collected at 4–5 kV for all the samples. A second SEM equipment (JEOL JSM-5600LV) with a microanalysis system (OXFORD-Link Isis series 300) was used to perform the morphological analysis.

**Photoluminescence characterization:** The emission spectra of  $\text{BiF}_3:\text{Ln}^{3+}$  ( $\text{Ln} = \text{Eu}, \text{Tb}, \text{Yb}, \text{Er}$ ) were recorded with a modular double grating excitation spectrofluorometer with an emission monochromator (TRIAx 320, Fluorolog-3, Horiba Scientific) coupled to a photomultiplier (R928 Hamamatsu) operating in the visible spectral range, using a front face configuration. A 450 W Xe arc lamp was used as the excitation source for the  $\text{Eu}^{3+}$ - $\text{Tb}^{3+}$  single-doped and co-doped samples. Both recorded emission and excitation spectra were corrected with the spectrofluorimeter optical spectral response and the spectral distribution of the lamp intensity using a photodiode reference detector, respectively. For recording the temperature-dependent upconversion spectra of  $\text{BiF}_3:\text{Yb}^{3+}/\text{Er}^{3+}$  sample, a continuous-wave 980 nm laser diode (BrixX 980-1000 HD, Omicron Laser) focused through a NIR optical lens (Thorlabs, 12 cm focal distance) was used as the excitation

source. The temperature was controlled using a temperature controller (IES-RD31) equipped with a Kapton thermofoil heater (Minco) mounted on a Cu-holder. The temperature was recorded using a thermocouple (Barnant 100 model 600-2820) with an accuracy of 0.1 K, accordingly to the manufacturer.

The emission spectra of  $\text{Yb-Ln}^{3+}$  ( $\text{Ln} = \text{Tm}, \text{Ho}$ ) were acquired at Ca' Foscari University of Venice in the 250–1,050 nm range using a portable spectrometer (QE65 Pro, Ocean Optics), and a continuous-wave laser diode peaking at 980 nm (CNI MDL-III-980) as the excitation source. The laser diode output power was 2 W, distributed on a  $5 \times 8 \text{ mm}^2$  spot, corresponding to a mean power density of  $5 \text{ W cm}^{-2}$ .

## Luminescence thermometry

The temperature (T) was accessed by the intensity ratio  $\Delta = I_H/I_S$ , where  $I_H$  and  $I_S$  the integrated areas of the  $\text{Er}^{3+}$  transitions  ${}^2\text{H}_{11/2} \rightarrow {}^4\text{I}_{15/2}$  and  ${}^4\text{S}_{3/2} \rightarrow {}^4\text{I}_{15/2}$ , respectively. The calculated temperature value is given by ([Balabhadra et al., 2017](#)):

$$\frac{1}{T} = \frac{1}{T_0} - \frac{k_B}{\Delta E} \ln \left( \frac{\Delta}{\Delta_0} \right) \quad (1)$$

where  $k_B$  is the Boltzmann constant,  $\Delta E$  is the energy gap between the barycenters of the  ${}^2\text{H}_{11/2} \rightarrow {}^4\text{I}_{15/2}$  and  ${}^4\text{S}_{3/2} \rightarrow {}^4\text{I}_{15/2}$  transitions,  $\Delta_0$  is the value of  $\Delta$  at the temperature  $T_0$  in the limit of null excitation power density. The performance of luminescent thermometers is quantified by the relative thermal sensitivity ( $S_r$ ) and temperature uncertainty ( $\delta T$ ). According to the corresponding definitions ([Brites et al., 2017](#)):

$$S_r = \frac{1}{\Delta} \left| \frac{\partial \Delta}{\partial T} \right| = \frac{\Delta E}{k_B T^2} \quad (2)$$

and

$$\delta T = \frac{1}{S_r} \frac{\delta \Delta}{\Delta} = \frac{k_B T^2}{\Delta E} \frac{\delta \Delta}{\Delta} \quad (3)$$

where  $\delta \Delta / \Delta$  is the relative uncertainty in  $\Delta$  estimated here for each temperature using the signal to noise ratio of the corresponding recorded emission spectrum.

## Results and discussion

### Synthesis, structure and morphology of the $\text{Ln}^{3+}$ -doped $\text{BiF}_3$ particles

The mechanism of formation of the sub-micro particles is not fully understood since the microwave-assisted reaction takes place very quickly ([Escudero et al., 2014](#)). [Figures 1A–F](#) shows the surface morphology of  $\text{BiF}_3$  sub-micro particles  $\text{Ln}^{3+}$ -doped and undoped obtained by microwave synthesis. It is assumed that spheres are initially formed which then evolve into octahedral



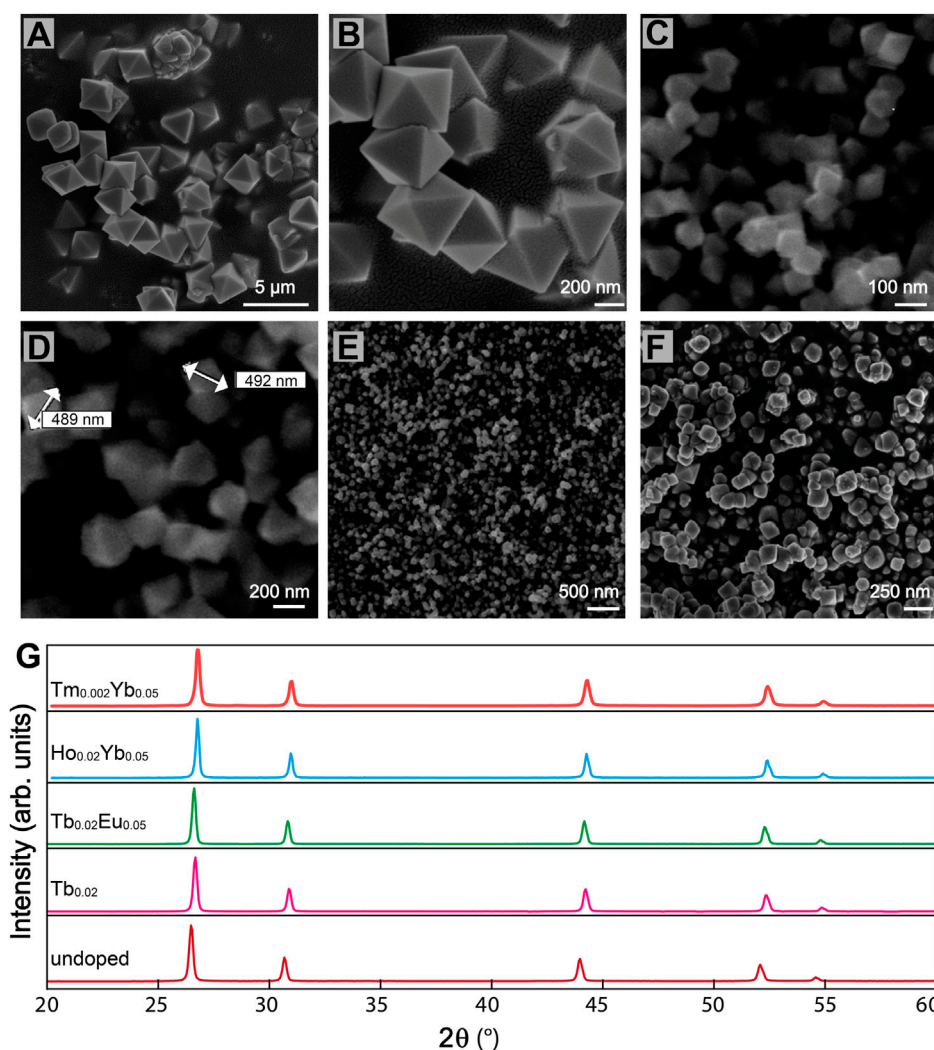


FIGURE 1

SEM micrographs of BiF<sub>3</sub> sub-micro particles (A) (B) Eu<sub>0.05</sub> doped, (C) (D) undoped, (E) Er<sub>0.02</sub> doped, (F) Er<sub>0.01</sub>Yb<sub>0.05</sub> co-doped. (G) XRD patterns of BiF<sub>3</sub> sample undoped and Ln<sup>3+</sup> single and co-doped.

shapes (Figures 1A–D), with an average size between 300 and 600 nm (Supplementary Figures S1A,B). As reported in the literature (Escudero et al., 2014), octahedral sub-micro particles are formed in a short time (30 s) as soon as the temperature reaches the set maximum (393 K). Smaller dimensions could be obtained using different molar ratios among reagents. For example, using a higher NaBF<sub>4</sub> concentration (Supplementary Table S1), resulted in a smaller size, around 130–150 nm (Supplementary Figure S2A). The decrease in the average size of the octahedral sub-micro particles is probably due to the largest number of nuclei involved during the reaction process.

On one hand, for samples with a low concentration of dopants octahedral is the predominant shape (Figure 1E), on the other hand, with a higher concentration of dopants, the

micrographs revealed agglomerated granules (Figure 1F). We observed that when the amount of Ln<sup>3+</sup> ions is higher than 5.0 atomic %, the thermodynamic equilibrium is altered and particles with different shapes are obtained (Supplementary Figure S2B).

Figure 1G suggests all the synthesized samples exhibit the same XRD pattern, attributable to α-BiF<sub>3</sub> cubic structure (ICSD#2452 card). The adopted microwave-assisted synthesis route can determine the incorporation of the oxygen into the α-BiF<sub>3</sub> structure that leads to the formation of BiO<sub>y</sub>F<sub>3–2y</sub> solid solutions (Escudero et al., 2014), and thus, diverse solid solutions based on the cubic fluorite, orthorhombic, monoclinic, rhombohedral, and hexagonal structures have been reported so far (Bervas et al., 2006).

The elemental mapping energy performed through X-ray (EDX) confirms the homogeneous distribution of elements in the

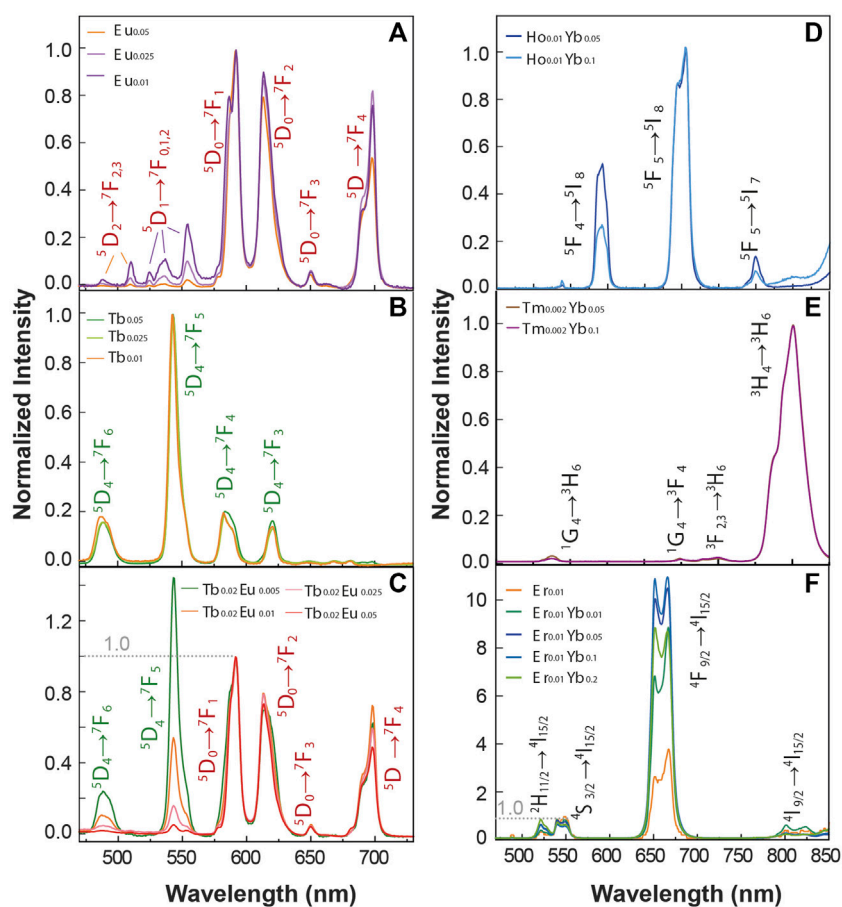


FIGURE 2

Emission spectra of (A)  $\text{Eu}^{3+}$  single-doped (B)  $\text{Tb}^{3+}$  single-doped, and (C)  $\text{Tb}^{3+}$ - $\text{Eu}^{3+}$  co-doped samples under 370 nm excitation. The transitions assigned the  $\text{Tb}^{3+}$  and  $\text{Eu}^{3+}$  ions are presented in green and red colors, respectively. Upconversion emission spectra of (D)  $\text{Yb}^{3+}$   $\text{Tm}^{3+}$  co-doped, (E)  $\text{Yb}^{3+}$   $\text{Ho}^{3+}$  co-doped and (F)  $\text{Yb}^{3+}$   $\text{Er}^{3+}$  co-doped and single doped  $\text{Er}^{3+}$  samples upon 980 nm excitation.

$\text{Ln}^{3+}$  doped particles. The elemental mapping of  $\text{BiF}_3$  confirmed that all the elements were finely dispersed over the entire analyzed area (Supplementary Figure S4).

## Photoluminescence characterization

It is widely known that the luminescence intensity of  $\text{Ln}^{3+}$  ions is sensitive to the concentration of the dopants. Looking forward to studying the optical properties of the material, we synthesized  $\text{BiF}_3$  particles incorporating different concentrations of  $\text{Ln}^{3+}$  ions. Figure 2 displays a series of  $\text{Ln}^{3+}$  single-doped and co-doped samples. Figures 2A–C shows the emission spectra for  $\text{Eu}^{3+}$  and  $\text{Tb}^{3+}$  single-doped and co-doped samples under 370 nm excitation. The narrow lines (FWHM <10 nm) are ascribed to the  $\text{Tb}^{3+}$  ( $^5\text{D}_4 \rightarrow ^7\text{F}_{3-6}$ ) and  $\text{Eu}^{3+}$  ( $^5\text{D}_0 \rightarrow ^7\text{F}_{0-4}$ ) transitions. The  $\text{Tb}^{3+}$  single-doped samples are normalized to the peak intensity of

$^5\text{D}_4 \rightarrow ^7\text{F}_4$  transition for comparison. The  $\text{Eu}^{3+}$  single-doped and  $\text{Tb}^{3+}$  co-doped samples instead are normalized to the peak intensity of  $^5\text{D}_0 \rightarrow ^7\text{F}_1$  transition. From the  $\text{Eu}^{3+}$  samples, the relative intensity of the  $^5\text{D}_1 \rightarrow ^7\text{F}_{0,3}$  and  $^5\text{D}_0 \rightarrow ^7\text{F}_{1,2}$  decreases as the  $\text{Eu}^{3+}$  concentration increases. One important transition is the  $\text{Eu}^{3+}$   $^5\text{D}_0 \rightarrow ^7\text{F}_1$  one (centered at 591 nm), a magnetic dipole transition (MD), allowed by the selection rules. The  $^5\text{D}_0 \rightarrow ^7\text{F}_1$  transition is usually less intense than the  $^5\text{D}_0 \rightarrow ^7\text{F}_2$  one (Binnemans, 2015). For the  $\text{BiF}_3$  host, however, the MD transition is most intense due to the  $\text{Eu}^{3+}$  cations occupying crystallographic sites with an inversion center, which is compatible with the replacement of  $\text{Bi}^{3+}$  by  $\text{Eu}^{3+}$  cations (Escudero et al., 2014). Moreover, emission bands originating from the  $^5\text{D}_1$  emitting level are clearly observed at low temperatures for the sample doped with a  $\text{Eu}^{3+}$  concentration of 5 mol% due to the suppression of non-radiative processes responsible for the thermal quenching at room temperature. We

stress the presence of  $^5D_1 \rightarrow ^7F_0$  transition that usually is not allowed for  $\text{Eu}^{3+}$  in centrosymmetric sites, in line with previous reports in other matrices with similar local symmetry (Tanner, 2013). The above-described  $\text{Eu}^{3+}$  transitions are usually observed in matrices with very low phonon energy, that are very convenient as hosts. In the  $\text{Eu}^{3+}/\text{Tb}^{3+}$  co-doped samples, there is evidence of a  $\text{Tb}^{3+}$ -to- $\text{Eu}^{3+}$  energy transfer as signed by the intra- $4f^8$  transitions lines observed in the  $\text{Eu}^{3+}$  excitation spectra (Supplementary Figure S5A), together with the decrease of the emission intensity for the  $\text{Tb}^{3+}$  transitions as the  $\text{Eu}^{3+}$  concentration increases (Figure 2C).

Figures 2D–F shows the upconversion emission spectra of a series of  $\text{Ln}^{3+}$  single-doped and  $\text{Yb}^{3+}\text{-Ln}^{3+}$  ( $\text{Er}^{3+}$ ,  $\text{Tm}^{3+}$ ,  $\text{Ho}^{3+}$ ) co-doped samples upon 980 nm excitation. The emission  $\text{Ho}^{3+}/\text{Yb}^{3+}$  co-doped samples (Figure 2D) show the emissions bands of  $\text{Ho}^{3+}$  ions in the green, red, and near-infrared spectral ranges, originating from the  $^5F_4 \rightarrow ^5I_8$  (~540 nm),  $^5F_5 \rightarrow ^5I_8$  (~650 nm), and  $^5F_4 \rightarrow ^5I_7$  (~750 nm) transitions, respectively. The emission spectra recorded for the  $\text{Tm}^{3+}/\text{Yb}^{3+}$  co-doped samples are presented in Figure 2E, and the peaks ascribed to the  $\text{Tm}^{3+}$  transitions  $^1G_4 \rightarrow ^3H_6$  at 475 nm,  $^1G_4 \rightarrow ^3F_4$  (~650 nm),  $^3F_{2,3} \rightarrow ^3H_6$  (~700 nm) and  $^3H_4 \rightarrow ^3H_6$  (~795 nm) are observed. Figure 2F presents the emission spectra of the  $\text{Er}^{3+}/\text{Yb}^{3+}$  co-doped samples, in which the emission bands ascribed to  $^2H_{11/2} \rightarrow ^4I_{15/2}$  (~520 nm),  $^4S_{3/2} \rightarrow ^4I_{15/2}$  (~550 nm) and  $^4F_{9/2} \rightarrow ^4I_{15/2}$  (~650 nm) transitions are observed. In all the  $\text{Yb}^{3+}\text{-Ln}^{3+}$  samples, the recorded upconverting emission involves the  $\text{Yb}^{3+} \rightarrow ^2F_{5/2}$  level population by ground state absorption, followed by  $\text{Yb}^{3+}$ -to-acceptor energy transfer mechanisms (Dong et al., 2015). The acceptor ions ( $\text{Ho}^{3+}$ ,  $\text{Tm}^{3+}$ ,  $\text{Er}^{3+}$ ) are first promoted to their respective excited states and then relax originating the observed spectral features. The energy diagram illustrating a possible route for the energy transfer processes is depicted in Supplementary Figure S6.

## Exploiting $\text{BiF}_3\text{:Yb}^{3+}/\text{Er}^{3+}$ particles for primary thermometry

Primary thermometers are temperature sensors in which the temperature determination is based on well-grounded physical principles. In 2017, Balabhadra et al. (2017) proposed a straightforward method to predict the temperature calibration curve of any upconverting thermometer based on two thermally coupled electronic levels using the Boltzmann statistics. Here, we selected an  $\text{Er}^{3+}/\text{Yb}^{3+}$  co-doped sample (1% of Er and 5% of Yb) hereafter denominated  $\text{BiF}_3\text{:YbEr}$ . Figure 3A displays the temperature-dependent upconversion emission spectra of  $\text{BiF}_3\text{:YbEr}$  recorded under 980 nm excitation between 298 and 363 K. Figure 3B shows the thermal dependence of the integrated areas of the  $\text{Er}^{3+}$  transitions  $^2H_{11/2} \rightarrow ^4I_{15/2}$  and  $^4S_{3/2} \rightarrow ^4I_{15/2}$  and corresponding to the  $I_H$  (510–533 nm) and  $I_S$  (533–570 nm),

respectively. We observe two regimes, depending on the temperature range: for  $T < 320$  K the  $I_H$  transition remains constant, and  $I_S$  decreases about 25%, whereas for higher temperatures both  $I_H$  and  $I_S$  increase. The parameter that allows the conversion of the integrated areas into temperature is the so-called thermometric parameter, defined as  $\Delta = I_H/I_S$  (Figure 3C).

According to the established methodology (S. Balabhadra et al., 2017), the calibration curve can be predicted if the energy separation between the emitting levels ( $\Delta E$ ) and the  $\Delta$  value in the limit of null excitation power density,  $\Delta_0$  (at temperature  $T_0$ , calculus in Supporting Information) can be obtained independently. The  $\Delta E$  value is calculated by the difference between the barycenter of the emission spectra recorded at room temperature, resulting  $\Delta E = 768 \pm 25 \text{ cm}^{-1}$  (calculus in Supporting Information). This value agrees with that reported for  $\text{Yb}^{3+}/\text{Er}^{3+}$  co-doped systems (Hernández-Rodríguez et al., 2021). The  $\Delta_0$  value, estimated at room temperature ( $T_0 = 298.0 \pm 0.1$  K) as the extrapolation for null excitation power densities of the thermometric parameter, is  $\Delta_0 = 0.16 \pm 0.01$ .

The maximum  $S_r$  value was observed for the lower temperature value tested (298 K) of  $1.3 \pm 0.1\% \text{ K}^{-1}$  and the minimum  $\delta T = 0.4$  K was estimated at the same temperature (Figure 3E,F). As the temperature increases,  $S_r$  decreases reaching  $0.9 \pm 0.1\% \text{ K}^{-1}$  at 365 K. The corresponding thermal uncertainty increases to 0.7 K. We conclude that  $\text{BiF}_3\text{:YbEr}$  sub-micro particles exhibited comparable  $S_r$  values to those reported for optical thermometers based on  $\text{Yb}^{3+}/\text{Er}^{3+}$  (Table 1) as expected since the  $\Delta E$  value obtained here (that is determining the maximum  $S_r$ ), is comparable to that found in the literature (Hernández-Rodríguez et al., 2021). The validity of Eq. 1 to predict the temperature was verified in the range 295–365 K. Figure 3D presents a comparison between measured (by a thermocouple, uncertainty of 0.1 K) and calculated temperature values in that temperature range. There is a perfect match between calculated and measured temperature values within the uncertainty of both quantities, thus attesting that the studied system is a primary thermometer with temperature determined via Eq. 1. These results sustain that  $\text{BiF}_3\text{:YbEr}$  sub-micro particles are primary luminescent thermometers working in a wide range of temperatures.

## Exploiting $\text{BiF}_3\text{:Yb}^{3+}/\text{Er}^{3+}$ particles for molecular logic

The  $\text{BiF}_3\text{:YbEr}$  particles present emission features that are dependent on the temperature and on the excitation power density employed. Rationalizing these observations in the context of molecular logic, we exploit external stimuli (e.g., excitation power density,  $P_D$ , and  $T$ ) and several logic outputs, considering the modifications induced in the emission spectra (Figures 4A,B). First, we calculate the intensity of some Stark

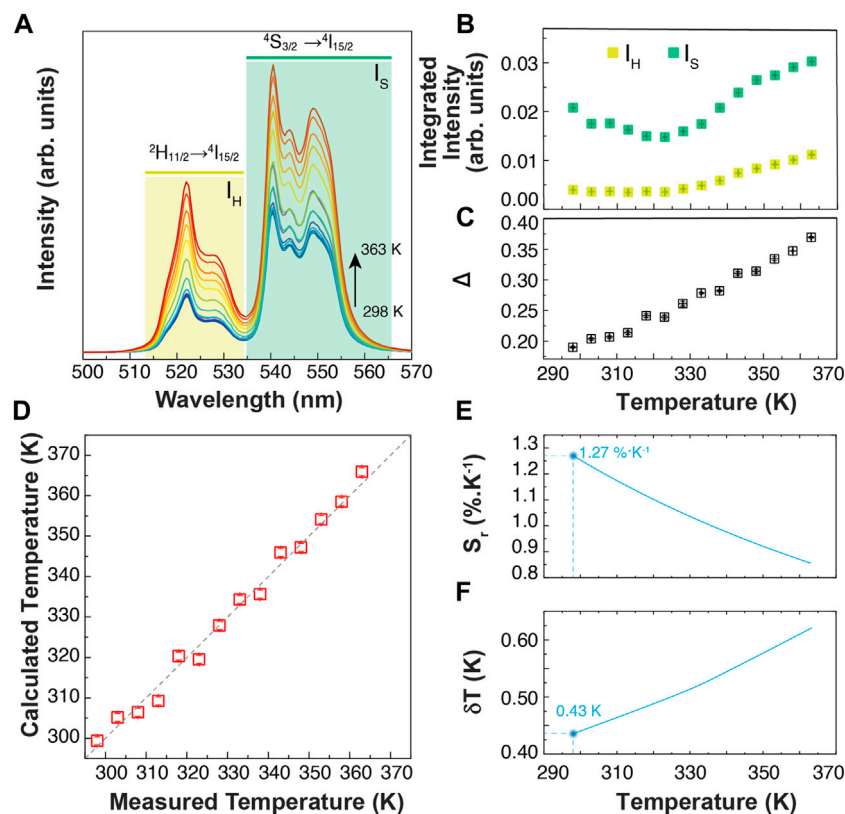


FIGURE 3

(A) Temperature-dependent upconversion emission spectra of BiF<sub>3</sub>:YbEr upon 980 nm excitation ( $P_D = 5 \text{ W cm}^{-2}$ ). The shadowed areas correspond to the integration ranges. (B) Temperature dependence of the emission band integrated areas related to the  $^2\text{H}_{11/2} \rightarrow ^4\text{I}_{15/2}$  ( $I_H$ ) and  $^4\text{S}_{3/2} \rightarrow ^4\text{I}_{15/2}$  ( $I_S$ ) Er<sup>3+</sup> transitions. The corresponding calibration curve is presented in (C). (D) Comparison between the measured (x-axis) and the calculated through Eq. 1 (y-axis) temperatures. The interrupted line is a guide to the eyes corresponding to  $y = x$ . (E) Relative thermal sensitivity and (F) temperature uncertainty of BiF<sub>3</sub>:YbEr expressed as  $S_r$  obtained through Eq. 2 and Eq. 3, respectively.

TABLE 1 Working temperature range, excitation wavelength ( $\lambda_x$ , nm), relative sensitivity ( $S_r$ , %K<sup>-1</sup>) and corresponding temperature value ( $T$ ) for which it is reported of illustrative Ln<sup>3+</sup>- based optical temperature sensors involving the ratio of the emission integrated areas of the Er<sup>3+</sup> transitions.

Compounds	Temperature range (K)	$\lambda_x$ (nm)	$S_r$ (%K <sup>-1</sup> )	$T$ (K)	Ref
NaYF <sub>4</sub> :Er <sup>3+</sup> /Yb <sup>3+</sup>	300–773	980	1.2	300	Li et al. (2019)
Ca <sub>3</sub> Al <sub>2</sub> O <sub>6</sub> :Er <sup>3+</sup> /Yb <sup>3+</sup>	298–573	980	0.8	145	Wang et al. (2019)
BiOF:Er <sup>3+</sup>	303–663	980	1.1	303	Wang et al. (2020a)
Bi <sub>2</sub> SiO <sub>5</sub> :Yb,Er@SiO <sub>2</sub>	80–800	980	1.1	300	Back et al. (2020a)
SrS:Ce <sup>3+</sup> /Er <sup>3+</sup>	100–300	410	0.3	100	Wei et al. (2022)
BiF <sub>3</sub> :ErYb	298–365	980	1.3	298	This work

components of the Er<sup>3+</sup> transitions  $^4\text{S}_{3/2}$ ,  $^2\text{H}_{11/2} \rightarrow ^4\text{I}_{15/2}$  transition, selecting the peak wavelengths, namely the 522.0 ( $I_1$ ) and 527.0 nm ( $I_2$ ) wavelengths, in the  $^4\text{S}_{3/2} \rightarrow ^4\text{I}_{15/2}$  transition, and the 540.5, 544.0, 549.0 and 552 nm wavelengths ( $I_3$  to  $I_6$ , respectively) in the  $^2\text{H}_{11/2} \rightarrow ^4\text{I}_{15/2}$  one. These intensities allow us to define four ratiometric outputs, as  $R_1 = I_1/I_3$ ;  $R_2 = I_1/I_2$ ;  $R_3 =$

$I_3/I_4$ , and  $R_4 = I_5/I_6$ . The ratiometric definition of the logic outputs guarantees that the system is independent of eventual fluctuations in the excitation source intensity and/or electrical drifts of the detection system. The temperature dependence of the intensity ratios is presented in Figures 4C,D for low (5 W·cm<sup>-2</sup>) and high (111 W·cm<sup>-2</sup>)  $P_D$  values. As the particles



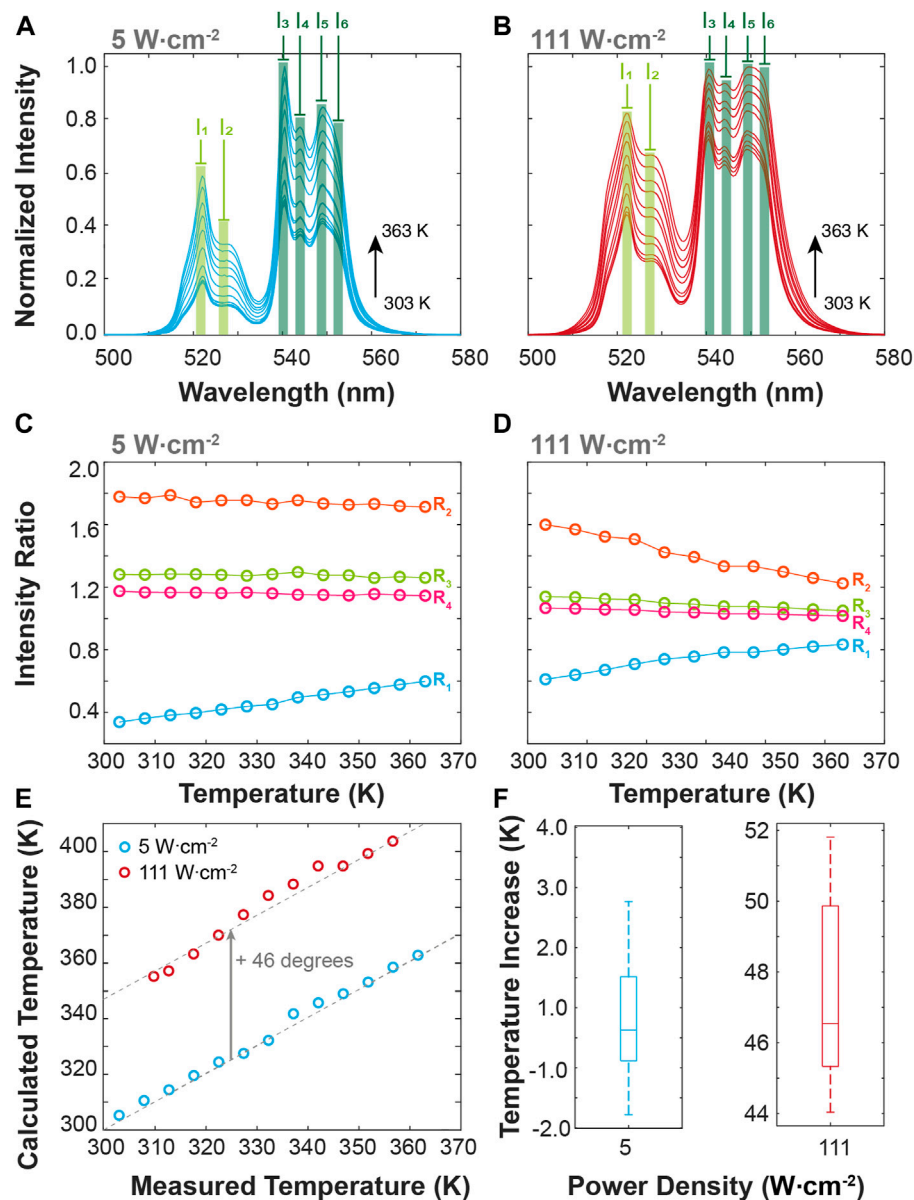


FIGURE 4

Temperature-dependent upconversion emission spectra of BiF<sub>3</sub>:YbEr upon 980 nm excitation at (A) 5 and (B) 111 W cm<sup>-2</sup>. (C) Intensities ratio as a function of the temperature calculated from the emission spectra at (C) 5 and (D) 111.1 W cm<sup>-2</sup>. (E) Comparison between the measured (set in the temperature controller) and the calculated (Eq. 1) temperature values for the 5 and 111 W cm<sup>-2</sup>. The interrupted lines are guides to the eyes corresponding to  $y = x$  (overlapping the blue symbols) and  $y = x + 46.3$  (overlapping the red symbols). The corresponding boxplots of the temperature increase are presented in (F).

are luminescent primary thermometers, we can determine the actual local temperature upon 980 nm irradiation. The comparison between the measured temperature (set in the temperature controller) and that calculated using Eq. 1 is presented in Figure 4E. As expected, the increase of the  $P_D$  value induces local heating on the particles independent of the temperature set in the controller, reaching a median value of 0.3° for 5 W cm<sup>-2</sup> (comparable to the temperature uncertainty of the

thermometer) and 43.3°C for 111 W cm<sup>-2</sup> (Figure 4F). These values are comparable to those reported by Bhiri *et al.* using GdVO<sub>4</sub>:Yb<sup>3+</sup>/Er<sup>3+</sup> microcrystals [~50°C at 100 W cm<sup>-2</sup>, (Bhiri *et al.*, 2022)].

To demonstrate the application of the BiF<sub>3</sub>:YbEr particles to molecular logic we represent the dependence of the intensity ratios defined above (R<sub>1</sub>-R<sub>4</sub>) on the temperature and the excitation power density, Figure 5A. The excitation

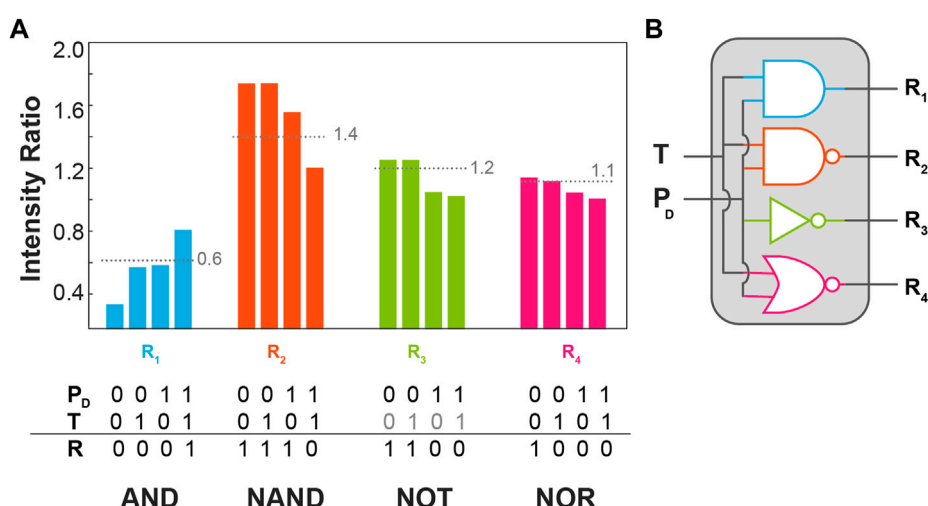


FIGURE 5

(A) Bar chart of the intensity ratios  $R_1$ – $R_4$  as a function of the temperature input ( $T$ ) and excitation power density ( $P_D$ ) presenting the corresponding threshold (pointed line) the truth tables in the bottom. (B) Schematic representation of the logic circuitry with the logic gates presented in (A).

radiation was not employed as a logic input being an *a priori* condition for the activation of the logic gate. The logic inputs are digitalized to 0 and 1 using the room temperature (305 K) set in the temperature controller as 0 and 360 K as 1. For  $P_D$  the logic input 0 was set to 5 W cm<sup>-2</sup> and the logical value 1–111 W cm<sup>-2</sup>. For each intensity ratio, a threshold value (pointed lines in Figure 5A) was arbitrarily set to get the higher number of distinct logic gates as possible. The corresponding truth tables were then constructed setting the logical values of 1 for the intensity ratios above the thresholds. The ratios  $R_1$ ,  $R_2$ , and  $R_4$  correspond to AND, NAND, and NOR logic gates whereas the ratio  $R_3$  is insensitive to the temperature, yielding simply a NOT gate on the logic input  $P_D$ . This is the first time the same upconversion emission is used to define multiple logic gates, constituting an equivalent molecular chipset as represented in Figure 5B.

## Conclusion

BiF<sub>3</sub>:Ln<sup>3+</sup> (Ln = Yb, Er, Tm, Eu, Tb) sub-micro particles were successfully prepared via microwave-assisted synthesis. Monodispersed octahedra sub-micro particles were obtained with Ln<sup>3+</sup> doping concentration <5 atomic %, while at higher concentrations of dopants the shape is no longer octahedral and spheres and aggregated are predominant. The crystalline structure of the materials is not altered by the concentration of the dopants. Through a microwave synthesis approach, we obtained samples with high reproducibility and the

possibility of a vast field of applications, even on the industrial scale.

All the prepared BiF<sub>3</sub>:Ln<sup>3+</sup> sub-micro particles display a detectable emission, both for downshifting and upconverting emission. We conclude that Ln<sup>3+</sup>-doped BiF<sub>3</sub> sub-micro particles synthesized through the microwave-assisted method are suitable for observing downshifting and upconversion emissions. The matrix has an important role due to the intrinsic low phonon energy that strongly determines the balance between the probabilities of radiative and non-radiative processes such as multiphonon relaxation and cross-relaxation mechanisms. The intrinsic low phonon energy of the BiF<sub>3</sub> host is an advantage that allows us to observe transitions that are obscured in other fluoride host matrixes such as NaYF<sub>4</sub>.

We characterized Er<sup>3+</sup>-Yb<sup>3+</sup> co-doped BiF<sub>3</sub> particles under 980 nm excitation for luminescence thermometry and molecular logic. We proved that these particles are luminescent primary thermometers with relative sensitivity up to 1.27% K<sup>-1</sup> and temperature uncertainty down to 0.4 K, values in good agreement with those in the literature for Yb<sup>3+</sup>/Er<sup>3+</sup> co-doped upconverting nanoparticles. Moreover, this sample presents emission features that are dependent on the excitation power density and the temperature, and thus, as an illustrative example, we defined a molecular chipset constituted of four independent logic gates (AND, NAND, NOR, and NOT) by analyzing the <sup>2</sup>H<sub>11/2</sub>→<sup>4</sup>I<sub>15/2</sub> and <sup>4</sup>S<sub>3/2</sub>→<sup>4</sup>I<sub>15/2</sub> Er<sup>3+</sup> transitions. The next challenge will be to employ these particles to define more complex operations involving more emitting centers and diverse external stimuli, looking forward to yielding logical reconfiguration, thus demonstrating that bismuth-based

materials are suitable for molecular computing in all-photonic logical devices.

## Data availability statement

The original contributions presented in the study are included in the article/Supplementary Materials, further inquiries can be directed to the corresponding author.

## Author contributions

SZ: Original draft and original figures preparation, synthesis of the particles, and photophysical characterization. ET, EM, AT, MB: Conceptualization, supervising the synthesis of the particles, data curation, and validation of the synthesis and structural characterization of the prepared particles. LC, RF, CB: Conceptualization of the luminescent thermometry and molecular logic experiments, methodology on photoluminescence measurements, data curation on photoluminescence for luminescent thermometry and molecular logic, software, validation, writing, reviewing, and editing on the final manuscript and figures.

## Funding

This work was developed within the scope of the project CICECO-Aveiro Institute of Materials, UIDB/50011/2020, UIDP/50011/2020 & LA/P/0006/2020, financed by national

funds through the FCT/MEC (PIDDAC). Financial support from the project LogicALL (PTDC/CTM-CTM/0298/2020) Portuguese funds through FCT/MCTES, is acknowledged. SZ acknowledges Fundação da Ciência e Tecnologia (Portugal) for a Ph.D. grant (SFRH/BD/144239/2019) financed by Portuguese national funds through the FCT/MEC and when appropriate co-financed by FEDER.

## Conflict of interest

The authors declare that the research was conducted in the absence of any commercial or financial relationships that could be construed as a potential conflict of interest.

## Publisher's note

All claims expressed in this article are solely those of the authors and do not necessarily represent those of their affiliated organizations, or those of the publisher, the editors and the reviewers. Any product that may be evaluated in this article, or claim that may be made by its manufacturer, is not guaranteed or endorsed by the publisher.

## Supplementary material

The Supplementary Material for this article can be found online at: <https://www.frontiersin.org/articles/10.3389/fphot.2022.1010958/full#supplementary-material>

## References

- Alivisatos, A. P. (1996). Semiconductor clusters, nanocrystals, and quantum dots. *Science* 271, 933–937. doi:10.1126/science.271.5251.933
- Andréasson, J., and Pischel, U. (2021). Light-stimulated molecular and supramolecular systems for information processing and beyond. *Coord. Chem. Rev.* 429, 213695. doi:10.1016/j.ccr.2020.213695
- Andréasson, J., Pischel, U., Straight, S. D., Moore, T. A., Moore, A. L., and Gust, D. (2011). All-photonic multifunctional molecular logic device. *J. Am. Chem. Soc.* 133, 11641–11648. doi:10.1021/ja203456h
- Back, M., Casagrande, E., Brondin, C. A., Ambrosi, E., Cristofori, D., Ueda, J., et al. (2020a). Lanthanide-doped Bi<sub>2</sub>SiO<sub>5</sub>@SiO<sub>2</sub> core-shell upconverting nanoparticles for stable ratiometric optical thermometry. *ACS Appl. Nano Mat.* 3, 2594–2604. doi:10.1021/acsanm.0c00003
- Back, M., Casagrande, E., Trave, E., Cristofori, D., Ambrosi, E., Dallo, F., et al. (2020b). Confined-melting-assisted synthesis of bismuth silicate glass-ceramic nanoparticles: Formation and optical thermometry investigation. *ACS Appl. Mat. Interfaces* 12, 55195–55204. doi:10.1021/acsami.0c17897
- Back, M., Ueda, J., Ambrosi, E., Cassandro, L., Cristofori, D., Ottini, R., et al. (2019). Lanthanide-doped bismuth-based fluoride nanocrystalline particles: Formation, spectroscopic investigation, and chemical stability. *Chem. Mat.* 31, 8504–8514. doi:10.1021/acs.chemmater.9b03164
- Bai, X., Caputo, G., Hao, Z. D., Freitas, V. T., Zhang, J. H., Longo, R. L., et al. (2014). Efficient and tuneable photoluminescent boehmite hybrid nanoplates lacking metal activator centres for single-phase white LEDs. *Nat. Commun.* 5, 5702. doi:10.1038/ncomms6702
- Balabhadra, S., Debasu, M. L., Brites, C. D. S., Ferreira, R. A. S., and Carlos, L. D. (2017). Upconverting nanoparticles working as primary thermometers in different media. *J. Phys. Chem. C* 121, 13962–13968. doi:10.1021/acs.jpcc.7b04827
- Bervas, M., Yakshinskiy, B., Klein, L. C., and Amatucci, G. G. (2006). Soft-chemistry synthesis and characterization of bismuth oxyfluorides and ammonium bismuth fluorides. *J. Am. Ceram. Soc.* 89, 645–651. doi:10.1111/j.1551-2916.2005.00721.x
- Bhiri, N. M., Dammak, M., Carvajal, J. J., Aguiló, M., Díaz, F., and Pujol, M. C. (2022). Excitation power density dependence of a primary luminescent thermometer based on Er<sup>3+</sup>, Yb<sup>3+</sup>: GdVO<sub>4</sub> microcrystals operating in the visible. *J. Alloys Compd.* 921, 166020. doi:10.1016/j.jallcom.2022.166020
- Binnemans, K. (2015). Interpretation of europium(III) spectra. *Coord. Chem. Rev.* 295, 1–45. doi:10.1016/j.ccr.2015.02.015
- Brites, C. D. S., Balabhadra, S., and Carlos, L. D. (2019). Lanthanide-based thermometers: At the cutting-edge of luminescence thermometry. *Adv. Opt. Mater.* 7, 1801239. doi:10.1002/adom.201801239
- Brites, C. D. S., Millán, A., and Carlos, L. D. (2017). “Lanthanides in luminescent thermometry,” in *Handbook on the Physics and chemistry of Rare Earths*. Editors J.-C. G. Bünzli and V. K. Pecharsky (Amsterdam: Elsevier Science).
- Bünzli, J.-C. G. (2015). On the design of highly luminescent lanthanide complexes. *Coord. Chem. Rev.* 293, 19–47. doi:10.1016/j.ccr.2014.10.013
- Casagrande, E., Back, M., Cristofori, D., Ueda, J., Tanabe, S., Palazzolo, S., et al. (2020). Upconversion-mediated Boltzmann thermometry in double-layered Bi

- 2 SiO<sub>5</sub>:Yb<sup>3+</sup>, Tm<sup>3+</sup>@ SiO<sub>2</sub> hollow nanoparticles. *J. Mat. Chem. C* 8, 7828–7836. doi:10.1039/d0tc01457e
- Chen, G., Yang, C., and Prasad, P. N. (2013). Nanophotonics and nanochemistry: Controlling the excitation dynamics for frequency up-and down-conversion in lanthanide-doped nanoparticles. *Acc. Chem. Res.* 46, 1474–1486. doi:10.1021/ar300270y
- Dąbrowska, S., Chudoba, T., Wojnarowicz, J., and Łojkowski, W. (2018). Current trends in the development of microwave reactors for the synthesis of nanomaterials in laboratories and industries: A review. *Crystals* 8, 379. doi:10.3390/cryst8100379
- De Silva, A. P., Gunaratne, N. H. Q., and McCoy, C. P. (1993). A molecular photoionic AND gate based on fluorescent signalling. *Nature* 364, 42–44. doi:10.1038/364042a0
- Deng, R., Qin, F., Chen, R., Huang, W., Hong, M., and Liu, X. (2015). Temporal full-colour tuning through non-steady-state upconversion. *Nat. Nanotechnol.* 10, 237–242. doi:10.1038/nnano.2014.317
- Dong, H., Sun, L.-D., and Yan, C.-H. (2015). Energy transfer in lanthanide upconversion studies for extended optical applications. *Chem. Soc. Rev.* 44, 1608–1634. doi:10.1039/c4cs00188e
- Erbaş-Cakmak, S., Kolemen, S., Sedgwick, A. C., Gunnlaugsson, T., James, T. D., Yoon, J., et al. (2018). Molecular logic gates: The past, present and future. *Chem. Soc. Rev.* 47, 2228–2248. doi:10.1039/c7cs00491e
- Escudero, A., Moretti, E., and Ocaña, M. (2014). Synthesis and luminescence of uniform europium-doped bismuth fluoride and bismuth oxyfluoride particles with different morphologies. *CrystEngComm* 16, 3274. doi:10.1039/c3ce42462f
- Gedye, R., Smith, F., Westaway, K., Ali, H., Baldiser, L., Laberge, L., et al. (1986). The use of microwave ovens for rapid organic synthesis. *Tetrahedron Lett.* 27, 279–282. doi:10.1016/s0040-4039(00)83996-9
- Hernández-Rodríguez, M. A., Kamada, K., Yoshikawa, A., Muñoz-Santiuste, J. E., Casanovas-Melián, A., Martín, I. R., et al. (2021). 1000 K optical radiometric thermometer based on Er<sup>3+</sup> luminescence in yttrium gallium garnet. *J. Alloys Compd.* 886, 161188. doi:10.1016/j.jallcom.2021.161188
- Jaque, D., and Vetrone, V. (2012). Luminescence nanothermometry. *Nanoscale* 4, 4301. doi:10.1039/c2nr30764b
- Kato, D., Hongo, K., Maezono, R., Higashi, M., Kunioku, H., Yabuuchi, M., et al. (2017). Valence band engineering of layered bismuth oxyhalides toward stable visible-light water splitting: Madelung site potential analysis. *J. Am. Chem. Soc.* 139, 18725–18731. doi:10.1021/jacs.7b11497
- Kumar, D., Sharma, S. K., Verma, S., Sharma, V., and Kumar, V. (2020). A short review on Rare earth doped NaYF<sub>4</sub> upconverted nanomaterials for solar cell applications. *Mater. Today Proc.* 21, 1868–1874. doi:10.1016/j.matpr.2020.01.243
- Kuriki, K., Koike, Y., and Okamoto, Y. (2002). Plastic optical fiber lasers and amplifiers containing lanthanide complexes. *Chem. Rev.* 102, 2347–2356. doi:10.1021/cr010309g
- Li, X., Yang, L., Zhu, Y., Zhong, J., and Chen, D. (2019). Upconversion of transparent glass ceramics containing β-NaYF<sub>4</sub>:Yb<sup>3+</sup>, Er<sup>3+</sup> nanocrystals for optical thermometry. *RSC Adv.* 9, 7948–7954. doi:10.1039/c9ra01088b
- Nicoli, F., Paltrinieri, E., Tranfić Bakić, M., Baroncini, M., Silvi, S., and Credi, A. (2021). Binary logic operations with artificial molecular machines. *Coord. Chem. Rev.* 428, 213589. doi:10.1016/j.ccr.2020.213589
- Nüchter, M., Ondruschka, B., Bonrath, W., and Gum, A. (2004). Microwave assisted synthesis – A critical technology overview. *Green Chem.* 6, 128–141. doi:10.1039/b310502d
- Piana, S., Reyhani, M., and Gale, J. D. (2005). Simulating micrometre-scale crystal growth from solution. *Nature* 438, 70–73. doi:10.1038/nature04173
- Sanna, S., Esposito, V., Andreasen, J. W., Hjelm, J., Zhang, W., Kasama, T., et al. (2015). Enhancement of the chemical stability in confined δ-Bi<sub>2</sub>O<sub>3</sub>. *Nat. Mat.* 14, 500–504. doi:10.1038/nmat4266
- Tanner, P. A. (2013). Some misconceptions concerning the electronic spectra of tri-positive europium and cerium. *Chem. Soc. Rev.* 42, 5090–5101. doi:10.1039/c3cs60033e
- Wang, C., Du, P., Li, W., and Luo, L. (2020a). Facile synthesis and photoluminescence performance of Er<sup>3+</sup>-activated BiOF sub-micro particles for radiometric thermometers. *J. Lumin.* 226, 117416. doi:10.1016/j.jlumin.2020.117416
- Wang, C., Ran, W., Du, P., Li, W., Luo, L., and Wang, D. (2020b). Enhanced visible light-driven photocatalytic activities and photoluminescence characteristics of BiOF nanoparticles determined via doping engineering. *Inorg. Chem.* 59, 11801–11813. doi:10.1021/acs.inorgchem.0c01811
- Wang, X., Wang, Y., Jin, L., Bu, Y., Yang, X. L., and Yan, X. (2019). Controlling optical temperature detection of Ca<sub>3</sub>Al<sub>2</sub>O<sub>6</sub>: Yb<sup>3+</sup>, Er<sup>3+</sup> phosphors through doping. *J. Alloys Compd.* 773, 393–400. doi:10.1016/j.jallcom.2018.09.229
- Wei, J., Liu, Y., Zhang, M., Zheng, W., Huang, P., Gong, Z., et al. (2022). Blue-LED-excitable NIR-II luminescent lanthanide-doped SrS nanoprobes for radiometric thermal sensing. *Sci. China Mat.* 65, 1094–1102. doi:10.1007/s40843-021-1801-8
- Xia, Y. N., Yang, P. D., Sun, Y. G., Wu, Y. Y., Mayers, B., Gates, B., et al. (2003). One-dimensional nanostructures: Synthesis, characterization, and applications. *Adv. Mat.* 15, 353–389. doi:10.1002/adma.200390087
- Xie, H.-H., Wen, Q., Huang, H., Sun, T.-Y., Li, P., Li, Y., et al. (2015). Synthesis of bright upconversion submicrocrystals for high-contrast imaging of latent fingerprints with cyanoacrylate fuming. *RSC Adv.* 5, 79525–79531. doi:10.1039/c5ra15255k
- Yi, G., Lu, H., Zhao, S., Ge, Y., Yang, W., Chen, D., et al. (2004). Synthesis, characterization, and biological application of size-controlled nanocrystalline NaYF<sub>4</sub>:Yb, Er infrared-to-visible up-conversion phosphors. *Nano Lett.* 4, 2191–2196. doi:10.1021/nl048680h
- Zaccariello, G., Back, M., Benedetti, A., Canton, P., Cattaruzza, E., Onoda, H., et al. (2019). Bismuth titanate-based UV filters embedded mesoporous silica nanoparticles: Role of bismuth concentration in the self-sealing process. *J. Colloid Interface Sci.* 549, 1–8. doi:10.1016/j.jcis.2019.04.042
- Zaccariello, G., Back, M., Zanello, M., Canton, P., Cattaruzza, E., Riello, P., et al. (2017). Formation and controlled growth of bismuth titanate phases into mesoporous silica nanoparticles: An efficient self-sealing nanosystem for UV filtering in cosmetic formulation. *ACS Appl. Mat. Interfaces* 9, 13252. doi:10.1021/acsami.6b13252
- Zanella, S., Hernández-Rodríguez, M. A., Carlos, L. D., Ferreira, R. A. S., and Brites, C. D. S. (2022). Reprogrammable and reconfigurable photonic molecular logic gates based on Ln<sup>3+</sup> ions. *Adv. Opt. Mat.* 10, 2200138. doi:10.1002/adom.202200138





## OPEN ACCESS

## EDITED BY

Zhen Ma,  
Fudan University, China

## REVIEWED BY

Sandip Kumar Singh,  
University of Kansas, United States  
Saikat Dutta,  
National Institute of Technology, India

## \*CORRESPONDENCE

Margarida M. Antunes,  
margarida.antunes@ua.pt  
Anabela A. Valente,  
ataav@ua.pt

## SPECIALTY SECTION

This article was submitted to Catalytic Reactions and Chemistry, a section of the journal Frontiers in Chemistry

RECEIVED 29 July 2022

ACCEPTED 06 September 2022

PUBLISHED 29 September 2022

## CITATION

Antunes MM, Silva AF, Fernandes A, Ribeiro F, Neves P, Pillinger M and Valente AA (2022), Micro/mesoporous LTL derived materials for catalytic transfer hydrogenation and acid reactions of bio-based levulinic acid and furanics.  
*Front. Chem.* 10:1006981.  
doi: 10.3389/fchem.2022.1006981

## COPYRIGHT

© 2022 Antunes, Silva, Fernandes, Ribeiro, Neves, Pillinger and Valente. This is an open-access article distributed under the terms of the [Creative Commons Attribution License \(CC BY\)](#). The use, distribution or reproduction in other forums is permitted, provided the original author(s) and the copyright owner(s) are credited and that the original publication in this journal is cited, in accordance with accepted academic practice. No use, distribution or reproduction is permitted which does not comply with these terms.

# Micro/mesoporous LTL derived materials for catalytic transfer hydrogenation and acid reactions of bio-based levulinic acid and furanics

Margarida M. Antunes<sup>1\*</sup>, Andreia F. Silva<sup>1</sup>, Auguste Fernandes<sup>2</sup>, Filipa Ribeiro<sup>2</sup>, Patrícia Neves<sup>1</sup>, Martyn Pillinger<sup>1</sup> and Anabela A. Valente<sup>1\*</sup>

<sup>1</sup>Department of Chemistry, CICECO—Aveiro Institute of Materials, University of Aveiro, Aveiro, Portugal, <sup>2</sup>Centro de Química Estrutural, Instituto Superior Técnico, Universidade de Lisboa, Lisboa, Portugal

The biomass-derived platform chemicals furfural and 5-(hydroxymethyl)furfural (HMF) may be converted to  $\alpha$ -angelica lactone (AnL) and levulinic acid (LA). Presently, LA (synthesized from carbohydrates) has several multinational market players. Attractive biobased oxygenated fuel additives, solvents, etc., may be produced from AnL and LA via acid and reduction chemistry, namely alkyl levulinates and  $\gamma$ -valerolactone (GVL). In this work, hierarchical hafnium-containing multifunctional Linde type L (LTL) related zeotypes were prepared via top-down strategies, for the chemical valorization of LA, AnL and HMF via integrated catalytic transfer hydrogenation (CTH) and acid reactions in alcohol medium. This is the first report of CTH applications (in general) of LTL related materials. The influence of the post-synthesis treatments/conditions (desilication, dealumination, solid-state impregnation of Hf or Zr) on the material properties and catalytic performances was studied. AnL and LA were converted to 2-butyl levulinate (2BL) and GVL in high total yields of up to ca. 100%, at 200°C, and GVL/2BL molar ratios up to 10. HMF conversion gave mainly the furanic ethers 5-(sec-butoxymethyl)furfural and 2,5-bis(sec-butoxymethyl)furan (up to 63% total yield, in 2-butanol at 200°C/24 h). Mechanistic, reaction kinetics and material characterization studies indicated that the catalytic results depend on a complex interplay of different factors (material properties, type of substrate). The recovered-reused solids performed steadily.

## KEYWORDS

heterogeneous catalysis, vegetable biomass, zeolite LTL, hafnium, levulinic acid,  $\gamma$ -valerolactone, furanics

## 1 Introduction

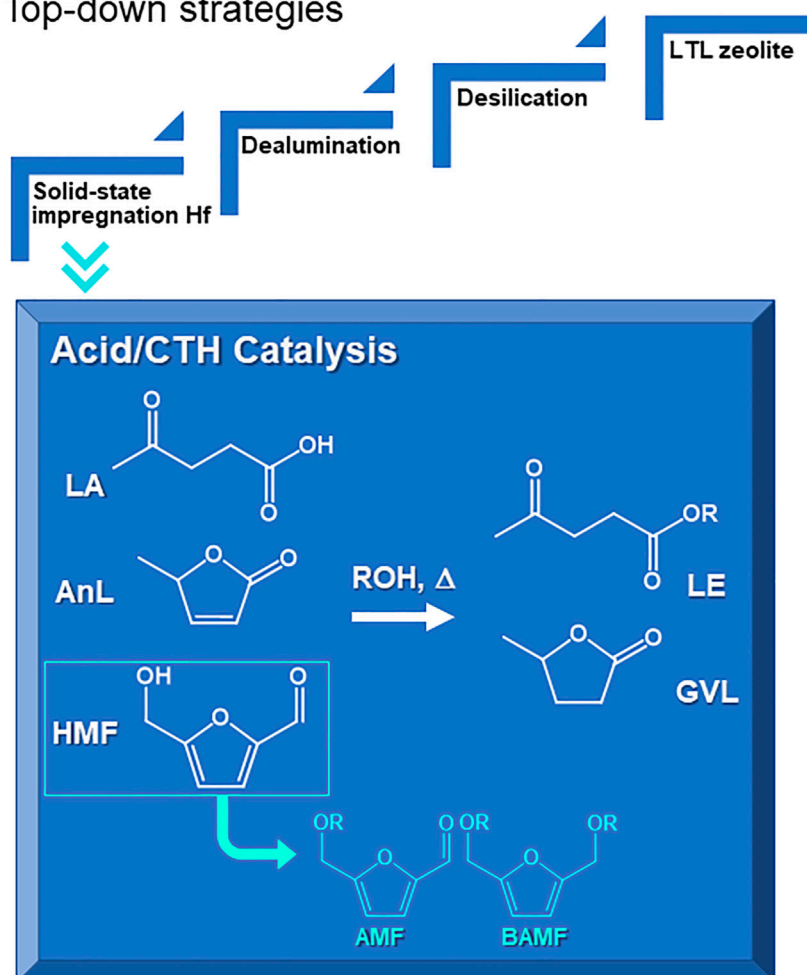
Global warming and energy security issues related to the intense use of fossil fuels may be alleviated by the alternative use of widespread renewable sources and waste/surpluses to produce bioenergy and bioproducts, thereby avoiding greenhouse gas emissions, environmental pollution, and waste management issues (Roy et al., 2021; Koul et al., 2022). Vegetable biomass existing in terrestrial and aquatic areas constitutes an abundant source of carbohydrates that are partly disposed of as agricultural surpluses/residues, municipal solid waste, industrial (e.g., biorefineries) waste, sewage sludge, etc. (Cheng and Brewer, 2021; Koul et al., 2022; Narisetty et al., 2022). Carbohydrates may be chemically valorized into useful bioproducts for several industrial sectors. The most important selective catalytic routes

of carbohydrates to bioproducts include the acid-catalyzed hydrolysis and dehydration reactions under relatively mild conditions, which lead to the bio-based furanic aldehyde platform chemicals 5-(hydroxymethyl)furfural (HMF) and furfural (FUR) (Liguori et al., 2015; Dutta, 2021; Fact, 2022).

HMF may be selectively converted to oxygenated fuel additives in alcohol media, namely 5-(alkoxymethyl)furfural (AMF) and 2,5-bis(alkoxymethyl)furan (BAMF) via etherification or reduction/etherification, respectively (Scheme 1) (Poullikkas, 2017; Kong et al., 2020; Hou et al., 2021). AMFs possess relatively high energy density, low toxicity and high stability (Li et al., 2016b; Kong et al., 2018; Hou et al., 2021; Liu et al., 2022). On the other hand, BAMFs may possess higher energy density, cetane number, miscibility and stability than AMFs, making them even more attractive fuel additives (Hu

### Multifunctional hierarchical catalysts

#### Top-down strategies



**SCHEME 1**

Hierarchical multifunctional LTL related materials prepared via top-down strategies for integrated catalytic transfer hydrogenation (CTH) and acid reactions of levulinic acid (LA),  $\alpha$ -angelica lactone (AnL) and 5-(hydroxymethyl)furfural (HMF) to useful bioproducts such as alkyl levulinates (LE) and  $\gamma$ -valerolactone (GVL), or (from HMF) 5-(alkoxymethyl)furfural (AMF) and 2,5-bis(alkoxymethyl)furan (BAMF).

et al., 2018, 2020); e.g., BAMFs synthesized using *n*-butanol (which may be renewable and synthesized via fermentation of hexoses (Cho et al., 2014)) or secondary and tertiary alcohols (Gruter, 2009).

On the other hand, HMF and FUR may be converted to  $\alpha$ -angelica lactone (AnL) and levulinic acid (LA), and AnL may be an intermediate to LA (Al-Shaal et al., 2015; Antonetti et al., 2016; Lima et al., 2018; Dutta and Bhat, 2021). LA was identified as one of the most valuable bioproducts derived from carbohydrates (Werpy and Petersen, 2004), and its market players include Biofine and DuPont (Fitzpatrick, 1995; Grand View Research, 2021). The growing LA market covers several sectors, from pharmaceuticals, agrochemicals, polymers, plasticizers, fuel and fuel additives to flavours, fragrances, cosmetics, and food additives (Morone et al., 2015; Dutta and Bhat, 2021; Di Bucchianico et al., 2022; Mordor Intelligence, 2022).

Both AnL and LA may be converted to alkyl levulinates (LE) and  $\gamma$ -valerolactone (GVL) (Manzer, 2005; Liguori et al., 2015; Zhang, 2016; Lima et al., 2018; Yu et al., 2019; Dutta and Bhat, 2021; Antunes et al., 2022a). LE and GVL are attractive oxygenated fuel additives (Morone et al., 2015); e.g., butyl levulinate blends can improve fuel properties such as conductivity, combustion emission, freezing point (Di Bucchianico et al., 2022). Furthermore, GVL has a growing market as a food flavouring agent and solvent, foreseen up to 2028 (Data Intelto, 2022), and is an interesting intermediate to diverse chemicals and fuels (Yu et al., 2019; Dutta and Bhat, 2021; Sajid et al., 2021).

The conversion of AnL and LA to GVL involves acid and reduction chemistry (Scheme 1). Hence, reducing agents are required, which may be  $H_2$  (for hydrogenation) or organic H-donors such as secondary alcohols or acids (for catalytic transfer hydrogenation (CTH)) (Dutta et al., 2019; Yu et al., 2019; Yu et al., 2020b, 2020a; Weng et al., 2020; Maumela et al., 2021). High GVL yields were reported for the reaction of LA with  $H_2$  (mainly produced from fossil fuels) using (expensive) noble metal catalysts (Huang et al., 2020; Bassi et al., 2021; Lu et al., 2022; Vu et al., 2022). However, the process economics and safety may be favoured by using (cheaper) non-noble metal catalysts (Xue et al., 2018; Dutta et al., 2019; Wang et al., 2020) and, on the other hand, organic H-donors instead of operating under high pressure  $H_2$  conditions, which requires robust, expensive infrastructures (Gilkey and Xu, 2016; Dutta et al., 2019; Nie et al., 2021).

A literature survey indicated that hafnium-containing catalysts may be effective for LA conversion to GVL via CTH chemistry, i.e., not requiring external  $H_2$  supply and noble metals, specifically: hafnium supported on organic supports such as sulfonated sugar cane bagasse (Huang et al., 2021), carbonized/sulfonated glucose (Jori and Jadhav, 2020), or graphite oxide (Li et al., 2020); hafnium-containing organic-inorganic coordination hybrids (including MOFs) (Xie et al.,

2016; Rojas-Buzo et al., 2018; Antunes et al., 2022b); and zeolites (BEA (Antunes et al., 2022a), FAU (Tang et al., 2019)). According to the literature, Hf-containing catalysts (zeolites, hybrids) may perform superiorly to the Zr-analogues in the conversion of LA and LE to GVL (Luo et al., 2014; Tang et al., 2019; Li et al., 2020; Antunes et al., 2022a; 2022b). Of these, the non-carbon-based catalysts may possess longer lifetimes and better resistance against regeneration treatments such as calcination of coke/humins, enhancing productivity. In this sense, zeolites may be promising.

Zeolites are (fully inorganic) crystalline microporous aluminosilicates used in the industry, and are particularly attractive for catalytic and adsorption processes (Čejka et al., 2020). They possess considerable specific surface area, tuneable acidity and selectivity properties (Li et al., 2016b; Mon and Leyva-Pérez, 2021). Different zeolite topologies are commercially available (Kuznetsova et al., 2018), which may be modified via top-down or bottom-up strategies, broadening and/or improving their catalytic applications. For example, hierarchical (micro/mesoporous) zeotype catalysts may be effective for multiple reactions (Serrano et al., 2018). The few literature studies on the conversion of LA to GVL over micro/mesoporous zeotypes led to 22–99% GVL yield (Antunes et al., 2022a): Sn-containing Beta (Antunes et al., 2015; Winoto et al., 2016); Zr-containing Beta (Antunes et al., 2016a, 2016b; Morales et al., 2019; López-Aguado et al., 2020); Hf-USY (Tang et al., 2019) and Hf-AlBeta (Antunes et al., 2022a) which surpassed the performances of Sn- and Zr-counterparts. These promising results motivated us to explore different commercially available zeolite topologies and post-synthesis treatments for GVL production.

Linde type L zeolites consist of a microporous aluminosilicate framework  $(K_6Na_3(H_2O)_{21}[Al_9Si_{27}O_{72}]$  for Si/Al = 3, but higher ratios are possible) with LTL topology, which allows diffusion along 1D 12-membered ring (MR) channels that have *ca.* 0.71 nm  $\times$  0.71 nm apertures and cages with *ca.* 1.2 nm diameter (Broach, 2010). The 1D 12 MR channel system is connected by a 3D 8 MR channel system (0.34 nm  $\times$  0.56 nm). LTL zeolites possess easily exchangeable cations located inside the 12 MR channels near the 8 MR windows. Although a literature survey indicates that LTL zeolitic catalysts are effective for hydrogenation reactions using externally supplied  $H_2$  (details discussed in the [Supplementary Material](#)), to the best of our knowledge, LTL catalysts were never reported in the literature for CTH reactions, in general.

Few hierarchical LTL type materials were prepared via different top-down strategies (e.g., with or without surfactants) and conditions (leading to enhanced mesopore volume ( $V_{meso}$ )), partly depending on the catalytic applications: alkane aromatization ( $V_{meso}$  increased from 0.079 to 0.44 cm<sup>3</sup> g<sup>-1</sup>) (Lee and Choi, 2016); Knoevenagel condensation ( $V_{meso}$  increased from 0.01 to 0.29 cm<sup>3</sup> g<sup>-1</sup>) (Nilesh et al., 2016); dealkylation of aromatics ( $V_{meso}$  increased from 0.08 to

0.28 cm<sup>3</sup> g<sup>-1</sup>) (Al-Ani et al., 2019); and hydrogenation of D-xylose to xylitol ( $V_{\text{meso}}$  increased from 0.010 to 0.14 cm<sup>3</sup> g<sup>-1</sup>) (Tangale et al., 2019). Al-Ani et al. (Al-Ani et al., 2019) proposed that the formation of mesopores in LTL via mixed alkaline plus surfactant treatment was gradual in relation to that for more open pore structures such as the FAU and BEA topologies, allowing some control over the features of the LTL pore system.

In this work, hierarchical multifunctional LTL zeotypes were prepared for integrated CTH and acid reactions of LA, AnL and HMF to useful bioproducts (Scheme 1). The catalysts were prepared from commercial KL zeolite via top-down strategies involving desilication, dealumination and solid-state impregnation (SSI) of hafnium (and zirconium for comparison). This is the first CTH application reported for the LTL family of zeolites. The influence of the post-synthesis treatments (e.g., with or without desilication) and conditions (e.g., acid concentration, hafnium loading) on the material properties and catalytic performances was studied. Mechanistic, reaction kinetics and material characterization studies indicated that the catalytic results depend on a complex interplay of different factors, and the relationships of material properties-catalytic performance may be different for different substrates.

## 2 Materials and methods

All reagents and solvents were obtained from commercial sources and used as received (purities and suppliers are indicated in [Supplementary Material](#)). The materials were characterized (details given in the [Supplementary Material](#)) by powder X-ray diffraction (PXRD; crystalline structure, relative crystallinity (RC)), scanning electron microscopy (SEM; morphology), elemental mappings (distributions of Hf, Zr, Si, Al) and energy dispersive X-ray spectroscopy (EDS; Si/Al, Si/Hf ratios), nitrogen sorption isotherms (textural properties and pore size distributions), <sup>27</sup>Al MAS NMR spectroscopy (types of Al sites), attenuated total reflectance Fourier Transform Infrared (ATR FT-IR) spectroscopy (surface chemistry), elemental analysis for carbon (adsorbed carbonaceous matter on the used catalysts), and FTIR of adsorbed pyridine (base probe) at 150 and 350°C (acid properties).

### 2.1 Preparation of the catalysts

Hafnium-containing hierarchical LTL zeotypes and a Zr-counterpart were prepared via post-synthesis partial dealumination using oxalic acid (oxac), desilication (D) using KOH treatments, followed by dealumination using H<sub>2</sub>SO<sub>4</sub>, solid-state impregnation (SSI) of hafnium acetylacetonate used as Hf precursor and finally calcination.

#### 2.1.1 Aluminosilicates

Commercial KL zeolite was mildly dealuminated using 0.08 M aq. oxalic acid (30 ml solution per gram of zeolite) at 80°C for 3 h, with stirring. The solid was separated by filtration, thoroughly washed with hot Milli-Q water until neutral pH, dried overnight at 100°C, and finally calcined at 550°C (1°C min<sup>-1</sup>) in static air for 5 h, giving KL(oxac). Literature studies reported alkaline treatments of LTL type materials, using NaOH or KOH in the concentrations range 0.04–2.8 M (Lee and Choi, 2016; Nilesh et al., 2016; Al-Ani et al., 2019; Tangale et al., 2019). KL(oxac) was subsequently desilicated (D) using 0.2 M aq. KOH (30 ml per gram of zeolite) at 65°C for 30 min, with stirring. The mixture was cooled in an ice bath during 10 min and the solid was separated by filtration, thoroughly washed with hot Milli-Q water until neutral pH, and dried overnight at 100°C, giving D-KL.

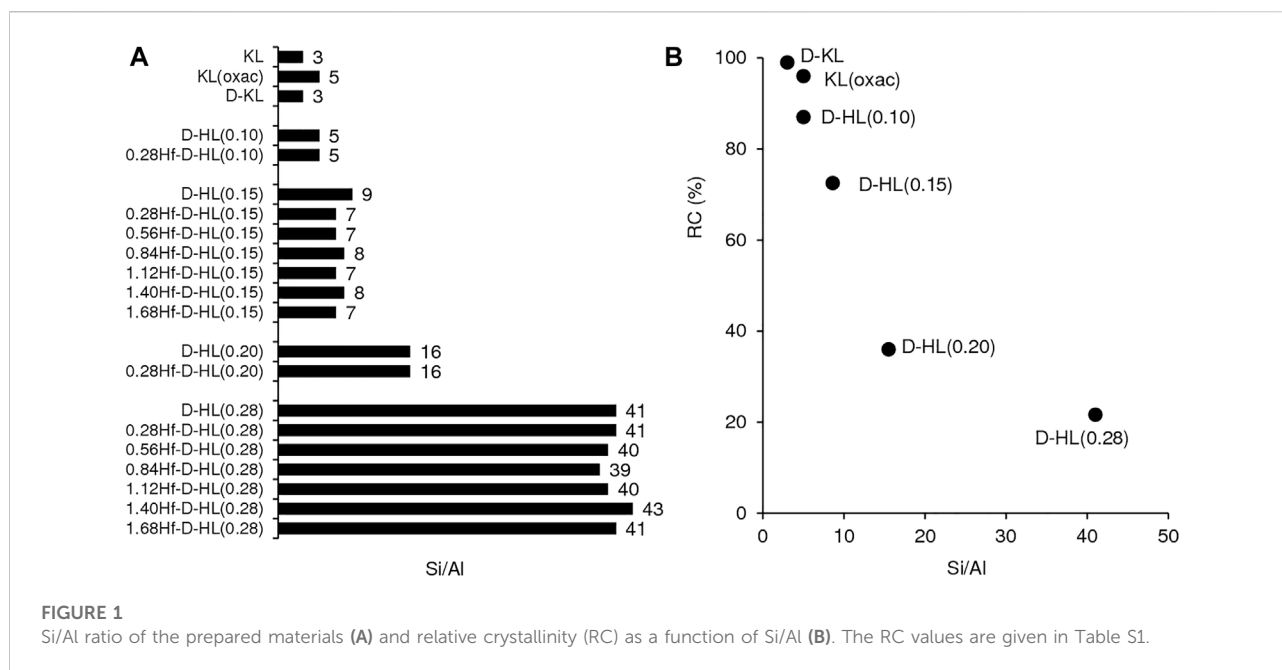
D-KL was simultaneously ion-exchanged and dealuminated using H<sub>2</sub>SO<sub>4</sub>. According to the literature, KL may tolerate 0.4 M H<sub>2</sub>SO<sub>4</sub> treatment for 1 h (Al-Ani et al., 2019); these conditions were applied to D-KL, but led to complete amorphization ([Supplementary Material](#) for details, [Supplementary Figure S1](#)). Hence, the concentration and time of the H<sub>2</sub>SO<sub>4</sub> treatment were reduced. Specifically, D-KL was treated with 0.10, 0.15, 0.20 or 0.28 M aq. H<sub>2</sub>SO<sub>4</sub> (30 ml per gram of zeolite) for 30 min at room temperature, with stirring. The solid was separated by filtration, thoroughly washed with hot Milli-Q water until neutral pH, and dried overnight at 100°C, giving D-HL(x), where x stands for the concentration of H<sub>2</sub>SO<sub>4</sub> (0.10 ≤ x < 0.28 M).

For comparison, a material denoted HL was prepared by subjecting commercial KL to dealumination with 0.15 M aq. H<sub>2</sub>SO<sub>4</sub> and then SSI of 0.28 mmol<sub>Hf</sub> g<sup>-1</sup> (the two treatments were carried out in a comparable fashion to that described above for the D-HL(x) materials). In a separate experiment, commercial KL was subjected to ion-exchange using 0.15 M aq. NH<sub>4</sub>NO<sub>3</sub>; the resultant material exhibited additional PXRD peaks, suggesting the presence of crystalline contaminations (which was reproducible; please see the [Supplementary Material](#) for details, [Supplementary Figure S2](#)), and, thus, this material was discarded.

#### 2.1.2 Hf-containing zeotypes and Zr-counterpart

The D-HL(x) precursors were subjected to SSI with Hf(acac)<sub>4</sub> and subsequent calcination, giving yHf-D-HL(x) where y is the hafnium concentration (in the range 0.28–1.68 mmol<sub>Hf</sub> g<sup>-1</sup>). The SSI process involved gentle grinding of 1 g of the aluminosilicate support with the desired amount of Hf(acac)<sub>4</sub> precursor for 30 min, using an agate pestle and mortar. The resultant material was calcined at 550°C (1°C min<sup>-1</sup>) under air flow (20 ml min<sup>-1</sup>) for 6 h. Zeolite 0.28Hf-HL was prepared in a similar fashion, albeit using the support HL and y = 0.28 mmol<sub>Hf</sub> g<sup>-1</sup>. The Zr-counterpart,





namely 0.28Zr-D-HL(0.15), was prepared by the same protocol, albeit using  $\text{Zr}(\text{acac})_4$  as precursor (0.158 g  $\text{Zr}(\text{acac})_4$  per g of D-HL(0.15)).

## 2.2 Catalytic tests

The catalytic reactions were carried out using homemade tubular glass batch reactors (*ca.* 8 cm length, *ca.* 11 mm internal diameter) with a conic-shaped bottom, equipped with a PTFE-coated magnetic stirring bar (Supelco) and a PTFE valve (Normax) for purging. Each reactor was loaded with LA (in a concentration ranging from 0.14 to 0.45 M), catalyst (25.5 g<sub>cat</sub> L<sup>-1</sup>) and 2BuOH. The reactions of AnL and HMF were carried out using an initial substrate concentration of 0.45 M in 2BuOH. Bulk  $\text{HfO}_2$  was used in an equivalent molar amount of hafnium to that added together with the catalysts 1.40Hf-D-HL(x) to the reactor. Prior to control tests using D-HL(x), these materials were calcined under similar conditions to those described above for the Hf-containing zeotypes.

The loaded reactors were immersed in a thermostatically controlled oil bath heated at 200°C and stirred to 850 rpm to favour uniform temperature distribution and avoid external diffusional limitations. Reaction time was counted from the instant that the reactors were immersed in the oil bath. After a given reaction time, the reactors were cooled to room temperature prior to sampling. Freshly prepared samples were analyzed by HPLC for quantification of HMF or by gas

chromatography (GC) for quantification of the reaction products and remaining substrates.

The HPLC analyses were carried out using a Knauer Smartline HPLC Pump 100 and a Shodex SH1011H + 300 mm × 8 mm (i.d.) ion exchange column (Showa Denko America, Inc. New York), coupled to a Knauer Smartline 2520 UV detector (254 nm). The column temperature was set at 50°C, and the mobile phase was 0.005 M aq.  $\text{H}_2\text{SO}_4$  at a flow rate of 0.8 ml min<sup>-1</sup>. The GC analyses were carried out using an Agilent 7820A GC equipped with a capillary column (HP-5, 30 m × 0.320 mm × 0.25 mm; 35–300°C), spit injector (240°C) and a flame ionization detector (320°C), using  $\text{H}_2$  as carrier gas. The quantification of the substrates and reaction products was based on calibration curves using internal standards. Individual experiments were performed for a given reaction time, and the presented results are the mean values of at least two replicates with an error <6%.

The reaction products were identified using a Shimadzu QP2010 ultra-GC-MS (Izasa Scientific, Lisbon, Portugal) equipped with a split injector (240°C), ion source (200°C), interface (300°C), a Zebron ZB-5ms capillary GC column (ZB-5, 30 m × 0.25 mm × 0.25 mm; 35–300°C) and He as carrier gas (supporting databases: Wiley229 and NIST14). The identified products were 2-butyl levulinate (2BL) and GVL from LA; LA, 2BL and GVL from AnL; 5-methylfurfural (5MF), 5-(*sec*-butoxymethyl)furfural (BMF) and 2,5-bis(*sec*-butoxymethyl) furan (BBMF) from HMF.

The conversion (%) of the substrate (Sub) at a reaction time *t* was calculated using the formula,  $100 \times [(\text{initial molar}$

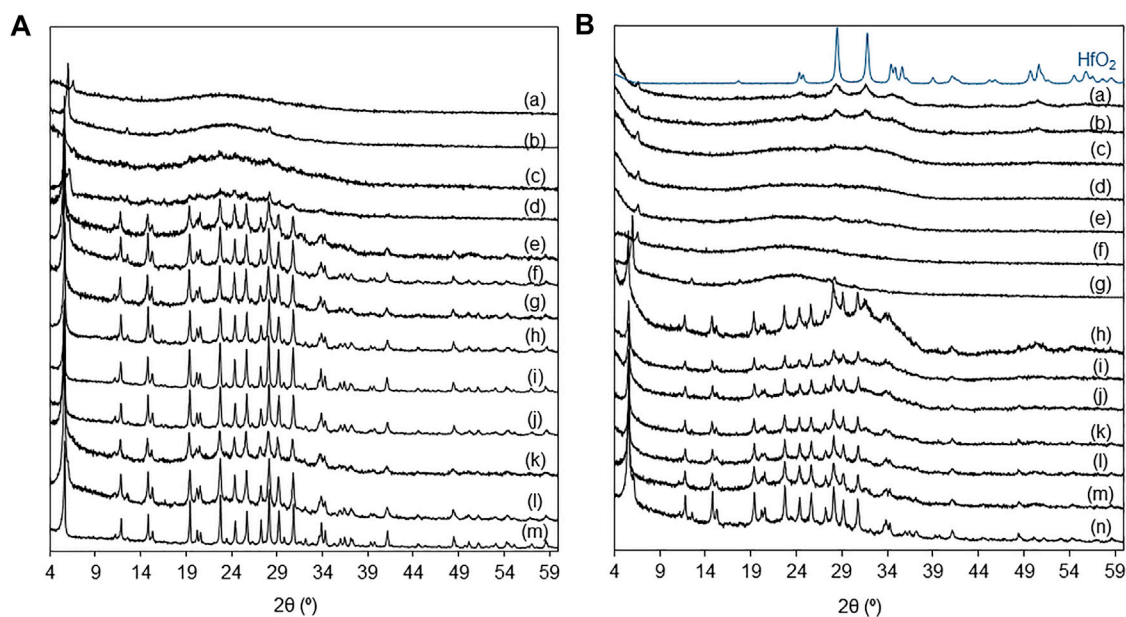


FIGURE 2

(A) PXRD patterns of (a) D-HL(x) with  $x = 0.28$  (b),  $0.20$  (d),  $0.15$  (f),  $0.10$  (h);  $0.28\text{Hf-D-HL}(x)$  with  $x = 0.28$  (a),  $0.20$  (c),  $0.15$  (e),  $0.10$  (g); D-KL (i); KL (oxac) (j);  $0.28\text{Hf-HL}$  (k); HL (l); KL (m). (B) PXRD patterns of  $y\text{Hf-D-HL}(0.28)$  with  $y = 1.68$  (a),  $1.40$  (b),  $1.12$  (c),  $0.84$  (d),  $0.56$  (e),  $0.28$  (f); D-HL( $0.28$ ) (g);  $y\text{Hf-D-HL}(0.15)$  with  $y = 1.68$  (h),  $1.40$  (i),  $1.12$  (j),  $0.84$  (k),  $0.56$  (l),  $0.28$  (m); D-HL( $0.15$ ) (n); bulk  $\text{HfO}_2$ .

concentration of Sub)—(molar concentration of Sub at reaction time  $t$ )/(initial molar concentration of Sub)], and product (Prod) yield was calculated using formula  $100 \times [(\text{molar concentration of Prod at time } t)/(\text{initial molar concentration of Sub})]$ . Catalytic activities ( $\text{mmol g}_{\text{cat}}^{-1} \text{h}^{-1}$ ) were calculated based on the substrate conversion at 5 h reaction.

The used catalysts were separated by centrifugation (10,000 rpm for *ca.* 5 min), thoroughly washed with the reaction solvent (2BuOH) and dried at  $85^\circ\text{C}$  overnight. The used catalysts were thermally regenerated at  $550^\circ\text{C}$  (heating rate of  $1^\circ\text{C min}^{-1}$ ) for 5 h, under an air flow ( $20 \text{ ml min}^{-1}$ ). Selected catalysts ( $1.40\text{Hf-D-HL}(0.15)$ ,  $1.12\text{Hf-D-HL}(0.28)$ ) were used for five consecutive 5 h-batch runs ( $0.45 \text{ M LA}$ ,  $2\text{BuOH}$ ,  $25.5 \text{ g}_{\text{cat}} \text{ L}^{-1}$ ,  $200^\circ\text{C}$ ).

Contact tests (CT) consisted of contacting the fresh catalysts  $1.40\text{Hf-D-HL}(0.15)$  and  $1.12\text{Hf-D-HL}(0.28)$  with  $2\text{BuOH}$  at  $200^\circ\text{C}$  for 5 h, under the same conditions as those used for a normal catalytic test, but without substrate; then, the solid was separated by centrifugation (10,000 rpm) and the supernatant liquid phase was passed through a  $220 \mu\text{m}$  pore size PTFE membrane; the substrate (LA) was added to this solution (to give an initial concentration of  $0.45 \text{ M}$ ) and left to react for 5 h at  $200^\circ\text{C}$  (giving LP-CT); finally, the homogeneous mixture was analyzed by GC and the results were compared to those without catalyst.

## 3 Results and discussion

### 3.1 Characterization of the catalysts

Multifunctional LTL related materials ( $y\text{Hf-D-HL}(x)$ ) were prepared from commercial KL ( $\text{Si/Al} = 3$ ) via top-down strategies for the target reactions of LA, AnL and HMF. The strategies consisted of mild dealumination (giving KL(oxac),  $\text{Si/Al} = 5$ ); desilication (D) to introduce mesoporosity (giving D-KL,  $\text{Si/Al} = 3$ ); dealumination using  $\text{H}_2\text{SO}_4$  (giving D-HL( $x$ ),  $\text{Si/Al}$  in the range 5–41); solid-state impregnation (SSI) of hafnium and calcination. The influence of the acid concentration ( $x$  in the range  $0.10$ – $0.28 \text{ M H}_2\text{SO}_4$ ) and Hf loading ( $y$  in the range  $0.28$ – $1.68 \text{ mmol}_{\text{Hf}} \text{ g}^{-1}$ ) on the material properties was studied. The characterization studies of the zirconium counterpart  $0.28\text{Zr-D-HL}(0.15)$  are discussed in the Supplementary Material (Supplementary Figure S3, Supplementary Table S1); the results were comparable to those for  $0.28\text{Hf-D-HL}(0.15)$ .

For the materials D-HL( $x$ ), increasing  $x$  led to increasing  $\text{Si/Al}$  ratio in the range 5–41, suggesting that partial removal of aluminum occurred (likely forming vacant sites) (Figure 1A, Supplementary Table S1). Although the materials HL ( $\text{Si/Al} = 6$ ) and D-HL( $0.15$ ) ( $\text{Si/Al} = 9$ ) were subjected to the same acid treatment using  $0.15 \text{ M H}_2\text{SO}_4$ , the latter possessed a higher  $\text{Si/Al}$  ratio, suggesting that the pretreatments facilitated dealumination. The SSI process did not significantly affect

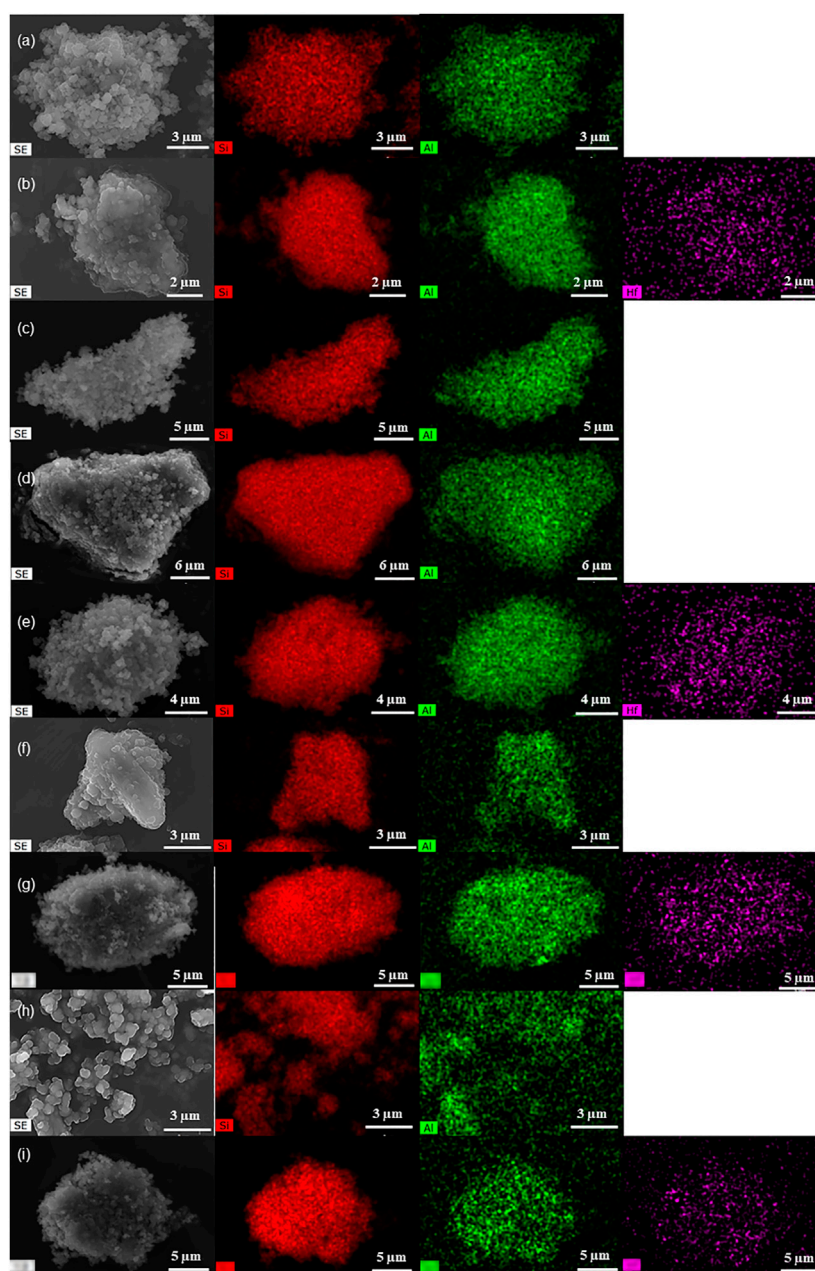


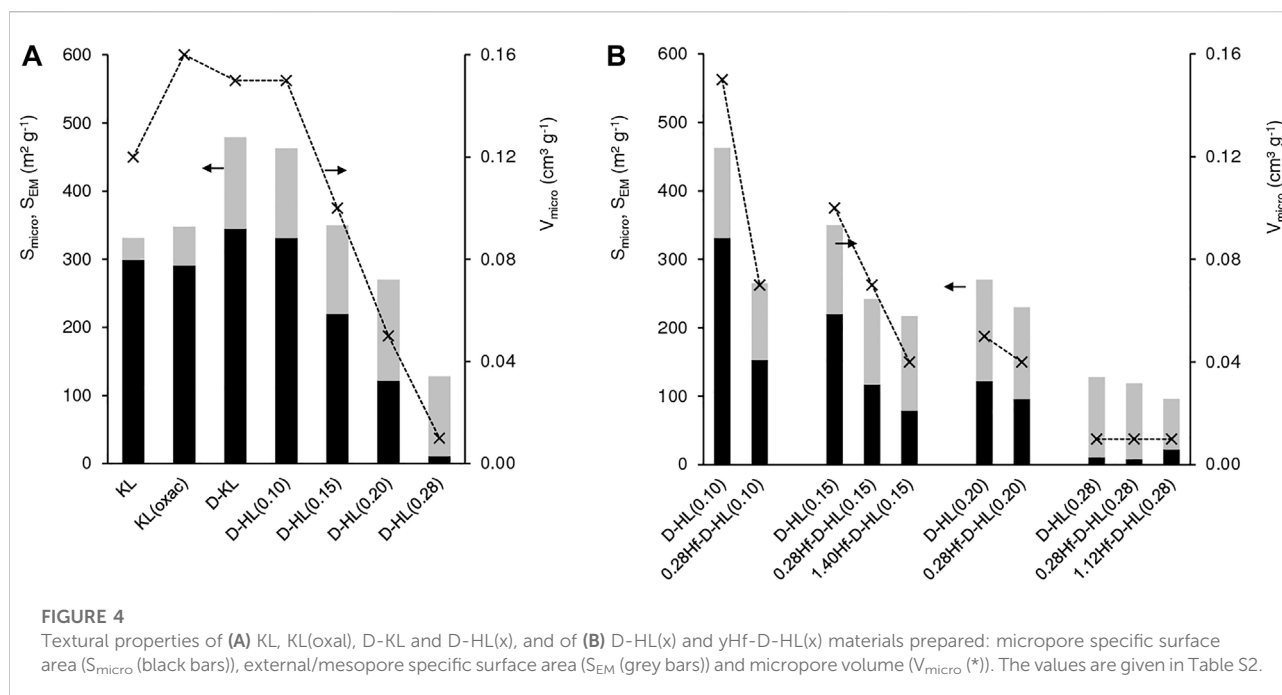
FIGURE 3

SEM images (left) and element mappings (Si–red, Al–green, Hf–purple) of KL (a), 5Hf–HL (b), D–KL (c), D–HL(x) ( $x = 0.15$  (d),  $0.20$  (f),  $0.28$  (h)) and  $0.28\text{Hf}$ –D–HL(x) ( $x = 0.15$  (e),  $0.20$  (g),  $0.28$  (i)).

the Si/Al ratio, *i.e.*, each pair of materials D–HL( $x$ ) and  $y\text{Hf}$ –D–HL( $x$ ) with the same  $x$  possessed similar Si/Al ratio. Since no wash/extraction/filtration operations were performed after SSI, the amount of hafnium introduced in the SSI step remained in the solids, giving  $y\text{Hf}$ –D–HL( $x$ ) with  $y$  in the range  $0.28$ – $1.68 \text{ mmol}_{\text{Hf}} \text{ g}^{-1}$  (Supplementary Table S1).

The PXRD patterns of the materials KL, KL(oxac), HL, D–KL, D–HL( $x$ ) and  $y\text{Hf}$ –D–HL( $x$ ) with  $x \leq 0.15$  indicated that the LTL

topology was preserved (Lee and Choi, 2016; Nilesh et al., 2016; Al-Ani et al., 2019; Tangale et al., 2019), whereas the materials with  $x = 0.20$  and  $0.28$  were mostly amorphous (Figure 2, Supplementary Table S1). The PXRD patterns of  $y\text{Hf}$ –D–HL( $0.15$ ) with  $y < 1.68 \text{ mmol}_{\text{Hf}} \text{ g}^{-1}$  and of  $y\text{Hf}$ –D–HL( $0.28$ ) with  $y < 1.40 \text{ mmol}_{\text{Hf}} \text{ g}^{-1}$  did not evidence the presence of other crystalline phases; peaks characteristic of hafnia monoclinic phase include *ca.*  $28.6^\circ$ ,  $31.8^\circ$  and  $34.7^\circ$  (ICDD PDF-4+



2020 reference code no. 04-005-4477) (Figure 2B). These results suggest that these materials possessed somewhat uniform metal/metalloid (Si, Al, Hf) distributions. The remaining materials with higher  $y$  exhibited weak reflections at *ca.* 28° and 32° assignable to polymeric hafnium oxide species. For the highest Hf loading of 1.68 mmol<sub>Hf</sub> g<sup>-1</sup> (for which formation of hafnium oxide particles may be more critical), the average crystallite size of the supported hafnium oxide particles (considering a spherical geometry) was very small, *ca.* 8–9 nm.

The oxalic acid and desilication treatments of KL did not significantly affect the relative crystallinity ( $RC \geq 96\%$ ) (Figure 1B, Supplementary Table S1). Increasing  $x$  led to decreasing RC of the D-HL( $x$ ) materials. Hence, the increasing Si/Al ratio was accompanied by decreasing RC. The D-HL( $x$ ) and 0.28Hf-D-HL( $x$ ) materials with the same  $x$ , possessed similar RC; *e.g.*, 73 and 71% RC for D-HL(0.15) and 0.28Hf-D-HL(0.15), respectively; 22 and 20% RC for D-HL(0.28) and 0.28Hf-D-HL(0.28), respectively. For the yHf-D-HL(0.15) materials, increasing  $y$  led to decreasing RC (Supplementary Table S1), which may be partly due to the presence of Hf species inside the pores, causing decreased scattering contrast and reduced intensities of the PXRD peaks. The range of RC of the yHf-D-HL( $x$ ) materials with  $x \leq 0.15$  and  $y \leq 0.84$  was comparable to that reported by Al-Ani *et al.* (Al-Ani *et al.*, 2019) for hierarchical LTL materials prepared via a surfactant templated approach, at 80–100°C (59–74% RC). The materials yHf-D-HL(0.28) possessed low RC (less than 24%) (Supplementary Table S1).

The SEM images showed that, in general, the materials consisted of aggregates of small pseudo-spherical particles

with sizes of up to *ca.* 30 nm (exemplified for some materials in Figure 3, Supplementary Figure S4, S5). The respective elemental mappings suggested somewhat uniform metal distributions (Figure 3, Supplementary Figure S4, S5) (noteworthy, it was not possible to discriminate HfO<sub>x</sub> nanocrystallites by SEM).

Commercial KL, HL, and KL(oxal) exhibited type I nitrogen sorption isotherms (Supplementary Figure S6A), characteristic of microporous materials (Gregg and Sing, 1982). The increasing N<sub>2</sub> uptake as the relative pressure ( $p/p_0$ ) approached unity may be attributed to N<sub>2</sub> sorption on the external surface of the relatively small crystallites. The desilicated materials D-KL and D-HL( $x$ ) exhibited type IV isotherms with an inflection point at  $p/p_0 > 0.9$  (inset of Supplementary Figure S6B), which is characteristic of mesoporous materials (Gregg and Sing, 1982). Whereas commercial KL possessed  $S_{\text{EM}} = 32 \text{ m}^2 \text{ g}^{-1}$  and  $V_{\text{micro}} = 0.12 \text{ cm}^3 \text{ g}^{-1}$ , the desilicated D-KL material possessed  $S_{\text{EM}} = 134 \text{ m}^2 \text{ g}^{-1}$  and  $V_{\text{micro}} = 0.15 \text{ cm}^3 \text{ g}^{-1}$ , *i.e.*, the alkaline treatment introduced mesoporosity without affecting significantly  $V_{\text{micro}}$  (Figure 4A, Supplementary Table S2). Consistently, D-HL( $x$ ) exhibited bimodal pore size distributions, in which the mesopore sizes were in the range 2.3–6 nm (Supplementary Figure S6C).

For D-HL( $x$ ), increasing  $x$  up to 0.20 essentially led to decreasing  $S_{\text{micro}}$  and  $V_{\text{micro}}$  without affecting considerably  $S_{\text{EM}}$  (130–148  $\text{m}^2 \text{ g}^{-1}$ ) (Figure 4A, Supplementary Table S2). Materials D-HL( $x$ ) with  $x \leq 0.15$  possessed comparable  $V_{\text{micro}}$  to literature data for surfactant-templated LTL type materials (Al-Ani *et al.*, 2019). For  $x = 0.28$ ,  $V_{\text{micro}}$  and  $S_{\text{micro}}$  decreased drastically to  $0.01 \text{ cm}^3 \text{ g}^{-1}$  and  $11 \text{ m}^2 \text{ g}^{-1}$ , respectively, and the



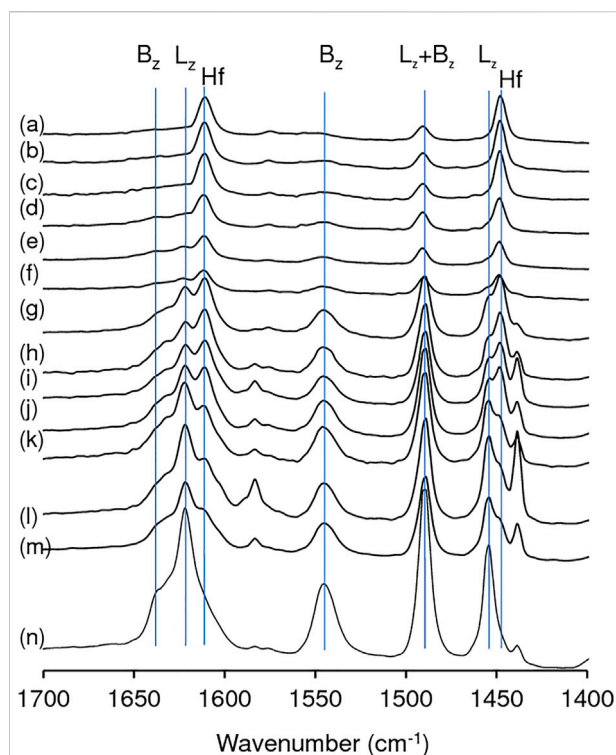


**FIGURE 5**

FT-IR spectra of adsorbed pyridine, at 150°C, for yHf-D-HL(0.28) with  $y = 1.40$  (a), 1.12 (b), 0.84 (c), 0.56 (d), 0.28 (e); 0.28Hf-D-HL(0.20) (f); yHf-D-HL(0.15) with  $y = 1.40$  (g), 1.12 (h), 0.84 (i), 0.56 (j), 0.28 (k); 0.28Hf-D-HL(0.10) (l); 0.28Hf-HL (m); HL (n). Hf signalizes the new bands which appeared after Hf introduction; B<sub>z</sub> and L<sub>z</sub> signalize typical bands associated with Brønsted and Lewis acid sites of a zeolitic type aluminosilicate framework.

material was essentially mesoporous ( $S_{EM} = 117 \text{ m}^2 \text{ g}^{-1}$ ). Based on these results and PXRD, harsh dealumination seems to cause partial destruction and/or blockage of the micropores (e.g., possibly by inorganic debris formed during post-synthesis treatments).

The introduction of Hf in D-HL( $x$ ) with  $x \leq 0.20$ , led to a decrease in  $S_{\text{micro}}$  and  $V_{\text{micro}}$ , suggesting that Hf sites are at least partly located on the internal micropore surface (Figure 4B, Supplementary Table S2). For  $x = 0.28$ , the introduction of Hf led to a decrease in  $S_{EM}$  ( $117$  and  $74 \text{ m}^2 \text{ g}^{-1}$  for D-HL(0.28) and 1.12Hf-D-HL(0.28), respectively), suggesting that Hf sites may be located on the mesopore surface.

Furthermore, the micropore size distribution curves of KL showed medians at ca. 0.55 and at 0.75 nm, assignable to the 8-MR (3D) and 12-MR (1D) channels. Especially the peak at ca. 0.55 nm was significantly attenuated for D-HL( $x$ ) with  $x \leq 0.20$  and negligible for D-HL(0.28) (Supplementary Figure S7A). This was more pronounced after introducing Hf, suggesting that a fraction of Hf species may be located inside micropores and/or at micropore mouths of yHf-D-HL( $x$ ) with

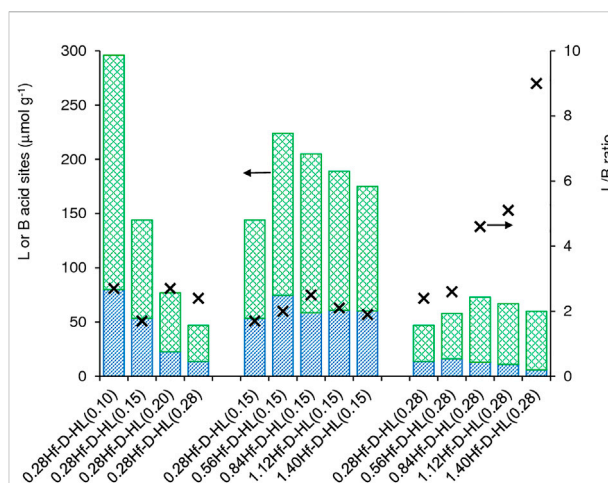


**FIGURE 6**

Acid properties of the materials prepared from commercial KL via post-synthesis modifications: L = Lewis acid sites (top green bar), B = Brønsted acid sites (bottom blue bar) and L/B ratio (x). The values are given in Table S3.

$x \leq 0.20$  (exemplified for 0.28Hf-D-HL( $x$ ) in Supplementary Figure S7B).

The  $^{27}\text{Al}$  MAS NMR spectra of KL, HL, Hf-HL, KL(oxac), D-KL, D-HL( $x$ ) and yHf-D-HL( $x$ ) with  $x \leq 0.15$  showed a prominent peak centered at ca. 63 ppm, assigned to Al sites in tetrahedral coordination ( $\text{Al}_{\text{tetra}}$ ) (Supplementary Figure S8). Increasing  $x$  above 0.15 led to the broadening of the  $\text{Al}_{\text{tetra}}$  peak and the appearance of a shoulder at ca. 53 ppm; the relative intensity of the latter peak increased with increasing  $x$ . These results suggest that the decreased crystallinity was accompanied by the formation of broader distributions of  $\text{Al}_{\text{tetra}}$  species (e.g., possessing different bond angles/lengths, coordination spheres). The materials D-HL( $x$ ) exhibited a weak resonance at ca. 0 ppm due to hexacoordinated (octahedral) Al species ( $\text{Al}_{\text{octa}}$ ), which was not verified for D-KL, suggesting that  $\text{Al}_{\text{octa}}$  was formed during the acid treatment. A comparison of the materials before and after the introduction of hafnium indicated no significant differences in the  $\text{Al}_{\text{tetra}}$  spectral region, but the  $\text{Al}_{\text{octa}}$  peak disappeared. Hence, it seems that  $\text{Al}_{\text{octa}}$  species were partially linked to the framework of D-HL( $x$ ) and converted to  $\text{Al}_{\text{tetra}}$  during SSI/calcination. According to the literature for zeolites,  $\text{Al}_{\text{octa}}$  and  $\text{Al}_{\text{tetra}}$  sites may interconvert (Mafra et al., 2012; Ravi et al., 2021); e.g., hydroxylated-hydrated  $\text{Al}_{\text{octa}}$  sites and hydroxylated  $\text{Al}_{\text{tetra}}$  sites may interconvert (Yakimov et al., 2022). Possibly the two resonances at ca. 63 and 53 ppm may include four coordinated hydroxylated ( $\text{Al}(\text{OSi})_{4-x}(\text{OH})_x$ ) and non-hydroxylated ( $\text{Al}(\text{OSi})_4$ ) aluminum sites.

The FT-IR spectrum of adsorbed pyridine for zeolite HL showed the typical bands associated with Al sites possessing Lewis (L) acidity (metal-pyridine complexes, which may possess extra framework metal sites) and Brønsted (B) acidity

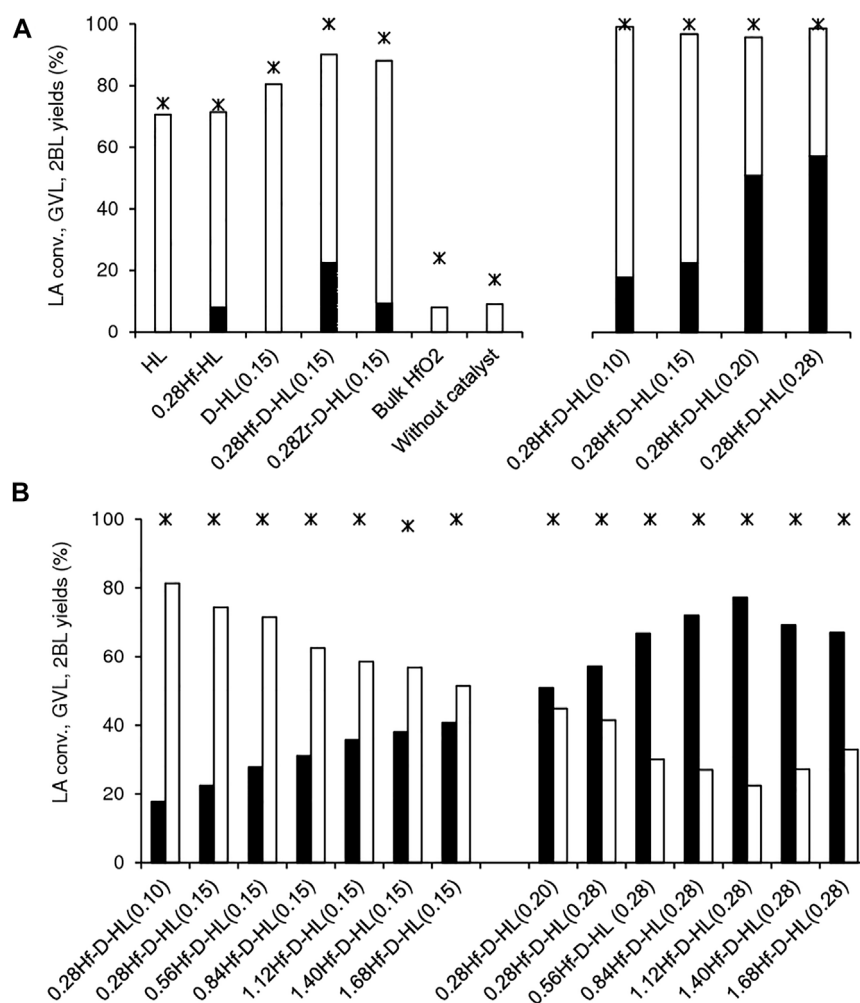


FIGURE 7

Catalytic performances of the prepared catalysts (A,B) for LA conversion (\*) to GVL (black bars) and 2BL (white bars). Tests without catalyst or in the presence of HfO<sub>2</sub> are included for comparison (A). Reaction conditions: 0.45 M LA in 2BuOH, 200°C, 24 h.

(pyridinium ions): *ca.* 1,620 cm<sup>-1</sup> and 1,454 cm<sup>-1</sup> (L); *ca.* 1,635 cm<sup>-1</sup> and 1,540 cm<sup>-1</sup> (B); and 1,490 cm<sup>-1</sup> (L + B) (Figure 5) (Zhu et al., 2016; Tang et al., 2019; Ravi et al., 2021). A band at 1,439 cm<sup>-1</sup> may be due to pyridine molecules interacting with weak acid sites. The relative intensities of the bands at 1,454 cm<sup>-1</sup> (L), 1,540 cm<sup>-1</sup> (B) and 1,635 cm<sup>-1</sup> (B) decreased after acid treatment and were hardly distinguishable in the spectra of the materials with *x* = 0.28. The introduction of hafnium led to the appearance of new bands at *ca.* 1,608 and 1,448 cm<sup>-1</sup> which became stronger with increasing *y* up to *ca.* 0.84 mmol<sub>Hf</sub> g<sup>-1</sup> (above this value the spectral differences in relative intensities were not so evident). Hence, these two new bands may be attributed to Hf-containing acid sites. The appearance of these new bands after introducing Hf is in agreement with that reported by Tang et al. for Hf-USY (Tang et al., 2019). For the yHf-D-HL(0.28) materials, the 1,608 and

1,448 cm<sup>-1</sup> bands predominated, suggesting that the acidity of these materials was essentially associated with Hf sites.

Increasing *x* of the materials 0.28Hf-D-HL(*x*) led to decreasing amount of L and B acid sites (Figure 6, Supplementary Table S3). On the other hand, the introduction of Hf in HL gave 0.28Hf-HL possessing higher amounts of B and L acid sites (L increased from 82 to 128 μmol g<sup>-1</sup>, and B increased from 45 to 71 μmol g<sup>-1</sup>, respectively (Supplementary Table S3)). These results parallel those reported in the literature for Beta zeolites with and without hafnium (Antunes et al., 2022a).

For each set of materials yHf-D-HL(0.15) and yHf-D-HL(0.28), a maximum amount of L acid sites was reached as a function of *y*; specifically, at *y* = 0.56 and 0.84 for materials with *x* = 0.15 and 0.28, respectively (Figure 6, Supplementary Table S3). For the lower range of Hf loading (*y*), the increasing L acidity with increasing *y* suggests that uniformly distributed Hf-sites

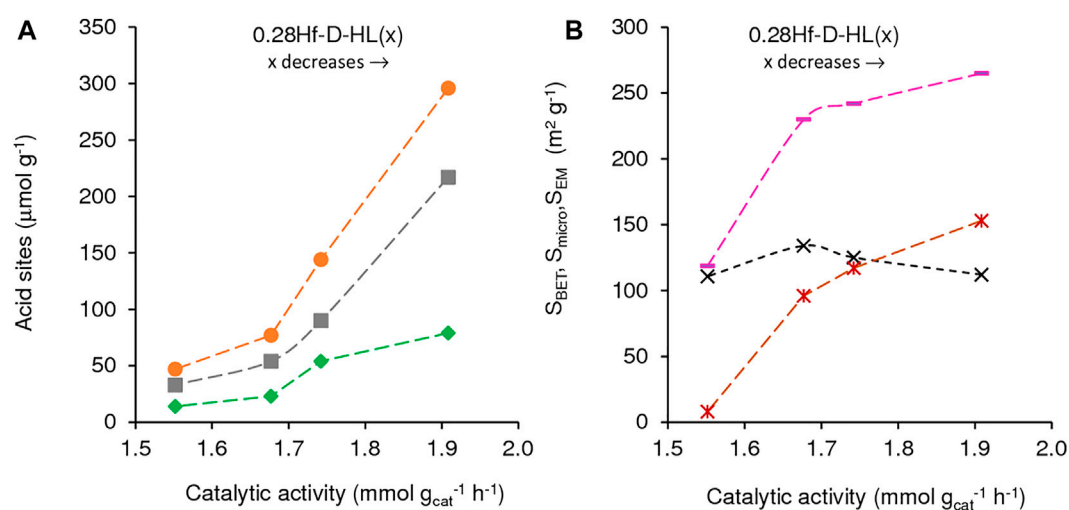


FIGURE 8

Influence of (A) the amount of acid sites (L (■), B (◆) and L + B (●)) and (B) textural properties (S<sub>BET</sub> (—), S<sub>EM</sub> (x), S<sub>micro</sub> (\*) on catalytic activity of 0.28Hf-D-HL(x) for LA conversion. Reaction conditions: 0.45 M LA in 2BuOH, 25.5 g<sub>cat</sub> L<sup>-1</sup>, 200°C, 5 h.

were introduced. On the other hand, for the higher range of Hf loadings, L may decrease due to 1) formation of dimeric/oligomeric Hf species which may possess reduced acidity and/or hinder the access of pyridine molecules to some acid sites of the aluminosilicate support, and 2) hafnium oxide nanoparticles formed at higher  $\gamma$  may possess inaccessible Hf sites. For  $\gamma$ Hf-D-HL(0.15), the L/B ratios (1.7–2.5) did not vary considerably with  $\gamma$ , whereas for  $\gamma$ Hf-D-HL(0.28) the L/B ratio (2.4–9.0) increased considerably with increasing  $\gamma$  in the range 0.28–1.68 mmol<sub>Hf</sub> g<sup>-1</sup> (Figure 6).

In general, the  $\gamma$ Hf-D-HL(x) materials possessed moderate to strong L acid sites (L<sub>350</sub>/L<sub>150</sub> up to ca. 0.33) and did not possess strong B acid sites (B<sub>350</sub>/B<sub>150</sub>  $\approx$  0), Supplementary Table S3. For the 0.28Hf-D-HL(x) materials (*i.e.*, Si/Al varied and Hf load was similar), the L acid strength increased with increasing  $x$  above 0.15 M H<sub>2</sub>SO<sub>4</sub> (L<sub>350</sub>/L<sub>150</sub> was similar for  $x$  = 0.10 and 0.15). On the other hand, the influence of  $\gamma$  on the L acid strength was not straightforward: for  $\gamma$ Hf-D-HL(0.15), the L acid strength decreased with increasing  $\gamma$ , whereas for  $\gamma$ Hf-D-HL(0.28) no straightforward relationship could be established. The acid properties may depend on several factors. The PXRD data indicated that condensed hafnium oxide species may be formed at higher  $\gamma$ , which may impact on the amount and strength of accessible acid sites. The materials  $\gamma$ Hf-D-HL(x) may possess different metal (Al, Hf) acid sites, chemical structures and coordination spheres, bond angles/lengths and binding energies (*e.g.*, distorted geometries), *etc.* For example, according to the literature, framework Lewis acid Hf sites may be hydrolyzed or non-hydrolyzed species, and the former may be stronger than the latter (Tang et al., 2019).

## 3.2 Catalytic studies

As mentioned in the Introduction, HMF, AnL and LA may be formed in carbohydrate conversion processes, and converted to GVL under acid and reduction conditions, and thus it is interesting to study their reactivities, envisaging future integrated reaction systems over multifunctional catalysts. The acid sites of the aluminosilicate LTL framework may promote the acid reactions (*e.g.*, esterification, etherification). On the other hand, desilication and partial dealumination of the framework may form vacant sites for introducing hafnium via SSI, furnishing the zeolite with CTH activity. In this fashion, multifunctional LTL type catalysts may be produced, capable of promoting several paths that lead to target bioproducts.

To study the influence of the post-synthesis conditions, the catalytic studies consisted of firstly studying the influence of the acid treatment (dealumination degree) of D-HL(x) ( $x$  = 0.10, 0.15, 0.20 or 0.28 M H<sub>2</sub>SO<sub>4</sub>) on the LA reaction, keeping constant the amount of impregnated hafnium ( $\gamma$  = 0.28 mmol<sub>Hf</sub> g<sup>-1</sup>). Subsequently, the influence of the Hf loading ( $\gamma$  in the range 0.28–1.68 mmol<sub>Hf</sub> g<sup>-1</sup>) was studied for two sets of materials, namely (crystalline micro/mesoporous)  $\gamma$ Hf-D-HL(0.15) and (mostly amorphous, mesoporous)  $\gamma$ Hf-D-HL(0.28). Kinetic, mechanistic, catalyst stability and finally substrate scope (AnL, HMF) were studied for selected catalysts.

### 3.2.1 LA to GVL

#### 3.2.1.1 General considerations

The reaction of LA in the presence of the  $\gamma$ Hf-D-HL(x) materials gave GVL and 2BL in a high total yield (>90%) with molar ratios GVL/2BL in the range 0.2–3.5, at 200°C, 24 h.

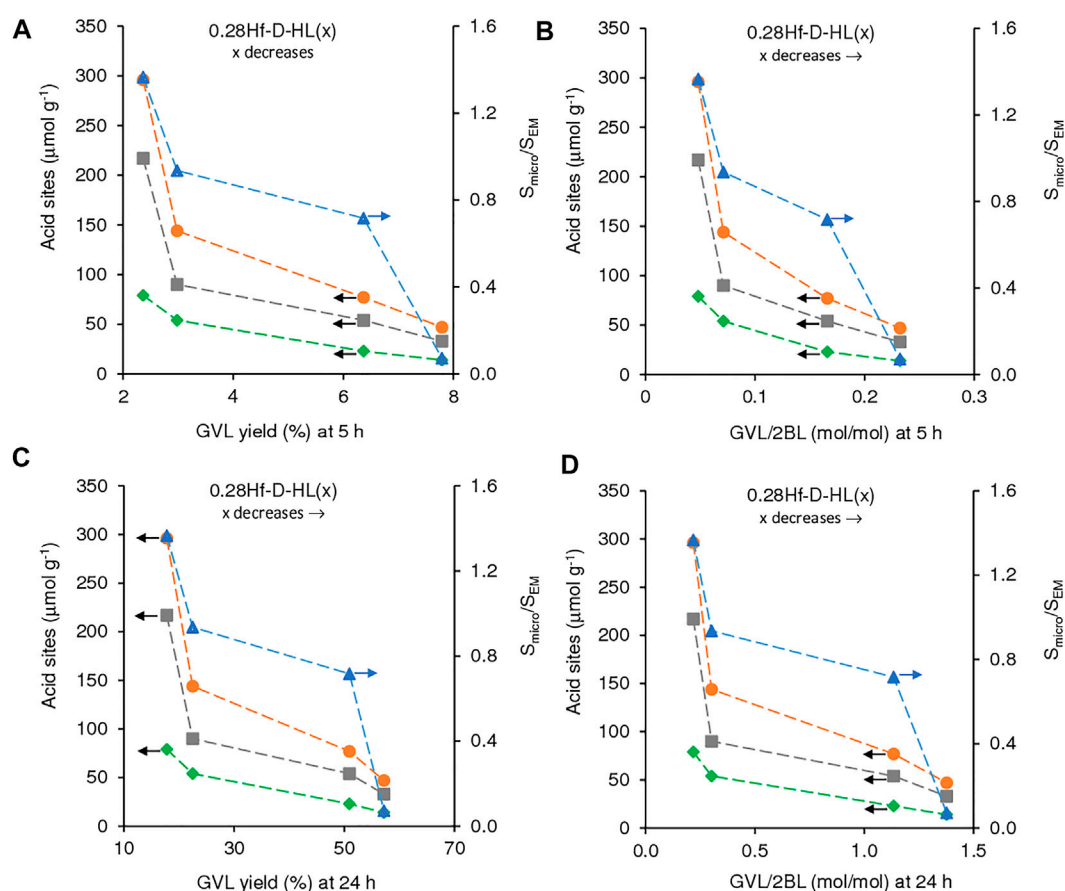


FIGURE 9

Influence of the amount of acid sites (L (■), B (◆) and L + B (●)) and  $S_{\text{micro}}/S_{\text{EM}}$  ratio (▲), on GVL yield ((A), (C)) and GVL/2BL molar ratio ((B), (D)), at 5 h ((A), (B)) and 24 h ((C), (D)) for the reaction of LA in the presence of 0.28Hf-D-HL(x). Reaction conditions: 0.45 M LA in 2BuOH, 25.5 g<sub>cat</sub> L<sup>-1</sup>, 200°C.

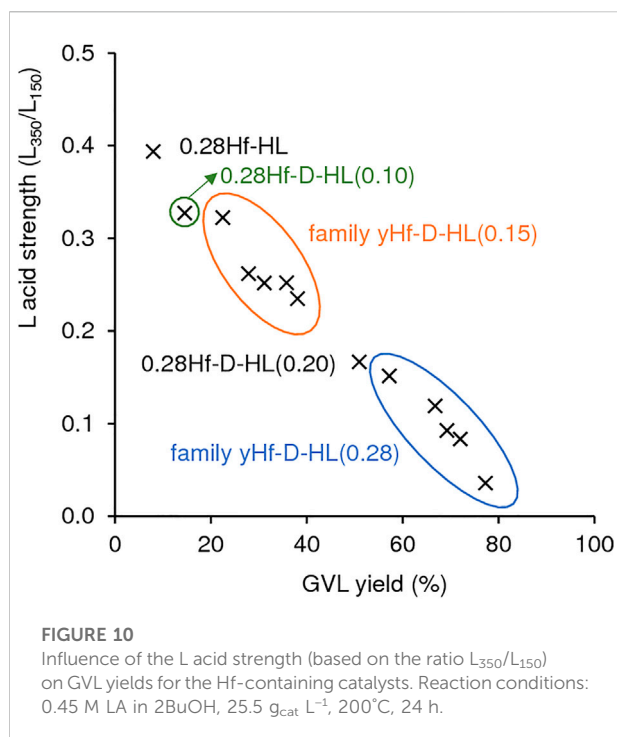
Without a catalyst, the reaction was much slower and GVL was not formed, under similar conditions (17% conversion, 9% 2BL yield) (Figure 7).

Literature studies suggest that the conversion of LA to GVL in alcohol medium may be favoured by L and B acidity (Li et al., 2017; Xu et al., 2017; Li et al., 2018; Tang et al., 2019; He et al., 2020; Li et al., 2021), such as Lewis acid Hf sites (Kumar et al., 2016; Tang et al., 2019). A comparative study for the aluminosilicates HL and D-HL(0.15) (both prepared via acid treatment using  $x = 0.15$  M H<sub>2</sub>SO<sub>4</sub>), and the respective Hf-containing materials 0.28Hf-HL and 0.28Hf-D-HL(0.15), indicated that the aluminosilicates effectively converted LA to 2BL, but failed to give GVL (Figure 7A). The formation of GVL required the presence of Hf sites. Nevertheless, bulk HfO<sub>2</sub> led to similar results to the blank test without catalyst (24% LA conversion, 8% 2BL yield, and GVL was not formed), suggesting that the type of Hf sites may be determinant for GVL formation.

The zirconium catalyst 0.28Zr-D-HL(0.15) was less effective than its counterpart 0.28Hf-D-HL(0.15); the former led to less than half the GVL yield reached in the presence of 0.28Hf-D-HL(0.15) (9 and 22% GVL yield, at 200°C/24 h) (Figure 7A). Hence, hafnium catalysts seem more promising for the target reaction, which parallels literature studies for Hf- versus Zr-Beta (Antunes et al., 2022a), and Hf- versus Zr- and Sn-USY (Tang et al., 2019).

A comparative study for (non-desilicated) 0.28Hf-HL and (desilicated) 0.28Hf-D-HL(0.15) (which possessed the same Hf loading ( $y = 0.28$  mmol<sub>Hf</sub> g<sup>-1</sup>) and were subjected to similar acid treatment using  $x = 0.15$  M H<sub>2</sub>SO<sub>4</sub>) indicated that the desilicated catalyst 0.28Hf-D-HL(0.15) was more active than 0.28Hf-HL (100.74% and LA conversion, respectively), led to higher 2BL + GVL total yield (90 and 71%, respectively) and higher GVL/2BL molar ratio (0.33 and 0.13, respectively) (Figure 7A), suggesting a favourable effect of desilication on the catalytic performance for targeting GVL.





### 3.2.1.2 Influence of acid treatment (x) and Hf loading (y)

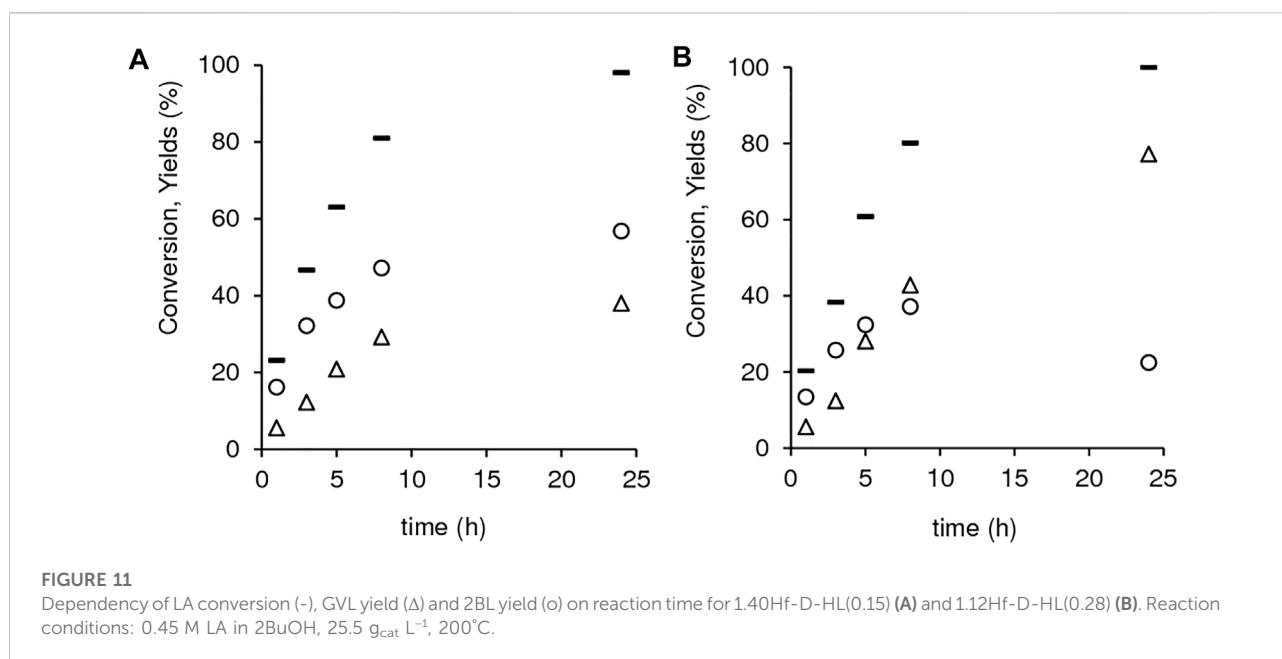
The influence of the acid treatment (dealumination degree) on the catalytic performance was studied keeping constant the Hf loading ( $y = 0.28 \text{ mmol}_{Hf} g^{-1}$ ), i.e., comparing the 0.28Hf-D-HL(x) catalysts (Figure 8, Figure 9). Catalysts 0.28Hf-D-HL(x) led mainly to 2BL and GVL, which were formed in high total

yield (96–99%, Figure 7), with GVL/2BL molar ratios in the range 0.2–1.4, at 24 h, 200°C. The activity ( $\text{mmol } g_{cat}^{-1} h^{-1}$ , based on conversion at 5 h) increased with decreasing x in the order  $1.55 (x = 0.28) < 1.68 (x = 0.20) < 1.74 (x = 0.15) < 1.91 (x = 0.10)$ , which correlated with the increasing amounts of B and L acid sites (Figure 8A) and increasing  $S_{BET}$  and  $S_{micro}$  (Figure 8B);  $S_{EM}$  was roughly constant, and no clear correlation could be established with the L/B ratio.

Although the activity of 0.28Hf-D-HL(x) decreased with increasing x, GVL yield and GVL/2BL ratios at 5 and 24 h increased (Figure 9). This may be partly due to a levelling off effect of the lower amounts of total acid sites for higher x, by a lower ratio  $S_{micro}/S_{EM}$  which may avoid steric hindrance effects, favouring GVL formation.

Further studies were carried out to check the influence of the Hf loading (y), specifically for the two sets of materials yHf-D-HL(x) with  $x = 0.15$  and 0.28. yHf-D-HL(0.15) led mainly to 2BL (51–71% yield), and GVL was formed in 22–38% yield at 200°C/24 h (Figure 7B), whereas yHf-D-HL(0.28) led mainly to GVL (57–77% yield), and 2BL was formed in 22–45% yield at 200°C/24 h (Figure 7B).

According to the literature, stronger L acidity may enhance CTH activity (Li et al., 2017). However, taking into consideration all the Hf-containing materials prepared (yHf-D-HL(x), 0.28Hf-HL), GVL yield increased somewhat linearly with decreasing L acid strength ( $R^2 = 0.9835$ ) (Figure 10). These results may be due to an interplay of several factors. For example, for materials with  $y = 0.28 \text{ mmol}_{Hf} g^{-1}$ , the L acid strength increased with increasing  $S_{micro}/S_{EM}$  (Supplementary Table S2, S3); specifically,  $L_{350}/L_{150}$  was  $0.39 (0.28Hf-HL) > 0.33 (0.28Hf-D-HL(0.10)) > 0.32 (0.28Hf-D-HL(0.15)) > 0.17 (0.28Hf-D-HL(0.20)) > 0.15$



(0.28Hf-D-HL(0.28)), and  $S_{\text{micro}}/S_{\text{EM}}$  followed a similar order,  $2.21$  (0.28Hf-HL)  $> 1.37$  (0.28Hf-D-HL(0.10))  $> 0.94$  (0.28Hf-D-HL(0.15))  $> 0.72$  (0.28Hf-D-HL(0.20))  $> 0.07$  (0.28Hf-D-HL(0.28)). Hence, for these materials with  $\gamma = 0.28 \text{ mmol}_{\text{Hf}} \text{ g}^{-1}$ , lower  $S_{\text{micro}}/S_{\text{EM}}$  may be a main factor in favour of GVL formation. For the remaining materials with  $\gamma > 0.28 \text{ mmol}_{\text{Hf}} \text{ g}^{-1}$ , the L acid strength dependency on  $\gamma$  (and thus on GVL yields) was not straightforward; higher  $\gamma$  may lead to relevant differences in surface chemistry, impacting on catalytic performances.

### 3.2.1.3 Mechanistic studies

In the conversion of LA to GVL, the secondary alcohol (2BuOH) plays multiple roles, *i.e.*, as solvent and as reducing, etherification and esterification agent. The acid-catalyzed esterification of LA gives alkyl levulinates (LE), and the CTH of LA and LE may give 4-hydroxypentanoic acid (HPA) and alkyl 4-hydroxypentanoates (HPE), respectively, *i.e.*, the carbonyl group in position C4 is reduced to an alcohol group. Literature studies reported that HPA/HPE may undergo etherification at the alcohol group in position C4, giving 4-alkoxypentanoic acid (APA) and alkyl 4-alkoxypentanoates (APE), respectively (Tang et al., 2015; Li et al., 2016a; Valekar et al., 2016; Wang et al., 2017). Although HPA/HPE/APA/APE were not identified for the  $\gamma\text{Hf-H-DL}(x)$  catalysts, one cannot exclude their possible formation and subsequent lactonization (and dealcoholation in the case of HPE/APE) to give GVL (Li et al., 2016a; Wang et al., 2017). According to the literature, even the intrinsic acidity of LA may promote relatively fast lactonization of HPA (Xie et al., 2016; Winoto et al., 2019).

To gain mechanistic insights, the kinetic curves of the reaction of LA were measured for (crystalline, micro/mesoporous) 1.40Hf-D-HL(0.15) and (mostly amorphous, mesoporous) 1.12Hf-D-HL(0.28), at 200°C (Supplementary Figure S9). For the two catalysts, the LA conversion versus time profiles were roughly coincident, and it was verified an approximately linear dependency ( $R^2 \geq 0.995$ ) of  $\ln([LA]_0/[LA])$  on reaction time (considering the integrated rate law:  $\ln([LA]_0/[LA]) = kt$ , where  $k$  is the kinetic constant and  $t$  is reaction time) (Supplementary Figure S9A). These results suggest that the reaction rate was apparently first order in LA concentration. Luo et al. reported a first order dependency on substrate concentration, for the reaction of LE to GVL over Hf-zeolites in 2BuOH (Luo et al., 2014).

Despite the similar catalytic activities, the two materials exhibited different kinetic curves of GVL and 2BL formation (Figure 11). For 1.40Hf-D-HL(0.15), GVL and 2BL were formed in parallel until *ca.* 98% conversion (Figure 11A), suggesting that GVL may be formed from LA without the intermediate formation of 2BL. Somewhat parallel formation of GVL and 2BL was also verified for 1.12Hf-D-HL(0.28) in an initial stage, but as LA conversion increased from 80 to 100% (20% difference), the 2BL yield dropped from 37 to 22% (15%

difference) and GVL yield increased considerably from 43 to 77% (34% difference) (Figure 11B). The increment in GVL yield (34%) was approximately equal to the total consumption of LA plus 2BL (35%) in the same time interval (8–24 h), suggesting that both LA and 2BL were converted to GVL.

One cannot rule out the hypothesis of other intermediates, besides 2BL, being involved in the formation of GVL. For example, the reaction of LA in the presence of 1.12Hf-D-HL(0.28) using lower  $[LA]_0$  of 0.11 M, was complete within 1 h and, yet GVL continued to be formed (64–91% GVL yield between 1 and 5 h), while 2BL concentration remained approximately constant (9–10% 2BL yield between 1 and 5 h) (Supplementary Figure S9B). Hence, it seems that the intermediates to GVL were not fully quantified. Possible explanations for this include: 1) some intermediates may be essentially adsorbed on the catalyst's surface and thus not analyzed in the liquid bulk; 2) some intermediates may be unstable under the analytical conditions.

In summary, 1.12Hf-D-HL(0.28) seems to effectively promote GVL formation via intermediate formation of 2BL. This catalyst possessed lower  $S_{\text{micro}}/S_{\text{EM}}$  than 1.40Hf-D-HL(0.15) (*ca.* 0.3 and 0.6, respectively), which may facilitate reaction pathways involving bulkier intermediates and transition states, *e.g.*, LE/HPE/APE are bulkier than LA/HPA/APA, respectively. Luo et al. reported for methyl levulinate conversion to GVL over Hf-Beta, in 2BuOH, a dual-binding mechanism where the alkyl levulinate and the alcohol H-donor interacted (involving a hydride shift) with a single metal site forming a voluminous six-membered transition state (Luo et al., 2014). Accordingly, steric hindrance may become important for catalysts possessing higher  $S_{\text{micro}}/S_{\text{EM}}$ .

### 3.2.1.4 Comparisons between $\gamma\text{Hf-D-HL}(x)$ and other materials

Based on the above results, it is interesting to compare the catalytic performances of  $\gamma\text{Hf-D-HL}(x)$  to hafnium silicates possessing high mesopore surface area, such as the mesoporous hafnium silicate Hf-TUD-1(50), previously described by our group (Antunes et al., 2021). Hf-TUD-1(50) possessed a similar Hf load of  $0.31 \text{ mmol}_{\text{Hf}} \text{ g}^{-1}$  to 0.28Hf-D-HL(0.28), but higher  $L + B = 130 \mu\text{mol g}^{-1}$ ,  $L/B = 12$  and mesopore specific surface area of *ca.*  $660 \text{ m}^2 \text{ g}^{-1}$  (Antunes et al., 2021); for 0.28Hf-D-HL(0.28),  $L + B = 47 \mu\text{mol g}^{-1}$ ,  $L/B = 2.4$  and  $S_{\text{BET}} = 119 \text{ m}^2 \text{ g}^{-1}$ . Hf-TUD-1(50) led to 29% GVL yield at 200°C/24 h (Supplementary Table S4, entry 6), which was approximately half of that for 0.28Hf-D-HL(0.28) (57% yield), under similar reaction conditions. Hence, the enhanced mesopore surface area of Hf-TUD-1(50) was not sufficient to warrant high GVL yield. Catalyst 0.28Hf-D-HL(0.28) possesses distinct surface chemistry partly because it has in its genesis an LTL type (starting) material.

To the best of our knowledge, this is the first study for LTL zeotype catalysts for LA conversion to GVL. Supplementary

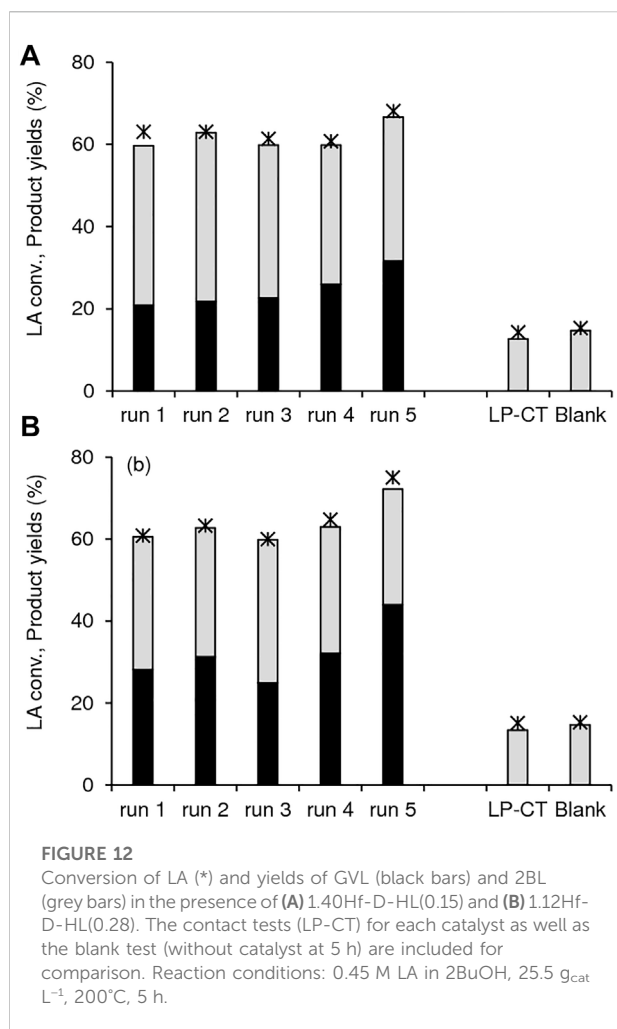


Table S4 further compares the catalytic performance of  $\gamma$ Hf-D-HL(x) to literature data for the reaction of LA to GVL, in the presence of micro/mesoporous zeotypes or mesoporous silicas/silicates, using an alcohol as reducing agent (Kuwahara et al., 2014; Antunes et al., 2015, 2016a, 2016b; Hengne et al., 2016; Winoto et al., 2016; Kuwahara et al., 2017; Xu et al., 2017; Zhou et al., 2018; Kumar and Srivastava, 2019; Morales et al., 2019; Tang et al., 2019; He et al., 2020; Kumaravel et al., 2020; López-Aguado et al., 2020; García et al., 2021; Ostovar et al., 2021; Antunes et al., 2022a). The different studies were carried out using different reaction conditions, making it difficult to establish clear comparisons. Without considering the differences in reaction conditions, and based solely on GVL yields, the best result for 0.28Hf-D-HL(0.28) (91% GVL yield, entry 5) was comparable to some of the best results indicated in Supplementary Table S4. GVL yields of at least 90% were reported for micro/mesoporous zeotypes such as Hf-WdeSAIBeta-m (entry 7) (Antunes et al., 2022a), Hf-USY (entry 17) (Tang et al., 2019) and Zr-AlBeta (entry 11) (López-Aguado et al., 2020) which led to 99% (180°C/24 h),

95% (150°C/10 h) and 92% GVL yield (170°C/6 h), respectively, and some Zr-containing mesoporous SBA-15 type catalysts (synthesized using the relatively expensive polymeric template Pluronic P123) which led to 90–95% GVL yield (entries 19, 20) (Kuwahara et al., 2014, 2017; Zhou et al., 2018). Catalyst 1.12Hf-D-HL(0.28) led to 64% GVL yield at 200°C/1 h (Figure 9B), which was higher than that reported for Ni-Sepiolite (<1% yield at 180°C/2 h, entry 25) (García et al., 2021). Moderate GVL yields were reported for a composite Zr-AlBeta/TUD-1 (31% at 150°C/72 h, entry 13) (Antunes et al., 2016b) and mesoporous Zr (7.6wt%)SBA-15-SGD (33% at 160°C/6 h, entry 18) (Ostovar et al., 2021). GVL was not formed for Zr-TUD-1 and ZrAl-TUD-1 at 120°C/24 h (entries 14 and 15, respectively) (Antunes et al., 2016b; 2016a).

### 3.2.1.5 Catalyst stability

The fresh and used catalysts 0.28Hf-D-HL(x) ( $x = 0.10, 0.15, 0.20, 0.28$ ) exhibited similar (white) colour, and the material balances closed in at least 91 mol%, considering GVL and 2BL as the useful bioproducts. ATR FT-IR spectroscopy indicated the presence of carbonaceous matter in the solids (exemplified for 0.28Hf-D-HL(0.15) in Supplementary Figure S10). The used catalyst exhibited new weak bands which were not verified for the fresh catalyst; *ca.* 1,460 cm<sup>-1</sup> assignable to C-H vibrations of adsorbed organic matter (O'Dell et al., 2008), *ca.* 1,377 cm<sup>-1</sup> assignable to metal-alkoxide type groups (Lynch et al., 1964), *ca.* 1,700 cm<sup>-1</sup> which may be associated with the carbonyl moiety of carboxylic acid or ester functional groups (Nandiyanto et al., 2019), and *ca.* 1,400 cm<sup>-1</sup> assignable to carboxylate groups (Nandiyanto et al., 2019). The thermal treatment of the catalyst at 550°C led to the disappearance of these new bands, and the spectrum was similar to that of the original catalyst. Hence, the surface chemistry was preserved during the catalytic and thermal regeneration processes. Furthermore, the PXRD patterns of the thermally regenerated solids were similar to those of the respective original catalysts (Supplementary Figure S11).

Elemental analysis of the washed-dried 0.28Hf-D-HL(x) catalysts (after a 5 h batch run) indicated that the carbon content (wt% C) increased with decreasing  $x$ , in the order 1.2 wt% ( $x = 0.28$ ) < 1.7 wt% ( $x = 0.20$ ) < 2.8 wt% ( $x = 0.15$ ) < 3.7 wt% ( $x = 0.10$ ). While enhanced adsorption of carbonaceous matter did not seem to negatively affect LA conversion (54, 49, 47 and 44% conversion for  $x = 0.10, 0.15, 0.20$  and 0.28, respectively), it led to decreasing GVL yields and GVL/2BL ratios.

The thermally regenerated solids 1.40Hf-D-HL(0.15) and 1.12Hf-D-HL(0.28) were reused and performed somewhat steadily for five consecutive 5 h-batch runs at 200°C (Figure 12). For the two catalysts, the contact tests (details in the experimental section) indicated that LP-CT led to similar results to those without catalyst; 14–15% LA conversion, 13–15% 2BL yield, and GVL was not formed (Figure 12). These results suggest that no active species were leached from the catalysts.

TABLE 1 Performance of the prepared catalysts in the reaction of  $\alpha$ -angelica lactone.<sup>a</sup>

Catalyst	AnL conversion (%)	Product yields (%)			
		LA	GVL	2BL	Total
HL	99	14	0	74	88
0.28Hf-HL	100	15	9	67	91
0.28Hf-D-HL(0.10)	98	0	18	75	93
D-HL(0.15)	98	8	0	89	97
0.28Hf-D-HL(0.15)	98	0	29	64	93
1.40Hf-D-HL(0.15)	99	0	34	60	94
0.28Hf-D-HL(0.20)	99	0	38	57	95
0.28Hf-D-HL(0.28)	100	0	45	49	94
1.12Hf-D-HL(0.28)	100	0	54	43	97

<sup>a</sup>Reaction conditions: 0.45 M AnL in 2BuOH, 25.5 g<sub>cat</sub> L<sup>-1</sup>, 200 °C, 24 h.  $\beta$ -Angelica lactone was formed for HL (0.8% yield); no measurable amounts of this isomer were obtained for the remaining catalytic tests.

TABLE 2 Performance of the prepared catalysts in the reaction of 5-(hydroxymethyl)furfural (HMF).<sup>a</sup>

Catalyst	HMF conversion (%)	Product yields (%)				
		5MF	2BL	BMF	BBMF	Total
HL	95	10	6	75	0	91
0.28Hf-HL	77	14	3	35	8	90
0.28Hf-D-HL(0.10)	92	9	2	59	4	74
D-HL(0.15)	90	8	4	73	0	85
0.28Hf-D-HL(0.15)	85	11	1	54	7	73
1.40Hf-D-HL(0.15)	68	9	1	10	7	16
0.28Hf-D-HL(0.20)	79	12	1	48	12	73
0.28Hf-D-HL(0.28)	71	22	4	20	21	67
1.12Hf-D-HL(0.28)	60	12	2	13	12	39

<sup>a</sup>Reaction conditions: 0.45 M HMF, in 2BuOH, 25.5 g<sub>cat</sub> L<sup>-1</sup>, 200°C, 24 h.

Consistently, EDS of the fresh and used catalysts indicated that Si/Al and Si/Hf remained similar: for fresh and used 1.40Hf-D-HL(0.15), Si/Al = 8 and Si/Hf = 8; for fresh and used 1.12Hf-D-HL(0.28), Si/Al = 40 and 44, respectively, and Si/Hf = 9 for the two solids. Not only the PXRD patterns (Supplementary Figure S11), but also the morphology and metal distributions (Supplementary Figure S12), textural and acid properties (Supplementary Table S5) of the fresh and used catalysts were roughly comparable, suggesting that the materials were relatively stable.

### 3.2.2 Reaction of $\alpha$ -angelica lactone

The reaction of AnL to GVL involves acid and reduction chemistry (e.g., hydration, CTH and lactonization) (Li et al., 2018; Antunes et al., 2022a, 2022b). According to the literature, the reversible reaction between AnL and LA may occur via

hydration-dehydration (Dutta and Bhat, 2021; Liu et al., 2021; Yuan et al., 2021), but AnL was not detected in the experiments using LA as substrate, whereas LA was formed using AnL as substrate. This is in agreement with literature studies for Hf-containing catalysts in alcohol media (Al-Shaal et al., 2015; Li et al., 2018; Antunes et al., 2022b, 2022a).

The reaction of AnL in the presence of HL and D-HL(0.15) gave LA and 2BL in high total yields (88 and 97% yield, respectively, at *ca.* 100% conversion, 200 °C/24 h), but no GVL was formed (Table 1). Hence, the aluminosilicate supports were essentially effective for converting AnL to 2BL.

The introduction of hafnium was required to confer CTH activity for GVL formation (Table 1). A comparison of 0.28Hf-HL (non-desilicated) and 0.28Hf-D-HL(0.15) (desilicated), both subjected to the same acid treatment ( $x = 0.15$  M H<sub>2</sub>SO<sub>4</sub>), indicates a favourable effect of desilication on GVL yield;



9 and 29% for the non-desilicated and the desilicated materials, respectively, at 91–93% AnL conversion, 200°C/24 h.

Increasing  $x$  from 0.10 to 0.28 led to 2BL plus GVL, which were formed in a total yield in the range 93–94% at 98–100% AnL conversion (Table 1). In parallel to that verified with LA as substrate, the GVL/2BL ratio (and GVL yields) increased with decreasing  $S_{\text{micro}}/S_{\text{EM}}$  (increasing  $x$ ) (Supplementary Figure S13A).

To check the influence of the Hf loading on the AnL reaction, comparative studies were carried out for  $\gamma\text{Hf-D-HL}(0.15)$  with  $y = 0.28$  and 1.40, and, on the other hand, for  $\gamma\text{Hf-D-HL}(0.28)$  with  $y = 0.28$  and 1.12 (Table 1). For each pair of materials with equal  $x$ , the GVL/2BL ratio and GVL yields were higher for the catalyst with higher  $y$ ; the best results were obtained for 1.12Hf-D-HL(0.28), i.e., 54% GVL yield and GVL/2BL = 1.26, at 100% AnL conversion, 200°C/24 h.

### 3.2.3 Reaction of 5-(Hydroxymethyl)furfural

Catalysts  $\gamma\text{Hf-D-HL}(x)$  were further explored for the reaction of HMF (Table 2). The aluminosilicates HL and D-HL(0.15) led to somewhat comparable results; 5-methylfurfural (5MF), 2BL and 5-(*sec*-butoxymethyl)furfural (BMF) were formed in total yields of 91 and 85%, at 95 and 90% HMF conversion, respectively, 200°C/24 h. The main product was BMF (73–75% yield) which may be formed via etherification of HMF. HMF to BMF may be enhanced by B acid sites (Ly et al., 2017). BMF may undergo acid-catalyzed ring-opening to 2BL, although the latter was formed in only 4–6% yield. On the other hand, 5MF was formed in 8–10% yield. Ly et al. reported minor amounts of 5MF formed in the reaction of HMF in the presence of Al/SiO<sub>2</sub> (aluminium supported on a commercial silica) in 2BuOH at 180°C/6 h (Ly et al., 2017). Elsayed et al. reported HMF to 5MF in 1-butanol, at 200°C, in the presence of Zr-Fe magnetic supported on activated carbon (Elsayed et al., 2021). Hence, 5MF may be a by-product in CTH/alcohol systems.

The introduction of hafnium in the materials led mainly to BMF (e.g., 35 and 54% yield for (non-desilicated) 0.28Hf-HL and (desilicated) 0.28Hf-D-HL(0.15), respectively). 2BL was formed in very low amounts, and thus the subsequent conversion of 2BL to GVL did not take place to a measurable extent (Table 2). The diether 2,5-bis(*sec*-butoxymethyl)furan (BBMF) was formed in up to 21% yield at 200°C/24 h, only in the presence of the Hf-containing catalysts. This path may involve integrated acid (etherification) and CTH (carbonyl group reduction) reactions.

Increasing  $x$  for the 0.28Hf-D-HL( $x$ ) materials led to decreasing HMF conversion and increasing BBMF yield (Table 2). Although the amounts of B and L acid sites decreased with increasing  $x$ ,  $S_{\text{micro}}/S_{\text{EM}}$  decreased, favouring BBMF formation (Supplementary Figure S13B). Steric effects may be important for materials with higher  $S_{\text{micro}}/S_{\text{EM}}$ , negatively impacting on the formation of the relatively bulky diether BBMF.

The effect of the Hf loading was studied for  $\gamma\text{Hf-D-HL}(0.15)$  ( $y = 0.28$ , 1.40 mmol<sub>Hf</sub> g<sup>−1</sup>) and  $\gamma\text{Hf-D-HL}(0.28)$  ( $y = 0.28$ , 1.12

(Table 2). A higher Hf loading did not enhance HMF conversion, total product yields or BBMF yields. No clear relationship could be established between the L acid strength of all the Hf-containing catalysts and BBMF yields. These results did not parallel those for the integrated acid-CTH reactions of LA. According to the literature, the optimal material properties (e.g., L acidity) of Hf-zeolites for CTH reaction systems may depend on the type of substrate (Luo et al., 2014). HMF is a relatively bulky molecule and somewhat less reactive than LA and AnL, which may pose different requirements on materials properties.

## 4 Conclusion

Hierarchical multifunctional LTL zeotypes were prepared for the chemical valorization of HMF, LA and AnL via integrated catalytic transfer hydrogenation (CTH) and acid reactions in 2-butanol (2BuOH) at 200°C. This is the first CTH application reported for LTL related materials.

The catalysts were prepared via top-down strategies involving desilication, dealumination ( $x = 0.10$ –0.28 M H<sub>2</sub>SO<sub>4</sub>) and solid-state impregnation (SSI) of different amounts of hafnium ( $y$ ), giving  $\gamma\text{Hf-D-HL}(x)$ . The influence of the Hf loading ( $y$ ) was studied for two groups of materials  $\gamma\text{Hf-D-HL}(x)$  with  $x = 0.15$  (crystalline micro/mesoporous) and  $x = 0.28$  (mostly amorphous, mesoporous).

Molecular level spectroscopic studies indicated: broader distributions of Al<sub>tetra</sub> sites with increasing  $x$ ; SSI/calcination introduced Lewis acid Hf sites; and the Hf loading ( $y$ ) may affect, to different extents, the textural properties, distributions and types (and strength) of acid sites, etc. Mechanistic and kinetic studies suggested that Al sites may promote esterification and etherification reactions (e.g., LA to 2BL), whereas Hf sites were required for CTH (e.g., GVL formation from LA and AnL).

For materials with  $y = 0.28$  mmol<sub>Hf</sub> g<sup>−1</sup> (lower Hf loading), GVL yields increased with decreasing Lewis acid strength and  $S_{\text{micro}}/S_{\text{EM}}$  ratio. The decreasing L acid strength may avoid strongly adsorbed carbonaceous matter on the catalysts, and, on the other hand, lower  $S_{\text{micro}}/S_{\text{EM}}$  may avoid steric hindrance and facilitate cyclization of intermediates (especially of relatively bulky ones, e.g., esters versus corresponding carboxylic acids), enhancing GVL formation. For materials with  $y > 0.28$  mmol<sub>Hf</sub> g<sup>−1</sup>, GVL formation may depend on an interplay of several factors, e.g., L acid strength, distribution and type of acid sites.

Although 0.28Hf-D-HL(0.28) was mostly amorphous and mesoporous, it performed far superiorly to ordered mesoporous hafnium silicate Hf-TUD-1 possessing similar Hf loading. The top-down strategy and, on the other hand, having an LTL zeolite in its genesis, may result in unique surface properties of  $\gamma\text{Hf-D-HL}(0.28)$  type materials. The 1.12Hf-D-HL(0.28) catalyst led to 77% GVL yield at 200°C/24 h (using 0.45 M initial LA

concentration), and 91% GVL yield at 200°C/5 h (0.11 M initial LA concentration).

HMF was a more demanding substrate than LA and AnL for the formation of GVL. The main product was BMF, and GVL was not formed in measurable amounts at 200°C/24 h. HMF conversion to BMF and 2BL did not require Hf sites (HL was effective), whereas the diether BBMF was solely formed in the presence of Hf-containing catalysts (21% yield for 0.28Hf-D-HL(0.28)).

Based on catalytic and characterization studies, the materials were relatively stable. The zirconium catalyst 0.28Zr-D-HL(0.15) possessed acid and CTH activity, but performed inferiorly to the analogue 0.28Hf-D-HL(0.15).

Overall, post-synthesis modifications of commercial LTL zeolites may broaden their catalytic application profiles. The top-down strategies and conditions may be optimized to tune material properties and meet superior catalytic performances. A challenge may be to further enhance mesoporosity without considerable reduction of crystallinity.

## Data availability statement

The original contributions presented in the study are included in the article/**Supplementary Material**, further inquiries can be directed to the corresponding authors.

## Author contributions

MA: data curation, formal analysis, investigation, methodology, conceptualization, writing—original draft preparation, validation, visualization, writing—review and editing. AFS: data curation, formal analysis, investigation, methodology, writing—original draft preparation. AF: data curation, formal analysis, investigation, methodology. FR: formal analysis, funding acquisition. PN: data curation, formal analysis. MP: visualization, writing—review and editing. AAV: conceptualization, validation, visualization, project administration, writing—review and editing, and supervision.

## Funding

This work was developed within the scope of the project CICECO-Aveiro Institute of Materials, UIDB/50011/2020, UIDP/50011/2020 & LA/P/0006/2020, financed by national funds through the FCT/MEC (PIDDAC). The positions held

by MMA and AF were funded by national funds (OE), through FCT, IP, in the scope of the framework contract foreseen in the numbers 4, 5 and 6 of article 23 of the Decree-Law 57/2016 of 29 August, changed by Law 57/2017 of 19 July. The position held by AFS was funded by Project POCI-01-0145-FEDER-030075 (COMPETE 2020 Operational Thematic Program for Competitiveness and Internationalization) co-financed by national funds through the FCT/MCTES and the European Union through the European Regional Development Fund under the Portugal 2020 Partnership Agreement. The NMR spectrometer used is part of the National NMR Network (PTNMR) and is partially supported by Infrastructure Project No 022161 (co-financed by FEDER through COMPETE 2020, POCI and PORL and FCT through PIDDAC).

## Acknowledgments

The authors are grateful to Dr. Rosário Soares from Chemistry Department, CICECO-Aveiro Institute of Materials (University of Aveiro) for the helpful measurements of RC (PXRD). The authors thank all funding institutions indicated in the previous section.

## Conflict of interest

The authors declare that the research was conducted in the absence of any commercial or financial relationships that could be construed as a potential conflict of interest.

## Publisher's note

All claims expressed in this article are solely those of the authors and do not necessarily represent those of their affiliated organizations, or those of the publisher, the editors and the reviewers. Any product that may be evaluated in this article, or claim that may be made by its manufacturer, is not guaranteed or endorsed by the publisher.

## Supplementary material

The Supplementary Material for this article can be found online at: <https://www.frontiersin.org/articles/10.3389/fchem.2022.1006981/full#supplementary-material>

## References

- Al-Ani, A., Haslam, J. J. C., Mordvinova, N. E., Lebedev, O. I., Vicente, A., Fernandez, C., et al. (2019). Synthesis of nanostructured catalysts by surfactant-templating of large-pore zeolites. *Nanoscale Adv.* 1, 2029–2039. doi:10.1039/c9na00004f
- Al-Shaal, M. G., Ciptonugroho, W., Holzhäuser, F. J., Mensah, J. B., Hausoul, P. J. C., and Palkovits, R. (2015). Catalytic upgrading of  $\alpha$ -angelica lactone to levulinic acid esters under mild conditions over heterogeneous catalysts. *Catal. Sci. Technol.* 5, 5168–5173. doi:10.1039/c5cy00446b
- Antonetti, C., Licursi, D., Fulignati, S., Valentini, G., and Galletti, A. M. R. (2016). New frontiers in the catalytic synthesis of levulinic acid: From sugars to raw and waste biomass as starting feedstock. *Catalysts* 6, 196. doi:10.3390/catal6120196
- Antunes, M. M., Lima, S., Neves, P., Magalhães, A. L., Fazio, E., Fernandes, A., et al. (2015). One-pot conversion of furfural to useful bio-products in the presence of a Sn, Al-containing zeolite beta catalyst prepared via post-synthesis routes. *J. Catal.* 329, 522–537. doi:10.1016/j.jcat.2015.05.022
- Antunes, M. M., Lima, S., Neves, P., Magalhães, A. L., Fazio, E., Neri, F., et al. (2016a). Integrated reduction and acid-catalysed conversion of furfural in alcohol medium using Zr, Al-containing ordered micro/mesoporous silicates. *Appl. Catal. B Environ.* 182, 485–503. doi:10.1016/j.apcatb.2015.09.053
- Antunes, M. M., Neves, P., Fernandes, A., Lima, S., Silva, A. F., Ribeiro, M. F., et al. (2016b). Bulk and composite catalysts combining BEA topology and mesoporosity for the valorisation of furfural. *Catal. Sci. Technol.* 6, 7812–7829. doi:10.1039/c6cy00223d
- Antunes, M. M., Silva, A. F., Bernardino, C. D., Fernandes, A., Ribeiro, F., and Valente, A. A. (2021). Catalytic transfer hydrogenation and acid reactions of furfural and 5-(hydroxymethyl)furfural over Hf-TUD-1 type catalysts. *Molecules* 26, 7203. doi:10.3390/molecules26237203
- Antunes, M. M., Silva, A. F., Fernandes, A., Pillinger, M., Ribeiro, F., and Valente, A. A. (2022a). Renewable bio-based routes to  $\gamma$ -valerolactone in the presence of hafnium nanocrystalline or hierarchical microcrystalline zeotype catalysts. *J. Catal.* 406, 56–71. doi:10.1016/j.jcat.2021.12.022
- Antunes, M. M., Silva, A. F., Fernandes, A., and Valente, A. A. (2022b).  $\gamma$ -Valerolactone synthesis from  $\alpha$ -angelica lactone and levulinic acid over biobased multifunctional nanohybrid catalysts. *Catal. Today* 394–396, 268–281. doi:10.1016/j.cattod.2021.08.027
- Bassi, R., Baeza, P., Sepulveda, C., Ghampson, I. T., Camu, E., Brückner, A., et al. (2021). Conversion of levulinic acid over rhenium oxide catalysts: Effect of metal content. *Appl. Catal. A Gen.* 625, 118328. doi:10.1016/j.apcata.2021.118328
- Broach, R. W. (2010). “Zeolite types and structures,” in *Zeolites in industrial separation and catalysis*. Editor Dr. Santi Kulprathipanja (Glasgow: Wiley-VCH Verlag GmbH & Co. KGaA), 27–59. doi:10.1002/9783527629565
- Čejka, J., Millini, R., Opanasenko, M., Serrano, D. P., and Roth, W. J. (2020). Advances and challenges in zeolite synthesis and catalysis. *Catal. Today* 345, 2–13. doi:10.1016/j.cattod.2019.10.021
- Cheng, F., and Brewer, C. E. (2021). Conversion of protein-rich lignocellulosic wastes to bio-energy: Review and recommendations for hydrolysis + fermentation and anaerobic digestion. *Renew. Sustain. Energy Rev.* 146, 111167. doi:10.1016/j.rser.2021.111167
- Cho, J., Kim, S., Lee, D., Kim, B.-R., and Jung, J.-W. (2014). Method for producing biofuel using marine algae-derived galactan. *US Pat. U. S.* 8, 795393.
- Data Intelo (2022). *Global gamma valerolactone (CAS 108-29-2) market by type (food grade, industrial grade), by application (food flavors, solvent, monomer intermediate, others) and by region (North America, Latin America, Europe, Asia Pacific, and Middle East and Africa)*. Ontario, United States. Available at: <https://dataintel.com/report/global-gamma-valerolactone-%28cas-108-29-2%29-market/> (Accessed July 24, 2022).
- Di Bucchianico, D. D. M., Wang, Y., Buvat, J. C., Pan, Y., Casson Moreno, V., and Leveneur, S. (2022). Production of levulinic acid and alkyl levulinates: A process insight. *Green Chem.* 24, 614–646. doi:10.1039/d1gc02457d
- Dutta, S., and Bhat, N. S. (2021). Recent advances in the value addition of biomass-derived levulinic acid: A review focusing on its chemical reactivity patterns. *ChemCatChem* 13, 3202–3222. doi:10.1002/cctc.202100032
- Dutta, S. (2021). Valorization of biomass-derived furfurals: Reactivity patterns, synthetic strategies, and applications. *Biomass Convers. Biorefin.* doi:10.1007/s13399-021-01924-w
- Dutta, S., Yu, I. K. M., Tsang, D. C. W., Ng, Y. H., Ok, Y. S., Sherwood, J., et al. (2019). Green synthesis of gamma-valerolactone (GVL) through hydrogenation of biomass-derived levulinic acid using non-noble metal catalysts: A critical review. *Chem. Eng. J.* 372, 992–1006. doi:10.1016/j.cej.2019.04.199
- Elsayed, I., Jackson, M. A., and Hassan, E. B. (2021). Catalytic hydrogenation and etherification of 5-Hydroxymethylfurfural into 2-(alkoxymethyl)-5-methylfuran and 2, 5-bis(alkoxymethyl)furan as potential biofuel additives. *Fuel Process. Technol.* 213, 106672. doi:10.1016/j.fuproc.2020.106672
- Fact, M. R. (2022). 5-Hydroxymethylfurfural market. Available at: <https://www.factmr.com/report/5-hydroxymethylfurfural-market> (Accessed July 24, 2022).
- Fitzpatrick, S. W. (1995). Production of levulinic acid from carbohydrate-containing materials. US 5608105A.
- García, A., Miguel, P. J., Pico, M. P., Álvarez-Serrano, I., López, M. L., García, T., et al. (2021).  $\gamma$ -valerolactone from levulinic acid and its esters: Substrate and reaction media determine the optimal catalyst. *Appl. Catal. A Gen.* 623, 118276. doi:10.1016/j.apcata.2021.118276
- Gilkey, M. J., and Xu, B. (2016). Heterogeneous catalytic transfer hydrogenation as an effective pathway in biomass upgrading. *ACS Catal.* 6, 1420–1436. doi:10.1021/acscatal.5b02171
- Grand View Research (2021). *Levulinic acid market demand to reach 3,820 tons by 2020*. Available at: <https://www.grandviewresearch.com/press-release/global-levulinic-acid-market> (Accessed July 24, 2022).
- Gregg, S. J., and Sing, K. S. W. (1982). *Adsorption surface area and porosity*. 2nd ed. London, UK: Academic Press.
- Gruter, G. J. M. (2009). *Hydroxymethylfurfural ethers from sugars or HMF and branched alcohols*. WO/2009/030506.
- He, J., Li, H., Xu, Y., and Yang, S. (2020). Dual acidic mesoporous KIT silicates enable one-pot production of  $\gamma$ -valerolactone from biomass derivatives via cascade reactions. *Renew. Energy* 146, 359–370. doi:10.1016/j.renene.2019.06.105
- Hengne, A. M., Kadu, B. S., Biradar, N. S., Chikate, R. C., and Rode, C. V. (2016). Transfer hydrogenation of biomass-derived levulinic acid to  $\gamma$ -valerolactone over supported Ni catalysts. *RSC Adv.* 6, 59753–59761. doi:10.1039/c6ra08637c
- Hou, Q., Qi, X., Zhen, M., Qian, H., Nie, Y., Bai, C., et al. (2021). Biorefinery roadmap based on catalytic production and upgrading 5-hydroxymethylfurfural. *Green Chem.* 23, 119–231. doi:10.1039/d0gc02770g
- Hu, L., Jiang, Y., Wang, X., He, A., Xu, J., and Wu, Z. (2020). Recent advances and mechanistic insights on the production of biomass-derived 2, 5-bis(alkoxymethyl) furans. *Biomass Convers. Biorefin.* doi:10.1007/s13399-020-01062-9
- Hu, L., Xu, J., Zhou, S., He, A., Tang, X., Lin, L., et al. (2018). Catalytic advances in the production and application of biomass-derived 2, 5-dihydroxymethylfuran. *ACS Catal.* 8, 2959–2980. doi:10.1021/acscatal.7b03530
- Huang, X., Liu, K., Vrijburg, W. L., Ouyang, X., Iulian Dugulan, A., Liu, Y., et al. (2020). Hydrogenation of levulinic acid to  $\gamma$ -valerolactone over Fe-Re/TiO<sub>2</sub> catalysts. *Appl. Catal. B Environ.* 278, 119314. doi:10.1016/j.apcatb.2020.119314
- Huang, R., Liu, Y., Zhang, J., Wei, J., Peng, L., and Tang, X. (2021). Catalytic transfer hydrogenation of levulinic acid to  $\gamma$ -valerolactone over an acids-base trifunctional Hf-bagase coordination complex derived catalyst. *Fuel* 305, 121557. doi:10.1016/j.fuel.2021.121557
- Jori, P. K., and Jadhav, V. H. (2020). Efficient synthesis of  $\gamma$ -valerolactone-A potential fuel from biomass derived levulinic acid using catalytic transfer hydrogenation over Hf@CCSO<sub>3</sub>H catalyst. *Catal. Lett.* 150, 2038–2044. doi:10.1007/s10562-020-03119-w
- Kong, Q. S., Li, X. L., Xu, H. J., and Fu, Y. (2020). Conversion of 5-hydroxymethylfurfural to chemicals: A review of catalytic routes and product applications. *Fuel Process. Technol.* 209, 106528. doi:10.1016/j.fuproc.2020.106528
- Kong, X., Zhu, Y., Fang, Z., Kozinski, J. A., Butler, I. S., Xu, L., et al. (2018). Catalytic conversion of 5-hydroxymethylfurfural to some value-added derivatives. *Green Chem.* 20, 3657–3682. doi:10.1039/c8gc00234g
- Koul, B., Yakoob, M., and Shah, M. P. (2022). Agricultural waste management strategies for environmental sustainability. *Environ. Res.* 206, 112285. doi:10.1016/j.envres.2021.112285
- Kumar, A., and Srivastava, R. (2019). CePO<sub>4</sub>, a multi-functional catalyst for carbohydrate biomass conversion: Production of 5-hydroxymethylfurfural, 2,5-diformylfuran, and  $\gamma$ -valerolactone. *Sustain. Energy Fuels* 3, 2475–2489. doi:10.1039/c9se00272c
- Kumar, V. V., Nareesh, G., Sudhakar, M., Anjaneyulu, C., Bhargava, S. K., Tardio, J., et al. (2016). An investigation on the influence of support type for Ni catalysed vapour phase hydrogenation of aqueous levulinic acid to  $\gamma$ -valerolactone. *RSC Adv.* 6, 9872–9879. doi:10.1039/c5ra24199e
- Kumaravel, S., Thiripuranthagan, S., Durai, M., Erusappan, E., and Vembuli, T. (2020). Catalytic transfer hydrogenation of biomass-derived levulinic acid to  $\gamma$ -

- valerolactone over Sn/Al-SBA-15 catalysts. *New J. Chem.* 44, 8209–8222. doi:10.1039/d0nj01288b
- Kuwahara, Y., Kaburagi, W., and Fujitani, T. (2014). Catalytic conversion of Levulinic Acid and its esters to  $\gamma$ -valerolactone over silica-supported zirconia catalysts. *Bull. Chem. Soc. Jpn.* 87, 1252–1254. doi:10.1246/bcsj.20140205
- Kuwahara, Y., Kaburagi, W., Osada, Y., Fujitani, T., and Yamashita, H. (2017). Catalytic transfer hydrogenation of biomass-derived levulinic acid and its esters to  $\gamma$ -valerolactone over ZrO<sub>2</sub> catalyst supported on SBA-15 silica. *Catal. Today* 281, 418–428. doi:10.1016/j.cattod.2016.05.016
- Kuznetsova, E. D., Blatova, O. A., and Blatov, V. A. (2018). Predicting new zeolites: A combination of thermodynamic and kinetic factors. *Chem. Mater.* 30, 2829–2837. doi:10.1021/acs.chemmater.8b00905
- Lee, K., and Choi, M. (2016). Hierarchically micro-/mesoporous Pt/KL for alkane aromatization: Synergistic combination of high catalytic activity and suppressed hydrogenolysis. *J. Catal.* 340, 66–75. doi:10.1016/j.jcat.2016.05.010
- Li, F., France, L. J., Cai, Z., Li, Y., Liu, S., Lou, H., et al. (2017). Catalytic transfer hydrogenation of butyl levulinate to  $\gamma$ -valerolactone over zirconium phosphates with adjustable Lewis and Brønsted acid sites. *Appl. Catal. B Environ.* 214, 67–77. doi:10.1016/j.apcatb.2017.05.013
- Li, H., Fang, Z., and Yang, S. (2016a). Direct catalytic transformation of biomass derivatives into biofuel component  $\gamma$ -valerolactone with magnetic nickel-zirconium nanoparticles. *ChemPlusChem* 81, 135–142. doi:10.1002/cplu.201500492
- Li, H., Yang, S., Riisager, A., Pandey, A., Sangwan, R. S., Saravanamurugan, S., et al. (2016b). Zeolite and zeotype-catalysed transformations of biofuranic compounds. *Green Chem.* 18, 5701–5735. doi:10.1039/c6gc02415g
- Li, H., Yang, T., and Fang, Z. (2018). Biomass-derived mesoporous Hf-containing hybrid for efficient Meerwein-Ponndorf-Verley reduction at low temperatures. *Appl. Catal. B Environ.* 227, 79–89. doi:10.1016/j.apcatb.2018.01.017
- Li, J., Zhao, S., Li, Z., Liu, D., Chi, Y., and Hu, C. (2021). Efficient conversion of biomass-derived levulinic acid to  $\gamma$ -valerolactone over polyoxometalate@Zr-based Metal–Organic frameworks: The synergistic effect of Brønsted and Lewis acidic sites. *Inorg. Chem.* 60, 7785–7793. doi:10.1021/acs.inorgchem.1c00185
- Li, X., Du, Z., Wu, Y., Zhen, Y., Shao, R., Li, B., et al. (2020). A novel hafnium-graphite oxide catalyst for the Meerwein-Ponndorf-Verley reaction and the activation effect of the solvent. *RSC Adv.* 10, 9985–9995. doi:10.1039/c9ra10795a
- Liguori, F., Moreno-Marroán, C., and Barbaro, P. (2015). Environmentally friendly synthesis of  $\gamma$ -valerolactone by direct catalytic conversion of renewable sources. *ACS Catal.* 5, 1882–1894. doi:10.1021/cs501922e
- Lima, C. G. S., Monteiro, J. L., de Melo Lima, T., Weber Paixão, M., and Corrêa, A. G. (2018). Angelica lactones: From biomass-derived platform chemicals to value-added products. *ChemSusChem* 11, 25–47. doi:10.1002/cssc.201701469
- Liu, X., Yu, D., Luo, H., and Li, C. (2022). Catalytic upgrading of lignocellulosic biomass sugars toward biofuel 5-ethoxymethylfurfural. *Front. Chem.* 9, 831102. doi:10.3389/fchem.2021.831102
- Liu, Y., Liu, X., Li, M., Meng, Y., Li, J., Zhang, Z., et al. (2021). Recyclable Zr/Hf-containing acid-base bifunctional catalysts for hydrogen transfer upgrading of biofurans: A review. *Front. Chem.* 9, 812331. doi:10.3389/fchem.2021.812331
- López-Aguado, C., Paniagua, M., Melero, J. A., Iglesias, J., Juárez, P., Granados, M. L., et al. (2020). Stable continuous production of  $\gamma$ -valerolactone from biomass-derived levulinic acid over Zr-Al-Beta zeolite catalyst. *Catalysts* 10, 678. doi:10.3390/catal10060678
- Lu, Y., Wang, Y., Tang, Q., Cao, Q., and Fang, W. (2022). Synergy in Sn-Mn oxide boosting the hydrogenation catalysis of supported Pt nanoparticles for selective conversion of levulinic acid. *Appl. Catal. B Environ.* 300, 120746. doi:10.1016/j.apcatb.2021.120746
- Luo, H. Y., Consoli, D. F., Gunther, W. R., and Román-Leshkov, Y. (2014). Investigation of the reaction kinetics of isolated Lewis acid sites in Beta zeolites for the Meerwein-Ponndorf-Verley reduction of methyl levulinate to  $\gamma$ -valerolactone. *J. Catal.* 320, 198–207. doi:10.1016/j.jcat.2014.10.010
- Ly, N., Al-Shamery, K., Chan-Thaw, C. E., Prati, L., Carniti, P., and Gervasini, A. (2017). Impact of support oxide acidity in Pt-catalyzed HMF hydrogenation in alcoholic medium. *Catal. Lett.* 147, 345–359. doi:10.1007/s10562-016-1945-9
- Lynch, C. T., Mazdiyasn, K. S., Smith, J. S., and Crawford, W. J. (1964). Infrared spectra of transition metal alkoxides. *Anal. Chem.* 36, 2332–2337. doi:10.1021/ac60218a034
- Mafra, L., Vidal-moya, J. A., and Blasco, T. (2012). “Structural characterization of zeolites by advanced solid state NMR spectroscopic methods,” in *Annual reports on NMR spectroscopy* (Elsevier B.V.), 259–351. doi:10.1016/B978-0-12-397020-6.00004-0
- Manzer, L. (2005). Preparation of levulinic acid esters from  $\alpha$ -angelic lactone and olefins; use of ester compositions as fuel additives. WO 2005/075405.
- Maumela, M., Marx, S., and Meijboom, R. (2021). Heterogeneous Ru catalysts as the emerging potential superior catalysts in the selective hydrogenation of bio-derived levulinic acid to  $\gamma$ -valerolactone: Effect of particle size, solvent, and support on activity, stability, and selectivity. *Catalysts* 11. doi:10.3390/catal11020292
- Mon, M., and Leyva-Pérez, A. (2021). “Chapter Two - zeolites catalyze selective reactions of large organic molecules,” in *Advances in catalysis*. Editors O. Diéguez, Montserrat, and Pàmies (Elsevier B.V.), 59–102.
- Morales, G., Melero, J. A., Iglesias, J., Paniagua, M., and López-Aguado, C. (2019). From levulinic acid biorefineries to  $\gamma$ -valerolactone (GVL) using a bi-functional Zr-Al-Beta catalyst. *React. Chem. Eng.* 4, 1834–1843. doi:10.1039/c9re00117d
- Mordor Intelligence (2022). Levulinic acid market- growth, trends, covid-19 impact, and forecasts (2022–2027). Available at: <https://www.mordorintelligence.com/industry-reports/levulinic-acid-market> (Accessed July 24, 2022).
- Morone, A., Apte, M., and Pandey, R. A. (2015). Levulinic acid production from renewable waste resources: Bottlenecks, potential remedies, advancements and applications. *Renew. Sustain. Energy Rev.* 51, 548–565. doi:10.1016/j.rser.2015.06.032
- Nandiyanto, A. B. D., Oktiani, R., and Ragadhita, R. (2019). How to read and interpret FTIR spectroscopy of organic material. *Indones. J. Sci. Technol.* 4, 97–118. doi:10.17509/ijost.v4i1.15806
- Narisetty, V., Cox, R., Bommarreddy, R., Agrawal, D., Ahmad, E., Pant, K. K., et al. (2022). Valorisation of xylose to renewable fuels and chemicals, an essential step in augmenting the commercial viability of lignocellulosic biorefineries. *Sustain. Energy Fuels* 6, 29–65. doi:10.1039/d1se00927c
- Nie, R., Tao, Y., Nie, Y., Lu, T., Wang, J., Zhang, Y., et al. (2021). Recent advances in catalytic transfer hydrogenation with formic acid over heterogeneous transition metal catalysts. *ACS Catal.* 11, 1071–1095. doi:10.1021/acscatal.0c04939
- Nilesh, Q., Tangale, P., Sonar, S. K., Niphadkar, P. S., and Joshi, P. N. (2016). Hierarchical K/LTL zeolites: Synthesis by alkali treatment, characterization and catalytic performance in Knoevenagel condensation reaction. *J. Ind. Eng. Chem.* 40, 128–136. doi:10.1016/j.jiec.2016.06.016
- Ostovar, S., Saravani, H., and Rodríguez-Padrón, D. (2021). Versatile functionalized mesoporous Zr/SBA-15 for catalytic transfer hydrogenation and oxidation reactions. *Renew. Energy* 178, 1070–1083. doi:10.1016/j.renene.2021.06.095
- O'Dell, L. A. G., Philips, N., Holland, M. A., Mountjoy, G., Pickup, D. M., Newport, R. J., et al. (2008). Characterisation of sol-gel prepared (HfO<sub>2</sub>)<sub>x</sub>(SiO<sub>2</sub>)<sub>1-x</sub> (x = 0.1, 0.2 and 0.4) by <sup>1</sup>H, <sup>13</sup>C, <sup>17</sup>O and <sup>29</sup>Si MAS NMR, FTIR and TGA. *Solid State Nucl. Magn. Reson.* 33, 16–24. doi:10.1016/j.ssnmr.2007.11.001
- Poullikkas, A., Omidvarborna, H., and Kim, D. S. (2017). A review on synthesis of alkoxymethyl furfural, a biofuel candidate. *Renew. Sustain. Energy Rev.* 71, 908–926. doi:10.1016/j.rser.2016.12.118
- Ravi, M., Sushkevich, V. L., and Bokhoven, J. A. V. (2021). On the location of Lewis acidic aluminum in zeolite mordenite and the role of framework-associated aluminum in mediating the switch between Brønsted and Lewis acidity. *Chem. Sci.* 12, 4094–4103. doi:10.1039/d0sc06130a
- Rojas-Buzo, S., García-García, P., and Corma, A. (2018). Catalytic transfer hydrogenation of biomass-derived carbonyls over hafnium-based metal-organic frameworks. *ChemSusChem* 11, 432–438. doi:10.1002/cssc.201701708
- Roy, S., Dikshit, P. K., Sherpa, K. C., Singh, A., Jacob, S., and Chandra Rajak, R. (2021). Recent nanobiotechnological advancements in lignocellulosic biomass valorization: A review. *J. Environ. Manage.* 297, 113422. doi:10.1016/j.jenvman.2021.113422
- Sajid, M., Farooq, U., Bary, G., Azim, M. M., and Zhao, X. (2021). Sustainable production of levulinic acid and its derivatives for fuel additives and chemicals: Progress, challenges, and prospects. *Green Chem.* 23, 9198–9238. doi:10.1039/d1gc02919c
- Serrano, D. P., Melero, J. A., Morales, G., Iglesias, J., and Pizarro, P. (2018). Progress in the design of zeolite catalysts for biomass conversion into biofuels and bio-based chemicals. *Catal. Rev.* 60, 1–70. doi:10.1080/01614940.2017.1389109
- Tang, B., Li, S., Song, W. C., Yang, E. C., Zhao, X. J., Guan, N., et al. (2019). Hierarchical FAU-type hafnosilicate zeolite as a robust Lewis acid catalyst for catalytic transfer hydrogenation. *ACS Sustain. Chem. Eng.* 7, 16329–16343. doi:10.1021/acssuschemeng.9b03347
- Tang, X., Zeng, X., Li, Z., Li, W., Jiang, Y., Hu, L., et al. (2015). *In situ* generated catalyst system to convert biomass-derived levulinic acid to  $\gamma$ -valerolactone. *ChemCatChem* 7, 1372–1379. doi:10.1002/cctc.201500115
- Tangale, N. P., Niphadkar, P. S., Joshi, P. N., and Dhepe, P. L. (2019). Hierarchical K/LTL zeolite as solid base for aqueous phase hydrogenation of xylose to xylitol. *Microporous Mesoporous Mater.* 278, 70–80. doi:10.1016/j.micromeso.2018.11.017
- Valekar, A. H., Cho, K. H., Chitale, S. K., Hong, D. Y., Cha, G. Y., Lee, U. H., et al. (2016). Catalytic transfer hydrogenation of ethyl levulinate to  $\gamma$ -valerolactone over



zirconium-based metal-organic frameworks. *Green Chem.* 18, 4542–4552. doi:10.1039/c6gc00524a

Vu, H. T., Harth, F. M., Goepel, M., Linares, N., García-Martínez, J., and Gläser, R. (2022). Enhanced activity of a bifunctional Pt/zeolite Y catalyst with an intracrystalline hierarchical pore system in the aqueous-phase hydrogenation of levulinic acid. *Chem. Eng. J.* 430, 132763. doi:10.1016/j.cej.2021.132763

Wang, J., Liu, J., Yu, X., Zhang, W., Zhang, G., Liu, M., et al. (2020). Non-noble metal catalysts for transfer hydrogenation of levulinic acid: The role of surface morphology and acid-base pairs. *Mat. Today Energy* 18, 100501. doi:10.1016/j.mtener.2020.100501

Wang, R., Wang, J., Zi, H., Xia, Y., Wang, H., and Liu, X. (2017). Catalytic transfer hydrogenation of ethyl levulinate to  $\gamma$ -valerolactone over zirconium(IV) Schiff base complexes on mesoporous silica with isopropanol as hydrogen source. *Mol. Catal.* 441, 168–178. doi:10.1016/j.mcat.2017.07.026

Weng, R., Yu, Z., Xiong, J., and Lu, X. (2020). Effects of water in the heterogeneous catalytic valorization of levulinic acid into  $\gamma$ -valerolactone and its derivatives. *Green Chem.* 22, 3013–3027. doi:10.1039/d0gc01082k

Werpy, T., and Petersen, G. (2004). *Top value added chemicals from biomass volume I*. United States: National Renewable Energy Lab, 76. doi:10.2172/15008859

Winoto, H. P., Ahn, B. S., and Jae, J. (2016). Production of  $\gamma$ -valerolactone from furfural by a single-step process using Sn-Al-Beta zeolites: Optimizing the catalyst acid properties and process conditions. *J. Ind. Eng. Chem.* 40, 62–71. doi:10.1016/j.jiec.2016.06.007

Winoto, H. P., Fikri, Z. A., Ha, J. M., Park, Y. K., Lee, H., Suh, D. J., et al. (2019). Heteropolyacid supported on Zr-Beta zeolite as an active catalyst for one-pot transformation of furfural to  $\gamma$ -valerolactone. *Appl. Catal. B Environ.* 241, 588–597. doi:10.1016/j.apcatb.2018.09.031

Xie, C., Song, J., Zhou, B., Hu, J., Zhang, Z., Zhang, P., et al. (2016). Porous hafnium phosphonate: Novel heterogeneous catalyst for conversion of levulinic acid and esters into  $\gamma$ -valerolactone. *ACS Sustain. Chem. Eng.* 4, 6231–6236. doi:10.1021/acssuschemeng.6b02230

Xu, S., Yu, D., Ye, T., and Tian, P. (2017). Catalytic transfer hydrogenation of levulinic acid to  $\gamma$ -valerolactone over a bifunctional tin catalyst. *RSC Adv.* 7, 1026–1031. doi:10.1039/c6ra25594a

Xue, Z., Liu, Q., Wang, J., and Mu, T. (2018). Valorization of levulinic acid over non-noble metal catalysts: Challenges and opportunities. *Green Chem.* 20, 4391–4408. doi:10.1039/c8gc02001a

Yakimov, A. V., Ravi, M., Verel, R., Sushkevich, V. L., Bokhoven, J. A. V., and Cop, C. (2022). Structure and framework association of Lewis acid sites in MOR zeolite. *J. Am. Chem. Soc.* 144, 10377–10385. doi:10.1021/jacs.2c02212

Yu, Z., Lu, X., Bai, H., Xiong, J., Feng, W., and Ji, N. (2020a). Effects of solid acid supports on the bifunctional catalysis of levulinic acid to  $\gamma$ -valerolactone: Catalytic activity and stability. *Chem. Asian J.* 15, 1182–1201. doi:10.1002/asia.202000006

Yu, Z., Lu, X., Liu, C., Han, Y., and Ji, N. (2019). Synthesis of  $\gamma$ -valerolactone from different biomass-derived feedstocks: Recent advances on reaction mechanisms and catalytic systems. *Renew. Sustain. Energy Rev.* 112, 140–157. doi:10.1016/j.rser.2019.05.039

Yu, Z., Lu, X., Xiong, J., Li, X., Bai, H., and Ji, N. (2020b). Heterogeneous catalytic hydrogenation of levulinic acid to  $\gamma$ -valerolactone with formic acid as internal hydrogen source. *ChemSusChem* 13, 2916–2930. doi:10.1002/cssc.2020000175

Yuan, Q., Van De Bovenkamp, H. H., Zhang, Z., Piskun, A. S., Sami, S., Havenith, R. W. A., et al. (2021). Mechanistic investigations into the catalytic levulinic acid hydrogenation, insight in H/D exchange pathways, and a synthetic route to  $d_8$ - $\gamma$ -valerolactone. *ACS Catal.* 11, 10467–10477. doi:10.1021/acscatal.1c02662

Zhang, Z. (2016). Synthesis of  $\gamma$ -valerolactone from carbohydrates and its applications. *ChemSusChem* 9, 156–171. doi:10.1002/cssc.201501089

Zhou, Y. H., Luo, Y. J., Lin, Y. T., and Huang, Y. B. (2018). Enhanced transfer hydrogenation activity of Zr-doped mesoporous silica through sol-gel method for the reduction of biomass-derived unsaturated carbon-oxygen bonds. *ChemistrySelect* 3, 11071–11080. doi:10.1002/slct.201802176

Zhu, Z., Xu, H., Jiang, J., Liu, X., Ding, J., and Wu, P. (2016). Applied Catalysis A: General Postsynthesis of FAU-type stannosilicate as efficient heterogeneous catalyst for Baeyer-Villiger oxidation. *Appl. Catal. A Gen.* 519, 155–164. doi:10.1016/j.apcata.2016.04.001



## OPEN ACCESS

## EDITED BY

Verónica De Zea Bermudez,  
University of Trás-os-Montes and Alto  
Douro, Portugal

## REVIEWED BY

Luiz Antônio S. Costa,  
Federal University of Juiz de Fora, Brazil  
Kiyoharu Tadanaga,  
Hokkaido University, Japan

## \*CORRESPONDENCE

Isabel S. Gonçalves,  
igoncalves@ua.pt  
J. Sérgio Seixas de Melo,  
sseixas@ci.uc.pt  
Martyn Pillinger,  
mpillinger@ua.pt

## SPECIALTY SECTION

This article was submitted to Inorganic  
Chemistry,  
a section of the journal  
Frontiers in Chemistry

RECEIVED 27 July 2022

ACCEPTED 26 September 2022

PUBLISHED 10 October 2022

## CITATION

Costa AL, Monteiro RP,  
Nunes Barradas PD, Ferreira SCR,  
Cunha C, Gomes AC, Gonçalves IS,  
Seixas de Melo JS and Pillinger M (2022),  
Enhanced thermal and photo-stability  
of a *para*-substituted dicumyl ketone  
intercalated in a layered  
double hydroxide.  
*Front. Chem.* 10:1004586.  
doi: 10.3389/fchem.2022.1004586

## COPYRIGHT

© 2022 Costa, Monteiro, Nunes  
Barradas, Ferreira, Cunha, Gomes,  
Gonçalves, Seixas de Melo and Pillinger.  
This is an open-access article  
distributed under the terms of the  
Creative Commons Attribution License  
(CC BY). The use, distribution or  
reproduction in other forums is  
permitted, provided the original  
author(s) and the copyright owner(s) are  
credited and that the original  
publication in this journal is cited, in  
accordance with accepted academic  
practice. No use, distribution or  
reproduction is permitted which does  
not comply with these terms.

# Enhanced thermal and photo-stability of a *para*-substituted dicumyl ketone intercalated in a layered double hydroxide

Ana L. Costa<sup>1</sup>, Rodrigo P. Monteiro<sup>1</sup>, Paulo D. Nunes Barradas<sup>2</sup>,  
Simone C. R. Ferreira<sup>2</sup>, Carla Cunha<sup>2</sup>, Ana C. Gomes<sup>1</sup>,  
Isabel S. Gonçalves<sup>1\*</sup>, J. Sérgio Seixas de Melo<sup>2\*</sup> and  
Martyn Pillinger<sup>1\*</sup>

<sup>1</sup>Department of Chemistry, CICECO—Aveiro Institute of Materials, University of Aveiro, Aveiro, Portugal, <sup>2</sup>Coimbra Chemistry Centre (CQC)-IMS, Department of Chemistry, University of Coimbra, Coimbra, Portugal

A ketodiacid, 4,4'-dicarboxylate-dicumyl ketone (**3**), has been intercalated into a Zn, Al layered double hydroxide (LDH) by a coprecipitation synthesis strategy. The structure and chemical composition of the resultant hybrid material (LDH-KDA3) were characterized by powder X-ray diffraction (PXRD), FT-IR, FT-Raman and solid-state <sup>13</sup>C{<sup>1</sup>H} NMR spectroscopies, scanning electron microscopy (SEM), energy-dispersive X-ray spectroscopy (EDS), thermogravimetric analysis (TGA), and elemental analysis (CHN). PXRD showed that the dicarboxylate guest molecules assembled into a monolayer to give a basal spacing of 18.0 Å. TGA revealed that the organic guest starts to decompose at a significantly higher temperature (ca. 330°C) than that determined for the free ketodiacid (ca. 230°C). Photochemical experiments were performed to probe the photoreactivity of the ketoacid in the crystalline state, in solution, and as a guest embedded within the photochemically-inert LDH host. Irradiation of the bulk crystalline ketoacid results in photodecarbonylation and the exclusive formation of the radical-radical combination product. Solution studies employing the standard myoglobin (Mb) assay for quantification of released CO showed that the ketoacid behaved as a photoactivatable CO-releasing molecule for transfer of CO to heme proteins, although the photoreactivity was low. No photoinduced release of CO was found for the LDH system, indicating that molecular confinement enhanced the photo-stability of the hexasubstituted ketone. To better understand the behavior of **3** under irradiation, a more comprehensive study, involving excitation of this compound in DMSO-d<sub>6</sub> followed by <sup>1</sup>H NMR, UV-Vis and fluorescence spectroscopy, was undertaken and further rationalized with the help of time-dependent density functional theory (TDDFT) electronic quantum calculations. The photophysical study showed the formation of a less emissive compound (or compounds). New signals in the <sup>1</sup>H NMR spectra were attributed to photoproducts obtained via Norrish type I α-cleavage decarbonylation and Norrish type II (followed by CH<sub>3</sub> migration) pathways. TDDFT calculations predicted that the formation of a

keto-enol system (*via* a CH<sub>3</sub> migration step in the type II pathway) was highly favorable and consistent with the observed spectral data.

#### KEYWORDS

hexasubstituted ketones, ketodiacid, photodecarbonylation, intercalation, layered double hydroxides, myoglobin assay, CO-releasing molecules, TDDFT calculations

## 1 Introduction

The decarbonylation of carbonyl compounds such as aldehydes and ketones is an important transformation in synthetic chemistry with broad application in the synthesis of natural products (Akanksha and Maiti, 2012; Morgan et al., 2010; Natarajan et al., 2007; Ng et al., 2004) and the upgrading of biomass-derived molecules to bio-fuels and feedstock chemicals (Geilen et al., 2011; Huang et al., 2013; Chatterjee et al., 2018). In organic synthesis, selective decarbonylation reactions are typically mediated by a transition metal complex, either in a stoichiometric or catalytic fashion (Lu et al., 2021). Metal-free decarbonylation may be achieved photochemically for certain families of carbonyl compounds (Houk, 1976; Suzuki et al., 2014), or, more rarely, by thermolysis [e.g., of *R*-(+)-lauroleal to give *R*-(+)-1,2,3-trimethylcyclopentene (Crawford and Tokunaga, 1980)] or by “on water” reactions in the presence of molecular oxygen (as in the specific case of tertiary aldehydes) (Rodrigues et al., 2011). Besides its use in decarbonylative organic synthesis, decarbonylation has found widespread use in carbonylative transformations in which the carbonyl compound is the source of carbon monoxide (usually termed CO surrogate), thereby eliminating the need to supply CO externally from a gas cylinder (Wu et al., 2014; Cao et al., 2017; Konishi and Manabe, 2019). Examples of common CO surrogates are formic acid, formates, formaldehyde, formamides, *N*-formylsaccharin, and silacarboxylic acids. In a parallel line of research, metal-free carbonyl compounds are attracting interest as pharmaceutical agents for the controlled delivery of therapeutic amounts of CO to treat inflammatory diseases (Antony et al., 2013; Peng et al., 2013; Anderson et al., 2015; Abeyrathna et al., 2017; Ji and Wang, 2018; Slanina and Šebej, 2018; Soboleva and Berreau, 2019). These prodrugs are referred to as organic CO-releasing molecules (oCORMs) and many of them work by photoinduced decarbonylation.

The chemistry of UV or near-UV light-induced liberation of CO from small organic carbonyl compounds has been well studied since the early 1970s (Collins et al., 1970; Horspool and Khandelwal, 1970; Chapman and McIntosh, 1971; Mikol and Boyer, 1972). Selective formation of decarbonylated products is possible for certain combinations of carbonyl-containing substrates (with the right structural features) and reaction conditions (type of solvent in the case of solution-phase photolysis, presence or absence of oxygen, excitation wavelength). Examples of monodecarbonylation syntheses are  $\alpha,\beta$ -unsaturated ketones from unsaturated lactones such as 2-

(3*H*)-furanones (Chapman and McIntosh, 1971; Lohray et al., 1984; Gopidas et al., 1987), olefins from  $\beta,\gamma$ -unsaturated aldehydes (Baggiolini et al., 1970; Houk, 1976), alkynes from cyclopropanones (Poloukhine and Popik, 2003), and various compounds from furan-2,3-diones [e.g., salicylic acid derivatives from coumarandiones in the presence of certain nucleophiles (Horspool and Khandelwal, 1970)]. A well-studied photobisdecarbonylation is the conversion of  $\alpha$ -diketones to acenes (Suzuki et al., 2014). These earlier studies laid the foundations for the recent and ongoing development of photoactivatable CORMs, which now encompass cyclic xanthene-9-carboxylic acid (Antony et al., 2013),  $\alpha$ -diketones (Peng et al., 2013), 3-hydroxyflavones (Anderson et al., 2015; Soboleva and Berreau, 2019), 3-hydroxy-4-oxoquinolines (Soboleva and Berreau, 2019), and diphenyl cyclopropanone-centered polymers (Shao et al., 2020), among others. Another highly productive and innovative branch of photodecarbonylation chemistry is the study of reactions in the solid state. Garcia-Garibay and co-workers have shown that the photoinduced decarbonylation of crystalline hexasubstituted ketones can cleanly and quantitatively afford compounds with adjacent quaternary stereogenic centers in one step (Mortko and Garcia-Garibay, 2005; Veerman et al., 2006; Family and Garcia-Garibay, 2009; Shiraki et al., 2011). In contrast, reactions in solution tend to yield mixtures of disproportionation and combination products. The high selectivity and specificity of the photodecarbonylation reactions in the crystalline state is due to confinement effects together with the geometrical constraints imposed by the rigid crystal lattice.

To the best of our knowledge, the photodecarbonylation of hexasubstituted ketones in the solid-state has only been studied for close-packed organic crystals. Supramolecular chemistry provides, however, several other strategies to control photoreactions through confinement of a substrate within an organizing medium, better known as host-guest chemistry (Ramamurthy and Gupta, 2015; Ramamurthy and Sivaguru, 2016). Examples of hosts which have been investigated include inorganic porous and layered materials [zeolites, clays, layered double hydroxides (LDHs)] (Ogawa and Kuroda, 1995; Scaiano and García, 1999; Shichi and Takagi, 2000; Ramamurthy, 2019), metallo-cages (Pd nanocage) (Karthikeyan and Ramamurthy, 2007; Ramamurthy and Gupta, 2015; Ramamurthy and Sivaguru, 2016), and organic molecular containers (cyclodextrins, cucurbiturils, calixarenes, octa-acid cavitand) (Karthikeyan and Ramamurthy, 2007; Ramamurthy,

2015; Ramamurthy and Gupta, 2015; Ramamurthy and Sivaguru, 2016; Pattabiraman et al., 2018). Among inorganic hosts, the interlayer region of LDHs provides an expandable two-dimensional (2D) reaction field for spatially controlled photochemical transformations (Ogawa and Kuroda, 1995; Newman and Jones, 1998). A range of organic guests may be incorporated (Newman and Jones, 1998). Normally, the geometrical constraint imposed by the host LDH layers leads to a highly ordered and well-defined arrangement of the guests inside the interlayer region. The main distinguishing feature of LDHs is that the guest species must possess a net negative charge to counterbalance the positive charge of the mixed metal hydroxide layers.

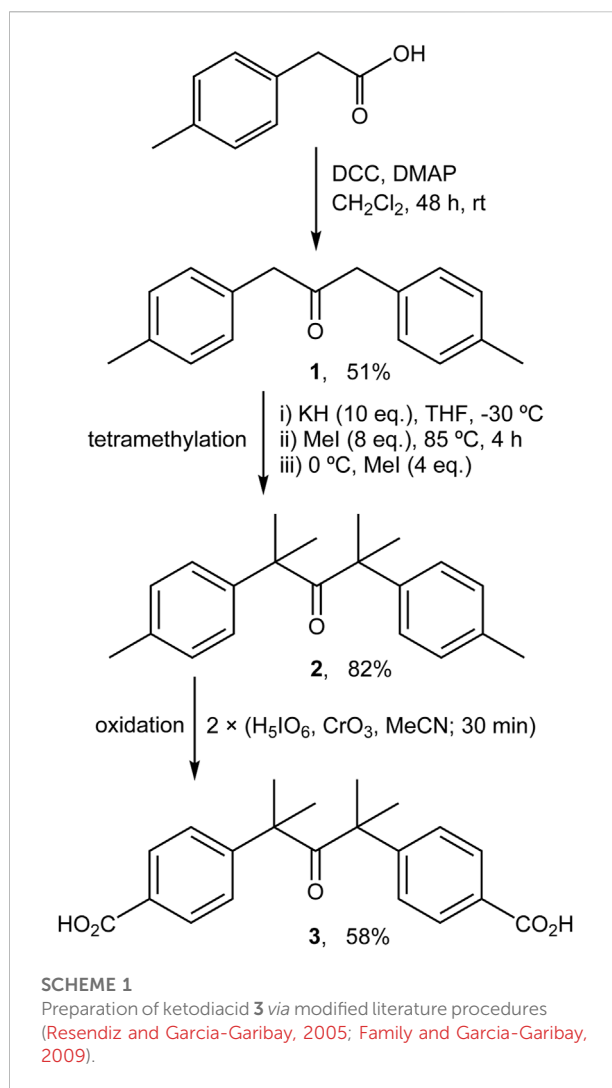
Among the hexasubstituted ketones studied by Garibay and co-workers, several of the photoreactive substrates were functionalized with carboxylate groups (Mortko and Garcia-Garibay, 2005; Family and Garcia-Garibay, 2009). These molecules should be ideal guests for LDHs. We therefore decided to prepare supramolecular LDH assemblies containing these ketoacids which would provide an opportunity to study the solid-state photodecarbonylation properties in a 2D reaction field. Here we report the synthesis and characterization of a zinc-aluminium LDH intercalated by a di-*p*-dicarboxylic acid derivative of dicumyl ketone, and a comparison of the photochemistry (in terms of photoproduct selectivities) of the ketodiacid in the crystalline state, in solution, and as a guest embedded within the LDH host.

## 2 Experimental

### 2.1 Materials and methods

The chemicals *N,N'*-dicyclohexylcarbodiimide, 4-(dimethylamino)pyridine, potassium hydride (30% in mineral oil), methyl iodide, periodic acid, chromium(VI) oxide,  $\text{Zn}(\text{NO}_3)_2 \cdot 6\text{H}_2\text{O}$  (98%, Fluka),  $\text{Al}(\text{NO}_3)_3 \cdot 9\text{H}_2\text{O}$  (98.5%, Riedel de-Haën), 1 M NaOH (Fluka),  $\text{Na}_2\text{S}_2\text{O}_4$  (Panreac), phosphate buffered saline (PBS) tablet, and 4-(2-hydroxyethyl)piperazine-1-ethanesulfonic acid (HEPES, 99.5%) were obtained from commercial sources (Sigma-Aldrich, unless otherwise indicated) and used as received. Lyophilized horse heart myoglobin and PBS solution were acquired from Sigma-Aldrich. THF (Aldrich) was dried over 4 Å molecular sieves. A nitrate-form Zn-Al LDH (denoted LDH- $\text{NO}_3$ ) with the composition  $\text{Zn}_4\text{Al}_2(\text{OH})_{12}(\text{NO}_3)_2 \cdot 2.5\text{H}_2\text{O}$  was prepared by using the standard method of coprecipitation of the  $\text{Zn}^{2+}$  and  $\text{Al}^{3+}$  hydroxides (initial  $\text{Zn}^{2+}/\text{Al}^{3+}$  molar ratio in solution = 2) in the presence of nitrate ions at a constant pH of 7.5–8 under nitrogen, followed by aging of the gel at 80°C for 20 h (Gomes et al., 2013; Costa et al., 2017).

FT-IR spectra were collected using KBr pellets and a Mattson-7000 infrared spectrophotometer. Solution  $^1\text{H}$  NMR



spectra were recorded either on a Bruker Avance III spectrometer operating at 400.13 MHz (for irradiated  $\text{DMSO-d}_6$  solutions) or (for all other measurements) a Bruker-AMX spectrometer. Solution  $^{13}\text{C}\{^1\text{H}\}$  NMR spectra were recorded on a Bruker-AMX spectrometer with an operating frequency of 101 MHz. Solid-state  $^{13}\text{C}\{^1\text{H}\}$  cross-polarization (CP) magic-angle spinning (MAS) NMR spectra were recorded using a wide-bore Bruker Avance III 400 spectrometer (9.4 T) at 100.62 MHz with 3.7  $\mu\text{s}$   $^1\text{H}$  90° pulses, 3.5 ms contact time, spinning rates of 12 kHz, and 5 s recycle delays.

Microanalyses for C, H, and N were carried out with a Truspec Micro CHNS 630-200-200 elemental analyzer. Powder X-ray diffraction (PXRD) data were collected at ambient temperature on a Philips Analytical Empyrean diffractometer equipped with a PIXcel 1D detector, with automatic data acquisition (X'Pert Data Collector software version 4.2) using monochromatized  $\text{Cu-K}\alpha$  radiation ( $\lambda = 1.54178 \text{ \AA}$ ). Intensity data were collected by the step-counting



method (step 0.02°), in continuous mode, in the  $2\theta$  range 3–70°. Scanning electron microscopy (SEM) images were obtained on a Hitachi SU-70 microscope at 15 kV. Samples were prepared by deposition on aluminium sample holders followed by carbon coating using an Emitech K 950 carbon evaporator. Thermogravimetric analysis (TGA) was performed using a Hitachi STA300 system at a heating rate of 5°C min<sup>-1</sup> under air.

Baseline-corrected absorption spectra for the Mb assays were measured from 200 to 800 nm at a scanning rate of 600 nm/min on a Cary 5000 UV-Vis-NIR spectrometer. Alternatively, a Shimadzu 2600 was used to obtain the UV-Vis absorption spectra, and a Horiba-Jobin-Yvon Spex Fluorolog 3-2.2. spectrophotometer, corrected for the instrumental response of the system, was used to record the fluorescence spectra.

Structural models and representations were generated using CrystalMaker software (CrystalMaker Software, 2017).

## 2.2 Synthesis

### 2.2.1 1,3-Di-*p*-tolylpropan-2-one (1)

The procedure described by Resendiz and Garcia-Garibay (2005) was followed with slight modifications (Scheme 1). A Schlenk tube was charged with dicyclohexylcarbodiimide (6.23 g, 30.2 mmol) and 4-(dimethylamino)pyridine (0.93 g, 7.61 mmol) in CH<sub>2</sub>Cl<sub>2</sub> (45 ml) under inert atmosphere. A solution of *p*-tolylacetic acid (4.50 g, 30.0 mmol) in CH<sub>2</sub>Cl<sub>2</sub> (40 ml) was then added dropwise with stirring. The resultant yellow-orange mixture was stirred for 48 h at room temperature, and then the precipitated solid was removed by filtration, washed with CH<sub>2</sub>Cl<sub>2</sub>, and volatiles were removed from the filtrate by evaporation under reduced pressure. Purification of the residue by chromatography (hexane/dichloromethane 97:3) gave the substituted dibenzyl ketone **1** (1.84 g, 51%). <sup>1</sup>H NMR (400 MHz, DMSO-*d*<sub>6</sub>):  $\delta$  = 2.27 (s, 6H, CH<sub>3</sub>), 3.75 (s, 4H, CH<sub>2</sub>), 7.03 (m, 4H, aryl-CH), 7.11 (m, 4H, aryl-CH).

### 2.2.2 2,4-Dimethyl-2,4-di-*p*-tolylpentan-3-one (2)

The procedure described by Resendiz and Garcia-Garibay (2005) was followed with slight modifications (Scheme 1). A solution of compound **1** (0.80 g, 3.36 mmol) in dry THF (30 ml) was added dropwise to a magnetically stirred and cooled (−30°C; acetone/liq. N<sub>2</sub> bath) suspension of potassium hydride (1.35 g, 33.6 mmol) in dry THF (50 ml). After dropwise addition of methyl iodide (1.68 ml, 26.8 mmol), the yellow suspension turned pale yellow, and was heated to 85°C and refluxed for 4 h, during which time a further color change to orange occurred. The mixture was cooled to 0°C in an ice bath and an additional amount of methyl iodide (0.84 ml, 13.4 mmol) was added. After evaporation of the solvent under reduced pressure, the residue was washed with water and extracted with diethyl ether. Concentration of the organic phase yielded the derivative **2** as

a pale yellow powder (0.81 g, 82%). <sup>1</sup>H NMR (400 MHz, DMSO-*d*<sub>6</sub>):  $\delta$  = 1.17 (s, 12H, CH<sub>3</sub>), 2.28 (s, 6H, CH<sub>3</sub>), 7.06 (m, 4H, aryl-CH), 7.12 (m, 4H, aryl-CH).

### 2.2.3 4,4'-(2,4-dimethyl-3-oxopentane-2,4-diyl)dibenzoic acid (3)

The procedure described by Family and Garcia-Garibay (2009) was followed with significant modifications (Scheme 1). A solution of periodic acid (2.31 g, 10.1 mmol) in acetonitrile (80 ml) was prepared with vigorous magnetic stirring. Then, chromium(VI) oxide (0.08 g, 0.75 mmol) was added and the color of the solution changed immediately to orange. Finally, compound **2** (0.57 g, 1.94 mmol) was added and the resultant yellow suspension was stirred for 30 min. At this point a second addition of a freshly prepared H<sub>5</sub>IO<sub>6</sub>/CrO<sub>3</sub>/MeCN mixture (in amounts equal to those used initially) was made and the mixture was stirred for a further 30 min. The solvent was then removed under reduced pressure and the resultant solid was washed several times with Milli-Q water. Purification of the product by recrystallization from acetone:water (20 ml: 40 ml) gave the ketodiacid **3** as a white powder (0.40 g, 58%). <sup>1</sup>H NMR (400 MHz, DMSO-*d*<sub>6</sub>):  $\delta$  = 1.25 (s, 12H, CH<sub>3</sub>), 7.28 (d, 4H, aryl-CH, *J* = 8.4 Hz), 7.85 (d, 4H, aryl-CH, *J* = 8.4 Hz). <sup>13</sup>C NMR (101 MHz, DMSO-*d*<sub>6</sub>):  $\delta$  = 27.5, 53.0, 126.0, 129.0, 129.5, 148.9, 167.1, 211.7.

### 2.2.4 Layered double hydroxide-KDA3

A solution of the sodium salt of the diacid **3** was prepared by dissolving **3** (0.66 g, 1.86 mmol) in decarbonated deionized (DD) water (30 ml) along with 2 equiv. of 0.25 M NaOH. A solution of Zn(NO<sub>3</sub>)<sub>2</sub>·6H<sub>2</sub>O (1.11 g, 3.74 mmol) and Al(NO<sub>3</sub>)<sub>3</sub>·9H<sub>2</sub>O (0.70 g, 1.87 mmol) in DD water (30 ml) was added dropwise to the above solution, under nitrogen atmosphere, and 0.25 M NaOH was added simultaneously to maintain the pH of the reaction mixture at 8. Once addition of the Zn<sup>2+</sup>/Al<sup>3+</sup> solution was complete, the resultant white suspension was stirred for 18 h at 65°C (final pH = 8.4). The solid product was recovered by filtration, washed several times with DD water (0.5 L), and dried at room temperature under reduced pressure in a vacuum desiccator.

	Anal.	Calcd	for
Zn <sub>4.3</sub> Al <sub>2</sub> (OH) <sub>12.6</sub> (C <sub>21</sub> H <sub>20</sub> O <sub>5</sub> ) <sub>0.92</sub> (NO <sub>3</sub> ) <sub>0.16</sub> (H <sub>2</sub> O) <sub>5</sub> (973.62):			
C,	23.83;		
H,	4.24;		
N,	0.23.		
Found:	C, 23.84;		
	H, 4.24;		
	N, 0.23%.		

EDS gave an average Zn/Al atomic ratio of 2.15 ± 0.05. TGA revealed a mass loss of 8.9% from ambient temperature up to 150°C (calcd for 5H<sub>2</sub>O: 9.2%).

## 2.3 Photolysis experiments

Photolysis experiments were carried out using a 158.5 W medium pressure Peschl Ultraviolet mercury arc lamp (catalog No. 50043) equipped with a circulating water cooled pyrex jacket. Supplementary Figure S1 shows a typical setup for a myoglobin

(Mb) UV-Vis assay in which the cuvette containing the test solution is placed at a distance of 5 cm from the lamp. A similar arrangement was used to irradiate solid samples or DMSO- $d_6$  solutions of **3** in an NMR tube.

## 2.4 Deintercalation tests

The stability of LDH-KDA3 in different aqueous media was explored through the following experiments: 1) A sample of LDH-KDA3 (27 mg) was irradiated in the solid-state for 12 h. The solid (iLDH) was then added to a solution of  $Na_2CO_3$  (125 mg, 1.18 mmol) in deionized water (7 ml), and the suspension was stirred overnight at rt. The resultant solid (designated iLDH<sup>DI</sup>, where DI stands for deintercalated) was recovered by filtration, washed with deionized water ( $2 \times 5$  ml), and vacuum-dried at rt. A second solid designated as iKDA<sup>DI</sup> was recovered from the filtrate by evaporation of the solution to dryness. This procedure was also performed for non-irradiated LDH-KDA3, giving the solids LDH<sup>DI</sup> and KDA<sup>DI</sup>. 2) In two parallel experiments, LDH-KDA3 (20 mg) was incubated in 0.01 M PBS or 0.01 M HEPES buffer solutions at rt for 5 h. The resultant solids, designated as LDH<sup>PBS</sup> and LDH<sup>HEPES</sup>, were recovered by filtration, washed with deionized water ( $2 \times 10$  ml), and vacuum-dried at rt.

## 2.5 Myoglobin assay

The photoinduced release of CO from the synthesized compounds was assessed by using the Mb assay, in which the conversion of deoxymyoglobin (deoxy-Mb) to carbonmonoxy-myoglobin (MbCO) can be spectrophotometrically measured (Mottetlini et al., 2002).

The heme group functions as the active site of Mb, originating two  $\pi \rightarrow \pi^*$  electronic transitions: one, very intense, at about 400 nm (Soret or B band), and a second at 500–600 nm (the Q bands). The wavelengths corresponding to these wavelength maxima are governed by the oxidation, spin, and coordination states of the heme iron. As a result, it is possible to distinguish between different forms of Mb by the respective peak positions and relative optical density values of the absorption spectra.

All experiments were performed by using a stock solution of Mb, which was freshly prepared by dissolving the protein in degassed ( $O_2$  free) 0.1 M PBS (pH = 7.4). An aliquot of this solution was taken and bubbled with gaseous nitrogen (99.99% pure), to which freshly prepared 1 M  $Na_2S_2O_4$  (300  $\mu$ l) was added to promote conversion of met-myoglobin into deoxy-Mb. While the solution was being bubbled, a solution (2 ml) of the ketone was added and the solution made up to 3 ml with 0.1 M PBS. After 15 min of bubbling, this solution was stored in quartz cuvettes with a magnetic stirring bar, with an optical path of 1 cm, and sealed

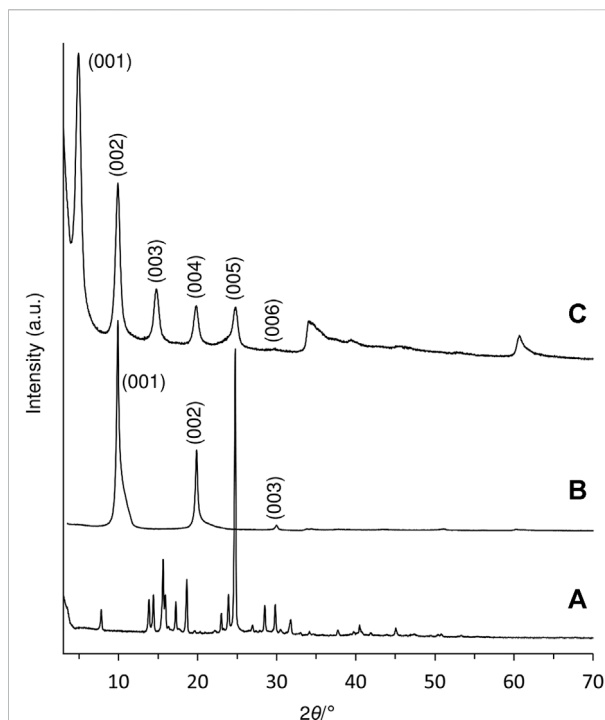


**FIGURE 1**  
PXRD patterns of (A) ketodiacid **3**, (B) LDH- $NO_3$ , and (C) LDH-KDA3.

with a Teflon stopper and parafilm to prevent any escape or entry of gas. An absorbance spectrum was immediately acquired after preparation of the samples. These were subsequently irradiated at room temperature and absorption spectra of the irradiated solutions were recorded periodically.

Blank solutions of deoxy-Mb with the same concentration for each experiment were prepared simultaneously and their absorption spectra were measured; these blank solutions were immediately saturated with CO gas at 10 bar for at least 1 h to promote a complete conversion of deoxy-Mb to MbCO using an autoclave reactor.

The CO released was quantified by following the absorbance of samples at 540 nm as reported previously (Atkin et al., 2011), using blank solutions and four isosbestic points between deoxy-Mb and MbCO in Q Bands to normalize data.

## 2.6 Time-dependent density functional theory studies

All theoretical calculations were of the DFT type, carried out using version R3 of GAMESS-US (Schmidt et al., 1993). A range-corrected LC-BPBE ( $\omega = 0.20$  au<sup>-1</sup>) functional, as implemented in GAMESS-US (Schmidt et al., 1993), was used in both ground- and excited-state calculations. TDDFT calculations, with similar

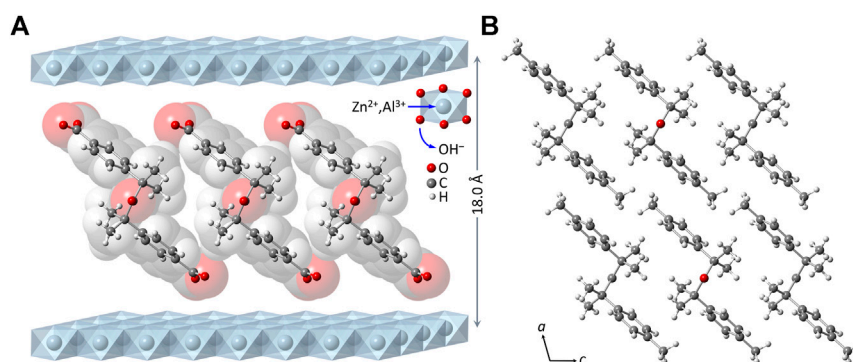


FIGURE 2

(A) Structural model (ball-and-stick diagram superimposed on a spacefilling, van der Waals-based representation) for the monolayer arrangement of 4,4'-(2,4-dimethyl-3-oxopentane-2,4-diyl)dibenzoate anions in the material LDH-KDA3. (B) View of the crystal packing of **2** down the crystallographic *b* axis.

functionals, were used to probe the excited-state potential energy surface (PES). A solvent was included using the polarizable continuum model with the solvation model density to add corrections for cavitation, dispersion, and solvent structure. In TDDFT calculation of FC (Franck-Condon) excitations the dielectric constant of the solvent was split into a “bulk” component and a fast component, which is essentially the square of the refractive index. In “adiabatic” conditions only the static dielectric constant is used. A 6-31G\*\* basis set was used in either DFT or TDDFT calculations. The results obtained with the LC-BPBE(20) functional are essentially unscaled raw data from calculations; for the  $S_0 \rightarrow S_n$  transitions, a small correction, which results in the subtraction of 0.05 eV, to account for the difference between zero point and the first vibronic level, was considered. For the resulting optimized geometries time dependent DFT calculations (using the same functional and basis set as those in the previous calculations) were performed to predict the vertical electronic excitation energies.

### 3 Results and discussion

#### 3.1 Intercalation of the ketodiacid **3** in a Zn-Al layered double hydroxide

A Zn-Al LDH intercalated by the deprotonated form of the diketoacid **3** was prepared by a direct coprecipitation method. The PXRD pattern of the resultant solid, designated as LDH-KDA3, is typical of LDHs containing organic guests (Figure 1C). Five equally spaced basal (00*l*) reflections are observed at  $2\theta$  angles below  $30^\circ$ . The sharpness of the basal reflections indicates that the layer structure is well-ordered, i.e., the interlayer spacing is highly regular. On the other hand, the presence of several weak, broad and asymmetric non-basal reflections at  $2\theta$  angles above  $30^\circ$  indicates disorder in the layer stacking, such as a turbostratic

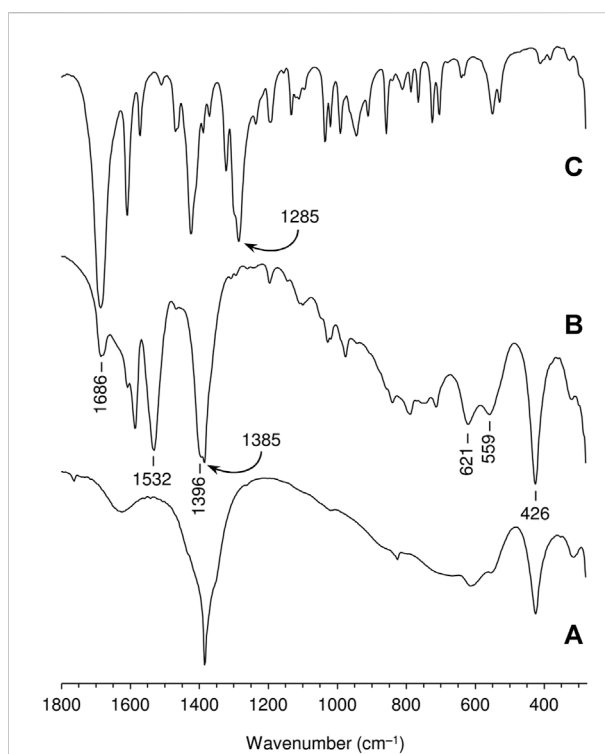
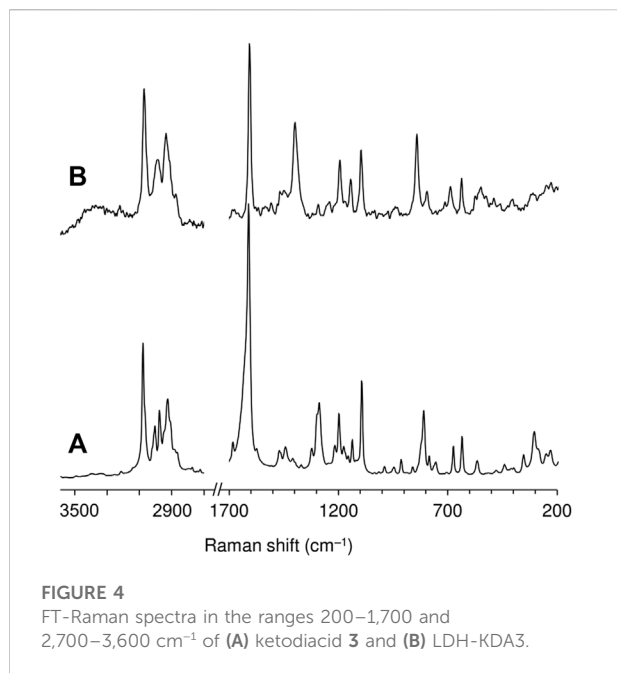


FIGURE 3

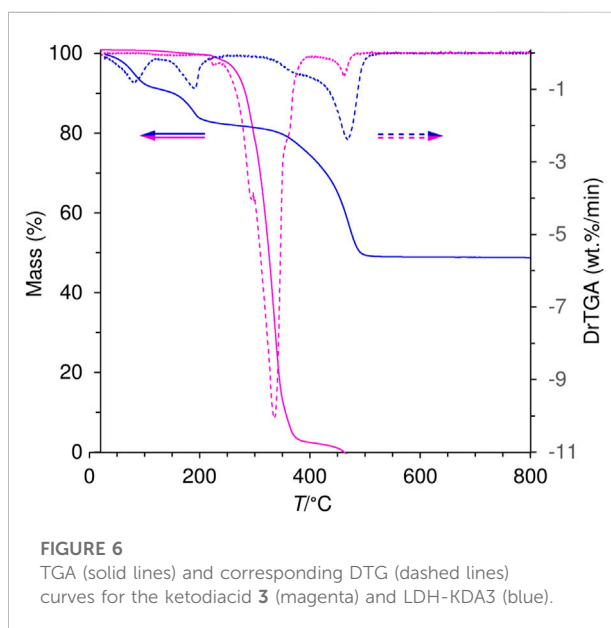
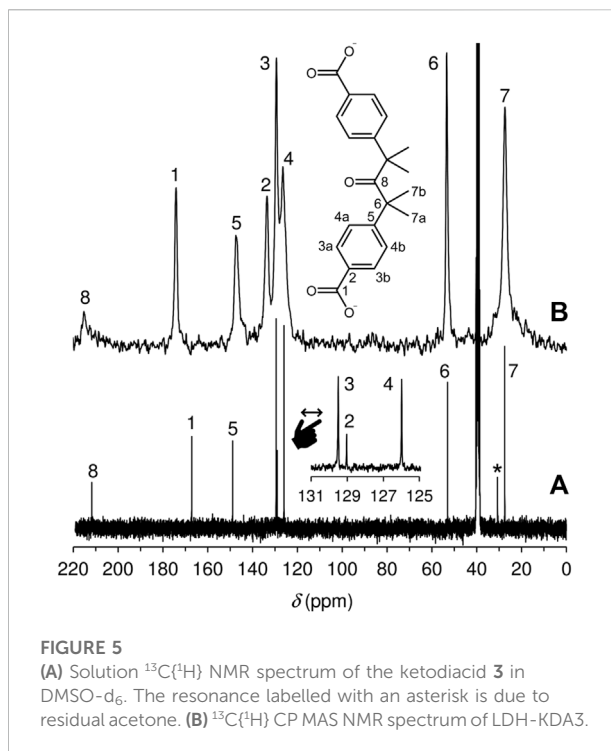
FT-IR spectra in the range 280–1800  $\text{cm}^{-1}$  of (A) LDH- $\text{NO}_3$ , (B) LDH-KDA3, and (C) ketodiacid **3**. The frequencies of selected bands are indicated.

distortion or an intergrowth of the rhombohedral and hexagonal polytypes (Bellotto et al., 1996; Evans and Slade, 2006). Since the type of polytype cannot be determined with any degree of certainty, the basal reflections have been indexed as a one-layer polytype (001, 002, 003, etc.). The interlayer spacing ( $c_0$ ) can be calculated from averaging the positions of the five 00*l*



harmonics:  $c_0 = (d_{001} + 2d_{002} + 3d_{003} + 4d_{004} + 5d_{005})/5 = 18.0 \text{ \AA}$ . This is almost exactly double the value of  $c_0$  (8.89  $\text{\AA}$ ) for the reference material LDH- $\text{NO}_3$  (Figure 1B).

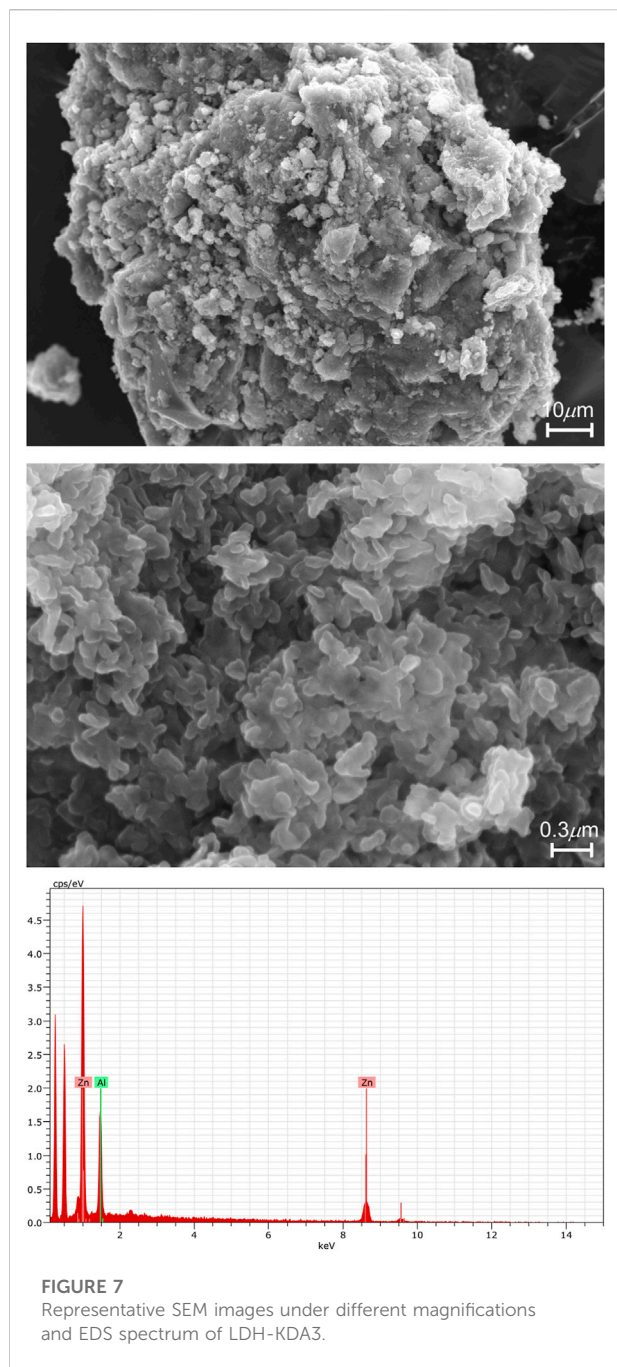
Subtracting the hydroxide layer thickness of 4.8  $\text{\AA}$  from the interlayer spacing of 18.0  $\text{\AA}$  for LDH-KDA3 gives a gallery height of 13.2  $\text{\AA}$ . To the best of our knowledge, no crystal structure has been reported for the ketodiacid **3**. A structure has, however, been deposited with the Cambridge Structural Database (Groom et al., 2016) for the synthetic precursor to **3**, i.e., 2,4-dimethyl-2,4-di-*p*-tolylpentan-3-one (**2**) (CSD Refcode WIVHOZ). A realistic model for the molecular structure of the deprotonated form of **3** was created by extracting a molecule of **2** from the crystal structure and replacing the *p*-tolyl methyl groups by carboxylate groups with a fixed C–O bond length of 1.25  $\text{\AA}$  and a  $\angle\text{OCO}$  angle of  $125^\circ$ . Figure 2 shows a schematic representation of a guest orientation that is calculated to give the experimentally observed gallery height of 13.2  $\text{\AA}$ . In this model, the guest molecules are markedly inclined from the normal to the hydroxide layers; the molecular axis defined by a vector joining the two carboxylate carbon atoms is at an angle of ca.  $52^\circ$  to the hydroxide surface of the layers. Apart from the fact that this arrangement gives a gallery height of 13.2  $\text{\AA}$ , there are other features that support this model: 1) hydrogen-bonding interactions between the carboxylate oxygen atoms and the layer hydroxyl groups are fortified, while positioning the hydrophobic dicumyl ketone section of the molecule towards the center of the interlayer region; 2) the inclined orientation may allow an efficient guest packing mode in which molecules can interlock as represented in Figure 2. The last argument is reinforced by the fact that a strikingly similar arrangement is present in the crystal



packing of compound **2**, when viewed down the crystallographic *b* axis, as shown in Figure 2B.

The FT-IR spectra of the free ketodiacid **3** and the intercalated material LDH-KDA3 are shown in Figure 3. The spectrum of **3** is dominated by the very strong absorption at  $1,686 \text{ cm}^{-1}$  assigned to overlapping  $\nu(\text{C}=\text{O})$  bands of the ketone and carboxylic acid groups. LDH-KDA3 displays this band at the





same frequency, albeit with reduced relative intensity, and it is therefore assigned to  $\nu(\text{C}=\text{O})$  of the ketone group. The deprotonation of the carboxylic acid groups of the guest molecules in LDH-KDA3 is confirmed by the appearance of two strong bands attributable to  $\nu_{\text{sym}}(\text{CO}_2)$  ( $1,396\text{ cm}^{-1}$ ) and  $\nu_{\text{asym}}(\text{CO}_2)$  ( $1,532\text{ cm}^{-1}$ ) vibrations, together with the absence of a  $\nu(\text{C}-\text{O})$  band (present at  $1,285\text{ cm}^{-1}$  for **3**). A weak, sharp band at  $1,385\text{ cm}^{-1}$  that overlaps with the  $\nu_{\text{sym}}(\text{CO}_2)$  band may be due to an asymmetric  $\nu_3$  stretching mode of nitrate ions (present *via*

cointercalation with **3** and/or formation of a secondary LDH- $\text{NO}_3$  phase). Bands at  $1,586$  and  $1,609\text{ cm}^{-1}$  for the intercalated LDH are assigned to aromatic ring stretching vibrations. Below  $700\text{ cm}^{-1}$ , the three main bands observed at  $426$ ,  $559$  and  $621\text{ cm}^{-1}$  are attributed to the characteristic Zn/Al-OH lattice translation modes of Zn-Al LDHs (Klopprogge et al., 2004). Similar lattice mode bands are observed for the reference nitrate-form material LDH- $\text{NO}_3$  (Figure 3A). The Raman spectrum of LDH-KDA3 is fully consistent with the FT-IR spectrum, showing a very strong band at  $1,606\text{ cm}^{-1}$  ( $\nu_{\text{ring}}$ ) and a strong band at  $1,399\text{ cm}^{-1}$  [ $\nu_{\text{sym}}(\text{CO}_2)$ ] (Figure 4).

The solid-state  $^{13}\text{C}\{^1\text{H}\}$  CP MAS NMR spectrum of LDH-KDA3 is shown in Figure 5 alongside the solution spectrum of the ketodiacid **3** in  $\text{DMSO}-d_6$ . The LDH displays eight distinct resonances that have a clear counterpart in the solution spectrum. Thus, the signals for the aliphatic (20–60 ppm), aromatic (120–150 ppm) and carbonyl (170–220 ppm) carbon atoms of LDH-KDA3 (and **3**, given in parentheses) are attributed as follows: ( $\delta$ , ppm)  $\text{CH}_3$  at 27.4 (27.5),  $\text{C}(\text{CH}_3)_2$  at 53.4 (53.0), phenylene-CH at 126.5, 129.4, 133.6, and 147.2 (126.0, 129.0, 129.5, 148.9),  $-\text{CO}_2^-$  at 174.1 (167.1), and  $\text{C}=\text{O}$  at 215.1 (211.7). Hence, as expected, the most significant change is the downfield shift of the carboxylate resonance owing to deprotonation.

TGA revealed that the organic guest anion in LDH-KDA3 starts to decompose at a significantly higher temperature than that determined for the free ketodiacid **3** (Figure 6). The intercalated LDH shows three main weight loss steps between ambient temperature and  $500^\circ\text{C}$  corresponding to removal of physisorbed and cointercalated water molecules (8.9% mass loss up to  $150^\circ\text{C}$ ), dehydroxylation of the hydroxide layers (6.9% loss in the range  $150$ – $210^\circ\text{C}$ ), and decomposition of the organic guest (31.2% loss in the range  $330$ – $500^\circ\text{C}$ ). The enhanced thermal stability of the intercalated ketodicarboxylate anions is underscored by the shift of the decomposition onset from about  $230^\circ\text{C}$  for **3** to  $330^\circ\text{C}$  for LDH-KDA3, as well as the shift of the maximum of the differential thermogravimetric (DTG) curve from  $335^\circ\text{C}$  for **3** to  $470^\circ\text{C}$  for LDH-KDA3. Comparable increases in thermal stability of organic carboxylates (vs. the initial free acid or sodium salt) have been reported for other systems, including Zn-Al LDHs containing intercalated benzenecarboxylate derivative anions, e.g., positive shifts of ca.  $150^\circ\text{C}$  for 5,5'-methylenedisalicylic acid (Cui et al., 2010),  $130^\circ\text{C}$  for aurintricarboxylic acid (Zhu et al., 2011), and  $50^\circ\text{C}$  for benzene carboxylate and 4-hydroxy-benzene carboxylate (Fleutot et al., 2012). These improvements in thermal stability are attributed to the formation of an ordered supramolecular structure with significant interactions (including electrostatic interaction between opposite charges, hydrogen bonding and van der Waals interactions) between the organic guest and the host layer.

The phase purity of the material LDH-KDA3 was verified by SEM and EDS (Figure 7). The morphology of the intercalated LDH consisted of large aggregates of irregular sheet-like nanoparticles. EDS analyses indicated a uniform Zn/Al atomic

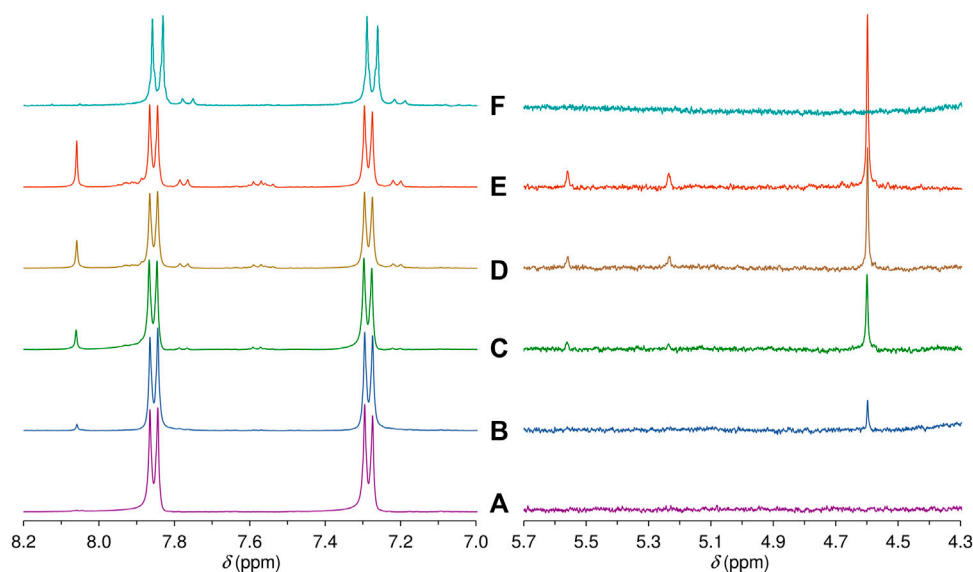
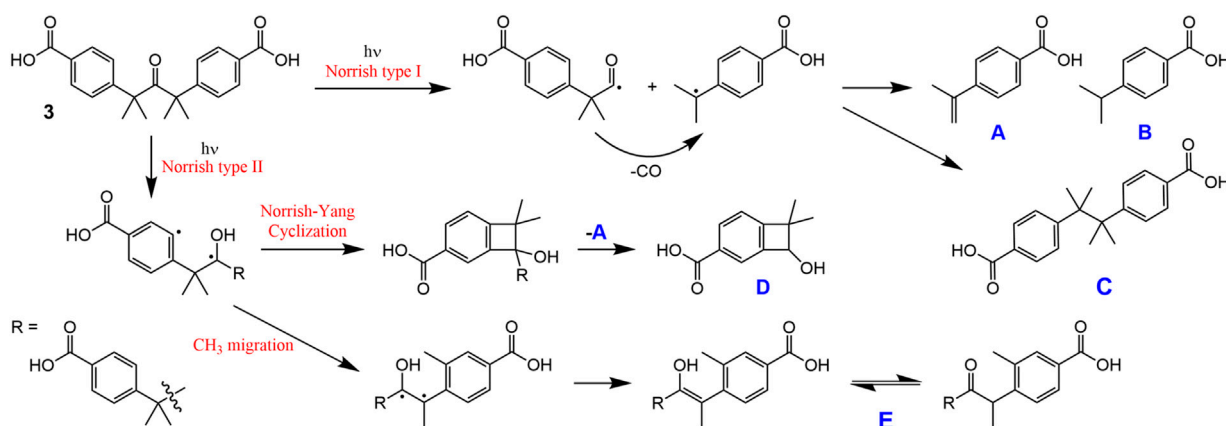


FIGURE 8

Aromatic and mid-field regions of the  $^1\text{H}$  NMR spectra obtained after irradiating a solution of the ketodiacid **3** in  $\text{DMSO}-d_6$  for (A) 0 h, (B) 3 h, (C) 5 h, (D) 8 h, and (E) 12 h. For comparison, (F) shows the same regions of the  $^1\text{H}$  NMR spectrum obtained in a  $\text{DMSO}-d_6$  solution of the irradiated solid **3** (see main text for details).



SCHEME 2

Possible photoproducts of **3** in solution.

ratio of  $2.15 \pm 0.05$ , which is quite close to the initial value of 2 in solution. The slight increase may have been caused by some leaching of aluminium during excessive washing with water. No evidence was found for secondary phases containing Zn (e.g., ZnO) and/or Al (e.g.,  $\text{Al}_2\text{O}_3$ ), in agreement with the PXRD data.

From CHN, EDS, and TGA analyses, together with the other characterization data, the formula  $\text{Zn}_{4.3}\text{Al}_2(\text{OH})_{12.6}(\text{C}_{21}\text{H}_{20}\text{O}_5)_{0.92}(\text{NO}_3)_{0.16}(\text{H}_2\text{O})_5$  is proposed

for the material LDH-KDA3. As discussed above, the presence of a small amount of nitrate ions was indicated by FT-IR spectroscopy, and the nitrate content in the formula is consistent with microanalyses for N. Since neither the IR spectrum nor the solid-state  $^{13}\text{C}\{^1\text{H}\}$  CP MAS NMR spectrum of LDH-KDA3 show peaks characteristic of carbonate ions, any interference from such species is deemed to be insignificant, and hence the presence of

$\text{CO}_3^{2-}$  (in addition to  $\text{NO}_3^-$ ) is not contemplated in the proposed formula.

To assess the stability of LDH-KDA3 in aqueous media, the material was incubated in two different biological buffers, 0.01 M PBS and 0.01 M HEPES, for 5 h at room temperature. No significant alterations in the IR spectrum or PXRD pattern of LDH-KDA3 were observed after these treatments (Supplementary Figures S2, S3), indicating that no structural changes took place, such as deintercalation of ketodicarboxylate anions by ion-exchange with phosphate ions in the PBS buffer solution.

## 3.2 Photolysis studies in the solid-state and in solution

### 3.2.1 Characterization of photoproducts

Solid samples of **3** and LDH-KDA3 were irradiated with UV light for 12 h at room temperature, giving materials designated as i**3** and iLDH. The  $^1\text{H}$  NMR spectrum of i**3** in  $\text{DMSO-d}_6$  was recorded and compared with that for **3** (Figure 8, spectra A and F). In the region containing the resonances for the phenyl group hydrogens, **3** displays a pair of doublets at 7.28 and 7.85 ppm. For the irradiated sample i**3**, an additional pair of weak doublets is observed at 7.20 and 7.76 ppm, which are attributed to the diphenylethane combination product of photodecarbonylation (structure C in Scheme 2) (Zhang et al., 2007; Family and Garcia-Garibay, 2009). Signals due to other photoproducts, e.g., disproportionation products A and B in Scheme 2 (Family and Garcia-Garibay, 2009), were not observed. The high chemoselectivity of the photodecarbonylation reaction in the solid-state agrees with results reported by Family and Garcia-Garibay (2009). On the other hand, the relatively low photoreactivity observed in our work does not tally with the results of Family and Garcia-Garibay (2009) who reported conversions of 33% and 100% after room-temperature photolysis of **3** for 1 h and 5–6 h (using a similar experimental setup). Differences in sample crystallinity and structure may account for the contrasting photoreactivities observed. Zhang et al. (2007) found that the photodecarbonylation of crystalline hexasubstituted ketones could be quenched by the formation of intermolecular H-bonds involving the carbonyl (C=O) group. Although the PXRD pattern of **3** (Figure 1A) matches quite well with that reported by Family and Garcia-Garibay (2009) in terms of peak positions and relative intensities, the crystallinity of the sample obtained in the present work may be higher, which could imply differences in the long-range crystal packing and H-bonding networks.

The FT-IR spectrum of the irradiated solid iLDH was identical to that of the parent material LDH-KDA3 (not shown here). There was no detectable alteration in the relative intensity of the band assigned to  $\nu(\text{C}=\text{O})$  of the ketone group, suggesting that very little or no photodecarbonylation had occurred. This was investigated further by performing deintercalation (DI) reactions in which LDH-KDA3 and iLDH were incubated overnight in a solution of  $\text{Na}_2\text{CO}_3$  at room

temperature. The PXRD patterns and FT-IR spectra of the resultant solids (designated as LDH<sup>DI</sup> and iLDH<sup>DI</sup>) confirmed that complete exchange of organic guest ions for carbonate ions had taken place to give Zn-Al- $\text{CO}_3$  LDHs with the characteristic interlayer spacing of 7.6 Å (exemplified in Supplementary Figures S2D, S3D for iLDH<sup>DI</sup>). Second solids designated as KDA<sup>DI</sup> and iKDA<sup>DI</sup> were recovered from these experiments by evaporation of the exchange solutions to dryness.  $^1\text{H}$  NMR analysis of the phenyl group hydrogens of iKDA<sup>DI</sup> confirmed, through comparison with the spectra for KDA<sup>DI</sup> and the disodium salt of **3**, the presence of the unchanged ketodiacid (as the disodium salt), in agreement with the FT-IR spectrum of iLDH (Supplementary Figure S4).

To compare with the solid-state photolysis results, a solution of **3** in  $\text{DMSO-d}_6$  was irradiated at room temperature with UV light and  $^1\text{H}$  NMR spectra were recorded for different irradiation times (Figure 8). After an irradiation time of 3 h, new signals start to appear in the aromatic region, and these grow in relative intensity with further irradiation up to 12 h. The new doublets at 7.21 and 7.77 ppm are assigned to the diphenylethane combination product C. In contrast to the photolysis of **3** in the solid-state, the photolysis of **3** in solution is less selective, with additional signals being observed in the aromatic region, namely several weak resonances in the spectral ranges of 7.52–7.62 and 7.88–7.95 ppm, and a relatively intense singlet at 8.06 ppm. The weaker resonances could be due to A and/or B (Scheme 2). The  $^1\text{H}$  NMR spectrum of B in  $\text{DMSO-d}_6$  has been independently reported by two groups, and in both studies the compound gave doublets at 7.36–7.37 ppm and 7.86–7.88 ppm (Yang et al., 2014; Liu et al., 2018). Since no doublet appeared around 7.36 ppm upon photolysis of the solution of **3** in  $\text{DMSO-d}_6$ , we exclude the formation of B, favoring instead the formation of A, which may be responsible for the weak doublet centered at 7.58 ppm and an additional signal in the 7.88–7.95 ppm range. These assignments are made by comparison with the spectrum reported for the methyl ester of A in  $\text{CDCl}_3$ , which exhibited doublets at 7.51 and 8.01 ppm (Matsumoto et al., 1994). The postulation of A as a photoproduct is further supported by the appearance of weak singlets at 5.23 and 5.56 ppm [cf. 5.19 and 5.46 ppm for methyl 4-isopropenylbenzoate (Matsumoto et al., 1994)], assigned to the vinylidene hydrogens (Figure 8).

In addition to the signals around 5.5 ppm, the mid-field region of the  $^1\text{H}$  NMR spectra of the irradiated  $\text{DMSO-d}_6$  solution of **3** shows the growth of a singlet resonance at 4.60 ppm (Figure 8). This signal and the one at 8.06 ppm are not due to any of the Norrish type I ( $\alpha$ -cleavage) photoproducts (A, B, and C) shown in Scheme 2. Hence, an alternative photoreaction sequence must be considered. One likelihood is the Norrish type II pathway (Oelgemöller and Hoffmann, 2016; Albini, 2021), which starts with the intramolecular abstraction of a  $\gamma$ -hydrogen to produce a 1,4-biradical (Scheme 2). In the case of **3**, the final products could include the dimethylbenzocyclobutenol derivative D (via Norrish-Yang cyclization) and the keto-enol system E (via a methyl migration

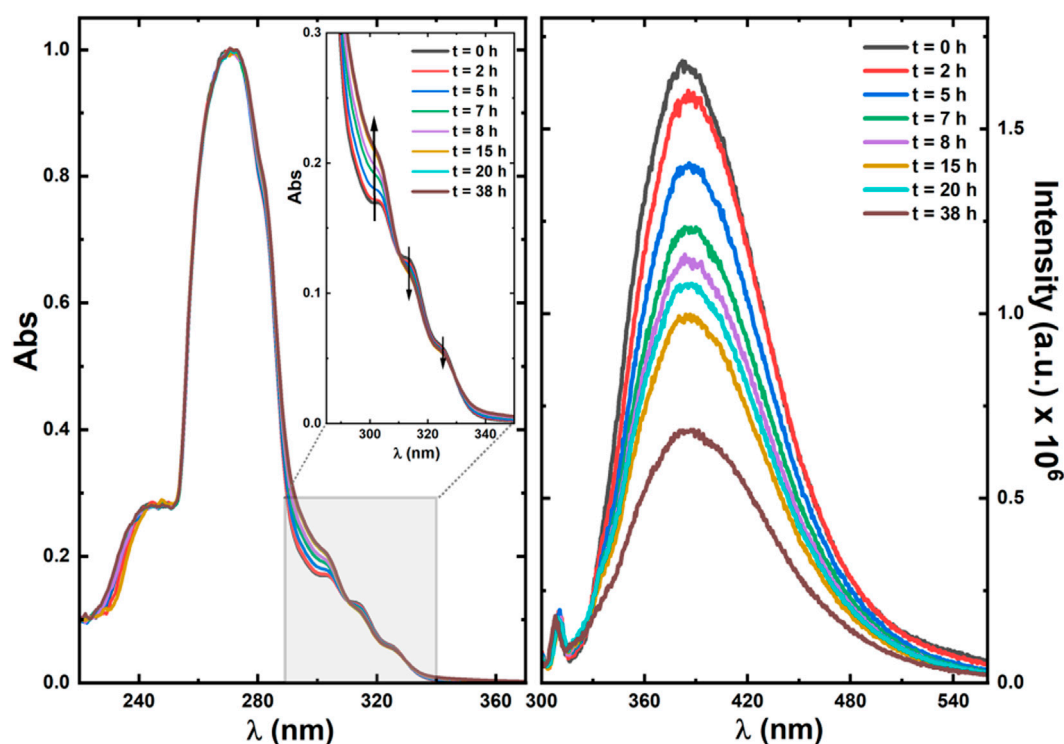


FIGURE 9

Normalized absorption (left) and fluorescence emission (right) spectra of ketodiacyd **3** in DMSO- $d_6$  solution with different irradiation times. In the absorption spectra the shape of the spectra for wavelength values below 260 nm mirrors the solvent's cut-off, and the vertical arrows indicate the increase ( $\sim 304$  nm) and decrease ( $\sim 314$  nm and  $\sim 327$  nm) of the absorption bands.

reaction) (Scheme 2), which could both explain the new singlet observed in the aromatic region of the  $^1\text{H}$  NMR spectra.

To better understand the behavior of **3** under irradiation, a more comprehensive photophysical study, involving excitation of this compound in DMSO- $d_6$  followed by UV-Vis and fluorescence spectroscopy, was undertaken. Figure 9 shows the absorption (left) and fluorescence (right) spectra upon irradiation for different periods up to a total time of 38 h (with the 158.5 W medium pressure Ultraviolet mercury arc lamp as described in Section 2.3).

The emission spectra were collected with excitation ( $\lambda_{\text{exc}}$ ) at 290 nm to avoid the superimposition of the Raman peak of the solvent. The dependence of the absorption spectra of ketoacid **3** on the irradiation time shows an increase of the 304 nm band and a decrease of the  $\sim 314$  nm and  $\sim 327$  nm bands. Although an isosbestic point could not be selected for excitation to obtain the emission spectra (to avoid the overlap of the Raman peak of the solvent in the emission spectra), with the  $\lambda_{\text{exc}} = 290$  nm used for excitation (close to the peak maximum of 304 nm) the absorbance value increases with the irradiation time, whereas the emission band (with peak maxima,  $\lambda_{\text{em}}$ , at 390 nm) decreases with the irradiation time. This shows that a new and less emissive compound is being formed at the expense of photodegradation of ketoacid **3** (see Figure 9).

Further rationalization of this behavior arrives with the predicted—from TDDFT calculations—absorption and emission maxima of ketoacid **3** and of the photoproducts (A–E). Indeed, for ketoacid **3** and photoproduct **E**, an absorption band (corresponding to an  $n, \pi^*$  transition) with maxima at ca. 316–317 nm (predicted from TDDFT calculations) matches with the longest wavelength vibronically resolved absorption band (wavelength range 290–350 nm, see Supplementary Table S1 and Supplementary Figure S5). The other photoproducts (compounds A–D) do not show evidence of theoretically predicted low energy  $n, \pi^*$  forbidden transitions. Moreover, the oscillator strength associated with the emission at 380 nm (Figure 9) of ketoacid **3** ( $f = 0.01$ ) is higher than that of photoproduct **E** ( $f = 0.002$ ), thus attesting, once more, that formation of this photoproduct is highly favorable and takes place through the proposed Norrish type mechanism (see Scheme 2; Supplementary Table S1).

Despite the above results, compound **D** is not excluded as a photoproduct formed from the photolysis of **3** in solution, since it appears to provide the best overall fit with the new NMR resonances, with the singlets at 4.60 and 8.06 ppm being assigned to the secondary alcohol methine proton and the isolated CH



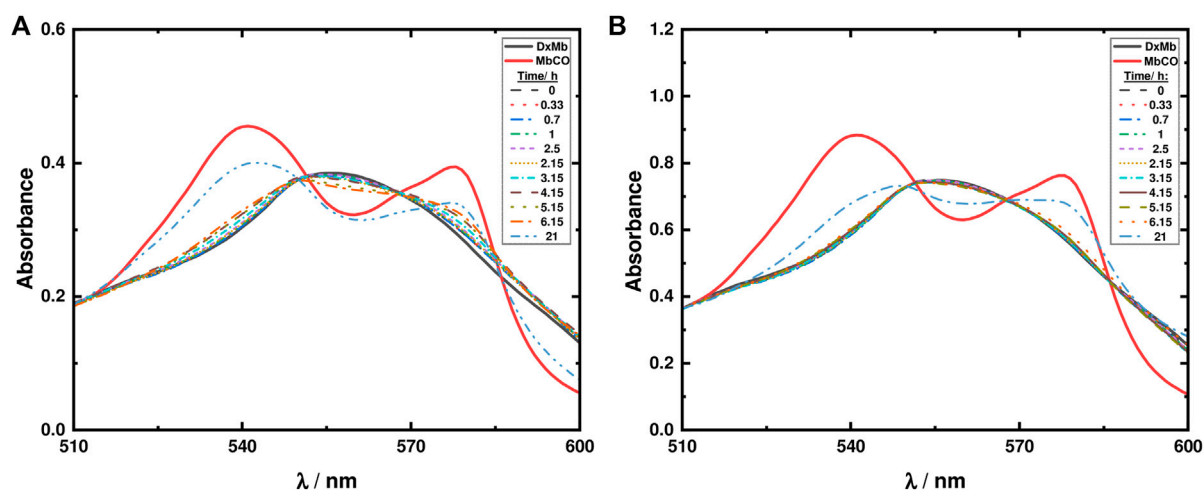


FIGURE 10

Mb assays for ketodiacid **3** (2.6 mM) using a deoxy-Mb (DxMb) concentration of approximately (A) 30  $\mu$ M and (B) 60  $\mu$ M.

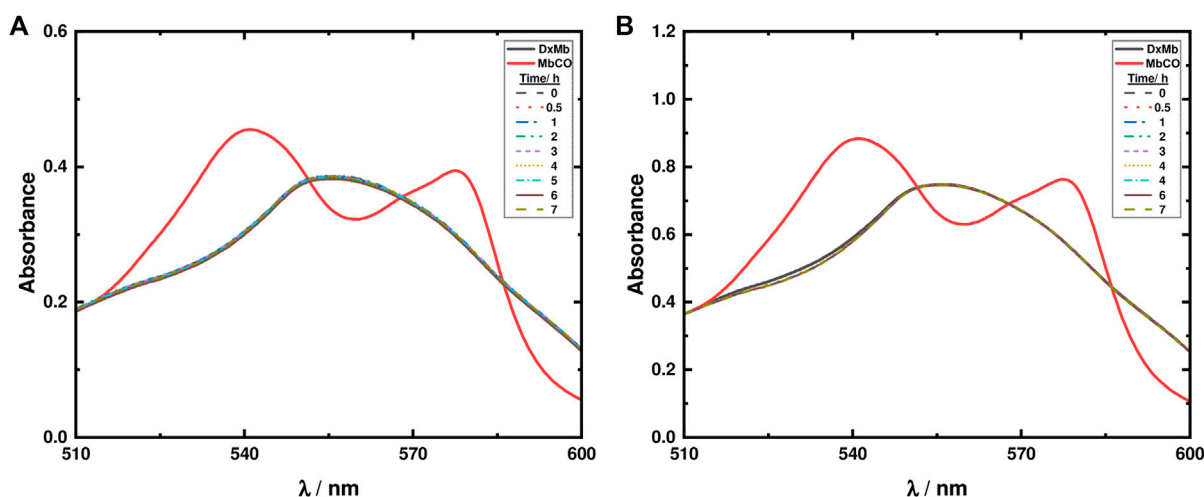


FIGURE 11

Mb assays for LDH-KDA3 (0.8 g/L) using a deoxy-Mb (DxMb) concentration of approximately (A) 30  $\mu$ M and (B) 60  $\mu$ M.

proton in the aromatic ring, respectively. The former assignment agrees with data recently reported for similar dimethylbenzocyclobutenols, differing only in the substituent on the benzene ring (F, Cl or Me instead of CO<sub>2</sub>H), which displayed the methine resonance in the range 4.7–4.8 ppm with CDCl<sub>3</sub> as solvent (Chen et al., 2021). The remaining two aromatic protons of compound **D** may be responsible for the weak doublet centered at 7.55 ppm and an additional signal in the 7.88–7.95 ppm range. It is noteworthy that the proposed pathway leading to **D** also leads to the formation of **A**, which strengthens the assignment of the new resonances at 5.23, 5.56, 7.58, and 7.88–7.95 ppm to **A**.

### 3.2.2 Myoglobin assays to measure photoinduced release of CO

The well-established Mb assay was used to assess the capabilities of ketodiacid **3** and LDH-KDA3 for the release of CO. The experiment, as previously described, relies on the spectrophotometric detection of the conversion of deoxy-Mb to MbCO (Motterlini et al., 2002).

With ketodiacid **3**, two different samples, with a final Mb concentration of approximately 30 and 60  $\mu$ M, and a final ketodiacid concentration of 2.6 mM, were simultaneously irradiated at room temperature. Two sets of parallel assays were performed—one for 7 h (Supplementary Figure S6) and

one for 21 h (Figure 10). Data in Figure 10 show the formation of MbCO, indicating photodecarbonylation of **3**. However, after 21 h of irradiation the maximum concentration of formed MbCO was found to be ca. 0.70% (0.07 equiv. MbCO based on **3**) in the two experiments with different Mb concentrations.

Regarding the material LDH-KDA3, suspensions of the solid in 0.1 M PBS buffer solution (0.8 g/L) were irradiated in the presence of two different concentrations of Mb (30 and 60  $\mu$ M). As shown in Figure 11, after 7 h of irradiation no changes are observed in the absorption spectra, thus showing that in the LDH hybrid system, photodecarbonylation of ketodiacid **3** is inhibited.

Further analysis of the photodecarbonylation of **2**, the ditolyl precursor of **3**, was performed. Due to the low solubility of **2** in aqueous solution, the Mb assay was performed with a solution of 1% DMSO to solubilize **2** (Mansour and Shehab, 2018; Toscani et al., 2021). In this case, 5 mg of **2** were dissolved in 1 ml of DMSO, and an aliquot of 30  $\mu$ l was taken to a final volume of 3 ml which contained a deoxy-Mb concentration of approximately 30  $\mu$ M. Under these experimental conditions, release of CO was not detected as shown in Supplementary Figure S7. This may be a consequence of the low concentration (poor solubility) of compound **2**.

In comparison with results of photodecarbonylation obtained for other dicumyl ketones (Resendiz and Garcia-Garibay, 2005; Veerman et al., 2006), ketodiacid **3** has shown an extremely low percentage of photodecarbonylation in aqueous dispersion followed by the Mb assay, and LDH-KDA3 was not reactive at all. For the ketodiacid **3**, the competing Norrish type II pathway proposed above, involving conversion of the carbonyl group to a ketyl radical, may partly explain the low extent of the Norrish type I photodecarbonylation reaction and hence the low yield of MbCO in the Mb assay. An additional explanation is that the presence of carboxylic acid groups stabilizes, by intermolecular and/or (in the case of the LDH system) host-guest interactions, the compound, thus inhibiting triplet formation and  $\alpha$ -cleavage to give an acyl-alkyl radical pair, followed by loss of CO from the acyl radical fragment. As mentioned above, other studies with crystalline dicumyl ketone derivatives are consistent with this observation since they showed that intermolecular hydrogen bonds can quench photodecarbonylation (Zhang et al., 2007).

## 4 Conclusion

In the present work we have demonstrated the enhanced thermal and photo-stability of a para-substituted dicumyl ketone intercalated in a layered double hydroxide. Due to the diminished photoreactivity, the study of the photochemistry of the ketodiacid (with respect to photoproduct selectivities) was limited to a comparison of results obtained for the compound in solution and in the crystalline state. The work has, nevertheless, worked as a proof of concept concerning the use

of LDHs as hosts for the supramolecular organization of hexasubstituted ketones. Concerning the photoreactivity of **3** in solution, from photophysical and NMR data, further rationalized by TDDFT calculations, the formation of a less emissive photoproduct (keto-enol system **E**) via a methyl migration reaction is proposed, although the co-formation of photoproduct **D** (through Norrish-Yang cyclization) cannot be discarded. In future work it would be desirable to study more photoreactive ketones to probe the influence of the supramolecular ordering on the photochemistry of the guest molecules.

## Data availability statement

The original contributions presented in the study are included in the article/Supplementary Material, further inquiries can be directed to the corresponding authors.

## Author contributions

IG, JM, and MP contributed to funding acquisition, project administration, supervision, conception and design of the study. AC, RM, and AG synthesized and characterized the compounds under the guidance of IG and MP. PB and SF performed the photolysis experiments and myoglobin assays under the guidance of JM. CC performed the TDDFT calculations and the fluorescence experiments under the guidance of JM. All authors contributed to manuscript preparation and revision and have read and approved the submitted version.

## Funding

This research was supported by the Associated Laboratory CICECO—Aveiro Institute of Materials (UIDB/50011/2020, UIDP/50011/2020 and LA/P/0006/2020), CQC—Coimbra Chemistry Center (UIDB/00313/2020 and UIDP/00313/2020), the CENTRO 2020 Regional Operational Programme (project references SASCOT-CENTRO-01-0145-FEDER-028031 and PTDC/QUI-QOR/28031/2017), and the COMPETE 2020 Operational Thematic Program for Competitiveness and Internationalization (project reference HYLIGHT-POCI-01-0145-FEDER-031625), financed by national funds through the FCT (Fundação para a Ciência e a Tecnologia)/MEC (Ministério da Educação e Ciência) (PIDDAC) and when appropriate co-financed by the European Union through the European Regional Development Fund under the Portugal 2020 Partnership Agreement. The PhD grant held by RPM (ref. 2020.04758.BD) was funded by the FCT and the European Social Fund (ESF). NMR data collected at the UC-NMR facility are supported in part by the EDRF through the COMPETE Program and by national

funds from the FCT through grants RECI/QEQ-QFI/0168/2012 and CENTRO-07-CT62-FEDER-002012, and also through support to Rede Nacional de Ressonância Magnética Nuclear (RNRMN) and to Coimbra Chemistry Centre through grant UID/QUI/00313/2019. AG thanks the FCT/MCTES for funding through the Individual Call to Scientific Employment Stimulus (CEECIND/02128/2017). CC thanks the FCT for a PhD Grant (ref. 2020.09661.BD).

## Conflict of interest

The authors declare that the research was conducted in the absence of any commercial or financial relationships that could be construed as a potential conflict of interest.

## References

- Abeyrathna, N., Washington, K., Bashur, C., and Liao, Y. (2017). Nonmetallic carbon monoxide releasing molecules (CORMs). *Org. Biomol. Chem.* 15, 8692–8699. doi:10.1039/C7OB01674C
- Akanksha, and Maiti, D. (2012). Microwave-assisted palladium mediated decarbonylation reaction: Synthesis of eulatachromene. *Green Chem.* 14, 2314–2320. doi:10.1039/c2gc35622h
- Albini, A. (2021). Norrish' type I and II reactions and their role in the building of photochemical science. *Photochem. Photobiol. Sci.* 20, 161–181. doi:10.1007/s43630-020-00003-9
- Anderson, S. N., Richards, J. M., Esquer, H. J., Benninghoff, A. D., Arif, A. M., and Berreau, L. M. (2015). A structurally-tunable 3-hydroxyflavone motif for visible light-induced carbon monoxide-releasing molecules (CORMs). *ChemistryOpen* 4, 590–594. doi:10.1002/open.201500167
- Antony, L. A. P., Slanina, T., Šebej, P., Šolomek, T., and Klán, P. (2013). Fluorescein analogue xanthene-9-carboxylic acid: A transition-metal-free CO releasing molecule activated by green light. *Org. Lett.* 15, 4552–4555. doi:10.1021/ol4021089
- Atkin, A. J., Lynam, J. M., Moulton, B. E., Sawle, P., Motterlini, R., Boyle, N. M., et al. (2011). Modification of the deoxy-myoglobin/carbonmonoxy-myoglobin UV-vis assay for reliable determination of CO-release rates from organometallic carbonyl complexes. *Dalton Trans.* 40, 5755–5761. doi:10.1039/C0DT01809K
- Baggiolini, E., Hamlow, H. P., and Schaffner, K. (1970). Photochemical reactions. LIX. On the mechanism of the photodecarbonylation of  $\beta,\gamma$ -unsaturated aldehydes. *J. Am. Chem. Soc.* 92, 4906–4921. doi:10.1021/ja00719a026
- Bellotto, M., Rebours, B., Clause, O., Lynch, J., Bazin, D., and Elkaïm, E. (1996). A reexamination of hydratalcite crystal chemistry. *J. Phys. Chem.* 100, 8527–8534. doi:10.1021/jp960039j
- Cao, J., Zheng, Z.-J., Xu, Z., and Xu, L.-W. (2017). Transition-metal-catalyzed transfer carbonylation with HCOOH or HCHO as non-gaseous C1 source. *Coord. Chem. Rev.* 336, 43–53. doi:10.1016/j.ccr.2017.01.005
- Chapman, O. L., and McIntosh, C. L. (1971). Photochemical decarbonylation of unsaturated lactones and carbonates. *J. Chem. Soc. D.* 383–384. doi:10.1039/C29710000383
- Chatterjee, M., Ishizaka, T., and Kawanami, H. (2018). Accelerated decarbonylation of 5-hydroxymethylfurfural in compressed carbon dioxide: A facile approach. *Green Chem.* 20, 2345–2355. doi:10.1039/c8gc00174j
- Chen, J., Shi, Z., Li, C., and Lu, P. (2021). Catalytic enantioselective synthesis of benzocyclobutenols and cyclobutanols via a sequential reduction/C–H functionalization. *Chem. Sci.* 12, 10598–10604. doi:10.1039/D1SC02119B
- Collins, P. M., Gupta, P., and Iyer, R. (1970). Photochemical decarbonylation of cyclic ketones in solution: Evidence for a biradical intermediate in the pyranosidulose-furanoside conversion. *J. Chem. Soc. D.* 1261–1262. doi:10.1039/C29700001261
- Costa, A. L., Gomes, A. C., Pillinger, M., Gonçalves, I. S., Pina, J., and Seixas de Melo, J. S. (2017). Insights into the photophysics and supramolecular organization of Congo red in solution and the solid state. *ChemPhysChem* 18, 564–575. doi:10.1002/cphc.201601236
- Crawford, R. J., and Tokunaga, H. (1980). A comparison of the stereochemistry and kinetics of thermolysis of *R*-(+)-Lauroleonic acid, *R*-(+)-Lauroleal, and *R*-(+)-Lauroleol. *Can. J. Chem.* 58, 463–465. doi:10.1139/v80-074
- CrystalMaker Software (2017). *CrystalMaker(R): A Crystal and Molecular Structures Modelling Program for Mac and Windows*, 9. Oxford, UK: CrystalMaker Software Ltd.
- Cui, G.-J., Xu, X.-Y., Lin, Y.-J., Evans, D. G., and Li, D.-Q. (2010). Synthesis and UV absorption properties of 5,5'-methylenedisalicylic acid-intercalated Zn-Al layered double hydroxides. *Ind. Eng. Chem. Res.* 49, 448–453. doi:10.1021/ie901151c
- Evans, D. G., and Slade, R. C. T. (2006). Structural aspects of layered double hydroxides. *Struct. Bond.* 119, 1–87. doi:10.1007/430\_005
- Family, F., and Garcia-Garibay, M. A. (2009). Photodecarbonylation of ketodiacids as ammonium salts: Efficient formation of C–C bonds between adjacent quaternary centers in the crystalline state. *J. Org. Chem.* 74, 2476–2480. doi:10.1021/jo802761t
- Fleutot, S., Dieudonné, B., Dupin, J. C., Renaudin, G., and Martinez, H. (2012). Thermal behaviors and grafting process of LDH/benzene derivative hybrid systems. *Thermochim. Acta* 538, 1–8. doi:10.1016/j.tca.2012.02.029
- Geilen, F. M. A., vom Stein, T., Engendahl, B., Winterle, S., Liauw, M. A., Klankermayer, J., et al. (2011). Highly selective decarbonylation of 5-(hydroxymethyl)furfural in the presence of compressed carbon dioxide. *Angew. Chem. Int. Ed.* 50, 6831–6834. doi:10.1002/anie.201100758†
- Gomes, A. C., Bruno, S. M., Gamelas, C. A., Valente, A. A., Abrantes, M., Gonçalves, I. S., et al. (2013). Intercalation of a molybdenum  $\eta^3$ -allyl dicarbonyl complex in a layered double hydroxide and catalytic performance in olefin epoxidation. *Dalton Trans.* 42, 8231–8240. doi:10.1039/C3DT50132A
- Gopidas, K. R., Cyr, D. R., Das, P. K., and George, M. V. (1987). Photochemical and thermal transformations of 3-benzyl-2(3H)-furanones and related substrates. *J. Org. Chem.* 52, 5505–5511. doi:10.1021/jo00234a002
- Grooms, C. R., Bruno, I. J., Lightfoot, M. P., and Ward, S. C. (2016). The Cambridge structural Database. *Acta Crystallogr. B Struct. Sci. Cryst. Eng. Mat.* B72, 171–179. doi:10.1107/S2052520616003954
- Horspool, W. M., and Khandelwal, G. D. (1970). Photo-decarbonylation of coumarandiones. *J. Chem. Soc. D.* 257–258. doi:10.1039/C29700000257
- Houk, K. N. (1976). The photochemistry and spectroscopy of  $\beta,\gamma$ -unsaturated carbonyl compounds. *Chem. Rev.* 76, 1–74. doi:10.1021/cr60299a001
- Huang, Y.-B., Yang, Z., Chen, M.-Y., Dai, J.-J., Guo, Q.-X., and Fu, Y. (2013). Heterogeneous palladium catalysts for decarbonylation of biomass-derived molecules under mild conditions. *ChemSusChem* 6, 1348–1351. doi:10.1002/cssc.201300190
- Ji, X., and Wang, B. (2018). Strategies toward organic carbon monoxide prodrugs. *Acc. Chem. Res.* 51, 1377–1385. doi:10.1021/acs.accounts.8b00019

## Publisher's note

All claims expressed in this article are solely those of the authors and do not necessarily represent those of their affiliated organizations, or those of the publisher, the editors and the reviewers. Any product that may be evaluated in this article, or claim that may be made by its manufacturer, is not guaranteed or endorsed by the publisher.

## Supplementary material

The Supplementary Material for this article can be found online at: <https://www.frontiersin.org/articles/10.3389/fchem.2022.1004586/full#supplementary-material>

- Karthikeyan, S., and Ramamurthy, V. (2007). Templating photodimerization of *trans*-cinnamic acid esters with a water-soluble Pd nanocage. *J. Org. Chem.* 72, 452–458. doi:10.1021/jo0617722
- Klopprogge, J. T., Hickey, L., and Frost, R. L. (2004). The effects of synthesis pH and hydrothermal treatment on the formation of zinc aluminum hydroxalicates. *J. Solid State Chem.* 177, 4047–4057. doi:10.1016/j.jssc.2004.07.010
- Konishi, H., and Manabe, K. (2019). Recent progress on catalytic Heck carbonylations using carbon monoxide surrogates. *Tetrahedron Lett.* 60, 151147. doi:10.1016/j.tetlet.2019.151147
- Liu, K.-J., Fu, Y.-L., Xie, L.-Y., Wu, C., He, W.-B., Peng, S., et al. (2018). Green and efficient: Oxidation of aldehydes to carboxylic acids and acid anhydrides with air. *ACS Sustain. Chem. Eng.* 6, 4916–4921. doi:10.1021/acssuschemeng.7b04400
- Lohray, B. B., Kumar, C. V., Das, P. K., and George, M. V. (1984). Photochemical and thermal transformations of 2(3*H*)-Furanones and bis(benzofuranones). A laser flash photolysis study. *J. Am. Chem. Soc.* 106, 7352–7359. doi:10.1021/ja00336a010
- Lu, H., Yu, T.-Y., Xu, P.-F., and Wei, H. (2021). Selective decarbonylation via transition-metal-catalyzed carbon-carbon bond cleavage. *Chem. Rev.* 121, 365–411. doi:10.1021/acs.chemrev.0c00153
- Mansour, A. M., and Shehab, O. R. (2018). Reactivity of visible-light induced CO releasing thiourea-based Mn(I) tricarbonyl bromide (CORM-NS1) towards lysozyme. *Inorganica Chim. Acta* 480, 159–165. doi:10.1016/j.ica.2018.05.009
- Matsumoto, T., Ishida, T., Takeda, Y., and Yagi, J. (1994). The enantioselective metabolism of 4-isopropenyltoluene in rabbits. *Biol. Pharm. Bull.* 17, 1441–1445. doi:10.1248/bpb.17.1441
- Mikol, G. J., and Boyer, J. H. (1972). Photo-induced decarbonylation of  $\beta$ -styryl isocyanates. *J. Chem. Soc. Chem. Commun.* 439–439. doi:10.1039/c39720000439
- Morgan, B. J., Mulrooney, C. A., and Kozlowski, M. C. (2010). Perylenequinone natural products: Evolution of the total synthesis of cercosporin. *J. Org. Chem.* 75, 44–56. doi:10.1021/jo9013854
- Mortko, C. J., and Garcia-Garibay, M. A. (2005). Green chemistry strategies using crystal-to-crystal photoreactions: Stereoselective synthesis and decarbonylation of *trans*- $\alpha,\alpha'$ -dialkenoylcyclohexanones. *J. Am. Chem. Soc.* 127, 7994–7995. doi:10.1021/ja0508166
- Motterlini, R., Clark, J. E., Foresti, R., Sarathchandra, P., Mann, B. E., and Green, C. J. (2002). Carbon monoxide-releasing molecules. Characterization of biochemical and vascular activities. *Circ. Res.* 90, e17–e24. doi:10.1161/hh0202.104530
- Natarajan, A., Ng, D., Yang, Z., and Garcia-Garibay, M. A. (2007). Parallel syntheses of (+)- and (-)- $\alpha$ -Cuparenone by radical combination in crystalline solids. *Angew. Chem. Int. Ed.* 46, 6485–6487. doi:10.1002/anie.200700679
- Newman, S. P., and Jones, W. (1998). Synthesis, characterization and applications of layered double hydroxides containing organic guests. *New J. Chem.* 22, 105–115. doi:10.1039/A708319J
- Ng, D., Yang, Z., and Garcia-Garibay, M. A. (2004). Total synthesis of ( $\pm$ )-Herbertenolide by stereospecific formation of vicinal quaternary centers in a crystalline ketone. *Org. Lett.* 6, 645–647. doi:10.1021/ol0499250
- Oelgemöller, M., and Hoffmann, N. (2016). Studies in organic and physical photochemistry – An interdisciplinary approach. *Org. Biomol. Chem.* 14, 7392–7442. doi:10.1039/c6ob00842a
- Ogawa, M., and Kuroda, K. (1995). Photofunctions of intercalation compounds. *Chem. Rev.* 95, 399–438. doi:10.1021/cr00034a005
- Pattabiraman, M., Sivaguru, J., and Ramamurthy, V. (2018). Cucurbiturils as reaction containers for photocycloaddition of olefins. *Isr. J. Chem.* 58, 264–275. doi:10.1002/ijch.201700100
- Peng, P., Wang, C., Shi, Z., Johns, V. K., Ma, L., Oyer, J., et al. (2013). Visible-light activatable organic CO-releasing molecules (photoCORMs) that simultaneously generate fluorophores. *Org. Biomol. Chem.* 11, 6671–6674. doi:10.1039/c3ob41385c
- Poloukhine, A., and Popik, V. V. (2003). Highly efficient photochemical generation of a triple bond: Synthesis, properties, and photodecarbonylation of cyclopropenones. *J. Org. Chem.* 68, 7833–7840. doi:10.1021/jo034869m
- Ramamurthy, V. (2019). Achiral zeolites as reaction media for chiral photochemistry. *Molecules* 24, 3570. doi:10.3390/molecules24193570
- Ramamurthy, V., and Gupta, S. (2015). Supramolecular photochemistry: From molecular crystals to water-soluble capsules. *Chem. Soc. Rev.* 44, 119–135. doi:10.1039/c4cs00284a
- Ramamurthy, V. (2015). Photochemistry within a water-soluble organic capsule. *Acc. Chem. Res.* 48, 2904–2917. doi:10.1021/acs.accounts.5b00360
- Ramamurthy, V., and Sivaguru, J. (2016). Supramolecular photochemistry as a potential synthetic tool: Photocycloaddition. *Chem. Rev.* 116, 9914–9993. doi:10.1021/acs.chemrev.6b00040
- Resendiz, M. J. E., and Garcia-Garibay, M. A. (2005). Hammett analysis of photodecarbonylation in crystalline 1,3-diarylacetonates. *Org. Lett.* 7, 371–374. doi:10.1021/ol0480527
- Rodrigues, C. A. B., de Matos, M. N., Guerreiro, B. M. H., Gonçalves, A. M. L., Romão, C. C., and Afonso, C. A. M. (2011). Water as efficient medium for mild decarbonylation of tertiary aldehydes. *Tetrahedron Lett.* 52, 2803–2807. doi:10.1016/j.tetlet.2011.03.012
- Scaiano, J. C., and García, H. (1999). Intrazeolite photochemistry: Toward supramolecular control of molecular photochemistry. *Acc. Chem. Res.* 32, 783–793. doi:10.1021/ar9702536
- Schmidt, M. W., Baldridge, K. K., Boatz, J. A., Elbert, S. T., Gordon, M. S., Jensen, J. H., et al. (1993). General atomic and molecular electronic structure system. *J. Comput. Chem.* 14, 1347–1363. doi:10.1002/jcc.540141112
- Shao, C., Duan, H., Min, Y., and Zhang, X. (2020). Diphenyl cyclopropenone-centered polymers for site-specific CO-releasing and chain dissociation. *Chin. Chem. Lett.* 31, 299–302. doi:10.1016/j.ccl.2019.03.053
- Shichi, T., and Takagi, K. (2000). Clay minerals as photochemical reaction fields. *J. Photochem. Photobiol. C Photochem. Rev.* 1, 113–130. doi:10.1016/S1389-5567(00)00008-3
- Shiraki, S., Natarajan, A., and Garcia-Garibay, M. A. (2011). The synthesis and stereospecific solid-state photodecarbonylation of hexasubstituted *meso*- and *d,l*-ketones. *Photochem. Photobiol. Sci.* 10, 1480–1487. doi:10.1039/c1pp05080j
- Slanina, T., and Šebej, P. (2018). Visible-light-activated photoCORMs: Rational design of CO-releasing organic molecules absorbing in the tissue-transparent window. *Photochem. Photobiol. Sci.* 17, 692–710. doi:10.1039/C8PP00096D
- Soboleva, T., and Berreau, L. M. (2019). 3-Hydroxyflavones and 3-Hydroxy-4-oxoquinolines as carbon monoxide-releasing molecules. *Molecules* 24, 1252. doi:10.3390/molecules24071252
- Suzuki, M., Aotake, T., Yamaguchi, Y., Noguchi, N., Nakano, H., Nakayama, K.-i., et al. (2014). Synthesis and photoreactivity of  $\alpha$ -diketone-type precursors of acenes and their use in organic-device fabrication. *J. Photochem. Photobiol. C Photochem. Rev.* 18, 50–70. doi:10.1016/j.jphotochemrev.2013.10.003
- Toscani, A., Hind, C., Clifford, M., Kim, S.-H., Gucic, A., Wooley, C., et al. (2021). Development of photoactivatable phenanthroline-based manganese(II) CO-releasing molecules (photoCORMs) active against ESKAPE bacteria and bacterial biofilms. *Eur. J. Med. Chem.* 213, 113172. doi:10.1016/j.ejmech.2021.113172
- Veeraman, M., Resendiz, M. J. E., and Garcia-Garibay, M. A. (2006). Large-scale photochemical reactions of nanocrystalline suspensions: A promising green chemistry method. *Org. Lett.* 8, 2615–2617. doi:10.1021/ol060978m
- Wu, L., Liu, Q., Jackstell, R., and Beller, M. (2014). Carbonylations of alkenes with CO surrogates. *Angew. Chem. Int. Ed.* 53, 6310–6320. doi:10.1002/anie.201400793
- Yang, H., Cui, X., Deng, Y., and Shi, F. (2014). Highly efficient carbon catalyzed aerobic selective oxidation of benzylic and allylic alcohols under transition-metal and heteroatom free conditions. *RSC Adv.* 4, 59754–59758. doi:10.1039/C4RA11148F
- Zhang, J., Gembicky, M., Messerschmidt, M., and Coppens, P. (2007). Hydrogen-bond quenching of photodecarbonylation in the solid state and recovery of reactivity by co-crystallization. *Chem. Commun.* 2399–2401. doi:10.1039/B700073A
- Zhu, H., Feng, Y., Tang, P., Cui, G., Evans, D. G., Li, D., et al. (2011). Synthesis and UV absorption properties of auranicarboxylic acid intercalated Zn-Al layered double hydroxides. *Ind. Eng. Chem. Res.* 50, 13299–13303. doi:10.1021/ie2016366





## OPEN ACCESS

## EDITED BY

Verónica de Zea Bermudez,  
University of Trás-os-Montes and Alto  
Douro, Portugal

## REVIEWED BY

Ramesh L. Gardas,  
Indian Institute of Technology Madras,  
India  
Oleksandr Tomchuk,  
Institute of Nuclear Physics, Polish  
Academy of Sciences, Poland  
Umapathi Reddicherla,  
Inha University, South Korea

## \*CORRESPONDENCE

Germán Pérez-Sánchez,  
gperez@ua.pt

## SPECIALTY SECTION

This article was submitted to Ceramics  
and Glass,  
a section of the journal  
Frontiers in Materials

RECEIVED 03 August 2022

ACCEPTED 23 September 2022

PUBLISHED 14 October 2022

## CITATION

Pérez-Sánchez G, Schaeffer N,  
Greaves TL, Pereira JFB and  
Coutinho JAP (2022), Tuning the ionic  
character of sodium dodecyl sulphate  
via counter-ion binding: An  
experimental and computational study.  
*Front. Mater.* 9:1011164.  
doi: 10.3389/fmats.2022.1011164

## COPYRIGHT

© 2022 Pérez-Sánchez, Schaeffer,  
Greaves, Pereira and Coutinho. This is  
an open-access article distributed  
under the terms of the [Creative  
Commons Attribution License \(CC BY\)](#).  
The use, distribution or reproduction in  
other forums is permitted, provided the  
original author(s) and the copyright  
owner(s) are credited and that the  
original publication in this journal is  
cited, in accordance with accepted  
academic practice. No use, distribution  
or reproduction is permitted which does  
not comply with these terms.

# Tuning the ionic character of sodium dodecyl sulphate *via* counter-ion binding: An experimental and computational study

Germán Pérez-Sánchez<sup>1\*</sup>, Nicolas Schaeffer<sup>1</sup>,  
Tamar L. Greaves<sup>2</sup>, Jorge F. B. Pereira<sup>3</sup> and João A. P. Coutinho<sup>1</sup>

<sup>1</sup>CICECO—Aveiro Institute of Materials, Department of Chemistry, University of Aveiro, Aveiro, Portugal, <sup>2</sup>STEM College, RMIT University, Melbourne, VIC, Australia, <sup>3</sup>CIEPQPF, Department of Chemical Engineering, University of Coimbra, Coimbra, Portugal

Solutions of surfactants exhibit remarkable features, such as a tunable amphiphilic character, which can further be varied for ionic surfactants through variations in their Coulombic interactions. These properties are very useful in many industrial applications such as in extraction, purification, and formulation processes, as detergents, wetting agents, or emulsifiers. Rather unexpectedly, the addition of tetrabutylammonium chloride ( $[N_{4,4,4,4}][Cl]$ ) to solutions of the ionic surfactant of sodium dodecyl sulphate (SDS) results in the appearance of a phase transition above the lower critical solution temperature (LCST), a property usually associated with non-ionic surfactants. The aim of this study is to provide a detailed nanoscopic scenario on the interaction between SDS micelles and  $[N_{4,4,4,4}][Cl]$  moieties to better understand the nature of the LCST cloud point and how to confer it to a given ionic surfactant system. A coarse-grained molecular dynamics (CG-MD) computational framework, under the latest MARTINI 3.0 force field, was developed and validated using available literature data. The impact of  $[N_{4,4,4,4}][Cl]$  concentration in the phase of SDS micellar aqueous solutions was then characterized and compared using experimental results. Specifically, dynamic light scattering (DLS) measurements and small-angle X-ray scattering (SAXS) profiles were obtained at different  $[N_{4,4,4,4}]^+/[DS]^-$  molar ratios (from 0.0 to 1.0) and compared with the CG-MD results. A good agreement between computer simulations and experimental findings was obtained, reinforcing the suitability of GC-MD to simulate complex phase behaviors. When the  $[N_{4,4,4,4}]^+/[DS]^-$  molar ratio is  $< 0.5$ , a weak impact of the cation in the micellar distribution was found whereas for ratios  $> 0.5$ , the system yielded clusters of enclosed small  $[DS]^-$  aggregates. Thus, the CG-MD simulations showed the formation of mixed  $[DS]^-$  and  $[N_{4,4,4,4}]^+$  aggregates with  $[N_{4,4,4,4}]^+$  cations acting as a bridge between small  $[DS]^-$  micelles. The CG-MD simulation framework developed in this work captured the role of  $[N_{4,4,4,4}]^+$  in the micellar phase transition whilst improving the results obtained with preceding computer models for which the limitations

on capturing SDS and  $[N_{4,4,4,4}]Cl$  mixtures in aqueous solutions are also shown in detail.

#### KEYWORDS

MARTINI 3.0, surfactant self-assembly, phase separation, thermo-responsive system, coarse-grained molecular dynamics simulations

## 1 Introduction

Stimuli-responsive systems can change their phase behavior after a temperature, magnetic field, light, or pH adjustment. Exploiting these properties allows for the design of novel and more efficient applications such as the purification of biomolecules, drug delivery nanocarriers, or the recovery of valuable compounds from wastewater (Ventura et al., 2017; Schaeffer et al., 2019a). Thermo-responsive systems can also be used for integrated reaction-separation processes (Ferreira et al., 2018; Morais et al., 2021). In this context, the reaction takes place under homogeneous conditions prior to the separation of products and catalysts/reactants into separate phases after the temperature change (Kohno et al., 2011; Ferreira et al., 2018). Thermo-responsive systems can exhibit an upper or lower critical solution temperature (UCST/LCST), depending on whether entropic (LCST) or enthalpic (UCST) terms dominate, led by solute-water interactions, mostly hydrogen bonding and strong polar interactions (Kohno and Ohno, 2012). Looking beyond the design of integrated reaction-separation systems, thermo-responsive systems were further demonstrated as draw solutions for forward osmosis desalination (Zhong et al., 2016) or heat storage media (Forero-Martinez et al., 2022).

Thermo-responsive systems presenting a LCST behavior are traditionally restricted to non-ionic polymeric and surfactant systems (Mukherjee et al., 2011) with few ionic systems exhibiting temperature dependent phase separation (Mukherjee et al., 2011; Naqvi and Kabir-ud-Din, 2018). However, aqueous solutions of bulky quaternary phosphonium or ammonium salts, often referred to as ionic liquids (ILs), were shown to phase separate upon heating with the cloud point dependent on the hydration properties of the anion (Gutowski et al., 2003; Martínez-Aragón et al., 2009; Freire et al., 2012; Schaeffer et al., 2018; Meyer et al., 2022). One example of such a system is the mixture of tetrabutylammonium halide ( $[N_{4,4,4,4}]X$  ( $X = Cl$  or  $Br$ ) with the anionic surfactant sodium dodecyl sulphate (SDS) (Chauhan and Kaur, 2017). As an example, this aqueous  $[N_{4,4,4,4}]Cl$ /SDS mixture was applied towards the one-pot process for the solid-liquid extraction of violacein from *Yarrowia lipolytica* yeast biomass and its purification by estimating the LCST point using the cloud-point method to analyze the separation from contaminant proteins (Schaeffer et al., 2019b). Interestingly, the  $[N_{4,4,4,4}]X$  and SDS mixtures exhibit an anomalous temperature dependent behavior as a function of the  $[N_{4,4,4,4}]Cl$  concentration in SDS aqueous solutions (Mata et al., 2004; Schaeffer et al., 2019a). This

system was experimentally characterized by cloud point measurements, dynamic light scattering (DLS), surface tension, (Bales and Zana, 2004; Mata et al., 2004), calorimetry (Mitra et al., 2007) or nuclear magnetic resonance (NMR) (Lin et al., 2013). Results indicate that the system properties result from extensive adsorption of the  $[N_{4,4,4,4}]^+$  cation of the  $[DS]^-$  micelles due to the low charge density, and therefore lower hydration, of the  $[DS]^-$  polar head, and large apolar volume of the symmetrical  $[N_{4,4,4,4}]^+$  ion. Nevertheless, these are all equilibrium-based measurements that only partially probe the dynamic nature of this system and the driving forces determining co-aggregation and phase separation. Considering the theoretical and practical relevance of conferring thermo-responsive behavior to ionic systems, a detailed understanding of the interactions and how these systematically vary with the molar ratio of  $[N_{4,4,4,4}]^+$  to  $[DS]^-$  is of interest.

The interactions at the nanoscale directing the self-assembly and aggregation in colloidal systems are rather complex and a difficult issue for experimentalists. Fortunately, molecular dynamics simulations provide the required level of detail to analyze the interactions between SDS and  $[N_{4,4,4,4}]Cl$  moieties and the complex cooperative self-assembly. For instance, E. Ritter et al. Berthod et al. (1991) carried out all-atom molecular dynamics (AA-MD) simulations with the COSMOmic (Klamt et al., 2008) package using preformed SDS micelles. In this work, a comprehensive analysis of micelle distributions for a wide number of surfactants (SDS, CTAB (cetyltrimethylammonium bromide),  $C_{12}E_{10}$ , Brij35,  $C_{12}E_{23}$ , Triton X-114 and Triton X-100) was developed, with good agreement to experiments, demonstrating that simulations can be a remarkable tool for predicting relevant properties of these micellar solutions. However, they were limited to study pre-assembled structures since AA-MD models cannot cope with the size/time scale to reproduce the self-assembly of relatively large structures. Manhub et al. Mahbub et al. (2019) studied the micellization of SDS and CTAB aqueous solutions and the impact of various salts at different temperatures using AA-MD simulations and the universal force field (UFF). They carried out experimental conductivity measurements to estimate the critical micelle concentrations, which was used as a reference for the MD simulations. MD results demonstrated that salts enhanced the interactions between the surfactants. The authors evaluated the formation of CTAB/SDS micelles and the complex interactions between both surfactants. The MD also demonstrated that the addition of salt enhanced the electrostatic interactions between SDS and CTAB moieties, in agreement with

the experimental results. Tang et al. [Tang et al. \(2014\)](#) evaluated the effect of the diverse available force fields on the aggregation of SDS in water using AA-MD simulations. Using preformed structures, they found a low impact from the force field choice with small SDS aggregates, but vesicles rather than the expected rod-like structures were found when the SDS aggregate size was increased. Closer to the identified problematic, Liu et al. [Liu et al. \(2016a\)](#), [Liu et al. \(2016b\)](#) studied the influence of different tetraalkylammonium counterions (tetraalkylammonium  $[N_{n,n,n,n}]^+$ , tetramethylammonium  $[N_{1,1,1,1}]^+$ , tetraethylammonium  $[N_{2,2,2,2}]^+$ , tetrapropylammonium  $[N_{3,3,3,3}]^+$  and  $[N_{4,4,4,4}]^+$ ) on  $[DS]^-$  micelles using AA-MD simulations, focusing on the analysis of systems containing a single pre-formed micelle to investigate the various interaction patterns between the components.

However, time and size scale restrictions inherent in molecular dynamics atomistic models (AA-MD) limits their use to the initial stages of micelle formation, leaving out the relevant study of any inter micelle interactions and phase behaviour. [Illa-Tuset et al., 2018](#)). The less detailed but more computationally efficient coarse-grained molecular dynamics (CG-MD) models can overcome such limitations, appearing as crucial tools to analyze the impact of  $[N_{4,4,4,4}]Cl$  on the phase behavior of SDS aqueous solutions. [Pérez-Sánchez et al., 2016](#); [Chien et al., 2017](#); [Illa-Tuset et al., 2018](#); [Pérez-Sánchez et al., 2020](#)). Progress towards this was made by Jalili et al. [Jalili and Akhavan \(2009\)](#) who used the MARTINI 2 CG-MD framework to model SDS aqueous solutions, with good agreement to previous AA-MD results [\(Gao et al., 2005; Sammalkorpi et al., 2007; Ritter et al., 2016\)](#) and to experimental micelle results. [\(Quina et al., 1995; Anachkov et al., 2012; Hammouda, 2013\)](#). LeBard et al. [Lebard et al. \(2012\)](#) performed CG-MD simulations to characterize the micellar distributions of three surfactants, including aqueous solutions of SDS. In that work, the authors conducted a comprehensive study regarding the impact of surfactant concentration on the aggregation number, noticing polydispersity of micelle sizes, and the impact that the type of hardware has on those values, with the CG-MD results compared with experimental literature data. The new method developed by the authors where CG-MD data is used as an input for the theoretical model, demonstrated that can predict critical micelle concentrations (CMC) in good agreement with literature data. However, LeBard et al. [Lebard et al. \(2012\)](#) used the HOOMD-Blue package for MD simulations and an *ad hoc* SDK force field for the SDS, with the consequence loss of transferability and generality offered by the MARTINI model and the GROMACS package. Ruiz-Morales et al. [Ruiz-Morales and Romero-Martínez \(2018\)](#) carried out CG-MD simulations with the MARTINI 2.2 model to evaluate the impact of the simulation box size on the critical micelle concentration and shear viscosity. They demonstrated the ability of MARTINI 2.2 for obtaining dynamic properties such as viscosity, finding a very good agreement with literature experimental data and improving upon the results of

more detailed AA-MD models. Recently, Anogiannakis et al. [Anogiannakis et al. \(2020\)](#) used MARTINI 2.2 to perform CG-MD simulations of SDS and CTAB aqueous solutions. In that work they estimated the CMC, aggregation numbers and small angle neutron scattering (SANS) patterns at low concentrations, as well as the liquid crystal phase behavior. Specifically, the authors used the Dry MARTINI 2.2 forcefield where some adjustments were introduced in the non-bonded interactions to find a good agreement with literature data. However, the Dry MARTINI 2.2 model has some inherent limitations when compared with the explicit water MARTINI 2.2 version, since a new parameterization of all interactions must be carried out when new moieties are included in the system.

With the aim to find a general, transferable, and reliable computer model to tackle SDS and  $[N_{4,4,4,4}]Cl$  aqueous solutions, the MARTINI 2.2 model was initially selected. The regular and polarizable water models were benchmarked, exhibiting both advantages and disadvantages when reproducing experimental results of micelle distribution and the impact of  $[N_{4,4,4,4}]Cl$  on SDS aqueous solutions. Fortunately, with the advent of the recently released MARTINI 3.0 [\(42\)](#) and the validated SDS and  $[N_{4,4,4,4}]Cl$  CG-MD models, the advantages and disadvantages converged in the new MARTINI 3.0 as detailed below. Thus, the manuscript is organized as follows; the technical aspects of the CG-MD simulations and ad hoc experiments are described in the Methods section, as well as the topology and model benchmark. This is followed by the CG-MD results on the impact of  $[N_{4,4,4,4}]Cl$  in SDS aqueous solutions, which are presented for the selected model. Simulation snapshots are discussed regarding the characterization of the phase behavior, along with computed Small-angle X-ray scattering (SAXS) profiles that are compared with experimental results obtained for this study. Additionally, dynamic light scattering (DLS) and NMR experimental data were used to characterize the phase behavior.

## 2 Methodology

### 2.1 Simulation details

All simulations were performed with the 2019 GROMACS package [\(Lindahl et al., 2018\)](#), which integrates the equations of motion using the leapfrog algorithm [\(Hockney et al., 1974\)](#) with a 20 fs time step. The total potential energy entails bonded interactions for bond stretching and angle bending—bonds were compelled with the LINear Constraint Solver (LINCS) [\(Hess et al., 1997\)](#)—whereas non-bonded ones used the Lennard-Jones (LJ) potential and the regular Coulomb interaction function—long-range electrostatic interactions were assessed using the Particle-Mesh-Ewald (PME). [\(Darden et al., 1993\)](#). The non-bonded interactions were calculated with the Verlet cutoff scheme (potential-shift-Verlet modifier) and a

cut-off of 1.2 nm. The temperature (298 K) and coupling time constant (1.0 ps) and pressure (1 bar and isotropic coupling with a time constant of 24.0 ps) were set with the velocity-rescaling thermostat (Bussi et al., 2007) and Parrinello-Rahman barostat, (Parrinello and Rahman, 1981), respectively. The simulation boxes were created with Packmol, (Martínez et al., 2009), setting the molecules randomly, with periodic boundary conditions in all directions.

Prior to the NpT ensemble production runs, an energy minimization step was done using the steepest descent algorithm to avoid close contacts between molecules which could occur in the preparation of the initial simulation boxes. Afterwards, two equilibrium MD simulations were carried out on the NVT and NpT ensembles to establish the desired temperature and density, respectively. The total potential energy, pressure, temperature, and densities were monitored alongside the equilibrium steps and production runs to ensure the thermodynamic equilibrium. The Visual Molecular Dynamics (VMD) software package (Humphrey et al., 1996) was used to visualize the systems. The micellar distributions were analyzed using an in-house code (Jorge, 2008) based in the Hoshen–Kopelman cluster counting algorithm (Hoshen and Kopelman, 1976). Computed SAXS profiles in the MD simulations were obtained with the gmx saxe Gromacs tool which calculates the SAXS structure factors for given coarse-grained form factors based on Cromer's method (Cromer and Mann, 1968).

## 2.2 Experimental methodology

Tetrabutylammonium chloride (97% purity) and sodium dodecyl sulfate (Pharmaceutical grade) were obtained from Sigma Aldrich (United States) and Panreac (Germany), respectively. A series of samples were prepared gravimetrically with varying proportions of SDS,  $[N_{4,4,4,4}]Cl$  and water molecules. The specific compositions are provided in [Supplementary Table S1](#). Ultrapure, double distilled water, passed through a reverse osmosis system and further treated with a Milli-Q plus 185 water purification apparatus, (18.2 MΩ.cm at 25°C) was used for all experiments.

Small angle X-ray scattering (SAXS) measurements were made of each of these samples at the SAXS/WAXS beamline of the Australian Synchrotron. Samples were loaded into 1.5 mm quartz capillaries and sealed with epoxy. Scattering patterns were acquired at room temperature over 1 s, using an X-ray energy of 11.5 keV and a scattering vector range of 0.01–0.44 Å<sup>-1</sup>. The 2D scattering profiles were converted to intensity vs. scattering vector, and the scattering contribution from an empty capillary subtracted, using the software Scatterbrain (<http://archive.synchrotron.org.au/aussynbeamlines/saxswaxs/software-saxswaxs>).

<sup>1</sup>H-NMR measurements were performed on a Bruker Avance 300 NMR spectrometer (Germany) operating at

300 MHz and 298 K. Samples were analyzed in a glass NMR tube with an added sealed capillary in a coaxial insert containing D<sub>2</sub>O and trimethylsilyl propanoic acid as an internal reference, both purchased from SigmaAldrich (United States). The formation of aggregates was followed by dynamic light scattering (DLS) using a Zetasizer Nano-ZS photometer from Malvern Instruments (United Kingdom). Sample preparation for NMR and DLS were identical and contained a fixed SDS concentration of 2 wt%, with all samples prepared gravimetrically. Following the weighing of SDS,  $[N_{4,4,4,4}]Cl$  and H<sub>2</sub>O, all samples were equilibrated for 24 h. Prior to the analyses, all samples were filtered through a nylon 0.45 μm syringe, sonicated in an ultrasonic bath for 5 min to promote particle dispersion and degassing and left to rest in a sealed quartz cuvette. DLS analyses were carried at 298 K, with an equilibration time of 120 s. Irradiation was performed at a wavelength of 565 nm by a helium-neon laser and scattered light was detected at a backscattering angle of 173°. The automatic mode was used for both measurements and data processing, the viscosity and refractive index of water was used. Analyses were performed in triplicate and extracted results are averages.

## 2.3 Molecular modelling and coarse-grained model validation

### 2.3.1 Validation of individual and mixed sodium dodecyl sulphate and $[N_{4,4,4,4}]Cl$ aqueous solutions in MARTINI 2.2

The MARTINI 2.2 model (Marrink et al., 2007) CG model was chosen initially since it reproduces reasonably well the micelle distribution of SDS aqueous solutions. Thus, three apolar C<sub>1</sub> beads for the alkyl-chain tail and a charged Q<sub>a</sub> (*a* meaning hydrogen bond acceptor) for the Sulphur head group were used (Jalili and Akhavan, 2009). The Q<sub>d</sub> (*d* meaning hydrogen bond donor) was selected for the Na<sup>+</sup> counterions whereas Q<sub>a</sub> was chosen for Cl<sup>-</sup>. For  $[N_{4,4,4,4}]^+$ , the ammonium center is represented with a Q<sub>0</sub> bead whilst the butyl groups are mapped with C<sub>3</sub> beads (Bastos et al., 2020). The P<sub>4</sub> and antifreeze BP<sub>4</sub> bead types, which implicitly include four water molecules, were selected to solvate the SDS system where 10% of BP<sub>4</sub> was included to avoid any unrealistic freezing of the regular MARTINI 2.2 water (Marrink et al., 2007). [Supplementary Figure S1](#) illustrates the MARTINI 2.2 CG mapping for all molecules. Initially, a CG-MD simulation test was run for 3 μs with the aim to reproduce the micellar distribution of a 2 wt% of SDS concentration in aqueous solution. A spherical micellar solution was found with an averaged micelle aggregation number of N<sub>agg</sub> = 60, in good agreement with experimental estimates N<sub>agg</sub> ~ 50–73 (Berthod et al., 1991; Itri and Amaral, 1991; Quina et al., 1995; Bales et al., 1998; Anachkov et al., 2012). [Supplementary Figure S2A](#) shows the final CG-MD simulation



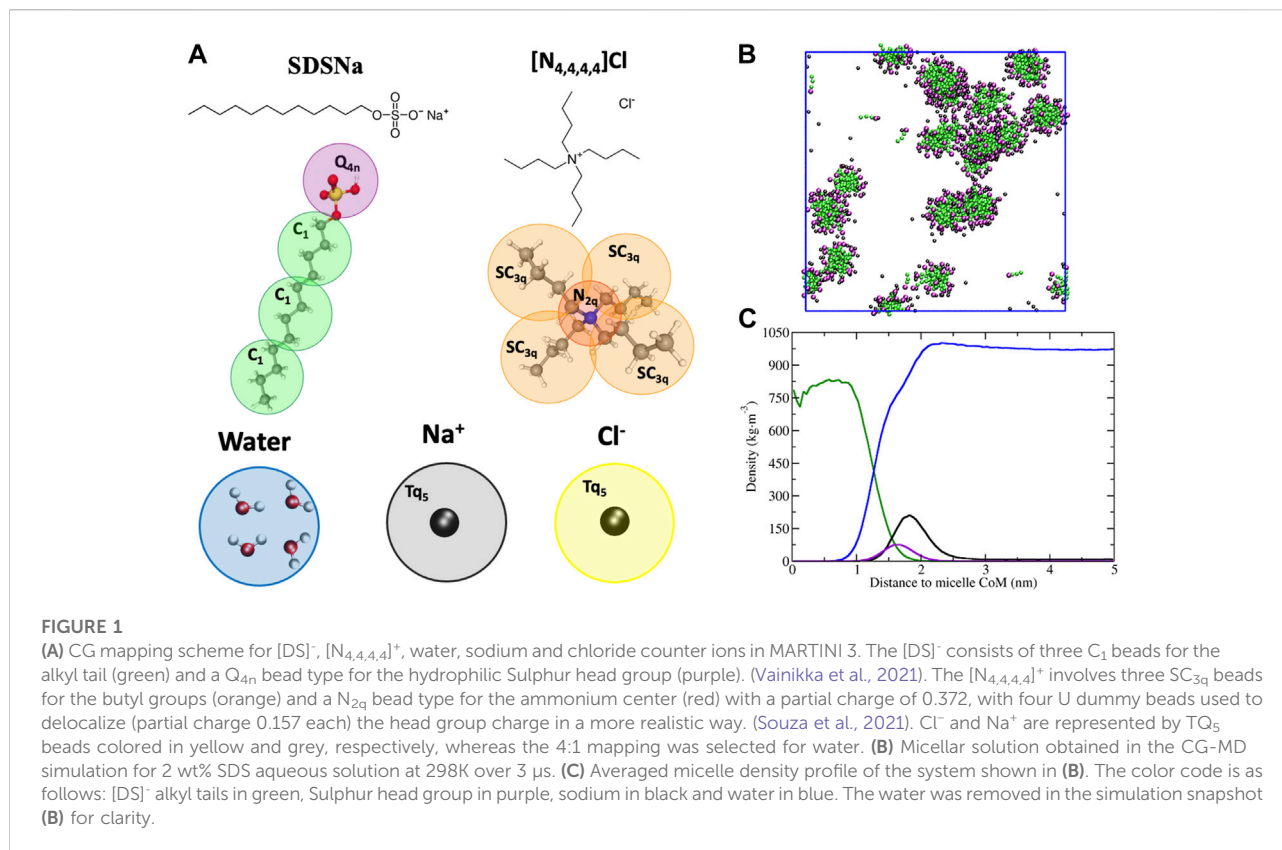
snapshot, and the micelle density profile was obtained with our cluster counting code displaying spherical micelles with an averaged diameter of  $\varnothing = 3.6$  nm. Similarly, the  $[N_{4,4,4,4}]^+$  CG model was previously developed (Bastos et al., 2020) consisting of three apolar  $C_3$  beads for the butyl groups and one  $Q_0$  (0 meaning no hydrogen bond donor/acceptor capability) to map the nitrogen charged center. The  $Q_a$  was selected for the  $Cl^-$  counterions. To ensure that this system does not excessively aggregate in line with reported polarizable AA-MD results, (Dong et al., 2017), a simulation test of a 6 wt% of  $[N_{4,4,4,4}]Cl$  in aqueous solution was also run over 3  $\mu s$ . As can be noticed in Supplementary Figure S2B, no evidence of aggregation was found where the simulation box density profile—obtained with the *gmx density* Gromacs tool—showed a homogeneous distribution of  $[N_{4,4,4,4}]Cl$  in the simulation box. The density of the simulation box was  $\rho = 0.93$  g cm $^{-3}$ , in reasonable agreement with the experimental result of  $\rho = 1.018$  g cm $^{-3}$  (Jain et al., 2013).

Then, different concentrations of  $[N_{4,4,4,4}]Cl$  were included in a 2 wt% of SDS aqueous solution where the systems were arranged by randomly placing all molecules in the simulation box using the Packmol code (Martínez et al., 2009). In this manner, 0.1, 0.3, 0.5, 0.7, and 1.0  $[N_{4,4,4,4}]^+/[DS]^-$  ratios were addressed to compare with DLS and NMR experiments carried out in this work. Therefore, the average hydrodynamic diameter (by volume) of aggregates in solution were obtained by DLS measurements and the results at different  $[N_{4,4,4,4}]^+/[DS]^-$  ratios are shown in Supplementary Figure S3A. Furthermore, Supplementary Figure S3B shows the NMR shift of the mixture relative to that of the pure compounds in water, which was obtained to highlight the difference between SDS,  $[N_{4,4,4,4}]Cl$  aqueous solutions and their mixtures. Supplementary Figure S4 shows the simulation snapshots for 0.3, 0.5, and 1.0  $[N_{4,4,4,4}]^+/[DS]^-$  ratios after 1.5  $\mu s$ . Therefore, while the MARTINI 2.2 model reproduced SDS aqueous solutions very well in terms of the micellar distribution (Berthod et al., 1991; Itri and Amaral, 1991; Quina et al., 1995; Bales et al., 1998; Anachkov et al., 2012), whilst no clumped structures were seen in the 6 wt%  $[N_{4,4,4,4}]Cl$  aqueous solution simulation. (Dong et al., 2017). In addition, the 2 wt% of SDS aqueous solution exhibited spherical micelles with an averaged diameter  $\varnothing \sim 3.6$  nm in reasonable agreement to what it was found in the DLS experiments at  $[N_{4,4,4,4}]^+/[DS]^- = 0.0$  (Supplementary Figure S3A). Unfortunately, the MARTINI 2.2 could not capture the micellar-to-clustered transition noticed in our experiments when  $[N_{4,4,4,4}]^+/[DS]^- > 0.5$  as shown in Supplementary Figure S3A. Conversely, prolate and rod like structures were obtained in our CG-MD simulations as shown in Supplementary Figure S4, mainly formed by small and joined  $[DS]^-$  aggregates, in contrast with the well-know SDS homogeneous micellar phase commonly found in the literature (Itri and Amaral, 1991; Bales et al., 1998). The solution with a ratio of 0.5  $[N_{4,4,4,4}]^+/[DS]^-$  shown in

Supplementary Figure S4B exhibited a spherical aggregate formed by clumped small  $[DS]^-$  aggregates with some interleaved  $[N_{4,4,4,4}]^+$  moieties in the center, acting as a bridge between them. Similarly, Supplementary Figure S4C displays a similar scenario for the solution with a ratio of  $[N_{4,4,4,4}]^+/[DS]^- = 1.0$  but the  $[N_{4,4,4,4}]^+$  moieties were homogeneously arranged in the spherical aggregate. Analogous scenarios were found for  $[N_{4,4,4,4}]^+/[DS]^-$  ratios of 0.1 and 0.7 (not shown in Supplementary Figure S4) indicating that the MARTINI 2.2 framework cannot capture the micellar-to-clustered transition above the 0.5 ratio as displayed in the experiments (Supplementary Figure S3A). The simplicity of the regular MARTINI 2.2 water model, with a very limited energy landscape among other limitations (use of water antifreeze beads), could be the reason behind this issue.

### 2.3.2 Validation of individual and mixed sodium dodecyl sulphate and $[N_{4,4,4,4}]Cl$ aqueous solutions with polarizable water in MARTINI 2.2

Since the polarizable water (PW) model available in MARTINI 2.2 offers a better perspective for the energy landscape, the PW model developed by Yesylevskyy et al. (2010) was used in the above systems. No clumping was found for the 6 wt%  $[N_{4,4,4,4}]Cl$  aqueous solution simulation test after 3  $\mu s$  from, in agreement with literature (Dong et al., 2017). Then, the SDS 2 wt% aqueous solution was run to evaluate the impact of the polarizable water in the SDS micelle distribution. Unfortunately, small spherical micelles with an averaged aggregation number of  $N_{agg} = 20$  were obtained after 1.5  $\mu s$ , distant from the experimentally accepted values that are in the range of  $N_{agg} \sim 50$ –73 (Berthod et al., 1991; Itri and Amaral, 1991; Quina et al., 1995; Bales et al., 1998; Anachkov et al., 2012). CG-MD simulations showed an averaged diameter of  $\varnothing \sim 3.0$  nm, exhibiting slightly smaller diameter when compared with the regular water model. Conversely, the polarizable water model offered a better perspective on tackling the impact of  $[N_{4,4,4,4}]Cl$  in the 2 wt% SDS aqueous solution as can be noticed in the experimental micelle size distribution when the for  $[N_{4,4,4,4}]Cl$  is increased as shown in Supplementary Figure S3A. Supplementary Figure S5 shows the CG-MD simulation snapshots for  $[N_{4,4,4,4}]^+/[DS]^-$  ratios of 0.1, 0.3, 0.5, 0.7 and 1, after 1.5  $\mu s$ . Consistent with experiments, Supplementary Figures 5A–C showed mono-phasic spherical  $[DS]^-$  micelle distributions surrounded by  $[N_{4,4,4,4}]^+$  moieties for  $[N_{4,4,4,4}]^+/[DS]^-$  ratios of 0.1, 0.3, and 0.5. For ratios above 0.5, a clumped and a biphasic system were formed for 0.7 and 1.0 ratios where a  $[N_{4,4,4,4}]^+/[DS]^-$  and water rich phase were found, as illustrated in Supplementary Figures 5D–E. The 0.5  $[N_{4,4,4,4}]^+/[DS]^-$  ratio system seems the threshold for the micellar-to-clustered transition as observed in the experiments (Supplementary Figure S3A). Thus, the more realistic PW model was able to



capture the impact of  $[N_{4,4,4,4}]Cl$  in SDS aqueous solution but this framework was limited by the poor SDS micelle size distribution obtained in the simulations.

### 2.3.3 Validation of individual and mixed sodium dodecyl sulphate and $[N_{4,4,4,4}]Cl$ aqueous solutions in MARTINI 3.0

The recently released MARTINI 3.0 model developed by Souza et al. (2021) potentially overcomes most of the limitations of MARTINI 2.2. The new MARTINI 3 offers new interaction energies as well as an enhanced water model, including three scale options namely, W, SW, and TW with 4:1, 3:1, and 2:1 mapping, respectively. The SDS MARTINI 3 model developed by Vainikka et al. (2021), shown in Figure 1A, was selected to investigate the 2 wt% of SDS aqueous solution previously attempted. The water model used was the W with the 4:1 mapping with four water molecules per CG bead. Figure 1B displays the simulation snapshot after 3  $\mu s$ , where spherical micelles were obtained with an averaged micelle aggregation number of  $N_{agg} = 35$ , slightly lower than literature results with an averaged diameter of  $\varnothing \sim 3.3$  nm (Supplementary Figure S6A), bigger than the DLS result as illustrated in Supplementary Figure S3A ( $\varnothing \sim 2.0$  nm at  $[N_{4,4,4,4}]^+/[DS]^- = 0$ ). However, it must be noted that this system displayed a polydisperse micelle size distribution with  $N_{agg}$  between 27 and 40, and  $\varnothing$  from 2.6 to 3.3 nm, close to the literature data and our DLS measurements (Itri and Amaral, 1991; Bales et al.,

1998; Anachkov et al., 2012). The micelle size distribution was monitored during the simulation, reaching the plateau after 1  $\mu s$  and continuing in equilibrium until the 3  $\mu s$  of simulation time was reached. Nevertheless, this simulation was extended for an additional 3  $\mu s$  with no trace of further micelle fusion processes, ensuring that micelle equilibrium was attained. Analogously, the new and more realistic  $[N_{4,4,4,4}]^+$  MARTINI 3 model (Souza et al., 2021) with four dummy beads (no mass and no Lennard-Jones interactions) with the aim to spread the charge around the ammonium center rather than a single point, was selected. The 6 wt%  $[N_{4,4,4,4}]Cl$  in aqueous solution simulation test was run for 3  $\mu s$  from which no clumping was found, consistent with literature (Dong et al., 2017). Remarkably, the density of the simulation box was  $\rho = 1.02$  g cm $^{-3}$ , in good agreement with the experimental density of  $\rho = 1.018$  g cm $^{-3}$  (Jain et al., 2013).

Thus, the SDS and  $[N_{4,4,4,4}]Cl$  CG-MD MARTINI 3 models developed by Vainikka et al. (2021) and the W water model were selected to analyze the impact of  $[N_{4,4,4,4}]Cl$  in a 2 wt% SDS aqueous solution.

## 3 Results and discussion

Five  $[N_{4,4,4,4}]^+/[DS]^-$  molar ratios, 0.0, 0.1, 0.3, 0.5, 0.7, and 1.0, were investigated in 2 wt% aqueous SDS solutions, with composition details provided in Supplementary Table S1,

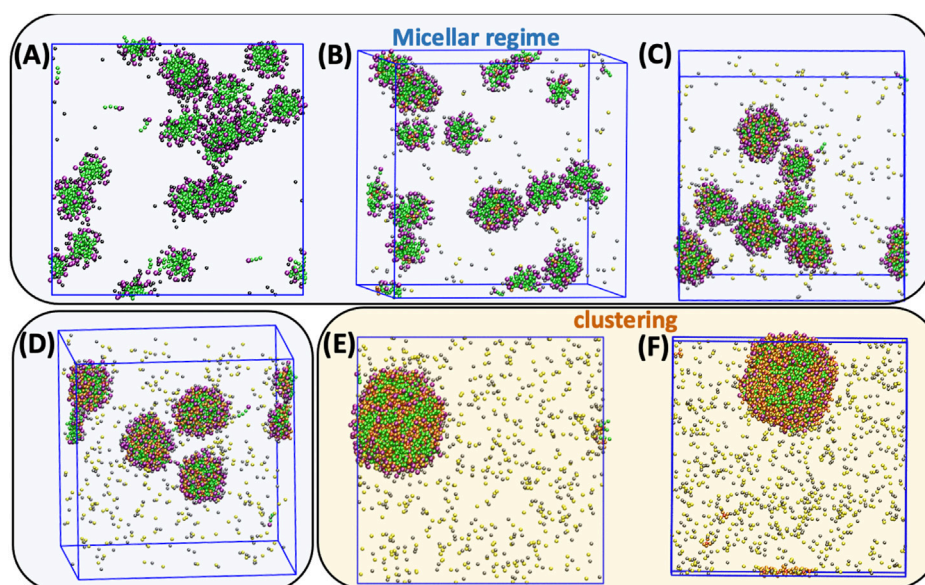


FIGURE 2

CG-MD simulation snapshots after for 2.5  $\mu$ s for (A) 0.0, (B) 0.1 and (C) 0.3, (D) 0.5, (E) 0.7 and (F) 1.0  $[N_{4,4,4,4}]^+/[DS]^-$  molar ratios in a 2 wt% of SDS aqueous solution at 298 K. The color code is as follows: SDS alkyl tails and Sulphur charged headgroups are colored in green and purple, respectively. Chlorides are yellow, sodium grey,  $[N_{4,4,4,4}]^+$  butyl groups orange, and the ammonium centers are red whilst the dummy beads and water were not represented for clarity.

TABLE 1 Micelle size distribution obtained in the CG-MD simulations for 0.0, 0.1, 0.3 0.5, 0.7, and 1.0  $[N_{4,4,4,4}]^+/[DS]^-$  ratios in the 2 wt% of SDS aqueous solution at 298 K.  $N_{agg}$  and  $\bar{\phi}$  are the averaged aggregation number and diameter of the aggregates, respectively, obtained throughout the last 0.5  $\mu$ s of simulation time.

$[N_{4,4,4,4}]^+/[DS]^-$	$N_{agg}$	$\bar{\phi}$ (nm)	$\bar{\phi}_{EXP}$ (nm)
0.0	35	3.3	1.9
0.1	35	3.3	2.2
0.3	71	4.6	3.1
0.5	100	4.9	4.0
0.7	1	8.6	8.6
1.0	1	9.0	9.1

Figure 2 shows the CG-MD simulation snapshots after 2.5  $\mu$ s of simulation time and Table 1 displays the  $N_{agg}$  and the averaged diameter,  $\bar{\phi}$ , for the obtained aggregates. A homogeneous micellar solution was found in the SDS aqueous solution without  $[N_{4,4,4,4}]^+$  and 0.1  $[N_{4,4,4,4}]^+/[DS]^-$  ratios as illustrated in Figures 2A,B, exhibiting micelles with  $N_{agg} \sim 35$  whilst a  $\bar{\phi} \sim 3.3$  nm was found in both systems (Table 1). The averaged micelle size obtained in the simulations were in good agreement with the DLS data displayed in Figure 3A where the solution without  $[N_{4,4,4,4}]Cl$  and for the  $[N_{4,4,4,4}]^+/[DS]^- = 0.1$  ratio exhibited similar micelle sizes  $\bar{\phi} \sim 2.0/3.0$  nm.

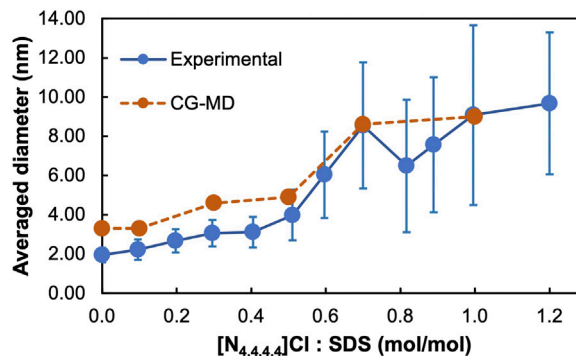


FIGURE 3

Experimental and CG-MD aggregate size distribution for the  $[N_{4,4,4,4}]^+/[DS]^-$  molar ratios shown in Figure 2. DLS was used to obtain the experimental data where additional  $[N_{4,4,4,4}]^+/[DS]^-$  molar ratios were measured. Bars in the experimental data correspond to half the base peak distribution and not the standard deviation.

The micelle density profile shown in Figure 4A is for the reference SDS aqueous solution (without  $[N_{4,4,4,4}]Cl$ ) whilst Figure 4B shows how the  $[N_{4,4,4,4}]^+$  moieties (orange) and the  $Cl^-$  and  $Na^+$  counterions (yellow and grey colors, respectively) were mainly arranged over the micelle surface (denoted by

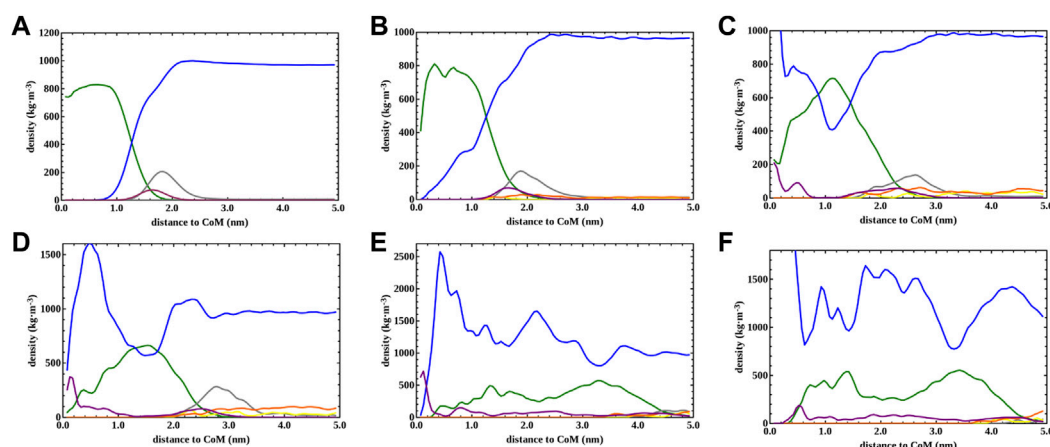


FIGURE 4

Averaged density profiles of the aggregates found in the CG-MD simulations for (A) 0.0, (B) 0.1, (C) 0.3, (D) 0.5, (E) 0.7 and (F) 1.0  $[N_{4,4,4,4}]^+/[DS]^-$  molar ratio systems shown in Figure 2. The last 0.5  $\mu$ s of the simulation was taken to obtain the density profiles. The color code is as follows:  $[DS]^-$  alkyl tails and Sulphur charged headgroups are colored in green and purple, respectively. Sodium, chloride and water are in grey, yellow and blue, respectively, whereas  $[N_{4,4,4,4}]^+$  was in orange.

maximum of the purple curve), and in the solution. A detailed perspective at the micelle surface for the above density profiles are provided in Supplementary Figures S6A–B. Similarly, the 0.3 ratio system yielded a homogeneous distribution of spherical micelles, as shown in Figure 2C, with  $N_{agg} \sim 71$  and  $\varnothing \sim 4.6$  nm (Table 1) but encompassing a slightly different micelle assembly. The DLS data pointed towards a similar micelle size with  $\varnothing \sim 3.0/4.0$  nm as shown in Figure 3A. The density profile shown in Figure 4C unveils the presence of SDS Sulphur headgroups (purple peaks) close to the aggregate center of mass (CoM) whereas the density of the  $[DS]^-$  alkyl tails (green) slightly decreased. This might indicate that  $[N_{4,4,4,4}]^+$  moieties were strongly absorbed and arranged in the micelle core. A detailed perspective can be seen in Supplementary Figure S6C showing that the  $[N_{4,4,4,4}]^+$  moieties and the  $Cl^-$  and  $Na^+$  counterions were arranged over the  $[DS]^-$  micelle surface as in the 0.1 ratio system.

This arrangement was more noticeable in the system with a ratio of 0.5, which also exhibited a homogeneous distribution of swelled micelles, as can be seen in Figure 2D, with  $N_{agg} \sim 100$  and  $\varnothing \sim 4.9$  nm (Table 1) in good agreement with DLS data (Figure 3A)  $\varnothing \sim 4.0$  nm. However, the density profile presented in Figure 4D points towards those micelles being an amalgam of small  $[DS]^-$  aggregates, somehow resembling the structure of a blackberry fruit. As a matter of fact, the increased  $[N_{4,4,4,4}]^+$  absorption promoted a  $[DS]^-$  micelle core breakdown, resembling the above mentioned blackberry like structure, also giving access to some water molecules arrange inside the core structure (denoted by the blue maximum close to the CoM shown in Figure 4). The arrangement of some  $[N_{4,4,4,4}]^+$  moieties (orange) in between the  $[DS]^-$  connected aggregates can be seen in Figure 2D besides a noticeable increase of the aggregate size, indicating that the increased number of available

$[N_{4,4,4,4}]^+$  moieties induced a micelle swell. A different scenario was observed in the 0.7 system displaying one cluster as shown in Figure 2E, with  $N_{agg} \sim 500$  and  $\varnothing \sim 8.6$  nm (Table 1) in very good agreement with DLS experiments  $\varnothing \sim 8.6$  nm (Figure 3A). The simulation snapshot highlights the singular blackberry like structure, with the  $[N_{4,4,4,4}]^+$  moieties connecting small  $[DS]^-$  aggregates. The density profile shown in Figure 4E displays a homogeneous distribution of the  $[DS]^-$  headgroups (purple) alongside the aggregate as well as the  $[N_{4,4,4,4}]^+$  moieties (orange) and the counterions (grey and yellow) as shown in detail in Supplementary Figure S6E. When the number of  $[N_{4,4,4,4}]^+$  matched the  $[DS]^-$  moieties (ratio 1.0) the system also yielded a cluster with a  $\varnothing \sim 8.7$  nm in line with DLS estimate ( $\varnothing \sim 9.1$  nm) shown in Figure 3A, displaying the same structure and size as in the 0.7 ratio system. The aggregate structure obtained in the CG-MD simulation is shown in Figure 2F with its density profile is displayed in Figure 4F. In fact, the density profile resembles the one found in the 0.7 system. Supplementary Figure S6F highlights the similar  $[N_{4,4,4,4}]^+$  and counterion arrangement at the cluster surface.

The solvent accessible surface area (SASA) was obtained for  $[N_{4,4,4,4}]^+$  and SDS moieties for all 0.1, 0.3 0.5, 0.7, and 1.0  $[N_{4,4,4,4}]^+/[DS]^-$  solutions throughout the SASA calculation. SASA provides an estimation of the level of hydration/dehydration and these profiles are shown in Figure 5. Figure 5A illustrates how  $[N_{4,4,4,4}]^+$  moieties dehydrate in the SDS solutions when the concentration is increased. Thus, the difference of SASA between the 0.1 and 1.0 solutions was  $1.5 \text{ nm}^2$ , highlighting the fact that at low  $[N_{4,4,4,4}]^+$  concentrations, the  $[N_{4,4,4,4}]^+$  were mostly arranged at the SDS micelle surface as shown in the density profiles (Figures 4B,C). However, at 0.5  $[N_{4,4,4,4}]^+/[DS]^-$  ratio, the  $[N_{4,4,4,4}]^+$



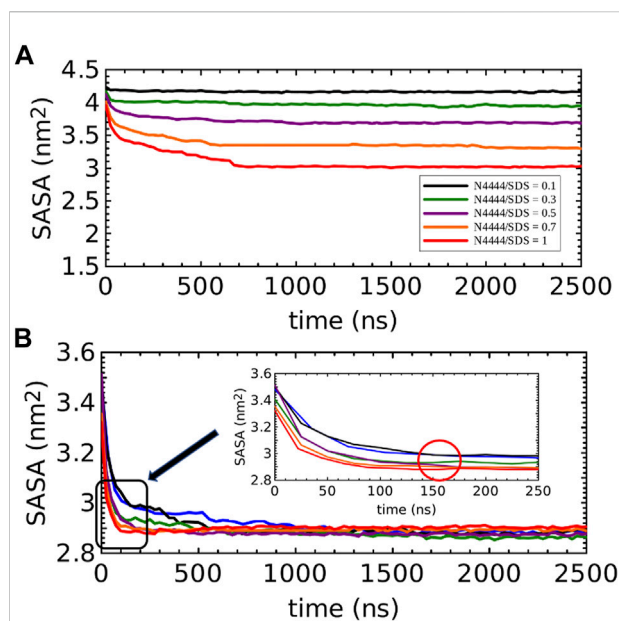


FIGURE 5

SASA profiles for the (A)  $[N_{4,4,4,4}]^+$  and (B)  $[DS]^-$  moieties, both for all 0.0, 0.1, 0.3, 0.5, 0.7, and 1.0  $[N_{4,4,4,4}]^+/[DS]^-$  molar ratio systems shown in Figure 2. The inset in Figure 5B zooms in the SASA profiles in the first 250 ns of simulation whilst the red circle guide the eye to emphasize the shift experienced for the 0.5  $[N_{4,4,4,4}]^+/[DS]^-$  ratio solution towards the SASA values of the clusters observed in the 0.7 and 1.0 solutions at 160 ns. SASA profile in (B) for the SDS solution without  $[N_{4,4,4,4}]^+$  is shown in blue color.

were not only arranged at the SDS micelle surface but also inside, losing access to water as shown in Figure 5A (purple). This dehydration was more dramatic at 0.7 and 1.0  $[N_{4,4,4,4}]^+/[DS]^-$  ratios, which can be seen by the shift between these and the regularly spaced SASA profiles observed in 0.1, 0.3, and 0.5 solutions. Thus, the noticeable change to lower SASA detected from 0.5 to 0.7 and 1.0 ratios (shift between purple and the orange and red color profiles) highlights the micellar-to-cluster phase transition also observed in the simulation snapshots of Figures 2E,F. Figure 5B displays the SASA for SDS moieties from higher-to-low SASA, the SDS at 0.0, 0.1, 0.3 and 0.5  $[N_{4,4,4,4}]^+/[DS]^-$  ratios exhibited a slightly higher access to water when compared with the 0.7 and 1.0 ratios as expected for micellar structures. In the first 250 ns of simulation, the 0.5 solution had a similar SASA profile to those of the 0.1 and 0.3 solutions. Then the SASA of the 0.5 solution rapidly dropped above 160 ns (see detail in the red circle in Figure 5B), displaying the same SASA seen for the 0.7 and 1.0 ratios, whereas the 0.1 and 0.3 profiles remained constant until 2,500 ns. Thus, an initial clustering process, promoted perhaps by a structural alteration of micelles promoted by the absorbed  $[N_{4,4,4,4}]^+$ , could be the reason behind this behavior since the 0.5  $[N_{4,4,4,4}]^+/[DS]^-$  ratio seems to be the threshold  $[N_{4,4,4,4}]^+$  concentration above which a

micellar-to-cluster transition occurred. In fact, the micelles observed in the simulation snapshots and density profiles in the 0.5 solution shown in Figure 2D and Figure 4D, respectively, resembled the blackberry fruit like structure denoted in the clusters for 0.7 and 1.0 ratios.

Overall, SASA results are in good agreement with our DLS and NMR experiments, revealing the micelle-to-clustering transition for  $[N_{4,4,4,4}]^+/[DS]^-$  ratios  $> 0.5$ , being a threshold from an ionic system to a pseudo-nonionic one, assuming  $[N_{4,4,4,4}]^+$  cations between  $[DS]^-$  head groups. This transition could be due to depletion of H-bonds of water molecules around the butyl chains of  $[N_{4,4,4,4}]^+$  besides the  $[DS]^-$  at the micelle surface. This is associated with the entropy gain which is the major thermodynamic factor related to micellar aggregation and LCST transition.

With the aim to provide a clearer picture of the phases found in the CG-MD simulations, the computed SAXS profiles for the 0.0, 0.1, 0.3, 0.5, 0.7, and 1.0  $[N_{4,4,4,4}]^+/[DS]^-$  ratio systems were obtained using the last 0.5  $\mu$ s of simulation time. In addition, experimental SAXS patterns were acquired of samples with these compositions. Figure 6 compares the computed SAXS profiles with their experimental counterparts. It must be pointed out that only a qualitative comparison between the computed and experimental SAXS profiles can be done due to the inherent size limitations of the simulation boxes. In fact, the simulation box sizes are  $\sim 24$  nm whereas the experimental samples are significantly larger. Additionally, the lack of atomistic details inherent in coarse-grained models make SAXS comparison with experiments even more difficult as also mentioned below. Furthermore, the experimental SAXS profiles were obtained using a 1 wt% SDS concentration, whilst 2 wt% was used in the CG-MD simulations due to the high computational cost of simulating diluted solutions. It must be noticed that the intensity of each computed SAXS profile was properly scaled with the aim to compare with the experimental ones. SAXS profiles can provide useful information of the phase behavior. In fact, in the pure SDS solution, the flat intensity profile at low  $q$  values indicates predominantly spherical or spheroidal micelles with repulsive interactions being the second the contribution of hydrophobic side chain distances. At higher  $[N_{4,4,4,4}]^+/[DS]^-$  ratios, the intensity at low  $q$  increases drastically indicating aggregation and phase transition where the lack of the first peak exhibits a transition from repulsive to attractive inter micellar interactions (Kabir-ud-Din et al., 2006; Schäfer et al., 2020). Figures 6A–D show a similar pattern between computed and experimental SAXS profiles for 0.0, 0.1, 0.3, and 0.5 ratios, which are in qualitative good agreement with a homogeneous micelle distribution as can be seen in Figures 2A–D exhibiting both profiles a down trend of the intensity when low  $q$  values are approached. For 0.7 and 1.0  $[N_{4,4,4,4}]^+/[DS]^-$  ratios, the computed and experimental SAXS profiles shown in Figures 6E,F displayed a similar pattern, both with an exponential increase of the intensity at low  $q$ , pointing towards a clustering process. This is in agreement with the  $[N_{4,4,4,4}]^+/[DS]^-$  clusters observed in the

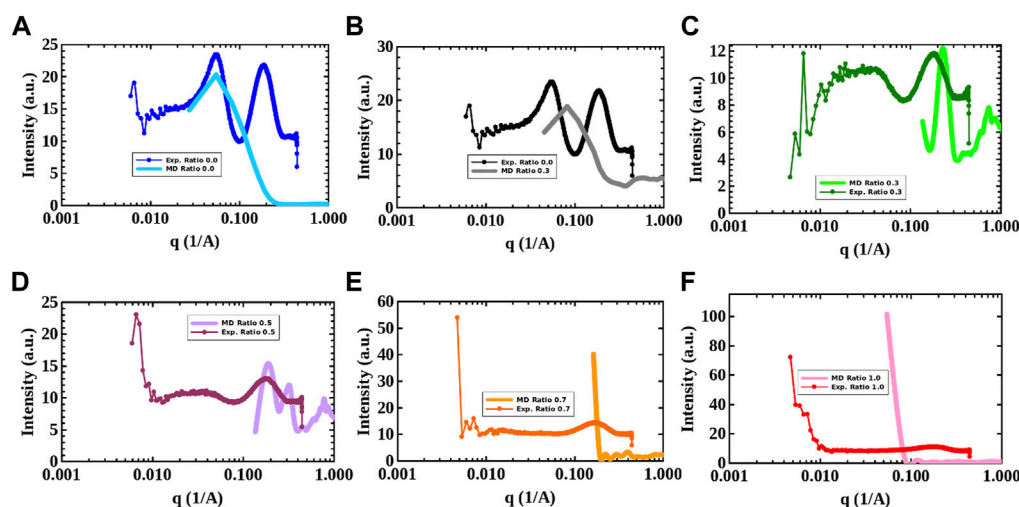


FIGURE 6

Computed and experimental SAXS profiles for the (A) 0.0, (B) 0.1, (C) 0.3, (D) 0.5, (E) 0.7, and (F) 1.0  $[N_{4,4,4,4}]^+/[DS]^-$  molar ratio systems shown in Figure 2. The SDS concentration in the experimental samples was 1wt% and the temperature was 298 K. Profiles colored in shadow are computed SAXS taken from the CG-MD simulations.

CG-MD simulations (*cf.* Figures 2E,F) with the above-mentioned blackberry like structure. In this manner, the CG-MD simulations disclosed the impact of  $[N_{4,4,4,4}]Cl$  in the phase behavior of the SDS micelles where the  $[N_{4,4,4,4}]^+$  provided a positive charge character inside the SDS hydrophobic core. Thereby, in a 2 wt% SDS aqueous solution, at low  $[N_{4,4,4,4}]Cl$  concentrations ( $[N_{4,4,4,4}]^+/[DS]^-$  ratios < 0.5) an homogeneous solution of  $[DS]^-$  micelles were in equilibrium and the inter micelle interactions were not affected by the absorbed  $[N_{4,4,4,4}]^+$  moieties. However, when the  $[N_{4,4,4,4}]Cl$  concentration is raised above the  $[N_{4,4,4,4}]^+/[DS]^-$  ratio > 0.5, the inner positive and outer negative charge balance of the SDS micelles promoted the formation of  $[N_{4,4,4,4}]^+/[DS]^-$  clusters as illustrated in Figures 2E,F. Thus, the electrostatic balance between the  $[DS]^-$  and  $[N_{4,4,4,4}]^+$  moieties seems to play the main role in the phase behavior as denoted in the evolution of the density profiles shown in Figure 4 and Supplementary Figure S6. In fact, if one focus in the second peaks of the experimental SAXS profiles as a function of the molar ratio displayed in Supplementary Figure S7, the trend could suggest a slight change in  $[DS]^-$  tail-tail distances. This might point towards that no micelle fusion but rather micelle clumping could be found resembling the above-mentioned blackberry structure.

The primary aim of this comparative study was to computationally capture the experimental change in the SAXS profiles, with a focus on the low  $q$  values. When the  $[N_{4,4,4,4}]^+/[DS]^-$  ratio is  $\leq 0.5$ , the computed SAXS profiles tended towards lower intensities at low  $q$  values whilst > 0.5 the intensity increased at low  $q$  values. Thus, this variation in the experimental SAXS trend at low  $q$  values below and above the 0.5 ratio corresponds to, and supports,

the micellar-to-clustering phase transition observed in the CG-MD simulation snapshots.

It must be pointed out that a direct correspondence of experimental and computed profiles is problematic due to the difference in molecular volumes when converting an atomistic description to a CG-bead one. Nevertheless, despite the expected discrepancies when comparing experimental and computed SAXS profiles, both clearly highlight a micellar-to-cluster phase transition when the  $[N_{4,4,4,4}]^+/[DS]^-$  ratio is above 0.5.

## 4 Conclusion

A new CG-MD approach based on the recently released MARTINI 3.0 model was developed to model SDS aqueous solutions, and evaluate the impact of  $[N_{4,4,4,4}]Cl$  on the phase behavior. Literature computational and experimental data were used in the validation procedure. The experimental aggregation number of SDS micelles in aqueous solution was taken as a reference to evaluate different CG beads available in MARTINI 3.0. The non-bonded interaction energies of a previous SDS model based in MARTINI 2.2 were taken as reference to find their counterparts in MARTINI 3.0. Afterwards, a SDS aqueous solution at a concentration in the micellar regime was simulated and the aggregation number was in good agreement with literature data. The  $[N_{4,4,4,4}]^+$  MARTINI 3.0 model was already available in the literature, nevertheless, a strength test was carried out simulating a diluted  $[N_{4,4,4,4}]Cl$  aqueous solution to ensure that no excessive aggregation is observed. Then, five SDS aqueous solutions at different  $[N_{4,4,4,4}]Cl$  concentrations

(0.1–1.0  $[N_{4,4,4,4}]^+/[DS]^-$  molar ratios) were simulated and the results were compared with SAXS experiments. The simulations showed how a regular SDS micellar solution (0.1 and 0.3  $[N_{4,4,4,4}]^+/[DS]^-$  ratios) yielded  $[DS]^-/[N_{4,4,4,4}]^+$  aggregates at higher  $[N_{4,4,4,4}]^+$  Cl concentrations (0.7 and 1.0  $[N_{4,4,4,4}]^+/[DS]^-$  ratios). The  $[N_{4,4,4,4}]^+/[DS]^-$  solution at 0.5 M ratio separates the above mentioned phase behavior regimes, in good agreement with experiments. Accessible solvent surface areas (SASA) were obtained for the  $[N_{4,4,4,4}]^+$  and SDS in all  $[N_{4,4,4,4}]^+/[DS]^-$  ratio solutions. The SASA profiles showed the dehydration of  $[N_{4,4,4,4}]^+$  moieties when their concentration is increased in the SDS solution, displaying the lowest values in 0.7 and 1.0 solutions when the system yielded clusters. In addition, experimental and computed SAXS profiles were obtained for the above  $[N_{4,4,4,4}]^+/[DS]^-$  aqueous solutions. Computed SAXS profiles for 0.1 and 0.3  $[N_{4,4,4,4}]^+/[DS]^-$  ratios displayed a profile of characteristic spherical aggregates, in agreement with their experimental counterparts. For the 0.5  $[N_{4,4,4,4}]^+/[DS]^-$  molar ratio, the computed SAXS profile pointed out a micellar solution (as illustrated in the simulation snapshot) whereas the experimental counterpart indicated the presence of a cluster as also revealed in the 0.7 and 1.0  $[N_{4,4,4,4}]^+/[DS]^-$  solutions. The computed SAXS profile for 0.7 and 1.0  $[N_{4,4,4,4}]^+/[DS]^-$  solutions exhibited the presence of clusters in conjunction with micelles, also noticed in the simulation snapshots and in agreement with the experimental ones. Analyzing the simulation snapshots for these systems, the cluster were assembled through small SDS aggregates linked by the absorbed  $[N_{4,4,4,4}]^+$  moieties somehow resembling a blackberry fruit. Thus, in a SDS micellar aqueous solution, as soon as the  $[N_{4,4,4,4}]^+$  concentration is increased, the SDS micelles are gaining  $[N_{4,4,4,4}]^+$  moieties, resulting in swelling of the micelles. However, above a certain  $[N_{4,4,4,4}]^+$  concentration threshold, the absorbed  $[N_{4,4,4,4}]^+$  split the SDS micelle core, as can be seen in the simulation snapshots, providing a positive charge inside the micelle core. As a matter of fact, when the positive load is at least half of the negative charge of the SDS micelle surface, this impacts the inter micelle interactions, promoting a micelle fusion process to form a clustered structure as observed in the 0.7 and 1.0  $[N_{4,4,4,4}]^+/[DS]^-$  solutions.

This work demonstrates that the CG-MD MARTINI 3.0 model is a powerful tool to analyze processes at the nanoscale the self-assembly of SDS and  $[N_{4,4,4,4}]Cl$  aqueous solutions, and provide useful to complement the information obtained from experimental approaches.

## Data availability statement

The original contributions presented in the study are included in the article/Supplementary Material, further inquiries can be directed to the corresponding author.

## Author contributions

GP—conceptualization, data curation, investigation, molecular simulations, validation, writing original draft, review, and editing. NS—data curation, experimental DLS and NMR measurements, review, and editing. TG—data curation, experimental SAXS measurements, review, and editing. JP—conceptualization, supervision, writing, review, and editing. JC—funding acquisition, conceptualization, supervision, writing, review, and editing.

## Acknowledgments

This work was developed within the scope of the project CICECO-Aveiro Institute of Materials, UIDB/50011/2020, UIDP/50011/2020 and LA/P/0006/2020, financed by national funds through the FCT/MEC (PIDDAC). CIEPQPF is supported by the Fundação para a Ciência e Tecnologia (FCT) through the projects UIDB/EQU/00102/2020 and UIDP/EQU/00102/2020. GáPé-Sá and NS acknowledge the national funds (OE), through FCT—Fundação para a Ciência e a Tecnologia, I.P., in the scope of the framework contract foreseen in the numbers 4, 5 and 6 of the article 23, of the Decree-Law 57/2016, of August 29<sup>th</sup>, changed by Law 57/2017, of July 19<sup>th</sup>. Part of this research was undertaken on the SAXS beamline at the Australian Synchrotron, part of ANSTO.

## Conflict of interest

The authors declare that the research was conducted in the absence of any commercial or financial relationships that could be construed as a potential conflict of interest.

## Publisher's note

All claims expressed in this article are solely those of the authors and do not necessarily represent those of their affiliated organizations, or those of the publisher, the editors and the reviewers. Any product that may be evaluated in this article, or claim that may be made by its manufacturer, is not guaranteed or endorsed by the publisher.

## Supplementary material

The Supplementary Material for this article can be found online at: <https://www.frontiersin.org/articles/10.3389/fmats.2022.1011164/full#supplementary-material>

## References

- Anachkov, S. E., Danov, K. D., Basheva, E. S., Kralchevsky, P. A., and Ananthapadmanabhan, K. P. (2012). Determination of the aggregation number and charge of ionic surfactant micelles from the stepwise thinning of foam films. *Adv. Colloid Interface Sci.* 183–184, 55–67. doi:10.1016/j.cis.2012.08.003, Available from: <https://linkinghub.elsevier.com/retrieve/pii/S0001868612001285>.
- Anogiannakis, S. D., Petris, P. C., and Theodorou, D. N. (2020). Promising Route for the Development of a computational framework for self-assembly and phase behavior prediction of ionic surfactants using MARTINI. *J. Phys. Chem. B* 124 (3), 556–567. doi:10.1021/acs.jpcc.9b09915, Available from: <https://pubs.acs.org/doi/10.1021/acs.jpcc.9b09915>.
- Bales, B. L., Messina, L., Vidal, A., Peric, M., and Nascimento, O. R. (1998). Precision relative aggregation number Determinations of SDS micelles using a Spin probe. A model of micelle surface hydration. *J. Phys. Chem. B* 102 (50), 10347–10358. doi:10.1021/jp983364a, Available from: <https://pubs.acs.org/doi/10.1021/jp983364a>.
- Bales, B. L., and Zana, R. (2004). Cloud point of aqueous solutions of tetrabutylammonium dodecyl sulfate is a function of the concentration of counterions in the aqueous phase. *Langmuir* 20 (5), 1579–1581. doi:10.1021/la0353935, Available from: <https://pubs.acs.org/doi/10.1021/la0353935>.
- Bastos, H., Bento, R., Schaeffer, N., Coutinho, J. A. P., and Pérez-Sánchez, G. (2020). Using coarse-grained molecular dynamics to rationalize biomolecule solubilization mechanisms in ionic liquid-based colloidal systems. *Phys. Chem. Chem. Phys.* 22 (42), 24771–24783. doi:10.1039/D0CP04942E, Available from: <http://xlink.rsc.org/?DOI=D0CP04942E>.
- Berthod, A., Borgerding, M. F., and Hinze, W. L. (1991). Investigation of the causes of reduced efficiency in micellar liquid chromatography. *J. Chromatogr. A* 556 (1–2), 263–275. doi:10.1016/s0021-9673(01)96226-0, Available from: <https://linkinghub.elsevier.com/retrieve/pii/S0021967301962260>.
- Bussi, G., Donadio, D., and Parrinello, M. (2007). Canonical sampling through velocity rescaling. *J. Chem. Phys.* 126 (1), 014101. doi:10.1063/1.2408420, Available from: <http://aip.scitation.org/doi/10.1063/1.2408420>.
- Chauhan, S., and Kaur, M. (2017). Modulation of aggregation behaviour of anionic surfactant in the presence of aqueous quaternary ammonium salts. *J. Surfactants Deterg.* 20 (3), 599–607. doi:10.1007/s11743-017-1949-5, Available from: <http://doi.wiley.com/10.1007/s11743-017-1949-5>.
- Chien, S.-C., Pérez-Sánchez, G., Gomes, J. R. B., Cordeiro, M. N. D. S., Jorge, M., Auerbach, S. M., et al. (2017). Molecular simulations of the Synthesis of periodic Mesoporous Silica phases at high surfactant concentrations. *J. Phys. Chem. C* 121 (8), 4564–4575. doi:10.1021/acs.jpcc.6b09429, Available from: <https://pubs.acs.org/doi/10.1021/acs.jpcc.6b09429>.
- Cromer, D. T., and Mann, J. B. (1968). X-ray scattering factors computed from numerical Hartree–Fock wave functions. *Acta Cryst. Sect. A* 24 (2), 321–324. doi:10.1107/S0567739468000550.
- Darden, T., York, D., and Pedersen, L. (1993). Particle mesh Ewald: An N-log(N) method for Ewald sums in large systems. *J. Chem. Phys.* 98 (12), 10089–10092. doi:10.1063/1.464397, Available from: <http://aip.scitation.org/doi/10.1063/1.464397>.
- Dong, D., Hooper, J. B., and Bedrov, D. (2017). Structural and dynamical properties of tetraalkylammonium bromide aqueous solutions: A molecular dynamics simulation study using a polarizable force field. *J. Phys. Chem. B* 121 (18), 4853–4863. doi:10.1021/acs.jpcc.7b01032, Available from: <https://pubs.acs.org/doi/10.1021/acs.jpcc.7b01032>.
- Ferreira, A. M., Passos, H., Okafuji, A., Tavares, A. P. M., Ohno, H., Freire, M. G., et al. (2018). An integrated process for enzymatic catalysis allowing product recovery and enzyme reuse by applying thermoreversible aqueous biphasic systems. *Green Chem.* 20 (6), 1218–1223. doi:10.1039/C7GC03880A, Available from: <http://xlink.rsc.org/?DOI=C7GC03880A>.
- Forero-Martinez, N. C., Cortes-Huerto, R., Benedetto, A., and Ballone, P. (2022). Thermoresponsive ionic liquid/water mixtures: From Nanostructuring to phase separation. *Molecules* 27 (5), 1647. doi:10.3390/molecules27051647, Available from: <https://www.mdpi.com/1420-3049/27/5/1647>.
- Freire, M. G., Cláudio, A. F. M., Araújo, J. M. M., Coutinho, J. A. P., Marrucho, I. M., Lopes, J. N. C., et al. (2012). Aqueous biphasic systems: A boost brought about by using ionic liquids. *Chem. Soc. Rev.* 41 (14), 4966. doi:10.1039/C2CS35151J, Available from: <http://xlink.rsc.org/?DOI=C2CS35151J>.
- Gao, J., Ge, W., Hu, G., and Li, J. (2005). From homogeneous dispersion to Micelles A molecular dynamics simulation on the Compromise of the hydrophilic and hydrophobic effects of sodium dodecyl sulfate in aqueous solution. *Langmuir* 21 (11), 5223–5229. doi:10.1021/la047121n, Available from: <https://pubs.acs.org/doi/10.1021/la047121n>.
- Gutowski, K. E., Broker, G. A., Willauer, H. D., Huddleston, J. G., Swatoski, R. P., Holbrey, J. D., et al. (2003). Controlling the aqueous Miscibility of ionic liquids: Aqueous biphasic systems of water-Miscible ionic liquids and water-Structuring salts for recycle, Metathesis, and separations. *J. Am. Chem. Soc.* 125 (22), 6632–6633. doi:10.1021/ja0351802, Available from: <https://pubs.acs.org/doi/10.1021/ja0351802>.
- Hammouda, B. (2013). Temperature effect on the Nanostructure of SDS micelles in water. *J. Res. Natl. Inst. Stand. Technol.* 118, 151. doi:10.6028/jres.118.008, Available from: <https://nvlpubs.nist.gov/nistpubs/jres/118/jres.118.008.pdf>.
- Hess, B., Bekker, H., Berendsen, H. J. C., and Fraaije, J. G. E. M. (1997). Lincs: A linear constraint solver for molecular simulations. *J. Comput. Chem.* 18 (12), 1463–1472. Available from: <http://doi.wiley.com/10.1002/%28SICI%291096-987X%28199709%2918%3A12%3C1463%3A%3AID-JCC4%3E3.0.CO%3B2-H>.
- Hockney, R., Goel, S., and Eastwood, J. (1974). Quiet high-resolution computer models of a plasma. *J. Comput. Phys.* 14 (2), 148–158. doi:10.1016/0021-9991(74)90010-2, Available from: <http://linkinghub.elsevier.com/retrieve/pii/0021999174900102>.
- Hoshen, J., and Kopelman, R. (1976). Percolation and cluster distribution. I. Cluster multiple labeling technique and critical concentration algorithm. *Phys. Rev. B* 14 (8), 3438–3445. Available from: <https://link.aps.org/doi/10.1103/PhysRevB.14.3438>.
- Humphrey, W., Dalke, A., and Schulten, K. (1996). Vmd: Visual molecular dynamics. *J. Mol. Graph.* 14 (1), 33–38. doi:10.1016/0263-7855(96)00018-5, Available from: <http://linkinghub.elsevier.com/retrieve/pii/0263785596000185>.
- Illa-Tuset, S., Malaspina, D. C., and Faraudo, J. (2018). Coarse-grained molecular dynamics simulation of the interface behaviour and self-assembly of CTAB cationic surfactants. *Phys. Chem. Chem. Phys.* 20 (41), 26422–26430. doi:10.1039/C8CP04505D, Available from: <http://xlink.rsc.org/?DOI=C8CP04505D>.
- Itri, R., and Amaral, L. Q. (1991). Distance distribution function of sodium dodecyl sulfate micelles by x-ray scattering. *J. Phys. Chem.* 95 (1), 423–427. doi:10.1021/j100154a074, Available from: <https://pubs.acs.org/doi/10.1021/j100154a074>.
- Jain, P., Sharma, S., and Shukla, R. K. (2013). Density and viscosity of tetrabutyl ammonium hydrogen sulphate and tetrabutyl ammonium chloride salts in aqueous and methanolic solution at 303 K. *Phys. Chem. Liq.* 51 (5), 547–566. doi:10.1080/00319104.2012.760084, Available from: <https://www.tandfonline.com/doi/full/10.1080/00319104.2012.760084>.
- Jalili, S., and Akhavan, M. (2009). A coarse-grained molecular dynamics simulation of a sodium dodecyl sulfate micelle in aqueous solution. *Colloids Surfaces A Physicochem. Eng. Aspects* 352 (1–3), 99–102. doi:10.1016/j.colsurfa.2009.10.007, Available from: <https://linkinghub.elsevier.com/retrieve/pii/S0927775709006104>.
- Jorge, M. (2008). Molecular dynamics simulation of self-assembly of n-Decyltrimethylammonium bromide micelles. *Langmuir* 24 (11), 5714–5725. doi:10.1021/la800291p, Available from: <http://pubs.acs.org/doi/abs/10.1021/la800291p>.
- Kabir-ud-Din, D. S., Sharma, D., Khan, Z. A., Aswal, V. K., and Kumar, S. (2006). Clouding phenomenon and SANS studies on tetra-n-butylammonium dodecylsulfate micellar solutions in the absence and presence of salts. *J. Colloid Interface Sci.* 302 (1), 315–321. doi:10.1016/j.jcis.2006.06.021, Available from: <https://linkinghub.elsevier.com/retrieve/pii/S0021979706005169>.
- Klamt, A., Huniar, U., Spycher, S., and Keldenich, J. (2008). COSMOmic: A Mechanistic approach to the calculation of Membrane–Water partition Coefficients and internal distributions within Membranes and micelles. *J. Phys. Chem. B* 112 (38), 12148–12157. doi:10.1021/jp801736k, Available from: <https://pubs.acs.org/doi/10.1021/jp801736k>.
- Kohno, Y., and Ohno, H. (2012). Ionic liquid/water mixtures: From hostility to conciliation. *Chem. Commun.* 48 (57), 7119. doi:10.1039/C2CC31638B, Available from: <http://xlink.rsc.org/?DOI=C2CC31638B>.
- Kohno, Y., Saita, S., Murata, K., Nakamura, N., and Ohno, H. (2011). Extraction of proteins with temperature sensitive and reversible phase change of ionic liquid/water mixture. *Polym. Chem.* 2 (4), 862. doi:10.1039/C0PY00364F, Available from: <http://xlink.rsc.org/?DOI=C0PY00364F>.
- Lebard, D. N., Levine, B. G., Mertmann, P., Barr, S. A., Jusufi, A., Sanders, S., et al. (2012). Self-assembly of coarse-grained ionic surfactants accelerated by graphics processing units. *Soft Matter* 8 (8), 2385–2397. doi:10.1039/c1sm06787g.
- Lin, J.-H., Chen, W.-S., and Hou, S.-S. (2013). NMR studies on effects of tetraalkylammonium bromides on micellization of sodium dodecylsulfate. *J. Phys. Chem. B* 117 (40), 12076–12085. doi:10.1021/jp403616p, Available from: <https://pubs.acs.org/doi/10.1021/jp403616p>.
- Lindahl, E., Abraham, M. J., Hess, B., and van der Spoel, D. (2018). GROMACS 2019 Source code. doi:10.5281/zenodo.2564764, Available at: <https://doi.org/10.5281/zenodo.2564764>.



- Liu, G., Li, R., Wei, Y., Gao, F., Wang, H., Yuan, S., et al. (2016). Molecular dynamics simulations on tetraalkylammonium interactions with dodecyl sulfate micelles at the air/water interface. *J. Mol. Liq.* 222, 1085–1090. doi:10.1016/j.molliq.2016.08.009, Available from: <https://linkinghub.elsevier.com/retrieve/pii/S0167732216307140>.
- Liu, G., Zhang, H., Liu, G., Yuan, S., and Liu, C. (2016). Tetraalkylammonium interactions with dodecyl sulfate micelles: A molecular dynamics study. *Phys. Chem. Chem. Phys.* 18 (2), 878–885. doi:10.1039/C5CP05639J Available from: <http://xlink.rsc.org/?DOI=C5CP05639J>.
- Mahbub, S., Molla, M. R., Saha, M., Shahriar, I., Hoque, M. A., Halim, M. A., et al. (2019). Conductometric and molecular dynamics studies of the aggregation behavior of sodium dodecyl sulfate (SDS) and cetyltrimethylammonium bromide (CTAB) in aqueous and electrolytes solution. *J. Mol. Liq.* 283, 263–275. doi:10.1016/j.molliq.2019.03.045, Available from: <https://linkinghub.elsevier.com/retrieve/pii/S0167732219300200>.
- Marrink, S. J., Risselada, H. J., Yefimov, S., Tieleman, D. P., and de Vries, A. H. (2007). The MARTINI force field: Coarse grained model for biomolecular simulations. *J. Phys. Chem. B* 111 (27), 7812–7824. doi:10.1021/jp071097f, Available from: <http://pubs.acs.org/doi/abs/10.1021/jp071097f>.
- Martínez, L., Andrade, R., Birgin, E. G., and Martínez, J. M. (2009). Packmol: A package for building initial configurations for molecular dynamics simulations. *J. Comput. Chem.* 30 (13), 2157–2164. doi:10.1002/jcc.21224.
- Martínez-Aragón, M., Burghoff, S., Goetheer, E. L. V., and de Haan, A. B. (2009). Guidelines for solvent selection for carrier mediated extraction of proteins. *Sep. Purif. Technol.* 65 (1), 65–72. doi:10.1016/j.seppur.2008.01.028, Available from: <https://linkinghub.elsevier.com/retrieve/pii/S1383586608000543>.
- Mata, J., Varade, D., Ghosh, G., and Bahadur, P. (2004). Effect of tetrabutylammonium bromide on the micelles of sodium dodecyl sulfate. *Colloids Surfaces A Physicochem. Eng. Aspects* 245 (1–3), 69–73. doi:10.1016/j.colsurfa.2004.07.009, Available from: <https://linkinghub.elsevier.com/retrieve/pii/S092777504004194>.
- Meyer, G., Schweins, R., Youngs, T., Dufrêche, J.-F., Billard, I., and Plazenet, M. (2022). How temperature Rise can Induce phase separation in aqueous biphasic solutions. *J. Phys. Chem. Lett.* 13 (12), 2731–2736. doi:10.1021/acs.jpclett.2c00146, Available from: <https://pubs.acs.org/doi/10.1021/acs.jpclett.2c00146>.
- Mitra, D., Chakraborty, I., Bhattacharya, S. C., and Moulik, S. P. (2007). Interfacial and solution properties of tetraalkylammonium bromides and their sodium dodecyl sulfate interacted products: A detailed Physicochemical study. *Langmuir* 23 (6), 3049–3061. doi:10.1021/la062830h, Available from: <https://pubs.acs.org/doi/10.1021/la062830h>.
- Morais, E. S., Schaeffer, N., Freire, M. G., Freire, C. S. R., Coutinho, J. A. P., and Silvestre, A. J. D. (2021). Integrated production and separation of Furfural using an acidic-based aqueous biphasic system. *ACS Sustain. Chem. Eng.* 9 (36), 12205–12212. doi:10.1021/acssuschemeng.1c03733, Available from: <https://pubs.acs.org/doi/10.1021/acssuschemeng.1c03733>.
- Mukherjee, P., Padhan, S. K., Dash, S., Patel, S., and Mishra, B. K. (2011). Clouding behaviour in surfactant systems. *Adv. Colloid Interface Sci.* 162 (1), 59–79. doi:10.1016/j.cis.2010.12.005.
- Naqvi, A. Z., and Kabir-ud-Din, D. S. (2018). Clouding phenomenon in amphiphilic systems: A review of five decades. *Colloids Surfaces B Biointerfaces* 165, 325–344. doi:10.1016/j.colsurfb.2018.01.060, Available from: <https://linkinghub.elsevier.com/retrieve/pii/S0927776518300687>.
- Parrinello, M., and Rahman, A. (1981). Polymorphic transitions in single crystals: A new molecular dynamics method. *J. Appl. Phys.* 52 (12), 7182–7190. doi:10.1063/1.328693, Available from: <http://aip.scitation.org/doi/10.1063/1.328693>.
- Pérez-Sánchez, G., Chien, S.-C., Gomes, J. R. B., Cordeiro Mn, D. S., Auerbach, S. M., Monson, P. A., et al. (2016). Multiscale model for the Templated Synthesis of Mesoporous Silica: The Essential role of Silica Oligomers. *Chem. Mat.* 28 (8), 2715–2727. doi:10.1021/acs.chemmater.6b00348, Available from: <https://pubs.acs.org/doi/10.1021/acs.chemmater.6b00348>.
- Pérez-Sánchez, G., Vicente, F. A., Schaeffer, N., Cardoso, I. S., Ventura, S. P. M., Jorge, M., et al. (2020). Unravelling the interactions between surface-active ionic liquids and Triblock Copolymers for the design of thermal responsive systems. *J. Phys. Chem. B* 124 (32), 7046–7058. doi:10.1021/acs.jpcc.0c02992, Available from: <https://pubs.acs.org/doi/10.1021/acs.jpcc.0c02992>.
- Quina, F. H., Nassar, P. M., Bonilha, J. B. S., and Bales, B. L. (1995). Growth of sodium dodecyl sulfate micelles with detergent concentration. *J. Phys. Chem.* 99 (46), 17028–17031. doi:10.1021/j100046a031, Available from: <https://pubs.acs.org/doi/10.1021/j100046a031>.
- Ritter, E., Yordanova, D., Gerlach, T., Smirnova, I., and Jakobtorweihen, S. (2016). Molecular dynamics simulations of various micelles to predict micelle water partition equilibria with COSMOmic: Influence of micelle size and structure. *Fluid Phase Equilib.* 422, 43–55. doi:10.1016/j.fluid.2016.03.006.
- Ruiz-Morales, Y., and Romero-Martínez, A. (2018). Coarse-grain molecular dynamics simulations to investigate the Bulk viscosity and critical micelle concentration of the ionic surfactant sodium dodecyl sulfate (SDS) in aqueous solution. *J. Phys. Chem. B* 122 (14), 3931–3943. doi:10.1021/acs.jpcc.7b10770, Available from: <https://pubs.acs.org/doi/10.1021/acs.jpcc.7b10770>.
- Sammalkorpi, M., Karttunen, M., and Haataja, M. (2007). Structural properties of ionic detergent aggregates: A large-scale molecular dynamics study of sodium dodecyl sulfate. *J. Phys. Chem. B* 111 (40), 11722–11733. doi:10.1021/jp072587a, Available from: <https://pubs.acs.org/doi/10.1021/jp072587a>.
- Schaeffer, N., Kholany, M., Veloso, T. L. M., Pereira, J. L., Ventura, S. P. M., Nicaud, J.-M., et al. (2019). Temperature-responsive extraction of violacein using a tuneable anionic surfactant-based system. *Chem. Commun.* 55 (59), 8643–8646. doi:10.1039/C9CC03831K Available from: <http://xlink.rsc.org/?DOI=C9CC03831K>.
- Schaeffer, N., Passos, H., Gras, M., Mogilreddy, V., Leal, J. P., Pérez-Sánchez, G., et al. (2018). Mechanism of ionic-liquid-based acidic aqueous biphasic system formation. *Phys. Chem. Chem. Phys.* 20 (15), 9838–9846. doi:10.1039/C8CP00937F Available from: <http://xlink.rsc.org/?DOI=C8CP00937F>.
- Schaeffer, N., Pérez-Sánchez, G., Passos, H., Gomes, J. R. B., Papaiconomou, N., and Coutinho, J. A. P. (2019). Mechanisms of phase separation in temperature-responsive acidic aqueous biphasic systems. *Phys. Chem. Chem. Phys.* 21 (14), 7462–7473. doi:10.1039/C8CP07750A Available from: <http://xlink.rsc.org/?DOI=C8CP07750A>.
- Schäfer, K., Kolli, H. B., Killingmoe Christensen, M., Bore, S. L., Diezemann, G., Gauss, J., et al. (2020). Supramolecular packing Drives Morphological transitions of charged surfactant micelles. *Angew. Chem. Int. Ed. Engl.* 132 (42), 18750–18757. doi:10.1002/ange.202004522, Available from: <https://onlinelibrary.wiley.com/doi/10.1002/ange.202004522>.
- Souza, P. C. T., Alessandri, R., Barnoud, J., Thallmair, S., Faustino, I., Grünewald, F., et al. (2021). Martini 3: A general purpose force field for coarse-grained molecular dynamics. *Nat. Methods* 18 (4), 382–388. doi:10.1038/s41592-021-01098-3, Available from: <http://www.nature.com/articles/s41592-021-01098-3>.
- Tang, X., Koenig, P. H., and Larson, R. G. (2014). Molecular dynamics simulations of sodium dodecyl sulfate micelles in water—the effect of the force field. *J. Phys. Chem. B* 118 (14), 3864–3880. doi:10.1021/jp410689m, Available from: <https://pubs.acs.org/doi/10.1021/jp410689m>.
- Vainikka, P., Thallmair, S., Souza, P. C. T., and Marrink, S. J. (2021). Martini 3 coarse-grained model for type III Deep Eutectic solvents: Thermodynamic, structural, and extraction properties. *ACS Sustain. Chem. Eng.* 9 (51), 17338–17350. doi:10.1021/acssuschemeng.1c06521, Available from: <https://pubs.acs.org/doi/10.1021/acssuschemeng.1c06521>.
- Ventura, S. P. M., e Silva, F. A., Quental, M. V., Mondal, D., Freire, M. G., and Coutinho, J. A. P. (2017). Ionic-liquid-Mediated extraction and separation processes for Bioactive compounds: Past, present, and Future trends. *Chem. Rev.* 117 (10), 6984–7052. doi:10.1021/acs.chemrev.6b00550, Available from: <https://pubs.acs.org/doi/10.1021/acs.chemrev.6b00550>.
- Yesylevskyy, S. O., Schäfer, L. V., Sengupta, D., and Marrink, S. J. (2010). Polarizable water model for the coarse-grained MARTINI force field. *PLoS Comput. Biol.* 6 (6), e1000810.
- Zhong, Y., Feng, X., Chen, W., Wang, X., Huang, K.-W., Gnanou, Y., et al. (2016). Using UCST ionic liquid as a draw solute in forward osmosis to Treat high-Salinity water. *Environ. Sci. Technol.* 50 (2), 1039–1045. doi:10.1021/acs.est.5b03747, Available from: <https://pubs.acs.org/doi/10.1021/acs.est.5b03747>.



## OPEN ACCESS

## EDITED BY

Verónica de Zea Bermudez,  
University of Trás-os-Montes and Alto  
Douro, Portugal

## REVIEWED BY

Ping Duan,  
China University of Geosciences  
Wuhan, China  
Arkamitra Kar,  
Birla Institute of Technology and  
Science, India

## \*CORRESPONDENCE

Inês Silveirinha Vilarinho,  
inessvilarinho@ua.pt  
João António Labrincha,  
jal@ua.pt

## SPECIALTY SECTION

This article was submitted to Ceramics  
and Glass,  
a section of the journal  
Frontiers in Materials

RECEIVED 29 July 2022

ACCEPTED 06 October 2022

PUBLISHED 18 October 2022

## CITATION

Vilarinho IS, Gameiro T, Capela MN,  
Carvalheiras J, Caetano APF, Novo C,  
Novais RM, Seabra MP and Labrincha JA  
(2022), Review of recycling alternatives  
for paper pulp wastes.  
*Front. Mater.* 9:1006861.  
doi: 10.3389/fmats.2022.1006861

## COPYRIGHT

© 2022 Vilarinho, Gameiro, Capela,  
Carvalheiras, Caetano, Novo, Novais,  
Seabra and Labrincha. This is an open-  
access article distributed under the  
terms of the [Creative Commons  
Attribution License \(CC BY\)](#). The use,  
distribution or reproduction in other  
forums is permitted, provided the  
original author(s) and the copyright  
owner(s) are credited and that the  
original publication in this journal is  
cited, in accordance with accepted  
academic practice. No use, distribution  
or reproduction is permitted which does  
not comply with these terms.

# Review of recycling alternatives for paper pulp wastes

Inês Silveirinha Vilarinho\*, Tânia Gameiro, Marinélia N. Capela,  
João Carvalheiras, Ana P. F. Caetano, Catarina Novo,  
Rui M. Novais, Maria Paula Seabra and João António Labrincha\*

Department of Materials and Ceramic Engineering, CICECO-Aveiro Institute of Materials, University of Aveiro, Aveiro, Portugal

The demand for products derived from the pulp and paper industry has been increasing over the past years and is projected to further increase over the coming decades. Although being one of Portugal's most relevant industrial activities, contributing to nearly 2.3% of the GDP, this sector is known to generate a variety of wastes including fly ashes, exhausted bed sands, green liquor dregs, grits, lime muds, biological and pulp and paper mill sludges, which have been mostly disposed of in landfills. This strategy is not aligned with the circular economy vision, and therefore it is imperative to develop new recycling routes for the different waste streams. This scenario has driven a significant research effort in the attempt to design sustainable recycling alternatives for the distinct wastes. This study summarizes the investigations focusing on the valorisation of these wastes in a wide range of applications, including the production of low carbon footprint binders or mortars for the construction sector, but also the production of novel materials for high added-value applications such as wastewater treatment and pH regulation. The present work also highlights the main bottlenecks and future prospects for the studied wastes.

## KEYWORDS

waste upcycling, clinker, portland cement, geopolymers, adsorbent, PH regulator

## 1 Introduction

Pulp and paper (P&P) production is one of the largest industrial activity in the world (Bajpai, 2017), and the fifth-largest energy consumer worldwide, behind industries such as chemical, iron and steel, and oil and gas refining (EIA, 2019). The demand for P&P products is increasing and, in 2020, its market size was evaluated at 355 billion € (FBI, 2021) with an expected annual growth rate of 4.08% from 2022 to 2026 (Cision, 2022). The new markets and applications P&P products such as cardboard, tissue paper, textile applications, or pulp for personal care products (Cherian and Siddiqua, 2019) have contributed to this growth. Further, the need to replace plastic (produced from non-renewable sources) with paper in packaging applications is also responsible for the expectable growth.

The members of the Confederation of European Paper Industries (CEPI) reached a total consumption of primary energy, in 2019, of 1.3 million TJ, which includes the use of

biomass and process residues (62%), gas (32%), coal (3%), fuel oil (1%) and other fuel sources. Electricity generated through combined (on-site) heat and power plants accounts for 96% of total electricity consumption (CEPI, 2021) and, for this reason, these industries are considered energy-intensive manufacturers (EIA, 2019). According to CEPI, the 495 pulp, paper and cardboard producing companies in 18 countries in Europe produced 36.2 million tons of pulp and 85.2 million tons of paper and cardboard in 2020 (CEPI, 2021). CEPI members account for 92% of the European P&P industries and represent 21% of the total world pulp production. Portugal is the third-largest European pulp producer, behind Sweden and Finland, being P&P production one of the most vital industrial activities. In terms of wood consumption for pulp manufacturing, 72% are softwood (such as pine and spruce) and 28% are hardwood, such as birch, eucalyptus, beech, ash, aspen, maple, acacia, oak, among others (CEPI, 2021).

## 2 Pulp manufacturing process

Pulp derived from wood is the main raw material in the production of different types of paper. Further, the pulp is also used as an absorbent material in diapers and other sanitary products (Cabrera, 2017). Considering the use of new wood materials, which represent a large share of pulp production, the process can be divided into three main steps: preparation of raw materials, separation of the fibres and bleaching process. The recovery of chemicals is also an important step that, although not directly in the pulp production process, contributes to its success and sustainability. The Kraft process is the most used pulping process by P&P industries worldwide (Santos et al., 2013) mainly because the pulp produced has superior strength, higher resistance to aging and the bleaching process is simplified.

### 2.1 Preparation of the raw materials and separation of fibres

Before the pulping process, the raw materials (softwoods, hardwoods and non-woody biomasses) are prepared, converting them into appropriate size and shape for the following processing. The logs are debarked and cleaned with water because the bark is a contaminant in the chemical pulping process. The clean logs are cut into identical small chips, maximizing in this way the efficiency of the process. Typically, very small or large chips are separated and used for energy recovery (biomass burning) or are reprocessed for further treatment (Kramer et al., 2009).

In the pulp-producing process, lignin, a resin that binds the wood fibres tightly, must be eliminated and only fibres (cellulose) must be extracted. Thus, the treatment process aims to separate the biomass components, namely, cellulose (40–50 wt.%),

hemicellulose (25–30 wt.%) and lignin (25–30 wt.%), into individual components (Naqvi et al., 2010). After separation, the fibres are suspended in a slurry, to be used in the papermaking process. The treatment process is performed by separation or solubilization of the lignocellulosic components. Pulping processes can be divided into mechanical, semi-chemical and chemical, according to the methodology and instruments used (Kumar et al., 2020). Chemical pulping is the most common pulping process used worldwide, possibly due to the high removal efficiency of lignin (Takada et al., 2020). In fact, in this route, the majority of the lignin and hemicellulose contents are removed, resulting in low pulp yields (40–55 wt.%), with a high degree of cellulose fibres (Meyer and Edwards, 2014). In this process, the lignin is separated from the remaining materials in a digester under pressure and using cooking chemicals. In the “cooking” of raw materials, such as wood chips, an aqueous chemical solution called “white liquor” is used, at high temperatures and pressure, to extract the pulp fibres. The three main chemical pulping processes are soda pulping (alkaline), sulphite pulping (acid) and Kraft or sulphate pulping (alkaline).

### 2.2 Kraft pulping process

A flowchart of the Kraft pulping process integrated into a P&P mill is presented in Figure 1. The process comprises chemical recovery steps, including the energy production from chemicals and biomass burning, and the connection between the pulp manufacture, the bleaching process and the paper manufacture. In addition, the main effluent and solid wastes generated in the process are highlighted in Figure 1.

The Kraft process was developed with the main goal of removing lignin while preserving carbohydrates. The “cooking” of wood is performed with the addition of white liquor, an alkaline mixture of sodium hydroxide and sodium sulphide, to promote lignin dissolution. The use of such chemicals is advantageous in terms of the final fibre strength but it leads to relatively low pulp yields, caused by the instability and degradation of carbohydrates during the alkaline reaction (Santos et al., 2013). The cooking of the wood chips is performed at elevated temperatures (150–170°C) and pressure. The lignin structure is modified and depolymerized by the action of the strong alkaline solution and the presence of hydrosulphide ions. In this digestion process, 90–95 wt.% of the lignin is solubilized in the pulping liquor. A wide variety of wood species can be processed by the Kraft pulping process and the exact conditions of the process depend on the type of wood used (softwood or hardwood) (Gellerstedt, 2015). After cooking for 2–4 h, the liquor and the pulp mixture are discharged from the digester. They are separated into a series of washers and, after the washing step, the pulp (fibres) is ready to be submitted to the bleaching process. The content in lignin of softwood pulps is

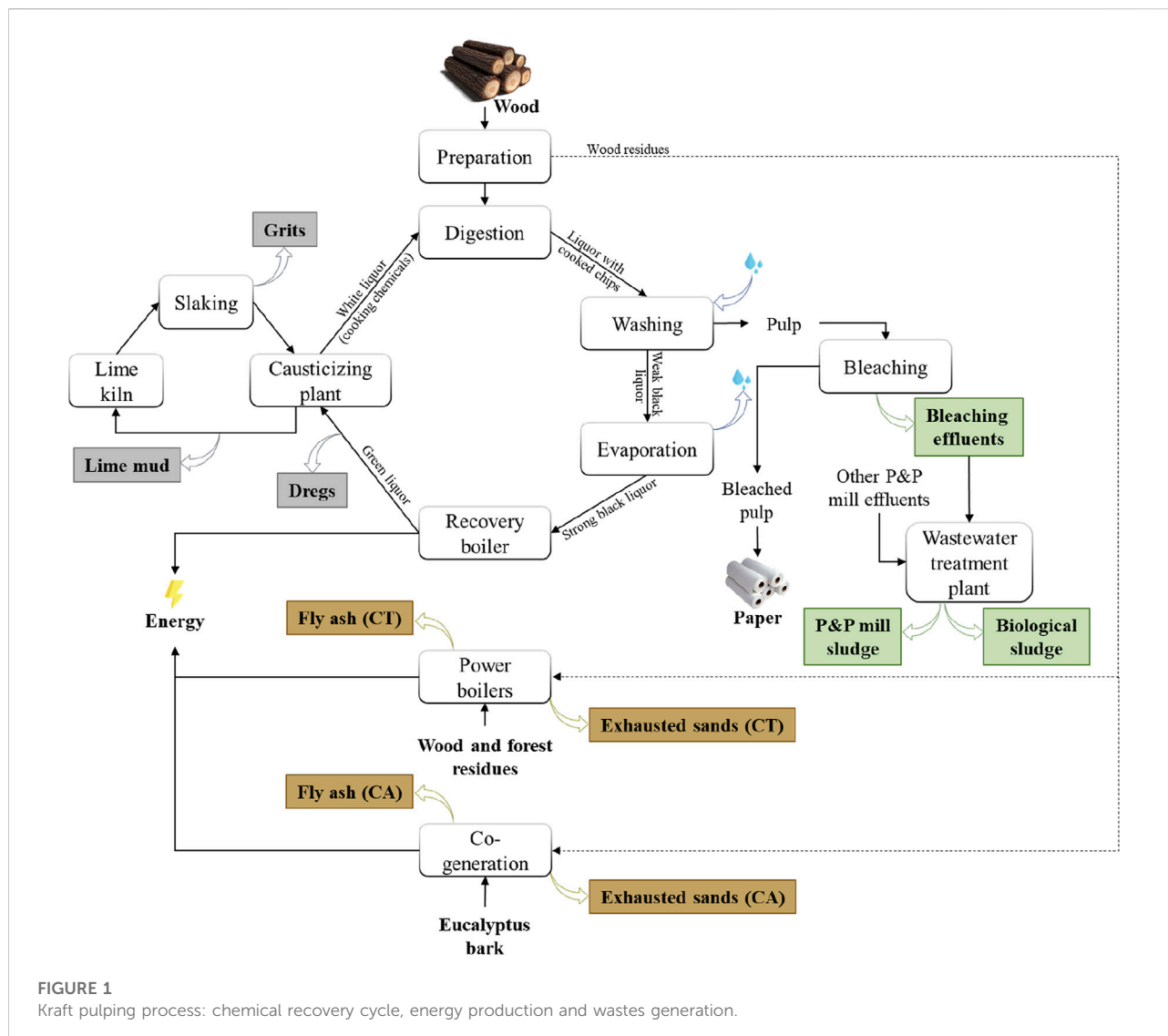


FIGURE 1

Kraft pulping process: chemical recovery cycle, energy production and wastes generation.

about 5 wt.%, and this residual lignin is removed in the bleaching process, obtaining a bright and high-quality pulp.

The Kraft process is the pulping process with maximum chemical recovery efficiency. The chemicals are collected after pulping and are set to the chemical recovery circuit. Figure 1 includes the three steps in the chemical recovery process, namely the black liquor concentration, the combustion of organic compounds and the causticizing and calcination. These steps are vital to the environmental and economic sustainability of the P&P industries, as they allow the reduction of costs and of the environmental impact of waste material (mainly black liquor), with the minimization of the raw materials used and with the recycling of chemical materials (Mesfun et al., 2014). In addition, the recovery of chemicals has the asset of co-generating steam and power, which is used as energy in the P&P mill.

In Kraft (and soda) pulp mills, the liquor from the cooking step is called “weak black liquor” and contains wood lignin, organic materials, oxidized inorganic compounds (such as  $\text{Na}_2\text{SO}_4$  and  $\text{Na}_2\text{CO}_3$ ) and white liquor (cooking chemicals such as  $\text{NaOH}$ —soda—or a mixture of  $\text{NaOH}$  and  $\text{Na}_2\text{S}$ —Kraft). The concentration of weak black liquor is performed by a series of evaporators, to increase the solids content from 12–15 wt.% to  $\approx 65$  wt.%. It forms the so-called “strong black liquor,” capable of being combusted in the recovery furnace (Verma et al., 2019), in the next chemical recovery step. The condensate from the evaporators contains high concentrations of methanol and is sent to the treatment plant (Meyer and Edwards, 2014). The combustion of organic compounds is performed in the recovery boiler, where “strong black liquor” is burned and the inorganic chemicals are reduced to a molten smelt, enriched with  $\text{Na}_2\text{S}$  and  $\text{Na}_2\text{CO}_3$ , after lignin



decomposition. They are recovered from the bottom of the boiler and refined (Kramer et al., 2009). This combustion process generates energy in the form of electricity, which, in combination with the energy produced by the power combustor (wood burning), is used in the plant. The inorganic salts recovered in combustion are dissolved in the weak wash water and form the “green liquor” (Naqvi et al., 2010), which is filtered/clarified to remove the green liquor dregs. “Green liquor” is causticized with the addition of lime, to convert the  $\text{Na}_2\text{CO}_3$  into  $\text{NaOH}$  (dos Santos et al., 2019). The calcium carbonate formed is removed as lime mud (He et al., 2009) and it is washed and the lime is regenerated in the lime kiln. The “white liquor” recovered is filtered and reused in the wood cooking process.

Typically, about 3.5 kg of steam is produced when 1 kg of black liquor solids is burned, depending on the efficiency of the recovery boiler. After the steam generation, it passes through a turbine to generate electricity and the amount generated depends on the turbine type and the quality of the steam. A mill, which produces 1000 ton/d of Kraft pulp, can generate 25–35 MW of electricity by burning 1500 ton/d of black liquor dry solids in the recovery boiler (Tran and Vakkilainen, 2008).

## 2.3 Bleaching process

After chemical or mechanical pulping processes, the pulp obtained still contains high amounts of lignin and other coloured compounds. To produce high-grade final products, the pulp must be bleached to remove the pulp colour caused by the presence of residual lignin, thus obtaining a light-coloured or white paper, preferred for many products and applications. The same bleaching process or sequence can be applied to any of the pulping processes (mechanical, semi-chemical, or chemical). The addition of two or more chemicals and the sequence in which they are used depends on several factors, including costs, the type of pulp to be bleached and the requirement for the final product. The addition of chemicals to the previously washed pulp is performed in stages in the bleaching towers. Between each stage, bleaching chemicals are removed from the washers. From these successive washes, the effluents generated are collected and sent to the wastewater treatment plant (EPA, 2010).

## 2.4 Wastes generated

In the P&P industry, several wastes are produced at different steps of the process and the amount of waste generated depends on the pulping process implemented (Cherian and Siddiqua, 2019). The Kraft pulping process generates about 100 kg of waste per ton of air-dry pulp ( $\text{kg/t}_{\text{AD}}$ ), whereas the semi-chemical and mechanical pulping process generates only about 60  $\text{kg/t}_{\text{AD}}$  (Monte et al., 2009). With the new approaches considered in

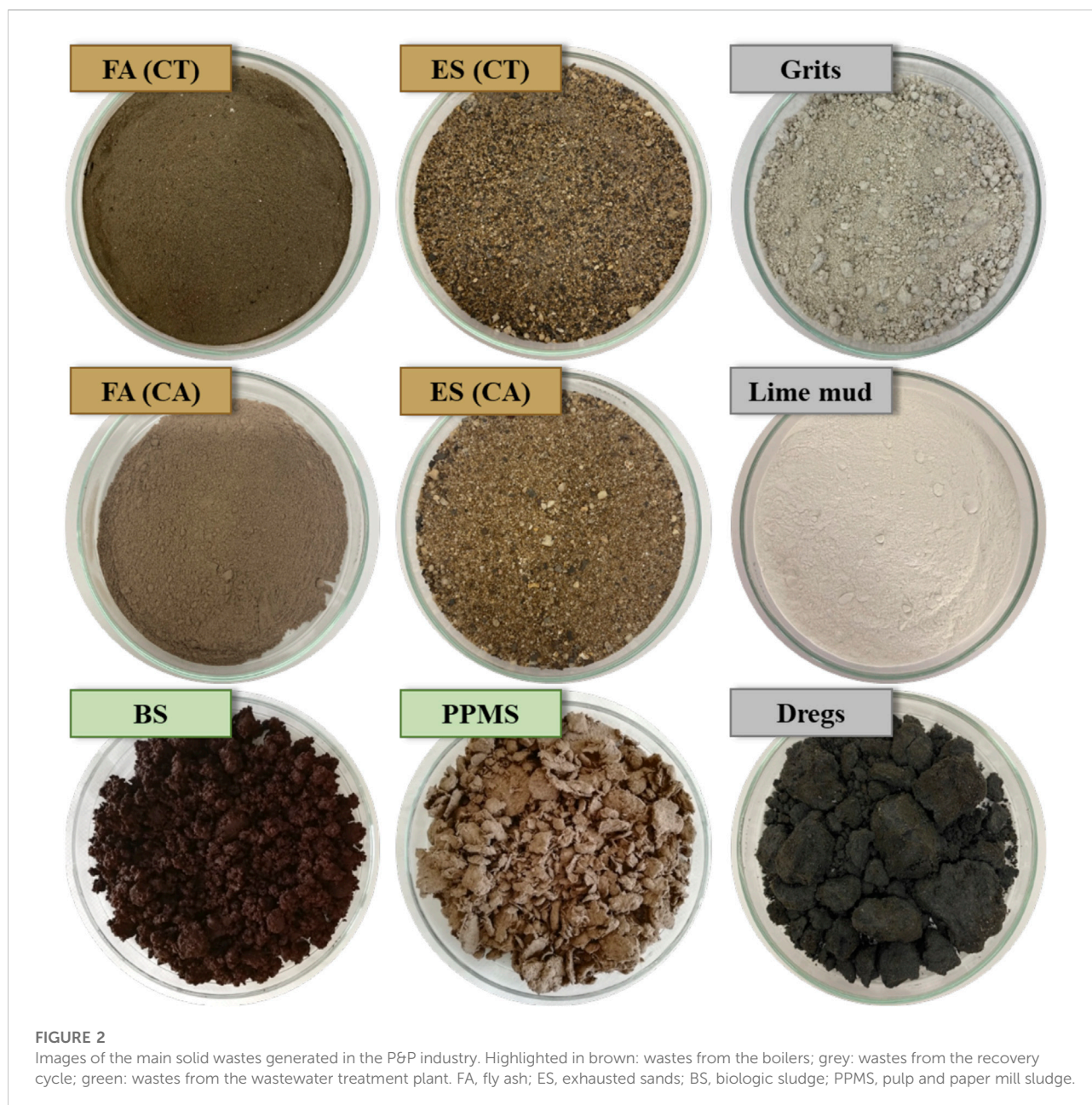
recent years for waste management, the use of different wastes generated in P&P mills as resources is a step towards green energy and environmental sustainability, moving from the conventional linear concept to the circular economy.

Figure 2 shows images of the main solid wastes generated in the P&P process. For the Kraft process, including the chemical recovery cycle, the main wastes generated are *fly ashes* (FA), *exhausted sands* (ES) from biomass boilers (CT) and co-generation plant (CA), *dregs* (also called green liquor sludge) from clarification of green liquor, *grits* from the regeneration of  $\text{CaO}$  after calcination in a lime kiln, *lime mud* from the causticizing process, *biological sludge* and *mill sludge* from the P&P mill wastewater treatment plant, as presented in Figure 1. Barks and other wood residues are burned for energy production, therefore, they are not considered wastes (Simão et al., 2018).

Fly ash and exhausted bed sand CT are generated in the combustion process of the power combustors, see Figures 1, 2. Herein, the fused particles of volatile matter and impurities are carried upwards with the flue gases and, as they approach the low-temperature zones, solidify to form fly ashes. These fine ashes are captured from the flue gases in the bag filters and electrostatic precipitators. The remaining residue is recovered at the bottom of the boiler and is called exhausted bed sand CT. Fresh sand (inert particles) is added to the fluidized bed biomass boiler which is a type of boiler recommended for biomass burning. The temperature of the bed ranges from 800°C to 900°C and the  $\text{O}_2$  concentration in the flue gas varies between 4 and 7 vol.% (dry basis) (Modolo et al., 2013). Fly ash and exhausted bed sands CA are generated in the co-generation power plant where heat and power are produced. Here, only eucalyptus barks are used whereas in the power boiler wood and forest residues are used. The worldwide amount of biomass fly ashes produced is estimated to be 10 million tonnes/year (Lamers et al., 2019).

Dregs are mainly composed of sodium and calcium carbonates, sodium sulphide, a low organic fraction that was not burned in the recovery boiler, and other salts from the pulp production process (Modolo et al., 2010; Novais et al., 2018f). Grits are a mixture of calcium carbonate and lime that did not react in the slaker (where causticization takes place). During causticization, the reaction between  $\text{Na}_2\text{CO}_3$  (in the green liquor) and lime (from the lime kiln) produces  $\text{NaOH}$  and calcium carbonate, which are the main components of the lime mud (Modolo et al., 2010). The pH of this waste is strongly alkaline (between 10.0 and 12.8) due to the presence of alkaline oxides (Manskinen et al., 2011).

Several wastewaters' streams with different compositions and volumes are generated in the different pulp and paper production stages. The bleaching process generates up to 85% of the total volume of effluent discharged in a P&P mill. These effluents formed in the pulp bleaching process have different characteristics, depending on the bleaching agent and generation stage, and are considered highly toxic (Kamali and



Khodaparast, 2015). These effluents from the bleaching process are rich in dissolved lignin, carbohydrates, colour, organic matter, adsorbable organic halogens (AOX) and inorganic chloride compounds, chlorophenols and halogenated hydrocarbons (Meyer and Edwards, 2014; Kamali and Khodaparast, 2015). The most problematic effluents are generated during the bleaching process with chlorine dioxide, due to the formation of complex and persistent organochlorine compounds, which can be genotoxic and are known to bioaccumulate in the aquatic food chain, mainly in the body fat of animals of higher trophic levels (Kamali et al., 2016). Usually, the alkaline effluent generated in the bleaching process is

called *Ep* and is generated in an alkali extraction step (e.g., using hydrogen peroxide) (Saeli et al., 2019c).

The typical wastewater treatment processes used in these plants are primary clarification by sedimentation and floatation followed by biological treatment (Faubert et al., 2016). These methods allow the removal of suspended and floating materials and toxic compounds from the wastewater streams that constitute the pulp and paper mill sludge (PPMS) (Kamali and Khodaparast, 2015), a mixture of primary and biological sludge. PPMS presents high composition variability, contains a large amount of water, and is produced in large quantities. It was estimated that 0.3–1 m<sup>3</sup> of primary sludge is generated per ton of

TABLE 1 Chemical composition of the wastes: fly ashes, sand, dregs, grits, lime mud, P&amp;P mill sludge.

Waste	Na <sub>2</sub> O	MgO	Al <sub>2</sub> O <sub>3</sub>	SiO <sub>2</sub>	P <sub>2</sub> O <sub>5</sub>	SO <sub>3</sub>	K <sub>2</sub> O	CaO	Fe <sub>2</sub> O <sub>3</sub>	LOI	Ref
CT Fly ashes	1.24–1.53	2.23–3.44	13.50–15.26	34.0–46.3	1.11–1.12	2.66–2.77	5.49–5.97	11.74–16.70	1.77–4.95	6.39–14.3	Novais et al. (2018d), Saeli et al. (2019b), Modolo et al. (2021)
CT Exhaust Sands	0.42–0.88	0.69–1.96	2.29–3.83	72.2–80.8	0.34	0.05	2.03	7.30–17.15	1.54	2.08–2.62	Modolo et al. (2013), Gonçalves et al. (2021b)
CA Fly ashes	1.50	3.10	13.50	34.0	—	2.80	5.50	16.50	5.00	14.30	Rossi et al. (2019)
CA Exhaust Sands	1.69	2.16	2.86	64.57	1.03	0.55	2.01	20.00	1.24	2.92	Gonçalves et al. (2021b)
Dregs	23.8	—	2.65	2.16	0.02	10.5	0.89	15.2	0.68	34.3	Novais et al. (2018f)
Grits	5.52	0.45	0.29	0.47	0.38	1.86	0.27	49.95	0.05	41.1	Saeli et al. (2019a)
LM	1.1–1.9	0.48–0.61	0.06–0.02	0.18–0.29	0.52–0.9	—	0.03–0.1	51.8–55	0.03	42.2–43.7	Modolo et al. (2014), Buruberry et al. (2015)
BS	0.58	0.79	0.97	1.89	2.31	4.9	0.32	4.53	0.34	83.8	Buruberry et al. (2015)
PPMS	0.67	0.32	13.24	5.34	1.83	—	0.30	2.14	0.75	74.84	Simão et al. (2017)

produced paper (Veluchamy and Kalamdhad, 2017) while the biological or secondary sludge (BS) is produced in less quantity than the primary sludge (Faubert et al., 2016).

### 3 Wastes characterization from a Portuguese paper and pulp industry

#### 3.1 Fly ashes and exhausted sands

The chemical composition of fly ashes and sand waste reported in the literature and measured by X-ray fluorescence (XRF) is presented in Table 1. Results show that the main components of both FA, CT and CA, are silica (SiO<sub>2</sub>), alumina (Al<sub>2</sub>O<sub>3</sub>) and calcium (CaO). Saeli et al. observed that, in CT, the sum of SiO<sub>2</sub> and Al<sub>2</sub>O<sub>3</sub> amounts was ~53 wt% and that iron was also present with an amount of 5.94 wt.% (Saeli et al., 2019b). The loss on ignition (LOI) at 1000°C was also determined in several works and vary between 6.39 and 14.3 wt.%. This wide range is mainly due to the type of material that is burned which can represent a drawback in the recycling route of this waste. X-ray diffraction (XRD) showed that the main crystalline phases of FA are: α-quartz, calcite, mica group mineral (like muscovite) and microcline, in agreement with the XRF results. Considering the particle size distribution, the mean particle size obtained for CT was 39 μm with a specific surface area (BET) of 3 m<sup>2</sup>/g (Saeli et al., 2019b) and for CA was 306.40 μm (Capela et al., 2021).

Regarding the exhausted sands (ES), the most abundant oxide, as expected, is SiO<sub>2</sub> which varies between 65 and 81 wt.%. CaO is also present, 7.3 to 20 wt.%, see Table 1. Another noteworthy factor is the LOI values, 2 to 2.9 wt.% which are much higher than the reference sand, 0.28 wt.%,

probably due to its chemical composition (presence of CaCO<sub>3</sub> and/or organic matter). The particle size distribution of the as-received sands was performed in the work of (Gonçalves et al., 2021b). The authors observed that the highest mass content was obtained for the fraction higher than 500 μm, 62%–71% of the total mass of the sands, CA and CT, respectively. For the reference sand the value was 57%.

#### 3.2 Dregs and grits

XRF analysis shows that the dominant oxides of dregs are MgO, CaO, Na<sub>2</sub>O and SO<sub>3</sub> (8.13, 15.2, 23.8 and 10.5 wt.%, correspondently) with a high LOI value (34.3 wt.%). These results are in line with the calcination of calcite and pirssonite, as well as some of the organic content present in such waste. The authors also raise concerns about SO<sub>3</sub> amount identified by XRF that suggests a poor deduction of the sulphur content in the boiler. The particles are irregular but very fine in size: all below 20 μm being the mean particle size near 6 μm (Novais et al., 2018f). It is also important to state that dregs contain, in its composition, several heavy metals as Novais et al. demonstrated (Novais et al., 2019a). Chromium, cobalt, copper, lead, nickel and zinc were all identified by XRF, at a ppm level between 50 and 150 except Cu which was found in much higher amount, around 3075 ppm (Novais et al., 2019a). This will have an impact on potential recycling methodologies as the possible heavy metals leaching from the wastes might limit their applications range for this challenging waste stream. Nevertheless, as it will show later in this review, recent studies suggest the feasibility of incorporating fairly high



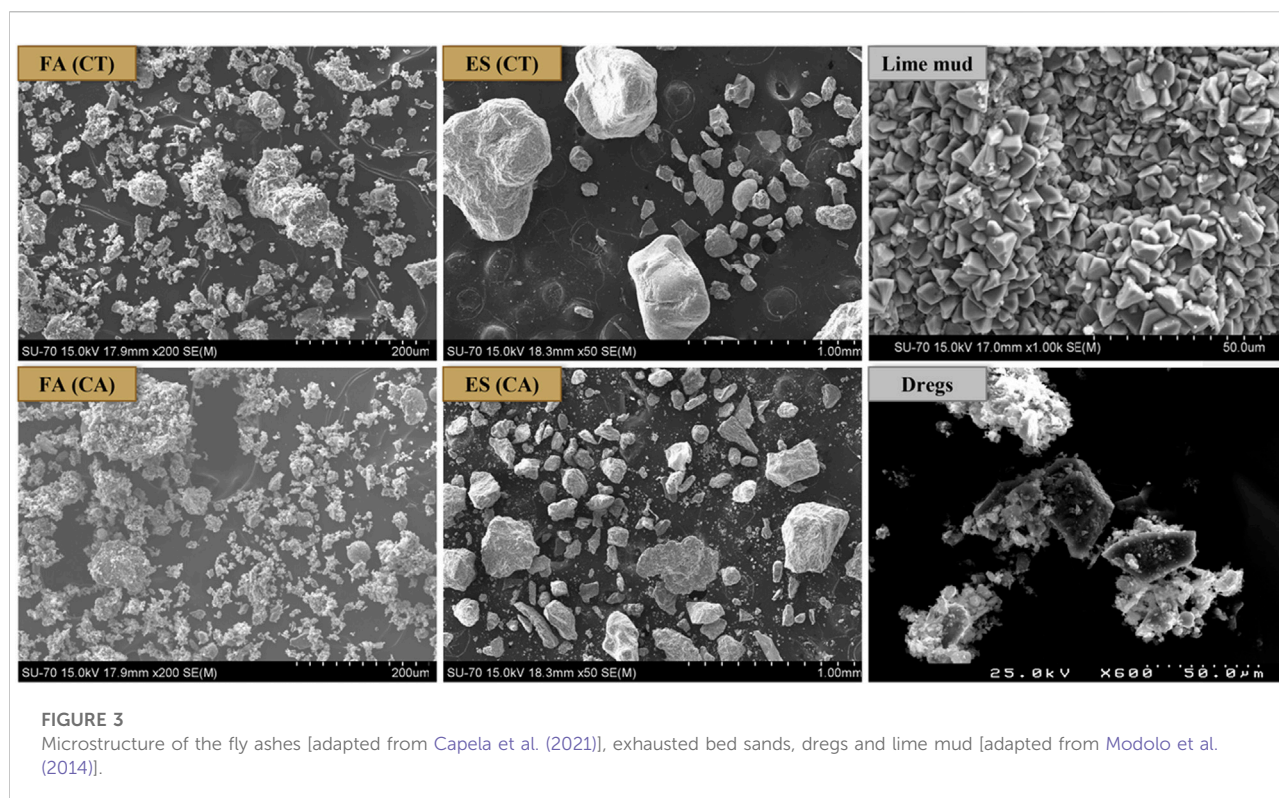


**FIGURE 3**  
Microstructure of the fly ashes [adapted from [Capela et al. \(2021\)](#)], exhausted bed sands, dregs and lime mud [adapted from [Modolo et al. \(2014\)](#)].

amounts of dregs in geopolymers, while trapping the hazardous components inside the binders' framework.

Grits were fully characterized by Saeli et al. [Saeli et al. \(2019a\)](#), [Saeli et al. \(2019b\)](#), [Saeli et al. \(2018\)](#). This residue presented a moisture content of ~7 wt.%. By XRF CaO is found to be the main constituent (49.45 wt.%) followed by Na<sub>2</sub>O (5.52 wt.%), while the other components are detected in much lower amounts (below 2 wt.%, as can be seen in [Table 1](#)). The LOI value of the waste was found to be 41.1 wt.%, attributed to the high-temperature decomposition of calcium carbonate and sodium bicarbonate. By XRD it was found that grits are mainly (>95 wt.%) constituted by calcium carbonate (CaCO<sub>3</sub>), also presenting some minor amounts of sodium bicarbonate (NaHCO<sub>3</sub>), results that are in accordance with the ones obtained by XRF. Grits presented a broad particle size distribution, ranging from 1 to 12.5 mm, but showing just a small percentage (2 wt.%) of particles with a diameter inferior to 1 mm.

### 3.3 Lime mud, biologic sludge and P&P mill sludge

Lime mud (LM) is mainly composed of CaO (51–55 wt.%). XRF analysis also identifies a large loss on ignition (LOI) at 1000°C (42–43.7 wt.%) associated with the thermal decomposition of calcium carbonate. In fact, differential thermal analysis shows a strong endothermic band centered at

828°C, typical of calcite decomposition ([Modolo et al., 2014](#); [Buruberry et al., 2015](#)). In line with the XRF, the XRD analysis only showed the presence of calcite (CaCO<sub>3</sub>). Further, LM is composed of finer particles, with a mean value of around 10–12 µm and a maximum size of 26 µm.

Biologic sludge (BS) concentration of solids was found to be 17.2 wt.%. BS's main chemical components are: SO<sub>3</sub> (4.90 wt.%), CaO (4.53 wt.%), P<sub>2</sub>O<sub>5</sub> (2.3 wt.%), and SiO<sub>2</sub> (1.89 wt.%), see [Table 1](#). BS shows high LOI values (83.80 wt.%), due to the presence of volatile components and organic compounds ([Buruberry et al., 2015](#)). BS particle size distribution was not evaluated because after being dried the sample was predominantly formed by aggregates.

PPMS is mainly composed of Al<sub>2</sub>O<sub>3</sub> (13.24 wt.%), SiO<sub>2</sub> (5.24 wt.%), CaO (2.14 wt.%), and P<sub>2</sub>O<sub>5</sub> (1.83 wt.%) ([Simão et al., 2017](#)). PPMS presented a lower LOI than BS (74.84 wt.%). The water content of PPMS is very high, ~86 wt.%, therefore a drying step is needed. PPMS showed low crystallinity, even so, quartz and calcite were detected. Its D<sub>50</sub> value was found to be 20.7 µm.

[Figure 3](#) presents the micrographs of some of the P&P wastes: fly ashes, exhausted bed sands, dregs and lime mud. Both FA and dregs are composed of irregularly shaped particles, presenting a rough surface and a broad particle size range (between a few microns and >100 µm) ([Novais et al., 2018f](#); [Capela et al., 2021](#)). Further, it can also be observed that CA presents much bigger particles than CT



which is in accordance with the laser diffraction results (Capela et al., 2021).

Gonçalves et al. (2021b) compared the exhausted sands with the commercial sand and, as observed in Figure 3, the waste sands are composed of irregular grains whereas the commercial sand has more regular rounded forms. However, as ES will be introduced as aggregate these forms might not have a negative influence on the mortar's properties. Lime mud presents crystals in its microstructure being those related to its composition, calcium carbonate (Modolo et al., 2014).

## 4 Possible applications for the P&P waste streams

The cement production process is, nowadays, responsible for up to 5% of the total CO<sub>2</sub> emissions (Statista, 2020a; 2020b). Hence, to turn this process more sustainable and meet the net zero emissions by 2050, lower carbon footprint materials have been investigated (Vass et al., 2021).

An overview of the different types of applications is described in the following section which is divided into subsections: 4.1 cement-based materials including clinker and dense materials; 4.2 alkali-activated materials including dense and porous materials, adsorption of pollutants, pH control; and 4.3 other applications.

### 4.1 Cement-based materials

#### 4.1.1 Clinker

Buruberri et al. studied the utilization of lime mud (LM), biological sludge (BS) and fly ash (FA) as secondary raw materials in the synthesis of belitic and Portland clinkers (Buruberri et al., 2015). For the clinker synthesis, eleven compositions were tested, starting from the mixture of different quantities of LM, BS and FA. The formulations were developed based on three principles: obtain a clinker with a composition rich in belite or Portland-type, maximize the incorporation of BS and lessen the moisture content. LM was used as the main source of CaO, BS besides adding energy to the system acted as a fluxing agent, and FA behaved as a fluxing agent and provided CaO, SiO<sub>2</sub>, Al<sub>2</sub>O<sub>3</sub> and Fe<sub>2</sub>O<sub>3</sub>. The prepared compositions were fired at four temperatures (1300, 1350, 1390 and 1455°C). The authors concluded that belitic and Portland clinkers were obtained from some of the tested formulations. It should be stressed that the obtained Portland clinker was fired at 1390°C, which represents a major energy gain compared to the temperature currently used in the industry (~1450°C). The obtained belite-based clinker was used to prepare CEM II A-L cement according to EN197-1:2011 (CEN: European Committee for Standardization, 2011) by being blended with LM and gypsum. This cement was then successively tested in the

production of mortars with a slump value of 167 ± 2 mm, proper for indoor and outdoor plastering applications, that were cured for 7, 28, and 90 days. The authors observed an increase of the compressive strength of the mortars with the rise of the curing time: 6.1, 10.2 and 13.3 MPa for 7, 28 and 90 days, respectively. Their density increased up to 28 days of curing and then remained unchanged, 2.03 g/cm<sup>3</sup>. It was concluded that the hardening of the mortars was caused by the clinker reaction with water that formed hydrated aluminates and silicates. After 7 days of curing the achieved compressive strength already meet the requirements for interior and exterior applications (6 N/mm<sup>2</sup>). The hardened mortars did not show the formation of efflorescences or other deterioration signs that could compromise their durability.

Simão et al. (2017) evaluated the preparation of clinker from LM, FA and pulp and paper mill sludge (PPMS). For the clinker synthesis, five formulations were prepared based on lime saturation factor, Bogue equations, moisture content and maximizing the content of the waste streams in the compositions. The formulations were fired at three temperatures (1350, 1400, and 1455°C). The obtained clinkers were mainly constituted of belite and alite but other phases like tricalciumaluminate, ferrite and, in some samples, lime were also present. These crystalline phases are those commonly found in commercial clinkers. A clinker that was prepared with the three wastes, heat-treated at 1455°C, presented a high amount of alite and the best fitting in the Rietveld quantification, was the one chosen to produce eco-cement. It was blended (95 wt.%) with gypsum (5 wt.%) and its strength development was tested in a mortar formulation. For comparison purposes, mortars with ordinary Portland cement were also prepared. The used water to binder ratio (w/b) of the cement-based mortars was 0.48. In the case of the eco-cement-based mortars, to achieve identical workability, the w/b had to be 0.75. Eco-cement-based mortars presented a compression strength of ~16 and 21 MPa after 7 and 28 days of curing, respectively. Lower values than the ones achieved by the cement-based mortars, ~32 MPa for 7 days of curing and 43 MPa for the longer curing time. The higher amount of water used in the preparation of eco-cement-based mortars was pointed out as the main factor responsible for the lower compression strength values. Nevertheless, the obtained results were considered satisfactory since eco-cement was produced, exclusively, from waste.

#### 4.1.2 Dense mortars

Rajamma et al. (2009) studied the replacement of Ordinary Portland cement (OPC) type I by different amounts of biomass fly ashes (10, 20 and 30 wt.%). The formulation with fly ash CA exhibited a heat of hydration similar to that of the pure cement paste and the hydration rate and phases formation depend on the alkali content and the water to binder ratio. The authors concluded that the replacement, up to 20 wt.%, of OPC by fly ash does not compromise the mechanical properties of the

material. Alkali-silica reaction is an undesired process as it causes the degradation of concrete structures. The effect of the presence of fly ash in the mitigation of the alkali-silica reaction was studied by (Esteves et al., 2012). The mortars were prepared with 20 and 30 wt.% of fly ash as a cement replacement. The following trends were reported: 1) the expansion of the mortars tend to reduce with the FA incorporation; 2) fly ash CA is more effective than CT, as the mortars prepared with CA present higher mechanical (compressive and flexural) strength; and 3) the addition of 10 wt.% of metakaolin increased the properties of the mortars and also significantly improved the expansion results mitigating the alkali-silica reactions. These findings suggest the feasibility of incorporating biomass fly ashes in concrete (Esteves et al., 2012).

Continuing the previous work, Rajamma et al. (2015) studied the effect of biomass fly ashes on the flow behaviour (workability and rheology), setting time, temperature of hydration and electrical resistivity. The authors observed that by increasing the percentage of fly ash more water was required to attain the same fresh conditions due to the smaller particle size of the FA, tendency to agglomerate and retention/absorption of water molecules. The setting time was also increased and the impedance measurements showed a lower resistivity than the reference when FA were used. This tendency might be explained by the higher concentration of mobile species, namely sodium ions, introduced by the FA. The authors also observed that the differences between the two types of ashes (CA and CT) are not expressive in the workability and setting time behaviour of the fresh pastes. Regarding the hydration temperature, the replacement of cement by FA decreased the hydration temperature which might indicate a delay in the hydration process. Concerning the hardened state properties, no significant differences were observed. Therefore, the authors concluded that the overall performance is acceptable and the incorporation of biomass fly ashes is a viable solution (Rajamma et al., 2015).

More recently, Capela et al. (2021) studied the recycling of biomass fly ash (FA), CA and CT, as supplementary cementitious material in a commercial screed mortar. A pre-treatment of the FA was conducted (sieving and grinding) and its impact was evaluated. The authors observed that the workability decreases with the increase of the FA content, either using FA as received or sieved. Increasing FA levels contributed to lower density, higher water absorption and lower strengths (compressive and flexural), coherent with porosity enhancement. When using grounded FA, this tendency is attenuated, this being related to the better homogeneity of the mixtures that resulted in better compactness. Density and water absorption values are closer to the ones of the standard composition. The samples proved to be resistant to 25 freeze-thaw cycles and the replacement of 17% of OPC with FA met the technical requirements for compressive strength (10 MPa) as well as for flexural strength (3 MPa) without any pre-treatment (Capela et al., 2021).

Modolo et al. (2013) evaluated the utilization of exhausted bed sands CT, produced from bubbling fluidized bed combustion of forest biomass residues, as a substitute of one of the aggregates (coarser sand) in a rendering mortar formulation. The ES was sieved (between 250 and 1000  $\mu\text{m}$ ) to obtain a particle size distribution similar to that of the commercial virgin sand and then washed in an industrial plant. By washing the ES its soluble chloride content was reduced by about 60%. This was an important achievement since Cl concentration determines the amount of ash that can be incorporated into a mortar/concrete formulation. According to EN 998-1:2016 the Cl content of a mortar/concrete formulation should be lower than 0.1 wt.%. Mortars with 0, 50 and 100 wt.% substitution of the coarser sand by the two types of pretreated ES were prepared. In all the ash-containing mortars, the onset of setting started slightly earlier, and the time interval between the beginning and final setting time was shortened, compared to the standard composition. This behavior was attributed to the higher content of chlorides in the ash than in the sand. In the hardened state, the sample's compressive strength, elasticity modulus and shrinkage were evaluated. The incorporation of ash induced small variations in the studied properties, with all formulations accomplishing the required specifications. From the obtained results it was assumed that the ES particles are not as inert as the sand. Nevertheless, further studies on the durability of the samples were suggested.

In a later work, Modolo et al. (2015) performed the physical, chemical and mineralogical characterization of ES CT, towards its landfilling classification and its valorization in an adhesive mortar formulation as a coarser sand replacement. Based on the obtained results ES was classified as a non-hazardous material for landfilling, according to 2003/33/CE (European Parliament and of the Council, E.C., 2003) and Decree-Law no 152/2002 Decree-Law 152/2002-Solid wastes (2002). The ES was sieved (between 250 and 1000  $\mu\text{m}$ ) and adhesive mortars with 0, 25, 50 and 100 wt.% of sand replacement by ES were produced. The ash containing formulations showed a lower water demand to get suitable workability (measured by the slump test). The ES containing mortars showed higher wettability than the standard formulation. From the transference test, it was observed that the non-filled area of the tiles covered with the standard formulation was higher than that of the ones covered with the ash containing mortars. For all the tested replacement percentages the values obtained for the transference capacity were superior to 70% after 40 min of testing. The observed results were attributed to physical differences between the ES and the sand. Namely, ES has particles with a rough surface and a higher percentage of smaller particles compared to commercial sand. In the hardened state, tensile adhesion strength was evaluated, and it was observed that it improved with the increase of ES content in samples with three storage conditions: standard, wet and heat. This result was attributed to the improved interfacial contact between the adhesive and the ceramic tile, due to the observed

increase in wetting and transfer capability demonstrated by the ash-containing samples. This tensile adhesion strength improvement led to a change in the failure pattern, from the tile–adhesive interface to a cohesive failure inside the adhesive.

Modolo et al. (2014) also studied the incorporation of LM in mortars. The samples containing 30 wt.% LM exhibited the highest torque and yield stress values, while the plastic viscosity remained almost constant. The spreading of these mortars decreased by about 15% compared with the reference. The setting time was also reduced but LM did not significantly influence the hydration kinetics. The compressive strength of the LM samples increased by around 8% at 28 days of curing (compared to the control sample) but in the mixtures with 30 wt.% there was a slight reduction after 28 days of curing. Although to use LM in dry-mixed industrial mortars, it is necessary to eliminate its moisture, it is possible to use this residue thus improving the economic and environmental aspects related to waste management and saving virgin raw materials (Modolo et al., 2014).

Biomass fly ash has been studied as supplementary cementitious material, as it can present pozzolanic activity. This behaviour is related to the sum of  $\text{SiO}_2$ ,  $\text{Al}_2\text{O}_3$ , and  $\text{Fe}_2\text{O}_3$  amounts available in its chemical composition (Rajamma et al., 2009; Berra et al., 2015; Capela et al., 2021), and to what extent these three oxides are present in the fly ash amorphous phase (Berra et al., 2015). Fly ash particle size reduction can also enhance the ashes' reactivity (Capela et al., 2021). The pozzolanic reaction is characterized by the reaction during cement hydration, of  $\text{Ca}(\text{OH})_2$  from clinker with  $\text{SiO}_2$  and  $\text{Al}_2\text{O}_3$  from fly ash, producing hydrated calcium aluminate (C-A-H) and hydrated calcium silicate (C-S-H) (Capela et al., 2021). Some biomass fly ash can possess hydraulic activity (Rajamma et al., 2009; Esteves et al., 2012; Capela et al., 2021), which can also contribute to mechanical strength development (Esteves et al., 2012). Like a hydraulic binder, it chemically reacts with water, sets, hardens and is capable of maintaining its strength and stability even beneath water, EN 197–1:2011 (CEN: European Committee for Standardization, 2011).

Modolo et al. (2015) concluded that LM particles agglomeration or tridimensionality structures formation can affect mortars' workability. Furthermore, LM incorporation will affect the pH of the hydration solution and influence the hydration mechanism. Other factors that may impact the setting mechanism, such as the presence of  $\text{Cl}^-$  ions on LM, the reaction between  $\text{Cl}^-$  ions and C3A (tricalcium aluminate) or C4AF (tetracalcium aluminoferrite) implies in the chloroaluminates formation that tend to expand and increase the amount of porosity.

## 4.2 Geopolymers

### 4.2.1 Dense materials

Saeli et al. (2019c) tested another pulp and paper industry residue in the production of geopolymeric binders and mortars

for construction, the alkaline effluent. The effluent replaced the distilled water used to dissolve NaOH pellets in the activator solution and several NaOH/ $\text{Na}_2\text{SiO}_3$  ratios and water to alkaline effluent substitutions were tested. The formulation with 70 wt% Biomass fly ash (BFA), 30 wt% MK, prepared with a solid/liquid ratio of 0.78 and a sodium hydroxide/sodium silicate ratio of 1:3 presented the best results and the differences between the samples prepared with alkaline effluent (instead of water) were not substantial, presenting environmental benefits. Mortars with the best binder and commercial sand were studied and the best formulation, with binder to aggregate ratio of 1:3, showed good workability and compressive strength higher than 20 MPa, being in class M20. Nevertheless, all the formulations were at least class M10 (Saeli et al., 2019c).

Saeli et al. (2019a) tested lime slaker grits as aggregate and biomass fly ash as precursor/binder of geopolymeric mortars. The influence of the aggregate granulometry and binder/aggregate ratio was accessed: the maximum size of the used grits was 12.5 mm. The use of finer grits decreases the consistency of the geopolymer mortars. The decrease of aggregates amount, by increasing the binder to aggregate ratio, improves the consistency. The same increase or the size enhancement improves the bulk density, while the water absorption decreases, and the capillary coefficient increases. As expected, the increase in the relative amount of aggregate decreases the compressive strength of the mortars. Anyway, the majority of formulations show compressive strength above 10 MPa, the limit for use in construction (Saeli et al., 2019b).

Another study conducted by the same authors (Saeli et al., 2019a) tested the use of BFA as a partial substitute of MK in the precursor mixture, while grits were used as aggregate with different binder/aggregate (B/A) ratios. To keep the same aggregate particle size distribution commercial siliceous sand was also used. The authors observed that geopolymer mortars with the incorporation of residues presents lower compressive strength than pure binder. The formulation that showed the highest mechanical resistance were the ones with 1:5 B/A ratio for both grits or grits + sand,  $18.89 \pm 1.26$  MPa and  $23.17 \pm 1.17$  MPa, respectively. The authors also observed that by increasing the aggregate amount, and by decreasing the binder to aggregates ratio, a more homogeneous paste and higher compressive strength values were obtained. All tested compositions are suitable for masonry applications in construction because mechanical strength higher than 10 MPa at 28 days of curing were achieved. Nevertheless, the authors propose the use of additional components in order to improve the workability of the paste, setting time, shrinkage and on the main engineering properties of the materials. Biomass fly ash, an aluminosilicate material, can act as a source of reactive silica and alumina in the production of geopolymer binders. Nevertheless, the reactivity of this waste stream is lower than that seen when using virgin and high purity precursors such as calcined kaolin.

Saeli et al. (2020) used lime mud (LM) as filler in geopolymeric mortars for construction. The experimental work was divided in two parts: 1) one with the addition of LM with no water adjustment to correct the workability; 2) the second one with water adjustment. The maximum LM amount was 12.5 wt% in the first case. The use of 7.5–12.5 wt% of LM proved to be beneficial to the mechanical strength of the material since it improves the classification of the mortars from M20 to M25. 10% LM assures a good compromise between workability and mechanical strength. The water adjustment to correct the workability allowed the use of higher LM amounts but then hardened properties were negatively affected (Saeli et al., 2020).

The grits coarser fractions were tested as aggregates of geopolymeric concrete (70% fly ash +30% metakaolin) by (Saeli et al., 2018). Two distinct granulometric fractions were used, one between 0.5 and 1.5 mm and the other from 0.5 to 5 mm. The authors also studied the influence of binder: aggregate ratio (1:1, 1:2 and 1:3). The use of coarser fractions will minimize the bending resistance, while the compressive strength tends to increase. As expected, the use of lower binder: aggregate ratios diminish the compressive strength of the samples. Samples prepared with 1:1 ratio show resistance values over 15 MPa (M15 classification). All other samples belong to M10 class.

The incorporation of dregs as filler in geopolymeric mortars was first considered in (Novais et al., 2018f), while a follow-up study evaluated also the heavy metals leaching by the dreg-containing geopolymers (Novais et al., 2019a). Results showed that increasing the amount of dregs affects the workability of the mortars and this was attributed to the fine particles of the dregs that absorb water and reduces workability (Novais et al., 2019a). Interestingly, the addition of dregs enhanced the compressive strength of the specimens. The formulation containing the highest amount of dregs (100 wt%) achieved a compressive strength of roughly 13 MPa at the 270th day of cure, and this without the appearance of efflorescences. Regarding the hazardous leached elements, the samples' proved to be capable of effectively immobilizing them within the geopolymer matrix. Only minor amounts of Cr and Cu were leached out, well below the contamination limit in soils (Novais et al., 2019a). Actually, samples containing an increasing amount of dregs show lower release of some toxic elements, namely As and Cr (notice that As is not present on dregs but in the fly ash), probably due to the achieved compactness increment. Novais et al. (2019a) showed that dregs are not involved in geopolymerization reaction once XRD of dregs-containing mortars clearly shows the presence of pirssonite, already detected in the waste. However, the major concern with this waste is its sodium content due to the possible formation of efflorescence. Through EDS analyses, no microstructural modification was observed. Further, even after water immersion followed by ambient drying, none of the prepared mortars showed the presence of efflorescence (Novais et al., 2018f). Consequently, the authors concluded that dregs do not negatively affect the geopolymer

microstructure and that stable long-term geopolymers were produced.

Novais et al. (2017a) studied the influence of glass fiber fabric (GFF) waste incorporation as a reinforcement agent on the properties of a metakaolin-based geopolymer. The used GFF comes from off-cuts generated in wind turbine blade production. The authors observed that the introduction of the fibers improved the ductility of the hardened samples and inhibited their complete fracture. Further, the incorporation of fibers improved the compressive and tensile strength of the samples, the best results being achieved with the utilization of 6 mm fibers. The incorporation of 2 wt.% of these fibers promoted an increase in the tensile strength of 77%, while with 3 wt.% the compressive strength raises ~162% when compared to results obtained for samples prepared without fibers. Based on these good results, the authors produce geopolymer-fiber composites using BFA as the main (70%) silica and alumina source blended with metakaolin (30%). The GFF was used as a reinforcement layer embedded in the geopolymer matrix. To evaluate the influence of the GFF amount on the properties of the cured samples, four formulations were prepared. One without the GFF (only the geopolymer matrix), and the other three containing one, two, and three layers of GFF arranged parallel to the base of the specimen and inserted between binder layers. In the 28 days cured samples it was observed that the density of the samples decreased with the addition of the GFF while the obtained values for the water absorption were similar in all samples. The authors also noticed that the introduction of the GFF layers improved the flexural strength (up to 144%) when compared to the specimen prepared only with the geopolymer matrix. It was verified that the flexural strength of the samples increased with the increment of the number of GFF layers and that its presence avoided the complete fracture/failure of the samples and increased their ductility.

Senff et al. (2020) concluded that the GFF 6 mm cuts can be used as a reinforcement agent in porous mortars formulations without negatively impacting their thermal conductivity. For that, the authors evaluated the influence of aluminum powder (AP), as a porogenic agent, and GFF, as a reinforcement agent, in the properties of geopolymeric porous mortars. Based on previous works (Novais et al., 2017a; Novais et al., 2018d), for the mortars production BFA was employed as the main aluminosilicate source and the GFF was used cut to 6 mm length fibers. From the flow table results, the incorporation of AP and fibers was limited to 0.2 and 2.0 wt.%, respectively. In the hardened samples, it was noticed that the increment in the added AP content ruled the observed decrease in the bulk density, and the increase in the total porosity and water absorption of the mortars. The 2.0 wt.% fibers incorporation ameliorated the flexural (23%) and compressive strength (30%) of the mortars prepared with 0.2 wt.% of AP. This behavior was explained by the fibers, by being randomly dispersed in the geopolymeric porous matrix, formed a holding frame that stabilized the microstructure.



TABLE 2 Comparison of the main properties and estimated classes of resistance (EN 998-2) of geopolymers synthesised using P&amp;P wastes.

Substitution	Waste used	Activators	L/S <sup>a</sup>	Curing condition	Workability [mm]	Bulk density [kg/m <sup>3</sup> ]	CS <sup>a</sup> [MPa]	Water Abs. [%]	Class	Ref.
Clinker substitution CEM II	14.3 wt.% of Lime mud + Biological sludge + FA	—	0.81	23°C and 95% RH	167 ± 2	2029	13	—	M10	Buruberri et al. (2015)
Clinker substitution	23.75 wt.% Gibbsite Lime Mud FA WWTP Sludge	—	0.75	22°C for 24 h and 27 days in immersed in saturated lime solution	78.5%	—	20.56 ± 4.93	—	M20	Simão et al. (2017)
MORTAR OPC type I (42.5 R) substitution	10 wt.% of FA CT	—	0.55	27 days immersed in water	120	2520 ± 20	43.31 ± 1.49	—	M40	Rajamma et al. (2009)
	10 wt.% of FA CA	—	0.55		120	2070 ± 10	35.76 ± 1.35	—	M35	
MORTAR OPC substitution	30 wt.% of FA CT	—	0.47	28 days in accelerated conditions, (ASTM C 1260)	115–133	2630	50.19	—	M50	Esteves et al. (2012)
	20 wt.% of FA CA	—	0.47		115–133	2250	42.45	—	M40	
MORTAR OPC CEM I 42.5 R substitution	10 wt.% FA CT	—	0.55	90 days	120	—	~43	—	M40	Rajamma et al. (2015)
	10 wt.% FA CA	—	0.55	90 days	120	—	~38	—	M35	
MORTAR OPC (CEM II/A–L 42.5 R) substitution	17 wt.% of FA CT	—	0.67	2 days in the mould, at 20°C, 95% HR.	105	1860	12.20	6.9	M10	Capela et al. (2021)
	17 wt.% of FA CA	—	0.67	Demolded and 5 days, at 20°C, 95% RH. Afterwards, 21 days at 20°C, 65% HR.	—	1850	12.16	6.6	M10	
MORTAR OPC type I (42.5 R) aggregate substitution	Exhausted sands	—		20°C and 65% RH	145	~1780	~10	97.24 ± 0.04	M10	Modolo et al. (2013)
MORTAR OPC I substitution	Exhausted Sand CT 9.6 wt.%	—	0.76	28 days at 23°C and 50% RH	—	1525	—	—	—	Modolo et al. (2015)
MORTAR OPC substitution	30 wt.% of Lime mud	—	0.62	90 days at 22°C and 65% RH	170	2120	22.6	10.6	M20	Modolo et al. (2014)
BINDER and MORTAR precursor and water substitution	70 wt% of FA	NaOH Na <sub>2</sub> SiO <sub>3</sub>	0.20	28 days at 65% HR and	200	1845 ± 18	>20	13 ± 1	M20	Saeli et al. (2019c)
MORTAR Aggregate substitution	70 wt% of FA Grits Binder/aggregate ratio 1:5	Na <sub>2</sub> SiO <sub>3</sub> SiO <sub>2</sub> /Na <sub>2</sub> O = 3.15 mixed with 10M NaOH	0.13	Ambient conditions	100	~1950	23.17 ± 1.17	~7.5	M20	Saeli et al. (2019c)
MORTAR aggregate substitution	70 wt.% of FA and 10 wt.% of Binder/Grits	Sodium hydroxide/silicate ratio equal to 1:3	—	28 days of curing–20°C and 65% RH	300	—	27	—	M25	Saeli et al. (2019a)
	70 wt.% of FA 1/3 Binder/Grits with 4–8 mm		—		210	2000	18	10	M15	
MORTAR aggregate substitution	75 wt. % of FA CDW (construction and demolition waste) 0.5–2.0 mm	NaOH Na <sub>2</sub> SiO <sub>3</sub>	—	28 days at 20°C, 68% RH	126	1290 ± 0.07	40	12.3 ± 0.1	M40	Rossi et al. (2019)

(Continued on following page)

TABLE 2 (Continued) Comparison of the main properties and estimated classes of resistance (EN 998-2) of geopolymers synthesised using P&amp;P wastes.

Substitution	Waste used	Activators	L/S <sup>a</sup>	Curing condition	Workability [mm]	Bulk density [kg/m <sup>3</sup> ]	CS <sup>a</sup> [MPa]	Water Abs. [%]	Class	Ref.
MORTAR filler	70 wt.% of FA Calcareous sludge	NaOH 10M Na <sub>2</sub> SiO <sub>3</sub>	0.18	20°C, 65% RH 24 h, RT until testing	160	~1925	28 ± 1	11.56	M25	Saeli et al. (2020)
MORTAR aggregate substitution	70 wt.% of FA Grits	NaOH 10M Na <sub>2</sub> SiO <sub>3</sub>	—	20°C, 65% RH	—	1500	18.1 ± 0.2	25	M15	Saeli et al. (2018)
MORTAR filler	70 wt.% of FA Green liquor dregs	NaOH 10M Na <sub>2</sub> SiO <sub>3</sub>	0.29	23°C, 65% RH 24 h, RT until testing	137.5	—	15	~8	M15	Novais et al. (2019a)
MORTAR aggregate substitution	Exhausted sands	Na <sub>2</sub> SiO <sub>3</sub> (solid)	0.29	ambient conditions	114	1820	56	0.7	M50	Gonçalves et al. (2021b)

<sup>a</sup>Liquid/solid.<sup>b</sup>Compressive strength.

Gonçalves et al. (2021b) investigated one-part alkali activated materials (AAMs) using only blast furnace slag as the solid precursor, and sodium metasilicate, as the solid activator. The authors developed, for the first time, mortars in which the commercial sand was replaced by exhausted bed sands from biomass burning boilers. The mortars prepared with commercial sand presented high compressive strength, 79 MPa, values obtained after 28 days of curing. The mortars developed with exhausted sands exhibit outstanding compressive strength values, from 70 to 86 MPa, not affecting the other material's properties (setting time, apparent density, and water absorption). This work suggests the feasibility of using exhausted bed sands, from biomass boilers, as aggregates in AAMs mortars production.

Table 2 presents a comparison of the main properties of all works described above (samples cured for 28 days) and reports the classes of resistance of the materials, according to EN 998-2. Each class have a specific application being: M2.5—non-load-bearing, M5—all types of exterior and interior walls, M10—masonry applications like indoor and outdoor wall, M15—structural reinforcement of masonry structures and M20.

## 4.2.2 Porous materials

### 4.2.2.1 Thermal insulation

The feasibility of using P&P wastes in the synthesis of low thermal conductivity geopolymers has been explored. The decrease in the geopolymers density can be achieved by the use of creating foaming agents, such as H<sub>2</sub>O<sub>2</sub> or Al powder (Novais et al., 2016c; Novais et al., 2019c; Senff et al., 2020), or by the incorporation of porous aggregates like cork or construction and demolition waste (Rossi et al., 2018; Novais et al., 2021), or a combination of both strategies (e.g., multi-layered materials) (Novais et al., 2020d). Table 3 summarises the most recent studies carried out using P&P wastes.

In one of the first studies, Novais et al. used different amounts of H<sub>2</sub>O<sub>2</sub> (0.03, 0.15, 0.30, 0.90 and 1.2 wt.%) to study the influence on thermal properties of FA based geopolymer. The XRD shows that increasing the amount of H<sub>2</sub>O<sub>2</sub> has no major influence on the mineral phases' formation. Nonetheless, the SEM and optical micrographs revealed strong microstructural changes, the increasing amount of H<sub>2</sub>O<sub>2</sub> effects especially the porosity as well as the pore size distribution. The authors studied the relationship between pore forming agent and average pore size, number of pores, area ratio, water absorption, apparent density, and total porosity. Typically, all parameters increased with the concentration of pore forming agent, except the apparent density that decreased. The thermal conductivity decreased with the increasing amount of foaming agent reaching a value as low as 107 mW/m K (Novais et al., 2016b).

Novais et al. also studied the influence of NaOH concentration and the influence of water amount on the properties and microstructure on FA based geopolymers, again using H<sub>2</sub>O<sub>2</sub> as a foaming agent. For that 0.72 wt.% and 1.35 wt.% of H<sub>2</sub>O<sub>2</sub> were added, 8 M 10 M and 12 M NaOH solutions were used, and the water content was also changed. Results showed that the water content and NaOH concentration strongly affect the viscosity of the pastes, while the H<sub>2</sub>O<sub>2</sub> content, at least in the studied range. The use of lower alkali concentration (NaOH) enhances the porosity and also changes the connectivity of the pores, as coalescence takes place resulting in a higher volume of open porosity. The thermal conductivity strongly decreased (up to 40%) when H<sub>2</sub>O<sub>2</sub> is added. This property is also controlled by the NaOH molarity: lower molarities led to smaller thermal conductivities, being 82 mW/m.K the minimum value achieved. This effect was attributed to viscosity changes of the slurries in the early stage of geopolymer formation. The NaOH concentration highly affects the apparent density of the samples, with a direct correspondence in the thermal

TABLE 3 Comparison of the thermal conductivity of the different alkali-activated materials reviewed.

Foaming agent		Aggregate	Thermal conductivity (mW/mK)	Reference
Type	Amount			
Al	0.2	Sand	216	Senff et al. (2020)
H <sub>2</sub> O <sub>2</sub>	0.45	CDW	190	Rossi et al. (2018)
H <sub>2</sub> O <sub>2</sub>	1.2	—	107	Novais et al. (2016b)
Al	0.1	Cork	94	Novais et al. (2020d)
H <sub>2</sub> O <sub>2</sub>	1.35	—	82	Novais et al. (2016b)
Al	0.08	—	78.6	Novais et al. (2018c)
—	—	Cork	72	Novais et al. (2019c)
—	—	Cork	68	Novais et al. (2020c)
—	—	Cork	68	Novais et al. (2021)

conductivity values. The attenuation of the thermal conductivity was more evident for compositions containing higher amounts of H<sub>2</sub>O<sub>2</sub>, which is consistent with the observed change in pore morphology (Novais et al., 2016a).

Rossi et al. (2018) also studied the influence of H<sub>2</sub>O<sub>2</sub> on waste-based mortars. The binder was produced using FA waste as a solid precursor and CDW as aggregate. In order to produce lightweight geopolymers Rossi et al. kept the solid to liquid ratio at low levels, so the reference mortar shows high porosity, around 44%. Nonetheless, when 0.45 wt.% of H<sub>2</sub>O<sub>2</sub> was added, the porosity increased to 55.9%. One of the major impacts was observed on the typical pore size of the samples that increased from 0.198 µm up to 31.88 µm with the highest amount of H<sub>2</sub>O<sub>2</sub> (0.45 wt.%), which also represents an increment on BET surface area from 18.93 to 26.7 m<sup>2</sup>/g. As it is shown in Table 3 the lowest value of thermal conductivity seen in this study was 190 mW/m K.

The influence of aluminium powder and water amount on the thermal conductivity of FA-containing geopolymers was studied by Novais et al. (2018a). The lowest thermal conductivity being 78.6 mW/m K.

Cork-containing samples show thermal conductivities between 94 and 68 mW/mK (Novais et al., 2019c; Novais et al., 2020b; Novais et al., 2020d; Novais et al., 2021).

#### 4.2.2.2 Moisture regulation

Moisture buffer value (MBV) tests were performed to verify the ability of samples to absorb and release water after exposure to daily/cyclic humidity fluctuations. In other words, MBV quantifies the amount of moisture (H<sub>2</sub>O) absorbed or released by a material when it is subjected to repeated daily fluctuations between two specified relative humidity levels. In the reviewed manuscripts, measurements were carried out according to the Nordtest protocol (Rode et al., 2005a), the equipment used was a climatic chamber (Fitoclima 300 EP10 from Aralab) and the mass variation was measured with a balance. The moisture buffer

value is given by the mass variation that is adsorbed and released from a given area of the material under a specific moisture variation and is given by the following equation:

$$MBV = \frac{\Delta m}{A \Delta \%RH}$$

Where  $\Delta m$  is the mass variation (g);  $A$  is the surface area exposed to humidity variation (m<sup>2</sup>);  $\Delta \%RH$  is the amplitude of relative humidity in the atmosphere (%). Different relative humidity amplitudes can be selected, but 75% HR for 8 h 33% HR for 16 h were the values used in order to simulate the working hours and corresponding to middle humidity levels, defined according to ISO 24353:2008 (Organization for Standardization, I., 2008). To increase the ability of mortars/pastes to control internal moisture fluctuations, foaming agents or porous/adsorbent aggregates can be used.

De Rossi et al. used waste-based geopolymer mortars (CDW as aggregate) with different porosities; the MBV for such samples fluctuate from 0.80 g/m<sup>2</sup>  $\Delta \%RH$  (reference mortar without foaming agent) to an impressive higher value of 5.61 g/m<sup>2</sup>  $\Delta \%RH$  (for the sample with the highest amount of foaming agent); this value is one of the highest ever reported to date for this type of materials (Rossi et al., 2018). This demonstrates that an improvement in moisture buffering capacity can be achieved by increasing the amount of foaming agent. It is important to mention that these values were obtained in a cycle of 12 h at 50 % RH + 12 h at 75%RH.

Rossi et al. (2019) combined biomass fly ash with construction and demolition waste (CDW), to produce geopolymer mortars. BFA was used as precursor while CDW partially substitute a commercial sand as aggregate. The use of CDW as fine aggregate instead of sand increases the compressive strength by 78% and the flexural strength by 115%. Regarding the fresh state properties, the use of CDW reduces the spread, and this effect was attributed to the fineness of the waste and its higher water absorption.

Gonçalves et al. (2021a) used bi-layered AMMs where only the porous surface was exposed to environmental changes (humidity fluctuation). The MBV achieved was  $2.71 \text{ g/m}^2 \Delta \% \text{ RH}$  which is considerably lower than that reported by Rossi et al., nevertheless, it is considered “Excellent” which is the top classification according to the Nordtest protocol (Rode et al., 2005a). This shows that bi-layered AMMs can be a good method to maximise the multifunctional behaviour of the samples.

The authors also investigated the influence of different types of cork as aggregate on the MBV capacity. Novais et al. (2020c) used black expanded cork (around 6 mm in size) as a lightweight aggregate. Not surprisingly, by increasing the amount of cork, the apparent density decreases to a value almost 7 times lower than the reference geopolymer, as seen above. As for the MBV, increasing the amount of cork in the samples resulted in a higher MBV (above  $1.37 \text{ g/m}^2 \text{ RH}$ ). With 75 vol.% cork MBV reached  $1.89 \text{ g/m}^2 \text{ RH}$ . The authors further enhanced the amount of cork, but with a negative effect on the specific MBV (lower values compared to the 75 vol.% sample); however, composites containing 87.5 and 90 vol.% cork show very reproducible absorption and desorption cycles, demonstrating a good ability to buffer the moisture fluctuations over time (Novais et al., 2020c).

In a similar work conducted by Novais et al. (2021), the authors investigated the influence of two types of cork “fine” and “coarse” (different sizes, 0.5 and 2 mm respectively). The incorporation of 20 vol.% of “coarse” cork resulted in a slightly higher MBV ( $1 \text{ g/m}^2 \Delta \% \text{ RH}$ ) compared to the reference sample (no cork added,  $0.89 \text{ g/m}^2 \Delta \% \text{ RH}$ ). Increasing the cork content to 80 vol% has a major impact on the moisture regulation ability: the composite containing the smaller size granules has a MBV of  $2.22 \text{ g/m}^2 \Delta \% \text{ RH}$ , which is 2.5 times higher than the reference. Further increasing cork volume up to 85 vol% did not induce better performance (MBV =  $1.97 \text{ g/m}^2 \Delta \% \text{ RH}$ ). In addition to cork volume, cork granule size was also found to have a large effect on moisture buffering capacity: the use of coarser granules resulted in lower MBV due to the lower storage and release capacity of these samples. However, it should be noted that although the performance is lower compared to the use of smaller sized cork granules, these composites still exhibit better buffering capacity compared to the reference matrix, not only in terms of practical MBV but also with respect to the absorption/desorption pattern.

These results show that geopolymeric foams or AAM composites have the potential necessary to be used as moisture regulators. Almost all samples show “good” or “excellent” MBV classification ( $1.0 < \text{MBV} < 2.0 \text{ g/m}^2 \% \text{ RH}$ ), and MBV  $> 2.0 \text{ g/m}^2 \% \text{ RH}$ , respectively, according the Nordtest protocol (Rode et al., 2005b).

## 4.2.3 Adsorption of pollutants

### 4.2.3.1 Heavy metals

Geopolymers exhibit interesting properties and their chemical structure presents a negatively charged

aluminosilicate framework and charge balancing cations ( $\text{Na}^+$ ,  $\text{K}^+$  or  $\text{Ca}^{2+}$ ). In fact, this property plays a fundamental role in the adsorption of heavy metals present in distinct streams (e.g., industrial wastewaters), where these cations can be exchanged with the positively charged metals present in the solution. This material is then converted into an environmentally acceptable waste for land disposal (Duxson et al., 2007). Heavy metals or dye molecules immobilization on a geopolymer matrix is a chemical and/or physical process and studies exploiting this potential were already conducted (Ji and Pei, 2019).

The first work conducted by our research group in this field involved the preparation of geopolymer monoliths, based on metakaolin and fly ash (FA), for lead adsorption. Since porosity plays a fundamental role in the adsorption process, hydrogen peroxide was used (between 0 and 1.2 wt%) as a foaming agent. The total porosities were successfully controlled, varying from 41.0 to 78.4%, while the corresponding apparent densities decreased from 1.21 to  $0.44 \text{ g/cm}^3$ . Due to alkali leaching from geopolymer samples and their influence on the solution pH, samples were washed until neutral pH was reached. Non-washed samples were also used. Cylindrical discs of 22 mm diameter and 3 mm thickness were immersed and shaken during 24 h at room temperature and after fixed periods, aliquots were taken and the  $\text{Pb}^{2+}$  concentration was measured by atomic absorption spectrometry. The maximum lead adsorption, obtained with the higher porosity samples (prepared with 1.2 wt%  $\text{H}_2\text{O}_2$ ), was  $6.34 \text{ mg}_{\text{lead}}/\text{g}_{\text{geopolymer}}$ . For desorption, samples were treated in water and acidic conditions. After 24 h, their recovery was not fully achieved, denoting strong fixation of lead onto the geopolymers matrix (Novais et al., 2016d). Another strategy involved the preparation of geopolymeric porous bulk-type samples for lead and zinc removal. These cubic samples presented total porosity of 84 vol% and bulk densities of  $408 \text{ kg/m}^3$  and  $258 \text{ kg/m}^3$  before and after washing, respectively. Metals removal by precipitation was obtained when using non-washes samples, while adsorption is the extraction mechanism when using the washed granules. Lead removal after 24 h of adsorption reached  $16.5 \text{ mg}_{\text{lead}}/\text{g}_{\text{geopolymer}}$ , while for zinc a value of  $20.4 \text{ mg/g}$  was obtained after 1 h precipitation.

Powdered materials show excellent pollutants removal efficiencies, but the experimental constraints in their collection post-use and the total cost are important drawbacks. Cm-size waste-based geopolymer foams (fly-ash based) were then prepared and tested for lead adsorption. In this case, NaOH molarity and the foaming agent content varied to evaluate the effect on the porosity. The highest removal efficiency was obtained with highly porous samples (100 ppm  $\text{Pb}^{2+}$ , 4 h contact). Using 800 ppm  $\text{Pb}^{2+}$  solution, the lead uptake was maximal ( $105.9 \text{ mg/g}$ ), and corresponds to the best value ever reported for bulk-type geopolymer adsorbents. The possibility of reusing these foams was also studied, after mild-acidic treatment and water washing, after contact with 100 ppm  $\text{Pb}^{2+}$  solution.



The samples with higher  $\text{Pb}^{2+}$  contents released 66.8% while the others containing lower  $\text{Pb}^{2+}$  concentrations released a lower amount (52.7% after 1 h immersion). With the obtained results the authors stated that mild acidic conditions promotes fast lead desorption, particularly in samples with high lead contents. After desorption, the samples were again reused in a  $\text{Pb}^{2+}$  100 ppm solution during 4 h presenting similar adsorption behaviour to the first using cycle. This confirms the feasibility to reuse them as lead adsorbents (Novais et al., 2020a).

Recent work involved the preparation of  $1\text{ cm}^3$  cubic foams and their performance as lead, copper, cadmium and zinc adsorbents in single, binary and multicomponent solutions. The foams were prepared considering previous studies by the authors (Novais et al., 2020a), using NaOH 8 M as activator agent. Regarding the physical properties of the cubic foams, the total porosity reaches 77.8% and bulk density is  $0.53\text{ g/cm}^3$ . The foams evaluation as heavy metals adsorbents was taken in 3 sorption tests: 1) single element ( $\text{Pb}^{2+}$ ,  $\text{Cd}^{2+}$ ,  $\text{Cu}^{2+}$  and  $\text{Zn}^{2+}$ ) with  $C_0$  between 1000 and 800 ppm and contact time of the adsorbent and the ion solution between 1 and 6 h; 2) binary systems with combination of two heavy metals,  $C_0 = 10\text{ ppm}$  with 6 h contact time; 3) multicomponent systems with  $C_0 = 10\text{ ppm}$  and 6 h contact time. Results showed that the removal efficiency is affected by the heavy metals nature and follows the sequence in terms of affinity in a single component system:  $\text{Pb}^{2+} > \text{Cd}^{2+} > \text{Zn}^{2+} > \text{Cu}^{2+}$ . This tendency is related, among others, to the hydrated ionic radius and hydration enthalpy of the different heavy metals (Caetano et al., 2022).

#### 4.2.3.2 Dyes

Colouring contamination of industrial effluents imposes serious threats on the environment and living organisms. Methylene Blue (MB) is a monovalent, cationic, aromatic organic compound, solid, basic, water-soluble and one of the most common dyes responsible for water contamination (Khan et al., 2022). Adsorption is a common method for dyes decontamination, turning porous geopolymers into feasible alternatives to be used as efficient precursors for dyes removal. The study by Li et al. (2006) was one of the first reports on the use of pulverized geopolymers in the removal of organic compounds from water, while the feasibility of using fly ash-based geopolymeric monoliths (not powders) was reported only in 2018 (Novais et al., 2018b). Geopolymers with distinct porosities were prepared and compared. As expected, especially for higher initial dye concentration ( $C_0$ ), highly porous samples exhibit higher adsorption performance, with uptake 3 times superior when the porosity doubles (from 40.7% to 80.6%). The reusability of these materials was also confirmed and after 5 cycles the removal efficiency was unaltered (Novais et al., 2018b). In a follow-up study, the preparation of geopolymer materials with higher specific surface area were studied. Fly ash-based geopolymeric spheres with 2.6 mm diameter were prepared and used as MB adsorbents from a

synthetic wastewater. Higher uptake values were obtained when  $C_0$  increases, from 1.1 to 30.1 mg/g when MB concentration is 10 and 250 ppm, respectively. After 24 h contact with the spheres, uptake reached 79.7 mg/g, exceeding the values already reported for geopolymeric materials. Thermal regeneration allows the reuse of the material. After 8 cycles the removal efficiency decayed only 17%. (Novais et al., 2019b).

Also taking into consideration that once exhausted, the recovery of samples is easier than powdered adsorbents, Capela et al. developed inexpensive porous adsorbent monoliths prepared only with CA and aluminum powder (as porogenic agent), taking advantage of the FA's self-hardening ability. The prepared monoliths were positively tested for MB adsorption. It was shown that the dye adsorption kinetics can be described by the pseudo-first-order equation and the adsorption process was characterised by the Type 2 Langmuir isotherm model with a maximum sorption capacity of  $\sim 0.66\text{ mg/g}$ , determined for the samples with the higher total porosity,  $\sim 72\%$  (Capela et al., 2022).

In a distinct approach, activated carbon was produced from cork wastes and activated with a mixture of alkaline wastewater from the pulp and paper industry (50 vol%) and commercial sodium hydroxide. The obtained activated carbon owned a very high specific surface area ( $1670\text{ m}^2/\text{g}$ ). This adsorbent shows extraordinary removal efficiency (99.9% in 5 min) and MB uptake of 350 mg/g, being part of one of the most promising activated carbons produced for methylene blue removal. (Novais et al., 2018d).

#### 4.2.4 pH buffering

In recent years, an innovative and greener alternative for pH regulation has been reported, involving the use of waste-containing geopolymer monoliths (Novais et al., 2016d) or spheres (Novais et al., 2017b). When immersed in water, these materials leach out significant amounts of hydroxyl ions from their structure. The presence of hydroxyl ions assures a prolonged pH adjustment, avoiding large fluctuations. Alkaline leaching from geopolymers can be controlled by the activator concentration (Zhang et al., 2014), nature of the binder (Novais et al., 2017b), solid-liquid ratio, and porosity (Novais et al., 2016d). Novais et al. (2016d) also suggested that the geometry of geopolymers has a major impact on their leaching behaviour, and the use of spheres instead of discs or cubes favoured the leaching of alkalis, due to the increase in the exposed area (Novais et al., 2016d). This pattern has been observed using both fly ash-based geopolymers and red mud-fly ash geopolymers, demonstrating an advantage of using mm size spheres as pH buffering materials (Novais et al., 2020c). Thus, waste-based geopolymers, including those prepared with P&P wastes, have the potential to be applied as pH buffering materials in systems such as anaerobic treatment for biogas production.

Novais et al. (2018g) studied the influence of the aluminosilicates source (metakaolin vs. fly ash) in the prolonged pH buffer of the complex anaerobic treatment of cheese whey. The authors tested the addition of spheres prepared from 33 wt.% of FA (MK-based spheres) and 75 wt.% of FA (FA-based spheres). After 70 days in an anaerobic digester, the addition of spheres assured pH stabilization at values close to those suitable for methane production by microorganisms (Gameiro et al., 2018). Also, the use of FA-based spheres improved the global methane production by 30% compared to methane production achieved with the use of MK-based spheres (Novais et al., 2018g).

The influence of the sphere's porosity in long-term methane production from cheese whey by an anaerobic system was studied by Gameiro et al. (2019, 2021). The authors tested two anaerobic cycles, to evaluate the spheres' capacity to continuously regulate the pH, even in stressful environmental conditions. The increased porosity of the FA-based spheres tested, induced by the addition of a foaming agent, enhanced the methane volume produced by two-fold and, in addition, improved the methane production rate by more than three-fold, leading to a stable anaerobic process after 87 days of operation (Gameiro et al., 2019). The authors also tested the performance of high porosity geopolymer spheres comparatively to the addition of alkaline chemicals for pH control. Once again, the spheres presented very good anaerobic performance after four cycles, with an improvement in methane yield produced of 25% (Gameiro et al., 2021).

Fly ash can also be used in the production of geopolymer spheres that incorporate bauxite residue (or red mud) in their composition (Novais et al., 2018e). The use of such spheres in anaerobic digestion systems was studied by Gameiro et al. (2020), which evaluate their performance in complex systems treating cheese whey, for 110 days. The use of red mud/fly ash geopolymer spheres promoted a prolonged pH stabilization, even after eleven anaerobic cycles, and improved by 94% the methane production, when compared with the addition of chemical alkalinity to stabilize the anaerobic system (Gameiro et al., 2020).

The use of fly ash-based geopolymer spheres for pH control and to promote the stability of anaerobic processes is an innovative and very promising strategy, thus contributing to the concept of circular economy, using wastes for the generation of new added-value products and obtaining sustainable energy sources, such as methane.

#### 4.2.5 Other applications

Modolo et al. (2014) aimed to regenerate the ES from the fluidized bed in order to recirculate the material and partially substitute the fresh bed sand (FBS) in industrial bubbling fluidized bed combustors. The authors observed that physical, chemical and mineralogical characteristics of the FBS and ES are strongly dependent on the forest biomass used. Nevertheless, the

authors state that by sieving the ES it is possible to recover almost 60% of the original ES particles (size between 0.3 and 1.0 mm), which have properties that allow its reuse as substitute of FBS for bed makeup in industrial bubbling fluidized bed combustors.

Rossi et al. (2019) synthesized faujasite and P zeolites through geopolymerization of biomass fly ash wastes at low temperature in a hermetic container. The raw materials were activated using a mixture of sodium silicate and sodium hydroxide, and then the specimens were cured at 60°C to obtain zeolite-containing geopolymers while hydrogen peroxide was used as a porogenic agent. XRD diffractograms showed the presence of faujasite zeolites regardless of the H<sub>2</sub>O<sub>2</sub> content. P zeolite was formed without porogenic agent addition, resulting in an increase in the surface area (56.35 m<sup>2</sup>/g) in comparison with samples cured in room conditions (40.69 m<sup>2</sup>/g). The presence of zeolites and faujasite was affected by the curing time and temperature. The cure in hydrothermal conditions was crucial for the development of zeolites since the sample cured at room temperature did not show the formation of such phases. The zeolites presented a mechanical strength of up to ~10 MPa which suggest applications as separation membranes or filters.

## 4 Conclusion

In this work, several case studies about possible valorisation strategies for the wastes generated in a pulp and paper mill, namely biomass fly ashes and exhausted sands from biomass boilers and co-generation plant, lime mud, grits and dregs from the chemical recovery cycle in the Kraft process, and biologic and P&P mill sludge from the wastewater treatment, were presented. The residues were successfully used in the laboratory production of new construction materials and adsorbents. The maximum incorporation or substitution content depends on the intended application but generally, 70 wt.% of wastes were used. Further, generically, no pre-treatment steps were applied to the wastes in order to ease its transition to an industrial application.

Despite the promising results presented here, it should be noted that one of the biggest constraints associated with the up-scaling of the various applications presented is related to the variation of the waste's properties over time, mainly the chemical composition, as evidenced in the results shown in Table 1. These variations make it more difficult to incorporate, on an industrial scale, wastes whose composition varies over time into new products. A future approach involves life cycle assessment (LCA) studies, which may encourage the translation of many of these studies to an industrial scale. In addition, an economic and environmental analysis should be done to determine the maximum incorporation level of each waste for the intended application.

Nevertheless, this innovative approach is a more sustainable alternative to the commonly used landfilling, as it allows a reduction in the consumption of natural raw materials and contributes to the establishment of a circular economy model.

## Author contributions

JL, MS, and RN contributed to conception, design and funding of the study. IV and TG wrote the first draft of the manuscript. MC, JC, AC, and CN wrote sections of the manuscript. All authors contributed to the final revision of the submitted version.

## Funding

This work was developed within the scope of the project CICECO-Aveiro Institute of Materials, UIDB/50011/2020, UIDP/50011/2020 and LA/P/0006/2020, financed by national funds through the FCT/MEC (PIDDAC).

## Acknowledgments

The authors would like to acknowledge the project ERA-MIN/0001/2019 (SMART-G—Smart Geopolymers) and

MAXIMUM (PTDC-CTM-CTM-2205-2020) supported by Foundation for Science and Technology (FCT). JC (SFRH/BD/144562/2019) wish to thank Fundação para a Ciência e Tecnologia (FCT) for supporting his work.

## Conflict of interest

The authors declare that the research was conducted in the absence of any commercial or financial relationships that could be construed as a potential conflict of interest.

## Publisher's note

All claims expressed in this article are solely those of the authors and do not necessarily represent those of their affiliated organizations, or those of the publisher, the editors and the reviewers. Any product that may be evaluated in this article, or claim that may be made by its manufacturer, is not guaranteed or endorsed by the publisher.

## References

- Bajpai, P. (2017). "Anaerobic technology in pulp and paper industry," in *SpringerBriefs in applied sciences and Technology*. 1st ed (Singapore: Springer Singapore). doi:10.1007/978-981-10-4130-3
- Berra, M., Mangialardi, T., and Paolini, A. E. (2015). Reuse of woody biomass fly ash in cement-based materials. *Constr. Build. Mat.* 76, 286–296. doi:10.1016/j.conbuildmat.2014.11.052
- Buruberry, L. H., Seabra, M. P., and Labrincha, J. A. (2015). Preparation of clinker from paper pulp industry wastes. *J. Hazard. Mat.* 286, 252–260. doi:10.1016/j.jhazmat.2014.12.053
- Cabrera, M. N. (2017). "Pulp mill wastewater: Characteristics and treatment," in *Biological wastewater treatment and resource recovery* (London, UK: InTech). doi:10.5772/67537
- Caetano, A. P. F., Carvalheiras, J., Senff, L., Seabra, M. P., Pullar, R. C., Labrincha, J. A., et al. (2022). Unravelling the affinity of alkali-activated fly ash cubic foams towards heavy metals sorption. *Materials* 15, 1453. doi:10.3390/ma15041453
- Capela, M. N., Cesconeto, F. R., Pinto, P. C., Tarelho, L. A. C., Seabra, M. P., and Labrincha, J. A. (2022). Biomass fly ash self-hardened adsorbent monoliths for methylene blue removal from aqueous solutions. *Appl. Sci. Switz.* 12, 5134. doi:10.3390/app12105134
- Capela, M. N., Tobaldi, D. M., Tarelho, L. A. C., Seabra, M. P., and Labrincha, J. A. (2021). Development of a commercial screed mortar with low OPC content by incorporation of biomass fly ash. *Appl. Sci. Switz.* 11, 9630. doi:10.3390/app11209630
- CEN (2011). *EN 197-1:2011 Cement Part 1: Composition, specifications and conformity criteria for common cements*. Brussels: European Committee for Standardization.
- Cepi (2021). *Key statistics 2020*. Brussels: European pulp & paper industry.
- Cherian, C., and Siddiqua, S. (2019). Pulp and paper mill fly ash: A review. *Sustainability* 11, 4394. doi:10.3390/su11164394
- Cision, P. N., 2022. Cision PR newswire, Available at: <https://www.prnewswire.com/news-releases/pulp-market-share-to-register-a-growth-of-usd-47-45-billion-at-a-cagr-of-4-08-increased-consumption-of-chemical-wood-pulp-to-boost-market-growth-technavio-301539679.html>, Accessed date: May 2022.
- Decree-Law 152/2002-Solid wastes (2002). *Landfills classification-Portuguese legislation (in Portuguese)*. Lisbon: Ministério do Ambiente e do Ordenamento do Território.
- dos Santos, V. R., Cabrelon, M. D., de Sousa Trichês, E., and Quinteiro, E. (2019). Green liquor dregs and slaker grits residues characterization of a pulp and paper mill for future application on ceramic products. *J. Clean. Prod.* 240, 118220. doi:10.1016/j.jclepro.2019.118220
- Duxson, P., Fernández-Jiménez, A., Provis, J. L., Lukey, G. C., Palomo, A., and van Deventer, J. S. J. (2007). Geopolymer technology: The current state of the art. *J. Mat. Sci.* 42, 2917–2933. doi:10.1007/s10853-006-0637-z
- EIA (2019). *International energy outlook 2019 with projections to 2050*. Washington, DC: U.S. Department of Energy.
- EPA (2010). *Available and emerging technologies for reducing greenhouse gas emissions from the pulp and paper manufacturing industry*. North Carolina, USA: U.S. Environmental Protection Agency.
- Esteves, T. C., Rajamma, R., Soares, D., Silva, A. S., Ferreira, V. M., and Labrincha, J. A. (2012). Use of biomass fly ash for mitigation of alkali-silica reaction of cement mortars. *Constr. Build. Mat.* 26, 687–693. doi:10.1016/j.conbuildmat.2011.06.075
- European Parliament and of the Council, E.C. (2003). *2003/33/CE: Criteria and procedures for the acceptance of waste at landfills*. Brussels: Official Journal of the European Communities.
- Faubert, P., Barnabé, S., Bouchard, S., Côté, R., and Villeneuve, C. (2016). Pulp and paper mill sludge management practices: What are the challenges to assess the impacts on greenhouse gas emissions? *Resour. Conserv. Recycl.* 108, 107–133. doi:10.1016/j.resconrec.2016.01.007
- FBI, 2021. Fortune business insights, Available at: <https://www.fortunebusinessinsights.com/pulp-and-paper-market-103447>, Accessed date: March 2022.
- Gellerstedt, G. (2015). Softwood kraft lignin: Raw material for the future. *Ind. Crops Prod.* 77, 845–854. doi:10.1016/j.indcrop.2015.09.040
- Gameiro, T., Correia, C. L., Novais, R. M., Seabra, M. P., Labrincha, J. A., and Capela, I. (2019). "pH control in anaerobic bioreactors using fly-ash based geopolymers as buffer material," in *Proceedings of the 2019 International Conference on Green Energy and Environmental Technology*, Paris, France, 24–26 July, 2019, 133.
- Gameiro, T., Novais, R. M., Correia, C. L., Carvalheiras, J., Seabra, M. P., Labrincha, J. A., et al. (2020). Red mud-based inorganic polymer spheres: Innovative and environmentally friendly anaerobic digestion enhancers. *Bioresour. Technol.* 316, 123904. doi:10.1016/j.biortech.2020.123904
- Gameiro, T., Novais, R. M., Correia, C. L., Carvalheiras, J., Seabra, M. P., Tarelho, L. A. C., et al. (2021). Role of waste-based geopolymer spheres addition for pH control and efficiency enhancement of anaerobic digestion process. *Bioprocess Biosyst. Eng.* 44, 1167–1183. doi:10.1007/s00449-021-02522-w

- Gameiro, T., Novais, R., Seabra, M. P., Tarelho, L. A. C., Labrincha, J. A., and Capela, I. (2018). "Geopolimeros para controlo de pH: Aplicação em processos de digestão anaeróbia," in Proceedings of the XI Conferência Internacional de Ambiente em Língua Portuguesa, Aveiro, Portugal, 8–10 May, 2018.
- Gonçalves, M., Novais, R. M., Senff, L., Carvalheiras, J., and Labrincha, J. A. (2021a). PCM-containing bi-layered alkali-activated materials: A novel and sustainable route to regulate the temperature and humidity fluctuations inside buildings. *Build. Environ.* 205, 108281. doi:10.1016/j.buildenv.2021.108281
- Gonçalves, M., Vilarinho, I. S., Capela, M., Caetano, A., Novais, R. M., Labrincha, J. A., et al. (2021b). Waste-based one-part alkali activated materials. *Materials* 14, 2911. doi:10.3390/ma14112911
- He, J., Lange, C. R., and Dougherty, M. (2009). Laboratory study using paper mill lime mud for agronomic benefit. *Process Saf. Environ. Prot.* 87, 401–405. doi:10.1016/j.psep.2009.08.001
- Ji, Z., and Pei, Y. (2019). Bibliographic and visualized analysis of geopolymer research and its application in heavy metal immobilization: A review. *J. Environ. Manage.* 231, 256–267. doi:10.1016/j.jenvman.2018.10.041
- Kamali, M., Gameiro, T., Costa, M. E. V., and Capela, I. (2016). Anaerobic digestion of pulp and paper mill wastes - an overview of the developments and improvement opportunities. *Chem. Eng. J.* 298, 162–182. doi:10.1016/j.cej.2016.03.119
- Kamali, M., and Khodaparast, Z. (2015). Review on recent developments on pulp and paper mill wastewater treatment. *Ecotoxicol. Environ. Saf.* 114, 326–342. doi:10.1016/j.ecoenv.2014.05.005
- Khan, I., Saeed, K., Zekker, I., Zhang, B., Hendi, A. H., Ahmad, A., et al. (2022). Review on methylene blue: Its properties, uses, toxicity and photodegradation. *Water (Basel)* 14, 242. doi:10.3390/w14020242
- Kramer, K. J., Masanet, E. Xu, T., and Worrell, E. (2009). *Energy efficiency improvement and cost saving opportunities for the pulp and paper industry*. Berkeley, CA: Environmental Energy Technologies Division.
- Kumar, M., Morya, R., Gupta, A., and Thakur, I. S. (2020). "Anaerobic biovalorization of pulp and paper mill waste," in *Biovalorisation of wastes to renewable chemicals and biofuels* (Amsterdam, Netherlands: Elsevier), 41–61. doi:10.1016/B978-0-12-817951-2.00003-1
- Lamers, A. S. F., Cremers, M., Matschegg, D., Schmidl, C., Hannam, K., Hazlett, P., et al. (2019). Options for increased use of ash from biomass combustion and co-firing. *IEA Bioenergy Task* 32, 1–61.
- Li, L., Wang, S., and Zhu, Z. (2006). Geopolymeric adsorbents from fly ash for dye removal from aqueous solution. *J. Colloid Interface Sci.* 300, 52–59. doi:10.1016/j.jcis.2006.03.062
- Manskinen, K., Nurmesniemi, H., and Pöykiö, R. (2011). Total and extractable non-process elements in green liquor dregs from the chemical recovery circuit of a semi-chemical pulp mill. *Chem. Eng. J.* 166, 954–961. doi:10.1016/j.cej.2010.11.082
- Mesfun, S., Lundgren, J., Grip, C.-E., Toffolo, A., Nilsson, R. L. K., and Rova, U. (2014). Black liquor fractionation for biofuels production – a techno-economic assessment. *Bioresour. Technol.* 166, 508–517. doi:10.1016/j.biortech.2014.05.062
- Meyer, T., and Edwards, E. A. (2014). Anaerobic digestion of pulp and paper mill wastewater and sludge. *Water Res.* 65, 321–349. doi:10.1016/j.watres.2014.07.022
- Modolo, R., Benta, A., Ferreira, V. M., and Machado, L. M. (2010). Pulp and paper plant wastes valorisation in bituminous mixes. *Waste Manag.* 30, 685–696. doi:10.1016/j.wasman.2009.11.005
- Modolo, R. C. E., Ascensão, G., Senff, L., Ribeiro, F. R. C., Tarelho, L. A. D. C., Ferreira, V. M., et al. (2021). Recycling of ashes from forest biomass combustion as raw material for mortars. *Mix Sustentável* 7, 137–146. doi:10.29183/2447-3073.mix2021.v7.n2.137-146
- Modolo, R. C. E., Ferreira, V. M., Tarelho, L. A., Labrincha, J. A., Senff, L., and Silva, L. (2013). Mortar formulations with bottom ash from biomass combustion. *Constr. Build. Mat.* 45, 275–281. doi:10.1016/j.conbuildmat.2013.03.093
- Modolo, R. C. E., Senff, L., Labrincha, J. A., Ferreira, V. M., and Tarelho, L. A. C. (2014). Lime mud from cellulose industry as raw material in cement mortars. *Mat. construcc.* 64, e033. doi:10.3989/mc.2014.00214
- Modolo, R. C. E., Silva, T., Senff, L., Tarelho, L. A. C., Labrincha, J. A., Ferreira, V. M., et al. (2015). Bottom ash from biomass combustion in BFB and its use in adhesive-mortars. *Fuel Process. Technol.* 129, 192–202. doi:10.1016/j.fuproc.2014.09.015
- Monte, M. C., Fuente, E., Blanco, A., and Negro, C. (2009). Waste management from pulp and paper production in the European Union. *Waste Manag.* 29, 293–308. doi:10.1016/j.wasman.2008.02.002
- Naqvi, M., Yan, J., and Dahlquist, E. (2010). Black liquor gasification integrated in pulp and paper mills: A critical review. *Bioresour. Technol.* 101, 8001–8015. doi:10.1016/j.biortech.2010.05.013
- Novais, R. M., Ascensão, G., Buruberri, L. H., Senff, L., and Labrincha, J. A. (2016a). Influence of blowing agent on the fresh- and hardened-state properties of lightweight geopolymers. *Mat. Des.* 108, 551–559. doi:10.1016/j.matdes.2016.07.039
- Novais, R. M., Ascensão, G., Ferreira, N., Seabra, M. P., and Labrincha, J. A. (2016b). Biomass fly ash geopolymer monoliths for effective methylene blue removal from wastewaters. *J. Clean. Prod.* 171, 783–794. doi:10.1016/j.jclepro.2017.10.078
- Novais, R. M., Buruberri, L. H., Ascensão, G., Seabra, M. P., and Labrincha, J. A. (2016b). Porous biomass fly ash-based geopolymers with tailored thermal conductivity. *J. Clean. Prod.* 119, 99–107. doi:10.1016/j.jclepro.2016.01.083
- Novais, R. M., Buruberri, L. H., Seabra, M. P., Bajare, D., and Labrincha, J. A. (2016c). Novel porous fly ash-containing geopolymers for pH buffering applications. *J. Clean. Prod.* 124, 395–404. doi:10.1016/j.jclepro.2016.02.114
- Novais, R. M., Buruberri, L. H., Seabra, M. P., and Labrincha, J. A. (2016d). Novel porous fly-ash containing geopolymer monoliths for lead adsorption from wastewaters. *J. Hazard. Mat.* 318, 631–640. doi:10.1016/j.jhazmat.2016.07.059
- Novais, R. M., Caetano, A. P. F., Seabra, M. P., Labrincha, J. A., and Pullar, R. C. (2018c). Extremely fast and efficient methylene blue adsorption using eco-friendly cork and paper waste-based activated carbon adsorbents. *J. Clean. Prod.* 197, 1137–1147. doi:10.1016/j.jclepro.2018.06.278
- Novais, R. M., Carvalheiras, J., Capela, M. N., Seabra, M. P., Pullar, R. C., and Labrincha, J. A. (2018d). Incorporation of glass fibre fabrics waste into geopolymer matrices: An eco-friendly solution for off-cuts coming from wind turbine blade production. *Constr. Build. Mat.* 187, 876–883. doi:10.1016/j.conbuildmat.2018.08.004
- Novais, R. M., Carvalheiras, J., Seabra, M. P., Pullar, R. C., and Labrincha, J. A. (2017a). Effective mechanical reinforcement of inorganic polymers using glass fibre waste. *J. Clean. Prod.* 166, 343–349. doi:10.1016/j.jclepro.2017.07.242
- Novais, R. M., Carvalheiras, J., Seabra, M. P., Pullar, R. C., and Labrincha, J. A. (2020a). Highly efficient lead extraction from aqueous solutions using inorganic polymer foams derived from biomass fly ash and metakaolin. *J. Environ. Manage.* 272, 111049. doi:10.1016/j.jenvman.2020.111049
- Novais, R. M., Carvalheiras, J., Seabra, M. P., Pullar, R. C., and Labrincha, J. A. (2018e). Innovative application for bauxite residue: Red mud-based inorganic polymer spheres as pH regulators. *J. Hazard. Mat.* 358, 69–81. doi:10.1016/j.jhazmat.2018.06.047
- Novais, R. M., Carvalheiras, J., Senff, L., and Labrincha, J. A. (2018f). Upcycling unexplored dregs and biomass fly ash from the paper and pulp industry in the production of eco-friendly geopolymer mortars: A preliminary assessment. *Constr. Build. Mat.* 184, 464–472. doi:10.1016/j.conbuildmat.2018.07.017
- Novais, R. M., Carvalheiras, J., Senff, L., Lacasta, A. M., Cantalapiedra, I. R., Giro-Paloma, J., et al. (2020b). Multifunctional cork – alkali-activated fly ash composites: A sustainable material to enhance buildings' energy and acoustic performance. *Energy Build.* 210, 109739. doi:10.1016/j.enbuild.2019.109739
- Novais, R. M., Carvalheiras, J., Senff, L., Seabra, M. P., Pullar, R. C., and Labrincha, J. A. (2019a). In-depth investigation of the long-term strength and leaching behaviour of inorganic polymer mortars containing green liquor dregs. *J. Clean. Prod.* 220, 630–641. doi:10.1016/j.jclepro.2019.02.170
- Novais, R. M., Carvalheiras, J., Tobaldi, D. M., Seabra, M. P., Pullar, R. C., and Labrincha, J. A. (2019b). Synthesis of porous biomass fly ash-based geopolymer spheres for efficient removal of methylene blue from wastewaters. *J. Clean. Prod.* 207, 350–362. doi:10.1016/j.jclepro.2018.09.265
- Novais, R. M., Gameiro, T., Carvalheiras, J., Seabra, M. P., Tarelho, L. A. C., Labrincha, J. A., et al. (2018g). High pH buffer capacity biomass fly ash-based geopolymer spheres to boost methane yield in anaerobic digestion. *J. Clean. Prod.* 178, 258–267. doi:10.1016/j.jclepro.2018.01.033
- Novais, R. M., Pullar, R. C., and Labrincha, J. A. (2020c). Geopolymer foams: An overview of recent advancements. *Prog. Mat. Sci.* 109, 100621. doi:10.1016/j.pmatsci.2019.100621
- Novais, R. M., Senff, L., Carvalheiras, J., and Labrincha, J. A. (2020d). Bi-layered porous/cork-containing waste-based inorganic polymer composites: Innovative material towards green buildings. *Appl. Sci. Switz.* 10, 2995. doi:10.3390/app10092995
- Novais, R. M., Seabra, M. P., and Labrincha, J. A. (2017b). Porous geopolymer spheres as novel pH buffering materials. *J. Clean. Prod.* 143, 1114–1122. doi:10.1016/j.jclepro.2016.12.008
- Novais, R. M., Senff, L., Carvalheiras, J., Lacasta, A. M., Cantalapiedra, I. R., and Labrincha, J. A. (2021). Simple and effective route to tailor the thermal, acoustic and



hygrothermal properties of cork-containing waste derived inorganic polymer composites. *J. Build. Eng.* 42, 102501. doi:10.1016/j.jobbe.2021.102501

Novais, R. M., Senff, L., Carvalheiras, J., Seabra, M. P., Pullar, R. C., and Labrincha, J. A. (2019c). Sustainable and efficient cork - inorganic polymer composites: An innovative and eco-friendly approach to produce ultra-lightweight and low thermal conductivity materials. *Cem. Concr. Compos.* 97, 107–117. doi:10.1016/j.cemconcomp.2018.12.024

Organization for Standardization, I. (2008). *ISO 24353, hygrothermal performance of building materials and products — determination of moisture adsorption/desorption properties in response to humidity variation*. Geneva, Switzerland: ISO.

Rajamma, R., Ball, R. J., Tarelho, L. A. C., Allen, G. C., Labrincha, J. A., and Ferreira, V. M. (2009). Characterisation and use of biomass fly ash in cement-based materials. *J. Hazard. Mat.* 172, 1049–1060. doi:10.1016/j.jhazmat.2009.07.109

Rajamma, R., Senff, L., Ribeiro, M. J., Labrincha, J. A., Ball, R. J., Allen, G. C., et al. (2015). Biomass fly ash effect on fresh and hardened state properties of cement based materials. *Compos. Part B Eng.* 77, 1–9. doi:10.1016/j.compositesb.2015.03.019

Rode, C., Peuhkuri, R. H. Hansen, K. K. Time, B., Svennberg, K. Arfvidsson, J., et al. (2005a). *NORDTEST project on moisture buffer value of materials*. In AIVC 26th conference: Ventilation in relation to the energy performance of buildings. Air Infiltration and Ventilation, 47–52.

Rode, C., Peuhkuri, R. Mortensen, L. H. Hansen, K. K. Time, B. Gustavsen, A., et al. (2005b). *Moisture buffering of building materials*. Technical University of Denmark, Department of Civil Engineering. BYG Report No. R-127.

Rossi, A., Carvalheiras, J., Novais, R. M., Ribeiro, M. J., Labrincha, J. A., Hotza, D., et al. (2018). Waste-based geopolymeric mortars with very high moisture buffering capacity. *Constr. Build. Mat.* 191, 39–46. doi:10.1016/j.conbuildmat.2018.09.201

Rossi, A., Ribeiro, M. J., Labrincha, J. A., Novais, R. M., Hotza, D., and Moreira, R. F. P. M. (2019). Effect of the particle size range of construction and demolition waste on the fresh and hardened-state properties of fly ash-based geopolymer mortars with total replacement of sand. *Process Saf. Environ. Prot.* 129, 130–137. doi:10.1016/j.psep.2019.06.026

Saeli, M., Novais, R. M., Seabra, M. P., and Labrincha, J. A. (2018). Green geopolymeric concrete using grits for applications in construction. *Mat. Lett.* 233, 94–97. doi:10.1016/j.matlet.2018.08.102

Saeli, M., Senff, L., Tobaldi, D. M., Carvalheiras, J., Seabra, M. P., and Labrincha, J. A. (2020). Unexplored alternative use of calcareous sludge from the paper-pulp industry in green geopolymer construction materials. *Constr. Build. Mat.* 246, 118457. doi:10.1016/j.conbuildmat.2020.118457

Saeli, M., Senff, L., Tobaldi, D. M., La Scalia, G., Seabra, M. P., and Labrincha, J. A. (2019a). Innovative recycling of lime slaker grits from paper-pulp industry reused as aggregate in ambient cured biomass fly ash-based geopolymers for sustainable construction material. *Sustain. Switz.* 11, 3481–3515. doi:10.3390/su11123481

Saeli, M., Senff, L., Tobaldi, D. M., Seabra, M. P., and Labrincha, J. A. (2019b). Novel biomass fly ash-based geopolymeric mortars using lime slaker grits as

aggregate for applications in construction: Influence of granulometry and binder/aggregate ratio. *Constr. Build. Mat.* 227, 116643. doi:10.1016/j.conbuildmat.2019.08.024

Saeli, M., Tobaldi, D. M., Seabra, M. P., and Labrincha, J. A. (2019c). Mix design and mechanical performance of geopolymeric binders and mortars using biomass fly ash and alkaline effluent from paper-pulp industry. *J. Clean. Prod.* 208, 1188–1197. doi:10.1016/j.jclepro.2018.10.213

Santos, R. B., Hart, P., Jameel, H., and Chang, H. (2013). Wood based lignin reactions important to the biorefinery and pulp and paper industries. *Bioresources* 8, 1456. doi:10.15376/biores.8.1.1456-1477

Senff, L., Novais, R. M., Carvalheiras, J., and Labrincha, J. A. (2020). Eco-friendly approach to enhance the mechanical performance of geopolymer foams: Using glass fibre waste coming from wind blade production. *Constr. Build. Mat.* 239, 117805. doi:10.1016/j.conbuildmat.2019.117805

Simão, L., Hotza, D., Raupp-Pereira, F., Labrincha, J. A., and Montedo, O. R. K. (2018). Wastes from pulp and paper mills - a review of generation and recycling alternatives. *Cerâmica* 64, 443–453. doi:10.1590/0366-69132018643712414

Simão, L., Jiusti, J., Löh, N. J., Hotza, D., Raupp-Pereira, F., Labrincha, J. A., et al. (2017). Waste-containing clinkers: Valorization of alternative mineral sources from pulp and paper mills. *Process Saf. Environ. Prot.* 109, 106–116. doi:10.1016/j.psep.2017.03.038

Statista, 2020a. Statista, Available at: <https://www.statista.com/statistics/276629/global-co2-emissions/>, Accessed date: May 2022.

Statista, 2020b. Statista, Available at: <https://www.statista.com/statistics/1299532/carbon-dioxide-emissions-worldwide-cement-manufacturing/>, Accessed date: May 2022.

Takada, M., Chandra, R., Wu, J., and Saddler, J. N. (2020). The influence of lignin on the effectiveness of using a chemithermomechanical pulping based process to pretreat softwood chips and pellets prior to enzymatic hydrolysis. *Bioresour. Technol.* 302, 122895. doi:10.1016/j.biortech.2020.122895

Tran, H., and Vakkilainen, E. K., 2008. The Kraft chemical recovery process, in: *Proceedings of the Tappi Kraft Pulping Short Course*. St. Petersburg, FL, USA, 7–10 January, 2008, pp. 1.1:1–1.1:8.

Vass, T., Levi, P., Gouy, A., and Mandová, H., 2021. International energy agency, Available at: <https://www.iea.org/reports/cement>, Accessed date: May 2022.

Veluchamy, C., and Kalamdhad, A. S. (2017). Influence of pretreatment techniques on anaerobic digestion of pulp and paper mill sludge: A review. *Bioresour. Technol.* 245, 1206–1219. doi:10.1016/j.biortech.2017.08.179

Verma, O. P., Manik, G., and Sethi, S. K. (2019). A comprehensive review of renewable energy source on energy optimization of black liquor in MSE using steady and dynamic state modeling, simulation and control. *Renew. Sustain. Energy Rev.* 100, 90–109. doi:10.1016/j.rser.2018.10.002

Zhang, Z., Provis, J. L., Reid, A., and Wang, H. (2014). Fly ash-based geopolymers: The relationship between composition, pore structure and efflorescence. *Cem. Concr. Res.* 64, 30–41. doi:10.1016/j.cemconres.2014.06.004



## OPEN ACCESS

## EDITED BY

Liang Zhou,  
Changchun Institute of Applied  
Chemistry (CAS), China

## REVIEWED BY

Yuhua Wang,  
Lanzhou University, China  
Xian Chen,  
Shenzhen University, China

## \*CORRESPONDENCE

Luís D. Carlos,  
lcarlos@ua.pt

## SPECIALTY SECTION

This article was submitted to Light  
Sources and Luminescent Materials,  
a section of the journal  
Frontiers in Photonics

RECEIVED 05 September 2022

ACCEPTED 18 October 2022

PUBLISHED 31 October 2022

## CITATION

Martins JC, Skripka A, Brites CDS,  
Benayas A, Ferreira RAS, Vetrone F and  
Carlos LD (2022), Upconverting  
nanoparticles as primary thermometers  
and power sensors.  
*Front. Photonics* 3:1037473.  
doi: 10.3389/fphot.2022.1037473

## COPYRIGHT

© 2022 Martins, Skripka, Brites, Benayas,  
Ferreira, Vetrone and Carlos. This is an  
open-access article distributed under  
the terms of the [Creative Commons  
Attribution License \(CC BY\)](https://creativecommons.org/licenses/by/4.0/). The use,  
distribution or reproduction in other  
forums is permitted, provided the  
original author(s) and the copyright  
owner(s) are credited and that the  
original publication in this journal is  
cited, in accordance with accepted  
academic practice. No use, distribution  
or reproduction is permitted which does  
not comply with these terms.

# Upconverting nanoparticles as primary thermometers and power sensors

Joana Costa Martins<sup>1</sup>, Artiom Skripka<sup>2</sup>, Carlos D. S. Brites<sup>1</sup>,  
Antonio Benayas<sup>3,4</sup>, Rute A. S. Ferreira<sup>1</sup>, Fiorenzo Vetrone<sup>2</sup> and  
Luís D. Carlos<sup>1\*</sup>

<sup>1</sup>Department of Physics, Phantom-G, CICECO–Aveiro Institute of Materials, University of Aveiro, Campus Universitário de Santiago, Aveiro, Portugal, <sup>2</sup>Centre Énergie, Matériaux et Télécommunications, Institut National de la Recherche Scientifique, Université du Québec, Varennes, QC, Canada, <sup>3</sup>Nanomaterials for Bioimaging Group (nanoBIG), Departamento de Física de Materiales, Facultad de Ciencias, Universidad Autónoma de Madrid, Madrid, Spain, <sup>4</sup>Nanomaterials for Bioimaging Group (nanoBIG), Instituto Ramón y Cajal de Investigación Sanitaria, Madrid, Spain

Luminescence thermometry is a spectroscopic technique for remote temperature detection based on the thermal dependence of the luminescence of phosphors, presenting numerous applications ranging from biosciences to engineering. In this work, we use the  $\text{Er}^{3+}$  emission of the  $\text{NaGdF}_4/\text{NaGdF}_4:\text{Yb}^{3+}, \text{Er}^{3+}/\text{NaGdF}_4$  upconverting nanoparticles upon 980 nm laser excitation to determine simultaneously the absolute temperature and the excitation power density. The  $\text{Er}^{3+} {}^2\text{H}_{11/2} \rightarrow {}^4\text{I}_{15/2}$  and  ${}^4\text{S}_{3/2} \rightarrow {}^4\text{I}_{15/2}$  emission bands, which are commonly used for thermometric purposes, overlap with the  ${}^2\text{H}_{9/2} \rightarrow {}^4\text{I}_{13/2}$  emission band, which can lead to erroneous temperature readout. Applying the concept of luminescent primary thermometry to resolve the overlapping  $\text{Er}^{3+}$  transitions, a dual nanosensor synchronously measuring the temperature and the delivered laser pump power is successfully realized holding promising applications in laser-supported thermal therapies.

## KEYWORDS

lanthanides (III), upconversion nanoparticles (UCNPs), luminescent nanothermometer, NIR radiation sensor, bioimaging

## Introduction

Luminescent nanothermometry exploits the temperature-dependent emission properties of luminescent nanoprobes, e.g., quantum dots, organic dyes, polymers, DNA or protein conjugated systems, transition-metal-based materials, or trivalent lanthanide ion ( $\text{Ln}^{3+}$ )-doped materials (Brites et al., 2012; Jaque and Vetrone, 2012; Brites et al., 2016). The latter systems feature unique characteristics, such as high photostability, narrow bandwidth, and efficient room-temperature emission, which make them suitable for different applications, particularly bioimaging-related ones (Jaque et al., 2014; Zhou et al., 2015; Brites et al., 2016; Dramicanin, 2018; Brites et al., 2019a).  $\text{Ln}^{3+}$  ions work in the spectral ranges where the biological tissue has minimal absorption and negligible autofluorescence, designated as biological imaging

windows. Therefore, luminescent thermometers based on  $\text{Ln}^{3+}$ -doped nanomaterials have been widely employed in intracellular measurements (Debasu et al., 2020; Piñol et al., 2020; Dantelle et al., 2021; Di et al., 2021; Kim et al., 2021; Dos Santos et al., 2022) and tumor temperature mapping during thermal therapies (Jaque et al., 2014; Carrasco et al., 2015; Zhu et al., 2016, 2018).

The most common approach to infer absolute temperature is based on the intensity ratio of two distinct transitions - ratiometric luminescence thermometry (Brites et al., 2016). In the last few years, primary thermometers based on luminescent nanoprobes have been studied which take advantage of the temperature-dependent intensity ratio of the two thermally coupled  $\text{Er}^{3+}$  levels,  $^2\text{H}_{11/2}$  and  $^4\text{S}_{3/2}$  (Balabhadra et al., 2017; Bastos et al., 2019; Brites et al., 2019b; Martínez et al., 2019; Borges et al., 2021; Martins et al., 2021; Dos Santos et al., 2022). A primary thermometer is characterized by a well-established emitting state population equation that follows Boltzmann statistics. Recently, a few works have drawn attention to the impact of the  $^2\text{H}_{9/2} \rightarrow ^4\text{I}_{13/2}$  emission band in temperature determination using  $\text{Er}^{3+}$  emission (Martins et al., 2021; Rühl et al., 2021; Van Swieten et al., 2021; Xia et al., 2021). Upon near-infrared (NIR) excitation, the  $^2\text{H}_{9/2}$  manifold of  $\text{Er}^{3+}$  is populated through a three-photon upconversion process (Cho et al., 2017). Emission of the  $^2\text{H}_{9/2} \rightarrow ^4\text{I}_{13/2}$  transition overlaps with the  $^4\text{S}_{3/2} \rightarrow ^4\text{I}_{15/2}$  one, which can lead to total intensity overestimation when  $^2\text{H}_{9/2} \rightarrow ^4\text{I}_{13/2}$  contribution is overlooked, and its contribution increases with the excitation power density ( $P_D$ ) (Zhou et al., 2013; Berry and May, 2015; Yuan et al., 2018, 2019; Rühl et al., 2021; Xia et al., 2021). This complicates accurate temperature readout but provides an opportunity to explore NIR  $P_D$  optical readout, as demonstrated herein. To the best of our knowledge, only one luminescent excitation density ratiometric sensor for the visible spectral range was reported by (Marciniak et al., 2022). There, the intensity ratio of  $^4\text{T}_{2(\text{g})} \rightarrow ^4\text{A}_{2(\text{g})}$  and  $^2\text{E}_{(\text{g})} \rightarrow ^4\text{A}_{2(\text{g})}$  transitions of  $\text{GdAl}_3(\text{BO}_3)_4:\text{Cr}^{3+}$  nanoparticles was used to measure the excitation power density at 445 nm and 532 nm. The authors designed the nanoparticles to enhance the probability of nonradiative processes to achieve an efficient radiation-to-heat conversion. The designed material reached temperatures as high as 143°C, even at low excitation power density. According to the excitation power density, the heat generated in the system leads to the thermalization of the  $^4\text{T}_{2(\text{g})}$  state inducing a change in the intensity ratio (Marciniak et al., 2022), and thus, the working principle of this  $\text{Cr}^{3+}$  ratiometric laser power meter is, in fact, temperature related.

The simultaneous measurement of temperature and incident  $P_D$  is critical for optimizing photon-based therapies, such as photothermal therapy (Jaque et al., 2014; Yang et al., 2017) and photobiomodulation (PBM) (Freitas and Hamblin, 2016), and preventing the surrounding tissue from overheating and deleterious damage (Shen et al., 2020). Photothermal therapy

uses light to generate heat from plasmonic or dielectric nanoparticles (Jaque et al., 2014), whereas PBM involves the use of a low-powered light source (lasers and LEDs) within the red and NIR wavelength range (~600–1,000 nm) to stimulate or inhibit cellular and biological processes (Freitas and Hamblin, 2016). In PBM applications, where the low-powered excitation source does not induce an evident temperature rise, the  $P_D$  quantization of the delivered light to the target could contribute to standardization, improving the reliability and reproducibility of the technique (Wang and Dong, 2020).

In this work, we study the thermometric features of  $\text{NaGdF}_4/\text{NaGdF}_4:\text{Yb}^{3+},\text{Er}^{3+}/\text{NaGdF}_4$  upconverting nanoparticles upon 980 nm laser excitation and show how they work as a primary luminescent thermometer once the decoupling procedure is applied to resolve the overlapping  $^2\text{H}_{9/2} \rightarrow ^4\text{I}_{13/2}$  and  $^4\text{S}_{3/2} \rightarrow ^4\text{I}_{15/2}$  emission bands. The passive-core/active-shell/passive-shell architecture of nanoparticles was chosen to promote  $\text{Er}^{3+}$  upconversion emission from the  $^2\text{H}_{9/2}$  excited state, through reduced energy migration and enhanced energy transfer upconversion (Chen et al., 2016; Wang, 2019). Taking advantage of the  $P_D$ -dependent  $^2\text{H}_{9/2} \rightarrow ^4\text{I}_{13/2}$  emission intensity, we characterize a ratiometric NIR radiation sensor. Thus, we have developed a versatile system capable of sensing both the local absolute temperature and the  $P_D$  delivered to the target using luminescence with future potential applications in PBM treatments or other laser-based thermal therapies.

Besides being a NIR radiation sensor, which is the radiation commonly used in biological applications, the monodisperse in size  $\text{NaGdF}_4/\text{NaGdF}_4:\text{Yb}^{3+},\text{Er}^{3+}/\text{NaGdF}_4$  nanoparticles can be patterned on various substrates as well as dispersed in different colloidal mixtures. Moreover, the intensity of the selected transitions to sense the delivered laser pump power are thermal independent, enabling the synchronous measurement of the temperature and  $P_D$ .

## Materials and methods

### Materials synthesis

$\text{NaGdF}_4/\text{NaGdF}_4$ : 2 mol%  $\text{Er}^{3+}$ , 20 mol%  $\text{Yb}^{3+}/\text{NaGdF}_4$  lanthanide-doped nanoparticles (Figure 1), were prepared by hot-injection thermal decomposition (Boyer et al., 2006; Skripka et al., 2020).

To synthesize the core, an initial mixture of 12.5 mL each of OA and ODE was prepared in a 100 mL three-neck round bottom flask (Solution A). Aside, 2.5 mmol of Na-TFA were added to the 2.5 mmol of dried Gd-TFA precursor together with 7.5 mL each of OA and ODE (Solution B). Both solutions A and B were degassed at 150°C under vacuum with magnetic stirring for 30 min. After degassing, solution A was placed under an Ar atmosphere and the temperature was raised to 315°C. Solution B was then injected into the reaction vessel containing solution A

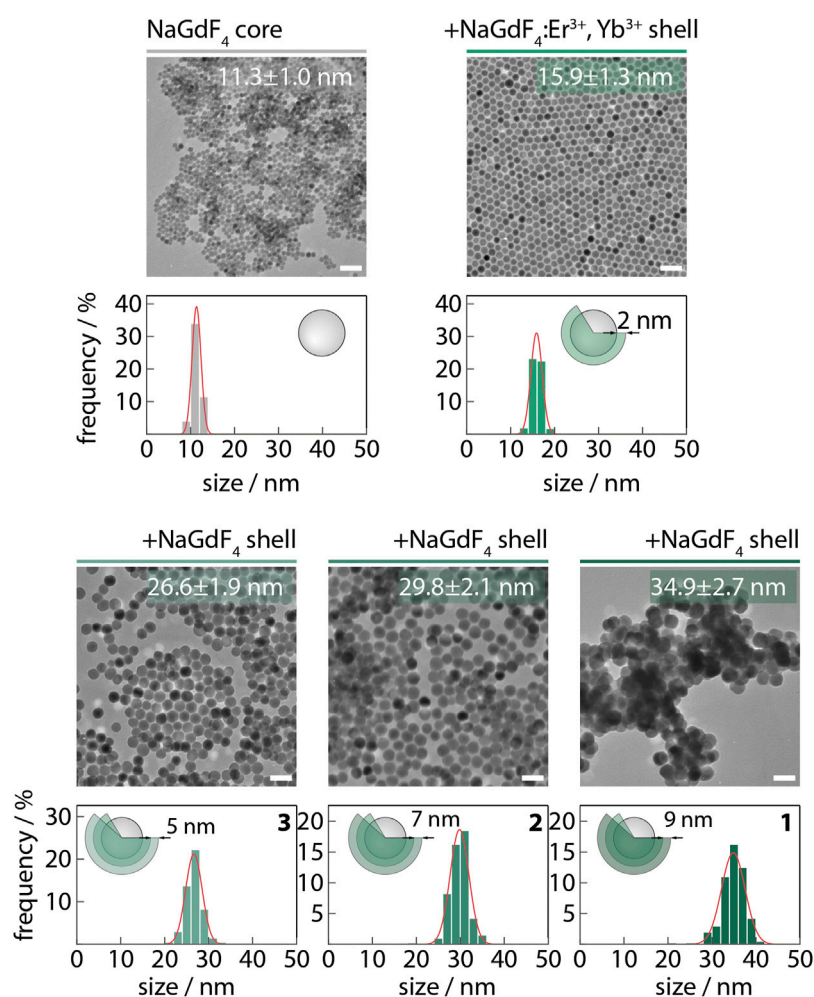


**FIGURE 1**

Representative TEM images of  $\text{Er}^{3+}$ -doped nanothermometers and their respective size distributions. The thickness of the outer  $\text{NaGdF}_4$  shell is represented in the scheme. The nanoparticles used in this work, 1, 2, and 3, are represented in the lower panel. The solid lines are the best fits to the experimental data using Gaussian distributions ( $r^2 > 0.99$ ). The scale bars correspond to 50 nm.

with a syringe and pump system at a 1.3 mL/min injection rate. The mixture was left at 315°C under vigorous stirring for 60 min. After cooling to room temperature, the as-synthesized cores (11.3 nm) were stored in a Falcon centrifuge tube under Ar for further synthesis steps. The core/shell  $\text{NaGdF}_4/\text{NaGdF}_4:\text{Er}^{3+}, \text{Yb}^{3+}$  nanoparticles were prepared by a subsequent shelling of the 2.5 mmol of core nanoparticles (solution A). Separately, solution B contained 3.5 mmol of Na-TFA precursors and 3.5 mmol of Gd,Yb,Er-TFA (2.73 mmol + 0.7 mmol + 0.07 mmol) together with 7.5 mL each of OA and ODE. Both solutions were degassed at 150°C under vacuum with magnetic stirring for 30 min. After degassing, solution A was placed under an Ar atmosphere and the temperature was raised to 315°C. Solution B was then injected at a 1 mL/min rate into solution A and left to react for 90 min. After, 15 mL of the reaction mixture containing core/shell1 nanoparticles (15.9 nm) was aliquoted for sampling.

The core/shell/shell  $\text{NaGdF}_4/\text{NaGdF}_4:\text{Er}^{3+}, \text{Yb}^{3+}/\text{NaGdF}_4$  with various thicknesses of the most-outer shell were prepared by subsequent injection of shelling precursors into the reaction. 8 mmol each of Na-TFA and Gd-TFA were dissolved and degassed in a mixture of 10 mL each of OA and ODE (solution C). Half (10 mL) of solution C was injected at 1 mL/min into the reaction flask and kept at a pre-set 315°C temperature for 60 min, 10 mL of the reaction mixture was aliquoted from the flask before injecting the rest of the solution C. After 60 min, 10 mL were aliquoted from the reaction flask, obtaining core/shell/shell RENPs with a 5.4 nm thick outer shell. Another 8 mmol each of Na-TFA and Gd-TFA were dissolved and degassed in a mixture of 10 mL each of OA and ODE (solution D) and injected (10 mL) into the reaction flask. After 60 min, 10 mL were aliquoted from the reaction obtaining core/shell/shell RENPs with 7.0 nm thick outer shell.



The remaining 10 mL of the solution D were then injected into the reaction mixture and allowed to react for 60 min, yielding core/shell/shell RENPs with a 9.5 nm thick outer shell. The mixture was cooled to room temperature, and core-only, core/shell, and core/shell/shell RENPs were precipitated with ethanol and washed three times with hexane/ethanol (1/4 v/v), followed by centrifugation (5400 RCF). Samples containing NaGdF<sub>4</sub>/NaGdF<sub>4</sub>:Er<sup>3+</sup>, Yb<sup>3+</sup>/NaGdF<sub>4</sub> RENPs with outer shell thicknesses of 9.5, 7.0, and 5.4 nm dispersed in water (nanofluids) were designated as **1**, **2** and **3**, respectively.

## Structural characterization methods

The morphology and size distribution of the core-only and core/shell UCNPs were investigated by transmission electron microscopy (TEM, Philips Tecnai 12). The particle size was determined from TEM images using ImageJ software with a minimum set size of 200 individual UCNPs per sample. The crystallinity and phase of all the UCNPs were determined *via* X-ray powder diffraction (XRD) analysis with a Bruker D8 Advance Diffractometer (USA) using Cu K<sub>α</sub> radiation.

## Power density and temperature-dependent photoluminescence measurements

The **1**, **2**, and **3** nanofluids were placed in a quartz cuvette (114F-10-40, Hellma Analytics) and were excited with a pulsed laser (BrixX 980-1000 HD, Omicron Laser) at a frequency of 1.5 MHz, to get an essentially continuous wave irradiation mode. The laser was focused through an optical lens of 7.5 cm focal distance (LA1145, Thorlabs) to enhance the power density ( $P_D$ ) that ranges from  $29.0 \pm 0.1$  to  $138.8 \pm 0.7$  W cm<sup>-2</sup>, estimated as previously reported (Caixeta et al., 2020). The emission light was guided through an optical fiber (P600-1-UV-VIS, Ocean Insight) and the laser contribution was cut out with a short-pass optical filter (FESH0750, Thorlabs). The emission spectra were recorded by a portable spectrometer (MAYA Pro 2000; Ocean Insight) using an acquisition window between 15–75 s (a total of 150 measurements with integration time ranging from 0.1 to 0.5 s), adjusting the acquisition conditions to obtain a similar signal-to-noise (SNR) ratio at the different excitation  $P_D$ . The spectrometer uses reference and dark measurements to correct the instrument response.

The quartz cuvette was placed in thermal contact with a homemade temperature controller containing a Peltier system and a thermocouple (K-type, 0.1 K accuracy) that was immersed near the laser spot, but away from the light path to monitor and measure the temperature ( $T$ ) of the nanofluid. We set the temperature controller at a fixed temperature and turned on the excitation laser at a fixed  $P_D$  inducing an additional temperature increment. After the nanofluid reaches thermal

equilibrium ( $t > 350$  s) the emission spectra and thermocouple reading are recorded. This process was repeated for  $P_D$  ranging from 19.0 to 138.8 W cm<sup>-2</sup> and for different set temperatures (297.6–315.3 K). At the lowest temperature used (room temperature), the temperature controller was kept off.

## Sensing parameters determination

Before the calculus of the thermometric parameter ( $\Delta$ ) and NIR radiation sensing parameter ( $\Delta_{\text{NIR}}$ ), a spectral deconvolution procedure based on a previously reported work (Martins et al., 2021) was applied to the emission spectra to decouple the overlapping transitions,  $^2\text{H}_{9/2} \rightarrow ^4\text{I}_{13/2}$  and  $^4\text{S}_{3/2} \rightarrow ^4\text{I}_{15/2}$ , using a routine in MatLab<sup>®</sup> software. The routine starts with a baseline subtraction to remove the remaining spectrometer electric noise, followed by the conversion of the signal of each emission spectrum from wavelength to energy units by applying the Jacobian transformation (Mooney and Kambhampati, 2013). Then, the [17,500, 19,500] cm<sup>-1</sup> spectral region was fitted using a multiparametric Gaussian function. Good fits to the experimental data ( $R^2 > 0.99$ ) were obtained with a minimum number of Gaussian functions equal to 10 (two, four, and four Gaussian functions described the  $^2\text{H}_{9/2} \rightarrow ^4\text{I}_{13/2}$ ,  $^4\text{S}_{3/2} \rightarrow ^4\text{I}_{15/2}$ , and  $^2\text{H}_{11/2} \rightarrow ^4\text{I}_{15/2}$  transitions, respectively). The intensities of the transitions were estimated by the sum of the fitted areas of the respectively assigned Gaussian functions. The parameters  $\Delta$  and  $\Delta_{\text{NIR}}$  are computed for the 150 recorded emission spectra for each  $P_D$  and  $T$ , where  $\Delta$ ,  $\Delta_{\text{NIR}}$  and the respective uncertainties ( $\delta\Delta$  and  $\delta\Delta_{\text{NIR}}$ , respectively) are extracted from the corresponding histograms (mean  $\pm$  standard deviation). To evaluate the performance of the luminescent thermometer, the relative thermal sensitivity,  $S_r$ , and the minimum temperature uncertainty,  $\delta T$ , are determined, as follows (Brites et al., 2016):

$$S_r = \frac{1}{\Delta} \left| \frac{\partial \Delta}{\partial T} \right| = \frac{\Delta E}{k_B T^2} \quad (1)$$

and

$$\delta T = \frac{1}{S_r} \frac{\delta \Delta}{\Delta} \quad (2)$$

where  $\delta\Delta$  is the uncertainty in the determination of  $\Delta$ .  $S_r$ , which represents the relative  $\Delta$  change per temperature degree, is an intrinsic property of the nanothermometer material (Brites et al., 2016).

## Results and discussion

### Primary thermometer

Figure 2 illustrates the emission spectra of **1** for selected  $P_D$  values exhibiting Er<sup>3+</sup> transitions in the green,  $^2\text{H}_{11/2} \rightarrow ^4\text{I}_{15/2}$  and

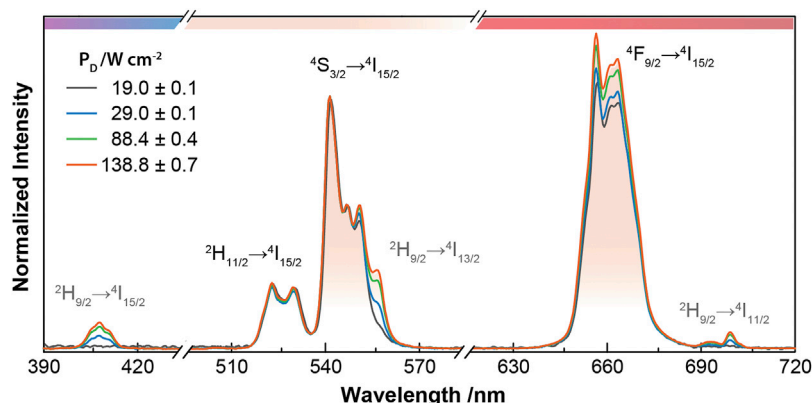


FIGURE 2

Normalized upconversion emission spectra of **1** as a function of  $P_D$  measured at room temperature. The spectra are normalized to the  $4S_{3/2} \rightarrow 4I_{15/2}$  transition.

$4S_{3/2} \rightarrow 4I_{15/2}$ , and red spectral regions,  $4F_{9/2} \rightarrow 4I_{15/2}$  (Auzel, 2004). Evidence of the  $2H_{9/2}$  level population can be found in the transitions in the blue,  $2H_{9/2} \rightarrow 4I_{15/2}$ , and red spectral region,  $2H_{9/2} \rightarrow 4I_{11/2}$ . Additionally, the band overlapping with the  $4S_{3/2} \rightarrow 4I_{15/2}$  emission corresponds to the  $2H_{9/2} \rightarrow 4I_{13/2}$  transition, whose intensity shows similar power-dependence to the  $2H_{9/2} \rightarrow 4I_{11/2,15/2}$  transitions (Berry and May, 2015; Cho et al., 2017). Since the population of the  $2H_{9/2}$  level is reached via a three-photon upconversion process, the intensity of radiative transitions from the  $2H_{9/2}$  level shows a different behavior with  $P_D$  than the  $2H_{11/2} \rightarrow 4I_{15/2}$  and  $4S_{3/2} \rightarrow 4I_{15/2}$  transitions (Renner-Lecuna et al., 2011; Zhou et al., 2013; Cho et al., 2017). A similar trend is observed for  $4F_{9/2} \rightarrow 4I_{15/2}$ , where, at higher  $P_D$ , the upper levels,  $2H_{11/2}$  and  $4S_{3/2}$  become saturated favoring the population of the  $4F_{9/2}$  emitting level due to nonradiative relaxations upon the local heating induced by the laser excitation (Kraft et al., 2018; Maturi et al., 2021). The emission spectra of **2** and **3** measured at the lowest measured  $P_D$  display analogous emission spectra of **1**, except for the worse SNR (Supplementary Figure S1). As the shell gets thicker, the luminescence quenching effects are reduced (Pini et al., 2022; Shi et al., 2022) leading to higher SNR and advantageously decreased temperature uncertainty. As initially proposed by some of us (Brites et al., 2016), and experimentally implemented by others (Van Swieten et al., 2021), the temperature uncertainty increases as the SNR degrades. The value of the relative thermal uncertainty for **1** is about 78% and 49% smaller than those obtained for **2** and **3**, respectively, in similar excitation and collection conditions (Supplementary Figure S2). For this reason, **1** was the chosen nanofluid to perform the onward photoluminescent measurements.

The  $Er^{3+}$  emission in the green spectral region, namely the  $2H_{11/2} \rightarrow 4I_{15/2}$  and  $4S_{3/2} \rightarrow 4I_{15/2}$  transitions, have been widely explored for thermometric purposes in light upconverting

nanoparticles since its first report in 2010 (Vetrone et al., 2010). The intensity ratio of these two transitions is temperature-dependent according to Boltzmann statistics, which governs the population distribution between the two thermally coupled levels,  $2H_{11/2}$  and  $4S_{3/2}$ . Recently, these thermometers have been explored as primary luminescent thermometers, in which the intensity ratio between  $2H_{11/2} \rightarrow 4I_{15/2}$  ( $I_H$ ) and  $4S_{3/2} \rightarrow 4I_{15/2}$  ( $I_S$ ) emissions bands are directly related to the absolute temperature,  $T$ , through a well-established equation of state population (Balabhadra et al., 2017; Brites et al., 2019b; Martínez et al., 2019; Back et al., 2020):

$$\frac{1}{T} = \frac{1}{T_0} - \frac{k_B}{\Delta E} \ln \frac{\Delta}{\Delta_0} \quad (3)$$

where  $k_B$  is the Boltzmann constant,  $\Delta E$  is the energy gap between the barycenters of the  $2H_{11/2}$  and  $4S_{3/2}$  levels, and  $\Delta = I_H/I_S$  the thermometric parameter with  $\Delta_0$  being the value at the temperature  $T_0$  (see Supporting Information for the calculus of  $\Delta E$  and  $\Delta_0$ ).

Regarding temperature determination through the intensity ratio between the  $2H_{11/2} \rightarrow 4I_{15/2}$  and  $4S_{3/2} \rightarrow 4I_{15/2}$ , a few works have been raising awareness of the impact of the  $2H_{9/2} \rightarrow 4I_{13/2}$  transition and how it can affect the temperature measurements, especially when a laser  $P_D$  variation is imposed (Martins et al., 2021; Rühl et al., 2021; Van Swieten et al., 2021; Xia et al., 2021).

Figure 3A shows the temperature dependence of the emission spectra of **1** excited at selected  $P_D$  values and set temperatures (297.6, 305.3, and 315.3 K). Since the  $2H_{9/2} \rightarrow 4I_{13/2}$  and  $4S_{3/2} \rightarrow 4I_{15/2}$  emission bands are overlapped, and Equation 3 accounts only for the emissions of the two thermally coupled levels ( $2H_{11/2}$  and  $4S_{3/2}$ ), the emission bands must be decoupled to correctly estimate  $I_S$ . Thus, a spectral deconvolution, consisting of a multiparametric Gaussian fit, is applied and the  $2H_{9/2} \rightarrow 4I_{13/2}$  ( $I_X$ ),  $4S_{3/2} \rightarrow 4I_{15/2}$  ( $I_S$ ), and  $2H_{11/2} \rightarrow 4I_{15/2}$  ( $I_H$ ) transitions

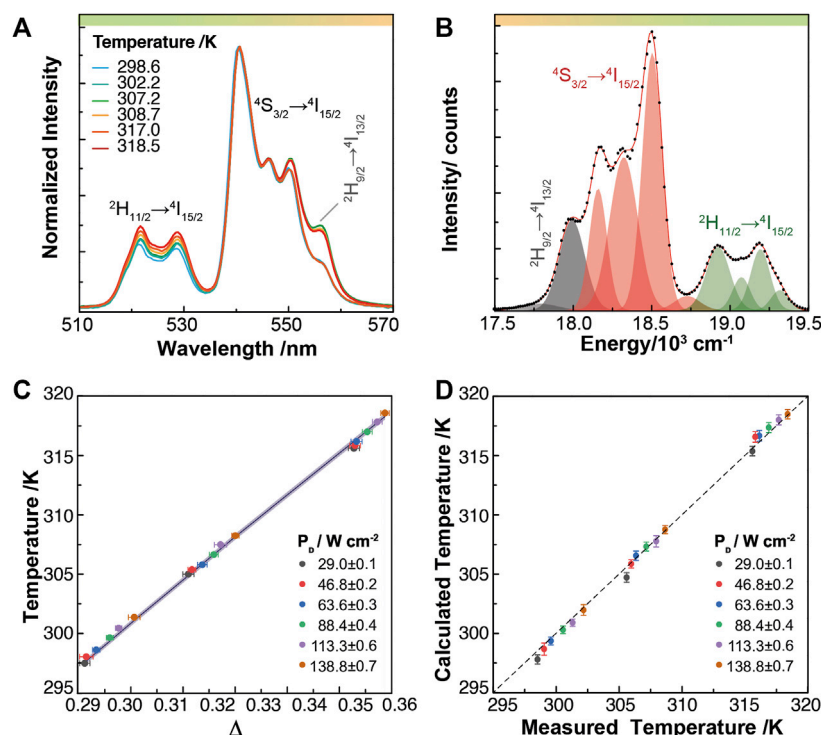


FIGURE 3

(A) Temperature-dependent upconversion emission spectra of **1** excited at 29.0, 88.4 and 138.8  $\text{W cm}^{-2}$ . (B) Spectral Gaussian deconvolution of the emission spectrum measured at 302.2 K and 138.8  $\text{W cm}^{-2}$ . The black dots and the red line represent the experimental data and the fit envelope of the spectrum, respectively. The shadowed areas correspond to the Gaussian functions assigned to the  $^2\text{H}_{9/2} \rightarrow ^4\text{I}_{13/2}$  (black),  $^4\text{S}_{3/2} \rightarrow ^4\text{I}_{15/2}$  (red), and  $^2\text{H}_{11/2} \rightarrow ^4\text{I}_{15/2}$  (green) transitions. (C) Temperature dependence of the experimental  $\Delta$  values determined under laser excitation at different  $P_D$  values. The horizontal error bars represent the error in the measured thermometric parameters (Supplementary Equation S1 in Supporting Information). The line is the theoretical prediction of the temperature (Equation 3) and the shadowed area is the corresponding uncertainty (Supplementary Equation S2 in Supporting Information). (D) Measured temperature (thermocouple reading) versus calculated temperature (Equation 3) under laser excitation at different  $P_D$  values. The vertical error bars correspond to the shadowed area of the line represented in C. The thermocouple accuracy is 0.1 K.

intensities are estimated by the sum of the fitted areas of the assigned Gaussians to the respective transitions (Figure 3B) (see further details in Materials and Methods).

We observe that the calculated  $\Delta$  are within the theoretical prediction by Equation 3, independently of the excitation  $P_D$  values (Figure 3C).  $\Delta$  is converted to absolute temperature substituting the corresponding parameters ( $\Delta_0$ ,  $T_0$ , and  $\Delta E$ , Supplementary Figures S3, S4 and Supporting Information for further details) in Equation 3. The calculated temperatures are in excellent agreement with the experimental ones, demonstrating that **1** works as a primary luminescent thermometer. Besides guaranteeing reliable temperature measurements, the primary luminescent thermometer demonstrated the correct decoupling of both transitions ( $^2\text{H}_{9/2} \rightarrow ^4\text{I}_{13/2}$  and  $^4\text{S}_{3/2} \rightarrow ^4\text{I}_{15/2}$ ) in the  $P_D$  range of 29.0–138.8  $\text{W cm}^{-2}$ . Moreover, it is experimentally verified, for the first time, the independence of the primary luminescent thermometer on excitation  $P_D$  (Figure 3D).

The  $S_r$  of **1** is within the commonly reported range for  $\text{Er}^{3+}$  based nanothermometers ( $\sim 0.2$ – $1\%$   $\text{K}^{-1}$ ), since  $\Delta E$  is not

considerably affected by its host matrix (Figure 4A). Besides the material,  $\delta T$  also depends on the SNR of the measurement, which means this figure of merit is strongly affected by the type and performance of the detector and experimental conditions, such as luminescent material quantity, acquisition time, and background noise, thus precluding a fair comparison with reported values in the literature (Brites et al., 2016; Van Swieten et al., 2022). Nevertheless, in this work, the minimum  $\delta T$  is 0.3 K at 297.5 K (Figure 4B), which is above 0.2 K, the minimum possible value, as reported by (Van Swieten et al. (2022)).

## NIR radiation sensor

The high sensitivity of the  $^2\text{H}_{9/2} \rightarrow ^4\text{I}_{13/2}$  intensity to  $P_D$  values led us to further study these luminescent nanoparticles as a potential NIR radiation sensor. Since emission intensities depend on a multitude of parameters (e.g., temperature,

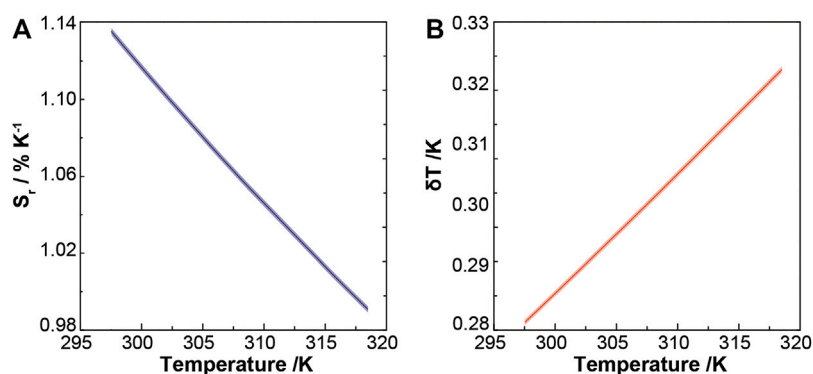


FIGURE 4

(A) Relative thermal sensitivity and (B) temperature uncertainty of **1**. The corresponding uncertainties (Supplementary Equations S3, S4 in Supporting Information) are represented by the shadowed areas.

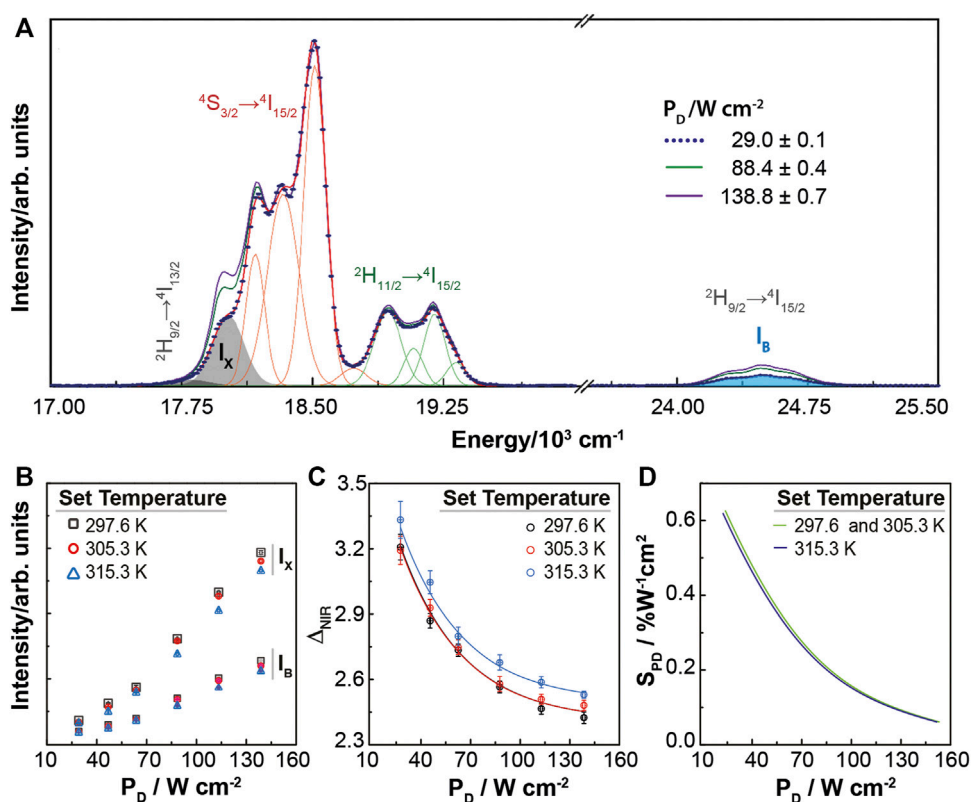


FIGURE 5

(A) Upconversion emission spectra of **1** for selected  $P_D$  values (297.6 K set temperature) depicting the spectral Gaussian deconvolution (green and red lines ascribed to  $^2H_{11/2} \rightarrow ^4I_{15/2}$  and  $^4S_{3/2} \rightarrow ^4I_{15/2}$  transitions) and the  $I_X$  and  $I_B$  areas for 29.0  $W\ cm^{-2}$  (grey and blue shadowed regions). Dependence on  $P_D$  of (B)  $I_X$  and  $I_B$  and (C)  $\Delta_{NIR}$ , for the indicated set temperatures. The lines correspond to the best fits to the experimental data using Equation 4 ( $r^2 > 0.98$ ). (D) Corresponding relative sensitivity to  $P_D$  of the NIR sensor based on **1**.



power density, sensor concentration, material inhomogeneities and optoelectronic drifts in detection) (Brites et al., 2012), we define the NIR radiation sensing parameter as an intensity ratio,  $\Delta_{\text{NIR}} = I_X/I_B$ , calculated using the emission intensity of the  $^2\text{H}_{9/2} \rightarrow ^4\text{I}_{15/2}$  ( $I_B$ ) and  $^2\text{H}_{9/2} \rightarrow ^4\text{I}_{13/2}$  ( $I_X$ ) transitions (Figure 5A).

The power-dependence of  $I_X$  and  $I_B$  is different (Figure 5B) resulting in a decreasing  $\Delta_{\text{NIR}}$  with  $P_D$  values (Figure 5C). Changing  $P_D$  for the set temperatures 297.6 and 305.3 K,  $\Delta_{\text{NIR}}$  is the same within the uncertainty, while at a higher set temperature (315.3 K) an offset in  $\Delta_{\text{NIR}}$  values is observed. Therefore, we characterize 1 as a NIR sensor with a specific calibration according to the working temperature ranges (298.5–308.7 K and 315.6–318.5 K, Figure 3D).

To determine a working calibration curve that describes  $\Delta_{\text{NIR}}$  variation in the measured  $P_D$  range, we assume a generic and empirical equation that better fits the experimental data since we lack a theoretical model. As the behavior observed for  $\Delta_{\text{NIR}}$  variation is similar in both temperature ranges and only differs by an offset, the following function:

$$\Delta_{\text{NIR}} = A \exp\left(-\frac{P_D}{t}\right) + y_0 \quad (4)$$

was fitted to both experimental datasets with  $A$  and  $t$  parameters shared between the two fits while  $y_0$  was kept free (Figure 5C). The resulting fitting parameters are  $A = 1.74 \pm 0.09$ ,  $t = 37 \pm 1 \text{ W cm}^{-2}$ ,  $y_{01} = 2.41 \pm 0.01$  and  $y_{02} = 2.50 \pm 0.01$ , corresponding to  $y_0$  in the 298.5–308.7 K and 315.6–318.5 K ranges, respectively. Inspired by the definition of the relative thermal sensitivity of a thermometer (Equation 1), we define the relative sensitivity to  $P_D$ ,  $S_{PD}$ , as a figure of merit to characterize the NIR sensor:

$$S_{PD} = \frac{1}{\Delta_{\text{NIR}}} \left| \frac{\partial \Delta_{\text{NIR}}}{\partial P_D} \right| = \left| \frac{-\Delta_{\text{NIR}} + y_0}{t \Delta_{\text{NIR}}} \right| \quad (5)$$

yielding a maximum value of  $0.5\% \text{ W}^{-1} \cdot \text{cm}^2$  at  $29.0 \text{ W cm}^{-2}$  (Figure 5D), which is higher than the value reported for the luminescent  $\text{Cr}^{3+}$ -based ratiometric radiation sensor,  $0.07\% \text{ W}^{-1} \text{ cm}^2$ , (Marciniak et al., 2022).

## Conclusion

The  $\text{Er}^{3+}$  emission of the  $\text{NaGdF}_4/\text{NaGdF}_4:\text{Yb}^{3+}, \text{Er}^{3+}/\text{NaGdF}_4$  upconverting nanoparticles upon 980 nm laser excitation was used to develop a luminescent dual nanosensor synchronously measuring the temperature and the delivered laser pump power. Both sensing capabilities use the same simple instrumentation, providing reliable temperature readout through the concept of luminescent primary thermometry to resolve the overlapping of the  $^2\text{H}_{9/2} \rightarrow ^4\text{I}_{13/2}$  and  $^4\text{S}_{3/2} \rightarrow ^4\text{I}_{15/2}$  emissions. Moreover, the measurements are independent and there are no temperature- $P_D$  crossover effects in the studied temperature. This dual-sensor

shows potential for laser-assisted biomedical applications, such as *in-vivo* real-time temperature monitoring during photothermal therapies, where human exposure to NIR laser radiation must be strictly controlled to avoid healthy tissue damage and, thus, ensuring a safe and efficient therapy implementation. In context, under the International Commission on Non-Ionizing Radiation Protection (ICNIRP) guidelines, skin exposure to 980 nm laser radiation is limited to  $0.73 \text{ W cm}^{-2}$  for exposures times of 10 s to 8 h (Ziegelberger, 2013). However, for deliberate exposure as part of medical treatment, these radiation limits vary according to the procedure and instrumentation regulated by U.S. Food and Drug Administration (FDA) (FDA, 2020), and thus demand for flexible in situ power verification.

## Data availability statement

The raw data supporting the conclusions of this article will be made available by the authors, without undue reservation.

## Author contributions

JM: Photoluminescence characterization, draft and figures preparation. AS, AB, and FV: Conceptualization, supervising the synthesis of the particles, data curation, and validation of the synthesis and structural characterization of the prepared particles. CB, RF, and LC: Conceptualization of the luminescent thermometry and delivered laser power density sensor, methodology of photoluminescence measurements, data curation on photoluminescence, validation, writing, reviewing, and editing on the final manuscript and figures.

## Funding

This work was developed within the scope of the project CICECO-Aveiro Institute of Materials, UIDB/50011/2020, UIDP/50011/2020 and LA/P/0006/2020, financed by national funds through the FCT/MEC (PIDDAC).

## Acknowledgments

JM and AS are grateful to FCT (SFRH/BD/139710/2018) and Fonds de Recherche du Québec-Nature et technologies (FRQNT) for financial support in the form of scholarships for doctoral studies, respectively. AB acknowledges funding support from Comunidad de Madrid through TALENTO grant ref. 2019-T1/IND-14014.

## Conflict of interest

The authors declare that the research was conducted in the absence of any commercial or financial relationships that could be construed as a potential conflict of interest.

## Publisher's note

All claims expressed in this article are solely those of the authors and do not necessarily represent those of their affiliated

organizations, or those of the publisher, the editors and the reviewers. Any product that may be evaluated in this article, or claim that may be made by its manufacturer, is not guaranteed or endorsed by the publisher.

## Supplementary material

The Supplementary Material for this article can be found online at: <https://www.frontiersin.org/articles/10.3389/fphot.2022.1037473/full#supplementary-material>

## References

- Auzel, F. (2004). Upconversion and anti-Stokes processes with  $f$  and  $d$  ions in solids. *Chem. Rev.* 104, 139–174. doi:10.1021/cr020357g
- Back, M., Casagrande, E., Brondin, C. A., Ambrosi, E., Cristofori, D., Ueda, J., et al. (2020). Lanthanide-doped  $\text{Bi}_2\text{SiO}_5/\text{SiO}_2$  core-shell upconverting nanoparticles for stable ratiometric optical thermometry. *ACS Appl. Nano Mat.* 3, 2594–2604. doi:10.1021/acsanm.0c00003
- Balabhadra, S., Debasu, M. L., Brites, C. D. S., Ferreira, R. A. S., and Carlos, L. D. (2017). Upconverting nanoparticles working as primary thermometers in different media. *J. Phys. Chem. C* 121, 13962–13968. doi:10.1021/acs.jpcc.7b04827
- Bastos, A. R. N., Brites, C. D. S., Rojas-Gutierrez, P. A., DeWolf, C., Ferreira, R. A. S., Capobianco, J. A., et al. (2019). Thermal properties of lipid bilayers determined using upconversion nanothermometry. *Adv. Funct. Mat.* 29, 1905474–1905510. doi:10.1002/adfm.201905474
- Berry, M. T., and May, P. S. (2015). Disputed mechanism for NIR-to-red upconversion luminescence in  $\text{NaYF}_4:\text{Yb}^{3+}, \text{Er}^{3+}$ . *J. Phys. Chem. A* 119, 9805–9811. doi:10.1021/acs.jpca.5b08324
- Borges, F. H., Martins, J. C., Caixeta, F. J., Pereira, R. R., Carlos, L. D., Ferreira, R. A. S., et al. (2021). Primary thermometers based on sol–gel upconverting  $\text{Er}^{3+}/\text{Yb}^{3+}$  Co-doped yttrium tantalates with high upconversion quantum yield and emission color tunability. *J. Sol-Gel Sci. Technol.* 102, 249–263. doi:10.1007/s10971-021-05673-0
- Boyer, J.-C., Vetrone, F., Cuccia, L. A., and Capobianco, J. A. (2006). Synthesis of colloidal upconverting  $\text{NaYF}_4$  nanocrystals doped with  $\text{Er}^{3+}$ ,  $\text{Yb}^{3+}$  and  $\text{Tm}^{3+}$ ,  $\text{Yb}^{3+}$  via thermal decomposition of lanthanide trifluoroacetate precursors. *J. Am. Chem. Soc.* 128, 7444–7445. doi:10.1021/ja061848b
- Brites, C. D. S., Balabhadra, S., and Carlos, L. D. (2019a). Lanthanide-based thermometers: At the cutting-edge of luminescence thermometry. *Adv. Opt. Mat.* 7, 1801239–1801330. doi:10.1002/adom.201801239
- Brites, C. D. S., Lima, P. P., Silva, N. J. O., Millán, A., Amaral, V. S., Palacio, F., et al. (2012). Thermometry at the nanoscale. *Nanoscale* 4, 4799–4829. doi:10.1039/c2nr30663h
- Brites, C. D. S., Martínez, E. D., Urbano, R. R., Rettori, C., and Carlos, L. D. (2019b). Self-calibrated double luminescent thermometers through upconverting nanoparticles. *Front. Chem.* 7, 267–310. doi:10.3389/fchem.2019.00267
- Brites, C. D. S., Millán, A., and Carlos, L. D. (2016). “Lanthanides in luminescent thermometry,” in *Handbook on the physics and chemistry of rare earths*. Editors J.-C. Bünzli and V. K. Pecharsky (Netherlands: Elsevier, B.V.), 339–427. doi:10.1016/b978-0-12-405183-2.0005
- Caixeta, F. J., Bastos, A. R. N., Botas, A. M. P., Rosa, L. S., Souza, V. S., Borges, F. H., et al. (2020). High-quantum-yield upconverting  $\text{Er}^{3+}/\text{Yb}^{3+}$ -organic-inorganic hybrid dual coatings for real-time temperature sensing and photothermal conversion. *J. Phys. Chem. C* 124, 19892–19903. doi:10.1021/acs.jpcc.0c03874
- Carrasco, E., Del Rosal, B., Sanz-Rodríguez, F., De La Fuente, Á. J., Gonzalez, P. H., Rocha, U., et al. (2015). Intratumoral thermal reading during photo-thermal therapy by multifunctional fluorescent nanoparticles. *Adv. Funct. Mat.* 25, 615–626. doi:10.1002/adfm.201403653
- Chen, X., Jin, L., Kong, W., Sun, T., Zhang, W., Liu, X., et al. (2016). Confining energy migration in upconversion nanoparticles towards deep ultraviolet lasing. *Nat. Commun.* 7, 10304. doi:10.1038/ncomms10304
- Cho, Y., Song, S. W., Lim, S. Y., Kim, J. H., Park, C. R., and Kim, H. M. (2017). Spectral evidence for multi-pathway contribution to the upconversion pathway in  $\text{NaYF}_4:\text{Yb}^{3+}, \text{Er}^{3+}$  phosphors. *Phys. Chem. Chem. Phys.* 19, 7326–7332. doi:10.1039/c7cp00048k
- Dantelle, G., Reita, V., and Delacour, C. (2021). Luminescent  $\text{Yb}^{3+}, \text{Er}^{3+}$ -doped  $\alpha\text{-La}(\text{IO}_3)_3$  nanocrystals for neuronal network bio-imaging and nanothermometry. *Nanomaterials* 11, 479. doi:10.3390/nano11020479
- Debasu, M. L., Oliveira, H., Rocha, J., and Carlos, L. D. (2020). Colloidal  $(\text{Gd}_{0.98}\text{Nd}_{0.02})_2\text{O}_3$  nanothermometers operating in a cell culture medium within the first and second biological windows. *J. Rare Earths* 38, 483–491. doi:10.1016/j.jre.2019.12.011
- Di, X., Wang, D., Zhou, J., Zhang, L., Stenzel, M. H., Su, Q. P., et al. (2021). Quantitatively monitoring in-situ mitochondrial thermal dynamics by upconversion nanoparticles. *Nano Lett.* 21, 1651–1658. doi:10.1021/acs.nanolett.0c04281
- Dos Santos, L. F., Martins, J. C., Lima, K. O., Gomes, L. F. T., De Melo, M. T., Tedesco, A. C., et al. (2022). In-vitro assays and nanothermometry studies of infrared-to-visible upconversion of nanocrystalline  $\text{Er}^{3+}, \text{Yb}^{3+}$  co-doped  $\text{Y}_2\text{O}_3$  nanoparticles for theranostic applications. *Phys. B Condens. Matter* 624, 413447. doi:10.1016/j.physb.2021.413447
- Dramicanin, M. (2018). *Luminescence thermometry: methods, materials, and applications*. Sawston: Woodhead Publishing.
- FDA (2020). Medical lasers - laws, regulations & performance standards. Radiation-Emitting Prod. Proced. Available at: <https://www.fda.gov/radiation-emitting-products/surgical-and-therapeutic-products/medical-lasers#lrps>.
- Freitas, L. F. de, and Hamblin, M. R. (2016). Proposed mechanisms of photobiomodulation or low-level light therapy. *IEEE J. Sel. Top. Quantum Electron.* 22, 348–364. doi:10.1109/JSTQE.2016.2561201
- Jaque, D., Martínez Maestro, L., Del Rosal, B., Haro-Gonzalez, P., Benayas, A., Plaza, J. L., et al. (2014). Nanoparticles for photothermal therapies. *Nanoscale* 6, 9494–9530. doi:10.1039/c4nr00708e
- Jaque, D., and Vetrone, F. (2012). Luminescence nanothermometry. *Nanoscale* 4, 4301–4326. doi:10.1039/c2nr30764b
- Kim, J. S., Lee, S. K., Doh, H., Kim, M. Y., and Kim, D. K. (2021). Real-time tracking of highly luminescent mesoporous silica particles modified with europium  $\beta$ -diketone chelates in living cells. *Nanomaterials* 11, 343–416. doi:10.3390/nano11020343
- Kraft, M., Würth, C., Muhr, V., Hirsch, T., and Resch-Genger, U. (2018). Particle-size-dependent upconversion luminescence of  $\text{NaYF}_4:\text{Yb}, \text{Er}$  nanoparticles in organic solvents and water at different excitation power densities. *Nano Res.* 11, 6360–6374. doi:10.1007/s12274-018-2159-9
- Marciniak, L., Szalkowski, M., Bednarkiewicz, A., and Elzbieciak-Piecka, K. (2022). A  $\text{Cr}^{3+}$  luminescence-based ratiometric optical laser power meter. *J. Mat. Chem. C* 10, 11040–11047. doi:10.1039/D2TC02348B
- Martínez, E. D., Brites, C. D. S., Carlos, L. D., García-Flores, A. F., Urbano, R. R., and Rettori, C. (2019). Electrochromic switch devices mixing small- and large-sized upconverting nanocrystals. *Adv. Funct. Mat.* 29, 1807758–1807812. doi:10.1002/adfm.201807758
- Martins, J. C., Bastos, A. R. N., Ferreira, R. A. S., Wang, X., Chen, G., and Carlos, L. D. (2021). Primary luminescent nanothermometers for temperature measurements reliability assessment. *Adv. Photonics Res.* 2, 2000169. doi:10.1002/adpr.202000169
- Maturi, F. E., Brites, C. D. S., Silva, R. R., Nigoghossian, K., Wilson, D., Ferreira, R. A. S., et al. (2021). Sustainable smart tags with two-step verification for

anticounterfeiting triggered by the photothermal response of upconverting nanoparticles. *Adv. Photonics Res.* 3, 2100227. doi:10.1002/adpr.202100227

Mooney, J., and Kambhampati, P. (2013). Get the basics right: Jacobian conversion of wavelength and energy scales for quantitative analysis of emission spectra. *J. Phys. Chem. Lett.* 4, 3316–3318. doi:10.1021/jz401508t

Pini, F., Francés-Soriano, L., Peruffo, N., Barbon, A., Hildebrandt, N., and Natile, M. M. (2022). Spatial and temporal resolution of luminescence quenching in small upconversion nanocrystals. *ACS Appl. Mat. Interfaces* 14, 11883–11894. doi:10.1021/acsami.1c23498

Piñol, R., Zeler, J., Brites, C. D. S., Gu, Y., Téllez, P., Carneiro Neto, A. N., et al. (2020). Real-time intracellular temperature imaging using lanthanide-bearing polymeric micelles. *Nano Lett.* 20, 6466–6472. doi:10.1021/acs.nanolett.0c02163

Ramalho, J. F. C. B., Dias, L. M. S., Fu, L., Botas, A. M. P., Carlos, L. D., Carneiro Neto, A. N., et al. (2021). Customized luminescent multiplexed quick-response codes as reliable temperature mobile optical sensors for eHealth and internet of things. *Adv. Photonics Res.* 3, 2100206. doi:10.1002/adpr.202100206

Renner-Lecuna, C., Martín-Rodríguez, R., Valiente, R., González, J., Rodríguez, F., Krämer, K. W., et al. (2011). Origin of the high upconversion green luminescence efficiency in  $\beta$ -NaYF<sub>4</sub>: 2%Er<sup>3+</sup>, 20%Yb<sup>3+</sup>. *Chem. Mat.* 23, 3442–3448. doi:10.1021/cm2004227

Rühl, P., Wang, D., Garwe, F., Müller, R., Haase, M., Krämer, K. W., et al. (2021). Notes on thermometric artefacts by Er<sup>3+</sup> luminescence band interference. *J. Lumin.* 232, 117860–117921. doi:10.1016/j.jlumin.2020.117860

Shen, Y., Santos, H. D. A., Ximenes, E. C., Lifante, J., Sanz-Portilla, A., Monge, L., et al. (2020). Ag<sub>2</sub>S nanoheaters with multiparameter sensing for reliable thermal feedback during *in vivo* tumor therapy. *Adv. Funct. Mat.* 30, 2002730–2002813. doi:10.1002/adfm.202002730

Shi, R., Brites, C. D. S., and Carlos, L. D. (2022). Understanding the shell passivation in In<sup>3+</sup>-doped luminescent nanocrystals. *Small Struct.* 3, 2100194. doi:10.1002/ssstr.202100194

Skripka, A., Benayas, A., Brites, C. D. S., Martín, I. R., Carlos, L. D., and Vetrone, F. (2020). Inert shell effect on the quantum yield of neodymium-doped near-infrared nanoparticles: The necessary shield in an aqueous dispersion. *Nano Lett.* 20, 7648–7654. doi:10.1021/acs.nanolett.0c03187

Van Swieten, T. P., Meijerink, A., and Rabouw, F. T. (2022). Impact of noise and background on measurement uncertainties in luminescence thermometry. *ACS Photonics* 9, 1366–1374. doi:10.1021/acsphotonics.2c00039

Van Swieten, T. P., Van Ommen, T., Van Den Heuvel, D. J., Vonk, S. J. W., Spruit, R. G., Meirer, F., et al. (2021). Mapping elevated temperatures with a micrometer resolution using the luminescence of chemically stable upconversion nanoparticles. *ACS Appl. Nano Mat.* 4, 4208–4215. doi:10.1021/acsanm.1c00657

Vetrone, F., Naccache, R., Zamarrón, A., De La Fuente, A. J., Sanz-Rodríguez, F., Maestro, L. M., et al. (2010). Temperature sensing using fluorescent nanothermometers. *ACS Nano* 4, 3254–3258. doi:10.1021/nn100244a

Wang, J., and Dong, J. (2020). Optical waveguides and integrated optical devices for medical diagnosis, health monitoring and light therapies. *Sensors* 20, 3981. doi:10.3390/s20143981

Wang, Y. (2019). The role of an inert shell in improving energy utilization in lanthanide-doped upconversion nanoparticles. *Nanoscale* 11, 10852–10858. doi:10.1039/C9NR03205C

Xia, X., Volpi, A., Roh, J. Y. D., De Siena, M. C., Gamelin, D. R., Hehlen, M. P., et al. (2021). The impact of <sup>2</sup>H<sub>9/2</sub> → <sup>4</sup>I<sub>13/2</sub> emission from Er<sup>3+</sup> ions on ratiometric optical temperature sensing with Yb<sup>3+</sup>/Er<sup>3+</sup> Co-doped upconversion materials. *J. Lumin.* 236, 118006. doi:10.1016/j.jlumin.2021.118006

Yang, T. D., Park, K., Kim, H.-J., Im, N.-R., Kim, B., Kim, T., et al. (2017). *In-vivo* photothermal treatment with real-time monitoring by optical fiber-needle array. *Biomed. Opt. Express* 8, 3482. doi:10.1364/boe.8.003482

Yuan, M., Wang, R., Zhang, C., Yang, Z., Cui, W., Yang, X., et al. (2018). Exploiting the silent upconversion emissions from a single  $\beta$ -NaYF<sub>4</sub>:Yb/Er microcrystal via saturated excitation. *J. Mat. Chem. C* 6, 10226–10232. doi:10.1039/c8tc02193g

Yuan, M., Wang, R., Zhang, C., Yang, Z., Yang, X., Han, K., et al. (2019). Revisiting the enhanced red upconversion emission from a single  $\beta$ -NaYF<sub>4</sub>:Yb/Er microcrystal by doping with Mn<sup>2+</sup> ions. *Nanoscale Res. Lett.* 14, 103. doi:10.1186/s11671-019-2931-0

Zhou, J., Liu, Q., Feng, W., Sun, Y., and Li, F. (2015). Upconversion luminescent materials: Advances and applications. *Chem. Rev.* 115, 395–465. doi:10.1021/cr400478f

Zhou, S., Deng, K., Wei, X., Jiang, G., Duan, C., Chen, Y., et al. (2013). Upconversion luminescence of NaYF<sub>4</sub>: Yb<sup>3+</sup>, Er<sup>3+</sup> for temperature sensing. *Opt. Commun.* 291, 138–142. doi:10.1016/j.optcom.2012.11.005

Zhu, X., Feng, W., Chang, J., Tan, Y. W., Li, J., Chen, M., et al. (2016). Temperature-feedback upconversion nanocomposite for accurate photothermal therapy at facile temperature. *Nat. Commun.* 7, 10437. doi:10.1038/ncomms10437

Zhu, X., Li, J., Qiu, X., Liu, Y., Feng, W., and Li, F. (2018). Upconversion nanocomposite for programming combination cancer therapy by precise control of microscopic temperature. *Nat. Commun.* 9, 2176. doi:10.1038/s41467-018-04571-4

Ziegelberger, G. (2013). ICNIRP guidelines on limits of exposure to laser radiation of wavelengths between 180 nm and 1,000  $\mu$ m. *Health Phys.* 105, 271–295. doi:10.1097/HP.0b013e3182983fd4



## OPEN ACCESS

## EDITED BY

Verónica de Zea Bermudez,  
University of Trás-os-Montes and Alto  
Douro, Portugal

## REVIEWED BY

Sabu Thomas,  
Mahatma Gandhi University, India  
Ruikang Zhang,  
Hebei Normal University, China

## \*CORRESPONDENCE

João Tedim,  
joao.tedim@ua.pt

## SPECIALTY SECTION

This article was submitted to Inorganic  
Chemistry,  
a section of the journal  
Frontiers in Chemistry

RECEIVED 19 September 2022

ACCEPTED 25 October 2022

PUBLISHED 18 November 2022

## CITATION

Tedim J, Galvão TLP, Yasakau KA,  
Bastos A, Gomes JRB and Ferreira MGS  
(2022), Layered double hydroxides for  
corrosion-related applications—Main  
developments from 20 years of  
research at CICECO.  
*Front. Chem.* 10:1048313.  
doi: 10.3389/fchem.2022.1048313

## COPYRIGHT

© 2022 Tedim, Galvão, Yasakau, Bastos,  
Gomes and Ferreira. This is an open-  
access article distributed under the  
terms of the [Creative Commons  
Attribution License \(CC BY\)](#). The use,  
distribution or reproduction in other  
forums is permitted, provided the  
original author(s) and the copyright  
owner(s) are credited and that the  
original publication in this journal is  
cited, in accordance with accepted  
academic practice. No use, distribution  
or reproduction is permitted which does  
not comply with these terms.

# Layered double hydroxides for corrosion-related applications —Main developments from 20 years of research at CICECO

João Tedim<sup>1\*</sup>, Tiago L. P. Galvão<sup>1</sup>, Kiryl A. Yasakau<sup>1</sup>,  
Alexandre Bastos<sup>1</sup>, José R. B. Gomes<sup>2</sup> and Mario G. S. Ferreira<sup>1</sup>

<sup>1</sup>CICECO-Aveiro Institute of Materials, Department of Materials and Ceramic Engineering, University of Aveiro, Campus Universitário de Santiago, Aveiro, Portugal, <sup>2</sup>CICECO-Aveiro Institute of Materials, Department of Chemistry, University of Aveiro, Campus Universitário de Santiago, Aveiro, Portugal

This work describes the main advances carried out in the field of corrosion protection using layered double hydroxides (LDH), both as additive/pigment-based systems in organic coatings and as conversion films/pre-treatments. In the context of the research topic “Celebrating 20 years of CICECO”, the main works reported herein are based on SECOP’s group (CICECO) main advances over the years. More specifically, this review describes structure and properties of LDH, delving into the corrosion field with description of pioneering works, use of LDH as additives to organic coatings, conversion layers, application in reinforced concrete and corrosion detection, and environmental impact of these materials. Moreover, the use of computational tools for the design of LDH materials and understanding of ion-exchange reactions is also presented. The review ends with a critical analysis of the field and future perspectives on the use of LDH for corrosion protection. From the work carried out LDH seem very tenable, versatile, and advantageous for corrosion protection applications, although several obstacles will have to be overcome before their use become commonplace.

## KEYWORDS

layered double hydroxides, corrosion, nanocontainer, coatings, films, corrosion detection, concrete, computational design

## 1 Introduction

Corrosion can be defined as the deterioration of a metal by chemical or electrochemical reactions with the surrounding environment (Revie and Uhlig, 2008; Jones, 2014). With a wide range of use of metallic substrates in different areas of society, from infrastructures to vehicles and biomedical implants, it is not surprising that its importance can be reflected on economy, efficiency, energy, safety, and conservation factors. All these aspects touch key points in a fast-developing world, still struggling to resume global activity after the COVID-19 pandemic, in parallel with important aspects for present and future generations that are addressed in the UN Sustainability goals, including climate change and circular economy.



TABLE 1 Overview of CICECO's functional LDH for corrosion-related applications.

LDH	Active species	Pigment/film	Type of coating/substrate	References
Zn (2)Al	nitrate	Pigment	AA2024-T3	Poznyak et al. (2009)
Zn (2)Al	quinaldate	Pigment	AA2024-T3	Poznyak et al. (2009)
Zn (2)Al	MBT <sup>-</sup>	pigment	AA2024-T3	Poznyak et al. (2009)
Mg (2)Al	nitrate	pigment	AA2024-T3	Poznyak et al. (2009)
Mg (2)Al	quinaldate	pigment	AA2024-T3	Poznyak et al. (2009)
Mg (2)Al	MBT <sup>-</sup>	pigment	AA2024-T3	Poznyak et al. (2009)
LDH intercalated with different organic corrosion inhibitors				
Zn (2)Al	vanadate	pigment	AA2024-T3	Tedim et al. (2010)
Zn (2)Al	phosphate	pigment	AA2024-T3	Tedim et al. (2010)
Zn (2)Al	MBT <sup>-</sup>	pigment	AA2024-T3	Tedim et al. (2010)
Enhancement of active corrosion protection by combination of inhibitor-loaded LDHs				
Zn (2)Al	vanadate	pigment	AA2024-T3	Zheludkevich et al. (2010)
Mg (2)Al	vanadate	pigment	AA2024-T3	Zheludkevich et al. (2010)
Active protection coatings based on LDH nanocontainers intercalated with corrosion inhibitors				
Zn (2)Al	nitrate	film	AA2024-T3	Tedim et al. (2011)
Zn (2)Al	pyrovanadate	film	AA2024-T3	Tedim et al. (2011)
Nanostructured LDH-container layer grown on top of AA2024 for corrosion protection				
Zn (2)Al	nitrate	pigment	polymer layer	Tedim et al. (2012)
Demonstration of LDH aggressive anion trapping ability in active protective coatings				
Zn (2)Al	MBT <sup>-</sup>	pigment	Galvanised steel	Montemor et al. (2012)
Combination of LDH and cerium molybdate nanocontainers filled with MBT corrosion inhibitor				
Zn (2)Al	vanadate	film	AA2024-T3	Tedim et al. (2013)
Dependence of the performance of LDH conversion films on the metal pre-treatment				
Zn (2)Al	nitrate	film	AA2024-T3	Tedim et al. (2014)
Zn (2)Al	vanadate	film	AA2024-T3	Tedim et al. (2014)
Influence of preparation conditions of LDH conversion films on their protection performance				
Zn (2)Al	MBT <sup>-</sup> and Ce <sup>3+</sup>	pigment	AA2024-T3	Carneiro et al. (2015)
MBT was intercalated, while Ce <sup>3+</sup> was fixed between polyelectrolyte layers on the LDH surface				
Zn (2)Al	nitrate	film	AA2024-T3	Tedim et al. (2016)
Zn (2)Al	vanadate	film	AA2024-T3	Tedim et al. (2016)
SVET analysis of the corrosion protection of LDH conversion films grown on AA2024				
Zn (2)Al	nitrate	pigment	-	Galvão et al. (2016a)
Density functional theory simulation of LDH-NO <sub>3</sub> XRD and interlayer structural features				
Zn (2)Al	vanadate	film	AA2024-T3	Kuznetsov et al. (2016)
Sealing of tartaric sulfuric anodized AA2024 with nanostructured LDH layers				

(Continued on following page)

TABLE 1 (Continued) Overview of CICECO's functional LDH for corrosion-related applications.

LDH	Active species	Pigment/film	Type of coating/substrate	References
Zn (2)Al Density functional theory simulation of LDH based conversion films	nitrate	film	AA2024-T3	Galvão et al. (2017)
Zn (2)Al An LDH layer was grown on PEO coatings for AA2024 and loaded with a corrosion inhibitor	vanadate	film	PEO coatings/AA2024	Mohedano et al. (2017)
Zn (2)Al Study of the antimicrobial activity of LDH-MBT	MBT	pigment	-	Kuznetsova et al. (2017)
Zn (2)Al Study of toxicity induced by LDH-MBT to clams	MBT	pigment	-	Martins et al. (2017b)
Zn (2)Al Study of toxicity induced by LDH-booster biocides to green microalgae, diatoms and mussels, brine shrimps, sea urchins	Cu and Zn pyrithiones	pigment		Gutner-Hoch et al. (2018) Gutner-Hoch et al. (2019)
Zn (2)Al Synergetic active corrosion protection with a cerium doped Y-type zeolite	MBT <sup>-</sup>	pigment	AA2024-T3	Abdolah Zadeh et al. (2018)
Zn (2)Al	nitrate	pigment	AA2024-T3	Yasakau et al. (2018)
Zn (2)Al	vanadate	pigment	AA2024-T3	Yasakau et al. (2018)
Mg (2)Al	chloride	pigment	-	Pérez-Sánchez et al. (2018)
Mg (2)Al	nitrate	pigment	-	Pérez-Sánchez et al. (2018)
Mg (2)Al	carbonate	pigment	-	Pérez-Sánchez et al. (2018)
Zn (2)Al	chloride	pigment	-	Pérez-Sánchez et al. (2018)
Zn (2)Al	nitrate	pigment	-	Pérez-Sánchez et al. (2018)
Zn (2)Al	carbonate	pigment	-	Pérez-Sánchez et al. (2018)
Development of a classic molecular dynamics framework to explore LDHs				
Zn (2)Al LDH-MBT film modified with hydrophobic silane with anticorrosion and antimicrobial properties	MBT	film	AA2024-T3	Neves et al. (2019)
Zn (2)Al One-step synthesis and growth mechanism of LDH based conversion coatings on zinc	nitrate	film	zinc	Mikhailau et al. (2019)
Mg (2)Al	phosphate	pigment	cast iron	Vieira et al. (2019)
Mg (2)Al Cast iron corrosion protection with LDHs	Ce <sup>3+</sup> /phosphate	pigment	cast iron	Vieira et al. (2019)
Zn (2)Al	nitrate	pigment	-	Novell-Leruth et al. (2020)
Zn (2)Al	MBT <sup>-</sup>	pigment	-	Novell-Leruth et al. (2020)
Molecular dynamics simulation of the structure and hydration of LDH-NO <sub>3</sub> and LDH-MBT				
Zn (2)Al	nitrate	film	AA2024-T3	Bouali et al. (2020a)
Zn (2)Al	nitrate	film	zinc	Bouali et al. (2020b)
Synchrotron high-resolution XRD was used to follow the anion exchange of nitrate by chloride				

(Continued on following page)

TABLE 1 (Continued) Overview of CICECO's functional LDH for corrosion-related applications.

LDH	Active species	Pigment/film	Type of coating/substrate	References
Zn (2)Al	nitrate	pigment	Steel-Reinforced Concrete	Gomes et al. (2020)
Zn (2)Al	nitrite	pigment	Steel-Reinforced Concrete	Gomes et al. (2020)
LDHs for controlling the corrosion of steel in reinforced concrete				
Zn (2)Al	nitrate	film	zinc	Iuzviuk et al. (2020)
<i>In situ</i> synchrotron XRD was used to follow the substitution with chloride, sulfate and vanadate				
Zn (2)Al	Hexacyanoferrate	pigment	carbon steel	Wilhelm et al. (2020)
Mg (2)Al	Hexacyanoferrate	pigment	carbon steel	Wilhelm et al. (2020)
Hexacyanoferrate-intercalated LDHs for steel corrosion detection				
Zn (2)Al	nitrite	pigment	cement	Mir et al. (2021)
Stability and chloride entrapping capacity of ZnAl-NO <sub>2</sub> in a cement model system				
Mg (2)Al	Ce <sup>3+</sup>	pigment	AA2024-T3	Vieira et al. (2022)
Mg (2)Al-Ce to prolong the service life of aluminum alloys				

There are several ways of preventing and protect metallic substrates against corrosion, being one of the most used, the application of protective coatings. With the increased awareness of society for human and environmental impact aspects, it became clear that several of the most effective solutions used to protect metals against corrosion lacked sufficient environmental friendliness. Hence, corrosion inhibitors such as those derived from Cr(VI) species were prohibited and, as a result, the whole field of science and corrosion engineering has been struggling to find equally effective additives and pigments, but less toxic and harmful, to replace chromates (Zheludkevich, 2009).

In this short review we address one of the materials which have been proposed and developed during the last 2 decades as promising for corrosion protection: layered double hydroxides (LDH). In the context of the Research Topic “Celebrating 20 Years of CICECO–Aveiro Institute of Materials”, this review is mostly focused on the main works developed in SECOP–Surface Engineering and Corrosion protection group over the last 15 years, giving proper context of those works with respect to current literature whenever relevant. Table 1 summarizes the main works which SECOP group at CICECO carried out over the years, some of them in collaboration with other groups. In addition, readers are entitled to read more

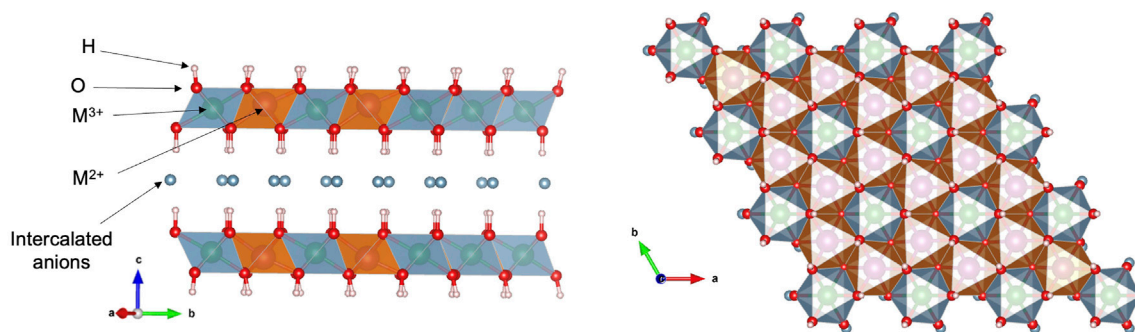


FIGURE 1

Schematic representation of the structure of a generic traditional layered double hydroxides (LDH) orthogonally and along the crystallographic axis c, depicting the distorted octahedral sheets. The figures of structural models have been constructed using VESTA software (Momma and Izumi, 2011; Leal et al., 2022). Reproduced from (Leal et al., 2022) with permission from Elsevier.

general and recent reviews on LDH applied to corrosion protection elsewhere (Bouali et al., 2020b; Mir et al., 2020; Tabish et al., 2021; Leal et al., 2022).

## 2 Layered double hydroxides

### 2.1 Structure and properties

LDH are a class of versatile materials with useful properties associated with their anion exchange abilities for a wide range of materials' applications including adsorbents, catalysts and its support, ceramic precursors, drug carriers, corrosion inhibitor carriers, supercapacitors, nanocomposites, energy conversion and storage, carbon dioxide sequestration, among many others (Wang and Ohare, 2012; Tian et al., 2016).

LDH are lamellar compounds having molecular formula  $[M(II)_{1-x}M(III)_x(OH)_2]^{x+}(A_{x/n}^{n-})_x \cdot mH_2O$ , where  $x$  ranges from 0.22 to 0.33,  $M$  is a metal and  $A^{n-}$  is a  $n^-$  valent anion. They are also called hydrotalcites since their structure is like that of the natural hydrotalcite, i.e.,  $Mg_6Al_2(OH)_{16}[CO_3] \cdot 4H_2O$ . This clay consists of positively charged brucite-like layers [brucite =  $Mg(OH)_2$ ] where the cations are octahedrally coordinated with  $OH^-$ , in slightly distorted octahedra that share their edges, forming the LDH layer, and of interlayer anions balancing the positive charge due to the partial substitution of bivalent  $Mg$  with trivalent  $Al$  and allowing the layers to stack onto one another by electrostatic forces.

Figure 1 shows a schematic representation of a generic LDH structure having molar ratio of  $M^{2+}:M^{3+}$  of 2:1, as frequently described in many minerals intercalated with hydrated carbonate anions (Guo et al., 2010; Wang and Ohare, 2012). The positions that the  $M^{3+}$  and  $M^{2+}$  octahedra adopt in the layer are well defined in the crystal lattice, although it depends on the ratio between the trivalent and the divalent species. In this case, the  $M^{2+}$  octahedra are in such configuration that resembles a dioctahedral-like sheet, in which the  $M^{3+}$  ions would occupy its vacancies (Leal et al., 2022).

The peculiar property of LDH is the possibility to exchange the interlayer anions; for this reason, they are also named anionic clays. LDH possess sandwich-like structure in which negative inorganic or organic anions are sandwiched into positively charged metal layers in a repeating manner. The hydroxide layers could be fabricated with combination of different divalent ( $Cd^{2+}$ ,  $Mn^{2+}$ ,  $Fe^{2+}$ ,  $Pb^{2+}$ ) and trivalent ( $Al^{3+}$ ,  $Cr^{3+}$ ,  $Fe^{3+}$ ) metal ions. The structural characteristics of the LDH allow the possibility to use a wide variety of intercalation compounds either by modification of the chemical composition of the hydroxide layer or by chemical/structural modification of the

interlayers. The particle size could change from nanometer (nm) to micrometer ( $\mu m$ ), depending on synthesis conditions.

Depending on the application, several methods (Bouali et al., 2020b) were reported for the formation of LDH powders relying mostly on chemical reactions (Levin et al., 1996; Takei et al., 2014), namely, co-precipitation, sol-gel method using alkoxides and/or acetylacetonate as starting precursors (Prinnetto et al., 2000), urea hydrolysis method (Hibino and Ohya, 2009), hydrothermal method (Zhi and Guo, 2005), reformation (Theiss et al., 2012) and mechanical milling (Qu et al., 2019). The co-precipitation method is the most straightforward and commonly applied. This method could involve one-step synthesis only, or be followed by anion exchange reactions between the interlayer anion and the targeted anion (two-step synthesis).

Typically, the synthesis by co-precipitation can be achieved at either variable pH (titration co-precipitation) or constant pH conditions. The latter option is preferable to obtain pure, crystalline LDH. During the reaction, the pH of the solution is kept constant by the simultaneous addition of an alkaline solution (e.g.,  $NaOH$  or  $NH_3 \cdot H_2O$ ) together with the precursor solution of mixed metal salts (metals that will be part of the LDH). Usually, an alkaline solution is chosen according to the corresponding metal salts and the desired anion to be intercalated between the LDH galleries. Additionally, since it is difficult to avoid the presence of  $CO_2$  in air, it is further advised to work under nitrogen or argon flow to avoid the formation of LDH structures with intercalated carbonate species, if these are not desirable.

The LDH product of the synthesis by co-precipitation relies upon a crucial control of the pH of the reaction medium, the concentration and nature of both alkaline and metal precursor solutions (besides the molar ratio of the metal cation itself), the temperature and aging time (Bouali et al., 2020b).

In the attempts to confer corrosion protection to metallic substrates "smart" active corrosion protective systems have been searched to replace chromate and pre-treatment containing coatings, due to the known health problems that  $Cr(VI)$  can originate. There are several reviews available in the literature listing numerous materials developed to replace chromates, including polymeric microcapsules, oxide nanoparticles (Zheludkevich, 2009; Zheludkevich et al., 2012; Zhang et al., 2018) and graphene (Kulyk et al., 2022), just to mention a few. Among those that have received the most attention are LDH. The reason behind the choice of selecting LDH for corrosion protection, to the detriment of other nanocontainers (Bouali et al., 2020b) can be explained by the fact that LDH have the remarkable option to be used both in form of anticorrosion pigments incorporated into a coating system (Zheludkevich et al.,



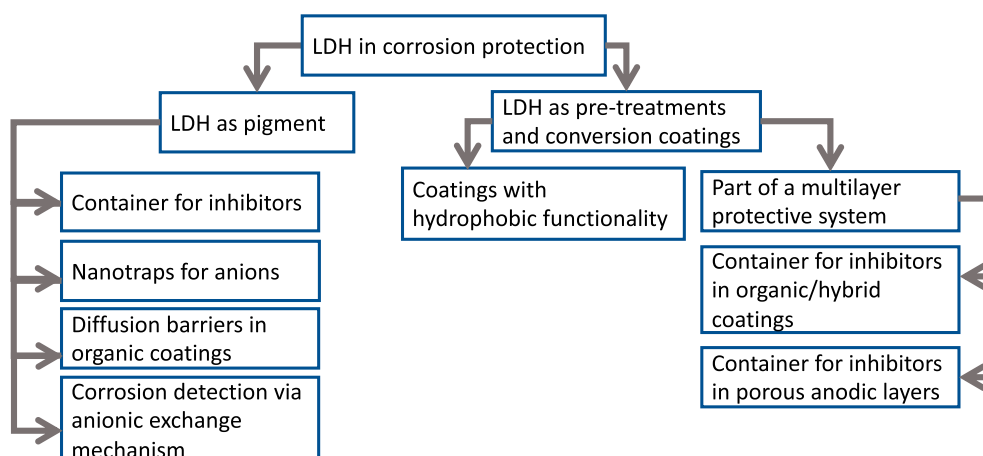


**FIGURE 2**  
Application of LDH in corrosion protection.

2012), as well as a conversion coating on the metal (Tedim et al., 2016). This means that it can be easily adapted according to different requirements. On one hand, LDH can be used as a powder/slurry to confer additional active protection properties to a barrier coating by the addition of a self-healing functionality (Zheludkevich et al., 2010). On the other hand, LDH can be applied directly to the metal surface as a conversion film/coating, similarly to Cr(VI) technology, if there is a need for the first coating layer (close to the metal) to be an active corrosion protective system (Tedim et al., 2011). LDH are among the most investigated and with more application potential anion exchange nanocontainers for “smart” active corrosion protection (Zheludkevich et al., 2010; Wang and Ohare, 2012; Zhang et al., 2015).

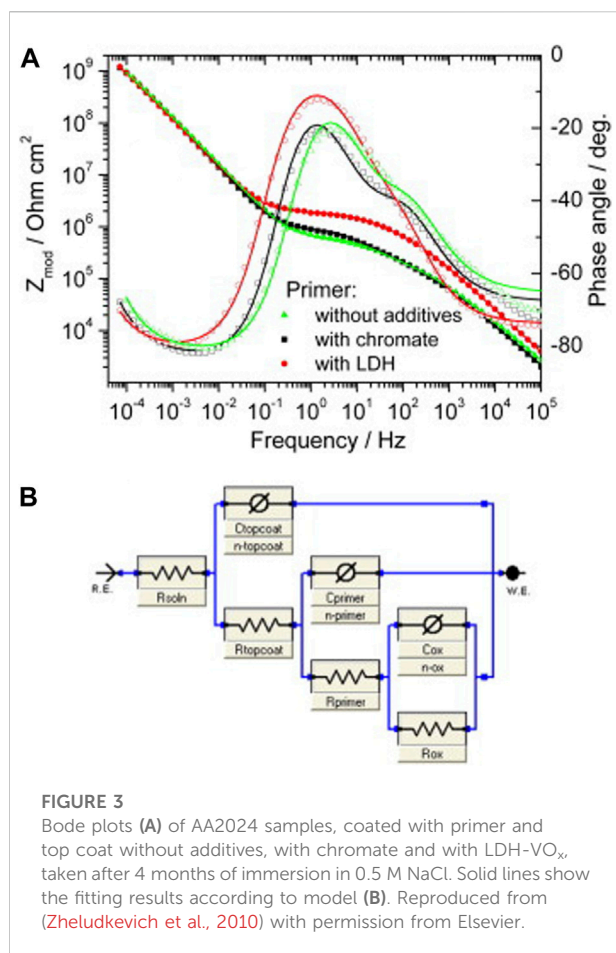
Keeping in mind that most well-known and studied LDH are based on compositions such as ZnAl or MgAl, attempts to develop LDH-based conversion films have occurred during the last 25 years (Leggat et al., 2002; Kuznetsov et al., 2016; Visser et al., 2016; Mikhailau et al., 2019; Iuzviuk et al., 2020). The simplest *in-situ* LDH growth can be achieved by a co-precipitation process, which is an extension of the LDH powder synthesis by co-precipitation. In this case, the substrate to be treated is also one of the precursors. In the case of Al substrate, M/Al LDH films can be fabricated by the immersion of the substrate in a bath containing a metal cation  $M^{2+}/M^+$  ( $Zn^{2+}$ ,  $Mg^{2+}$ ,  $Li^+$ , etc.) precursor in certain conditions (pH, temperature, concentration etc.), while the  $Al^{3+}$  ions are generated by the dissolution of the Al substrate. Specific anions could be carried out through anion exchange reaction by simple immersion of the LDH treated Al alloy into a solution containing the respective species at a specific pH, concentration, and temperature.

## 2.2 Application of LDH in corrosion

The corrosion protection performance of LDH mainly comes from its structural and chemical properties, including the formation of physical protective films, presence of inhibitors contained in the LDH nanostructure and self-healing effect. The controlled release of inhibitors from LDH occurs by anion exchange, normally with chloride ions present in the aggressive medium, leading to their capture, and then a double protection effect. Figure 2 summarizes the main roles that LDH can play in the context of corrosion protection.

The breadth of works reporting layered double hydroxides-based materials, both as particle-like (so-called nanocontainers) and as conversion coatings, dates back to the mid 1990s—beginning of 2000s, with pioneering works by Buchheit (Buchheit et al., 2002; Zhang and Buchheit, 2002; Buchheit et al., 2003), Williams and McMurray (McMurray and Williams, 2004; Williams and McMurray, 2004). Both conversion coatings and active corrosion protection pigments based on LDH aimed at replacing hexavalent Cr, particularly in applications where Cr(VI)-based pre-treatments and primers had been the main solution for anti-corrosion protection: the aerospace industry (Twite and Bierwagen, 1998). Hence, it is not surprising that these early works have focused mostly on aluminum alloys.

With respect to the use of LDH as anticorrosion pigments in organic coatings, Williams and McMurray investigated nitrate-, carbonate- and chromate-containing Mg-Al LDH, which were added to a polyvinyl butyral (PVB) coating applied onto AA2024-T3 substrates to investigate how these pigments could affect the development of filiform corrosion (McMurray and Williams, 2004). In all the LDH-modified coatings, the rates



of coating delamination were reduced and the inhibiting efficiency of the LDHs was found to be dependent on the nature of the intercalating anion, with the chromate-containing LDH displaying the best result. In another work by the same authors (Williams and McMurray, 2004), different organic corrosion inhibitors, namely benzotriazole, ethyl xanthate and oxalate were anion-exchanged in LDH and their effect on filiform corrosion of a PVB-coated AA2024-T3 substrate were surveyed. Benzotriazole was found to render the best inhibition efficiency.

In an independent contemporary study by Buchheit and colleagues (Buchheit et al., 2003), the preparation of Zn-Al LDH intercalated with decavanadate was described and the effect of this LDH material was surveyed in an epoxy resin coating. The resulting Zn-Al LDH was prepared firstly by modifying the vanadate speciation from meta to decavanadate form and then obtained the LDH material by direct coprecipitation in a carbonate-free environment. The structural analysis performed by XRD, unambiguously showed the expansion of galleries when decavanadate was present in the interlayer spacing between the mixed-metal hydroxide sheets, with respect to chloride-containing LDH. Release studies were

also performed in 0.5 M NaCl solution, revealing leaching of both Zn and V species, with the latter ascribed to anion-exchange reaction between chlorides and vanadates. On the other hand, Zn release was claimed to be associated with co-intercalation of Zn<sup>2+</sup> or with formation of a hetero-polyoxometalate of Zn and V, which became subsequently immobilized in the LDH galleries. Furthermore, corrosion inhibition studies demonstrated a clear protective effect of the coatings loaded with V-containing LDH (salt spray tests and electrochemical impedance spectroscopy, EIS, studies). In addition, the same work described the possibility of using LDH as a corrosion sensing pigment as XRD analysis of LDH-vanadate (LDH-VO<sub>x</sub>) exposed to NaCl solution, directly as powder or embedded within the epoxy resin, reveals the occurrence of a second LDH phase associated with intercalation of chlorides, constituting a way of detecting the earlier uptake of electrolyte by the coating (corrosion sensing).

As mentioned earlier, the works by Buchheit's group have not been restricted to the use of LDH as pigments in organic coatings. They also laid the foundations for some of the most trending works in terms of active protection, Cr-free, surface pre-treatments and Li-based pigments for organic coatings (Liu et al., 2016). In their works, Buchheit and colleagues used different oxidizing bath chemistries to obtain LiAl LDH (Buchheit et al., 1994; Buchheit et al., 2002; Zhang and Buchheit, 2002), in an attempt to reduce processing times for coating formation and increase in corrosion resistance. The results showed that nitrate/persulfate bath chemistries gave rise to better corrosion resistance when compared to carbonate or nitrate-only based chemistries. The healing characteristics of the obtained coatings was ascribed to competition between chloride attack and sealing of coatings formed under oxidizing chemistries. In another work (Buchheit et al., 2002) a Ce LDH conversion coating was investigated as a potential self-healing protective system using a simulated scratch cell. The healing effect of this system was associated to the introduction of Ce in the LDH as a soluble, high-oxidation state species which in presence of solution dissolve and Ce<sup>4+</sup> is reduced and precipitated as Ce<sup>3+</sup> compound on the exposed Al sites.

## 2.2.1 LDH as reservoirs for corrosion inhibitors in coatings

### 2.2.1.1 New LDH compositions for active corrosion protection

The first few works describing layered double hydroxides in the literature revealed promising properties of this class of materials for corrosion protection. They were reported right after the concept of self-healing being described by White et al. (White et al., 2001) and, as a result, the concept was also adapted to the field of anti-corrosion protective coatings. Healing in this context does not necessarily imply a healing of defects in polymeric systems *via* recovery of structural integrity

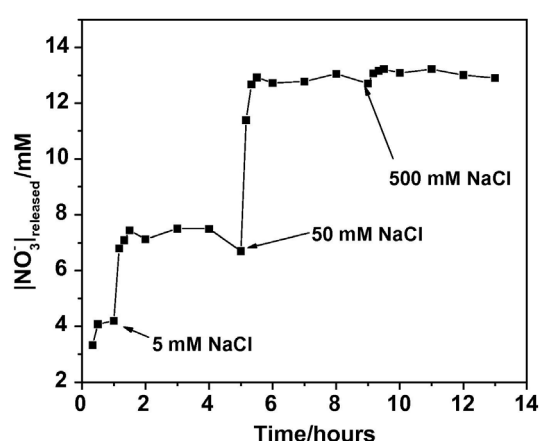


**FIGURE 4**  
Release profiles of  $\text{NO}_3^-$  from Zn-Al- $\text{NO}_3$  LDH (0.5 wt.%) in solution, in the presence of increasing amounts of NaCl. Reproduced from (Tedim et al., 2012) with permission from Elsevier.

of the protective coating only (e.g., healing by polymerization), but also the controlled release of active species such as water-displacing hydrophobic agents and corrosion inhibitors, from the so-called *smart micro and nanocontainers* which are embedded within polymeric matrices and are able to protect the exposed surface—*functional self-healing*. Several works have reported a wide range of materials as potential systems for active corrosion protection, from mesoporous particles to polymeric microcapsules (Zheludkevich et al., 2012; Zhang et al., 2018). In this section the most relevant work published by our group using LDH as smart nanocontainers for corrosion protection is revisited.

The early works reported by our group on LDH have been based on ZnAl and MgAl compositions, intercalated with different corrosion inhibitors. Vanadate-intercalated ZnAl and MgAl LDH were prepared by direct co-precipitation and ion-exchange (Zheludkevich et al., 2010). Vanadates were intercalated in the pyrovanadate ( $\text{V}_2\text{O}_7^{4-}$ ) form by careful control of pH conditions. Structural studies revealed that LDH- $\text{VO}_x$  prepared by ion-exchange of LDH- $\text{NO}_3$  were more crystalline when compared to LDH- $\text{VO}_x$  prepared by direct coprecipitation. Furthermore, ion exchange studies revealed the release of V-containing species and EIS measurements demonstrated the inhibiting properties of these LDH against corrosion of AA2024-T3 in NaCl solution. The performance of ZnAl LDH- $\text{VO}_x$  prepared by ion-exchange was compared against strontium chromate pigment, using both type of pigments in an epoxy-resin primer, as part of a coating multilayer system composed of anodizing layer, water-based primer and water-based epoxy topcoat layers. EIS measurements showed that ZnAl LDH- $\text{VO}_x$  lead to an increase on both the oxide resistance and pore resistance of

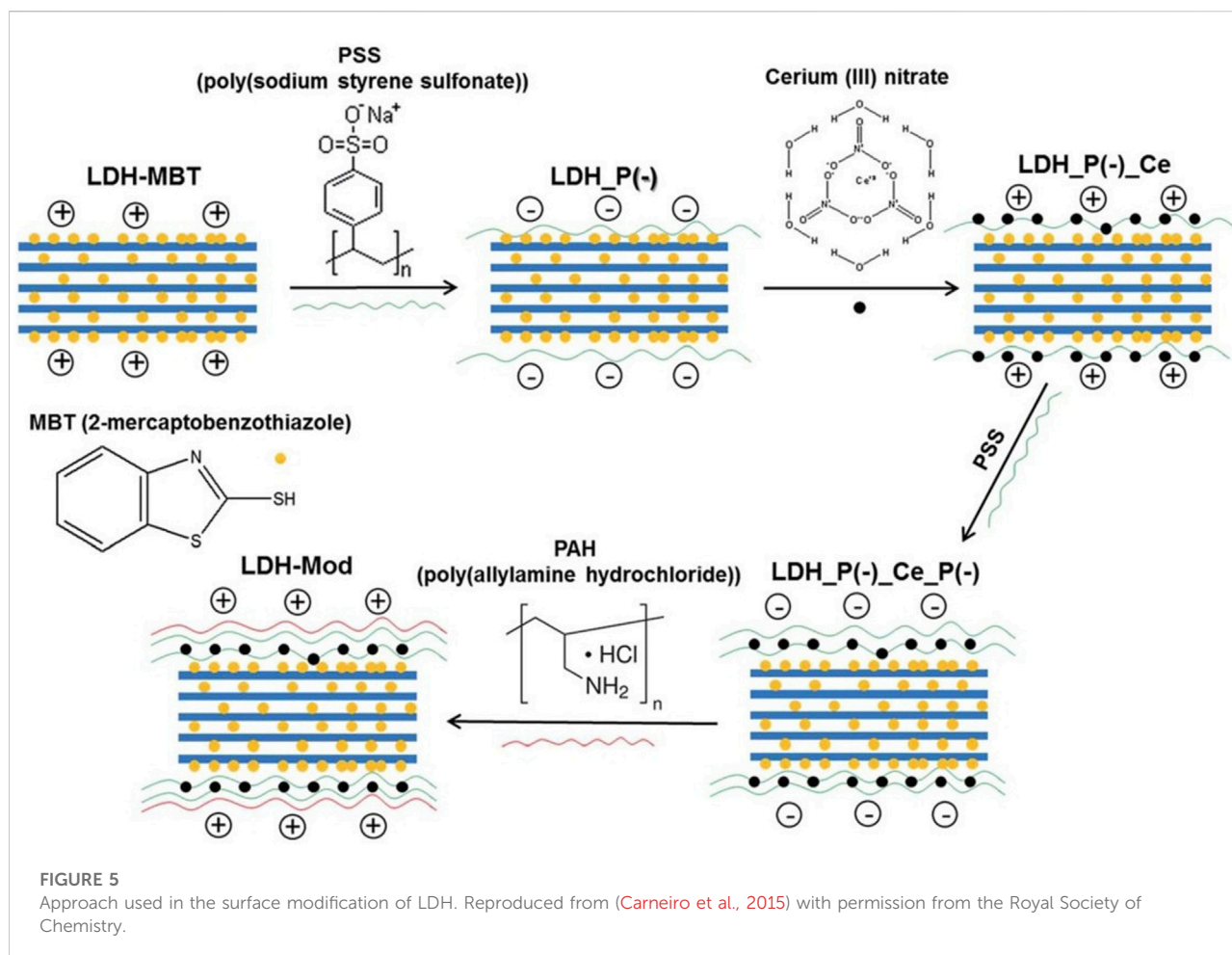
the organic coating system, when compared to the chromate-base pigment (Figure 3). Moreover, accelerated tests were also performed. The results showed that the chromate-based paint system was better than the LDH-based paint system in terms of neutral salt spray and resistance to osmotic blistering but worst against filiform corrosion.

In a detailed XRD work by Salak and colleagues (Salak et al., 2010), the authors went deeper on understanding structural changes occurring in LDH when nitrates were exchanged with pyrovanadates. The results from this study revealed that when anion exchange occurs between nitrates and vanadates, there is a decrease on the average crystallite size of LDH, which was ascribed to mechanical fragmentation of the crystallites because of the fast anion exchange reaction.

In another work, different organic inhibitors, namely quinaldate (QA) and 2-mercaptobenzothiazolate (MBT) anions were intercalated in MgAl and ZnAl LDH by ion exchange. XRD patterns and FTIR spectra revealed the presence of these anions within the LDH galleries. Release studies performed in aqueous NaCl solutions with different concentrations demonstrated that higher amounts of MBT were released in more concentrated NaCl solutions, which is consistent with an equilibrium-driven ion-exchange mechanism (Poznyak et al., 2009). The EIS studies showed that in the beginning of immersion tests, uncoated AA2024-T3 samples exhibited relatively low impedance values, probably due to the increase of solution pH associated with the release of QA and MBT. However, as the immersion time progressed a thick layer composed of corrosion products and inhibitor protected the substrate in the presence of ZnAl LDH-MBT, leading to an overall increase of impedance in the presence of this material. These results were discussed in terms of differences between inhibiting effect rendered by QA and MBT under different pH conditions. The way MBT and benzotriazole (BTA) arrange within Zn-Al and Mg-Al LDH galleries was also evaluated in a different work by *in-situ* XRD measurements (Serdechnova et al., 2016). Herein, the authors found out that upon the formation of LDH-MBT and LDH-BTA, there is occurrence of an additional LDH-OH phase, while in the (ZnAl or MgAl) LDH-MBT and MgAl LDH-BTA phases these organic anions form a double layer arrangement with tilted orientation with respect to the metal hydroxide sheets. In the case of ZnAl LDH, exchange between nitrates and BTA was not possible due to the formation of a compound based on zinc oxide and BTA.

#### 2.2.1.2 The chloride entrapment effect

Having been reported in the literature the effect of ion-exchange on inhibitor modified LDH, the sole effect associated with chloride entrapment within LDH and its contribution for the electrolyte permeability through a coating layer, had not been addressed before. In the work carried out by Tedim and colleagues (Tedim et al., 2012), Zn-Al LDH loaded with



nitrates and chlorides were used as “empty” and “full” forms of LDH. Organic coatings loaded with ZnAl LDH-NO<sub>3</sub> exhibited lower permeability to chlorides, which was demonstrated to be associated with exchange of chlorides with nitrates, while the coating with ZnAl LDH-Cl revealed a permeability to chlorides even higher than the reference coating (i.e., without LDH). Authors claimed that this increase in the coating permeability could be due to the combining effects of LDH not being able to entrap chlorides and to the disruption of coating barrier properties due to agglomeration of LDH particles during coating preparation. Equally relevant was the release/ion-exchange experiments performed, which unambiguously revealed the controlled release capacity of LDH to exchange anions with the surrounding environment, as a function of the concentration of chlorides available in the medium (Figure 4).

### 2.2.1.3 Combination of inhibitors in micro- and nanocontainers

In a work published in 2010, the effect of combining LDH with different corrosion inhibitors, namely MBT, vanadates and phosphates, was reported (Tedim et al., 2010). Herein, authors

found that when LDH intercalated with different corrosion inhibitors were combined in solution, the overall impedance associated with AA2024-T3 in 0.05 M NaCl was larger than for each individual LDH. This was the first report on the combination of different nanocontainers rendering a positive effect in terms of corrosion protection. However, when the same strategy was attempted within coatings, the results were found to be different: when both LDH-MBT and LDH-VO<sub>x</sub> were added to the primer or to the sol-gel layer, the impedance was lower than when LDH-MBT was added to the sol-gel pre-treatment and LDH-VO<sub>x</sub> was added to the primer. Overall, this work revealed that compatibility between the nanocontainer and the coating matrix is of paramount importance when designing a protective coating system and that the availability of inhibitors in the pre-treatment sol-gel layer for short timescale action combined with vanadates in the primer layer to render long-term protection was a promising way of combining these two LDH.

In another work carried out in collaboration with Montemor, Kordas and colleagues (Montemor et al., 2012), LDH and cerium molybdate nanocontainers, both loaded with MBT, were combined to render corrosion protection to galvanized steel.



In this work, although the inhibitor was the same, the release-driven mechanisms and release timescales were expectedly different. Several electrochemical techniques, namely the scanning vibrating electrode technique (SVET) and EIS were used to investigate the self-healing ability of epoxy-based organic coatings modified with these two types of nanocontainers. The results obtained revealed a positive effect in combining the two nanocontainers, with LDH-MBT displaying a fast, short-term response whereas CeMo-MBT provided a long-term inhibition effect to protect metallic substrate. More recently, a joint work with Garcia and colleagues demonstrated that the combination of LDH-MBT with a Ce(III)-loaded zeolite provided superior protection to AA2024-T3, when the micro and nanocontainers were both added to the same water-based epoxy coating in a specific proportion (10:90) between LDH and the zeolite (Abdolah Zadeh et al., 2018).

Another strategy that was explored using LDH and combination of different corrosion inhibitors relied on the surface modification of LDH with polyelectrolyte shells (Carneiro et al., 2015). It is well-known in the literature that polyelectrolytes are sensitive to changes in pH, which can be used as a triggering condition for release of corrosion inhibitors, as anodic and cathodic reactions associated with corrosion processes may lead to local pH changes (Shchukin et al., 2006). Hence, we decided to use LDH-MBT modified with polyelectrolyte shells, between which  $\text{Ce}^{3+}$  was immobilized (Figure 5). The EIS results revealed that the modification of LDH-MBT with polyelectrolyte shells had to main effects: first, there was an increase in the impedance magnitude of AA2024-T3 directly exposed to the these modified LDH, when compared to LDH-MBT, which was interpreted as a combination of having the two inhibiting species being released from the nanocontainer; second, the effect of polyelectrolytes on not letting the pH in solution increase as much as when MBT was released from LDH-MBT, as shown previously (Poznyak et al., 2009), thus contributing for an high stability of the native aluminum oxide layer. Furthermore, the presence of the polyelectrolyte shells also led to a change in the release mechanism of MBT, with MBT being released more extensively under alkaline conditions rather than more concentrated NaCl solutions. Finally, the polyelectrolyte shells contributed to a better compatibility of the LDH with a sol-gel coating system used as model formulation in this work, by reducing the exposure of the sol-gel matrix to MBT and  $\text{Ce}^{3+}$  during coating preparation.

#### 2.2.1.4 Sonication route for the synthesis of LDH

One of the most used routes for the synthesis of LDH is based on direct coprecipitation of a mixed metal salts solution under controlled pH, followed by hydrothermal treatment for several hours to promote crystallization of the LDH. However, for the sake of industrial production, any process that can lead to shorter production times and reduction of water consumption is welcomed. Recently, Salak and colleagues developed a

sonication-based procedure to produce MgAl LDH. In a joint work with the group of Kareiva and co-workers (Sokol et al., 2019), they obtained MgAl LDH- $\text{H}_2\text{PO}_4$  via a sol-gel route, combined with successive anion-exchange processes between  $\text{OH}^-$  and  $\text{Cl}^-$  and between  $\text{Cl}^-$  and  $\text{H}_2\text{PO}_4^-$ . They observed that the use of ultrasound treatment with 1.5 kW power accelerated the anion-exchange step. A similar approach was applied to obtain a MgAl, Ce LDH- $\text{PO}_4$ . The resulting LDH material was studied as an anti-corrosion nanomaterial for corrosion inhibition of cast iron (Vieira et al., 2019). In another study, the authors applied the sonication treatment during the crystallization step for 5 min to obtain a MgAl, Ce LDH- $\text{NO}_3$  by co-precipitation. When exposed to UV radiation, the obtained material was found to degrade and the release of  $\text{Ce}^{3+}$  was accelerated (Vieira et al., 2022).

#### 2.2.2 LDH: From nanocontainers to pre-treatments

LDH nanocontainers have proven to be an effective means of enhancing the anticorrosion capabilities of organic coatings applied to metallic substrates. Despite that, there are several drawbacks associated with the use of nanocontainers in coatings. For instance, agglomerates formed when mixing nanocontainers with the liquid coating formulation may disrupt the barrier properties of the coating matrix in which the particles are distributed. If the coating matrix has high barrier properties LDH could effectively lower the barrier properties of such coatings leading to faster deterioration of the protection system. When the nanocontainers are located far away from the metallic surface the transport of the inhibitive species from the LDH to the metallic surface may be limited due to diffusion. However, if LDH are distributed close to the metallic surface, it will be much easier for the inhibiting species to reach the surface and provide inhibiting action. One of the ways to achieve this objective is by surface modification of a metallic surface via conversion films based on LDH.

In general, there are more methodologies to produce LDH coatings than LDH powders, and some of them are often separated into different groups (Guo et al., 2018; Tabish et al., 2021; Cao et al., 2022): *in situ* hydrothermal treatment, steam coating (Ishizaki et al., 2013; Kamiyama et al., 2016), spin coating (Zhang et al., 2008), co-precipitation (Zhou et al., 2015; Zhou et al., 2017), electrochemical deposition (Indira and Vishnu Kamath, 1994; He et al., 2020). The *in situ* hydrothermal methods are commonly used for the synthesis of LDH films on a broad range of metallic substrates using different water chemistry, concentration, pH of solutions, and temperature conditions. Typically, the solutions for LDH growth contain metal salts precursors and auxiliary salts and the growth is done at a high temperature directly at the metal surface (Buchheit et al., 2002). For the hydrothermal method, specific conditions are used i.e., temperature  $>100^\circ\text{C}$  and pressure  $>1$  bar under which LDH growth is performed most notably on Al alloys (Mohammadi et al., 2021) and Mg alloys (Wang et al., 2010; Ye et al., 2018). When there is slow kinetics of dissolution of metallic substrates that supply the

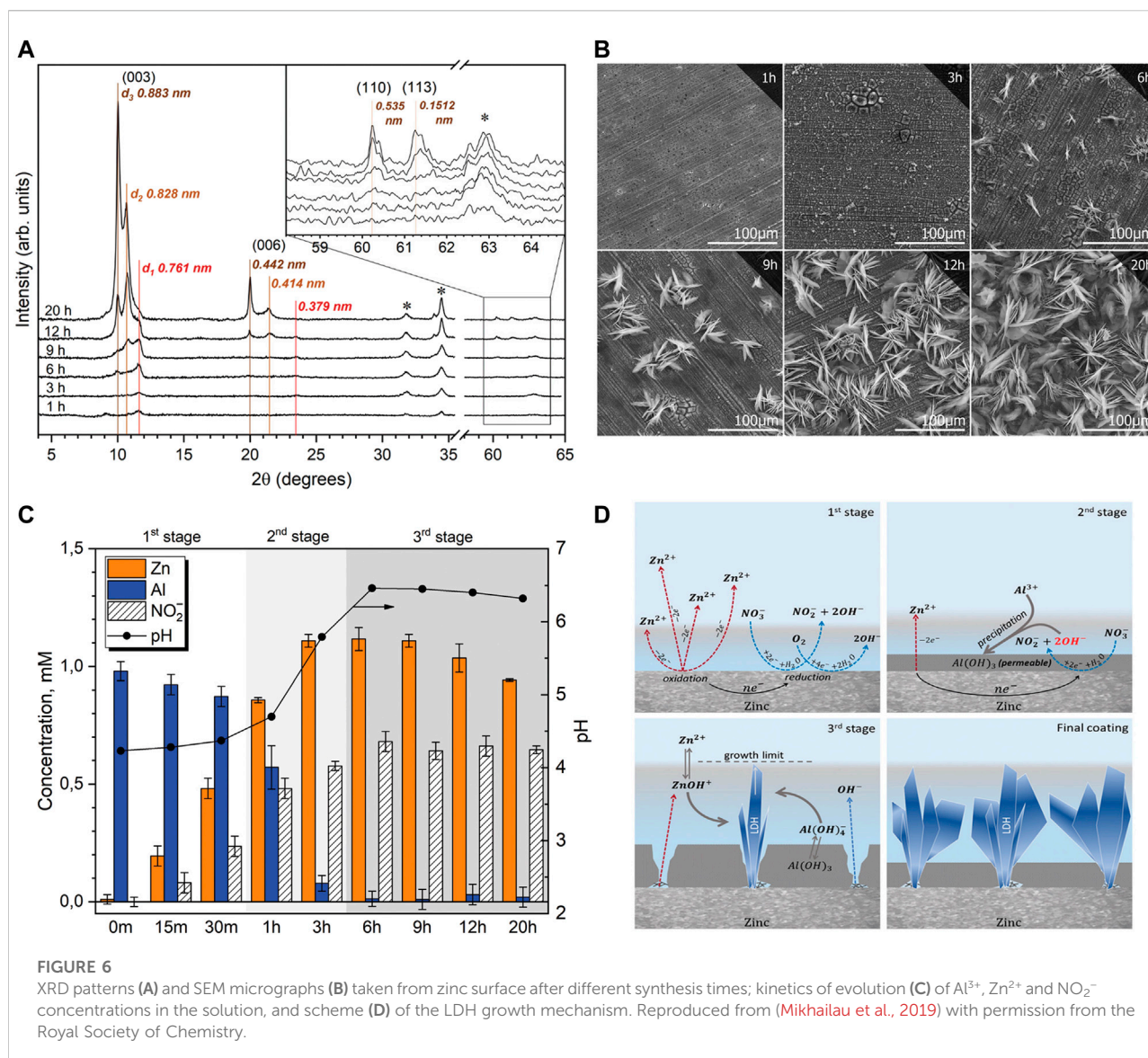


FIGURE 6

XRD patterns (A) and SEM micrographs (B) taken from zinc surface after different synthesis times; kinetics of evolution (C) of Al<sup>3+</sup>, Zn<sup>2+</sup> and NO<sub>2</sub><sup>-</sup> concentrations in the solution, and scheme (D) of the LDH growth mechanism. Reproduced from (Mikhailau et al., 2019) with permission from the Royal Society of Chemistry.

cations for the LDH growth, organic and inorganic complexants e.g., NH<sub>3</sub> (Guo et al., 2009; Lei et al., 2013), nitrilotriacetic acid (NTA) or ethylenediaminetetraacetic acid (EDTA) (Shulha et al., 2018) can be used to control the concentration of soluble metal species in the solution. The steam growth method (Ishizaki et al., 2013; Kamiyama et al., 2016) was proposed as an alternative to the classical hydrothermal method. Its main difference compared with the latter is that the metallic samples are placed in a hydrothermal capsule above the liquid level, so the steam reacts with the substrate surface forming the LDH. Next, the methods such as spin coating and co-precipitation often employ the hydrothermal treatment as part of the process, however, the obtained coatings lack necessary adhesion towards the metal surface, which prevents their application in corrosion protection. Although the electrochemical deposition of LDH coatings has been known for decades (Indira and Vishnu

Kamath, 1994), there are shortcomings due to fast hydrogen evolution kinetics. Nonetheless, there are reports on the efficiency of corrosion protection of these LDH coatings (Wu et al., 2014; He et al., 2020). In more complex cases the various methods can be combined, which was exploited by some researchers to develop multistep LDH coating formation routes (Chen et al., 2012; Wu et al., 2017).

Buchheit et al. presented one of the first attempts to grow *in situ* hydrotalcite (HT) films on metallic surfaces such as galvanized steel and AA 2024 (Buchheit et al., 1994; Buchheit et al., 2002; Zhang and Buchheit, 2002; Buchheit and Cuan, 2004). It is noteworthy that HT is essentially a LDH and it has a general formula Mg<sub>6</sub>Al<sub>2</sub>CO<sub>3</sub>(OH)<sub>16</sub>·4H<sub>2</sub>O. The XRD patterns collected on samples coated with various HTs do show typical reflections (003) and (006) belonging to the layered structure of

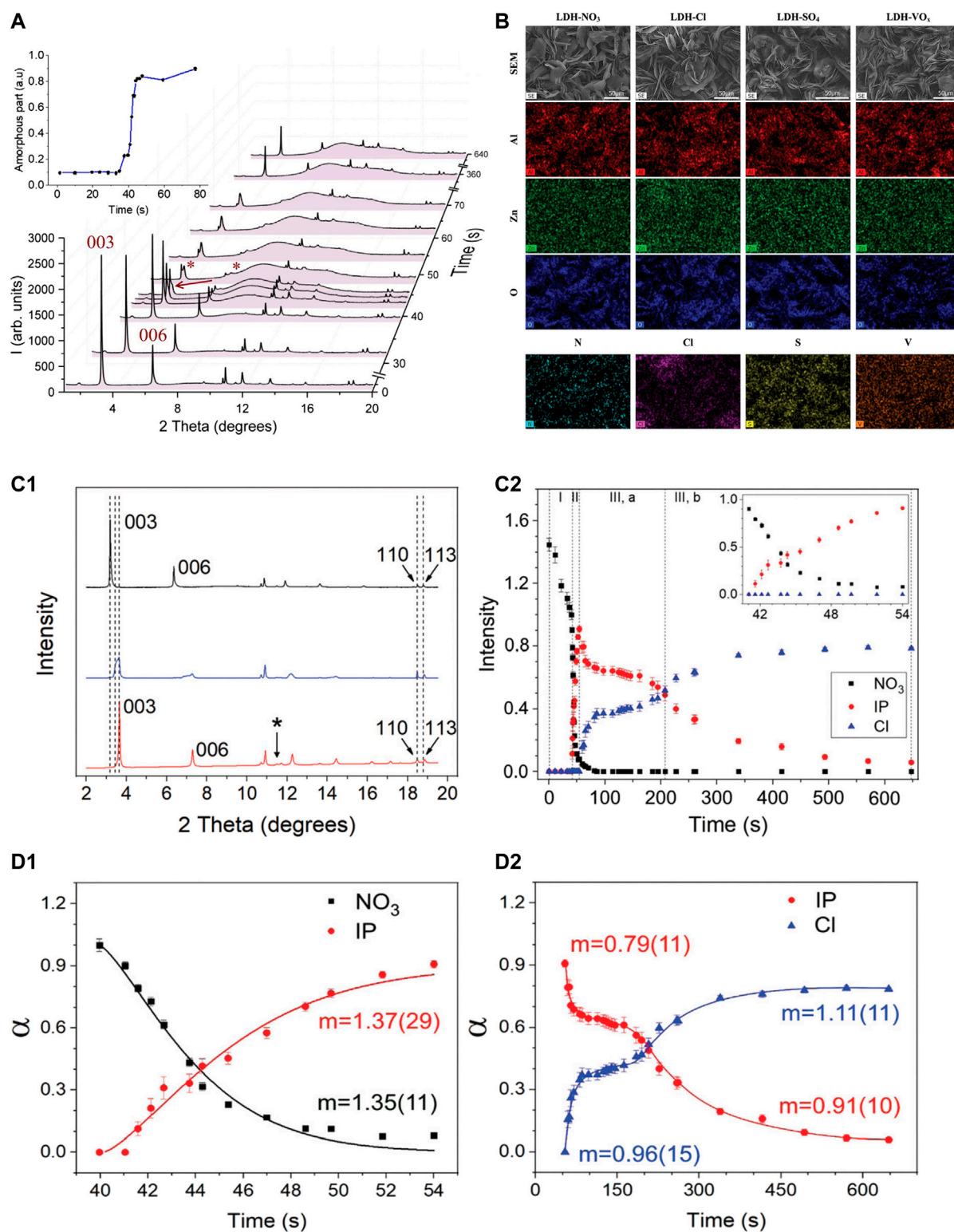


FIGURE 7

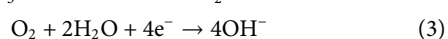
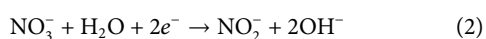
XRD patterns (A) for  $\text{Cl}^-$  intercalation process on Zn coated with LDH (Bouali et al., 2020a); SEM-images and EDS maps (B) of LDHs with  $\text{NO}_3^-$ ,  $\text{Cl}^-$ ,  $\text{SO}_4^{2-}$ ,  $\text{VO}_3^{3-}$ ; (C1) XRD patterns of initial LDH- $\text{NO}_3$  (black), state of coexistence of initial and final phases (blue) and final LDH- $\text{Cl}$  (red) phases; (C2) time evolution of the integral intensity of 003 peaks of the initial (LDH- $\text{NO}_3$ , squares), intermediate (IP, circles) and final (LDH- $\text{Cl}$ , triangles) phases; Kinetic dependences of the degree of substitution of  $\text{NO}_3^-$  by  $\text{Cl}^-$  in Zn-LDH: (D1) interval II: release of  $\text{NO}_3^-$  (black squares), IP formation (red circles); (D2) interval III: IP decrease and formation of the final crystalline phase with  $\text{Cl}^-$ -intercalated (blue triangles). Solid lines are the fittings of the AE model. Reproduced from (Iuzviuk et al., 2020) with permission from the Royal Society of Chemistry.



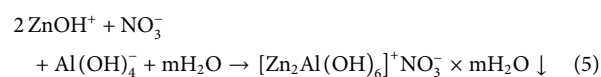
LDH (Buchheit and Cuan, 2004). Albeit HT coatings demonstrate improved corrosion protective properties HT has poor anionic exchange capabilities and cannot contribute to building active corrosion protective coatings based on intercalation of corrosion inhibitive species. Therefore, more elaborate synthesis methods of LDH films were developed. Although later Hoshino et al. (Hoshino et al., 2018) developed a process in which carbonate anions incorporated in LDHs grown on galvanized steel surfaces are substituted by nitrate anions, the process involved methanol as a solvent. A more environmentally safe route is necessary.

One-step *in situ* synthesis of nitrate substituted LDH on zinc surface was demonstrated for the first time in a recent study (Mikhailau et al., 2019). The synthesis was carried out at 90 °C in the solution of 1 mM  $\text{Al}(\text{NO}_3)_3$  and 0.1 M  $\text{NaNO}_3$ . Figure 6A depicts the evolution of diffraction patterns taken from the zinc surface after different immersion times. Figure 6A reveals a pronounced growth of the diffraction peaks at about  $10^\circ 2\theta$  and  $20^\circ 2\theta$  that were assigned to different LDH phases with distinct values of the interlayer distances (basal spacing,  $d$ ), namely  $d_1 = 0.761$  nm,  $d_2 = 0.828$  nm, and  $d_3 = 0.883$  nm. Interestingly the last two  $d$ -values were assigned to the two different LDH phases namely  $d_3$  -  $\text{Zn}_{0.67}\text{Al}_{0.33}\text{-NO}_3$  and  $d_2$  -  $\text{Zn}_{0.75}\text{Al}_{0.25}\text{-NO}_3$ . The  $d_3$  value was comparable to the results obtained in (Salak et al., 2012), while the  $d_2$  value corresponds to the phase in which the ratio of Zn/Al cations increased. The difference between the two phases was due to different tilt angles of  $\text{NO}_3^-$  anions against the layer plane in the LDH gallery with the tilt angle being smaller for the  $d_2$  phase and higher for the  $d_3$  phase. The  $d_1$  LDH phase having the smallest interlayer distance was ascribed to the carbonate intercalated LDH that forms when the solution contained dissolved  $\text{CO}_2$ . The paper states that there were no purification steps performed to remove an excess of  $\text{CO}_2$  thus its intercalation into the LDH gallery as carbonate anions could affect the synthesis. SEM observations revealed a step-by-step evolution of the surface microstructure starting from the appearance of Al hydroxide film on top of the zinc surface, followed by gradually appearance of footprints of zinc oxide interweaved with the crystalline network that could correspond to the  $d_1$  LDH phase (Figure 6B). It was proposed that the  $d_1$  phase served as nucleation site for the growth of the  $d_2$  and  $d_3$  phases.

The growth mechanism suggested in the work (Mikhailau et al., 2019) emphasized several key processes that involved electrochemical oxidation/reduction reactions of zinc (1), nitrate (2) and oxygen (3) and chemical precipitation at the zinc surface described below.



These processes have been experimentally confirmed by analytical measurements of concentrations of the respective species (Figure 6C) and by EDS analysis of the surface at the initial immersion time that suggested the presence of Al oxide/hydroxide film. The scheme presented in Figure 6D shows the main steps by which the LDH growth process occurs namely oxidation-reduction processes that give rise to pH increase, deposition of Al hydroxide layer and gradual growth of LDH. The chemical equation of LDH precipitation is presented in Eq. 5 and involves soluble species of zinc and aluminum that form LDH in the narrow pH region on Pourbaix diagrams as proposed in (Mikhailau et al., 2019).



Anionic exchange properties of such LDH films grown on zinc and in particular changes in crystalline lattice and kinetics of anionic exchange processes have been explored in the following works (Bouali et al., 2020a; Iuzviuk et al., 2020). The XRD analysis was the main method for evaluating the changes in the crystalline structure of the LDHs and was performed at the PETRA III synchrotron radiation source (DESY, Hamburg, Germany) with an X-ray energy of 25 KeV. The diffraction patterns were collected from the samples coated with LDH films in the *in-situ* flow cell that allowed monitoring changes by the minute in the crystalline lattice of LDH during the anion exchange process. Several water-based solutions relevant for corrosion applications containing anionic species such as chloride ( $\text{Cl}^-$ ), sulphate ( $\text{SO}_4^{2-}$ ) and vanadate ( $\text{VO}_x^{y-}$ ) were used for *in situ* intercalation experiments.

Figure 7A presents XRD patterns taken from the zinc surface coated with LDH before (0 time) and during immersion in  $\text{Cl}^-$  containing solution (Bouali et al., 2020a). The intensities of (003) and (006) Bragg peaks decrease upon exposure to the solution and new Bragg peaks associated with a new LDH phase containing  $\text{Cl}^-$  appear after an induction period. In addition to the changes in the crystalline lattice of LDH, a strong signal of the amorphous phase appears on diffractograms that can be seen on the inset in Figure 7A. Such phase was ascribed to scattering from water, though decomposition of the main LDH phase was also considered as a possible contribution to the amorphous halo. The kinetics of the intercalation process with other anions like  $\text{SO}_4^{2-}$  and vanadate  $\text{VO}_x^{y-}$  have been studied in (Iuzviuk et al., 2020) using the same methodology as presented above. An extensive assessment of LDH microstructure and composition revealed little changes in the morphology of LDH films before and after the anionic exchange process which was confirmed not only by



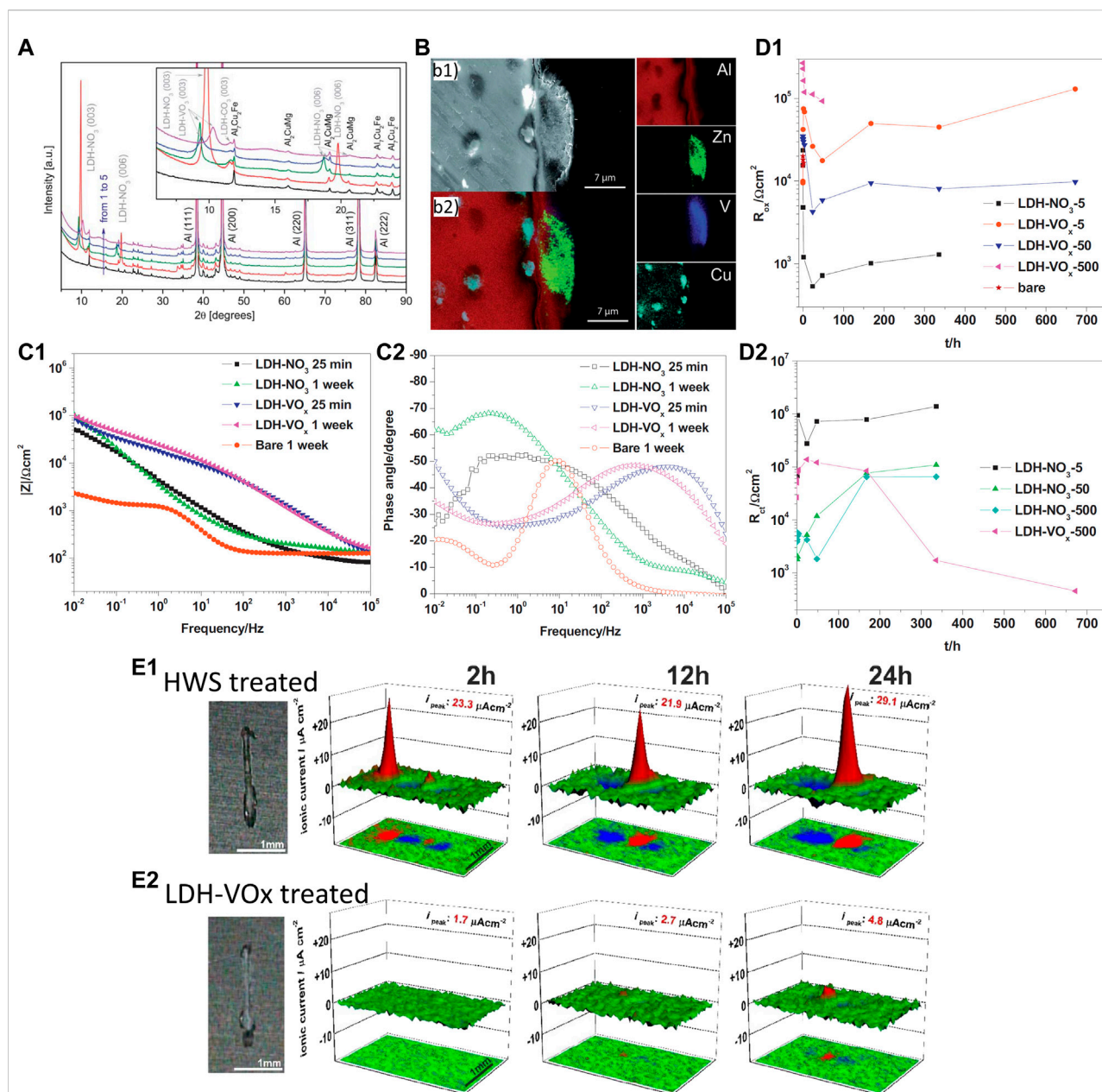


FIGURE 8

XRD patterns (A) of the AA2024 samples: untreated (1), covered with ZnAl LDH-NO<sub>3</sub> (2), and ZnAl LDH-V<sub>2</sub>O<sub>7</sub> as prepared (3) or immersed in 0.05 M NaCl for 2 weeks (4) and for 1 month (5). Reproduced from (Tedim et al., 2011) with permission from the Royal Society of Chemistry. The inset shows the patterns for the (003) and (006) diffraction reflections; SEM images (cross-section) of ZnAl LDH intercalated with vanadates (B1) and its corresponding EDS analysis (B2); EIS spectra (C1,C2) acquired for AA2024-T3 in 0.05 M NaCl after growth of LDH-NO<sub>3</sub> and LDH-VO<sub>x</sub> conversion films (prepared with 5 mM Zn<sup>2+</sup> solution); evolution of  $R_{ox}$  (D1) and  $R_{ct}$  (D2) as a function of immersion time. Reprinted from (Tedim et al., 2014) with permission from Elsevier; Microphotographs, SVET profiles and projection for the samples with HWS (E1) and LDH-VO<sub>x</sub> (E2). Reproduced from (Kuznetsov et al., 2016) with permission from The Royal Society of Chemistry.

the shift of Bragg peaks (003) and (006) positions but also *via* X-ray maps of different species (Figure 7B). The anionic exchange kinetics was analysed by the changes of intensities from the (003) basal plane as the most intense peak belonging to

the LDH phases as presented in Figures 7C1,C2. For the analysis of the time dependencies of the anionic exchange reactions, the equation of Avrami-Erofeev (AE) 6) has been utilized.

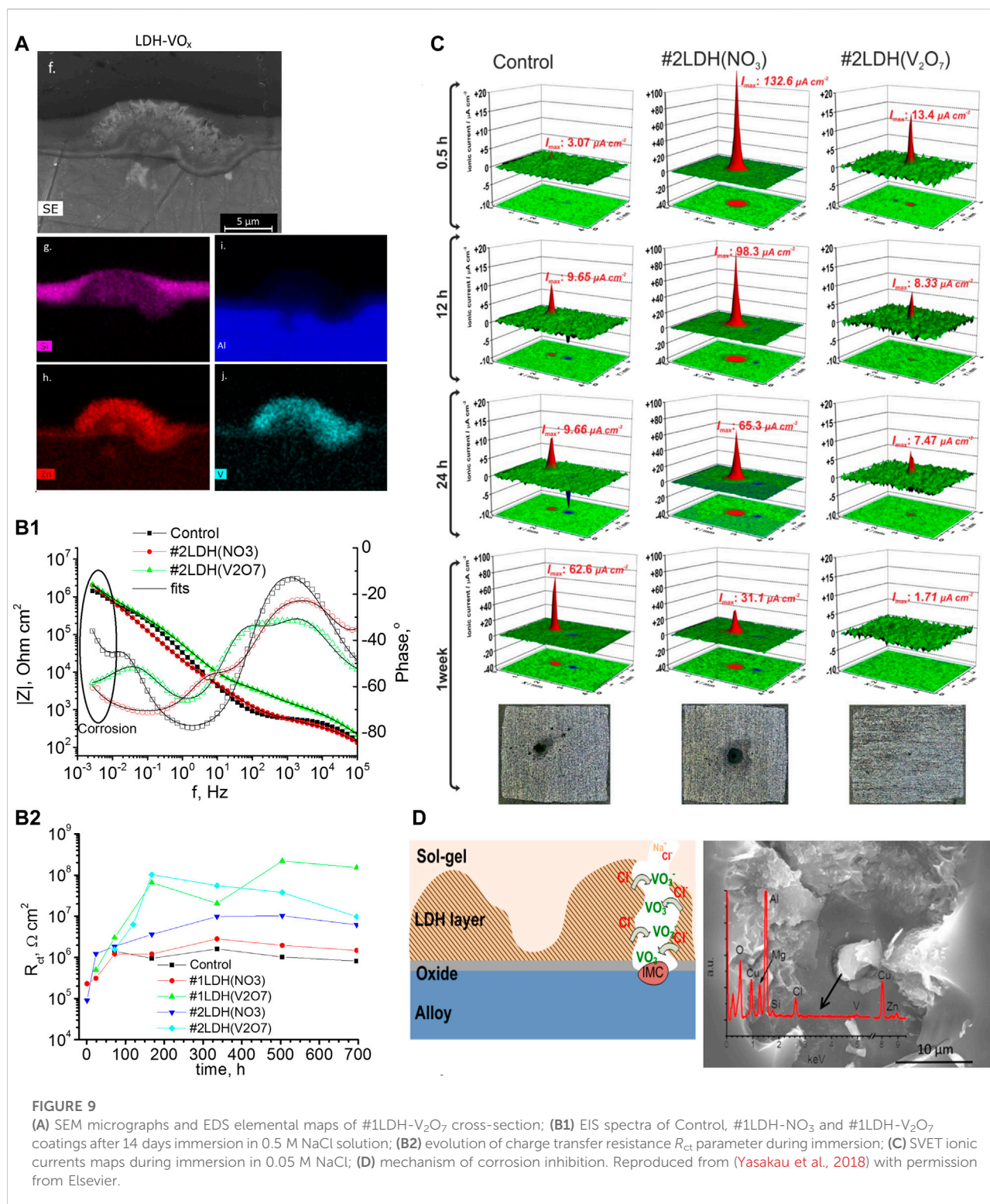
$$a(t) = 1 - \exp[-k(t - t_0)^m] \quad (6)$$

Where ( $\alpha$ ) is the reaction extent obtained as the ratio of the integral intensity of (003) reflections at a time ( $t$ ) to the maximal integral intensity, ( $t_0$ ) is the time of induction period, ( $m$ ) is a single reaction index that combines the nucleation rate law with the growth mechanism of the nucleus, and the parameter ( $k$ ) characterizes the reaction rate. The fitting of the kinetic dependencies has been done using the AE equation and the results are presented in **Figures 7D1,D2**. The obtained values of the ( $m$ ) parameter for the disappearing phase with  $\text{NO}_3^-$  suggested that the reaction mechanism is a two-dimensional diffusion-controlled one including a decelerated nucleation (**Figure 7D1**). Likewise, the formation of the phase containing  $\text{Cl}^-$  anions are better described by the AE equation than the others, though the values of ( $m$ ) suggest a one-dimensional diffusion-controlled reaction taking place with a decreasing rate of nucleation. Other anions such as  $\text{SO}_4^{2-}$ ,  $\text{VO}_x^{y-}$  reveal slower kinetics of anionic exchange compared with  $\text{Cl}^-$  ones. Moreover, the intercalation process of  $\text{SO}_4^{2-}$  corresponds to a one-dimensional diffusion-controlled reaction with the effect of decelerator nucleation, while the process for  $\text{VO}_x^{y-}$  is characterized by a two-dimensional diffusion-controlled reaction following instantaneous nucleation. This study provided fundamental characterization of the anionic exchange properties of LDH films synthesized on zinc metal surface which opens further applications of such LDH films in the development of intelligent corrosion protection schemes for zinc-based substrates.

As stated earlier in this section various methods for growing LDH coatings have been developed. Nevertheless, the methodologies are sometimes too complex and require harsh conditions, and the LDH films most often contain carbonate, hydroxide, and hydrophobic species that afford passive protection against corrosion. For Mg alloys, the hydrothermal synthesis of LDH is state of the art (**Wang et al., 2010; Ye et al., 2018**). However, it was shown that the LDH films intercalated with nitrate anions are successfully grown on aluminum alloys at a temperature  $<100^\circ\text{C}$  in simple bath chemistry (**Tedim et al., 2011; Tedim et al., 2014**). Cleaned AA2024-T3 plates were immersed in the solution of  $\text{Zn}(\text{NO}_3)_2$  in the neutral pH range for a few hours at  $T < 100^\circ\text{C}$ . Afterwards, the plates were washed with ultrapure water and ethanol and dried in air and the obtained samples were designated as ZnAl LDH- $\text{NO}_3$ . The anionic exchange process for vanadate anions was carried out in 0.1 M  $\text{NaVO}_3$  solution at  $T < 50^\circ\text{C}$  for a few hours (**Tedim et al., 2011**). The vanadate species have been chosen as they offer superior corrosion inhibiting performance. **Figure 8A** displays diffractograms of the AA2024 substrates with and without LDH coatings. The distinction between the ZnAl LDH- $\text{NO}_3$  (2) and ZnAl LDH- $\text{V}_2\text{O}_7$  (3) is visible since the reflexes (003) and (006) are shifted to lower  $2\theta$  angles as was shown in a previous study (**Salak et al., 2010**). The patterns also reveal shifts in positions and some broadening of (003) reflexes after immersion in 0.05 M NaCl solution for 2 weeks (4) and

1 month (5). To understand how much vanadates anions have been substituted by  $\text{Cl}^-$  ones the changes in basal spacings were analyzed by a superlinear function (**Tedim et al., 2011**), which suggested that approximately 50% and 90% of the vanadates intercalated in the LDH were substituted by the end of 2 weeks and 1 month of immersion respectively. The study also revealed that the intermetallics such as S-phase ( $\text{Al}_2\text{CuMg}$ ) were the preferred places for the growth of LDH as can be seen on the cross-section SEM picture and EDS maps of different elements (**Figure 8B**). The authors proposed that at the places of intermetallics aluminum oxide/hydroxide films is broken and dissolution of aluminum at such places is higher, which explained thick LDH deposits found preferentially on S-phase particles (**Figure 8B**).

The follow-up study (**Tedim et al., 2014**) explored in more detail the corrosion protective capabilities of the LDH coatings grown on AA2024 substrates. A broad range of concentrations of  $\text{Zn}(\text{NO}_3)_2$ , i.e., 5 mM 50 mM and 500 mM was used for LDH growth producing the coatings abbreviated respectively as follows LDH- $\text{NO}_3$ -5, LDH- $\text{NO}_3$ -50 and LDH- $\text{NO}_3$ -500. The anionic exchange process was done similarly as described in the paragraph above, and the resulting samples were named LDH- $\text{VO}_x$ -5, LDH- $\text{VO}_x$ -50 and LDH- $\text{VO}_x$ -500. Initially, the microstructural information was obtained from the coated samples. It appeared that the LDH coatings became denser with increasing the concentration of  $\text{Zn}(\text{NO}_3)_2$ . Following that, the assessment of corrosion protection was done using the EIS method during immersion in 50 mM NaCl solution and some results are presented in **Figure 8C**. Interestingly, although all the coatings presented a higher impedance at a low frequency than the bare uncoated alloy, the coatings containing vanadate (LDH- $\text{VO}_x$ ) displayed higher barrier properties than the nitrate-based coatings (LDH- $\text{NO}_3$ ) (**Figures 8C1,C2**). The impedance spectra were fitted to appropriate equivalent circuit models describing in a physical way the phenomena occurring in the coatings, oxide films and at the electrode/electrolyte interface. the protective efficiency of the denser coatings was much inferior to that of the thinner coating. Kinetic dependencies of oxide resistance ( $R_{\text{ox}}$ ) and charge transfer resistance ( $R_{\text{ct}}$ ) are presented in **Figures 8D1,D2**. These parameters represent the corrosion protection efficiency and the higher the values the better the protection of a system. The results revealed that only the thin coatings prepared LDH- $\text{VO}_x$ -5 and LDH- $\text{VO}_x$ -50 show the best performance in terms of active corrosion protection since the  $R_{\text{ct}}$  was too high and thus was not included in **Figure 8**. Although LDH- $\text{NO}_3$  showed some protection according to electrochemical results, the optical picture taken from the surface did show significant corrosion. These studies provided a solid ground for the development of intelligent complex protection systems involving a combination of anodic oxide with LDH layers, and sol-gel coatings with LDH layers that will be briefly discussed below.



The aerospace industry utilizes state-of-the-art conversion treatments of the aluminum alloys employing tartaric sulfuric acid anodizing (TSA), phosphoric sulfuric acid anodizing (PSA) processes as an example (Martínez-Viademonte et al., 2020),

which exclude highly carcinogenic Cr(VI) species formerly employed in the chromic acid anodizing (CAA) process (Critchlow et al., 2006). The latter process passivates the surface of aluminum alloy and enhances its active corrosion



protective properties due to the presence of Cr(VI) species. However, the TSA and PSA processes provide only passive protection and in case of damage to the coating, uncontrolled corrosion will start in the place of the defect. Since anodized coatings possess intrinsic porosity, it opens a pathway to seal the pores with LDH. The development of LDH coating capable of delivering corrosion inhibitors in the defects of the TSA anodic layer was presented in ref. (Kuznetsov et al., 2016). The AA2024 substrate was cleaned using a standard 3-step pre-treatment employed in the aerospace industry and anodized at 14 V for 25 min in a tartaric/sulfuric acid bath containing 0.53 M  $C_4H_6O_6$  and 0.46 M  $H_2SO_4$  at 37°C. The anodized samples were immersed for 30 min in a solution of 0.01 M  $Zn(NO_3)_2$  and 0.06 M  $NH_4NO_3$  with a pH of 6.5 and a temperature of 95°C. Afterwards, the samples were rinsed with deionized water and dried in air and the samples were designated as LDH- $NO_3$ . An additional anionic exchange process was carried out in the solution of  $NaVO_3$  at different immersion times such as 30 min and 60 min, which produced LDH coated samples with incorporated vanadate anions (LDH- $VO_x$ ). Finally, an additional process such as hot water sealing (HWS) was applied to make an adequate comparison for the LDH-coated samples. The samples containing LDH- $VO_x$  revealed better corrosion performance in EIS tests and also demonstrated efficient active corrosion protection in local measurements of ionic currents performed by the SVET technique on the scratched surface during immersion in 0.05 M NaCl solution (Figures 8E1,E2). Ionic currents normally increase due to uncontrolled corrosion at the metal surface. However, in the case of LDH- $VO_x$  coating, the SVET maps showed small and almost unchanging corrosion activity (Figure 8E2) which was attributed to the active role of vanadate species released from the coating.

Another work studied the protective capabilities of bi-layer protective systems comprised of LDH conversion treatments and sol-gel pre-treatment in corrosion protection of AA 2024 (Yasakau et al., 2018). The main idea was to explore long-term corrosion protection and active corrosion protection with general (EIS) and local (SVET) electrochemical methods of analysis. Before LDH growth, the alloy samples were cleaned with two processes: a simplified procedure involving 0.1 M NaOH and 0.1 M  $HNO_3$  and denominated as (#1), and a three-step industrial process denominated as (#2), more details in (Yasakau et al., 2018). The LDHs conversion treatment was done in the same way as reported above (Tedim et al., 2011) and involved initially the preparation of nitrate containing LDH in which nitrate anions were consecutively substituted by vanadates. Subsequently, a model hybrid sol-gel formulation was applied, and three coating systems were produced, namely the sol-gel coatings only (Control), the sol-gel coating atop an LDH layer with intercalated nitrates (#1LDH- $NO_3$ ), and sol-gel coating atop an LDH layer with intercalated nitrates (#1LDH- $V_2O_7$ ).

Figure 9A shows a selected cross-section of the coating #2LDH- $V_2O_7$  and corresponding signals from Si, V and Zn which point out to the place of the sol-gel and LDH respectively. The EIS results revealed rather complicated spectra (Figure 8B1) which were fitted with equivalent circuit models considering the properties of the barrier coating, oxide layer and corrosion process. The latter was characterized by charge transfer resistance ( $R_{ct}$ ) and its kinetics were plotted in Figure 9B2. In comparison to the Control and #1LDH- $NO_3$  or #2LDH- $NO_3$  coating systems the #1LDH- $V_2O_7$  and #2LDH- $V_2O_7$  ones revealed the highest  $R_{ct}$  and consequently the best performance during immersion in 0.5 M NaCl. Moreover, it also revealed active corrosion capabilities and self-healing events that were picked up by SVET measurements displayed in Figure 9C. In addition, the results pointed out that the LDH- $NO_3$  coating also improved corrosion protection according to the EIS results, which is similar to the results of the previous study (Tedim et al., 2014). Finally, the corrosion protection mechanism involved the release of vanadate anions which acted as the corrosion inhibitor toward the localized corrosion involving the intermetallics and aluminum matrix (Figure 9D).

In a more recent work, authors grew spatially resolved LDH film on AA2024-T3 substrate and modified the resulting film, first by intercalating MBT, and then by modifying the resulting film with an hydrophobic silane (Neves et al., 2019). The intercalation of MBT led to a decrease in the thickness of the LDH film, while the functionalization of LDH-MBT with silane increased the water contact angle almost into the superhydrophobic domain (144°). Moreover, the resulting film was found to exhibit high corrosion resistance and anti-microbial action.

### 2.2.3 Use of LDH for controlling the corrosion of steel in reinforced concrete

Another area of research where LDH are being tested is in concrete, particularly in the corrosion control of the reinforcing steel. Concrete is the world's most used construction material. The cement production is responsible for 8% of the anthropogenic  $CO_2$  emissions (Wu et al., 2022). Hence, extending the lifetime of concrete structures has a societal, economic, and environmental impact. Concrete alone has a very high durability but once steel is placed inside (reinforced concrete) its lifespan is significantly reduced (Bertolini et al., 2013). This is due to the corrosion of steel inside concrete. At the beginning, the steel bars in concrete are in the passive state due to the high pH of concrete (12.5–13.5). With time, atmospheric  $CO_2$  penetrates the concrete pores and reacts with  $Ca(OH)_2$  leading to the carbonation of concrete, with the formation of  $CaCO_3$  and a local decrease in pH. When the carbonation front reaches the reinforcing bars the steel passivation is lost, and corrosion can start. The corrosion products of iron are more voluminous than the metal. The extra volume creates internal stresses leading to cracking and spalling of the concrete cover. This exposes the steel



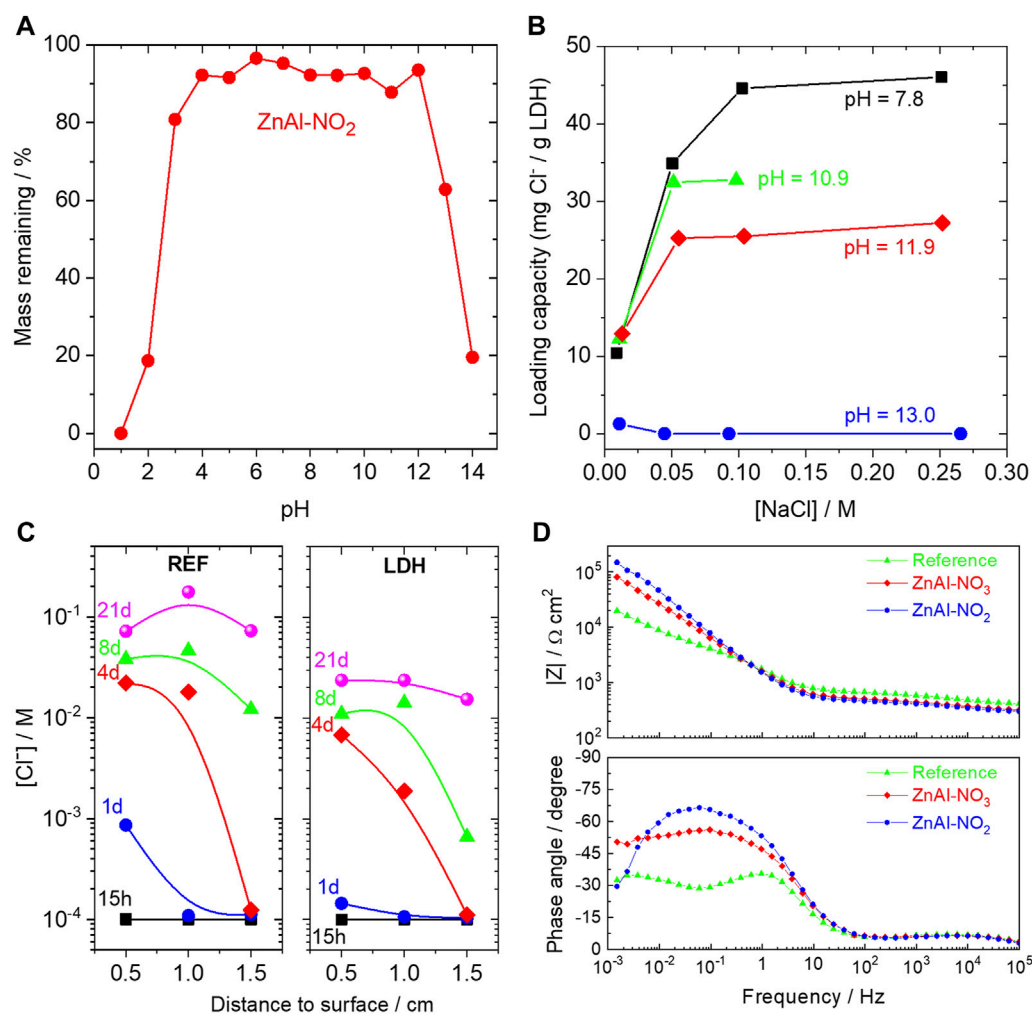


FIGURE 10

(A) LDH powder remaining after 1 month of immersion in water with pH from 1 to 14; (B) Chloride loading capacity of ZnAl LDH-NO<sub>2</sub> at different pH; (C) Profiles of chloride ion inside mortars with LDH and without (REF) exposed to 0.5 M NaCl; (D) Impedance response of mortars with steel bar immersed in 3.5% NaCl without and with 0.3% (2% with respect to cement) ZnAl LDH-NO<sub>3</sub> or ZnAl LDH-NO<sub>2</sub> LDHs.

bar to the environment further accelerating the corrosion process. Consequently, there is a great economic and technological interest in controlling this degradation phenomenon.

It is in this context that LDH are being tested to verify their ability to increase the service life of concrete structures. This can be achieved using two properties of LDH referred above, namely, the release of intercalated corrosion inhibitors and the capture of aggressive anions (chloride for example). The first reported attempt to counteract the ingress of chloride ions in concrete using LDH was made in 2003 with a CaAl-NO<sub>2</sub> added to the concrete mixture (Tatematsu and Sasaki, 2003). The action of the LDH involved the ionic exchange between the nitrite in the interlayer with the chloride inside the concrete. As a result, in the

concrete pore solution the amount of free chloride decreased and the concentration of corrosion inhibitor (NO<sub>2</sub><sup>-</sup>) increased, both contributing to the enhanced corrosion resistance of the steel reinforcement. At about the same time, in 2004, CaAl LDH with intercalated organic acids were used for controlling the cement hydration kinetics (Raki et al., 2004). This is another application of LDH in concrete, together with its use for improving the mechanical properties (compressive strength and flexural strength). Notwithstanding, most of the research is dedicated to the corrosion protection of the steel rebars in concrete with a significant number of papers being published in the last years. An overview of these works can be found in few reviews (Yang et al., 2013; Mir et al., 2020; Yang et al., 2021). There it becomes clear that MgAl is the most studied LDH with cement, mortar, or

concrete, followed by CaAl, and then by modified or unmodified hydrotalcite. The main intercalated ions are nitrate, carbonate, and chloride.

Recently, we have studied ZnAl LDH in mortar samples. This LDH has been studied in our group before, as an additive in coatings for corrosion control or as surface pre-treatment. This time the objective was to assess the advantage of using this LDH with intercalated nitrate or nitrite to extend the lifetime of reinforced concrete (Gomes et al., 2020). ZnAl-NO<sub>3</sub> works as a chloride trap while ZnAl LDH-NO<sub>2</sub> has the additional ability of releasing a corrosion inhibitor. The work analysed the stability of the LDH in different pH, the ability to capture chloride in solutions of different pH, and the impact in slowing the ingress of chloride and in preventing the corrosion of steel bars inside mortar. Figure 10 summarizes the main findings. One important feature to consider is the stability of the LDH in the service environment. Figure 10A shows that ZnAl LDH is unstable at low and high pH. It dissolves in the high pH values found in concrete (e.g., about 40% in pH = 13). XRD analysis of the remaining powder (Mir et al., 2021) showed the appearance of peaks of aluminium and zinc oxides and hydroxides above pH = 12.5, and the absence of LDH structure above pH 13.5. This has a great impact on the expected action of LDH inside concrete because the pH of concrete lies precisely within these values. Equally important is the capability of the LDH to capture chloride and the effect of pH in the process. This is shown in Figure 10B where a substantial amount of chloride is captured by ZnAl LDH in near neutral solutions. However, as the pH increases the capturing capacity declines. At pH 11.9 the capacity is reduced to about 55% and is lost at pH = 13. The reason is the increasing concentration of hydroxide ion which competes with chloride and is preferentially captured. Again, this occurs at the high pH characteristic of concrete. The low LDH stability and its weak capacity to capture chloride at high pH indicate that this might be a bad choice for use in concrete. However, the results of embedded chloride sensors inside mortar with and without LDH revealed a smaller amount of chloride ions in the pore solution of the mortar with LDH, as shown in Figure 10C. This clearly indicates a positive effect of the addition of the ZnAl LDH. Moreover, corrosion tests made on steel bars embedded in mortars containing either no LDH (reference samples) or ZnAl-NO<sub>3</sub> or ZnAl-NO<sub>2</sub> LDH, showed better corrosion resistance on samples with LDH, higher for the one containing corrosion inhibitor. The impedance spectra presented in Figure 10D were measured after 70 days of immersion in 3.5% NaCl. The reference sample showed a lower charge transfer resistance and presence of a diffusional process. In contrast, much higher impedance was measured on the other two samples, with a capacitive response dominating at the middle and lower frequency ranges, indicative of passivation of the steel bar. This can be attributed to the chloride capture by ZnAl-NO<sub>3</sub> and the capture + inhibition by ZnAl-NO<sub>2</sub> (Gomes et al., 2020). However, these results seem to be inconsistent with

the previous observations of partial dissolution and low Cl<sup>-</sup> capture capacity of the ZnAl LDH at high pH. A tentative explanation is that the LDH dissolution brings local increment of aluminium ions which in the presence of high chloride concentration might precipitate as Friedel's salt. This could explain the sequestration of chloride ions. The inhibitor is released when the LDH structure is destroyed and becomes readily available to act. Work is ongoing to verify this hypothesis.

The above findings put in perspective many of the works published so far since most of them were done in simulated pore solution (typically saturated calcium hydroxide but in some cases near neutral solutions), just a few in mortar and only one in real concrete (Tatematsu and Sasaki, 2003). It becomes clear that stability and ionic exchange tests must be performed in conditions close to the service environment. Ultimately, only tests in real mortar or concrete samples will allow the correct assessment of the practical use of these new materials.

## 2.2.4 LDH in corrosion detection

In the field of corrosion protection, there is a need to extend the service life of structures by not only improving the anti-corrosion protection but also provide additional functionalities which may somehow aid on the earlier detection of corrosion onset. While most works published in the literature have focused on the use of pH indicators and fluorescent molecules (Li and Calle, 2008), there is also the possibility to use complexing agents that can react with corrosion products and thereby signal corrosion processes.

In a recent work by Wilhelm and co-workers (Wilhelm et al., 2020), hexacyanoferrate salts were investigated as indicators for early detection of corrosion in carbon steel. Both syntheses of MgAl and ZnAl LDH intercalated with hexacyanoferrate salts were attempted, but only MgAl LDH was found suitable for intercalation of this anion, as Zn in ZnAl LDH tends to react with hexacyanoferrate and form a brownish insoluble precipitate. XRD and FTIR revealed the presence of different forms of hexacyanoferrate within LDH, which can both react with Fe cations and form intense blue precipitates (Turnbull's Blue and Prussian Blue). Release studies performed under different conditions showed that hexacyanoferrate is preferentially released under high NaCl concentrations. In addition, electrochemical studies (potentiodynamic polarization and EIS) demonstrated that corrosion of carbon steel increases when this anion is fully available in solution, with this effect being minimized when the anion is intercalated within LDH. Visual analysis of exposed carbon steel substrates to LDH in aqueous NaCl solution and simulated FeCl<sub>2</sub> solution revealed the formation of the blue precipitates, which underlines the success of this approach. The next step was to carry out similar studies in coatings modified with LDH-hexacyanoferrate. Indeed, the combination between electrochemical and visual analysis of the substrate shows that the appearance of dark blue spots at

the metal coating interface is associated with the decrease of overall impedance and initiation of corrosion processes, before the appearance of iron-based corrosion products (Sushkova et al., 2021).

### 2.2.5 Environmental and biological aspects associated with LDH

One of the requirements associated to the use of micro and nanocontainers is that these systems can not pose environmentally negative effects as those associated with Cr(VI)-derived species. They shall also contribute for a lower availability of the active species in the surrounding media when they are not necessary. This can contribute for a long-term protective action, while at the same time reducing the harmful effects associated with intercalated toxic species.

Having carried out several works on the assessment of LDH-MBT and knowing that MBT displays biocidal properties, we decided to investigate the antibacterial effect of MBT when intercalated in Zn-Al LDH (Kuznetsova et al., 2017). Different conditions of salinity (1, 2 and 3% NaCl) and pH (4, 5, 6 and 7) were used and the biological effects of MBT immobilized and released from LDH were monitored using an assay based on bacterial bioluminescence of either *Allivibrio fischeri* or a recombinant strain of *Escherichia coli*. While release studies carried out by UV-Visible spectrophotometry run under similar conditions of salinity and pH indicated that MBT is released swiftly, with high extent of release in 3% NaCl and under alkaline conditions, the biological studies revealed a more pronounced toxic effect (decrease of cell viability) in 1% NaCl solution. The differences observed between extent of released MBT and toxicity measured imply that the toxic effect induced in the bacteria was a function of both extent of released MBT and optimal salinity conditions for the growth of model bacteria. Also relevant is the fact that ZnAl LDH-NO<sub>3</sub> did not induce any light emission by the bioluminescent bacteria.

The toxicity induced by ZnAl LDH-MBT to the clam *Ruditapes philippinarum* was also studied in a joint work with Martins and Loureiro (Martins et al., 2017b). The results obtained demonstrated that the immobilization of MBT in the LDH provides some protection effect for the clams, reducing both physiological and lethal effects, though still presenting some hazardous effects. The chemical toxicity was ranked as being the highest for MBT and the lowest for LDH. In another work in collaboration with Martins and Loureiro, zinc and copper pyrithione booster biocides were immobilized into Zn-Al LDH and the anti-fouling efficacy and toxicity of the materials obtained was tested using green microalgae *Tetraselmis chuii* (non-target species) and the diatom *Phaeodactylum tricornutum* and the mussel *Mytilus edulis* (target species) (Avelelas et al., 2017b). When comparing the free form of the biocides, biocide-free LDH and biocide-containing LDH, the results obtained indicated that

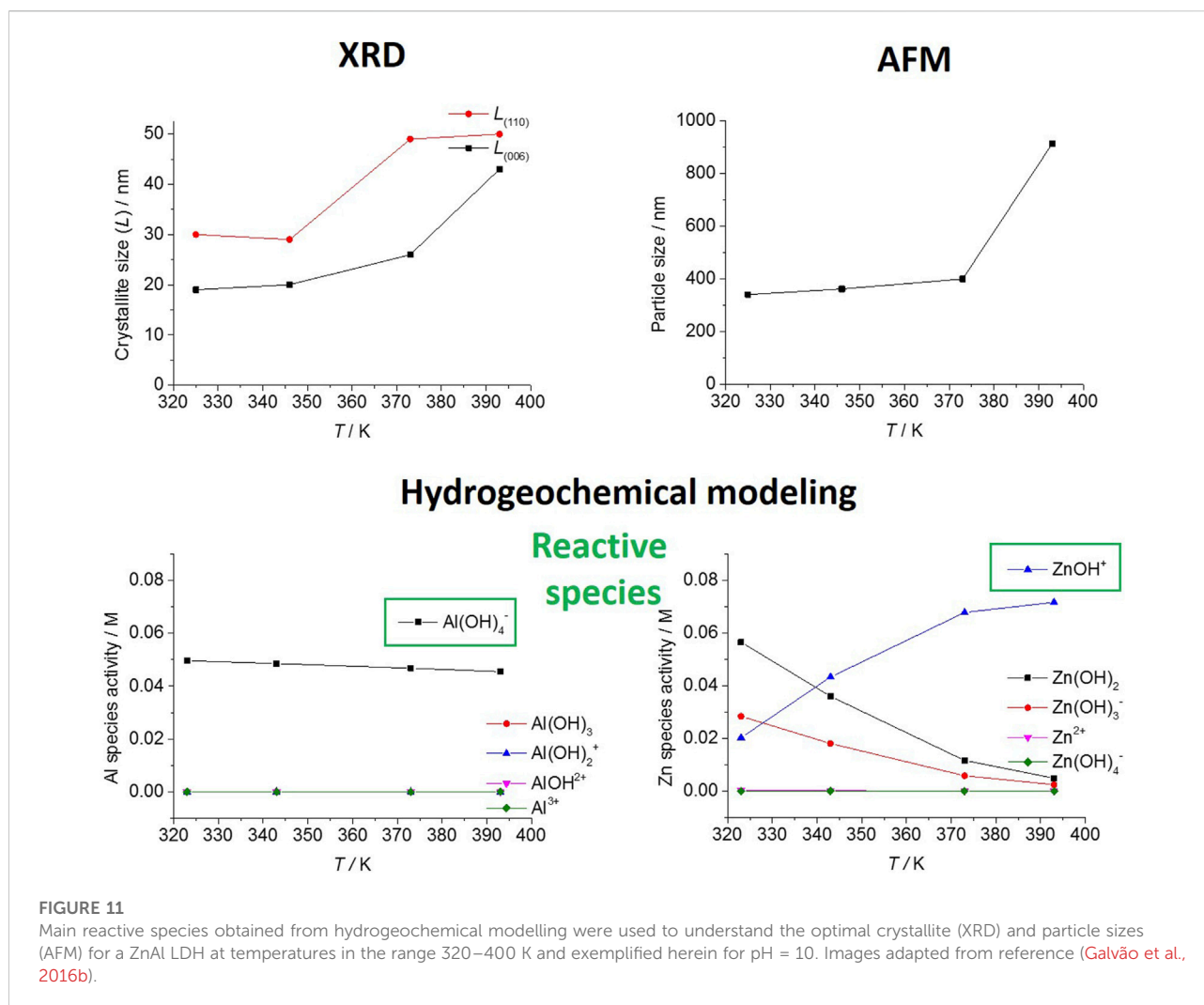
incorporation of zinc pyrithione in LDH was found to be an environmentally friendly way of using the biocides, without compromising the antifouling efficacy compared to the free biocide. In another joint work with Martins and Loureiro, and with Benayahu and co-workers (Gutner-Hoch et al., 2018), the anti-macrofouling efficacy of Zn-Al LDH loaded with zinc and copper pyrithione was investigated. In this study, adult mussels from Atlantic Ocean, Mediterranean Sea and Red Sea, together with larvae of bryozoan *Bugula neritina* from Mediterranean Sea and Red Sea were used. The results obtained demonstrated that LDH with zinc pyrithione could be used in lower quantities with respect to other compounds used currently to render anti-macrofouling effects and the fact that LDH can provide controlled release of the compound, thereby allowing targeted foulers to be tackled while still limiting the release of the active compounds to ambient waters. Similar trends were found in another study conducted on larval stage of the brine shrimp *Artemia salina*, and on embryonic European purple sea urchin *Paracentrotus lividus* (Gutner-Hoch et al., 2019). Overall, the results support the use of LDH as eco-friendly nanomaterials for development of high-performing protective coatings.

## 3 Exploring LDH via computational tools

### 3.1 The role of computational tools

During the last few years, our research team has been using different computational tools to explore the structure, reactivity, and properties of LDH at different scales. As highlighted above, LDH not only play a key role in the field of corrosion protection as nanocontainers through hosting corrosion inhibitors or molecules capable of signaling corrosion but have been finding application in a wide range of fields. For this reason, some of the conclusions obtained using computational tools to gather insights into the structure and properties of LDH, their interlamellar reactivity and dynamics, have also been important to other fields.

Unfortunately, information about the structure, stability and kinetics of these bulk systems is difficult to obtain by experimental techniques alone, despite some notable efforts (Kameda et al., 2021), due to their high degree of complexity, regarding different parts of system, notably, 1) the order, types of atoms and defects of the cationic layer; 2) the orientation, conformation, reactivity, and solvation degree of the interlayer molecular contents, and 3) the surrounding conditions in terms of types of species, their concentration, pH and other physicochemical properties, which, in turn, can influence the cationic layer and interlayer contents themselves. Therefore, computational, and molecular modelling tools play a key role in the understanding of these systems, providing unprecedented mechanistic details about the different processes and applications in



which LDHs are involved, eventually potentiating and accelerating the design of more efficient and sustainable materials.

In this section, we will review recent advances made with the following tools:

- 1) Hydrogeochemical modeling rendered insights on the chemical speciation of different metal cations in solution during the synthesis of LDH, which leads to its proposal as a promising solution to model and optimize the production of LDH.
- 2) Density functional theory (DFT) was used to characterize the crystalline structure of LDH, which allowed to understand and simulate their XRD spectra, while also explaining the shape of LDH particles, the exfoliation of LDH particles to form nanosheets, and the formation of conversion films on top of metallic surfaces.
- 3) Classical molecular dynamics (MD) simulations allowed to reach larger time and length scales of realistic models of LDHs, which was key to understand the reactivity and role of solvation inside the interlayer galleries.

Some of these works developed in CICECO had a seminal character, which subsequently led to their use and citation by other authors. Therefore, their impact within the LDH community will also be discussed herein.

### 3.2 Hydrogeochemical modeling

Hydrogeochemical modelling can render insights into the chemical speciation of different metal cations in solution. Therefore, this simulation tool was proposed to model, understand, and optimize the synthesis of LDH based materials (Galvão et al., 2016b).

The more traditional method of LDH synthesis usually involves the co-precipitation of the metals in solution to form the cationic layer and the appearance of the first crystallites with the known layered structure, followed by hydrothermal treatment during which the initial material grows into fully formed LDH particles, usually in the form of hexagonal plates (Galvão et al., 2016b, 2017). Usually, a labile anion



(nitrate, for example) is intercalated during this step, which can then be replaced by a functional molecule, also in the anionic form, during a subsequent anion-exchange process. Due to the wide range of applications of LDH (Galvão et al., 2020b), often, there is the need to establish the large-scale production of these materials. For this reason, the relation between the physicochemical properties capable of influencing the synthesis (pH, time and temperature), and the crystallite and hydrodynamic particle sizes of the produced LDH were investigated, and subsequently correlated with the concentration of the metals in solution during the synthesis (Galvão et al., 2016b).

An hydrogeochemical modelling software (Parkhurst and Appelo, 2013) was used to estimate the concentrations of different species of aluminum and zinc in aqueous solution under synthesis conditions, considering different temperatures ( $T = 323, 343, 373$  and  $393$  K) and pHs (8.5 and 10), thus allowing to understand the influence of hydrothermal treatment. It was proved that hydrothermal treatments performed at the higher temperatures lead to larger crystallites than treatments at the lower temperatures. Moreover, it was found that the temperature influenced the rate of crystallite reorganization in solution and the equilibrium of aluminum and zinc chemical species. According to the Al and Zn chemical speciation obtained from hydrogeochemical modelling calculations,  $\text{Al}(\text{OH})_4^-$  was the only Al species present in solution. In the case of Zn, at pH = 10,  $\text{Zn}(\text{OH})_2$ ,  $\text{Zn}(\text{OH})_3^-$  and  $\text{ZnOH}^+$  were the favored species in solution. However, among these species, only  $\text{ZnOH}^+$  increased its concentration in solution as the temperature increased, thus accompanying the occurrence of larger crystallites and particle sizes. The results shown in Figure 11 supported the important role of  $\text{Al}(\text{OH})_4^-$  and  $\text{ZnOH}^+$  in the formation of LDH (Galvão et al., 2016b). Despite the chemical speciation in solution was already proposed by other authors (Zhi and Guo, 2005) as preponderant for the LDH formation mechanism, to the best of our knowledge, for the first time a hydrogeochemical modelling tool was used to help identify the reactive species in solution. The potential of this strategy was recognized by other authors (Conterposito et al., 2018). Subsequently, the identified species were used to propose a reaction mechanism for the LDH formation (Mohedano et al., 2017; Serdechnova et al., 2017). This indicates that hydrogeochemical modelling can be a solution to accelerate the scale-up and increase the efficiency of LDH synthesis.

### 3.3 Density functional theory with periodic models

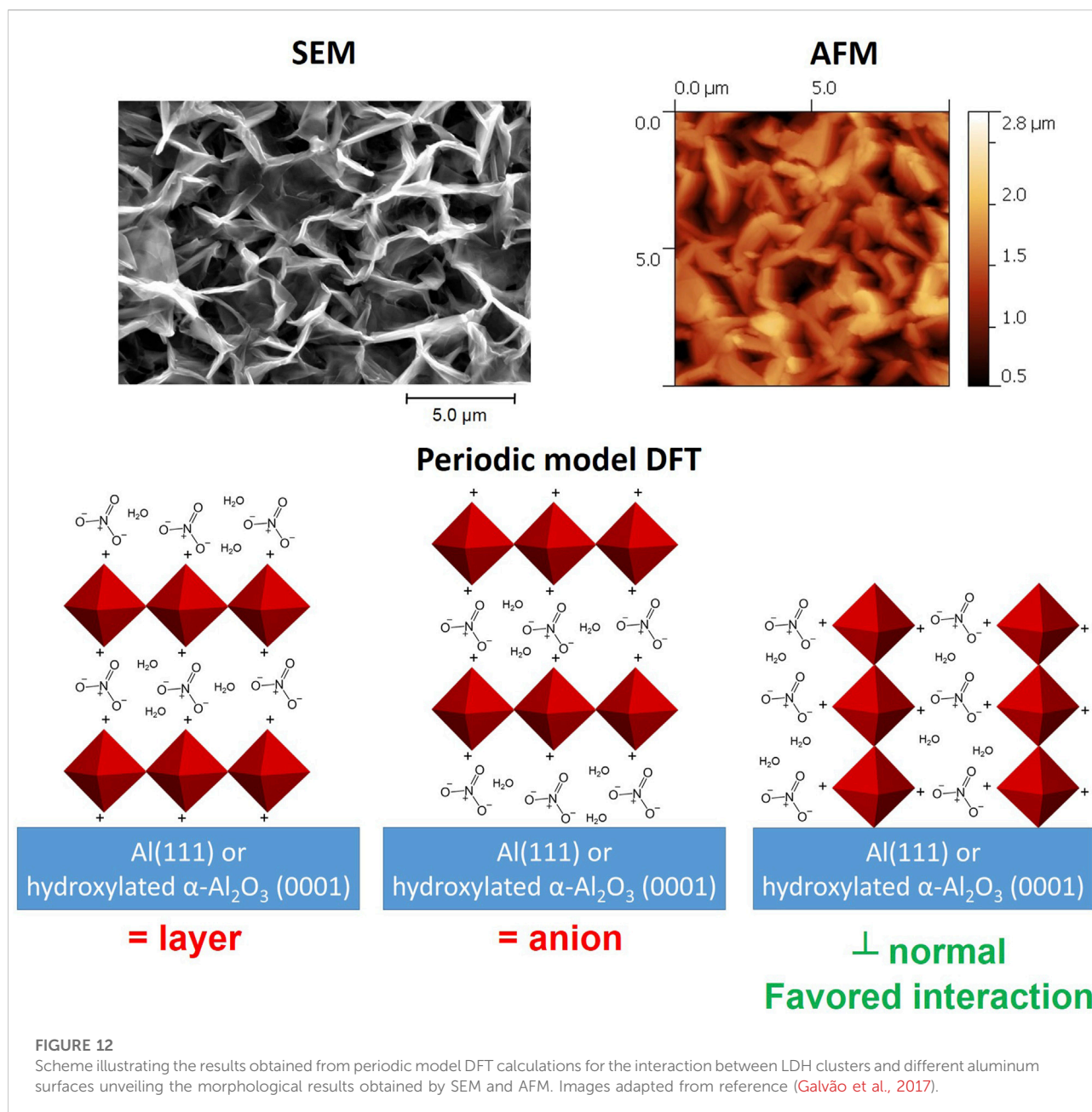
The crystal structure of LDH can be difficult to determine by XRD due to the poor crystallinity of these materials (Thomas and Kamath, 2006). This makes density functional theory (DFT) calculations with expanded periodic models (a.k.a. periodic model DFT) an ideal technique to gain insights into the inner structural features of new LDH materials. The first DFT studies used LDH structural models based on anhydrous supercells

(Trave et al., 2002) or small cluster models (Yan et al., 2008) to reduce the computational cost of the simulations. Afterwards, Costa, Leitão and co-workers designed more realistic periodic models with an ideal size for DFT studies (Costa et al., 2008; Costa et al., 2010; Costa et al., 2012). Inspired on Costa et al. works, a DFT periodic model of the LDH structure was used by us (Galvão et al., 2016b) to unveil the orientation of the nitrate anion inside the interlayer structure of a ZnAl LDH, which was still a matter of uncertainty at the time, regarding the parallel (Xu and Zeng, 2001; Xu et al., 2009) vs. tilted (Costa et al., 2012; Salak et al., 2012) orientation of nitrate anions relative to the cationic layer.

Afterwards, it was explored the structural and energetic driving forces behind the morphology of zinc-aluminum LDH particles, single layer nanosheets and protective conversion films grown on top of aluminum alloys (Galvão et al., 2017).

Periodic model DFT was employed to obtain surface and interaction energies of different orientations of the LDH structure. These results were combined with Atomic Force Microscopy (AFM) and XRD measurements to understand how LDH polycrystalline particles are formed. Fully formed LDH particles, have a plate-like shape, where the lateral size is larger than the particle height. LDH polycrystalline particles seem to be defined by 1–3 crystallites forming the plate height and between 8 and 11 crystallites forming the plate length. Computed surface energies show that particles grow larger in terms of length than in terms of height to minimize the surface energy of particles, since the lateral side of the particles is less stable than the top and bottom of the plates. Moreover, interaction energies show that crystallites have more favorable interaction energies when they interact side-by-side, thus extending the formation of the cationic layers to form the plate shape. On the contrary, crystallites interact less favorably when stacking cationic layers and interlayers one over the other, thus resulting in lower heights than widths. This view of the relation between the plate-like morphology and the inner structure of LDH has already allowed a better understanding of the morphology of LDH based structures in other works (Li et al., 2018; Prestopino et al., 2019; Wu et al., 2019; Aleshin et al., 2020; Roberts et al., 2020).

The literature is vast in what concerns the delamination of LDH when they are dispersed in formamide (Liu et al., 2006; Ma et al., 2006; Han et al., 2008; Abellán et al., 2010; Song and Hu, 2014), even without thermal treatment (Ma et al., 2006). Ma et al. (Ma et al., 2006) proposed a two-stage delamination mechanism for LDH in formamide, i.e., rapid swelling and subsequent slow exfoliation, but confirmation with atomistic detail could be obtained only after computational studies. DFT calculations revealed that formamide conserve or even increase the network of hydrogen bonds in the interlayer, while increasing the distance between cationic layers, when they enter the interlayer to substitute crystalline water molecules, usually intercalated during the synthesis. As the formamide treatment progresses and more formamide molecules substitute water molecules in the interlayer, this is accompanied by a decrease of the layer separation energy for formamide in comparison



with water. These structural and energetic tendencies show why formamide can be a good agent to delaminate LDH. The conclusions obtained in that work (Galvão et al., 2017) contributed to subsequent DFT studies on the exfoliation of LDH (Tavares et al., 2020b; Tavares et al., 2021).

Regarding LDH conversion films grown on top of aluminum alloys, it is well documented the preference for LDH plates of conversion films to grow perpendicularly to the aluminum substrate, rather than lying flat on top of the aluminum surface and growing in terms of height (Tedim et al., 2011; Tedim et al., 2013; Tedim et al., 2014). For LDH particles and nanosheets it was

shown that cationic layers grow longitudinally in parallel to the plate like morphology of LDH. Therefore, in the case of conversion films, the cationic layers should also be perpendicular to the aluminum substrate. However, in order to explore this hypothesis and unveil the relation between atomic structure and morphology of conversion films, the interface between ZnAl LDH-NO<sub>3</sub> conversion films and the aluminum surface was studied considering the bare metal (Al (111)), more common under extreme pH conditions (Tait, 2012), and the hydroxylated aluminum oxide [ $\alpha\text{-Al}_2\text{O}_3$ (0001)] predominant under near neutral pH (Tait, 2012). The conversion films were approximated computationally using LDH clusters with different

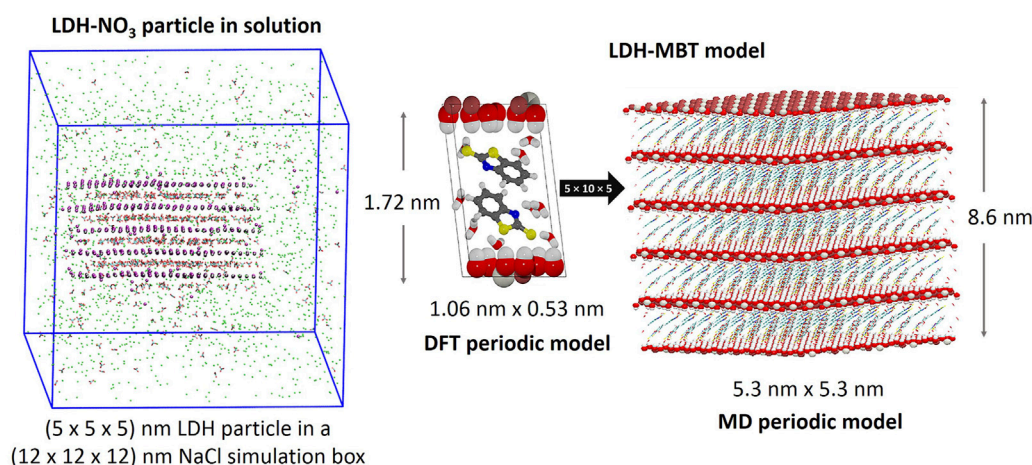


FIGURE 13

MD simulation snapshot of an LDH-NO<sub>3</sub> particle in a sodium chloride solution simulating a corrosion medium, showing the stability of the system after 20 ns (left). DFT periodic model, and expanded MD periodic model used for the MD simulation of LDH-MBT (Colour code for spheres: silver, Al; scarlet, Zn; red, O; white, H; grey, C; blue, N; and yellow, S). Images adapted from references (Pérez-Sánchez et al., 2018; Novell-Leruth et al., 2020).

orientations and sizes, and, for both aluminum surfaces, it was found that the most favorable interaction was with the cationic layers perpendicular to the aluminum surfaces, thus allowing to understand the SEM and AFM results obtained for these systems. In the case of Al (111), the hydroxyl groups of the cationic layer coordinate with the aluminum atoms of the surface, whereas for  $\alpha$ -Al<sub>2</sub>O<sub>3</sub>(0001) the metallic atoms of the LDH cationic layer coordinate with the hydroxyl groups resulting from the hydroxylation of the oxide surface in water (Rohmann et al., 2014). These results also elucidate the crystallization mechanism of LDH films. The mechanism has been rationalized by other authors (Guo et al., 2009; Lee et al., 2015) in terms of an initial random grow of crystal seeds. The DFT results point to a preferential orientation of the seeds with the cationic layers normal to the surface even during early stages of crystal grow. After this early stage, even if seeds crystallize away from the surface in other directions, these eventually meet crystals growing with the cationic layers normal to the surface, thus preventing the former from continuing the growing process (Guo et al., 2009; Lee et al., 2015). Part of the experimental and computational results obtained in that work for conversion films (Galvão et al., 2017) are illustrated in Figure 12.

### 3.4 Molecular dynamics

Classical molecular dynamics (MD) has been the main computational approach for the atomistic simulation of LDHs and other clay-like materials (Cygan et al., 2004; Greenwell et al., 2006; Cygan et al., 2009), since it allows to examine models with thousands of atoms in a computational efficient manner. However, despite several works could be found in the

literature about the structure and dynamics of the LDH's interlayer contents (Kim et al., 2005; Lombardo et al., 2005; Kim et al., 2007; Pisson et al., 2008; Tran et al., 2008), it was lacking a straightforward MD procedure, with supercell models, MD steps and parametrization, which could be readily adapted for the simulation of different LDH systems. Therefore, Pérez-Sánchez et al. (Pérez-Sánchez et al., 2018) developed a straightforward framework based on the GROMACS open-source code to perform MD simulations of LDH, which can be easily modified to consider a wide range of inorganic and organic anions intercalated. The developed procedure enables to run simulations for long timescales (>100 ns) with all atomic positions allowed to move freely, while maintaining intact the integrity of the LDH structure. It was demonstrated for different cationic mixtures (e.g., MgAl and ZnAl LDHs) and different intercalated anions (chloride, nitrate and carbonate) that the model and partial charges parametrization allow to study interlayer equilibrium processes in detail. This is an especially important feature of the developed MD framework, since, as far as we know, none of the previous computational models (Rad et al., 2016; Tsukanov and Psakhie, 2016) were able to reproduce realistic experimental conditions for LDH immersed in solution as nanocontainers of active functional species.

The model considers the periodic expansion of the LDH structure in the directions parallel and perpendicular to the cationic layers (Thyveetil et al., 2008; Lv et al., 2012; Makaremi et al., 2015). Based on the excellent agreement between calculated and experimental data, the model can be considered to simulate the application of LDH in a wide range of fields, having the potential to predict the controlled release of functional anions, such as corrosion inhibitors (Poznyak

et al., 2009) or pharmaceuticals (Senapati et al., 2016), the trapping of aggressive or hazardous anions (Lu et al., 2016) or to simulate the influence of pH or other electrolytes on the controlled release of intercalated active compounds (Carneiro et al., 2015). As a test case, LDH particles with intercalated nitrate anions were introduced in a sodium chloride water solution, to simulate an aggressive corrosion environment. Encouragingly, it was found that the layered structure of the LDH was kept stable within the timeframe of a 20 ns MD simulation, as shown in Figure 13, paving the way to study an ion or solvent exchange between the LDH and the surrounding solution that require much longer simulation times.

The model presented for LDH materials is ready to be used with different intercalated anions with the well-known open-source code for MD simulations, GROMACS (Abraham et al., 2015). Therefore, all the necessary parameters and inputs to carry out the MD simulations are available for download (<http://sweet.ua.pt/jrgomes/SELMA/MD-LDH/>). This framework has already been used by other researchers to model LDH, particularly dealing with the removal of hazardous materials (Zhu et al., 2022), the examination of the undulation of the cationic layers of exfoliated LDHs (Tavares et al., 2020a), following the MD procedure to evaluate the structure of LDH as drug nanocarriers (Pšenička et al., 2020), and taking the partial charge parametrization of the force field to evaluate the hydration states of the interlayer contents (Li et al., 2022).

One key aspect for the application of LDH as nanostructured coating additives for corrosion protection is the choice of the inhibitor to be intercalated. To facilitate this selection, an open cloud database to search for corrosion inhibitors, their respective inhibition efficiencies and measurement conditions was also built (Galvão et al., 2022), and a machine learning approach to evaluate new inhibitors is being developed (Galvão et al., 2020a). One particularly efficient inhibitor is 2-mercaptobenzothiazole (MBT), which was previously studied regarding its tautomeric, acid-base and ion-pair formation equilibrium in aqueous solution (Galvão et al., 2016a), as well as its ability to adsorb onto aluminum surfaces (Galvão et al., 2018). To understand its acid-base equilibrium, conformation and degree of solvation inside the interlayer galleries, the LDH-MBT system was studied by classical MD (Novell-Leruth et al., 2020) using the model presented in Figure 13. The MD model is a  $5 \times 10 \times 5$  expansion of the smaller DFT periodic model, thus allowing to simulate more realistic structural features and follow complex dynamic processes. That work showed how MD simulations can complement the experimental characterization of LDHs, providing atomistic and dynamic insights into the interlayer distance and other structural information obtained by XRD and the solvating degree indicated by TGA.

## 4 Summary and conclusion

Since 2004 the SECOP group at University of Aveiro has been heavily involved in searching for new chemical alternatives to the replacement of traditional applications of Cr(VI) in corrosion protection. This went through doped sol-gel coatings, self-assembled networks as nanostructured reservoirs for self-healing anticorrosion pre-treatments, silanes and rare-earth salts as corrosion inhibitors, zeolites and oxide nanoparticles nano/micro reservoirs for storage of corrosion inhibitors, layer by layer assembled nanocontainers, LDHs nanocontainers filled with corrosion inhibitors, etc.

Among these strategies LDH seem very tenable, versatile, and advantageous for corrosion protection applications. Moreover, they are environmentally friendly, accessible, and applicable to a wide range of metal substrates. In our Laboratory we have investigated and developed the synthesis, characterization, and anti-corrosion properties of these materials as nanoparticles (to be used in paints) or as conversion coatings formed directly on metals. The studies mainly concerned the protection of aluminum alloys, in particular AA2024 used in aeronautics. Nevertheless, other substrates were used, as magnesium alloys and galvanized steel and in a few cases steel.

These materials demonstrate very good ion-exchange capacity, which is very useful for corrosion protection applications since the LDH can provide a simultaneous double-function on removing (trapping) aggressive species from the medium and releasing inhibiting species on-demand for protecting the metallic substrate. Moreover, this mechanism often provides a fast protective response (self-healing) conferring active corrosion protection, triggered by presence of aggressive ions ( $\text{Cl}^-$ ) or mechanical damage, acting in specific sites and avoiding the uncontrolled leaching of the inhibitor, with improvement in the corrosion protection efficiency and increase of the duration of the coatings (Leal et al., 2022).

In the context of corrosion protection, LDH are still in the process of development and some problems must be overcome before taking full advantage of them. In the case of nanoparticles, challenges as the dispersion and the compatibility of the nanoparticles with the coating formulation, amount of nanoparticles introduced, carbonate contamination during LDH synthesis and storing, difficulties to intercalate large anions or neutral molecules, and instability in acidic or very alkaline media, good corrosion inhibitors in certain media, high cost, among others, must be considered.

However, there are a few companies that have dedicated their R&D to focus in this area of expertise. For instance, KISUMA Chemicals (Innovation - Kisuma Chemicals), a world leader in the production of hydrotalcites, possesses a branch specifically devoted to the development and optimization of LDH pigments for corrosion protection. SMALLMATEK Lda. (Smallmatek-Small Materials and Technologies), which was created as a start-up at the



University of Aveiro, produces and performs research on LDH additives mainly for the purpose of corrosion protection. Their pigments can be incorporated into coatings and integrated in a multi-level corrosion protective scheme.

The possibility to use LDH nanocontainers as a post-sealing treatment for anodized and plasma electrolytic oxidation (PEO) coatings has generated a lot of interest in the corrosion field. However, the growth on certain PEO coatings remains challenging (Bouali et al., 2020a).

## 5 Future perspectives and outlook

Despite the scientific achievements and promising potential for use of LDH into real coating systems, the work is yet not complete. LDH need to fit into other requirements such as processing parameters, compatibility with other coatings and adhesion performance. These factors can be overcome by further optimization of the LDH both in form of pigments and conversion coatings. It is important to perform more systematic studies on environmentally friendly inhibitors for specific media/metals that could be intercalated in the galleries, since active corrosion protection comes from them.

Overall, any major development in Materials Science in general and Corrosion Science and Engineering in particular, requires the pursuing of new ways of designing materials and testing them: from application of bio-inspired approaches to design new additives and multifunctional coatings, to the use of AI for design and optimization of materials in ways otherwise not accessible to more traditional trial-and-error, incremental approaches. SECOP group is currently carrying out activities in this direction in collaboration with industry, namely by developing organic coatings from bio-based sources combined with LDH-based nanoadditives (COAT4LIFE) with active corrosion protection and corrosion detection functionalities, developing biocompatible surface treatments for Mg alloys used in biomedical implants and by implementing data-driven approaches to find efficient corrosion inhibitors for different metals (DATACOR) to be subsequently loaded into LDH.

## Author contributions

JT designed the manuscript, reviewed the literature, wrote and revised the manuscript. TG reviewed the literature, wrote, compiled all contributions and revised the manuscript. KY, AB, JG, and MF reviewed the literature, wrote and revised the

manuscript. All authors contributed to the article and approved the submitted version.

## Funding

This work was developed within the scope of the project CICECO-Aveiro Institute of Materials, UIDB/50011/2020, UIDP/50011/2020 and LA/P/0006/2020, financed by national funds through the FCT/MEC (PIDDAC). It was also financed in the framework of projects SELMA (POCI-01-0145-FEDER-016594 and PTDC/QEQ-QFI/4719/2014), DataCor (POCI-01-0145-FEDER-030256 and PTDC/QUI-QFI/30256/2017, <https://datacorproject.wixsite.com/datacor>), NATURAL (CENTRO-01-0247-FEDER-047080), and the European Union's Horizon 2020 research and innovation programme under the Marie Skłodowska-Curie grant agreement ID 101007430 (COAT4LIFE).

## Acknowledgments

On a final note, we would like to thank our present and former SECOP colleagues which contributed to this research, in particular Prof. Mikhail Zheludkevich which was one of the driving forces for several of the works reported herein, and with whom we collaborate till the present day. Acknowledgments are also due to all the other groups, duly cited in this document, with whom we have been collaborating over the years and have helped us to bring new knowledge to the corrosion science and engineering field.

## Conflict of interest

The authors declare that the research was conducted in the absence of any commercial or financial relationships that could be construed as a potential conflict of interest.

## Publisher's note

All claims expressed in this article are solely those of the authors and do not necessarily represent those of their affiliated organizations, or those of the publisher, the editors and the reviewers. Any product that may be evaluated in this article, or claim that may be made by its manufacturer, is not guaranteed or endorsed by the publisher.

## References

Abdolah Zadeh, M., Tedim, J., Zheludkevich, M., van der Zwaag, S., and Garcia, S. J. (2018). Synergetic active corrosion protection of AA2024-T3 by 2D- anionic and

3D-cationic nanocontainers loaded with Ce and mercaptobenzothiazole. *Corros. Sci.* 135, 35–45. doi:10.1016/j.corsci.2018.02.018

- Abellán, G., Coronado, E., Martí-Gastaldo, C., Pinilla-Cienfuegos, E., and Ribera, A. (2010). Hexagonal nanosheets from the exfoliation of  $\text{Ni}^{2+}$ - $\text{Fe}^{3+}$  LDHs: A route towards layered multifunctional materials. *J. Mat. Chem.* 20, 7451–7455. doi:10.1039/c0jm01447h
- Abraham, M. J., Murtola, T., Schulz, R., Páll, S., Smith, J. C., Hess, B., et al. (2015). Gromacs: High performance molecular simulations through multi-level parallelism from laptops to supercomputers. *SoftwareX* 1–2, 19–25. doi:10.1016/j.softx.2015.06.001
- Aleshin, D. K., Mashkovtsev, M. A., Rychkov, V. N., Bunkov, G. M., Baksheev, E. O., and Zhirenkina, N. V. (2020). Evolution of layered yttrium hydroxide nitrate particles during controlled double-jet precipitation. *Powder Technol.* 376, 12–21. doi:10.1016/j.powtec.2020.08.013
- Avelas, F., Martins, R., Oliveira, T., Maia, F., Malheiro, E., Soares, A. M. V. M., et al. (2017a). Efficacy and ecotoxicity of novel anti-fouling nanomaterials in target and non-target marine species. *Mar. Biotechnol.* 19 (2), 164–174. doi:10.1007/s10126-017-9740-1
- Bertolini, L., Elsener, B., Pedferri, P., Redaelli, E., and Polder, R. B. (2013). *Corrosion of steel in concrete: Prevention, diagnosis, repair*. Weinheim, Germany: Wiley-VCH Verlag GmbH & Co. KGaA.
- Bouali, A. C., Iuzviuk, M. H., Serdechnova, M., Yasakau, K. A., Wieland, D. C. F., Dovzhenko, G., et al. (2020a). Zn-Al LDH growth on AA2024 and zinc and their intercalation with chloride: Comparison of crystal structure and kinetics. *Appl. Surf. Sci.* 501, 144027. doi:10.1016/j.apsusc.2019.144027
- Bouali, A. C., Serdechnova, M., Blawert, C., Tedim, J., Ferreira, M. G. S., and Zheludkevich, M. L. (2020b). Layered double hydroxides (LDHs) as functional materials for the corrosion protection of aluminum alloys: A review. *Appl. Mat. Today* 21, 100857. doi:10.1016/j.apmt.2020.100857
- Buchheit, R. C., and Cuan, H. (2004). Formation and characteristics of Al–Zn hydroxalite coatings on galvanized steel. *J. Coat. Technol. Res.* 1, 277–290. doi:10.1007/S11998-004-0030-2
- Buchheit, R. G., Bode, M. D., and Stoner, G. E. (1994). Corrosion-resistant, chromate-free talc coatings for aluminum. *Corrosion* 50, 205–214. doi:10.5006/1.3293512
- Buchheit, R. G., Mamidipally, S. B., Schmutz, P., and Guan, H. (2002). Active corrosion protection in Ce-modified hydrotalcite conversion coatings. *Corrosion* 58, 3–14. doi:10.5006/1.3277303
- Buchheit, R. G., Guan, H., Mahajanam, S., and Wong, F. (2003). Active corrosion protection and corrosion sensing in chromate-free organic coatings. *Prog. Org. Coat.* 47, 174–182. doi:10.1016/j.porgcoat.2003.08.003
- Cao, Y., Zheng, D., Zhang, F., Pan, J., and Lin, C. (2022). Layered double hydroxide (LDH) for multi-functionalized corrosion protection of metals: A review. *J. Mat. Sci. Technol.* 102, 232–263. doi:10.1016/j.jmst.2021.05.078
- Carneiro, J., Caetano, A. F., Kuznetsova, A., Maia, F., Salak, A. N., Tedim, J., et al. (2015). Polyelectrolyte-modified layered double hydroxide nanocontainers as vehicles for combined inhibitors. *RSC Adv.* 5, 39916–39929. doi:10.1039/C5RA03741G
- Chen, J., Song, Y., Shan, D., and Han, E. H. (2012). Study of the *in situ* growth mechanism of Mg–Al hydrotalcite conversion film on AZ31 magnesium alloy. *Corros. Sci.* 63, 148–158. doi:10.1016/j.corsci.2012.05.022
- Conterosito, E., Gianotti, V., Palin, L., Boccacali, E., Viterbo, D., and Milanese, M. (2018). Facile preparation methods of hydrotalcite layered materials and their structural characterization by combined techniques. *Inorganica Chim. Acta* 470, 36–50. doi:10.1016/j.ica.2017.08.007
- Costa, D. G., Rocha, A. B., Souza, W. F., Chiaro, S. S. X., and Leitão, A. A. (2008). Structural and energetic analysis of  $\text{Mg}_3\text{M}_{1-x}(\text{OH})_2$  ( $\text{M} = \text{Zn}, \text{Cu}$  or  $\text{Ca}$ ) brucite-like compounds by DFT calculations. *J. Phys. Chem. C* 112, 10681–10687. doi:10.1021/jp8016453
- Costa, D. G., Rocha, A. B., Diniz, R., Souza, W. F., Chiaro, S. S. X., and Leitão, A. A. (2010). Structural model proposition and thermodynamic and vibrational analysis of hydrotalcite-like compounds by DFT calculations. *J. Phys. Chem. C* 114, 14133–14140. doi:10.1021/jp1033646
- Costa, D. G., Rocha, A. B., Souza, W. F., Chiaro, S. S. X., and Leitão, A. A. (2012). Comparative Structural, thermodynamic and electronic analyses of ZnAlAn-hydrotalcite-like compounds ( $\text{A}^n = \text{Cl}^-, \text{F}^-, \text{Br}^-, \text{OH}^-, \text{CO}_3^{2-}$  or  $\text{NO}_3^-$ ): An *ab initio* study. *Appl. Clay Sci.* 56, 16–22. doi:10.1016/j.clay.2011.11.014
- Critchlow, G. W., Yendall, K. A., Bahrani, D., Quinn, A., and Andrews, F. (2006). Strategies for the replacement of chromic acid anodising for the structural bonding of aluminium alloys. *Int. J. Adhes. Adhes.* 26, 419–453. doi:10.1016/j.ijadhadh.2005.07.001
- Cygan, R. T., Greathouse, J. A., Heinz, H., and Kalinichev, A. G. (2009). Molecular models and simulations of layered materials. *J. Mat. Chem.* 19, 2470. doi:10.1039/b819076c
- Cygan, R. T., Liang, J.-J., and Kalinichev, A. G. (2004). Molecular models of hydroxide, oxyhydroxide, and clay phases and the development of a general force field. *J. Phys. Chem. B* 108, 1255–1266. doi:10.1021/jp0363287
- Galvão, T. L. P., Ferreira, I., Kuznetsova, A., Novell-Leruth, G., Song, C., Feiler, C., et al. (2022). Cordata: An open data management web application to select corrosion inhibitors. *npj Mat. Degrad.* 6, 48. doi:10.1038/s41529-022-00259-9
- Galvão, T. L. P., Kuznetsova, A., Gomes, J. R. B., Zheludkevich, M. L., Tedim, J., and Ferreira, M. G. S. (2016a). A computational UV–Vis spectroscopic study of the chemical speciation of 2-mercaptobenzothiazole corrosion inhibitor in aqueous solution. *Theor. Chem. Acc.* 135, 78. doi:10.1007/s00214-016-1839-3
- Galvão, T. L. P., Neves, C. S., Caetano, A. P. F., Maia, F., Mata, D., Malheiro, E., et al. (2016b). Control of crystallite and particle size in the synthesis of layered double hydroxides: Macromolecular insights and a complementary modeling tool. *J. Colloid Interface Sci.* 468, 86–94. doi:10.1016/j.jcis.2016.01.038
- Galvão, T. L. P., Neves, C. S., Zheludkevich, M. L., Gomes, J. R. B., Tedim, J., and Ferreira, M. G. S. (2017). How density functional theory surface energies may explain the morphology of particles, nanosheets, and conversion films based on layered double hydroxides. *J. Phys. Chem. C* 121, 2211–2220. doi:10.1021/acs.jpcc.6b10860
- Galvão, T. L. P., Sousa, I., Wilhelm, M., Carneiro, J., Opršal, J., Kukačková, H., et al. (2018). Improving the functionality and performance of AA2024 corrosion sensing coatings with nanocontainers. *Chem. Eng. J.* 341, 526–538. doi:10.1016/j.cej.2018.02.061
- Galvão, T. L. P., Novell-Leruth, G., Kuznetsova, A., Tedim, J., and Gomes, J. R. B. (2020a). Elucidating structure-property relationships in aluminum alloy corrosion inhibitors by machine learning. *J. Phys. Chem. C* 124, 5624–5635. doi:10.1021/acs.jpcc.9b09538
- Galvão, T. L. P., Wilhelm, M., Gomes, J. R. B., and Tedim, J. (2020b). “Emerging trends in smart nanocontainers for corrosion applications,” in *Smart Nanocontainers*. Editors P. Nguyen-Tri, T.-O. Do, and T. A. Nguyen (Elsevier), Chap. 22, 385–398. doi:10.1016/B978-0-12-816770-0.00022-8
- Gomes, C., Mir, Z., Sampaio, R., Bastos, A., Tedim, J., Maia, F., et al. (2020). Use of ZnAl-layered double hydroxide (LDH) to extend the service life of reinforced concrete. *Mater. (Basel)* 13, 1769. doi:10.3390/MA13071769
- Greenwell, H. C., Jones, W., Coveney, P. V., and Stackhouse, S. (2006). On the application of computer simulation techniques to anionic and cationic clays: A materials chemistry perspective. *J. Mat. Chem.* 16, 708–723. doi:10.1039/B506932G
- Guo, L., Wu, W., Zhou, Y., Zhang, F., Zeng, R., and Zeng, J. (2018). Layered double hydroxide coatings on magnesium alloys: A review. *J. Mat. Sci. Technol.* 34, 1455–1466. doi:10.1016/j.jmst.2018.03.003
- Guo, X., Xu, S., Zhao, L., Lu, W., Zhang, F., Evans, D. G., et al. (2009). One-step hydrothermal crystallization of a layered double hydroxide/alumina bilayer film on aluminum and its corrosion resistance properties. *Langmuir* 25, 9894–9897. doi:10.1021/la901012w
- Guo, X., Zhang, F., Evans, D. G., and Duan, X. (2010). Layered double hydroxide films: Synthesis, properties and applications. *Chem. Commun.* 46, 5197–5210. doi:10.1039/c0cc00313a
- Gutner-Hoch, E., Martins, R., Maia, F., Oliveira, T., Shpigel, M., Weis, M., et al. (2019). Toxicity of engineered micro- and nanomaterials with antifouling properties to the brine shrimp *Artemia salina* and embryonic stages of the sea urchin *Paracentrotus lividus*. *Environ. Pollut.* 251, 530–537. doi:10.1016/j.envpol.2019.05.031
- Gutner-Hoch, E., Martins, R., Oliveira, T., Maia, F., Soares, A., Loureiro, S., et al. (2018). Antimicrofouling efficacy of innovative inorganic nanomaterials loaded with booster biocides. *J. Mar. Sci. Eng.* 6, 6. doi:10.3390/jmse6010006
- Han, J. B., Lu, J., Wei, M., Wang, Z. L., and Duan, X. (2008). Heterogeneous ultrathin films fabricated by alternate assembly of exfoliated layered double hydroxides and polyanion. *Chem. Commun.* 41, 5188–5190. doi:10.1039/b807479h
- He, Q. Q., Zhou, M. J., and Hu, J. M. (2020). Electrodeposited Zn–Al layered double hydroxide films for corrosion protection of aluminum alloys. *Electrochim. Acta* 355, 136796. doi:10.1016/j.electacta.2020.136796
- Hibino, T., and Ohya, H. (2009). Synthesis of crystalline layered double hydroxides: Precipitation by using urea hydrolysis and subsequent hydrothermal reactions in aqueous solutions. *Appl. Clay Sci.* 45, 123–132. doi:10.1016/j.clay.2009.04.013
- Hoshino, K., Furuya, S., and Buchheit, R. G. (2018). Effect of  $\text{NO}_3^-$  intercalation on corrosion resistance of conversion coated Zn–Al– $\text{CO}_3$  LDHs on electrogalvanized steel. *J. Electrochem. Soc.* 165, C461–C468. doi:10.1149/2.0091809jes
- Indira, L., and Vishnu Kamath, P. (1994). Electrogenation of base by cathodic reduction of anions: Novel one-step route to unary and layered double hydroxides (LDHs). *J. Mat. Chem.* 4, 1487–1490. doi:10.1039/JM9940401487
- Innovation - Kisuma chemicals Available at: <https://www.kisuma.com/Innovation> [Accessed September 8, 2022].
- Ishizaki, T., Chiba, S., Watanabe, K., and Suzuki, H. (2013). Corrosion resistance of Mg–Al layered double hydroxide container-containing magnesium hydroxide

- films formed directly on magnesium alloy by chemical-free steam coating. *J. Mat. Chem. A Mat.* 1, 8968–8977. doi:10.1039/C3TA11015J
- Iuzviuk, M. H., Bouali, A. C., Serdechnova, M., Yasakau, K. A., Wieland, D. C. F., Dovzhenko, G., et al. (2020). *In situ* kinetics studies of Zn–Al LDH intercalation with corrosion related species. *Phys. Chem. Chem. Phys.* 22, 17574–17586. doi:10.1039/D0CP01765E
- Jones, D. (2014). *Principles and prevention of corrosion*. 2nd ed. Essex: Pearson Education Limited.
- Kameda, T., Horikoshi, K., Kikuchi, H., Kitagawa, F., Kumagai, S., Saito, Y., et al. (2021). Kinetic and equilibrium analyses of lactate adsorption by Cu–Al and Mg–Al layered double hydroxides (Cu–Al LDH and Mg–Al LDH) and Cu–Al and Mg–Al layered double oxides (Cu–Al LDO and Mg–Al LDO). *Nano-Structures Nano-Objects* 25, 100656. doi:10.1016/j.NANOSO.2020.100656
- Kamiyama, N., Panomsuwan, G., Yamamoto, E., Sudare, T., Saito, N., and Ishizaki, T. (2016). Effect of treatment time in the Mg(OH)<sub>2</sub>/Mg–Al LDH composite film formed on Mg alloy AZ31 by steam coating on the corrosion resistance. *Surf. Coat. Technol.* 286, 172–177. doi:10.1016/j.SURFCOAT.2015.11.051
- Kim, N., Kim, Y., Tsotsis, T. T., and Sahimi, M. (2005). Atomistic simulation of nanoporous layered double hydroxide materials and their properties. I. Structural modeling. *J. Chem. Phys.* 122, 214713. doi:10.1063/1.1902945
- Kim, N., Harale, A., Tsotsis, T. T., and Sahimi, M. (2007). Atomistic simulation of nanoporous layered double hydroxide materials and their properties. II. Adsorption and diffusion. *J. Chem. Phys.* 127, 224701. doi:10.1063/1.2799985
- Kulyk, B., Freitas, M. A., Santos, N. F., Mohseni, F., Carvalho, A. F., Yasakau, K., et al. (2022). A critical review on the production and application of graphene and graphene-based materials in anti-corrosion coatings. *Crit. Rev. Solid State Mater. Sci.* 47, 309–355. doi:10.1080/10408436.2021.1886046
- Kuznetsov, B., Serdechnova, M., Tedim, J., Starykevich, M., Kallip, S., Oliveira, M. P., et al. (2016). Sealing of tartaric sulfuric (TSA) anodized AA2024 with nanostructured LDH layers. *RSC Adv.* 6, 13942–13952. doi:10.1039/C5RA27286F
- Kuznetsova, A., Domingues, P. M., Silva, T., Almeida, A., Zheludkevich, M. L., Tedim, J., et al. (2017). Antimicrobial activity of 2-mercaptobenzothiazole released from environmentally friendly nanostructured layered double hydroxides. *J. Appl. Microbiol.* 122, 1207–1218. doi:10.1111/jam.13433
- Leal, D. A., Kuznetsova, A., Silva, G. M., Tedim, J., Wypych, F., and Marino, C. E. B. (2022). Layered materials as nanocontainers for active corrosion protection: A brief review. *Appl. Clay Sci.* 225, 106537. doi:10.1016/j.clay.2022.106537
- Lee, W., Kim, E., Choi, J., and Lee, K. B. (2015). Kinetic analysis of secondary crystal growth for hydrotalcite film formation. *Cryst. Growth Des.* 15, 884–890. doi:10.1021/cg5016737
- Leggat, R. B., Zhang, W., Bucheit, R. G., and Taylor, S. R. (2002). Performance of hydrotalcite conversion treatments on AA2024-T3 when used in a coating system. *Corrosion* 58, 322–328. NACE-02040322. doi:10.5006/1.3287681
- Lei, X., Wang, L., Zhao, X., Chang, Z., Jiang, M., Yan, D., et al. (2013). Oriented CuZnAl ternary layered double hydroxide films: *In situ* hydrothermal growth and anticorrosion properties. *Ind. Eng. Chem. Res.* 52, 17934–17940. doi:10.1021/IE403299U
- Levin, D., Soled J. S. L., and Ying, A. Y. (1996). Chimie douce synthesis of nanostructured layered materials. *ACS Symp. Ser. Am. Chem. Soc.* 622, 237–249. doi:10.1021/BK-1996-0622.CH016
- Li, W., and Calle, L. M. (2008). “Review of pH and electrochemical responsive materials for corrosion control applications,” in NACE - CORROSION, New Orleans, LA, 08214.
- Li, W., Liu, A., Tian, H., and Wang, D. (2018). Controlled release of nitrate and molybdate intercalated in Zn–Al-layered double hydroxide nanocontainers towards marine anticorrosion applications. *Colloid Interface Sci. Commun.* 24, 18–23. doi:10.1016/J.COLCOM.2018.03.003
- Li, X., Würger, T., Feiler, C., Meißner, R. H., Serdechnova, M., Blawert, C., et al. (2022). Atomistic insight into the hydration states of layered double hydroxides. *ACS Omega* 7, 12412–12423. doi:10.1021/ACSOMEGA.2C01115
- Liu, Z., Ma, R., Osada, M., Iyi, N., Ebina, Y., Takada, K., et al. (2006). Synthesis, anion exchange, and delamination of Co–Al layered double hydroxide: Assembly of the exfoliated nanosheet/polyanion composite films and magneto-optical studies. *J. Am. Chem. Soc.* 128, 4872–4880. doi:10.1021/ja0584471
- Liu, Y., Visser, P., Zhou, X., Lyon, S. B., Hashimoto, T., Curioni, M., et al. (2016). Protective film formation on AA2024-T3 aluminum alloy by leaching of lithium carbonate from an organic coating. *J. Electrochem. Soc.* 163, C45–C53. doi:10.1149/2.0021603jes
- Lombardo, G. M., Pappalardo, G. C., Punzo, F., Costantino, F., Costantino, U., and Sisani, M. (2005). A novel integrated X-ray powder diffraction (XRPD) and molecular dynamics (MD) approach for modelling mixed-metal (Zn, Al) layered double hydroxides (LDHs). *Eur. J. Inorg. Chem.* 2005, 5026–5034. doi:10.1002/ejic.200500666
- Lu, Y., Jiang, B., Fang, L., Ling, F., Gao, J., Wu, F., et al. (2016). High performance NiFe layered double hydroxide for methyl orange dye and Cr(VI) adsorption. *Chemosphere* 152, 415–422. doi:10.1016/j.chemosphere.2016.03.015
- Lv, K., Kang, H., Zhang, H., and Yuan, S. (2012). Molecular simulation studies for intercalation of photoactive dyes into layered double hydroxide. *Colloids Surfaces A Physicochem. Eng. Aspects* 402, 108–116. doi:10.1016/j.colsurfa.2012.03.032
- Ma, R., Liu, Z., Li, L., Iyi, N., and Sasaki, T. (2006). Exfoliating layered double hydroxides in formamide: A method to obtain positively charged nanosheets. *J. Mat. Chem.* 16, 3809–3813. doi:10.1039/b605422f
- Makaremi, M., Jordan, K. D., Guthrie, G. D., and Myshakin, E. M. (2015). Multiphase Monte Carlo and molecular dynamics simulations of water and CO<sub>2</sub> intercalation in montmorillonite and beidellite. *J. Phys. Chem. C* 119, 15112–15114. doi:10.1021/acs.jpcc.5b01754
- Martínez-Viademonte, M. P., Abrahami, S. T., Hack, T., Burchardt, M., and Terryn, H. (2020). A review on anodizing of aerospace aluminum alloys for corrosion protection. *Coatings* 10, 1106. doi:10.3390/COATINGS10111106
- Martins, R., Oliveira, T., Santos, C., Kuznetsova, A., Ferreira, V., Avelelas, F., et al. (2017b). Effects of a novel anticorrosion engineered nanomaterial on the bivalve *Ruditapes philippinarum*. *Environ. Sci. Nano* 4, 1064–1076. doi:10.1039/C6EN00630B
- McMurray, H. N., and Williams, G. (2004). Inhibition of filiform corrosion on organic-coated aluminum alloy by hydrotalcite-like anion-exchange pigments. *Corrosion* 60, 219–228. doi:10.5006/1.3287724
- Mikhailau, A., Maltanova, H., Poznyak, S. K., Salak, A. N., Zheludkevich, M. L., Yasakau, K. A., et al. (2019). One-step synthesis and growth mechanism of nitrate intercalated ZnAl LDH conversion coatings on zinc. *Chem. Commun.* 55, 6878–6881. doi:10.1039/C9CC02571E
- Mir, Z. M., Bastos, A., Höche, D., and Zheludkevich, M. L. (2020). Recent advances on the application of layered double hydroxides in concrete—a review. *Materials* 13, 1426. doi:10.3390/ma13061426
- Mir, Z. M., Gomes, C., Bastos, A. C., Sampaio, R., Maia, F., Rocha, C., et al. (2021). The stability and chloride entrapping capacity of ZnAl–NO<sub>2</sub> LDH in high-alkaline/cementitious environment. *Corros. Mater. Degrad.* 2, 78–99. doi:10.3390/CMD2010005
- Mohammadi, I., Shahrabi, T., Mahdavian, M., and Izadi, M. (2021). Zn–Al layered double hydroxide as an inhibitive conversion coating developed on AA2024-T3 by one-step hydrothermal crystallization: Crystal structure evolution and corrosion protection performance. *Surf. Coat. Technol.* 409, 126882. doi:10.1016/J.SURFCOAT.2021.126882
- Mohedano, M., Serdechnova, M., Starykevich, M., Karpushenkov, S., Bouali, A. C., Ferreira, M. G. S., et al. (2017). Active protective PEO coatings on AA2024: Role of voltage on *in-situ* LDH growth. *Mat. Des.* 120, 36–46. doi:10.1016/J.MATDES.2017.01.097
- Momma, K., and Izumi, F. (2011). VESTA 3 for three-dimensional visualization of crystal, volumetric and morphology data. *J. Appl. Crystallogr.* 44, 1272–1276. doi:10.1107/S0021889811038970
- Montemor, M. F., Snihrova, D. V., Taryba, M. G., Lamaka, S. V., Kartsonakis, I. A., Balaskas, A. C., et al. (2012). Evaluation of self-healing ability in protective coatings modified with combinations of layered double hydroxides and cerium molibdate nanocontainers filled with corrosion inhibitors. *Electrochim. Acta* 60, 31–40. doi:10.1016/j.electacta.2011.10.078
- Neves, C. S., Bastos, A. C., Salak, A. N., Starykevich, M., Rocha, D., Zheludkevich, M. L., et al. (2019). Layered double hydroxide clusters as precursors of novel multifunctional layers: A bottom-up approach. *Coatings* 9, 328. doi:10.3390/coatings9050328
- Novell-Leruth, G., Pérez-Sánchez, G., Galvão, T. L. P., Boiba, D., Poznyak, S., Carneiro, J., et al. (2020). Unveiling the local structure of 2-mercaptobenzothiazole intercalated in (Zn<sub>2</sub>Al) layered double hydroxides. *Appl. Clay Sci.* 198, 105842. doi:10.1016/j.clay.2020.105842
- Parkhurst, D. L., and Appelo, C. A. J. (2013). Description of input and examples for PHREEQC version 3: A computer program for speciation, batch-reaction, one-dimensional transport, and inverse geochemical calculations. *Tech. Methods* 6, 497. doi:10.3133/TM6A43
- Pérez-Sánchez, G., Galvão, T. L. P., Tedim, J., and Gomes, J. R. B. (2018). A molecular dynamics framework to explore the structure and dynamics of layered double hydroxides. *Appl. Clay Sci.* 163, 164–177. doi:10.1016/J.CLAY.2018.06.037
- Pisson, J., Morel, J. P., Morel-Desrosiers, N., Taviot-Guého, C., and Malreay, P. (2008). Molecular modeling of the structure and dynamics of the interlayer species of ZnAlCl layered double hydroxide. *J. Phys. Chem. B* 112, 7856–7864. doi:10.1021/JP800574D



- Poznyak, S. K., Tedim, J., Rodrigues, L. M., Salak, A. N., Zheludkevich, M. L., Dick, L. F. P., et al. (2009). Novel inorganic host layered double hydroxides intercalated with guest organic inhibitors for anticorrosion applications. *ACS Appl. Mat. Interfaces* 1, 2353–2362. doi:10.1021/am900495r
- Prestopino, G., Arrabito, G., Generosi, A., Mattoccia, A., Paci, B., Perez, G., et al. (2019). Emerging switchable ultraviolet photoluminescence in dehydrated Zn/Al layered double hydroxide nanoplatelets. *Sci. Rep.* 9, 11498. doi:10.1038/s41598-019-48012-8
- Prinetto, F., Ghiotti, G., Graffin, P., and Tichit, D. (2000). Synthesis and characterization of sol-gel Mg/Al and Ni/Al layered double hydroxides and comparison with co-precipitated samples. *Microporous Mesoporous Mater.* 39, 229–247. doi:10.1016/S1387-1811(00)00197-9
- Pšenička, M., Škoda, J., and Pospíšil, M. (2020). Structural arrangement and properties of layered double hydroxide drug nanocarrier intercalated by sulindac and mefenamic acid solved by molecular simulation methods. *Appl. Clay Sci.* 189, 105560. doi:10.1016/J.CLAY.2020.105560
- Qu, J., Sha, L., Wu, C., and Zhang, Q. (2019). Applications of mechanochemically prepared layered double hydroxides as adsorbents and catalysts: A mini-review. *Nanomaterials* 9, 80. doi:10.3390/NANO9010080
- Rad, F. A., Rezvani, Z., and Khodam, F. (2016). Molecular design confirmation for proposition of improved photophysical properties in a dye-intercalated layered double hydroxides. *RSC Adv.* 6, 11193–11203. doi:10.1039/C5RA19209A
- Raki, L., Beaudoin, J. J., and Mitchell, L. (2004). Layered double hydroxide-like materials: Nanocomposites for use in concrete. *Cem. Concr. Res.* 34, 1717–1724. doi:10.1016/J.CEMCONRES.2004.05.012
- Revie, R. W., and Uhlig, H. H. (2008). *Corrosion and corrosion control: An introduction to corrosion science and engineering*. Fourth Edition. John Wiley & Sons. doi:10.1002/9780470277270
- Roberts, J., Song, Y., Crocker, M., and Risko, C. (2020). A genetic algorithmic approach to determine the structure of Li-Al layered double hydroxides. *J. Chem. Inf. Model.* 60, 4845–4855. doi:10.1021/acs.jcim.0c00493
- Rohmann, C., Metson, J. B., and Idriss, H. (2014). A DFT study on carbon monoxide adsorption onto hydroxylated  $\alpha$ -Al<sub>2</sub>O<sub>3</sub>(0001) surfaces. *Phys. Chem. Chem. Phys.* 16, 14287–14297. doi:10.1039/c4cp01373e
- Salak, A. N., Tedim, J., Kuznetsova, A. I., Ribeiro, J. L., Vieira, L. G., Zheludkevich, M. L., et al. (2012). Comparative X-ray diffraction and infrared spectroscopy study of Zn–Al layered double hydroxides: Vanadate vs nitrate. *Chem. Phys.* 397, 102–108. doi:10.1016/J.CHEMPHYS.2012.01.026
- Salak, A. N., Tedim, J., Kuznetsova, A. I., Zheludkevich, M. L., and Ferreira, M. G. S. (2010). Anion exchange in Zn–Al layered double hydroxides: *In situ* X-ray diffraction study. *Chem. Phys. Lett.* 495, 73–76. doi:10.1016/J.CPLETT.2010.06.041
- Senapati, S., Thakur, R., Verma, S. P., Duggal, S., Mishra, D. P., Das, P., et al. (2016). Layered double hydroxides as effective carrier for anticancer drugs and tailoring of release rate through interlayer anions. *J. Control. Release* 224, 186–198. doi:10.1016/j.jconrel.2016.01.016
- Serdechnova, M., Mohedano, M., Bouali, A., Höche, D., Kuznetsov, B., Karpushenkov, S., et al. (2017). Role of phase composition of PEO coatings on AA2024 for *in-situ* LDH growth. *Coatings* 7, 190. doi:10.3390/coatings7110190
- Serdechnova, M., Salak, A. N., Barbosa, F. S., Vieira, D. E. L., Tedim, J., Zheludkevich, M. L., et al. (2016). Interlayer intercalation and arrangement of 2-mercaptobenzothiazolate and 1, 2, 3-benzotriazolate anions in layered double hydroxides: *In situ* X-ray diffraction study. *J. Solid State Chem.* 233, 158–165. doi:10.1016/j.jssc.2015.10.023
- Shchukin, D. G., Zheludkevich, M., Yasakau, K., Lamaka, S., Ferreira, M. G. S., and Möhwald, H. (2006). Layer-by-Layer assembled nanocontainers for self-healing corrosion protection. *Adv. Mat.* 18, 1672–1678. doi:10.1002/adma.200502053
- Shulha, T. N., Serdechnova, M., Lamaka, S. V., Wieland, D. C. F., Lapko, K. N., and Zheludkevich, M. L. (2018). Chelating agent-assisted *in situ* LDH growth on the surface of magnesium alloy. *Sci. Rep.* 8, 16409–16410. doi:10.1038/s41598-018-34751-7
- Smallmteak – small materials and Technologies Available at: <https://www.smallmteak.pt/> [Accessed September 8, 2022].
- Sokol, D., Vieira, D. E. L., Zarkov, A., Ferreira, M. G. S., Beganskiene, A., Rubanik, V. V., et al. (2019). Sonication accelerated formation of Mg–Al-phosphate layered double hydroxide via sol-gel prepared mixed metal oxides. *Sci. Rep.* 9, 10419–9. doi:10.1038/s41598-019-46910-5
- Song, F., and Hu, X. (2014). Exfoliation of layered double hydroxides for enhanced oxygen evolution catalysis. *Nat. Commun.* 5, 4477. doi:10.1038/ncomms5477
- Sushkova, A., Wilhelm, M., Montes, R., Paulino, T., Galvão, T., Neves, C., et al. (2021). “Development of nanoadditives for detection of early-stage corrosion of carbon steel” in EUROCORR, September 20–24, 2021.
- Tabish, M., Yasin, G., Anjum, M. J., Malik, M. U., Zhao, J., Yang, Q., et al. (2021). Reviewing the current status of layered double hydroxide-based smart nanocontainers for corrosion inhibiting applications. *J. Mater. Res. Technol.* 10, 390–421. doi:10.1016/j.jmrt.2020.12.025
- Tait, W. S. (2012). “Corrosion prevention and control of chemical processing equipment,” in *Handbook of environmental degradation of materials*. Second Edition (Oxford: William Andrew Publishing), 863–886. doi:10.1016/B978-1-4377-3455-3.00028-6
- Takei, T., Miura, A., and Kumada, N. (2014). Soft-chemical synthesis and catalytic activity of Ni–Al and Co–Al layered double hydroxides (LDHs) intercalated with anions with different charge density. *J. Asian Ceram. Soc.* 2, 289–296. doi:10.1016/J.JASCER.2014.06.002
- Tatematsu, H., and Sasaki, T. (2003). Repair materials system for chloride-induced corrosion of reinforcing bars. *Cem. Concr. Compos.* 25, 123–129. doi:10.1016/S0958-9465(01)00059-2
- Tavares, S. R., Haddad, J. F. S., Ivo, R., Moraes, P., and Leitão, A. A. (2020a). Computational exploration of the anion exchange on the basal surface of layered double hydroxides by molecular dynamics. *Appl. Surf. Sci.* 513, 145743. doi:10.1016/J.APSUSC.2020.145743
- Tavares, S. R., Nangoi, I. M., and Leitão, A. A. (2020b). Computational investigation of two-dimensional LDHs and the modification of their electronic structure induced by defects. *Appl. Surf. Sci.* 532, 147159. doi:10.1016/J.APSUSC.2020.147159
- Tavares, S. R., Moraes, P. I. R., and Leitão, A. A. (2021). DFT and force-field based MD simulations of formamide intercalation in LDH and its exfoliated form. *Appl. Surf. Sci.* 552, 149450. doi:10.1016/J.APSUSC.2021.149450
- Tedim, J., Poznyak, S. K., Kuznetsova, A., Raps, D., Hack, T., Zheludkevich, M. L., et al. (2010). Enhancement of active corrosion protection via combination of inhibitor-loaded nanocontainers. *ACS Appl. Mat. Interfaces* 2, 1528–1535. doi:10.1021/am100174t
- Tedim, J., Zheludkevich, M. L., Salak, A. N., Lisenkov, A., and Ferreira, M. G. S. (2011). Nanostructured LDH-container layer with active protection functionality. *J. Mat. Chem.* 21, 15464–15470. doi:10.1039/c1jm12463c
- Tedim, J., Kuznetsova, A., Salak, A. N., Montemor, F., Snihirova, D., Pilz, M., et al. (2012). Zn–Al layered double hydroxides as chloride nanotraps in active protective coatings. *Corros. Sci.* 55, 1–4. doi:10.1016/j.corsci.2011.10.003
- Tedim, J., Zheludkevich, M. L., Bastos, A. C., Salak, A. N., Carneiro, J., Maia, F., et al. (2013). Effect of surface treatment on the performance of LDH conversion films. *ECS Electrochem. Lett.* 3, C4–C8. doi:10.1149/2.005401eel
- Tedim, J., Zheludkevich, M. L., Bastos, A. C., Salak, A. N., Lisenkov, A. D., and Ferreira, M. G. S. (2014). Influence of preparation conditions of Layered Double Hydroxide conversion films on corrosion protection. *Electrochim. Acta* 117, 164–171. doi:10.1016/j.electacta.2013.11.111
- Tedim, J., Bastos, A. C., Kallip, S., Zheludkevich, M. L., and Ferreira, M. G. S. (2016). Corrosion protection of AA2024-T3 by LDH conversion films. Analysis of SVET results. *Electrochim. Acta* 210, 215–224. doi:10.1016/j.electacta.2016.05.134
- Theiss, F. L., Palmer, S. J., Ayoko, G. A., and Frost, R. L. (2012). Sulfate intercalated layered double hydroxides prepared by the reformation effect. *J. Therm. Anal. Calorim.* 107, 1123–1128. doi:10.1007/s10973-011-1369-0
- Thomas, G. S., and Kamath, P. V. (2006). Line broadening in the PXRD patterns of layered hydroxides: The relative effects of crystallite size and structural disorder. *J. Chem. Sci. (Bangalore)* 118, 127–133. doi:10.1007/BF02708774
- Thyveetil, M.-A., Coveney, P. V., Greenwell, H. C., and Suter, J. L. (2008). Role of host layer flexibility in DNA guest intercalation revealed by computer simulation of layered nanomaterials. *J. Am. Chem. Soc.* 130, 12485–12495. doi:10.1021/ja8037068
- Tian, R., Liang, R., Wei, M., Evans, D. G., and Duan, X. (2016). Applications of layered double hydroxide materials: Recent advances and perspective. *Struct. Bond* 172, 65–84. doi:10.1007/430\_2015\_205
- Tran, P., Smith, S., Zhang, H., Xu, Z. P., Wong, Y., and Lu, G. Q. (2008). Molecular dynamic simulations of interactions between LDH and NO<sup>3-</sup> intercalates in aqueous solution. *J. Phys. Chem. Solids* 69, 1044–1047. doi:10.1016/J.JPCS.2007.10.063
- Trave, A., Selloni, A., Goursot, A., Tichit, D., and Weber, J. (2002). First principles study of the structure and chemistry of Mg-based hydrotalcite-like anionic clays. *J. Phys. Chem. B* 106, 12291–12296. doi:10.1021/JP026339K



- Tsukanov, A. A., and Psakhie, S. G. (2016). Energy and structure of bonds in the interaction of organic anions with layered double hydroxide nanosheets: A molecular dynamics study. *Sci. Rep.* 6, 19986. doi:10.1038/srep19986
- Twite, R. L., and Bierwagen, G. P. (1998). Review of alternatives to chromate for corrosion protection of aluminum aerospace alloys. *Prog. Org. Coat.* 33, 91–100. doi:10.1016/S0300-9440(98)00015-0
- Vieira, D. E. L., Sokol, D., Smalenskaite, A., Kareiva, A., Ferreira, M. G. S., Vieira, J. M., et al. (2019). Cast iron corrosion protection with chemically modified MgAl layered double hydroxides synthesized using a novel approach. *Surf. Coat. Technol.* 375, 158–163. doi:10.1016/J.SURFCOAT.2019.07.028
- Vieira, D. E. L., Salak, A. N., Ferreira, M. G. S., Vieira, J. M., and Brett, C. M. A. (2022). Ce-substituted Mg-Al layered double hydroxides to prolong the corrosion protection lifetime of aluminium alloys. *Appl. Surf. Sci.* 573, 151527. doi:10.1016/J.APSUSC.2021.151527
- Visser, P., Lutz, A., Mol, J. M. C., and Terryn, H. (2016). Study of the formation of a protective layer in a defect from lithium-leaching organic coatings. *Prog. Org. Coat.* 99, 80–90. doi:10.1016/J.PORGCOAT.2016.04.028
- Wang, J., Li, D., Yu, X., Jing, X., Zhang, M., and Jiang, Z. (2010). Hydrotalcite conversion coating on Mg alloy and its corrosion resistance. *J. Alloys Compd.* 494, 271–274. doi:10.1016/J.JALLCOM.2010.01.007
- Wang, Q., and Ohare, D. (2012). Recent advances in the synthesis and application of layered double hydroxide (LDH) nanosheets. *Chem. Rev.* 112, 4124–4155. doi:10.1021/cr200434v
- White, S. R., Sottos, N. R., Geubelle, P. H., Moore, J. S., Kessler, M. R., Sriram, S. R., et al. (2001). Autonomic healing of polymer composites. *Nature* 409, 794–797. doi:10.1038/35057232
- Wilhelm, M., Quevedo, M. C., Sushkova, A., Galvão, T. L. P., Bastos, A., Ferreira, M., et al. (2020). Hexacyanoferrate-intercalated layered double hydroxides as nanoadditives for the detection of early-stage corrosion of steel: The revival of prussian blue. *Eur. J. Inorg. Chem.* 2020, 2063–2073. doi:10.1002/EJIC.202000144
- Williams, G., and McMurray, H. N. (2004). Inhibition of filiform corrosion on polymer coated AA2024-T3 by hydrotalcite-like pigments incorporating organic anions. *Electrochem. Solid-State Lett.* 7, B13. doi:10.1149/1.1691529
- Wu, F., Liang, J., Peng, Z., and Liu, B. (2014). Electrochemical deposition and characterization of Zn-Al layered double hydroxides (LDHs) films on magnesium alloy. *Appl. Surf. Sci.* 313, 834–840. doi:10.1016/J.APSUSC.2014.06.083
- Wu, J., Peng, D., He, Y., Du, X., Zhang, Z., Zhang, B., et al. (2017). *In situ* formation of decavanadate-intercalated layered double hydroxide films on AA2024 and their anti-corrosive properties when combined with hybrid sol gel films. *Materials* 10, 426. doi:10.3390/MA10040426
- Wu, L., Peng, B., Li, Q., Wang, Q., Yan, X., Lin, Q., et al. (2019). Formation of high crystalline LDH sludge for removing Cu and Zn from wastewater by controlled double-jet precipitation. *Environ. Sci. Pollut. Res.* 26, 19665–19675. doi:10.1007/s11356-019-05161-7
- Wu, T., Ng, S. T., and Chen, J. (2022). Deciphering the CO<sub>2</sub> emissions and emission intensity of cement sector in China through decomposition analysis. *J. Clean. Prod.* 352, 131627. doi:10.1016/J.JCLEPRO.2022.131627
- Xu, Q., Ni, Z. M., and Mao, J. H. (2009). First principles study of microscopic structures and layer-anion interactions in layered double hydroxides intercalated various univalent anions. *J. Mol. Struct. THEOCHEM* 915, 122–131. doi:10.1016/J.THEOCHEM.2009.08.033
- Xu, Z. P., and Zeng, H. C. (2001). Abrupt structural transformation in hydrotalcite-like compounds  $Mg_{1-x}Al_x(OH)_2(NO_3)_x \cdot nH_2O$  as a continuous function of nitrate anions. *J. Phys. Chem. B* 105, 1743–1749. doi:10.1021/JP0029257
- Yan, H., Lu, J., Wei, M., Ma, J., Li, H., He, J., et al. (2008). Theoretical study of the hexahydrated metal cations for the understanding of their template effects in the construction of layered double hydroxides. *J. Mol. Struct. THEOCHEM* 866, 34–45. doi:10.1016/J.THEOCHEM.2008.06.031
- Yang, Z., Fischer, H., and Polder, R. (2013). Modified hydrotalcites as a new emerging class of smart additive of reinforced concrete for anticorrosion applications: A literature review. *Mater. Corros.* 64, 1066–1074. doi:10.1002/maco.201206915
- Yang, H., Xiong, C., Liu, X., Liu, A., Li, T., Ding, R., et al. (2021). Application of layered double hydroxides (LDHs) in corrosion resistance of reinforced concrete-state of the art. *Constr. Build. Mat.* 307, 124991. doi:10.1016/j.conbuildmat.2021.124991
- Yasakau, K. A., Kuznetsova, A., Kallip, S., Starykevich, M., Tedim, J., Ferreira, M. G. S., et al. (2018). A novel bilayer system comprising LDH conversion layer and sol-gel coating for active corrosion protection of AA2024. *Corros. Sci.* 143, 299–313. doi:10.1016/J.CORSCI.2018.08.039
- Ye, X., Jiang, Z., Li, L., and Xie, Z. H. (2018). *In-situ* growth of NiAl-layered double hydroxide on AZ31 Mg alloy towards enhanced corrosion protection. *Nanomaterials* 8, 411. doi:10.3390/NANO8060411
- Zhang, F., Sun, M., Xu, S., Zhao, L., and Zhang, B. (2008). Fabrication of oriented layered double hydroxide films by spin coating and their use in corrosion protection. *Chem. Eng. J.* 141, 362–367. doi:10.1016/J.CEJ.2008.03.016
- Zhang, F., Zhang, C. L., Song, L., Zeng, R. C., Liu, Z. G., and Cui, H. Z. (2015). Corrosion of *in-situ* grown MgAl-LDH coating on aluminum alloy. *Trans. Nonferrous Metals Soc. China* 25, 3498–3504. doi:10.1016/S1003-6326(15)63987-5
- Zhang, F., Ju, P., Pan, M., Zhang, D., Huang, Y., Li, G., et al. (2018). Self-healing mechanisms in smart protective coatings: A review. *Corros. Sci.* 144, 74–88. doi:10.1016/J.CORSCI.2018.08.005
- Zhang, W., and Buchheit, R. G. (2002). Hydrotalcite coating formation on Al-Cu-Mg alloys from oxidizing bath chemistries. *Corrosion* 58, 591–600. doi:10.5006/1.3277650
- Zheludkevich, M. L., Poznyak, S. K., Rodrigues, L. M., Raps, D., Hack, T., Dick, L. F., et al. (2010). Active protection coatings with layered double hydroxide nanocontainers of corrosion inhibitor. *Corros. Sci.* 52, 602–611. doi:10.1016/J.CORSCI.2009.10.020
- Zheludkevich, M. L., Tedim, J., and Ferreira, M. G. S. (2012). Smart coatings for active corrosion protection based on multi-functional micro and nanocontainers. *Electrochim. Acta* 82, 314–323. doi:10.1016/j.electacta.2012.04.095
- Zheludkevich, M. (2009). “Self-healing anticorrosion coatings,” in *Self-healing materials: Fundamentals, design strategies, and applications*, 101–139. doi:10.1002/9783527625376.CH4
- Zhi, P. X., and Guo, Q. L. (2005). Hydrothermal synthesis of layered double hydroxides (LDHs) from mixed MgO and Al<sub>2</sub>O<sub>3</sub>: LDH formation mechanism. *Chem. Mat.* 17, 1055–1062. doi:10.1021/cm048085g
- Zhou, M., Pang, X., Wei, L., and Gao, K. (2015). *In situ* grown superhydrophobic Zn-Al layered double hydroxides films on magnesium alloy to improve corrosion properties. *Appl. Surf. Sci.* 337, 172–177. doi:10.1016/J.APSUSC.2015.02.086
- Zhou, M., Yan, L., Ling, H., Diao, Y., Pang, X., Wang, Y., et al. (2017). Design and fabrication of enhanced corrosion resistance Zn-Al layered double hydroxides films based anion-exchange mechanism on magnesium alloys. *Appl. Surf. Sci.* 404, 246–253. doi:10.1016/J.APSUSC.2017.01.161
- Zhu, S., Khan, M. A., Kameda, T., Xu, H., Wang, F., Xia, M., et al. (2022). New insights into the capture performance and mechanism of hazardous metals Cr<sup>3+</sup> and Cd<sup>2+</sup> onto an effective layered double hydroxide based material. *J. Hazard. Mat.* 426, 128062. doi:10.1016/J.JHAZMAT.2021.128062



## OPEN ACCESS

## EDITED BY

Verónica de Zea Bermudez,  
University of Trás-os-Montes and Alto  
Douro, Portugal

## REVIEWED BY

Ping Wang,  
Jiangnan University, China  
Pei Xu,  
Sun Yat-Sen University, China

## \*CORRESPONDENCE

Ana P. M. Tavares,  
aptavares@ua.pt

<sup>†</sup>These authors have contributed equally  
to this work and share first authorship

## SPECIALTY SECTION

This article was submitted to  
Biomaterials,  
a section of the journal  
Frontiers in Bioengineering and  
Biotechnology

RECEIVED 05 September 2022

ACCEPTED 15 November 2022

PUBLISHED 28 November 2022

## CITATION

Magalhães FF, Pereira AF, Freire MG and  
Tavares APM (2022), New liquid  
supports in the development of  
integrated platforms for the reuse of  
oxidative enzymes and  
polydopamine production.  
*Front. Bioeng. Biotechnol.* 10:1037322.  
doi: 10.3389/fbioe.2022.1037322

## COPYRIGHT

© 2022 Magalhães, Pereira, Freire and  
Tavares. This is an open-access article  
distributed under the terms of the  
[Creative Commons Attribution License](#)  
(CC BY). The use, distribution or  
reproduction in other forums is  
permitted, provided the original  
author(s) and the copyright owner(s) are  
credited and that the original  
publication in this journal is cited, in  
accordance with accepted academic  
practice. No use, distribution or  
reproduction is permitted which does  
not comply with these terms.

# New liquid supports in the development of integrated platforms for the reuse of oxidative enzymes and polydopamine production

Flávia F. Magalhães<sup>†</sup>, Ana F. Pereira<sup>†</sup>, Mara G. Freire and  
Ana P. M. Tavares\*

Department of Chemistry, CICECO-Aveiro Institute of Materials, University of Aveiro, Aveiro, Portugal

Polydopamine (PDA), a bioinspired polymer from mussel adhesive proteins, has attracted impressive attention as a novel coating for (nano) materials with an adequate conformal layer and adjustable thickness. Currently, PDA is obtained from dopamine chemical oxidation under alkaline conditions, limiting its use in materials sensible to alkaline environments. Envisaging a widespread use of PDA, the polymerization of dopamine by enzymatic catalysis allows the dopamine polymerization in a large range of pHs, overcoming thus the limitations of conventional chemical oxidation. Moreover, the conventional method of polymerization is a time-consuming process and produces PDA films with poor stability, which restricts its applications. On the other hand, the main bottleneck of enzyme-based biocatalytic processes is the high cost of the single use of the enzyme. In this work, laccase was used to catalyze dopamine polymerization. To improve its performance, a liquid support for integrating the laccase and its reuse together with the PDA production and recovery was developed using aqueous biphasic systems (ABS). Firstly, dopamine polymerization by laccase was optimized in terms of pH, temperature and initial dopamine concentration. It was demonstrated that the highest enzymatic polymerization of dopamine was achieved at pH 5.5, 30°C and 2 mg ml<sup>-1</sup> of dopamine. Then, ABS composed of polymers, salts and ionic liquids were evaluated to optimize the laccase confinement in one phase while PDA is recovered in the opposite phase. The most promising ABS allowing the separation of laccase from the reaction product is composed of polypropylene glycol (400 g mol<sup>-1</sup>) and K<sub>2</sub>HPO<sub>4</sub>. The polymerization of dopamine in ABS leads to a remarkable improvement of polymerization of 3.9-fold in comparison to the conventional chemical PDA polymerization. The phase containing the confined laccase was reused for four consecutive reaction cycles, with a relative polymerization of 68.9% in the last cycle. The results of this work proved that ABS are a promising approach to create a liquid support for enzyme reuse allowing the process intensification efforts. The use of biocatalysts in ABS emerges as sustainable and alternative platforms from environmental and techno-economic points of view.

## KEYWORDS

laccase, polymerization of dopamine, polydopamine, aqueous biphasic systems, ionic liquids, integrated process

## 1 Introduction

Polydopamine (PDA) is a bioinspired polymer from mussel adhesive proteins, and has attracted relevant attention as a novel coating for (nano) materials with adequate conformational layer and adjustable thickness (Lee et al., 2007). PDA was first introduced in 2007 by Lee et al. (2007) as a multifunctional coating for different materials including noble metals, oxides, ceramics and polymers (Cai et al., 2018; Song et al., 2021; Teng et al., 2021). Since then, PDA has been widely used in the modification and functionalization of several (nano) materials, providing them new functionalities for a diversity of applications, especially in the field of biomedicine (Cai et al., 2018; Tripathi et al., 2018; Wu et al., 2022). Currently, PDA can be used as surface modifier for tissue engineering, cell adhesion, capsules, biosensing and drug delivery (Ding et al., 2016; Ball, 2018; Singh et al., 2021). The outstanding adhesive properties of PDA are attributed to the presence of catechol, amino and imine functional groups which can bind by covalent bonds or physical adsorption (Yan et al., 2020). Moreover, the (nano) materials modified with PDA present biocompatibility, biodegradability and antioxidative properties (Zhou et al., 2020). Comparing to other coating methodologies, such as chemical vapor deposition and layer-by-layer deposition (complex, expensive equipment, multiple steps and only applicable to certain materials) PDA coating can be achieved in a single-step (easy processing) allowing the functionalization of a large number of surfaces (El Yakhlifi and Ball, 2020).

The conventional method for dopamine polymerization is under alkaline conditions (pH > 8.5) that leads to spontaneously dopamine self-polymerization. However, it is a time-consuming process requiring a long reaction time, 24 h, and oxidant agents such as O<sub>2</sub>, NaIO<sub>4</sub> or KClO<sub>3</sub> (Wei et al., 2010; Li et al., 2018). These hard conditions have a lot of drawbacks when coating biological, alkali-sensitive or other surfaces that are not compatible with the reaction conditions such as polyester, phenolic resin and proteins, thus, limiting the widespread applications of PDA coatings (Li et al., 2018). In addition, the use of hazardous chemicals produces large quantities of insoluble precipitates, besides leading to rough surfaces and difficulty in controlling PDA film thickness (Lee et al., 2007). To overcome these limitations, a biocompatible, efficient, and environmentally friendly approach based on biocatalysis with oxidative enzymes has been recently proposed for the polymerization of dopamine since a well-controlled and material-efficient thin film formation can be produced (Kobayashi and Makino, 2009; Milyaeva et al., 2020). Laccases (oxygen oxidoreductase, EC 1.10.3.2) are multicopper oxidases with high catalytic efficiency for the degradation of both phenolic and non-phenolic compounds

and for the synthesis of polymers (Walde et al., 2019; Mayolo-Deloya et al., 2020). Moreover, due to their broad substrate range and diversity of biotechnological applications they are widely employed in the industrial sector (Zdarta et al., 2018; Mayolo-Deloya et al., 2020; Othman et al., 2022). Therefore, because of the diphenolic structure of dopamine, laccases are a potential biocatalyst for its oxidative polymerization in a large range of pH values (Olmeda et al., 2021). For example, Li et al. (2018) compared the enzymatic polymerization of dopamine using free laccase from *Trametes versicolor* with the conventional method. According to this study, the enzymatic polymerization of dopamine at pH 5.5 was ~3.4-fold higher and the obtained PDA films were more uniform and stable than the films produced by the conventional method (pH 8.5 under aerobic conditions) (Li et al., 2018). However, the use of free laccase has some limitations such as the loss of activity and stability as well as difficulties in its recovery and reusability increasing the process costs (Ferreira et al., 2018; Zhang et al., 2020; Adamian et al., 2021). To boost the economic and sustainable viability of the enzymatic process for dopamine polymerization with laccase, the reuse of the enzyme without loss in its biological properties is an ever-increasing demand for industrial applications (Zdarta et al., 2018). In this context, the most used approach is the enzyme immobilization on a solid support (Gan et al., 2021). Nevertheless, this strategy might lead to activity loss and conformational changes in the enzyme structure (Shakerian et al., 2020). Therefore, there is an urgent need to find alternative techniques to overcome such problems and ensure the biocatalyst's recovery and reusability from the reaction medium. When appropriately designed, aqueous biphasic systems (ABS), which are composed of water and at least two water-soluble components [e.g., polymers, salts, ionic liquids (ILs)], appear as an excellent and promising alternative with outstanding environmental and economic points of view. ABS consist of two immiscible aqueous-rich phases formed when water-soluble components are mixed above given concentrations (Freire et al., 2012; Pereira et al., 2020). Recently, ABS systems have been investigated as reaction media and liquid supports for enzymes since they provide a suitable and friendly environment for the maintenance of the enzymatic activity and its reuse (Ferreira et al., 2018; Capela et al., 2020; Ferreira et al., 2021; Muñoz-Mouro et al., 2021). Another advantage and application of this approach is the possibility of simultaneous extract and concentrate the reaction product by manipulating the volume of the ABS phases, using the tie-line of binodal curves (Dinis et al., 2018), while maintaining the enzyme in the opposite phase. Besides, the process integration is the principal strength of this technique: enzymatic reactions can be integrated with the

separation step, thus, making an integrated biocatalytic process (Pereira et al., 2020; Magalhães et al., 2021). Thereby, it is possible the separation of the target product and the reuse of the enzyme in a unique step, contributing to a reduction in process costs and time. In a recent study assessed by Ferreira et al. (2021) it was demonstrated the recovery and reuse of laccase in an integrated reaction-separation process by applying thermoreversible ABS. No losses in the enzymatic activity were observed for at least five consecutive cycles of enzymatic reaction with 2,2'-azino-bis (3-ethylbenzothiazoline-6-sulphonic acid) (ABTS). In the work performed by Muñiz-Mouro et al. (2021), the oligomerization of rutin using laccase as the biocatalyst was carried out in ABS. It was verified a preferential migration of laccase to the opposite phase of the product throughout the cycles and its reuse in three reaction-separation cycles was achieved.

This work aims the development of an integrated and sustainable platform for the enzymatic production and recovery of PDA and biocatalyst reuse using ABS. The biocatalytic process for the polymerization of dopamine was carried out using laccase as the biocatalyst and ABS composed of polymers, salts, and ILs. ABS was used for the first time as reaction media and liquid support for laccase allowing the simultaneous separation of product, soluble PDA intermediate species (PDA<sub>i</sub>), and the reuse of the enzyme. The potential of laccase in polymerization is herein exploited and compared with the non-enzymatic method. Several parameters including the temperature, pH of the medium and initial dopamine concentrations on the dopamine polymerization were also investigated and optimized.

## 2 Materials and methods

### 2.1 Materials

Polypropylene glycol with a molecular weight of 400 g mol<sup>-1</sup> (PPG 400), polyethylene glycol with a molecular weight of 400 g mol<sup>-1</sup> (PEG 400), ABTS (≥ 98 wt% purity) and dopamine hydrochloride (98 wt% purity) were acquired from Sigma-Aldrich. The ILs, cholinium dihydrogen phosphate ([Ch][DHP], >98 wt% purity) and cholinium acetate ([Ch][Acet], 98 wt% purity) were both purchased from IoLiTec, and cholinium dihydrogen citrate ([Ch][DHC], ≥98 wt% purity) from Sigma-Aldrich. Dipotassium hydrogen phosphate trihydrate (K<sub>2</sub>HPO<sub>4</sub>·3H<sub>2</sub>O, 98 wt% purity) was purchased from Scharlau.

Commercial laccase from *Trametes versicolor* (10 U mg<sup>-1</sup>) was acquired from Sigma-Aldrich. Sodium acetate (CH<sub>3</sub>COONa) pure from AnalaR Normapur and acetic acid (CH<sub>3</sub>COOH, 99 wt% purity) from Fisher Chemical was used to prepare sodium acetate buffer; disodium phosphate (Na<sub>2</sub>HPO<sub>4</sub>, 99 wt% purity) and citric

acid (C<sub>6</sub>H<sub>8</sub>O<sub>7</sub>, 99.5 wt% purity), both acquired from Panreac were used to prepare citrate-phosphate buffer; Tris-HCl buffer was prepared by using tris (hydroxymethyl) aminomethane [NH<sub>2</sub>C(CH<sub>2</sub>OH)<sub>3</sub>, >99 wt% purity] from PRONALAB and a hydrochloric acid solution (HCl, 1 M).

### 2.2 Optimization of the enzymatic polymerization of dopamine

Enzymatic polymerization of dopamine was performed according to the adapted procedure by Li et al. (2018). To optimise the dopamine polymerization into PDA<sub>i</sub> using laccase, several reactional parameters were studied, namely pH, temperature, and initial dopamine concentrations.

The pH effect on enzymatic polymerization was studied using sodium acetate buffer for pHs 4.5 and 5.5; phosphate buffer for pH 6.5 and Tris-HCl buffer for pH 7.5 and 8.5 (0.05 M). Dopamine solution (2.00 mg ml<sup>-1</sup>) was prepared in the multiple buffers and laccase (1.00 mg ml<sup>-1</sup>) was added to perform the enzymatic reaction. The reactions were kept at a controlled temperature (30°C) and continuously magnetic stirred (350 rpm) at atmospheric air for 1 h.

The influence of temperature was investigated. The assay was performed by adding a dopamine solution (2.00 mg ml<sup>-1</sup>) prepared in sodium acetate buffer at pH 5.5 (0.05 M) and laccase (1.00 mg ml<sup>-1</sup>). The reactions were performed at a controlled temperature in a range from 20 to 40°C and continuously magnetic stirred (350 rpm) at atmospheric air for 1 h.

The effect of dopamine concentration was evaluated by adding a dopamine solution with different concentrations ranging from 0.25 to 3.00 mg ml<sup>-1</sup> prepared in sodium acetate buffer at pH 5.5 (0.05 M) and laccase (1.00 mg ml<sup>-1</sup>). The reactions were kept at a controlled temperature (30°C) and continuously magnetic stirred (350 rpm) at atmospheric air for 1 h. Each assay was performed in triplicate. Reactions without laccase under the same conditions were carried out and considered as control.

UV-vis spectroscopy was employed to monitor the oxidation of dopamine. The degree of dopamine polymerization was indirectly monitored at 305 and 480 nm using a UV-Vis spectrophotometer (Shimadzu UV-1800 Spectrometer). Both wavelengths correspond to PDA<sub>i</sub>. For this purpose, spectra were acquired in wavelength range from 250 to 500 nm.

The relative enzymatic polymerization of dopamine in relation to the non-enzymatic was determined according to Eq. 1. The absorbance of the non-enzymatic polymerization was obtained after 1 h of reaction under the best conditions previously optimised (35°C, pH 8.5 and dopamine 2.00 mg ml<sup>-1</sup>) and was used as a reference value in the calculation of the relative enzymatic polymerization.



$$\text{Relative Polymerization (fold)} = \frac{\text{abs (enzymatic)}}{\text{abs (non - enzymatic)}} \quad (1)$$

where abs (enzymatic) and abs (non-enzymatic) correspond to the absorbance values at 480 nm of the laccase-catalysed polymerization and non-enzymatic polymerization, respectively.

## 2.3 Laccase activity method

The laccase activity was measured by adding 50  $\mu\text{l}$  of sample to 250  $\mu\text{l}$  of ABTS aqueous solution and 700  $\mu\text{l}$  of citrate phosphate buffer (0.1 M, pH 4.5). The increase in absorbance per min was spectrophotometrically measured at 420 nm and expressed in  $\text{U}\cdot\text{L}^{-1}$ . Each measurement was analysed in triplicate. 1 Unit (U) of laccase activity corresponds to the amount of enzyme necessary for the oxidation of 1  $\mu\text{mol}$  of the substrate (ABTS) per min ( $\epsilon = 36.000 \text{ M}^{-1} \text{ cm}^{-1}$ ).

### 2.3.1 Effect of dopamine and PDAi in the laccase activity method

The enzymatic activity of laccase was evaluated in the presence of dopamine by adding 200  $\mu\text{l}$  of dopamine solution with different concentrations ranging from 0.10 to 1.00  $\text{mg ml}^{-1}$  [prepared in Tris-HCl buffer at pH 8.5 (0.05 M)] and 200  $\mu\text{l}$  of laccase (0.60  $\text{mg ml}^{-1}$ ) + 600  $\mu\text{l}$  Tris-HCl buffer. Then, laccase activity was measured as previously described. The laccase activity measured in Tris-HCl buffer pH 8.5 was considered as the control (100%).

To evaluate the influence of PDA<sub>i</sub> in the laccase activity method, the polymerization of dopamine was carried out by the traditional method using Tris-HCl buffer at pH 8.5 (0.05 M). 200  $\mu\text{l}$  of PDA<sub>i</sub> solution was added to 200  $\mu\text{l}$  of laccase solution (0.60  $\text{mg ml}^{-1}$ ) + 600  $\mu\text{l}$  Tris-HCl. Then, laccase activity was measured as previously described. The laccase activity in the Tris-HCl buffer pH 8.5, used in the production of PDA<sub>i</sub>, was considered as the control (100%).

## 2.4 Evaluation of the extraction efficiency of laccase, dopamine and polydopamine in ABS

The extraction efficiency of active laccase ( $EE_{\text{Laccase}}\%$ ), dopamine ( $EE_{\text{dopamine}}\%$ ) and PDA<sub>i</sub> ( $EE_{\text{PDA}}\%$ ) was evaluated in five different ABS. The ABS ternary mixture compositions used were based on the previous binodal curves reported in the literature (Pereira et al., 2015; Sadeghi and Maali, 2016): 45 wt% PPG 400 + 7 wt% [Ch][DHP] + 48 wt%  $\text{H}_2\text{O}$ ; 46 wt% PPG 400 + 16 wt% [Ch][DHC] + 38 wt%  $\text{H}_2\text{O}$ ; 51 wt% PPG 400 + 6 wt% [Ch][Acet] + 43 wt%  $\text{H}_2\text{O}$ ; 33 wt% PPG 400 + 6.4 wt%  $\text{K}_2\text{HPO}_4$  + 60.6 wt%  $\text{H}_2\text{O}$  and 46 wt% PPG 400 + 24 wt% PEG 400 + 30 wt%  $\text{H}_2\text{O}$ .

$EE_{\text{Laccase}}\%$  was determined by adding 10 wt% of an aqueous laccase solution (1.00  $\text{mg ml}^{-1}$ ) to the ABS mixture compositions described above, replacing the water content, to attain a total ABS weight of 2 g. After the homogenization of the ABS, the phase separation was carried out by centrifugation at 3,500 rpm for 20 min at 25°C. The  $EE_{\text{Laccase}}\%$  was considered as the percentage ratio between the laccase activity in the bottom phase (bot) to that in the opposite top phase (top), according to Eq. 2. For each experiment three replicates were prepared.

$$EE_{\text{Laccase}}\% = \frac{\text{Laccase activity (bot)} \cdot W(\text{bot})}{\text{Laccase activity (bot)} \cdot W(\text{bot}) + \text{Laccase activity (top)} \cdot W(\text{top})} \times 100 \quad (2)$$

where W (bot) and W (top) correspond to the weight of the bottom and top phases, respectively.

To evaluate  $EE_{\text{dopamine}}\%$  for each ABS mentioned, 20 wt% of an aqueous dopamine solution (2.00  $\text{mg ml}^{-1}$ ) was added to the ABS mixture compositions described above, replacing the water content, attaining a total ABS weight of 2 g. After the homogenization of the ABS, the phase separation was carried out by centrifugation at 3,500 rpm for 20 min at 25°C. The absorbance of each phase was measured at 280 nm using a Shimadzu UV-Vis spectrometer.  $EE_{\text{dopamine}}\%$  was determined according to Eq. 3. For each experiment three replicates were prepared.

To evaluate  $EE_{\text{PDA}}\%$ , produced by the enzymatic catalysis, the polymerization of dopamine was carried out using the previously mentioned five ABS at the same compositions. For each ABS, 20 wt% of dopamine solution (2.0  $\text{mg ml}^{-1}$ ) and 10 wt% laccase aqueous solution (1.0  $\text{mg ml}^{-1}$ ) were added to the ABS mixture compositions, replacing water content, for total ABS weight of 2 g. The reaction was incubated at 25°C and stirred for 1 h. Afterwards, both phases of the ABS were separated after centrifugation at 3,500 rpm for 30 min at 25°C. PDA<sub>i</sub> partition was assessed by recording the UV-Vis absorbance spectra ranging between 250 and 500 nm, through the analysis of absorbance at 480 nm.  $EE_{\text{PDA}}\%$  was determined according to Eq. 3. For each experiment three replicates were prepared.

$$EE_{\text{dopamine/PDA}}\% = \frac{\text{abs (top)} \cdot \text{DF (top)} \cdot W(\text{top})}{\text{abs (top)} \cdot \text{DF (top)} \cdot W(\text{top}) + \text{abs (bot)} \cdot \text{DF (bot)} \cdot W(\text{bot})} \times 100 \quad (3)$$

where abs (top) and abs (bot) correspond to the absorbance values at 280 nm (for dopamine partition) or 480 nm (for PDA<sub>i</sub> partition) of the top and bottom phases, respectively. DF corresponds to the dilution factor of each phase, W (top) to the weight of the top phase and W (bot) the weight of the bottom phase.

## 2.5 Evaluation of the dopamine concentration in the enzymatic polymerization using ABS

Laccase-catalysed dopamine polymerization was carried out in the selected ABS composed of 33 wt% PPG 400 + 6.4 wt% K<sub>2</sub>HPO<sub>4</sub> + 20 wt% dopamine solutions (0.50–3.50 mg ml<sup>-1</sup>) + 40.6 wt% laccase solution at 2.56 mg ml<sup>-1</sup>. The reactions were performed for 1 h, incubated at 30°C and continuously under magnetic stirring (350 rpm). After 1 h, the phase separation was carried out by centrifugation at 3,500 rpm for 30 min at 25°C. Relative polymerization (fold) was determined according to Eq. 1. Different final dopamine concentrations from 0.10 to 0.70 mg ml<sup>-1</sup> were evaluated. The conventional method of polymerization (without laccase) was also carried out in the same ABS and was considered as the reference: 33 wt% PPG 400 + 6.4 wt% K<sub>2</sub>HPO<sub>4</sub> + 20 wt% dopamine solution (0.50–3.50 mg ml<sup>-1</sup>) + 40.6 wt% H<sub>2</sub>O at 30°C.

### 2.5.1 Laccase activity in presence of ABS bottom phase

To evaluate the effect of the ABS bottom phase in the laccase activity, the selected ABS composed of 33 wt% PPG 400 + 6.4 wt% K<sub>2</sub>HPO<sub>4</sub> was prepared and the phase separation was carried out by centrifugation at 3,500 rpm for 30 min at 25°C. The laccase activity was determined in the bottom phase of the ABS that was used as a medium for laccase incubation. The laccase activity measured in water at the same conditions (final enzyme concentration at 0.60 mg ml<sup>-1</sup> and after 1 h of incubation time at 25°C) was considered as the control (100%).

## 2.6 Laccase recovery and reuse using ABS

ABS is used to recovery and reuse of the enzyme by confining the enzyme in the bottom phase. For the study of recovery and reuse of laccase, four consecutive cycles of dopamine polymerization were performed using the optimised ABS composed of 33 wt% PPG 400 + 6.4 wt% K<sub>2</sub>HPO<sub>4</sub> + 20 wt% dopamine solution (3.00 mg ml<sup>-1</sup>) + 40.6 wt% laccase solution (1.00 mg ml<sup>-1</sup>). After the first reaction cycle, the PDA<sub>i</sub>-enriched top phase was removed, and the same volume of a solution containing the respective top polymer-rich phase constituents (determined by the tie-line) (Ferreira et al., 2021) was added to the remaining laccase-rich bottom phase. Dopamine solution was added to reach a final concentration of 0.60 mg ml<sup>-1</sup> in the ABS and a new biocatalytic cycle started. This step was repeated for four consecutive reaction cycles. After each cycle, the ABS was centrifuged at 3,500 rpm for 30 min and both phases were separated. Laccase reuse is confirmed by the increase in dopamine polymerization.

Relative polymerization (%) was defined as the ratio between the obtained absorbance at the end of each cycle with respect to that obtained in the first cycle and was calculated according to Eq. 4:

$$\text{Relative polymerization (\%)} = \frac{\text{abs (n cycle)}}{\text{abs (1st cycle)}} \times 100 \quad (4)$$

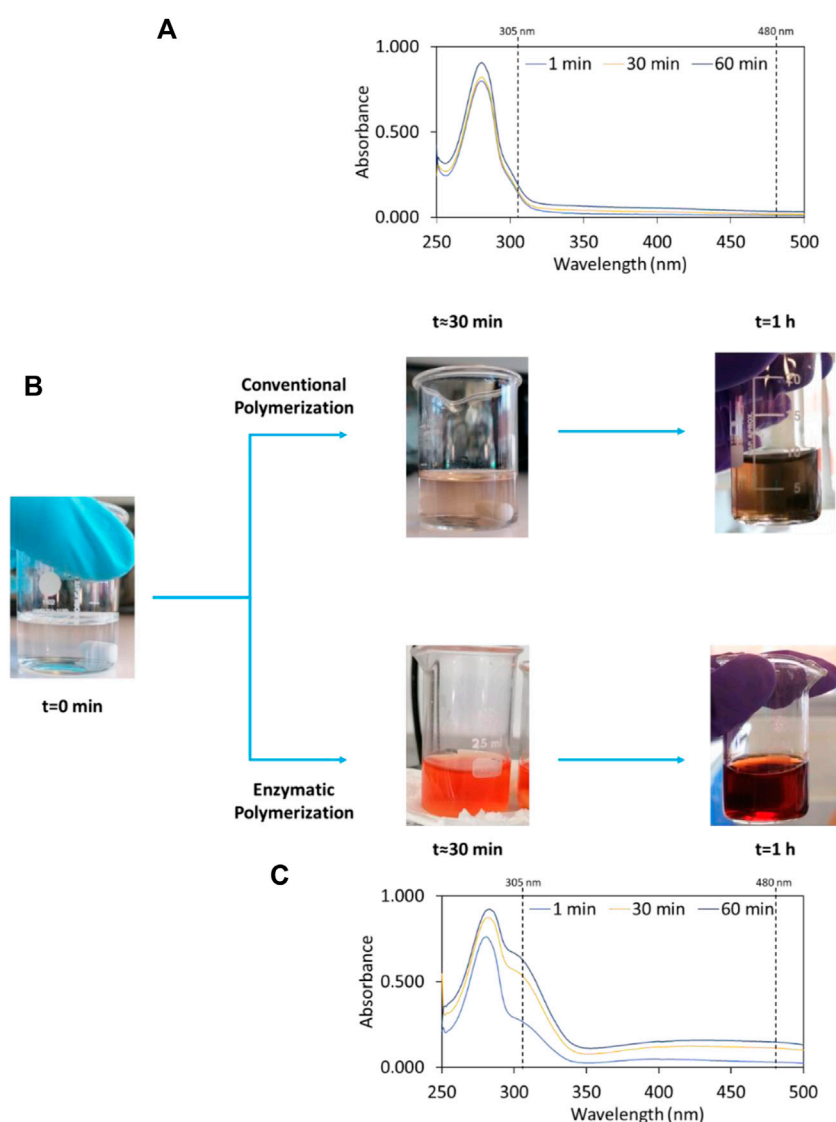
where abs<sub>(n cycle)</sub> and abs<sub>(1st cycle)</sub> correspond to the absorbance values at 480 nm obtained in the ABS top phase each cycle and the first cycle of reaction, respectively.

## 3 Results and discussion

### 3.1 Optimization of the enzymatic polymerization of dopamine

To explore the potential of laccase in the polymerization of dopamine, the enzymatic polymerization was investigated at pH 5.5 and compared to the alkaline conventional method at pH 8.5. Both reactions were carried out at 30°C for 1 h. In the presence of laccase, the colourless of the initial dopamine solution rapidly (~1 min) changed to a reddish solution, indicating the fast polymerization of dopamine. After 1 h of reaction, the red colour became more intense (dark red) (Figure 1B). Comparatively, in the non-enzymatic polymerization, the colourless solution turned into pale yellow and after 1 h into grey. Small PDA films were also observed at the surface of the solution (although not so notable), as well as grains in the bulk (Figure 1B).

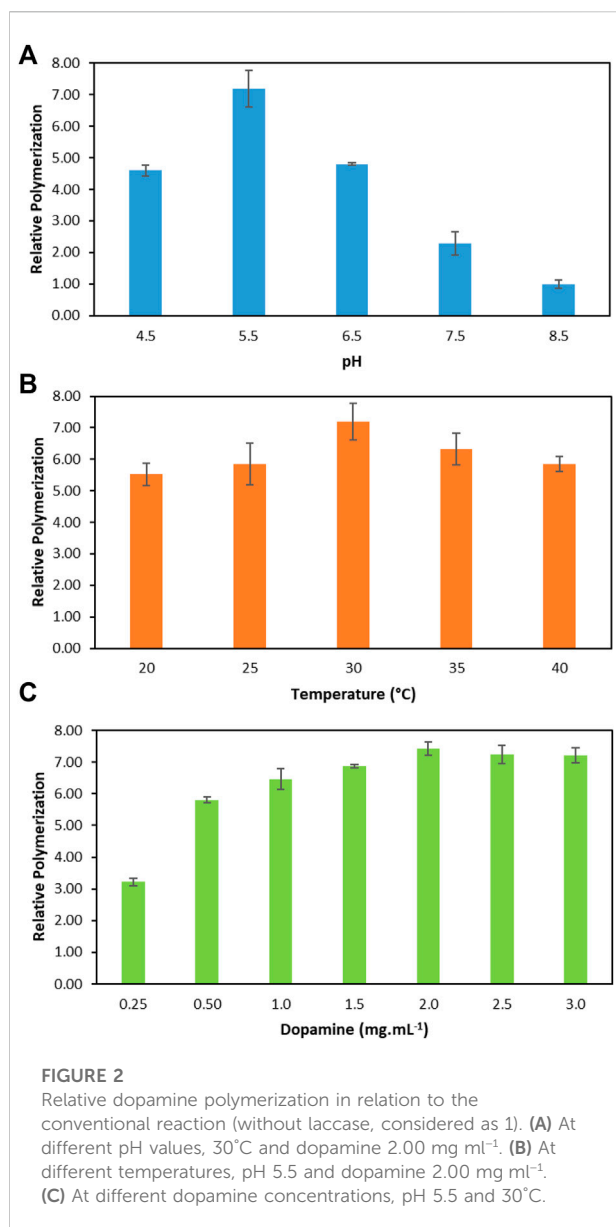
The oxidation of dopamine into PDA<sub>i</sub> was assessed by UV-Vis absorption intensities at 305 and 480 nm, which correspond to the formation of dopamine semiquinone and dopaminechrome intermediate species, respectively. The subsequent oxidation of these species leads to the formation of PDA (Wei et al., 2010; Salomäki et al., 2018). In this study, the absorbance value chosen to evaluate and calculate the relative polymerization was 480 nm, since it corresponds to the intermediate species to produce PDA during the polymerization reaction. All UV-Vis absorbance spectra during the time of both reactions and the detailed analysis and discussion of the intermediate species are reported in the Supplementary Figures S1–S4. According to Figure 1C, there is a fast increase in absorption intensities at 305 and 480 nm of the enzymatic polymerization during the reaction time. In contrast, for the conventional non-enzymatic reaction (Figure 1A), the absorption peaks intensity remains unaltered in all wavelength ranges during the reaction time, which indicates that the polymerization of dopamine into PDA<sub>i</sub> is very slow. The dopamine polymerization reaction was improved in the presence of laccase since for the same reaction time the conventional polymerization was significantly inferior. Relatively to the absorbance at 305 nm, for the enzymatic method, an absorbance increase of ~4.6-fold in relation to the non-enzymatic method is obtained after 1 h. Regarding the absorbance at 480 nm, an increase of ~7-fold after 1 h was obtained when compared to the non-enzymatic dopamine polymerization. These results are consistent with those reported by Li et al. (2018), in which the spectra follow the same trend at the same wavelength values.

**FIGURE 1**

Colour changes of initial solutions of dopamine after 30 min and 1 h (B) and time-dependent UV-Vis absorbance spectra for: Conventional polymerization of dopamine, pH 8.5 and 30°C (A) and enzymatic polymerization of dopamine, pH 5.5 and 30°C (C).

To improve the performance of the enzymatic polymerization of dopamine, the following reaction parameters were optimised: pH, temperature, and initial dopamine concentrations. Figure 2 depicts the relative increase in the polymerization of dopamine with laccase in relation to the conventional reaction (without laccase) at the best reaction condition: pH 8.5, 30°C and  $2.00 \text{ mg ml}^{-1}$ . Conventional reaction was considered as the control (1-fold). It should be noted that the conventional dopamine polymerization was also evaluated at a pH range between 4.5 and 7.5 and, as expected, no polymerization was observed. The respective detailed data are reported in the Supplementary Tables S1–S3.

Firstly, the effect of the pH on the enzymatic dopamine polymerization was evaluated since the pH affects the oxidation and polymerization by laccase. The pH dependence of laccase was studied at pH values ranging from 4.5 to 8.5. The respective relative polymerization values are depicted in Figure 2A. All reactions were carried out with an initial dopamine concentration of  $2.00 \text{ mg ml}^{-1}$  at 30°C. According to the results, it is evident that the optimal pH for the enzymatic polymerization of dopamine was pH 5.5. The efficiency of the enzymatic reaction at pH 5.5 was improved by approximately 7.2-fold. In addition, all pHs ranging from 4.5 to 7.5 present better relative dopamine polymerization than the conventional polymerization. As



expected, the lowest polymerization value corresponds to pH 8.5 which is similar to the conventional approach. This can be explained by the higher pH since the laccase performance decreases due to the inhibitory effect of OH<sup>-</sup> on the active site of the enzyme (Tan et al., 2010). This result indicates that laccase exhibits a low capacity for dopamine polymerization in high pHs values which is in agreement with the literature (Arregui et al., 2019; Yin et al., 2019). Considering the laccase activity and relative polymerization, pH 5.5 was chosen for dopamine polymerization.

After selecting the best pH of 5.5, the temperature from 20 to 40°C was evaluated in the relative dopamine polymerization (Figure 2B). The temperature that led to the high relative dopamine polymerization was 30°C, with an increase of 7.2-fold when compared to the conventional method. In addition, an

increase of 6.3-fold, 5.8-fold and 5.8-fold in the relative dopamine polymerization was obtained for 35, 40 and 25°C, respectively. These results indicate that laccase is able to polymerize dopamine in a significant temperature range. According to the literature, laccase from *T. versicolor* shows an increase in its activity with the increase in the temperature up to 60°C, however, its thermal stability stands between 10 and 30°C (Kurniawati and Nicell, 2008). The results obtained agree with these data since the best temperature to work with laccase is 30°C, where the enzyme has a good thermal stability.

At the optimum pH and temperature (pH 5.5 and 30°C), the initial dopamine concentration was optimised in the range of 0.25–3.00 mg mL<sup>-1</sup>. The relative dopamine polymerization values are depicted in Figure 2C. There is an increase in the relative polymerization values as the dopamine concentration increases up to 2.00 mg mL<sup>-1</sup>, leading to the highest relative dopamine polymerization of 7.4-fold. From 2.00 mg mL<sup>-1</sup>, the relative dopamine polymerization remained constant, which indicates the saturation of the enzyme by the dopamine. After the enzyme reaches its saturation point, the increase of dopamine concentration did not affect the reaction rate, creating the same amount of PDA<sub>i</sub> in 1 h. Moreover, it is important to highlight that even at the lowest dopamine concentration (0.25 mg mL<sup>-1</sup>) a relative polymerization increase of ~3-fold was obtained in relation to the maximum value observed for the conventional non-enzymatic method at 2.00 mg mL<sup>-1</sup>.

The parameters for the enzymatic dopamine polymerization were optimised (pH 5.5, 30°C and dopamine 2.00 mg mL<sup>-1</sup>). Under these conditions, the relative enzymatic dopamine polymerization achieves 7.4-fold in comparison to the conventional dopamine polymerization. These results confirm that the use of laccase has many advantageous for the PDA<sub>i</sub> production. In addition, the laccase reuse is important to achieve a more sustainable and economic process. Therefore, the reuse of laccase in ABS is further investigated to improve the process.

## 3.2 ABS as integrated platform for the polydopamine production and laccase reuse

### 3.2.1 Extraction efficiency of laccase, PDA<sub>i</sub> and dopamine

Enzyme reuse and substrate recovery need to be considered when developing a sustainable and economical process. The reuse of enzymes using liquid supports can provide a novel opportunity to surpass the major challenge of biocatalyst recovery and reuse while improving its stability, activity, biocompatibility and reaction rates (Ferreira et al., 2021; Muñoz-Mouro et al., 2021; Baptista et al., 2022). To this end, ABS approach was chosen as excellent liquid supports to develop an integrated and sustainable platform for enzymatic catalysis. This approach allows PDA<sub>i</sub> to be recovered in one



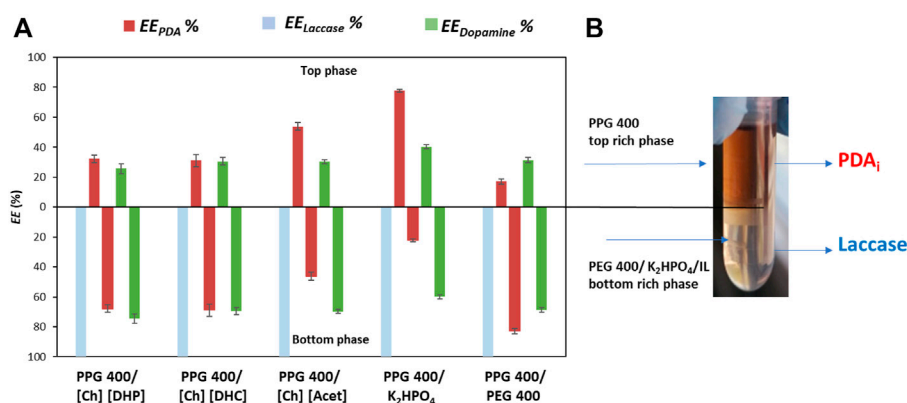


FIGURE 3

(A) Extraction efficiency of PDA<sub>i</sub> ( $EE_{PDA}$  %, red bars), laccase ( $EE_{Laccase}$  %, blue bars) and dopamine ( $EE_{Dopamine}$  %, green bars) in the top and bottom-phase. (B) PPG 400 + K<sub>2</sub>HPO<sub>4</sub> ABS after the enzymatic polymerization of dopamine and phases separation.

phase while the enzyme is confined into the opposite phase for further reuse.

To develop this multifunctional platform, it is mandatory that PDA<sub>i</sub> migrate to the opposite phase of laccase. Thus, it was firstly evaluated the  $EE_{PDA}$  %,  $EE_{Laccase}$  %, and  $EE_{Dopamine}$  % in five different ABS composed of PPG 400 and [Ch][DHP], [Ch][DHC], [Ch][Acet], PEG 400 or K<sub>2</sub>HPO<sub>4</sub>. The ternary mixture compositions of the ABS were selected according to the literature (Ferreira et al., 2021) and correspond to a mixture point that leads to a biphasic system with an approximately equal ratio of both phases. Thus, it is possible to ensure enough mass in each phase for laccase reaction and reuse and product recovery. The  $EE_{PDA}$  and  $EE_{Laccase}$  % are shown in Figure 3A and an image of the PPG 400 + K<sub>2</sub>HPO<sub>4</sub> ABS after the enzymatic polymerization reaction is shown in Figure 3B. The respective detailed data are reported in the (Supplementary Tables S4–S6).

The results depicted in Figure 3A show a selective partition of laccase for the bottom phase (IL-, K<sub>2</sub>HPO<sub>4</sub>- or PEG-rich phase) of all ABS, with an  $EE_{Laccase}$  of 100%. These results are in accordance with previous works demonstrating that proteins and enzymes have a high affinity for the more hydrophilic phase (Ferreira et al., 2018; Capela et al., 2020; Ferreira et al., 2021). For example, the study carried out by Capela et al. (2020) proved that using ABS composed of cholinium-based ILs or PEG 400 + PPG 400, laccase complete partitioned for the more hydrophilic phase namely IL- or PEG 400- rich phase with an  $EE_{Laccase}$  of 100%.

Regarding the  $EE_{PDA}$  %, for the ABS composed of PPG 400 + [Ch][Acet], PDA preferentially migrates to the top phase ( $EE_{PDA}$  of 53.8%), whereas for PPG 400 + [Ch][DHP], PPG 400 + [Ch][DHC], and PPG 400 + PEG 400, PDA<sub>i</sub> and laccase preferentially migrate to the bottom-phase, with an  $EE_{PDA}$  to the top-phase ranging from 17.2 to 32.2%. Thus, these ABS were excluded for further studies since the PDA<sub>i</sub> was in the same phase of laccase.

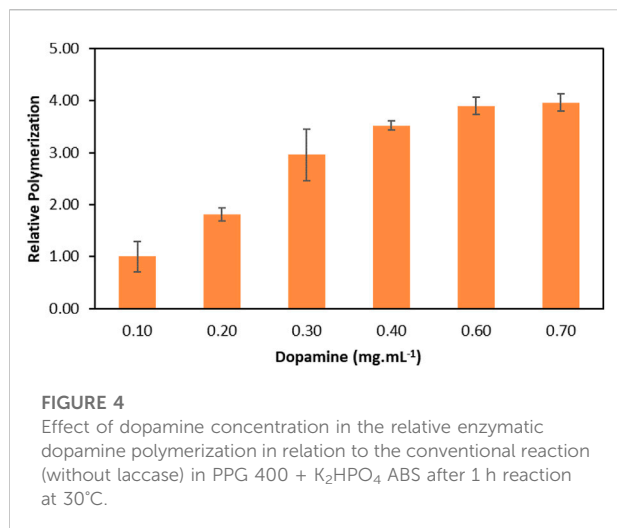
On the other hand, the ABS composed of PPG 400 + K<sub>2</sub>HPO<sub>4</sub> led to the best  $EE_{PDA}$  of 77.8%. PDA<sub>i</sub> preferentially migrated to the PPG-rich top phase while laccase complete migrated to the salt-rich bottom phase. Thus, this ABS was the most promising system for the separation of PDA<sub>i</sub> while allowing the recovery and reuse of laccase. In addition, the colour obtained in the top phase after 1 h of reaction confirmed that the dopamine polymerization was successfully catalysed by laccase, Figure 3B.

From an integrated and sustainable process perspective, the dopamine partition is also important to better comprehend the composition of the phases and their reuse. Therefore,  $EE_{dopamine}$  % was determined and the results are depicted in Figure 3A. Dopamine preferentially migrated to the bottom phase for all ABS investigated, with an  $EE_{dopamine}$  for the bottom phase from 59.8 to 74.4%. Since dopamine is more hydrophilic than PDA<sub>i</sub>, this behaviour is expected due to the hydrophilic character of the bottom phase (You et al., 2017; Zhang et al., 2018). These results are promising, both dopamine and laccase migrate for the same phase, thus, allowing the recovery and reuse of the dopamine, that is not consumed by the enzymatic reaction, for posterior cycles of reaction.

Based on the obtained results, the ABS constituted by PPG 400 + K<sub>2</sub>HPO<sub>4</sub> allowed a remarkable  $EE_{Laccase}$  of 100% for the bottom phase and PDA<sub>i</sub> to the opposite top phase. Thus, this ABS was selected for further studies of enzyme reuse.

### 3.2.2 Effect of dopamine concentration on the laccase-catalysed PDA<sub>i</sub> using ABS

The polymerization of dopamine in the selected ABS was evaluated. Using the conditions previously selected, the reaction was carried out in a system composed of PPG 400 + K<sub>2</sub>HPO<sub>4</sub>/KH<sub>2</sub>PO<sub>4</sub> at 30°C, pH 5.5 and initial dopamine concentration of 2.00 g ml<sup>-1</sup>. However, under these conditions, the formation of a precipitate was observed (Supplementary Figure S5,



Supplementary Material), which did not allow to quantify the PDA<sub>i</sub>, the aim of this work. Thus, all the enzymatic reaction performed in ABS was carried out using the original pH of the system (pH 8.8).

The optimisation of the laccase-catalysed dopamine polymerization was carried out in the selected ABS composed of PPG 400 + K<sub>2</sub>HPO<sub>4</sub> by determining the ideal initial dopamine concentration in the ABS. The optimisation was evaluated based on the relative polymerization increase using different concentrations of dopamine, from 0.10 to 0.70 mg mL<sup>-1</sup> after 1 h of reaction. Figure 4 depicts the relative polymerization fold of dopamine with laccase in the ABS, in relation to conventional reaction at the same conditions without laccase (considered as the control, 1-fold). The respective detailed data are reported in the Supplementary Material (Supplementary Table S7).

The results depicted in Figure 4 show an increase in the relative dopamine polymerization from 1.0 to 3.9-fold when dopamine concentration increases from 0.10 mg mL<sup>-1</sup> up to 0.60 mg mL<sup>-1</sup>, respectively. Above this value, the relative dopamine polymerization remains constant, following a similar trend to that previously observed in Figure 2, which indicates enzyme saturation. Also, it is possible to conclude that all reactions with dopamine above 0.1 mg mL<sup>-1</sup> lead to an outstanding polymerization increase in comparison with the conventional polymerization method performed without laccase, again demonstrating the high efficiency of the laccase-catalysed reaction.

Comparing to the performance of laccase in aqueous solution, a decrease in optimum dopamine concentration is observed. To explain this behaviour, the enzymatic activity of laccase was evaluated in the bottom phase of the ABS composed of PPG 400 + K<sub>2</sub>HPO<sub>4</sub>. Compared to the control (laccase in water at the same conditions), the laccase maintains 80% of the enzymatic activity in the K<sub>2</sub>HPO<sub>4</sub> rich-phase. The decrease in laccase activity in the bottom phase can explain the difference in

the relative polymerization between the results in the ABS and in aqueous solution. However, despite some loss in enzymatic activity in the ABS, this technique allows the recovery and reuse of the enzyme with good performance.

Since above 0.60 mg mL<sup>-1</sup> the polymerization remains constant, this concentration was chosen for further assays. The choice of the initial concentration of dopamine is important to make the process profitable, making it more sustainable and economical, and avoiding the unnecessary use of the substrate.

### 3.3 ABS as liquid support for laccase recovery and reuse

After selecting the optimum dopamine concentration (0.60 mg mL<sup>-1</sup>), an integrated platform for laccase reuse and PDA<sub>i</sub> recovery was developed using the ABS composed of PPG 400 + K<sub>2</sub>HPO<sub>4</sub>. The polymerization reaction was carried out in the ABS for four consecutive cycles. A scheme of the integrated reaction—extraction platform developed, including the recycling of the laccase and dopamine and the K<sub>2</sub>HPO<sub>4</sub>-rich phase is illustrated in Figure 5A. The enzymatic reaction in the ABS was carried out with continuous stirring for 1 h (heterogeneous medium). Then, the ABS was centrifuged, and the phases recovered. The relative polymerization, in relation to the first cycle, was determined, in Figure 5B [Detailed data are reported in the Supplementary Material (Supplementary Table S8)].

The enzymatic cycles were evaluated through the polymerization of dopamine into PDA<sub>i</sub> (relative polymerization), Figure 5B. Overall, the recovery and reuse of laccase were possible for at least four reaction cycles, as can be confirmed by the obtained values of the relative polymerization (%) (Figure 5B). Despite some decrease in relative polymerization from the first to the second cycle, a remarkable relative polymerization of ~70% in the last cycle was achieved. The decrease in the polymerization may be caused by the physical forces used, such as constant stirring and centrifugation throughout the four cycles of reaction, leading to enzymatic activity loss or by laccase inhibition caused by PDA<sub>i</sub>. Similar behaviour is reported in the literature, where intermediates of certain laccase reactions (e.g., lignin degradation) act as laccase inhibitors decreasing the enzyme activity (Pamidipati and Ahmed, 2020). To understand if a decrease in the enzymatic activity occurred, laccase activity was measured with ABTS substrate at the end of each cycle. A high decrease in laccase activity was obtained compared to the slight decrease in the relative polymerization (relative polymerization yield ~70%, cycle 4). Thus, the influence of soluble PDA intermediates (PDA<sub>i</sub> produced by the traditional method) in the laccase activity tests with ABTS was evaluated and compared to the control (activity of laccase in the presence of the

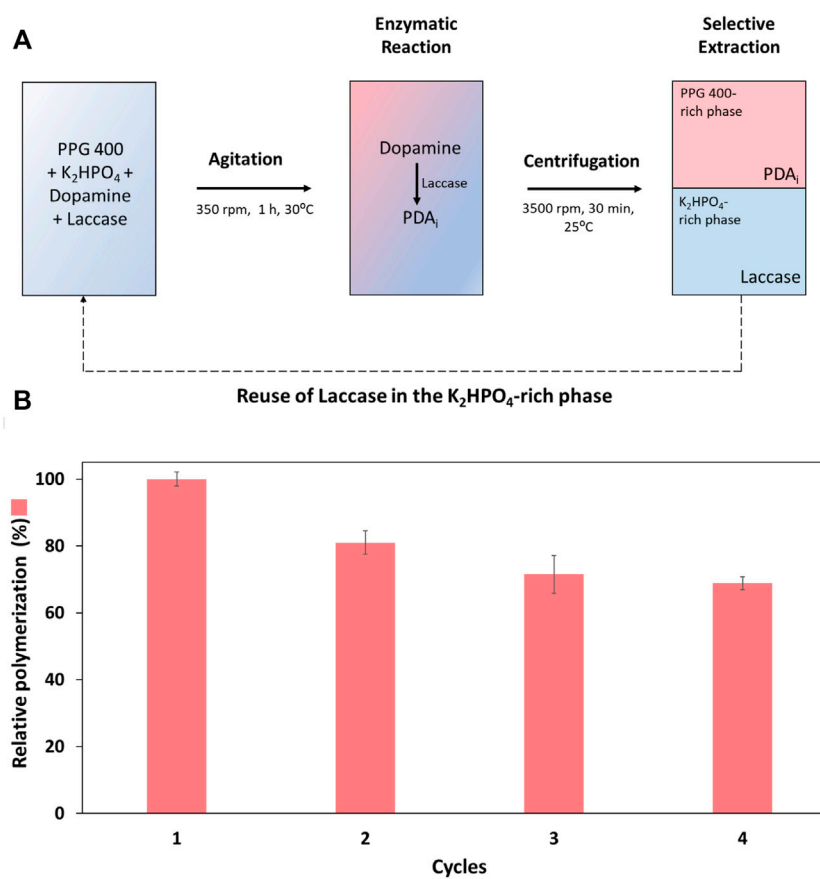


FIGURE 5

(A) Scheme of the integrated reaction—extraction process developed by applying ABS consisting of PPG 400 and  $K_2HPO_4$ , 30°C, including the recycling of the laccase and the  $K_2HPO_4$ -rich phase. (B) Relative dopamine polymerization (%) in four reaction cycles of the polymerization reaction (in relation to the first cycle).

buffer used in the production of  $PDA_i$ , considered 100%). The results presented in [Supplementary Table S9](#) revealed a high influence of these compounds in the ABTS quantification method, the enzyme activity relative to the control is only 8.2%. Since soluble  $PDA_i$  are also laccase substrates for the formation of solid  $PDA_i$ , more than one substrate is competing for the active site of laccase during the measurement with ABTS and consequently contributing for the decrease in the values of enzyme activity during the cycles. In addition, the influence of dopamine in the ABTS method was also evaluated and as expected once dopamine is also laccase substrate, the enzyme activity relative to the control was 6% ([Supplementary Table S9](#)).

$EE_{Laccase}$  % and  $EE_{PDA}$  % were also determined for all polymerization cycles ([Supplementary Material, Supplementary Table S10](#)). An  $EE_{Laccase}$  of 100% was obtained to the bottom phase throughout the four reaction cycles. Regarding  $EE_{PDA}$  %, 75.1% of  $PDA_i$  migrated to the top phase in the first reaction cycle, but it should be noted that some

selectivity was lost at the end of the fourth cycle with an  $EE_{PDA}$  of 48.0%. However, in a continuous process of recycling, the  $PDA_i$  that migrated to the bottom phase will be returned along with the reused phase, before starting a new biocatalytic cycle, making the loss of  $PDA_i$  to the bottom phase not relevant.

According to the literature, only one work can be found on polymerization studies using laccase and ABS. This work studied the oligomerization of rutin in ABS composed of PEG 600 and [Ch][DHP] ([Muñiz-Mouro et al., 2021](#)). A total of three reaction cycles were achieved, with an oligomerization yield of 89% in the last one. It also verified a preferential migration of the laccase to the opposite phase of the product throughout the cycles ( $EE_{Laccase}$  % of ~94% to the IL-rich phase). The  $EE$  of oligorutin was 67% and it was similar to that obtained in this study for  $PDA_i$  in the first cycle (~75%).

The outcomes from successive cycles, considering good relative dopamine polymerization values, demonstrate the robustness of the reaction-extraction process proposed with ABS for integrated biocatalytic processes.

## 4 Conclusion

Laccase improves the dopamine polymerization reaction, achieving high polymerization rates when compared with the conventional polymerization method. The results show that PPG 400 + K<sub>2</sub>HPO<sub>4</sub> ABS enable enzymatic processes while simultaneously extracting the products to the opposite phase. This selectivity demonstrates that it is possible to reuse the enzyme in a liquid support matching the ABS phase by allowing the extraction of the products from the enzyme. Therefore, ABS was here demonstrated as an efficient, and integrated reaction—separation platform to carry out the biocatalytic polymerization reactions, further allowing the reuse of the enzyme without compromising high polymerization rates and performance. For four consecutive reaction cycles, the phase containing the confined laccase was reused, with the final cycle having a relative polymerization of 68.9%. To sum up, it was found that the PPG 400 + K<sub>2</sub>HPO<sub>4</sub> ABS is an efficient system since it allows the separation of PDA<sub>i</sub> and laccase to opposite phases and the confinement and further reuse of laccase, thus, being an adequate liquid support for biocatalytic reactions and processes integration.

## Data availability statement

The original contributions presented in the study are included in the article/Supplementary Material, further inquiries can be directed to the corresponding author.

## Author contributions

FM: Conceptualization, Methodology, Validation, Formal analysis, Data Curation, Writing-Original Draft, and Editing. AP: Methodology, Validation, Formal analysis, Data Curation, Writing-Original Draft, and Editing. MF: Conceptualization, Writing—Review and Editing, Supervision, Funding acquisition. AT: Conceptualization, Writing—Review and

Editing, Supervision, Project administration, Funding acquisition.

## Funding

This work was developed within the scope of the project CICECO-Aveiro Institute of Materials, UIDB/50011/2020, UIDP/50011/2020 and LA/P/0006/2020, financed by national funds through the FCT/MCTES (PIDDAC). AT acknowledges FCT for the research contract CEECIND/2020/01867. FM acknowledges the SPQ/FCT PhD grant (SFRH/BD/150669/2020). AP acknowledges the FCT PhD grant (2022/13247/BD).

## Conflict of interest

The authors declare that the research was conducted in the absence of any commercial or financial relationships that could be construed as a potential conflict of interest.

## Publisher's note

All claims expressed in this article are solely those of the authors and do not necessarily represent those of their affiliated organizations, or those of the publisher, the editors and the reviewers. Any product that may be evaluated in this article, or claim that may be made by its manufacturer, is not guaranteed or endorsed by the publisher.

## Supplementary material

The Supplementary Material for this article can be found online at: <https://www.frontiersin.org/articles/10.3389/fbioe.2022.1037322/full#supplementary-material>

## References

- Adamian, Y., Lonappan, L., Alokpa, K., Agathos, S. N., and Cabana, H. (2021). Recent developments in the immobilization of laccase on carbonaceous supports for environmental applications - a critical review. *Front. Bioeng. Biotechnol.* 9, 778239–778329. doi:10.3389/fbioe.2021.778239
- Arregui, L., Ayala, M., Gómez-Gil, X., Gutiérrez-Soto, G., Hernández-Luna, C. E., Herrera De Los Santos, M., et al. (2019). Laccases: Structure, function, and potential application in water bioremediation. *Microb. Cell. Fact.* 18, 200. doi:10.1186/s12934-019-1248-0
- Ball, V. (2018). Polydopamine nanomaterials: Recent advances in synthesis methods and applications. *Front. Bioeng. Biotechnol.* 6, 109–112. doi:10.3389/fbioe.2018.00109
- Baptista, I. O., Ferreira, A. M., Magalhães, F. F., Freire, M. G., Tavares, A. P. M., and Coutinho, J. A. P. (2022). "Biocatalysis in biphasic systems based on ionic liquids," in *Biocatalysis in green solvents*. Editor P. Lozano (Amsterdam, Netherlands: Elsevier), 183–208.
- Cai, W., Wang, J., Pan, Y., Guo, W., Mu, X., Feng, X., et al. (2018). Mussel-inspired functionalization of electrochemically exfoliated graphene: Based on self-polymerization of dopamine and its suppression effect on the fire hazards and smoke toxicity of thermoplastic polyurethane. *J. Hazard. Mat.* 352, 57–69. doi:10.1016/j.jhazmat.2018.03.021
- Capela, E. V., Valente, A. I., Nunes, J. C. F., Magalhães, F. F., Rodríguez, O., Soto, A., et al. (2020). Insights on the laccase extraction and activity in ionic-liquid-based aqueous biphasic systems. *Sep. Purif. Technol.* 248, 117052. doi:10.1016/j.seppur.2020.117052
- Ding, Y. H., Floren, M., and Tan, W. (2016). Mussel-inspired polydopamine for bio-surface functionalization. *Biosurface Biotribology* 2, 121–136. doi:10.1016/j.bsbt.2016.11.001
- Dinis, T. B. V., Passos, H., Lima, D. L. D., Sousa, A. C. A., Coutinho, J. A. P., Esteves, V. I., et al. (2018). Simultaneous extraction and concentration of water



pollution tracers using ionic-liquid-based systems. *J. Chromatogr. A* 1559, 69–77. doi:10.1016/j.chroma.2017.07.084

El Yakhlifi, S., and Ball, V. (2020). Polydopamine as a stable and functional nanomaterial. *Colloids Surfaces B Biointerfaces* 186, 110719. doi:10.1016/j.colsurfb.2019.110719

Ferreira, A. M., Passos, H., Okafuji, A., Tavares, A. P. M., Ohno, H., Freire, M. G., et al. (2018). An integrated process for enzymatic catalysis allowing product recovery and enzyme reuse by applying thermoreversible aqueous biphasic systems. *Green Chem.* 20, 1218–1223. doi:10.1039/C7GC03880A

Ferreira, A. M., Valente, A. I., Castro, L. S., Coutinho, J. A. P., Freire, M. G., and Tavares, A. P. M. (2021). Sustainable liquid supports for laccase immobilization and reuse: Degradation of dyes in aqueous biphasic systems. *Biotechnol. Bioeng.* 118, 2514–2523. doi:10.1002/bit.27764

Freire, M. G., Cláudio, A. F. M., Araújo, J. M. M., Coutinho, J. A. P., Marrucho, I. M., Canongia Lopes, J. N., et al. (2012). Aqueous biphasic systems: A boost brought about by using ionic liquids. *Chem. Soc. Rev.* 41, 4966–4995. doi:10.1039/c2cs35151j

Gan, J. S., Bagheri, A. R., Aramesh, N., Gul, I., Franco, M., Almulaiky, Y. Q., et al. (2021). Covalent organic frameworks as emerging host platforms for enzyme immobilization and robust biocatalysis – a review. *Int. J. Biol. Macromol.* 167, 502–515. doi:10.1016/j.ijbiomac.2020.12.002

Kobayashi, S., and Makino, A. (2009). Enzymatic polymer synthesis: An opportunity for green polymer chemistry. *Chem. Rev.* 109, 5288–5353. doi:10.1021/cr900165z

Kurniawati, S., and Nicell, J. A. (2008). Characterization of *Trametes versicolor* laccase for the transformation of aqueous phenol. *Bioresour. Technol.* 99, 7825–7834. doi:10.1016/j.biortech.2008.01.084

Lee, H., Dellatore, S. M., Miller, W. M., and Messersmith, P. B. (2007). Mussel-Inspired surface chemistry for multifunctional coatings. *Sci. (80-. )* 318, 426–430. doi:10.1126/science.1147241

Li, F., Yu, Y., Wang, Q., Yuan, J., Wang, P., and Fan, X. (2018). Polymerization of dopamine catalyzed by laccase: Comparison of enzymatic and conventional methods. *Enzyme Microb. Technol.* 119, 58–64. doi:10.1016/j.enzmictec.2018.09.003

Magalhães, F. F., Tavares, A. P. M., and Freire, M. G. (2021). Advances in aqueous biphasic systems for biotechnology applications. *Curr. Opin. Green Sustain. Chem.* 27, 100417. doi:10.1016/j.cogsc.2020.100417

Mayolo-Delouis, K., González-González, M., and Rito-Palmares, M. (2020). Laccases in food industry: Bioprocessing, potential industrial and biotechnological applications. *Front. Bioeng. Biotechnol.* 8, 222–228. doi:10.3389/fbioe.2020.00222

Milyaeva, O. Y., Bykov, A. G., Campbell, R. A., Loglio, G., Miller, R., and Noskov, B. A. (2020). The dynamic properties of PDA-laccase films at the air-water interface. *Colloids Surfaces A Physicochem. Eng. Aspects* 599, 124930. doi:10.1016/j.colsurfa.2020.124930

Muñiz-Mouro, A., Ferreira, A. M., Coutinho, J. A. P., Freire, M. G., Tavares, A. P. M., Gullón, P., et al. (2021). Integrated biocatalytic platform based on aqueous biphasic systems for the sustainable oligomerization of rutin. *ACS Sustain. Chem. Eng.* 9, 9941–9950. doi:10.1021/acssuschemeng.1c03399

Olmeda, I., Casino, P., Collins, R. E., Sendra, R., Callejón, S., Huesa, J., et al. (2021). Structural analysis and biochemical properties of laccase enzymes from two *Pedococcus* species. *Microb. Biotechnol.* 14, 1026–1043. doi:10.1111/1751-7915.13751

Othman, A. M., Rodriguez-Couto, S., and Mechichi, T. (2022). Editorial: Microbial laccases: Recent advances and biotechnological applications. *Front. Bioeng. Biotechnol.* 10, 922223. doi:10.3389/fbioe.2022.922223

Pamidipati, S., and Ahmed, A. (2020). A first report on competitive inhibition of laccase enzyme by lignin degradation intermediates. *Folia Microbiol. (Praha)* 65, 431–437. doi:10.1007/s12223-019-00765-5

Pereira, J. F. B., Freire, M. G., and Coutinho, J. A. P. (2020). Aqueous two-phase systems : Towards novel and more disruptive applications. *Fluid Phase Equilib.* 505, 112341. doi:10.1016/j.fluid.2019.112341

Pereira, M. M., Pedro, S. N., Quental, M. V., Lima, Á. S., Coutinho, J. A. P., and Freire, M. G. (2015). Enhanced extraction of bovine serum albumin with aqueous biphasic systems of phosphonium- and ammonium-based ionic liquids. *J. Biotechnol.* 206, 17–25. doi:10.1016/j.jbiotec.2015.03.028

Sadeghi, R., and Maali, M. (2016). Toward an understanding of aqueous biphasic formation in polymer-polymer aqueous systems. *Polymer* 83, 1–11. doi:10.1016/j.polymer.2015.11.032

Salomäki, M., Marttila, L., Kivelä, H., Ovinen, T., and Lukkari, J. (2018). Effects of pH and oxidants on the first steps of Polydopamine Formation: A thermodynamic approach. *J. Phys. Chem. B* 122, 6314–6327. doi:10.1021/acs.jpcc.8b02304

Shakerian, F., Zhao, J., and Li, S. P. (2020). Recent development in the application of immobilized oxidative enzymes for bioremediation of hazardous micropollutants – a review. *Chemosphere* 239, 124716. doi:10.1016/j.chemosphere.2019.124716

Singh, I., Dhawan, G., Gupta, S., and Kumar, P. (2021). Recent advances in a polydopamine-mediated antimicrobial adhesion system. *Front. Microbiol.* 11, 607099. doi:10.3389/fmicb.2020.607099

Song, D., Chen, L., Li, T., and Xu, Z.-R. (2021). A polydopamine-coated mesoporous nanocomposite with robust affinity to horseradish peroxidase based on catecholic adhesion. *Colloid Interface Sci. Commun.* 40, 100340. doi:10.1016/j.colcom.2020.100340

Tan, Y., Deng, W., Li, Y., Huang, Z., Meng, Y., Xie, Q., et al. (2010). Polymeric bionanocomposite cast thin films with *in situ* laccase-catalyzed polymerization of dopamine for biosensing and biofuel cell applications. *J. Phys. Chem. B* 114, 5016–5024. doi:10.1021/jp100922t

Teng, R., Meng, Y., Zhao, X., Liu, J., Ding, R., Cheng, Y., et al. (2021). Combination of polydopamine coating and plasma pretreatment to improve bond ability between PEEK and primary teeth. *Front. Bioeng. Biotechnol.* 8, 630094–630099. doi:10.3389/fbioe.2020.630094

Tripathi, B. P., Das, P., Simon, F., and Stamm, M. (2018). Ultralow fouling membranes by surface modification with functional polydopamine. *Eur. Polym. J.* 99, 80–89. doi:10.1016/j.eurpolymj.2017.12.006

Walde, P., Kashima, K., and Čirić-Marjanović, G. (2019). Synthesizing polyaniline with laccase/O<sub>2</sub> as catalyst. *Front. Bioeng. Biotechnol.* 7, 165–210. doi:10.3389/fbioe.2019.00165

Wei, Q., Zhang, F., Li, J., Li, B., and Zhao, C. (2010). Oxidant-induced dopamine polymerization for multifunctional coatings. *Polym. Chem.* 1, 1430–1433. doi:10.1039/c0py00215a

Wu, H., Zhao, C., Lin, K., and Wang, X. (2022). Mussel-Inspired polydopamine-based multilayered coatings for enhanced bone formation. *Front. Bioeng. Biotechnol.* 10, 952500–952521. doi:10.3389/fbioe.2022.952500

Yan, J., Wu, R., Liao, S., Jiang, M., and Qian, Y. (2020). Applications of polydopamine-modified scaffolds in the peripheral nerve tissue engineering. *Front. Bioeng. Biotechnol.* 8, 590998–591007. doi:10.3389/fbioe.2020.590998

Yin, Q., Zhou, G., Peng, C., Zhang, Y., Kües, U., Liu, J., et al. (2019). The first fungal laccase with an alkaline pH optimum obtained by directed evolution and its application in indigo dye decolorization. *Amb. Express* 9, 151. doi:10.1186/s13568-019-0878-2

You, I., Jeon, H., Lee, K., Do, M., Seo, Y. C., Lee, H. A., et al. (2017). Polydopamine coating in organic solvent for material-independent immobilization of water-insoluble molecules and avoidance of substrate hydrolysis. *J. Ind. Eng. Chem.* 46, 379–385. doi:10.1016/j.jiec.2016.11.007

Zdarta, J., Meyer, A. S., Jesionowski, T., and Pinelo, M. (2018). Developments in support materials for immobilization of oxidoreductases: A comprehensive review. *Adv. Colloid Interface Sci.* 258, 1–20. doi:10.1016/j.cis.2018.07.004

Zhang, C., Gong, L., Mao, Q., Han, P., Lu, X., and Qu, J. (2018). Laccase immobilization and surface modification of activated carbon fibers by bio-inspired poly-dopamine. *RSC Adv.* 8, 14414–14421. doi:10.1039/c8ra01265b

Zhang, H., Lu, M., Jiang, H., Wu, Z.-Y., Zhou, D.-D., Li, D.-Q., et al. (2020). Tyrosinase-mediated dopamine polymerization modified magnetic alginate beads for dual-enzymes encapsulation: Preparation, performance and application. *Colloids Surfaces B Biointerfaces* 188, 110800. doi:10.1016/j.colsurfb.2020.110800

Zhou, Z., Zheng, B., Gu, Y., Shen, C., Wen, J., Meng, Z., et al. (2020). New approach for improving anticorrosion and biocompatibility of magnesium alloys via polydopamine intermediate layer-induced hydroxyapatite coating. *Surfaces Interfaces* 19, 100501. doi:10.1016/j.surfin.2020.100501



## OPEN ACCESS

## EDITED BY

Verónica de Zea Bermudez,  
University of Trás-os-Montes and Alto  
Douro, Portugal

## REVIEWED BY

Atakan Tevlek,  
Middle East Technical University, Turkey  
Bartłomiej Kryszak,  
Wrocław University of Science and  
Technology, Poland

## \*CORRESPONDENCE

Artur Ferreira,  
artur.ferreira@ua.pt

## SPECIALTY SECTION

This article was submitted to  
Biomaterials,  
a section of the journal *Frontiers in  
Bioengineering and Biotechnology*

RECEIVED 01 September 2022

ACCEPTED 10 November 2022

PUBLISHED 30 November 2022

## CITATION

Godinho B, Gama N and Ferreira A  
(2022), Different methods of  
synthesizing poly(glycerol sebacate)  
(PGS): A review.  
*Front. Bioeng. Biotechnol.* 10:1033827.  
doi: 10.3389/fbioe.2022.1033827

## COPYRIGHT

© 2022 Godinho, Gama and Ferreira.  
This is an open-access article  
distributed under the terms of the  
[Creative Commons Attribution License](#)  
(CC BY). The use, distribution or  
reproduction in other forums is  
permitted, provided the original  
author(s) and the copyright owner(s) are  
credited and that the original  
publication in this journal is cited, in  
accordance with accepted academic  
practice. No use, distribution or  
reproduction is permitted which does  
not comply with these terms.

# Different methods of synthesizing poly(glycerol sebacate) (PGS): A review

Bruno Godinho<sup>1</sup>, Nuno Gama<sup>1</sup> and Artur Ferreira<sup>1,2\*</sup>

<sup>1</sup>CICECO-Aveiro Institute of Materials, University of Aveiro, Aveiro, Portugal, <sup>2</sup>ESTGA-Águeda School of Technology and Management, Águeda, Portugal

Poly(glycerol sebacate) (PGS) is a biodegradable elastomer that has attracted increasing attention as a potential material for applications in biological tissue engineering. The conventional method of synthesis, first described in 2002, is based on the polycondensation of glycerol and sebacic acid, but it is a time-consuming and energy-intensive process. In recent years, new approaches for producing PGS, PGS blends, and PGS copolymers have been reported to not only reduce the time and energy required to obtain the final material but also to adjust the properties and processability of the PGS-based materials based on the desired applications. This review compiles more than 20 years of PGS synthesis reports, reported inconsistencies, and proposed alternatives to more rapidly produce PGS polymer structures or PGS derivatives with tailor-made properties. Synthesis conditions such as temperature, reaction time, reagent ratio, atmosphere, catalysts, microwave-assisted synthesis, and PGS modifications (urethane and acrylate groups, blends, and copolymers) were revisited to present and discuss the diverse alternatives to produce and adapt PGS.

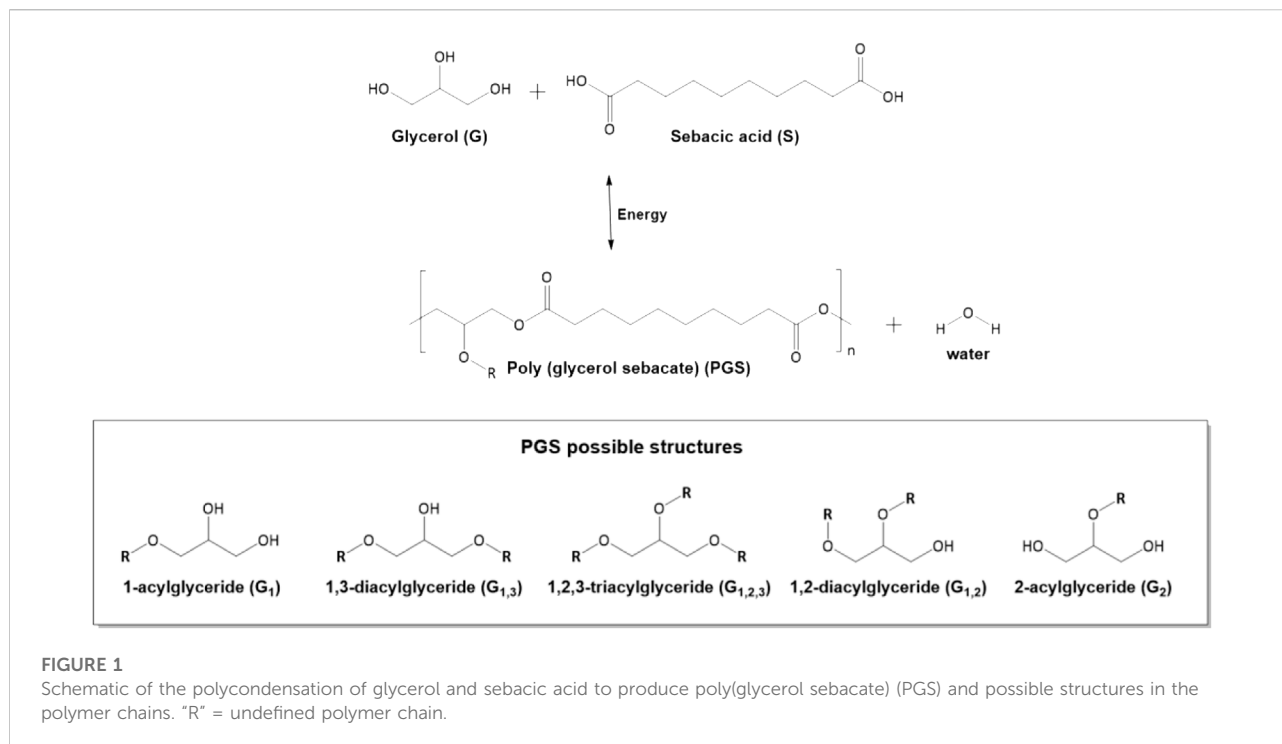
## KEYWORDS

poly(glycerol sebacate) (PGS), microwave-assisted synthesis, enzymatic synthesis, polycondensation synthesis, PGS-based materials

## 1 Introduction of poly (glycerol sebacate) (PGS)

Poly(glycerol sebacate) (PGS) is a polyester elastomer conventionally produced through the esterification of glycerol with sebacic acid (Figure 1). It is bioresorbable and biodegradable; moreover, its degradation results in non-toxic products. Since its first report as a biocompatible material in 2002 (Wang et al., 2002), PGS has been a research focus of many groups. However, publications before Wang et al. (2002) by Nagata et al. (1996; 1999) described the synthesis of a PGS film (considered a biodegradable polyester) via polycondensation, which was identified as “Yg10” rather than PGS (Nagata et al., 1996; Nagata et al., 1999). The absence of these terms may explain why they have been somewhat forgotten in the literature. Some review articles erroneously consider Wang et al. (2002) the first report of PGS synthesis (Loh et al., 2015; Halil Murat, 2017; Sha et al., 2021; Vogt et al., 2021; Wu et al., 2021).

Several studies have targeted the comprehension and optimization of PGS synthesis and its properties, which have analyzed numerous variables (Liu et al., 2007a; Liu et al.,



2007b; Kossivas et al., 2012; Li et al., 2013a; Li et al., 2013b; Guo et al., 2014; Li et al., 2015; Moorhoff et al., 2015; Conejero-García et al., 2017; Gadomska-Gajadur et al., 2018; Matyszczyk et al., 2020; Perin and Felisberti, 2020; Vilariño-Feltrer et al., 2020; Martín-Cabezuelo et al., 2021a; Martín-Cabezuelo et al., 2021b; Wrzecionek et al., 2021; Ning et al., 2022). In addition to these fundamental studies, PGS has been used as a component of polymer blends (Frydrych et al., 2015a; Tallawi et al., 2016; Salehi et al., 2017; Gultekinoglu et al., 2019; Saudi et al., 2019; Fakhrali et al., 2020; Flaig et al., 2020; Gorgani et al., 2020; Kaya et al., 2020; Stowell et al., 2020; Xuan et al., 2020; Behtaj et al., 2021a; Behtaj et al., 2021b; Fakhari et al., 2021; Hanif et al., 2021; Mokhtari and Zargar Kharazi, 2021; Varshosaz et al., 2021; Zhang et al., 2021; Fakhrali et al., 2022), other composite materials (Redenti et al., 2009; Chen et al., 2010; Liang et al., 2011; Gaharwar et al., 2015; Zhou et al., 2015; Rosenbalm et al., 2016; Souza et al., 2017; Tevlek et al., 2017; Zhang et al., 2017; Chen S et al., 2018; Abudula et al., 2020; Fu et al., 2020a; Aghajan et al., 2020; Sencadas et al., 2020a; Lau et al., 2020; Luginina et al., 2020; Rezk et al., 2020; Ruther et al., 2020; Tallá Ferrer et al., 2020; Touré et al., 2020; Zanzanizadeh Ezazi et al., 2020; Piszko et al., 2021a; Atya et al., 2021; Fakhrali et al., 2021; Rastegar et al., 2021; Talebi et al., 2021; Wang et al., 2021; Davoodi et al., 2022), or chemically modified/integrated in the development of PGS copolymers (Tang et al., 2006; Wu Y et al., 2014; Aydin et al., 2016; Jia et al., 2016; Choi et al., 2017; Tang et al., 2017; Zhao et al., 2017; Wang et al., 2018; Wilson et al., 2018; Lang et al., 2020; Rostamian et al., 2020; Chang and Yeh, 2021; Azerêdo

et al., 2022; Ruther et al., 2022). PGS-based polymers have been widely employed in electrospinning to produce fibers (Yi and La Van, 2008; Jeffries et al., 2015; Rai et al., 2015; Tallawi et al., 2015; Hou et al., 2017; Hu et al., 2017; Vogt et al., 2018; Wu H. J. et al., 2019; Saudi et al., 2019; Vogt et al., 2019; Abudula et al., 2020; Apsite et al., 2020; Fakhrali et al., 2020; Flaig et al., 2020; Gorgani et al., 2020; Jafari et al., 2020; Keirouz et al., 2020; Silva et al., 2020; Stowell et al., 2020; Touré et al., 2020; Abazari et al., 2021; Bellani et al., 2021; Fakhari et al., 2021; Flaig et al., 2021; Mokhtari and Zargar Kharazi, 2021; Varshosaz et al., 2021; Zhang et al., 2021; Behtouei et al., 2022; Heydari et al., 2022; Rekabgarden et al., 2022; Saudi et al., 2022) and also studied for 3D printing (Yeh et al., 2016; Yeh et al., 2017; Chen S et al., 2018; Pashneh-Tala et al., 2018; Kazemzadeh Farizhandi et al., 2020; Touré et al., 2020; Tsai et al., 2020; Liu et al., 2021; Ruther et al., 2022).

The major focus of PGS-inspired polymers is the development of scaffold material for biological tissue engineering (Wang et al., 2002; Gao et al., 2006; Gao et al., 2007; Jeong and Hollister, 2010; Kemppainen and Hollister, 2010; Masoumi et al., 2013; Khosravi et al., 2016; Ma et al., 2016; Zhang et al., 2016; Nadim et al., 2017; Hsu et al., 2018; Wu W et al., 2019; Hu et al., 2019; Jiang et al., 2019; Xiao et al., 2019; Abudula et al., 2020; Fu et al., 2020a; Apsite et al., 2020; Fu et al., 2020b; Sencadas et al., 2020b; Jafari et al., 2020; Keirouz et al., 2020; Liang et al., 2020; Martín-Pat et al., 2020; Pashneh-Tala et al., 2020; Xuan et al., 2020; Abazari et al., 2021; Behtaj et al., 2021a; Piszko et al., 2021a; Liu et al., 2021; Rastegar et al., 2021;

Ângelo et al., 2021; Chen et al., 2022; Fukunishi et al., 2022; Saudi et al., 2022), although many other purposes have been identified for these materials. PGS-based materials have been investigated as drug delivery systems (Sun et al., 2009; Sun et al., 2013; Yang et al., 2017; Ayati Najafabadi et al., 2018; Desai et al., 2018; Oklu et al., 2018; Zhu et al., 2018; Rezk et al., 2020; Zanzanizadeh Ezazi et al., 2020; Sivanesan et al., 2021; Torabi et al., 2021; Heydari et al., 2022; Mehta et al., 2022), adhesives (Mahdavi et al., 2008; Tevlek et al., 2017; Azerêdo et al., 2022), sealants (Chen et al., 2011), coatings (Kim et al., 2014; Lin et al., 2015; Jiang et al., 2020; Zbinden et al., 2020; Zhang et al., 2020; Martín-Cabezuelo et al., 2021b; Ghafarzadeh et al., 2021), biosorbents (Rostamian et al., 2022), membranes for solvents/water pervaporation (Chang et al., 2021), and components for electronic applications (Chen S et al., 2018; Sencadas et al., 2020a; Kazemzadeh Farizhandi et al., 2020; Zhang et al., 2020; Hanif et al., 2021). Their memory shape properties have also been studied (Cai and Liu, 2007; Wu T et al., 2014; Rosenbalm et al., 2016; Wu et al., 2016; Coativy et al., 2017; Tevlek et al., 2020; Xuan et al., 2020). Several reviews have also compiled the research, developments, and applications of PGS and PGS-based materials (Rai et al., 2012; Loh et al., 2015; Halil Murat, 2017; Valerio et al., 2018; Piszko et al., 2021b; Sha et al., 2021; Vogt et al., 2021; Wu et al., 2021; Zulkifli et al., 2022).

The literature used for the present review was identified through searches of the Scopus, Web of Science, Google Scholar, and ResearchGate databases in the Mendeley<sup>®</sup> application, which was also used to store the database of identified studies. Additionally, we thank the reviewers who also suggested relevant publications to enrich this review article. The search included the following keywords and phrases: “PGS,” “poly(glycerol sebacate),” “poly(glycerol-co-diacids),” “enzymatic synthesis polyesters,” “glycerol polyesters,” “microwave-assisted polyester synthesis,” “PGS-based materials,” etc.

We did not limit the search to any specific period; thus, this review includes relevant publications from 1996 up to 2022.

This review focused on the different synthesis routes used to produce PGS, including its variables and how they influence the polymer properties. The review begins with the conventional method for PGS synthesis *via* the polycondensation of glycerol with sebacic acid, followed by polycondensation at higher temperatures and microwave-assisted polycondensation. Next, the review describes enzymatic synthesis and the use of other monomers to obtain PGS. Under each of these topics, efforts were made to ensure that the review followed the chronological order of publications whenever possible. We believe that this chronological organization of the publications allows readers to better understand the origin and evolution of knowledge. The following sections present publications on the use of other catalysts and other monomers to obtain the polymer structure of PGS, cross-linking of PGS by photopolymerization, and urethane bonds. The review ends with the properties of PGS

and PGS-based materials, where the degradative behavior of these materials is presented in detail (e.g., *in vitro*, *in vitro* enzymatic, and *in vivo*).

This review consolidates the PGS and PGS-based materials synthesis comprehension in their several variables and routes. Therefore, this is a tribute to the knowledge developed over more than 20 years of research, especially publications from the 1990s that were somewhat overlooked, and that also provided fundamental knowledge on the field of PGS.

## 2 PGS synthesis

### 2.1 PGS polycondensation synthesis (conventional method)

Traditional PGS synthesis is an energy-intensive and time-consuming process. However, it is considered an economic material (Li et al., 2013a; Kafouris et al., 2013). The conventional method involves a two-step procedure that incorporates a prepolymerization step to form low molecular weight polymers/oligomers, followed by a curing step to cross-link these products and shape the final material. Both steps are normally performed at around 120–150°C, under an inert atmosphere or vacuum, and without catalysts or solvents. Wang et al. (2002) proposed a procedure to produce PGS; subsequent works suggested changes or small adjustments based on those processes (Table 1).

Studies on the reaction kinetics have shown that the activation energy decreases with increasing molar ratios of glycerol to sebacic acid, which indicates that the reaction is favored at an equimolar ratio of reactants. The reaction kinetics also increase with increasing temperature, showing classical Arrhenius behavior (Maliger et al., 2013; Matyszczyk et al., 2020).

Initially, the kinetic control of the reaction advances with first-order kinetics with respect to the monomer. When a given conversion is achieved, the viscosity of the medium increases by changing the reaction to a diffusion-controlled process, which makes it difficult to transfer mass in the system to continue the reaction (Valerio et al., 2018).

PGS properties can be modified by changing the reaction conditions (time, temperature, or reagent ratios) to produce a wide range of mechanical properties (Table 2). Liu et al. (2007a, 2007b) reported that PGS can be a thermoset (TS)PGS or a thermoplastic (TM)PGS depending on the molecular size of the prepolymer used to obtain cured PGS. This may influence the properties and final degradation rate of PGS. Different molecular weights cause the prepolymers to present different viscosities and reactivities in the curing step, which result in distinct branching degrees on the final products.

Li et al. (2013a) identified inconsistencies in PGS properties among research groups using similar synthesis conditions. For



TABLE 1 Synthesis conditions for PGS and PGS-based materials.

Application/Objective	Molar ratio G:S	Prepolymerization stage The (number) means steps order	Curing step	References
Ancient article (year 1996) before the “PGS” expression Properties assessment (time of cure effect)	2:3	200°C, 2 h, nitrogen  PGS prepolymer (called Yg10 by the authors)	Film cast (20 wt% DMF solution 80°C)  Aluminum plate mold 230°C, 30 min, 1, 2, 4, and 6 h, nitrogen  Transparent and flexible film of Yg10 (insoluble in organic solvents for polyesters)	Nagata et al. (1996)
Ancient article (year 1999) before the “PGS” expression Properties assessment (effect of sebacic acid progressive substitution by other diacids to produce PGS copolymers)	2:3	200°C, 43 min, nitrogen  PGS prepolymer (called Yg10 by the authors)	Film cast (17 wt% DMF solution 80°C)  Aluminum plate mold 230°C, 4 h, nitrogen  Transparent and flexible film of Yg10 (insoluble in organic solvents for polyesters)	Nagata et al. (1999)
Wang et al. (2002) procedure (beginning of the “PGS” expression year 2002) Porous scaffold for soft tissue engineering	1:1	(1) 120°C, 24 h, argon  (2) 120°C, 1 torr to 40 mTorr (5 h) (3) 120°C., 48 h, 40 mTorr	NaCl particles  1,3-dioxilane PTFE mold 120°C, 100 mTorr	Wang et al. (2002), Mitsak et al. (2012)
Soft tissue engineering	1:1	(1) 120°C, 24 h, nitrogen (2) 120°C., 24 h, 40 mTorr Highly viscous liquid (pale yellow)	THF Salt mold disk 150°C, 48 h, 100 mTorr	Gao et al. (2006), Gao et al. (2007), Sales et al. (2007), Jeong and Hollister. (2010)
Soft tissue engineering (myocardial tissue PGS match properties)	1:1	(1) 110 or 120 or 130°C, 24 h, argon (2) 110 or 120 or 130°C, 1 torr to 50 mmHg (5 h) (3) 110 or 120 or 130°C, 48 h, 50 mTorr	Sheet forming mold 110 or 120 or 130°C, 48 h, vacuum oven 50 mmHg	Chen et al. (2007)
Soft tissue engineering (heart valve)	1:1	(1) 120°C, 24 h, nitrogen  (2) 120°C, 24 h, high vacuum (<50 mTorr)  Viscous PGS prepolymer (hot) Soft waxy prepolymer (room temperature)	Sucrose coated glass microscope slides (mold) with prepolymer spread uniformly 120°C, 8, 12 or 16 h, high vacuum (<50 mTorr) Thin PGS membranes (~250 nm)	Masoumi et al. (2013)
Cardiac tissue engineering	1:1	(1) 120°C, 24 h, nitrogen  (2) 120°C., 48 h, 40 mTorr PGS prepolymer	Prepolymer “spinned” to fibers produce 130°C, 24 h PGS fibers	Ravichandran et al. (2012)
Cardiac support devices	1:1	(1) 120°C, 24 h, nitrogen (2) Prepolymer mixed with nanoBioglass® at 50°C	120°C, 2 or 3 days, under vacuum Thin sheets (0.2–0.3 mm) PGS–Bioglass® composites	Chen et al. (2010)
Scaffolds for skin tissue engineering	1:1	(1) 150°C, 12 h, nitrogen (2) 150°C, 12 h, vacuum Highly viscous prepolymer (pale yellow)	Teflon circular mold 140°C, 8, 9, 10, 12 or 13 h, vacuum oven	Zhang et al. (2016)
3D scaffolds for cartilage	4:3 1:1 3:4	(1) 120°C, 24 h, nitrogen (2) 120°C., 48 h, 50 mTorr	Teflon/hydroxyapatite mold 150°C, 24, 48 or 72 h, 100 mTorr	Kemppainen and Hollister (2010)
Scaffolds for adipose tissue engineering	1:1	120°C, 72 h, nitrogen low flow	Prepolymer heated at 80°C and distributed in Teflon molds	Frydrych et al. (2015a)

(Continued on following page)

TABLE 1 (Continued) Synthesis conditions for PGS and PGS-based materials.

Application/Objective	Molar ratio G:S	Prepolymerization stage The (number) means steps order	Curing step	References
Neural tissue engineering	1:0.8	PGS prepolymer	Degassed film, 80°C vacuum oven, until void-free film	Saudi et al. (2019)
		170°C, 3, 5 or 7 h, nitrogen	120°C, 36 h, vacuum oven PGS to blend with poly(lactic acid) PGS/PLA	
Nerve guide material	1:1	PGS prepolymer	Prepolymer blended with poly(vinyl alcohol)	Sundback et al. (2005)
		(1) 120°C, 24 h, argon (2) 120°C, 48 h, 40 mTorr	Electrospinning of fibers (pPGS/PVA) 120°C, 24 h, 60 mmHg pressure PGS-based fibers	
Musculoskeletal tissue engineering	1:1	Viscous PGS prepolymer	THF film cast	Gaharwar et al. (2015)
		(1) 130°C, 2 h, argon (2) 130°C, 1 torr to 50 mTorr (5 h) (3) 120°C, 24 h, 50 mTorr	THF/prepolymer solution mixed with carbon nanotubes (CNTs) Teflon flat petri dish. (THF evaporated overnight) 130°C, 40 h, vacuum	
Sterilization effects and cytotoxicity and soft tissue engineering (cardiac patch)	1:1	Prepolymer (Mw: 3960 g/mol)	PGS/CNTs nanocomposite scaffolds	Rai et al. (2013a), Rai et al. (2013b)
		120°C, 24 h, nitrogen Transparent viscous liquid prepolymer	Teflon molds 120°C, 4 days, under vacuum (1.3–2.5 × 10 <sup>-2</sup> mbar) for 4 days PGS transparent film (1.5 mm)	
Scaffolds to restoring a wounded rat uterus	1:1	(1) 120°C, 24 h, nitrogen (2) 120°C, 24 h, 1 torr	Solvent cast and particles leaching (THF and NaCl)	Xiao et al. (2019)
		PGS prepolymer	Disciform mold 150°C, 24 h, 1 torr	
Properties assessment (thermoplastic and thermoset PGS)	2:2.5	(1) 130°C, 1 kPa, nitrogen (2:2) (2) Sebacic acid (0.5) addition	Hot-pressed, 130°C, 15 MPa Cold-pressed and molded, room °C, 20min	Liu et al. (2007a), Liu et al. (2007b)
		(3) 130°C, 1 kPa, nitrogen	Thermoplastic (TM)PGS	
Properties assessment (temperature of cure effect)	1:1	(1) 120°C, 24 h, nitrogen (2) 120°C, 48 h, -20 kPa (instantly)	120, 130, 140, 150 or 165°C, 24 h, vacuum oven (-20 kPa) or 165°C, 2, 4, 10 or 48 h, same vacuum conditions	Jaafar et al. (2010)
Properties assessment (molar ratio effect)	2:1	(1) 120°C, 24 h, dry argon	Prepolymer transfer to mold at 120°C	Kossivas et al. (2012), Kafouris et al. (2013)
	2:2	(2) 120°C, 48 h, under vacuum	120°C, 24 h, under vacuum	
	2:3	Viscous branched PGS prepolymer		
	2:4	Prepolymer properties assessment		
	2:5			
Properties assessment (ratio G:S optimization for cell culture)	1:0.8	(1) 180°C, 2.5 h, nitrogen	NaCl mix with prepolymer	Guo et al. (2014)
	1:1	(2) 180°C, 1 h, vacuum	150°C, 24 h, vacuum	
	1:1.2			
Properties assessment	1:1	130°C, 24 h, nitrogen (130 cm <sup>3</sup> min <sup>-1</sup> flow) Or	THF solvent Film cast PGS prepolymer in glass slide molds	Li et al. (2013a), Li et al. (2013b), Moorhoff et al. (2015)

(Continued on following page)

TABLE 1 (Continued) Synthesis conditions for PGS and PGS-based materials.

Application/Objective	Molar ratio G:S	Prepolymerization stage  The (number) means steps order	Curing step	References
Synthesis for tailored mechanical properties	1:1	150°C, 8 h, nitrogen (130 cm <sup>3</sup> min <sup>-1</sup> flow)  PGS prepolymer (1) Mix the two reagents at room temperature (2) 120, 130 or 140°C, 24 h, convection oven under nitrogen (no agitation)  Waxy or liquid like prepolymers (room temperature)	130°C, 24, 48, 72, 96, 144 or 168 h, under vacuum  PGS gel sheets (0.5–0.9 mm)  Prepolymer/THF solution cast to aluminum mold  120, 130 or 140°C, 6–66 h, vacuum oven	Li et al. (2015)
Assessments for correlating properties with synthesis parameters of PGS.	2:1 1:1 1:2	130°C, 24 h, nitrogen  Viscous PGS prepolymer	Teflon square mold  130°C, 24, 48, 72 or 96 h, ventilated oven or  110, 120, 140, 150°C, 48 h, ventilated oven	Conejero-García et al. (2017)
Optimization synthesis of PGS for biomedical purposes (maximization aims degree of esterification and conversion of monomers)	1:1 2:1 3:1	(1) 130, 140, and 150°C as temperature variables and 4, 5 and 6 h as time reaction variables, under argon atmosphere (2) Distillation, 40°C, 18 mbar (3) Purification  Dioxane/prepolymer solution, 24 h mixing  Cold distilled water addition for precipitation  Filtration and desiccation of PGS at 45°C, 24 h  Pure PGS prepolymer	—	Gadomska-Gajadur et al. (2018)
Material evaluation properties	1:1	(1) 130°C, 24 h, nitrogen  (2) Prepolymer/ethanol solution mixed with cellulose nanocrystals (CNC) at room temperature	Teflon mold, ethanol evaporated at 60°C  130°C, 48 h, under vacuum  PGS/CNCs composite	Zhou et al. (2015)
Drug carrier	1:1	150°C, 4 h, nitrogen  Addition of 5-fluorouracil drug	150°C, 30 h, under vacuum  PGS wafers 1–1.5 mm thickness	Sun et al. (2009)
Drug release (brain gliomas)	1:1.2	(1) 170°C, 1 h, nitrogen  (2) 170°C, pressure reduce slow until vacuum, end after no bubble occurred  PGS prepolymer  Or (1) (2) Same procedure, but 185°C  PGS-curcumin prepolymer	170°C, 24 h, vacuum drying chamber  PGS polymer  or  Same procedure, but at 185°C  PGS-curcumin polymer	Sun et al. (2013)
Local drug delivery	1:1	(1) Evenly mixed reagents at room temperature (2) 120°C, 24 h, nitrogen in vacuum oven (no agitation)	120°C, 72 h, vacuum oven  PGS drug load	Yang et al. (2017)
Memory shape material	1:1	(1) 120°C, 24 h, argon (2) 120°C., 48 h, 0.1 MPa  Viscous PGS prepolymer	THF  Films mold  120°C, 24 h, 0.1 MPa  PGS films 1 mm thickness	Cai and Liu, (2007)
Memory shape material	1:1	(1) 120°C, 8 h, nitrogen (2) 120°C, 16 h, vacuum oven	Prepolymer reacted with HDI to produce PGS urethane (PGSU)	Wu T et al. (2014)

(Continued on following page)

TABLE 1 (Continued) Synthesis conditions for PGS and PGS-based materials.

Application/Objective	Molar ratio G:S	Prepolymerization stage The (number) means steps order	Curing step	References
Coating	1:1	Viscous prepolymer (1) 130°C, 3 h, argon (2) 120°C, 45 h, 40 mTorr (Yield for viscous liquid phase prepolymer, above 80%)	and mix with cellulose nanocomposites Electrospray coating of nitinol stent with PGS prepolymer 100°C, 48 h, vacuum oven	Kim et al. (2014)
Assessments material for tissue engineering	1:1	(1) 130°C, 2 h, argon (2) 130°C, 1 torr to 40 mTorr (5 h) (3) 130°C, 48 h, 40 mTorr PGS prepolymer	Teflon crucibles mold 130°C, 48 h, vacuum oven PGS polymer to copolymerize with poly(ethylene glycol)	Patel et al. (2013)

example, [Chen et al. \(2007\)](#) and [Jaafar et al. \(2010\)](#) produced PGS with very different Young's modulus of 1.2 and 0.12 MPa, respectively, despite identical reported synthesis conditions.

As previously stated, different synthesis conditions produce PGS with different properties. [Chen et al. \(2011\)](#) demonstrated some of these differences among research groups and proposed several explanations. For example, the temperature uniformity inside a vacuum oven is  $\pm 1^\circ\text{C}$  at best and is typically  $\pm 2.5^\circ\text{C}$  for most ovens ([Chen et al., 2011](#)). A difference of  $5^\circ\text{C}$  can significantly change the cross-linking kinetics of PGS, according to their experiences. Additionally, glycerol loss is problematic and inevitable. The purging flow rate with inert gas and the capacity of the vacuum pump can greatly affect glycerol loss during synthesis, altering the molar relationship of the reagents. Therefore, different research groups report different results, despite using apparently identical synthesis conditions ([Chen et al., 2011](#)).

[Li et al. \(2013a\)](#) confirmed that glycerol evaporation is the major cause of irreproducibility. This problem is aggravated when synthesis is performed at high temperatures. At the level of mechanical properties, Young's modulus of PGS increases with longer cure duration and higher curing temperatures, while the ultimate strength at break decreased. The authors performed detailed  $^1\text{H}$  NMR and  $^{13}\text{C}$  NMR analyses. The results of the NMR analyses show that secondary hydroxyl groups, responsible for cross-link, reacted more slowly than primary hydroxyl groups. Thus, NMR techniques provided qualitative and semi-quantitative structural information on the synthesized PGS. The different structures of acylglycerides identified in PGS are shown in [Figure 1](#).

[Li et al. \(2015\)](#) also identified glycerol loss as a problem. For example, the molar ratios of glycerol to sebacic acid decreased from 0.80 to 0.75 when the curing temperature increased from 120 to  $140^\circ\text{C}$ . The authors proposed the use of the degree of

esterification to precisely predict the physical status, mechanical properties, and degradation of PGS. Young's modulus linearly increased with the degree of esterification. Young's modulus also increased as the total cure time increased, while the elongation at break decreased. [Figure 2](#) illustrates the relationship between the degree of esterification (%) and the physical appearance of PGS at room temperature according to production time and temperature conditions ([Li et al., 2015](#)). [Figure 2](#) shows the five physical states that can be observed at room temperature for the production of PGS at different times and temperatures. PGS starts in a waxy solid state, changing to a viscous liquid (gel state), and finally returning to a solid state.

[Kafouris et al. \(2013\)](#) also focused on understanding PGS synthesis by testing different molar ratios of G:S (glycerol:sebacic acid) to produce PGS (2:1, 2:2, 2:3, 2:4, and 2:5), using three reaction steps at  $120^\circ\text{C}$  ([Table 1](#)). All prepolymers were low molecular weight oligomers, between dimers and nonamers. They concluded that the properties of PGS elastomers are highly dependent on the composition. For example, PGS 2:3 elastomer was the stiffest, with the lowest degree of swelling and sol fraction, while the PGS 2:5 elastomer was one of the softest, exhibiting the highest degree of swelling and sol fraction. The elastomers with compositions far from stoichiometry were softer due to the lower cross-linking density.

In 2017, [Conejero-García et al. \(2017\)](#) assumed a disruptive approach face to the conventional method. It was the first work without vacuum steps and showed the second-highest Young's modulus reported in the PGS literature (4.7 MPa). The prepolymerization step was conducted at  $130^\circ\text{C}$  under an inert atmosphere for 24 h. The curing step was performed in a forced ventilation oven. The resulting films were transparent, soft, and flexible, and became more yellowish and harder with increasing temperature or curing time. This yellowing may be related to the oxidation of the material due to the normal and ventilated



TABLE 2 Mechanical properties of PGS and PGS-based materials.

Material	Young's modulus (MPa)	Tensile strength (MPa)	Elongation (%)	Compression strength (MPa)	References
PGS or PGS backbone type (PSeD)					
Poly(glycerol sebacate) (PGS)	0.017–6.86	0.1–1.96	10–448	2.75–4.74 (54–70% deform)	Nagata et al. (1999), Wang et al. (2002), Chen et al. (2007), Mitsak et al. (2012), Patel et al. (2013), Gaharwar et al. (2015), Loh et al. (2015), Conejero-García et al. (2017), Tevlek et al. (2017), Wilson et al. (2018), Sencadas et al. (2020b), Lang et al. (2020), Tallá Ferrer et al. (2020), Atya et al. (2021)
Poly(sebacoyl diglyceride) (PSeD)	1.57	1.83	409	—	You et al. (2010)
PGS copolymers					
Poly(glycerol glycol sebacate) PGGS	0.42–0.49	0.50–0.63	108–198	—	Tang et al. (2006)
PGS-co-poly(ethylene glycol) (PGS-co-PEG)	0.040–1.590	0.026–0.388	39–100% (190% hydrated polymer)	1.88–2.99 (55–69% deform)	Patel et al. (2013)
Poly(glycerol sebacate citrate) (PGSC)	6.9	2.7	40	—	Liu et al. (2009)
PGS-co-lactic Acid (PGS-co-LA)	Sealant gel				Chen et al. (2011)
Poly(glycerol sebacate urethane) (PGSU)	0.1–20	0.14–12.1	78–516	0.13–0.75 (75% deform) Scaffold material	Pereira et al. (2013), Wu T et al. (2014), Frydrych and Chen. (2017), Wang et al. (2018)
PGS-ureido-pyrimidinone-HDI (PGS-U)	0.4–32.8	0.2–4.6	610–260		Wu et al. (2016)
Urethane-based PEGylated PGS	1.0–6.4 (dry) 0.6–4.7 (hydrated)	0.32–4.3 (dry) 0.14–3.7 (hydrated)	53.6–272.8 (dry) 25.7–329.2 (hydrated)		Wang et al. (2018)
PGS-acrylate (PGSA)	0.05–30	0.01–1.36	5–200	—	Nijst et al. (2007), Ifkovits et al. (2008), Chen J.-Y et al. (2018)
PGS-poly(caprolactone) (PGS-PCL) fibers	5.6–15.7	2–3	142–900	—	Rai et al. (2015), Hou et al. (2017)
PGSA-co-polycaprolactone diacrylate (PGSA-co-PCLDA)	0.67–7	0.14–0.69	11.28–45.95	—	Chen S et al. (2018)
PGSA-co-poly(ethylene glycol) diacrylate (PGSA-co-PEGDA)	4.22–10.54	0.61–1.97	12.96–25.96	—	Chen S et al. (2018)
PGSA-co-PEGDA co-PCLDA	3.84–8.78	1.01–1.37	20.61–40.31	—	Chen S et al. (2018)
PGS-b-PTMO-Hytrel 3078	0.018	2.1	2574	—	Wilson et al. (2018)
Poly(glycerol-1,8-octanediol-sebacate) (PGOS)	106.1	4.94	23	—	Lang et al. (2020)
Palmitate-PGS (PPGS)	<0.3	<0.20	70–100	—	Fu et al. (2020b), Ding et al. (2020)
PGS-co-Zein	0.021–2.9	0.020–1.4	21–63	—	Ruther et al. (2022)
PGS-Citrate	0.12–1.29	±0.1–0.4	±30–120	—	Risley et al. (2021)
PGS composites/blends					
PGS/carbon nanotubes (PGS-CNT) nanocomposites	0.28–1.01	0.13–0.275	38–99	—	Gaharwar et al. (2015)
Multi-walled carbon nanotubes/(PGSC) (MWCNTs/PGSC)	0.85–9.9	0.9–4.4	40–325	—	Liu et al. (2009), Yan et al. (2018)
PLC/PGS/graphene	11.4–21.7	2.35–3.02	82.6–122.8	—	Fakhrli et al. (2021)
PGS/cellulose nanocrystals (PGS/CNCs)	1.0–1.9	0.62–1.5	80–100	—	Zhou et al. (2015)

(Continued on following page)

TABLE 2 (Continued) Mechanical properties of PGS and PGS-based materials.

Material	Young's modulus (MPa)	Tensile strength (MPa)	Elongation (%)	Compression strength (MPa)	References
PGSU/cellulose nanocrystals (PGSU/CNCs)	1.38–47.96	12.4	396	—	Wu T et al. (2014)
PGS/bacterial cellulose (PGS/BC)	1.21	0.32	25	—	Wang et al. (2021)
PGS/silk fibroin (PGS/SF)	1.5–2.5	1–6.5	100–325	—	Zhang et al. (2021)
PGS- $\beta$ -tricalcium phosphate (PGS- $\beta$ -TCP) bi-layered composites	1.95	0.21	24	14 (85% deform)	Tevlek et al. (2017)
( $\beta$ -TCP/PGS content 15%) scaffolds	—	—	375	1.73	Yang et al. (2015)
PGS/Bioglass®	0.4–1.6	0.8–1.53	150–550	—	Chen et al. (2010), Rai et al. (2012)
PCL-PGS/bioactive glass	240–311	3–8	<5%	—	Touré et al. (2020)

atmosphere. The yellowing of polymeric materials due to oxidation is well known (Allen et al., 2022). PGS cured at low temperatures has more non-cross-linked chains and, thus, rinsing promotes a significant loss of mass. In comparison, curing at high temperatures results in more effective cross-linking. The curing time is also important in cross-linking, with mass losses ranging from 6% to 20% for PGS cured at 130°C/48 h and 130°C/24 h, respectively.

The ratio of reagents also influences the efficiency of cross-linking. Similar to Kafouris et al. (2013), Conejero-García et al. (2017) reported superior cross-link density at closer hydroxyl/carboxylic group equilibrium ratios, leading to more robust PGS.

Gadomska-Gajadur et al. (2018) proposed an optimization of PGS prepolymer (pPGS) synthesis using the Box–Behnken design based on three variables (temperature, G:S molar ratio, and reaction time). The optimization criteria maximized the degree of esterification of PGS and the conversion of monomers. The optimal conditions resulted in a 2:1 molar ratio synthesis at 150°C for 5 h at reflux with stirring (200 rpm), argon atmosphere, and without a catalyst. The resulting pPGS showed a high conversion of the carboxylic groups (~89%) and a very high degree of esterification (~82%). The total process time to obtain pure material suitable for medical and pharmaceutical applications was >50 h (Table 1).

While the influences of temperature, time, and reagent molar ratio have been evaluated intensively, the effects of the atmosphere in the PGS reaction have been relatively neglected until recently.

In 2021, Martín-Cabezuelo et al. (2021a) reported the results of a study that aimed to better understand the effect of inert (argon and nitrogen) and oxidative (oxygen, dry air, and humid air) atmospheres in PGS synthesis. The prepolymerization step was performed at 130°C for 24 h with a 1:1 (G:S) molar ratio and different gases flowing through the reactor. The curing step was performed in an oven with forced ventilation at atmospheric

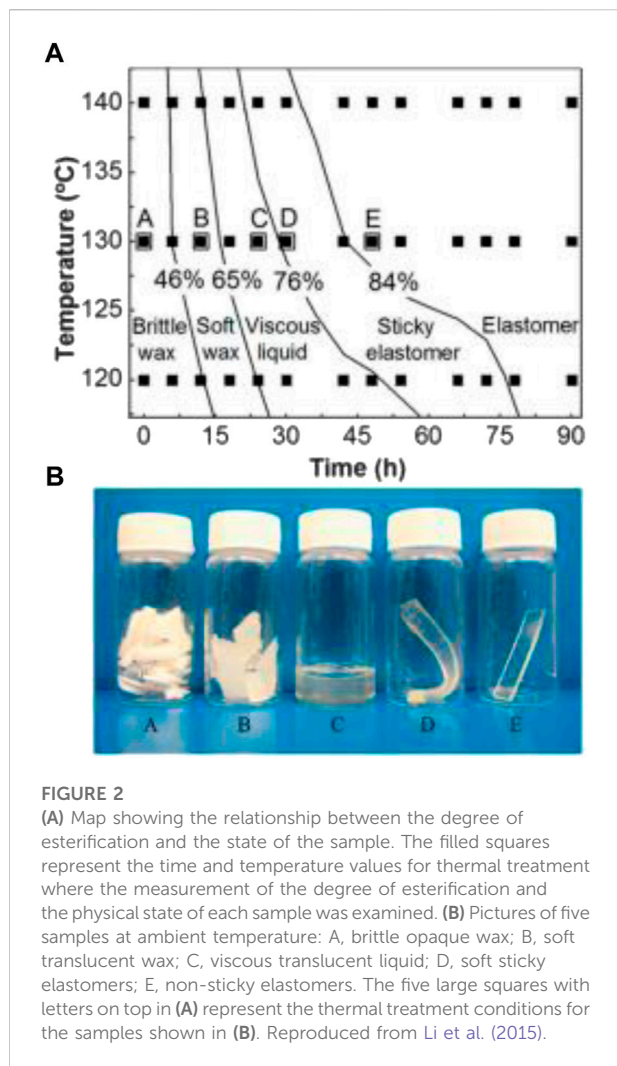
pressure (130°C for 48 h). Synthesis at different atmosphere conditions led to PGS networks with significantly different properties. The prepolymerization step showed great extension when performed under oxidative atmospheres, but in a branched way due to the simultaneous formation of oxidized species that boost the reactivity of secondary hydroxyls from glycerol. In contrast, inert atmospheres (Ar even more than N<sub>2</sub>) promote linear growth of oligomers and low branching. As a result, the increase in viscosity was more gradual in pPGS obtained under inert atmospheres, so the gel point takes longer. After curing, PGS obtained from pPGS produced under oxidative atmospheres is less elastic and softer (Martín-Cabezuelo et al., 2021a).

## 2.2 PGS polycondensation synthesis (higher temperature approach)

The conventional method of PGS synthesis requires days to complete. To reduce PGS synthesis time, some research groups have used higher temperatures ( $\geq 170^\circ\text{C}$ ) (Sun et al., 2013; Guo et al., 2014; Gadomska-Gajadur et al., 2018; Saudi et al., 2019; Riaz et al., 2022). This strategy is described in this section; some examples are also listed in Table 1.

Before the conventional method and the term “PGS” for this polymer were established, the first polycondensation of glycerol with sebacic acid and the production of PGS film (Yg10) were reported by Nagata et al. (1996 and 1999). The temperatures used for synthesis were extremely high and the researchers also used the two-step methodology. Prepolymerization and curing were performed at 200°C and 230°C, respectively, in both publications (Nagata et al., 1996; Nagata et al., 1999).

In 1996, Nagata et al. (1996) prepared aliphatic polyesters from glycerol and a series of various-length aliphatic dicarboxylic acids and analyzed the effects of the methylene chain length on the structure and physicochemical properties,



as well as enzymatic degradation. The PGS film was prepared with various curing times (Table 1), which influenced the degree of reaction (%) and, consequently, the enzymatic degradation rate of the film. The PGS films with the best resistance to enzymatic degradation were produced with 2 h of prepolymerization followed by 2 h or 4 h of curing. At 6 h of curing time, the degree of reaction (%) was lower than that at 4 h. Therefore, 6 h was excessive, resulting in thermal degradation of the polymer (Nagata et al., 1996). This PGS film with 6 h of curing was also less resistant to enzymatic degradation.

In 1999, Nagata et al. (1999) prepared PGS copolymers by progressively replacing sebacic acid with other diacids and evaluated the physicochemical and thermal properties, as well as enzymatic degradation. The PGS film was obtained with 43 min of prepolymerization and 4 h of curing time. This very fast synthesis resulted in a material with 1.96 MPa of tensile strength, Young's modulus of 6.86 MPa, and 27%

elongation. Based on these values, this was the strongest and toughest PGS that we found in the literature.

Sun et al. (2013) were the first to report pPGS synthesis and cure at 170°C, significantly reducing the duration of this process. Furthermore, PGS-curcumin polymer was prepared at 185°C. Guo et al. (2014) also produced pPGS at 180°C in only 3.5 h (Table 1).

Matyszczyk et al. (2020) created a kinetic model of the polycondensation of sebacic acid with glycerol based on infrared (IR) spectra during the reactions, which allowed the determination of the parameters of the Arrhenius equation over a wide temperature range (130°C–170°C). The polycondensation reaction was performed in an equimolar ratio of reactants at temperatures of 130°C, 150°C, and 170°C for 5–8 h, without any catalyst and under an argon atmosphere at 200 rpm. The disappearance of the 1410 cm<sup>-1</sup> peak generated by the acid and an increasing intensity of the 1185 cm<sup>-1</sup> ester peak were observed in the real-time IR measurement of the reactions. The polycondensation kinetics were determined based on changes in the intensity of these IR signals.

Saudi et al. (2019) synthesized pPGS under nitrogen gas at 170°C. Glycerol and sebacic acid were combined in a 1:0.8 (G:S) molar ratio as this ratio is more hydrophilic and suitable for cell adhesion and proliferation than other ratios (Guo et al., 2014). Under these conditions, the authors tested three reaction times (3, 5, and 7 h) and analyzed pPGS by Fourier transforming infrared (FTIR). They observed that, beyond 3 h, the sharp carbonyl peak at 1733 cm<sup>-1</sup> shifted to 1691 cm<sup>-1</sup> and its intensity increased. The sharp peak observed at 1691 cm<sup>-1</sup> was related to carbonyl stretching of the unreacted free sebacic acid. Under these conditions, with increasing reaction time, the ester bonds were broken or degraded and a greater proportion of free sebacic acid remained after prepolymer formation. Based on these observations and compared to FTIR of the conventional pPGS synthesis in other studies, the authors suggested 3 h as the ideal reaction time.

The FTIR observations of Saudi et al. (2019) are contrary to the real-time IR spectra of pPGS synthesis reported by Matyszczyk et al. (2020). At 5 h, the IR spectra showed a more intense peak related to ester groups compared to that at 3 h. For similar reaction conditions (only a slight ratio change of G:S, 1:0.8 and 1:1), the progression of reactions differed significantly between these studies (Saudi et al., 2019; Matyszczyk et al., 2020).

Riaz et al. (2022) synthesized pPGS, mixing the reagents thoroughly for 15 min to ensure homogeneity, heating the reaction mixture at 180°C for 3 h, under continuous nitrogen flow, for use as an ultrasound contrast agent.

Synthesis by the conventional method can take several days without polymer degradation. At very high temperatures, polymer degradation can occur within hours, as reported by Nagata et al. (1996) and Saudi et al. (2019). These higher temperatures can also lead to a severe loss of glycerol. The

temperature increase rate must be slow for the monomers to react, forming small monoglycerides (less volatile than glycerol) before reaching high temperatures. Users of this methodology should select the reaction time with care.

## 2.3 PGS microwave-assisted synthesis

Microwave-assisted synthesis (MwAS) is a time- and energy-efficient pathway to polycondensation reactions. The production of polyesters using microwaves is a relatively solid technology, with application on a non-laboratory scale. For example, in 2009, the first commercial plant for the mass production of poly(lactic acid) *via* microwave method was developed in Japan (Aydin et al., 2013).

MwAS significantly increases the esterification reaction rate by generating heat homogeneously in a bulk solution *via* dipole rotation, in which the polar species (e.g., glycerol and lactic acid) align themselves with a rapidly changing electric field produced by the microwaves such that the reactants can be activated selectively. Microwave irradiation provides heat internally and tends to eliminate the “thermal wall effect.” Hence, the condensed water molecules are evaporated faster in the microwave due to their large dielectric constant, which further enhances the polymerization reaction (Coativy et al., 2016; Lau et al., 2017).

Aydin et al. (2013) reported the first attempt to produce PGS using MwAS. The authors proposed an alternative for the initial prepolymerization step in 3 min instead of days, without purge gas, catalyst, vacuum, and agitation. Curing was performed at 150°C and 5 Torr for different time periods. They achieved a PGS after 3 min of prepolymerization and 16 h of cure with Young's modulus of  $0.50 \pm 0.02$  MPa, tensile strength of  $0.27 \pm 0.06$  MPa, and an elongation of approximately 180%.

However, this MwAS reaction produced a polymer with a molar ratio different from the initial molar composition (G:S, 1:1 to 0.22:0.78). The process resulted in a severe loss of glycerol due to the reaction temperature during the first prepolymerization step, which resulted in the boiling of glycerol monomers, as well as the higher curing temperatures in the second step. The authors also suggested that, since the boiling point of glycerol is 290°C, the decreased time required for polymerization was caused by extremely high temperatures (Aydin et al., 2013).

Li et al. (2015) also performed a MwAS synthesis for prepolymerization. They demonstrated that 15 min of microwave time was as efficient as the conventional prepolymerization method in a nitrogen atmosphere for 6 h at 130°C. However, this rapid synthesis method causes severe glycerol evaporation, resulting in a large alteration in the ratio of the monomers, leading to a more rigid PGS produced under similar curing conditions compared to the conventional prepolymerization method. The temperature of the mixture in

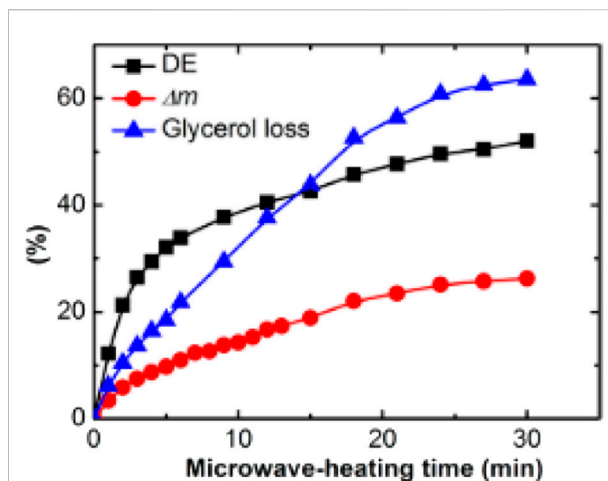


**FIGURE 3**  
Evolution of the degree of esterification (DE), mass loss ( $\Delta m$ ), and glycerol loss values with increasing prepolymerization time during microwave heating (Li et al., 2015).

the microwave heating process reached 170°C. The glycerol loss was 63% after 30 min of microwave time. This value was significantly higher than the 5%–10% glycerol loss value for the samples prepolymerized for 24 h in a nitrogen atmosphere at 1 atm at 120–140°C.

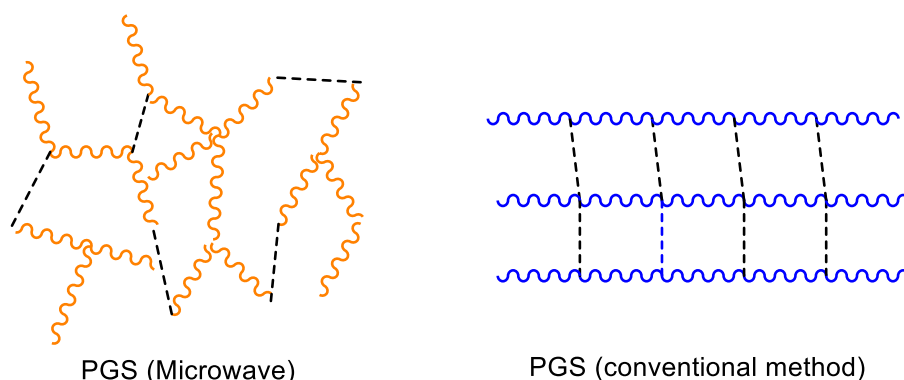
The results presented in Figure 3 (evolution of the degree of esterification (DE), mass loss ( $\Delta m$ ), glycerol loss values, and prepolymerization time) indicate that the rate of esterification decreases faster after 3 min and show a severe loss of glycerol. Thus, the 3 min time is a trade-off between efficient prepolymerization and severe glycerol loss. The authors reported a PGS with Young's modulus of 0.25 MPa, tensile strength of 0.25 MPa, and an elongation of approximately 190% for a microwave prepolymerization step lasting 3 min and a 48 h cure at 130°C in a vacuum, with a total loss of glycerol of 60%. The PGS properties are close to those reported by Aydin et al. (2013).

Tevlek et al. (2017) also produced pPGS in a microwave oven for 3 min at 650 W to mix with  $\beta$ -tricalcium phosphate ( $\beta$ -TCP) to create a bone-soft tissue interface. The mechanical properties of this material are shown in Table 2.

Recently, Tevlek et al. (2020) reported equimolar PGS with good elasticity ( $212.75 \pm 37.25\%$  elongation) and  $0.09 \pm 0.03$  MPa (Young's modulus) produced from microwave prepolymerization (4 min, with 10 s intervals every 1 min), followed by curing in a vacuum oven (150°C, 12 h).

Tevlek et al. (2022) also performed PGS prepolymerization in a microwave reactor (White-Westinghouse, United States) at 650 W without any catalyst or extra chemical material. The process was completed by exposing the reagents to microwaves for a total of five times, at 15 s intervals for 1 min. Curing was performed in a vacuum oven at 150°C and



**FIGURE 4**

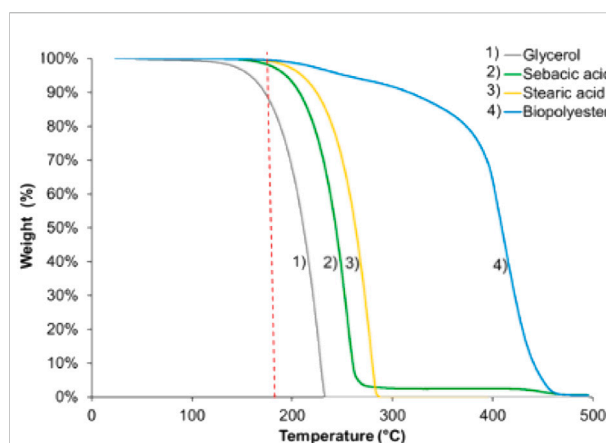
Proposed images of the possible structures of PGS prepolymerized via microwave and conventional methods. Dashed line: cross-linking. Images inspired by Lau et al. (2017).

10 mbar for 10, 12, and 14 h, to assess the impact of various cross-linking times on PGS membranes properties. More time (14 h) led to a PGS elastomer with more cross-link density, better biocompatibility, increased tensile strength, and lower elasticity.

Deniz et al. (2020) used a microwave oven (Samsung, Korea) at 650 W and high/medium settings. An equimolar sample of sebacic acid and glycerol mixture was exposed to five rounds of electromagnetic waves for 1 min each at 10-s intervals in the prepolymerization step.

Lau et al. (2017, 2020) proposed a solvent-based system (toluene) to provide better control of the reaction temperature in a microwave cavity and minimize monomer evaporation. Water was collected to measure the degree of esterification. The authors performed MwAS in a CEM Discover SP system, with the reaction maximum temperature well controlled at 130°C. This type of accuracy is impossible in conventional microwave ovens, similar to those used by Aydin et al. (2013) and Li et al. (2015). The curing step was performed at 120°C in a vacuum oven. MwAS was six times faster than conventional heating (CH). For example, 12 min of heating in MwAS, showed a DE of 66%; a similar value of CH required around 75 min. Furthermore, the results of NMR and MALDI-TOF analyses showed that the pPGS produced by MwAS was more branched than that produced by the conventional method without changing the molar ratio of glycerol and sebacic acid. Figure 4 shows proposed PGS structures by both methods. The microwave radiation interacts strongly with glycerol, leading to the activation of both alcohol groups (primary and secondary), which react more efficiently with sebacic acid compared to that in the CH approach.

The higher branching of the pPGS achieved by MwAS facilitates the formation of a cross-linked PGS in a very short curing time. For example, by reducing the curing time to 2 h, PGS specimens prepared by MwAS (DE = 66.82%) showed faster toughening compared to CH samples (DE = 68.18%). The PGS

**FIGURE 5**

Thermogravimetric analysis: variation in reagent weight and biopolyesters under nitrogen flow with a heating ramp of 10°C/min (Coativy et al., 2016)

showed Young's modulus values between 0.7 and 3.14 MPa and elongation between 60% and 15%, depending on curing time. A longer curing time resulted in higher Young's modulus value and lower elasticity.

Coativy et al. (2016, 2017) also used a microwave approach to synthesize a modified PGS with stearic acid (a Microwave Synthesis Labstation MicroSYNTH with constant agitation). The reaction was performed at 180°C until the viscosity suddenly increased, resulting in the end of magnetic stirring. Stearic acid was used to limit cross-linking to adjust the original properties of PGS to produce a polymer with a memory shape (Coativy et al., 2017). This modified PGS was blended with PLA to increase its ductility (Coativy et al., 2016). Thermogravimetric analysis was performed on pure reagents and the formed polymer (Figure 5). These results were important to explain the glycerol

loss behavior with temperature and gas flow. Glycerol showed two mass losses: a small 1% loss between room temperature and 150°C and a severe loss between 150°C and 220°C. This result highlights that glycerol, which is liquid, can be evaporated at a much lower temperature than its boiling point (290°C, 1 atm).

In addition to the boiling point, the flash point of a substance is also an important property to consider in evaporation processes. The flash point of glycerol is 160°C (Quispe et al., 2013), which confirms the observations of thermogravimetric analysis for the beginning of glycerol mass loss (Figure 5).

Lee et al. (2018) used a microwave reactor (Biotage® Initiator, Charlotte, NC) to cure PGS. The microwave-cured PGS elastomers were similar to PGS elastomers produced by the conventional polycondensation method. The results showed that the microwave curing of PGS is feasible and eight times faster than the conventional curing process, with a maximum cross-link of PGS using a gradual heating up to 160°C for 3 h.

## 2.4 PGS enzymatic synthesis

Biosynthesis is an alternative to the conventional chemical process of polyester synthesis. Lipase-catalyzed polymerization has been widely investigated because it allows high catalytic activity and high selectivity at mild reaction conditions (preventing side reactions), without harmful components or metallic traces from inorganic catalysts. Enzymatic polymerization was demonstrated as a new methodology in polymer synthesis. Several reviews have addressed this topic (Kobayashi, 2010; Yang et al., 2011; Yu et al., 2012; Zhang et al., 2013; Zhang et al., 2014), including extensive backgrounds on the lipase-catalyzed synthesis of polyesters from polyols and diacids.

Uyama et al. (1999) and Uyama et al. (2001) reported the lipase-catalyzed regioselective polymerization of divinyl sebacate and triols (glycerol-included). These studies produced acylglyceride products through the polymerization of divinyl sebacate and glycerol using *Candida antarctica* lipase as the catalyst. The reactions were performed at 60°C for 8 h with different reagent ratios. The obtained products were characterized by NMR and SEC analysis. A polymer yield of 63% was obtained in mass after washing. The main unit achieved was 1,3-diacylglyceride with a small amount of the branching unit 1,2,3-triacylglyceride. The reagent ratios greatly affected the microstructure of the polymer (molecular mass and glyceride distribution).

Choi and Yoon (2010) registered a patent for the preparation of a biodegradable polymer using an enzyme catalyst. Different sebacate-based polymers are mentioned, including PGS produced by enzyme B as a catalyst, in toluene medium.

Godinho et al. (2018) reported the successful synthesis of pPGS with *Candida antarctica* lipase B free (CALB) and lipase B immobilized Novozym 435 (N435) with crude glycerol, a by-

product of biodiesel production, and glycerol. An equimolar G:S ratio was used, with the reactions performed at 60°C for 24 h in a *t*-butanol solvent. The products were characterized by MALDI-ToF-MS and NMR. The acid consumption (titration method) was around 75% for the immobilized enzyme and 68% for the free enzyme after 24 h. After rinsing with water, viscous liquid prepolymers were obtained at room temperature, consistent with the PGS map by Li et al. (2015). The MALDI analysis showed that the crude glycerol is favorable for producing cyclic structures, mainly with N435 as a catalyst. Although a clear explanation for this finding is lacking, it may be related to the interaction of NaCl (present in crude glycerol) with the formed oligomers and the enzyme catalytic center. The enzyme types showed differences in acid consumption, and N435 produced richer prepolymer in the range of longer oligomers. In general, multibranched (oligomer with more than one triglyceride structure) or hyperbranched (no free -OH groups in the oligomer) oligomers were not detected, and the 1,3-diacylglyceride unit was the predominant structure. All prepolymers were mainly composed of low-mass oligomers (<1000 g mol<sup>-1</sup>), but tridecamers were also detected (<1600 g mol<sup>-1</sup>).

Perin and Felisberti (2020) used immobilized CALB to produce PGS in mild reaction conditions and studied the kinetics, chain growth, and branching behavior in different reaction conditions (solvents, temperatures, CALB amount, reagents feed ratio). These findings showed that, during the polycondensation reaction, CALB-catalyzed esterification and acyl migration occurred simultaneously. Thus, the PGS architecture changed from linear to branched throughout the progression of the reaction, with the branching resulting from the simultaneous CALB-catalyzed esterification and acyl migration. The different solvents strongly influenced the chain growth. The reactions performed in acetone, at temperatures ranging from 30°C to 50°C, had a higher molecular weight distribution (>10 kDa) compared to those for tetrahydrofuran, *t*-butanol, or acetonitrile (<3.5 kDa), under the same conditions. Contrary to the conventional method, the increase in temperature did not necessarily mean a faster reaction and higher molecular weight. In acetone, 40°C performed better than 50°C (Perin and Felisberti, 2020).

Avoiding solvents, some works adopted a hybrid way to produce pPGS using enzymatic synthesis. First, the prepolymerization mixture was heated to 120°C, under N<sub>2</sub> protection, to form a homogenous transparent liquid mixture. After a 24 h reaction, the temperature was reduced to 90°C and N435 (around 10%–15% of the mass of the starting reagents) was added. The N<sub>2</sub> atmosphere was then removed, and vacuum was applied progressively until the end of the reaction, which could take > 60 h (total time) (Lang et al., 2020; Ning et al., 2022). With these reaction procedures, Lang et al. (2020) produced PGS with Mn, Mw, and Đ values of 3700 g/mol, 63,900 g/mol, and 16.9, respectively, after 71 h.

More recently, Ning et al. (2022) demonstrated that N435 catalysis in bulk leads to higher molecular weight PGS compared to that for the conventional method. They also reached an acid consumption of 82% without the formation of a gel fraction, in equimolar reaction conditions, without solvents, at 90°C. The N435 catalysis restricted the interchain cross-linking relations, preventing the gel fraction products, and offered higher selectivity for the reaction of primary hydroxyl units. The N435-catalyzed synthesis enabled the preparation of PGS with  $M_n$ ,  $M_w$ , and  $\bar{D}$  values of 6000 g/mol, 59,400 g/mol, and 10 at 67 h, respectively. The authors also explored the application of non-solvents to enrich PGS in higher molecular weight chains by solvent fractionation, with methanol showing the best results.

The use of enzymatic catalysis avoids glycerol loss and significantly reduces the pPGS synthesis time compared to the conventional method. Enzymatic synthesis allows greater control in obtaining oligomers with a linear structure, leaving cross-linking for the curing step. This may be relevant for PGS modifications with alternative cross-linkers, such as acrylate or isocyanate moieties.

## 2.5 PGS polymer structure synthesis using other catalysts and reagents

PGS has been synthesized mainly by esterification reactions between glycerol and sebacic acid without catalysts. The previous section described some studies using enzymes as catalysts. Two of these studies replaced sebacic acid with divinyl sebacate (Uyama et al., 1999; Uyama et al., 2001). Several publications reported the use of other monomers and catalysts to obtain PGS structures. This section describes publications that used non-enzymatic catalysis and other monomers for PGS-type structure synthesis.

Organometallic catalysts are widely used in industry and research in the polymers field. Wyatt et al. (2012) used dibutyltin (IV)oxide as a catalyst to produce poly(glycerol-co-diacid)s, where sebacic acid was not selected. However, in a recent work, Wilson et al. (2018) used FASCAT 9100 (butylstannic acid) catalyst to produce pPGS. After curing, a PGS with a tensile strength of 0.84 MPa was produced. In this work, a block copolymer of PGS with poly(tetramethylene oxide) glycol (PTMO) and a mixture of PGS-b-PTMO with a poly(ester-ether) thermoplastic elastomer (Hytrel 3078) was synthesized, producing a polymer, PGS-b-PTMO-Hytrel 3078, with extreme elasticity (2574% elongation).

Diarylborinic acid catalysts promote the formation of linear polyesters from glycerol. Slavko and Taylor (2017) used organoboron catalysts to produce polymers that were essentially free of branching or cross-linking. Sebacoyl chloride was used instead of sebacic acid, and PGS synthesis was performed in THF solvent at 70°C (Slavko and Taylor, 2017). Using sebacoyl chloride and glycerol as monomers and diarylborinic acids as catalysts, a high fraction of 1,3-

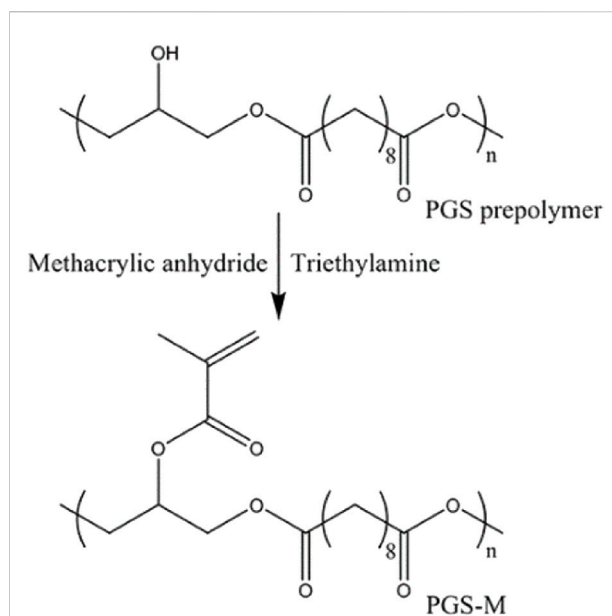


**FIGURE 6**  
Synthesis schemes for PGS prepolymer and PGS-Methacrylate (PGS-M). Scheme from Pashneh-Tala et al. (2018).

diacylglyceride units was found in NMR analysis (Slavko and Taylor, 2017). These findings demonstrated the production of PGS with an essentially linear structure.

Another alternative to PGS synthesis is the ring-opening reaction of diglycidyl sebacate with sebacic acid. Here, diglycidyl sebacate replaces glycerol. This approach aims to produce a linear PGS backbone. This reaction yielded a well-defined linear structure known as poly(sebacoyl diglyceride) PSeD, suitable for functionalization (You et al., 2010; Chen et al., 2016; Wang et al., 2016).

Wrzeczniak et al. (2021) developed a method to obtain linear PGS by catalyst-free polytransesterification using glycerol and dimethyl sebacate (2:1 molar ratio, respectively). The authors fixed the molar ratio of the reactants and varied the time and temperature. The synthesis was optimized to minimize the degree of branching and maximize the molecular weight. The optimal parameters obtained for this process were 160°C and 30 h, which produced PGS with a branching degree of 3.5% and a molecular weight of 1.6 kDa.

## 2.6 PGS photopolymerization (acrylate cross-linking)

The photopolymerization method has been used to obtain a final polymer by introducing reactive acrylate groups into pPGS to form PGS photocurable materials (Figure 6). This approach makes it possible to produce a wide range of physical properties under mild conditions using ultraviolet (UV) light



**FIGURE 7**

Methacrylated PGS nerve guidance conduits: the left is compressed to highlight the elastic properties, while the right shows the final 3D-printed product ready for implantation (Singh et al., 2018).

photopolymerization and to reduce the curing step to a few minutes instead of days as in the traditional thermo-curing process. However, the preparation of these photocurable pPGS can also take a long time in functionalization reactions with acrylate groups (Nijst et al., 2007; Ifkovits et al., 2008; Mahdavi et al., 2008; Wu Y et al., 2014; Yeh et al., 2016; Wang M et al., 2017; Wang L et al., 2017; Hu et al., 2017; Yeh et al., 2017; Pashneh-Tala et al., 2018; Chen J.-Y et al., 2018; Singh et al., 2018; Farr et al., 2020; Kazemzadeh Farizhandi et al., 2020; Liang et al., 2020; Pashneh-Tala et al., 2020).

Nijst et al. (2007) synthesized PGS acrylate (PGSA) using acryloyl chloride and a photoinitiator (2,2-dimethoxy-2-phenylacetophenone). The synthesis of pPGS followed the traditional method and then was performed with the addition of acrylate moieties. The UV curing step required only 10 min. The elastomers showed Young's modulus values of 0.05–1.38 MPa, an ultimate tensile strength of 0.05–0.50 MPa, and an elongation at break of 42–189%, depending on the degree of acrylation. Increasing acrylate led to an increased Young's modulus and decreased elongation capacity. Photocured PGSA networks showed biocompatibility *in vitro* as assessed by human primary cell adherence and subsequent proliferation into a confluent monolayer. The copolymerization of poly(ethylene glycol) diacrylate with PGSA was also tested and allowed for additional control of final material properties.

Ifkovits et al. (2008) similarly synthesized PGSA as Nijst et al. (2007), with the same conclusions. In general, Young's modulus increased with an increasing degree of acrylation. The elongation at break increased with increasing molecular weight for a constant degree of acrylation. In their study, the PGSA mechanical properties were 0.15–30 MPa (Young's modulus) and 5%–200% (elongation). Not all macromers formed an elastomeric network. High acrylation values led to the formation of a very stiff PGSA with low elastomeric characteristics.

Acrylated and methacrylated PGS are biocompatible materials for use in biological tissue engineering applications.

These types of materials have been proposed as aid materials for wound dressing (Mahdavi et al., 2008) and nerve guidance conduits (Hu et al., 2017; Singh et al., 2018).

Mahdavi et al. (2008) developed a synthetic gecko-inspired adhesive tissue in PGSA that may be useful for a range of medical applications, including sealing wounds and replacing sutures/staples.

Methacrylated PGS has been proposed for nerve tissue applications (Hu et al., 2017; Singh et al., 2018). Because pPGS is a difficult material to electrospin into nanofibers, Hu et al. (2017) synthesized PGS-based copolymers with methyl methacrylate (MMA), a more easily processed material. Singh et al. (2018) used PGS methacrylate to produce nerve guidance conduits *via* stereolithography for peripheral nerve injury repair (Figure 7). The material showed appropriate mechanical properties and supported neuronal and glial cell growth *in vitro* and *in vivo*.

Yeh et al. (2016) reported the extrusion-based 3D printing of PGSA to produce scaffolds with elastic properties. This method showed great potential to originate complex biocompatible elastomeric tissues. In the same line of studies, the authors also developed a norbornene-modified PGS (Nor-PGS) that cross-linked faster under ultraviolet light (<1 min), suitable for extrusion-based 3D printing (Yeh et al., 2016).

Tsai et al. (2020) developed a new type of photocurable and elastomeric hydrogel using Nor-PGS-co-polyethylene glycol (Nor-PGS-co-PEG). The norbornene functional groups allowed hydrogel cross-linking *via* thiol-norbornene photochemistry. The cross-linking process was rapid in the presence of a photoinitiator and UV light (<3 min). Several properties of this material can be easily fine-tuned by adding different amounts of cross-linker. The Nor-PGS-co-PEG can be processed using electrospinning and 3D printing techniques to generate microfibrillar scaffolds and printed structures, respectively. The material showed excellent elongation (around 950%) and good cytocompatibility in *in vitro* studies.



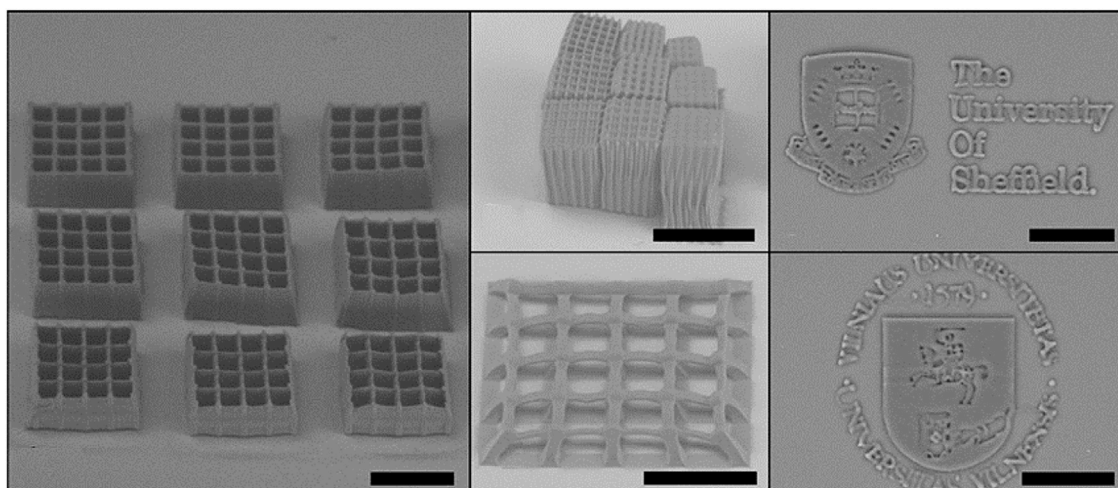


FIGURE 8

PGS-M 3D structures produced by DLW-2PP. Images collected and adapted from Pashneh-Tala et al. (2018).

Nor-PGS-co-PEG is a promising elastomer with highly tailorable properties for biomedical applications.

Chen J.-Y et al. (2018) described the tunable mechanical and degradation properties for the selection of biodegradable photocurable polymers that may be useful in 3D printing. The authors produced biodegradable photocurable copolymers by copolymerizing polycaprolactone diacrylate (PCLDA) and/or poly(ethylene glycol) diacrylate (PEGDA) with PGSA to form a polymer network. PCLDA and PEGDA are two common choices used in biomedical research. However, the degradation rates of these polymers *in vivo* are low, limiting their applications. The formation of several copolymers generated a database with selectable properties. The overall degradation rate was significantly higher than those for pure substances.

The direct use of PGS-based biomaterials in *in situ* tissue and cell encapsulation applications is limited due to their low water uptake. Therefore, Wu Y et al. (2014) developed injectable photocurable biodegradable hydrogels and microgels based on methacrylate poly(ethylene glycol)-co-poly(glycerol sebacate) copolymers. These gels showed good hydration properties and an easy *in situ* gelation process by photopolymerization under physiological conditions, thus demonstrating their potential as injectable tissue engineering scaffolds.

Pashneh-Tala et al. (2018) and Pashneh-Tala et al. (2020) developed a photocurable PGS methacrylate (PGS-M) prepolymer by functionalization of secondary hydroxyl groups with methacrylic anhydride and triethylamine as catalyst. The authors used different approaches to define the shape of the final material. The authors filled molds with pPGS-M, applied UV light, and photopolymerized a generic disc shape to be CNC carved, creating different objects from digital designs with excellent manufacturing quality and a highly porous structure

(Pashneh-Tala et al., 2020). The DLW-2PP (direct laser writing two-photon polymerization) laser technique to obtain 3D structures (Figure 8) was also used to produce PGS-M objects (Pashneh-Tala et al., 2018).

Wang M et al. (2017) produced a photo/thermo dual curable polymer based on PGS. The functionalization of PGS with 2-isocyanatoethyl methacrylate (IM) quickly produced a methacrylated PGS (PGS-IM). The PGS-IM was synthesized only by mixing PGS with IM at 80°C for 20 min in DMF solvent and without additional reagents/catalysts. After this process, PGS-IM scaffolds were produced by three curing approaches. The thermo-cured scaffolds used a vacuum oven at 150°C at 1 Torr for 12 h. The photo-cured scaffolds were produced using an Irgacure 2959 and UV light for 10 min. The dual-cured scaffold was produced by consecutively applying the previous two curing approaches. The photo-curing was applied first and then the thermo-curing. The combination of these curing processes provided a further way to modulate the properties of the resultant porous scaffolds. All PGS-IM scaffolds showed good elasticity, biodegradability, and cytocompatibility with L929 fibroblast cells. The cross-linking in PGS-IM comprised both acrylate and urethane bonds.

The next section describes the cross-linking of PGS by urethane bonds.

## 2.7 PGS urethane cross-linking

The use of isocyanates for pPGS cross-linking is another alternative to avoid the long curing times in the conventional process and to produce PGS-derived polymers with improved properties (Pereira et al., 2013; Li et al., 2015; Frydrych and Chen,

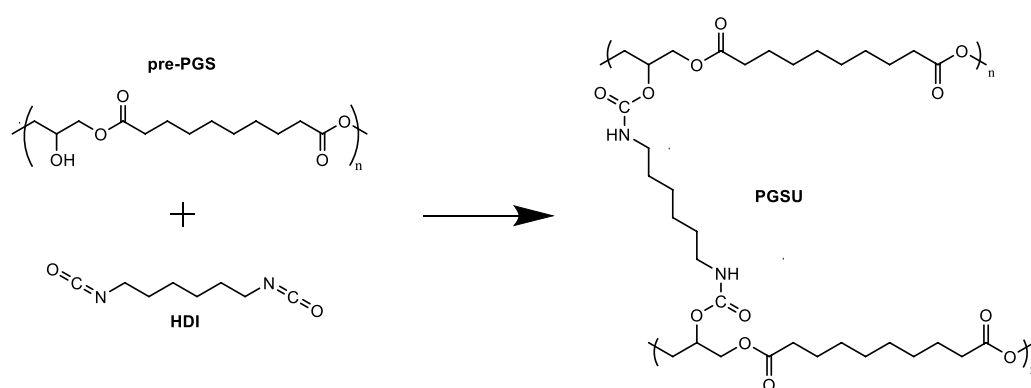


FIGURE 9

Reaction scheme for PGSU synthesis using HDI as a pre-PGS cross-linker. Scheme inspired by [Pereira et al. \(2013\)](#).

2017; Monem et al., 2022). The reaction between isocyanate and free hydroxyl groups occurs rapidly under mild conditions.

Pereira et al. (2013) produced a PGS urethane (PGSU) biocompatible and mechanically tunable elastomer suitable for encapsulation and controlled drug delivery systems. PGSU was synthesized with hexamethylene diisocyanate (HDI) as the cross-linker and tin (II) 2-ethylhexanoate as the catalyst (Figure 9). Pereira et al. (2013) synthesized PGSU films under two conditions: with solvent and solvent free. The solvent-free approach reduced the quantity of solvent traditionally used in film cast and produced films in <36 h. Pereira et al. (2013) reported a wide range of mechanical properties (Young's modulus from 0.1 MPa to 20 MPa and elongations >400%) for their PGSU films, replicating the characteristics of some biological tissues. The *in vitro* assessment of the biodegradation and cytocompatibility demonstrated that the degradation profile depended on the degree of cross-linking. Increasing urethane content resulted in slower degradation rates. The degradation rates for all PGSU derivatives were generally slower than that for PGS. Testing of the cytocompatibility of the PGSU materials in human mesenchymal stem cells showed identical metabolism to cells placed in tissue culture polystyrene (TCP) after 8 days of cell proliferation. The inflammatory reaction *in vivo* of PGSU was significantly lower than that observed for poly(lactic-co-glycolic acid) (PLGA), a degradable material that has been FDA-approved for internal use.

Frydrych and Chen (2017) synthesized three-dimensional biodegradable PGSU scaffolds and films *via* solvent-based synthesis using HDI, tin (II) 2-ethylhexanoate, and 1,4-dioxane as solvent. The PGSU scaffolds showed good hydrophilic characteristics and high-water absorption abilities. *In vitro* tests, the PGSU scaffolds demonstrated variable degradation rates and mass losses of 10%–16% and 30%–62%, without and with the presence of lipase enzyme, respectively,

after 112 days. The results demonstrated that the degradation kinetics of the PGSU scaffolds depended on the urethane content in the PGSU specimens, in which slower degradation rates were linked to higher urethane group numbers, and *vice versa*, similar to the findings reported by Pereira et al. (2013).

Frydrych et al. (2015b) produced polyester-based polyurethane (PEU) hydrogels based on PGS and poly(ethylene glycol)s (PEG)s. The hydrogels were thermoresponsive, stretchable, biodegradable, and biocompatible. The hydrogels had a tensile Young's modulus, ultimate tensile strength, and elongation at break in the range of 0.02–0.20 MPa, 0.05–0.47 MPa, and 426%–623%, respectively. *In vitro* cell tests showed that some of the hydrogels were suitable for culturing adipose-derived stem cells and dermal fibroblasts. These results showed the versatility of these PEU hydrogels for biomedical and engineering applications.

Wang et al. (2018) synthesized PGSU and urethane-based PEGylated PGS elastomers using HDI, tin (II) 2-ethylhexanoate, and pPGS and pPEGs. These mixtures were allowed to react at 55°C with stirring for 5 h and under argon flow for cross-linking. By tailoring the PEG and HDI contents, elastomers were produced with broad ranges of mechanical properties and customized hydrophilicities. The mechanical properties of these elastomers are shown in Table 2. Increasing PEG decreased the water contact angle (WCA) to between 28.6–71.5°. The HDI amount had almost no influence on the hydrophobicity of polymers but influenced Young's modulus and tensile strength. The degradation rate depended on the urethane content in the elastomers, as reported previously (Pereira et al., 2013; Frydrych and Chen, 2017). These elastomers showed favorable biocompatibility *in vitro* and mild host response *in vivo*. The results showed that these elastomers could be easily produced into various shapes and be tailored for diverse applications in biomedical research.

Monem et al. (2022) also synthesized PGSU using HDI, tin (II) 2-ethylhexanoate, and 1,4-dioxane as a solvent. In this study, a series of PGSU nanocomposites were synthesized and characterized to produce desirable elastomeric materials. These nanocomposites were prepared with two kinds of nanoclay under the commercial names of Cloisite Na<sup>+</sup> and Cloisite 10 A. The results indicated that both nanoclays enhanced the storage modulus. Hydrolytic degradation of the nanocomposites indicated that the degradation behaviors of the samples were highly affected by their hydrophilicity properties. The neat PGSU showed a mass loss of  $63.5 \pm 1\%$  after 30 days (degradation rate  $\sim 15\%$  per week) and a WCA close to  $80^\circ$ . The more resistant PGSU nanocomposite to degradation showed a mass loss of  $48.9 \pm 1\%$  after 30 days (degradation rate  $\sim 11\%$  per week) and a WCA close to  $90^\circ$ .

Golbaten-Mofrad et al. (2021) similarly produced PGSU using HDI, tin (II) 2-ethylhexanoate, and a solvent mixture of DMSO:DMF (70:30 wt%). The solution was stirred at  $55^\circ\text{C}$  for 15 min. In this research experiment, a series of PGSU scaffolds with various cross-link densities were prepared for subsequent polypyrrole polymerization and insertion of zinc oxide (ZnO) nanoparticles. The mechanical performance of the scaffolds under dry and hydrated conditions was evaluated by compression tests. Hydrated low urethane content scaffolds presented Young's modulus and compression stress at 75% strain in the ranges of 8.1–9.4 kPa and 26.6–29.8 kPa, respectively. In contrast, the high urethane content scaffolds displayed higher Young's modulus values and compression stress at 75% strain in the ranges of 48.8–122.5 kPa and 927.9–1014.5 kPa, respectively. The ZnO nanoparticles improved the surface hydrophilicity (WCA  $86^\circ$ ) and added anti-bacterial behavior (WCA  $97.2^\circ$ ). The high HDI molar ratio intensified the samples' surface hydrophobicity (WCA  $102.9^\circ$ ).

Li et al. (2015) also synthesized PGSU, but with methylene diphenyl diisocyanate (MDI) as the cross-linker. They observed that MDI resulted in a more rigid polymer compared to PGS. Thus, isocyanate introduction must be moderate because excessive amounts remove the elastomeric properties of the final material.

### 3 PGS material properties

PGS is presently characterized as a material that resembles soft biological tissues. Its mechanical properties (Table 2) are close to those of some biological tissues, such as the cornea, the arteries/veins, the spinal cord, the gray matter, and some muscles (McKee et al., 2011). Because sebacic acid and glycerol both have endogenous natures, PGS and PGS-based materials are considered to be biocompatible (Piszko et al., 2021b). Moreover, glycerol and sebacic acid have been approved by the FDA; therefore, PGS degradation products are considered

safe (Kemppainen and Hollister, 2010; Sha et al., 2021). PGS polyester elastomer can appear as transparent, almost odorless, and colorless or slightly yellow (depending on oxygen present during the reaction) (Halil Murat, 2017; Piszko et al., 2021b). PGS forms a covalently cross-linked 3D network of random coils with hydroxyl groups on the backbone (Sha et al., 2021). The PGS density is around  $1.13 \text{ g/cm}^3$  (Nagata et al., 1996; Pomerantseva et al., 2009).

pPGS is soluble in many available organic solvents, including 1,3-dioxolane, THF, dimethyl carbonate, ethanol, isopropanol, DMF, dioxane, acetic acid, formic acid, and acetone (Halil Murat, 2017; Piszko et al., 2021b). This makes processing easier and allows the use of a variety of techniques.

The physicochemical properties of PGS are commonly assessed by FTIR and NMR. These analyses are useful for screening the synthesis progress and characterizing the final material. FTIR confirms the presence of all important bonds and functional groups including polar hydroxyl, terminal carboxyl groups, ester bonding, and aliphatic backbone. NMR analysis allows for effective structural characterization of the prepolymer before subsequent cross-linking or modification, as well as analyses of the molecular chain topology (Wyatt et al., 2012; Li et al., 2013a; Halil Murat, 2017; Perin and Felisberti, 2020; Piszko et al., 2021a; Piszko et al., 2021b; Ning et al., 2022).

The thermal stability of PGS, as evaluated by thermal gravimetric analysis (TGA), is consistent throughout the literature. PGS is stable up to  $250^\circ\text{C}$  and shows a single weight loss step between  $320^\circ\text{C}$  and  $475^\circ\text{C}$  (Gaharwar et al., 2015; Tang et al., 2017; Aghajan et al., 2020; Rostamian et al., 2020; Martín-Cabezuelo et al., 2021a; Chang et al., 2021). The initial degradation temperature starts between  $320^\circ\text{C}$  and  $350^\circ\text{C}$ , with a peak degradation temperature typically between  $435^\circ\text{C}$  and  $440^\circ\text{C}$  (Gaharwar et al., 2015; Aghajan et al., 2020; Martín-Cabezuelo et al., 2021a; Piszko et al., 2021a). However, Martín-Cabezuelo et al. (2021a) studied the effects of the PGS synthesis under different atmospheres and observed a lower peak of thermal degradation ( $415^\circ\text{C}$  and  $425^\circ\text{C}$  for hydrated and dry air, respectively) when PGS was synthesized using air (Martín-Cabezuelo et al., 2021a).

The thermal properties of PGS, as assessed by differential scanning calorimetry (DSC), are also consistent in the literature. PGS is a semi-crystalline polymer, with properties that depend on the glass transition temperature ( $T_g$ ) of the amorphous phase and melting temperature ( $T_m$ ) of the crystalline phase (Cai and Liu, 2007; Jaafar et al., 2010). The degree of crystallization decreases significantly with the extent of cure (Jaafar et al., 2010; Guo et al., 2014). The  $T_g$  of PGS ranged between  $-40^\circ\text{C}$  and  $-15^\circ\text{C}$ , with a broad melting transition between  $-20^\circ\text{C}$  and  $40^\circ\text{C}$  according to the DSC diagrams (Cai and Liu, 2007; Jaafar et al., 2010; Conejero-García et al., 2017). PGS is completely amorphous  $>35^\circ\text{C}$  (Cai and Liu, 2007; Jaafar et al., 2010; Rostamian et al., 2020). The dynamic mechanical thermal analysis (DMTA) results are consistent across many

publications. The temperature at the maximum of the associated peak in  $\tan \delta$  shifts accordingly to lower temperatures, around  $-20^{\circ}\text{C}$ , which characterizes the main relaxation process associated with the  $T_g$  of PGS (Aghajan et al., 2020; Rostamian et al., 2020; Martín-Cabezuelo et al., 2021a; Chang et al., 2021).

The crystallinity and morphology of PGS can be assessed by X-ray diffraction (XRD) analysis. PGS shows a broad amorphous peak at about  $2\theta = 20^{\circ}$  which is related to the short-range regular ordered structure of both free and cured chains along with the disordered structure of the amorphous phase of the PGS matrix (Nagata et al., 1996; Nagata et al., 1999; Chen et al., 2007; Guo et al., 2014; Aghajan et al., 2020).

PGS is considered hydrophilic, with a WCA around  $38\text{--}94^{\circ}$  (Guo et al., 2014; Gaharwar et al., 2015; Aghajan et al., 2020; Chang et al., 2021; Martín-Cabezuelo et al., 2021a; Tevlek et al., 2022). A higher glycerol ratio synthesis promotes decreased WCA as it increases the number of hydroxyl groups. However, a higher ratio of sebacic acid increases the hydrophobic group content and WCA values (Guo et al., 2014). For PGS produced from a molar reagent ratio of 1:1 (G:S), the increase in cross-link density, which consumes more hydroxyl groups, provides more wettable surfaces (Conejero-García et al., 2017; Tevlek et al., 2022). However, when the cross-link density increases by urethane (Golbaten-Mofrad et al., 2021) or methacrylate (Singh et al., 2018) bonds, the WCA value increases (Singh et al., 2018; Golbaten-Mofrad et al., 2021). This can be contradictory. However, the hydrophilicity of PGS elastomers is related not only to the presence of hydroxyl groups but also to the polar end groups and inter-molecular hydrogen bonds (Conejero-García et al., 2017; Tevlek et al., 2022). The WCA value of a PGS material is a good indicator of cell viability as more wettable surfaces promote better cell adhesion and propagation (Fakhari et al., 2021; Tevlek et al., 2022).

Based on the ISO 10,993-5 standard, materials with cell viability  $<70\%$  are considered toxic. PGS can cause cytotoxicity *in vitro* due to acidic components released into the culture medium because of surface degradation (Li et al., 2013b; Tevlek et al., 2022). PGS elastomers with lower cross-link density degrade faster than those with higher cross-link density, in the same environmental conditions. The unreacted carboxylic acid groups and/or the carboxylic acids produced by the hydrolysis of ester groups can cause severe acidification of the medium (Li et al., 2013b), leading to higher cytotoxicity of PGS elastomers with lower cross-link density (Chen et al., 2011; Li et al., 2013b; Tevlek et al., 2022). Moreover, Liu et al. (2009) reported high cytotoxicity of a PGS elastomer modified with citric acid (PGSC). After 7 days, the accumulated acidity of the acidic sols inhibited the growth of L-929 cells, causing most of the cells to die (Liu et al., 2009). These findings confirmed that excessive acidity caused by elastomer degradation leads to high cytotoxicity levels.

However, the addition of another acid monomer to the polymer structure does not necessarily imply increased

cytotoxicity. Chen et al. (2011) reported that the addition of lactic acid to PGS to obtain (PGS-co-LA) significantly improved the cytocompatibility of the final materials compared to the PGS alone.

PGS and PGS-based materials are non-toxic when synthesized properly. The cytocompatibility of PGS has been demonstrated in NIH 3T3 fibroblasts (Wang et al., 2002), 3T3 fibroblasts (Rai et al., 2013a; Jeffries et al., 2015), MC3T3 osteoblasts (Wu et al., 2016), chondrocytes (Wu et al., 2016), human umbilical artery smooth muscle cells (HUASMCs) (You et al., 2016; Hsu et al., 2018; Wu H. J et al., 2019), SNL mouse fibroblasts (Chen et al., 2011; Li et al., 2013b; Xu et al., 2015), L-929 fibroblasts, (Conejero-García et al., 2017; Varshosaz et al., 2021; Wang et al., 2021; Jia et al., 2016; Tang et al., 2017; Wu et al., 2016; Wang M et al., 2017) human umbilical vein endothelial cells (HUVECs) (Wang et al., 2021; Zhang et al., 2021; Tevlek et al., 2022), hFOB1.19 human fetal osteoblasts (cytocompatibility and osteoconductivity) (Piszko et al., 2021a), Schwann cells (Sundback et al., 2005; Singh et al., 2018), bone marrow stromal cells (BMSCs) (Wang et al., 2018), human mesenchymal stem cells (hMSCs) (Pereira et al., 2013), and human dermal fibroblasts (Pashneh-Tala et al., 2020).

PGS and PGS-based material biocompatibility has been demonstrated *in vivo* in BALB/c adult mice (Piszko et al., 2021a), CD<sup>®</sup> (Sprague-Dawley) IGS rats (Fu et al., 2020b), Sprague-Dawley rats (Wang et al., 2002; Ifkovits et al., 2008; Jia et al., 2016; Ma et al., 2016; Wu et al., 2016; Xiao et al., 2019), Wistar rats (Mahdavi et al., 2008; Sun et al., 2009), Fisher rats (Sundback et al., 2005), rabbits (osteoconductive to bone regeneration) (Zaky et al., 2017), C57 rats (Wang et al., 2018), YFP+ mice (Singh et al., 2018), and Lewis rats (Pomerantseva et al., 2009; Pereira et al., 2013). *In vivo*, some mild and temporary inflammatory responses typical of implantable biodegradable polymers have been reported with PGS and PGS-based materials; however, necrosis or tissue degradation have not been reported (Ifkovits et al., 2008; Pomerantseva et al., 2009; Sun et al., 2009; Wu et al., 2016; Fu et al., 2020b).

Table 2 presents the mechanical properties of different PGS-based materials found in the bibliography. The data shows how compliant PGS can be with other elements, allowing the production of new materials with different or improved mechanical properties.

### 3.1 PGS degradation (*in vitro* hydrolytic, *in vitro* enzymatic, and *in vivo*)

PGS degradation can be evaluated by three methods: *in vitro* hydrolysis degradation, *in vitro* enzymatic degradation, and *in vivo* degradation. Independent of the degradation type, the PGS degradation process follows the surface erosion mechanism (Wang et al., 2003; Sundback et al., 2005; Pomerantseva et al., 2009; Guo et al., 2014; Kim et al., 2014; Li et al., 2015; Souza et al.,



2017; Zhang et al., 2020; Tevlek et al., 2022). This mechanism is characterized by linear mass loss and corresponding volume decrease while preserving the shape, surface integrity, and mechanical properties. The surface erosion mechanism has also been observed in many PGS-based materials such as PGSU (Pereira et al., 2013; Frydrych and Chen, 2017), PGS-M (Pashneh-Tala et al., 2018), and other PGS-based materials (Ma et al., 2016; Lang et al., 2020).

However, Shi et al. (2020) demonstrated that induced cracks overcome erosion in PGS and lead to the premature loss of the mechanical properties and morphology of the material. The crack progression depends on pH, humidity, and applied forces (Shi et al., 2020).

The degradation rate, for the same conditions, is related to the cross-link density of PGS materials, in which materials with higher cross-link densities show more resistance to degradation (Pereira et al., 2013; Li et al., 2015; Frydrych and Chen, 2017; Lau et al., 2017; Singh et al., 2018; Krook et al., 2020).

Krook et al. (2020) investigated the degradation of porous PGS, reporting that the polymer properties change rapidly with degradation in the case of materials with lower cross-link density.

### 3.1.1 *In vitro* hydrolytic degradation

The *in vitro* hydrolytic degradation is typically performed in a buffered aqueous solution (pH 7.4), at 37°C under agitation. This type of degradation is the slowest.

One study reported that the PGS samples lost 15%–30% of the mass, depending on the cross-link density, during the 28-day process of hydrolytic degradation (Li et al., 2015). In another study, the PGS slowly degraded, losing only 17% of the mass in 60 days (Sundback et al., 2005).

In another study, PGS-IM scaffolds degraded *in vitro* showed mass losses of 12.2% (photo-cured), 11.9% (thermo-cured), and 5.9% (dual-cured), respectively, at day 28. The dual-cured scaffolds showed the lowest mass loss rate, likely due to their highest cross-link density (Wang M et al., 2017). Once again, this process of degradation is slower.

### 3.1.2 *In vitro* enzymatic degradation

The *in vitro* enzymatic degradation is usually performed in an aqueous buffered solution (pH 7.4), with enzymes (e.g., lipases and esterases), at 37°C, and under agitation. The use of enzymes accelerates the degradation process.

Nagata et al. (1996) performed the *in vitro* degradation of PGS films with lipase. After 6 h, a weight loss of 80 g/m<sup>2</sup> was observed for PGS films, with a reaction degree of 83%. The degree of reaction affected the degradation. PGS films with higher degrees of reaction showed higher resistance to degradation.

Nagata et al. (1999) performed *in vitro* degradation of PGS copolymers films with lipase. The films were obtained by incorporating other diacids in the polymer synthesis. The various PGS copolymers films produced were compared after 2 h of enzymatic degradation. The PGS film had a weight loss of

50 g/m<sup>2</sup>; however, the addition of other diacids increased the resistance of the copolymer films. For example, replacing 10% (mol) of sebacic acid with succinic acid resulted in a PGS-co-succinate film, “Yg-10/4 (90/10)”, which had a weight loss of 22 g/m<sup>2</sup>, an increase in degradation resistance of >50%, compared to PGS.

Tevlek et al. (2022) cured three sets of PGS elastomers for different times (14, 12, and 10 h) and performed *in vitro* hydrolytic and enzymatic degradations in a 28-day process. The hydrolytic mass losses were 9.65%, 13.79%, and 24.82%, and the enzymatic degradation mass losses were 12.75%, 19.54%, and 43.75%, respectively. The cross-link densities were 70.33, 33.79, and 14.77 mol/m<sup>3</sup>, respectively. Their data confirmed that enzymatic degradation was faster than hydrolytic degradation and that the degradation rate of both depended on the cross-link density.

In a 4-day process, Pereira et al. (2013) performed *in vitro* enzymatic degradation in PGS and PGSU with different degrees of urethane cross-linking. The PGS samples were completely degraded in 4 days, while the mass was progressively lost in the PGSU samples due to their cross-link density. The PGSU samples with the highest cross-link densities showed 0% mass loss (no degradation).

Frydrych and Chen (2017) performed *in vitro* degradation tests in PGSU scaffolds, which showed adjustable degradation rates and mass losses of 8.7%–16.3% and 10.7%–20.7% without and with the presence of enzyme, respectively, after 31 days. Enzymatic degradation was faster than hydrolytic degradation.

Singh et al. (2018) performed PGS-M hydrolytic degradation studies after 40 days, in which the implants showed no change in mass (no degradation). Enzymatic degradation results indicated a decrease in the degradation rate of the polymer with an increased degree of methacrylation. The results of enzymatic degradation showed a decreased rate of polymer degradation with an increased degree of methacrylation. At the highest methacrylation cross-linking the degradation rate was null (no degradation).

The information presented thus far in this review showed that the modification of PGS can lead to significantly increased resistance to degradation.

### 3.1.3 *In vivo* degradation

*In vivo* degradation is performed by placing the object to degrade inside an animal (e.g., mice or rats). In *in vivo* trials, the environment is more dynamic, with a more fluid exchange of molecules and removal of any degradation products around the implant. The presence of various enzymes in their natural environment also has a greater impact on degradation, compared to *in vitro* trials (Ifkovits et al., 2008; Pomerantseva et al., 2009). The *in vivo* degradation rate of PGS is much faster than the *in vitro* degradation rate.

Wang et al. (2002) demonstrated the differences between *in vitro* and the *in vivo* PGS degradation. In the 60-day trials, the

measured *in vitro* hydrolytic degradation of PGS resulted in a 17.6% mass loss, while PGS implanted in Sprague-Dawley rats were completely consumed in the same time.

Wang et al. (2003) implanted PGS samples subcutaneously in female Sprague-Dawley rats and evaluated them after 35 days. The PGS implants maintained their geometries throughout the time periods. The implants lost weight gradually and linearly over the test period of 35 days, during which time >70% of their mass.

Another study implanted PGS samples in male Fisher rats, after which the degradation was evaluated for 60 days. After 35 days, the geometry of the PGS implants was the same as that on day 1; however, the volume was almost half that measured initially. The implants gradually decreased in size, consistent with a mechanism of surface erosion. After 60 days, the implants were difficult to detect and no dimensional data were obtained (Sundback et al., 2005).

The PGS was almost completely degraded within 14 days in the arterial circulation of Sprague-Dawley IGS rats (Fu et al., 2020a).

Ding et al. (2017) added tyramine (TA) to PGS and placed the PGS-TA and PGS in male BALB/c mice. After 14 days, both implants had completely degraded *in vivo*.

The rapid degradation of PGS may limit its use in tissues that require long-term mechanical support but may be useful for the controlled release of drugs in short-term treatments.

PGS implants loaded with 5-fluorouracil (5-FU-PGS) placed in Wistar rats maintained their geometries and decreased in bulk throughout the degradation period of 30 days. The mass loss *in vivo* (30%) was much higher than that *in vitro* (10%). The results of the *in vitro* anti-tumor activity assay suggested the anti-tumor activity of 5-FU-PGSs exhibited through sustained drug release. These results showed that PGS is a good candidate for drug delivery systems (Sun et al., 2009).

The rapid hydrolysis of PGS limits its application as a scaffold material in tissue engineering applications, particularly when healing is slow (i.e., from months to years) (Lang et al., 2020).

However, PGS showed good results for guided tissue regeneration. Upon implanting PGS in the rabbit ulnar defect, histology and tomography analysis at 8 weeks showed that gap filling with the new bone, guided by the PGS elastomer (Zaky et al., 2017).

Another way to use PGS for long-term treatment is by mixing it with other components.

PGS combined with chondroitinase ABC (ChABC) promoted spinal cord repair in rats in 12 weeks. The combination of PGS and ChABC resulted in augmented nerve regeneration and partial functional recovery, better than PGS or ChABC independently (Pan et al., 2018). A recent study used PGS scaffolds to restore a wounded rat uterus, which promoted BMSC attachment and growth and increased blood vessel regeneration in 90 days (Xiao et al., 2019).

PGS modification by functionalization of the hydroxyl groups with palmitates (palmitate-PGS) has been successfully

shown to delay degradation (Fu et al., 2020b; Ding et al., 2020). *In vivo* tests with CD<sup>®</sup> (Sprague-Dawley) IGS rats showed that palmitate-PGS degraded over 4–12 weeks compared to only 2 weeks for PGS alone (Fu et al., 2020b).

PGSA samples were implanted in Sprague-Dawley rats. After 4 weeks, the *in vivo* mass loss (25%) was greater than *in vitro* hydrolytic (12%). Past 8 weeks, the *in vivo* mass loss (37%) was nearly the same at the *in vitro* hydrolytic mass loss (33%) (Ifkovits et al., 2008).

## 4 Outlook/Conclusion

PGS is an elastomer-type polymer with great potential in the biomedical field because its biocompatibility and properties can be tailored to biological tissues. PGS is typically produced through the polycondensation of glycerol and sebacic acid. However, its synthesis has also been reported using divinyl sebacate or sebacyl chloride with glycerol. Another alternative method of producing PGS is by ring-opening reaction of diglycidyl sebacate with sebacic acid, which results in a well-defined linear structure known as PSeD.

PGS was mainly produced by the conventional method, which is energy-intensive and time-consuming without the use of solvents or catalysts. One strategy to reduce the reaction time is increasing the temperature to >150°C. However, this option can lead to a significant loss of glycerol and an increased number of branches and/or cross-links in the polymer chain and, thus, a more rigid material.

MwAS reportedly produces pPGS in minutes instead of hours or days and is mainly mixed with other materials. Microwave radiation promotes the growth of undifferentiated polymers, in which the primary and secondary hydroxyl groups have the same reactivity with carboxylic acid groups. This type of pre-PGS is richer in cross-linked structures (triacylglycerides) and requires less time to cure.

The use of catalysts is the least often described approach to potentially reduce reaction time. Enzymes and diarylborinic acids can be used to reduce the reaction time and temperature by promoting linear structures. However, the use of solvents requires polymer separation and purification steps.

Another strategy to reduce the PGS synthesis time is the modification of pPGS with cross-linkers such as isocyanates and acrylates that speed curing. Isocyanates allow fast cross-linking *via* urethane bonds, while acrylate and methacrylate allow fast cross-linking by photopolymerization.

PGS has been frequently combined with other molecules and polymers to produce materials with more desirable properties. Individually, PGS has a high biodegradability *in vivo* that is not suitable for long-term applications. However, its biocompatibility and safety are well proven, which makes PGS a

valid polymer for the development of materials for biomedical applications.

## Author contributions

All authors have made substantial, direct, and intellectual contributions to the work and approved its publication.

## Funding

This work was developed within the scope of the project CICECO-Aveiro Institute of Materials (UIDB/50011/2020, UIDP/50011/2020, and LA/P/0006/2020), financed by national funds through the FCT/MEC (PIDDAC).

## References

- Abazari, M. F., Zare Karizi, S., Samadian, H., Nasiri, N., Askari, H., Asghari, M., et al. (2021). Poly (glycerol sebacate) and polyhydroxybutyrate electrospun nanocomposite facilitates osteogenic differentiation of mesenchymal stem cells. *J. Drug Deliv. Sci. Technol.* 66, 102796. doi:10.1016/j.jddst.2021.102796
- Abudula, T., Gauthaman, K., Hammad, A., Joshi Navare, K., Alshahrie, A., Bencherif, S., et al. (2020). Oxygen-releasing antibacterial nanofibrous scaffolds for tissue engineering applications. *Polym. (Basel)* 12, 1233. doi:10.3390/polym12061233
- Aghajani, M. H., Panahi-Sarmad, M., Alikarami, N., Shojaei, S., Saeidi, A., Khonakdar, H. A., et al. (2020). Using solvent-free approach for preparing innovative biopolymer nanocomposites based on PGS/gelatin. *Eur. Polym. J.* 131, 109720. doi:10.1016/j.eurpolymj.2020.109720
- Allen, N. S., Edge, M., and Hussain, S. (2022). Perspectives on yellowing in the degradation of polymer materials: inter-relationship of structure, mechanisms and modes of stabilisation. *Polym. Degrad. Stab.* 201, 109977. doi:10.1016/j.polymdegradstab.2022.109977
- Angelo, D. F., Wang, Y., Morouco, P., Monje, F., Monico, L., Gonzalez-Garcia, R., et al. (2021). A randomized controlled preclinical trial on 3 interpositional temporomandibular joint disc implants: TEMPOJIMS—phase 2. *J. Tissue Eng. Regen. Med.* 15, 852–868. doi:10.1002/term.3230
- Apsite, I., Constante, G., Dulle, M., Vogt, L., Caspari, A., Boccaccini, A. R., et al. (2020). 4D Biofabrication of fibrous artificial nerve graft for neuron regeneration. *Biofabrication* 12, 035027. doi:10.1088/1758-5090/ab94cf
- Atya, A. M. N., Tevlek, A., Almemar, M., Gökçen, D., and Aydin, H. M. (2021). Fabrication and characterization of carbon aerogel/poly(glycerol-sebacate) patches for cardiac tissue engineering. *Biomed. Mat.* 16, 065027. doi:10.1088/1748-605x/ac2dd3
- Ayati Najafabadi, S. A., Shirazaki, P., Zargar Kharazi, A., Varshosaz, J., Tahriri, M., and Tayebi, L. (2018). Evaluation of sustained ciprofloxacin release of biodegradable electrospun gelatin/poly(glycerol sebacate) mat membranes for wound dressing applications. *Asia. Pac. J. Chem. Eng.* 13, e2255. doi:10.1002/apj.2255
- Aydin, H. M., Salimi, K., Rzaev, Z. M. O., and Pişkin, E. (2013). Microwave-assisted rapid synthesis of poly(glycerol-sebacate) elastomers. *Biomater. Sci.* 1, 503. doi:10.1039/c3bm00157a
- Aydin, H. M., Salimi, K., Yilmaz, M., Turk, M., Rzaev, Z. M. O., and Pişkin, E. (2016). Synthesis and characterization of poly(glycerol-co-sebacate-co-ε-caprolactone) elastomers. *J. Tissue Eng. Regen. Med.* 10, E14–E22. doi:10.1002/term.1759
- Azerêdo, M. S., Nunes, M. A. B. S., Figueiredo, L. R. F., Oliveira, J. E., Tonoli, G. D., de Barros, S., et al. (2022). Environmentally friendly adhesives derived from glycerol-based polymers. *J. Adhes. Sci. Technol.* 36, 98–108. doi:10.1080/01694243.2021.1915619
- Behtaj, S., Karamali, F., Masaeli, E., Anissimov, G. Y., and Rybachuk, M. (2021). Electrospun PGS/PCL, PLLA/PCL, PLGA/PCL and pure PCL scaffolds for retinal progenitor cell cultivation. *Biochem. Eng. J.* 166, 107846. doi:10.1016/j.bej.2020.107846
- Behtaj, S., Karamali, F., Najafian, S., Masaeli, E., Esfahani, M. H. N., and Rybachuk, M. (2021). The role of PGS/PCL scaffolds in promoting differentiation of human embryonic stem cells into retinal ganglion cells. *Acta Biomater.* 126, 238–248. doi:10.1016/j.actbio.2021.03.036
- Behtouei, E., Zandi, M., Askari, F., Daemi, H., Zamanlui, S., Arabsorkhi-Mishabi, A., et al. (2022). Bead-free and tough electrospun PCL/gelatin/PGS ternary nanofibrous scaffolds for tissue engineering application. *J. Appl. Polym. Sci.* 139, 51471. doi:10.1002/app.51471
- Bellani, C. F., Yue, K., Flaig, F., Hebraud, A., Ray, P., Annabi, N., et al. (2021). Sutureless elastomeric tubular grafts with patterned porosity for rapid vascularization of 3D constructs. *Biofabrication* 13, 035020. doi:10.1088/1758-5090/abdf1d
- Cai, W., and Liu, L. (2007). Shape-memory effect of poly (glycerol-sebacate) elastomer. *Mat. Lett.* 62, 2171–2173. doi:10.1016/j.matlet.2007.11.042
- Chang, C., and Yeh, Y. (2021). Poly(glycerol sebacate) co-poly(ethylene glycol)/gelatin hybrid hydrogels as biocompatible biomaterials for cell proliferation and Spreading. *Macromol. Biosci.* 21, 2100248. doi:10.1002/mabi.202100248
- Chang, P.-Y., Wang, J., Li, S.-Y., and Suen, S.-Y. (2021). Biodegradable polymeric membranes for organic solvent/water pervaporation applications. *Membr. (Basel)* 11, 970. doi:10.3390/membranes11120970
- Chen, J.-Y., Hwang, J., Ao-leong, W. S., Lin, Y. C., Hsieh, Y. K., Cheng, Y. L., et al. (2018). Study of physical and degradation properties of 3D-printed biodegradable, photocurable copolymers, PGSA-co-PEGDA and PGSA-co-PCLDA. *Polym. (Basel)* 10, 1263. doi:10.3390/polym10111263
- Chen, Q.-Z., Bismarck, A., Hansen, U., Junaid, S., Tran, M. Q., Harding, S. E., et al. (2007). Characterisation of a soft elastomer poly(glycerol sebacate) designed to match the mechanical properties of myocardial tissue. *Biomaterials* 29, 47–57. doi:10.1016/j.biomaterials.2007.09.010
- Chen, Q., Jin, L., Cook, W. D., Mohn, D., Lagerqvist, E. L., Elliott, D. A., et al. (2010). Elastomeric nanocomposites as cell delivery vehicles and cardiac support devices. *Soft Matter* 6, 4715. doi:10.1039/c0sm00213e
- Chen, Q., Liang, S., and Thouas, G. A. (2011). Synthesis and characterisation of poly(glycerol sebacate)-co-lactic acid as surgical sealants. *Soft Matter* 7, 6484. doi:10.1039/c1sm05350g
- Chen, S., Bi, X., Sun, L., Gao, J., Huang, P., Fan, X., et al. (2016). Poly(sebacoyl diglyceride) cross-linked by dynamic hydrogen bonds: A self-healing and functionalizable thermoplastic Bioelastomer. *ACS Appl. Mat. Interfaces* 8, 20591–20599. doi:10.1021/acsami.6b05873
- Chen, S., Huang, T., Zuo, H., Qian, S., Guo, Y., Sun, L., et al. (2018). Wearable electronics: A single integrated 3D-printing process Customizes elastic and sustainable Triboelectric Nanogenerators for Wearable electronics (Adv. Funct. Mater. 46/2018). *Adv. Funct. Mat.* 28, 1870331. doi:10.1002/adfm.201870331

## Conflict of interest

The authors declare that the research was conducted in the absence of any commercial or financial relationships that could be construed as a potential conflict of interest.

## Publisher's note

All claims expressed in this article are solely those of the authors and do not necessarily represent those of their affiliated organizations, or those of the publisher, the editors, and the reviewers. Any product that may be evaluated in this article, or claim that may be made by its manufacturer, is not guaranteed or endorsed by the publisher.

- Chen, W., Xiao, W., Liu, X., Yuan, P., Zhang, S., Wang, Y., et al. (2022). Pharmacological manipulation of macrophage autophagy effectively rejuvenates the regenerative potential of biodegrading vascular graft in aging body. *Bioact. Mat.* 11, 283–299. doi:10.1016/j.bioactmat.2021.09.027
- Choi, I., and Yoon, K. (2010). *Process of preparing A biodegradable polymer using an enzyme catalyst and A biodegradable polymer prepared through the process.* US7642075B2. United States.
- Choi, S. M., Lee, Y., Son, J. Y., Bae, J. W., Park, K. M., and Park, K. D. (2017). Synthesis and characterization of *in situ* gellable poly(glycerol sebacate)-co-poly(ethylene glycol) polymers. *Macromol. Res.* 25, 85–91. doi:10.1007/s13233-017-5007-y
- Coativy, G., Misra, M., and Mohanty, A. K. (2016). Microwave synthesis and Melt blending of glycerol based toughening agent with poly(lactic acid). *ACS Sustain. Chem. Eng.* 4, 2142–2149. doi:10.1021/acssuschemeng.5b01596
- Coativy, G., Misra, M., and Mohanty, A. K. (2017). Synthesis of shape memory poly(glycerol sebacate)-Stearate polymer. *Macromol. Mat. Eng.* 302, 1600294–1600296. doi:10.1002/mame.201600294
- Conejero-García, Á., Gimeno, H. R., Saez, Y. M., Vilarino-Feltré, G., Ortuno-Lizaran, I., and Valles-Lluch, A. (2017). Correlating synthesis parameters with physicochemical properties of poly(glycerol sebacate). *Eur. Polym. J.* 87, 406–419. doi:10.1016/j.eurpolymj.2017.01.001
- Davoodi, B., Goodarzi, V., Hosseini, H., Tigrar, M., Shojaei, S., Asefnejad, A., et al. (2022). Design and manufacturing a tubular structures based on poly( $\epsilon$ -caprolactone)/poly(glycerol-sebacic acid) biodegradable nanocomposite blends: Suggested for applications in the nervous, vascular and renal tissue engineering. *J. Polym. Res.* 29, 54. doi:10.1007/s10965-021-02881-8
- Deniz, P., Guler, S., Çelik, E., Hosseini, P., and Aydin, H. M. (2020). Use of cyclic strain bioreactor for the upregulation of key tenocyte gene expression on Poly(glycerol-sebacate) (PGS) sheets. *Mater. Sci. Eng. C* 106, 110293. doi:10.1016/j.msec.2019.110293
- Desai, P., Venkataramanan, A., Schneider, R., Jaiswal, M. K., Carrow, J. K., Purwada, A., et al. (2018). Self-assembled, ellipsoidal polymeric nanoparticles for intracellular delivery of therapeutics. *J. Biomed. Mat. Res. A* 106, 2048–2058. doi:10.1002/jbm.a.36400
- Ding, X., Chen, Y., Chao, C. A., Wu, Y., and Wang, Y. (2020). Control the mechanical properties and degradation of poly(glycerol sebacate) by substitution of the hydroxyl groups with palmitates. *Macromol. Biosci.* 20, 2000101. doi:10.1002/mabi.202000101
- Ding, X., Wu, Y. L., Gao, J., Wells, A., Lee, K. W., and Wang, Y. (2017). Tyramine functionalization of poly(glycerol sebacate) increases the elasticity of the polymer. *J. Mat. Chem. B* 5, 6097–6109. doi:10.1039/c7tb01078h
- Fakhari, Z., Nouri Khorasani, S., Alihosseini, F., Nasr Esfahani, M. H., Karamali, F., and Khalili, S. (2021). Core-shell nanofibers of poly (glycerol sebacate) and poly (1, 8 octanediol citrate) for retinal regeneration. *Polym. Bull.* 79, 7161–7176. doi:10.1007/s00289-021-03850-3
- Fakhrali, A., Nasari, M., Poursharifi, N., Semnani, D., Salehi, H., Ghane, M., et al. (2021). Biocompatible graphene-embedded PCL/PGS-based nanofibrous scaffolds: A potential application for cardiac tissue regeneration. *J. Appl. Polym. Sci.* 138, 51177. doi:10.1002/app.51177
- Fakhrali, A., Semnani, D., Salehi, H., and Ghane, M. (2022). Electro-conductive nanofibrous structure based on PGS/PCL coated with PPy by *in situ* chemical polymerization applicable as cardiac patch: Fabrication and optimization. *J. Appl. Polym. Sci.* 139, 52136. doi:10.1002/app.52136
- Fakhrali, A., Semnani, D., Salehi, H., and Ghane, M. (2020). Electrospun PGS/PCL nanofibers: From straight to sponge and spring-like morphology. *Polym. Adv. Technol.* 31, 3134–3149. doi:10.1002/pat.5038
- Farr, N., Pashneh-Tala, S., Stehling, N., Claeysens, F., Green, N., and Rodenburg, C. (2020). Characterizing cross-linking within polymeric biomaterials in the SEM by secondary Electron Hyperspectral imaging. *Macromol. Rapid Commun.* 41, 2070006. doi:10.1002/marc.202070006
- Flaig, F., Bellani, C. F., Uyumaz, Ö., Schlatter, G., and Hébraud, A. (2021). Elaboration and mechanical properties of elastomeric fibrous scaffolds based on crosslinked poly(glycerol sebacate) and cyclodextrin for soft tissue engineering. *Mat. Adv.* 2, 1284–1293. doi:10.1039/d0ma00673d
- Flaig, F., Ragot, H., Simon, A., Revet, G., Kitsara, M., Kitasato, L., et al. (2020). Design of functional electrospun scaffolds based on poly(glycerol sebacate) elastomer and poly(lactic acid) for cardiac tissue engineering. *ACS Biomater. Sci. Eng.* 6, 2388–2400. doi:10.1021/acsbomaterials.0c00243
- Frydrych, M., and Chen, B. (2017). Fabrication, structure and properties of three-dimensional biodegradable poly(glycerol sebacate urethane) scaffolds. *Polymer* 122, 159–168. doi:10.1016/j.polymer.2017.06.064
- Frydrych, M., Román, S., Green, N. H., MacNeil, S., and Chen, B. (2015). Thermoresponsive, stretchable, biodegradable and biocompatible poly(glycerol sebacate)-based polyurethane hydrogels. *Polym. Chem.* 6, 7974–7987. doi:10.1039/c5py01136a
- Frydrych, M., Román, S., MacNeil, S., and Chen, B. (2015). Biomimetic poly(glycerol sebacate)/poly(L-lactic acid) blend scaffolds for adipose tissue engineering. *Acta Biomater.* 18, 40–49. doi:10.1016/j.actbio.2015.03.004
- Fu, J., Ding, X., Stowell, C. E. T., Wu, Y.-L., and Wang, Y. (2020). Slow degrading poly(glycerol sebacate) derivatives improve vascular graft remodeling in a rat carotid artery interposition model. *Biomaterials* 257, 120251. doi:10.1016/j.biomaterials.2020.120251
- Fu, J., Wang, M., De Vlaminc, I., and Wang, Y. (2020). Thick PCL fibers improving host remodeling of PGS-PCL composite grafts implanted in rat common carotid arteries. *Small* 16, 2004133. doi:10.1002/smll.202004133
- Fukunishi, T., Lui, C., Ong, C. S., Dunn, T., Xu, S., Smoot, C., et al. (2022). Extruded poly (glycerol sebacate) and polyglycolic acid vascular graft forms a neoartery. *J. Tissue Eng. Regen. Med.* 16, 346–354. doi:10.1002/term.3282
- Gadomska-Gajadur, A., Wrzecieć, M., Matyszczyk, G., Pietowski, P., Wicław, M., and Ruskowski, P. (2018). Optimization of poly(glycerol sebacate) synthesis for biomedical purposes with the design of experiments. *Org. Process Res. Dev.* 22, 1793–1800. doi:10.1021/acs.oprd.8b00306
- Gaharwar, A. K., Patel, A., Dolatshahi-Pirouz, A., Zhang, H., Rangarajan, K., Iviglia, G., et al. (2015). Elastomeric nanocomposite scaffolds made from poly(glycerol sebacate) chemically crosslinked with carbon nanotubes. *Biomater. Sci.* 3, 46–58. doi:10.1039/c4bm00222a
- Gao, J., Crapo, P. M., and Wang, Y. (2006). Macroporous elastomeric scaffolds with extensive micropores for soft tissue engineering. *Tissue Eng.* 12, 917–925. doi:10.1089/ten.2006.12.917
- Gao, J., Ensley, A. E., Nerem, R. M., and Wang, Y. (2007). Poly(glycerol sebacate) supports the proliferation and phenotypic protein expression of primary baboon vascular cells. *J. Biomed. Mat. Res. A* 83A, 1070–1075. doi:10.1002/jbm.a.31434
- Ghafarzadeh, M., Kharaziha, M., and Atapour, M. (2021). Bilayer micro-arc oxidation-poly (glycerol sebacate) coating on AZ91 for improved corrosion resistance and biological activity. *Prog. Org. Coat.* 161, 106495. doi:10.1016/j.porgcoat.2021.106495
- Godinho, B., Gama, N., Barros-Timmons, A., and Ferreira, A. (2018). “Enzymatic synthesis of poly(glycerol sebacate) pre-polymer with crude glycerol, by-product from biodiesel production,” in AIP Conference Proceedings, Ischia, Italy, July 2018 (AIP Publishing LLC), 020031.
- Golbaten-Mofrad, H., Seyfi Sahzabi, A., Seyfekar, S., Salehi, M. H., Goodarzi, V., Wurm, F. R., et al. (2021). Facile template preparation of novel electroactive scaffold composed of polypyrrole-coated poly(glycerol-sebacate-urethane) for tissue engineering applications. *Eur. Polym. J.* 159, 110749. doi:10.1016/j.eurpolymj.2021.110749
- Gorgani, S., Zargar Kharazi, A., Haghighi Javanmard, S., and Rafiinia, M. (2020). Improvement of endothelial cell performance in an optimized electrospun pre-polyglycerol sebacate-poly lactic acid scaffold for Reconstruction of Intima in Coronary arteries. *J. Polym. Environ.* 28, 2352–2363. doi:10.1007/s10924-020-01749-0
- Gultekinoglu, M., Öztürk, Ş., Chen, B., Edirisinghe, M., and Ulubayram, K. (2019). Preparation of poly(glycerol sebacate) fibers for tissue engineering applications. *Eur. Polym. J.* 121, 109297. doi:10.1016/j.eurpolymj.2019.109297
- Guo, X.-L., Lu, X.-L., Dong, D.-L., and Sun, Z.-J. (2014). Characterization and optimization of glycerol/sebacate ratio in poly(glycerol-sebacate) elastomer for cell culture application. *J. Biomed. Mat. Res. A* 102, 3903–3907. doi:10.1002/jbm.a.35066
- Halil Murat, A. (2017). Poly(Glycerol-Sebacate) elastomer: A Mini review. *Orthoplastic Surg. Orthop. Care Int. J.* 1. doi:10.31031/oij.2017.01.000507
- Hanif, A., Ghosh, G., Meeseepong, M., Haq Choudhry, H., Bag, A., Chinnamani, M., et al. (2021). A composite microfiber for biodegradable stretchable electronics. *Micromachines* 12, 1036. doi:10.3390/mi12091036
- Heydari, P., Zargar Kharazi, A., Asgari, S., and Parham, S. (2022). Comparing the wound healing effect of a controlled release wound dressing containing curcumin/ciprofloxacin and simvastatin/ciprofloxacin in a rat model: A preclinical study. *J. Biomed. Mat. Res. A* 110, 341–352. doi:10.1002/jbm.a.37292
- Hou, L., Zhang, X., Mikael, P. E., Lin, L., Dong, W., Zheng, Y., et al. (2017). Biodegradable and Bioactive PCL-PGS core-shell fibers for tissue engineering. *ACS Omega* 2, 6321–6328. doi:10.1021/acsomega.7b00460
- Hsu, C.-N., Lee, P.-Y., Tuan-Mu, H.-Y., Li, C.-Y., and Hu, J.-J. (2018). Fabrication of a mechanically anisotropic poly(glycerol sebacate) membrane for tissue engineering. *J. Biomed. Mat. Res.* 106, 760–770. doi:10.1002/jbm.b.33876
- Hu, J., Kai, D., Ye, H., Tian, L., Ding, X., Ramakrishna, S., et al. (2017). Electrospinning of poly(glycerol sebacate)-based nanofibers for nerve tissue engineering. *Mater. Sci. Eng. C* 70, 1089–1094. doi:10.1016/j.msec.2016.03.035



- Hu, T., Wu, Y., Zhao, X., Wang, L., Bi, L., Ma, P. X., et al. (2019). Micropatterned, electroactive, and biodegradable poly(glycerol sebacate)-aniline trimer elastomer for cardiac tissue engineering. *Chem. Eng. J.* 366, 208–222. doi:10.1016/j.cej.2019.02.072
- Ifkovits, J. L., Padera, R. F., and Burdick, J. A. (2008). Biodegradable and radically polymerized elastomers with enhanced processing capabilities. *Biomed. Mat.* 3, 034104. doi:10.1088/1748-6041/3/3/034104
- Jaafar, I. H., Ammar, M. M., Jedlicka, S. S., Pearson, R. A., and Coulter, J. P. (2010). Spectroscopic evaluation, thermal, and thermomechanical characterization of poly(glycerol-sebacate) with variations in curing temperatures and durations. *J. Mat. Sci.* 45, 2525–2529. doi:10.1007/s10853-010-4259-0
- Jafari, Fatemeh, Khorasani, S. N., Alihosseini, F., Semnani, D., Khalili, S., and Neisiany, R. E. (2020). Development of an electrospun scaffold for retinal tissue engineering. *Polym. Sci. Ser. B* 62, 290–298. doi:10.1134/s156090420030069
- Jeffries, E. M., Allen, R. a., Gao, J., Pesce, M., and Wang, Y. (2015). Highly elastic and suturable electrospun poly(glycerol sebacate) fibrous scaffolds. *Acta Biomater.* 18, 30–39. doi:10.1016/j.actbio.2015.02.005
- Jeong, C. G., and Hollister, S. J. (2010). A comparison of the influence of material on *in vitro* cartilage tissue engineering with PCL, PGS, and POC 3D scaffold architecture seeded with chondrocytes. *Biomaterials* 31, 4304–4312. doi:10.1016/j.biomaterials.2010.01.145
- Jia, Y., Wang, W., Zhou, X., Nie, W., and Chen, L. (2016). Synthesis and characterization of poly(glycerol sebacate)-based elastomeric copolymers for tissue engineering applications. *Polym. Chem.* 7, 2553–2564. doi:10.1039/c5py01993a
- Jiang, L., Jiang, Y., Stiadle, J., Wang, X., Wang, L., Li, Q., et al. (2019). Electrospun nanofibrous thermoplastic polyurethane/poly(glycerol sebacate) hybrid scaffolds for vocal fold tissue engineering applications. *Mater. Sci. Eng. C* 94, 740–749. doi:10.1016/j.msec.2018.10.027
- Jiang, W., Zhang, C., Tran, L., Wang, S. G., Hakim, A. D., and Liu, H. (2020). Engineering Nano-to-Micron-patterned polymer coatings on bioresorbable Magnesium for controlling human endothelial cell adhesion and morphology. *ACS Biomater. Sci. Eng.* 6, 3878–3898. doi:10.1021/acsbiomaterials.0c00642
- Kafouris, D., Kossivas, F., Constantinides, C., Nguyen, N. Q., Wesdemiotis, C., and Patrickios, C. S. (2013). Biosourced amphiphilic degradable elastomers of poly(glycerol sebacate): Synthesis and network and oligomer characterization. *Macromolecules* 46, 622–630. doi:10.1021/ma3016882
- Kaya, M., Ahi, Z. B., Ergene, E., Yilgor Huri, P., and Tuzlakoglu, K. (2020). Design of a new dual mesh with an absorbable nanofiber layer as a potential implant for abdominal hernia treatment. *J. Tissue Eng. Regen. Med.* 14, 347–354. doi:10.1002/term.3000
- Kazemzadeh Farizhandi, A. A., Khalajabadi, S. Z., Krishnadoss, V., and Noshadi, I. (2020). Synthesized biocompatible and conductive ink for 3D printing of flexible electronics. *J. Mech. Behav. Biomed. Mat.* 110, 103960. doi:10.1016/j.jmbbm.2020.103960
- Keirouz, A., Zakharova, M., Kwon, J., Robert, C., Koutsos, V., Callanan, A., et al. (2020). High-throughput production of silk fibroin-based electrospun fibers as biomaterial for skin tissue engineering applications. *Mater. Sci. Eng. C* 112, 110939. doi:10.1016/j.msec.2020.110939
- Kemppainen, J. M., and Hollister, S. J. (2010). Tailoring the mechanical properties of 3D-designed poly(glycerol sebacate) scaffolds for cartilage applications. *J. Biomed. Mat. Res. A* 94A, 9–18. doi:10.1002/jbm.a.32653
- Khosravi, R., Best, C. A., Allen, R. A., Stowell, C. E. T., Onwuka, E., Zhuang, J. J., et al. (2016). Long-term functional Efficacy of a novel electrospun poly(glycerol sebacate)-based arterial graft in mice. *Ann. Biomed. Eng.* 44, 2402–2416. doi:10.1007/s10439-015-1545-7
- Kim, M. J., Hwang, M. Y., Kim, J., and Chung, D. J. (2014). Biodegradable and elastomeric poly(glycerol sebacate) as a coating material for nitinol bare stent. *Biomed. Res. Int.* 2014, 1–7. doi:10.1155/2014/956952
- Kobayashi, S. (2010). Lipase-catalyzed polyester synthesis-a green polymer chemistry. *Proc. Jpn. Acad. Ser. B. Phys. Biol. Sci.* 86, 338–365. doi:10.2183/pjab.86.338
- Kossivas, F., Angeli, S., Kafouris, D., Patrickios, C. S., Tzagarakis, V., and Constantinides, C. (2012). MRI-based morphological modeling, synthesis and characterization of cardiac tissue-mimicking materials. *Biomed. Mat.* 7, 035006. doi:10.1088/1748-6041/7/3/035006
- Krook, N. M., Jaafar, I. H., Sarkhosh, T., LeBlon, C., Coulter, J. P., and Jedlicka, S. S. (2020). *In vitro* examination of poly(glycerol sebacate) degradation kinetics: Effects of porosity and cure temperature. *Int. J. Polym. Mater. Polym. Biomaterials* 69, 535–543. doi:10.1080/00914037.2019.1596907
- Lang, K., Bhattacharya, S., Ning, Z., Sanchez-Leija, R. J., Bramson, M. T. K., Centore, R., et al. (2020). Enzymatic polymerization of poly(glycerol-1, 8-octanediol-sebacate): Versatile poly(glycerol sebacate) Analogues that form Monocomponent biodegradable fiber scaffolds. *Biomacromolecules* 21, 3197–3206. doi:10.1021/acs.biomac.0c00641
- Lau, C. C., Al Qaysi, M., Owji, N., Bayazit, M., Xie, J., Knowles, J., et al. (2020). Advanced biocomposites of poly(glycerol sebacate) and  $\beta$ -tricalcium phosphate by *in situ* microwave synthesis for bioapplication. *Mat. Today Adv.* 5, 100023. doi:10.1016/j.mtadv.2019.100023
- Lau, C. C., Bayazit, M. K., Knowles, J. C., and Tang, J. (2017). Tailoring degree of esterification and branching of poly(glycerol sebacate) by energy efficient microwave irradiation. *Polym. Chem.* 8, 3937–3947. doi:10.1039/c7py00862g
- Lee, S. H., Lee, K.-W., Gade, P. S., Robertson, A. M., and Wang, Y. (2018). Microwave-assisted facile fabrication of porous poly (glycerol sebacate) scaffolds. *J. Biomaterials Sci. Polym. Ed.* 29, 907–916. doi:10.1080/09205063.2017.1335076
- Li, X., Hong, A. T.-L., Naskar, N., and Chung, H.-J. (2015). Criteria for quick and consistent synthesis of poly(glycerol sebacate) for tailored mechanical properties. *Biomacromolecules* 16, 1525–1533. doi:10.1021/acs.biomac.5b00018
- Li, Y., Cook, W. D., Moorhoff, C., Huang, W.-C., and Chen, Q.-Z. (2013). Synthesis, characterization and properties of biocompatible poly(glycerol sebacate) pre-polymer and gel. *Polym. Int.* 62, 534–547. doi:10.1002/pi.4419
- Li, Y., Huang, W., Cook, W. D., and Chen, Q. (2013). A comparative study on poly(xylitol sebacate) and poly(glycerol sebacate): Mechanical properties, biodegradation and cytocompatibility. *Biomed. Mat.* 8, 035006. doi:10.1088/1748-6041/8/3/035006
- Liang, B., Shi, Q., Xu, J., Chai, Y.-M., and Xu, J.-G. (2020). Poly (glycerol sebacate)-based bio-artificial Multiporous matrix for bone regeneration. *Front. Chem.* 8, 603577. doi:10.3389/fchem.2020.603577
- Liang, S., Cook, W. D., and Chen, Q. (2011). Physical characterization of poly(glycerol sebacate)/Bioglass<sup>®</sup> composites. *Polym. Int.* 61, 17–22. doi:10.1002/pi.3165
- Lin, D., Yang, K., Tang, W., Liu, Y., Yuan, Y., and Liu, C. (2015). A poly(glycerol sebacate)-coated mesoporous bioactive glass scaffold with adjustable mechanical strength, degradation rate, controlled-release and cell behavior for bone tissue engineering. *Colloids Surfaces B Biointerfaces* 131, 1–11. doi:10.1016/j.colsurfb.2015.04.031
- Liu, Q., Tian, M., Ding, T., Shi, R., Feng, Y., Zhang, L., et al. (2007). Preparation and characterization of a thermoplastic poly(glycerol sebacate) elastomer by two-step method. *J. Appl. Polym. Sci.* 103, 1412–1419. doi:10.1002/app.24394
- Liu, Q., Tian, M., Shi, R., Zhang, L., Chen, D., and Tian, W. (2007). Structure and properties of thermoplastic poly(glycerol sebacate) elastomers originating from prepolymers with different molecular weights. *J. Appl. Polym. Sci.* 104, 1131–1137. doi:10.1002/app.25606
- Liu, Q., Wu, J., Tan, T., Zhang, L., Chen, D., and Tian, W. (2009). Preparation, properties and cytotoxicity evaluation of a biodegradable polyester elastomer composite. *Polym. Degrad. Stab.* 94, 1427–1435. doi:10.1016/j.polymdegradstab.2009.05.023
- Liu, X., Chen, W., Shao, B., Zhang, X., Wang, Y., Zhang, S., et al. (2021). Mussel patterned with 4D biodegrading elastomer durably recruits regenerative macrophages to promote regeneration of craniofacial bone. *Biomaterials* 276, 120998. doi:10.1016/j.biomaterials.2021.120998
- Loh, X. J., Abdul Karim, A., and Owh, C. (2015). Poly(glycerol sebacate) biomaterial: Synthesis and biomedical applications. *J. Mat. Chem. B* 3, 7641–7652. doi:10.1039/c5tb01048a
- Luginina, M., Schuhladen, K., Orru, R., Cao, G., Boccaccini, A. R., and Liverani, L. (2020). Electrospun PCL/PGS composite fibers incorporating bioactive glass Particles for soft tissue engineering applications. *Nanomaterials* 10, 978. doi:10.3390/nano10050978
- Ma, Y., Zhang, W., Wang, Z., Wang, Z., Xie, Q., Niu, H., et al. (2016). PEGylated poly(glycerol sebacate)-modified calcium phosphate scaffolds with desirable mechanical behavior and enhanced osteogenic capacity. *Acta Biomater.* 44, 110–124. doi:10.1016/j.actbio.2016.08.023
- Mahdavi, A., Ferreira, L., Sundback, C., Nichol, J. W., Chan, E. P., Carter, D. J. D., et al. (2008). A biodegradable and biocompatible gecko-inspired tissue adhesive. *Proc. Natl. Acad. Sci. U. S. A.* 105, 2307–2312. doi:10.1073/pnas.0712117105
- Maliger, R., Halley, P. J., and Cooper-White, J. J. (2013). Poly(glycerol-sebacate) bioelastomers-kinetics of step-growth reactions using Fourier Transform (FT)-Raman spectroscopy. *J. Appl. Polym. Sci.* 127, 3980–3986. doi:10.1002/app.37719
- Martín-Cabezuelo, R., Rodríguez-Hernández, J. C., Vilarinho-Feltrre, G., and Vallés-Lluch, A. (2021). Role of curing temperature of poly(glycerol sebacate) Substrates on protein-cell interaction and early cell adhesion. *Polym. (Basel)* 13, 382. doi:10.3390/polym13030382

- Martín-Cabezuelo, R., Vilarinho-Feltrer, G., and Vallés-Lluch, A. (2021). Influence of pre-polymerisation atmosphere on the properties of pre- and poly(glycerol sebacate). *Mater. Sci. Eng. C* 119, 111429. doi:10.1016/j.msec.2020.111429
- Martín-Pat, G. E., Rodríguez-Fuentes, N., Cervantes-Uc, J. M., Rosales-Ibanez, R., Carrillo-Escalante, H. J., Ku-Gonzalez, A. F., et al. (2020). Effect of different exposure times on physicochemical, mechanical and biological properties of PGS scaffolds treated with plasma of iodine-doped polypyrrole. *J. Biomater. Appl.* 35, 485–499. doi:10.1177/0885328220941466
- Masoumi, N., Jean, A., Zugates, J. T., Johnson, K. L., and Engelmayr, G. C. (2013). Laser microfabricated poly(glycerol sebacate) scaffolds for heart valve tissue engineering. *J. Biomed. Mat. Res. A* 101A, 104–114. doi:10.1002/jbm.a.34305
- Matyszczyk, G., Wrzecionek, M., Gadowska-Gajadur, A., and Ruśkowski, P. (2020). Kinetics of polycondensation of sebacic acid with glycerol. *Org. Process Res. Dev.* 24, 1104–1111. doi:10.1021/acs.oprd.0c00110
- McKee, C. T., Last, J. A., Russell, P., and Murphy, C. J. (2011). Indentation versus tensile measurements of Young's modulus for soft biological tissues. *Tissue Eng. Part B Rev.* 17, 155–164. doi:10.1089/ten.teb.2010.0520
- Mehta, M., Zhao, C., Liu, A., Innocent, C., and Kohane, D. S. (2022). Prolonged Retrobulbar local Anesthesia of the cornea does not cause Keratopathy in mice. *Transl. Vis. Sci. Technol.* 11, 33. doi:10.1167/tvst.11.1.33
- Mitsak, A. G., Dunn, A. M., and Hollister, S. J. (2012). Mechanical characterization and non-linear elastic modeling of poly(glycerol sebacate) for soft tissue engineering. *J. Mech. Behav. Biomed. Mat.* 11, 3–15. doi:10.1016/j.jmbm.2011.11.003
- Mokhtari, N., and Zargar Kharazi, A. (2021). Blood compatibility and cell response improvement of poly glycerol sebacate/poly lactic acid scaffold for vascular graft applications. *J. Biomed. Mat. Res. A* 109, 2673–2684. doi:10.1002/jbm.a.37259
- Monem, M., Ahmadi, Z., Fakhri, V., and Goodarzi, V. (2022). Preparing and characterization of poly(glycerol-sebacic acid-urethane) (PGSU) nanocomposites: Clearing role of unmodified and modified clay nanoparticles. *J. Polym. Res.* 29, 25. doi:10.1007/s10965-021-02866-7
- Moorhoff, C., Li, Y., Cook, W. D., Braybrook, C., and Chen, Q.-Z. (2015). Characterization of the prepolymer and gel of biocompatible poly(xylitol sebacate) in comparison with poly(glycerol sebacate) using a combination of mass spectrometry and nuclear magnetic resonance. *Polym. Int.* 64, 668–688. doi:10.1002/pi.4831
- Nadim, A., Khorasani, S. N., Kharaziha, M., and Davoodi, S. M. (2017). Design and characterization of dexamethasone-loaded poly (glycerol sebacate)-poly caprolactone/gelatin scaffold by coaxial electro spinning for soft tissue engineering. *Mater. Sci. Eng. C* 78, 47–58. doi:10.1016/j.msec.2017.04.047
- Nagata, M., Kiyotsukuri, T., Ibuki, H., Tsutsumi, N., and Sakai, W. (1996). Synthesis and enzymatic degradation of regular network aliphatic polyesters. *React. Funct. Polym.* 30, 165–171. doi:10.1016/1381-5148(95)00107-7
- Nagata, M., Machida, T., Sakai, W., and Tsutsumi, N. (1999). Synthesis, characterization, and enzymatic degradation of network aliphatic copolyesters. *J. Polym. Sci. A. Polym. Chem.* 37, 2005–2011. doi:10.1002/(sici)1099-0518(19990701)37:13<2005:aid-pola14>3.0.co;2-h
- Nijst, C. L. E., Bruggeman, J. P., Karp, J. M., Ferreira, L., Zumbuehl, A., Bettinger, C. J., et al. (2007). Synthesis and characterization of photocurable elastomers from poly(glycerol-co-sebacate). *Biomacromolecules* 8, 3067–3073. doi:10.1021/bm070423u
- Ning, Z., Lang, K., Xia, K., Linhardt, R. J., and Gross, R. A. (2022). Lipase-catalyzed synthesis and characterization of poly(glycerol sebacate). *Biomacromolecules* 23, 398–408. doi:10.1021/acs.biomac.1c01351
- Oklu, R., Rezaei Nejad, H., Chen, A. Z., Ju, J., Tamayol, A., Liu, X., et al. (2018). Fracture-resistant and bioresorbable drug-Eluting poly(glycerol sebacate) coils. *Adv. Ther. (Weinh.)* 2 (3), 1800109. doi:10.1002/adtp.201800109
- Pan, Q., Guo, Y., and Kong, F. (2018). Poly(glycerol sebacate) combined with chondroitinase ABC promotes spinal cord repair in rats. *J. Biomed. Mat. Res.* 106, 1770–1777. doi:10.1002/jbm.b.33984
- Pashneh-Tala, S., Moorehead, R., and Claeysens, F. (2020). Hybrid manufacturing strategies for tissue engineering scaffolds using methacrylate functionalised poly(glycerol sebacate). *J. Biomater. Appl.* 34, 1114–1130. doi:10.1177/0885328219898385
- Pashneh-Tala, S., Owen, R., Bahmaee, H., Rekstyte, S., Malinauskas, M., and Claeysens, F. (2018). Synthesis, characterization and 3D micro-structuring via 2-photon polymerization of poly(glycerol sebacate)-methacrylate-an elastomeric degradable polymer. *Front. Phys.* 6, 41. doi:10.3389/fphy.2018.00041
- Patel, A., Gaharwar, A. K., Ivgilia, G., Zhang, H., Mukundan, S., Mihaila, S. M., et al. (2013). Highly elastomeric poly(glycerol sebacate)-co-poly(ethylene glycol) amphiphilic block copolymers. *Biomaterials* 34, 3970–3983. doi:10.1016/j.biomaterials.2013.01.045
- Pereira, M. J. N., Ouyang, B., Sundback, C. A., Lang, N., Friehs, I., Mureli, S., et al. (2013). A highly tunable biocompatible and multifunctional biodegradable elastomer. *Adv. Mat.* 25, 1209–1215. doi:10.1002/adma.201203824
- Perin, G. B., and Felisberti, M. I. (2020). Enzymatic synthesis of poly(glycerol sebacate): Kinetics, chain growth, and branching behavior. *Macromolecules* 53, 7925–7935. doi:10.1021/acs.macromol.0c01709
- Piszko, P., Kryszak, B., Piszko, A., and Szustakiewicz, K. (2021). Brief review on poly(glycerol sebacate) as an emerging polyester in biomedical application: Structure, properties and modifications. *Polim. Med.* 51, 43–50. doi:10.17219/pim/139585
- Piszko, P., Włodarczyk, M., Zielinska, S., Gazinska, M., Płocinski, P., Rudnicka, K., et al. (2021). PGS/HAP Microporous composite scaffold obtained in the TIPS-TCL-SL method: An Innovation for bone tissue engineering. *Int. J. Mol. Sci.* 22, 8587. doi:10.3390/ijms22168587
- Pomerantseva, I., Krebs, N., Hart, A., Neville, C. M., Huang, A. Y., and Sundback, C. A. (2009). Degradation behavior of poly(glycerol sebacate). *J. Biomed. Mat. Res. A* 91A, 1038–1047. doi:10.1002/jbm.a.32327
- Quispe, C. a. G., Coronado, C. J. R., and Carvalho, J. (2013). a. Glycerol: Production, consumption, prices, characterization and new trends in combustion. *Renew. Sustain. Energy Rev.* 27, 475–493.
- Rai, R., Tallawi, M., Barbani, N., Frati, C., Madeddu, D., Cavalli, S., et al. (2013). Biomimetic poly(glycerol sebacate) (PGS) membranes for cardiac patch application. *Mater. Sci. Eng. C* 33, 3677–3687. doi:10.1016/j.msec.2013.04.058
- Rai, R., Tallawi, M., Frati, C., Falco, A., Gervasi, A., Quaini, F., et al. (2015). Bioactive electrospun fibers of poly(glycerol sebacate) and poly( $\epsilon$ -caprolactone) for cardiac patch application. *Adv. Healthc. Mat.* 4, 2012–2025. doi:10.1002/adhm.201500154
- Rai, R., Tallawi, M., Grigore, A., and Boccaccini, A. R. (2012). Synthesis, properties and biomedical applications of poly(glycerol sebacate) (PGS): A review. *Prog. Polym. Sci.* 37, 1051–1078. doi:10.1016/j.progpolymsci.2012.02.001
- Rai, R., Tallawi, M., Roether, J. A., Detsch, R., Barbani, N., Rosellini, E., et al. (2013). Sterilization effects on the physical properties and cytotoxicity of poly(glycerol sebacate). *Mat. Lett.* 105, 32–35. doi:10.1016/j.matlet.2013.04.024
- Rastegar, S., Mehdikhani, M., Bigham, A., Poorazizi, E., and Rafienia, M. (2021). Poly glycerol sebacate/polycaprolactone/carbon quantum dots fibrous scaffold as a multifunctional platform for cardiac tissue engineering. *Mat. Chem. Phys.* 266, 124543. doi:10.1016/j.matchemphys.2021.124543
- Ravichandran, R., Venugopal, J. R., Sundarajan, S., Mukherjee, S., Sridhar, R., and Ramakrishna, S. (2012). Minimally invasive injectable short nanofibers of poly(glycerol sebacate) for cardiac tissue engineering. *Nanotechnology* 23, 385102. doi:10.1088/0957-4484/23/38/385102
- Redenti, S., Neeley, W. L., Rompani, S., Saigal, S., Yang, J., Klassen, H., et al. (2009). Engineering retinal progenitor cell and scrollable poly(glycerol-sebacate) composites for expansion and subretinal transplantation. *Biomaterials* 30, 3405–3414. doi:10.1016/j.biomaterials.2009.02.046
- Rekabgardan, M., Rahmani, M., Soleimani, M., Hossein Zadeh, S., Roozafzoon, R., Parandakh, A., et al. (2022). A Bilayered, electrospun poly(glycerol-sebacate)/polyurethane-polyurethane scaffold for engineering of endothelial Basement membrane. *ASAIO J.* 68, 123–132. doi:10.1097/mat.0000000000001423
- Rezk, A. I., Kim, K.-S., and Kim, C. S. (2020). Poly( $\epsilon$ -Caprolactone)/Poly(Glycerol sebacate) composite nanofibers incorporating hydroxyapatite nanoparticles and simvastatin for bone tissue regeneration and drug delivery applications. *Polym. (Basel)* 12, 2667. doi:10.3390/polym12112667
- Riaz, R., Abbas, S. R., and Iqbal, M. (2022). Synthesis, rheological characterization, and proposed application of pre-polyglycerol sebacate as ultrasound contrast agent based on theoretical estimation. *J. Appl. Polym. Sci.* 139, 51963. doi:10.1002/app.51963
- Risley, B. B., Ding, X., Chen, Y., Miller, P. G., and Wang, Y. (2021). Citrate crosslinked poly(glycerol sebacate) with tunable elastomeric properties. *Macromol. Biosci.* 21, 2000301. doi:10.1002/mabi.202000301
- Rosenbalm, T. N., Teruel, M., Day, C. S., Donati, G. L., Morykwas, M., Argenta, L., et al. (2016). Structural and mechanical characterization of bioresorbable, elastomeric nanocomposites from poly(glycerol sebacate)/nanohydroxyapatite for tissue transport applications. *J. Biomed. Mat. Res.* 104, 1366–1373. doi:10.1002/jbm.b.33467
- Rostamian, M., Hosseini, H., Fakhri, V., Talouki, P. Y., Farahani, M., Gharehtapeh, A. J., et al. (2022). Introducing a bio sorbent for removal of methylene blue dye based on flexible poly(glycerol sebacate)/chitosan/graphene oxide ecofriendly nanocomposites. *Chemosphere* 289, 133219. doi:10.1016/j.chemosphere.2021.133219

- Rostamian, M., Kalaei, M. R., Dehkordi, S. R., Panahi-Sarmad, M., Tirgar, M., and Goodarzi, V. (2020). Design and characterization of poly(glycerol-sebacate)-co-poly(caprolactone) (PGS-co-PCL) and its nanocomposites as novel biomaterials: The promising candidate for soft tissue engineering. *Eur. Polym. J.* 138, 109985. doi:10.1016/j.eurpolymj.2020.109985
- Ruther, F., Roether, J. A., and Boccaccini, A. R. (2022). 3D printing of mechanically resistant poly (glycerol sebacate) (PGS)/zein scaffolds for potential cardiac tissue engineering applications. *Adv. Eng. Mat.* 24, 2101768. doi:10.1002/adem.202101768
- Ruther, F., Zimmermann, A., Engel, F. B., and Boccaccini, A. R. (2020). Improvement of the layer adhesion of composite cardiac patches. *Adv. Eng. Mat.* 22, 1900986. doi:10.1002/adem.201900986
- Salehi, S., Czugala, M., Stafiej, P., Fathi, M., Bahnert, T., Gutmann, J. S., et al. (2017). Poly (glycerol sebacate)-poly ( $\epsilon$ -caprolactone) blend nanofibrous scaffold as intrinsic bio- and immunocompatible system for corneal repair. *Acta Biomater.* 50, 370–380. doi:10.1016/j.actbio.2017.01.013
- Sales, V. L., Engelmayr, G. C., Johnson, J. A., Gao, J., Wang, Y., Sacks, M. S., et al. (2007). Protein Precoating of elastomeric tissue-engineering scaffolds increased Cellularity, enhanced Extracellular matrix protein production, and differentially Regulated the Phenotypes of circulating endothelial progenitor cells. *Circulation* 116, 155–163. doi:10.1161/circulationaha.106.6806637
- Saudi, A., Rafienia, M., Zargar Kharazi, A., Salehi, H., Zarrabi, A., and Karevan, M. (2019). Design and fabrication of poly (glycerol sebacate)-based fibers for neural tissue engineering: Synthesis, electrospinning, and characterization. *Polym. Adv. Technol.* 1, 1427–1440. doi:10.1002/pat.4575
- Saudi, A., Zebarjad, S. M., Salehi, H., Katouezadeh, E., and Alizadeh, A. (2022). Assessing physicochemical, mechanical, and *in vitro* biological properties of polycaprolactone/poly(glycerol sebacate)/hydroxyapatite composite scaffold for nerve tissue engineering. *Mat. Chem. Phys.* 275, 125224. doi:10.1016/j.matchemphys.2021.125224
- Sencadas, V., Sadat, S., and Silva, D. M. (2020). Mechanical performance of elastomeric PGS scaffolds under dynamic conditions. *J. Mech. Behav. Biomed. Mat.* 102, 103474. doi:10.1016/j.jmbbm.2019.103474
- Sencadas, V., Tawk, C., and Alici, G. (2020). Environmentally friendly and biodegradable Ultrasensitive Piezoresistive Sensors for Wearable electronics applications. *ACS Appl. Mat. Interfaces* 12, 8761–8772. doi:10.1021/acsami.9b21739
- Sha, D., Wu, Z., Zhang, J., Ma, Y., Yang, Z., and Yuan, Y. (2021). Development of modified and multifunctional poly(glycerol sebacate) (PGS)-based biomaterials for biomedical applications. *Eur. Polym. J.* 161, 110830. doi:10.1016/j.eurpolymj.2021.110830
- Shi, M., Steck, J., Yang, X., Zhang, G., Yin, J., and Suo, Z. (2020). Cracks outrun erosion in degradable polymers. *Extreme Mech. Lett.* 40, 100978. doi:10.1016/j.eml.2020.100978
- Silva, J. C., Udangawa, R. N., Chen, J., Mancinelli, C. D., Garrudo, F. F., Mikael, P. E., et al. (2020). Kartogenin-loaded coaxial PGS/PCL aligned nanofibers for cartilage tissue engineering. *Mater. Sci. Eng. C* 107, 110291. doi:10.1016/j.msec.2019.110291
- Singh, D., Harding, A. J., Albadawi, E., Boissonade, F. M., Haycock, J. W., and Claeysens, F. (2018). Additive manufactured biodegradable poly(glycerol sebacate methacrylate) nerve guidance conduits. *Acta Biomater.* 78, 48–63. doi:10.1016/j.actbio.2018.07.055
- Sivanesan, D., Verma, R. S., and Prasad, E. (2021). 5FU encapsulated polyglycerol sebacate nanoparticles as anti-cancer drug carriers. *RSC Adv.* 11, 18984–18993. doi:10.1039/d1ra01722e
- Slavko, E., and Taylor, M. S. (2017). Catalyst-controlled polycondensation of glycerol with diacyl chlorides: Linear polyesters from a trifunctional monomer. *Chem. Sci.* 8, 7106–7111. doi:10.1039/c7sc01886j
- Souza, M. T., Tansaz, S., Zannotto, E. D., and Boccaccini, A. R. (2017). Bioactive glass fiber-reinforced PGS matrix composites for cartilage regeneration. *Materials* 10, 83. doi:10.3390/ma10010083
- Stowell, C. E. T., Li, X., Matsunaga, M. H., Cockreham, C. B., Kelly, K. M., Cheetham, J., et al. (2020). Resorbable vascular grafts show rapid cellularization and degradation in the ovine carotid. *J. Tissue Eng. Regen. Med.* 14, 1673–1684. doi:10.1002/term.3128
- Sun, Z.-J., Chen, C., Sun, M. Z., Ai, C. H., Lu, X. L., Zheng, Y. F., et al. (2009). The application of poly (glycerol-sebacate) as biodegradable drug carrier. *Biomaterials* 30, 5209–5214. doi:10.1016/j.biomaterials.2009.06.007
- Sun, Z.-J., Sun, B., Tao, R. B., Xie, X., Lu, X. L., and Dong, D. L. (2013). A poly(glycerol-sebacate-curcumin) polymer with potential use for brain gliomas. *J. Biomed. Mat. Res. A* 101A, 253–260. doi:10.1002/jbm.a.34319
- Sundback, C. A., Shyu, J., Wang, Y., Faquin, W., Langer, R., Vacanti, J., et al. (2005). Biocompatibility analysis of poly(glycerol sebacate) as a nerve guide material. *Biomaterials* 26, 5454–5464. doi:10.1016/j.biomaterials.2005.02.004
- Talebi, A., Labbaf, S., Atari, M., and Parhizkar, M. (2021). Polymeric nanocomposite structures based on functionalized graphene with tunable properties for nervous tissue replacement. *ACS Biomater. Sci. Eng.* 7, 4591–4601. doi:10.1021/acsbomaterials.1c00744
- Tallá Ferrer, C., Vilariño-Feltrer, G., Rizk, M., Sydow, H. G., and Vallés-Lluch, A. (2020). Nanocomposites based on poly(glycerol sebacate) with silica nanoparticles with potential application in dental tissue engineering. *Int. J. Polym. Mater. Polym. Biomaterials* 69, 761–772. doi:10.1080/00914037.2019.1616197
- Tallawi, M., Dippold, D., Rai, R., D'Atri, D., Roether, J., Schubert, D., et al. (2016). Novel PGS/PCL electrospun fiber mats with patterned topographical features for cardiac patch applications. *Mater. Sci. Eng. C* 69, 569–576. doi:10.1016/j.msec.2016.06.083
- Tallawi, M., Zebrowski, D. C., Rai, R., Roether, J. A., Schubert, D. W., El Fray, M., et al. (2015). Poly(glycerol sebacate)/poly(butylene succinate-butylene diolinate) fibrous scaffolds for cardiac tissue engineering. *Tissue Eng. Part C. Methods* 21, 585–596. doi:10.1089/ten.tec.2014.0445
- Tang, B. C., Yao, C. L., Xieh, K. Y., and Hong, S. G. (2017). Improvement of physical properties of poly(glycerol sebacate) by copolymerization with polyhydroxybutyrate-diols. *J. Polym. Res.* 24, 215. doi:10.1007/s10965-017-1371-8
- Tang, J., Zhang, Z., Song, Z., Chen, L., Hou, X., and Yao, K. (2006). Synthesis and characterization of elastic aliphatic polyesters from sebacic acid, glycol and glycerol. *Eur. Polym. J.* 42, 3360–3366. doi:10.1016/j.eurpolymj.2006.09.008
- Tevele, A., Agacik, D. T., and Aydin, H. M. (2020). Stretchable poly(glycerol-sebacate)/ $\beta$ -tricalcium phosphate composites with shape recovery feature by extrusion. *J. Appl. Polym. Sci.* 137, 48689. doi:10.1002/app.48689
- Tevele, A., Hosseini, P., Ogutcu, C., Turk, M., and Aydin, H. M. (2017). Bi-layered constructs of poly(glycerol-sebacate)- $\beta$ -tricalcium phosphate for bone-soft tissue interface applications. *Mater. Sci. Eng. C* 72, 316–324. doi:10.1016/j.msec.2016.11.082
- Tevele, A., Topuz, B., Akbay, E., and Aydin, H. M. (2022). Surface channel patterned and endothelialized poly(glycerol sebacate) based elastomers. *J. Biomater. Appl.* 37, 287–302. doi:10.1177/08853282221085798
- Torabi, H., Mehdikhani, M., Varshosaz, J., and Shafiee, F. (2021). An innovative approach to fabricate a thermosensitive melatonin-loaded conductive pluronic/chitosan hydrogel for myocardial tissue engineering. *J. Appl. Polym. Sci.* 138, doi:10.1002/app.50327
- Touré, A. B. R., Mele, E., and Christie, J. K. (2020). Multi-layer scaffolds of poly(caprolactone), poly(glycerol sebacate) and bioactive Glasses manufactured by combined 3D printing and electrospinning. *Nanomaterials* 10, 626. doi:10.3390/nano10040626
- Tsai, Y.-T., Chang, C.-W., and Yeh, Y.-C. (2020). Formation of highly elastomeric and property-tailorable poly(glycerol sebacate)-co-poly(ethylene glycol) hydrogels through thiol-norbornene photochemistry. *Biomater. Sci.* 8, 4728–4738. doi:10.1039/d0bm00632g
- Uyama, H., Inada, K., and Kobayashi, S. (1999). Regioselective polymerization of divinyl sebacate and triols using lipase catalyst. *Macromol. Rapid Commun.* 174, 171–174. doi:10.1002/(sici)1521-3927(19990401)20:4<171:aid-marc171>3.0.co;2-2
- Uyama, H., Inada, K., and Kobayashi, S. (2001). Regioselectivity control in lipase-catalyzed polymerization of divinyl sebacate and triols. *Macromol. Biosci.* 1, 40–44. doi:10.1002/1616-5195(200101)1:13.3.CO;2-K
- Valerio, O., Misra, M., and Mohanty, A. K. (2018). Poly(glycerol-co-diacids) polyesters: From glycerol Biorefinery to sustainable engineering applications, A review. *ACS Sustain. Chem. Eng.* 6, 5681–5693. doi:10.1021/acssuschemeng.7b04837
- Varshosaz, J., Choopannejad, Z., Minaiyan, M., and Kharazi, A. Z. (2021). Rapid hemostasis by nanofibers of polyhydroxyethyl methacrylate/polyglycerol sebacic acid: An *in vitro/in vivo* study. *J. Appl. Polym. Sci.* 138, 49785. doi:10.1002/app.49785
- Vilariño-Feltrer, G., Muñoz-Santa, A., Conejero-García, Á., and Vallés-Lluch, A. (2020). The effect of salt fusion processing variables on structural, physicochemical and biological properties of poly(glycerol sebacate) scaffolds. *Int. J. Polym. Mater. Polym. Biomaterials* 69, 938–945. doi:10.1080/00914037.2019.1636247
- Vogt, L., Liverani, L., Roether, J. A., and Boccaccini, A. R. (2018). Electrospun zein fibers incorporating poly(glycerol sebacate) for soft tissue engineering. *Nanomaterials* 8, 150. doi:10.3390/nano8030150
- Vogt, L., Rivera, L. R., Liverani, L., Piegat, A., El Fray, M., and Boccaccini, A. R. (2019). Poly( $\epsilon$ -caprolactone)/poly(glycerol sebacate) electrospun scaffolds for cardiac tissue engineering using benign solvents. *Mater. Sci. Eng. C* 103, 109712. doi:10.1016/j.msec.2019.04.091
- Vogt, L., Ruther, F., Salehi, S., and Boccaccini, A. R. (2021). Poly(Glycerol sebacate) in biomedical applications—a review of the recent literature. *Adv. Healthc. Mat.* 10, 2002026. doi:10.1002/adhm.202002026



- Wang, B., Ji, P., Ma, Y., Song, J., You, Z., and Chen, S. (2021). Bacterial cellulose nanofiber reinforced poly(glycerol-sebacate) biomimetic matrix for 3D cell culture. *Cellulose* 28, 8483–8492. doi:10.1007/s10570-021-04053-9
- Wang, L., Xu, K., Hou, X., Han, Y., Liu, S., Wiraja, C., et al. (2017). Fluorescent poly(glycerol-co-sebacate) acrylate nanoparticles for stem cell Labeling and Longitudinal Tracking. *ACS Appl. Mat. Interfaces* 9, 9528–9538. doi:10.1021/acsami.7b01203
- Wang, M., Lei, D., Liu, Z., Chen, S., Sun, L., Lv, Z., et al. (2017). A poly(glycerol sebacate) based photo/thermo dual curable biodegradable and biocompatible polymer for biomedical applications. *J. Biomaterials Sci. Polym. Ed.* 28, 1728–1739. doi:10.1080/09205063.2017.1348927
- Wang, S., Jeffries, E., Gao, J., Sun, L., You, Z., and Wang, Y. (2016). Polyester with Pendent Acetylcholine-mimicking Functionalities promotes neurite growth. *ACS Appl. Mat. Interfaces* 8, 9590–9599. doi:10.1021/acsami.5b12379
- Wang, Y., Ameer, G. A., Sheppard, B. J., and Langer, R. (2002). A tough biodegradable elastomer. *Nat. Biotechnol.* 20, 602–606. doi:10.1038/nbt0602-602
- Wang, Y., Kim, Y. M., and Langer, R. (2003). *In vivo* degradation characteristics of poly(glycerol sebacate). *J. Biomed. Mat. Res.* 66A, 192–197. doi:10.1002/jbm.a.10534
- Wang, Z., Ma, Y., Wang, Y., Liu, Y., Chen, K., Wu, Z., et al. (2018). Urethane-based low-temperature curing, highly-customized and multifunctional poly(glycerol sebacate)-co-poly(ethylene glycol) copolymers. *Acta Biomater.* 71, 279–292. doi:10.1016/j.actbio.2018.03.011
- Wilson, R., Divakaran, A. V., Varyambath, A., Kumaran, A., Sivaram, S., et al. (2018). Poly(glycerol sebacate)-based polyester-Polyether copolymers and their semi-Interpenetrated networks with thermoplastic poly(ester-ether) elastomers: Preparation and properties. *ACS Omega* 3, 18714–18723. doi:10.1021/acsomega.8b02451
- Wrzecionek, M., Howis, J., Marek, P. H., Ruśkowski, P., and Gadomska-Gajadur, A. (2021). The catalyst-free polytransesterification for obtaining linear PGS optimized with use of 22 factorial design. *Chem. Process Eng. - Inz. Chem. i Proces.* 42, 43–52.
- Wu, H.-J., Hu, M.-H., Tuan-Mu, H.-Y., and Hu, J.-J. (2019). Preparation of aligned poly(glycerol sebacate) fibrous membranes for anisotropic tissue engineering. *Mater. Sci. Eng. C* 100, 30–37. doi:10.1016/j.msec.2019.02.098
- Wu, T., Frydrych, M., O'Kelly, K., and Chen, B. (2014). Poly(glycerol sebacate urethane)-cellulose nanocomposites with water-Active shape-memory effects. *Biomacromolecules* 15, 2663–2671. doi:10.1021/bm500507z
- Wu, W., Jia, S., Chen, W., Liu, X., and Zhang, S. (2019). Fast degrading elastomer stented fascia remodels into tough and vascularized construct for tracheal regeneration. *Mater. Sci. Eng. C* 101, 1–14. doi:10.1016/j.msec.2019.02.108
- Wu, Y., Wang, L., Guo, B., and X Ma, P. (2014). Injectable biodegradable hydrogels and microgels based on methacrylated poly(ethylene glycol)-co-poly(glycerol sebacate) multi-block copolymers: Synthesis, characterization, and cell encapsulation. *J. Mat. Chem. B* 2, 3674. doi:10.1039/c3tb21716g
- Wu, Y., Wang, L., Zhao, X., Hou, S., Guo, B., and Ma, P. X. (2016). Self-healing supramolecular bioelastomers with shape memory property as a multifunctional platform for biomedical applications via modular assembly. *Biomaterials* 104, 18–31. doi:10.1016/j.biomaterials.2016.07.011
- Wu, Z., Jin, K., Wang, L., and Fan, Y. (2021). A review: Optimization for poly(glycerol sebacate) and fabrication techniques for its Centered scaffolds. *Macromol. Biosci.* 21, 2100022. doi:10.1002/mabi.202100022
- Wyatt, V. T., Strahan, G. D., Wyatt, V. T., and Strahan, G. D. (2012). Degree of branching in hyperbranched poly(glycerol-co-diacid)s synthesized in toluene. *Polym. (Basel)* 4, 396–407. doi:10.3390/polym4010396
- Xiao, B., Yang, W., Lei, D., Huang, J., Yin, Y., Zhu, Y., et al. (2019). PGS scaffolds promote the *In vivo* Survival and Directional differentiation of bone marrow mesenchymal stem cells restoring the morphology and function of wounded rat uterus. *Adv. Healthc. Mat.* 8, 1801455. doi:10.1002/adhm.201801455
- Xu, B., Li, Y., Zhu, C., Cook, W. D., Forsythe, J., and Chen, Q. (2015). Fabrication, mechanical properties and cytocompatibility of elastomeric nanofibrous mats of poly(glycerol sebacate). *Eur. Polym. J.* 64, 79–92. doi:10.1016/j.eurpolymj.2014.12.008
- Xuan, H., Hu, H., Geng, C., Song, J., Shen, Y., Lei, D., et al. (2020). Biofunctionalized chondrogenic shape-memory ternary scaffolds for efficient cell-free cartilage regeneration. *Acta Biomater.* 105, 97–110. doi:10.1016/j.actbio.2020.01.015
- Yan, Y., Sencadas, V., Jin, T., Huang, X., Lie, W., Wei, D., et al. (2018). Effect of multi-walled carbon nanotubes on the cross-linking density of the poly(glycerol sebacate) elastomeric nanocomposites. *J. Colloid Interface Sci.* 521, 24–32. doi:10.1016/j.jcis.2018.03.015
- Yang, B., Lv, W., and Deng, Y. (2017). Drug loaded poly(glycerol sebacate) as a local drug delivery system for the treatment of periodontal disease. *RSC Adv.* 7, 37426–37435. doi:10.1039/c7ra02796f
- Yang, K., Zhang, J., Ma, X., Ma, Y., Kan, C., Ma, H., et al. (2015).  $\beta$ -Tricalcium phosphate/poly(glycerol sebacate) scaffolds with robust mechanical property for bone tissue engineering. *Mater. Sci. Eng. C* 56, 37–47. doi:10.1016/j.msec.2015.05.083
- Yang, Y., Yu, Y., Zhang, Y., Liu, C., Shi, W., and Li, Q. (2011). Lipase/esterase-catalyzed ring-opening polymerization: A green polyester synthesis technique. *Process Biochem.* 46, 1900–1908. doi:10.1016/j.procbio.2011.07.016
- Yeh, Y.-C., Highley, C. B., Ouyang, L., and Burdick, J. A. (2016). 3D printing of photocurable poly(glycerol sebacate) elastomers. *Biofabrication* 8, 045004. doi:10.1088/1758-5090/8/4/045004
- Yeh, Y.-C., Ouyang, L., Highley, C. B., and Burdick, J. A. (2017). Norbornene-modified poly(glycerol sebacate) as a photocurable and biodegradable elastomer. *Polym. Chem.* 8, 5091–5099. doi:10.1039/c7py00323d
- Yi, F., and La Van, D. A. (2008). Poly(glycerol sebacate) nanofiber scaffolds by core/shell electrospinning. *Macromol. Biosci.* 8, 803–806. doi:10.1002/mabi.200800041
- You, Z., Cao, H., Gao, J., Shin, P. H., Day, B. W., and Wang, Y. (2010). A functionalizable polyester with free hydroxyl groups and tunable physiochemical and biological properties. *Biomaterials* 31, 3129–3138. doi:10.1016/j.biomaterials.2010.01.023
- You, Z. R., Hu, M. H., Tuan-Mu, H. Y., and Hu, J. J. (2016). Fabrication of poly(glycerol sebacate) fibrous membranes by coaxial electrospinning: Influence of shell and core solutions. *J. Mech. Behav. Biomed. Mat.* 63, 220–231. doi:10.1016/j.jmbbm.2016.06.022
- Yu, Y., Wu, D., Liu, C., Zhao, Z., Yang, Y., and Li, Q. (2012). Lipase/esterase-catalyzed synthesis of aliphatic polyesters via polycondensation: A review. *Process Biochem.* 47, 1027–1036. doi:10.1016/j.procbio.2012.04.006
- Zaky, S. H., Lee, K., Gao, J., Jensen, A., Verdelis, K., Wang, Y., et al. (2017). Poly(glycerol sebacate) elastomer supports bone regeneration by its mechanical properties being closer to osteoid tissue rather than to mature bone. *Acta Biomater.* 54, 95–106. doi:10.1016/j.actbio.2017.01.053
- Zanjanizadeh Ezazi, N., Ajdary, R., Correia, A., Makila, E., Salonen, J., Kemell, M., et al. (2020). Fabrication and characterization of drug-loaded conductive poly(glycerol sebacate)/Nanoparticle-based composite patch for myocardial Infarction applications. *ACS Appl. Mat. Interfaces* 12, 6899–6909. doi:10.1021/acsami.9b21066
- Zbinden, J. C., Blum, K. M., Berman, A. G., Ramachandra, A. B., Szafron, J. M., Kerr, K. E., et al. (2020). Tissue-engineered vascular grafts: Effects of Braiding parameters on tissue engineered vascular graft development. *Adv. Healthc. Mat.* 9, 2070086. doi:10.1002/adhm.202070086
- Zhang, C., Wen, T. H., Razak, K. A., Lin, J., Xu, C., Seo, C., et al. (2020). Magnesium-based biodegradable microelectrodes for neural recording. *Mater. Sci. Eng. C* 110, 110614. doi:10.1016/j.msec.2019.110614
- Zhang, J., Shi, H., Wu, D., Xing, Z., and Zhang, A. (2014). Recent developments in lipase-catalyzed synthesis of polymeric materials. *Process Biochem.* 49, 797–806. doi:10.1016/j.procbio.2014.02.006
- Zhang, X., Jia, C., Qiao, X., Liu, T., and Sun, K. (2016). Porous poly(glycerol sebacate) (PGS) elastomer scaffolds for skin tissue engineering. *Polym. Test.* 54, 118–125. doi:10.1016/j.polymertesting.2016.07.006
- Zhang, X., Jia, C., Qiao, X., Liu, T., and Sun, K. (2017). Silk fibroin microfibers and chitosan modified poly(glycerol sebacate) composite scaffolds for skin tissue engineering. *Polym. Test.* 62, 88–95. doi:10.1016/j.polymertesting.2017.06.012
- Zhang, Y., Liu, Y., Jiang, Z., Wang, J., Xu, Z., Meng, K., et al. (2021). Poly(glycerol sebacate)/silk fibroin small-diameter artificial blood vessels with good elasticity and compliance. *Smart Mat. Med.* 2, 74–86. doi:10.1016/j.smaim.2021.01.001
- Zhang, Y., Spinella, S., Xie, W., Cai, J., Yang, Y., Wang, Y. Z., et al. (2013). Polymeric triglyceride analogs prepared by enzyme-catalyzed condensation polymerization. *Eur. Polym. J.* 49, 793–803. doi:10.1016/j.eurpolymj.2012.11.011
- Zhao, X., Wu, H., Guo, B., Dong, R., Qiu, Y., and Ma, P. X. (2017). Antibacterial anti-oxidant electroactive injectable hydrogel as self-healing wound dressing with hemostasis and adhesiveness for cutaneous wound healing. *Biomaterials* 122, 34–47. doi:10.1016/j.biomaterials.2017.01.011
- Zhou, L., He, H., Jiang, C., and He, S. (2015). Preparation and characterization of poly(glycerol sebacate)/cellulose nanocrystals elastomeric composites. *J. Appl. Polym. Sci.* 132, 27. doi:10.1002/app.42196
- Zhu, C., Rodda, A. E., Truong, V. X., Shi, Y., Zhou, K., Haynes, J. M., et al. (2018). Increased Cardiomyocyte Alignment and intracellular calcium Transients using Micropatterned and drug-releasing poly(glycerol sebacate) elastomers. *ACS Biomater. Sci. Eng.* 4, 2494–2504. doi:10.1021/acsbomaterials.8b00084
- Zulkifli, Z., Tan, J. J., Ku Marsilla, K. I., Rusli, A., Abdullah, M. K., Shuib, R. K., et al. (2022). Shape memory poly(glycerol sebacate)-based electrospun fiber scaffolds for tissue engineering applications: A review. *J. Appl. Polym. Sci.* 139, 52272. doi:10.1002/app.52272





## OPEN ACCESS

## EDITED BY

Florent Allais,  
AgroParisTech Institut des Sciences et  
Industries du Vivant et de  
L'environnement, France

## REVIEWED BY

Wendy Schluchter,  
University of New Orleans, United States  
Jianan Sun,  
Ocean University of China, China

## \*CORRESPONDENCE

Sónia P. M. Ventura,  
spventura@ua.pt

## SPECIALTY SECTION

This article was submitted to  
Green and Sustainable Chemistry,  
a section of the journal  
Frontiers in Chemistry

RECEIVED 09 October 2022

ACCEPTED 14 November 2022

PUBLISHED 01 December 2022

## CITATION

Kovaleski G, Kholany M, Dias LMS,  
Correia SFH, Ferreira RAS, Coutinho JAP  
and Ventura SPM (2022), Extraction and  
purification of phycobiliproteins from  
algae and their applications.  
*Front. Chem.* 10:1065355.  
doi: 10.3389/fchem.2022.1065355

## COPYRIGHT

© 2022 Kovaleski, Kholany, Dias,  
Correia, Ferreira, Coutinho and Ventura.  
This is an open-access article  
distributed under the terms of the  
[Creative Commons Attribution License](#)  
(CC BY). The use, distribution or  
reproduction in other forums is  
permitted, provided the original  
author(s) and the copyright owner(s) are  
credited and that the original  
publication in this journal is cited, in  
accordance with accepted academic  
practice. No use, distribution or  
reproduction is permitted which does  
not comply with these terms.

# Extraction and purification of phycobiliproteins from algae and their applications

Gabriela Kovaleski<sup>1,2</sup>, Mariam Kholany<sup>1</sup>, Lília M. S. Dias<sup>2</sup>,  
Sandra F. H. Correia<sup>3</sup>, Rute A. S. Ferreira<sup>2</sup>, João A. P. Coutinho<sup>1</sup>  
and Sónia P. M. Ventura<sup>1\*</sup>

<sup>1</sup>Department of Chemistry, CICECO—Aveiro Institute of Materials, University of Aveiro Campus  
Universitário de Santiago, Aveiro, Portugal, <sup>2</sup>Department of Physics, CICECO—Aveiro Institute of  
Materials, University of Aveiro Campus Universitário de Santiago, Aveiro, Portugal, <sup>3</sup>Instituto de  
Telecomunicações, University of Aveiro, Aveiro, Portugal

Microalgae, macroalgae and cyanobacteria are photosynthetic microorganisms, prokaryotic or eukaryotic, living in saline or freshwater environments. These have been recognized as valuable carbon sources, able to be used for food, feed, chemicals, and biopharmaceuticals. From the range of valuable compounds produced by these cells, some of the most interesting are the pigments, including chlorophylls, carotenoids, and phycobiliproteins. Phycobiliproteins are photosynthetic light-harvesting and water-soluble proteins. In this work, the downstream processes being applied to recover fluorescent proteins from marine and freshwater biomass are reviewed. The various types of biomasses, namely macroalgae, microalgae, and cyanobacteria, are highlighted and the solvents and techniques applied in the extraction and purification of the fluorescent proteins, as well as their main applications while being fluorescent/luminescent are discussed. In the end, a critical perspective on how the phycobiliproteins business may benefit from the development of cost-effective downstream processes and their integration with the final application demands, namely regarding their stability, will be provided.

## KEYWORDS

phycobiliproteins, R-phycoerythrin, extraction, purification, applications

## Introduction

Marine biomass is recognized worldwide as a valuable carbon source, which can be used for food, feed, chemicals, and biopharmaceuticals of paramount industrial relevance (Merlo et al., 2021). Algae are mostly known for their use in the production of biomaterials and biofuels, due to their high content of fats or polysaccharides (Pham et al., 2013). Nonetheless, new fields of application arise with a greater focus on the remaining compounds with multiple uses in the food, medical, pharmaceutical, and cosmetic industries. Both academia and industry have invested significant efforts during the last decades in the exploration of valuable bioproducts that can be sourced

from algae, and which can allow the development of a biorefinery focusing on a blue economy. Plenty of high-value compounds such as proteins, antioxidants, vitamins, minerals, lipids, pigments, biopolymers (chitosan and sodium alginate), and polyunsaturated fatty acids are already being explored for this purpose (Barkia et al., 2019; Novak et al., 2019; Cuellar-Bermudez et al., 2014).

Microalgae, macroalgae, and cyanobacteria are photosynthetic microorganisms, prokaryotic or eukaryotic, living in saline or freshwater environments. The cell wall of macroalgae consists of polysaccharides (agar and cellulose), which are an obstacle to cell rupture during the extraction of their bioactive compounds (Mittal et al., 2017).

The species selection and cultivation strategies are considered essential to producing each compound of interest (López-Rodríguez et al., 2020), further boosting their industrial potential. Included in the set of bioactive compounds of most interests to academia and industry are the pigments, including chlorophylls, carotenoids, and phycobiliproteins (Pagels et al., 2019).

Phycobiliproteins are photosynthetic light-harvesting proteins present in cyanobacteria, red algae, cryptomonads, and cyanelles. They are water-soluble proteins, covalently bound *via* cysteine amino acid chromophores called phycobilins, which are open-chain tetrapyrroles (Mulders et al., 2014; Pagels et al., 2019), and organized in supramolecular structures called phycobilisomes, located in the stroma of the cells (Dumay et al., 2014).

The presence of phycobiliproteins in some organisms allows the transfer of light energy in spectral zones that cannot be used by chlorophyll *a* (responsible for the photosynthesis mechanism to occur), thus allowing the photosynthesis and the survival of living organisms even at low light intensities (Dumay et al., 2014). The phycobilisome works as an energetic funnel, allowing the energy transfer through chromophores to the reaction centers (Roy et al., 2011).

All phycobiliproteins have the same monomer as the basic unit, composed of  $\alpha$  and  $\beta$  subunits. Each monomer can carry either one, two, or three chromophores, depending on the molecular species. These phycobilin chromophores are phycoerythrobilin (PEB), phycocyanobilin (PCB) and phycobiliviolin (PVB) (Bryant, 1982). Depending on the phycobiliprotein, different phycobilin combinations may occur leading to their specific spectral and optical identity (Glazer, 1994): Phycoerythrin with maximum absorption wavelengths ( $\lambda_{\text{max}}$ ) ranging between 490 and 570 nm (with three-peak absorption maxima at 565, 539, and 498 nm) (Liu et al., 2005); phycocyanin ( $\lambda_{\text{max}}$  = 610–620 nm) (Dias et al., 2022) allophycocyanin ( $\lambda_{\text{max}}$  = 650–655 nm), and phycoerythrocyanin ( $\lambda_{\text{max}}$  = 560–600 nm) (Munier et al., 2014). Given that, phycobiliproteins differ in the amino-acid sequence, the number of chromophores per subunit, and the type of chromophores. Based on their structure

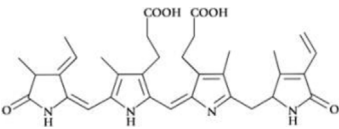
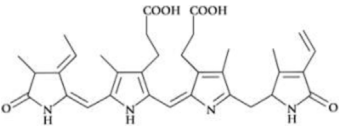
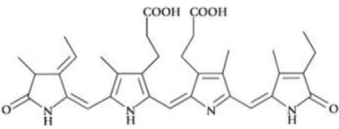
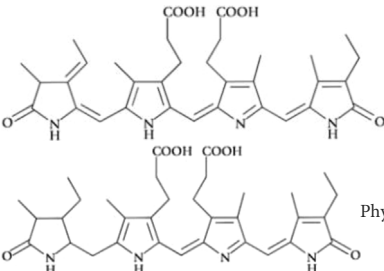
and properties, specifically on their radiation absorption ability, phycobiliproteins are divided into four main types, namely phycoerythrin (PE), phycocyanin, phycoerythrocyanin, and allophycocyanin, as detailed in Table 1 (Pagels et al., 2019).

PE is found in the chloroplasts of red algae, cyanobacteria, being generally composed of ( $\alpha\beta$ )  $6\gamma$  complexes ( $\alpha$ , 18–20 kDa;  $\beta$ , 19.5–21 kDa; and  $\gamma$ , 30 kDa) (Munier et al., 2014), with a total molecular weight around 240 kDa (Table 1). PE can be classified into four classes: B-PE (Bangiophyceae PE, containing PEB only or containing PEB and phycourobilin) C-PE (cyanobacterial-PE), and R-PE (Rhodophyta-PE). The increment of the  $\gamma$  subunit in R-PE in comparison with other phycobiliproteins confers additional stability since this subunit is in the center of the molecule linking the ( $\alpha\beta$ ) 3 trimers (Wang et al., 1998). Indeed, R-PE is recognized for its stability towards several denaturant agents, namely temperature and pH (Galland-Irmouli et al., 2000). The high solubility in water and stability associated with R-PE has increased industrial interest. R-PE is commonly used as a natural colouring agent (Kamble et al., 2018), fluorescent label probe (Wang et al., 2020), and as an ingredient in pharmaceutical formulations (Sekar and Chandramohan, 2007). Many studies show the various biological activities of R-PE, namely its antioxidant and anti-cancer properties (Pan et al., 2013; Jung et al., 2016; Tan et al., 2016).

Given the broad range of applications of phycobiliproteins, particularly of R-PE, and their consequent economic value, there is a growing interest in the development of more sustainable and efficient extraction and purification techniques for their recovery. These methods are dependent on the biomass and should be tailored in accordance (Ranjitha and Kaushik, 2005). Cell disruption, primary recovery, and purification are the three main steps for the recovery of pure R-PE. The polysaccharides present in the algal cell wall, such as agar and cellulose, interfere with cell disruption during extractions, so there is a need for a suitable method for PE extraction (Mittal et al., 2017). The purity index expressed as the  $A_{565\text{ nm}}/A_{280\text{ nm}}$  ratio indicates the purity of PE for different applications, where a value of 0.7 represents a protein with food-grade purity, 3.9 as a reactive grade, and greater than 4.0 as analytical grade (Rito-Palomares et al., 2001). Some other variables to be considered are the recovery, the yield of extraction, the extraction efficiency, and the purity level, which will be further described and analysed in this work.

This review will focus on the different downstream schemes reported so far for the recovery of phycobiliproteins from marine and freshwater biomass, highlighting the different sources, namely macroalgae, microalgae, and cyanobacteria, the solvents and techniques applied in the extraction and purification of the fluorescent proteins, as well as their main

TABLE 1 Main properties and characteristics of phycobiliproteins.

Phycobiliprotein	Absorption maxima (nm) (Liu et al., 2005)	Chemical structure (Li et al., 2019)	Molecular weight (kDa)	Chromophore ID and structure
Phycoerythrin	490–570	( $\alpha\beta$ ) <sub>6</sub> γ complexes	240	 Phycoerythrobilin (PEB)
Phycoerythrocyanin	560–600	( $\alpha\beta$ ) <sub>3</sub>		 Phycoerythrobilin (PEB)
Phycocyanin	610–625	( $\alpha\beta$ ) <sub>3</sub>	30	 Phycocyanobilin (PCB)
Allophycocyanin	650–660	( $\alpha\beta$ ) <sub>3</sub>	104	 PCB and Phycobiliviolin (PVB)

applications while being fluorescent/luminescent. In the end, a critical perspective on how the sector of phycobiliproteins may benefit from the development of cost-effective downstream processes and their integration with the final application demands, namely regarding their stability, will be provided.

## Downstream processing

A downstream process is traditionally defined by two or three main steps, which depend on the compounds to be recovered from the biomass being produced extra or intracellularly. Moreover, the downstream processes to apply, depends not only on the type of biomolecule(s) to recover (considering the physical, chemical, and optical properties) but also on the morphology of the raw material, in the specific case of this review, cyanobacteria, macro or microalgae.

Considering that the focus of this review is the phycobiliproteins, the downstream processes associated with their production are composed of three main steps: 1) cell disruption and pigments' release, 2) extraction of phycobiliproteins 3) purification of phycobiliproteins by separating them from the other contaminants. As recently

discussed by Martins and Ventura (2020), the traditional schemes of cell disruption and biomolecules release are based on mechanical and/or chemical treatments. Included in the mechanical treatments, and considering specifically the release of phycobiliproteins, the effect of maceration, freeze-thaw, ultrasounds, and microwaves have been evaluated. In addition to the mechanical treatments, two other techniques are explored to recover phycobiliproteins, namely the use of specific solvents in the solid-liquid extraction of the pigments and the enzymatic hydrolysis (as described in Tables 2, 3). Furthermore, with a much lower incidence of investigation are the extraction schemes considering the combination of mechanical and chemical treatments (Martínez et al., 2019). Normally, the first step for the recovery of a valuable compound produced intracellularly by any organism is cell disruption with the consequent release of the cell components (Günerken et al., 2015). Disruption processes have been effectively performed to release R-PE from algae by applying the techniques of maceration, freeze-thaw, ultrasound, microwave irradiation and enzymatic hydrolysis. Normally these techniques are used in conjunction with solid-liquid extraction, which can be water or other solvents. In the next section of this review, a brief analysis of the techniques applied to extract phycobiliproteins from 1) macroalgae and 2) microalgae/cyanobacteria.

TABLE 2 Extraction methods applied so far to the recovery of phycobiliproteins from macroalgae.

Species	Tissue disruption/ Extraction method	Yield/Extraction efficiency PE	Yield/Extraction efficiency PC	Yield/ Extraction efficiency	R-PE purity index (A <sub>565</sub> /A <sub>280</sub> )	References
<i>Gracilaria gracilis</i>	Maceration (mortar and pestle)	3.58 ± 0.03 mg g <sup>-1</sup>	0.62 ± 0.02 mg g <sup>-1</sup>	—	—	Pereira et al. (2020)
	Ultrasonic bath	1.60 ± 0.12 mg g <sup>-1</sup>	0.37 ± 0.03 mg g <sup>-1</sup>	—	—	
	Ultrasonic probe	1.57 ± 0.10 mg g <sup>-1</sup>	0.44 ± 0.01 mg g <sup>-1</sup>	—	—	
	High pressure	0.25 ± 1.27 mg g <sup>-1</sup>	—	—	—	
	Freeze-thawing	1.51 ± 0.03 mg g <sup>-1</sup>	—	—	—	
	Maceration with pestle and mortar	7 mg g <sup>-1</sup> d.w.	2 mg g <sup>-1</sup> d.w.	—	—	
<i>Gelidium pusillum</i>	Aqueous solutions of ionic liquids	0.4 mg g <sup>-1</sup> fresh biomass	-	—	—	Francavilla et al. (2015)
						Martins et al. (2016)
	Ultrasonication	0.16 ± 0.01 mg g <sup>-1</sup>	0.11 ± 0.01 mg g <sup>-1</sup>	—	—	Mittal et al. (2017)
	Maceration using mortar and pestle	1.19 ± 0.03 mg g <sup>-1</sup>	0.81 ± 0.03 mg g <sup>-1</sup>	—	—	
	Maceration in liquid nitrogen	0.54 ± 0.05 mg g <sup>-1</sup>	0.34 ± 0.03 mg g <sup>-1</sup>	—	—	
	Homogenization	1.29 ± 0.04 mg g <sup>-1</sup>	0.80 ± 0.07 mg g <sup>-1</sup>	—	—	
	Freezing-thawing	0.17 ± 0.04 mg g <sup>-1</sup>	0.29 ± 0.02 mg g <sup>-1</sup>	—	—	
	Maceration + freezing-thawing	0.9 ± 0.03 mg g <sup>-1</sup>	0.61 ± 0.02 mg g <sup>-1</sup>	—	—	
	Homogenization + ultrasonication.	1.41 ± 0.01 mg g <sup>-1</sup>	0.95 ± 0.01 mg g <sup>-1</sup>	—	—	
<i>Grateloupia turuturu</i>	Maceration + ultrasonication	1.56 ± 0.01 mg g <sup>-1</sup>	1.19 ± 0.01 mg g <sup>-1</sup>	—	—	Guillard et al. (2015)
	Ultrasound-assisted	—	—	—	—	
<i>Porphyridium purpureum</i>	Ultrasound-assisted extraction + enzymatic hydrolysis	3.6 mg g <sup>-1</sup> (22°C)	—	—	—	Juin et al. (2014)
	Microwave-Assisted (40°C)	73.7 ± 2.3 µg mg <sup>-1</sup>	34.8 ± 6.4 µg mg <sup>-1</sup>	—	—	
<i>Porphyridium cruentum</i>	Fresh: Freeze-thawing (−20°C and 20–25°C)	71 ± 4%	—	—	—	Lauceri et al. (2019)
	Fresh: Freeze-thawing + Ultrasound	69 ± 3%	—	—	—	
	Freeze dried: Freeze-thawing (−20°C and 20–25°C)	69 ± 5%	—	—	—	
	Freeze dried: Freeze-thawing + Ultrasound	62%	—	—	—	
	50 mM acetate buffer at pH 5.5) + five repeated freeze-thaw cycles	0.27 mg ml <sup>-1</sup>	—	—	—	
<i>Pyropia yezoensis</i>	Freeze-thaw (−20°C and 4°C)	—	—	3.766 ± 0.021 mg g <sup>-1</sup> dw	0.195 ± 0.015	Wang et al. (2020)
	Maceration	—	—	2.465 ± 0.017 mg g <sup>-1</sup> dw	0.176 ± 0.014	
	Hydrolysis	—	—	2.087 ± 0.022 mg g <sup>-1</sup> dw	0.147 ± 0.012	
	Enzymatic hydrolysis (agarase and cellulase)	—	—	6.953 ± 0.020 mg g <sup>-1</sup> dw	0.287 ± 0.014	
	Enzymatic hydrolysis (xylanase)	—	—	1.99 mg g <sup>-1</sup> dw	0.36	
<i>Mastocarpus stellatus</i>	Enzymatic digestion (xylanase)	—	—	3.28 ± 0.64 (g.kg <sup>-1</sup> dw)	0.14 ± 0.03	Dumay et al. (2013)
<i>Palmaria palmata</i>	After optimization	—	—	12.36 ± 0.37 (g.kg <sup>-1</sup> dw)	0.40 ± 0.04	
<i>Gracilaria verrucosa</i>	Enzymatic hydrolysis (endocellulase and βxylanase)	—	—	6.25 mg g <sup>-1</sup>	-	Mensi et al. (2011)

d.w. (dry weigh).

[PE], phycoerythrin concentration; [PC], phycocyanin concentration.



TABLE 3 Extraction methods applied so far to the recovery of phycobiliproteins from microalgae and cyanobacteria.

Species	Tissue disruption/Extraction method	Yield/Extraction efficiency PE	Yield/Extraction efficiency PC	References
<i>Spirulina maxima</i>	Ultrasonication	0.8 mg ml <sup>-1</sup>	11.3 mg ml <sup>-1</sup>	Choi and Lee (2018)
<i>Spirulina platensis</i>	Ultrasonication + protic ionic liquids (2-HEAA + 2-HEAF)	—	0.75 g.L <sup>-1</sup>	Rodrigues et al. (2018)
	Mechanical agitation + thermal heating + protic ionic liquids (2-HEAA + 2-HEAF)	—	1.65 g.L <sup>-1</sup>	Rodrigues et al. (2019)
<i>Pseudanabaena catenate</i>	Three cycles of repeated freezing in liquid nitrogen + maceration mortar and pestle.	25.5 ± 5.1 mg.L <sup>-1</sup>	28.8 ± 2.8 mg.L <sup>-1</sup>	Khan et al. (2018)
<i>Pseudanabaena amphigranulata</i>	Three cycles of repeated freezing in liquid nitrogen + maceration mortar and pestle.	10.2 ± 3.9 mg.L <sup>-1</sup>	86 ± 14.7 mg.L <sup>-1</sup>	Khan et al. (2018)
<i>Arthrospira platensis</i> GL	Fresh: Freeze-thawing (−20°C and 20–25°C)	—	77 ± 6%	Lauceri et al. (2019)
	Fresh: Freeze-thawing + Ultrasound	—	76 ± 6%	
	Freeze dried: Freeze-thawing (−20°C and 20–25°C)	—	81 ± 2%	
	Freeze dried: Freeze-thawing + Ultrasound	—	79 ± 1%	
<i>Porphyridium cruentum</i>	50 mM acetate buffer at pH 5.5) + five repeated freeze-thaw cycles	0.27 mg ml <sup>-1</sup>	—	Ibáñez-González et al. (2016)
	Fresh: Freeze-thawing (−20°C and 20–25°C)	71 ± 4%	—	Lauceri et al. (2019)
	Fresh: Freeze-thawing + Ultrasound	69 ± 3%	—	
	Freeze dried: Freeze-thawing (−20°C and 20–25°C)	69 ± 5%	—	
	Freeze dried: Freeze-thawing + Ultrasound	62%	—	
<i>Porphyridium purpureum</i>	Microwave-Assisted (40°C)	73.7 ± 2.3 µg mg <sup>-1</sup>	34.8 ± 6.4 µg mg <sup>-1</sup>	Juin et al. (2014)

## Extraction processes applied to macroalgae

### Conventional techniques

Macroalgae, also known as seaweeds, are multicellular, macroscopic algae, which may belong to different groups of multicellular algae: green, red, and brown algae (Suganya et al., 2016). Due to their desirable characteristics, such as high photosynthetic efficiency, high biomass conversion rate, ease of handling, and fast growth rate, they are considered a promising raw material for biotechnological valorization answering the needs of a marine biorefinery (Francavilla et al., 2015). The cell wall of macroalgae consists of polysaccharides (agar and cellulose), which are an obstacle to cell rupture during the extraction of their bioactive compounds (Mittal et al., 2017). Maceration and milling are often used, with liquid nitrogen freezing to yield better results. However, at least some of these cell disruption approaches require increased time, specific equipment, and higher overall costs. An example is the use of liquid nitrogen at a lab scale which is impossible to apply in higher scales, but nevertheless, it can be replaced by a cryogenic mill operational unit. Ultrasonication is a technique where biomass breaks down by the compression and decompression cycles resulting from sound waves at frequencies normally higher than 20 kHz, also requires less time and lower temperature (Guillard et al., 2015; Mittal et al., 2017). Table 2 describes

the yields of extraction and purities obtained by the application of different conventional methods.

In 2015, Francavilla et al. (2015) used maceration to extract phycobiliproteins from *Gracilaria gracilis*, which was used as the first step of a complex biorefinery cascade, achieving a yield of 7 mg PE. g<sup>-1</sup> d. w. and 2 PC. g<sup>-1</sup> d. w. Later, Pereira and co-authors (2018) compared five techniques for the extraction of R-PE from the same algae, namely maceration, ultrasonic bath, ultrasonic probe, high pressure, and freeze-thawing. Using a Response Surface Methodology for optimization of the extraction method, a greater efficiency was attained through maceration with mortar and pestle yielding an extraction of 3.58 ± 0.03 mg PE. g<sup>-1</sup> and 0.62 ± 0.02 mg PC. g<sup>-1</sup>, confirming that PE is the most abundant phycobiliprotein in *Gracilaria gracilis*. Still, in the study of red macroalgae, various extraction methods were tested on *Gelidium pusillum*, namely maceration with freezing-thawing, homogenization and ultrasonication, and maceration and ultrasonication, the latter being more effective in the R-PE and R-PC extraction, 77%, and 93%, respectively (Mittal et al., 2019). Guillard et al. (2015) compared two extraction processes with *Grateloupia turuturu*, ultrasound-assisted extraction and ultrasound-assisted with enzymatic hydrolysis. Despite the higher complexity of an enzymatic step, normally a better performance is achieved considering the specificity of the enzymes to break the bonds between the constituents of the biomass (3.6 mg g<sup>-1</sup> at 22°C). Finally, in 2017, Sharmila et al (2017) used different cell disruption schemes,

which included the maceration using mortar and pestle, the freeze-thaw, the use of lysozyme and sonication for the extraction of phycobiliproteins from *Kappaphycus alvarezii*. In this work, the authors have also investigated different process conditions, namely, three temperatures for the freeze-thaw, the best extraction using freeze-thaw at a temperature of  $-20^{\circ}\text{C}$ – $25^{\circ}\text{C}$ .

## Solvent-and solvent-assisted extraction

Another approach for the extraction of molecules is the use of solvents. Phycobiliproteins are hydrophilic proteins, thus, conventional solvents used in their extraction are mainly water or buffers (to control the media pH). These solutions can be phosphate buffer, ethylenediamine tetra-acetic acid (EDTA), acetate buffer, or even water. For the optimization of the extraction, Hemlata et al. (2018) have used five different buffers as solvents to extract phycoerythrin from *Microchaete*, namely the citrate buffer (pH-5.0; 0.1 M), acetate buffer (pH-6.0; 0.1 M), carbonate buffer (pH 9.6; 0.1 M), Tris-HCl buffer (pH-7.2; 0.05 M) and the sodium phosphate buffer (pH-7.0; 0.1 M). After optimization, a higher yield of extraction ( $65.21\text{ mg g}^{-1}$ ) was obtained with the acetate buffer (pH-6.0; 0.1 M). They also showed the antioxidant, antibacterial, anticancer, antifungal activities of *Microchaete*'s PE. Sfriso et al. (2018) used different concentrations of buffers, phosphate buffer (0.1, 1, 10, and 100 mM), and EDTA (0.1, 1, 10, and 100 mM), to later investigate the fluorescence of PE. Sharmila et al. (2017) also optimized the process with different buffers at different pH conditions, followed by different cell disruption methods, and this result was found for different temperatures. The results were better with sodium phosphate pH 7.2 and using freeze-thaw at  $-20^{\circ}\text{C}$ – $25^{\circ}\text{C}$ . Sintra and co-authors (2021) also used sodium phosphate for extraction and achieved 90% of recovery of C-PC.

Meanwhile, Nguyen et al. (2016) compared different concentrations of phosphate buffer (20 mM, 50 mM, and 0.1 M) with tap and pure water with maceration in liquid nitrogen. It was found that the solution of phosphate buffer 20 mM with pH 7.1 showed better results for PE in *Mastocarpus stellatus*. Sudhakar et al. (2015) also purchased the extractions of the algae *Gracilaria crassa* with water (distilled water and seawater) and phosphate buffer (0.1 M), and found a better yield for distilled water for PE ( $0.35\text{ mg g}^{-1}$ ) and PC ( $0.18\text{ mg g}^{-1}$ ). The use of solvents was also reported by its combination with microwave irradiation. Microwave irradiation consists of instantaneous and homogeneous heat transfer in the sample to break the cell wall. Juin et al. (2014) achieved maximum extraction efficiency of PE ( $73.7 \pm 2.3\text{ }\mu\text{g mg}^{-1}$ ) with just 10 s of irradiation, at  $40^{\circ}\text{C}$ , showing that this procedure is fast and has high yields, but for PC the efficiency was lower ( $34.8 \pm 6.4\text{ }\mu\text{g mg}^{-1}$ ) with 10 s but with a temperature of  $100^{\circ}\text{C}$ , describing that: "The weak extractability of the two pigments tightly bound to the thylakoid membrane

compared to PE." Martins et al., 2016 compared the extraction of PBPs in *Gracilaria* sp. between sodium phosphate and different ionic liquids, finding cholinium chloride as the best solvent, with an increase of 45% in yield and represented by high selectivity since practically no chlorophylls were extracted simultaneously. Pressurized liquids extraction (PLE), which is a method that uses solvents at high temperatures and pressures for the extraction of compounds, has the advantage of being a faster process and using less solvent. This method was applied in the extraction of PE and proved to be efficient when the temperatures were lower and with pressurized water ( $16.51 \pm 0.21\text{ mg g}^{-1}$  of PE) (Gallego et al., 2019).

## Extraction processes applied to microalgae and cyanobacteria

### Conventional techniques

Cyanobacteria are unique photosynthetic organisms present in almost all habitats all over the world, as pointed out by the World Health Organization (WHO, 2021). They have a small cell size and can be unicellular, filamentous, or colonial, being sometimes large enough to be visible by the human eye, especially during the occurrence of natural blooms (Macário et al., 2021). These bacteria have been studied for their morphology, photosynthesis, and nitrogen fixation mechanisms, but also for certain aspects of their structure namely in what concerns the part of the cell driving photosynthesis. As recurrently reported, the cyanobacteria photosynthetic apparatus is composed of three light-harvesting systems, namely the two main photosystems found in other photosynthetic organisms and a phycobilisome (Masojídek et al., 2013). The phycobilisome of these organisms is mainly composed of phycobiliproteins, the phycobilisome composition varying from species to species.

Microalgae are microscopic algae, unicellular, which may vary in size from a few micrometers to a few hundred of micrometers (Suganya et al., 2016). They can produce hydrogen, hydrocarbons, fats and carbohydrates, as well as be able to use different water sources, such as fresh, saline, and wastewater (Randrianarison and Ashraf, 2017). Most microalgae/cyanobacteria produce more phycobiliproteins under stressful environmental conditions, especially light (Manirafasha et al., 2016). Microalgae have already been incorporated, with good acceptability, in dairy products as bioactive compounds (Caporgno and Mathys, 2018).

Although most works report the recovery of phycobiliproteins from macroalgae, Choi and Lee (2018) have extracted phycobiliproteins from *Spirulina* sp. (a cyanobacterium commonly used as a functional food) with ultrasound and obtained very high amounts of phycocyanin ( $11.3\text{ mg ml}^{-1}$ ) when compared to conventional water extraction at  $4^{\circ}\text{C}$

TABLE 4 Purification methods applied to the fractionation of phycobiliproteins.

Type of algae	Species	Tissue disruption/ Extraction method	Purification method	Yield/Extraction efficiency/ Recovery/PE purity index	Yield/Extraction efficiency/ Recovery/PC purity index	References
Macroalgae	Gracilaria gracilis	Phosphate buffer 20 mM	Anion-exchange chromatography (DEAE Sepharose)	$0.24 \pm 0.01 \text{ mg g}^{-1}$ $A_{565}/A_{280} = 3.25 \pm 0.01$	—	Nguyen et al. (2019)
		Maceration	Induced precipitation + ultrafiltration (Poly (acrylic acid) sodium salts)	79.5% yield	—	Martins et al. (2021)
	Pyropia haitanensis residue	Freeze-thaw	Expanded-bed chromatographic (DEAE-Sepharose.)	[PE] $247.13 \text{ mg.L}^{-1}$ $OD_{565}/OD_{280} = 4.01$	—	Zhao et al. (2019)
	Halymenia floresia	0.05 M phosphate buffer at pH 7.0	Polyacrylamide Gel Using Electrophoretic elution technique (Preparative Native PAGE + dialyzed)	41.1% yield $A_{565}/A_{280} = 5.9$	—	MalairajMuthu et al. (2016)
	Grateloupia turuturu	Liquid nitrogen + sodium phosphate buffer (20 mM; pH 7.1)	Ammonium sulfate precipitation 85%	$A_{565}/A_{280} = 1.22$	—	Munier et al. (2015)
			+ Anion-exchange chromatography (DEAE-Cellulose)	$A_{565}/A_{280} = 2.89$	—	
	Porphyra yezoensis Ueda	Phosphate buffered saline + EDTA	Continuous precipitation with ammonium sulfate at different concentrations (10%, 20%, 40% and 50%) + Hydroxylapatites chromatography (HAC)	$A_{565}/A_{280} = 5.50$	$A_{615}/A_{280} = 5.10$	Cai et al. (2014)
	Gracilaria corticata	Phosphate buffer (0.1 M)	65% ammonium sulphate + dialyzed	$0.24 \text{ mg g}^{-1}$	$0.11 \text{ mg g}^{-1}$	Sudhakar et al. (2014)
			+ Anion-exchange chromatography (DEAE-Cellulose)	$A_{565}/A_{280} = 1.10$	—	
	Portieria hornemannii	0.02 mM phosphate buffer at pH 7.2 + freezing-thawing	Ammonium sulfate (55%) + anion exchange column chromatography (Q-Sepharose)	$A_{562}/A_{280} = 5.2$	—	Senthilkumar et al. (2013)
	Gracilaria lemaneiformis	10 mM phosphate buffer (pH 6.8) + agar + freeze-thaw	Anion-exchange chromatography (DEAE-Sepharose)	Recovery 16%	$OD_{565}/OD_{280}=3.2$	Niu et al. (2013)
	Porphyra yezoensis	10 mM phosphate buffer (pH 6.8) + freeze-thaw	Expanded bed chromatography (Phenyl-sepharose)	$0.96 \text{ mg g}^{-1}$	$OD_{565}/OD_{280} = 2.0-2.5$	Niu et al. (2010)
			Anion-exchange chromatography (DEAE-Sepharose)	$0.82 \text{ mg g}^{-1}$	$OD_{565}/OD_{280} = 4.5$	
Microalgae or cyanobacteria	Corallina elongata	10 mM sodium phosphate Ph7+filtration	Hydroxyapatite chromatography	$A_{566}/A_{280} = 6.67$	—	Rossano et al. (2003)
	Ceramium isogonum	1 mM K-phosphate (pH 6.8)	Ion-exchange chromatography (DEAE)	$A_{565}/A_{280} = 2.10$	—	Kaixian et al. (1993)
	Porphyridium marinum	Sodium phosphate buffer (20 mM, pH = 7.2) + freezing-freezing + ultrasound	Two steps of precipitation with ammonium sulfate + Dialyzed + anion exchange chromatography (DEAE-Cellulose)	$57 \text{ mg g}^{-1}$ dry weight Recovery = 72% $A_{545}/A_{280} = 5$	—	Gargouch et al. (2018)
	Bangia atropurpurea	50 mM phosphate buffer (pH 7.2) + sonicated	35% saturated ammonium sulfate + dialyzed	64.8% recovery $A_{562}/A_{280} = 2.47$	54.7% recovery $A_{615}/A_{280} = 0.77$	Punampalam et al. (2018)
			Gel filtration with Sephadex G-200	91.3% recovery $A_{562}/A_{280} = 4.76$	68.3% recovery $A_{615}/A_{280} = 2.80$	
			Reverse Phase-High Performance Liquid Chromatography (RP-HPLC)	100% recovery $A_{562}/A_{280} = 5.42$	100% recovery $A_{615}/A_{280} = 3.95$	

(Continued on following page)

TABLE 4 (Continued) Purification methods applied to the fractionation of phycobiliproteins.

Type of algae	Species	Tissue disruption/ Extraction method	Purification method	Yield/Extraction efficiency/ Recovery/PE purity index	Yield/Extraction efficiency/ Recovery/PC purity index	References
	Nostoc sp. strain HKAR-2	50 mM potassium phosphate buffer (pH 7.0) + sonication + repeated freezing	Ammonium sulfate precipitation (20–70%) + Dialyzed + Gel filtration chromatography (Sephacryl S-100 HR)	$A_{563}/A_{280} = 7.2$	$A_{615}/A_{280} = 3.18$	Kannaujiya and Sinha (2016b)
	Nostoc sp. strain HKAR-11	50 mM phosphate buffer (PB) (pH 7.0) + mortar and pestle + repeated freeze	Ammonium sulfate precipitation + Gel filtration chromatography (Sephacryl S-100 HR) + Hydrophobic interaction chromatography	97% recovery $A_{563}/A_{280} = 1.10$ 89%, recovery $A_{563}/A_{280} = 6.37$ 83% recovery $A_{563}/A_{280} = 11.53$	96% recovery $A_{615}/A_{280} = 0.92$ 80% recovery $A_{615}/A_{280} = 1.36$ 73% recovery $A_{615}/A_{280} = 5.75$	Kannaujiya and Sinha (2016a)
	Porphyra yezoensis	10 mM phosphate buffer (pH 6.8) + freeze-thaw	Expanded bed chromatography (Phenyl-sepharose) Anion-exchange chromatography (DEAE-Sephacryl)	0.96 mg g <sup>-1</sup> 0.82 mg g <sup>-1</sup>	OD <sub>565</sub> /OD <sub>280</sub> = 2.0–2.5 OD <sub>565</sub> /OD <sub>280</sub> = 4.5	Niu et al. (2010)

(9.8 mg ml<sup>-1</sup>) and 25°C (5.7 mg ml<sup>-1</sup>). For PE a low yield of 0.8 mg ml<sup>-1</sup> was obtained, demonstrating that PE is not an abundant phycobiliprotein in this species. In the same year, Khan et al. (2018) studied the production of PC and PE in two different strains of *Pseudanabaena*. *P. catenata* produced more PE in green light (25.5 ± 5.1 mg.L<sup>-1</sup>) but *P. amphigranulata* produced 86 ± 15 mg.L<sup>-1</sup> of PC in red light. For that, the authors have used three cycles of freezing-thawing of biomass in liquid nitrogen and then maceration using a mortar and pestle.

Included in the criteria to select the species to explore in the recovery of phycobiliproteins should also be the need for a pre-treatment of the cells before cell disruption. Following this rationale, the difference between the use of fresh or freeze-dried biomass was evaluated with the freeze-thawing and freeze-thawing + ultrasound process by Lauceri et al. (2019). For *Arthrospira platensis* GL the yield of PC was 81% for the frozen microalgae in freeze-thawing extraction, whereas in *Porphyridium cruentum* the higher recovery yield with the fresh algae (71%) was obtained for PE, which was independent of the method of extraction employed. Another study with fresh *Porphyridium cruentum*, using five repeated freeze-thaw fresh cycles was carried reporting a higher recovery yield of 86.6%, this value representing a concentration of 0.27 mg ml<sup>-1</sup> of R-PE (Ibáñez-González et al., 2016).

## Solvent and solvent-assisted extraction

For the optimization of the extraction, Hemlata et al. (2018) have used five different buffers as solvents to extract phycoerythrin from *Microchaete*, namely the citrate (pH-5.0; 0.1 M), acetate (pH-6.0; 0.1 M), carbonate (pH9.6; 0.1 M), Tris-

HCl (pH-7.2; 0.05 M) and the sodium phosphate buffers (pH-7.0; 0.1 M). After optimization, a higher yield of extraction (65.21 mg g<sup>-1</sup>) was obtained with the acetate buffer (pH-6.0; 0.1 M). They also showed the antioxidant, antibacterial, anticancer, and antifungal activities of *Microchaete*'s PE. Sfriso et al. (2018) used different concentrations of buffers, phosphate buffer (0.1, 1, 10, and 100 mM), and EDTA (0.1, 1, 10, and 100 mM), to later investigate the fluorescence of PE. Sharmila et al. (2017) also optimized the process with different buffers at different pH conditions, followed by different cell disruption methods and this result was found for different temperatures. The results were better with sodium phosphate pH 7.2 and using freeze-thaw at -20°C/-25°C. Sintra et al. (2021) also used sodium phosphate for extraction and achieved 90% of recovery of C-PC.

The use of protic ionic liquids (PIL) was also studied since the operating conditions required are softer compared to other alternatives. As ILs are expensive, PILs were investigated for their lower price. Rodrigues et al. (2018) used the PILs on *Spirulina* (*Arthrospira*) *platensis* in combination with ultrasonic and obtained a PC concentration of 0.75 g.L<sup>-1</sup> with PIL 2-HEAA + 2-HEAF. In 2019, Rodrigues et al. (2019) were able to double the concentration (PC concentration of 1.65 g.L<sup>-1</sup>) when PILs were used with mechanical agitation and thermal heating in *Spirulina platensis* and with the same PIL (2-HEAA + 2-HEAF).

At this point, and considering the works reviewed, it is not completely clear what should be considered the most appropriate technique to extract the phycobiliproteins from the different algal matrices. However, it is clear from the data that techniques like a microwave- and ultrasound-assisted extractions, as well as the use of only buffers as solvents, although less expensive, do not



TABLE 5 ABS applied to the purification of phycobiliproteins.

Species	Tissue disruption/ Extraction method	System parameters	Yield/Extraction efficiency/Recovery/ PE purity index/ Selectivity	Yield/Extraction efficiency/Recovery/PC purity index	References
<i>Porphyridium cruentum</i>	Phosphate potassium buffer + Bead mill	Bead mill + isoelectric precipitation + ABS (PEG-potassium phosphate) + ultrafiltration $V_r = 3.0$ PEG 1000 g.gmol <sup>-1</sup> TLL 45% (w/w) System pH 7.0	54%	$A_{545}/A_{280} = 4.2$	Ruiz-Ruiz et al. (2013)
<i>Porphyridium cruentum</i>	—	Polyethylene glycol (PEG)	$A_{545}/A_{280} = 3.2$ 92% recovery	—	Benavides and Rito-Palomares (2008)
<i>Porphyridium cruentum</i>	Ultrasonic bath	PEG/sulphate + isoelectric precipitation $V_r = 1.0$ PEG 1000 g.gmol <sup>-1</sup> System pH 7.0	$A_{545}/A_{280} = 4.1$ 72% yield	—	Hernandez-Mireles and Rito-Palomares (2006)
<i>Porphyridium cruentum</i>	Glass beads	Polyethylene glycol-phosphate $V_R = 1.0$ PEG 1000 g.gmol <sup>-1</sup> TLL 50%w/w System pH 7.0 $V_R = 0.3$ PEG 1450 g.gmol <sup>-1</sup> TLL 3%w/w System pH 7.0	$A_{545}/A_{280} = 2.8 \pm 0.2$ 82% yield     —	     $A_{615}/A_{280} = 2.1 \pm 0.2$ 98% yield	Benavides and Rito-Palomares (2005)
<i>Porphyridium cruentum</i>	Glass beads	Polyethylene glycol-phosphate $V_r = 1.0$ PEG 1450 g.gmol <sup>-1</sup> TLL 24.9% w/w System pH 8.0	$A_{545}/A_{280} = 2.9$ 77% yield	—	Benavides and Rito-Palomares (2004)
<i>Anabaena cylindrica</i>	Sodium phosphate (20 nM, pH 7.0)	Dextran T6 + Copolymer Pluronic PE 6400	—	$A_{620}/A_{280} = 2.16$	Sintra et al. (2021)
<i>Gracilaria</i> sp.	Maceration	10 wt% of surfactant and 0 or 0.3 wt% of SAIL	Recovery of PE = $78.8 \pm 0.8\%$	Selectivity = $13.6 \pm 0.1$ $0.047 \pm 0.004$	Vicente et al. (2019)
	Maceration + microfluidics + ultrafiltration	10 wt% of surfactant and 0 or 0.3 wt% of SAIL	416 mg of R-PE/g dry biomass		Seručník et al. (2020)

allow the development of processes of extraction with high selectivity. Nevertheless, it seems that *Spirulina* species is one of the simplest to process since the yields of extraction are higher than the ones obtained for the remaining species analysed. Moreover, the comparison between the results presented in Table 3 seems to suggest that ultrasonication combined with the use of ionic liquids is the best approach to extracting phycocyanin. Nevertheless, it should also be pointed out that the number of works is not so significant to allow us to define some heuristic rules on the best mechanical approaches or even on the best solvents to apply. One point is, however, clear; ionic

liquids are normally recognized as being more selective solvents (Martins et al., 2016), although the selectivity was not checked in the works analysed.

## Purification

Depending on the final application envisioned for PE, namely in the energy, food, cosmetic, or pharmaceutical industries, different purities are required, which greatly affect the production cost and the product price (Torres-Acosta et al.,

2016). Regardless of its efficiency, the extraction process often lacks selectivity. Low selectivity means the low purity of the extracts obtained. Solutions of purified phycobiliproteins are expensive, considering the established markets (e.g., as natural food colorants), but also new market applications with high economic and industrial relevance (energy, medical, pharmaceutical, and cosmetic). For reference, a purity index, expressed as the A565 nm/A280 nm ratio, of 0.7 represents a protein with food-grade purity, 3.9 as a reactive grade, and greater than 4.0 as analytical grade (Rito-Palomares et al., 2001).

## Chromatographic techniques

The most extensively used purification technique is chromatography, which can be ion-exchange, expanded-bed adsorption, or reverse-phase (Table 4). Often, the purification consists of a combination of techniques to reach higher purity levels. A typical example is the use of precipitation followed by chromatography. Nguyen et al. (2019) achieved a high purity index (3.3) of R-PE from *Gracilaria gracilis* after purification on DEAE-Sephacryl fast flow chromatography. The use of ammonium sulfate before chromatography is very common since it can remove amino acids, and consequently increase the purity of PE (Lee et al., 2017). Gargouch et al. (2018) used two-step precipitation with ammonium sulfate (first 20% and second 40%) before extraction on DEAE-Cellulose in the *Porphyridium marinum* algae and achieved a high PE purity (5.0). Senthilkumar et al. (2013) used only precipitation by ammonium sulfate (55%), obtaining a high PE purity (5.2) from red alga *Portieria hornemannii*. The use of ultrafiltration before anion exchange chromatography (SOURCE 15Q) was evaluated in the microalgae *Porphyridium cruentum*, achieving an analytical grade B-PE at the commercial level (purity index of 5.1). Munier et al. (2015) studied the difference between using only ammonium sulfate precipitation for PE purification and in combination with anion-exchange chromatography (DEAE-Cellulose), with the purity index increasing from 1.2 to 2.9.

Sudhakar et al. (2014) purified the PE from red seaweed *Gracilaria corticate* found abundantly in Indian waters throughout the seasons, through anion-exchange chromatography, to study the stability in carbonated drinks as a natural coloring, concluding that PE can be used in cool, sweetened, and carbonated drinks. The use of gel filtration (Sephacryl S-300) before anion-exchange chromatography was found for the extraction of PE in *Lyngbya arboricola* and *Synechococcus* sp., with a purity index of  $A_{560}/A_{280} = 5.2$  and  $A_{542}/A_{280} = 3.4$ , respectively (Tripathi et al., 2007; Kim et al., 2010).

Expanded bed adsorption chromatography is a suitable technique for protein recovery without the need for prior clarification. Bermejo et al. (2007) used this technique with *Porphyridium cruentum* achieving 66% of PE recovered. Niu

et al. (2010) compared the expanded bed and anion-exchange chromatography in *Porphyra yezoensis*, the largest and most important aquaculture species in China, achieving a higher yield from expanded bed adsorption but a higher purity ratio in anion-exchange chromatography. The use of this technique was efficient for the purification of PE in *Pyropia haitanensis* residue, with a concentration of 247.13 mg.L<sup>-1</sup> and purity index of 4.1 (Zhao et al., 2019).

Rossano et al. (2003) used hydroxyapatite for the purification of PE, which is a chromatographic resin that can be produced at a very low cost, achieving an optimal purity index of 6.7. Another study on *Porphyra yezoensis* Ueda used chromatography with hydroxyapatite as adsorbent material after continuous precipitation with ammonium sulfate and obtained a purity ratio of 5.5 of PE and 5.1 of PC (Cai et al., 2014).

The cyanobacterium *Nostoc* sp. has proved to be an excellent source of PE. Kannaujiya and Sinha, (2016) performed the purification with ammonium sulfate precipitation and gel filtration chromatography (Sephacryl S-100 HR) obtaining a high purity of PE (7.2). In another study, another purifying process was added, namely a hydrophobic interaction chromatography, allowing to obtain a purity of 11.5. Punampalam et al. (2018) extracted phycobiliproteins with saturated ammonium and isolated PE and PC by gel filtration (Sephadex G-200) and further purified by Reverse Phase-High Performance Liquid Chromatography (RP-HPLC), demonstrating a higher extraction and purity ratio for PE, while the protein had its antioxidant activity improved. MalairajMuthu et al. (2016) obtained the optimum purity of 5.9 from *Halymenia floresia* using an alternative to chromatography, the electrophoretic elution technique. Another purification used as ultrafiltration. Marcati et al. (2014) used ultrafiltration to separate PE from high molecular weight polysaccharides in *Porphyridium cruentum*, first using a 300,000 Da membrane and then a second with 10,000, leaving PE with a purity index of 2.3. Finally, in 2021, Martins et al. (2021) found that precipitation with ammonium sulfate has a good yield for R-PE and R-PC (100% and 81.1%, respectively), however, it was not selective for any of the PBPs, unlike using poly (acrylic acid) sodium salts as precipitation agents and conjugated with an ultrafiltration step (in this case R-PE was precipitated after extraction from *Gracilaria gracilis*, with a yield of 79.5%.

## Aqueous biphasic systems

ABS consists of a liquid-liquid extraction, where the biphasic system can be achieved by mixing two hydrophilic and non-miscible polymers or one salt and one polymer. Table 5 summarizes the conditions, yields of extraction and purities attained for the extraction of PE and PC using ABS in the various reports on the subject.

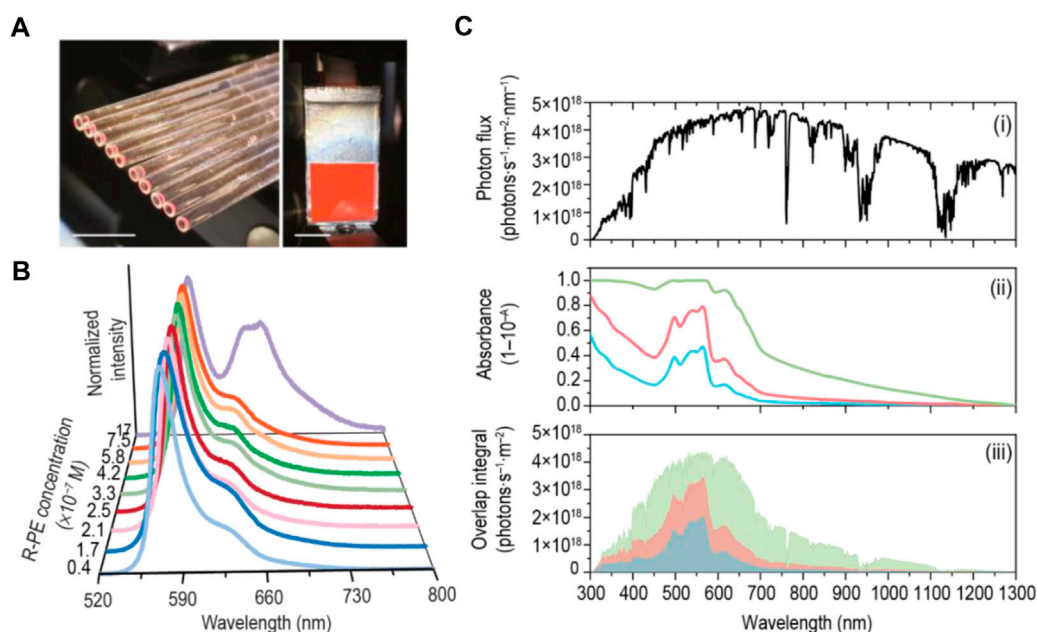


FIGURE 1

(A) Photographs of a bundle of cylindrical LSCs and a planar LSC based on R-PE solutions under AM1.5G. Scale bars: 1 cm; (B) Emission spectra of the R-PE solutions excited at 498 nm; (C) (i) Solar photon flux on Earth at AM1.5G, (ii) absolute absorbance of  $1.7 \times 10^{-7}$  M (blue line),  $3.3 \times 10^{-7}$  M (red line), and  $17 \times 10^{-7}$  M (green line), and (iii) integral overlap between the solar photon flux and the absolute absorbance. Reproduced with permission from Frias et al., 2019. Copyright 2019, Wiley-VCH Verlag GmbH & Co. KGaA, Weinheim.

The first work done in this context was by Benavides and Rito-Palomares (2004). In this work, the authors studied polyethylene glycol (PEG) with different molecular weights, 1,000, 1,450, 3,350, and 8,000 g.  $\text{gmol}^{-1}$ , obtaining the best purity for PE with PEG 1450, TLL 24.9% (w/w) at a pH of 8.0. Later, they showed that the best purity of PE was obtained for PEG 1000, (TLL 50% w/w and system pH 7.0) and PEG 1450 for PC. Later, Antelo et al. (2007) continued to test conventional ABS. Benavides and Rito-Palomares (2008) found that PEG 1000, beyond the higher yield for PE, induced the change of two conditions of the system: increased volume ratio (1.0 for 4.5) and decreased the TLL (50% for 45%), allowing to achieve a purity of 3.2.

The ABS process can also be used combined with other processes, such as isoelectric precipitation. Hernandez-Mireles and Rito-Palomares (2006) used three processes for PE extraction: cell disruption behind sonification, isoelectric precipitation with the addition of HCl, and PEG/phosphate ABS extraction achieving an excellent purity of 4.1. Ruiz-Ruiz et al. (2013) obtained an excellent purity (4.2) through four steps: cell disruption through bead mill, isoelectric precipitation, ABS, and lastly ultrafiltration. Later, in 2020, Sintra and collaborators (2020) used ABS based on copolymers and dextran to improve the purity and stability of C-PC. The extraction with sodium phosphate produced an extract with a purity of 0.52, and after purification, the purity was increased by 4-fold. Vicente et al.

(2019) tested several surfactants to isolate and maintain the R-PE structural integrity, identifying benzyldodecyltrimethylammonium bromide as the most adequate. Later, the same author studied the effect of using microfluidic devices to make the intensification of the process of purification of phycoerythrin, achieving very good results as well (Seručnik et al., 2020).

## Phycobiliproteins applications

The study of phycobiliproteins as bioactive compounds has been growing in different areas including cosmetics, food, textile, and pharmaceutical, because they are obtained from renewable abundant sources, have good stability, biocompatibility, and bioactivity (Guedes et al., 2011; Manivasagan et al., 2017). In this section, studies of the application of phycobiliproteins for different purposes will be reviewed and discussed.

## Food applications

The use of synthetic dyes in the food industry is potentially harmful to human health, due to their toxicity. Phycobiliproteins may play a major role as natural food colorants in their water-soluble protein-bound forms. Generally, these pigments present an enhanced solubility as well as high stability in the pH range of

TABLE 6 Reports of LSCs incorporating phycobiliproteins from algae and comparison of their performance with that of other natural-based molecules.

	Solvent	Fluorophore/Host matrix	Dimensions (cm <sub>3</sub> )	G	$\eta_{opt}$ (%)	PCE (%)	Ref.
Natural molecules	Triton X-100	Phycobilisomes/Acrylamide	2.2 × 2.2×0.05	44	12.5	—	Vossen et al. (2016)
	DCM	Chlorophyll/t-U (5,000)	1.0 × 1.0×0.3	3.3	3.70	0.10	Frias et al. (2018)
	Water	R-PE/Glass container	2.0 × 2.0×1.0	2	6.88	0.27	Frias et al. (2019)
		mScarlet/PDMS slab	2.5 × 2.5×0.6	0.54	2.58	—	Sadeghi et al. (2019)
		eGFP/Glass container	2.0 × 2.0×1.0	2	3.30	0.35	Carlos et al. (2020)
			4.0 × 2.0×1.0	4		0.12	Correia et al. (2022)
Carbon dots		PC/Glass container			2.65	0.21	
		N-CDs/PMMA	2.5 × 1.6×0.1	4.88	4.75	3.94	Li et al. (2017)
		N-CDs/PMMA	2.0 × 2.0×0.2	10	12.2	2.63	Gong et al. (2018)
		N-CDs/PVP	1.8 × 1.8×0.11	4.09	5.02	4.97	Wang et al. (2018)
		N-CDs/custom glass	5 × 2.5×0.42	5.5	4.52	2.49	Mateen et al. (2019)
		N-GQDs/PMMA	2 × 2×0.3	6.7	—	8.77	Saeidi et al. (2020)
		UV-CDs/PVP	10 × 10×0.2	50	1.10	—	Zhou et al. (2018)
		NaOH-CDs/PVP					
		Narrow sized CDs/PVP	10 × 10×nd	4.5	2.70	1.04	Zhao et al. (2021)
			15 × 15×nd	6.8	2.20	1.13	
	Ethanol	CDs/PVP	10 × 10×0.9	2.8	1.60	0.7	Zhao et al. (2019)
	DMF		10 × 10×1	2.5	0.92	—	Zhao (2019)
		OLA-CDs/PLMA	10 × 1.5×0.2	10	1.20	4.65	Zhou et al. (2018)
	Water	N-CDs/PVP	2.5 × 2×0.2	5.5	5.20	4.06	Ma et al. (2019)
	Acetic acid	TPFE-Rho/PMMA	2.5 × 2×0.2	2.8	5.20	4.06	
	Water	b-CDs/PVA	8 × 8×0.8	10	2.30	—	Zdrasil et al. (2020)
	Ethanol	g-CDs/PVP					
		r-CDs/PVP + PEI					
	Methanol	Y-CD/PVP	10 × 10×0.9	2.5	4.3	3.8	Li et al. (2021)
		R-CD/PVP					

t-U(5,000), tri-ureasil organic-inorganic hybrid; PDMS, polydimethylsiloxane; eGFP, enhanced Green Fluorescent Protein; N-CDs, nitrogen-doped CDs; PMMA, polymethylmethacrylate; PVP, polyvinylpyrrolidone; N-GQDs, nitrogen-doped graphene quantum dots; UV-CDs, ultraviolet active carbon-dots; NaOH-CDs, NaOH, treated carbon-dots; OLA, oleylamine; PLMA, poly (lauryl methacrylate); b-CDs, blue-emitting carbon dots; g-CDs, green-emitting carbon dots; r-CDs, red-emitting carbon dots; PEI, polyethylenimine; Y-CDs, yellow carbon dots; R-CDs, red carbon dots.

4–10 (Galland-Irmouli et al., 2000; Munier et al., 2014). Phycoerythrin holds potential as an alternative red natural food colorant. Yet more relevant, allophycocyanin and PC present bluish-green and dark blue hues, respectively, which are rarely found in other natural sources. However, to guarantee the stability of the phycobiliproteins in the desired final product, some conditions must be considered, such as temperature, pH, and light (Manirafasha et al., 2016).

The addition of acids, salts, and sucrose was proven to help prevent the denaturation of phycobiliproteins. Mishra et al. (2010) found that among the preservatives studied: citric acid, sucrose, sodium chloride, and calcium chloride, citric acid was the best preservative for C-PE as it acts as a chelator and reduces the pH preventing protein degradation. The stability of PE applied in three carbonated drinks, namely, Lehar soda, 7'UP, and TATA mineral water were evaluated. Although for the 7'UP drink, the color was

retained for more than 30 days, for the other drinks it was stable for only 3 days. The authors argue that the sugar present in 7'UP acted as a preservative retaining the colour for longer times (Sudhakar et al., 2014). The study of thermokinetic stability in PC and PE extracted from *Nostoc sp.* in preservatives showed that for both phycobiliproteins, benzoic acid is the best preservative at 4°C compared to citric acid, sucrose, ascorbic acid, and calcium chloride, at 4°C, 25°C, and 40°C (Kannaujiya and Sinha 2016b). Zhang et al. (2020) evaluated the stability of C-PC in whey protein in acidified conditions during light storage. It was found that whey protein helped protect C-PC from color degradation in light. The color stability of PE from a crude extract from *Rhodomonas salina* was studied, the best conditions being established under white fluorescent light for 8 h, a maximum temperature of 40°C, 20% (v/v) of ethanol, and pH range of 3.9–8. (Marraskuranto et al., 2019).



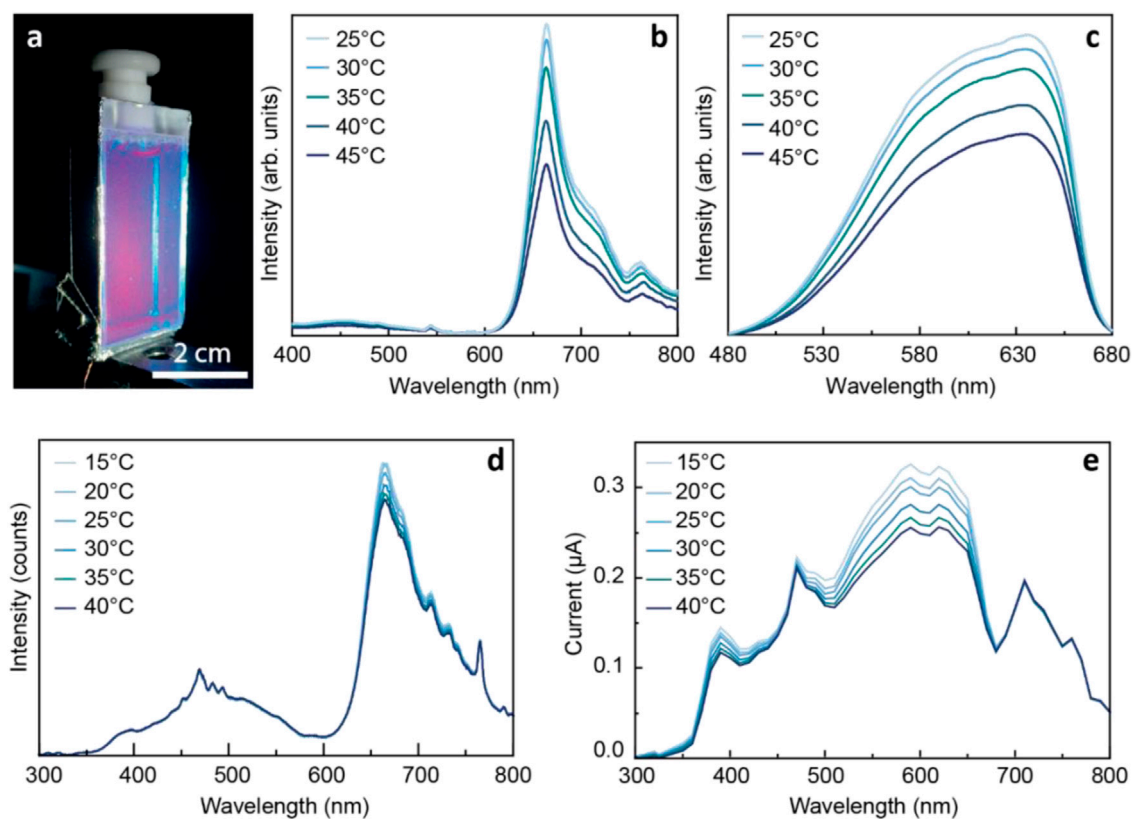


FIGURE 2

(A) Photograph of the LSC/sensor based on a glass container filled with PC-based aqueous solutions under AM1.5G illumination. The PV cell is located at the bottom edge. PC-based optical sensors temperature-dependent (B) emission and (C) excitation spectra excited at 380 nm and monitored at 715 nm, respectively, and (D) emission spectra and (E) generated short-circuit current under solar simulator irradiation. Reproduced from (Correia et al., 2022) under a CC BY 4.0 license.

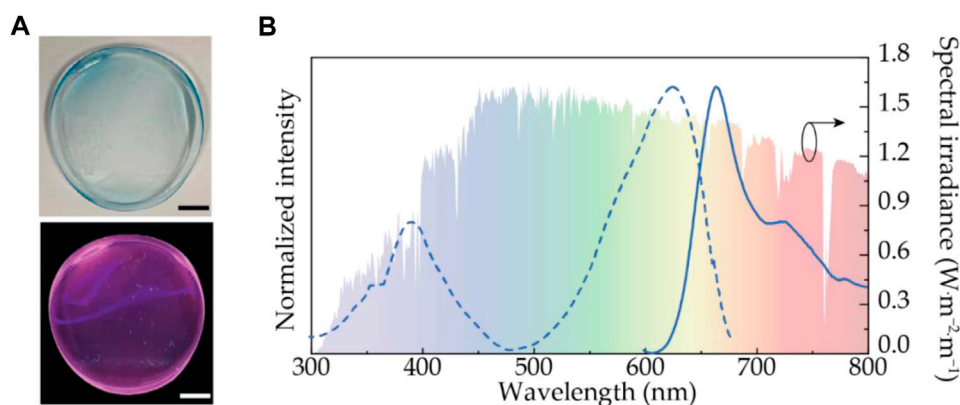


FIGURE 3

(A) Photographs of PC incorporated in PVA (Dias et al., 2022) under white light (top) and UV irradiation at 365 nm (bottom). Scale bars:  $10^{-2}$  m. (B) Emission and excitation spectra excited at 575 nm and monitored at 720 nm, respectively. The c-Si spectral response is shown on the right y-axis. (B) Excitation spectra for R-PE/PVA, C-PC/PVA, and FX/PVA monitored at 720 nm. The shadowed area represents the AM1.5G solar spectrum (right y-axis). Reproduced from (Dias et al., 2022) under a CC BY 4.0 license.

The impact of the addition of these pigments in dairy products was also evaluated by some authors. PE and PC extracted from Atacama Cyanobacteria had chemical stability at pH 5-8 and temperature up to 50°C. The addition of the pigments to skim milk fortified allowed for higher scores in sensory tests (Galetović et al., 2020). In another study, three types of milk bases were compared: milkshakes, liquid yogurts, and yogurts. Successfully, all the products evaluated exhibited the pink color of B-PE, with proven stability (García et al., 2021). One technique used to improve pigment stability is microencapsulation, which consists of protecting some material from the environment in which it is contained. Ganesan and Shanmugam (2020) encapsulated PE with kappa-carrageenan and guar-gum to enhance the stability and functionality of the pigment in ice cream, resulting in better rheology and augmented intensity of pink color over 90 days of storage.

## Nutraceutical and pharmaceutical applications

Oxidative stress is the imbalance between free radicals and antioxidants in the body. This imbalance can cause various diseases such as diabetes, cancer, and inflammation, just to mention a few. To prevent and treat these diseases, there are already some phytochemicals such as tocopherol, caffeic acid, and zeaxanthin (Pagels et al., 2019). PC and PE have also been studied for this purpose due to their antioxidant, antibacterial, anticancer, and anti-inflammatory activities. The antioxidant activity of PC isolated from *Anabaena* biomass proved to be good against DPPH (2,2-diphenyl-1-picrylhydrazyl) and ABTS (2,2'-azinobis-3-ethylbenzothiazoline-6-sulfonic acid) free radical and was able to attenuate the liver structural deformations caused by carbon tetrachloride (CCl<sub>4</sub>) in rats (Osman et al., 2020). Fernández-Rojas et al. (2015) were the first to report that C-PC prevents mitochondrial dysfunction and increases oxidative defense in mice. This study motivated Wang et al. (2020) to study the effects of PC against doxorubicin (DOX), a chemotherapeutic agent that causes Chemotherapy-Induced Cognitive Impairment (CICI), a common detrimental effect of cancer treatment. Studies in mice have shown that PC has the potential to treat CICI as it improves established DOX-induced cognitive deficits, due to the inhibition of neuroinflammatory and oxidant stress and attenuation of mitochondrial and synaptic dysfunction. In addition to the antioxidant activator, PE is also known to be effective against age-related diseases. In *in vitro* experiments, the antioxidant and immunomodulation potential of C-PC extracted from *Spirulina* were also evaluated, without revealing any toxicity in the mice (Grover et al., 2021). Yoshimoto et al. (2019) also found immunomodulation activity, as well as anti-inflammatory actions in the mucosal immune responses. R-PE can inhibit

the growth of subcutaneous transplanted tumors, repair damaged mucosa to protect the intestinal barrier, and regulate the immune function of mice (Qi et al., 2019). Regarding PC, studies have indicated that this pigment can induce apoptosis, one of the important mechanisms in the inhibition of cancer cell proliferation, of multiple non-small cell lung cancer cells and colorectal cancer cells (Hao et al., 2019; Hamdan et al., 2021).

Photodynamic therapy (PDT) is a treatment that combines light and photosensitizing agents to destroy cancer cells. Phycobiliproteins can be used as photosensitizers because they can emit strong fluorescence after being irradiated with a laser (Li et al., 2019). A study on the inhibition of  $\beta$ -site amyloid precursor protein cleaving enzyme-1 (BACE1) by PE revealed potential in the application of C-PE as a therapeutic agent in Alzheimer's disease (Chaubey et al., 2019). Lian et al. (2020) found that treatment in rats with C-PC attenuated gastric ulcers by suppressing oxidation and inflammation and increasing gastroprotection.  $\beta$ -carotene and PC added to the standard diet of Nile tilapia, allowed us to conclude that the fish with a diet supplemented with PC had a higher survival rate, with an increase in intestinal digestive enzymes such as amylase, trypsin, and lipase, and improved hematological parameters such as immunoglobulin M (IgM), catalase, and total antioxidant capacity (T-AOC) (Hassaan et al., 2021).

## Fluorescence applications: Sensing and solar energy harvesting and conversion

Besides the application of phycobiliproteins in photodynamic therapy, another application is their use as fluorescent probes for analyte sensing. You et al. (2020) developed a luminescent nanoprobe based on the upconversion of nanoparticles conjugated with PC to detect the bioactivity of myeloperoxidase, a protein that causes inflammation-related diseases. Yang et al. (2020) have found a viable method for the detection of ochratoxin A and zearalenone, a quantitative fluorescence image analysis based on multicolor upconversion nanocrystal (UCN)-encoded microspheres. PE was also used for the detection of transcription factors and as a fluorescent label in the microsphere (Sun et al., 2021).

Metals are by-products of several industrial processes that present toxic, corrosive, and malodorous properties. The study of PE as a hydrosulphide selective optical probe has shown promising results in freshwater and effluent samples through the fluorescence 'turn off' phenomenon, (Ghosh and Mishra 2020). The same mechanism was applied to mercury, in which C-PE was successfully used as a natural agent for the selective detection of environmentally hazardous Hg<sup>2+</sup> (Ghosh et al., 2020). R-PE has shown potential when conjugated with silver nanoparticles (AgNPs) for the detection of Cu<sup>2+</sup>. Xu et al. (2019) reported that the addition of the ion Cu<sup>2+</sup> to R-PE-AgNPs leads to a decrease in fluorescence and color change due to the

increasing size of the particle diameter. This change in fluorescence was directly proportional to the concentration of  $\text{Cu}^{2+}$ , therefore this method can be applied to real wastewater samples.

Ghosh et al. (2020b) developed a natural protein-based DNA sensor with PC and graphene oxide, a complex which allowed differentiating DNA from a mixture of other biomolecules (amino acids, sugars, polydispersed exopolysaccharides, other proteins) through 'turn off, turn on fluorescence. The detailed study of the structure and composition of phycobiliproteins can be an obstacle to their use as proteins from natural sources. Studies have found that the central subunits of PC and PE complexes, although absent from the crystal structures, may be crucial for their stability, and even that PE is the best phycobiliprotein to be used as a fluorescent probe due to the stabilizing effect of its  $\gamma$  subunits (Leney et al., 2017; Kaldmäe et al., 2019).

Another field where R-PE stands out due to its fluorescence is bio-based luminescent solar concentrators (LSCs, Figure 1A). Frias et al. (2019) used R-PE aqueous solutions to fabricate planar and cylindrical LSCs with maximum optical conversion efficiency values of 6.88%, being the largest among other biomolecules studied such as chlorophyll or Green Fluorescent Protein, Table 6. The high figures of merit arise from the photoluminescence features of the R-PE, namely the emission in the absorption region of typical Si photovoltaic devices (Figure 1B) and high spectral overlap between the R-PE absorption and the sunlight (Figure 1C), which indicated that the most concentrated aqueous solution has the potential to absorb  $\approx 27\%$  of the solar photon flux on the Earth ( $4.3 \times 10^{21}$  photons $\cdot\text{s}^{-1}\cdot\text{m}^{-2}$ ) (Frias et al., 2019).

Combining the sensing ability with that of sunlight harvesting, Correia et al. (2022) reported a surprising example of a novel application by fabricating a sustainable solar optical temperature sensor based on PC aqueous solutions (Figure 2A). As PC optical features are temperature-dependent (Figures 2B,C), the electrical output of the PC-based LSC also varies (Figure 2D). After calibration, this device allows us to infer the temperature values from the output voltage of the photovoltaic cell coupled to the LSC. Moreover, the electrical power delivered by the coupled PV cells under solar radiation was enough to power a small circuit able to read voltage values, convert it to temperature and send real-time data through Wi-Fi to a smartphone app or website, bridging these sensors to the Internet of Things (IoT). The goal here was the building integration of photovoltaic and sensing units as smart windows, which could contribute to the future design of zero-energy buildings with enhanced energy consumption management (Correia et al., 2022).

To improve the processability of the phycobiliproteins, the PC molecules were entrapped into solid matrices, such as poly (vinyl alcohol (PVA) (Dias et al., 2022). It was demonstrated that the ability to down-shift the UV radiation observed for the

biomolecules in solution (Figure 2) was kept after their incorporation into the host, Figure 3. Nonetheless, it was observed a decrease in the emission quantum yield ( $0.09 \pm 0.01$ ) when compared to the value found for the aqueous solution together with poor photostability, which suggests molecular aggregation (Zhao et al., 2021). Therefore, this preliminary study reinforces the need for further optimization of the incorporation procedures.

## Conclusion and future perspectives

In this work, the downstream processes reported to recover phycobiliproteins from marine and freshwater biomass were reviewed. The different sources were highlighted (macroalgae, microalgae, and cyanobacteria), and the solvents and techniques used in the extraction and purification of the fluorescent proteins, as well as their main applications taking advantage of being fluorescent/luminescent, were assessed. Most articles reviewed in this work focus only on conventional approaches to extraction and purification, at a laboratory scale paying attention only to the extraction yield and purity level obtained. However, some disadvantages remain, such as poor selectivity, high energetic costs, and high investment in equipment, for example considering the chromatographic techniques (Bleakley and Hayes, 2017). From the publications analysed, it seems that the majority is still using the most conventional solvents, without considering their low selectivity. In this sense, the use of more task-specific solvents is advised. Some authors briefly started to evaluate the effect of some ILs, however, there is a need of choosing the best ones only by their capacity to extract the phycobiliproteins, however without considering too much their economic, environmental impact, safety, or even their potential to develop processes appropriate to scale-up. Taking this into consideration, some other solvents are being used in other fields, but not so much in the marine biorefinery field, although the best results were obtained. Examples of these classes of eco-solvents are the eutectic solvents and more recently, the bio-solvents. Indeed, eutectic solvents were applied in the solid-liquid extraction of proteins as performance boosters (Yue et al., 2021). These are composed of a hydrogen bond acceptor and a hydrogen bond donor and are prepared by mixing natural starting materials with a high melting point, in different molar ratios, to form a liquid. They are simpler to prepare and purify, and of lower costs (Wahlström et al., 2016). Also, they form aqueous biphasic systems (ABS) capable to perform the separation/purification of proteins in a single-step [9], without using chromatography. Bio-solvents, by their turn, are solvents prepared from natural sources, with high biodegradability, abundance, and green credentials, being cyrene the most popular up to now (Sherwood et al., 2014). The set of bio-solvents although small is expanding, and with this expansion more task-specific bio-solvents will be produced on industrial

scale, allowing thus to consider them as good alternatives for the development of downstream processes of lower environmental and economic impact, while maintaining or even increasing their capacity as solvents. Nevertheless, aiming at a possible application of some of these processes at an industrial scale much more needs to be defined and investigated, namely the economic and environmental impact of the overall process and stability of the fluorescent proteins. Promising food and pharmaceutical applications of PE were demonstrated primarily at the laboratory scale as pigments and potent antioxidants. Additionally, the photosensitizing and fluorescent properties of these proteins show great potential in varied fields including photodynamic cancer therapy and as organic sunlight harvesters for the improved efficacy of solar panels.

Some works approached the question of the chemical stability of these fluorescent proteins. However, little is known regarding their optical stability. Considering that part of the applications with the highest interest from an economic point of view is related to the optical activity of the phycobiliproteins, the development of strategies to improve the optical stability is a crucial demand, not only in liquid samples but also very important in solid matrices.

## Author contributions

GK and MK contributed to conception and design of the study. GK, MK, LD, and SC organized the database. GK and MK wrote the first draft of the manuscript. LD and SC wrote sections of the manuscript. SV, RF, and JC revised the first draft of the manuscript. All authors read, and approved the submitted version.

## References

- Antelo, F. S., Anschau, A., Costa, J. A. V., and Kalil, S. J. (2007). Extraction and purification of C-phycoerythrin from *Spirulina platensis* in conventional and integrated aqueous two-phase systems. *J. Braz. Chem. Soc.* 21, 921–926. doi:10.1590/S0103-50532010000500022
- Barkia, I., Saari, N., and Manning, S. R. (2019). Microalgae for high-value products towards human health and nutrition. *Mar. Drugs* 17, 304. doi:10.3390/md17050304
- Benavides, J., and Rito-Palmares, M. (2004). Bioprocess intensification: A potential aqueous two-phase process for the primary recovery of B-phycoerythrin from *Porphyridium cruentum*. *J. Chromatogr. B* 807, 33–38. doi:10.1016/j.jchromb.2004.01.028
- Benavides, J., and Rito-Palmares, M. (2008). Generic application of polyethylene glycol-salt Aqueous Two-Phase Systems for the development of processes to biological products primary recovery. *Rev. Mex. De Ing. Quimica* 7 (2), 99–111.
- Benavides, J., and Rito-Palmares, M. (2005). Potential aqueous two-phase processes for the primary recovery of colored protein from microbial origin. *Eng. Life Sci.* 5, 259–266. doi:10.1002/elsc.200420073
- Bermejo, R., Ruiz, E., and Acien, F. G. (2007). Recovery of B-phycoerythrin using expanded bed adsorption chromatography: Scale-up of the process. *Enzyme Microb. Technol.* 40, 927–933. doi:10.1016/j.enzmictec.2006.07.027
- Bleakley, S., and Hayes, M. (2017). Algal proteins: Extraction, application, and challenges concerning production. *Foods* 6 (5), 33. doi:10.3390/foods6050033
- Bryant, D. A. (1982). Phycoerythrocyanin and phycoerythrin: properties and occurrence in cyanobacteria. *J. Gen. Microbiol.* 128, 835–844.
- Cai, C., Wang, Y., Li, C., Guo, Z., Jia, R., Wu, W., et al. (2014). Purification and photodynamic bioactivity of phycoerythrin and phycocyanin from *Porphyra yezoensis* Ueda. *J. Ocean. Univ. China* 13, 479–484. doi:10.1007/s11802-014-2148-x
- Caporgno, M. P., and Mathys, A. (2018). Trends in microalgae incorporation into innovative food products with potential health benefits. *Front. Nutr.* 5, 58–10. doi:10.3389/fnut.2018.00058
- Carlos, C. P. A., Correia, S. F. H., Martins, M., Savchuk, O. A., Coutinho, P. J. A., André, P. S., et al. (2020). Environmentally friendly luminescent solar concentrators based on an optically efficient and stable green fluorescent protein. *Green Chem.* 22, 4943–4951. doi:10.1039/D0GC01742F
- Cuellar-Bermudez, S. P., Aguilar-Hernandez, I., Cardenas-Chavez, D. L., Ornelas-Soto, N., Romero-Ogawa, M. A., and Parra-Saldivar, R. (2014). Extraction and purification of high-value metabolites from microalgae: essential lipids, astaxanthin and phycobiliproteins. *Microb. Biotechnol.* 8 (2), 190–209. doi:10.1111/1751-7915.12167
- Chaubey, M. G., Patel, S. N. K., Rastogi, R. P., Srivastava, P. L., Singh, A. K., Madamwar, D., et al. (2019). Therapeutic potential of cyanobacterial pigment protein phycoerythrin: In silico and in vitro study of BACE1 interaction and in vivo  $\alpha\beta$  reduction. *Int. J. Biol. Macromol.* 134, 368–378. doi:10.1016/j.jbiomac.2019.05.006

## Funding

This work was developed within the scope of the project CICECO-Aveiro Institute of Materials, UIDB/50011/2020, UIDP/50011/2020 and LA/P/0006/2020, and Instituto de Telecomunicações, UIDB/50008/2020-UIDP/50008/2020 and the projects SOLPOWINS (PTDC/CTM-REF/4304/2020) and PLANETa (CENTRO-01-0247-FEDER-181242) financed by national funds through the FCT/MEC (PIDDAC). S. F. H. C. thanks European Space Agency (ESA STAR AO 2-1790/21/NL/GLC/ov). GK acknowledges the financial support through BD/REITORIA/9328/2020, MK and LD thank FCT for the financial support through SFRH/BD/138413/2018 and UI/BD/153491/2022, respectively. The authors also thank the financial support from FCT considering the following references: UI/BD/153491/2022, LD UI/BD/153491/2022, and PTDC/BTA-BTA/30914/2017.

## Conflict of interest

The authors declare that the research was conducted in the absence of any commercial or financial relationships that could be construed as a potential conflict of interest.

## Publisher's note

All claims expressed in this article are solely those of the authors and do not necessarily represent those of their affiliated organizations, or those of the publisher, the editors and the reviewers. Any product that may be evaluated in this article, or claim that may be made by its manufacturer, is not guaranteed or endorsed by the publisher.



- Choi, W., and Lee, H. (2018). Effect of ultrasonic extraction on production and structural changes of C-phycoerythrin from marine *Spirulina maxima*. *Int. J. Mol. Sci.* 19, 220–311. doi:10.3390/ijms19010220
- Correia, S. F. H., Bastos, A. R. N., Martins, M., Macário, I. P. E., Veloso, T., Pereira, J. L., et al. (2022). Bio-based solar energy harvesting for onsite mobile optical temperature sensing in smart cities. *Adv. Sci. (Weinh.)* 9, 2104801–2104810. doi:10.1002/advs.202104801
- Dias, L. M. S., Kovaleski, G., Fu, L., Dias, T. R., Macário, I. P. E., Correia, S. F. H., et al. (2022). Uncovering the use of fucoxanthin and phycobiliproteins into solid matrices to increase their emission quantum yield and photostability. *Appl. Sci. (Basel)* 12, 5839–5911. doi:10.3390/app12125839
- Dumay, J., Clément, N., Moranchais, M., and Fleurence, J. (2013). Optimization of hydrolysis conditions of *Palmaria palmata* to enhance R-phycoerythrin extraction. *Bioresour. Technol.* 131, 21–27. doi:10.1016/j.biortech.2012.12.146
- Dumay, J., Moranchais, M., Munier, M., Le Guillard, C., and Fleurence, J. (2014). Sea plants. *Adv. Botanical Res.* 71.
- Fernández-Rojas, B., Rodríguez-Rangel, D. S., Granados-Castro, L. F., Negrette-Guzmán, M., León-Contreras, J. C., Hernández-Pando, R., et al. (2015). C-phycoerythrin prevents cisplatin-induced mitochondrial dysfunction and oxidative stress. *Mol. Cell. Biochem.* 406, 183–197. doi:10.1007/s11010-015-2436-9
- Francavilla, M., Manara, P., Kamaterou, P., Monteleone, M., and Zabaniotou, A. (2015). Cascade approach of red macroalgae *Gracilaria gracilis* sustainable valorization by extraction of phycobiliproteins and pyrolysis of residue. *Bioresour. Technol.* 184, 305–313. doi:10.1016/j.biortech.2014.10.147
- Frias, A. R., Correia, S. F. H., Martins, M., Ventura, S. P. M., Pecoraro, E., Ribeiro, S. J. L., et al. (2019). Sustainable liquid luminescent solar concentrators. *Adv. Sustain. Syst.* 3, 1800134–1800210. doi:10.1002/adsu.201800134
- Frias, A. R., Pecoraro, E., Correia, S. F. H., Minas, L. M. G., Bastos, A. R., Garcia-Revilla, S., et al. (2018). Sustainable luminescent solar concentrators based on organic-inorganic hybrids modified with chlorophyll. *J. Mat. Chem. A Mat.* 6, 8712–8723. doi:10.1039/C8TA01712C
- Galetović, A., Seura, F., Gallardo, V., Graves, R., Cortés, J., Valdivia, C., et al. (2020). Use of phycobiliproteins from atacama cyanobacteria as food colorants in a dairy beverage prototype. *Foods* 9 (244), 244–313. doi:10.3390/foods9020244
- Galland-Irmouli, A. V., Pons, L., Luçon, M., Villaume, C., Mrabet, N. T., Guéant, J. L., et al. (2000). One-step purification of R-phycoerythrin from the red macroalga *Palmaria palmata* using preparative polyacrylamide gel electrophoresis. *J. Chromatogr. B Biomed. Sci. Appl.* 739, 117–123. doi:10.1016/S0378-4347(99)00433-8
- Gallego, R., Martínez, M., Cifuentes, A., Ibáñez, E., and Herrero, M. (2019). Development of a green downstream process for the valorization of *Porphyridium cruentum* biomass. *Molecules* 24, 1564. doi:10.3390/molecules24081564
- Ganesan, A. R., and Shanmugam, M. (2020). Isolation of phycoerythrin from *Kappaphycus alvarezii*: A potential natural colourant in ice cream. *J. Appl. Phycol.* 32, 4221–4233. doi:10.1007/s10811-020-02214-0
- García, A. B., Longo, E., Murillo, M. C., and Ana Bermejo, R. (2021). Using a B-phycoerythrin extract as a natural colorant: Application in milk-based products. *Molecules* 26, 297–313. doi:10.3390/molecules26020297
- Gargouch, N., Karkouch, I., Elleuch, J., Elkhoui, S., Michaud, P., Abdelkafi, S., et al. (2018). Enhanced B-phycoerythrin production by the red microalga *Porphyridium marinum*: A powerful agent in industrial applications. *Int. J. Biol. Macromol.* 120, 2106–2114. doi:10.1016/j.ijbiomac.2018.09.037
- Ghosh, T., Chatterjee, S., Bhayani, K., and Mishra, S. (2020). A natural cyanobacterial protein C-phycoerythrin as an Hg<sup>2+</sup> selective fluorescent probe in aqueous systems. *New J. Chem.* 44, 6601–6609. doi:10.1039/D0NJ01059F
- Ghosh, T., and Mishra, S. (2020). A natural cyanobacterial protein C-phycoerythrin as an HS<sup>−</sup> selective optical probe in aqueous systems. *Spectrochimica Acta Part A Mol. Biomol. Spectrosc.* 239, 118469. doi:10.1016/j.saa.2020.118469
- Ghosh, T., Mondal, A., Vyas, A., and Mishra, S. (2020). A “one-tube” synthesis of a selective fluorescence “turn off/on” DNA probe based on a C-phycoerythrin-graphene oxide (CPC-GO) bio composite. *Int. J. Biol. Macromol.* 163, 977–984. doi:10.1016/j.ijbiomac.2020.06.286
- Glazer, A. N. (1994). Phycobiliproteins—a family of valuable, widely used fluorophores. *J. Appl. Phycol.* 6, 105–112.
- Gong, X., Ma, W. W., Li, Y. X., Zhong, L. Q., Li, W. J., and Zhao, X. J. (2018). Fabrication of high-performance luminescent solar concentrators using N-doped carbon dots/PMMA mixed matrix slab. *Org. Electron.* 63, 237–243. doi:10.1016/j.orgel.2018.09.028
- Grover, P., Bhatnagar, A., Kumari, N., Bhatt, A. N., Nishad, D. K., and Purkayastha, J. (2021). C-Phycocyanin-a novel protein from *Spirulina platensis*-in vivo toxicity, antioxidant and immunomodulatory studies. *Saudi J. Biol. Sci.* 28, 1853–1859. doi:10.1016/j.sjbs.2020.12.037
- Guedes, A. C., Amaro, H. M., and Malcata, F. X. (2011). Microalgae as sources of carotenoids. *Mar. Drugs* 9, 625–644. doi:10.3390/md9040625
- Guillard, L. C., Dumay, J., Donnay-Moreno, C., Bruzac, S., Ragon, J.-Y., Fleurence, J., et al. (2015). Ultrasound-assisted extraction of R-phycoerythrin from *Grateloupia turuturu* with and without enzyme addition. *Algal Res.* 12, 522–528. doi:10.1016/j.algal.2015.11.002
- Günkerken, E., D'Hondt, E., Eppink, M. H. M., Garcia-Gonzalez, L., Elst, K., and Wijffels, R. H. (2015). Cell disruption for microalgal biorefineries. *Biotechnol. Adv.* 33, 243–260. doi:10.1016/j.biotechadv.2015.01.008
- Hamdan, N., Jwad, B. A. A. A., and Jasim, S. A. (2021). Synergistic anticancer effects of phycocyanin and *Citrullus colocynthis* extract against WiDr, HCT-15 and HCT-116 colon cancer cell lines. *Gene Rep.* 22, 100972. doi:10.1016/j.genrep.2020.100972
- Hao, S., Li, S., Wang, J., Zhao, L., Yan, Y., Wu, T., et al. (2019). C-phycoerythrin suppresses the in vitro proliferation and migration of non-small-cell lung cancer cells through reduction of RIPK1/NF-κB activity. *Mar. Drugs* 17, 362. doi:10.3390/md17060362
- Hassan, M. S., Mohammady, E. Y., Soaudy, M. R., Sabae, S. A., Mahmoud, A. M. A., and El-Haroun, E. R. (2021). Comparative study on the effect of dietary β-carotene and phycocyanin extracted from *Spirulina platensis* on immune-oxidative stress biomarkers, genes expression and intestinal enzymes, serum biochemical in Nile tilapia, *Oreochromis niloticus*. *Fish. Shellfish Immunol.* 108, 63–72. doi:10.1016/j.fsi.2020.11.012
- Hemlata, V., Afreen, S., and Fatma, T. (2018). Extraction, purification and characterization of phycoerythrin from *Microchaete* and its biological activities. *Biocatal. Agric. Biotechnol.* 13, 84–89. doi:10.1016/j.bcab.2017.11.012
- Hernandez-Mireles, T., and Rito-Palomares, M. (2006). Improved recovery of B-phycoerythrin produced by the red microalga *Porphyridium cruentum*. *J. Chem. Technol. Biotechnol.* 81, 989–996. doi:10.1002/jctb.1503
- Ibáñez-González, M. J., Mazzuca-Sobczuk, T., Redondo-Miranda, R. M., Molina-Grima, E., and Cooney, C. L. (2016). A novel vortex flow reactor for the purification of B-phycoerythrin from *Porphyridium cruentum*. *Chem. Eng. Res. Des.* 111, 24–33. doi:10.1016/j.cherd.2016.03.032
- Juin, C., Chérouvier, J.-R., Thiéry, V., Gagez, A.-L., Bérard, J.-B., Joguet, N., et al. (2014). Microwave-assisted extraction of phycobiliproteins from *Porphyridium purpureum*. *Appl. Biochem. Biotechnol.* 175, 1–15. doi:10.1007/s12010-014-1250-2
- Jung, S.-M., Park, J. S., Shim, H. J., Kwon, Y. S., Kim, H. G., and Shin, H. S. (2016). Antioxidative effect of phycoerythrin derived from *Grateloupia filicina* on rat primary astrocytes. *Bioprocess Eng.* 21, 676–682. doi:10.1007/s12257-016-0369-0
- Kaixian, Q., Franklin, M., and Borowitzka, M. A. (1993). The study for isolation and purification of R-phycoerythrin from a red alga. *Appl. Biochem. Biotechnol.* 43, 133–139. doi:10.1007/BF02916437
- Kaldmæ, M., Sahin, C., Saluri, M., Marklund, E. G., and Landreh, M. (2019). A strategy for the identification of protein architectures directly from ion mobility mass spectrometry data reveals stabilizing subunit interactions in light harvesting complexes. *Protein Sci.* 28, 1024–1030. doi:10.1002/pro.3609
- Kamble, S. P., Vikhe, G. P., and Chamle, D. R. (2018). Extraction and purification of phycoerythrin-A natural colouring agent from *Spirulina platensis*. *J. Pharm. Chem. Biol. Sci.* 6, 78–84.
- Kannaujiya, V. K., and Sinha, R. P. (2016b). An efficient method for the separation and purification of phycobiliproteins from a rice-field cyanobacterium *Nostoc sp.* Strain HKAR-11. *Chromatographia* 79, 335–343. doi:10.1007/s10337-016-3025-0
- Kannaujiya, V. K., and Sinha, R. P. (2016a). Thermokinetic stability of phycocyanin and phycoerythrin in food-grade preservatives. *J. Appl. Phycol.* 28, 1063–1070. doi:10.1007/s10811-015-0638-x
- Khan, Z., Omar, W. M. W., Merican, F., Convey, P., Najimudin, N., and Alias, S. A. (2018). A comparative study of phycobiliprotein production in two strains of *Pseudanabaena* isolated from Arctic and tropical regions in relation to different light wavelengths and photoperiods. *Polar Sci.* 20, 3–8. doi:10.1016/j.polar.2018.10.002
- Kim, J.-J., Jeon, Y.-M., Noh, J.-H., and Lee, M.-Y. (2010). Isolation and characterization of a new phycoerythrin from the cyanobacterium *Synechococcus sp.* ECS-18. *J. Appl. Phycol.* 23, 137–142. doi:10.1007/s10811-010-9554-2
- Lauceri, R., Zittelli, C. G., and Torzillo, G. (2019). A simple method for rapid purification of phycobiliproteins from *Arthrospira platensis* and *Porphyridium cruentum* biomass. *Algal Res.* 44, 101685. doi:10.1016/j.algal.2019.101685
- Lee, D., Nishizawa, M., Shimizu, Y., and Saeki, H. (2017). Anti-inflammatory effects of dulce (*Palmaria palmata*) resulting from the simultaneous water-

extraction of phycobiliproteins and chlorophyll a. *Food Res. Int.* 100, 514–521. doi:10.1016/j.foodres.2017.06.040

Leney, A. C., Tschanz, A., and Heck, A. J. R. (2017). Connecting color with assembly in the fluorescent B-phycoerythrin protein complex. *FEBS J.* 285, 178–187. doi:10.1111/febs.14331

Li, J. R., Zhao, H. G., Zhao, X. J., and Gong, X. (2021). Red and yellow emissive carbon dots integrated tandem luminescent solar concentrators with significantly improved efficiency. *Nanoscale* 13, 9561–9569. doi:10.1039/D1NR01908B

Li, W., Su, H.-N., Pu, Y., Chen, J., Liu, L.-N., Liu, Q., et al. (2019). Phycobiliproteins: Molecular structure, production, applications, and prospects. *Biotechnol. Adv.* 37, 340–353. doi:10.1016/j.biotechadv.2019.01.008

Li, Y. X., Miao, P., Zhou, W., Gong, X., and Zhao, X. J. (2017). N-doped carbon-dots for luminescent solar concentrators. *J. Mat. Chem. A* 5, 21452–21459. doi:10.1039/C7TA05220K

Lian, Y. Z., Lin, I.-H., Yang, Y.-C., and Chao, J. C.-J. (2020). Gastroprotective effect of Lycium barbarum polysaccharides and C-phycoerythrin in rats with ethanol-induced gastric ulcer. *Int. J. Biol. Macromol.* 165, 1519–1528. doi:10.1016/j.ijbiomac.2020.10.037

Liu, L.-N., Chen, X.-L., Zhang, X.-Y., Zhang, Y.-Z., and Zhou, B.-C. (2005). One-step chromatography method for efficient separation and purification of R-phycoerythrin from *Polysiphonia urceolata*. *J. Biotechnol.* 116, 91–100. doi:10.1016/j.jbiotec.2004.09.017

López-Rodríguez, M., Cerón-García, M. C., López-Rosales, L., Navarro-López, E., Sánchez-Mirón, A., Molina-Miras, A., et al. (2020). Improved extraction of bioactive compounds from biomass of the marine dinoflagellate microalga *Amphidinium carterae*. *Bioresour. Technol.* 31, 123518. doi:10.1016/j.biortech.2020.123518

Ma, W. W., Li, W. J., Liu, R. Y., Cao, M. Y., Zhao, X. J., and Gong, X. (2019). Carbon dots and AIE molecules for highly efficient tandem luminescent solar concentrators. *Chem. Commun.* 55, 7486–7489. doi:10.1039/C9CC02676B

Macário, I. P. E., Ventura, S. P. M., Gonçalves, F. J. M., Torres-Acosta, M. A., and Pereira, J. L. (2021). The “bright side” of cyanobacteria: Revising the nuisance potential and prospecting innovative biotechnology-based solutions to integrate water management programs. *ACS Sustain. Chem. Eng.* 9 (21), 7182–7197. doi:10.1021/acssuschemeng.1c00458

Malairaj, S., Muthu, S., Gopal, V. B., Perumal, P., and Ramasamy, R. (2016). Qualitative and quantitative determination of R-phycoerythrin from *Halymenia floresia* (Clemente) C. Agardh by polyacrylamide gel using electrophoretic elution technique. *J. Chromatogr. A* 1454, 120–126. doi:10.1016/j.chroma.2016.05.063

Manirafasha, E., Ndikubwimana, T., Zeng, X., Lu, Y., and Jing, K. (2016). Phycobiliprotein: Potential microalgae derived pharmaceutical and biological reagent. *Biochem. Eng. J.* 109, 282–296. doi:10.1016/j.bej.2016.01.025

Manivasagan, P., Bharathiraja, S., Moorthy, S. M., Mondal, S., Seo, H., Dae Lee, K., et al. (2017). Marine natural pigments as potential sources for therapeutic applications. *Crit. Rev. Biotechnol.* 38, 745–761. doi:10.1080/07388551.2017.1398713

Marcati, A., Ursu, A. V., Laroche, C., Soanen, N., Marchal, L., Jubeau, S., et al. (2014). Extraction and fractionation of polysaccharides and B-phycoerythrin from the microalga *Porphyridium cruentum* by membrane technology. *Algal Res.* 5, 258–263. doi:10.1016/j.algal.2014.03.006

Marraskuranto, E., Raharjo, T. J., Kasiandari, R. S., and Nuringtyas, T. R. (2019). Color stability of phycoerythrin crude extract (PECE) from *Rhodomonas salina* toward physicochemical factors. *Squalen Bull. Mar. Fish. Postharvest Biotech.* 14, 21–31. doi:10.15578/squalen.v14i1.379

Martínez, J. M., Delso, C., Álvarez, I., and Raso, J. (2019). Pulsed electric field permeabilization and extraction of phycoerythrin from *Porphyridium cruentum*. *Algal Res.* 37, 51–56. doi:10.1016/j.algal.2018.11.005

Martins, M., Vieira, F. A., Correia, I., Ferreira, R. A. S., Abreu, H., Coutinho, J. A. P., et al. (2016). Recovery of phycobiliproteins from the red macroalga *Gracilaria sp.* using ionic liquid aqueous solutions. *Green Chem.* 18, 4287–4296. doi:10.1039/c6gc01059h

Martins, M., and Ventura, S. P. M. (2020). Emerging seaweed extraction techniques using ionic liquids, in Editors M. D. Torres, S. Kraan, and H. Dominguez. *Sustain. Seaweed Technol.* Amsterdam, Netherlands: Elsevier, 287–311. doi:10.1016/b978-0-12-817943-7.00011-1

Martins, M., Soares, B. P., Santos, J. H. P. M., Bharmoria, P., Acosta, M. A. T., Dias, A. C. R. V., et al. (2021). Sustainable strategy based on induced precipitation for the purification of phycobiliproteins. *ACS Sustain. Chem. Eng.* 9, 3942–3954. doi:10.1021/acssuschemeng.0c09218

Masojidek, J., Torzillo, G., and Koblížek, M. (2013). *Photosynthesis in microalgae: Handbook of microalgal culture*. New Jersey, United States: John Wiley & Sons, 21–36.

Mateen, F., Ali, M., Oh, H., and Hong, S. K. (2019). Nitrogen-doped carbon quantum dot based luminescent solar concentrator coupled with polymer dispersed

liquid crystal device for smart management of solar spectrum. *Sol. Energy* 178, 48–55. doi:10.1016/j.solener.2018.12.013

Mensi, F., Ksouri, J., Seale, E., Romdhane, M. S., and Fleurence, J. (2011). A statistical approach for optimization of R-phycoerythrin extraction from the red algae *Gracilaria verrucosa* by enzymatic hydrolysis using central composite design and desirability function. *J. Appl. Phycol.* 24, 915–926. doi:10.1007/s10811-011-9712-1

Merlo, S., Durany, X. G., Tonon, A. p., and Rossi, S. (2021). Marine microalgae contribution to sustainable development. *Water* 13, 1373. doi:10.3390/w13101373

Mishra, S. K., Shrivastav, A., Pancha, I., Jain, D., and Mishra, S. (2010). Effect of preservatives for food grade C-phycoerythrin, isolated from marine cyanobacteria *Pseudanabaena sp.* *Int. J. Biol. Macromol.* 47, 597–602. doi:10.1016/j.ijbiomac.2010.08.005

Mittal, R., Sharma, R., and Raghavarao, K. (2019). Aqueous two-phase extraction of R-Phycoerythrin from marine macro-algae, *Gelidium pusillum*. *Gelidium Pusillum. Bioresour. Technol.* 280, 277–286. doi:10.1016/j.biortech.2019.02.044

Mittal, R., Tavanandi, H. A., Mantri, V. A., and Raghavarao, K. S. M. S. (2017). Ultrasound assisted methods for enhanced extraction of phycobiliproteins from marine macro-algae, *Gelidium pusillum* (Rhodophyta). *Ultrason. Sonochem.* 38, 92–103. doi:10.1016/j.ultsonch.2017.02.030

Mulders, K. J. M., Lamers, P. P., Martens, D. E., and Wijffels, R. H. (2014). Phototrophic pigment production with microalgae: Biological constraints and opportunities. *J. Phycol.* 50, 229–242. doi:10.1111/jpy.12173

Munier, M., Jubeau, S., Wijaya, A., Morancès, M., Dumay, J., Marchal, L., et al. (2014). Physicochemical factors affecting the stability of two pigments: R-Phycoerythrin of *Grateloupia turururu* and B-phycoerythrin of *Porphyridium cruentum*. *Food Chem.* 150, 400–407. doi:10.1016/j.foodchem.2013.10.113

Munier, M., Morancès, M., Dumay, J., Jaouen, P., and Fleurence, J. (2015). One-step purification of R-phycoerythrin from the red edible seaweed *Grateloupia turururu*. *J. Chromatogr. B* 992, 23–29. doi:10.1016/j.jchromb.2015.04.012

Nguyen, H. P. T., Morancès, M., Déléris, P., Fleurence, J., Nguyen-Le, C. T., Vo, K. H., et al. (2019). Purification of R-phycoerythrin from a marine macroalga *Gracilaria gracilis* by anion-exchange chromatography. *J. Appl. Phycol.* 32, 553–561. doi:10.1007/s10811-019-01947-x

Nguyen, H. P. T., Morancès, M., Fleurence, J., and Dumay, J. (2016). *Mastocarpus stellatus* as a source of R-phycoerythrin: Optimization of enzyme assisted extraction using response surface methodology. *J. Appl. Phycol.* 29, 1563–1570. doi:10.1007/s10811-016-1024-z

Niu, J.-F., Chen, Z.-F., Wang, G.-C., and Cheng, Z. (2010). Purification of phycoerythrin *Porphyra yezoensis* Ueda (Bangiales, Rhodophyta) using expanded bed absorption. *J. Appl. Phycol.* 22, 25–31. doi:10.1007/s10811-009-9420-2

Niu, J., Xu, M., Wanf, G., Zhang, K., and Peng, G. (2013). Comprehensive extraction of agar and R-phycoerythrin from *Gracilaria lemaneiformis* (bangiales, rhodophyta). *J. Geo-Marine Sci.* 42, 21–28.

Novak, U., Bajić, M., Körge, K., Oberlinter, A., Murn, J., Lokar, K., et al. (2019). From waste/residual marine biomass to active biopolymer-based packaging film materials for food industry applications – A review. *Phys. Sci. Rev.* 5, doi:10.1515/psr-2019-0099

Osman, A., Salama, A., Mahmoud, K. E., and Sitohy, M. (2020). Alleviation of carbon tetrachloride-induced hepatocellular damage and oxidative stress in rats by *Anabaena oryzae* phycocyanin. *J. Food Biochem.* 45, e13562. doi:10.1111/jfbc.13562

Pagels, F., Guedes, A. C., Amaro, H. M., Kijjoa, A., and Vasconcelos, V. (2019). Phycobiliproteins from cyanobacteria: Chemistry and biotechnological applications. *Biotechnol. Adv.* 37, 422–443. doi:10.1016/j.biotechadv.2019.02.010

Pan, Q., Chen, M., Li, J., Wu, Y., Zhen, C., and Liang, B. (2013). Antitumor function and mechanism of phycoerythrin from *Porphyra haitanensis*. *Biol. Res.* 46, 87–95. doi:10.4067/S0716-97602013000100013

Pereira, T., Barroso, S., Mendes, S., Amaral, R. A., Dias, J. R., Baptista, T., et al. (2020). Optimization of phycobiliprotein pigments extraction from red algae *Gracilaria gracilis* for substitution of synthetic food colorants. *Food Chem.* 321, 126688. doi:10.1016/j.foodchem.2020.126688

Pham, T. N., Um, Y. J., and Yoon, H. H. (2013). Pretreatment of macroalgae for volatile fatty acid production. *Bioresour. Technol.* 146, 754–757. doi:10.1016/j.biortech.2013.07.080

Punampalam, R., Khoo, K. S., and Sit, N. W. (2018). Evaluation of antioxidant properties of phycobiliproteins and phenolic compounds extracted from *Bangia atropurpurea*. *Mal. J. Fund. Appl. Sci.* 14, 289–297. doi:10.11113/mjfas.v14n2.1096

Qi, H., Liu, Y., Qi, X., Liang, H., Chen, H., Jiang, P., et al. (2019). Dietary recombinant phycoerythrin modulates the gut microbiota of H22 tumor-bearing mice. *Mar. Drugs* 17, 665. doi:10.3390/md17120665

- Randrianarison, G., and Ashraf, M. A. (2017). Microalgae: A potential plant for energy production. *Geol. Ecol. Landscapes* 1 (2), 104–120. doi:10.1080/24749508.2017.1332853
- Ranjitha, K., and Kaushik, B. D. (2005). Purification of phycobiliproteins from *Nostoc muscorum*. *J. Sci. Industrial Res.* 64, 372–375.
- Rito-Palmares, M., Nuñez, L., and Amador, D. (2001). Practical application of aqueous two-phase systems for the development of a prototype process for c-phycoerythrin recovery from *Spirulina maxima*. *J. Chem. Technol. Biotechnol.* 76, 1273–1280. doi:10.1002/jctb.507
- Rodrigues, R. D. P., Castro, F. C., Santiago-Aguiar, R. S., and Rocha, M. V. P. (2018). Ultrasound-assisted extraction of phycobiliproteins from *Spirulina (Arthrospira) platensis* using protic ionic liquids as solvent. *Algal Res.* 31, 454–462. doi:10.1016/j.algal.2018.02.021
- Rodrigues, R. D. P., Lima, P. F., Santiago-Aguiar, R. S., and Rocha, M. V. P. (2019). Evaluation of protic ionic liquids as potential solvents for the heating extraction of phycobiliproteins from *Spirulina (Arthrospira) platensis*. *Algal Res.* 38, 101391. doi:10.1016/j.algal.2018.10.1391
- Rossano, R., Ungaro, N., D'Ambrosio, A., Liuzzi, G., and Riccio, P. (2003). Extracting and purifying R-phycoerythrin from mediterranean red algae corallina elongata ellis & solander. *J. Biotechnol.* 101, 289–293. doi:10.1016/S0168-1656(03)00002-6
- Roy, S., Llewellyn, C. A., Egeland, S. E., and Johnsen, G. (2011). *Phytoplankton pigments: Characterization, chemotaxonomy and applications in oceanography*. Cambridge, United Kingdom: Cambridge University Press.
- Ruiz-Ruiz, F., Benavides, J., and Rito-Palmares, M. (2013). Scaling-up of a B-phycoerythrin production and purification bioprocess involving aqueous two-phase systems: Practical experiences. *Process Biochem.* 48, 738–745. doi:10.1016/j.procbio.2013.02.010
- Sadeghi, S., Melikov, R., Jalali, H. B., Karatum, O., Srivastava, S. B., Conkar, D., et al. (2019). Ecofriendly and efficient luminescent solar concentrators based on fluorescent proteins. *ACS Appl. Mat. Interfaces* 11, 8710–8716. doi:10.1021/acsami.9b00147
- Saiedi, S., Rezaei, B., Irannejad, N., and Ensafi, A. A. (2020). Efficiency improvement of luminescent solar concentrators using upconversion nitrogen-doped graphene quantum dots. *J. Power Sources* 476, 228647. doi:10.1016/j.jpowsour.2020.228647
- Sekar, S., and Chandramohan, M. (2007). Phycobiliproteins as a commodity: Trends in applied research, patents and commercialization. *J. Appl. Phycol.* 20, 113–136. doi:10.1007/s10811-007-9188-1
- Senthilkumar, N., Suresh, V., Thangam, R., Kurinjimalar, C., Kavitha, G., Murugan, P., et al. (2013). Isolation and characterization of macromolecular protein R-Phycocyanin from *Portieria hornemannii*. *Int. J. Biol. Macromol.* 55, 150–160. doi:10.1016/j.ijbiomac.2012.12.039
- Seručník, M., Vicente, F. A., Brečko, Ž., Coutinho, J. A. P., Ventura, S. P. M., and Žnidaršič-Plazl, P. (2020). Development of a microfluidic platform for R-phycoerythrin purification using an aqueous micellar two-phase system. *ACS Sustain. Chem. Eng.* 46, 17097–17105. doi:10.1021/acssuschemeng.0c05042
- Sfriso, A. A., Gallo, M., and Baldi, F. (2018). Phycoerythrin productivity and diversity from five red macroalgae. *J. Appl. Phycol.* 30, 2523–2531. doi:10.1007/s10811-018-1440-3
- Sharmila, B. V. M., Santhosi, S., Hemalatha, V., Venkatakrishnan, V., and Dhandapani, R. (2017). Optimization study on extraction & purification of phycoerythrin from red algae *Kappaphycus alvarezii*. *Asian J. Pharm. Clin. Res.* 10, 297–306. doi:10.22159/ajpcr.2017.v10i2.15598
- Sherwood, J., Bruyn, M., Constantinou, A., Moity, L., McElroy, C. R., Farmer, T. J., et al. (2014). Dihydroxycyclohexenone (cyrene) as a bio-based alternative for dipolar aprotic solvents. *Chem. Commun.* 50, 9650–9652. doi:10.1039/c4cc04133j
- Sintra, T. E., Bagagem, S. S., Ghazizadeh, A. F., Fernandes, A., Martins, M., Macário, I. P. E., et al. (2021). Sequential recovery of C-phycoerythrin and chlorophylls from *Anabaena cylindrica*. *Sep. Purif. Technol.* 255, 117538. doi:10.1016/j.seppur.2020.117538
- Sudhakar, M. P., Jagatheesan, A., Perumal, K., and Arunkumarm, K. (2015). Methods of phycobiliprotein extraction from *Gracilaria crassa* and its applications in food colorants. *Algal Res.* 8, 115–120. doi:10.1016/j.algal.2015.01.011
- Sudhakar, M. P., Saraswathi, M., and Nair, B. B. (2014). Extraction, purification and application study of R-phycoerythrin from *Gracilaria corticata* (J. Agardh) J. Agardh var. *corticata*. *Indian J. Nat. Prod. Resour.* 5, 371–374.
- Suganya, T., Varman, M., Masjuki, H. H., and Renganathan, S. (2016). Macroalgae and microalgae as a potential source for commercial applications along with biofuels production: A biorefinery approach. *Renew. Sustain. Energy Rev.* 55, 909–941. doi:10.1016/j.rser.2015.11.026
- Sun, Y., Zang, L., Lau, C., Zhang, X., and Lu, J. (2021). Sensitive detection of transcription factor by coupled fluorescence-encoded microsphere with exonuclease protection. *Talanta* 229, 122272. doi:10.1016/j.talanta.2021.122272
- Tan, H., Gao, S., Zhuang, Y., Dong, Y., Guan, W., Zhang, K., et al. (2016). R-phycoerythrin induces SGC-7901 apoptosis by arresting cell cycle at S phase. *Mar. Drugs* 14, 166. doi:10.3390/md14090166
- Torres-Acosta, M. A., Ruiz-Ruiz, F., Aguilar-Yáñez, J. M., Benavides, J., and Rito-Palmares, M. (2016). Economic analysis of pilot-scale production of B-phycoerythrin. *Biotechnol. Prog.* 32, 1472–1479. doi:10.1002/btpr.2344
- Tripathi, S. N., Kapoor, S., and Shrivastava, A. (2007). Extraction and purification of an unusual phycoerythrin in a terrestrial desiccation tolerant cyanobacterium *Lyngbya arboricola*. *J. Appl. Phycol.* 19, 441–447. doi:10.1007/s10811-006-9151-6
- Vicente, F. A., Cardoso, I. S., Martins, M., Gonçalves, C. V. M., Dias, A. C. R. V., Domingues, P., et al. (2019). R-phycoerythrin extraction and purification from fresh *Gracilaria* sp. using thermo-responsive systems. *Green Chem.* 21, 3816–3826. doi:10.1039/C9GC00104B
- Vossen, F. M., Aarts, M. P. J., and Debije, M. G. (2016). Visual performance of red luminescent solar concentrating windows in an office environment. *Energy Build.* 113, 123–132. doi:10.1016/j.enbuild.2015.12.022
- Wahlström, R., Hiltunen, J., Sirkka, M. P. S. N., Vuoti, S., and Kruus, K. (2016). Comparison of three deep eutectic solvents and 1-ethyl-3-methylimidazolium acetate in the pretreatment of lignocellulose: Effect on enzyme stability, lignocellulose digestibility and one-pot hydrolysis. *RSC Adv.* 6, 68100–68110. doi:10.1039/C6RA11719H
- Wang, C., Shen, Z., Cui, X., Jiang, Y., and Jiang, X. (2020). Response surface optimization of enzyme-assisted extraction of R-phycoerythrin from dry *Pyropia yezoensis*. *J. Appl. Phycol.* 32, 1429–1440. doi:10.1007/s10811-019-01963-x
- Wang, C., Zhao, Y., Wang, L., Pan, S., Liu, Y., Li, S., et al. (2020). C-Phycocyanin mitigates cognitive impairment in doxorubicin-induced chemobrain: Impact on neuroinflammation, oxidative stress, and brain mitochondrial and synaptic alterations. *Neurochem. Res.* 46, 149–158. doi:10.1007/s10642-020-03164-2
- Wang, G., Zhou, B., and Zeng, C. (1998). Isolation, properties and spatial site analysis of gamma subunits of B-phycoerythrin and R-phycoerythrin. *Sci. China Ser. C -Life. Sci.* 41, 9–17. doi:10.1007/BF02882700
- Wang, Z. J., Zhao, X. J., Guo, Z. Z., Miao, P., and Gong, X. (2018). Carbon dots based nanocomposite thin film for highly efficient luminescent solar concentrators. *Org. Electron.* 62, 284–289. doi:10.1016/j.orgel.2018.08.020
- WHO (2021). World health organization. Available at [https://www.who.int/water\\_sanitation\\_health/diseases-risks/diseases/cyanobacteria/en/](https://www.who.int/water_sanitation_health/diseases-risks/diseases/cyanobacteria/en/).
- Xu, Y., Hou, Y., Wang, Y., Wang, Y., Li, T., Song, C., et al. (2019). Sensitive and selective detection of Cu<sup>2+</sup> ions based on fluorescent Ag nanoparticles synthesized by R-phycoerythrin from marine algae *Porphyra yezoensis*. *Ecotoxicol. Environ. Saf.* 168, 356–362. doi:10.1016/j.ecoenv.2018.10.102
- Yang, M., Cui, M., Wang, W., Yang, Y., Chang, J., Hao, J., et al. (2020). Background-free upconversion-encoded microspheres for mycotoxin detection based on a rapid visualization method. *Anal. Bioanal. Chem.* 412, 81–91. doi:10.1007/s00216-019-02206-1
- Yoshimoto, S., Okada, K., and Hayashi, O. (2019). Immuno-regulatory and anti-inflammatory actions of phycocyanin on Caco-2/U937 cells co-culture as a model of the intestinal barrier. *Funct. Foods Health Dis.* 9, 466–483. doi:10.31989/fhd.v9i7.611
- You, Y., Cheng, S., Zhang, L., Zhu, Y., Zhang, C., and Xian, Y. (2020). Rational modulation of the luminescence of upconversion nanomaterials with phycocyanin for the sensing and imaging of myeloperoxidase during an inflammatory process. *Anal. Chem.* 92, 5091–5099. doi:10.1021/acs.analchem.9b05468
- Yue, J., Zhu, Z., Yi, J., Lan, Y., Chen, B., and Rao, J. (2021). Structure and functionality of oat protein extracted by choline chloride–dihydric alcohol deep eutectic solvent and its water binary mixtures. *Food Hydrocoll.* 112, 106330–106338. doi:10.1016/j.foodhyd.2020.106330
- Zdržal, L., Kalytchuk, S., Hla, K., Petr, M., Zmeskal, O., Kment, S., et al. (2020). A carbon dot-based tandem luminescent solar concentrator. *Nanoscale* 12, 6664–6672. doi:10.1039/C9NR10029F
- Zhang, S., Zhang, Z., Dadmohammadi, Y., Li, Y., Jaiswal, A., and Abbaspourrad, A. (2020). Whey protein improves the stability of C-phycoerythrin in acidified conditions during light storage. *Food Chem.* 344, 128642. doi:10.1016/j.foodchem.2020.128642
- Zhao, H. G., Liu, G. J., and Han, G. T. (2019). High-performance laminated luminescent solar concentrators based on colloidal carbon quantum dots. *Nanoscale Adv.* 1, 4888–4894. doi:10.1039/C9NA00527G
- Zhao, H. G., Liu, G. J., You, S. J., Camargo, F. V. A., Zavelani-Rossi, M., Wang, X. H., et al. (2021). Gram-scale synthesis of carbon quantum dots with a large Stokes shift for the fabrication of eco-friendly and high-efficiency luminescent solar concentrators. *Energy Environ. Sci.* 14, 396–406. doi:10.1039/D0EE02235G
- Zhao, H. G. (2019). Refractive index dependent optical property of carbon dots integrated luminescent solar concentrators. *J. Luminescence* 211, 150–156. doi:10.1016/j.jlumin.2019.03.039
- Zhou, Y. F., Benetti, D., Tong, X., Jin, L., Wang, Z. M. M., Ma, D. L., et al. (2018). Colloidal carbon dots based highly stable luminescent solar concentrators. *Nano Energy* 44, 378–387. doi:10.1016/j.nanoen.2017.12.017





## OPEN ACCESS

## EDITED BY

Vadim G. Kessler,  
Swedish University of Agricultural  
Sciences, Sweden

## REVIEWED BY

Rocco Di Girolamo,  
University of Naples Federico II, Italy  
Patrizia Cinelli,  
University of Pisa, Italy

## \*CORRESPONDENCE

Mariela M. Nolasco,  
mnolasco@ua.pt  
Andreia F. Sousa,  
andreiafs@ua.pt

## SPECIALTY SECTION

This article was submitted to Polymer  
Chemistry,  
a section of the journal  
Frontiers in Chemistry

RECEIVED 28 September 2022

ACCEPTED 21 November 2022

PUBLISHED 06 December 2022

## CITATION

Nolasco MM, Rodrigues LC, Araújo CF,  
Coimbra MM, Ribeiro-Claro P, Vaz PD,  
Rudić S, Silvestre AJD, Bouyahya C,  
Majdoub M and Sousa AF (2022), From  
PEF to PBF: What difference does the  
longer alkyl chain make a computational  
spectroscopy study of  
poly(butylene 2,5-furandicarboxylate).  
*Front. Chem.* 10:1056286.  
doi: 10.3389/fchem.2022.1056286

## COPYRIGHT

© 2022 Nolasco, Rodrigues, Araújo,  
Coimbra, Ribeiro-Claro, Vaz, Rudić,  
Silvestre, Bouyahya, Majdoub and  
Sousa. This is an open-access article  
distributed under the terms of the  
[Creative Commons Attribution License](#)  
(CC BY). The use, distribution or  
reproduction in other forums is  
permitted, provided the original  
author(s) and the copyright owner(s) are  
credited and that the original  
publication in this journal is cited, in  
accordance with accepted academic  
practice. No use, distribution or  
reproduction is permitted which does  
not comply with these terms.

# From PEF to PBF: What difference does the longer alkyl chain make a computational spectroscopy study of poly(butylene 2,5-furandicarboxylate)

Mariela M. Nolasco<sup>1\*</sup>, Leonor C. Rodrigues<sup>1</sup>, Catarina F. Araújo<sup>1</sup>,  
Mariana M. Coimbra<sup>1</sup>, Paulo Ribeiro-Claro<sup>1</sup>, Pedro D. Vaz<sup>2</sup>,  
Svemir Rudić<sup>3</sup>, Armando J. D. Silvestre<sup>1</sup>, Chaima Bouyahya<sup>1,4</sup>,  
Mustapha Majdoub<sup>4</sup> and Andreia F. Sousa<sup>1,5\*</sup>

<sup>1</sup>CICECO, Departamento de Química, Universidade de Aveiro, Aveiro, Portugal, <sup>2</sup>Champalimaud Foundation, Champalimaud Centre for the Unknown, Lisboa, Portugal, <sup>3</sup>ISIS Neutron & Muon Source, STFC Rutherford Appleton Laboratory, Didcot, United Kingdom, <sup>4</sup>Laboratoire des Interfaces et Matériaux Avancés, Université de Monastir, Monastir, Tunisia, <sup>5</sup>Centre for Mechanical Engineering, Materials and Processes, Department of Chemical Engineering, University of Coimbra, Coimbra, Portugal

This work explores the conformational preferences and the structure-property correlations of poly(butylene 2,5-furandicarboxylate) (PBF), a longer chain analogue of the most well-known biobased polyester from the furan family, poly(ethylene 2,5-furandicarboxylate) (PEF). A thorough computational spectroscopic study—including infrared, Raman and inelastic neutron scattering spectroscopy, combined with discrete and periodic density functional theory calculations—allowed the identification of dominant structural motifs in the amorphous and crystalline regions. Discrete calculations and vibrational spectroscopy of semi-crystalline and amorphous samples strongly support the predominance of *gauche*, *trans*, *gauche* conformations of the butylene glycol fragment in both the crystalline and amorphous domains. In what concerns the furandicarboxylate fragment, amorphous domains are dominated by *syn,syn* conformations, while in the crystalline domains the *anti,anti* forms prevail. A possible crystalline structure—built from these conformational preferences and including a network of C-H...O hydrogen bond contacts—was optimized using periodic density functional theory. This proposed crystal structure avoids the unrealistic structural features of the previously proposed X-ray structure, provides an excellent description of the inelastic neutron scattering spectrum of the semi-crystalline form, and allows the correlation between microscopic structure and macroscopic properties of the polymer.



## KEYWORDS

computational spectroscopy, inelastic neutron scattering (INS), C-H...O hydrogen bond, molecular interpretation, physical properties, 2,5-furan dicarboxylate, butylene glycol

## Introduction

Progress in renewable based polymers has accelerated since they offer the possibility to reduce the environmental impact of plastics, paving the way to the UN Sustainable Development Goals (United Nations, 2020) and towards a circular economy as set forth by the European Commission (European Commission, 2015). Despite this, biobased polymers still represent today a minor fraction of all commercial polymers produced yearly (*ca.* 864 tonnes in 2021), accounting for less than 1% of the global production (European Bioplastics, 2021). A complex set of factors underlie this fact, in which economic constraints (high production costs) and their typical inferior mechanical and thermal properties have limited its market production and penetration. Nevertheless, the extensive research carried out by both academia and industry have brought new prospects with the arising of the 2,5-furandicarboxylic acid (FDCA)—a key building-block for polymers development which can impart high performance to the polymers thereof (Werpy and Petersen, 2004; Bozell and Petersen, 2010; Loos et al., 2020; de Jong et al., 2022).

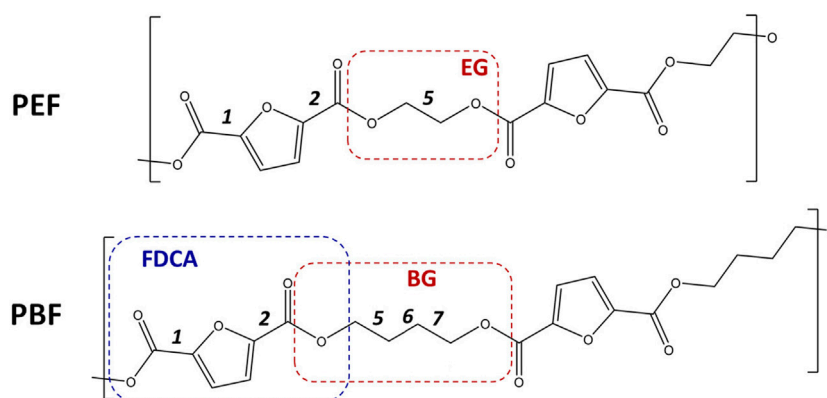
Poly(ethylene 2,5-furandicarboxylate) (PEF) and poly(butylene 2,5-furandicarboxylate) (PBF)—Figures 1 – are among the most interesting FDCA-based polymers because, besides having a renewable origin and a more favorable sustainable performance, they have improved properties arising from their chemical structure. The in-depth characterization carried out so far focused mostly on PEF, due to its potential to replace the fossil-based poly(ethylene terephthalate) (PET) on packaging, *e.g.* plastic bottles (Fei et al., 2020; de Jong et al., 2022). Our group reported a vibrational spectroscopy and computational modeling study on this polymer, shedding light on important structure-property correlations (Araujo C. F. et al., 2018). A clear picture emerged, then, on how the most favorable conformational preferences both in the amorphous and crystalline regions, as well as  $\alpha$  and  $\beta$  polymorphs, are built in. Results show that, in the amorphous domains, PEF chains prefer a winding structure based on energetically favorable gauche conformation of the ethylene-glycol fragment. Yet, in the crystalline domains, polymeric chains adopt an energetically unfavorable extended *all-trans* geometry, which is stabilized by a network of C-H...O bonds linking adjacent chains. Interestingly the INS spectrum, revealing distinct low-frequency vibrational profiles for PEF and PET, confirmed the furanic “ring flipping” hindrance and stiffer polymeric chains, typically associated with enhanced O<sub>2</sub>, CO<sub>2</sub>, and H<sub>2</sub>O gas barrier properties (Burgess et al., 2014a; 2014c; 2014b, 2015), as well as a higher Young’s modulus. To the best of our knowledge, a similar picture has not been

drawn for PBF, besides an attempt study made by (Zhu et al., 2013). Indeed, most studies focus instead on its synthesis (Carlos Morales-Huerta et al., 2016), thermal and crystallinity properties (Ma et al., 2012; Sousa et al., 2018), mechanical behavior (Zhu et al., 2013; Robles-Hernandez et al., 2020), molecular dynamics (Soccio et al., 2017; Papamokos et al., 2019; Guidotti et al., 2020; Klonos et al., 2020; Bianchi et al., 2021; Fosse et al., 2022; Pouloupoulou et al., 2022) or in some of these aspects (Matos et al., 2018).

Recent publications demonstrate the high-quality simulations of the vibrational spectra of crystals using periodic boundary conditions, usually described as periodic density functional theory (DFT) calculations. Inelastic neutron scattering (INS) intensities, which are a straightforward result of the eigenvectors (atomic displacements) determined for the vibrational normal modes, are particularly well-predicted from periodic DFT, allowing the confident assignment of molecular and lattice modes in the crystal. In the case of amorphous polymer samples—or in absence of a reliable crystal structure for the crystalline domains in a semi-crystalline sample—discrete (or molecular) calculations have been used with success (Araujo C. et al., 2018; Vilela et al., 2020; Druzicki et al., 2021; Stroupe et al., 2022). In this case, the possible polymer chain structures are simulated by resorting to short polymer fragments, typically triads. Then, the experimental spectra can be matched to a combination of proposed structures whose spectral contributions are determined from calculations. Due to the high reliability of calculations, structures that fail to adequately contribute to the experimental spectra can be excluded. This approach applies to infrared (IR) and Raman spectroscopy with some caveats, since selection rules could provide different weightings for different geometries, resulting in a non-quantitative intensity/population relationship. However, the approach is particularly suitable for INS spectroscopy, because the INS spectrum is a quantitative measurement of the vibrational density of states—i.e., it is a direct sum of contributions from the different populations—and so the INS scattering profile can be decomposed into a linear combination of contributions from dominant structural motifs (see, *e.g.* (Harrelson et al., 2017)). Despite the potential of the combination of these approaches they have not yet been used to describe PBF.

Further, a comparison between PEF and PBF conformational preferences and related properties was missing, apart from the obvious gain in flexibility due to the extra methylene groups of PBF. All in all, what difference does the longer alkyl chain make?

In this vein, in this work, the computational spectroscopy approach was extended to biobased PBF and a comparison with

**FIGURE 1**

Skeletal formulas of the repeating units for poly(ethylene 2,5-furandicarboxylate) (PEF, top) and poly(butylene 2,5-furandicarboxylate) (PBF, bottom). Dashes delimit the 1,2- and 1,4-alkyl glycol moieties—EG, BG—and the first 2,5-furandicarboxylic acid moiety—FDCA. The labels 1, 2, five to seven identify the single bonds for which rotational freedom exists. For 1 and 2, the orientation of C=O bonds relative to ring C=C bonds are described as *syn* or *anti*. For five EG and 5,6,7 BG bonds, conformations are either *trans* or *gauche*. In this way, the PBF structure shown here is described as *anti,anti-trans,trans, trans, or aa-ttt* for short.

PEF is provided. By combining vibrational spectroscopy techniques—including infrared absorption (IR), Raman scattering and inelastic neutron scattering (INS)—and quantum mechanical calculations at the density functional theory (DFT) level, new insights on the structure and properties of this polymer, compared to PEF were herein achieved.

The *syn/anti* terms refer to the orientation of C=O bonds relative to the nearest ring C=C bond. In the previous work with PEF (Araujo C. F. et al., 2018), the terms *syn/anti* were defined relative to the position of furanic oxygen atom; using the more adequate definition herein adopted simply reverses the *anti/syn* meaning.

## Experimental details

### Synthesis of PBF

Dimethyl 2,5-furandicarboxylate (DMFDC) was synthesized following a previously reported procedure (Matos et al., 2017). Briefly, DMFDC was prepared by refluxing FDCA (5 g, 32.0 mmol) with an excess of methanol, under acidic conditions (HCl) at 80°C, for 15 h. Then, the reaction mixture was cooled down to room temperature and the resulting insoluble product was filtered off in *ca.* 70% yield.

PBF was synthesized by an adapted polytransesterification reaction procedure previously reported (Matos et al., 2018). In a first stage, DMFDC (8 g, 43.5 mmol), 1,4-butanediol (6 g, 66.5 mmol) and titanium(IV) butoxide (20 mg, 0.1 wt%) were allowed to react under a nitrogen atmosphere from 190°C up to 210°C, for 7–8 h. During the second stage, a high vacuum of

10<sup>−3</sup> mbar was gradually applied, and the reaction was carried out at 210°C for 3 h. Then, the reaction was stopped and cooled down to room temperature. The polymer was purified by dissolving in a chloroform–trifluoroacetic acid mixture (6:1) and poured in an excess of methanol, filtered and dried in a vacuum oven at 40°C. The ensuing PBF was isolated in *ca.* 70% yield. The amorphous and semi-crystalline samples of PBF were obtained as described for PEF (Araujo C. F. et al., 2018) and characterized from powder X-ray diffraction (XRD). The XRD pattern of the amorphous sample did not reveal the presence of a crystalline fraction. The crystallinity of the semi-crystalline sample, estimated from its XRD pattern, was *ca.* 60%.

### X-ray diffraction

PBF samples were analyzed using X-ray diffraction studies. XRD powder patterns were collected at room temperature on a Panalytical Empyrean instrument operating with CuK $\alpha$  radiation at 40 kV and 50 mA. Samples were scanned in the 2 $\theta$  range of 5°–70° with a step size of 0.026° and step time of 67 s.

### Vibrational spectra

PBF samples were studied using optical techniques (IR, Raman) and inelastic neutron scattering (INS). FTIR-ATR spectra were measured at room temperature using a FT Bruker IFS 55 spectrometer with a Golden Gate ATR accessory with a resolution of 2 cm<sup>−1</sup>. Raman spectra were collected at room temperature on a Bruker MultiRAM FT-Raman instrument with an Nd:YAG laser and using a

resolution of  $2\text{ cm}^{-1}$ . The INS spectra of PBF samples were collected in the scope of project RB2000214 (Nolasco et al., 2021), using the TOSCA instrument (Parker et al., 2014; Pinna et al., 2018) at the ISIS Neutron and Muon Source of STFC's Rutherford Appleton Laboratory (Chilton, United Kingdom) (ISIS, 2022). The samples, weighing 0.5–1 g, were placed inside a flat thin-walled aluminum can, which was then mounted perpendicular to the incident beam using a regular TOSCA centered stick. Spectra were collected below 20 K and samples were “shock-frozen” by quenching in liquid nitrogen before placement in the beam path, in order to preserve the room-temperature morphology of possible amorphous and crystalline regions. The contribution of aluminum can to the final INS spectra was found to be not negligible and has been removed by subtraction.

## Quantum chemical calculations

**Discrete (molecular) calculations:** Geometry optimizations and vibrational frequency calculations of PBF oligomers (triads,  $\text{BG}_3\text{FDCA}_3$ ) were computed using the Gaussian 09 software, using the B3LYP density functional with the 6–311G (d,p) basis set. This method was found to provide a reliable description of the conformational preferences of molecular models and allows a direct comparison with previous results for PEF (Araujo C. F. et al., 2018; Papamokos et al., 2019). The initial structures were based on the well-known minima for these systems (see, e.g. (Papamokos et al., 2019)) described in Figure 1. Optimizations were performed without constraints and all the optimized structures were found to be real minima, with no imaginary frequencies. For calculated Raman and infrared spectra, vibrational frequencies were scaled by a factor of 0.967 (NIST Computational Chemistry Comparison and Benchmark Database, 2022). The inelastic neutron scattering simulated intensities were estimated from the calculated eigenvectors using the AbINS software (Dymkowski et al., 2018), a part of the Mantid package (Arnold et al., 2014). The energy values mentioned throughout the text refer to the electronic energy without zero-point correction.

**Periodic DFT calculations:** calculations were performed using the plane wave pseudopotential method as implemented in CASTEP 8.0 code (Clark et al., 2005; Refson et al., 2006). All calculations were done using the Perdew–Burke–Ernzerhof (PBE) functional based on the generalized gradient gauge (GGA) approximation (Perdew et al., 1996) supplemented with the semi-empirical dispersion correction of Tkatchenko and Scheffler (Tkatchenko and Scheffler, 2009). The plane-wave cutoff energy was set at 830 eV. Brillouin zone sampling of electronic states was performed on  $2\times 4\times 5$  Monkhorst–Pack grid. The initial structures were built from selected triads, considering a triclinic crystal with P1 symmetry, or obtained from (Zhu et al., 2013). Geometry optimizations were carried out

with no constraints (i.e., both cell parameters and internal coordinates were relaxed) and accuracy of the optimization requested residual forces to fall below  $0.005\text{ eV \AA}^{-1}$ . Phonon frequencies were obtained by diagonalization of dynamical matrices calculated using density-functional perturbation theory (Milman et al., 2009). The calculated atomic displacements in each mode that are part of the CASTEP output enable visualization of the atomic motions and support the assignment of vibrational modes. The simulated inelastic neutron scattering intensities were predicted from the calculated eigenvectors using AbINS, and values were not scaled.

## Results and discussion

### Conformational landscape (from discrete molecular modelling)

The existence of a crystalline model structure is a prerequisite to periodic DFT calculations. In the case of PBF, Zhu et al. proposed a crystal structure from fiber X-ray diffraction scans on a stretched PBF film (Zhu et al., 2013). However, the proposed structure presents several unrealistic structural features that cast serious doubts on its reliability and render it unavailing for structural characterization of the system. Among other geometrical issues, the BG alkyl chain presents C–C–C angles up to  $129^\circ$ , far from acceptable values for an alkyl chain. In the absence of doubtless crystallographic data, discrete (or molecular) calculations on polymer fragments offer a reliable alternative to assess conformational preferences of the polymer chain.

In this way, the conformational landscape of PBF was explored through DFT calculations on  $\text{BG}_3\text{FDCA}_3$  triads. Due to the large number of possible combinations for this oligomer, calculations were performed for uniform conformations along the  $\text{BG}_3\text{FDCA}_3$  chain. For instance, the lowest energy conformation for  $\text{BG}_3\text{FDCA}_3$  was found to be *ss-gtg*, which means that all three FDCA fragments have *syn-syn* orientation and all three BG chains have *gauche-trans-gauche* conformations (see Figure 1). This “uniform chain” approach is the model expected to prompt easiest close packing of chains and, thus, to better describe the crystalline domains in the polymer. Of course, a variety of non-uniform sequences are predictable for the amorphous domains.

Figure 2 compares the structure and energies of the lower energy triads found for PEF and PBF. These triads present uniform conformations, resulting from the internal rotation around FDCA bonds labelled 1,2 and EG and BG bonds labelled 5 and 5,6,7 in Figure 1, respectively.

As in the case of PEF, in the FDCA fragment the *syn* orientation is clearly preferred over the *anti* orientation, while the alkoxy CC–CO fragments prefer the *gauche* conformation relative to the *trans* conformation. The longer alkyl chain in PBF brings an additional CC–CC torsion angle with a preference for the *trans* conformation.

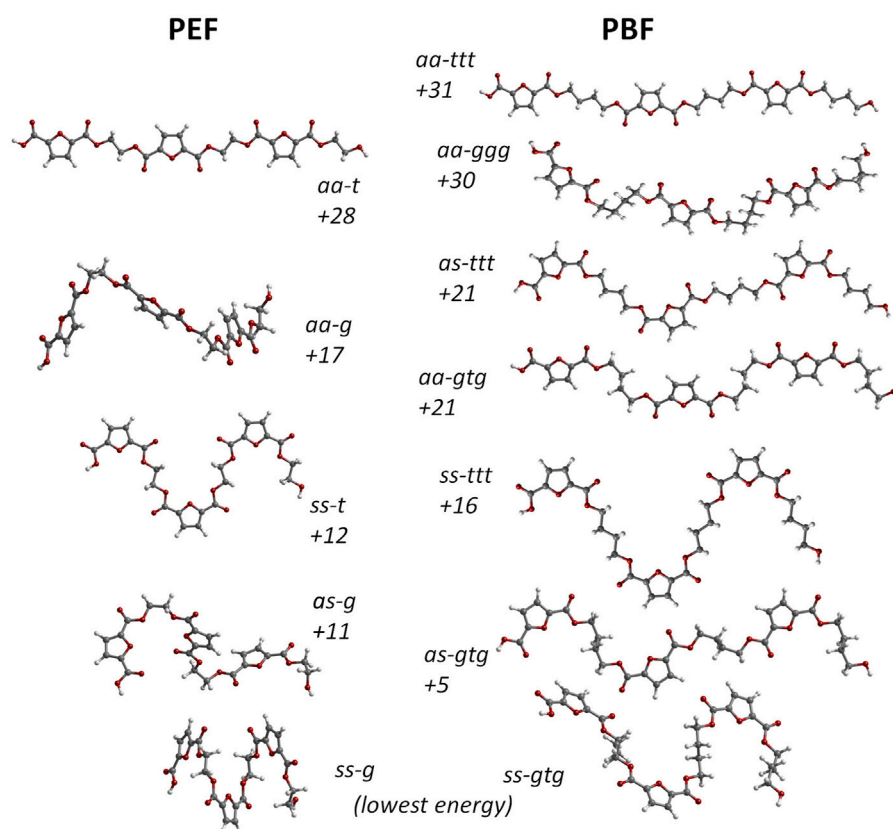


FIGURE 2

Comparison between the molecular structure of PBF triads BG<sub>3</sub>FDCA<sub>3</sub> (right) and PEF triads EG<sub>3</sub>FDCA<sub>3</sub> (left). The numbers indicate their relative stability expressed in terms of electronic energy, at the B3LYP/6311G (d,p) level, in kJ/mol. The *aa*, *as* and *ss* labels indicate the *anti*- and *syn*-orientation of the carbonyl bonds relative to nearest ring C=C bond in each FDCA fragment; for PBF, *ttt* and *gtg* indicate *trans*- and *gauche*-conformations along the BG skeleton. The *as* structures with alternate sequence *as-sa-as* for the three FDCA fragments present marginally lower energy than structures with *as-as-as* sequence and are used in this figure. Only the three *ttt* forms present a fully planar skeleton.

Hence, the lowest energy conformation in PBF is *ss-gtg* and energy raises *ca.* 30 kJ/mol up to the *aa-ggg* and *aa-ttt* conformations. The high energy *aa-ggg* structure results from the optimization of a triad extracted from the defective X-ray structure of Zhu et al., discussed above. Due to the correction of unrealistic geometrical parameters during the geometry optimization, this triad adopts the curved shape evident in Figure 2.

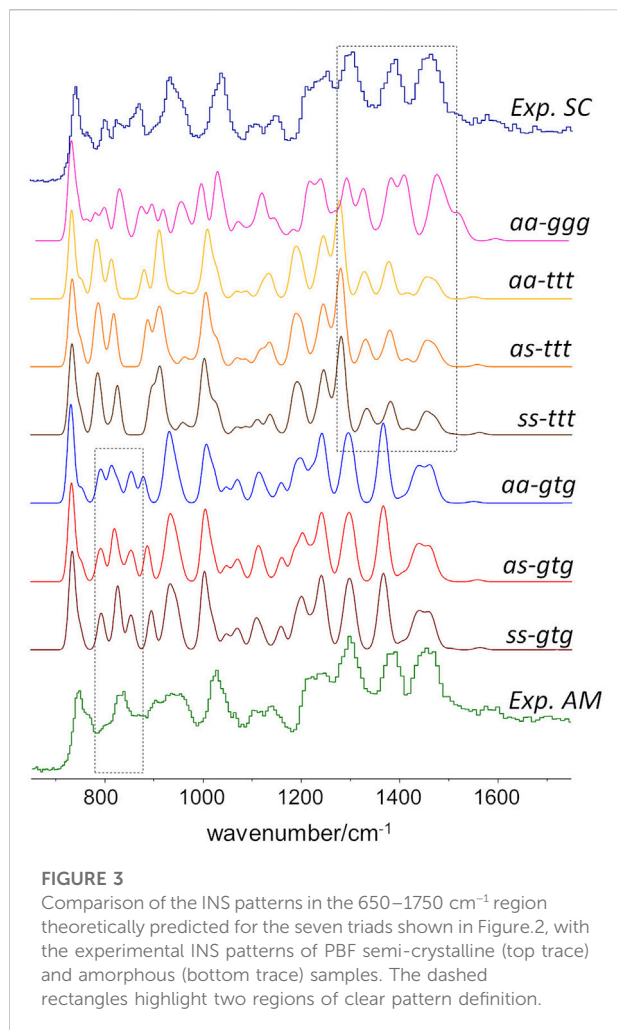
A noticeable feature of Figure 2 is the correlation between PBF and PEF triads and their relative energies. For instance, the lowest energy *ss-g* PEF form directly correlates with the lowest energy *ss-gtg* PBF form. In the same way, *as-g* (PEF) correlates with *as-gtg* (PBF), but the energy gap to the lowest energy form is substantially lower for PBF: 5 kJ/mol vs 11 kJ/mol. More interesting is the correlation between the “crystal-prone” (non-winding) structures in both polymers: due to the longer alkyl chain of PBF, the *aa-t* form of PEF correlates with both the *aa-ttt* and *aa-gtg* forms of PBF. And while *aa-t* and *aa-ttt* present similar energy values relative to the minima (28 and 31 kJ/mol, respectively), the *aa-gtg* form is *ca.* 7 kJ/mol below *aa-t*.

On average, the change from *gtg* to *ttt* conformation in a single BG fragment has an energy penalty of *ca.* 5 kJ/mol. Changes to mixed conformations, such as *gtt* or *tgg*, will require a fraction of this value. The energy penalty for a single *syn*-to-*anti* change in a single FDCA fragment falls in the range of *ca.* 2–3.5 kJ/mol. These values turn a large number of conformations accessible for the amorphous domain at room temperature, and, from this point of view (energetic considerations alone) also for crystalline forms. However, it is possible to discriminate the conformational preferences for crystalline and amorphous domains from a computational spectroscopy approach, as described below.

## INS spectroscopic patterns

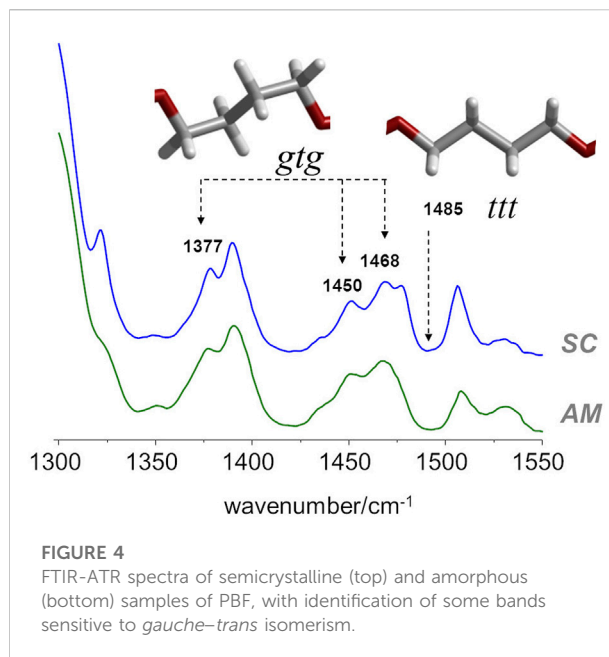
As stated above, since the INS intensities are relatively easy to simulate and predict, it is possible to generate reliable INS spectrum for each triad on Figure 2 and, thus, identify the





INS patterns associated with each conformation. The conformations with dominant contribution to the crystalline and amorphous domains are selected from the patterns that best match the experimental spectrum of semi-crystalline and amorphous samples. Figure 3 shows the INS spectra predicted for the seven uniform triads considered, compared with the experimental INS spectra for amorphous and semi-crystalline samples.

As it can be seen, the triads bearing a BG group with *ttt* conformation fail to reproduce the intensity pattern in the ca. 1200–1450  $\text{cm}^{-1}$  region (associated with  $\text{CH}_2$  bending modes). Since the intensity pattern associated with the *gtg* conformation is observed for both amorphous and semi-crystalline samples, it can be assumed that this conformation dominates both crystalline and amorphous domains. It should be mentioned that the *all-trans* (*ttt*) conformation of the alkyl chain was observed for the crystalline domains of PEF and PET, and has been reported for one polymorphic form of PBT (poly(2,5-butylene terephthalate)) (Milani and Galimberti, 2014). However, the herein described results do not support a similar behavior on PBF.



A noticeable difference between the INS spectra of amorphous and semi-crystalline samples occurs in the region of ca. 800–900  $\text{cm}^{-1}$  (which embraces the out-of-plane bending of the furanic C-H bonds and the stretching of the butylene O- $\text{CH}_2$  bonds). In this case, the triads combining *gtg* with *syn, syn* or *syn, anti* conformations provide a better description of the INS spectrum of the amorphous sample. The *anti, anti-gtg* triad (Figure 3, middle blue trace) relates better with the INS spectrum of the semi-crystalline sample, suggesting the predominance of this conformation in the crystalline domains, hence shedding light into the crystalline structure puzzle of PBF.

## Further details from IR and Raman spectroscopy

For PEF, it was possible to infer the conformational preferences of the crystalline and amorphous domains from optical spectroscopy, i.e., infrared and Raman spectroscopy (Araujo C. F. et al., 2018). In particular, the *trans* vs. *gauche* infrared profiles could be related with similar cases previously described (namely, from PET studies). The *anti* vs. *syn* forms of FDCA fragment were identified with support from discrete quantum mechanical frequency calculations of PEF triads.

In the case of PBF, and regarding the conformation of the butylene chain, the comparison with the PBT analogue is the most straightforward. According to Milani et al. (Milani and Galimberti, 2014), there are several infrared markers associated with *gauche* and *trans* orientations of the butylene chain in PBT. For instance, the 917  $\text{cm}^{-1}$  band is an unambiguous marker of the PBT polymorph with *gtg* chain ( $\alpha$  polymorph) and the one at

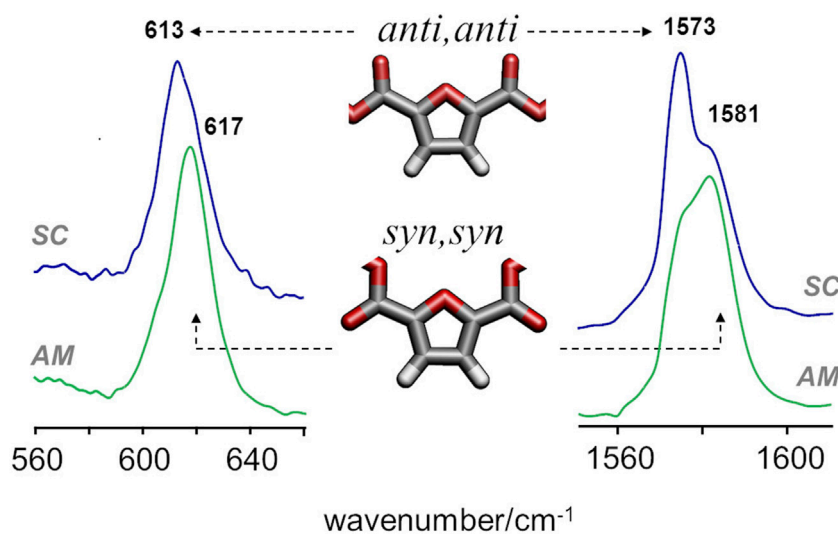


FIGURE 5

FTIR-ATR spectra of semicrystalline (top) and amorphous (bottom) samples of PBF, with identification of the bands sensitive to *syn-anti* isomerism.

960  $\text{cm}^{-1}$  is a marker of the crystal form possessing chains in *all-trans* conformation ( $\beta$  polymorph). Other  $\alpha/\beta$  markers in PBT are observed in the 1300–1550  $\text{cm}^{-1}$  region (Milani and Galimberti, 2014). Unfortunately, in the case of PBF, the infrared spectra in these regions are not unambiguous. Nevertheless, the infrared spectra of amorphous and semi-crystalline PBF samples (Figure 4), when compared with spectra of the  $\alpha/\beta$  forms of PBT in the same region, evidences a few features compatible with the prevalence of *gtg* configuration in both the crystalline and amorphous domains.

In particular, both samples present the same general profile of the *a* polymorph, with bands at 1377, 1450 and 1468  $\text{cm}^{-1}$ , and the absence of the  $\beta$  polymorph marker at 1485  $\text{cm}^{-1}$ . It should be mentioned that in the case of PEF, there are large intensity changes from the amorphous to the semi-crystalline samples in this region, signaling the change from *gauche* to *trans* conformation in the BG fragment. The absence of such changes in PBF is indirect evidence of the commonness of *gtg* forms in both amorphous and crystalline domains.

A more definite conclusion can be drawn from the infrared bands associated with *syn* and *anti* conformations of the FDCA moiety. For PEF, the frequencies of two vibrational modes - ring out-of-plane deformation and C=C stretching—were found to be sensitive to the *syn/anti* conformation (Araujo C. F. et al., 2018). In PBF triads, these modes are consistently predicted to fall in the same wavenumbers and follow the same pattern, with the lowest wavenumbers associated with *anti,anti* conformation and the highest wavenumbers associated with the *syn,syn* conformation. Figure 5 compares the infrared spectra of amorphous and semi-

crystalline samples in the relevant regions. The semi-crystalline sample is richer in the *anti*-FDCA forms, while the *syn*-FDCA forms are dominant in the amorphous sample.

These observations concerning the *syn-anti* conformations are consistent with the energetic profile described above and the expected changes upon crystalline packing. As observed for PEF, the *syn,syn* conformation has lower energy (and hence dominates the amorphous regions) but the *anti,anti* conformation is crucial for the establishment of C-H...O hydrogen bonds that stabilize the crystalline domains.

In the case of PEF, the presence of C-H...O hydrogen bond interactions was inferred from a few spectroscopic changes, namely, those observed for the in-plane deformation ( $\delta$ ) and the stretching ( $\nu$ ) of furanic C-H modes and the stretching of the carbonyl C=O mode (Araujo C. F. et al., 2018). In PBF, these vibrational modes follow the same trends reported for PEF, as shown in Figure 6: from the amorphous to semicrystalline samples, the  $\nu_{\text{sym}}$  CH<sub>ring</sub> mode displays a pronounced intensification in infrared intensity, along with a red-shift from 3125 to 3118  $\text{cm}^{-1}$ , a behaviour associated with the formation of C-H...O bonds; The blue-shift of the  $\delta$ CH<sub>ring</sub> deformation mode, clearly observed in the Raman spectra, is also a direct consequence of the restricted motion of CH<sub>ring</sub> moieties due to the formation of C-H...O bonds; And the band profile of carbonyl stretching mode shows the competing effects already discussed for PEF, with a broad profile characteristic of the amorphous sample and two sharper maxima emerging with increasing crystallinity.

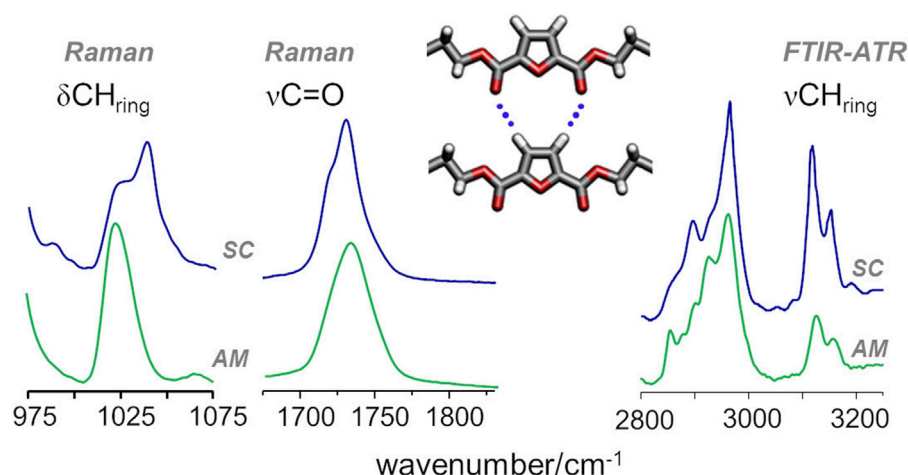


FIGURE 6

Raman and infrared spectra of amorphous (bottom) and semicrystalline (top) samples of PBF, highlighting the CH deformation ( $\delta\text{CH}_{\text{ring}}$ ) and stretching ( $\text{vCH}_{\text{ring}}$ ) and the C=O stretching ( $\text{vC=O}$ ) vibrational modes of FDCA moieties.

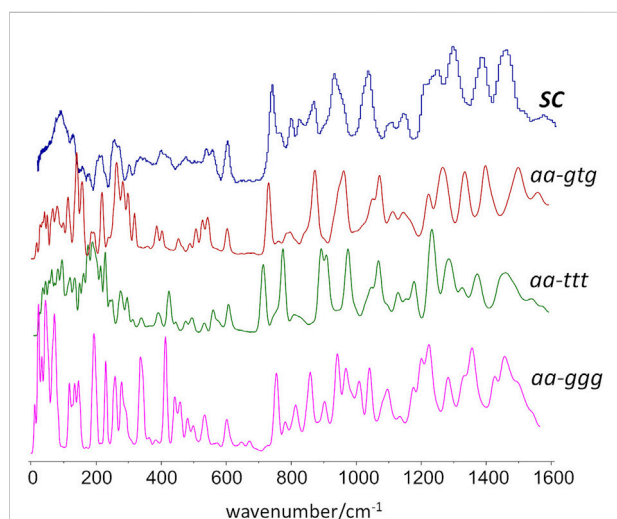


FIGURE 7

Experimental and calculated INS spectra obtained from periodic DFT calculations based on different conformational arrangements of the butylene skeleton. From top to bottom, experimental spectrum, calculated spectra for crystalline models with *gtg*, *ttt*, and *ggg* conformations.

## Crystal structure: What can be learned from computational spectroscopy?

On the whole, what can be said about the amorphous and crystalline domains of PBF?

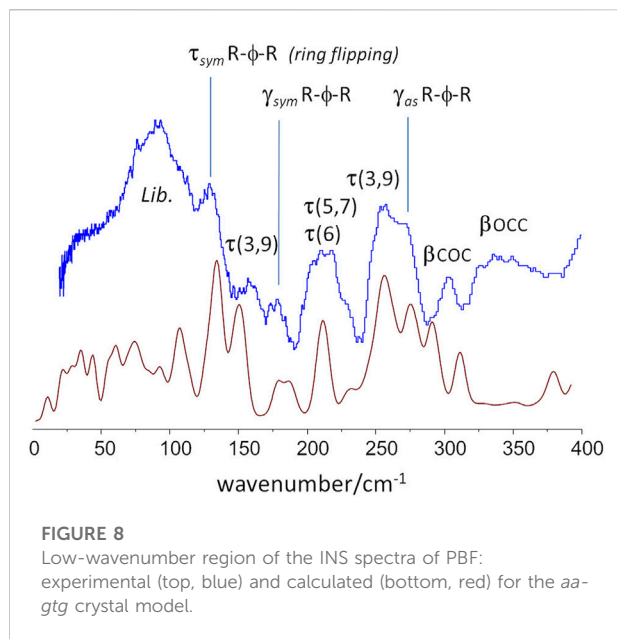
The amorphous domains are dominated by *gtg*-BG and *ss*-FDCA conformations, with contributions from *aa*-FDCA.

“Mixed” conformations, such as *gtt*- or *ggt*-BG and *as*-FDCA forms are also probable, considering the energy balances within the amorphous polymer chain.

For the crystalline domains, the most reasonable structures stem from “extended” conformations, such as the ones observed for *aa*-*ttt* or *aa*-*gtg*. “Winding” conformations, such as those observed for the lower energy triads are not prone to crystal packing. In addition, the above mentioned observations strongly support the existence of hydrogen-bonded FDCA fragments (which requires *anti*, *anti* orientation of the carbonyl groups) and the prevalence of *gtg* BG chains. In this way, periodic DFT calculations were performed for a crystalline structure based on the *aa*-*gtg* triad. In order to have a comparison set, similar calculations were performed for two other starting structures: 1) a crystal structure built from the most linear triad (*aa*-*ttt*), that mimics the planar structure observed for PEF; 2) a crystal using the reported X-ray as a starting point for geometry optimization. In this last case, (and as already mentioned for discrete calculations, above) the required geometry optimization corrected the unrealistic structural parameters, and led to a geometry that can be described as *aa*-*ggg*.

Figure 7 compares the experimental INS spectrum of the semi-crystalline sample with the simulated INS spectra for the three crystal models. As it can be seen, the best match is provided by the periodic structure based on the *aa*-*gtg* conformation.

For instance, the “intensity gap” at ca. 700  $\text{cm}^{-1}$  was only correctly predicted for the *aa*-*gtg*. Above this region, the *aa*-*ttt* structure clearly failed to reproduce the observed intensities for the  $\text{CH}_2$  rock, twist, wag and scissor modes at ca. 1200–1450  $\text{cm}^{-1}$ , as already observed from discrete calculations with the molecular triad models. The *aa*-*ggg* spectrum produced a large number of bands in the region of



900–1200  $\text{cm}^{-1}$ , whose general profile did not match the experimental spectrum. In what concerns the 300–600  $\text{cm}^{-1}$  interval, the bands of the experimental spectrum are nearly described by a one-to-one match to the *aa-gtg* spectrum, while both *aa-ggg* and *aa-ttt* forms deviate from this profile. Of course, below 200  $\text{cm}^{-1}$ , the intensities become increasingly “external” - or intermolecular - modes, and more dependent on crystal packing details. The description of external modes is generally known to be hampered by natural limitations of the periodic calculations (e.g. harmonic oscillator approximation, incomplete description of dispersion interactions, energy cut-offs, and the sum of numerical errors, which accumulate in the low wavenumber modes). Nevertheless, the simulated spectrum for the *aa-gtg* crystal structure provides a reasonable description of this region, allowing a reliable assignment of the low wavenumber bands, as shown in Figure 8.

This Figure 8 reveals some dynamical properties of crystalline PBF, which can be related with the longer alkyl chain of the BG fragment. For instance, the ring flipping mode, identified at *ca.* 160  $\text{cm}^{-1}$  in PEF is observed at *ca.* 130  $\text{cm}^{-1}$  in PBF. This significant reduction of the barrier to rotation of the furanic ring can be ascribed to a larger flexibility of the longer BG chain in the *gtg* conformation—corroborated from the presence multiple torsional modes in the 160–260  $\text{cm}^{-1}$  range. This larger flexibility is expected to affect the polymer properties, as discussed below.

An important vibrational mode in the comparison between 2,5-PEF and 2,4-PEF was the low-wavenumber mode described as “asymmetric out-of-plane bend of ring substituents” (Nolasco et al., 2020). In 2,4-PEF the mode was found to be sensitive to 2,4-FDCA orientation, becoming a broad band due to the random

orientation of furanic rings. In the symmetrical 2,5-analogue the mode occurs as a sharp band at 272  $\text{cm}^{-1}$ , very close to the value of 270  $\text{cm}^{-1}$  in PBF, indicating that this mode is not sensitive to the length or conformation of the alkyl chain.

How to derive macroscopic properties from the microscopic structure?

The in-depth understanding (or even prediction) of PBF macroscopic properties—namely, thermal and mechanical properties—using microscopic structure insights is the ultimate goal of the computational spectroscopy approach used in this study, and a highly desired exponent of polymer physics. However, it still remains a challenge, in large part due to the diversity of processes which ramp up into measurable properties, depending on such diverse factors such as the fine structure, chain regularity/symmetry and the chain flexibility, together with the intermolecular forces.

In addition, properties are dependent on factors such as average molecular weight, degree of crystallinity, and thermal history of the polymer sample (see, e.g. (Terzopoulou et al., 2020)).

The melting ( $T_m$ ) and the glass transition ( $T_g$ ) temperatures are thermal properties whose enthalpic component can be straightforwardly related to the intermolecular forces within the polymer bulk. While  $T_m$  is dependent on the interactions in the crystalline domains,  $T_g$  depends on cohesion of the amorphous form. Both transition temperatures are assumed to decrease with the increase of chain mobility and flexibility (Balani et al., 2015).

Crystal packing of PBF chains relies on the same intermolecular forces as PEF, namely the C-H...O contacts forming a planar layer, but the interactions between layers is hampered the *gtg* “ladder” motif of PBF, absent in PEF. This is in line with the  $T_m$  values of 211°C and 170°C reported for PEF and PBF, respectively (Burgess et al., 2014b; Guidotti et al., 2020). In what concerns the  $T_g$ , both intermolecular forces and chain stiffness are in the equation. The presence of some C-H...O contacts, even in the amorphous form, can be assumed for both PEF and PBF. However, in PBF the longer alkyl chain reduces the probability of C-H...O contacts in the amorphous domains, thus favouring an increase in free volume and reducing chain stiffness (due to the several *gauche/trans* conformations available). All these effects contribute to the huge decrease of  $T_g$ , from *ca.* 85°C in PEF to *ca.* 39°C in PBF (Burgess et al., 2014b; Guidotti et al., 2020).

The increased chain mobility of PBF relative to PEF brought by the presence of the longer alkyl chain spacer is expected to also affect properties such as gas permeation and elasticity. The gas barrier properties of PEF have been related with the restriction of the ring flipping motion (Burgess et al., 2014b; Araujo C. F. et al., 2018). As mentioned above, the ring flipping mode, identified at *ca.* 160  $\text{cm}^{-1}$  in PEF is observed at *ca.* 130  $\text{cm}^{-1}$  in PBF, signalling a significant reduction of the barrier to ring rotation. Hence, larger gas permeability can be predicted for PBF compared to



PEF, a prediction in agreement with the recently reported values (Guidotti et al., 2020; Zhao et al., 2021).

A relevant mechanical parameter of polymeric materials due to its relevance for applications is the Young's modulus,  $E$ , which is a measure of the elastic response to applied stress. For this property, which is more dependent on the above mentioned sample composition and processing, the experimental results are somewhat scattered. Nevertheless, a recent review (Terzopoulou et al., 2020) lists six values for PEF Young's modulus with average value of 2.5 GPa, and twelve values for PBF Young's modulus with average value of 1.4 GPa. Assuming a connection between the dihedral angles flexibility and polymer elasticity during the viscoelastic regime—an assumption that gets grounds on the molecular interpretation of Stirnemann (Stirnemann, 2022) for protein elasticity—the presence of a longer alkyl chain in PBF, with multiple low energy torsional modes, clearly supports the reduced stiffness of PBF relative to PEF, and, thus, in accordance with a lower PBF modulus.

## Conclusion

This work explores the conformational preferences and the structure-property correlations of biobased PBF, a longer chain analogue of PEF, from a computational spectroscopy approach, i.e., combining experimental results with computational chemistry. The approach combined infrared, Raman and inelastic neutron scattering spectroscopy with discrete and periodic density functional theory calculations, aiming at the identification of dominant structural motifs in the amorphous and crystalline regions—and, from this information at the microscopic level, predict and describe the macroscopic properties of the material.

In comparison with PEF, PBF presents higher conformational flexibility due to the presence of additional torsional degrees of freedom in the alkyl chain. Discrete calculations for triad models revealed a large number of conformations energetically accessible at room temperature, for both amorphous and crystalline forms. Nevertheless, it was possible to discriminate the conformational preferences for crystalline and amorphous domains by comparing the predicted and observed INS spectroscopic patterns and analyzing the infrared and Raman profiles in regions previously known to be sensitive to structural motifs.

The results strongly support the predominance of *gtg* conformations of the BG fragment in both the crystalline and amorphous domains. In what concerns the furandicarboxylate fragment, amorphous domains are dominated by *syn,syn* conformations, while in the crystalline domains the *anti,anti* form prevails. In addition, Raman and infrared spectra of the semi-crystalline sample unveil the spectral signature of the C-H...O hydrogen bond contacts, as found for PEF.

A possible crystalline structure, built from these conformational preferences (*aa-gtg*) and including a network of C-H...O hydrogen bond contacts, was optimized using periodic density functional theory. The *gtg* conformation of the BG fragment leads to a “ladder-like” chain. This is a relevant difference relative to PEF, for which only the fully planar *aa-t* structure allows the formation of the C-H...O hydrogen bond network. In PBF, a fully planar chain is also possible from the *ttt* conformation of the BG fragment, but with a substantially higher energy cost (ca. 10 kJ/mol per triad, as shown in Figure 2). This energy penalty is probably determinant in crystallization of PBF. Nevertheless, the existence of a higher energy PBF polymorph based on *aa-ttt* conformation cannot be discarded (and the INS main features for such *aa-ttt* polymorph are predicted from periodic DFT calculations in Figure 7).

As an ultimate goal of the computational spectroscopy approach herein described, some correlations between microscopic structure and macroscopic properties of PBF were addressed. In comparison with PEF, differences in melting and glass transition temperatures, as well as in elastic modulus and gas permeability can generally be understood at a deeper level. Furthermore, the experimental trend on lower thermal and Young's modulus of PBF could be predicted from the increased molecular flexibility resulting from the longer alkyl chain.

## Data availability statement

The datasets presented in this study can be found in online repositories. The names of the repository/repositories and accession number(s) can be found below: <http://www.crystallography.net/tcod/index.php>, 30000103 and 30000104; <https://data.isis.stfc.ac.uk/doi/INVESTIGATION/113612429/>.

## Author contributions

All authors contributed toward the planning, preparation and implementation of the fieldwork, data analysis and interpretation, and writing the manuscript. In addition, AFS and MMN were the principal investigators for ‘polymer science’ and ‘computational chemistry’ tasks, respectively; MMN was responsible for INS project at ISIS (DOI: 10.5286/ISIS.E.RB2000214); PDV and MMN were responsible for periodic DFT calculations; LCR was responsible for initial laboratory work and discrete DFT calculations, as a part of her graduation thesis under supervision of AFS and PR-C; PR-C, CFA, and MMC were engaged in discrete DFT calculations and sample environment, data acquisition and data processing tasks; SR, the instrument scientist at ISIS, provided the expertise on INS data collection and analysis; AFS and AJDS provided student supervision for preparation,

processing, and physical characterization of polymer samples; CB and MM were engaged in the synthesis and processing of polymer samples.

## Funding

This work was developed within the scope of the project CICECO-Aveiro Institute of Materials, UIDB/50011/2020, UIDP/50011/2020 and LA/P/0006/2020, financed by national funds through the FCT/MCTES (PIDDAC). This research is also sponsored by FEDER funds through the program COMPETE—Programa Operacional Factores de Competitividade—and by national funds through the FCT under the project UID/EMS/00285/2020. FCT is also acknowledged for the research contract under Scientific Employment Stimulus to AFS (CEECIND/02322/2020) and for the grant to CFA (SFRH/BD/129040/2017). The STFC Rutherford Appleton Laboratory is thanked for access to neutron beam facilities (TOSCA/RB2000214, DOI: 10.5286/ISIS.E.RB2000214). CASTEP calculations were made possible due to the computing resources provided by

STFC Scientific Computing Department's SCARF cluster. This publication was also supported by COST Action FUR4Sustain—European network of FURan based chemicals and materials FOR a Sustainable development, CA18220.

## Conflict of interest

The authors declare that the research was conducted in the absence of any commercial or financial relationships that could be construed as a potential conflict of interest.

## Publisher's note

All claims expressed in this article are solely those of the authors and do not necessarily represent those of their affiliated organizations, or those of the publisher, the editors and the reviewers. Any product that may be evaluated in this article, or claim that may be made by its manufacturer, is not guaranteed or endorsed by the publisher.

## References

- Araujo, C. F., Nolasco, M. M., Ribeiro-Claro, P. J., Rudić, S., Silvestre, A. J., Vaz, P. D., et al. (2018). Inside PEF: Chain conformation and dynamics in crystalline and amorphous domains. *Macromolecules* 51, 3515–3526. doi:10.1021/acs.macromol.8b00192
- Araujo, C., Freire, C. S. R., Nolasco, M. M., Ribeiro-Claro, P. J. A., Rudić, S., Silvestre, A. J. D., et al. (2018). Hydrogen bond dynamics of cellulose through inelastic neutron scattering spectroscopy. *Biomacromolecules* 19, 1305–1313. doi:10.1021/acs.biomac.8b00110
- Arnold, O., Bilheux, J. C., Borreguero, J. M., Buts, A., Campbell, S. I., Chapon, L., et al. (2014). Mantid—data analysis and visualization package for neutron scattering and  $\mu$  SR experiments. *Nucl. Instrum. Methods Phys. Res. Sect. A Accel. Spectrom. Detect. Assoc. Equip.* 764, 156–166. doi:10.1016/j.nima.2014.07.029
- Balani, K., Verma, V., Agarwal, A., and Narayan, R. (2015). *Biosurfaces: A materials science and engineering perspective*. United States: Wiley.
- Bianchi, E., Soccio, M., Siracusa, V., Gazzano, M., Thiagarajan, S., and Lotti, N. (2021). Poly(butylene 2, 4-furanoate), an added member to the class of smart furan-based polyesters for sustainable packaging: Structural isomerism as a key to tune the final properties. *ACS Sustain. Chem. Eng.* 9, 11937–11949. doi:10.1021/acssuschemeng.1c04104
- Bozell, J., and Petersen, G. R. (2010). Technology development for the production of biobased products from biorefinery carbohydrates - the US Department of Energy's "top 10" revisited. *Green Chem.* 12, 539–554. doi:10.1039/b922014c
- Burgess, S. K., Karvan, O., Johnson, J. R., Kriegel, R. M., and Koros, W. J. (2014a). Oxygen sorption and transport in amorphous poly(ethylene furanoate). *Polymer* 55, 4748–4756. doi:10.1016/j.polymer.2014.07.041
- Burgess, S. K., Kriegel, R. M., and Koros, W. J. (2015). Carbon dioxide sorption and transport in amorphous poly(ethylene furanoate). *Macromolecules* 48, 2184–2193. doi:10.1021/acs.macromol.5b00333
- Burgess, S. K., Leisen, J. E., Kraftschik, B. E., Mubarak, C. R., Kriegel, R. M., and Koros, W. J. (2014b). Chain mobility, thermal, and mechanical properties of poly(ethylene furanoate) compared to poly(ethylene terephthalate). *Macromolecules* 47, 1383–1391. doi:10.1021/ma5000199
- Burgess, S. K., Mikkilineni, D. S., Yu, D. B., Kim, D. J., Mubarak, C. R., Kriegel, R. M., et al. (2014c). Water sorption in poly(ethylene furanoate) compared to poly(ethylene terephthalate). Part 2: Kinetic sorption. *Polymer* 55, 6870–6882. doi:10.1016/j.polymer.2014.10.065
- Carlos Morales-Huerta, J., Martínez de Ilarduya, A., and Muñoz-Guerra, S. (2016). Poly(alkylene 2, 5-furandicarboxylate)s (PEF and PBF) by ring opening polymerization. *Polymer* 87, 148–158. doi:10.1016/j.polymer.2016.02.003
- Clark, S. J., Segall, M. D., Pickard, C. J., Hasnip, P. J., Probert, M. I. J., Refson, K., et al. (2005). First principles methods using CASTEP. *Cryst. Mat.* 220, 567–570. doi:10.1524/zkri.220.5.567.65075
- NIST Computational Chemistry Comparison Database, B. (2022). NIST stand. Ref. Database number 101. Available at: <https://cccbdb.nist.gov/vibscalejustx.asp> (Accessed September 15, 2022).
- de Jong, E., Visser, H. A., Dias, A. S., Harvey, C., and Gruter, G. J. M. (2022). The road to bring FDCA and PEF to the market. *Polym. (Basel)* 14, 943–1032. doi:10.3390/polym14050943
- Druzicki, K., Gaboardi, M., and Fernandez-Alonso, F. (2021). Dynamics & spectroscopy with neutrons—recent developments & emerging opportunities. *Polym. (Basel)* 13, 1440. doi:10.3390/polym13091440
- Dymkowski, K., Parker, S. F., Fernandez-Alonso, F., and Mukhopadhyay, S. (2018). AbINS: The modern software for INS interpretation. *Phys. B Condens. Matter* 551, 443–448. doi:10.1016/j.physb.2018.02.034
- European Bioplastics (2021). European bio-plastics. Available at: <https://www.european-bioplastics.org/market/>.
- European Commission (2015). COMMUNICATION FROM THE COMMISSION TO THE EUROPEAN PARLIAMENT, THE COUNCIL, THE EUROPEAN ECONOMIC AND SOCIAL COMMITTEE AND THE COMMITTEE OF THE REGIONS Closing the loop—An EU action plan for the Circular Economy Available at: <https://eur-lex.europa.eu/legal-content/EN/TXT/?uri=CELEX:52015DC0614>.
- Fei, X., Wang, J., Zhu, J., Wang, X., and Liu, X. (2020). Biobased poly(ethylene 2, 5-furanoate): No longer an alternative, but an irreplaceable polyester in the polymer industry. *ACS Sustain. Chem. Eng.* 8, 8471–8485. doi:10.1021/acssuschemeng.0c01862
- Fosse, C., Esposito, A., Thiagarajan, S., Soccio, M., Lotti, N., Dargent, E., et al. (2022). Cooperativity and fragility in furan-based polyesters with different glycolic subunits as compared to their terephthalic counterparts. *J. Non-Crystalline Solids* 597, 121907. doi:10.1016/j.jnoncrysol.2022.121907

- Guidotti, G., Soccio, M., Cruz Garcia-Gutierrez, M., Ezquerro, T., Siracusa, V., Gutierrez-Fernandez, E., et al. (2020). Fully biobased superpolymers of 2, 5-furandicarboxylic acid with different functional properties: From rigid to flexible, high performant packaging materials. *ACS Sustain. Chem. Eng.* 8, 9558–9568. doi:10.1021/acssuschemeng.0c02840
- Harrelson, T. F., Cheng, Y. Q., Li, J., Jacobs, I. E., Ramirez-Cuesta, A. J., Faller, R., et al. (2017). Identifying atomic scale structure in undoped/doped semicrystalline P3HT using Inelastic Neutron Scattering. *Macromolecules* 50, 2424–2435. doi:10.1021/acs.macromol.6b02410
- ISIS (2022). ISIS facility INS/TOSCA. Available at: <https://www.isis.stfc.ac.uk/Pages/tosca.aspx> (Accessed September 15, 2022).
- Klonos, P. A., Papadopoulos, L., Terzopoulou, Z., Papageorgiou, G. Z., Kyritsis, A., and Bikiaris, D. N. (2020). Molecular dynamics in nanocomposites based on renewable poly(butylene 2, 5-furan-dicarboxylate) *in situ* reinforced by montmorillonite nanoclays: Effects of clay modification, crystallization, and hydration. *J. Phys. Chem. B* 124, 7306–7317. doi:10.1021/acs.jpcc.0c04306
- Loos, K., Zhang, R., Pereira, I., Agostinho, B., Hu, H., Maniar, D., et al. (2020). A perspective on PEF synthesis, properties, and end-life. *Front. Chem.* 8, 585–618. doi:10.3389/fchem.2020.00585
- Ma, J., Yu, X., Xu, J., and Pang, Y. (2012). Synthesis and crystallinity of poly(butylene 2, 5-furandicarboxylate). *Polym. Guildf.* 53, 4145–4151. doi:10.1016/j.polymer.2012.07.022
- Matos, M., Sousa, A. F., Silva, N. H. C. S., Freire, C. S. R., Andrade, M., Mendes, A., et al. (2018). Furanate-based nanocomposites: A case study using poly(butylene 2, 5-furanate) and poly(butylene 2, 5-furanate)-co-(butylene diglycolate) and bacterial cellulose. *Polymers* 10 (1–16), 810. doi:10.3390/polym10080810
- Matos, M., Sousa, A. F., and Silvestre, A. J. D. (2017). Improving the thermal properties of poly(2, 5-furandicarboxylate)s using cyclohexylene moieties: A comparative study. *Macromol. Chem. Phys.* 218 (1–10), 1600492. doi:10.1002/macp.201600492
- Milani, A., and Galimberti, D. (2014). Polymorphism of poly(butylene terephthalate) investigated by means of periodic density functional theory calculations. *Macromolecules* 47, 1046–1052. doi:10.1021/ma402602f
- Milman, V., Perlov, A., Refson, K., Clark, S. J., Gavartin, J., and Winkler, B. (2009). Structural, electronic and vibrational properties of tetragonal zirconia under pressure: A density functional theory study. *J. Phys. Condens. Matter* 21, 485404. doi:10.1088/0953-8984/21/48/485404
- Nolasco, M. M., Araujo, C. F., Ribeiro-Claro, P., Rudic, S., and Vaz, P. D. (2021). Inside bio-based furan polymers: Conformation and dynamics in crystalline and amorphous domains. *STFC ISIS Neutron Muon Source*. doi:10.5286/ISIS.E.RB2000214
- Nolasco, M. M., Araujo, C. F., Thiagarajan, S., Rudic, S., Vaz, P. D., Silvestre, A. J. D., et al. (2020). Asymmetric monomer, amorphous polymer structure–property relationships in 2, 4-FDCA and 2, 4-PEF. *Macromolecules* 53, 1380–1387. doi:10.1021/acs.macromol.9b02449
- Papamokos, G., Dimitriadis, T., Bikiaris, D. N., Papageorgiou, G. Z., and Floudas, G. (2019). Chain conformation, molecular dynamics, and thermal properties of poly(n-methylene 2, 5-furanates) as a function of methylene unit sequence length. *Macromolecules* 52, 6533–6546. doi:10.1021/acs.macromol.9b01320
- Parker, S. F., Fernandez-Alonso, F., Ramirez-Cuesta, A. J., Tomkinson, J., Rudic, S., Pinna, R. S., et al. (2014). “Recent and future developments on TOSCA at ISIS,” in *J. Phys.: Conf. Ser.*. Editors S. JimenezRuiz and M. Parker 554, 012003. doi:10.1088/1742-6596/554/1/012003
- Perdew, J. P., Burke, K., and Ernzerhof, M. (1996). Generalized gradient approximation made simple. *Phys. Rev. Lett.* 77, 3865–3868. doi:10.1103/PhysRevLett.77.3865
- Pinna, R. S., Rudic, S., Parker, S. F., Armstrong, J., Zanetti, M., Škoro, G., et al. (2018). The neutron guide upgrade of the TOSCA spectrometer. *Nucl. Instrum. Methods Phys. Res. Sect. A Accel. Spectrom. Detect. Assoc. Equip.* 896, 68–74. doi:10.1016/j.nima.2018.04.009
- Pouloupoulou, N., Nikolaidis, G. N., Ioannidis, R. O., Efstathiadou, V. L., Terzopoulou, Z., Papageorgiou, D. G., et al. (2022). Aromatic but sustainable: Poly(butylene 2, 5-furandicarboxylate) as a crystallizing thermoplastic in the bioeconomy. *Ind. Eng. Chem. Res.* 61, 13461–13473. doi:10.1021/acs.iecr.2c02069
- Refson, K., Tulip, P. R., and Clark, S. J. (2006). Variational density-functional perturbation theory for dielectrics and lattice dynamics. *Phys. Rev. B* 73, 155114. doi:10.1103/PhysRevB.73.155114
- Robles-Hernandez, B., Soccio, M., Castrillo, I., Guidotti, G., Lotti, N., Alegria, A., et al. (2020). Poly(alkylene 2, 5-furanate)s thin films: Morphology, crystallinity and nanomechanical properties. *Polym. Guildf.* 204, 122825. doi:10.1016/j.polymer.2020.122825
- Soccio, M., Martinez-Tong, D. E., Alegria, A., Munari, A., and Lotti, N. (2017). Molecular dynamics of fully biobased poly(butylene 2, 5-furanate) as revealed by broadband dielectric spectroscopy. *Polym. Guildf.* 128, 24–30. doi:10.1016/j.polymer.2017.09.007
- Sousa, A. F., Guigo, N., Pożycka, M., Delgado, M., Soares, J., Mendonça, P. V., et al. (2020). Tailored design of renewable copolymers based on poly(1, 4-butylene 2, 5-furandicarboxylate) and poly(ethylene glycol) with refined thermal properties. *Polym. Chem.* 9, 722–731. doi:10.1039/c7py01627a
- Stirnemann, G. (2022). Molecular interpretation of single-molecule force spectroscopy experiments with computational approaches. *Chem. Commun.* 58, 7110–7119. doi:10.1039/D2CC01350A
- Stroupe, Z. D., Strange, N. A., Daemen, L. L., and Larese, J. Z. (2022). Inelastic neutron scattering from thin film biaxially oriented polyethylene terephthalate. *J. Phys. Chem. A* 126, 7491–7501. doi:10.1021/acs.jpca.2c05397
- Terzopoulou, Z., Papadopoulos, L., Zamboulis, A., Papageorgiou, D. G., Papageorgiou, G. Z., and Bikiaris, D. N. (2020). Tuning the properties of furandicarboxylic acid-based polyesters with copolymerization: A review. *Polym. (Basel)* 12. doi:10.3390/polym12061209
- Tkatchenko, A., and Scheffler, M. (2009). Accurate molecular van der Waals interactions from ground-state electron density and free-atom reference data. *Phys. Rev. Lett.* 102, 073005. doi:10.1103/PhysRevLett.102.073005
- United Nations (2020). Sustainable development goals. Available at: <https://unstats.un.org/sdgs/report/2020/> (Accessed September 15, 2022).
- Vilela, C., Freire, C. S. R., Araújo, C., Rudic, S., Silvestre, A. J. D., Vaz, P. D., et al. (2020). Understanding the structure and dynamics of nanocellulose-based composites with neutral and ionic poly(methacrylate) derivatives using inelastic neutron scattering and DFT calculations. *Molecules* 25, 1689. Article Number 1689. doi:10.3390/molecules25071689
- Werpy, T., and Petersen, G. (2004). *Top value added chemicals from biomass. Volume I—results of screening for potential candidates from sugars and synthesis gas*. United States: US Department of Energy. doi:10.2172/926125
- Zhao, M., Zhang, C., Yang, F., and Weng, Y. (2021). Gas barrier properties of furan-based polyester films analyzed experimentally and by molecular simulations. *Polym. Guildf.* 233, 124200. doi:10.1016/j.polymer.2021.124200
- Zhu, J., Cai, J., Xie, W., Chen, P.-H., Gazzano, M., Scandola, M., et al. (2013). Poly(butylene 2, 5-furan dicarboxylate), a biobased alternative to PBT: Synthesis, physical properties, and crystal structure. *Macromolecules* 46, 796–804. doi:10.1021/ma3023298



## OPEN ACCESS

## EDITED BY

Sidney J.L. Ribeiro,  
São Paulo State University, Brazil

## REVIEWED BY

Nuno Gonçalo Azoia,  
Aquitex S.A., Portugal  
Theo G.M. Van De Ven,  
McGill University, Canada

## \*CORRESPONDENCE

Carmen S. R. Freire,  
cfreire@ua.pt

## SPECIALTY SECTION

This article was submitted to  
Biomaterials,  
a section of the journal  
Frontiers in Bioengineering and  
Biotechnology

RECEIVED 30 September 2022

ACCEPTED 25 November 2022

PUBLISHED 13 December 2022

## CITATION

Silva ACQ, Silvestre AJD, Vilela C and  
Freire CSR (2022), Cellulose and protein  
nanofibrils: Singular biobased  
nanostructures for the design of  
sustainable advanced materials.  
*Front. Bioeng. Biotechnol.* 10:1059097.  
doi: 10.3389/fbioe.2022.1059097

## COPYRIGHT

© 2022 Silva, Silvestre, Vilela and Freire.  
This is an open-access article  
distributed under the terms of the  
[Creative Commons Attribution License](#)  
(CC BY). The use, distribution or  
reproduction in other forums is  
permitted, provided the original  
author(s) and the copyright owner(s) are  
credited and that the original  
publication in this journal is cited, in  
accordance with accepted academic  
practice. No use, distribution or  
reproduction is permitted which does  
not comply with these terms.

# Cellulose and protein nanofibrils: Singular biobased nanostructures for the design of sustainable advanced materials

Ana C. Q. Silva, Armando J. D. Silvestre, Carla Vilela and  
Carmen S. R. Freire\*

Department of Chemistry, CICECO—Aveiro Institute of Materials, University of Aveiro, Aveiro, Portugal

Polysaccharides and proteins are extensively used for the design of advanced sustainable materials. Owing to the high aspect ratio and specific surface area, ease of modification, high mechanical strength and thermal stability, renewability, and biodegradability, biopolymeric nanofibrils are gaining growing popularity amongst the catalog of nanostructures exploited in a panoply of fields. These include the nanocomposites, paper and packaging, environmental remediation, electronics, energy, and biomedical applications. In this review, recent trends on the use of cellulose and protein nanofibrils as versatile substrates for the design of high-performance nanomaterials are assessed. A concise description of the preparation methodologies and characteristics of cellulosic nanofibrils, namely nanofibrillated cellulose (NFC), bacterial nanocellulose (BNC), and protein nanofibrils is presented. Furthermore, the use of these nanofibrils in the production of sustainable materials, such as membranes, films, and patches, amongst others, as well as their major domains of application, are briefly described, with focus on the works carried out at the BioPol4Fun Research Group (Innovation in BioPolymer based Functional Materials and Bioactive Compounds) from the Portuguese associate laboratory CICECO—Aveiro Institute of Materials (University of Aveiro). The potential for partnership between both types of nanofibrils in advanced material development is also reviewed. Finally, the critical challenges and opportunities for these biobased nanostructures for the development of functional materials are addressed.

## KEYWORDS

cellulose, proteins, nanofibrils, nanostructured materials, advanced materials, sustainability

## Introduction

The transition towards a more sustainable society, aligned with the 2030 Agenda for Sustainable Development (United Nations, 2015), demands a considerable change in the overall design and manufacturing practices, regarding consumer items and materials with advanced functionalities (Silva et al., 2021b). In this perspective, naturally abundant and



renewable biobased feedstocks are increasingly being exploited as eco-friendly building blocks for the development of sustainable materials with diverse morphologies and applications (Silva et al., 2014a; Silva et al., 2021b; Shaghaleh et al., 2018; Mohammadian et al., 2020; Shen et al., 2021; Teixeira et al., 2022a).

The advent of nanotechnology and nanoscience has created an opportunity to control materials at the nanoscale, enabling the tailored design of complex nanostructures such as nanotubes, nanowires, nanofibrils, and nanoparticles (Krishnaswamy and Orsat, 2017; Carvalho et al., 2021b). Nanofibrils, i.e., fibers with diameter in the nanoscale and significantly longer lengths (up to several micrometers), have attracted the interest of researchers as essential building blocks in the development of innovative functional materials, owing to their outstanding mechanical properties (Barhoum et al., 2018; Barhoum et al., 2019). Particularly, nanofibrils obtained from polysaccharides (e.g., cellulose, chitosan/chitin) (Raza et al., 2021) and proteins (e.g., silk fibroin, soy protein, zein) (Babitha et al., 2017) combine the unique features of nanofibrils with biocompatibility, biodegradability, and in some cases specific biological properties, that can be exploited for the preparation of functional materials, such as membranes (Galiano et al., 2018), hydrogels (Ling et al., 2018b; Du et al., 2019), and films (Lendel and Solin, 2021), among others (Knowles and Mezzenga, 2016; Owolabi et al., 2020; Santos et al., 2021). These nanomaterials find application in high-tech applications, as for example, in enzyme immobilization (Frazão et al., 2014), functional textiles (Silva et al., 2021a), active food packaging (Cazón and Vázquez, 2021; Danilowski et al., 2021), tissue engineering and wound healing (Carvalho et al., 2019; Chen et al., 2022; Soroush et al., 2022), drug delivery (Almeida et al., 2014; Silvestre et al., 2014), cosmetic applications (Almeida et al., 2021; Meftahi et al., 2022), sensors and semiconductors (Cherian et al., 2022; Qiu et al., 2022), fuel cells (Vilela et al., 2019e), and environmental remediation (Muqet et al., 2020; Abdelhamid and Mathew, 2021; Peydayesh and Mezzenga, 2021; Raza et al., 2021).

As the most abundant polysaccharide on Earth, cellulose has attracted increased scientific and economic interest in materials development (Charreau et al., 2020; Meftahi et al., 2021), particularly in its nanometric forms, *viz.* cellulose nanocrystals (CNCs), nanofibrillated cellulose (NFC) and bacterial nanocellulose (BNC) (Freire et al., 2013; Figueiredo et al., 2014; Freire and Vilela, 2022). The majority of literature in this field addresses both established and novel methods for isolating and modifying nanocelluloses (Abdul Khalil et al., 2012; Meftahi et al., 2021; Sayyed et al., 2021; Hamimed et al., 2022; Pradhan et al., 2022) and their application in materials science (Carvalho et al., 2019; Vilela et al., 2019e; Wang et al., 2020; Subhedar et al., 2021; Wang et al., 2022). Thus, NFC and BNC will be the focus of this review concerning cellulose nanofibrils application in this field.

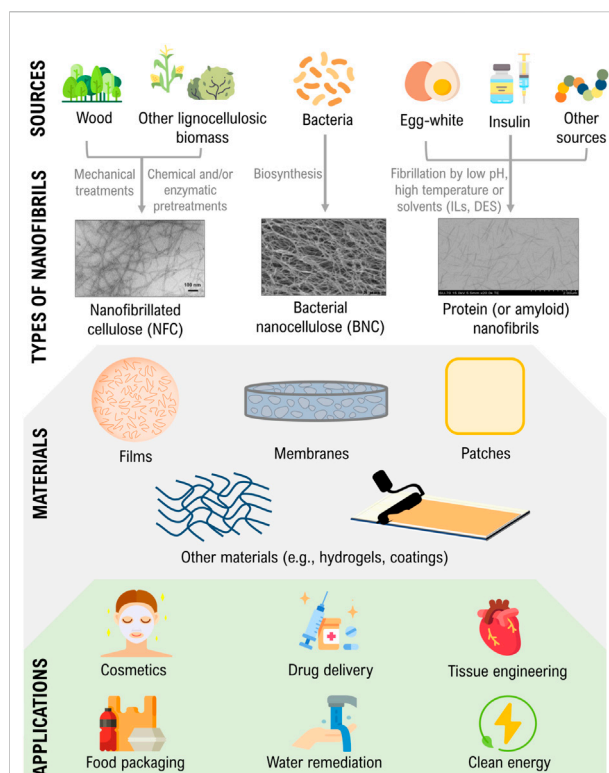
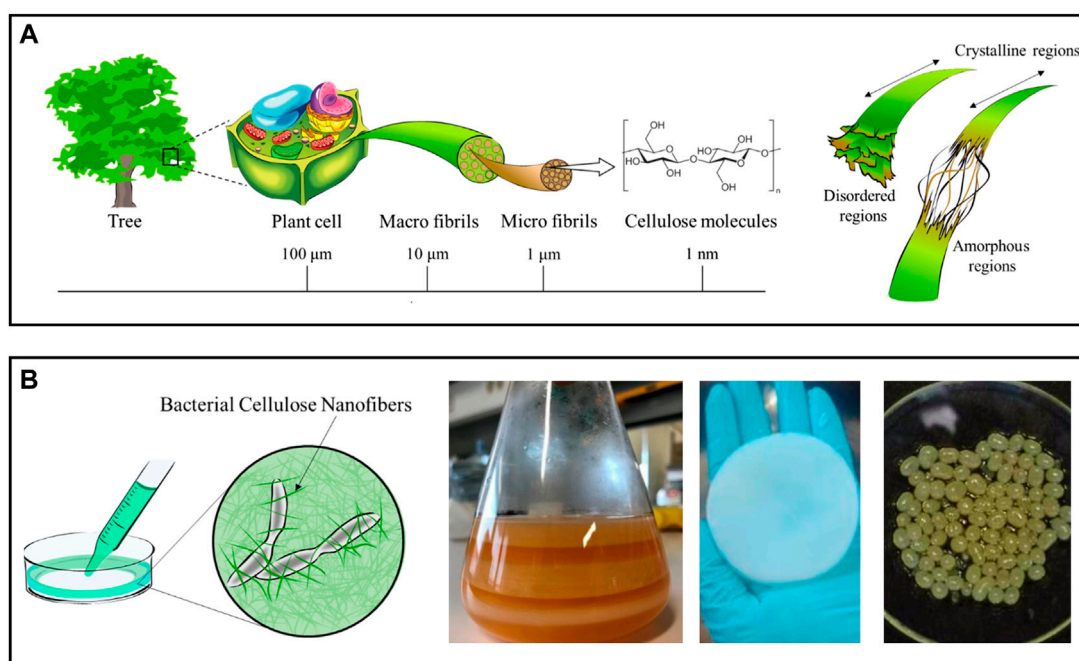


FIGURE 1

Illustration of the sources and production of nanocellulose and protein nanofibrils, their use in materials design, and critical areas of application. Transmission electron microscopy (TEM) micrographs are adapted and reprinted with permission from (Nazrin et al., 2020). Copyright Frontiers, 2020; and (Silva et al., 2018c). Copyright Elsevier, 2018.

On the other hand, owing to the recent advances in protein fibrillation mechanisms and methodologies (Wang et al., 2021), protein nanofibrils (also known as amyloid fibrils) obtained from both animal and plant-based origins (Meng et al., 2022) have stepped forward as promising nanostructures for the development of materials with a variety of functional properties that are gaining attention for packaging purposes (Danilowski et al., 2021; Hadidi et al., 2022), environmental remediation (Peydayesh and Mezzenga, 2021; Vinayagam et al., 2022), and biomedical applications (Silva et al., 2014a; Mohammadian et al., 2020), amongst others.

The production, modification, and applications of cellulose and protein nanofibrils have already been extensively reviewed, as proven by the number of review articles and book chapters *supra* cited. Nevertheless, as far as our research could go, only one review by Ling et al. (2018a) provided an overview of both polysaccharide and protein-based nanofibrils, specifically cellulose, chitin, silk, and collagen nanofibrils, for material production. This comprehensive work provides a detailed outline of the four most abundant biopolymer nanofibrils in terms of structure, computational models, processing

**FIGURE 2**

(A) Schematic representation of the hierarchical structure of cellulose obtained from plants, with detail in the crystalline and amorphous regions of the cellulose nanofibrils. Adapted and reprinted with permission from (Miyashiro et al., 2020). Copyright MDPI, 2020; (B) Diagram of a bacterial nanocellulose culture and digital photographs of membranes produced in static culture before (left) and after cleaning (center), and of spherical particles obtained in agitated culture conditions (right). Adapted and reprinted with permission from (Miyashiro et al., 2020). Copyright MDPI, 2020; and (Almeida et al., 2021). Copyright MDPI, 2021.

methodologies, and applications. Nonetheless, the authors only offer information regarding fibrous proteins (i.e., silk and collagen) despite the growing interest in the fibrillation process of globular proteins [e.g.,  $\beta$ -lactoglobulin (Loveday et al., 2017), lysozyme (Mohammadian and Madadlou, 2018)] with more complex structural levels and essential biological properties.

The present review will focus on nanocellulose fibrils, namely NFC and BNC, and protein amyloid nanofibrils, to design advanced and sustainable materials. Though cellulose nanocrystals (CNCs) are isolated from cellulosic feedstocks, the resulting highly-crystalline rod-like nanostructures contain all three exterior dimensions at the nanoscale and are classified as cellulose nanoparticles (Barhoun et al., 2019). As a result, this cellulose nanoform is beyond the scope of this review. Nonetheless, the reader can find more information about recent advances in the preparation and modification of CNCs, material fabrication, and significant application areas elsewhere (Long et al., 2021; Rana et al., 2021; Shojaeiarani et al., 2021).

Thus, this review provides a succinct overview regarding the fabrication methodologies and properties of nanocellulose and protein nanofibrils, their use in materials design, and critical areas of application (Figure 1), with emphasis on the works

developed in the latter years at the BioPol4Fun Research Group (Innovation in BioPolymer based Functional Materials and Bioactive Compounds) from the Portuguese associate laboratory CICECO—Aveiro Institute of Materials (University of Aveiro). The combination of both types of nanofibrils is also examined before concluding with some prospects for the exploitation of these nanostructures for materials research. Since it is impossible to dive into the detail of every cited work, a few key examples and features of representative materials have been chosen for a more elaborated discussion in the following sections. Further information concerning the type, composition, fabrication methodologies, and critical properties and applications of each material is summarized on Tables 1–5.

## Exploiting nanocellulose fibrils for the production of novel materials

With an estimated annual production of  $10^{11}$ – $10^{12}$  tonnes, cellulose is considered the most prevalent natural polymer and can be extracted from many sources, mostly from plants (lignocellulosic biomass), but also from algae, bacteria, and

tunicates (Nechporchuk et al., 2016; Trache et al., 2020). This linear polysaccharide is comprised of D-glucose units linked *via*  $\beta$ -(1 $\rightarrow$ 4) glycosidic bonds. Due to the strong intra- and intermolecular hydrogen bond network and the intermolecular van der Waals forces, the cellulose chains arrange themselves into a distinctive three-dimensional structure of microfibrils that contain crystalline (highly ordered) and amorphous domains (Figure 2A) (Noremylia et al., 2022). The intertwining of microfibrils culminates in the formation of macrofibrils.

As overviewed by Klemm et al. (2018), Thomas et al. (2020) and, more recently, by Noremylia et al. (2022), nanocelluloses can be extracted from native cellulose using top-down approaches, or obtained by bottom-up methodologies, producing nanostructures with distinct morphological features. According to their characteristics, three types of nanocellulose can be identified: 1) Cellulose nanocrystals (CNCs), also known as “nanocrystalline cellulose” or “cellulose nanowhiskers,” 2) Nanofibrillated cellulose (NFC), also commonly referred to as “microfibrillated cellulose” or “cellulose nanofibrils,” and 3) Bacterial nanocellulose (BNC), also denominated “microbial cellulose,” “biocellulose” or “biotech cellulose” (Klemm et al., 2018). As previously stated, this section will provide a brief rundown of the fabrication processes and attributes of NFC and BNC. Regardless, the reader is encouraged to examine the publications mentioned in each section, which provide a comprehensive overview of these topics.

Plant cellulose can be used to obtain nanofibrils (NFC) with a diameter of 5–60 nm and a length of a few micrometers, which contain both amorphous and crystalline regions (Figure 2A) (Nechporchuk et al., 2016). Delamination of cellulose fibers is most frequently accomplished in an aqueous medium through intense mechanical treatments (e.g., high-pressure homogenization, grinding, and refining), resulting in suspensions of NFC with low solid content (<5 wt%) (Nechporchuk et al., 2016; Noremylia et al., 2022). Despite the high energy consumption associated with these processes, this is the most scalable methodology and, as a result, the preferred option for industrial applications. Nonetheless, chemical and enzymatic pretreatments are also proposed to minimize the energy consumption in mechanical processing, while also increasing the degree of fibrillation of NFC, as these pretreatments disturb the hydrogen bond network (Pradhan et al., 2022; Squinca et al., 2022). Nevertheless, depending on the selection and combination of pretreatments and extraction processes, various grades of NFC with variable dimensions and properties (e.g., crystallinity, rheological behavior, surface chemistry) can be obtained (Nechporchuk et al., 2016). Non-traditional processes, such as extrusion, ball milling, steam explosion, aqueous counter collision, cryocrushing, and ultrasonication, have been proposed to govern the fibrillation process yielding NFC with more predictable properties (Wang et al., 2021).

In contrast, BNC results from a bottom-up process in which non-pathogenic bacterial strains synthesize the nanofibrils through a sequence of biochemical reactions driven by specific enzymes and cofactors (Manan et al., 2022). Most common BNC-producing species belong to the *Komagataeibacter* genus (previously known as *Gluconacetobacter* (Trovatti et al., 2011a)), although the list may include organisms from the *Agrobacterium*, *Rhizobium*, and *Pseudomonas* genus. In practice, BNC is a three-dimensional nanofiber network resulting from a fermentation process taking place in a nutrient-enriched culture medium (Klemm et al., 2018). Depending on the culture conditions, this network can be produced with tailored shapes and sizes, ranging from planar hydrogel pellicles, formed at the air-water interface of the culture media in static cultures, to sphere-like particles in agitated cultures (Figure 2B) (Chandana et al., 2022). The use of bioreactor systems with complex geometries is known to improve BNC yield, enabling the production of BNC on a larger scale (Chandana et al., 2022). Compared to NFC, bacterial nanocellulose has a high degree of crystallinity because it is free of hemicelluloses, lignin, and other minor compounds found in plant-lignocellulosic biomass (Klemm et al., 2018). BNC also has an exceptional water retention ability since it contains nearly 99% water.

Overall, cellulosic nanofibrils have remarkable properties, such as high surface area, high aspect ratio, tailorable surface chemistry, high mechanical strength, rheological behavior, high water absorption capacity, non-cytotoxicity, non-genotoxicity, and inherent renewability (Chandana et al., 2022; Noremylia et al., 2022), which elevate this polysaccharide out of the shadows of the pervasive pulp and paper industries to produce sophisticated materials, with diverse types and functionalities. However, due to the presence of three hydroxyl groups per anhydroglucose unit, these nanofibers are extremely hydrophilic, which can be seen as a benefit in applications in which water compatibility is an advantage (e.g., most often in biomedical applications) or as a drawback when compatibilization with hydrophobic domains is essential, thus requiring adequate modifications towards their hydrophobization.

The following sections illustrate some of the most recent and relevant contributions about the use of NFC and BNC to assemble membranes, films, patches and other materials.

## Membranes

The simplicity of creating membranes with tailored size and shape that do not disintegrate when exposed to water-rich environments is a particular advantage of BNC materials in several sectors. NFC-based membranes can also be produced by simple methodologies, like casting or filtration (Table 1). Moreover, cellulose nanofibrils have a high surface area and are simple to modify. As such, the properties of BNC and NFC can be

TABLE 1 Examples of membranes produced with cellulosic nanofibrils.

Type of nanofibrils	Other compounds	Methodology	Key properties and applications	Reference(s)
BNC	APS	Chemical grafting	Antibacterial activity: <i>E. coli</i> ; <i>S. aureus</i> Non-cytotoxic (adipose-derived stem cells)	Fernandes et al. (2013)
BNC	APS, AEAPS	Chemical grafting	Antibacterial activity: <i>S. aureus</i>	Chantereau et al. (2019a)
BNC	Fucoidan (0.5 and 0.75) <sup>a</sup>	Diffusion of aqueous solutions in the BNC matrix	Ion-exchange membranes for fuel cells Maximum ionic conductivity: 1.6 mS cm <sup>-1</sup>	Vilela et al. (2020c)
BNC	Lignosulfonates (0.5 and 0.75) <sup>a</sup>	Diffusion of aqueous solutions in the BNC matrix	Ion-exchange membranes for fuel cells Maximum ionic conductivity: 23 mS cm <sup>-1</sup>	Vilela et al. (2020b)
BNC	Nafion <sup>®</sup> (0.5) <sup>a</sup>	Diffusion of the ionomer in the BNC matrix	Ion-exchange membranes for fuel cells Maximum ionic conductivity: 140 mS cm <sup>-1</sup>	Gadim et al. (2016)
BNC	P(bis-MEP) (3 and 5) <sup>a</sup>	<i>in situ</i> free radical polymerization	Ion-exchange membranes for fuel cells Maximum ionic conductivity: 30 mS cm <sup>-1</sup>	Vilela et al. (2018b)
BNC	PAEM (6) <sup>a</sup>	<i>in situ</i> free radical polymerization	Antibacterial activity: <i>E. coli</i> Improvement of the thermal stability and water uptake capacity	Figueiredo et al. (2015a)
BNC	PGMA (2.0 and 20.0) <sup>a</sup>	<i>in situ</i> free radical polymerization	Improvement of the thermal stability and water uptake capacity Decrease in hydrophobicity	Faria et al. (2019a); Faria et al. (2019b)
BNC	PMACC (2, 5, 8 and 10) <sup>a</sup>	<i>in situ</i> free radical polymerization	Ion-exchange membranes for fuel cells Maximum ionic conductivity: 10 mS cm <sup>-1</sup>	Vilela et al. (2017)
BNC	PMMA, PBA	<i>in situ</i> atom transfer radical polymerization	Improvement of the thermal stability Increased hydrophobicity	Lacerda et al. (2013)
BNC	PMOEP (3, 5 and 10) <sup>a</sup>	<i>in situ</i> free radical polymerization	Ion-exchange membranes for fuel cells Maximum ionic conductivity: 100 mS cm <sup>-1</sup>	Vilela et al. (2016)
BNC	PMPC (3 and 5) <sup>a</sup>	<i>in situ</i> free radical polymerization	Antibacterial activity: <i>E. coli</i> ; <i>S. aureus</i> Water remediation (removal of cationic and anionic organic dyes)	Vilela et al. (2019b)
BNC	PSSA (5) <sup>a</sup>	<i>in situ</i> free radical polymerization	Ion-exchange membranes for fuel cells Maximum ionic conductivity: 185 mS cm <sup>-1</sup> Application in a microbial fuel cell with <i>Shewanella frigidimarina</i>	Gadim et al. (2014); Gadim et al. (2017); Vilela et al. (2020a)

<sup>a</sup>Nominal composition represented as the mass ratio of other compounds in relation to the nanofibrils ( $W_{\text{other compounds}}/W_{\text{nanofibrils}}$ ).

Abbreviations: AEAPS, (2-aminoethyl)-3-aminopropyl-trimethoxysilane; APS, 3-aminopropyl-trimethoxysilane; BNC, bacterial nanocellulose; P(bis-MEP), poly(bis[2-(methacryloyloxy)ethyl] phosphate); PAEM, poly(2-aminoethyl methacrylate); PBA, poly(butyl acrylate); PGMA, poly(glycidyl methacrylate); PMACC, poly(methacryloylcholine chloride); PMMA, poly(methyl methacrylate); PMOEP, poly(methacryloyloxyethyl phosphate); PMPC, poly(2-methacryloyloxyethyl phosphorylcholine); PSSA, poly(4-styrene sulfonic acid).

customized to accomplish specific functions (Shen et al., 2020). For instance, the chemical grafting of amino moieties grants antibacterial activity to BNC fibrils (Fernandes et al., 2013; Chantereau et al., 2019a), and the *in situ* atom transfer radical polymerization reaction of acrylate monomers onto the BNC nanofibrils surface can improve the hydrophobicity of the membranes (Lacerda et al., 2013). Additionally, the *in situ* free radical polymerization of acrylate monomers inside the 3D-network of BNC can increase their water uptake capacity (Figueiredo et al., 2015a), depending on the starting monomers and conditions. To illustrate, the grafting of poly(methyl methacrylate) in the BNC network increased the water static contact angle of the membrane from 32° up to 134°, thus enhancing its hydrophobic behavior (Lacerda et al., 2013). Owing to the properties mentioned above, allied with their tunable porous structure, nanocellulose-based materials are receiving significant attention for the fabrication of high-

performance membranes for environmental remediation purposes, with application as ion-selective separators for clean energy, in water purification, air filtration, and carbon dioxide sieving (Wang et al., 2022).

In the energy field, nanocellulose membranes are being exploited to design components of energy storage systems, in the development of electrodes *via* direct carbonization of the cellulose nanofibrils or incorporation of conductive polymers (e.g., polypyrrole), carbon (e.g., carbon nanotubes) and metal/metal oxides (e.g., silver, manganese dioxide) phases (Xiao et al., 2022). Nanocelluloses are also being explored as alternatives for components in energy generators like fuel cells, particularly as replacements for the ion-exchange membranes (Vilela et al., 2019e). Nanocelluloses do not naturally possess the ionic conductivity required for this application; however, this problem can be solved by incorporating ion-conducting phases either through the direct diffusion of ionomers, like Nafion<sup>®</sup>, into the



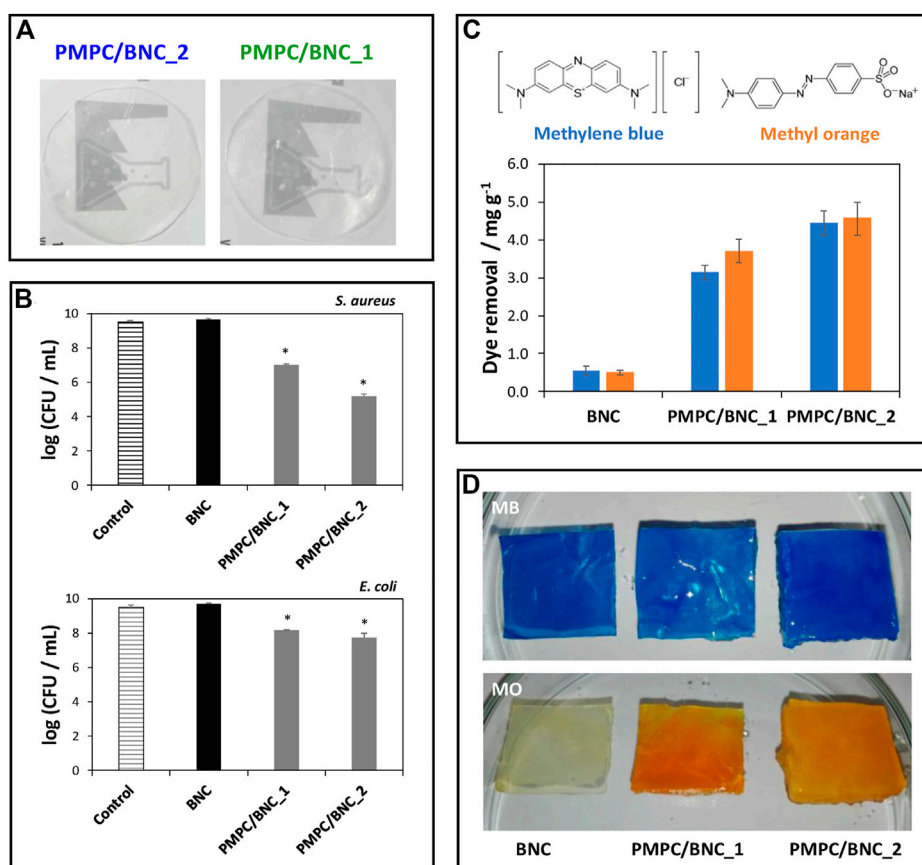


FIGURE 3

(A) Digital photographs of the zwitterionic membranes; (B) Graphical representation of the antibacterial activity of the membranes against *S. aureus* and *E. coli* after 24 h of exposure; (C) Chemical structures of the methylene blue (MB) and methylene orange (MO) dyes and graphical representation of the dye removal capacity of the BNC membranes with different compositions; (D) Digital photographs of the membranes after immersion in the aqueous dye solutions for 12 h. Reprinted with permission from (Vilela et al., 2019b). Copyright MDPI, 2019.

BNC 3D-nanofibrillar structure (Gadim et al., 2016) or via the *in situ* free-radical polymerization under green conditions of adequate synthetic monomers to generate polyelectrolytes, such as poly(4-styrene sulfonic acid) (Gadim et al., 2014, 2017; Vilela et al., 2020a), poly(methacryloyloxyethyl phosphate) (Vilela et al., 2016), poly(methacryloylcholine chloride) (Vilela et al., 2017) and poly(bis[2-(methacryloyloxy)ethyl] phosphate) (Vilela et al., 2018b). More recently, BNC and naturally derived macromolecules rich in ion-conducting functional groups have been combined to create fully biobased ion-exchange membranes. Fucoidan, an algal polysaccharide (Vilela et al., 2020c), and lignosulfonates, a by-product of the sulfite pulping process (Vilela et al., 2020b), are examples of this practice. Despite the ionic conductivity of some of these systems being two orders of magnitude lower than Nafion®, the benchmark for this application, these findings show the immense potential of cellulose nanofibrils for creating environmentally friendly separators.

Sorbents of modified nanocellulose membranes have been described to remove heavy metal ions, dyes, pesticides, pharmaceuticals, and other dissolved organic pollutants from contaminated waters (Muqheet et al., 2020; Abdelhamid and Mathew, 2021). Since cellulosic nanofibrils have low affinity for ionic species, it is necessary their combination with materials with high adsorption capacity (e.g., graphene oxide) (Abdelhamid and Mathew, 2021) or modification with adequate functional groups (e.g., carboxylate or quaternary ammonium moieties) to which metal ions, dyes or other contaminants (e.g., sulfate and fluoride anions) can bind to. Functional groups can also be imparted to cellulose nanofibers during the production stages, in the case of NFC, or by post-modification (Abdelhamid and Mathew, 2021). A common example is the introduction of carboxyl groups (COO⁻) via TEMPO-mediated oxidation of the C6 primary hydroxyl group, which is often used in the nanocellulose production stages. Cellulose nanofibrils with anionic functional groups (e.g., COO⁻) ensure high adsorption

TABLE 2 Examples of films produced with cellulosic nanofibrils.

Type of nanofibrils	Other compounds	Methodology	Key properties and applications	Reference(s)
BNC	PEDOT:PSS	Ink-jet printing	Reduced impedance and the 1/f <sup>2</sup> noise Application in sensors (glioma cells)	Inácio et al. (2020)
BNC	PSBMA (3 and 5) <sup>a</sup>	<i>in situ</i> free radical polymerization	UV-light barrier function Antibacterial activity: <i>E. coli</i> ; <i>S. aureus</i> Maximum ionic conductivity: 1.5 mS cm <sup>-1</sup> Application in active food packaging	Vilela et al. (2019c)
BNC (0, 0.5, 0.1, 0.2, 0.4 and 0.6) <sup>b</sup>	Pullulan	Solvent casting	Improvement of the thermal stability and mechanical properties	Trovatti et al. (2012a)
NFC (0.05, 0.10, 0.25, 0.50 and 0.75) <sup>b</sup>	Arabinoxylans, ferulic acid, or feruloylated arabinoxylo-oligosaccharides	Solvent casting	UV-light barrier function Antibacterial activity: <i>E. coli</i> ; <i>S. aureus</i> Antifungal activity: <i>C. albicans</i> Antioxidant activity: ca. 90%, DPPH assay Application in active food packaging	Moreirinha et al. (2020)
NFC	Mango leaf extract (0.1, 0.2, and 0.3) <sup>a</sup>	Supercritical solvent impregnation	UV-light barrier function Antibacterial activity: <i>E. coli</i> ; <i>S. aureus</i> Antioxidant activity: ca. 84%, DPPH assay Application in active food packaging	Bastante et al. (2021)
NFC (0, 0.5, 0.1, 0.2, 0.4 and 0.6) <sup>b</sup>	Pullulan	Solvent casting	Improvement of the thermal stability and mechanical properties	Trovatti et al. (2012b)

<sup>a</sup>Nominal composition represented as the mass ratio of other compounds in relation to the nanofibrils ( $W_{\text{other compounds}}/W_{\text{nano fibrils}}$ ).

<sup>b</sup>Nominal composition represented as the mass ratio of nanofibrils in relation to other compounds ( $W_{\text{nano fibrils}}/W_{\text{other compounds}}$ ).

Abbreviations: BNC, bacterial nanocellulose; DPPH, 2,2-diphenyl-1-picrylhydrazyl; NFC, nanofibrillated cellulose; PEDOT:PSS, poly(3,4-ethylenedioxythiophene):polystyrene sulfonate; PSBMA, poly(sulfobetaine methacrylate); UV, ultraviolet.

toward cationic contaminants. In contrast, nanofibrils bearing cationic groups can be effective sorbents for anionic compounds (e.g., fluoride) (Abdelhamid and Mathew, 2021).

However, the affinity towards both positively and negatively charged molecules is highly desirable in this field. To address that challenge, cellulose nanofibrils can be combined with zwitterionic polymers, such as the non-toxic poly(2-methacryloyloxyethyl phosphorylcholine), that contains a phosphate anion and a trimethylammonium cation (Vilela et al., 2019b). It was shown that this BNC/zwitterionic polymer membrane effectively collected cationic (methylene blue) and anionic (methylene orange) model dyes from contaminated water (ca. 4.4–4.5 mg g<sup>-1</sup>) and limited the growth of pathogens commonly observed in these environments (up to 4.3- and 1.8-log CFU reduction for *Staphylococcus aureus* and *Escherichia coli*, respectively), owing to the antimicrobial action of the polymer, highlighting the effective dual action of the biosorbents in the retrieval of contaminants (Figure 3). Overall, reusable nanocellulose membranes hold the potential for contaminant removal and salvage and repurposing of valuable waste matter, such as metals.

## Films

The fundamental shift towards a more environmentally conscious society has increased the demand for packaging

materials made from sustainable resources to reduce the volume and impact of the typical petroleum-based plastics we are accustomed to (Silva et al., 2021b) (Table 2). The inclusion of cellulose nanofibrils in polymeric films results in improved thermal and mechanical properties that are often vital for their target applications (Amara et al., 2021; Cazón and Vázquez, 2021). For instance, both BNC (Trovatti et al., 2012a) and NFC (Trovatti et al., 2012b) have been employed as reinforcing elements in homogeneous and translucent pullulan films *via* the simple solvent casting of aqueous suspensions, leading to nanocomposites films with improved thermal (increase in the maximum degradation temperature, compared to the neat pullulan films) and mechanical (e.g., a 22 times increase in the Young's modulus value with the inclusion of 10% of BNC, compared to unfilled pullulan matrices) properties.

Films that also offer active and intelligent functions are becoming ever more relevant in the food industry sector, as packaging acts as both a method of transportation and a mean of preserving the food contained within (Vilela et al., 2018a; Carvalho et al., 2021a). In this sense, films that incorporate additives with antimicrobial (e.g., metal nanoparticles, chitosan), antioxidant (e.g., plant extracts, phenolic compounds), and gas scavenging (e.g., metal oxides) functions can extend the shelf life of packed products, resulting in less food spoilage and waste (Vilela et al., 2018a). As an illustrative example, NFC-based films containing arabinoxylans obtained from brewers' spent grains and ferulic acid or feruloylated arabinoxylo-oligosaccharides displayed good antioxidant activity (ca. 90%, assessed by the DPPH radical scavenging

TABLE 3 Examples of patches produced with cellulosic nanofibrils.

Type of nanofibrils	Other compounds	Methodology	Key properties and applications	Reference(s)
BNC	Lidocaine (4.2 mg cm <sup>-2</sup> ) Ibuprofen (1.9 mg cm <sup>-2</sup> )	Diffusion of aqueous or ethanolic solutions in the BNC matrix	Incorporation of hydrophilic or hydrophobic drugs Application in drug delivery	Trovatti et al. (2011b); Trovatti et al. (2012c)
BNC	Diclofenac (1 and 2 mg cm <sup>-2</sup> )	Diffusion of aqueous solutions in the BNC matrix	Fast cumulative release (ca. 90%, after 10 min) Permeation studies in the skin ( <i>in vitro</i> ) Application in drug delivery	Silva et al. (2014c)
BNC	Diclofenac (2.1 mg cm <sup>-2</sup> ) Ibuprofen (1.9 mg cm <sup>-2</sup> ) Caffeine (8.0 mg cm <sup>-2</sup> ) Lidocaine (4.2 mg cm <sup>-2</sup> )	Diffusion of aqueous solutions in the BNC matrix	No noticeable alterations in morphology and release profile after accelerated stability tests Application in drug delivery	Silva et al. (2020c)
BNC	Alginate Chitosan Dexpanthenol (0.32 mg cm <sup>-2</sup> )	Layer-by-layer technology	Modulatory drug release depending on the number of layers of the patch Antibacterial activity: <i>S. aureus</i> Non-cytotoxic (HaCaT cells) Promote cell migration Application in wound healing	Fonseca et al. (2020)
BNC	Caffeine (8.0 mg cm <sup>-2</sup> )	Diffusion of aqueous solutions in the BNC matrix	Highly conformable Application in skin treatment (cellulite)	Silva et al. (2014b)
BNC	<i>E. globulus</i> leaves hydro-distillation extract (1.0, 1.5, 2.0 and 3.0 µg cm <sup>-2</sup> )	Diffusion of aqueous solutions in the BNC matrix	Antioxidant activity Non-cytotoxic (NIH/3T3, HaCaT cells) Minimized senescence of NIH/3T3 cells Application in skin treatment (antiaging)	Almeida et al. (2022)
BNC	Hyaluronic acid (0.62 mg cm <sup>-2</sup> ) Diclofenac (1.56 and 3.12 mg cm <sup>-2</sup> )	Diffusion of aqueous solutions in the BNC matrix	Fast cumulative release (max. 90% after 4 min) Adherent to oral mucosa simulant Non-cytotoxic (HaCaT cells) Application in drug delivery	Carvalho et al. (2020)
BNC	Hyaluronic acid Rutin (14.5 µg cm <sup>-2</sup> )	Micromoulding	The BNC backing layer delays drug release Antioxidant activity Non-cytotoxic (HaCaT cells) Application in drug delivery No adverse skin effects in human participants	Fonseca et al. (2021)
BNC	NSAIDs-based ILs (2.5 mg cm <sup>-2</sup> )	Diffusion of aqueous solutions in the BNC matrix	Increase in drug solubility (up to 100-fold) Fast cumulative release (ca. 90% after 2 h, for most of the systems) Non-cytotoxic (Raw 264.7 macrophages) Anti-inflammatory activity (in macrophages) Application in drug delivery	Chanterreau et al. (2019b)
BNC	Phenolic-based ILs (2.5 mg cm <sup>-2</sup> )	Diffusion of aqueous solutions in the BNC matrix	Antioxidant activity Bolus release, followed by a gradual release up to 24 h Non-cytotoxic (Raw 264.7 macrophages, HaCaT cells) Anti-inflammatory activity Application in skin treatment	Morais et al. (2019)
BNC	PMETAC (1.5 and 5) <sup>a</sup>	<i>in situ</i> free radical polymerization	Increase in high water uptake capacity Antifungal activity: <i>C. albicans</i> Non-cytotoxic (HaCaT cells) Application in the treatment of fungal infections	Vilela et al. (2019d)
BNC	PMGly (1, 2 and 3) <sup>a</sup> Diclofenac (5 mg cm <sup>-2</sup> )	<i>in situ</i> free radical polymerization	pH-dependent drug release Non-cytotoxic (HaCaT cells) Application in drug delivery	Saidi et al. (2017)

(Continued on following page)

TABLE 3 (Continued) Examples of patches produced with cellulosic nanofibrils.

Type of nanofibrils	Other compounds	Methodology	Key properties and applications	Reference(s)
BNC	Vitamin B-based ILs (2.5 mg cm <sup>-2</sup> )	Diffusion of aqueous solutions in the BNC matrix	Increase in vitamin B bioavailability (up to 30.6-fold) Increase in high water uptake capacity Fast cumulative release (at least 66% after 5 min) Non-cytotoxic (HaCaT cells) Application in skin treatment	Chantereau et al. (2020)

\*Nominal composition represented as the mass ratio of other compounds in relation to the nanofibrils ( $W_{\text{other compounds}}/W_{\text{nanofibrils}}$ ).

Abbreviations: BNC, bacterial nanocellulose; ILs, ionic liquids; NSAIDs, non-steroidal anti-inflammatory drugs; PMETAC, poly([2-(methacryloyloxy)ethyl]trimethylammonium chloride); PMGly, poly(*N*-methacryloyl glycine).

activity), which is essential to control the oxidative reactions and maintain the sensory properties of the foodstuff (Moreirinha et al., 2020). Furthermore, these films showed antimicrobial activity toward common food pathogens, i.e., Gram-positive (*S. aureus*) and Gram-negative (*E. coli*) bacteria and fungi (*Candida albicans*). The inclusion of these active compounds also offers the opportunity to improve the UV-light properties (decrease in the transmittance values of the films in the UVC (100–280 nm), UVB (280–320 nm) and UVA (320–400 nm) regions) and gas barrier of the films, while retaining the mechanical strength (Young's modulus up to 7.5 GPa) and flexibility characteristic of the cellulose nanofibrils (Moreirinha et al., 2020). NFC has also been combined with a mango leaf extract using conventional solvent-casting methodologies and alternatively by supercritical solvent impregnation (Bastante et al., 2021). The ensuing films displayed good antioxidant (ca. 84%, using the DPPH assay) and antimicrobial activity (ca. 37% and 91% growth inhibition of *S. aureus* and *E. coli*, correspondingly), which was more pronounced in the films prepared by the non-conventional supercritical solvent impregnation methodology, highlighting the potential of this eco-friendly technique in the production of bioactive films with improved functional properties.

Film packaging materials can house molecules that interact with internal (e.g., food) or external factors (e.g., temperature) and provide dynamic feedback regarding the condition of packed goods (Amin et al., 2022). These intelligent films can respond to environmental changes, such as variation in pH levels, gaseous composition, and microbial activity metabolites (e.g., hydrogen sulfide). The incorporation of these types of molecules in inherently biodegradable matrices (such as NFC and BNC) can be an appealing platform for the mitigation of the environmental footprint imposed by packaging goods. A case in point is the incorporation of poly(sulfobetaine methacrylate) in BNC films (Vilela et al., 2019c). This zwitterionic polymer endows antibacterial activity against *S. aureus* and *E. coli*, while also providing proton conductivity to the material (maximum of 1.5 mS

cm<sup>-1</sup>), which can be advantageous for the implementation as sensors to monitor food humidity levels.

## Patches

Nanostructured cellulose-based patches are attractive for a wide range of cosmetic and biomedical applications, including wound healing (Carvalho et al., 2019), drug delivery (Silvestre et al., 2014; Raghav et al., 2021), and skin care (Almeida et al., 2021), due to their inherent biodegradability, biocompatibility, capacity to avoid immunological reactions, and potential to be combined with other components, in particular, bioactive molecules and drugs (Table 3).

In the cosmetics industry, cellulose nanofibrils have been widely employed as stabilizers and thickening agents in cream and liquid formulations, as well as moisturizing agents and polymeric matrices (particularly BNC) in facial sheet masks and skin patches (Meftahi et al., 2022). In this latter application, BNC has emerged as an appealing substitute for cotton-based and synthetic polymer-based patches owing to its versatile production with tailored shapes and sizes and capacity to retain a broad range of compounds that can be delivered to the skin in a controlled and sustained manner (Almeida et al., 2021). As such, BNC can act as a carrier of skin-active substances such as caffeine (Silva et al., 2014b), commonly used in cellulite treatment, or plant-based extracts (Almeida et al., 2022), ionic liquids based on phenolic acids (Morais et al., 2019) and complex-B vitamins (Chantereau et al., 2020), which can be used in antiaging formulations. The formulation of these active principles as ionic liquids is aimed at modulating their water solubility and, thus, the resulting release profile. For instance, Chantereau et al. (2020) described an enhancement of the solubility of complex-B vitamins ionic liquids, composed of the vitamin anion and the cholinium cation, compared to the solubility of the original vitamins in water, thereby increasing their bioavailability (up to 30-fold). Moreover, including these active principles in BNC leads to a more complete and faster release of the compounds, which is attractive for short-term applications. BNC has also been reported as the backing layer of microneedles, i.e., arrays of micron-sized needles with



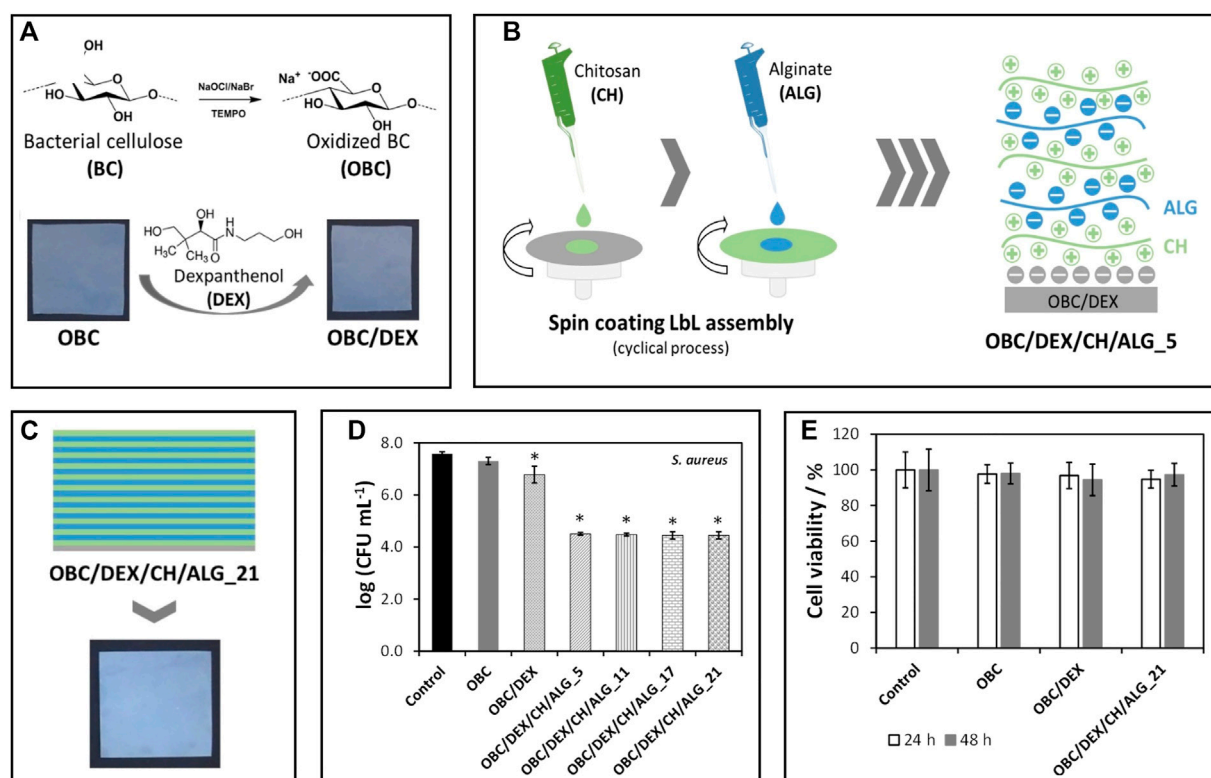


FIGURE 4

(A) Representation of the preparation of TEMPO-mediated oxidized BNC (OBC) and incorporation of dexpanthenol (DEX); (B) Scheme of the layer-by-layer spin coating assembly of the patches using alginate and chitosan, and (C) Digital photograph of the multilayered patches with 21 layers; Graphical representation of the (D) antibacterial activity of the patches against *Staphylococcus aureus* after 24 h of exposure and (E) cell viability of HaCaT cells after 24 and 48 h of exposure. Reprinted with permission from (Fonseca et al., 2020). Copyright MDPI, 2020.

25–2000 µm in height (Fonseca et al., 2019), to support the incorporation of bioactive molecules (e.g., rutin) and delay the release of active pharmaceutical ingredients (APIs) to the skin (delayed cumulative release plateau from 3 to 6.5 h) (Fonseca et al., 2021).

NFC (Raghav et al., 2021) and BNC (Silvestre et al., 2014) based materials can be employed as oral, buccal, or topical drug delivery systems for hydrophilic and hydrophobic APIs. BNC displays its supremacy yet again by facilitating the manufacture of pharmacological patches or other carriers *via* the simple diffusion of APIs aqueous solutions across its three-dimensional porous network. Among the numerous works, we highlight the use of BNC in combination with lidocaine (Trovatti et al., 2011b; 2012c), ibuprofen (Trovatti et al., 2012c), diclofenac (Silva et al., 2014c; Saïdi et al., 2017), diclofenac/hyaluronic acid (Carvalho et al., 2020), and non-steroidal anti-inflammatory drugs (NSAIDs)-based ionic liquids (Chantreau et al., 2019b).

Even when subjected to accelerated testing settings at varying temperatures and relative humidity, BNC patches retain their morphological integrity and release profile

(Silva et al., 2020c). In the cases mentioned above, the release of the drugs is essentially governed by their hydrophobic/hydrophilic character diffusion through the 3D network of BNC. However, the modulation of drug release is highly desirable in drug delivery. For instance, Saïdi et al. (2017) modified BNC, under green reaction conditions, with polymers containing amino acid pending moieties to produce patches with pH-responsive behavior.

In wound healing, BNC is once more the material of choice for most applications due to its high purity and similarity to the extracellular matrix (Carvalho et al., 2019). BNC-based wound dressings provide an adequate moist environment with selective oxygen and water permeability, while simultaneously protecting the injured area from the entry of pathogens and removing the exudates from the site (Carvalho et al., 2019). Additionally, they are simple to detach from the area without inflicting pain or dislodging the newly formed tissue. BNC patches can be functionalized with hemostatic and antimicrobial agents or other bioactive molecules that improve skin cell proliferation and accelerate wound healing. For instance, Fonseca et al. (2020) prepared BNC

TABLE 4 Examples of other functional materials produced with cellulosic nanofibrils.

Type of nanofibrils	Other compounds	Methodology	Key properties and applications	Reference(s)
BNC	Graphene oxide (0.025, 0.05 and 0.10) <sup>a</sup> Phase change materials (0.05 and 0.10) <sup>a</sup>	Solvent casting	Flame retardancy Increased hydrophobicity and hydrophobic behavior Application as thermal/sound insulator materials	Pinto et al. (2020b)
BNC	PCL (2.5, 5, 10 and 20 g L <sup>-1</sup> )	Addition of PCL in the BNC growth media, followed by hot-pressing	Blend of hydrophobic matrices (PCL) and hydrophilic fibers (BNC) Improvement of the mechanical properties	Figueiredo et al. (2015b)
BNC (0.01, 0.04 and 0.06) <sup>b</sup>	PLA	Melt-mixing	Improvement of the thermal stability and mechanical properties	Tomé et al. (2011)
NFC	AgNPs	Electrostatic assembly	Antibacterial activity: <i>S. aureus</i> ; <i>K. pneumoniae</i> Application in paper coatings	Martins et al. (2012)
NFC	CuNWs (0.01, 0.05, 0.10, 0.20, and 0.50) <sup>a</sup>	Vacuum filtration	Electroconductivity Application in paper coatings	Pinto et al. (2020a)
NFC modified with cationic latex nanoparticles (0.01, 0.05 and 0.075) <sup>b</sup>	PCL	Melt-mixing	Increase compatibility of the fibrils with the matrix due to the cationic latex nanoparticles Enzymatically degradable nanocomposites	Vilela et al. (2019a)
NFC	ZnO NPs	Electrostatic assembly	Antibacterial activity: <i>S. aureus</i> ; <i>K. pneumoniae</i> ; <i>B. cereus</i> Application in paper coatings	Martins et al. (2013)

<sup>a</sup>Nominal composition represented as the mass ratio of other compounds in relation to the nanofibrils ( $W_{\text{other compounds}}/W_{\text{nanofibrils}}$ ).

<sup>b</sup>Nominal composition represented as the mass ratio of nanofibrils in relation to other compounds ( $W_{\text{nanofibrils}}/W_{\text{other compounds}}$ ).

Abbreviations: AgNPs, silver nanoparticles; BNC, bacterial nanocellulose; CuNWs, copper nanowires; NFC, nanofibrillated cellulose; NPs, nanoparticles; PCL, poly( $\epsilon$ -caprolactone); PLA, poly(lactic) acid.

patches loaded with dexamethenol, an API used in the treatment of dermatological conditions as a topical protectant and moisturizing agent, and spin-coated the patches with varying layers of alginate and chitosan (Figure 4). The multilayered patches presented antibacterial activity against *S. aureus*, mainly due to the presence of chitosan, a polysaccharide with well-known antimicrobial activity (Wang et al., 2020). They also promoted cell migration and wound closure (*in vitro*) by the inclusion of dexamethenol in the non-sacrificial BNC matrix. Furthermore, the *in vitro* release profile of the API could be modulated by the number of layers of the polysaccharides, with an extended timeframe of drug delivery as the number of layers increased (Fonseca et al., 2020).

## Other materials

Over the years, researchers have been exploring the exceptional mechanical properties and thermal stability of cellulose nanofibrils for application as reinforcing agents in thermoplastic matrices to improve the properties of the ensuing composites (Shen et al., 2020) (Table 4). BNC has

been used as a reinforcement of poly(lactic acid) (PLA) membranes with visible improvements on the mechanical (higher Young's modulus, compared to neat PLA) and thermal (increase in the initial and maximum degradation temperatures, compared to neat PLA) properties of the materials (Tomé et al., 2011). Unmodified and modified NFC also was used to reinforce poly( $\epsilon$ -caprolactone) (PCL) matrices using a melt-mixing approach, wherein the nanofillers are directly dispersed in the melted polymer and extruded to produce the final nanocomposite materials (Vilela et al., 2019a). The inclusion of NFC modified with cationic latex nanoparticles had no noticeable impact on the composite's thermal properties (thermal stability up to 335–340°C). However, it improved the mechanical properties (increase in Young's modulus of the PCL matrices from 41.1 to 52.5 MPa, with the inclusion of only 7.5 wt% of modified NFC) and accelerated the rate of enzymatic degradation of the nanocomposites (from 1.40% for the pure PCL to 1.67–2.21% for the modified nanocomposites, after 10 weeks). This study demonstrated the application of environmentally friendly techniques that improve the compatibility of cellulose nanofibrils with hydrophobic matrices and accelerate the rate at which composites biodegrade. Following a different strategy,

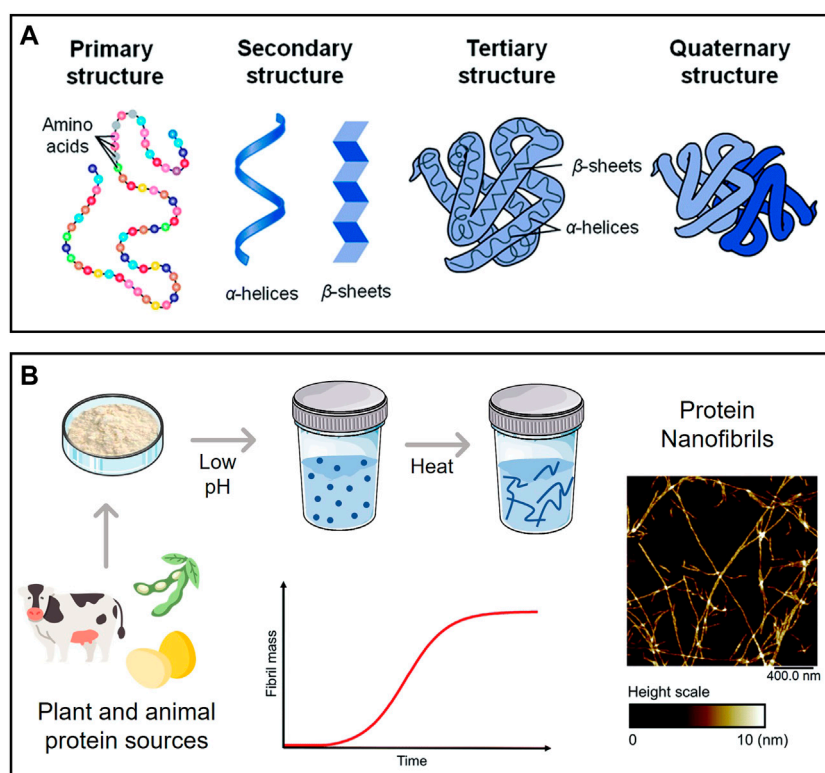


FIGURE 5

(A) Levels of protein organization; (B) Schematic representation of a typical process of protein nanofibril production using low pH and elevated temperature, with an illustrative example of their morphology (atomic force microscopy micrograph). Adapted and reprinted with permission from (Silva et al., 2014a). Copyright The Royal Society of Chemistry, 2014; and (Lendel and Solin, 2021). Copyright The Royal Society of Chemistry, 2021.

Figueiredo et al. (2015b) produced BNC/PCL composites through the addition of the powdered PCL to the culture media, followed by hot pressing of the ensuing membranes, to melt the PCL that was retained inside the porous cellulose network.

As shown in the previous sections, nanocelluloses can harbor molecules with known functional roles using simple and cost-effective techniques. Nanopapers with inherent conductivity can be prepared by the simple vacuum filtration of NFC suspensions containing copper nanowires (Pinto et al., 2020a), and nanocomposite foams with enhanced fire-retardancy and thermal energy storage capacity may be prepared by solvent casting and freeze-drying of disintegrated BNC nanofibrils, graphene oxide, and phase change materials (Pinto et al., 2020b). Cellulose-based functional coatings prepared *via* the functionalization of nanofibrils with antibacterial moieties [e.g., silver (Martins et al., 2012) and zinc oxide nanoparticles (Martins et al., 2013)] are desirable for many substrates, namely paper materials for packaging solutions. Highly porous nanocellulose materials (e.g., aerogels, cryogels, xerogels, foams, and sponges) are of great interest not only in environmental remediation and

catalysis but also in the construction field as thermal and sound insulators (Sun et al., 2021).

Since BNC nanofibrils are analogous to the fibrillar component of the extracellular matrix, nanostructured implantable materials (e.g., injectable hydrogels, tubular grafts, and scaffolds) have been extensively reported in the field of tissue engineering to promote cell regeneration in damaged sites (Carvalho et al., 2019). BNC and NFC nanofibrils can be manipulated to fabricate biomimetic spherical microparticles or microcapsules for cell culture applications (Carvalho et al., 2021b). Cellulosic nanofibrils have also been described as reinforcement additives in the development of bioinks for the 3D printing of hydrogel scaffolds, with application in tissue engineering and 3D cell culture (Teixeira et al., 2022a).

## Exploiting protein fibrils for the production of novel materials

Proteins (or polypeptides) are among the most prevalent organic macromolecules in living organisms, taking part in

TABLE 5 Examples of functional materials produced with protein-based nanofibrils.

Type of nanofibrils	Other compounds	Methodology	Key properties and applications	Reference(s)
<b>Films</b>				
LNFs (0, 0.01, 0.03, 0.05, 0.10 and 0.15) <sup>a</sup>	Pullulan	Solvent casting	Improvement of the mechanical properties Antioxidant activity: ca. 77%, DPPH assay Antibacterial activity: <i>S. aureus</i> Application in active food packaging	Silva et al. (2018b)
LNFs/NFC (2:1, 1:1 and 1:2 mass ratios)		Vacuum filtration	Improvement of the mechanical properties pH-dependent metal sorption capacity (ca. 99%, at pH 11) Application in water remediation (removal of Hg <sup>2+</sup> )	Silva et al. (2020a)
<b>Patches</b>				
LNFs (0, 0.05 and 0.10) <sup>a</sup>	Gelatin Curcumin	Electrospinning	Improvement of the mechanical properties Antioxidant activity: ca. 80%, DPPH assay Reduced bioresorbability rate from 45 to 30–35 days Burst release of curcumin, followed by a constant release for the next 21 days Non-cytotoxic (H9c2 cells, human dermal fibroblasts) Application in tissue regeneration (myocardium)	Carvalho et al. (2022)
LNFs/NFC (1:1 mass ratio)		Vacuum filtration	Antioxidant activity: 76–79%, DPPH assay Antibacterial activity: <i>S. aureus</i> Non-cytotoxic (L929 fibroblast cells) Promote cell migration Application in wound healing	Silva et al. (2020b)
<b>Other materials</b>				
LNFs (0.01, 0.05 and 0.10) <sup>a</sup>	Alginate	3D Bioprinting	Non-cytotoxic (HaCaT cells) Promote cell proliferation for up to 7 days after bioprinting Application in bioink formulation (cell-laden scaffolds)	Teixeira et al. (2022b)

<sup>a</sup>Nominal composition represented as the mass ratio of nanofibrils in relation to other compounds ( $W_{nanofibrils}/W_{other\ compounds}$ ).

Abbreviations: DPPH, 2,2-diphenyl-1-picrylhydrazyl; LNFs, lysozyme nanofibrils; NFC, nanofibrillated cellulose.

important structural and biological roles (Silva et al., 2014a). As illustrated in Figure 5A, they are comprised of a linear sequence of amino acids (primary structure) with a specific local conformation (secondary structure) and a three-dimensional spatial arrangement (tertiary structure). Some proteins can also display a quaternary structure, resulting from the non-covalent interaction between different tertiary structures. These macromolecules can self-assemble into highly ordered amyloid nanofibrils with diameters of 5–10 nm, lengths of several micrometers, and aligned cross- $\beta$  structures connected by a strong network of hydrogen bonds (Ye et al., 2019). The fibrillation phenomenon is typically linked to the misfolding of soluble proteins and accumulation of agglomerated amyloid nanofibrils (i.e., amyloid plaques) present in neurodegenerative conditions like Parkinson's and Alzheimer's (Salahuddin et al., 2021). Several biological proteins are known to self-assemble both *in vivo* and *in vitro* into nanofibrils with non-toxic and functional properties, such as the chorion proteins that protect silkworm eggs and the Pmel17 that is involved in human melanin formation (Ye et al., 2019).

Amyloid nanofibrils can be produced *in vitro* from animal proteins, such as whey protein and hen egg white lysozyme, as

study models to examine the principles and mechanisms governing protein self-assembly and fibrillation (Loveday et al., 2017). These protein nanofibrils are formed by partially or entirely unfolding the native structure of the protein, revealing potential amyloidogenic regions in the chain that can assemble into fibrils under specific conditions (Ye et al., 2019). Exposure to low pH (ca. 2) and high temperature is known to promote protein fibrillation (Figure 5B), as is the addition of certain chemicals (e.g., urea, alcohols) and enzymes (e.g., trypsin). The morphology and yield can be adjusted by varying the incubation time, temperature, pH, and ionic strength (Moayedzadeh et al., 2015). Furthermore, microwave irradiation (Carvalho et al., 2016) can shorten the time required to obtain the protein nanofibrils from days to a couple of hours. The use of alternative solvents with benign character as fibrillation agents (e.g., ionic liquids (Silva et al., 2018a) and deep eutectic solvents (Silva et al., 2018c)) is also able to reduce the fibrillation time.

Aside from providing new insights into the pathophysiology triggered by the formation of amyloid nanofibrils, the ability to obtain proteinaceous nanofibrils with exceptional mechanical and thermal stability from animal (e.g., whey protein, hen egg white lysozyme, milk casein) and plant-based (e.g., soy protein isolate,



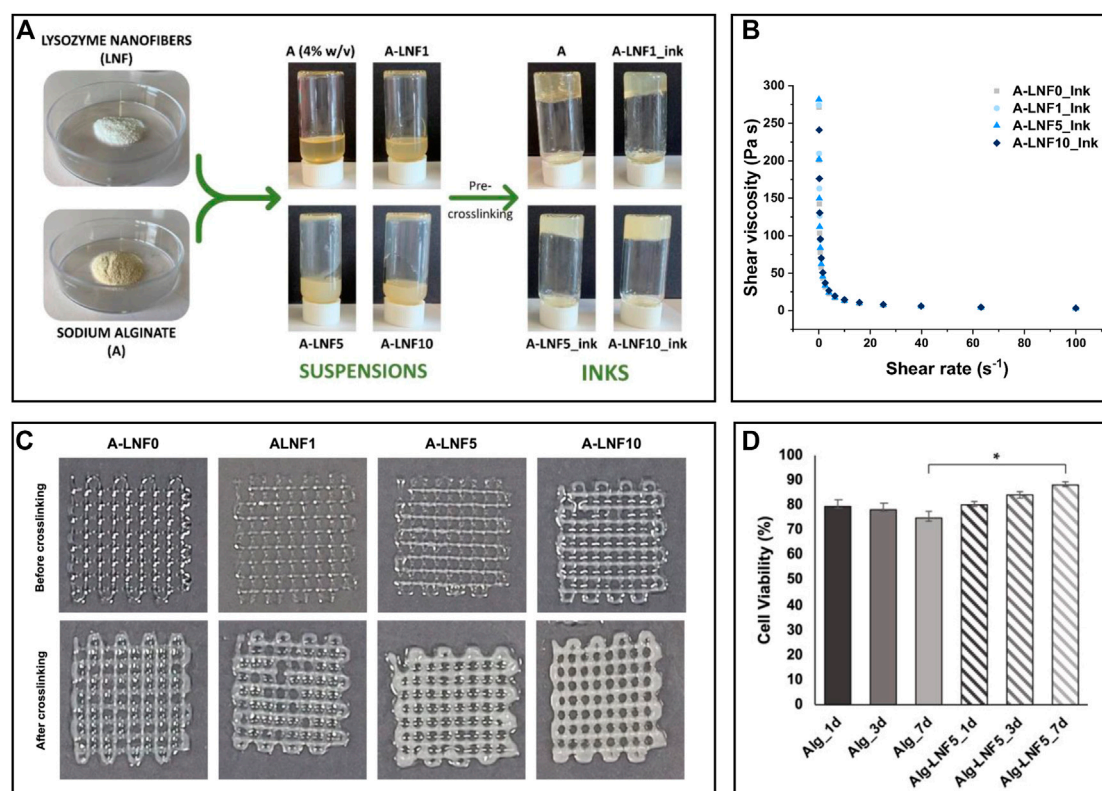


FIGURE 6

(A) Illustration of the preparation of the alginate and lysozyme nanofibrils (LNFs) bioinks; (B) Graphical representation of the shear viscosity of the inks with different contents of LNFs; (C) Optical micrographs of the printed scaffolds (2 layers) before and after crosslinking with  $\text{CaCl}_2$ ; (D) Graphical representation of the cell viability of HaCaT cells incorporated in the scaffolds after 1, 3 and 7 days of bioprinting. Reproduced with permission from (Teixeira et al., 2022b). Copyright MDPI, 2022.

rice glutelin,  $\alpha$ -zein) proteins offer an opportunity to use these renewable resources for the development of innovative materials with a high added value (Knowles and Mezzenga, 2016; Lendel and Solin, 2021; Meng et al., 2022). Furthermore, the discovery of functional nanofibrils *in vivo* opens the door to the laboratory synthesis of protein nanofibrils that preserve the inherent biological features of parent proteins, e.g., the antibacterial capabilities of lysozyme (Sarkar et al., 2020), which might be imparted onto the final materials (Table 5).

In the next sections, relevant examples of the development of new nanomaterials (films, patches and other materials) based on protein nanofibrils will be discussed in detail.

## Films

Protein nanofibrils are incredibly robust, with mechanical strength akin to spider silk and far superior to most biological filaments, and interestingly, also show higher thermochemical stability than their native counterparts (Knowles and Mezzenga, 2016). Nevertheless, the inability of protein nanofibrils to form

freestanding films, together with their distinct size and morphology, underline the unique role of protein nanofibrils as nanofillers or templates for the creation of innovative nanocomposite films (Ye et al., 2019). For instance, lysozyme nanofibrils (LNFs) can be combined with the filmogenic polysaccharide pullulan using a simple solvent casting technique (Silva et al., 2018b). The incorporation of LNFs imparted mechanical reinforcement abilities, as demonstrated by the increase in Young's modulus from 1.69 to 2.50 GPa, and the reduction in the elongation at break from 6.63% to 1.34%, with the addition of 15 wt% of nanofibrils to the pullulan films. Moreover, the inclusion of LNFs endowed antioxidant (ca. 77%, using the DPPH assay) and antimicrobial properties (towards *S. aureus*) to the films, which are highly desirable for application in the food packaging sector.

## Patches

Electrospinning approaches can be employed to obtain other nanomaterials with planar structures, such as patches, from protein suspensions (Lendel and Solin, 2021). For example, amyloid-like

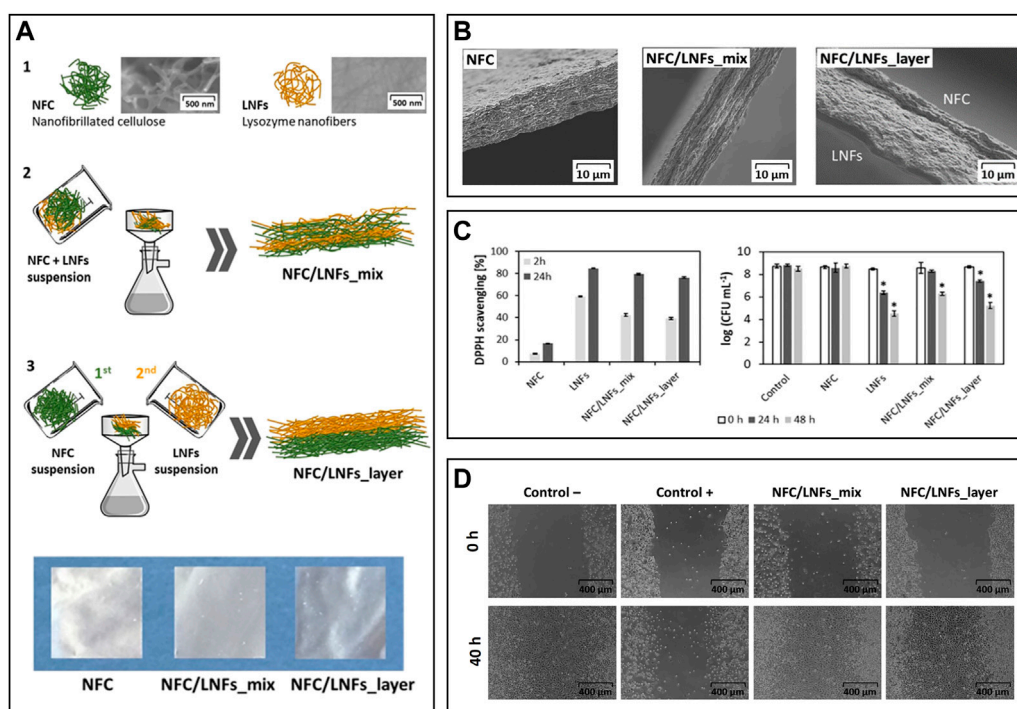


FIGURE 7

(A) Overview of the constituents (1) and the preparation of the nanocellulose (herein represented as NFC) and lysozyme nanofibrils (LNFs) patches via vacuum filtration by direct mixing of the suspensions (2) or using a layered approach (3), and digital photographs of the dry patches; (B) Scanning electron microscopy micrographs of the cross-section of the patches; (C) *In vitro* antioxidant activity (left) and antimicrobial activity (right) of the functional patches; (D) Optical micrographs of the scratch assay of the fibroblast cells after 40 h of exposure to both patches. Reproduced with permission from (Silva et al., 2020b). Copyright Elsevier, 2020.

bovine serum albumin fibrils were combined with ampicillin to produce electrospun patches that enabled the controlled release of the hydrophilic drug (Kabay et al., 2017). Moreover, even after treatment with solvents prior to the electrospinning process and application of high voltages, the drug retained its antimicrobial action towards *S. aureus* and *E. coli*. In another work, gelatin/LNFs electrospun patches were designed for tissue regeneration, specifically as an implant for infarcted myocardium tissues (Carvalho et al., 2022). The patches displayed excellent mechanical properties (increase in Young's modulus from 3 to 6 MPa, in wet state) and enhanced antioxidant activity (ca. 80%, using the DPPH assay), ascribed to the reinforcement with the protein nanofibrils. Furthermore, the materials had an increased bioresorbability rate compared to patches comprised only of gelatin (reduction in 10–15 days), highlighting the immense potential of LNFs as functional reinforcements.

## Other materials

Owing to the increase in viscosity during fibrillation, which is related to the interfibrillar interactions facilitated by the high

aspect ratio of the nanofibrils, protein nanofibril dispersions demonstrate impressive gelation capabilities, even at low concentrations (Lendel and Solin, 2021). This ability is responsible for the formation of hydro/aero-gels with high stability, which find applicability in the biomedical field as scaffolds for cell and tissue growth and bioink formulations used in 3D printing technology (Veiga et al., 2021). In this realm, composite hydrogels of LNFs and alginate were produced to formulate bioinks for extrusion-based 3D bioprinting (Figure 6A) (Teixeira et al., 2022b). The reinforcement of the alginate matrix with the protein nanofibrils was responsible for improving the shear-thinning behavior, which is crucial in the printing process (Figures 6B,C). As a proof of concept, the gels were loaded with immortalized human keratinocytes (HaCaT cells). After printing the scaffold structures, the suitability of the hydrogels was evaluated *via* cell viability. Not only were the structures able to maintain the cells alive during the studied time (7 days), but the structures printed with the bioinks containing LNFs showed enhanced cell proliferation (cell viability of ca. 88%) compared to the cell-laden hydrogels without the protein nanofibrils (cell viability of 75%), highlighting their bioactive role (Figure 6D).

The addition of protein nanofibrils is also known to alter the mechanical behavior of thermoplastic matrices. For instance, the blend of bovine insulin nanofibrils with poly(vinyl alcohol) resulted in increased stiffness of the films compared with the addition of the same amount (1 wt%) of non-fibrillar bovine insulin (Rao et al., 2012). The increase of other mechanical properties, such as elongation at break and elastic modulus, has also been reported with the blend of LNFs with poly(lactic acid) (Byrne et al., 2011) and a silicone elastomer (Oppenheim et al., 2010), respectively.

## The partnership between nanocellulose and protein fibrils

The use of cellulose nanofibers or protein fibrils in combination with other (bio)polymers or bioactive molecules results in nanostructured materials with promising physicochemical properties and functionalities, which can take the form of membranes, films, patches, and other materials, as illustrated in the works mentioned above (Tables 1–5). Given the tremendous potential of cellulose and protein nanofibrils on the design of new functional materials, their assembly will certainly result in fibrillar materials with unique properties. Nonetheless, as far as we could gather, only three publications to date dealing with the joint use of nanocellulose and protein nanofibrils in advanced material production, namely in films and aerogels with application in water remediation (Silva et al., 2020a; Sorriaux et al., 2021) and patches for wound healing (Silva et al., 2020b), have been reported (Table 5).

Silva et al. (2020a) described for the first time the preparation of NFC/LNFs biobased films using a simple methodology of vacuum filtration of the water-based suspensions of nanocellulose (obtained from softwood) and protein nanofibrils (extracted from hen egg white). The dual nanofibrillar films exhibited superior mechanical properties compared to neat NFC films (which already have remarkable mechanical properties), namely an increase up to 2 GPa of the Young's modulus and a concomitant decrease in the elongation at break. These results highlighted the structural reinforcement role of the lysozyme nanofibrils in the system, possibly due to the interactions between the hydroxyl and carboxyl groups of the nanocellulose fibrils and the amide groups of the LNFs. The adequacy of the NFC/LNFs films as biosorbents was evaluated in mercury-contaminated ultrapure and spring waters. After 24 h of contact at pH 11 (close to the isoelectric point of the lysozyme), the removal effectiveness reached a maximum of 99% and a residual concentration below the threshold value in waters intended for human consumption. The presence of amino acid side chains with multiple binding sites plays a crucial role in the adsorption of the  $Hg^{2+}$  ions.

In the same field,  $\beta$ -lactoglobulin nanofibrils were combined with polydopamine-coated cellulose nanofibrils (NFC) and

crosslinked *via* periodate oxidation to produce biosorbent aerogels (Sorriaux et al., 2021). The adsorption capability of the aerogels was evaluated in water contaminated with an assortment of pollutants (e.g., dyes, pesticide/pharmaceutical agents, and heavy metal ions), with good efficiencies and fast adsorption rates in the removal of crystal violet dye (93%, 30 min), bisphenol A (92%, 5 min) and  $Pb^{2+}$  ions (95%, 5 min), specifically. In this case, the adsorption is facilitated by the presence of various functional groups (e.g., catechols, quinones amines, and aromatic moieties) in the polydopamine functional coating.

The combination of NFC and LNFs was also evaluated in the preparation of nanofibrillated patches for wound healing following two different approaches, *viz.*, patches produced *via* vacuum filtration of the mixed NFC and LNF dispersions *versus* ones obtained through the sequential filtration of NFC and LNFs, respectively (Figure 7A) (Silva et al., 2020b). Scanning electron microscopy analysis revealed the excellent compatibility between NFC and LNF in the mixed nanofibrils patch and in the two distinct layers in the patch obtained by sequential deposition of NFC and LNF (Figure 7B). The mechanical properties differed due to the varying layouts. Compared to the pure NFC patch, the blended nanofibrils patch displayed an increase in Young's modulus, as expected, from 4.4 to 6.7 GPa. This trend, however, was not mirrored in the layered nanofibrils patch, which exhibited a lower Young's modulus than neat NFC (3.7 GPa), most likely due to the exclusive establishment of interfacial interactions between the functional groups of both nanofibrils. The inclusion of proteinaceous nanofibrils provided the patches with good UV-barrier properties, high antioxidant activity (up to 79.5%, using the DPPH assay), and antimicrobial activity against *S. aureus* (up to 3.5-log CFU mL<sup>-1</sup> reduction), which was slightly higher in the layered patch due to the bacterium's direct contact with the LNFs side (Figure 7C). Both NFC/LNFs patches were biocompatible toward the L929 fibroblast cell line and, in contrast to the pure NFC patch, promoted cell adhesion with high viability values (Figure 7C). The *in vitro* wound healing assay exhibited good migratory capacity of the cells on the surface of the patches, resulting in nearly complete occlusion of the simulated wound (Figure 7D). These findings point to the potential of the dual nanofibrils patches in wound healing improvement.

## Conclusion and future perspectives

In this review, we outlined the properties of cellulose and protein (amyloid) nanofibrils in the development of ecofriendly and sustainable advanced materials, namely membranes, films, and patches, among others (Tables 1–5). Owing to their excellent mechanical strength, these biobased nanofibrils are frequently used as reinforcement agents by compounding with thermoplastics such as PLA (Tomé et al., 2011) and PCL

(Figueiredo et al., 2015b; Vilela et al., 2019a), or through combination with biopolymeric matrices like pullulan (Trovatti et al., 2012a; Trovatti et al., 2012b), resulting in materials with improved mechanical and thermal properties.

Apart from the reinforcement role, the remarkable physicochemical properties of nanofibrils (e.g., high water absorption capacity, high surface area, biocompatibility and biodegradability) are being exploited in the development of advanced functional materials (Tables 1–4). BNC is particularly interesting for some applications since its membranes are simple to obtain in tailored shapes and sizes (*in situ* moldability) to better suit the target application. Combining BNC with bioactive molecules or polymers with different functionalities can produce materials for widely different applications, which explains the deluge of works reported using this nanocellulosic form.

Overall, materials produced with BNC and NFC have received much attention in a variety of emerging fields, including fuel cell components (Gadim et al., 2014; Gadim et al., 2016; Vilela et al., 2016; Gadim et al., 2017; Vilela et al., 2017; Vilela et al., 2018b; Vilela et al., 2020a; Vilela et al., 2020c; Vilela et al., 2020b), water remediation (Vilela et al., 2019b), active food packaging (Vilela et al., 2019c; Moreirinha et al., 2020; Bastante et al., 2021), skin treatment (Silva et al., 2014b; Morais et al., 2019; Chantereau et al., 2020; Almeida et al., 2022), wound healing (Fonseca et al., 2020) and drug delivery (Trovatti et al., 2011b; Trovatti et al., 2012c; Silva et al., 2014c; Silva et al., 2020c; Saïdi et al., 2017; Chantereau et al., 2019b; Carvalho et al., 2020; Fonseca et al., 2021).

Contrary to cellulose nanofibrils, protein amyloid nanofibrils, apart from their excellent mechanical properties, biodegradability and biocompatibility, also carry the functional groups of their native amino acid chains, avoiding an additional step in modification. Given so, the ability to hold intrinsic functional properties, paired with their high surface area and capacity to mimic non-cellular components, is attracting tremendous interest in the use of protein nanofibrils as functional reinforcements for the development of films, patches and other materials (Table 5) with application in areas like active food packaging (Silva et al., 2018b), bioinks formulation (Teixeira et al., 2022b) and tissue regeneration (Carvalho et al., 2022).

Moreover, the design of dual-fibrillar systems comprising both nanocellulose and protein nanofibrils seems to be a promising approach, still in its infancy. Regardless, their successful partnership is notorious, particularly in the formulation of patches for biomedical treatments (Silva et al., 2020b) and in the development of films (Silva et al., 2020a) and aerogels (Sorriaux et al., 2021) for environmental remediation strategies. In these studies, only NFC and two protein nanofibrils (lysozyme and  $\beta$ -lactoglobulin) have been used; therefore, plenty of materials can be foreseen by the combination of other nanocelluloses with nanofibrils obtained from other protein sources.

Even though the transition to more sustainable biopolymeric nanofibrillated materials remains limited to the establishment of

straightforward, economically viable, and speedier methods for nanofibril production, there is a clear potential for economic expansion in this field. The global nanocellulose market is estimated to reach USD 1,053.09 million by 2027, with a compound annual growth rate (CAGR) of 19.9% throughout the forecast period (2020–2027), demonstrating the clear interest in cellulosic nanofibrils (Fortune Business Insights, 2021). The functional protein industry is still primarily driven by uses for animal feed, nutraceuticals, and food and beverage supplementation (Markets and Markets, 2021). However, the growing interest in this research field over the past few years might be a driving factor towards the development of functional materials (Ye et al., 2019; Daniloski et al., 2021; Lendel and Solin, 2021; Peydayesh and Mezzenga, 2021; Vinayagam et al., 2022). Protein nanofibrils have significant advantageous characteristics and can be valuable building blocks in the creation of sophisticated nanostructured materials with intrinsic functional properties. Despite the significant progress that remains to be accomplished in this field, we foresee a growing interest in the use of nanocellulosic and protein nanofibrils, as well as their blends, as we begin to witness the merits of this partnership (Silva et al., 2020a; Silva et al., 2020b; Sorriaux et al., 2021).

## Author contributions

Conceptualization, CSRF; writing–original draft preparation, ACQS; writing–review and editing, ACQS, AJDS, CV, CSRF; supervision, AJDS, CV, CSRF; funding acquisition, AJDS, CV, CSRF. All authors have read and agreed to the published version of the manuscript.

## Funding

This work was developed within the scope of the project CICECO–Aveiro Institute of Materials, UIDB/50011/2020, UIDP/50011/2020 and LA/P/0006/2020, financed by national funds through the FCT/MCTES (PIDDAC) and project Cell4Janus: Engineering self-propelled cellulose-based Janus microrobots (PTDC/BII-BIO/1901/2021), financially supported by national funds (OE), through FCT/MCTES. FCT is also acknowledged for the doctoral grant to ACQS (SFRH/BD/140230/2018), and the research contracts under Scientific Employment Stimulus to CV (CEECIND/00263/2018 and 2021.01571.CEECIND) and CSRF (CEECIND/00464/2017).

## Conflict of interest

The authors declare that the research was conducted in the absence of any commercial or financial relationships that could be construed as a potential conflict of interest.



## Publisher's note

All claims expressed in this article are solely those of the authors and do not necessarily represent those of their affiliated

## References

- Abdelhamid, H. N., and Mathew, A. P. (2021). Cellulose-based materials for water remediation: Adsorption, catalysis, and antifouling. *Front. Chem. Eng.* 3, 790314. doi:10.3389/fceng.2021.790314
- Abdul Khalil, H. P. S., Bhat, A. H., and Ireana Yusra, A. F. (2012). Green composites from sustainable cellulose nanofibrils: A review. *Carbohydr. Polym.* 87, 963–979. doi:10.1016/j.carbpol.2011.08.078
- Almeida, I. F., Pereira, T., Silva, N. H. C. S., Gomes, F. P., Silvestre, A. J. D., Freire, C. S. R., et al. (2014). Bacterial cellulose membranes as drug delivery systems: An *in vivo* skin compatibility study. *Eur. J. Pharm. Biopharm.* 86, 332–336. doi:10.1016/j.ejpb.2013.08.008
- Almeida, T., Moreira, P., Sousa, F. J., Pereira, C., Silvestre, A. J. D., Vilela, C., et al. (2022). Bioactive bacterial nanocellulose membranes enriched with Eucalyptus globulus labill. Leaves aqueous extract for anti-aging skin care applications. *Materials* 15, 1982. doi:10.3390/ma15051982
- Almeida, T., Silvestre, A. J. D., Vilela, C., and Freire, C. S. R. (2021). Bacterial nanocellulose toward green cosmetics: Recent progresses and challenges. *Int. J. Mol. Sci.* 22, 2836. doi:10.3390/ijms22062836
- Amara, C., El Mahdi, A., Medimagh, R., and Khwaldia, K. (2021). Nanocellulose-based composites for packaging applications. *Curr. Opin. Green Sustain. Chem.* 31, 100512. doi:10.1016/j.cogsc.2021.100512
- Amin, U., Khan, M. K. I., Maan, A. A., Nazir, A., Riaz, S., Khan, M. U., et al. (2022). Biodegradable active, intelligent, and smart packaging materials for food applications. *Food Packag. Shelf Life* 33, 100903. doi:10.1016/j.fpsl.2022.100903
- Babitha, S., Rachita, L., Karthikeyan, K., Shoba, E., Janani, I., Poornima, B., et al. (2017). Electrospun protein nanofibers in healthcare: A review. *Int. J. Pharm. X.* 523, 52–90. doi:10.1016/j.ijpharm.2017.03.013
- Barhoum, A., Pal, K., Rahier, H., Uludag, H., Kim, I. S., and Bechelany, M. (2019). Nanofibers as new-generation materials: From spinning and nano-spinning fabrication techniques to emerging applications. *Appl. Mat. Today* 17, 1–35. doi:10.1016/j.apmt.2019.06.015
- Barhoum, A., Rasouli, R., Yousefzadeh, M., Rahier, H., and Bechelany, M. (2018). "Nanofiber technology: History and developments," in *Handbook of nanofibers*. Editors H. Barhoum, M. Bechelany, and A. S. H. Makhlof (Cham: Springer International Publishing), 1–42. doi:10.1007/978-3-319-42789-8\_54-1
- Bastante, C. C., Silva, N. H. C. S., Cardoso, L. C., Serrano, C. M., Martínez de la Ossa, E. J., Freire, C. S. R., et al. (2021). Biobased films of nanocellulose and mango leaf extract for active food packaging: Supercritical impregnation versus solvent casting. *Food Hydrocoll.* 117, 106709. doi:10.1016/j.foodhyd.2021.106709
- Byrne, N., Hameed, N., Werzer, O., and Guo, Q. (2011). The preparation of novel nanofilled polymer composites using poly(l-lactic acid) and protein fibers. *Eur. Polym. J.* 47, 1279–1283. doi:10.1016/J.EURPOLYMJ.2010.12.002
- Carvalho, J. P. F., Freire, C. S. R., and Vilela, C. (2021a). "Active packaging," in *Sustainable food processing and engineering challenges*. Editor C. Galanakis (London: Academic Press, Elsevier), 315–341. doi:10.1016/B978-0-12-822714-5.00009-7
- Carvalho, J. P. F., Silva, A. C. Q., Bastos, V., Oliveira, H., Pinto, R. J. B., Silvestre, A. J. D., et al. (2020). Nanocellulose-based patches loaded with hyaluronic acid and diclofenac towards aphthous stomatitis treatment. *Nanomaterials* 10, 628. doi:10.3390/nano10040628
- Carvalho, J. P. F., Silva, A. C. Q., Silvestre, A. J. D., Freire, C. S. R., and Vilela, C. (2021b). Spherical cellulose micro and nanoparticles: A review of recent developments and applications. *Nanomaterials* 11, 2744. doi:10.3390/nano11102744
- Carvalho, T., Ezazi, N. Z., Correia, A., Vilela, C., Santos, H. A., and Freire, C. S. R. (2022). Gelatin-lysozyme nanofibrils electrospun patches with improved mechanical, antioxidant, and bioresorbability properties for myocardial regeneration applications. *Adv. Funct. Mat.* 32, 2113390. doi:10.1002/adfm.202113390
- Carvalho, T., Guedes, G., Sousa, F. L., Freire, C. S. R., and Santos, H. A. (2019). Latest advances on bacterial cellulose-based materials for wound healing, delivery systems, and tissue engineering. *Biotechnol. J.* 14, 1900059. doi:10.1002/biot.201900059
- Carvalho, T., Pinto, R. J. B., Martins, M. A., Silvestre, A. J. D., and Freire, C. S. R. (2016). Timesaving microwave assisted synthesis of insulin amyloid fibrils with enhanced nanofiber aspect ratio. *Int. J. Biol. Macromol.* 92, 225–231. doi:10.1016/j.ijbiomac.2016.07.008
- Cazón, P., and Vázquez, M. (2021). Bacterial cellulose as a biodegradable food packaging material: A review. *Food Hydrocoll.* 113, 106530. doi:10.1016/j.foodhyd.2020.106530
- Chandana, A., Mallick, S. P., Dikshit, P. K., Singh, B. N., and Sahi, A. K. (2022). Recent developments in bacterial nanocellulose production and its biomedical applications. *J. Polym. Environ.* 30, 4040–4067. doi:10.1007/s10924-022-02507-0
- Chantereau, G., Brown, N., Dourges, M.-A., Freire, C. S. R., Silvestre, A. J. D., Sebe, G., et al. (2019a). Silylation of bacterial cellulose to design membranes with intrinsic anti-bacterial properties. *Carbohydr. Polym.* 220, 71–78. doi:10.1016/j.carbpol.2019.05.009
- Chantereau, G., Sharma, M., Abednejad, A., Neves, B. M., Sêbe, G., Coma, V., et al. (2019b). Design of nonsteroidal anti-inflammatory drug-based ionic liquids with improved water solubility and drug delivery. *ACS Sustain. Chem. Eng.* 7, 14126–14134. doi:10.1021/acssuschemeng.9b02797
- Chantereau, G., Sharma, M., Abednejad, A., Vilela, C., Costa, E. M., Veiga, M., et al. (2020). Bacterial nanocellulose membranes loaded with vitamin B-based ionic liquids for dermal care applications. *J. Mol. Liq.* 302, 112547. doi:10.1016/j.molliq.2020.112547
- Charreau, H., Cavallo, E., and Foresti, M. L. (2020). Patents involving nanocellulose: Analysis of their evolution since 2010. *Carbohydr. Polym.* 237, 116039. doi:10.1016/j.carbpol.2020.116039
- Chen, C., Ding, W., Zhang, H., Zhang, L., Huang, Y., Fan, M., et al. (2022). Bacterial cellulose-based biomaterials: From fabrication to application. *Carbohydr. Polym.* 278, 118995. doi:10.1016/j.carbpol.2021.118995
- Cherian, R. M., Tharayil, A., Varghese, R. T., Antony, T., Kargazadeh, H., Chirayil, C. J., et al. (2022). A review on the emerging applications of nano-cellulose as advanced coatings. *Carbohydr. Polym.* 282, 119123. doi:10.1016/j.carbpol.2022.119123
- Daniloski, D., Petkoska, A. T., Lee, N. A., Bekhit, A. E.-D., Carne, A., Vaskoska, R., et al. (2021). Active edible packaging based on milk proteins: A route to carry and deliver nutraceuticals. *Trends Food Sci. Technol.* 111, 688–705. doi:10.1016/j.tifs.2021.03.024
- Du, H., Liu, W., Zhang, M., Si, C., Zhang, X., and Li, B. (2019). Cellulose nanocrystals and cellulose nanofibrils based hydrogels for biomedical applications. *Carbohydr. Polym.* 209, 130–144. doi:10.1016/j.carbpol.2019.01.020
- Faria, M., Vilela, C., Mohammadkazemi, F., Silvestre, A. J. D., Freire, C. S. R., and Cordeiro, N. (2019a). Poly(glycidyl methacrylate)/bacterial cellulose nanocomposites: Preparation, characterization and post-modification. *Int. J. Biol. Macromol.* 127, 618–627. doi:10.1016/j.ijbiomac.2019.01.133
- Faria, M., Vilela, C., Silvestre, A. J. D., Deepa, B., Resnik, M., Freire, C. S. R., et al. (2019b). Physicochemical surface properties of bacterial cellulose/polymethacrylate nanocomposites: An approach by inverse gas chromatography. *Carbohydr. Polym.* 206, 86–93. doi:10.1016/j.carbpol.2018.10.110
- Fernandes, S. C. M., Sadocco, P., Alonso-Varona, A., Palomares, T., Eceiza, A., Silvestre, A. J. D., et al. (2013). Bioinspired antimicrobial and biocompatible bacterial cellulose membranes obtained by surface functionalization with aminoalkyl groups. *ACS Appl. Mat. Interfaces* 5, 3290–3297. doi:10.1021/am400338n
- Figueiredo, A. R. P., Figueiredo, A. G. P. R., Silva, N. H. C. S., Barros-Timmons, A., Almeida, A., Silvestre, A. J. D., et al. (2015a). Antimicrobial bacterial cellulose nanocomposites prepared by *in situ* polymerization of 2-aminoethyl methacrylate. *Carbohydr. Polym.* 123, 443–453. doi:10.1016/j.carbpol.2015.01.063
- Figueiredo, A. R. P. P., Vilela, C., Neto, C. P., Silvestre, A. J. D. D., and Freire, C. S. R. (2014). "Bacterial cellulose-based nanocomposites: Roadmap for innovative

materials," in *Nanocellulose polymer nanocomposites*. Editor V. K. Thakur (Hoboken, NJ, USA: John Wiley & Sons), 17–64. doi:10.1002/9781118872246.ch2

Figueiredo, A. R. P., Silvestre, A. J. D., Neto, C. P., and Freire, C. S. R. (2015b). *In situ* synthesis of bacterial cellulose/polycaprolactone blends for hot pressing nanocomposite films production. *Carbohydr. Polym.* 132, 400–408. doi:10.1016/j.carbpol.2015.06.001

Fonseca, D. F. S., Carvalho, J. P. F., Bastos, V., Oliveira, H., Moreirinha, C., Almeida, A., et al. (2020). Antibacterial multi-layered nanocellulose-based patches loaded with dexpantenol for wound healing applications. *Nanomaterials* 10, 2469. doi:10.3390/nano10122469

Fonseca, D. F. S., Vilela, C., Pinto, R. J. B., Bastos, V., Oliveira, H., Catarino, J., et al. (2021). Bacterial nanocellulose-hyaluronic acid microneedle patches for skin applications: *In vitro* and *in vivo* evaluation. *Mater. Sci. Eng. C* 118, 111350. doi:10.1016/j.msec.2020.111350

Fonseca, D. F. S., Vilela, C., Silvestre, A. J. D., and Freire, C. S. R. (2019). A compendium of current developments on polysaccharide and protein-based microneedles. *Int. J. Biol. Macromol.* 136, 704–728. doi:10.1016/j.ijbiomac.2019.04.163

Fortune Business Insights (2021). Nanocellulose market size, growth and industry trends. Available at: <https://www.fortunebusinessinsights.com/nanocellulose-market-104565> (Accessed June 13, 2022).

Frazão, C. J. R., Silva, N. H. C., Freire, C. S. R., Silvestre, A. J. D., Xavier, A. M. R. B., and Tavares, A. P. M. (2014). Bacterial cellulose as carrier for immobilization of laccase: Optimization and characterization. *Eng. Life Sci.* 14, 500–508. doi:10.1002/elsc.201400054

Freire, C. S. R., Fernandes, S. C. M., Silvestre, A. J. D., and Pascoal Neto, C. (2013). Novel cellulose-based composites based on nanofibrillated plant and bacterial cellulose: Recent advances at the university of Aveiro – a review. *Holzforschung* 67, 603–612. doi:10.1515/hf-2012-0127

Freire, C. S. R., and Vilela, C. (2022). Advanced nanocellulose-based materials: Production, properties, and applications. *Nanomaterials* 12, 431. doi:10.3390/nano12030431

Gadim, T. D. O., Figueiredo, A. G. P. R., Rosero-Navarro, N. C., Vilela, C., Gamelas, J. A. F., Barros-Timmons, A., et al. (2014). Nanostructured bacterial cellulose–poly(4-styrene sulfonic acid) composite membranes with high storage modulus and protonic conductivity. *ACS Appl. Mat. Interfaces* 6, 7864–7875. doi:10.1021/am501191t

Gadim, T. D. O., Loureiro, F. J. A., Vilela, C., Rosero-Navarro, N., Silvestre, A. J. D., Freire, C. S. R., et al. (2017). Protonic conductivity and fuel cell tests of nanocomposite membranes based on bacterial cellulose. *Electrochim. Acta* 233, 52–61. doi:10.1016/j.electacta.2017.02.145

Gadim, T. D. O., Vilela, C., Loureiro, F. J. A., Silvestre, A. J. D., Freire, C. S. R., and Figueiredo, F. M. L. (2016). Nafion® and nanocellulose: A partnership for greener polymer electrolyte membranes. *Ind. Crops Prod.* 93, 212–218. doi:10.1016/j.indcrop.2016.01.028

Galiano, F., Briceño, K., Marino, T., Molino, A., Christensen, K. V., and Figoli, A. (2018). Advances in biopolymer-based membrane preparation and applications. *J. Memb. Sci.* 564, 562–586. doi:10.1016/j.memsci.2018.07.059

Hadidi, M., Jafarzadeh, S., Forough, M., Garavand, F., Alizadeh, S., Salehabadi, A., et al. (2022). Plant protein-based food packaging films; recent advances in fabrication, characterization, and applications. *Trends Food Sci. Technol.* 120, 154–173. doi:10.1016/j.tifs.2022.01.013

Hamimed, S., Abdeljelil, N., Landoulsi, A., Chatti, A., Aljabali, A. A., and Barhoum, A. (2022). "Bacterial cellulose nanofibers," in *Handbook of nanocelluloses* (Cham: Springer International Publishing), 1–38. doi:10.1007/978-3-030-62976-2\_15-1

Inácio, P. M. C., Medeiros, M. C. R., Carvalho, T., Félix, R. C., Mestre, A., Hubbard, P. C., et al. (2020). Ultra-low noise PEDOT:PSS electrodes on bacterial cellulose: A sensor to access bioelectrical signals in non-electrogenic cells. *Org. Electron.* 85, 105882. doi:10.1016/j.orgel.2020.105882

Kabay, G., Meydan, A. E., Kaleli Can, G., Demirci, C., and Mutlu, M. (2017). Controlled release of a hydrophilic drug from electrospun amyloid-like protein blend nanofibers. *Mater. Sci. Eng. C* 81, 271–279. doi:10.1016/j.msec.2017.08.003

Klemm, D., Cranston, E. D., Fischer, D., Gama, M., Kedzior, S. A., Kralisch, D., et al. (2018). Nanocellulose as a natural source for groundbreaking applications in materials science: Today's state. *Mat. TodayKidlingt.* 21, 720–748. doi:10.1016/j.mattod.2018.02.001

Knowles, T. P. J., and Mezzenga, R. (2016). Amyloid fibrils as building blocks for natural and artificial functional materials. *Adv. Mat.* 28, 6546–6561. doi:10.1002/adma.201505961

Krishnaswamy, K., and Orsat, V. (2017). "Sustainable delivery systems through green nanotechnology," in *Nano- and microscale drug delivery systems* (Amsterdam: Elsevier), 17–32. doi:10.1016/B978-0-323-52727-9.00002-9

Lacerda, P. S. S., Barros-Timmons, A. M. M. V., Freire, C. S. R., Silvestre, A. J. D., and Neto, C. P. (2013). Nanostructured composites obtained by ATRP sleeving of bacterial cellulose nanofibers with acrylate polymers. *Biomacromolecules* 14, 2063–2073. doi:10.1021/bm400432b

Sendel, C., and Solin, N. (2021). Protein nanofibrils and their use as building blocks of sustainable materials. *RSC Adv.* 11, 39188–39215. doi:10.1039/D1RA06878D

Ling, S., Chen, W., Fan, Y., Zheng, K., Jin, K., Yu, H., et al. (2018a). Biopolymer nanofibrils: Structure, modeling, preparation, and applications. *Prog. Polym. Sci.* 85, 1–56. doi:10.1016/j.procpolymsci.2018.06.004

Ling, S., Kaplan, D. L., and Buehler, M. J. (2018b). Nanofibrils in nature and materials engineering. *Nat. Rev. Mat.* 3, 18016. doi:10.1038/natrevmat.2018.16

Long, W., Ouyang, H., Hu, X., Liu, M., Zhang, X., Feng, Y., et al. (2021). State-of-art review on preparation, surface functionalization and biomedical applications of cellulose nanocrystals-based materials. *Int. J. Biol. Macromol.* 186, 591–615. doi:10.1016/j.ijbiomac.2021.07.066

Loveday, S. M., Anema, S. G., and Singh, H. (2017).  $\beta$ -Lactoglobulin nanofibrils: The long and the short of it. *Int. Dairy J.* 67, 35–45. doi:10.1016/j.idairyj.2016.09.011

Manan, S., Ullah, M. W., Ul-Islam, M., Shi, Z., Gauthier, M., and Yang, G. (2022). Bacterial cellulose: Molecular regulation of biosynthesis, supramolecular assembly, and tailored structural and functional properties. *Prog. Mat. Sci.* 129, 100972. doi:10.1016/j.pmatsci.2022.100972

Markets and Markets (2021). Functional proteins market [2020–2025]. Available at: <https://www.marketsandmarkets.com/Market-Reports/functional-protein-market-140299581.html> (Accessed July 21, 2022).

Martins, N. C. T., Freire, C. S. R., Neto, C. P., Silvestre, A. J. D., Causio, J., Baldi, G., et al. (2013). Antibacterial paper based on composite coatings of nanofibrillated cellulose and ZnO. *Colloids Surfaces A Physicochem. Eng. Aspects* 417, 111–119. doi:10.1016/j.colsurfa.2012.10.042

Martins, N. C. T., Freire, C. S. R., Pinto, R. J. B., Fernandes, S. C. M., Pascoal Neto, C., Silvestre, A. J. D., et al. (2012). Electrostatic assembly of Ag nanoparticles onto nanofibrillated cellulose for antibacterial paper products. *Cellulose* 19, 1425–1436. doi:10.1007/s10570-012-9713-5

Meftahi, A., Momeni Heravi, M. E., Baroum, A., Samyn, P., Najarzadeh, H., and Alibakhshi, S. (2021). "Cellulose nanofibers," in *Handbook of nanocelluloses*. Editor A. Barhoum (Cham: Springer International Publishing), 1–30. doi:10.1007/978-3-030-62976-2\_13-1

Meftahi, A., Samyn, P., Geravand, S. A., Khajavi, R., Alibakhshi, S., Bechelany, M., et al. (2022). Nanocelluloses as skin biocompatible materials for skincare, cosmetics, and healthcare: Formulations, regulations, and emerging applications. *Carbohydr. Polym.* 278, 118956. doi:10.1016/j.carbpol.2021.118956

Meng, Y., Wei, Z., and Xue, C. (2022). Protein fibrils from different food sources: A review of fibrillation conditions, properties, applications and research trends. *Trends Food Sci. Technol.* 121, 59–75. doi:10.1016/j.tifs.2022.01.031

Miyashiro, D., Hamano, R., and Umemura, K. (2020). A review of applications using mixed materials of cellulose, nanocellulose and carbon nanotubes. *Nanomaterials* 10, 186. doi:10.3390/nano10020186

Moayedzadeh, S., Madadlou, A., and Khosrowshahi asl, A. (2015). Formation mechanisms, handling and digestibility of food protein nanofibrils. *Trends Food Sci. Technol.* 45, 50–59. doi:10.1016/j.tifs.2015.05.005

Mohammadian, M., and Madadlou, A. (2018). Technological functionality and biological properties of food protein nanofibrils formed by heating at acidic condition. *Trends Food Sci. Technol.* 75, 115–128. doi:10.1016/j.tifs.2018.03.013

Mohammadian, M., Waly, M. I., Moghadam, M., Emam-Djomeh, Z., Salami, M., and Moosavi-Movahedi, A. A. (2020). Nanostructured food proteins as efficient systems for the encapsulation of bioactive compounds. *Food Sci. Hum. Wellness* 9, 199–213. doi:10.1016/j.fshw.2020.04.009

Moraes, E. S., Silva, N. H. C. S., Sintra, T. E., Santos, S. A. O., Neves, B. M., Almeida, I. F., et al. (2019). Anti-inflammatory and antioxidant nanostructured cellulose membranes loaded with phenolic-based ionic liquids for cutaneous application. *Carbohydr. Polym.* 206, 187–197. doi:10.1016/j.carbpol.2018.10.051

Moreirinha, C., Vilela, C., Silva, N. H. C. S., Pinto, R. J. B., Almeida, A., Rocha, M. A. M., et al. (2020). Antioxidant and antimicrobial films based on brewers spent grain arabinoxylans, nanocellulose and feruloylated compounds for active packaging. *Food Hydrocoll.* 108, 105836. doi:10.1016/j.foodhyd.2020.105836

Muqet, M., Mahar, R. B., Gadhi, T. A., and Ben Halima, N. (2020). Insight into cellulose-based-nanomaterials - a pursuit of environmental remedies. *Int. J. Biol. Macromol.* 163, 1480–1486. doi:10.1016/j.ijbiomac.2020.08.050

Nazrin, A., Sapuan, S. M., Zuhri, M. Y. M., Ilyas, R. A., Syafiq, R., and Sherwani, S. F. K. (2020). Nanocellulose reinforced thermoplastic starch (TPS), polylactic acid

- (PLA), and polybutylene succinate (PBS) for food packaging applications. *Front. Chem.* 8, 213. doi:10.3389/fchem.2020.00213
- Nechyporchuk, O., Belgacem, M. N., and Bras, J. (2016). Production of cellulose nanofibrils: A review of recent advances. *Ind. Crops Prod.* 93, 2–25. doi:10.1016/j.indcrop.2016.02.016
- Noremylia, M. B., Hassan, M. Z., and Ismail, Z. (2022). Recent advancement in isolation, processing, characterization and applications of emerging nanocellulose: A review. *Int. J. Biol. Macromol.* 206, 954–976. doi:10.1016/j.ijbiomac.2022.03.064
- Oppenheim, T., Knowles, T. P. J., Lacour, S. P., and Welland, M. E. (2010). Fabrication and characterisation of protein fibril–elastomer composites. *Acta Biomater.* 6, 1337–1341. doi:10.1016/j.ACTBIO.2009.10.013
- Owolabi, F. A. T., Deepu, A. G., Thomas, S., Shima, J., Rizal, S., Sri Aprilia, N. A., et al. (2020). “Green composites from sustainable cellulose nanofibrils,” in *Encyclopedia of renewable and sustainable materials* (Amsterdam: Elsevier), 81–94. doi:10.1016/B978-0-12-803581-8.11422-5
- Peydayesh, M., and Mezzenga, R. (2021). Protein nanofibrils for next generation sustainable water purification. *Nat. Commun.* 12, 3248. doi:10.1038/s41467-021-23388-2
- Pinto, R. J. B., Martins, M. A., Lucas, J. M. F., Vilela, C., Sales, A. J. M., Costa, L. C., et al. (2020a). Highly electroconductive nanopapers based on nanocellulose and copper nanowires: A new generation of flexible and sustainable electrical materials. *ACS Appl. Mat. Interfaces* 12, 34208–34216. doi:10.1021/acsmi.0c09257
- Pinto, S. C., Silva, N. H. C. S., Pinto, R. J. B., Freire, C. S. R., Duarte, I., Vicente, R., et al. (2020b). Multifunctional hybrid structures made of open-cell aluminum foam impregnated with cellulose/graphene nanocomposites. *Carbohydr. Polym.* 238, 116197. doi:10.1016/j.carbpol.2020.116197
- Pradhan, D., Jaiswal, A. K., and Jaiswal, S. (2022). Emerging technologies for the production of nanocellulose from lignocellulosic biomass. *Carbohydr. Polym.* 285, 119258. doi:10.1016/j.carbpol.2022.119258
- Qiu, J., Li, M., Ding, M., and Yao, J. (2022). Cellulose tailored semiconductors for advanced photocatalysis. *Renew. Sustain. Energy Rev.* 154, 111820. doi:10.1016/j.rser.2021.111820
- Raghav, N., Sharma, M. R., and Kennedy, J. F. (2021). Nanocellulose: A mini-review on types and use in drug delivery systems. *Carbohydr. Polym. Technol. Appl.* 2, 100031. doi:10.1016/j.carpta.2020.100031
- Rana, A. K., Frollini, E., and Thakur, V. K. (2021). Cellulose nanocrystals: Pretreatments, preparation strategies, and surface functionalization. *Int. J. Biol. Macromol.* 182, 1554–1581. doi:10.1016/j.ijbiomac.2021.05.119
- Rao, S. P., Meade, S. J., Healy, J. P., Sutton, K. H., Larsen, N. G., Staiger, M. P., et al. (2012). Amyloid fibrils as functionalizable components of nanocomposite materials. *Biotechnol. Prog.* 28, 248–256. doi:10.1002/btpr.726
- Raza, Z. A., Munim, S. A., and Ayub, A. (2021). Recent developments in polysaccharide-based electrospun nanofibers for environmental applications. *Carbohydr. Res.* 510, 108443. doi:10.1016/j.carres.2021.108443
- Saïdi, L., Vilela, C., Oliveira, H., Silvestre, A. J. D., and Freire, C. S. R. (2017). Poly(N-methacryloyl glycine)/nanocellulose composites as pH-sensitive systems for controlled release of diclofenac. *Carbohydr. Polym.* 169, 357–365. doi:10.1016/j.carbpol.2017.04.030
- Salahuddin, P., Fatima, M. T., Uversky, V. N., Khan, R. H., Islam, Z., and Furkan, M. (2021). The role of amyloids in Alzheimer’s and Parkinson’s diseases. *Int. J. Biol. Macromol.* 190, 44–55. doi:10.1016/j.ijbiomac.2021.08.197
- Santos, R. F., Ribeiro, J. C. L., Franco de Carvalho, J. M., Magalhães, W. L. E., Pedroti, L. G., Nalon, G. H., et al. (2021). Nanofibrillated cellulose and its applications in cement-based composites: A review. *Constr. Build. Mat.* 288, 123122. doi:10.1016/j.conbuildmat.2021.123122
- Sarkar, S., Gulati, K., Mishra, A., and Poluri, K. M. (2020). Protein nanocomposites: Special inferences to lysozyme based nanomaterials. *Int. J. Biol. Macromol.* 151, 467–482. doi:10.1016/j.ijbiomac.2020.02.179
- Sayyed, A. J., Pinjari, D. V., Sonawane, S. H., Bhanvase, B. A., Sheikh, J., and Sillanpää, M. (2021). Cellulose-based nanomaterials for water and wastewater treatments: A review. *J. Environ. Chem. Eng.* 9, 106626. doi:10.1016/j.jece.2021.106626
- Shaghaleh, H., Xu, X., and Wang, S. (2018). Current progress in production of biopolymeric materials based on cellulose, cellulose nanofibers, and cellulose derivatives. *RSC Adv.* 8, 825–842. doi:10.1039/C7RA11157F
- Shen, R., Xue, S., Xu, Y., Liu, Q., Feng, Z., Ren, H., et al. (2020). Research progress and development demand of nanocellulose reinforced polymer composites. *Polymers* 12, 2113. doi:10.3390/polym12092113
- Shen, Y., Levin, A., Kamada, A., Toprakcioglu, Z., Rodriguez-Garcia, M., Xu, Y., et al. (2021). From protein building blocks to functional materials. *ACS Nano* 15, 5819–5837. doi:10.1021/acsnano.0c08510
- Shojaeiarani, J., Bajwa, D. S., and Chanda, S. (2021). Cellulose nanocrystal based composites: A review. *Compos. Part C. Open Access* 5, 100164. doi:10.1016/j.jcomc.2021.100164
- Silva, A. C. Q., Silvestre, A. J. D., Freire, C. S. R., and Vilela, C. (2021a). in *Fundamentals of natural Fibres and textiles*. Editor M. I. H. Mondal (Cambridge: Woodhead Publishing, Elsevier). doi:10.1016/C2019-0-03400-0
- Silva, A. C. Q., Silvestre, A. J. D., Vilela, C., and Freire, C. S. R. (2021b). Natural polymers-based materials: A contribution to a greener future. *Molecules* 27, 94. doi:10.3390/molecules27010094
- Silva, N. H. C. S. C. S., Vilela, C., Marrucho, I. M., Freire, C. S. R., Pascoal Neto, C., and Silvestre, A. J. D. D. (2014a). Protein-based materials: From sources to innovative sustainable materials for biomedical applications. *J. Mat. Chem. B* 2, 3715. doi:10.1039/c4tb00168k
- Silva, N. H. C. S., Drumond, I., Almeida, I. F., Costa, P., Rosado, C. F., Neto, C. P., et al. (2014b). Topical caffeine delivery using biocellulose membranes: A potential innovative system for cellulite treatment. *Cellulose* 21, 665–674. doi:10.1007/s10570-013-0114-1
- Silva, N. H. C. S., Figueira, P., Fabre, E., Pinto, R. J. B., Pereira, M. E., Silvestre, A. J. D., et al. (2020a). Dual nanofibrillar-based bio-sorbent films composed of nanocellulose and lysozyme nanofibrils for mercury removal from spring waters. *Carbohydr. Polym.* 238, 116210. doi:10.1016/j.carbpol.2020.116210
- Silva, N. H. C. S., Garrido-Pascual, P., Moreirinha, C., Almeida, A., Palomares, T., Alonso-Varona, A., et al. (2020b). Multifunctional nanofibrous patches composed of nanocellulose and lysozyme nanofibers for cutaneous wound healing. *Int. J. Biol. Macromol.* 165, 1198–1210. doi:10.1016/j.ijbiomac.2020.09.249
- Silva, N. H. C. S., Mota, J. P., Santos de Almeida, T., Carvalho, J. P. F., Silvestre, A. J. D., Vilela, C., et al. (2020c). Topical drug delivery systems based on bacterial nanocellulose: Accelerated stability testing. *Int. J. Mol. Sci.* 21, 1262. doi:10.3390/ijms21041262
- Silva, N. H. C. S., Pinto, R. J. B., Martins, M. A., Ferreira, R., Correia, I., Freire, C. S. R., et al. (2018a). Ionic liquids as promoters of fast lysozyme fibrillation. *J. Mol. Liq.* 272, 456–467. doi:10.1016/j.molliq.2018.08.064
- Silva, N. H. C. S., Rodrigues, A. F., Almeida, I. F., Costa, P. C., Rosado, C., Neto, C. P., et al. (2014c). Bacterial cellulose membranes as transdermal delivery systems for diclofenac: *In vitro* dissolution and permeation studies. *Carbohydr. Polym.* 106, 264–269. doi:10.1016/j.carbpol.2014.02.014
- Silva, N. H. C. S., Vilela, C., Almeida, A., Marrucho, I. M., and Freire, C. S. R. (2018b). Pullulan-based nanocomposite films for functional food packaging: Exploiting lysozyme nanofibers as antibacterial and antioxidant reinforcing additives. *Food Hydrocoll.* 77, 921–930. doi:10.1016/j.foodhyd.2017.11.039
- Silva, N. H. C. S., Vilela, C., Pinto, R. J. B., Martins, M. A., Marrucho, I. M., and Freire, C. S. R. (2018c). Tuning lysozyme nanofibers dimensions using deep eutectic solvents for improved reinforcement ability. *Int. J. Biol. Macromol.* 115, 518–527. doi:10.1016/j.ijbiomac.2018.03.150
- Silvestre, A. J. D., Freire, C. S. R., and Neto, C. P. (2014). Do bacterial cellulose membranes have potential in drug-delivery systems? *Expert Opin. Drug Deliv.* 11, 1113–1124. doi:10.1517/17425247.2014.920819
- Soroush, E., Mohammadpour, Z., Kharaziha, M., Bakhsheshi-Rad, H. R., and Berto, F. (2022). Polysaccharides-based nanofibrils: From tissue engineering to biosensor applications. *Carbohydr. Polym.* 291, 119670. doi:10.1016/j.carbpol.2022.119670
- Sorriaux, M., Sorieul, M., and Chen, Y. (2021). Bio-based and robust polydopamine coated nanocellulose/amyloid composite aerogel for fast and wide-spectrum water purification. *Polymers* 13, 3442. doi:10.3390/polym13193442
- Squinca, P., Bilatto, S., Badino, A. C., and Farinas, C. S. (2022). The use of enzymes to isolate cellulose nanomaterials: A systematic map review. *Carbohydr. Polym. Technol. Appl.* 3, 100212. doi:10.1016/j.carpta.2022.100212
- Subhedar, A., Bhadauria, S., Ahankari, S., and Kargazadeh, H. (2021). Nanocellulose in biomedical and biosensing applications: A review. *Int. J. Biol. Macromol.* 166, 587–600. doi:10.1016/j.ijbiomac.2020.10.217
- Sun, Y., Chu, Y., Wu, W., and Xiao, H. (2021). Nanocellulose-based lightweight porous materials: A review. *Carbohydr. Polym.* 255, 117489. doi:10.1016/j.carbpol.2020.117489
- Teixeira, M. C., Lameirinhas, N. S., Carvalho, J. P. F., Silvestre, A. J. D., Vilela, C., and Freire, C. S. R. (2022a). A guide to polysaccharide-based hydrogel bioinks for 3D bioprinting applications. *Int. J. Mol. Sci.* 23, 6564. doi:10.3390/ijms23126564
- Teixeira, M. C., Lameirinhas, N. S., Carvalho, J. P. F., Valente, B. F. A., Luís, J., Pires, L., et al. (2022b). Alginate-lysozyme nanofibers hydrogels with improved rheological behavior, printability and biological properties for 3D bioprinting applications. *Nanomaterials* 12, 2190. doi:10.3390/nano12132190
- Thomas, P., Duolikun, T., Rumjit, N. P., Moosavi, S., Lai, C. W., Bin Johan, M. R., et al. (2020). Comprehensive review on nanocellulose: Recent developments,



challenges and future prospects. *J. Mech. Behav. Biomed. Mat.* 110, 103884. doi:10.1016/j.jmbbm.2020.103884

Tomé, L. C., Pinto, R. J. B., Trovatti, E., Freire, C. S. R., Silvestre, A. J. D., Neto, C. P., et al. (2011). Transparent bionanocomposites with improved properties prepared from acetylated bacterial cellulose and poly(lactic acid) through a simple approach. *Green Chem.* 13, 419. doi:10.1039/c0gc00545b

Trache, D., Tarchoun, A. F., Derradji, M., Hamidon, T. S., Masruchin, N., Brosse, N., et al. (2020). Nanocellulose: From fundamentals to advanced applications. *Front. Chem.* 8, 392. doi:10.3389/fchem.2020.00392

Trovatti, E., Fernandes, S. C. M., Rubatat, L., Freire, C. S. R., Silvestre, A. J. D., and Neto, C. P. (2012a). Sustainable nanocomposite films based on bacterial cellulose and pullulan. *Cellulose* 19, 729–737. doi:10.1007/s10570-012-9673-9

Trovatti, E., Fernandes, S. C. M., Rubatat, L., Perez, D., da, S., Freire, C. S. R., et al. (2012b). Pullulan–nanofibrillated cellulose composite films with improved thermal and mechanical properties. *Compos. Sci. Technol.* 72, 1556–1561. doi:10.1016/j.compscitech.2012.06.003

Trovatti, E., Freire, C. S. R., Pinto, P. C., Almeida, I. F., Costa, P., Silvestre, A. J. D., et al. (2012c). Bacterial cellulose membranes applied in topical and transdermal delivery of lidocaine hydrochloride and ibuprofen: *In vitro* diffusion studies. *Int. J. Pharm.* X, 435, 83–87. doi:10.1016/j.ijpharm.2012.01.002

Trovatti, E., Serafim, L. S., Freire, C. S. R., Silvestre, A. J. D., and Neto, C. P. (2011a). Gluconacetobacter sacchari: An efficient bacterial cellulose cell-factory. *Carbohydr. Polym.* 86, 1417–1420. doi:10.1016/j.carbpol.2011.06.046

Trovatti, E., Silva, N. H. C. S., Duarte, I. F., Rosado, C. F., Almeida, I. F., Costa, P., et al. (2011b). Biocellulose membranes as supports for dermal release of lidocaine. *Biomacromolecules* 12, 4162–4168. doi:10.1021/bm201303r

United Nations (2015). Transforming our world: The 2030 Agenda for sustainable development. *U. N. Gen. Assem.* 1, 529–567. doi:10.1891/9780826190123.ap02

Veiga, A., Silva, I. V., Duarte, M. M., and Oliveira, A. L. (2021). Current trends on protein driven bioinks for 3D printing. *Pharmaceutics* 13, 1444. doi:10.3390/pharmaceutics13091444

Vilela, C., Cordeiro, D. M., Boas, J. V., Barbosa, P., Nolasco, M., Vaz, P. D., et al. (2020a). Poly(4-styrene sulfonic acid)/bacterial cellulose membranes: Electrochemical performance in a single-chamber microbial fuel cell. *Bioresour. Technol. Rep.* 9, 100376. doi:10.1016/j.biteb.2019.100376

Vilela, C., Engström, J., Valente, B. F. A., Jawerth, M., Carlmark, A., and Freire, C. S. R. (2019a). Exploiting poly( $\epsilon$ -caprolactone) and cellulose nanofibrils modified with latex nanoparticles for the development of biodegradable nanocomposites. *Polym. Compos.* 40, 1342–1353. doi:10.1002/pc.24865

Vilela, C., Gadim, T. D. O., Silvestre, A. J. D., Freire, C. S. R., and Figueiredo, F. M. L. (2016). Nanocellulose/poly(methacryloyloxyethyl phosphate) composites as proton separator materials. *Cellulose* 23, 3677–3689. doi:10.1007/s10570-016-1050-7

Vilela, C., Kurek, M., Hayouka, Z., Röcker, B., Yildirim, S., Antunes, M. D. C., et al. (2018a). A concise guide to active agents for active food packaging. *Trends Food Sci. Technol.* 80, 212–222. doi:10.1016/j.tifs.2018.08.006

Vilela, C., Martins, A., Sousa, N., Silvestre, A., Figueiredo, F., and Freire, C. (2018b). Poly(bis[2-(methacryloyloxy)ethyl] phosphate)/bacterial cellulose nanocomposites: Preparation, characterization and application as polymer electrolyte membranes. *Appl. Sci. (Basel)* 8, 1145. doi:10.3390/app8071145

Vilela, C., Morais, J. D., Silva, A. C. Q., Muñoz-Gil, D., Figueiredo, F. M. L. L., Silvestre, A. J. D. D., et al. (2020b). Flexible nanocellulose/lignosulfonates ion-

conducting separators for polymer electrolyte fuel cells. *Nanomaterials* 10, 1713. doi:10.3390/nano10091713

Vilela, C., Moreirinha, C., Almeida, A., Silvestre, A. J. D., and Freire, C. S. R. (2019b). Zwitterionic nanocellulose-based membranes for organic dye removal. *Materials* 12, 1404. doi:10.3390/ma12091404

Vilela, C., Moreirinha, C., Domingues, E. M., Figueiredo, F. M. L., Almeida, A., and Freire, C. S. R. (2019c). Antimicrobial and conductive nanocellulose-based films for active and intelligent food packaging. *Nanomaterials* 9, 980. doi:10.3390/nano9070980

Vilela, C., Oliveira, H., Almeida, A., Silvestre, A. J. D., and Freire, C. S. R. (2019d). Nanocellulose-based antifungal nanocomposites against the polymorphic fungus *Candida albicans*. *Carbohydr. Polym.* 217, 207–216. doi:10.1016/j.carbpol.2019.04.046

Vilela, C., Silva, A. C. Q., Domingues, E. M., Gonçalves, G., Martins, M. A., Figueiredo, F. M. L., et al. (2020c). Conductive polysaccharides-based proton-exchange membranes for fuel cell applications: The case of bacterial cellulose and fucoidan. *Carbohydr. Polym.* 230, 115604. doi:10.1016/j.carbpol.2019.115604

Vilela, C., Silvestre, A. J. D., Figueiredo, F. M. L., and Freire, C. S. R. (2019e). Nanocellulose-based materials as components of polymer electrolyte fuel cells. *J. Mat. Chem. A* 7, 20045–20074. doi:10.1039/C9TA07466j

Vilela, C., Sousa, N., Pinto, R. J. B., Silvestre, A. J. D., Figueiredo, F. M. L., and Freire, C. S. R. (2017). Exploiting poly(ionic liquids) and nanocellulose for the development of bio-based anion-exchange membranes. *Biomass Bioenergy* 100, 116–125. doi:10.1016/j.biombioe.2017.03.016

Vinayagam, V., Murugan, S., Kumaresan, R., Narayanan, M., Sillanpää, M., Vo, D.-V. N., et al. (2022). Protein nanofibrils as versatile and sustainable adsorbents for an effective removal of heavy metals from wastewater: A review. *Chemosphere* 301, 134635. doi:10.1016/j.chemosphere.2022.134635

Wang, L., Li, K., Copenhaver, K., Mackay, S., Lamm, M. E., Zhao, X., et al. (2021). Review on nonconventional fibrillation methods of producing cellulose nanofibrils and their applications. *Biomacromolecules* 22, 4037–4059. doi:10.1021/acs.biomac.1c00640

Wang, Q., Liu, S., Liu, J., Sun, J., Zhang, Z., and Zhu, Q. (2022). Sustainable cellulose nanomaterials for environmental remediation - achieving clean air, water, and energy: A review. *Carbohydr. Polym.* 285, 119251. doi:10.1016/j.carbpol.2022.119251

Wang, W., Xue, C., and Mao, X. (2020a). Chitosan: Structural modification, biological activity and application. *Int. J. Biol. Macromol.* 164, 4532–4546. doi:10.1016/j.ijbiomac.2020.09.042

Wang, X., Wang, Q., and Xu, C. (2020b). Nanocellulose-based inks for 3D bioprinting: Key aspects in research development and challenging perspectives in applications—a mini review. *Bioengineering* 7, 40. doi:10.3390/bioengineering7020040

Xiao, J., Li, H., Zhang, H., He, S., Zhang, Q., Liu, K., et al. (2022). Nanocellulose and its derived composite electrodes toward supercapacitors: Fabrication, properties, and challenges. *J. Bioresour. Bioprod.* 7, 245–269. doi:10.1016/j.jobab.2022.05.003

Ye, X., Lendel, C., Langton, M., Olsson, R. T., and Hedenqvist, M. S. (2019). “Protein nanofibrils: Preparation, properties, and possible applications in industrial nanomaterials,” in *Industrial applications of nanomaterials*. Editors S. Thomas, Y. Grohens, and Y. B. Pottathara (Amsterdam: Elsevier), 29–63. doi:10.1016/B978-0-12-815749-7.00002-5





## OPEN ACCESS

## EDITED BY

Sidney JL Ribeiro,  
São Paulo State University, Brazil

## REVIEWED BY

Kalipada Das,  
University of Calcutta, India

## \*CORRESPONDENCE

V. S. Amaral,  
✉ vamaral@ua.pt

## SPECIALTY SECTION

This article was submitted to  
Computational Materials Science, a  
section of the journal Frontiers in Materials

RECEIVED 05 September 2022

ACCEPTED 23 January 2023

PUBLISHED 03 February 2023

## CITATION

Amaral JS and Amaral VS (2023), Simulating  
the giant magnetocaloric effect—from  
mean-field theory to microscopic models.  
*Front. Mater.* 10:1037396.  
doi: 10.3389/fmats.2023.1037396

## COPYRIGHT

© 2023 Amaral and Amaral. This is an  
open-access article distributed under the  
terms of the [Creative Commons Attribution  
License \(CC BY\)](#). The use, distribution or  
reproduction in other forums is permitted,  
provided the original author(s) and the  
copyright owner(s) are credited and that  
the original publication in this journal is  
cited, in accordance with accepted  
academic practice. No use, distribution or  
reproduction is permitted which does not  
comply with these terms.

# Simulating the giant magnetocaloric effect—from mean-field theory to microscopic models

J. S. Amaral and V. S. Amaral\*

Departamento de Física and CICECO—Aveiro Institute of Materials, University of Aveiro, Aveiro, Portugal

Magnetocaloric materials are recognized as one of the major classes of magnetic materials for energy applications, and can be either employed as refrigerants in heat-pumping devices, or in thermomagnetic generators for energy conversion/harvesting. For both applications, having a material that presents a first-order magnetic phase transition is advantageous, as this typically leads to enhanced values of magnetization change in temperature (relevant to energy conversion) and of the magnetocaloric effect (relevant to heat-pumping). We present a brief overview of selected models applied to the simulation of applied magnetic field and temperature-dependent magnetization and magnetic entropy change of first-order magnetic phase transition systems, covering mean-field models such as the Landau theory of phase transitions and the Bean-Rodbell model, up to more recent developments using a Ising-like microscopic model with magnetovolume coupling effects. We highlight the fundamental and practical limitations of employing these models and compare predicted thermodynamic properties.

## KEYWORDS

magnetic materials, magnetic refrigeration, energy harvesting, first-order phase transitions, magnetovolume coupling

## 1 Introduction

Magnetic materials have had, for several decades, wide-spread use in energy applications, including power generation, conditioning, conversion and transportation (Gutfleisch et al., 2011). Since the discovery of the giant magnetocaloric effect (GMCE) in the late 1990s (Pecharsky and Gschneidner, 1997), the use of magnetic materials for room-temperature refrigeration has been gathering the attention from both the scientific and industrial communities (Pecharsky and Gschneidner, 2008). The GMCE is typically observed only for first-order magnetic phase transition (FOMPT) materials, where a strong magnetovolume coupling is present. As the designation implies, the GMCE is considerably larger than the MCE of second-order magnetic phase transition (SOMPT) systems. While technologically challenging, the development and use of FOMPT materials for use in refrigeration devices is now commonplace, as seen from the number of current prototypes using these materials as refrigerants (Kitanovski et al., 2015). More recently, the use of magnetocaloric materials for energy generation from near room temperature thermal energy harvesting has also gathered attention (Waske et al., 2019). In this case, the sharp dependence of magnetization ( $M$ ) on temperature ( $T$ ) near the Curie temperature  $T_C$  of a FOMPT material enhances the energy-harvesting potential of a device, in a tunable operating temperature window. In short, for both refrigeration and thermal energy harvesting, the use of a first-order magnetic phase transition (FOMPT) material presents considerable advantages. The search for new and optimized

magnetocaloric materials for these applications is an on-going effort from the community. In this context, the use of magnetism models to both interpret experimental data and predict the magnetic and magnetocaloric performance of materials are valuable tools. Naturally, correctly describing the thermodynamics of a FOMPT is required to ensure the physical soundness of calculations. Nevertheless, when choosing a model to use, practical questions come into play, and in the end, the choice of a particular model becomes the result of the balance between the complexity of the model, the information being sought, and the computational cost.

In this work, we consider three distinct models which have been employed to describe quantitatively describe FOMPT materials, from mean-field models such as the Landau theory of phase transitions, the Bean-Rodbell model, and a microscopic Ising-like model with magnetovolume interactions. We employ these models to simulate both SOMPT and FOMPT systems with similar thermodynamic properties, such as a  $T_C \sim 300$  K for the SOMPT, same spin values and saturation magnetization, and a similar value of critical field for the FOMPT system. Both magnetic field ( $H$ ) and  $T$  dependent  $M$  and magnetic entropy change ( $\Delta S_M$ ) are simulated for the three considered models. The aim is to compare the obtained results both qualitatively and quantitatively, highlighting the fundamental and practical limitations of employing these models to describe real materials.

## 2 The Landau theory of phase transitions

The Landau theory of phase transitions has been previously employed to describe the GMCE of FOMPT systems, from describing the magnetoelastic coupling influence on the magnetocaloric effect in ferromagnetic materials (Amaral and Amaral, 2004), and the effect of magnetic irreversibility on estimating the magnetocaloric effect from magnetization measurements (Amaral and Amaral, 2009). The model starts from an expansion of the (Gibbs) Free Energy  $G$  on even powers of  $M$ , together with an Zeeman-like external field interaction term.

$$G(T, M) = G_0 + \frac{1}{2}A(T)M^2 + \frac{1}{4}B(T)M^4 + \frac{1}{6}C(T)M^6 - M.H, \quad (1)$$

where  $A$ ,  $B$ , and  $C$  are the temperature-dependent Landau coefficients. Typically  $A$  is assumed to be linear in temperature, establishing the Curie temperature  $T_C$  of the system:  $A(T) = A'(T - T_C)$ . This linear relation is valid in the susceptibility regime, obeying the Curie law:

$$\frac{H}{M} = \frac{C_{Curie}}{T - T_C}, \quad (2)$$

where  $C_{Curie}$  is the Curie constant of the system. For low  $M$  values, the  $A'$  parameter is then equal to the inverse Curie constant. Minimizing the free energy expression of Eq 1, an equation of state is derived:

$$\frac{H}{M} = A(T) + B(T)M^2 + C(T)M^4, \quad (3)$$

with a structure that allows fitting the well-known isothermal Arrott plot ( $H/M$  versus  $M^2$ ) construction to determine the Landau coefficients' dependence on temperature from magnetization data. This approach was employed for both FOMPT (Amaral and Amaral, 2004) and SOMPT (Amaral et al., 2005) systems.

Here, we consider a trial system with  $A' = 1.5 \times 10^2$ , and constant  $B$  and  $C$  coefficients,  $\pm 5 \times 10^{-1}$  and  $1 \times 10^{-4}$  respectively in cgs units, with  $T_C = 300$  K. The  $A'$  value was chosen to correspond to the inverse Curie constant of a molecular mean-field system with spin  $S = 1/2$ , and a saturation magnetization of 100 emu/g. The chosen  $B$  value leads, when negative, to a critical field of  $\sim 25$  kOe which is within values achievable in commercially available magnetometers with superconducting coils as applied field source.

The  $M(H, T)$  and  $\Delta S_M(H, T)$  data of Figure 1, using a positive  $B$  coefficient, show how a system with thermomagnetic behavior comparable to real SOMPT systems is obtained, with  $M$  around 40 emu/g at 50 kOe near  $T_C$ , and a maximum value of  $\Delta S_M$  around 12 J/(K.kg) for a field change from 0 to 50 kOe.

When considering a negative  $B$  coefficient value, the system now shows a FOMPT, where discontinuities are present in both the magnetization and magnetic entropy change dependence in  $T$  and  $H$ , as shown in Figure 2.

As expected, the maximum  $\Delta S_M$  increases considerably, up to values  $\sim 40$  J/(K.kg). The FOMPT nature is clearly visible in the discontinuities in both  $M(H, T)$  and  $\Delta S_M(H, T)$  data. One of the main limitations of the Landau theory of phase transitions, in this context, is visible when the system reaches higher values of  $M$ . Due to the equation of state originating from a power expansion in  $M$ , the validity of this expansion fails for high  $M$  values, and the magnetization does not saturate even at very low  $T$ . This is an important fact that is often overlooked when fitting or extrapolating Arrott plots of experimental data in the high-magnetization regime. There is also no deep physical insight from the values of the  $B$  and  $C$  Landau parameters. One can observe a negative  $B$  value and justify its occurrence with effects such as magnetovolume coupling and electron condensation, depending on the particular physics of the system under study, but a quantitative analysis is typically not the objective of employing this model. As we will see in the next section, the use of the Bean-Rodbell model, overcomes some of these limitations.

## 3 The Bean-Rodbell model

The Bean-Rodbell model is an extension to the Weiss molecular field model, and was first reported in a study on the magnetic properties of MnAs, a system well-known to have strong magneto-volume coupling (Bean and Rodbell, 1962). The model imposes a linear relation between  $T_C$  and volume, as shown in Eq. 4.

$$T_C = T_0 \left( 1 + \beta \left( \frac{v - v_0}{v_0} \right) \right), \quad (4)$$

where  $\beta$  is positive and constant,  $v$  is volume,  $v_0$  the equilibrium volume with no magnetic interactions, and  $T_0$  the Curie temperature of the rigid system with  $v = v_0$ .

For a sufficiently large linear dependence of  $T_C$  on volume (large  $\beta$  value), the magnetic transition becomes first-order. The crossover point is established via the  $\eta$  parameter, which is defined for a system with compressibility  $K$ :

$$\eta = 40Nk_BKT_0\beta^2 \frac{(S(S+1))^2}{(2S+1)^4 - 1}, \quad (5)$$

where  $S$  is the spin quantum number,  $N$  the spin density and  $k_B$  the Boltzmann constant. The transition is second-order for  $0 < \eta \leq 1$ , while for  $\eta > 1$  the transition is first-order.

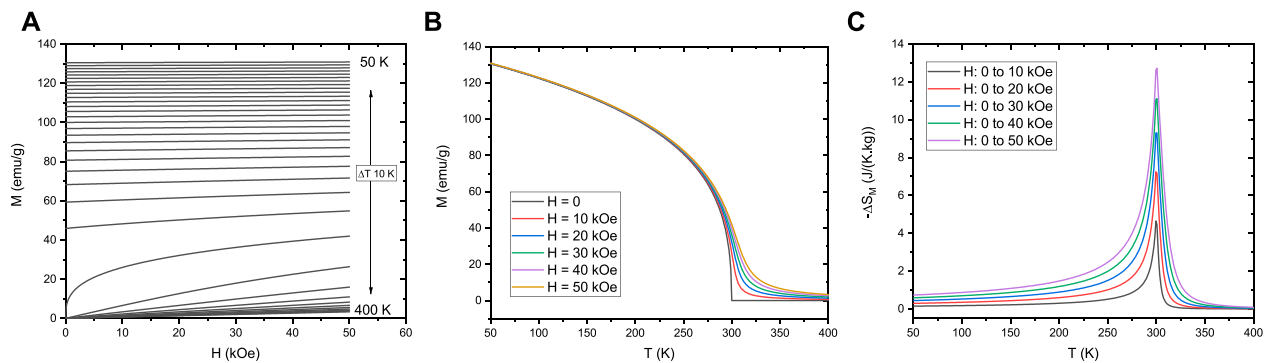


FIGURE 1

(A) Isothermal magnetization  $M$  versus applied magnetic field  $H$ , of a SOMPT system simulated by the Landau theory of phase transitions. Simulation parameters were chosen to correspond to a magnetic material with spin 1/2 and a saturation magnetization value of 100 emu/g. (B) Isofield  $M$  versus temperature  $T$  behavior, for  $H$  between 0 and 50 kOe. (C) Magnetic entropy change  $\Delta S_M$  dependence on  $H$  change and  $T$ .

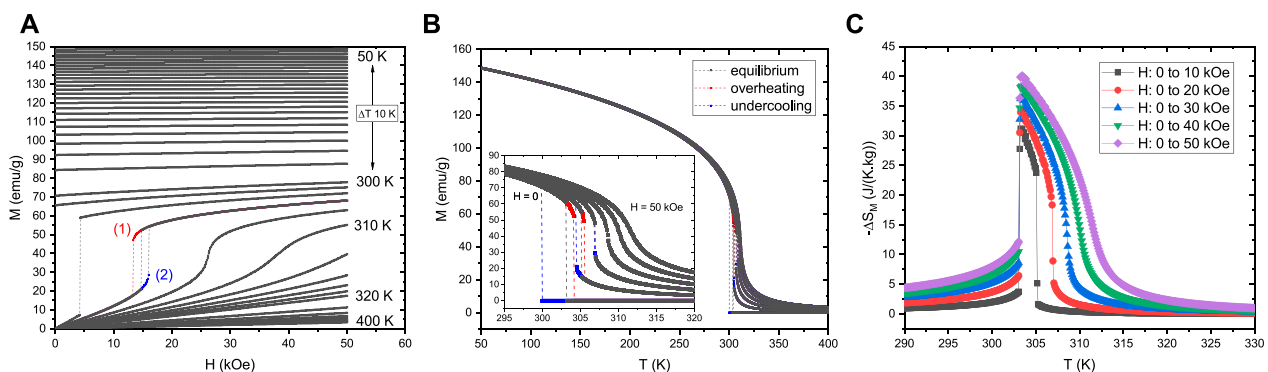


FIGURE 2

(A) Isothermal magnetization  $M$  versus applied magnetic field  $H$ , of a FOMPT system simulated by the Landau theory of phase transitions. Simulation parameters were chosen to correspond to a magnetic material with spin 1/2 and a saturation magnetization value of 100 emu/g, with a critical field value  $\sim 25$  kOe. (B) Isofield  $M$  versus temperature  $T$  behavior, for  $H$  between 0 and 50 kOe. (C) Magnetic entropy change  $\Delta S_M$  dependence on  $H$  change and  $T$ .

For a comparable system with the previous simulations using the Landau theory of phase transitions, we consider the following parameters for our Bean-Rodbell model calculations:  $S = 1/2$ ,  $T_0 = 300$  K, and a  $N$  value of  $1.077 \times 10^{22}$  spins/g, which corresponds to a saturation magnetization of 100 emu/g. For simulating a SOMPT, a null  $\eta$  value is used, with data for magnetization and magnetic entropy change shown in Figure 3.

For simulating a FOMPT, an  $\eta$  value of 1.35 is used, which increases the  $T_C$  to around 304 K, and leads to a critical field around 2.5 kOe, together with an increase in magnetic entropy change, as shown in Figure 4.

The Bean-Rodbell model simulation results are quite similar to those obtained by the Landau theory of phase transitions, for both the SOMPT and FOMPT. This could only be achieved by establishing comparable systems with the same Curie constant, and adjusting the values of the Landau  $B$  and the Bean-Rodbell  $\eta$  parameters to lead to similar values of the critical field. Note, however, how for the Bean-Rodbell data, the  $M(H, T)$  data clearly saturates. The use of the model in the high- $M$  region was useful in the simulation of mixed-phase FOMPT materials, and the validity of the use of the Maxwell relation in estimating  $\Delta S_M$  in strongly first-order systems

(Amaral and Amaral, 2009; Amaral and Amaral, 2010). It is also worth highlighting that, as opposed to the Landau theory of phase transitions, the fact that physically meaningful parameters such as spin and compressibility are defined in the model, a quantitative analysis of experimental data using the Bean-Rodbell model is possible, for both FOMPT and SOMPT systems (Amaral et al., 2007). Simulations using this model are computationally inexpensive, and it is possible to consider smooth distributions of  $T_C$  values, with hundreds of points, to describe disordered SOMPT (Amaral et al., 2008; Bahl et al., 2012) and FOMPT (Amaral and Amaral, 2014; Nielsen et al., 2017) systems.

While widely employed in the study of both SOMPT and FOMPT materials, the Bean-Rodbell model is not the right model for predicting a given material's magnetic and magnetocaloric performance. For this, an *ab initio* approach is required, which can start from using Density Functional Theory (DFT) to estimate relevant magnetic and physical properties of a given system. DFT calculations are typically performed at 0 K, so it is required to feed this parameters to a given model for estimating thermodynamic properties. A relatively straightforward approach is to estimate the Heisenberg exchange parameter  $J$  of a given material using DFT, and then use the calculated value in an Ising or Heisenberg model.

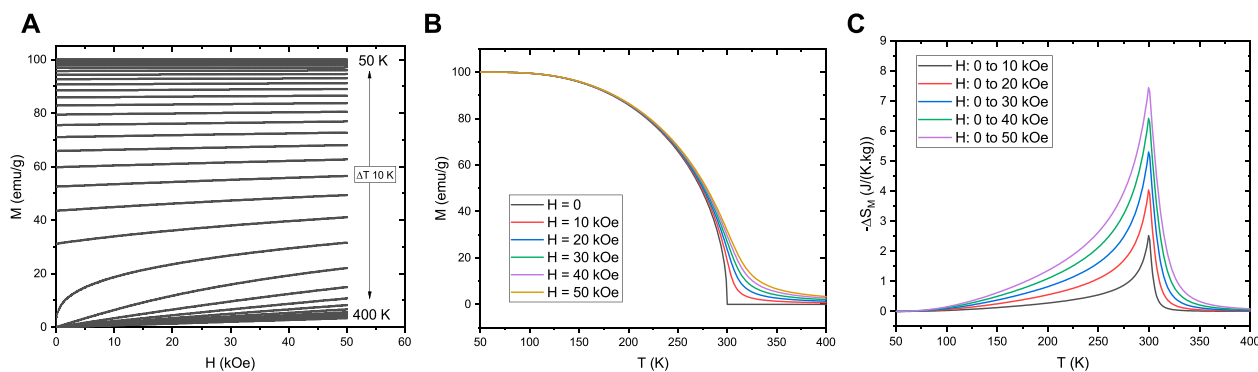


FIGURE 3

(A) Isothermal magnetization  $M$  versus applied magnetic field  $H$ , of a SOMPT system ( $\eta = 0$ ) simulated by the Bean-Rodbell model, with spin 1/2 and a saturation magnetization value of 100 emu/g. (B) Isofield  $M$  versus temperature  $T$  behavior, for  $H$  between 0 and 50 kOe. (C) Magnetic entropy change  $\Delta S_M$  dependence on  $H$  change and  $T$ .

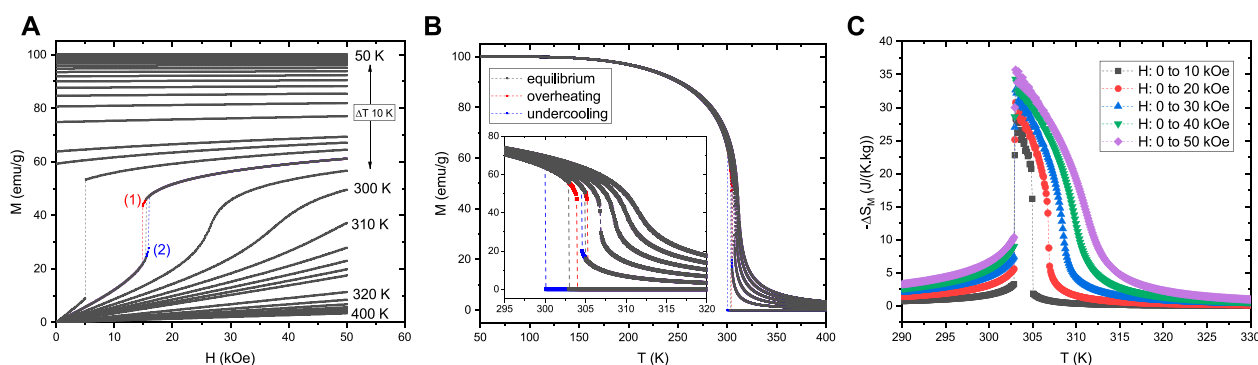


FIGURE 4

(A) Isothermal magnetization  $M$  versus applied magnetic field  $H$ , of a FOMPT system ( $\eta = 1.35$ ) simulated by the Bean-Rodbell model, with spin 1/2 and a saturation magnetization value of 100 emu/g. (B) Isofield  $M$  versus temperature  $T$  behavior, for  $H$  between 0 and 50 kOe. (C) Magnetic entropy change  $\Delta S_M$  dependence on  $H$  change and  $T$ .

Naturally, for describing a magneto-volume driven FOMPT, the model needs to include this coupling. In the next section, we will consider an Ising-like microscopic model with magnetovolume interactions.

## 4 Microscopic model with magnetovolume interactions

A FOMPT system can be described in simple microscopic models, such as the Ising and Heisenberg models, by including an explicit dependence of the magnetic exchange parameter  $J$ , together with a volume energy potential (Amaral et al., 2016):

$$\mathcal{H} = -\frac{1}{2} \sum_{ij} [J(v) S_i \cdot S_j] + \frac{1}{2} K v^2 - M H, \quad (6)$$

where  $J$  is the magnetic exchange parameter between  $S_i$  and  $S_j$  nearest-neighbour spins,  $v$  volume and  $K$  compressibility.

All the parameters required to simulate a given (real) magnetic system using this approach can be readily obtained by existing DFT packages. Estimating  $J$  for multi-component alloys is particularly relevant in the study of magnetocaloric materials, so the use of the

Liechtenstein method (Liechtenstein et al., 1987) in systems where fractional site occupancy is accurately described by the Coherent Potential Approximation (Yonezawa and Morigaki, 1973) is a practical approach. These capabilities are available in the SPR-KKR (Ebert, 2005) and openmx (Ozaki et al., 2013) DFT packages. The estimate of the full  $M(H, T)$  and  $\Delta S_M(H, T)$  dependencies can be challenging using the standard Monte Carlo Metropolis method (Metropolis et al., 1953), as each  $(H, T)$  pair will require an independent calculation, and for the case of FOMPT the stabilization of the two order parameters,  $M$  and  $v$  is difficult and time-consuming. Another approach is to obtain the thermodynamic properties of the system with previously calculated Joint Density of States (JDOS) estimates. The JDOS of a given model (discrete or continuous) and of a given lattice (e. g. 2D, 3D) can be calculated by Monte Carlo methods such as the Wang-Landau method (Wang and Landau, 2001; Zhou et al., 2006), Random Path Sampling (Amaral et al., 2014) and the recently reported Flat Scan Sampling method (Inácio et al., 2022). As the JDOS is  $T$ ,  $H$  and  $v$  independent, the full calculation of  $M(H, T)$  and  $\Delta S_M(H, T)$  dependencies for both SOMPT and FOMPT systems is robust and quickly achievable using a regular personal computer.



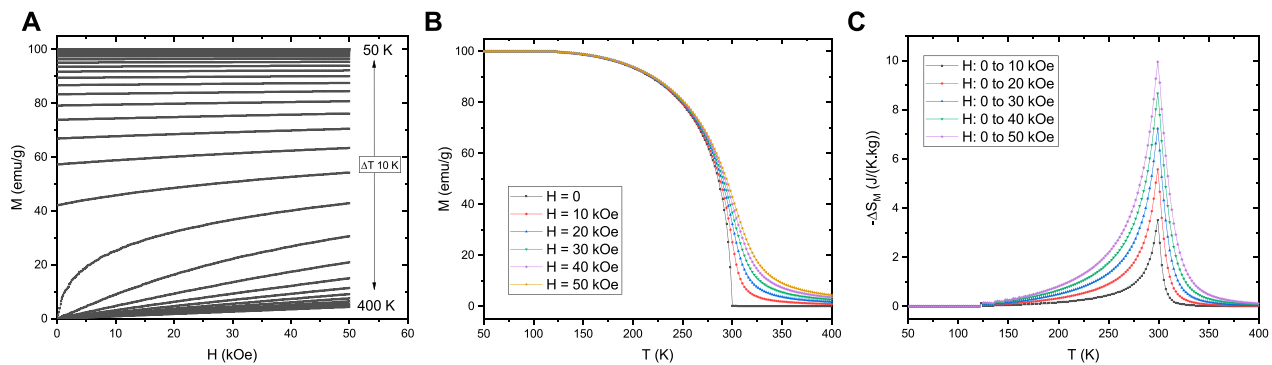


FIGURE 5

(A) Isothermal magnetization  $M$  versus applied magnetic field  $H$ , of a SOMPT system ( $J' = 0$ ) from a Ising spin 1/2 3D lattice with 512 spins, considering a saturation magnetization of 100 emu/g and a magnetic moment value of  $1 \mu_B$  per spin. (B) Isofield  $M$  versus temperature  $T$  behavior, for  $H$  between 0 and 50 kOe. (C) Magnetic entropy change  $\Delta S_M$  dependence on  $H$  change and  $T$ .

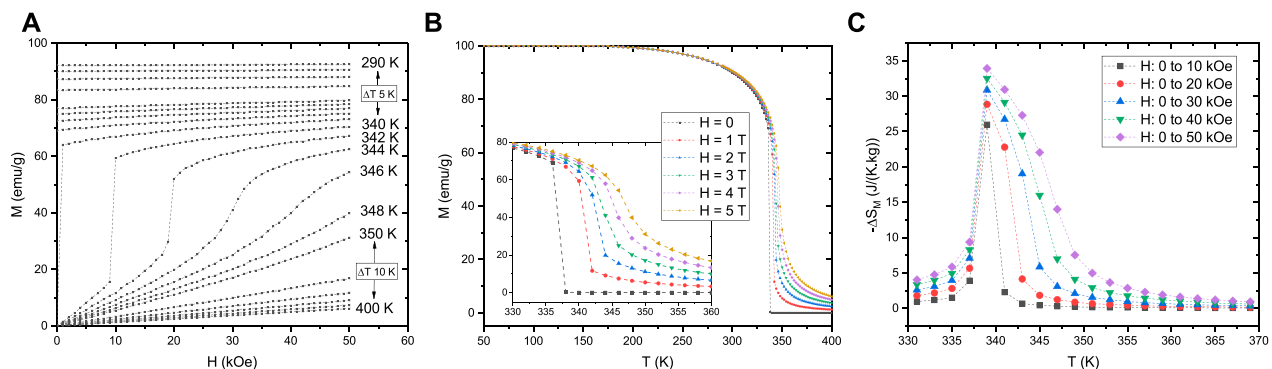


FIGURE 6

(A) Isothermal magnetization  $M$  versus applied magnetic field  $H$ , of a FOMPT system ( $J' = 2.8$ ) from a compressible Ising spin 1/2 3D lattice with 512 spins, considering a saturation magnetization of 100 emu/g and a magnetic moment value of  $1 \mu_B$  per spin. (B) Isofield  $M$  versus temperature  $T$  behavior, for  $H$  between 0 and 50 kOe. (C) Magnetic entropy change  $\Delta S_M$  dependence on  $H$  change and  $T$ .

For describing a comparable system to the previous mean-field simulations, we consider the Ising model of 512 spin 1/2 particles in a 3D lattice. In the case of the rigid system with a SOMPT, the  $J$  value is chosen to lead to a  $T_C$  of 300 K. The field interaction is calculated with a magnetic moment value of  $1 \mu_B$  per spin. Imposing a 100 emu/g saturation magnetization, a similar behavior compared to the previous mean-field models is obtained for magnetization and magnetic entropy change, as seen in Figure 5.

Considering now a compressible system, with a linear dependence of  $J$  on volume,  $J(v) = J_0 + J'(v - v_0)/v_0$  and a  $K$  value of 50, a  $J'$  value of 2.8 (in units of  $J_0$ ) leads to a FOMPT with a critical field of  $\sim 25$  kOe, comparable to the previous simulations of the Landau Theory of phase transitions and the Bean-Rodbell model, as shown in Figure 6.

While qualitatively the behavior of the Ising model simulations for both SOMPT and FOMPT systems are similar to the results of the mean-field models, a quantitative comparison highlights some differences. While for the mean-field models the change of  $T_C$  between the SOMPT and FOMPT is relatively small at around 3 K ( $\sim 1\%$  of  $T_C$ ), for the case of the microscopic model, this value is substantially higher at  $\sim 40$  K ( $\sim 13\%$  of  $T_C$ ). In terms of the observed maximum values of  $-\Delta S_M$  for an applied field of 50 kOe, for both SOMPT and

FOMPT systems the obtained results are similar for all the considered models. These increase from  $\sim 10$  J/(K.kg) of the SOMPT systems, to values  $\sim 35$  J/(K.kg) for the FOMPT systems. These results highlight how these fundamentally different models can lead to quantitatively similar behaviors for both the  $M(H, T)$  and  $\Delta S_M(T, H)$  dependencies, with results comparable to real SOMPT and FOMPT materials.

## 5 Overview

In this work, we have explored three distinct magnetic models that can simulate the relevant thermodynamic properties of both SOMPT and FOMPT systems for application in magnetic refrigeration and thermal energy harvesting. One of the main objectives was to consider equivalent SOMPT and FOMPT magnetic systems with  $T_C$  values around room temperature, and to compare the simulated results, particularly  $M(H, T)$  and  $\Delta S_M(H, T)$ , which are the main thermodynamic properties for these applications.

Landau theory allows to easily interpret experimental magnetization data by fitting the isothermal Arrott plots. The observation of negative values of the  $B$  coefficient (negative slopes

in the Arrott plots) is a sign of a FOMPT. With a full description of the temperature dependence of the  $A$ ,  $B$  and  $C$  coefficients, it is straightforward to smooth, interpolate and, away from saturation, to extrapolate the  $(H, T)$  dependence of magnetization and magnetic entropy change data. Still, while it is possible to qualitatively interpret the values of the model parameters, they do not have a straightforward or quantitative physical interpretation. Nevertheless, the obtained  $M(H, T)$  and  $\Delta S_M(H, T)$  data are physically and quantitatively sound.

The Bean-Rodbell model, as an extension of the Weiss molecular mean-field model, while also a phenomenological model, has physical meaning to all its parameters. This allows to interpret experimental data of both SOMPT and FOMPT systems and estimate fundamental system properties such as spin value and quantify magnetovolume coupling. The validity of the simulations near  $M$  saturation, in contrast to the Landau theory, allows for accurate description of GMCE systems in a wider temperature range, including disordered and mixed phase systems. While the Bean-Rodbell simulation parameters have physical meaning, it is impossible to directly obtain input values of  $T_O$  and  $\beta$  from *ab initio* calculations at 0 K. To allow the prediction of the properties of a given material from DFT calculations at 0K, then a different approach is required.

A microscopic model approach, while typically more expensive in terms of computational cost, allows for more intricate and detailed simulation of model systems. As the main simulation parameter  $J$ , together with its dependence on system volume  $J(v)$ , are obtainable *via* DFT calculations, an *in silico* approach to predict the thermo-magnetic properties of new and optimized magnetic materials is possible. The use of prior JDOS of models such as the Ising and Heisenberg models, lowers computational cost for simulation of materials for arbitrary values of  $J$  and  $J(v)$ , and allows the description of the full  $M(H, T)$  and  $\Delta S_M(H, T)$  dependencies.

Our simulation results for the three models, for both SOMPT and FOMPT systems are both qualitatively and quantitatively in agreement. The  $M(H, T)$  and  $\Delta S_M(H, T)$  behaviors are similar, particularly the increase of the maximum  $\Delta S_M$  value due to the change of a SOMPT to a FOMPT. The most notable difference between our obtained results is the larger change of  $T_C$  of the FOMPT system

compared to the SOMPT, in the case of the compressible Ising model simulations. We highlight that all three models are physically sound, and the choice of which one to use will depend if the purpose is to interpret experimental data, or the *in silico* prediction of the performance of new and optimized magnetic refrigerants and ferromagnets for thermal energy harvesting.

## Author contributions

All authors listed have made a substantial, direct, and intellectual contribution to the work and approved it for publication.

## Funding

This work was developed within the scope of the project CICECO-Aveiro Institute of Materials, UIDB/50011/2020, UIDP/50011/2020 and LA/P/0006/2020, financed by national funds through the FCT/MEC (PIDDAC).

## Conflict of interest

The authors declare that the research was conducted in the absence of any commercial or financial relationships that could be construed as a potential conflict of interest.

## Publisher's note

All claims expressed in this article are solely those of the authors and do not necessarily represent those of their affiliated organizations, or those of the publisher, the editors and the reviewers. Any product that may be evaluated in this article, or claim that may be made by its manufacturer, is not guaranteed or endorsed by the publisher.

## References

- Amaral, J. S., and Amaral, V. S. (2014). Disorder effects in giant magnetocaloric materials. *Phys. Stat. Sol. A* 211, 971–974. doi:10.1002/pssa.201300749
- Amaral, J. S., and Amaral, V. S. (2010). On estimating the magnetocaloric effect from magnetization measurements. *J. Magn. Magn. Mat.* 322, 1552–1557. doi:10.1016/j.jmmm.2009.06.013
- Amaral, J. S., and Amaral, V. S. (2009). The effect of magnetic irreversibility on estimating the magnetocaloric effect from magnetization measurements. *Appl. Phys. Lett.* 94, 042506. doi:10.1063/1.3075851
- Amaral, J. S., Fortunato, N. M., Amorim, C. O., Gonçalves, J. N., and Amaral, V. S. (2016). “Giant magnetocaloric effect of compressible ising and heisenberg lattices,” in Proceedings of the 7th International Conference on Magnetic Refrigeration at Room Temperature (Thermag VII), Turin, Italy, 11 - 14 September 2016, 30019341. doi:10.18462/iir.thermag.2016.0200
- Amaral, J. S., Gonçalves, J. N., and Amaral, V. S. (2014). Thermodynamics of the 2-D ising model from a random path sampling method. *IEEE Trans. Magn.* 50, 1–4. doi:10.1109/tmag.2014.2326713
- Amaral, J. S., Reis, M. S., Amaral, V. S., Mendonça, T. M., Araújo, J. P., Sá, M. A., et al. (2005). Magnetocaloric effect in Er- and Eu-substituted ferromagnetic La-Sr manganites. *J. Magn. Magn. Mat.* 290–291, 686–689. doi:10.1016/j.jmmm.2004.11.337
- Amaral, J. S., Silva, N. J. O., and Amaral, V. S. (2007). A mean-field scaling method for first- and second-order phase transition ferromagnets and its application in magnetocaloric studies. *Appl. Phys. Lett.* 91, 172503. doi:10.1063/1.2801692
- Amaral, J. S., Tavares, P. B., Reis, M. S., Araújo, J. P., Mendonça, T. M., Amaral, V. S., et al. (2008). The effect of chemical distribution on the magnetocaloric effect: A case study in second-order phase transition manganites. *J. Non-cryst. Sol.* 354, 5301–5303. doi:10.1016/j.jnoncrysol.2008.05.078
- Amaral, V. S., and Amaral, J. S. (2004). Magnetoelastic coupling influence on the magnetocaloric effect in ferromagnetic materials. *J. Magn. Magn. Mat.* 272–276, 2104–2105. doi:10.1016/j.jmmm.2003.12.870
- Bahl, C. R. H., Bjørk, R., Smith, A., and Nielsen, K. K. (2012). Properties of magnetocaloric materials with a distribution of curie temperatures. *J. Magn. Magn. Mat.* 324, 564–568. doi:10.1016/j.jmmm.2011.08.044
- Bean, C. P., and Rodbell, D. S. (1962). Magnetic disorder as a first-order phase transformation. *Phys. Rev.* 126, 104–115. doi:10.1103/PhysRev.126.104
- Ebert, H. (2005). The Munich SPR-KKR package. version 6.3.
- Gutfleisch, O., Willard, M. A., Brück, E., Chen, C. H., Sankar, S. G., and Liu, J. P. (2011). Magnetic materials and devices for the 21st century: Stronger, lighter, and more energy efficient. *Adv. Mater.* 23, 821–842. doi:10.1002/adma.201002180

- Inácio, J. C., Ferreira, A. L., and Amaral, J. S. (2022). Accurate estimate of the joint density of states via flat scan sampling. *arXiv arXiv:2203.02718*. doi:10.48550/arXiv.2203.02718
- Kitanovski, A., Tušek, J., Tomc, U., Plaznik, U., Ošbolt, M., and Poredoš, A. (2015). *Magnetocaloric energy conversion - from theory to applications*. Berlin: Springer.
- Liechtenstein, A. I., Katsnelson, M. I., Antropov, V. P., and Gubanov, V. A. (1987). Local spin density functional approach to the theory of exchange interactions in ferromagnetic metals and alloys. *J. Magn. Magn. Mat.* 67, 65–74. doi:10.1016/0304-8853(87)90721-9
- Metropolis, N., Rosenbluth, A. W., Rosenbluth, M. N., Teller, A. H., and Teller, E. (1953). Equation of state calculations by fast computing machines. *J. Chem. Phys.* 21, 1087–1092. doi:10.1063/1.1699114
- Nielsen, K. K., Bahl, C. R. H., Smith, A., and Bjørk, R. (2017). Spatially resolved modelling of inhomogeneous materials with a first order magnetic phase transition. *J. Phys. D: Appl. Phys.* 50, 414002. doi:10.1088/1361-6463/aa86e2
- Ozaki, T., Kino, H., and Yu, J. (2013) Openmx (open source package for material explorer). ver. 3.7.
- Pecharsky, V. K., and Gschneidner, K. A. Jr (1997). Giant magnetocaloric effect in  $\text{Gd}_5(\text{Si}_2\text{Ge}_2)$ . *Phys. Rev. Lett.* 78, 4494–4497. doi:10.1103/PhysRevLett.78.4494
- Pecharsky, V. K., and Gschneidner, K. A. Jr (2008). Thirty years of near room temperature magnetic cooling: Where we are today and future prospects. *Int. J. Refrig.* 31, 945–961. doi:10.1016/j.ijrefrig.2008.01.004
- Wang, F., and Landau, D. P. (2001). Efficient, multiple-range random walk algorithm to calculate the density of states. *Phys. Rev. Lett.* 86, 2050–2053. doi:10.1103/physrevlett.86.2050
- Waske, A., Dzekan, D., Sellschopp, K., Berger, D., Stork, A., Nielsch, K., et al. (2019). Energy harvesting near room temperature using a thermomagnetic generator with a pretzel-like magnetic flux topology. *Nat. Energy* 4, 68–74. doi:10.1038/s41560-018-0306-x
- Yonezawa, F., and Morigaki, K. (1973). Coherent potential approximation. basic concepts and applications. *Prog. Theor. Phys. Suppl.* 53, 1–76. doi:10.1143/PTPS.53.1
- Zhou, S. T. C., Schulthess, T. C., and Landau, D. P. (2006). Wang-Landau algorithm for continuous models and joint density of states. *Phys. Rev. Lett.* 96, 120201. doi:10.1103/physrevlett.96.120201



## OPEN ACCESS

## EDITED BY

Vadim G. Kessler,  
Swedish University of Agricultural  
Sciences, Sweden

## REVIEWED BY

Ana Margarida Goncalves Carvalho Dias,  
New University of Lisbon, Portugal  
Iris Luz Batalha,  
Institute for Bioengineering of Catalonia  
(IBEC), Spain

## \*CORRESPONDENCE

Mara G. Freire,  
✉ maragfreire@ua.pt

## SPECIALTY SECTION

This article was submitted to  
Biomaterials,  
a section of the journal  
Frontiers in Bioengineering and  
Biotechnology

RECEIVED 05 September 2022

ACCEPTED 23 January 2023

PUBLISHED 07 February 2023

## CITATION

Almeida C, Pedro AQ, Tavares APM,  
Neves MC and Freire MG (2023), Ionic-  
liquid-based approaches to improve  
biopharmaceuticals downstream  
processing and formulation.  
*Front. Bioeng. Biotechnol.* 11:1037436.  
doi: 10.3389/fbioe.2023.1037436

## COPYRIGHT

© 2023 Almeida, Pedro, Tavares, Neves  
and Freire. This is an open-access article  
distributed under the terms of the [Creative  
Commons Attribution License \(CC BY\)](#).  
The use, distribution or reproduction in  
other forums is permitted, provided the  
original author(s) and the copyright  
owner(s) are credited and that the original  
publication in this journal is cited, in  
accordance with accepted academic  
practice. No use, distribution or  
reproduction is permitted which does not  
comply with these terms.

# Ionic-liquid-based approaches to improve biopharmaceuticals downstream processing and formulation

Catarina Almeida, Augusto Q. Pedro, Ana P. M. Tavares,  
Márcia C. Neves and Mara G. Freire\*

CICECO-Aveiro Institute of Materials, Department of Chemistry, University of Aveiro, Aveiro, Portugal

The emergence of biopharmaceuticals, including proteins, nucleic acids, peptides, and vaccines, revolutionized the medical field, contributing to significant advances in the prophylaxis and treatment of chronic and life-threatening diseases. However, biopharmaceuticals manufacturing involves a set of complex upstream and downstream processes, which considerably impact their cost. In particular, despite the efforts made in the last decades to improve the existing technologies, downstream processing still accounts for more than 80% of the total biopharmaceutical production cost. On the other hand, the formulation of biological products must ensure they maintain their therapeutic performance and long-term stability, while preserving their physical and chemical structure. Ionic-liquid (IL)-based approaches arose as a promise alternative, showing the potential to be used in downstream processing to provide increased purity and recovery yield, as well as excipients for the development of stable biopharmaceutical formulations. This manuscript reviews the most important progress achieved in both fields. The work developed is critically discussed and complemented with a SWOT analysis.

## KEYWORDS

biopharmaceuticals, ionic liquids, biomanufacturing, downstream processing, purification platforms, formulation, ionic liquid-based approaches, biopharmaceuticals administration

## Introduction

Due to the massive growth and aging of global population and to the high incidence of autoimmune and chronic diseases, there is a huge demand for effective and safe drugs (Kesik-Brodacka, 2018; Tavares et al., 2019; O'Flaherty et al., 2020). The pharmaceutical industry is majorly governed by traditional low molecular weight and synthetic pharmaceuticals, which represent more than 90% of all drugs currently available (Ferreira et al., 2016; Tavares et al., 2019). However, a relatively new class of therapeutic molecules, known as biopharmaceuticals, has been gaining increasing traction. Biopharmaceuticals, also known as biologics or biologic drugs, were first introduced in the 1980s and refer to all pharmaceutical products with therapeutic activity that are derived from biological sources (Chen et al., 2018; Hong et al., 2018; US Food and Drug Administration, 2018; Tavares et al., 2019; O'Flaherty et al., 2020; Pereira et al., 2021). They represent an important fast-growing sector within the global pharmaceutical industry, constituting *ca.* one-third of all drugs currently under development (Moorkens et al., 2017; Tavares et al., 2019; Pereira et al., 2021).

The manufacturing of biopharmaceuticals, also known as biomanufacturing, comprises two main stages—the upstream and downstream processing (Jozala et al., 2016; Hong et al., 2018; Tavares et al., 2019). The upstream processing encompasses several events responsible to



promote the growth of the host cell that will further express and produce the biomolecule of interest. Afterwards, during the downstream processing, the target biomolecule is isolated and purified (Jozala et al., 2016). Biomanufacturing itself demands a multistep approach, in which precise quality control and accurate monitoring must be carried out to assure some criteria, including the biomolecule's identity/quality, purity and stability (Tavares et al., 2019; Pereira et al., 2021). Purification strategies are currently dominated by chromatographic techniques, which are needed to efficiently remove all cell-, process- and product-associated impurities, while being of easy scale-up, reliable, and highly robust (Jozala et al., 2016). However, their main disadvantage is their high cost (Jozala et al., 2016; Castro et al., 2019; Tavares et al., 2019). It is, therefore, crucial to either develop novel cost-effective purification platforms or to find new ways to improve existent workflows, providing a high-quality and high-purity product, while simultaneously meeting regulatory requirements (Castro et al., 2019; Pereira et al., 2021).

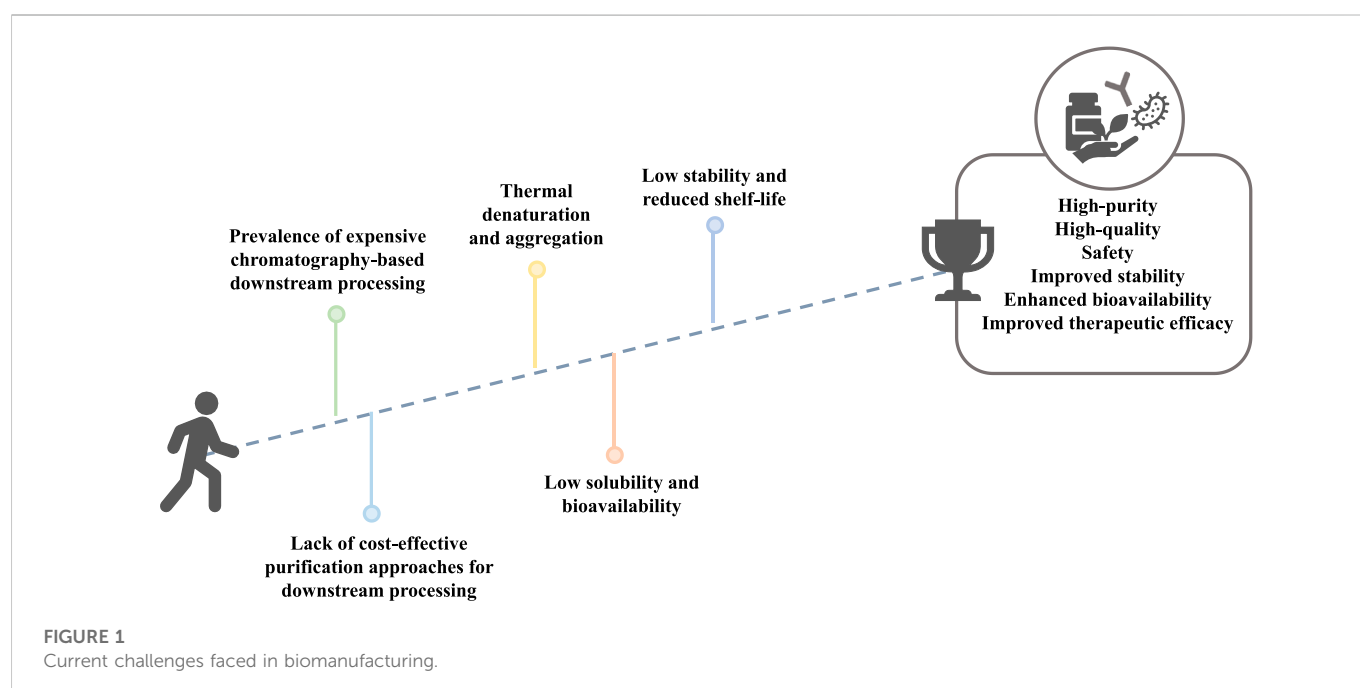
Contrarily to synthetic drugs, due to their complexity and natural origin, biopharmaceuticals are often unstable (Lin et al., 2021; Loureiro et al., 2022). Thus, biopharmaceuticals formulation must ensure their long-term stability through the preservation of their structural integrity and bioactivity (Loureiro et al., 2022). This can be achieved by adding excipients to the final formulation or by employing costly preservation techniques that improve shelf-life and durability (Lin et al., 2021). Another important bottleneck is their low bioavailability *in vivo* after the administration, which can significantly alter pharmacokinetic properties and therapeutic efficacy (Lin et al., 2021; Loureiro et al., 2022). Altogether, these issues compromise the development of high-quality, effective, and safe biopharmaceuticals, which are major requirements in the sector (Tavares et al., 2019). The major challenges currently faced in the biopharmaceutical field are summarized in Figure 1.

ILs are salts formed by the combination of organic cations and organic or inorganic anions, resulting in salts with low charge distribution and low melting points, some of them liquid at room

temperature, and capable of establishing a plethora of interactions (Pereira et al., 2021; Castro et al., 2019; e Silva et al., 2017). IL's outstanding properties make them attractive for catalysis, electrochemistry, separation, and extraction, among others (Fontanals et al., 2009; Kianfar and Mafi, 2020). Although less investigated, within the pharmaceutical field, ILs have already shown to be important enhancers of the solubility, activity, permeability, and stability of several synthetic drugs (Pedro et al., 2020) and biopharmaceuticals (Vijayaraghavan et al., 2010; Byrne et al., 2012; Foureau et al., 2012; Kumar and Venkatesu, 2013; Mukesh et al., 2013; Kumar and Venkatesu, 2014; Mazid et al., 2015; Todinova et al., 2016; Banerjee et al., 2018; Jagannath et al., 2018; Pedro et al., 2018; Reslan et al., 2018; Guncheva et al., 2019; Lin et al., 2019; Quental et al., 2019; Mandal et al., 2020; Lin et al., 2021; Dhiman et al., 2022; Vicente et al., 2022), and also in the extraction and purification of these biomolecules (Shu et al., 2010; Qu et al., 2012; Yuan et al., 2012; Chen et al., 2015; Ding et al., 2015; Ren et al., 2015; Taha et al., 2015; Ferreira et al., 2016; Mondal et al., 2016; Ramalho et al., 2018; Santos et al., 2018; Song et al., 2018; Xu et al., 2018; Capela et al., 2019; Magri et al., 2019; Marchel et al., 2019; Quental et al., 2019; Vicente et al., 2019; Castro et al., 2020; Neves et al., 2020; Vicente et al., 2022; Capela et al., 2023).

## Biopharmaceuticals manufacturing

Most biopharmaceuticals are obtained through recombinant deoxyribonucleic acid (DNA) technology, in which a given gene is introduced in the genetic code of the host organism to produce the biomolecule of interest. Innovations have been achieved in this field, allowing to shift from production approaches based on non-mammalian systems to mammalian cell cultures (Tavares et al., 2019; Rasmussen et al., 2021). Within biopharmaceuticals are included vaccines, nucleic acids, cell or gene therapies, plant extracts, allergens, cytokines, tissue growth factors, blood components or derivatives, peptides, enzymes and recombinant

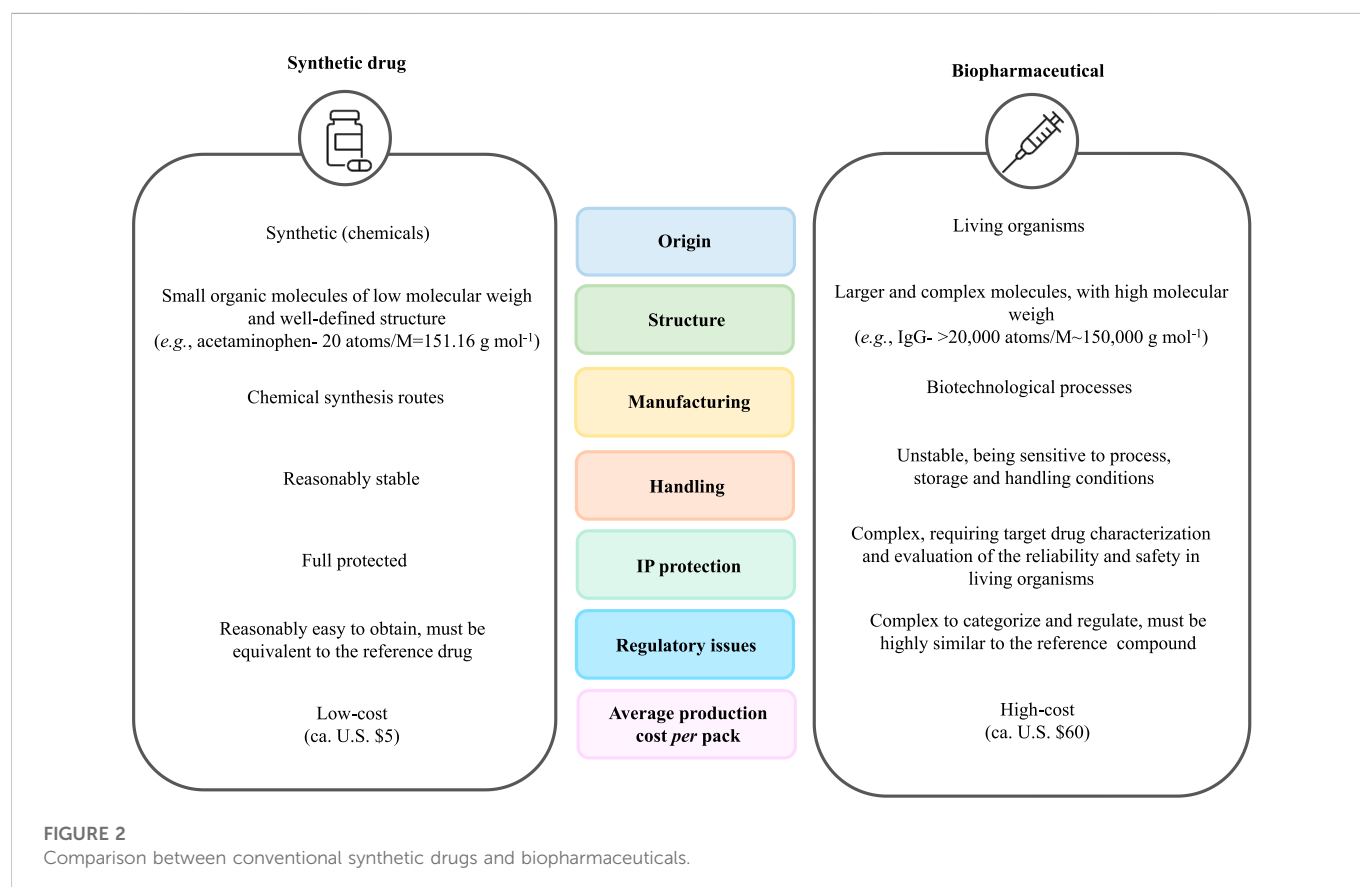


therapeutic proteins, including monoclonal antibodies (mAbs) (Rosa et al., 2010; Foldvari et al., 2016; Chen et al., 2018; Tavares et al., 2019; O'Flaherty et al., 2020). The oldest biopharmaceutical approved by the U.S Food and Drug Administration (FDA) regulatory agency—a recombinant DNA human insulin produced in *Escherichia coli*—dates back to 1982 (The, 1989; O'Flaherty et al., 2020). Between 2013 and 2016, a total of 73 biopharmaceuticals were approved to be used in humans (Jozala et al., 2016). In 2016, this number increased, with the introduction of approximately 200 biopharmaceuticals in the market (Rasmussen et al., 2021). Later, in 2018, ca. 374 biopharmaceuticals obtained approval for therapeutic purposes in the European Union (EU) and the United States of America (United States of America) for the treatment of cancer, infectious and autoimmune diseases, and HIV-AIDS-associated disorders (Foldvari et al., 2016; Walsh, 2018; Parker and Li, 2021). Overall, the global market associated with biopharmaceuticals accounted for U.S. \$237.2 billion in 2018 and it is expected to increase to U.S. \$389 billion by 2024, with a compound annual growth rate (CAGR) of 8.59% (O'Flaherty et al., 2020). Antibodies correspond to the largest fraction of the biopharmaceutical market, in which monoclonal antibodies (mAbs) accounted for the highest sale numbers, with projections pointing out a market value of U.S. \$200 billion by 2023 (Hong et al., 2018; Kesik-Brodacka, 2018; Grilo and Mantalaris, 2019; O'Flaherty et al., 2020). Although mAbs currently represent the largest segment of the biopharmaceutical sector (Jozala et al., 2016; Castro et al., 2019; Tavares et al., 2019; Castro et al., 2020), ground-breaking research for the development of safe and effective delivery platform technologies to deliver nucleic acids has been at the forefront of

the global efforts to fight the COVID-19 pandemic. Nucleic acids are gaining momentum within the biopharmaceutical sector, from which an ever-growing number of different products have received regulatory approval (Kulkarni et al., 2021).

Due to their safety, high specificity, and efficiency to tackle numerous diseases, in which a targeted therapy is provided instead of symptomatic therapy, biopharmaceuticals are gradually replacing synthetic therapies (Rosa et al., 2010; Kesik-Brodacka, 2018; Tavares et al., 2019; O'Flaherty et al., 2020). Biopharmaceuticals significantly differ from the common synthetic drugs, namely concerning their origin, structure, manufacturing process, final formulation, handling conditions, dosing, immunogenicity, intellectual property (IP) issues, regulations and marketing, and cost, as summarized in Figure 2 (Rader, 2008; Kesik-Brodacka, 2018; Tavares et al., 2019).

In contrast to biopharmaceuticals, which possess a biological nature, synthetic drugs are products resulting from chemical synthetic routes (Kesik-Brodacka, 2018; Tavares et al., 2019). The latter are generally small organic molecules with low molecular weight and a simple and well-identified structure (e.g., acetaminophen has 20 atoms and a molecular weight of  $151.16 \text{ g mol}^{-1}$ ) (Information NC for B, 2007; Kesik-Brodacka, 2018; Tavares et al., 2019; Rasmussen et al., 2021). In contrast, biopharmaceuticals are compounds of high molecular mass, being 200 to 1000 times larger than conventional drugs (e.g., IgG has more than 20,000 atoms and a molecular weight of ca.  $150,000 \text{ g mol}^{-1}$ ) (Tsang and Cortez, 2010; Mitrageotri et al., 2014; Kesik-Brodacka, 2018; Tavares et al., 2019; Rasmussen et al., 2021). Moreover, whereas synthetic drugs are characterized through well-established analytical techniques, the accurate characterization of biopharmaceuticals is more challenging. For instance, recombinant



proteins, such as fragment crystallizable (Fc)-fusion proteins and mAbs, can undergo several post-translational modifications (proteolysis, glycosylation, among others), making their accurate bioprocessing and, consequently, their characterization, difficult to achieve (Jenkins et al., 2008). Moreover, biopharmaceuticals are more unstable and sensitive to the conditions employed during the manufacturing process, storage, and handling, such as temperature and pH (Kesik-Brodacka, 2018; Tavares et al., 2019; Lin et al., 2021). Since biopharmaceuticals are highly prone to denaturation and degradation events, as well as to modifications in their amino acid and sugar patterns, the manufacturing conditions must be strictly controlled (Kesik-Brodacka, 2018; Lin et al., 2021). As such, well-designed stabilization systems/excipients for these biomolecules are required to guarantee their long-term stability and preservation. Notwithstanding their outstanding properties, the IP protection and the regulatory approval pathways for biopharmaceuticals are more complex due to their manufacturing processes, since the characterization of the target drug and the evaluation of the reproducibility and safety of the production approach are mandatory (Tavares et al., 2019). Moreover, biopharmaceuticals are more expensive to produce (average production cost per pack was *ca.* U.S. \$60 for biopharmaceuticals, in contrast with U.S. \$5 per pack of small-molecule drugs) (Makurvet, 2021). A representative overview of the biomanufacturing of mAbs, including all steps required in the upstream and downstream stages, is provided in Figure 3. The upstream processing starts with the cell culture in optimal conditions designed to assure the proper cell growth in the culture media (Jozala et al., 2016; Hong et al., 2018). This process is then scaled up through a sequence of various bioreactor stages; the obtained cell mass is then transferred to the final bioreactor to allow the expression and production of the target biomolecule (Shukla and Thömmes, 2010; Hong et al., 2018). Afterwards, cells and cell debris are separated from the culture broth by a sequence of cell harvesting steps, involving centrifugation and/or filtration approaches, to obtain a clarified broth

(Shukla and Thömmes, 2010; Jozala et al., 2016; Hong et al., 2018). The next stage of the manufacturing of biopharmaceuticals relies on downstream processing, during which, through a series of multiple steps, the biopharmaceutical is isolated and purified (Conner et al., 2014; Jozala et al., 2016; Hong et al., 2018; Tavares et al., 2019). The initial recovery of the target compound depends on the cellular localization of the biomolecule; for instance in the cases where the target compound is produced extracellularly, the clarified broth is concentrated by ultrafiltration and then purified, whereas when it is produced intracellularly, the cell is subjected to lysis after harvesting, and then clarified to remove the resultant cell debris (Jozala et al., 2016). The second step in the downstream processing corresponds to the purification of the target biomolecule, during which all impurities related to the cell (e.g., DNA and host cell proteins), the process (e.g., antifoam agents, leached ligands, and buffers), or the impurities associated to the product (fragments, clipped species, and aggregates) are removed (Azevedo et al., 2009; Conner et al., 2014; Rathore and Kapoor, 2015; Jozala et al., 2016). During this step, several techniques can be employed, such as chromatography, filtration, diafiltration, tangential flow filtration, as well as the use of aqueous biphasic systems (ABS) (Azevedo et al., 2009; Conner et al., 2014; Jozala et al., 2016; Hong et al., 2018; Tavares et al., 2019). The selection of the purification technique is also dependent on the cellular localization of the biopharmaceutical; for instance, if it is extracellularly produced, it can be purified by ultrafiltration, precipitation, and chromatography, whereas if it is intracellularly produced, it can be purified by precipitation and chromatography after cell lysis (Jozala et al., 2016).

The final goal of biomanufacturing is to obtain a safe and high-quality biopharmaceutical with high purity, high yield, low-cost, and within the shortest time (Jozala et al., 2016). Downstream strategies are currently dominated by liquid chromatography due to its high selectivity and high resolution (Azevedo et al., 2009; Fields et al., 2016; Jozala et al., 2016; Castro et al., 2019). Chromatographic techniques

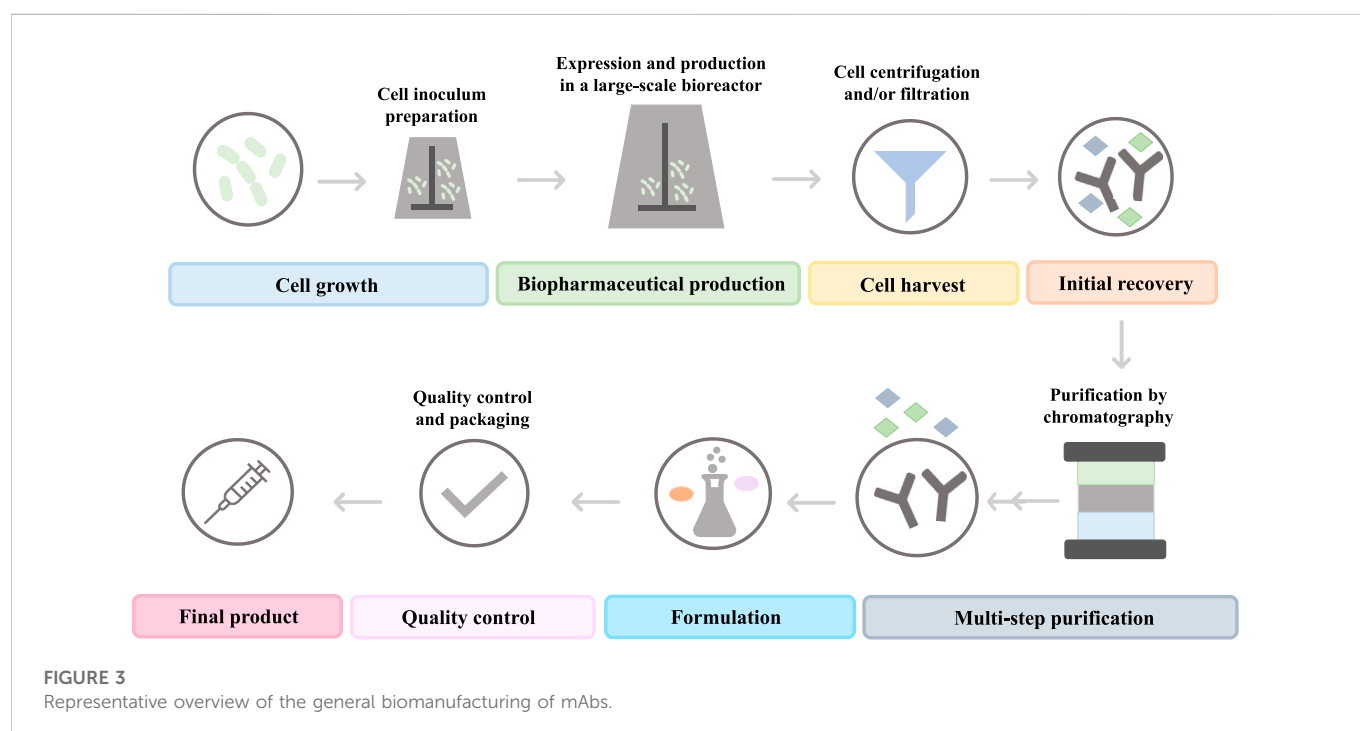
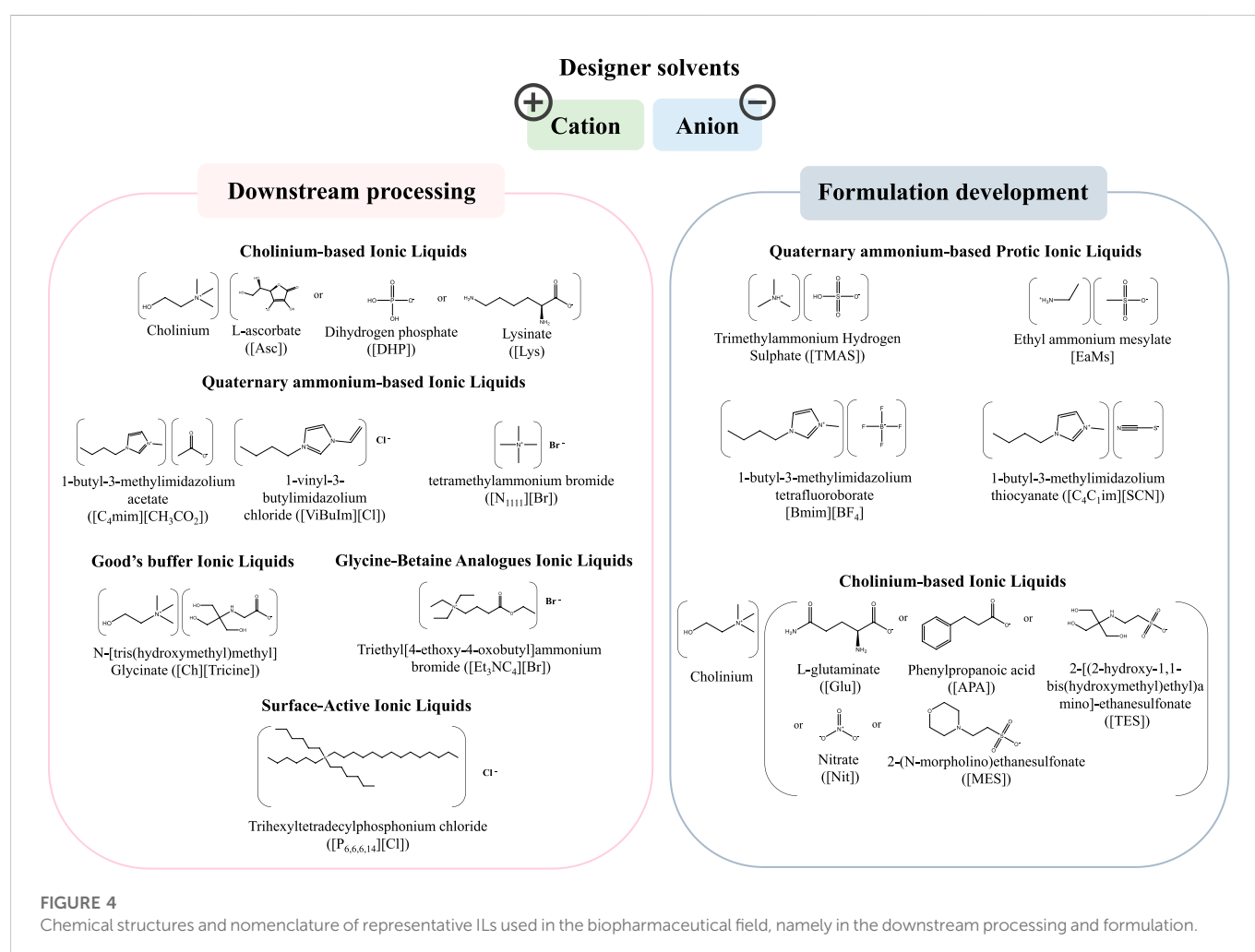


**FIGURE 3**  
Representative overview of the general biomanufacturing of mAbs.

include affinity chromatography, which is based on the selective molecular recognition between an affinity ligand and the target molecule; reverse-phase and hydrophobic interaction chromatography, which separate molecules according to their hydrophobicity; size-exclusion and ion-exchange chromatography, in which the separation is achieved according to the molecular size and charge, respectively; and mixed-mode chromatography, which is a combination of the previously mentioned approaches (Saraswat et al., 2013; Hanke and Ottens, 2014; Jozala et al., 2016; Tavares et al., 2019). For example, the purification of mAbs generally requires a sequence of three chromatographic steps (Shukla et al., 2007; Azevedo et al., 2009). The mAbs capture step employs Protein A affinity chromatography, a technique based on the specific interaction between the mAbs Fc region and the Protein A ligand—a recombinant protein derived from *Staphylococcus aureus*—that is immobilized in a resin support (Shukla et al., 2007). Afterwards, two more chromatographic steps are required to polish the final product by removing impurities, such as aggregates of high molecular mass, host cell proteins, clipped species of low molecular mass, DNA, and leached Protein A.

Despite the high selectivity, high resolution and high purity of the product, chromatography also exhibits some limitations, namely low associated throughputs, low proteolytic and chemical stabilities when biological ligands are used, high scale pressure drops, time-consuming nature, and high costs, which hinder the production of biopharmaceuticals at low cost (Rosa

et al., 2010; Jozala et al., 2016; Castro et al., 2019; Castro et al., 2020). To surpass these limitations, research has focused on the development of chromatographic ligands with enhanced selectivity, robustness, and reproducibility (Martins et al., 2014), as well as on non-chromatographic strategies, such as affinity precipitation (Hoffman et al., 2001; Roque et al., 2007), preparative electrophoresis (Thomas et al., 2002), high-performance tangential flow filtration (Lazarova et al., 2001), membrane filtration (Castilho et al., 2002), precipitation (dos Santos et al., 2017), aqueous biphasic systems (Zijlstra et al., 1998; Azevedo et al., 2009), non-chromatographic magnetic separation (Karl and Schwa, 2005), high-gradient magnetic separation (Akgo et al., 2004; Gomes et al., 2018), and crystallization (dos Santos et al., 2017). Nevertheless, the progress made in this field is still far from that required, and downstream processing continues to account for the most expensive part of biomanufacturing (Azevedo et al., 2009). More than 80% of the total production costs of a biopharmaceutical are allocated to downstream processing, in which approximately 20% results from the recovery, isolation, and polishing steps, and more than 70% from the purification step (Azevedo et al., 2009). After the final polishing stage, filling and finishing steps are applied, in which the biopharmaceutical is placed in the final formulation (Azevedo et al., 2009; Rosa et al., 2010; Conner et al., 2014; Jozala et al., 2016; Castro et al., 2021). Conventional approaches to enhance and/or





maintain the stability of therapeutic biomolecules are focused on the addition of several compounds, acting as excipients, such as sugars, salts, amino acids, surfactants and polymers (Frokjaer and Otzen, 2005; Kerwin, 2008; Qian et al., 2008; Wang, 2015; Castro et al., 2021; Lin et al., 2021). These allow to prevent their denaturation and increase their bioactivity and shelf-life.

## Ionic-liquid-based approaches in the biopharmaceuticals field

The outstanding properties of ILs in the biomedicine field have spurred a high interest within the scientific community (Kianfar and Mafi, 2020; Curreri et al., 2021; Bernardo et al., 2022). ILs are organic salts displaying a set of relevant properties, e.g., tailored polarity, non-flammability and non-volatility at ambient conditions, low-vapor or negligible pressure, high thermal and chemical stabilities and high solvation ability, making them attractive for a variety of applications (Castro et al., 2019; Kianfar and Mafi, 2020; Jadhav et al., 2021). ILs are considered “designer solvents” since their cations and anions can be carefully selected to provide a variety of compounds with unique physicochemical properties and biological activity (Castro et al., 2019; Curreri et al., 2021; Jadhav et al., 2021; Bernardo et al., 2022). In the biomedical and pharmaceuticals fields, ILs were mostly investigated to develop anti-cancer drugs (Yen and Chu, 2004), antimicrobial compounds (Pernak et al., 2003), and controlled drug release systems (Jaitely et al., 2008), to improve the catalytic efficiency of enzymes and to increase the thermal stability of proteins (Erbeldinger et al., 2000; Baker et al., 2004; Kumar et al., 2017; Schindl et al., 2019), and to act as excipients in synthetic drugs formulation to improve the solubility, permeability, activity, bioavailability, and stability (Moniruzzaman et al., 2010; Pedro et al., 2020; Lin et al., 2021). The application of ILs in the pharmaceutical field regarding their use with small molecules and synthetic drugs has been comprehensively reviewed elsewhere (Pedro et al., 2020) and is out of the scope of the current review. Here, we will focus on the application of ILs in the production of biopharmaceuticals, a field that is still in its infancy, but evolving at a high pace (Lin et al., 2021). The chemical structures and nomenclature of representative ILs used in the downstream processing and formulation of biopharmaceuticals, and addressed in the works herein reviewed, are compiled in Figure 4.

## Ionic liquids in the downstream processing of biopharmaceuticals

Several IL-based approaches, namely liquid-liquid and solid-liquid extractions, have been proposed for the efficient recovery and purification of a myriad of compounds, such as therapeutic enzymes (Santos et al., 2018), antibodies (Taha et al., 2015; Ferreira et al., 2016; Mondal et al., 2016; Ramalho et al., 2018; Capela et al., 2019; Vicente et al., 2022), nucleic acids (Pereira et al., 2021), viruses (Marchel et al., 2019), and interferons (Castro et al., 2020). Liquid-liquid extraction based on ILs has been proposed for the recovery and purification of a variety of biopharmaceuticals, most of them relying on the use of IL-based Aqueous Biphasic Systems (IL-ABS). In ABS the IL can either act as a phase-forming component (Taha et al., 2015; Mondal et al., 2016; Ramalho et al., 2018; Song et al., 2018; Xu et al., 2018; Capela et al., 2019; Magri et al., 2019; Quental et al., 2019;

Vicente et al., 2019; Vicente et al., 2022) or as an adjuvant (Ferreira et al., 2016; Santos et al., 2018; Marchel et al., 2019; Castro et al., 2020). In addition to IL-ABS, other liquid-liquid strategies have been reported, namely Thermoresponsive Aqueous Micellar Two-Phase Systems (AMTPS) and Three-Phase Partitioning (TPP) systems. Representative works regarding the recovery and purification of biopharmaceuticals using liquid-liquid approaches based on ILs are summarized in Table 1. ILs abbreviations are provided in the footnote of Table 1.

ABS comprise two non-miscible aqueous-rich phases, formed by polymer-polymer, polymer-salt, or salt-salt combinations (Carapito, 2019; Castro et al., 2019; Bento et al., 2021). Above particular concentrations of the phase-forming components, the systems separate into two coexisting phases, each of them enriched in one component (Carapito, 2019; Castro et al., 2020). ABS display high performance, high biocompatibility, low energy consumption, allow continuous operation, and are of low-cost. By including ILs as phase-forming component/adjuvant, ABS may be designed to display different polarities and affinities to target compounds (Carapito, 2019). In addition, being aqueous systems, ABS maintain the stability of biological compounds during downstream processing. A schematic representation of a liquid-liquid extraction process using IL-ABS for the recovery and purification of biopharmaceuticals is given in Figure 5.

Mondal et al. (2016) investigated polymer-salt-based ABS formed by a combination of polypropylene glycol (PPG 400), phosphate-buffered saline (PBS) and several biobased cholinium-containing ILs, for the recovery and purification of immunoglobulin G (IgG) from rabbit serum. Systems comprising [Ch][Pyr], [Ch][Gly], [Ch][D-Gal], [Ch][Qui], and [Ch][Asc] ILs were able to form ABS and to completely extract IgG to the IL-rich phase in one-step. The [Ch][Asc]-based ABS was the most promising system, allowing a 58% enhancement in the IgG purity compared with its purity in rabbit serum samples. This study pioneeringly demonstrated the potential of ILs as phase-forming components of ABS to extract and purify antibodies. Similarly, Ramalho et al. (2018) prepared ABS formed by PPG 400 and several cholinium-based ILs, which allowed to extract commercial IgG to the IL-rich phase with extraction efficiencies ranging from 93 to 100% and recovery yields ranging from 20 to 100%. ABS formed by [Ch][Lac] and [Ch][DHP] ILs presented extraction efficiencies of 100% and allowed to purify IgG to the IL-rich phase, in one step, with 47 and 49% purity, respectively. A subsequent ultrafiltration step further increased the IgG purity up to 66% (Ramalho et al., 2018) - the highest value obtained so far for this type of system. Ferreira et al. (2016) used polymer-salt-based ABS composed of polyethylene glycol 400 g mol<sup>-1</sup> (PEG 400), a buffered salt and several imidazolium-, quaternary ammonium-, and phosphonium-based ILs acting as adjuvants, for the extraction and purification of IgG from rabbit serum. ABS without ILs were able to recover IgG with 19% purity and 42% of recovery yield. The IL addition to the ABS allowed 100% extraction of IgG to the polymer-rich phase in one step, being the [C<sub>4</sub>mim][CH<sub>3</sub>CO<sub>2</sub>]-based ABS the best system with a recovery yield of 46% and a purity enhancement of 37% when compared to the ABS without IL. This study showed that low amounts of ILs (5 wt%) can be used in the preparation of ABS for antibody purification.

Immunoglobulin Y (IgY) antibodies, found in chicken's egg yolk, are an important class of antibodies for therapeutic

**TABLE 1 Representative works regarding the recovery and purification of biopharmaceuticals using liquid-liquid approaches based on ILs.**

Biopharmaceutical	Biological source	Recovery/Purification system	IL	Role of IL	System composition	Recovery yield and purity	References
Immunoglobulin G (IgG) antibody	Rabbit serum	Aqueous biphasic systems (ABS)	Cholinium-based ILs, comprising [Ch][Gly], [Ch][Pyr], [Ch][Asc], [Ch][D-Gal] and [Ch][Qui]	Phase-forming component	30 wt% PPG 400 + 25 wt% IL + 45 wt% IgG	Rabbit serum/pure IgG: 85%/100% recovery yield +~58% purity enhancement	Mondal et al. (2016)
IgG	Rabbit serum	ABS	Cholinium-based ILs, comprising [Ch][Lac], [Ch][Gly], [Ch][Prop], [Ch][But], [Ch]Cl, [Ch][Bit], [Ch][DHCit], [Ch][DHP] and [Ch][Ac]	Phase-forming component	45 wt% PPG 400, 30 wt% PBS +25 wt% IL	Rabbit serum IgG: >80% recovery yield/49% purity	Ramvalho et al. (2018)
IgG	Rabbit serum	ABS	Imidazolium, ammonium and phosphonium-based ILs comprising [C <sub>4</sub> mim][N(CN) <sub>2</sub> ], [C <sub>4</sub> mim][CH <sub>3</sub> CO <sub>2</sub> ], [C <sub>4</sub> mim]Cl, [C <sub>4</sub> mim]Br [N <sub>1111</sub> ][Br] and [N <sub>4444</sub> ][Br]	Adjuvant	25 wt% PEG 400 + 25 wt% C <sub>6</sub> H <sub>5</sub> K <sub>3</sub> O <sub>7</sub> /C <sub>6</sub> H <sub>6</sub> O <sub>2</sub> -buffer +5 wt% IL + 45 wt% rabbit serum	42–47% recovery yield/21–26% purity	Ferreira et al. (2016)
Avian immunoglobulin Y (IgY) antibody	Water-Soluble Protein Fraction (WSPF) from chicken egg yolk	ABS	Good's buffer ILs (GB-ILs) comprising [Ch][MES], [Ch][TES], [Ch][Tricine], [Ch][CHES] and [Ch][HEPES]	Phase-forming component	50 wt% PPG 400 +7–10 wt% IL + 40–43 wt% WSPF	-	Taha et al. (2015)
Anti-Interleukin-8 (Anti-IL-8) monoclonal antibodies (mAbs)	Chinese Hamster Ovary (CHO) cell culture supernatants	ABS, Three-Phase Partitioning (TPP) systems and hybrid processes combining ultrafiltration	Glycine-Betaine Analogues ILs (AGB-ILs), comprising [Et <sub>3</sub> NC <sub>4</sub> ][Br], [Pr <sub>3</sub> NC <sub>4</sub> ][Br], [Bu <sub>3</sub> NC <sub>4</sub> ][Br] and [MepyrNC <sub>4</sub> ][Br]	Phase-forming component	15 wt% K <sub>2</sub> HPO <sub>4</sub> /KH <sub>2</sub> PO <sub>4</sub> + 25,30, and 40 wt% IL + 37.5 wt% CHO cell culture supernatant	ILs-ABS: 100% recovery yield/1.6 purification factor ILs-TPP: 41% recovery yield/2.7 purification factor (60.9% purity)	Capela et al. (2019)
Recombinant interferon alpha-2b (IFNα-2b)	<i>E. coli</i> lysates	ABS	[C <sub>2</sub> mim]Cl, [C <sub>4</sub> mim]Cl, [C <sub>6</sub> mim]Cl, [C <sub>4</sub> mim]Br, [C <sub>4</sub> mim][CH <sub>3</sub> COO], [N <sub>4444</sub> ]Cl and [Ch]Cl	Adjuvant	15 wt% phosphate salt +30 wt% PEG600 + 30 wt% PPG400 + 5 wt% IL	6.77 purification factor	Castro et al. (2020)
L-asparaginase	<i>E. coli</i> BL21 (DE3)	ABS	Imidazolium-based ILs, comprising [C <sub>4</sub> mim]Cl, [C <sub>4</sub> mim][DMP], [C <sub>4</sub> mim][CH <sub>3</sub> SO <sub>3</sub> ] and [C <sub>4</sub> mim][CF <sub>3</sub> SO <sub>3</sub> ]	Adjuvant	15 wt% PEG 6000 + 15 wt% citrate buffer +5 wt% IL	87.9% recovery yield/20.09 purification factor	Santos et al. (2018)
L-asparaginase	Aqueous solution of L-Asparaginase	ABS	[Ch]Cl and [Ch][Ac]	Phase-forming component	50 wt% PEG 600 + 30 wt% IL, 30 wt% PPG 400 + 16 wt% IL +	—	Magri et al. (2019)
Green fluorescent protein	BL21 (DE3) pLysS	ABS	DIMCARB	Phase-forming component	42 wt% PPG 1000 + 4.4 wt% DIMCARB +10% wt feedstock pH 8	98.8% recovery yield	Song et al. (2018)
enveloped Hepatitis C virus pseudoparticles (HCVpp)	HEK 293 (ATCC CRL-1573) cell supernatants	ABS	Imidazolium and bromide-based ILs, comprising [C <sub>4</sub> mim]Cl, [C <sub>4</sub> mim][CH <sub>3</sub> O <sub>2</sub> ] and [N <sub>4444</sub> ][Br]	Adjuvant	PEG 400 + citrate buffer +5 wt% IL	40–70% purity	Marchel et al. (2019)

(Continued on following page)

**TABLE 1 (Continued) Representative works regarding the recovery and purification of biopharmaceuticals using liquid-liquid approaches based on ILs.**

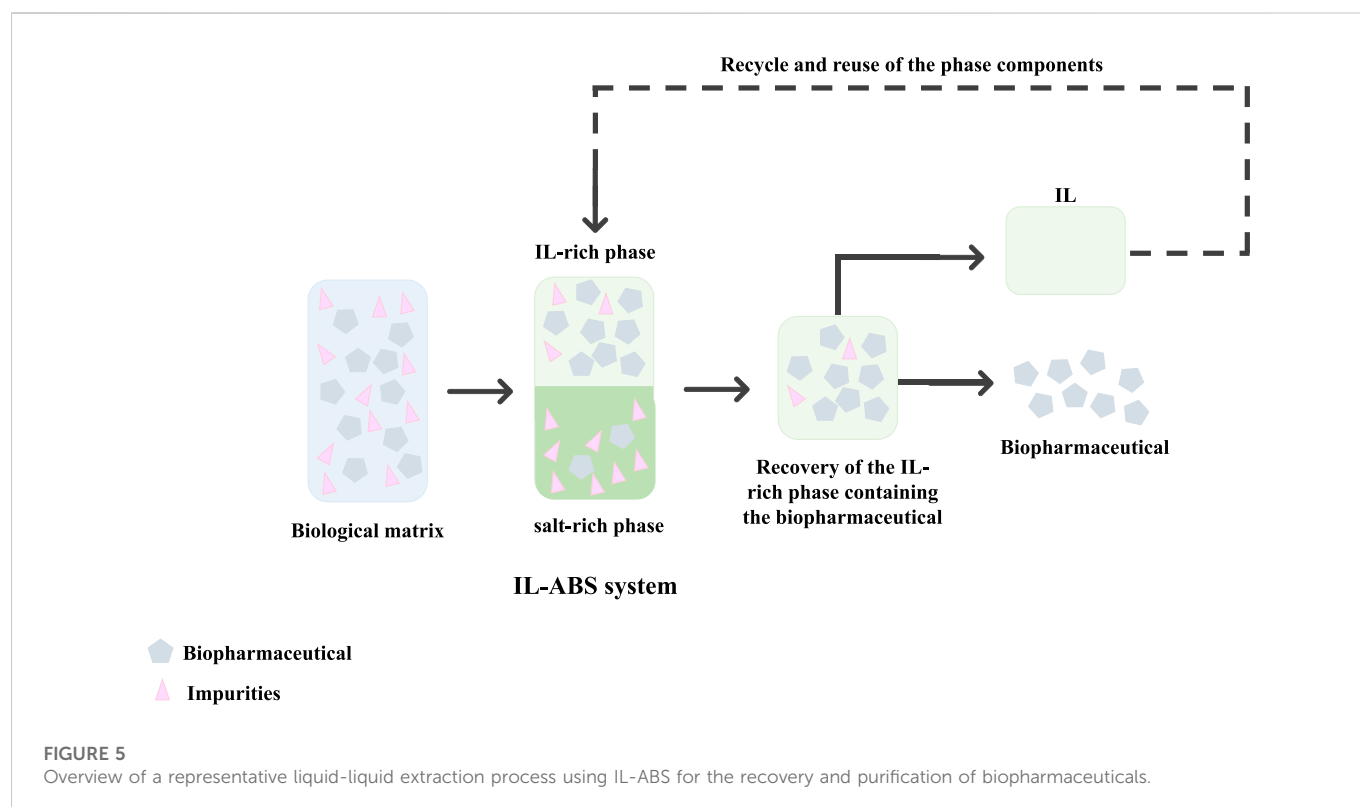
Biopharmaceutical	Biological source	Recovery/Purification system	IL	Role of IL	System composition	Recovery yield and purity	References
Ribonucleic acid (RNA)	Bacterial lysate	ABS	Amino-acid-based ILs (AA-ILs), comprising [Ch][Lys], [Ch][Arg], [Ch][Glu] and [Ch][Asp]	Phase-forming component	20 wt% PPG 400 + 20 wt% IL + 60 wt % RNA	—	Quental et al. (2019)
Salmon DNA	Standard aqueous solution containing cytochrome c	ABS	Betaine-based ILs, [Be][For], [Be][Ac], [Be][Prop], [Be][Buty]	Phase-forming component	[TBAB][PPG 400] + [Be][For] + 2 mg DNA + 2 mg Cyt c	—	Xu et al. (2018)
IgG and Human Serum Albumin (HSA)	Human expired plasma	AMTPS	Surface-Active ILs (SAILs), comprising [C <sub>14</sub> mim]Cl and [P <sub>4,4,4,14</sub> ]Cl	Co-surfactant	15.2 wt% Tergitol 15-S-7 + 0.3 wt% SAIL + 10 wt% plasma	1.14-fold purification of IgG and 1.36-fold purification for HSA	Vicente et al. (2019)
IgY	Water-Soluble Protein Fraction (WSPF) from chicken egg yolk	Thermoresponsive AMTPS	Surface-Active ILs (SAILs), comprising [C <sub>10</sub> mim]Cl, [C <sub>12</sub> mim]Cl, [C <sub>14</sub> mim]Cl, [C <sub>16</sub> mim]Cl, [C <sub>18</sub> mim]Cl, [P <sub>6,6,6,14</sub> ]Cl, [P <sub>6,6,6,14</sub> ]Br, [P <sub>6,6,6,14</sub> ][Dec] and [P <sub>6,6,6,14</sub> ][TMPP]	Co-surfactant	20 wt% Triton X-114 + 0.3 or 0.5 wt % SAIL + 25 wt% WSPF + McIlvaine buffer pH 6.0	69% purity	Vicente et al. (2022)
Hexahistidine-tagged (His-tagged) proteins	<i>E. coli</i> crude BL21 (DE3)	Adsorption	Triazacyclononane-based IL namely tacn-attached 6,7-dihydro-5H-pyrrolo [1,2-a] imidazolium and [Bmim][NTf <sub>2</sub> ]	Chelating ligand	—	—	Ren et al. (2015)

Abbreviations: [Be][For], betaine formate; [Be][Ac], betaine acetate; [Be][Prop], betaine propionate; [Be][Buty], betaine butyrate; [C<sub>2</sub>mim][C<sub>2</sub>SO<sub>4</sub>], 1-ethyl-3-methylimidazolium ethylsulfate; [C<sub>2</sub>mim][[(C<sub>2</sub>H<sub>5</sub>)<sub>2</sub>PO<sub>4</sub>]], 1-ethyl-3-methylimidazolium diethyl phosphate; [C<sub>2</sub>mim][HSO<sub>4</sub>], 1-ethyl-3-methylimidazolium hydrogen sulphate; [C<sub>6</sub>mim]Cl, 1-hexyl-3-methylimidazolium chloride; [P<sub>4,4,4,14</sub>]Cl, tributyltetradecylphosphonium chloride; [C<sub>10</sub>mim]Cl, 1-decyl-3-methylimidazolium chloride; [C<sub>12</sub>mim]Cl, 1-dodecyl-3-methylimidazolium chloride; [C<sub>14</sub>mim]Cl, 1-tetradecyl-3-methylimidazolium chloride; [C<sub>16</sub>mim]Cl, 1-hexadecyl-3-methylimidazolium chloride; [C<sub>18</sub>mim]Cl, 1-octadecyl-3-methylimidazolium chloride; [P<sub>6,6,6,14</sub>]Cl, trihexyltetradecylphosphonium chloride; [P<sub>6,6,6,14</sub>]Br, trihexyltetradecylphosphonium bromide; [P<sub>6,6,6,14</sub>][Dec], trihexyltetradecylphosphonium decanoate; [P<sub>6,6,6,14</sub>][TMPP], trihexyltetradecylphosphonium bis (2,4,4-trimethyl (pentyl)phosphinate); [C<sub>4</sub>mim][N(CN)<sub>2</sub>], 1-butyl-3-methylimidazolium dicyanamide; [C<sub>4</sub>mim][CH<sub>3</sub>CO<sub>2</sub>], 1-butyl-3-methylimidazolium acetate; [C<sub>4</sub>mim]Cl, 1-butyl-3-methylimidazolium chloride; [C<sub>4</sub>mim]Br, 1-ethyl-3-methylimidazolium bromide; [N<sub>1111</sub>]Br, tetramethylammonium bromide; [N<sub>4444</sub>]Br, tetrabutylammonium bromide; [Ch][Gly], cholinium glycolate; [Ch][Pyr], cholinium pyruvate; [Ch][Asc], cholinium-L-ascorbate; [Ch][D-Gal], cholinium-D-galacturonate; [Ch][Qui], cholinium-D-(-)-quinate; [Ch][Lac], cholinium lactate; [Ch][Prop], cholinium propanoate; [Ch][But], cholinium butanoate; [Ch][Abt], cholinium abietate; [Ch][C<sub>3</sub>C], cholinium coumarine-3-carboxylate; [Ch][Gen], cholinium gentisate; [Ch][MES], cholinium 2-(N-morpholino) ethanesulfonate; [Ch][TES], cholinium 2-[(2-hydroxy-1,1-bis(hydroxy methyl)ethyl)amino]ethane sulfonate; [Ch][Tricine], cholinium N-[tris(hydroxymethyl)methyl]glycinate; [Ch][CHES], cholinium 2-cyclohexylamino)ethanesulfonate; [Ch][HEPES], cholinium 2-[4-(2-hydroxyethyl)piperazin-1-yl]ethanesulfonate; [Ch]Cl, cholinium chloride; [Ch][Bit], cholinium bitartrate; [Ch][DHCit], cholinium dihydrogen citrate; [Ch][DHP], cholinium dihydrogen phosphate; [Ch][Ac], cholinium acetate; DIMCARB, N,N-dimethylammonium N',N'-dimethylcarbamate; [C<sub>4</sub>mim][CH<sub>3</sub>O<sub>2</sub>], 1-butyl-3-methylimidazolium acetate; [Ch][Lys], cholinium L-lysinate; [Ch][Arg], cholinium L-argininate; [Ch][Glu], cholinium L-glutamate; [Ch][Asp], cholinium DL-aspartate; [TBAB], tetrabutylammonium bromide; [Et<sub>3</sub>NC<sub>4</sub>]Br, triethyl[4-ethoxy-4-oxobutyl]ammonium bromide; [Pr<sub>3</sub>NC<sub>4</sub>]Br, tri(n-propyl)[4-ethoxy-4-oxobutyl]ammonium bromide; [Bu<sub>3</sub>NC<sub>4</sub>]Br, tri(n-butyl)[4-ethoxy-4-oxobutyl]ammonium bromide; [MepyrNC<sub>4</sub>]Br, N-(1-methylpyrrolidyl-4-ethoxy-4-oxobutyl)ammonium bromide; [C<sub>2</sub>mim]Cl, 1-Ethyl-3-methylimidazolium chloride; [C<sub>4</sub>mim]Cl, 1-Butyl-3-methylimidazolium chloride; [C<sub>6</sub>mim]Cl, 1-Hexyl-3-methylimidazolium chloride; [C<sub>4</sub>mim]Br, 1-Butyl-3-methylimidazolium bromide; [C<sub>4</sub>mim][CH<sub>3</sub>COO], 1-butyl-3-methylimidazolium acetate; [C<sub>4</sub>mim][CH<sub>3</sub>SO<sub>3</sub>], 1-butyl-3-methylimidazolium methanesulfonate; [C<sub>4</sub>mim][CF<sub>3</sub>SO<sub>3</sub>], 1-butyl-3-methylimidazolium triflate, and [Bmim][NTf<sub>2</sub>], 1-butyl-3-methylimidazolium bis(trifluoromethylsulfonyl)imide.

applications; however, since they derive from a complex matrix, a sequence of several steps for their purification is generally required, and mostly resorting to chromatography (Vicente et al., 2022). Taha et al. (2015) prepared polymer-salt-based ABS formed by PPG 400 and several Good's buffer ILs (GB-ILs) to recover and purify IgY from the Water-Soluble Protein Fraction (WSPF) of egg yolk (Taha et al., 2015). It was shown that GB-ILs present a high ability to form ABS with PPG 400, in which IgY extraction efficiencies between 79 and 94% were obtained (Taha et al., 2015). Furthermore, ABS containing [Ch][Tricine] and [Ch][HEPES] GB-ILs led to the highest IgY extraction efficiencies with values above 90% achieved in a single step (Taha et al., 2015). Herein, the self-buffering nature of GB-ILs allowed to

keep the pH within the physiological range without the addition of external buffers, contributing to maintain the stability of biopharmaceuticals.

The previously described studies investigated the use of ABS to purify polyclonal antibodies. However, mAbs represent the largest fraction of the biopharmaceuticals market. They are currently used in immunization, vaccination, and treatment of life-threatening diseases; nevertheless, their recovery and purification from their complex biological sources, i.e., cell culture media, also require a multi-step and expensive approach (Capela et al., 2019). To surpass these limitations and decrease all the associated burdens, Capela et al. (2019) used ABS based on glycine-betaine analogue ILs (AGB-ILs) to isolate anti-interleukin-8 (anti-IL-8) mAbs from Chinese Hamster



Ovary (CHO) cell culture supernatants. Together with ABS, other strategies were also assessed, *i.e.*, TPP systems and hybrid strategies of ABS and TPP systems with ultrafiltration. ABS containing AGB-ILs allowed the recovery of the target biomolecule to the IL-rich phase with an overall yield of 100% and a purification factor of more than 1.6 (Capela et al., 2019). When the IL-based TPP system was applied, anti-IL-8 mAbs were recovered in the ABS interface with a lower yield (41%) but with an increased purification factor of 2.7 (60.9% purity) (Capela et al., 2019). Competitive enzyme-linked immunosorbent assays (ELISAs) were performed for the IL-rich phase and the precipitate after the last ultrafiltration step, as well as for the CHO cell culture for comparison purposes. It was shown that mAbs were able to maintain their biological activity after all purification and recovery stages. The recyclability of ILs was finally evaluated, showing that the separation performance was not significantly changed during three separation cycles.

Interferon alpha-2b (IFN $\alpha$ -2b) is an important therapeutic product in the treatment of chronic Hepatitis C and hairy cell leukaemia; however, its downstream processing is hindered by the high cost of conventional purification strategies (Castro et al., 2020). Castro et al. (2020) used ABS composed of two polymers, namely PEG of 600 g mol<sup>-1</sup> (PEG 600) and PPG 400, and several ILs acting as adjuvants, for the purification of IFN $\alpha$ -2b from *E. coli* lysates. The addition of ILs to the ABS enhanced the IFN $\alpha$ -2b purification factor from 2.28 to 6.77, in which the biomolecule preferentially migrated to the PEG-rich phase (also the phase enriched in the IL) (Castro et al., 2020). Furthermore, ILs containing aromatic cations combined with high hydrogen basicity anions boosted the purity level of the protein, while maintaining its secondary structure. The IFN $\alpha$ -2b recovered in the PEG-rich phase was shown to be immunologically active.

L-asparaginase, also known as L-asparagine amidohydrolase enzyme, is a biopharmaceutical mostly produced by *E. coli* with therapeutic activity against acute lymphoblastic leukaemia (ALL) in humans and canine lymphosarcoma (Santos et al., 2018). Aiming to address the purification of L-asparaginase from crude enzyme extract, Santos et al. (2018) used ABS composed of PEG, citrate buffer, and several imidazolium-based ILs acting as adjuvants, combined with cell membrane permeabilization. The ABS comprising the [C<sub>4</sub>mim][CH<sub>3</sub>SO<sub>3</sub>] IL was identified as the best system for the enzyme recovery to the PEG-rich phase, in which a yield of approximately 87.9% and a purity factor of 20.09 were obtained (Santos et al., 2018). Moreover, the best results were achieved when ABS comprising ILs were combined with a previous enzyme purification step through ammonium sulphate precipitation, allowing to obtain a higher purification factor (Santos et al., 2018). In a different study, Magri et al. (2019) studied the partition of L-asparaginase using a series of polymer/salt-based ABS including, among others, PEGs of different molecular weights (PEG 600, polyethylene glycol of 2,000 g mol<sup>-1</sup> (PEG 2000)) and PPG 400, to understand the mechanisms behind the separation of the enzyme. The following ABS were studied: PEG 600 + phosphate buffer, PEG 2000 + phosphate buffer, PEG 600 + citrate buffer, PEG 600 + sodium sulphate, PEG 600 + [Ch][Cl], PEG 2000 + citrate buffer, PEG 2000 + sodium sulphate, PPG 400 + [Ch][Cl], and PPG 400 + [Ch][Ac]. The obtained results demonstrated that by changing the relative hydrophobicity of the polymers, the systems induce the inversion of the enzyme partitioning, being preferentially partitioned to the polymer-rich phase in ABS composed of IL-PEG 600 since it is constituted by the polymer that is more hydrophilic, and to the IL-rich phase using PPG 400-based ABS, formed by the polymer that is more hydrophobic. PEG 600-IL-based ABS lead to a decrease in its biocatalytic activity, whereas systems comprising PPG



400 maintained the relative activity of L-asparaginase around 100%. Then, L-asparaginase purification from the fermentation broth was conducted and the purification performance of the systems in study was optimized. It was found that the ABS comprising PEG 2000 and phosphate buffer was the most effective with a purification factor of *ca.* 2.4, while preserving the activity of L-asparaginase.

Green fluorescent protein (GFP) is a protein exhibiting bright green fluorescence when exposed to light in the blue to ultraviolet range. Therefore, it can be used as a powerful biomarker and visualization tool in diverse cellular processes. Song et al. (2018) investigated the recovery of GFP from *E. coli* using ABS constituted by PPG 1000 and the *N,N*-dimethylammonium *N',N'*-dimethylcarbamate (DIMCARB) IL. This IL may represent a more environmentally friendly option, since it presents a simpler and cheaper synthesis route, as well as enhanced biodegradability, and biocompatibility. Furthermore, this CO<sub>2</sub>-based alkyl carbamate IL can be distilled at a relatively low temperature under vacuum, allowing a simple recovery of the IL for subsequent extraction processes. The authors found that GFP was preferentially partitioned to the IL-rich phase in ABS composed of 42 wt% of PPG 1000 and 4.4 wt% of DIMCARB, with a GFP selectivity of 1.2 and 98.8% of yield. The system could be scaled up 50 times without compromising the purification performance, and DIMCARB was successfully recycled and reused in three consecutive GFP purification processes. The process did not affect the GFP stability. Also, Soares et al. (2021) investigated the continuous purification of the variant enhanced GFP (EGFP) through a fast centrifugal partition chromatography (FCPC) using ABS formed by polyethylene glycol (PEG 8000), sodium polyacrylate (NaPA 8000), and sodium sulphate (Na<sub>2</sub>SO<sub>4</sub>) acting as an electrolyte. The most effective ABS, *i.e.*, the one formed by 15 wt% PEG 8000 with 4.5 wt% NaPA 8,000 and 2.5 wt% Na<sub>2</sub>SO<sub>4</sub> was selected and applied for FCPC. This combination of FCPC with ABS led to an EGFP recovery yield of 82.3% and a purification of 89.93%.

Virus-like particles (VLPs) are also considered promising biopharmaceuticals, particularly in VLP-based vaccination and cancer therapy; however, conventional VLPs separation techniques (gradient ultracentrifugation, ultrafiltration, precipitation, size-exclusion chromatography) are still challenged by the low yield, low selectivity, and difficulties in scale-up, limiting their widespread application (Marchel et al., 2019). To overcome these drawbacks, Marchel et al. (2019) performed a high-throughput screening on a liquid handling station to select the most appropriate ILs to be used as adjuvants in polymer-salt-based ABS, followed by the application of the prepared systems for the extraction and purification of enveloped Hepatitis C virus pseudoparticles (HCVpp), a VLP able to infect liver cells resulting in liver disease and cirrhosis, and ultimately in hepatic failure and death (Marchel et al., 2019). ABS composed of PEG 400, citrate buffer, and bromide-based ILs acting as adjuvants, allowed 100% extraction of the target VLPs to the PEG-rich phase (Marchel et al., 2019). Moreover, when no IL was present in the ABS, a purity degree of 53% was obtained, contrasting with the purity range of 40–70% obtained when ILs were used as adjuvants (Marchel et al., 2019). This study demonstrated that it is possible to increase the purity of viral particles by using appropriate ILs as adjuvants able to modulate the properties of the ABS, thus requiring lower amounts of ILs.

Nucleic acids, including RNAs, play key roles in the diagnosis and treatment of diseases. Current methods available for their isolation include phenol/chloroform-based extraction and Solid-Phase

Extraction (SPE), whereas for their purification chromatographic techniques (e.g., gel filtration, reverse-phase, ion-pairing, and ion-exchange chromatography) and denaturing polyacrylamide gel electrophoresis are usually applied (Ferreira et al., 2000; Quental et al., 2019; Neves et al., 2020; Pereira et al., 2021). In addition to resorting to hazardous organic solvents, these conventional strategies are time-consuming, laborious, and lead to low recovery yields (Neves et al., 2020). With this challenge in mind, Quental et al. (2019) used ABS formed by PPG- 400 and several cholinium-based ILs comprising anions derived from amino acids (AA-ILs) to purify ribonucleic acid (RNA) from bacterial lysate samples, while preserving its stability. These ILs were selected given the previously shown potential of columns modified with amino acids to purify nucleic acids (Pereira et al., 2014a; Pereira et al., 2014b). RNA was successfully extracted from bacterial lysate samples to the IL-rich phase without compromising its integrity and stability. Moreover, it was possible to recover RNA from the IL-rich phase through ethanol precipitation, as well as to recover and reuse the phase-forming components of the ABS in new purification steps. Xu et al. (2018) investigated ABS comprising deep eutectic solvents (DES) and betaine-based ILs to extract DNA from salmon testes. The DES used in ABS preparation were formed by different molar ratios of hydrogen bond acceptor (HBA), hydrogen bond donor (HBD) and water (HBA:HBD:H<sub>2</sub>O). The ability of these systems to extract DNA was amplified by [TBAB] [PPG 400] and by the IL [Be][For], being observed that experimental parameters such as temperature, mass of IL, mass of DES, extraction time, pH, and ionic strength have a significant effect on the DNA extraction efficiency. Under these conditions, proteins with higher isoelectric points (pI) such as cytochrome c (pI = 10) are preferentially partitioned to the DES-rich phase, thus allowing their separation from DNA, which is preferentially enriched in the IL-rich phase. Furthermore, it was shown that the structural integrity and chemical stability of DNA, before and after its extraction, were preserved.

As mentioned previously, in addition to ABS, other liquid-liquid systems such as AMTPS have also been investigated for purification purposes. AMTPS are mainly constituted by water and a surfactant, resulting in two-phase liquid systems at given temperatures and surfactant concentrations (Vicente et al., 2022). If properly designed, AMTPS exhibit higher percentages of water in comparison to traditional ABS, being therefore able to preserve the original conformation and biological activity of biomolecules. Vicente et al. (2019) investigated the potential of using AMTPS formed by non-ionic surfactants, namely Triton X-114 or Tergitol 15-S-7, to concurrently separate IgG and Human Serum Albumin (HSA) from human expired plasma. After optimization of the conditions with the previous AMTPS systems, the ability of mixed AMTPS composed of Tergitol 15-S-7 and several surface-active ionic liquids (SAILs) acting as cosurfactants to tailor the IgG and HSA partition between the two phases was investigated. In this way, the mixed AMTPS formed by Tergitol 15-S-7 and tributyltetradecylphosphonium chloride IL as the cosurfactant at pH 8.0 was able to enhance the simultaneous separation of IgG and HSA to the opposing phases of the system. A 1.14-fold purification of IgG and a 1.36-fold purification for HSA were obtained in the surfactant-poor and the surfactant-rich phases, respectively. Vicente et al. (2022) studied the potential of AMTPS formed by the non-ionic surfactant Triton X-114 and several imidazolium- and phosphonium-based SAILs acting as co-surfactants for the isolation and purification of IgY antibodies from

the WSPF of chicken's egg yolk. In this study, the AMTPS comprising the  $[C_{18}mim]Cl$  SAIL was able to enhance the recovery of IgY to the surfactant-poor phase, in a single-step, with a purity of 69%, whereas traditional AMTPS allowed a purity of 54% (Vicente et al., 2022). Moreover, it was shown that after applying three successive cycles of purification using consecutively the surfactant-poor phase of the  $[C_{14}mim]Cl$ -based AMTPS, the purity improved to up to 73% (Vicente et al., 2022).

Although the majority of works regarding the recovery and purification of biopharmaceuticals by IL-based approaches are established on liquid-liquid extraction, pertinent scientific evidence has been recently published showing the potential of solid-phase extraction (SPE) to enhance the downstream processing of therapeutic biomolecules. The field of SPE involving IL-modified materials, known as Supported Ionic Liquids (SILs), is gaining increasing traction. SILs are usually obtained by the immobilization of ILs in a suitable solid support, e.g., silica or polymeric support, combining the ILs properties with the advantages exhibited by materials (e.g., high specific surface area, and mechanical properties, among others) (Lemus et al., 2011; Pedro et al., 2019; Bento et al., 2021). This led to a modified material with adjustable properties that are coupled to an efficient immobilization on a confined environment. They can be considered “designer surfaces” since the properties of ILs are transferred to the solid surfaces, thus constituting attractive materials (Fehrmann et al., 2014). Depending on the interactions established between the IL and the support material, the immobilization of these solvents can be attained by two pathways (Tavares et al., 2019): physical confinement of the IL in the materials, i.e., physisorption, through van der Waals and dipole forces; or by 2) covalent bonding between the support and the IL, i.e., chemisorption (Tavares et al., 2019; Bento et al., 2021). SILs obtained by the first approach are generally present as a multilayer in which properties of the neat ILs are almost maintained, being mainly applied in gas capture (Giacalone and Gruttadauria, 2016; Bento et al., 2021). In contrast, by applying a chemisorption process to immobilize the IL onto the support through covalent binding, the ILs leaching from the material will be avoided (Pedro et al., 2019), being thus relevant to be applied in SPE dealing with liquid samples. Figure 6 depicts the general application of SILs in the SPE of biopharmaceuticals. SILs have been applied in SPE and chromatography to separate proteins and enzymes by taking advantage of some specific properties of ILs, in which high adsorption capacities and selectivity were achieved (Itoh and Koo,

2019). Most of these studies involve SILs in which silica or polymers were used as supports; however, it is important to highlight that this field is still in the early stages of development, with most works published dealing with the adsorption of model proteins from aqueous solutions (Bento et al., 2021). Few scientific works reported the application of SILs in the separation or recovery of biomolecules from complex biological mixtures, including nucleic acids (Neves et al., 2020; Pereira et al., 2021), bovine serum albumin (Liu et al., 2014; Song et al., 2016; Jia et al., 2019), haemoglobin (Zhao et al., 2013), cytochrome-c (Yuan et al., 2012; Liu et al., 2014), lysozyme (Yuan et al., 2012; Liu et al., 2014), and bovine haemoglobin (Liu et al., 2014; Song et al., 2016). Representative works regarding the recovery and purification of biopharmaceuticals using solid-liquid approaches based on SILs are compiled in Table 2. ILs abbreviations are provided in the footnote of Table 2.

Pereira et al. (2021) used silica modified with chloride-based ILs to isolate bacterial RNAs from *E. coli* lysates. SILs comprising  $[C_3C_{1im}]Cl$  and  $[N_{3114}]Cl$  were the best adsorbent materials for the effective and selective isolation of the target compound, with binding capacities of 16.3 and 15.6  $\mu mol\ g^{-1}$ , respectively (Pereira et al., 2021). It is important to highlight that this remarkable applicability of ILs as chromatographic ligands results from ILs diversity in terms of the chemical structures and functional groups, allowing the establishment of a variety of interactions with the target biomolecule, such as hydrophobic and electrostatic interactions, as reviewed by Bento et al. (2021) and Bernardo et al. (2022). The potential of using macroporous polymeric supports functionalized with ILs to purify nucleic acids was reported by Neves et al. (2020).  $[C_3C_{1im}]Cl$  was identified as the most promising ligand to be used in preparative liquid chromatography. The prepared support material allowed to purify, in a single-step and with high selectivity and dynamic binding capacity, different classes of nucleic acids, namely small RNAs, ribosomal RNA, and genomic DNA, from a bacterial lysate. In this work, it was pioneeringly shown that ILs behave as multimodal ligands. Moreover, these IL-based materials were regenerated using NaOH and HCl aqueous solutions and reused without compromising their separation performance.

In addition to nucleic acids, SILs have been applied in the purification of both monoclonal and polyclonal IgG antibodies. Capela et al. (2023) investigated the use of SILs, namely with the IL ligands  $[C_3C_{1im}]Cl$ ,  $[N_{3444}]Cl$ , and  $[N_{3888}]Cl$  in silica supports to capture and purify IgG from complex biological samples, i.e., human

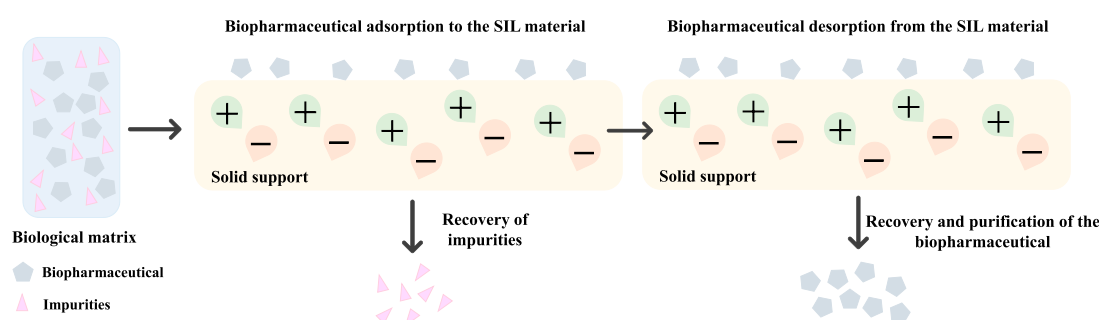


FIGURE 6

Overview of a representative SPE process using SILs for the purification of biopharmaceuticals.

**TABLE 2** Representative works regarding the recovery and purification of biopharmaceuticals using solid-liquid approaches based on SILs.

Biopharmaceutical	Source	Solid support	IL	References
Ribonucleic acid (RNA)	<i>E. coli</i> DH5a	Silica-modified materials	Chloride-based ILs comprising [C <sub>3</sub> C <sub>1</sub> im]Cl, [N <sub>3222</sub> ]Cl, [N <sub>3114</sub> ]Cl, and [N <sub>3888</sub> ]Cl	Pereira et al. (2021)
Small RNAs, ribosomal RNA, and genomic DNA	<i>E. coli</i> DH5a lysate	Commercial macroporous resin named Toyopearl AF-Epoxy-650M	[C <sub>3</sub> C <sub>1</sub> im]Cl	Neves et al. (2020)
Immunoglobulin G (IgG)	Human serum, rabbit serum and Chinese hamster ovary (CHO) cell culture supernatants	Silica-modified materials	[C <sub>3</sub> C <sub>1</sub> im]Cl, [N <sub>3444</sub> ]Cl and [N <sub>3888</sub> ]Cl	Capela et al. (2023)
Lysozyme, cytochrome-c, and haemoglobin	Standard aqueous solutions	Polyvinyl chloride (PVC) materials	Imidazolium-based ILs comprising [Nmim]Cl	Shu et al. (2010)
Lysozyme, cytochrome-c, bovine serum albumin, bovine haemoglobin and equine myoglobin	Standard aqueous solutions	Macroporous polymer material modified	Imidazolium-based ILs comprising [ViBuIm]Cl	Yuan et al. (2012)
Lysozyme, bovine serum albumin, trypsin and ovalbumin	Standard aqueous solutions	Magnetic multiwall CNTs	Dual hydroxyl functional ILs	Chen et al. (2015)
Lysozyme	Standard aqueous solutions	Graphene oxide	Guanidinium-based IL comprising [diBOHTMG]Cl	Ding et al. (2015)

Abbreviations: [C<sub>3</sub>C<sub>1</sub>im]Cl, 1-methyl-3-propylimidazolium chloride; [N<sub>3222</sub>]Cl, triethylpropylammonium chloride; [N<sub>3444</sub>]Cl, propyltributylammonium chloride; [N<sub>3114</sub>]Cl, dimethylbutylpropylammonium chloride; [N<sub>3888</sub>]Cl, trioctylpropylammonium chloride; [Nmim]Cl, N-methylimidazole; [ViBuIm]Cl, 1-vinyl-3-butylimidazolium chloride, and [diBOHTMG]Cl, hexabutylguanidinium chloride.

and rabbit sera and CHO cell culture supernatants. By using the 1-methyl-3-propylimidazolium-based supported material, IgG was directly recovered from the aqueous solution (diluted human serum) with a yield of 59% and a purity degree of 84%. On the other hand, by using the propyltrioctylammonium-based supported material, IgG was adsorbed from human serum samples onto the surface of the material with a recovery yield of 76% and a purity of 100%. The same conditions were also applied to recover IgG from other biological sources, namely rabbit serum and CHO cell culture supernatants, demonstrating the versatility and reproducibility of the used SILs. This work showed that SILs are customizable materials, in which the bind-and-elute and flowthrough-like modes can be applied just by changing the IL chemical structure.

Shu et al. (2010) prepared [Nmim]Cl/polyvinyl chloride (PVC) materials by immobilizing imidazolium cations, namely [Nmim]<sup>+</sup> moieties, onto a PVC support to extract lysozyme and cytochrome-c from prepared aqueous solutions. Cytochrome c is a small mitochondrial electron transport heme protein that has been used in several bioelectrochemical and therapeutic applications, for instance as a biosensor and anticancer drug (Santos et al., 2022), whereas lysozyme is a therapeutic compound used in gastrointestinal infections (Sava, 1996). These [Nmim]Cl/PVC materials were able to adsorb both proteins with high efficiency (97–98%). Also, Yuan et al. (2012) prepared a macroporous polymeric material that was modified with [ViBuIm]Cl, to selectively adsorb cytochrome-c and lysozyme, as well as three other proteins, including bovine serum albumin, bovine haemoglobin, and equine myoglobin. The synthesized SIL presented a strong binding capacity for the proteins, in particular for lysozyme, presenting a maximum capacity of 755.1 mg g<sup>-1</sup>.

Carbon-based materials, including carbon nanotubes (CNTs) (Chen et al., 2015) and graphene oxide (Ding et al., 2015) have also been successfully used to immobilize ILs. Chen et al. (2015) used magnetic multiwall CNTs modified with dual hydroxyl

functional ILs to extract lysozyme. The maximum adsorption capacity attained by the enzyme was 94.6 mg g<sup>-1</sup>, with a desorption ratio and recovery of 91.6% and 97.8%, respectively (Chen et al., 2015). For comparison purposes, the extraction of standard proteins and enzymes, namely with bovine serum albumin, trypsin, and ovalbumin, was additionally studied. It was shown that the extraction efficiency decreases in the following order: lysozyme (94.6 mg g<sup>-1</sup>) > trypsin (73.3 mg g<sup>-1</sup>) > ovalbumin (39.6 mg g<sup>-1</sup>) > bovine serum albumin (31.4 mg g<sup>-1</sup>). This tendency can be explained by the PI and the size of proteins. The pIs of bovine serum albumin (BSA) and ovalbumin are between 4.7 and 4.8, while lysozyme and trypsin pIs are, respectively, 10.8 and 10.5. Therefore, and considering the pH in study (Pereira et al., 2021), bovine serum albumin and ovalbumin will be predominantly negatively charged, whereas lysozyme and trypsin will be positively charged. In these conditions, the surfaces of the material (pI = 6.3) are negatively charged. Due to the electrostatic interactions between negatively charged and positively charged nanoparticles, the amount of lysozyme and trypsin that are extracted is higher than the amount of bovine serum albumin and ovalbumin extracted. Moreover, a small sized protein, i.e., lysozyme and trypsin, makes easier its extraction. The manuscript was slightly modified accordingly (Chen et al., 2015). Ding et al. (2015) used a magnetic chitosan and graphene oxide functionalized with a guanidinium IL, namely [diBOHTMG]Cl, composite to extract lysozyme and were able to obtain a value of 38.4 mg g<sup>-1</sup>. Moreover, the material was easily regenerated and reused three times without significant losses on the adsorption efficiency of the protein. As highlighted previously, also this set of works was carried out with prepared aqueous solutions containing a mixture of proteins, requiring additional studies with real matrices.

Despite the limited research that has been carried out so far on the use of IL-based SPE for the recovery and purification of biopharmaceuticals, the evidence gathered up to date indicates that SILs materials could be a promising approach for this purpose, in

which different types of interactions could be investigated and tailored.

## Ionic liquids in the formulation of biopharmaceuticals

IL-based approaches have been proposed to surpass the shortcomings still faced in the formulation development stage of biomanufacturing, namely to improve the stability of biopharmaceuticals, including insulin (Kumar and Venkatesu, 2013; Kumar and Venkatesu, 2014; Todinova et al., 2016; Banerjee et al., 2018; Guncheva et al., 2019), interleukins (Foureaux et al., 2012; Jagannath et al., 2018), cortisol (Jagannath et al., 2018), antibodies (Mazid et al., 2015; Ferreira et al., 2016; Reslan et al., 2018; Vicente et al., 2022), nucleic acids (Vijayaraghavan et al., 2010; Mukesh et al., 2013; Pedro et al., 2018), and viruses (Byrne et al., 2012; Lin et al., 2019). Most ILs investigated enhanced or maintained the biomolecules' thermal and chemical stabilities, inhibiting their aggregation, denaturation, and enzymatic degradation, while promoting long-term stability and prolonged shelf-life. A flowchart illustrating the integration between downstream processing and formulation development stages of biopharmaceuticals using IL-based approaches, accompanied by the general effects of ILs in biopharmaceutical's stability is presented in Figure 7. This integrated approach was pioneeringly proposed by Quental et al. (2019) for the extraction-preservation of RNA, discussed before.

Representative works regarding the application of ILs in the formulation of biopharmaceuticals are compiled in Table 3. ILs abbreviations are provided in the footnote of Table 3. Todinova et al. (2016) studied the effect of several imidazolium-based ILs on the stability of the monomeric form of insulin under acidic pH conditions.

It was shown that, among all studied ILs, the  $[C_4C_1im]Cl$  IL increased the transition temperature ( $T_m$ ) of insulin from approximately 75.4°C (when no IL was present) to 86.9°C at IL concentrations of 0.3 mol L<sup>-1</sup>, while preserving its helicoidal structure (Todinova et al., 2016). Moreover, no aggregation events were observed in the presence of the studied ILs, demonstrating the potentiality of these solvents for the maintenance and/or enhancement of insulin stability (Todinova et al., 2016). Kumar and Venkatesu (2014) also studied the stability of insulin in the presence of imidazolium-based ILs. It was demonstrated that  $[C_4C_1im]Br$  and  $[C_4C_1im]Cl$  were able to stabilize the native form of the protein, whereas the remaining ILs, comprising  $[SCN]^-$ ,  $[HSO_4]^-$  and  $[CH_3COO]^-$ , led to insulin denaturation (Kumar and Venkatesu, 2014). In the same line, Kumar and Venkatesu (2013) reported the use of ammonium-based protic ILs (PILs) to prevent aggregation and preserve the thermal stability of insulin. Through the application of several analytical techniques, including UV-Visible Spectroscopy, Circular Dichroism (CD), Dynamic Light Scattering (DLS) and Fluorescence Spectroscopy, it was shown that the ammonium-based IL formed by  $[TEAP]$  hindered the formation of inactive forms of the protein while maintaining its thermal stability (Kumar and Venkatesu, 2013). Also, Guncheva et al. (2019) synthesized a total of six biocompatible cholinium-based ILs containing several amino acids as anions and evaluated their effects on the secondary structure of insulin (Guncheva et al., 2019). Its  $T_m$  increased by 9.7 and 4.5°C in the presence of  $[Ch][Glu]$  and  $[Ch]_2[Asp]$  ILs, respectively (Guncheva et al., 2019). The synthesized cholinium-based ILs contributed to increasing the  $\beta$ -sheet conformations in comparison to the  $\alpha$ -helix ones and led to molecular rearrangements within the protein. Furthermore,  $[Ch][Lys]$  and  $[Ch][Arg]$  inhibited insulin aggregation and fibrillation; however, it was observed a decrease in thermal stability (Guncheva et al., 2019). Finally, the ILs cytotoxicity on murine embryonic fibroblasts (3T3) (ATCC) was assessed, showing that all ILs, applied at the

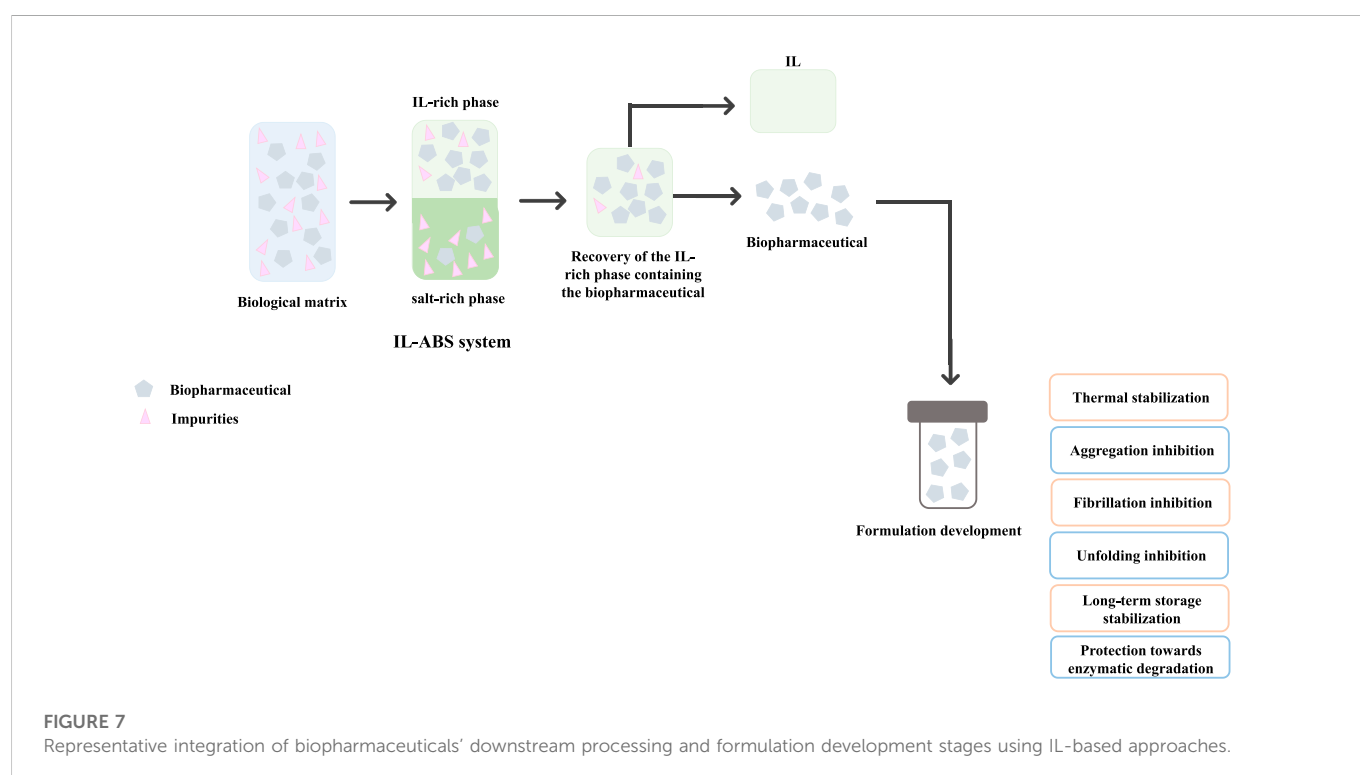




TABLE 3 Representative works regarding the use of ILs in biopharmaceutical formulations.

Biopharmaceutical	Biological source	IL	Role of IL	References
Insulin	—	Ammonium-based protic ILs (PILs) comprising [TMA], [TEAS], [TMAP], [TEAP] and [TMAA]	Thermal stabilization and inhibition of the formation of inactive forms of the protein	Kumar and Venkatesu (2013)
Insulin	Porcine pancreas	Cholinium-based ILs in the presence of amino acids, comprising [Ch][Glu] and [Ch] <sub>2</sub> [Asp]	Inhibition of aggregation and fibrillation of the protein	Guncheva et al. (2019)
Insulin	Porcine pancreatic B-cells	Imidazolium-based ILs comprising [C <sub>4</sub> C <sub>1</sub> im][CH <sub>3</sub> COO], [C <sub>4</sub> C <sub>1</sub> im][Cl], [C <sub>4</sub> C <sub>1</sub> im][CF <sub>3</sub> COO], [C <sub>4</sub> C <sub>1</sub> im][SCN] and [C <sub>4</sub> C <sub>1</sub> im][N(CN) <sub>2</sub> ]	Stabilization and improvement of the helical structure of the protein	Todinova et al. (2016)
Insulin	—	Cholinium and geranate (CAGE) ILs	Protection from enzymatic degradation	Banerjee et al. (2018)
NFKBIZ small interfering RNA (siRNA)	—	Cholinium-based ILs comprising [Ch][AGE], [Ch][ADA], [Ch][AVA], [Ch][APA], [Ch][ASA], [Ch][APP] and [Ch][ABA]	Preservation of the secondary structure of the protein	Mandal et al. (2020)
Insulin	—	Imidazolium-based ILs comprising Br <sup>−</sup> and Cl <sup>−</sup> anions	Stabilization of the native form	Kumar and Venkatesu (2014)
Recombinant human interleukin-2 (rhIL-2)	—	Cholinium-based ILs comprising [Ch][DHP]	Thermal stabilization	Foureau et al. (2012)
Interleukin-6 (IL-6) and cortisol antibodies	Human sweat	Cholinium and imidazolium-based ILs comprising [Ch][DHP] and [Bmim][BF <sub>4</sub> ]	Stabilization	Jagannath et al. (2018)
Epidermal Growth Factor Receptor (EGFR) mAb	—	Cholinium-based buffered ILs (BILs) comprising [Ch][DHP]	Stabilization and inhibition of protein fragmentation	Mazid et al. (2015)
Herceptin <sup>®</sup> (trastuzumab) mAb	—	Cholinium-based ILs comprising [Ch][DHP]	Inhibition of the unfolding and	Reslan et al. (2018)
Immunoglobulin G (IgG)	Human serum	Cholinium-based ILs comprising [Ch][Ac], [Ch][Cl], [Ch][DHC] and [Ch][DHP]	Enhancement of the thermal and chemical stability, and preservation of the protein	Dhiman et al. (2022)
Immunoglobulin Y (IgY)	Water-Soluble Protein Fraction (WSPF) from chicken egg yolk	Surface-Active ILs (SAILs), comprising [C <sub>14</sub> mim]Cl	Stabilization	Vicente et al. (2022)
Deoxyribonucleic acid (DNA)	Salmon testes	Cholinium-based IL comprising [Ch][IAA]	Chemical and structural stabilization and inhibition of the protein degradation	Mukesh et al. (2013)
Deoxyribonucleic acid (DNA)	Salmon testes	Cholinium-based ILs comprising [Ch][Lac], [Ch][DHP] and [Ch][Nit]	Structure preservation and long-term storage stabilization	Vijayaraghavan et al. (2010)
Double stranded Deoxyribonucleic acid (dsDNA)	Salmon testes	Cholinium-, tetrabutylammonium-, tetrabutylphosphonium-, and imidazolium-based ILs comprising [N <sub>4444</sub> Br], [P <sub>4444</sub> Br], [C <sub>2</sub> C <sub>1</sub> im]Br, [Ch]Br, [Ch]Cl, [Ch][DHP], [Ch][Ac] and [Ch][Gly]	Preservation media	Dinis et al. (2020)
Recombinant small ribonucleic acid (RNA)	<i>E. coli</i> DH5α strain	Self-buffering cholinium-based Good's buffers ILs (GB-ILs) comprising [Ch][HEPES], [Ch][MES], [Ch][Tricine] and [Ch][TES]	Preservation media	Pedro et al. (2018)
RNA	Bacterial lysates	Amino-acid-based ILs (AA-ILs) comprising [Ch][Lys], [Ch][Arg], [Ch][Glu] and [Ch][Asp]	Preserve stability	Quental et al. (2019)
Tobacco Mosaic Virus (TMV)	<i>Nicotiana tabacum</i> plants infected with TMV	Protic ILs comprising [EaMs], [DeaMs] and [TeaMs] anions	Improvement of the shelf-life, without structural losses	Byrne et al. (2012)
Inactivated Foot-and-Mouth Disease Virus (iFMDV)	—	Cholinium-based ILs comprising [Ch][Cl], [Ch][SO <sub>4</sub> ] and [Ch][H <sub>2</sub> PO <sub>4</sub> ]	Enhancement of the thermal and long-term stability	Lin et al. (2019)

Abbreviations: TMA, trimethylammonium hydrogen sulphate; TEAS, triethylammonium hydrogen sulphate; TMAP–trimethylammonium dihydrogen phosphate; TEAP, triethylammonium dihydrogen phosphate; TMAA, trimethylammonium acetate; [C<sub>4</sub>C<sub>1</sub>im][CH<sub>3</sub>COO], 1-butyl-3-methylimidazolium acetate; [C<sub>4</sub>C<sub>1</sub>im][Cl], 1-Butyl-3-methylimidazolium chloride; [C<sub>4</sub>C<sub>1</sub>im][CF<sub>3</sub>COO], 1-butyl-3-methylimidazolium trifluoroacetate; [C<sub>4</sub>C<sub>1</sub>im][SCN], 1-butyl-3-methylimidazolium thiocyanate; [C<sub>4</sub>C<sub>1</sub>im][N(CN)<sub>2</sub>], 1-butyl-3-methylimidazolium dicyanamide; [Ch][AGE], cholinium geranate; [Ch][ADA], cholinium dimethylacrylic acid; [Ch][AVA], cholinium iso-valeric acid; [Ch][APA], cholinium phenylpropanoic acid; [Ch][ASA], cholinium 4-phenolsulfonic acid; [Ch][APP], cholinium phenyl-phosphoric acid; [Ch][ABA], cholinium biphenyl-3-carboxylic acid; [Br]<sup>−</sup>, bromide anion; [Cl]<sup>−</sup>, chloride anion; [Ch][Glu], cholinium L-glutamate; [Ch]<sub>2</sub>[Asp], cholinium L-asparaginate; [Ch][DHP], cholinium dihydrogen phosphate; [Bmim][BF<sub>4</sub>], 1-butyl-3-methylimidazolium tetrafluoroborate; [P<sub>4444</sub>Br], tetrabutylphosphonium bromide; [N<sub>4444</sub>Br], tetrabutylammonium bromide; [C<sub>4</sub>mim][Cl], 1-butyl-3-methylimidazolium chloride; [C<sub>4</sub>mim][Br], 1-ethyl-3-methylimidazolium bromide; [C<sub>4</sub>mim][N(CN)<sub>2</sub>], 1-butyl-3-methylimidazolium dicyanamide; [C<sub>4</sub>mim][CH<sub>3</sub>CO<sub>2</sub>], 1-butyl-3-methylimidazolium acetate; [C<sub>14</sub>mim]Cl, 1-tetradecyl-3-methylimidazolium chloride; [Ch][IAA], cholinium-indole-3-acetate; [Ch][Lac], cholinium lactate; [Ch][Nit], cholinium nitrate; [N<sub>4444</sub>Br], tetrabutylammonium bromide; [P<sub>4444</sub>Br], tetrabutylphosphonium bromide; [C<sub>2</sub>C<sub>1</sub>im]Br, 1-ethyl-3-methylimidazolium bromide; [Ch]Br, cholinium bromide; [Ch]Cl, cholinium chloride; [Ch][DHP], cholinium dihydrogen phosphate; [Ch][Ac], cholinium acetate; [Ch][Gly], cholinium glycolate; [Ch][HEPES], 2-[4-(2-hydroxyethyl)piperazin-1-yl]ethanesulfonate; [Ch][MES], cholinium 2-(N-morpholino)ethanesulfonate; [Ch][Tricine], cholinium N- tris(hydroxymethyl)methylglycinate; [Ch][TES], cholinium 2-[(2-hydroxy-1, 1-bis(hydroxymethyl)ethyl)amino]-ethanesulfonate; [EaMs], ethyl ammonium mesylate; [DeaMs], diethylammonium mesylate; [TeaMs], triethylammonium mesylate; [Ch][Cl], cholinium chloride, [Ch][SO<sub>4</sub>], cholinium sulphate; [Ch][H<sub>2</sub>PO<sub>4</sub>], cholinium dihydrogen phosphate; [Ch][Arg], cholinium L-argininate; [Ch][Asp], cholinium DL-aspartate; [Ch][Lys], (2-hydroxyethyl) trimethylammonium (cholinium) L-lysinate.

concentrations of 0.05 and 0.5 mmol L<sup>-1</sup>, did not affect fibroblast proliferation for 48 h; however, a significant reduction of the cell growth of more than 50% and a moderate anti-proliferative activity of more than 25% were achieved with [Ch][Arg] and [Ch][Glu], respectively, in the experiments in which the highest concentration was tested. Overall, it was concluded that cholinium-based ILs can be considered potential stabilizing agents for relevant therapeutic proteins, such as insulin; however, it is crucial to properly select the IL nature and concentration, when envisioning their application in the biopharmaceutical field. Still regarding the same target molecule, Banerjee et al. (Banerjee et al., 2018) showed the potential of choline and geranate (CAGE) ILs for oral insulin delivery, showing that these solvents can protect insulin from enzymatic degradation.

Foureau et al. (2012) studied the effect of [Ch][DHP] on the functional and structural integrity of recombinant human interleukin-2 (rhIL-2), a protein that is used for the treatment of advanced melanoma. It was shown that for rhIL-2 formulations comprising 680 mmol L<sup>-1</sup> IL, the IL was able to preserve the binding activity of rhIL-2 after a thermal treatment, in which temperatures of 23.3°C above the protein T<sub>m</sub> were applied (Foureau et al., 2012). Cytotoxicity assays were also performed to evaluate the safety of [Ch][DHP], being observed that it presents a non-toxic profile against primary splenocytes or B16F10 cell lines (Foureau et al., 2012). The [Ch][DHP] IL increased the thermal stability of rhIL-2, while being non-toxic, confirming its potential to prepare safe and stable formulations of therapeutic proteins (Foureau et al., 2012). In the study conducted by Jagannath et al. (2018), the ability of [Ch][DHP] and [C<sub>4</sub>C<sub>1</sub>im][BF<sub>4</sub>] ILs to stabilize interleukin-6 (IL-6) and cortisol antibodies was evaluated. It was shown that upon the addition of [Ch][DHP] to the final formulation at concentrations higher than 60% (v/v), it was able to stabilize both proteins, avoiding aggregation (Jagannath et al., 2018).

In the antibody field, Reslan et al. (2018) studied the effect of [Ch][DHP] IL on the stability of Herceptin® (trastuzumab) mAb. To achieve this purpose, several formulations containing different concentrations of the IL and the mAb were prepared, in the presence and in the absence of other excipient compounds that are typically used in conventional Herceptin® formulations (Reslan et al., 2018). Overall, it was shown that [Ch][DHP] inhibited the aggregation and unfolding of the protein and that its stability could be significantly enhanced when the IL was combined with other excipients (Reslan et al., 2018). Moreover, in formulations containing 53% (w/v) of [Ch][DHP], the transition temperature and the onset temperature of aggregation (T<sub>agg</sub>) of 20 mg mL<sup>-1</sup> of trastuzumab, increased by 5.6 and 10.4°C, respectively (Reslan et al., 2018). The effect of cholinium-based buffered ILs (BILs), comprising again [Ch][DHP], in the structural and chemical stability of the Epidermal Growth Factor Receptor (EGFR) mAb was also studied (Mazid et al., 2015). It was demonstrated that the introduction of BILs in the EGFR mAb formulations inhibits protein fragmentation, preserves its α-helix conformation, prolongs its stability and activity in the presence of proteinases, and maintains its biological activity during storage (Mazid et al., 2015). This study disclosed the potential of BILs as storage buffers for mAbs, decreasing the necessity to apply other preservation techniques, such as lyophilisation and refrigeration. Dhiman et al. (2022) investigated the use of cholinium-based ILs as stabilizers of polyclonal IgG antibodies. It was shown that these solvents do not lead to IgG aggregation or fragmentation, being [Ch][Ac] and [Ch]Cl the ILs with higher ability to improve the thermal stability of the protein.

Vicente et al. (2022) studied the effect of SAILs-based AMTPS on the structural stability of IgY antibodies. This work disclosed that, even when IgY antibody is effectively recovered from its biological source with IL-based AMTPS, its stability is preserved.

In addition to protein-based pharmaceuticals, a set of works has shown the ability of ILs to improve the stability of nucleic acids. In the work conducted by Mukesh et al. (2013), two cholinium-based ILs were studied with DNA from salmon testes. DNA denaturation occurred when it was formulated with the [Ch][IBA] IL, whereas the introduction of the [Ch][IAA] IL enabled to dissolve DNA up to 3.5% (w/w) and to maintain its long-term chemical and structural stabilities (Mukesh et al., 2013). Similarly, Vijayaraghavan et al. (2010) demonstrated the ability of cholinium-based ILs to maintain the structural conformation and storage stability of salmon testes DNA. The [Ch][Lac] IL was able to preserve the double-helical structure of the nucleic acid during its long-term storage of 6 months at room temperature (Vijayaraghavan et al., 2010). Moreover, Dinis et al. (2020) investigated the use of aqueous solutions of ILs, formed by the combination of cholinium, tetrabutylammonium, tetrabutylphosphonium, and 1-ethyl-3-methylimidazolium cations with bromide, chloride, dihydrogen phosphate, acetate, and glycolate anions, as preservation media for double-stranded DNA (dsDNA). Cholinium-based ILs shown to be most effective in preserving the structure of the dsDNA majorly due to the electrostatic interactions established between the cholinium cation and the phosphate groups of dsDNA, which were determined by <sup>31</sup>P NMR spectroscopy. Moreover, the denaturation of dsDNA mainly arose with ILs comprising more hydrophobic cations that are capable to establish dispersive interactions with the nucleobases environment of dsDNA. It was also demonstrated that, in contrast to the IL cation, the anion component of the IL has a lower effect in the interaction with dsDNA.

Pedro et al. (2018) evaluated the potential of several self-buffering cholinium-based Good's buffer ILs (GBILs) at 20 and 50% (w/w) as structural preservation media of recombinant small RNAs (sRNAs) from *E. coli* DH5α strain comprising the therapeutic pre-miR-29. It was found that GBILs were able to increase the stability of the nucleic acid for at least up to 30 days at room temperature and 4°C, allowing to increment the overall shelf-life of the molecule. The ILs [Ch][HEPES] and [Ch][MES] were identified as the best ones in increasing the integrity and stability of sRNAs (Pedro et al., 2018). Their thermal stability was significantly improved, being observed an increase of 14°C in the respective biopolymer melting point. Moreover, no cytotoxicity was observed in two human cell lines for the RNA formulated in ILs solutions at 20% (w/w). This work revealed the potential of using aqueous solutions of GB-ILs as stabilizing and preservation media for recombinant sRNAs at room temperature, avoiding the employment of conventional freezing methodologies during storage. In the same way, Quental et al. (2019) confirmed the RNA stability and integrity for 15 days in aqueous solutions of ILs comprising anions derived from amino acids (AA-ILs). Furthermore, the authors propose an integrated extraction-preservation approach for RNA, in which after extraction-purification of RNA to the IL-rich phase, it can be preserved in that same phase/solution up to its use.

Byrne et al. (2012) studied the effect of ILs as solvents for the solubilisation and stabilization of Tobacco Mosaic Virus (TMV). It was demonstrated that when TMV was formulated with Protic ILs (PILs), the IL enabled to increase its shelf-life to 4 months without significant losses on its tertiary structure (Byrne et al.,

2012). In contrast, when TMV was formulated with a conventional buffer solution, its degradation occurred after 3 weeks (Byrne et al., 2012). Therefore, ILs can be seen as promising stabilizing agents for TMV, being this observation highly important for the development of safe viral formulations with therapeutic activity. Also, Lin et al. (2019) studied the effect of biocompatible cholinium-based ILs on the stability of foot-and-mouth disease virus (iFMDV) particles. It was shown that [Ch] [Cl] and [Ch][SO<sub>4</sub>] were able to enhance the thermal and long-term stability of the virus, inhibiting its dissociation (Lin et al., 2019). The results obtained in this work showed that if a proper selection of the anion component of the IL is carried out, cholinium-based ILs can be seen as promising stabilizing agents for iFMDV particles, enabling the development of more stable formulations of these products.

In summary, the described works demonstrated the outstanding performance of ILs to improve and/or maintain the stability of relevant biopharmaceuticals, opening the door for their use in formulation development.

## SWOT analysis of Ionic liquid-based approaches in biomanufacturing

This review has given the reader an overview of the potential of IL-based strategies in biomanufacturing namely, to improve the performance of the downstream processing and formulation development stages of biopharmaceuticals. Despite the significant research advances made in the last few decades, there is still a long road to walk until ILs are widely approved by regulatory agencies and



**FIGURE 8**

SWOT analysis emphasizing the major strengths, weaknesses, opportunities, and threats of the application of IL-based approaches for the downstream processing and formulation of biopharmaceuticals.

employed at an industrial scale. As summary of the previous discussion, a SWOT analysis (strengths, weaknesses, opportunities, and threats) analysis is presented in Figure 8.

It is important to highlight that a comprehensive SWOT analysis has been previously made by Soares et al. (2015) concerning the use of ABS for the partitioning of biomolecules. The effectiveness, simplicity, biocompatibility, selectivity, integrability, scalability, as well as the possibility of being applied in a continuous operation mode, were referred as ABS major strengths for biomolecule purification. On the opposite, as weaknesses, there is a lack of knowledge concerning the installation, validation, and operation of ABS-based technologies, and a limited predictive design. Regarding IL-based strategies in the downstream processing of biopharmaceuticals, including not only IL-ABS but also SILs, there are three major strengths: i) their versatility and improved/tailored separation performance for different types of biopharmaceuticals from a myriad of sources; ii) the possibility of process integration; iii) and scalability. Due to the outstanding properties presented by ILs, that are transferred to SILs, it is possible to design numerous combinations of ionic components to improve the performance of the envisioned application (Castro et al., 2019; Kianfar and Mafi, 2020; Curreri et al., 2021; Jadhav et al., 2021; Bernardo et al., 2022). However, a proper selection of the cation and anion should consider the envisaged physicochemical properties of the final formulation, the formulation biocompatibility, and the biological activity of the biomolecules. Running the production and purification processes in a continuous mode during biomanufacturing, by integrating the production and purification stages and/or the different purification steps, as shown with the use of ABS in CPC (Soares et al., 2021), use of SILs in preparative liquid chromatography (Neves et al., 2020), and integrated extraction-preservation approaches (Quental et al., 2019), could contribute to further improve the cost-effectiveness and potential application at large-scale of these processes.

Notwithstanding the benefits previously mentioned, there are still two major weaknesses limiting the broad application of IL-based approaches in biomanufacturing (Tavares et al., 2019): the concerns regarding the biocompatibility, biodegradability, and cytotoxicity of ILs, and (Kesik-Brodacka, 2018) the limited predictive design of IL-ABS. Furthermore, before their use in the biopharmaceuticals field can become a reality, a long path including *in vivo* preclinical studies and long and expensive human clinical trials to assess safety and efficacy is still needed. Since the evaluation of ILs cytotoxicity and biocompatibility is mandatory when envisioning their application in the biopharmaceutical field (Lin et al., 2021), ILs comprising cations and anions from a natural source and/or already approved as safe ingredients by regulatory entities should be preferably selected.

Several opportunities could be pointed out for IL-based approaches in biomanufacturing, among them (Tavares et al., 2019): the fact that the number of approved nucleic-acid-based therapeutics and respective market shares is growing, in part due to the emergence of the COVID-19 mRNA vaccines (Kesik-Brodacka, 2018); the possibility of designing integrated preservation-extraction strategies and continuous purification processes (O'Flaherty et al., 2020); the existence of a panoply of ILs and IL-modified materials allowing to tailor separation performance; and (Ferreira et al., 2016) the possibility of performing computational investigations to predict the best IL to a given purpose. IL-based strategies still cope with some

threats that limit their use in bioprocesses, namely the unwillingness of some industries to substitute their current and well-established processes, the lack of appropriate industrial downstream processing plants for operating IL-ABS, and the complex and expensive regulatory approval processes required for the use of biopharmaceuticals in humans.

## Conclusions and future perspectives in the field

ILs and IL-modified materials can be considered highly promising tools to improve the downstream processing and formulation approaches of biopharmaceuticals. Several IL-based approaches, most of them relying on IL-ABS and SILs, have been proposed confirming their outstanding performance to enhance the recovery yields and purification efficiency of a myriad of biomolecules, including therapeutic enzymes, antibodies, nucleic acids, viruses, and interferons. The attractiveness of using IL-based approaches in the biopharmaceutical field is due to their remarkable properties, particularly versatility and “designer” nature, allowing them to modulate the final properties and outcomes of a specific process/application and therefore, to surpass the challenges related to the lack of robust, selective, and easy to scale-up approaches for the recovery, purification, and formulation of biopharmaceuticals.

In the downstream processing, IL-based ABS/ATPMS/TPP and SILs have shown the ability to improve the purity and yield of a myriad of biopharmaceuticals. Research showing the possibility of performing biomolecules' purification in continuous mode with ABS and CPC, and the identification of ILs as multimodal ligands in preparative liquid chromatography, seems particularly relevant. It is also important to emphasize the capacity of ILs to be recovered and reused, contributing to the development of more sustainable and low-cost processes. In the formulation field, ILs have been shown to have high potential to improve the thermal and chemical stability of several therapeutic compounds, and to inhibit their aggregation, denaturation, enzymatic degradation, and fragmentation.

Other factors, such as the safety profile and costs, also need to be adequately assessed before considering market introduction. However, ILs and SILs-based processes represent good alternatives when aiming to reduce biomanufacturing-associated environmental, economic and health burdens. Although there is still a long path ahead, the research conducted so far and here reviewed shows the remarkable potential of IL-based approaches in the biopharmaceutical field, challenging researchers to go above and beyond.

## Author contributions

CA: writing—original draft preparation and review and editing; methodology; visualization; formal analysis. AQP: writing—review and editing; supervision; visualization; funding acquisition. APMT: conceptualization; writing—review and editing. visualization; supervision; MCN: conceptualization; writing—review and editing; supervision; visualization. MGF: conceptualization; writing—review and editing; supervision; project administration; funding acquisition. All authors have read and agreed to the published version of the manuscript.



## Funding

This work is financed by Portugal 2020 through European Regional Development Fund (ERDF) in the frame of CENTRO2020 in the scope of the project AntYmicrob, CENTRO-01-0145-FEDER-181219 and in the scope of the project CICECO—Aveiro Institute of Materials, UIDB/50011/2020 and UIDP/50011/2020 and LA/P/0006/2020, financed by national funds through the FCT/MEC (PIDDAC). This work was additionally developed within the scope of the EIC-Pathfinder YSCRIPT project with reference 101047214, supported by the budgets of the Horizon Europe Program.

## Acknowledgments

CA acknowledge FCT for the doctoral grant 2022.11570.BD. AQP, MCN, and APMT acknowledge FCT respectively, for the research

## References

- Agko, S., Denizli, A., and Canak, Y. (2004). A novel magnetic adsorbent for immunoglobulin-G purification in a magnetically stabilized fluidized bed. *Biotechnol. Prog.* 20, 1169–1175. doi:10.1021/bp049896s
- Azevedo, A. M., Rosa, P. A. J., Ferreira, I. F., and Aires-barros, M. R. (2009). Chromatography-free recovery of biopharmaceuticals through aqueous two-phase processing. *Trends Biotechnol.* 27 (4), 240–247. doi:10.1016/j.tibtech.2009.01.004
- Baker, S. N., McCleskey, T. M., Pandey, S., and Baker, G. A. (2004). Fluorescence studies of protein thermostability in ionic liquids. *Chem. Commun.* 4 (8), 940. Available at: <http://xlink.rsc.org/?DOI=b401304m>. doi:10.1039/b401304m
- Banerjee, A., Ibsen, K., Brown, T., Chen, R., Agatemor, C., and Mitragotri, S. (2018). Ionic liquids for oral insulin delivery. *Proc. Natl. Acad. Sci.* 115 (28), 7296–7301. [Internet]. doi:10.1073/pnas.1722338115
- Bento, R. M. F., Almeida, C. A. S., Neves, M. C., Tavares, A. P. M., and Freire, M. G. (2021). Advances achieved by ionic-liquid-based materials as alternative supports and purification platforms for proteins and enzymes. *Nanomater. (Basel)*. 11 (10), 2542. doi:10.3390/nano11102542
- Bernardo, S. C., Carapito, R., Neves, M. C., Freire, M. G., and Sousa, F. (2022). Supported ionic liquids used as chromatographic matrices in bioseparation—an overview. *Molecules* 27 (5), 1618. doi:10.3390/molecules27051618
- Byrne, N., Rodoni, B., Constable, F., Varghese, S., and Davis, J. H. (2012). Enhanced stabilization of the Tobacco mosaic virus using protic ionic liquids. *Phys. Chem. Chem. Phys.* [Internet] 14 (29), 10119. Available at: <http://xlink.rsc.org/?DOI=c2cp41625e>. doi:10.1039/C2CP41625E
- Capela, E. V., Bairos, J., Pedro, A. Q., Neves, M. C., Raquel Aires-Barros, M., Azevedo, A. M., et al. (2023). Supported ionic liquids as customizable materials to purify immunoglobulin G. *Sep. Purif. Technol.* 305, 122464. doi:10.1016/j.seppur.2022.122464
- Capela, E. V., Santiago, A. E., Rufino, A. F. C. S., Tavares, A. P. M., Pereira, M. M., Mohamadou, A., et al. (2019). Sustainable strategies based on glycine-betaine analogue ionic liquids for the recovery of monoclonal antibodies from cell culture supernatants. *Green Chem.* 21 (20), 5671–5682. doi:10.1039/c9gc02733e
- Carapito, A. R. M. (2019). *Ionic liquids for the purification and stabilization of nucleic acids*. Covilhã, Portugal: Universidade da Beira Interior. [Internet] Available at: <http://hdl.handle.net/10400.6/10162>.
- Castilho, L. R., Anspach, F. B., and Deckwer, W. (2002). Comparison of affinity membranes for the purification of immunoglobulins. *J. Memb. Sci.* 207, 253–264. doi:10.1016/S0376-7388(02)00257-0
- Castro, L., Pereira, P., Freire, M., and Pedro, A. (2019). Progress in the development of aqueous two-phase systems comprising ionic liquids for the downstream processing of protein-based biopharmaceuticals. *Am. Pharm. Rev.* 1–6.
- Castro, L. S., Lobo, G. S., Freire, M. G., Neves, M. C., and Pedro, A. Q. (2021). Interferon-based biopharmaceuticals: Overview on the production, purification, and formulation. *Vaccines* 9 (4), 328. doi:10.3390/vaccines9040328
- Castro, L. S., Pereira, P., Passarinha, L. A., Freire, M. G., and Pedro, A. Q. (2020). Enhanced performance of polymer-polymer aqueous two-phase systems using ionic liquids as adjuvants towards the purification of recombinant proteins. *Sep. Purif. Technol.* 248, 117051. [Internet]. doi:10.1016/j.seppur.2020.117051
- contracts CEEC-IND/02599/2020, CEECIND/00383/2017, and CEECIND/01867/2020 under the Scientific Stimulus—Individual Call.
- ## Conflict of interest
- The authors declare that the research was conducted in the absence of any commercial or financial relationships that could be construed as a potential conflict of interest.
- ## Publisher's note
- All claims expressed in this article are solely those of the authors and do not necessarily represent those of their affiliated organizations, or those of the publisher, the editors and the reviewers. Any product that may be evaluated in this article, or claim that may be made by its manufacturer, is not guaranteed or endorsed by the publisher.
- Chen, J., Wang, Y., Huang, Y., Xu, K., Li, N., Wen, Q., et al. (2015). Magnetic multiwall carbon nanotubes modified with dual hydroxy functional ionic liquid for the solid-phase extraction of protein. *Analyst* 140 (10), 3474–3483. doi:10.1039/c5an00201j
- Chen, Y.-C., and Yeh, M.-K. (2018). “Biopharmaceuticals,” in *Biopharmaceuticals*. Editors M.-K. Yeh and Y.-C. Chen (London: InTech), 138. Available at: <http://www.intechopen.com/books/biopharmaceuticals/introductory-chapter-biopharmaceuticals>.
- Conner, J., Wuchterl, D., Lopez, M., Minshall, B., Prusti, R., Bocclair, D., et al. (2014). “The biomanufacturing of biotechnology products,” in *Biotechnology entrepreneurship: Starting, managing, and leading biotech companies [internet]*. Editor C. Shimasaki (Academic Press), 351–385. doi:10.1016/B978-0-12-404730-3.00026-9
- Curreri, A. M., Mitragotri, S., and Tanner, E. E. L. (2021). Recent advances in ionic liquids in biomedicine. *Adv. Sci. [Internet]* 8 (17), 2004819. doi:10.1002/advs.202004819
- Dhiman, D., Bisht, M., Tavares, A. P. M., Freire, M. G., and Venkatesu, P. (2022). Cholinium-based ionic liquids as efficient media for improving the structural and thermal stability of immunoglobulin G antibodies. *ACS Sustain. Chem. Eng.* 10 (17), 5404–5420. doi:10.1021/acssuschemeng.1c07979
- Ding, X., Wang, Y., Wang, Y., Pan, Q., Chen, J., Huang, Y., et al. (2015). Preparation of magnetic chitosan and graphene oxide-functional guanidinium ionic liquid composite for the solid-phase extraction of protein. *Anal. Chim. Acta* 861, 36–46. doi:10.1016/j.aca.2015.01.004
- Dinis, T. B. V., Sousa, F., and Freire, M. G. (2020). Insights on the DNA stability in aqueous solutions of ionic liquids. *Front. Bioeng. Biotechnol.* 8, 547857. doi:10.3389/fbioe.2020.547857
- dos Santos, R., Carvalho, A. L., and Roque, A. C. A. (2017). Renaissance of protein crystallization and precipitation in biopharmaceuticals purification. *Biotechnol. Adv. [Internet]* 35 (1), 41–50. doi:10.1016/j.biotechadv.2016.11.005
- e Silva, F. A., Pereira, J. F. B., Kurnia, K. A., Ventura, S. P. M., Silva, A. M. S., Rogers, R. D., et al. (2017). Temperature dependency of aqueous biphasic systems: An alternative approach for exploring the differences between coulombic-dominated salts and ionic liquids. *Chem. Commun. [Internet]* 53 (53), 7298–7301. Available from: doi:10.1039/C7CC02294H
- Erbeldinger, M., Mesiano, A. J., and Russell, A. J. (2000). Enzymatic catalysis of formation of Z-aspartame in ionic liquid an alternative to enzymatic catalysis in organic solvents. *Biotechnol. Prog.* 16, 1129–1131. [Internet]. doi:10.1021/bp000094g
- Fehrmann, R., Haumann, M., and Riisager, A. (2014). *Supported ionic liquids: Fundamentals and applications, introduction*. Hoboken, NJ, USA: John Wiley & Sons, 1–9.
- Ferreira, A. M., Faustino, V. F. M., Mondal, D., Coutinho, J. A. P., and Freire, M. G. (2016). Improving the extraction and purification of immunoglobulin G by the use of ionic liquids as adjuvants in aqueous biphasic systems. *J. Biotechnol.* 236, 166–175. doi:10.1016/j.jbiotec.2016.08.015
- Ferreira, G., Monteiro, G., Prazeres, D., and Cabral, J. (2000). Downstream processing of plasmid DNA for gene therapy and DNA vaccine applications. *Trends Biotechnol.* 18 (9), 380–388. doi:10.1016/S0167-7799(00)01475-x
- Fields, C., Li, P., Mahony, J. J. O., and Lee, G. U. (2016). Advances in affinity ligand-functionalized nanomaterials for biomagnetic separation. *Biotechnol. Bioeng.* 113 (1), 11–25. doi:10.1002/bit.25665

- Foldvari, M., Chen, D. W., Nafissi, N., Calderon, D., Narsineni, L., and Rafiee, A. (2016). Non-viral gene therapy: Gains and challenges of non-invasive administration methods. *J. Control Release* 240, 165–190. [Internet]. doi:10.1016/j.jconrel.2015.12.012
- Fontanal, N., Ronka, S., Borrell, F., Trochimczuk, A. W., and Marcé, R. M. (2009). Supported imidazolium ionic liquid phases: A new material for solid-phase extraction. *Talanta* 80 (1), 250–256. doi:10.1016/j.talanta.2009.06.068
- Foureaux, D. M., Vrikakis, R. M., Jones, C. P., Weaver, K. D., MacFarlane, D. R., Salo, J. C., et al. (2012). *In vitro* assessment of choline dihydrogen phosphate (CDHP) as a vehicle for recombinant human interleukin-2 (rhIL-2). *Cell Mol. Bioeng.* 5 (4), 390–401. [Internet]. doi:10.1007/s12195-012-0243-x
- Frokjaer, S., and Otzen, D. E. (2005). Protein drug stability: A formulation challenge. *Nat. Rev. Drug Discov.* [Internet] 4 (4), 298–306. doi:10.1038/nrd1695
- Giacalone, F., and Gruttadauria, M. (2016). Covalently supported ionic liquid phases: An advanced class of recyclable catalytic systems. *ChemCatChem* 8, 664–684. doi:10.1002/cctc.201501086
- Gomes, C. S., Fashina, A., Fernández-Castané, A., Overton, T. W., Hobley, T. J., Theodosiou, E., et al. (2018). Magnetic hydrophobic-charge induction adsorbents for the recovery of immunoglobulins from antiserum feedstocks by high-gradient magnetic fishing. *J. Chem. Technol. Biotechnol.* [Internet] 93 (7), 1901–1915. doi:10.1002/jctb.5599
- Grilo, A. L., and Mantalaris, A. (2019). The increasingly human and profitable monoclonal antibody market. *Trends Biotechnol.* [Internet] 37 (1), 9–16. doi:10.1016/j.tibtech.2018.05.014
- Guncheva, M., Ossowicz, P., Janus, E., Todinova, S., and Yancheva, D. (2019). Elucidation of the effect of some cholinium amino acid ionic liquids on the thermal and the conformational stability of insulin. *J. Mol. Liq.* [Internet] 283, 257–262. doi:10.1016/j.molliq.2019.03.074
- Hanke, A. T., and Ottens, M. (2014). Purifying biopharmaceuticals: Knowledge-based chromatographic process development. *Trends Biotechnol.* [Internet] 32 (4), 210–220. doi:10.1016/j.tibtech.2014.02.001
- Hoffman, A. S., Letourneur, D., Pelle, A., and Letourneur, D. (2001). New antibody purification procedure using a thermally responsive poly (N-isopropylacrylamide)-dextran derivative conjugate. *J. Chromatogr. B* 761, 247–254. doi:10.1016/s0378-4347(01)00336-x
- Hong, M. S., Severson, K. A., Jiang, M., Lu, A. E., Love, J. C., and Braatz, R. D. (2018). Challenges and opportunities in biopharmaceutical manufacturing control. *Comput. Chem. Eng.* 110, 106–114. doi:10.1016/j.compchemeng.2017.12.007
- Information NC for B (2007). “PubChem compound summary for CID 1983,” in *Acetaminophen*.
- Itoh, T., and Koo, Y.-M. (2019). *Application of ionic liquids in Biotechnology*. Berlin/Heidelberg, Germany: Springer, 343.
- Jadhav, N. R., Bhosale, S. P., Bhosale, S. S., Mali, S. D., Toraskar, P. B., and Kadam, T. S. (2021). Ionic liquids: Formulation avenues, drug delivery and therapeutic updates. *J. Drug Deliv. Sci. Technol.* 65, 102694. [Internet]. doi:10.1016/j.jddst.2021.102694
- Jagannath, B., Muthukumar, S., and Prasad, S. (2018). Electrical double layer modulation of hybrid room temperature ionic liquid/aqueous buffer interface for enhanced sweat based biosensing. *Anal. Chim. Acta* [Internet] 1016, 29–39. doi:10.1016/j.aca.2018.02.013
- Jaitely, V., Karatas, A., and Florence, A. T. (2008). Water-immiscible room temperature ionic liquids (RTILs) as drug reservoirs for controlled release. *Int. J. Pharm.* [Internet] 354 (1–2), 168–173. doi:10.1016/j.jipharm.2008.01.034
- Jenkins, N., Murphy, L., and Tyther, R. (2008). Post-translational modifications of recombinant proteins: Significance for biopharmaceuticals. *Mol. Biotechnol.* 39 (2), 113–118. doi:10.1007/s12033-008-9049-4
- Jia, X., Hu, X., Wang, W., and Du, C. (2019). Non-covalent loading of ionic liquid-functionalized nanoparticles for bovine serum albumin: Experiments and theoretical analysis. *RSC Adv.* 9 (33), 19114–19120. doi:10.1039/c9ra02265a
- Jozala, A. F., Galdes, D. C., Tundisi, L. L., Feitosa, V. de A., Breyer, C. A., Cardoso, S. L., et al. (2016). Biopharmaceuticals from microorganisms: From production to purification. *Braz. J. Microbiol.* [Internet] 47, 51–63. doi:10.1016/j.bjm.2016.10.007
- Karl, H., and Schwa, A. (2005). Preparative purification of antibodies with protein A — An alternative to conventional chromatography. *J. Magn. Magn. Mater* 293, 345–348. doi:10.1016/j.jmmm.2005.02.050
- Kerwin, B. A. (2008). Polysorbates 20 and 80 used in the formulation of protein biotherapeutics: Structure and degradation pathways. *J. Pharm. Sci.* [Internet] 97 (8), 2924–2935. doi:10.1002/jps.21190
- Kesik-Brodacka, M. (2018). Progress in biopharmaceutical development. *Biotechnol. Appl. Biochem.* 65 (3), 306–322. doi:10.1002/bab.1617
- Kianfar, E., and Mafi, S. (2020). Ionic liquids: Properties, application, and synthesis. *Fine Chem. Eng.*, 22–31. [Internet]. Available at: <http://127.0.0.1:8320/index.php/FCE/article/view/693>. doi:10.37256/fce.212021693
- Kulkarni, J. A., Witzigmann, D., Thomson, S. B., Chen, S., Leavitt, B. R., Cullis, P. R., et al. (2021). The current landscape of nucleic acid therapeutics. *Nat. Nanotechnol.* [Internet] 16 (6), 630–643. doi:10.1038/s41565-021-00898-0
- Kumar, A., Bisht, M., and Venkatesu, P. (2017). Biocompatibility of ionic liquids towards protein stability: A comprehensive overview on the current understanding and their implications. *Int. J. Biol. Macromol.* [Internet] 96, 611–651. doi:10.1016/j.ijbiomac.2016.12.005
- Kumar, A., and Venkatesu, P. (2013). Prevention of insulin self-aggregation by a protic ionic liquid. *RSC Adv.* 3 (2), 362–367. Available at: <http://xlink.rsc.org/?DOI=C2RA22277A>. doi:10.1039/C2RA22277A
- Kumar, A., and Venkatesu, P. (2014). The stability of insulin in the presence of short alkyl chain imidazolium-based ionic liquids. *RSC Adv.* [Internet] 4 (9), 4487–4499. Available at: <http://xlink.rsc.org/?DOI=C3RA44477E>. doi:10.1039/C3RA44477E
- Lazarova, Z., Beschkov, V., and Velizarov, S. (2001). Membrane separations in biotechnology. *Curr. Opin. Biotechnol.* 12, 208–211. doi:10.1016/s0958-1669(00)00201-9
- Lemus, J., Palomar, J., Gilarranz, M. A., and Rodriguez, J. J. (2011). Characterization of supported ionic liquid phase (SILP) materials prepared from different supports. *Adsorpt. Bost.* 17 (3), 561–571. doi:10.1007/s10450-011-9327-5
- Lin, X., Su, Z., Yang, Y., and Zhang, S. (2021). The potential of ionic liquids in biopharmaceutical engineering. *Chin. J. Chem. Eng.* [Internet] 30, 236–243. doi:10.1016/j.cjche.2020.11.015
- Lin, X., Yang, Y., Li, S., Song, Y., Ma, G., Su, Z., et al. (2019). Unique stabilizing mechanism provided by biocompatible choline-based ionic liquids for inhibiting dissociation of inactivated foot-and-mouth disease virus particles. *RSC Adv.* [Internet] 9 (24), 13933–13939. Available at: <http://xlink.rsc.org/?DOI=C9RA02722J>. doi:10.1039/c9ra02722j
- Liu, Y., Ma, R., Deng, Q., Zhang, L., Liu, C., and Wang, S. (2014). Preparation of ionic liquid polymer materials and their recognition properties for proteins. *RSC Adv.* 4 (94), 52147–52154. doi:10.1039/c4ra05713a
- Loureiro, A. M., Tavares, A. P. M., and Freire, M. G. (2022). An overview on the recent advances in alternative solvents as stabilizers of proteins and enzymes. *Chemengineering* 6 (4), 51. doi:10.3390/chemengineering6040051
- Magri, A., Pimenta, M. V., Santos, J. H., Coutinho, J. A., Ventura, S. P., Monteiro, G., et al. (2019). Controlling the L-asparaginase extraction and purification by the appropriate selection of polymer/salt-based aqueous biphasic systems. *J. Chem. Technol. Biotechnol.* [Internet] 55 (16), 6281. doi:10.1002/jctb.6281
- Makurvet, F. D. (2021). Biologics vs. small molecules: Drug costs and patient access. *Med. Drug Discov.* 9, 100075. doi:10.1016/j.medidd.2020.100075
- Mandal, A., Kumbhokar, N., Reilly, C., Dharamdasani, V., Ukidve, A., Ingber, D. E., et al. (2020). Treatment of psoriasis with NFKBIZ siRNA using topical ionic liquid formulations. *Sci. Adv.* [Internet] 6 (30), eabb6049–9. doi:10.1126/sciadv.abb6049
- Marchel, M., Soares, H. R., Vormittag, P., Hubbuck, J., Coroadinha, A. S., and Marrucho, I. M. (2019). High-throughput screening of aqueous biphasic systems with ionic liquids as additives for extraction and purification of enveloped virus-like particles. *Eng. Rep.* 1 (1), 1–16. doi:10.1002/eng2.12030
- Martins, R., Queiroz, J. A., and Sousa, F. (2014). Ribonucleic acid purification. *J. Chromatogr. A* [Internet] 1355, 1–14. doi:10.1016/j.chroma.2014.05.075
- Mazid, R. R., Vijayaraghavan, R., MacFarlane, D. R., Cortez-Jugo, C., and Cheng, W. (2015). Inhibited fragmentation of mAbs in buffered ionic liquids. *Chem. Commun.* [Internet] 51 (38), 8089–8092. doi:10.1039/C5CC01877C
- Mitragotri, S., Burke, P. A., and Langer, R. (2014). Overcoming the challenges in administering biopharmaceuticals: Formulation and delivery strategies. *Nat. Rev. Drug Discov.* [Internet] 13 (9), 655–672. doi:10.1038/nrd4363
- Mondal, D., Sharma, M., Quental, M. V., Tavares, A. P. M., Prasad, K., and Freire, M. G. (2016). Suitability of bio-based ionic liquids for the extraction and purification of IgG antibodies. *Green Chem.* [Internet] 18 (22), 6071–6081. Available at: <http://xlink.rsc.org/?DOI=C6GC01482H>. doi:10.1039/C6GC01482H
- Moniruzzaman, M., Tahara, Y., Tamura, M., Kamiya, N., and Goto, M. (2010). Ionic liquid-assisted transdermal delivery of sparingly soluble drugs. *Chem. Commun.* 46 (9), 1452. [Internet]. Available at: <http://xlink.rsc.org/?DOI=b907462g>. doi:10.1039/b907462g
- Moorkens, E., Meuwissen, N., Huys, I., Declercq, P., Vulto, A. G., and Simoons, S. (2017). The market of biopharmaceutical medicines: A snapshot of a diverse industrial landscape. *Front. Pharmacol.* 8, 314. doi:10.3389/fphar.2017.00314
- Mukesh, C., Mondal, D., Sharma, M., and Prasad, K. (2013). Rapid dissolution of DNA in a novel bio-based ionic liquid with long-term structural and chemical stability: Successful recycling of the ionic liquid for reuse in the process. *Chem. Commun.* [Internet] 49 (61), 6849. Available at: <http://xlink.rsc.org/?DOI=c3cc42829j>. doi:10.1039/C3CC42829J
- Neves, M. C., Pereira, P., Pedro, A. Q., Martins, J. C., Trindade, T., Queiroz, J. A., et al. (2020). Improved ionic-liquid-functionalized macroporous supports able to purify nucleic acids in one step. *Mater Today Bio* [Internet] 8, 100086. doi:10.1016/j.mtbio.2020.100086
- O’Flaherty, R., Bergin, A., Flampouri, E., Mota, L. M., Obaidi, I., Quigley, A., et al. (2020). Mammalian cell culture for production of recombinant proteins: A review of the critical steps in their biomanufacturing. *Biotechnol. Adv.* 43, 107552. doi:10.1016/j.biotechadv.2020.107552
- Parker, M., and Li, Z. (2021). “Biotechnology and drugs,” in *Remington* (Elsevier), 397–415. doi:10.1016/B978-0-12-820007-0.00022-2
- Pedro, A., Coutinho, J. A. P., and Freire, M. G. (2019). “Immobilization of ionic liquids, types of materials, and applications,” in *Encyclopedia of ionic liquids* (Berlin/Heidelberg, Germany: Springer), 1–12.
- Pedro, A. Q., Pereira, P., Quental, M. J., Carvalho, A. P., Santos, S. M., Queiroz, J. A., et al. (2018). Cholinium-based Good’s buffers ionic liquids as remarkable stabilizers and recyclable preservation media for recombinant small RNAs. *ACS Sustain. Chem. Eng.* [Internet] 6 (12), 16645–16656. doi:10.1021/acssuschemeng.8b03900

- Pedro, S. N., Freire Cs, R., Silvestre, A. J. D., and Freire, M. G. (2020). The role of ionic liquids in the pharmaceutical field: An overview of relevant applications. *Int. J. Mol. Sci.* 21 (21), 8298. [Internet]. doi:10.3390/ijms21218298
- Pereira, P., Pedro, A. Q., Neves, M. C., Martins, J. C., Rodrigues, I., Freire, M. G., et al. (2021). Efficient isolation of bacterial RNAs using silica-based materials modified with ionic liquids. *Life* 11 (10), 1090. doi:10.3390/life11101090
- Pereira, P., Sousa, A., Queiroz, J., Correia, I., Figueiras, A., and Sousa, F. (2014). Purification of pre-miR-29 by arginine-affinity chromatography. *J. Chromatogr. B* 951–952, 16–23. doi:10.1016/j.jchromb.2014.01.020
- Pereira, P., Sousa, A., Queiroz, J., Figueiras, A., and Sousa, F. (2014). New approach for purification of pre-miR-29 using lysine-affinity chromatography. *J. Chromatogr. A* 1331, 129–132. doi:10.1016/j.chroma.2014.01.033
- Pernak, J., Sobaszekiewicz, K., and Mirska, I. (2003). Anti-microbial activities of ionic liquids. *Green Chem.* 5 (1), 52–56. Available at: <http://xlink.rsc.org/?DOI=b207543c>. doi:10.1039/B207543C
- Qian, J., Tang, Q., Cronin, B., Markovich, R., and Rustum, A. (2008). Development of a high performance size exclusion chromatography method to determine the stability of Human Serum Albumin in a lyophilized formulation of Interferon alfa-2b. *J. Chromatogr. A* 1194 (1), 48–56. [Internet]. doi:10.1016/j.chroma.2008.01.040
- Qu, Q., Gu, C., and Hu, X. (2012). Capillary coated with graphene and graphene oxide sheets as stationary phase for capillary electrochromatography and capillary liquid chromatography. *Anal. Chem.* 84 (20), 8880–8890. doi:10.1021/ac3023636
- Quental, M. V., Pedro, A. Q., Pereira, P., Sharma, M., Queiroz, J. A., Coutinho, J. A. P., et al. (2019). Integrated extraction-preservation strategies for RNA using biobased ionic liquids. *ACS Sustain. Chem. Eng.* [Internet] 7 (10), 9439–9448. doi:10.1021/acssuschemeng.9b00688
- Rader, R. A. (2008). (Re)defining biopharmaceutical. *Nat. Biotechnol.* 26 (7), 743–751. doi:10.1038/nbt0708-743
- Ramalho, C. C., Neves, C. M. S. S., Quental, M. V., Coutinho, J. A. P., and Freire, M. G. (2018). Separation of immunoglobulin G using aqueous biphasic systems composed of cholinium-based ionic liquids and poly(propylene glycol). *J. Chem. Technol. Biotechnol.* [Internet] 93 (7), 1931–1939. doi:10.1002/jctb.5594
- Rasmussen, A. S. B., Hammou, A., Poulsen, T. F., Laursen, M. C., and Hansen, S. F. (2021). Definition, categorization, and environmental risk assessment of biopharmaceuticals. *Sci. Total Environ.* 789, 147884. doi:10.1016/j.scitotenv.2021.147884
- Rathore, A. S., and Kapoor, G. (2015). Application of process analytical technology for downstream purification of biotherapeutics. *J. Chem. Technol. Biotechnol.* 90 (2), 228–236. doi:10.1002/jctb.4447
- Ren, G., Gong, X., Wang, B., Chen, Y., and Huang, J. (2015). Affinity ionic liquids for the rapid liquid-liquid extraction purification of hexahistidine tagged proteins. *Sep. Purif. Technol.* 146, 114–120. doi:10.1016/j.seppur.2015.03.025
- Reslan, M., Ranganathan, V., Macfarlane, D. R., and Kayser, V. (2018). Choline ionic liquid enhances the stability of Herceptin® (trastuzumab). *Chem. Commun.* 54 (75), 10622–10625. Available at: <http://xlink.rsc.org/?DOI=C8CC06397D>. doi:10.1039/C8CC06397D
- Roque, A. C. A., Silva, S. O., and Angela, M. (2007). Affinity-based methodologies and ligands for antibody purification: Advances and perspectives. *J. Chromatogr. A* 1160, 44–55. doi:10.1016/j.chroma.2007.05.109
- Rosa, P. A. J., Ferreira, I. F., Azevedo, A. M., and Aires-Barros, M. (2010). Aqueous two-phase systems: A viable platform in the manufacturing of biopharmaceuticals. *J. Chromatogr. A* [Internet] 1217, 2296–2305. doi:10.1016/j.chroma.2009.11.034
- Santos, J. H. P. M., Feitosa, V. A., Meneguetti, G. P., Carretero, G., Coutinho, J. A. P., Ventura, S. P. M., et al. (2022). Lysine-PEGylated cytochrome C with enhanced shelf-life stability. *Biosens. (Basel)*. 12 (2), 94. doi:10.3390/bios12020094
- Santos, J. H. P. M., Flores-santos, J. C., Meneguetti, G. P., Rangel-yagui, C. O., Coutinho, A. P., Vitolo, M., et al. (2018). *In situ* purification of periplasmatic L-asparaginase by aqueous two phase systems with ionic liquids (ILs) as adjuvants. *J. Chem. Technol. Biotechnol.* 93, 1871–1880. doi:10.1002/jctb.5455
- Saraswat, M., Musante, L., Ravidá, A., Shortt, B., Byrne, B., and Holthofer, H. (2013). Preparative purification of recombinant proteins: Current status and future trends. *Biomed. Res. Int.* 2013, 1–18. doi:10.1155/2013/312709
- Sava, G. (1996). Pharmacological aspects and therapeutic applications of lysozymes. *EXS* 75, 433–449. doi:10.1007/978-3-0348-9225-4\_22
- Schindl, A., Hagen, M. L., Muzammal, S., Gunasekera, H. A. D., and Croft, A. K. (2019). Proteins in ionic liquids: Reactions, applications, and futures. *Front. Chem.* [Internet] 7, 1–31. doi:10.3389/fchem.2019.00347/full
- Shu, Y., Chen, X. W., and Wang, J. H. (2010). Ionic liquid-polyvinyl chloride ionomer for highly selective isolation of basic proteins. *Talanta* 81 (1–2), 637–642. doi:10.1016/j.talanta.2009.12.059
- Shukla, A. A., Hubbard, B., Tressel, T., Guhan, S., and Low, D. (2007). Downstream processing of monoclonal antibodies — application of platform approaches. *J. Chromatogr. B* 848, 28–39. doi:10.1016/j.jchromb.2006.09.026
- Shukla, A. A., and Thömmes, J. (2010). Recent advances in large-scale production of monoclonal antibodies and related proteins. *Trends Biotechnol.* [Internet] 28 (5), 253–261. doi:10.1016/j.tibtech.2010.02.001
- Soares, B. P., Santos, J. H. P. M., Martins, M., Almeida, M. R., Santos, N. V., Freire, M. G., et al. (2021). Purification of green fluorescent protein using fast centrifugal partition chromatography. *Sep. Purif. Technol.* 257, 117648. doi:10.1016/j.seppur.2020.117648
- Soares, R. R. G., Azevedo, A. M., Van Alstine, J. M., and Aires-Barros, M. R. (2015). Partitioning in aqueous two-phase systems: Analysis of strengths, weaknesses, opportunities and threats. *Biotechnol. J.* [Internet] 10 (8), 1158–1169. doi:10.1002/biot.201400532
- Song, C. P., Liew, P. E., Teh, Z., Lim, S. P., Show, P. L., and Ooi, C. W. (2018). Purification of the recombinant green fluorescent protein using aqueous two-phase system composed of recyclable CO<sub>2</sub>-based alkyl carbamate ionic liquid. *Front. Chem.* 6, 1–10. doi:10.3389/fchem.2018.00529/full
- Song, H., Yang, C., Yohannes, A., and Yao, S. (2016). Acidic ionic liquid modified silica gel for adsorption and separation of bovine serum albumin (BSA). *RSC Adv.* 6 (109), 107452–107462. doi:10.1039/c6ra23372d
- Taha, M., Almeida, M. R., Silva, F. A. e., Domingues, P., Ventura, S. P. M., Coutinho, J. A. P., et al. (2015). Novel biocompatible and self-buffering ionic liquids for biopharmaceutical applications. *Chem. - A Eur. J.* [Internet] 21 (12), 4781–4788. doi:10.1002/chem.201405693
- Tavares, A. P. M., Neves, M. C., Trindade, T., and Freire, M. G. (2019). “Recovery and purification of (bio) pharmaceuticals using (nano) materials,” in *Recent advances in analytical techniques*, 1–36.
- The, M.-J. (1989). Human insulin: DNA technology’s first drug. *Am. J. Heal. Pharm.* 46, S9–S11. Available at: [https://academic.oup.com/ajhp/article/46/11\\_Suppl/S9/5179129](https://academic.oup.com/ajhp/article/46/11_Suppl/S9/5179129).
- Thomas, T. M., Shave, E. E., Bate, I. M., Gee, S. C., Franklin, S., and Rylatt, D. B. (2002). Preparative electrophoresis: A general method for the purification of polyclonal antibodies. *J. Chromatogr. A* 944, 161–168. doi:10.1016/s0021-9673(01)01283-3
- Todinova, S., Guncheva, M., and Yancheva, D. (2016). Thermal and conformational stability of insulin in the presence of imidazolium-based ionic liquids. *J. Therm. Anal. Calorim.* 123 (3), 2591–2598. [Internet]. doi:10.1007/s10973-016-5287-z
- Tsang, L., and Cortez, N. (2010). “Biopharmaceuticals: Definition and regulation,” in *Pharmaceutical Sciences encyclopedia* [internet] (Hoboken, NJ, USA: John Wiley & Sons), 1–18. doi:10.1002/9780470571224.pse160
- US Food and Drug Administration (2018). *What are “biologics” questions and answers.* [Internet]. [cited 2022 Oct 20]. Available at: <https://www.fda.gov/about-fda/center-biologics-evaluation-and-research-cber/what-are-biologics-questions-and-answers>.
- Vicente, F. A., Bairos, J., Roque, M., Coutinho, J. A. P., Ventura, S. P. M., and Freire, M. G. (2019). Use of ionic liquids as cosurfactants in mixed aqueous micellar two-phase systems to improve the simultaneous separation of immunoglobulin G and human serum albumin from expired human plasma. *ACS Sustain. Chem. Eng.* [Internet] 7 (17), 15102–15113. doi:10.1021/acssuschemeng.9b03841
- Vicente, F. A., Castro, L. S., Mondal, D., Coutinho, J. A. P., Tavares, A. P. M., Ventura, S. P. M., et al. (2022). Purification of immunoglobulin Y from egg yolk using thermoresponsive aqueous micellar two-phase systems comprising ionic liquids. *Sep. Purif. Technol.* [Internet] 288, 120589. doi:10.1016/j.seppur.2022.120589
- Vijayaraghavan, R., Izgorodin, A., Ganesh, V., Surianarayanan, M., and MacFarlane, D. R. (2010). Long-term structural and chemical stability of DNA in hydrated ionic liquids. *Angew. Chem. Int. Ed.* 49 (9), 1631–1633. [Internet]. doi:10.1002/anie.200906610
- Walsh, G. (2018). Biopharmaceutical benchmarks 2018. *Nat. Biotechnol.* 36 (12), 1136–1145. doi:10.1038/nbt.4305
- Wang, W. (2015). Advanced protein formulations. *Protein Sci.* [Internet] 24 (7), 1031–1039. doi:10.1002/pro.2684
- Xu, P., Wang, Y., Chen, J., Wei, X., Xu, W., Ni, R., et al. (2018). A novel aqueous biphasic system formed by deep eutectic solvent and ionic liquid for DNA partitioning. *Talanta* 189, 467–479. doi:10.1016/j.talanta.2018.07.035
- Yen, Y.-H., and Chu, Y.-H. (2004). Synthesis of tetrahydro- $\beta$ -carboline-diketopiperazines in [bdmim][PF<sub>6</sub>] ionic liquid accelerated by controlled microwave heating. *Tetrahedron Lett.* [Internet] 45 (44), 8137–8140. doi:10.1016/j.tetlet.2004.09.056
- Yuan, S., Deng, Q., Fang, G., Pan, M., Zhai, X., and Wang, S. (2012). A novel ionic liquid polymer material with high binding capacity for proteins. *J. Mater. Chem.* 22 (9), 3965–3972. doi:10.1039/c2jm14577d
- Zhao, G., Chen, S., Chen, X. W., and He, R. H. (2013). Selective isolation of hemoglobin by use of imidazolium-modified polystyrene as extractant. *Anal. Bioanal. Chem.* 405 (15), 5353–5358. doi:10.1007/s00216-013-6889-y
- Zijlstra, G. M., Michielsen, M. J. F., Gooijer, C. D. D., PolVan Der, L. A., and Tramper, J. (1998). IgG and hybridoma partitioning in aqueous two-phase systems containing a dye-ligand. *Bioseparation* 7, 117–126. doi:10.1023/a:1008079626929





## OPEN ACCESS

## EDITED BY

Sidney J. L. Ribeiro,  
São Paulo State University, Brazil

## REVIEWED BY

Wenli Zhang,  
Guangdong University of Technology,  
China  
Qian Mao,  
The Pennsylvania State University (PSU),  
United States

## \*CORRESPONDENCE

Priscilla Brosler,  
✉ [broslerp@ua.pt](mailto:broslerp@ua.pt)

## SPECIALTY SECTION

This article was submitted to  
Carbon-Based Materials,  
a section of the journal  
Frontiers in Materials

RECEIVED 16 August 2022

ACCEPTED 14 March 2023

PUBLISHED 23 March 2023

## CITATION

Brosler P, Girão AV, Silva RF, Tedim J and  
Oliveira FJ (2023), In-house vs.  
commercial boron-doped diamond  
electrodes for electrochemical  
degradation of water pollutants: A  
critical review.  
*Front. Mater.* 10:1020649.  
doi: 10.3389/fmats.2023.1020649

## COPYRIGHT

© 2023 Brosler, Girão, Silva, Tedim and  
Oliveira. This is an open-access article  
distributed under the terms of the  
[Creative Commons Attribution License](https://creativecommons.org/licenses/by/4.0/)  
(CC BY). The use, distribution or  
reproduction in other forums is  
permitted, provided the original author(s)  
and the copyright owner(s) are credited  
and that the original publication in this  
journal is cited, in accordance with  
accepted academic practice. No use,  
distribution or reproduction is permitted  
which does not comply with these terms.

# In-house vs. commercial boron-doped diamond electrodes for electrochemical degradation of water pollutants: A critical review

Priscilla Brosler\*, Ana Violeta Girão, Rui F. Silva, João Tedim and  
Filipe J. Oliveira

Department of Materials and Ceramic Engineering, CICECO—Aveiro Institute of Materials, University of Aveiro, Aveiro, Portugal

Boron-doped diamond (BDD) electrodes are eco-friendly and widely used in efficient water remediation through electrochemical advanced oxidation processes (EAOPs). These anodes can completely mineralize a wide range of pollutants, only requiring electrical energy. Over the last 2 decades, numerous commercially available BDD electrodes have emerged, but little is known about their electrooxidation performance, particularly if compared to laboratory-produced anodes by different research groups. In this critical review, a comparison between in-house-made and commercially available BDD electrodes based on a systematic literature review (SLR) is carried out. SLR was quite useful in locating and selecting the scientific publications relevant to the topic, enabling information gathering on dissemination, growth, and trends in the application of BDD electrodes in the degradation of water pollutants. More specifically, data concerning the origin of the employed BDD electrodes, and their physicochemical properties were extracted from a thorough selection of articles. Moreover, a detailed analysis of the main parameters affecting the BDD electrodes' performance is provided and includes selection and pre-treatment of the substrate material, chemical vapor deposition (CVD) method, deposition parameters, characterization methods, and operational conditions. This discussion was carried out fully based on the numerous performance indicators found in the literature. Those clearly revealed that there are only a few analogous points across works, demonstrating the challenge of establishing an accurate comparison methodology. In this context, we propose a figure-of-merit equation which aims at normalizing BDD degradation results for a specific contaminant, even if working under different experimental conditions. Two case studies based on the degradation of solutions spiked with phenol and landfill leachate treatment with commercial or in-house-made BDD electrodes are also presented. Although it was not possible to conclude which electrode would be the best choice, we propose a set of guidelines detailing a consistent experimental procedure for comparison purposes in the future.

## KEYWORDS

bibliometrics, doped diamond, cvd, electrooxidation, wastewater, commercial electrodes, energy consumption



## 1 Introduction

Over the last 2 decades, boron-doped diamond (BDD) has gained increased attention and has been extensively studied for electrochemical applications due to its distinct physical and chemical properties from conventional electrode materials. These include a wide electric potential window in aqueous and non-aqueous solutions (Swain et al., 2013; Martin et al., 2019), good stability and corrosion resistance (Ramesham and Rose, 1997; Swain, 2019), inert surface with low adsorption (Swain, 1994), low double-layer capacitance and background current (Swain and Ramesham, 2002), high current density electrolysis ( $1\text{--}10\text{ A.cm}^{-2}$ ) (Luong et al., 2009), and high overpotential for both hydrogen and oxygen evolution (Martin et al., 2019).

The electric potential window of BDD electrodes is much wider than that of any other material (Brillas and Martínez-Huitle, 2011), with the hydrogen evolution reaction (HER) starting at about  $-1.2\text{ V/SHE}$  (Standard hydrogen electrode) and the oxygen evolution reaction (OER) at approximately  $+2.3\text{ V/SHE}$  (Swain et al., 2013; Martin et al., 2019). This broad potential window arises from the BDD's high overvoltage for water splitting (Brillas and Martínez-Huitle, 2011). The HER and OER are inner-sphere reactions that generally consist of multi-step electron transfer reactions that depend on reaction intermediates' adsorption (He et al., 2019). The carbon  $\text{sp}^3$ -hybridized orbitals in diamond show weak adsorption ability towards these intermediates and, consequently, the catalytic effect for HER and OER in BDD electrodes is weak (Brillas and Martínez-Huitle, 2011). The diamond  $\text{sp}^3$ -hybridized orbitals form strong covalent bonds and are responsible for the BDD's good stability and corrosion resistance. Studies have shown that BDD electrodes are stable in strong acid media, even for long-term cycling of potential ranging from hydrogen to oxygen evolution reaction overpotentials (Ramesham and Rose, 1997; Swain, 2019). Electrodes based on conventional materials such as glassy carbon or graphite usually have higher surface adsorption ability, forming a polymeric adhesive film on their surface, leading to electrode fouling (Luong et al., 2009). The  $\text{sp}^2$ -hybridized orbitals present in the surface of these electrodes increase the adsorption strength (Medeiros de Araújo et al., 2014), while the  $\text{sp}^3$ -hybridized orbitals present in the diamond structure shows weak adsorption capacity (Brillas and Martínez-Huitle, 2011). Electrode fouling is easily avoided in BDD electrodes if working above the potential region of water splitting (Iniesta, 2001). BDD electrodes can also be self-cleaned through the polarization of such polymeric films (Ryl et al., 2016). The surface of BDD electrodes resists deactivation processes, showing stable voltametric responses towards  $\text{Fe}(\text{CN})_6^{4-/3-}$  even after 2 weeks of continuous potential cycling (Swain, 1994). BDD electrodes are also particularly interesting for electroanalysis and sensing applications since they present low background current and consequent low double-layer capacitance, resulting in lower detection limits for trace analysis when compared to other sensors (Stanković and Kalcher, 2016). The above-mentioned excellent electrochemical behavior of BDD electrodes can vary drastically depending on their physicochemical properties.

More important is the role BDD anodes are currently playing in water remediation through OER and the generated oxygen-based radicals that can completely eliminate a wide range of pollutants,

including non-biodegradable compounds (Cornejo et al., 2021). Recent reviews on the electrochemical degradation of contaminants with BDD electrodes can be found in the literature (Cobb et al., 2018; Freitas et al., 2019; Ganiyu and Martínez-Huitle, 2019; He et al., 2019; McBeath et al., 2019; Nidheesh et al., 2019; Trellu et al., 2019; Cornejo et al., 2020; Clematis and Panizza, 2021a; Karim et al., 2021; Bogdanowicz and Ryl, 2022; Crispim et al., 2022; De Luna and Bensalah, 2022; He et al., 2022; Mousset, 2022; Oliveira et al., 2022; Wang et al., 2022). These include studies performed using BDD anodes prepared by chemical vapor deposition (CVD), commercially available and in-house-made, and applied in spiked water and real wastewater treatment systems.

In this critical review, we will evaluate if it is possible to compare the performance of commercial BDD electrodes with those produced in-house towards electrooxidation of water pollutants. We will also discuss how the CVD deposition conditions, the physicochemical properties of the anodes, and the electrooxidation process influence the interpretation of the degradation efficiency results. This assessment will be carefully carried out using bibliometric analysis. Afterwards, an attempt will be made to reach a consensus on possible guidelines and/or degradation performance indicators for future comparison of BDD electrodes from different origins.

## 2 Electrochemical degradation of contaminants with BDD electrodes: A bibliometric analysis

Bibliometrics is a research method that uses quantitative and statistical analysis to describe patterns in publications. Bibliometric studies are frequently used to investigate structural interrelationships and to increase the understanding of a specific subject state of the art (Donthu et al., 2021). In order to properly carry out these studies, it is essential to know Lotka's inverse square laws regarding the calculation of authors' productivity, Bradford's law for the dispersion of authors in different journals, and Zipf's law concerning the frequency of words in each document (Guedes and Borschiver, 2005; Araújo, 2006). Systematic literature review (SLR) was chosen as the method of searching for publications since it is widely used and because it is a structured way of locating and selecting the relevant publications, increasing the reproducibility and reliability of the method (Donthu et al., 2021).

In this work, bibliometric analysis was used 1) to identify the growth and trends in the application of BDD in the degradation of contaminants; 2) to identify the dissemination of information with quantification of publications by journals, universities, and research centers, and by country; and 3) to verify the keywords relationship between themes through their co-occurrence in a network graph. The tools used to visualize the results and create the graphics were Microsoft Excel and VOSViewer (van Eck and Waltman, 2010).

The bibliometric search of the topic "electrochemical degradation of contaminants with BDD electrodes" was carried out by a Boolean advanced search query in the Scopus database through a search string connecting the topics by the title field of publications in April 2022. The details of this search query can be found in the [Supplementary Table S1](#). A total of 875 articles meeting the established criteria were obtained. The search was restricted to

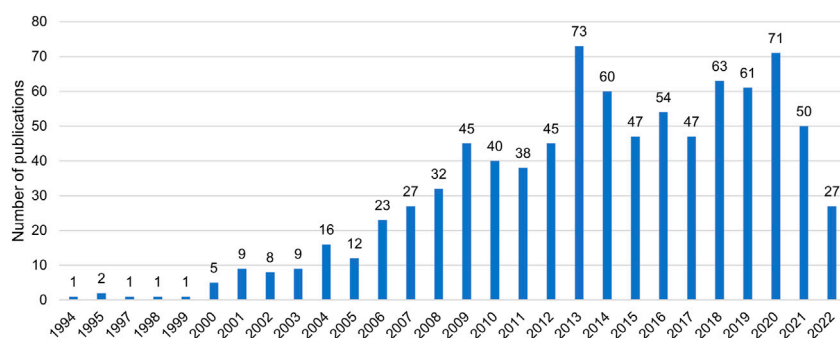


FIGURE 1

Number of publications per year on BDD as an electrode for electrooxidation of contaminants, based on the Scopus database (source: the authors).

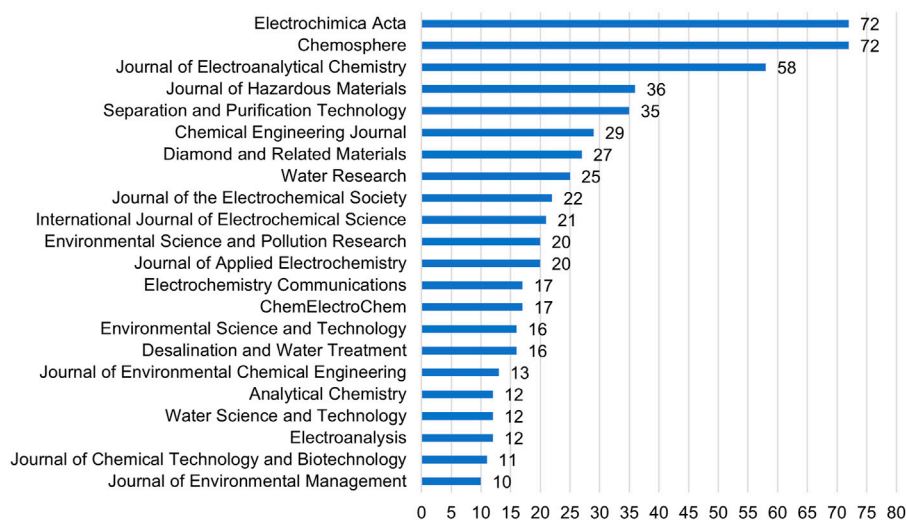


FIGURE 2

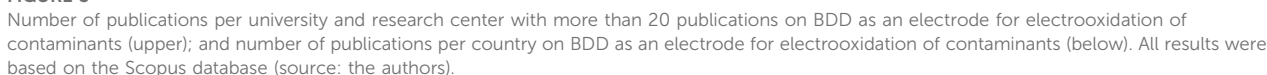
Number of publications per journal with more than 10 publications on BDD as an electrode for electrooxidation of contaminants, based on the Scopus database (source: the authors).

scientific articles as the document type and only to the English language. This result went through a process of elimination of duplicates and irrelevant results (not related to the subject), reaching a final number of 868 publications for further bibliometric analysis. The list of strings used in the search query was defined based on a previous broader search in which the fundamental terms used to describe the electrochemical degradation of contaminants were identified (Supplementary Table S2). Figure 1 illustrates the number of publications per year on BDD as an electrode for electrooxidation of contaminants.

The first publication identified in the SLR was published in 1994 (Mitra et al., 1994), although the first one ever reported on the electrochemical behavior of CVD diamond dates back to 1987 (Pelskov et al., 1987). However, the latter does not address pollutant degradation studies. In the early 1990s, studies of BDD used as electrodes began to emerge all over the world: Japan (Patel et al., 1992), the United States (Swain, 1994; Swain and Ramesham, 2002) or China (Zhu J. Z. et al., 1995; Zhu P. et al., 1995). The

number of publications increased rapidly in the 2000s, reaching a peak of 73 publications in one single year (2013). Nearly the same number of publications was achieved again in 2020. By the time these data were gathered, early 2022 already accounted for 27 publications, clearly indicating that the topic has excellent scientific relevance and is still extensively explored. The dissemination of information was identified through the analysis of publications by journals, as shown in Figure 2.

Articles on the topic were published in more than 160 different journals. *Chemosphere*, *Electrochimica Acta*, and *Journal of Electroanalytical Chemistry* published around 23% of all the articles on BDD as an electrode for electrooxidation of contaminants. Therefore, researchers on this subject should consult information primarily in these three journals. Figure 3 presents the bibliometric study finding the dissemination of information by universities and research centers with more than 20 publications on the topic, as well as the number of publications per country.



across the literature. In the red cluster, pesticides appear as the primarily studied pollutant. The purple cluster represents the analysis of energy consumption by the electrooxidation processes using BDD anodes, and the cyan cluster is mainly related to wastewater disinfection. BDD electrochemistry, electrochemical oxidation of phenol and dyes, and the toxicity of the resulting by-products are featured in the green cluster. The blue one involves water treatment containing pharmaceuticals (primarily studied contaminants) by different EAOPs (anodic oxidation, electro-Fenton, and photoelectron-Fenton). This cluster includes intermediate oxidation products such as carboxylic acids (oxalic, acetic, or formic), often used as models to investigate the reaction mechanisms and electrocatalytic properties of the anode materials (de Queiroz et al., 2017). The yellow group gathers information on the production of hydroxyl radicals and carboxylic acid intermediates during the final

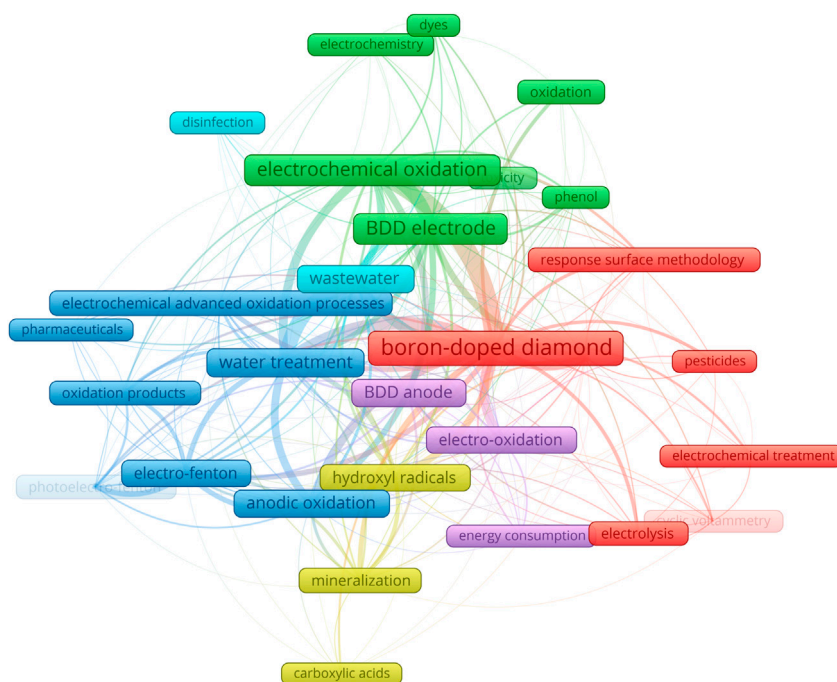


**FIGURE 4**

Keywords co-occurrence network (minimum of 10 occurrences) representation of the trends on the application of BDD anodes in the degradation of contaminants and corresponding relationship within the main themes, sorted in six clusters represented in different colors, based on the Scopus database and VOSviewer as the bibliometric network graph software (source: the authors).

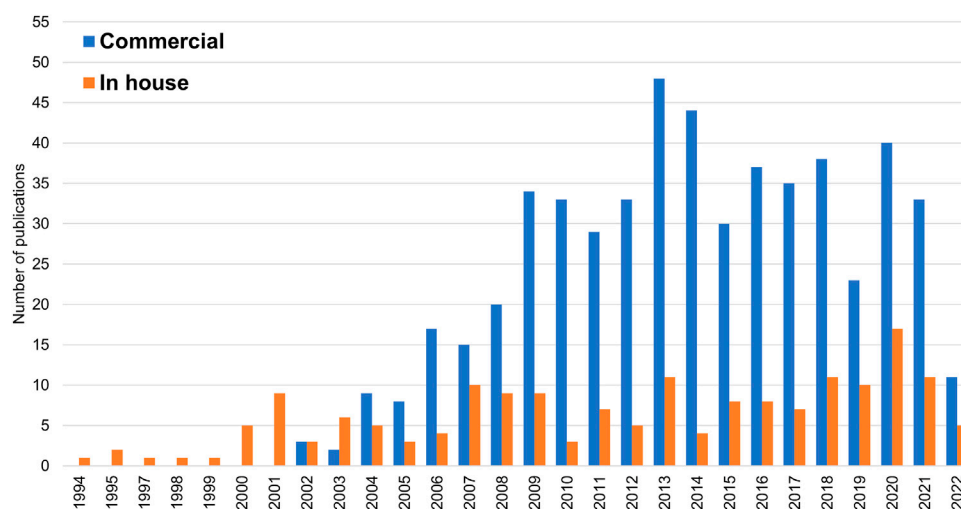


**FIGURE 5**

Number of publications per year on commercial and in-house BDD anodes in the degradation of contaminants, based on the bibliometric analysis search (source: the authors).

mineralization process. Overall, the keyword network graph in Figure 4 reveals that BDD anodes for water remediation have been primarily used in the electrooxidation of pharmaceuticals, pesticides, carboxylic acids, phenolic compounds, dyes, and for water disinfection of bacteria and viruses.

SLR verified that the degradation of water pollutants through BDD electrodes is a subject particularly targeted in the last 2 decades, highly relevant (mentioned in more than 160 journals) and studied on all continents. The keywords co-occurrence network map allowed the identification of the most studied types of water



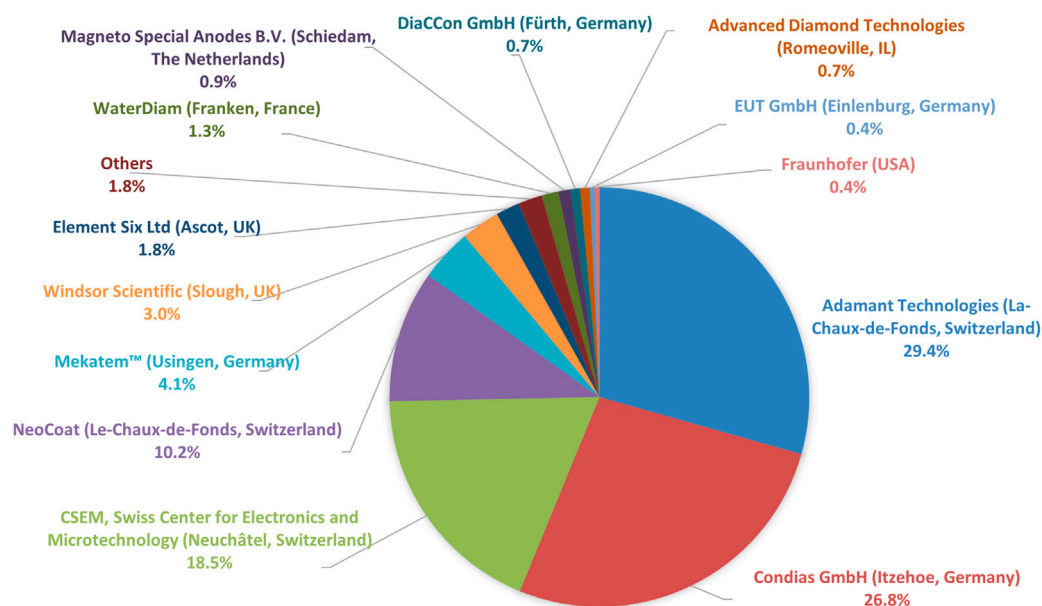


**FIGURE 6**  
Commercial BDD manufacturer preference based on the bibliometric analysis search (source: the authors).

pollutants and applied EAOPs, as well as other relevant issues to the degradation process: the generation of by-products and their toxicity and associated energy consumption/costs.

### 3 Utilization of laboratory produced and commercial BDD electrodes

From 1994 to 2001, electrooxidation of pollutants using BDD anodes was exclusively performed with lab-made electrodes (Figure 5). Commercial BDD electrodes started to gain ground and were first reported in 2002. The number of studies considering the application of commercial BDD anodes increased, and since 2006 they are around 4 times greater (average) than those using in-house-made electrodes. However, only 20% of the 868 identified publications were related to laboratory-made BDD anodes, and 63% applied commercially available electrodes. The remaining unspecified 17% of the reported studies can probably be associated with commercial BDD electrodes, which would sum up to 80% of the publications implementing such electrodes. Such a high percentage of the use of commercial electrodes may indicate the technology's maturity is being achieved.

Figure 6 shows the distribution of the companies whose BDD electrodes were used in the analyzed publications. A list of commercial BDD suppliers, including companies that did not appear in the articles from the SLR, is available in the Supplementary Table S3. Commercial electrodes from Adamant Technologies (Switzerland) and NeoCoat (Switzerland), which are spin-off companies of CSEM (Switzerland), together with those manufactured by CSEM itself, sum up to 58% of presence in the articles from the SLR, followed by 26.8% from Condias GmbH (Germany), and 4.1% from Mekatem™ (Germany).

Commercially manufactured BDD electrodes may offer greater reproducibility since companies are committed to delivering high quality and reproducible materials to their clients but are also costly and with a fixed set of morphological and electrochemical characteristics, such as  $sp^3/sp^2$  ratio, boron doping level, film morphology and thickness, electrochemical potential window, capacitance, among others. Nevertheless, they enable numerous research groups without in-house CVD equipment to explore the use of such BDD electrodes in their studies, further expanding their application range and effectively contributing to knowledge expansion of these thin films.

The main advantage of producing in-house BDD electrodes is growing customizable films by exploring and controlling their properties, such as the  $sp^3/sp^2$  ratio, thickness, boron doping level, growth rate, and grain size. These properties strongly define the working potential window of the electrode, its conductivity and selectivity. Hence, in theory, precise BDD films can be created and adapted to each type of target pollutant. In addition, in-house BDD deposition allows the exploration of different deposition conditions and/or substrate materials. The full potential of BDD electrodes can only be attained by appropriate and specific electrode design for each application and/or target contaminant (Bogdanowicz and Ryl, 2022).

Nonetheless, in-house BDD film deposition may also imply lower reproducibility, depending on the CVD reactors used and their operability. Additionally, the overall area of the BDD films is limited by the volume and operation design of the CVD chamber reactor (Mehedi et al., 2014), typically smaller than the commercial ones. The in-house production of BDD electrodes is expensive for universities and research centers, when including the cost of the CVD equipment and the process associated costs such as electricity consumption, water cooling system, and reactive gases (Railkar et al., 2000). Furthermore, a well-prepared infrastructure is mandatory to

meet all the necessary safety requirements, including electrical hazards and the use of dangerous reactive gases. These, and the lack of know-how, contribute to limiting the spread of such equipment in laboratories working mostly on water purification processes.

## 4 BDD electrodes from different sources

It is a challenge to compare the performance of different in-house BDD electrodes regarding the electrooxidation of water pollutants. First, the design and working conditions of the adopted CVD technique can vary widely: the deposition method (hot-filament -HFCVD, or microwave plasma -MPCVD); the experimental deposition parameters ( $\text{CH}_4/\text{H}_2$  ratio, pressure, substrate temperature, boron doping source,  $[\text{B}]/[\text{C}]$  ratio); and the substrate material and its prior preparation (Gracio et al., 2010; May et al., 2011). Altogether, these parameters will influence the final physicochemical properties of the BDD electrode, such as  $\text{sp}^3/\text{sp}^2$  ratio, effective boron doping level, grain size, film thickness, electrical conductivity, electrochemical potential window, oxygen evolution potential (OEP), electron transfer rate, surface roughness, and surface termination (May et al., 2011; Salgueiredo et al., 2011; Huang et al., 2021; Sharma et al., 2022).

Second, the application of the BDD anodes in the electrooxidation of contaminants includes several other accountable factors such as the degradation conditions used in the experiments (current density, type of EAOP, pH and type of electrolyte, active electrode area, volume of solution, type and concentration of the pollutant, electrochemical cell design, or fluid dynamics), and the water system itself (spiked water or real wastewater) (Sires et al., 2014; Cano et al., 2016; Xu, 2016; Ma et al., 2018).

The number of publications concerning BDD anodes in electrochemistry has drastically increased due to the emergence of commercial BDD manufacturers. It broadened the application of BDD electrodes resulting in high-quality publications but further entangled possible comparisons between electrodes' performance. Most reports on tested commercial BDD electrodes lack information on their physicochemical properties and preparation process. The manufacturing process of such complex thin films dictates their performance (Einaga et al., 2014), and it may vary significantly from one company to another. In this section, we discuss how these factors control the final physicochemical properties of BDD coatings, hence their implementation in degrading pollutants present in water systems.

### 4.1 Substrate material and preparation

In the preparation of BDD electrodes, the primary function of the substrate for electrochemical applications is to allow the flow of electric current through the electrode, providing physical support to the thin film and conferring enough mechanical stability to the electrode (Chen, 2004). The first thing to keep in mind is that the substrate nature might influence the BDD final properties. Thus, its selection must meet criteria such as stability under extreme

conditions (high current density, intense erosive and/or abrasive wear, and strong acids or bases media) (Yang et al., 2022).

Ideally, the substrate material must withstand the CVD deposition conditions, present high affinity towards diamond thin film growth, high mechanical strength, good electrical conductivity, and electrochemical inertness or the ability to easily form a protective passivation layer on its surface (Chen, 2004; He et al., 2019). A carbide buffer layer may be formed during CVD deposition, restricting further substrate carburization and promoting easy diamond nucleation and crystal growth (Xiang-Liu et al., 1991). Furthermore, a substrate material with low carbon solubility and diffusion coefficient yields higher diamond nucleation rates (Yang et al., 2022). Temperature gradients interfere with the surface reactions and diamond growth kinetics (Bushuev et al., 2017). Therefore, the diffusion coefficient of the carbon atoms, the substrate thermal conductivity, and its coefficient of thermal expansion (CTE) influence the adhesion strength of the diamond thin film, grain size, growth rate, and residual stress, dictating its service life (Yang et al., 2022).

Several materials have been proved suitable substrates for BDD deposition, including Si, Nb, Ta, W, Mo, Ti, Zr, and graphite (Fryda et al., 1999; Shaw et al., 2002; Chaplin et al., 2011); dielectric ceramics (Neto et al., 2012); high pressure-high temperature (HPHT) diamond (Denisenko et al., 2008); carbon fibers (Jian et al., 2021);  $\text{SiO}_2$  fibers (Zhang et al., 2020); carbon nanotubes (Zanin et al., 2014);  $\text{TiO}_2$  nanotubes (Vernasqui et al., 2021); or metal foams (Zhang J. et al., 2019). Polished silicon wafers are by far the most applied substrate material, being identified in more than 36% of the published articles (Supplementary Figure S1), especially *p*-doped Si commercial wafers. Their characteristic low electrochemical activity and ability to form stable and compact oxide films help prevent film delamination (Brito et al., 2018). However, Si substrates still have many limitations for large-scale applications since they are not suitable in aggressive water treatment environments, mainly due to their relatively low conductivity and brittleness (Yu et al., 2014). Contrary to Si substrates' short durability, Nb/BDD electrodes have shown a lifetime of more than 850 h during electrolysis (0.5 M  $\text{H}_2\text{SO}_4$ ) at very high current densities such as 10 A/cm<sup>2</sup> (Fryda et al., 1999). The SLR indicates that currently, the second most used substrate material is Nb, followed by Ti and Ta, which are metals capable of forming stable and protective passivation layers. It is important to emphasize that Nb became the preferred choice of substrate material over the years (Supplementary Figure S2) and, since 2013, started to surpass the use of Si substrates. Roughly, the approximate substrate stability for diamond film deposition obeys the following order: Ta > Si > Nb > W > Ti (Chaplin et al., 2011). The CTE of the substrate material is the main factor influencing its compatibility with the BDD film deposition and ideally, it should be as close as possible to that of diamond ( $0.7\text{--}2.0 \times 10^{-6} \text{ K}^{-1}$ ) (Moelle et al., 1997; Luong et al., 2009; Gracio et al., 2010). A CTE mismatch can cause delamination of the BDD film with possible consequent corrosion of the substrate due to electrolyte permeation through the thin film (Chaplin et al., 2011). Nevertheless, the high cost of Nb, Ta, and W substrates makes them unattainable for widespread use in large-scale applications (Nidheesh et al., 2019). Ti has been considered a desirable substrate among those mentioned above due to its lower cost, high conductivity, corrosion resistance, and

excellent mechanical properties (Braga et al., 2009). Yet, Ti/BDD electrodes have shown short service life due to the formation of a TiC intermediate layer generated by the diffusion of carbon species onto the metal during the deposition, resulting in a rough and porous structure that promotes early deterioration of the BDD film adhesion and stability (Fryda et al., 1999; Lim et al., 2008; He et al., 2019). The most likely reasons of electrode failure are assumed to be the TiC layer corrosion at the substrate/film interface, the quality and adhesion of the BDD film, the residual stress produced in the CVD process, and the degradation of the diamond film (Lu X. R. et al., 2019). According to Lu et al., the delamination process occurs in two main stages. The first stage of electrode failure is caused mainly by pore-type defects in the BDD films that allow the electrolyte to penetrate the BDD film and corrode the TiC intermediate layer, which is unstable and quickly decomposes causing the BDD film to delaminate from the substrate. The second stage is caused primarily by corrosion holes created in the Ti substrate. Several attempts have been made to improve the service life of Ti/BDD electrodes, such as developing multilayered structures or increasing the boron concentration in the CVD deposition to inhibit the TiC layer growth, with different levels of success (Guo and Chen, 2007; Gerger and Haubner, 2008; Sun et al., 2012; Kwon et al., 2019).

Following the choice of the appropriate substrate material, its pre-treatment for CVD deposition may also affect the final characteristics of the BDD film. The surface properties of the substrate influence the diamond film roughness, adhesion strength, and electroactivity (Guimaraes et al., 2020). Diamond growth over non-diamond materials usually requires pre-treatment of their surface by a seeding stage (Spitsyn et al., 1981). This is necessary to obtain proper diamond nucleation density with a complete and packed growth of the thin film, without any substrate area exposed to the solution, which could compromise the working electrode. An effective seeding process depends on the size of the diamond abrasive particles, processing time, and the adopted method (e.g., manually scratching, ultrasonic bath). There are a few studies reporting on the effect of substrate preparation on the nucleation and growth of BDD films (Chaplin et al., 2011; da Silva et al., 2018) showing that ultrasonic seeding is more effective than seeding through manual scratching. In addition, a rougher Nb substrate prepared by sandblasting with alumina particles (75–106 µm) resulted in the most effective electrode lifetime compared to that with the untreated substrate or the sandblasted one with smaller alumina particles (Choi et al., 2017).

Considering the direct influence of the substrate material on the electrochemical properties of BDD, when Nb/BDD (planar) and Ti/BDD (Ti mesh) electrodes were compared for phenol degradation, Nb/BDD showed the best performance (Hangarter et al., 2015). However, the electrodes had different geometries (consequently, different specific areas), boron doping levels, and different film thicknesses, limiting comparisons between the different metallic substrates. Si/BDD and Nb/BDD electrodes have been compared in different studies for the electrooxidation of acid violet 7 dye (Brito et al., 2018) and norfloxacin (da Silva et al., 2018). In both cases, the Si/BDD electrode showed higher removal rates with lower associated energy consumption. BDD films deposited over Nb, Si, Ti, and TiNx/Ti by HFCVD were compared in terms of their performance, particularly chemical oxygen demand (COD) removal and

*Escherichia coli* sterilization from livestock wastewaters (Kwon et al., 2019). The TiNx/Ti/BDD electrode with a TiNx intermediate layer showed better performance and higher service life than Nb/BDD, Si/BDD, and Ti/BDD. It is quite difficult to evaluate the effect of the substrate material on the BDD electrodes' performance since the published experimental conditions and parameters are not described in detail. Finally, a recent study (Yang et al., 2022) is perhaps the most systematic and complete comparison to determine the substrate effect, providing enough detailed information on the BDD deposition and substrate preparation conditions and characterization. The influence of the substrate material (Si, Ta, Nb, and Ti substrates) was examined in terms of electrochemical properties, microstructure, degradation of the antibiotic tetracycline, and service life of the identically deposited BDD films. Their results showed that the physicochemical properties of the substrate have a significant impact on the growth and microstructure of the BDD film, and the growth rate followed: Si > Ta > Nb >> Ti. In addition, the surface finish of both substrate and BDD film also influenced the performance of the BDD electrode. The Ti/BDD electrode showed the best performance in terms of OEP, background current, electron transfer kinetics, and energy consumption, but far shorter service life than Si/BDD, Ta/BDD, and Nb/BDD. In terms of tetracycline removal and current efficiency, the performance of the electrodes followed: Si/BDD > Ti/BDD > Nb/BDD > Ta/BDD. Yang et al. indicated that the type of substrate does not significantly affect the boron doping level and diamond quality of BDD electrodes. However, they suggest that the degradation performance of BDD electrodes is affected by the intermediate carbide interlayers formed in the interface between the substrate and the BDD film during CVD deposition. These interlayers are closely related to the substrate material and affect film thickness, grain size, and electron transfer resistance, thus the surface state of BDD films and, consequently, their organics electrooxidation capability.

Laboratory and pilot tests on wastewaters have been successful in showing the feasibility of BDD electrodes (Li et al., 2014; Bergmann et al., 2015; Wu et al., 2015; Alvarez Pugliese et al., 2016; Souza et al., 2016; Naji et al., 2017; Durán et al., 2018; Salmerón et al., 2019; Roccamante et al., 2020; Tawabini et al., 2020; Maldonado et al., 2021; Monteil et al., 2021; Salmeron et al., 2021), but the absence of a universally appropriate and accepted substrate with a defined size and established durability are a tremendous challenge for large scale application of such anodes. Furthermore, practical long-term application of BDD electrodes (highly stable under anodic polarization) in the degradation of pollutants is still subjected to failure at high applied current densities (e.g., 1 A.cm<sup>-2</sup>), mainly due to poor film adhesion with consequent film delamination (Chaplin, 2014).

The above literature analysis demonstrates that evaluation of the substrate effect on the BDD electrode final performance is not straightforward. It depends on numerous factors leading to very different conclusions. Hence, a further detailed and systematic research is required, and it should also include the complete analysis of the microstructure and physicochemical properties of BDD films like grain size, surface roughness, growth rate, conductivity, sp<sup>3</sup>/sp<sup>2</sup> ratio, residual stress, adhesion strength, electron transfer rate, OEP, electrochemical potential window,

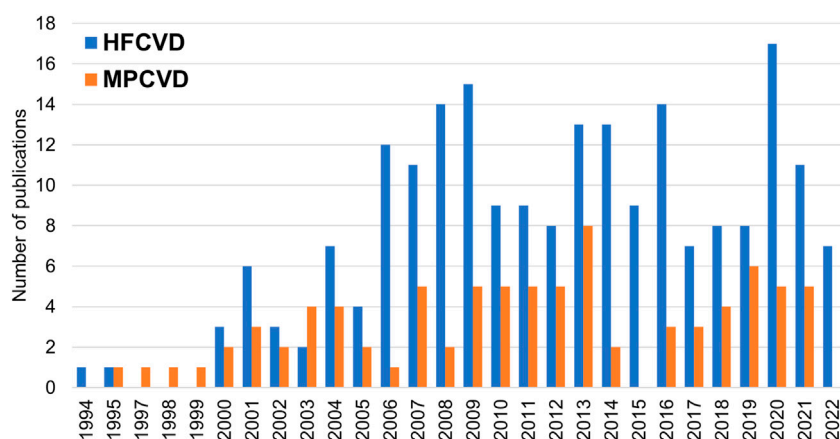


FIGURE 7

Number of publications per year on commercial and in-house BDD anodes, employing HF or MPCVD deposition methods, based on the bibliometric analysis search (source: the authors).

background current, and boron doping level, deposited under the same CVD deposition conditions over several different substrate materials. Then, possible guidelines may be provided for adequate selection of substrate material for the deposition of BDD thin films for specific water treatment applications.

## 4.2 The chemical vapor deposition process

CVD diamond thin films are usually carried out by activating a mixture of a carbon-containing gas (usually methane in low concentration) with molecular hydrogen. During its course, carbon radicals are generated and react with dissociated hydrogen in high concentration to give the diamond growth precursors (Yang et al., 2019). Chemical vapor deposition techniques include hot-filament (HFCVD), RF-plasma (RFCVD), microwave plasma (MPCVD), and related DC plasma, DC arc-jet, or oxy-acetylene flame (Srikanth and Jiang, 2011). Regarding BDD film deposition, SLR detailed analysis indicates that 71.2% of the articles employed hot-filament (HFCVD) and 28.8% microwave plasma (MPCVD), as illustrated in Figure 7.

In HFCVD deposition, an appropriate filament temperature will guarantee molecular hydrogen dissociation, usually obtained at temperatures above 2000°C. The melting point and purity of the metallic filaments (e.g., W, Ta, and Re) are always considered to avoid or minimize their degradation, which causes film contamination (Mehta Menon et al., 1999). Suitable diamond growth kinetics is also dependent on the distance between each of the filaments and that between them and the substrate's surface. In MPCVD, the microwave power and frequency are the important parameters that require careful control and optimization. Microwave frequency can vary from 300 MHz to 300 GHz, with most depositions performed in commercial reactors (e.g., Seki-ASTeX reactors) typically at 2.45 GHz (Schwander and Partes, 2011). MPCVD depositions using higher microwave powers exhibit increased feed gas temperature and dissociation efficiency,

resulting in larger grain sizes and improved growth rates (Tang et al., 2011).

Manufacturers of commercial diamond films tend to adopt the HFCVD method due to the possibility of growing films over large surface areas, similarly to some authors who implemented such method to deposit BDD films over areas as large as 0.5 m<sup>2</sup> (Haenni et al., 2004). In contrast, MPCVD enables higher growth rates, higher phase purity, and better reproducibility since HFCVD temperatures are limited to the filaments' melting point, restricting the concentration of dissociated hydrogen atoms (Macpherson, 2015). The latter is the main reason for using MPCVD in free-standing diamond deposition (Schwander and Partes, 2011). In addition, the degradation of the filaments used in HFCVD can promote metal contamination of the films (Schwander and Partes, 2011), interfering with the quality of the final films and, for example, hindering the film adhesion to the substrate or inducing graphitization points (Griesser et al., 1994; Mehta Menon et al., 1999; Lee et al., 2022). On the other hand, the plasma area is limited by the wavelength of the microwave radiation in the MPCVD method (Macpherson, 2015), greatly restricting industrial-scale production of BDD electrodes for pollutant degradation. The preference for HFCVD is also explained by the simplicity of its apparatus and lower cost compared to MPCVD (Gracio et al., 2010).

As demonstrated in the previous section, a comparison between the distinct deposition parameters used in the production of commercial and in-house electrodes constitutes a challenge. Each CVD reactor has specific dimensions and characteristics, as well as optimized deposition parameters (Einaga et al., 2014). For example, two different reactors using the same deposition conditions will not necessarily yield similar BDD films with the very same characteristics due to geometric constraints within the reactor that directly affect the deposition kinetics (Parikh and Adomaitis, 2006). Tables 1, 2 summarize some of the HFCVD and MPCVD deposition parameters respectively, found in the articles within the SLR.



**TABLE 1** HFCVD deposition conditions present in the literature based on the bibliometric analysis search.

University, research center, or commercial manufacturer	Substrate	CH <sub>4</sub> /H <sub>2</sub> (%)	Boron source	Filament temperature (°C)	Substrate temperature (°C)	Pressure (mbar)	[B]/[C] (ppm)	Ref.
Adamant Technologies (Switzerland)	p-Si; Ti	1.0%	Trimethylborane	2,440–2,560	830	—	100–8,000	Pujol et al. (2020)
Condias GmbH (Germany)	Nb	0.5%–2.5%	Diborane	2,200–2,600	700–925	10–50	500–8,000	Chen et al. (2014)
CSEM, Swiss Center for Electronics and Microtechnology (Switzerland)	p-Si	1.0%	Trimethylborane	2,440–2,560	830	—	800–8,000	Machini et al. (2016)
Central South University, China	Si; Ta; Nb; Ti	1%–4%	Diborane	2,200–2,400	650–850	30	2000–20,000	Zhu et al. (2018), Miao et al. (2022)
	Si	3.0%	Diborane	—	850	20	—	Li et al. (2020)
École Polytechnique Fédérale de Lausanne (EPFL), Switzerland	p-Si	1.0%	Trimethylborane	2,440–2,560	830	—	2,500–10,000	Kapalka et al. (2009)
	—	1.0%	Trimethylborane	—	760–870	10–100	600	Lévy-Clément et al. (2003)
Instituto Nacional de Pesquisas Espaciais (INPE), Brazil	Ti	0.5%–5.0%	B <sub>2</sub> O <sub>3</sub>	—	650	53–67	100–30,000	Migliorini et al. (2016)
Jilin University, China	Ti	1.0%	Trimethylborate	2,000	—	70	8,000	He et al. (2016)
Slovak University of Technology in Bratislava, Slovak Republic	n-Si	1.0%	Trimethylborane	—	650 ± 20	30	10,000	Kuchtová et al. (2020)
	Si	2.0%	Trimethylborane	2,100	650	30	10,000	Mackuľak et al. (2020)
Tianjin University of Technology, China	Ta	2.0%	Trimethylborate	—	950	50	—	Li et al. (2018)
	Ta	0.7%	B <sub>2</sub> O <sub>3</sub>	—	800–1,000	~67	—	Jiang et al. (2008)
	Ta	0.7%	B <sub>2</sub> O <sub>3</sub>	2,000	800	25	—	Chang et al. (2009)
Zhejiang University, China	Ta	2.0%	Diborane	2,500	800	50	—	Li et al. (2015)

\*TMD, trimethylborane

CVD polycrystalline diamond deposition is generally performed using a CH<sub>4</sub>/H<sub>2</sub> gas mixture, with microcrystalline (MCD) and nanocrystalline diamond (NCD) being typically grown under hydrogen-rich gas mixtures. The introduction of argon into the gas mixture increases the diamond re-nucleation rate, preventing enlargement of the crystallites, and ultra-nanocrystalline diamond (UNCD) is usually grown under argon-rich CVD environments (Gracio et al., 2010). According to the van der Drift regime (van der Drift, 1967; Gracio et al., 2010), MCD and NCD grain size and thickness are determined by the deposition time, while UNCD presents a nodular morphology with negligible crystal faceting, disobeying the standard regime (van der Drift, 1967; Yang et al., 2019). Some researchers also add small amounts (<2%) of O<sub>2</sub> to the gas mixture to limit impurity incorporation and non-epitaxial defect formation (Teraji et al., 2015). The gas mixture influences the grain

size, diamond quality, and the surface finish of the diamond film (Neto et al., 2016). The temperature of the substrate plays a significant role in the film growth kinetics. MPCVD diamond growth was evaluated over HPHT diamond substrates in a broad range of substrate temperatures (750°C–1,150°C) and CH<sub>4</sub>/H<sub>2</sub> gas mixture ratios (1%–13%) (Bushuev et al., 2017). Results showed that an appropriate substrate temperature could significantly improve growth rate, and higher CH<sub>4</sub>/H<sub>2</sub> ratios favor enhanced growth rates. Increasing CH<sub>4</sub> content leads to enhanced non-diamond carbon incorporation. Competitive etching by atomic hydrogen showed a strong effect at low CH<sub>4</sub>/H<sub>2</sub> ratios (1%), and a transition from growth to etching was observed at substrate temperatures higher than 1,000°C and low CH<sub>4</sub> concentrations (1%–4%).

Application of a direct bias current between the filaments and the substrate is not mandatory, but doing so can enhance nucleation

TABLE 2 MPCVD deposition conditions present in the literature based on the bibliometric analysis search.

University, research center, or commercial manufacturer	Substrate	CH <sub>4</sub> /H <sub>2</sub> (%)	Boron source	Substrate temperature (°C)	Pressure (mbar)	Power (kW)	[B]/[C] (ppm)	Ref.
Keio University, Japan	p-Si	—	Trimethylborate	—	—	5	2000–10000	Triana et al. (2020)
	Si	—	Trimethylborane	—	~113	5	—	Yamaguchi et al. (2019)
Michigan State University, United States	p-Si	0.5%–1%	B <sub>2</sub> O <sub>3</sub>	850	~47	1.0–1.3	100–1,000	Witek and Swain (2001)
Peking University, China	Ti	1%–2%	Diborane	800	~53	1.2	1,000–5,000	Wei et al. (2011)
University of Technology, Poland	p-Si	1.0%	Diborane	1,000	~67	1.3	1,000–10000	Ryl et al. (2019)
University of Tokyo, Japan	n-Si	0.5%	B <sub>2</sub> O <sub>3</sub>	800–900	~153	1.5	8,000	Lévy-Clément et al. (2003)
	p-Si	3.0%	Diborane	880	40	—	6,000	Lévy-Clément et al. (2003)
	n-Si; p-Si	3% ± 1%	B <sub>2</sub> O <sub>3</sub>	800–900	~153	5	10000	Mitadera et al. (2004), Kondo et al. (2007)
Utsunomiya University, Japan	p-Si	—	B <sub>2</sub> O <sub>3</sub>	540	~93	1.4	10000	Muruganathan et al. (2011)

\*TMD, trimethylborane.

density during the deposition and improve diamond quality (Sein et al., 2006). The gas pressure may change the mean free path of particles (primarily hydrocarbons radicals) and, in consequence, their activity due to the absorption of energy from electrons provided by the filaments (Jia et al., 2010). In addition, pressure has been shown to affect film quality, boron-doping concentration, and diamond crystallographic plane growth direction (Jia et al., 2010). During the CVD diamond deposition process, the crystal morphology and orientation are directly related to the growth parameter, which specifies the ratio of the growth rates on different grain orientations [namely, between the (100) and (111) crystallographic planes for CVD diamond] (Lu X. R. et al., 2019). The growth parameter is mainly determined by different deposition parameters such as pressure, gas composition, and the temperature of the substrate (Wild et al., 1990; Wild et al., 1994; Paritosh et al., 1999; Tamor and Everson, 2011).

The choice of boron doping source and its concentration in the gas mixture significantly affect the BDD's molecular structure, electronic properties, composition, impurities, and direction of crystallographic diamond facets (Bogdanowicz and Ryl, 2022). The most used sources of boron in CVD diamond growth are gases such as trimethylborane [B(CH<sub>3</sub>)<sub>3</sub>], trimethylborate [B(OCH<sub>3</sub>)<sub>3</sub>], or diborane (B<sub>2</sub>H<sub>6</sub>). Solid-state sources such as boron oxide (B<sub>2</sub>O<sub>3</sub>) diluted in ethanol or methanol have also been successfully used (Brillas and Martínez-Huitle, 2011; Neto et al., 2016). Controlling the [B]/[C] ratio in the feed gas inside the reactor is established by determining appropriate mixing ratios based on Raoult's law (Einaga, 2018). Different boron sources may require different CVD growth conditions since boron incorporation depends on its source type. Gaseous boron precursors enable more precise control of the boron doping level over a wide concentration range (Cifre et al., 1994).

In addition to the commonly reported parameters, other factors related to the CVD reactor design and operation also affect the final characteristics of the BDD electrode. For example, the temperature measurement instruments and their position (thermocouple, pyrometer), the gas inlet point(s) in the reactor chamber, the direction of the gases' extraction, the chamber volume, or residence time of the gas mixture (depends on the chamber volume and gas flow/pressure). Slow cooling rates favor film adhesion due to lower residual stress caused by the CTE mismatch between the substrate material and the diamond film (Wei and Chen, 2008). The cooling atmosphere will also affect diamond surface chemical termination (Vanhove et al., 2007).

Both in-house and commercially made BDD electrodes show strong heterogeneities in their final characteristics due to the diverse deposition conditions and methods applied. The development of new technology or modified CVD reactors delivering homogeneous power into the diamond growth surface, together with selective BDD surface modifications, would be possible solutions to help minimize the currently found heterogeneities of BDD films (Bogdanowicz and Ryl, 2022).

### 4.3 Characterization of boron-doped diamond coatings

The microstructure, growth rate, sp<sup>3</sup>/sp<sup>2</sup> ratio, boron doping level, and surface termination are key factors that determine the electrochemical properties of BDD. These characteristics significantly control their conductivity, OEP, electrochemical potential window, molecular adsorption, and electron transfer kinetics. Thus, a detailed characterization of a BDD film is also

an important point when comparing BDD electrodes from different sources.

In this section, the properties that most influence the electrochemical performance of the BDD electrodes will be discussed to better understand the efficiency of pollutants removal. The difficulty in comparing the diamond quality and boron doping levels in BDD thin films when determined by different characterization methods will also be addressed. One should bear in mind that the following considerations refer to BDD electrodes with planar geometry since distinct diamond-based architectures (e.g., BDD particles, nanostructured BDD, diamond-nanocarbon structures) may exhibit different behaviors (Baluchová et al., 2019; Bogdanowicz and Ryl, 2022).

### 4.3.1 Presence of non-diamond carbon

Raman spectroscopy is the most accepted and used technique for diamond quality assessment. It enables the detection of non-diamond carbon (NDC), allowing the determination of the carbon  $sp^3$  (diamond-like)/ $sp^2$  (graphite-like) ratio, which is the commonly adopted diamond quality indicator. The presence of NDC in the BDD films significantly influences their electrocatalytic properties, particularly the voltametric background current, potential window, molecular adsorption, and electron transfer kinetics (Macpherson, 2015). High NDC content affects the electrocatalytic inertia of the electrode (Macpherson, 2015) and modifies its adsorption characteristics, decreasing the potential window (Medeiros de Araújo et al., 2014) and increasing fouling susceptibility (Patel et al., 2013). Relevant presence of  $sp^2$  carbon in the BDD films may induce voltametric responses like glassy carbon and graphite (He et al., 2019). The substantial presence of NDC in the grain boundaries of the diamond film causes lower electrode stability when under anodic polarization and, ultimately, the disintegration of the electrode (Read and Macpherson, 2016). The NDC content is also related to higher background current and double-layer capacitance (Bennett et al., 2004). For water treatment applications, a lower level of  $sp^2$  carbon favors the ability for the mineralization of organics, and electrochemical combustion over conversion, thus avoiding the generation of hazardous by-products (Medeiros de Araújo et al., 2014).

Different laser wavelengths ranging from 257 to 1,064 nm have been used in Raman spectroscopy to evaluate the quality of the diamond thin films (Prawer and Nemanich, 2004). The determination of the  $sp^3/sp^2$  ratio strongly depends on the excitation wavelength, and it increases with the increasing energy of the used laser (Prawer and Nemanich, 2004; Jagannadham et al., 2010). Typically, the peaks used for  $sp^3/sp^2$  calculations are the first-order diamond band ( $sp^3$ ) at  $1,332\text{ cm}^{-1}$ ; the G-band between  $1,500$  and  $1,600\text{ cm}^{-1}$  (related to the C=C  $sp^2$  bond stretching mode); and the D-band usually located at  $1,345\text{ cm}^{-1}$  (represents most  $sp^2$  structures) (Ballutaud et al., 2008; Dychalska et al., 2015). In the case of nanocrystalline diamond films, the first-order diamond peak is only detected under UV excitation (Prawer and Nemanich, 2004).

The comparison of different  $sp^3/sp^2$  ratios is only accurate if the same excitation energy is used to acquire the spectra and if determined by the same method and mathematical expression. Several authors have used the ratio between the integral intensity of the diamond band ( $I_{\text{diamond}}$ ) and the integral intensity of the

G-band ( $I_G$ ) (Issihi et al., 2012). Others divide  $I_{\text{diamond}}$  by the total integrated intensity of the Raman spectrum ( $I_{\text{total}}$ ) (Salgueiredo et al., 2011; Štenclová et al., 2019). The full width at half maximum (FWHM) of the first-order peak for diamond has also often been used to estimate its crystalline quality and dopant concentration since lower FWHM values indicate lesser structural defects and/or grain boundaries, hence higher diamond quality (Gheeraert et al., 1993; Ferrari and Robertson, 2004; Prawer and Nemanich, 2004; Kowalska et al., 2020). Different expressions for the calculation of the diamond quality are found in the literature, depending on the applied excitation wavelength. For example, if the 514 nm excitation line is used, authors usually determine the diamond quality by Eq. 1 (Espinoza et al., 2019), Eq. 2 (McNamara et al., 1992), or Eq. 3 (Vorlíček et al., 1997).

$$sp^3/sp^2 \text{ ratio} = \frac{I_{\text{diamond}}}{250 \times \sum I_{\text{non-diamond}}} \quad (1)$$

$$sp^3/sp^2 \text{ ratio} = 100 \times \frac{I_G}{75 \times I_{\text{diamond}} + I_G} \quad (2)$$

$$\beta = \frac{I_{\text{diamond}}}{I_{\text{diamond}} + I_{\text{total}}} \quad (3)$$

In Eq. 1,  $I_{\text{non-diamond}}$  is the integral intensity of non-diamond bands of the Raman spectrum, and 250 is the factor related to the Raman scattering efficiencies between the  $sp^3$  band and other forms of non-diamond carbon. In Eq. 3,  $\beta$  is the figure-of-merit or the Raman quality fraction (Vorlíček et al., 1997). If the 488 nm excitation wavelength is used to acquire the Raman spectra, then the purity of the CVD diamond can be expressed by  $C_{\text{diamond}}$ , as seen in equation Eq. 4, where 50 is a correction factor for the substantial resonant Raman scattering effect of  $sp^2$  bonded carbons (Shroder et al., 1990; Kowalska et al., 2020).

$$C_{\text{diamond}} = 100 \times \frac{I_{\text{diamond}}}{I_{\text{diamond}} + I_G/50} \quad (4)$$

It is important to emphasize that all the above equations for diamond quality assessment should be used with caution since several other factors influence the  $sp^3/sp^2$  ratio. For instance, the polarization changes if micro or macro-Raman measurements are employed or if measurements are carried out over grains with different orientations (especially in micro-Raman) (Prawer and Nemanich, 2004).

### 4.3.2 Surface morphology and roughness

Scanning electron microscopy (SEM), atomic force microscopy (AFM), and 3D optical profilometry easily provide surface morphology and roughness analysis information. In polycrystalline BDD, the crystal defects are usually linked to NDC, mainly located in the grain boundaries. Therefore, higher surface roughness arises from large grain sizes and low grain boundary density, indicating a reduced amount of NDC present at the BDD surface (Williams, 2011; Gomez-Ruiz et al., 2019). Except in the case of UNCD films, CVD diamond films usually grow according to the van der Drift regime, in which the average grain size increases with the increasing film thickness (van der Drift, 1967). Therefore, grain size, roughness, and film thickness are closely related to the BDD surface's electrochemical properties, which, in their turn, are highly influenced by variation in the

amount of NDC. Consequently, the overpotential for oxygen evolution is lower for thinner films (and finer grains), and the capacitance of BDD electrodes is also related to surface roughness (Pleskov, 2011).

### 4.3.3 Boron doping level

The conversion of insulator diamond to metal-like conductivity is required for effective practical electrochemical applications and attained at certain doping levels (Yang et al., 2019). The evolution of resistivity in diamond as a function of boron concentration ([B]) in BDD thin films has been studied (Lagrange et al., 1998). For [B] below  $10^{19} \text{ cm}^{-3}$ , the conduction in diamond is dominated by free electrons within the valence band. Up to  $3 \times 10^{20} \text{ cm}^{-3}$ , the conduction is of the hopping type, diamond behaves as a semiconductor, and the resistivity decreases strongly with the increase of boron content. Diamond reaches metal-like conductivity when [B] is above  $3 \times 10^{20} \text{ cm}^{-3}$ .

Nevertheless, effective doping is not linear since boron does not homogeneously incorporate diamond, being simultaneously substitutional and interstitially distributed within the crystalline framework. Thus, effective boron doping does not linearly increase with the boost of boron concentration in the CVD feed gas (Sharma et al., 2022). Boron preferentially incorporates the (111) diamond facets compared to (100) facets (Spitsyn et al., 1981; Larsson, 2020). Electric conductivity in (111) planes is estimated to be approximately  $10^4$  times higher than that in (100) planes (Spitsyn et al., 1981), with consequent faster electron transfer kinetics in (111) planes (Bogdanowicz and Ryl, 2022). Furthermore, boron atoms are not electrically active when incorporated within the grain boundaries (Lu et al., 2012), which means that the measured doping level is usually higher than the effective carrier concentration (holes) (Yang et al., 2019). Several techniques have been used for quantitative and/or semiquantitative determination of the boron doping level in BDD films. It includes secondary ion mass spectrometry (SIMS), X-ray photoelectron spectroscopy (XPS), electron energy-loss spectroscopy (EELS), and neutron depth profile (NDP). However, these methods are time-consuming, expensive, and difficult to apply, especially when a full depth analysis of boron distribution within the diamond lattice is desired (Sharma et al., 2022). Recently, pulsed RF glow discharge optical emission spectroscopy (GDOES) has been used to semi-quantify boron doping levels, and it was demonstrated that the technique provides high-speed depth profiles (Sharma et al., 2022). In the case of heavily doped BDD films, many authors use a non-destructive and contactless measurement using Raman spectroscopy data to estimate the boron doping concentration. The following equation (Eq. 5) was proposed, and it is valid for boron doping concentration within the  $2 \times 10^{20} \sim 10^{22} \text{ cm}^{-3}$  range (Bernard et al., 2004):

$$[B] \text{ cm}^{-3} = 8.44 \times 10^{30} \exp(-0.048\omega) \quad (5)$$

where  $\omega$  is the wavenumber ( $\text{cm}^{-1}$ ) of the Lorentzian component of the Raman peak at about  $500 \text{ cm}^{-1}$ . Care must be taken when using this method since the intensity of the Raman peaks varies with the wavelength of the used laser (Prawer and Nemanich, 2004).

Understanding the electrical conductivity of BDD electrodes is complex and is not solely determined by the efficient amount of

boron incorporation. Heterogeneities such as NDC content, lattice hydrogen, and dangling bonds also affect such property (Einaga et al., 2014). Enhanced BDD electrochemical performance is commonly linked to high boron doping levels, which provide higher carrier concentration and electrical conductivity (Einaga et al., 2014), thus electrochemical reactions are faster for heavier doped BDD electrodes (Pleskov, 2011). The doping level influence on the chemical surface of diamond electrodes was studied, and results indicate that highly doped diamond films show more reversible performances in the electrochemical response to the  $\text{Fe}(\text{CN})_6^{4-/3-}$  redox couple (Azevedo et al., 2013). Conversely, in the same study, other results indicate that increased doping level is associated with smaller grain size, with consequent increase of the grain boundary density that leads to a higher amount of NDC and surface oxidation states. The doping level effect of boron on the width of the electrochemical potential window of the electrodes revealed that low boron doping levels led to a broader potential range and slower response to the overpotential of both HER and OER (Salazar-Banda et al., 2010). This behavior is related to the minor concentration of boron-rich sites on the surface, blocking both hydrogen and oxygen adsorption steps required for HER and OER, respectively. Increasing boron content led to smaller electrochemical windows, as well as higher electron transfer rate constants and active electrochemical areas (Liu et al., 2018). Boron concentration also affects the adhesion strength of the film (Gerger and Haubner, 2008), diamond nucleation density, grain size, and overall diamond quality (Wang et al., 1992). Most published works on the electrochemical degradation of pollutants using BDD anodes do not provide information on effective boron content determination. In some cases, a rough estimative is expressed based on the [B]/[C] ratio in the feed gas during the CVD process. This estimate is inaccurate since boron incorporation in the diamond lattice is not linearly related to the feeding concentration, as previously demonstrated. An optimum balance between doping level and diamond quality must be reached to produce BDD electrodes with the desired and top electrochemical performance. Proper and accurate determination of the effective boron doping level is required to fine-tune the electrochemical properties of BDD films, although for practical applications the electrical conductivity can be used as a proxy for doping efficiency.

### 4.3.4 Surface termination

The surface termination of BDD electrodes can drastically influence their electrochemical kinetics (Yagi et al., 1999; Notsu et al., 2001). Hydrogen is the foremost gas used in the CVD growth of diamond films, and their surface presents a hydrogen-terminated surface if cooled down to room temperature under such flow. These surfaces are hydrophobic and show typical water contact angles around  $90^\circ$  (Neto et al., 2016). However, H-terminated diamond surfaces slowly oxidize with time when in contact with air, becoming more hydrophilic (Salazar-Banda et al., 2006; Vanhove et al., 2007). Several studies demonstrate that O-terminated BDD surfaces present a wider potential window, lower background current, and higher surface resistivity when compared to H-terminated surfaces (Yagi et al., 1999; Liu et al., 2007; Yano et al., 2019a; Yano et al., 2019b). Anodic polarization (Hutton et al., 2013) and oxygen plasma treatment are common means to obtain O-terminated BDD surfaces (Brillas and Martínez-Huitle, 2011). Oxidation of



the BDD surface can also be achieved by adding small amounts of O<sub>2</sub> or using an oxygen-containing boron source during the CVD deposition (Neto et al., 2016). The oxygen atoms incorporate the doped films by bonding with carbon atoms, mainly as C–O–C and C=O terminating groups (Neto et al., 2016). Evidence shows that increased boron doping levels lead to higher oxygen amounts with a consequent decrease in the water contact angle, showing a more hydrophilic character (Azevedo et al., 2013). O-terminated diamond surfaces show water contact angles ranging from 0.6° to 65° (Macpherson, 2015). The difference between H and O-terminated diamond surfaces is mainly associated with their electronic structures and surface bandgap (opposite bond polarities) (Liu et al., 2007). The former (–C<sup>δ−</sup>–H<sup>δ+</sup>) increases the energy levels of the valence (E<sub>VB</sub>) and conduction bands (E<sub>CB</sub>), as well as the negative electron affinity. The latter (C<sup>δ+</sup>–O<sup>δ−</sup>) lowers the energy levels and shows higher positive electron affinity (Macpherson, 2015).

The functional groups terminating the surface of BDD electrodes strongly influence the electron transfer kinetics of inner-sphere redox couples (Bard, 2010). The H-terminated BDD functional groups are usually =CH<sub>2</sub> and ≡C–H groups that, when oxidized under anodic polarization, show hydroxyl (≡C–OH), carbonyl (≡C=O), carboxylic (–COOH), carbon radical (≡C•), and hydroxyl radical (≡C–O•) functional groups (Chaplin, 2014). These functional groups may vary according to the chosen anodic polarization procedure and the different grain orientations on the polycrystalline diamond surface (Yuan et al., 2021). Diamond surfaces with (111) orientation tend to be dominated by hydroxyl groups since only one chemical bond to a single carbon atom is available at the first surface layer. The latter then inhibits the formation of carbonyl and ether groups at the surface of the electrode (Chaudhuri et al., 2022). Diamond surfaces with (100) texture present two available chemical bonds for a single carbon atom, promoting carbonyl and ether group formation (Chaudhuri et al., 2022). For example, the Fe(CN)<sub>6</sub><sup>4−/3−</sup> redox system exhibits slow electron transfer for O-terminated surfaces but fast electron transfer for H-terminated surfaces (Yagi et al., 1999). In addition, H-terminated surfaces show narrower solvent potential windows than those O-terminated (Tryk et al., 2001).

Electrochemical pre-treatments and polishing have been carried out to enhance the BDD electroanalytical performance, increase the electrochemically active surface area, lower detection limits, and broader linearity ranges (Lourenco et al., 2020).

### 4.3.5 Electrochemical characterization

In a summarized way, the four main points to be taken into account in the electrochemical characterization of BDD electrodes are (Macpherson, 2015): good electrical contact to avoid ohmic drop effects, the cell apparatus, quantification of the capacitance and solvent potential window of the electrode, and assessment of the electron transfer kinetics with outer-sphere redox mediators.

Assessment of the solvent potential window is essential because it specifies the potential range over which the anode works prior to the electrolysis of the solvent (Macpherson, 2015). The electrochemical potential window will be the first quality indicator to be considered for the evaluation of the electrode performance, particularly if important information on the electrode is known (sp<sup>3</sup>/sp<sup>2</sup> ratio, conductivity, surface

termination, and morphology). The window range is pH-dependent and may vary depending on the electrolyte concentration, the electrode geometry, potential/current value, scan rate, and temperature. Electrolyte solutions commonly reported include KNO<sub>3</sub> (Yoon et al., 2012), H<sub>2</sub>SO<sub>4</sub> (Kornienko et al., 2011), HClO<sub>4</sub> (Inieta, 2001), Na<sub>2</sub>SO<sub>4</sub> (Chen et al., 2022), NaBr, NaCl (Zhang et al., 2018), within a wide range of concentrations.

As already stated in the present review, the lack of information for comparison purposes includes the experiment temperature, whose increase leads to narrower electrochemical potential windows (McLaughlin et al., 2020). Another one is the adopted methodology regarding the determination of the solvent window (from the voltammogram), which is commonly carried out by applying a method based on defining the window at an arbitrary current density cut-off (J<sub>cut-off</sub>) value or a linear fit method (Olson and Bühlmann, 2012). The arbitrary method is highly influenced by the mass transport of the electrolyte (McLaughlin et al., 2020), and the setting of J<sub>cut-off</sub> values has been diversely defined in the literature, limiting possible comparison of the obtained results (Mousavi et al., 2015). On the other hand, the linear fit method is less affected by the experimental conditions for each measurement system, becoming the recommended one for accurately comparing solvent potential windows (McLaughlin et al., 2020).

The OEP of an electrode material and the enthalpy of adsorption of the hydroxyl radicals on its surface are the main factors that determine its oxidation power (Comninellis et al., 2008). This parameter is simple to obtain, it is also a good indicator of electrode quality, and it should be carefully evaluated. OEP determines if the anode presents an active or a non-active behavior (Comninellis et al., 2008). Usually, BDD is considered a non-active anode due to its high OEP, which indicates a more significant restriction of the oxygen evolution from water electrolysis and the production of hydroxyl radicals at the surface of the electrode (Lee et al., 2017). Comparison of OEP values is only valid if obtained for the same solution concentration and electrolyte.

Determination of the double-layer capacitance (C<sub>dl</sub>) is also a helpful indicator of electrode quality (Macpherson, 2015). C<sub>dl</sub> can be calculated from cyclic voltammetry applying Eq. 6 or through electrochemical impedance spectroscopy (EIS) measurements.

$$C_{dl} = \frac{i_{av}}{A\nu} \quad (6)$$

where i<sub>av</sub> is the average current from the forward and reverse sweep, A is the electroactive area, and ν is the scan rate. Nevertheless, the application of this equation becomes challenging due to the topographic nature of the BDD surface (especially in MCD), which restricts the accurate determination of the electroactive area (Macpherson, 2015).

The electron transfer kinetics may be evaluated from cyclic voltammogram measurements for inner-sphere and outer-sphere redox couples. The most studied redox couples are the inner-sphere Fe(CN)<sub>6</sub><sup>−3/−4</sup> and the outer-sphere Ru(NH<sub>3</sub>)<sub>6</sub><sup>3+/2+</sup> redox couples. The latter is valuable for qualitative estimation of the boron doping level. BDD films with a dominant electrical transport mechanism (i.e., metal-like conductivity) show a reversible or quasi-reversible faradaic peak current response under conditions where the electron transfer rate is much faster than the diffusional rate (Macpherson,

**TABLE 3** Accelerated life test results and experimental conditions found for several studied BDD electrodes.

Electrolyte	Substrate material	Current density (A/cm <sup>2</sup> )	Accelerated life test result (h)	Ref.
0.5 M H <sub>2</sub> SO <sub>4</sub>	Nb	10	850	Fryda et al. (1999)
1 M H <sub>2</sub> SO <sub>4</sub>	Nb	1.32	88–130	Choi et al. (2017)
		1	484	Lu et al. (2019a)
	Si	1	262	Miao et al. (2020)
	Ti	1	127	Lu et al. (2018), Lu et al. (2019b)
3 M H <sub>2</sub> SO <sub>4</sub>	Nb	1	>1,600	Yang et al. (2022)
	Si	1	>1,600	Yang et al. (2022)
	Ta	1	>1,600	Yang et al. (2022)
	Ti	1	1,530	Yang et al. (2022)
		1	264	Chen et al. (2005)
		1	95	Chen and Chen (2004)
		0.5	89	He et al. (2015)
6 M HNO <sub>3</sub>	Nb	0.5	1,620–1810	Groenen Serrano et al. (2015)

2015). However, the oxidation and reduction reaction rate of Ru(NH<sub>3</sub>)<sub>6</sub><sup>2+/3+</sup> is little affected by surface defects, film microstructure, adsorbed sp<sup>2</sup> carbon, or surface terminations like oxygen-containing groups (Ueda et al., 2009; Dettlaff et al., 2021). On the contrary, the Fe(CN)<sub>6</sub><sup>3-/4-</sup> redox couple electron transfer rate is significantly affected by the surface chemistry of the BDD coating and the presence of defects such as NDC impurities (Dettlaff et al., 2021).

#### 4.3.6 Electrode service life

Ultimately, comparing the service time of different BDD electrodes is equally important to balance performance and lifetime service with optimal cost-benefit in large-scale water treatment applications. Accelerated life tests are a practical way of evaluating the BDD's electrochemical stability over time (Zhang C. et al., 2019). Accelerated service life tests have been performed on BDD films deposited over various substrate materials (e.g., Nb, Si, Ti, Ta) through electrolysis at high current densities ranging from 0.5 to 10 A/cm<sup>2</sup> in concentrated electrolyte solutions of H<sub>2</sub>SO<sub>4</sub> or HNO<sub>3</sub>. Table 3 shows the accelerated life tests and their experimental conditions found in the literature.

### 4.4 Design of pollutant degradation experiments

The mineralization efficiency is influenced by the applied current density, EAOP, pollutant concentration, properties of the degraded pollutant, pH of the solution, supporting electrolyte, temperature, the volume of solution, fluid dynamics, dissolved oxygen, electrode configuration, active electrode area, cell design, and agents added in the solution, e.g., chloride, sulfate, phosphate, carbonate, and oxygen (Brillas et al., 2005; Enache et al., 2009; Panizza and Cerisola, 2009; Macpherson, 2015; Cano et al., 2016; Rubí-Juárez et al., 2016; Xu, 2016; McLaughlin et al., 2020).

Comparing the degradation performance of BDD electrodes is again a repetitive challenge.

#### 4.4.1 Electrochemical advanced oxidation process

In EAOPs, the primary processes are classified as anodic oxidation (AO) *via* intermediates of oxygen evolution and electro-Fenton-based processes. Anodic oxidation *via* intermediates (hydroxyl radicals formed from water oxidation at the anode surface) resulting from oxygen evolution may directly destroy organic pollutants (Belhadj Tahar and Savall, 2019). Electrogeneration of H<sub>2</sub>O<sub>2</sub>, denominated AO with electrogenerated H<sub>2</sub>O<sub>2</sub> (AO-H<sub>2</sub>O<sub>2</sub>), is another anodic oxidation method (Brillas et al., 2008). The efficiency of both methods depends on the type of material used as anode and must present high OEP (Moreira et al., 2017). Anodic oxidation can also be accomplished by adding anions to the bulk solution, such as chloride, sulfate, phosphate, and carbonate, that generate oxidants like active chlorine, persulfate, perphosphate, and percarbonate species, respectively (Panizza and Cerisola, 2009). The electro-Fenton (EF) process arises from the electrochemical production of H<sub>2</sub>O<sub>2</sub> with the addition of Fe<sup>2+</sup> in the bulk solution producing additional hydroxyl radicals as a by-product of the Fenton's reaction (Brillas et al., 2004). Photoelectro-Fenton (PEF) and solar photoelectro-Fenton (SPEF) are a combination of the EF method with the irradiation of UV light and natural sunlight, respectively, that enhance degradation efficiency (Brillas, 2014). The sonoelectro-Fenton (SEF) process is performed under EF conditions and simultaneous application of ultrasound radiation (Oturan et al., 2008). Electrochemical degradation experiments combining UV or ultrasound irradiation demonstrated improved outcomes if compared to direct anodic oxidation (Hurwitz et al., 2014; Vidales et al., 2014; Vieira Dos Santos et al., 2017). Ultrasound radiation improves the transfer of pollutants to the BDD surface though it requires higher energy consumption; and UV irradiation increases hydroxyl radical generation (Vidales et al., 2014),

preventing the formation of undesirable and hazardous by-products (e.g., chlorate and perchlorates) during the electrochemical degradation process (Cotillas et al., 2016). The key EAOPs are AO, AO-H<sub>2</sub>O<sub>2</sub>, EF, PEF, and SPEF (Sires et al., 2014). Other EAOPs such as peroxi-coagulation (Brillas and Casado, 2002) and Fered-Fenton (Huang et al., 2001) are also proposed for remediation of various pollutants in wastewater.

The main disadvantages of EAOPs are high energy consumption and mandatory solution high conductivity which is directly correlated to lower energy conditions (Clematis and Panizza, 2021b). The effluents from several industries and urban wastewater have low conductivities, but adding a supporting electrolyte enables water treatment by direct application of electrochemical processes (Ma et al., 2018). Still, this extra leads to increased operational costs and/or toxic by-products (Clematis and Panizza, 2021b). Alternatives include reduction of ohmic resistances and increasing the mass transport of the pollutants towards the surface of the electrode through a solid polymer electrolyte (SPE) (Clematis et al., 2017), or capillary microfluidic cells (Ma et al., 2018), respectively. A review on the electrochemical oxidation of organic pollutants in low conductive solutions can be found elsewhere (Clematis and Panizza, 2021b).

#### 4.4.2 Cell design

Various configurations and apparatus have been used in pollutant degradation with BDD electrodes, including simple electrochemical cells under static conditions and commercial multi-cell flow reactors. Thus, the influence of the electrode configuration and cell design on the intrinsic fluid dynamics (e.g., volumetric flow, Reynolds number, and mass transport) is an important factor (Cano et al., 2016; Xu, 2016).

Cells are usually equipped with two types of electrode configurations: monopolar and bipolar designs (Cano et al., 2016). In the first one, the anode is BDD, and the cathode is another material, usually a stainless-steel plate. In bipolar design, BDD is used as both anode and cathode. Both configurations under the same operating conditions were tested, and the bipolar electrodes provided higher efficiency in water disinfection (Cano et al., 2016). Moreover, reactors designed for cells with bipolar configuration allow switching the polarity of electrodes to electrochemically clean their surface and prevent electrode deactivation (Murugananthan et al., 2007). Nevertheless, one should bear in mind that monopolar electrodes consume less energy (Cano et al., 2016).

The type and geometry of the cell and the BDD electrodes are essential aspects since they will determine the flow dispersion and consequent mass transport within the container. The latter will directly influence the potential and current distribution of the working electrode, affecting the current efficiency and overall energy consumption associated with the degradation process (Rivera et al., 2015; Cornejo et al., 2020).

#### 4.4.3 Operating conditions

According to the literature, the adopted operating conditions to perform electrochemical oxidation of contaminants in wastewater are diverse. However, the removal of organic carbon from treated solutions is mainly influenced by the applied current density, mass

transfer effects, and the properties of degraded pollutants (Xu, 2016).

Many degradation experiments are performed with the addition of a supporting electrolyte, particularly in high concentrations (higher solution conductivity) where electrooxidation proficiency is enhanced (Ma et al., 2018). The effect of different supporting electrolytes in phenol degradation using BDD electrodes has been assessed (de Souza and Ruotolo, 2013). In the absence of chloride ions, the oxidation kinetics constants follows the order: Na<sub>2</sub>SO<sub>4</sub> ≈ Na<sub>2</sub>CO<sub>3</sub> > H<sub>2</sub>SO<sub>4</sub> > H<sub>3</sub>PO<sub>4</sub>. In chloride-mediated process, the reaction kinetics considerably increases with a new order: H<sub>2</sub>SO<sub>4</sub> > Na<sub>2</sub>SO<sub>4</sub> > Na<sub>2</sub>CO<sub>3</sub>. Therefore, the supporting electrolyte plays a crucial role in generating different oxidative species like peroxocarbonate, peroxosulfate, or hypochlorite (Rubí-Juárez et al., 2016). The choice of electrolyte will affect the pH value, and acidic media is correlated to the improvement of pollutant degradation efficiency, benefiting the production of hydroxyl radicals at the anode surface (Zhou et al., 2011a; Daskalaki et al., 2013; Espinoza-Montero et al., 2013; Fabianska et al., 2014). However, in terms of pH effect, there are diverse and even contradictory results which are dependent on the pollutant chemistry (Brillas et al., 2005; Zhou et al., 2011b; Xu, 2016). Ideally, the electrochemical behavior of BDD electrodes should be evaluated in different pH and electrolyte solutions before the degradation experiments (Enache et al., 2009).

Mineralization rates are linearly related to the current density ( $j_{\text{appl}}$ ) with two different operating regimes depending on it: current and mass transport-controlled oxidations (Brillas et al., 2005). In these regimes, the limiting current density ( $j_{\text{limit}}$ ) for electrooxidation of the organic pollutant is estimated according to the following equation:

$$j_{\text{limit}} = n k_m F [\text{Pollutant}] = 4 k_m F \text{COD} \quad (7)$$

where  $j_{\text{limit}}$  is the limiting current density, [Pollutant] is the organic pollutant concentration,  $k_m$  is the mass-transfer coefficient,  $n$  is the number of electrons exchanged in the oxidation of a molecule of the pollutant,  $F$  is the Faraday constant, and COD is the chemical oxygen demand. Current-controlled oxidation takes place when  $j_{\text{appl}} < j_{\text{limit}}$ , and the contaminant concentration decreases linearly over time with a current efficiency of 100% (Panizza et al., 2001). On the other hand, mass transport-controlled oxidation occurs when  $j_{\text{appl}} > j_{\text{limit}}$ , and secondary reactions like oxygen evolution occur. In this case, the contaminant degradation follows an exponential trend, and the current efficiency is below 100% (Panizza et al., 2001).

The geometric area of the BDD anode should be controlled since its conductivity is not entirely uniform along with the film due to its surface heterogeneities. Restricted areas prevent poor current density distribution and, consequently, lower degradation efficiency and possible formation of undesired by-products (Cano et al., 2016). The relationship between the electrode area and the applied current density is meaningful: the same degradation performance with a reduced electrode area is achieved by increasing the current density. Its maximum is defined by the quality, defect density, and adhesion strength of the BDD film to the substrate. Still, lower current densities may avoid the production of non-desired or hazardous by-products (chlorate, perchlorate, or organo-chlorinates) (Cano et al., 2011).

The total volume of solution affects the residence time and, consequently, the degradation efficiency (Lacasa et al., 2013). In addition, high pollutant concentration leads to lower mineralization rates but higher temperature promotes faster mineralization rates due to further mass transfer towards the anode surface (Brillas et al., 2005).

#### 4.4.4 Performance indicators for pollutant degradation

The measurement of COD in the solution containing the contaminant under study is the most applied approach to assess the degradation performance of BDD electrodes. Some authors also evaluate the total organic carbon (TOC) of the solution, or both COD and TOC, and others prefer to express degradation results as a function of the contaminant concentration. The latter is usually determined by UV-vis spectroscopy and/or high-performance liquid chromatography (HPLC).

The COD method is used to quantify the performance of the electrodes. It determines the average current efficiency (ACE) and instantaneous current efficiency (ICE) of the BDD electrode, expressed in Eqs 8, 9, respectively (Comninellis and Pulgarin, 1991):

$$ACE = \frac{FV(COD_0 - COD_t)}{8I\Delta t} \quad (8)$$

$$ICE = \frac{FV(COD_t - COD_{t+\Delta t})}{8I\Delta t} \quad (9)$$

where  $F$  is the Faraday constant ( $96485 \text{ C mol}^{-1}$ );  $t$  is the time (s);  $V$  is the volume of the electrolyte ( $\text{dm}^3$ );  $COD_0$  is the initial COD concentration ( $\text{gO}_2 \text{ dm}^{-3}$ );  $COD_t$  and  $COD_{t+\Delta t}$  are the COD concentration at times  $t$  and  $t+\Delta t$  (s), respectively;  $I$  is the applied current (A); and  $8$  is the dimensional factor for unit consistency (meaning  $32 \text{ g of O}_2/4 \text{ mol e}^- \text{ mol}^{-1} \text{ of O}_2$ ).

Likewise, current efficiency results have also been measured as a function of TOC. For example, the mineralization current efficiency (MCE) is calculated considering TOC removal (Eq. 10) (Flox et al., 2007). In addition, the combustion efficiency (Eq. 11) can be determined by calculating the ratio between the TOC and the COD decrease rates (Pacheco et al., 2007):

$$MCE = \frac{nFV\Delta TOC}{4.32 \times 10^7 m I t} \quad (10)$$

$$\eta_c = \frac{32}{12} \left( \frac{n}{4m} \right) \frac{dTOC}{dCOD} \quad (11)$$

where  $n$  is the number of electrons required for the complete combustion of the organic pollutant,  $m$  is the number of carbon atoms in the molecule of the organic pollutant,  $F$  is the Faraday constant,  $V$  is the volume of the electrolyte (L),  $I$  is the applied current (A),  $t$  is the time (h),  $\Delta TOC$  is the total organic carbon reduction ( $\text{mg/L}$ ),  $dTOC$  is the TOC decrease rate, and  $dCOD$  is the COD decrease rate.

If the concentration of the pollutant is evaluated over its electrooxidation time, the results are usually demonstrated in plots of removal percentage, or contaminant concentration, against the charge amount  $Q^t$  (Eq. 12).

$$Q^t (\text{Ah/L}) = \frac{jAt}{V} \quad (12)$$

However,  $Q^t$  does not consider the total removed concentration of the pollutant from the solution. Therefore, we propose a different approach to determine the degradation performance, which enables comparison between the reported results. It starts by calculating the average  $Q'$  ( $\text{Ah/kg}$ ) required for the pollutant degradation, expressed through Eq. 13.

$$Q' (\text{Ah/kg}_{\text{pollutant}}) = Q^t \times \frac{1}{\Delta C_{\text{pollutant}}} = \frac{jAt}{V \Delta C_{\text{pollutant}}} \quad (13)$$

We propose  $Q'$ , a new figure-of-merit to be used when COD and TOC are undetermined and the cell potential value is unavailable, i.e., when the calculation of energy consumption is not possible.  $Q'$  is a base parameter to enable comparison between different performances of the BDD electrodes from different sources (in-house and commercially manufactured). Energy consumption values have been reported in several ways as a function of the removed concentration of the studied analyte (Eq. 14), COD (Eq. 15), and TOC (Eq. 16). Additionally, some authors have expressed energy consumption values only as a function of the volume of the treated solution (Eq. 17). However, the latter expression of consumption does not consider the pollutant concentration and may induce misinterpretation of the electrode performance.

$$\text{Energy consumption} \left( \frac{\text{kWh}}{\text{kg}_{\text{pollutant}}} \right) = Q^t \times \frac{E}{\Delta C_{\text{pollutant}}} = \frac{EjAt}{V \Delta C_{\text{pollutant}}} \quad (14)$$

$$\text{Energy consumption} \left( \frac{\text{kWh}}{\text{kg}_{\text{COD}}} \right) = Q^t \times \frac{E}{\Delta COD} = \frac{EjAt}{V \Delta COD} \quad (15)$$

$$\text{Energy consumption} \left( \frac{\text{kWh}}{\text{kg}_{\text{TOC}}} \right) = Q^t \times \frac{E}{\Delta TOC} = \frac{EjAt}{V \Delta TOC} \quad (16)$$

$$\text{Energy consumption} (\text{kWh/m}^3) = Q^t \times E = \frac{EjAt}{V} \quad (17)$$

where  $Q^t$  is the charge ( $\text{Ah/dm}^3$ ) at time  $t$  (h),  $j$  is the applied current density ( $\text{A dm}^{-2}$ ),  $t$  is the electrolysis time (h),  $A$  is the BDD electrode geometric area ( $\text{dm}^2$ ),  $V$  is the volume ( $\text{dm}^3$ ) of the solution,  $E$  is the average electrode potential (V),  $\Delta C_{\text{pollutant}}$  is the total concentration of pollutant removed from the solution ( $\text{kg/dm}^3$ ),  $\Delta COD$  is the total amount of COD removed ( $\text{kg/dm}^3$ ), and  $\Delta TOC$  is the total amount of TOC removed ( $\text{kg/dm}^3$ ).

The previous equations allow normalization of the BDD degradation results for a specific contaminant (Eq. 14) or complex matrixes (Eqs 15, 16) based on diverse experimental conditions like applied current density, electrode potential, geometric electrode area, degradation time, the volume of solution, and initial pollutant concentration. Although one may use such figures-of-merit, understanding the different results is only achieved through proper and complete characterization of the BDD films, as discussed in the previous sections. In addition, a comparison of the results is only possible within each specific calculation method. For example, the COD method (ICE, ACE, energy consumption in  $\text{kWh/kg}_{\text{COD}}$ ), TOC (MCE,  $\eta_c$ , energy consumption in  $\text{kWh/kg}_{\text{TOC}}$ ), and pollutant concentration ( $Q'$ , and energy consumption in  $\text{kWh/kg}_{\text{pollutant}}$ ). A summary of the figures of merit discussed in this section is provided in Table 4.



TABLE 4 Summary of figures of merit used as performance indicators for pollutant degradation.

Figure-of-merit (FOM)	Pros	Cons
$ACE = \frac{FV(COD_0 - COD_t)}{8I\Delta t}$	Most used FOMs, allowing comparison with most published results COD measurements are less expensive than TOC	Does not give information on the oxidation of a specific pollutant The COD analysis uses hazardous reagents (dichromate), can be time-consuming, have a relatively high detection limit, and may suffer interference from inorganics. In addition, dichromate does not oxidize some organic species, which can imply false low COD values
$EC_{COD} = \frac{EjAt}{V\Delta COD}$		
$ICE = \frac{FV(COD_0 - COD_{(t-\Delta t)})}{8I\Delta t}$	Provide instantaneous current efficiency data	
$MCE = \frac{nFV\Delta TOC}{4.32 \times 10^6 mIt}$	TOC analyses are usually faster than COD and often result in accuracy over an extensive range of concentrations from 1 to 50,000 ppm	TOC measurements require expensive equipment and complicated analysis
$EC_{TOC} = \frac{EjAt}{V\Delta TOC}$		
$\eta_c = \frac{32}{12} \left( \frac{n}{4m} \right) \frac{dTOC}{dCOD}$		Requires both COD and TOC measurements
$Q' = \frac{jAt}{V\Delta C_{pollutant}}$	Ideal for comparing results when the cell potential value is unavailable Does not require COD and/or TOC analysis	Requires pollutant quantification techniques (e.g., UV-vis spectroscopy, HPLC)
$EC_{Pollutant} = \frac{EjAt}{V\Delta C_{pollutant}}$	Does not require COD and/or TOC analysis	
$Q' = \frac{iAt}{V}$	Does not require quantification methods (e.g., pollutant concentration, COD or TOC)	Does not consider the pollutant concentration or any other water quality parameter, which may lead to misinterpretation
$EC_{Volume} = \frac{EjAt}{V}$		

\*EC, energy consumption.

## 5 Case studies and comparisons according to the literature

There are only a few studies comparing in-house electrodes with commercial ones (Hutton et al., 2013; Huang et al., 2021). For example, eleven different BDD electrodes over Nb substrates by HFCVD were produced by varying the B(OCH<sub>3</sub>)<sub>3</sub>/CH<sub>4</sub> gas mixture (0.125%–0.75%), CH<sub>4</sub>/H<sub>2</sub> ratio (0.5%–1.0%), and gas pressure (5–15 torr) (Huang et al., 2021). They were then compared to commercial BDDs manufactured by Neocoat and Diachem in terms of electrochemical degradation of guaifenesin (pharmaceutical) and TOC removal. Four in-house prepared BDD electrodes showed more significant OEP values reaching a value of 2.45 V against 2.36 V (vs. Ag/AgCl) (commercial). The in-house electrodes [B(OCH<sub>3</sub>)<sub>3</sub>/CH<sub>4</sub> ratio of 0.75%, CH<sub>4</sub>/H<sub>2</sub> ratio of 1%, 5 torr pressure] exhibited the second-best performance in terms of electrochemical degradation of the contaminant as well as TOC removal. The best-performance in-house produced electrode showed a pseudo-first-order reaction rate constant for guaifenesin degradation of 0.33 min<sup>−1</sup>, compared to 0.35 min<sup>−1</sup> (Neocoat) and 0.27 min<sup>−1</sup> (Diachem). After 120 min of electrolysis, the TOC removal efficiency was 100% for the in-house electrode, 100% for Neocoat and 97% for Diachem. Thus, in-house produced BDD anodes may exhibit similar or even superior performance than commercial ones. However, for such statement it is necessary to ensure that the electrodes performance data are reliable and statistically relevant.

According to SLR, phenol and landfill leachate appeared as the analytes with the highest occurrence among articles that use BDD electrodes for electrochemical degradation of water pollutants. In this section, we will discuss most of the published results (to the best of our knowledge) and the diversity of operating conditions when degrading spiked solutions with phenol (Supplementary Table S4) or treating landfill leachate (Supplementary Table S5). One should note that the information included in the previous tables only relates to results obtained using planar BDD electrodes under the simplest

operating conditions for each published article. Moreover, when results were absent along the text and tables of the analyzed articles, data was extracted from plotted graphs using the WebPlotDigitizer tool (Rohatgi, 2019).

The operating conditions used for the electrochemical treatment of phenol and landfill leachate are diverse. In the case of phenol (Supplementary Table S4), ACE values range from 12.3% to 87%, and energy consumption from 26.6 to 475 kWh/kg<sub>COD</sub>. The average ACE for in-house electrodes is 32.4%, against 44% for commercial electrodes. Energy consumption data is insufficient to establish further comparisons since it is presented in different units (e.g., kWh/kg<sub>COD</sub>, kWh/kg<sub>TOC</sub>, kWh/kg<sub>phenol</sub>, and kWh/m<sup>3</sup>). Overall data analysis indicate that commercial electrodes appear to consume less energy and present better current efficiency for phenol degradation. Nevertheless, it is impossible to unambiguously confirm this trend due to the different operating conditions and configuration variability of the electrodes and reactors.

Considering landfill leachate treatment (Supplementary Table S5), ACE values range from 14.4% to 193%, and energy consumption from 5.7 to 285 kWh/kg<sub>COD</sub>. Disregarding experimental conditions, in-house electrodes present higher ACE values but higher energy consumption when compared to commercial ones. Again, one should note that the operating conditions are significantly divergent, and that landfill leachates are complex and variable mixtures that may interfere with synergistic or antagonistic effects.

This review largely reflects the significant variability within the results and the influence of several parameters on the performance of the BDD electrodes (summarized in Figure 8). Considering the few possible comparisons withdrawn in this work, it is not possible to conclude which electrode would be the best choice. Such decision highly depends on proper and effective comparisons under the same degradation conditions and electrochemical cell configuration for a wide range of model pollutants and real wastewater systems. Only then it will be possible to properly evaluate and compare in-house electrodes with commercial ones.

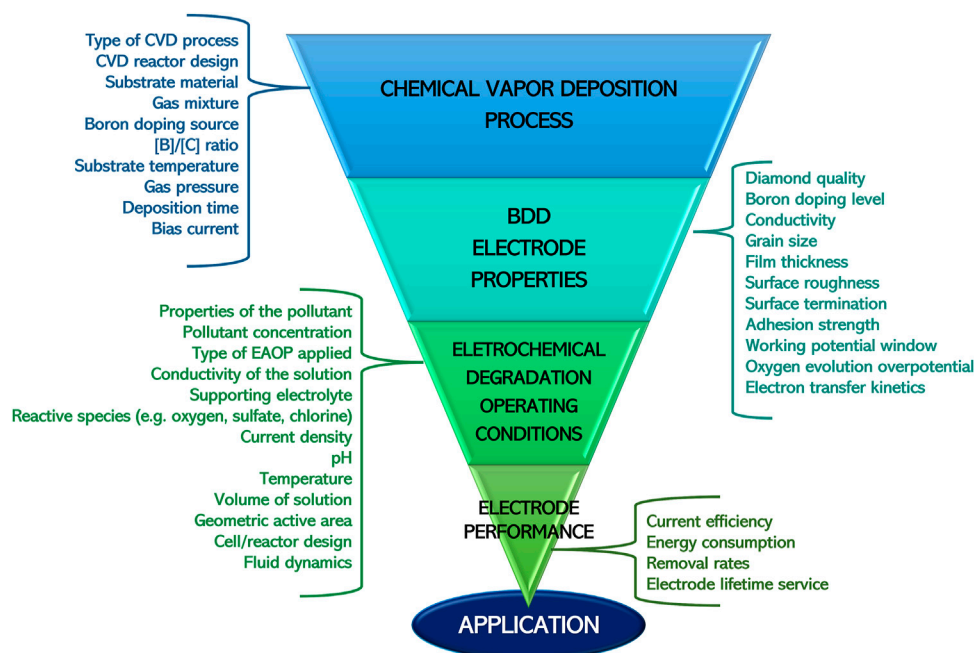


FIGURE 8

Main factors influencing the performance of BDD electrodes in the electrochemical degradation of pollutants (source: the authors).

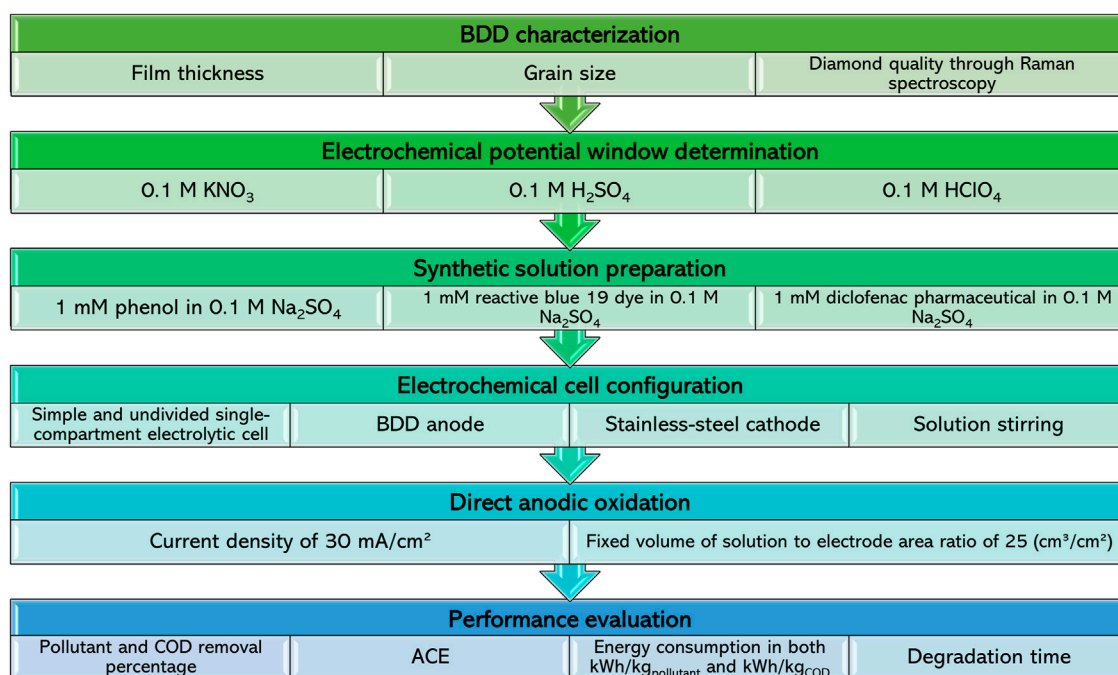


FIGURE 9

Experimental procedure proposed for evaluating BDD electrodes (source: the authors).

## 6 Critical perspectives and future outlook

In this critical review, a detailed discussion of the most relevant parameters that influence the performance of BDD electrodes in the

electrooxidation of water pollutants was carried out. The SLR and bibliometric network graphs were valuable tools to identify the most studied water pollutants, applied EAOPs, and relevant issues such as energy consumption, by-products and toxicity of the treated waters. Based on the gathered information, an attempt was made to

compare the electrooxidation performance between in-house and commercially available BDD electrodes. Both types of electrodes show strong heterogeneities in their final physicochemical characteristics due to the diversity of deposition conditions and applied methods. The comparison attempt is further complicated by the variety of methods, parameters, or electrochemical cells used in the pollutant degradation experiments. Due to the lack of essential information for such comparison, it is not possible to state which one would be the best.

Over the years, many different figures-of-merit based on COD, TOC, or the concentration of the pollutant studied, have been proposed to determine the performance of BDD electrodes. Here, we propose a figure-of-merit equation which normalizes BDD degradation results for a specific contaminant, even if working under different experimental conditions like applied current density or initial pollutant concentration. This is however a remedial solution to allow comparing data obtained under very different conditions.

Data analysis for phenol degradation and landfill leachate treatment generally suggest that commercial BDD electrodes appear to consume less energy and present better current efficiency than in-house prepared anodes. These indications are subjective to a certain point since there is significant variability in the reported operating conditions, which precludes unequivocal conclusions to be made. Nevertheless, there is a strong indication that if in-house electrodes are further optimized, they could reach or surpass the performance of those commercially available. This analysis also points ways for these companies to improve the efficiency of their products.

Our suggestion is to create a uniform reporting/testing procedure: authors could provide further details on the produced BDD electrodes (film thickness, grain size, diamond quality through Raman spectroscopy, resistivity, and working potential window) in three model electrolytes (e.g., 0.1 M KNO<sub>3</sub>, 0.1 M H<sub>2</sub>SO<sub>4</sub>, and 0.1 M HClO<sub>4</sub>). Based on the case study of phenol, we further suggest that all laboratories could perform three water electrooxidation tests, each one with a different model pollutant (e.g., phenol, reactive blue 19 dye, diclofenac pharmaceutical), through direct anodic oxidation in an undivided single-compartment electrolytic cell, under constant stirring, using a BDD anode and a stainless-steel cathode (same geometric area). Moreover, a pollutant concentration of 1 mM, applied current density of 30 mA/cm<sup>2</sup>, electrolyte solution of Na<sub>2</sub>SO<sub>4</sub> for fixing solution conductivity and pH, and a fixed volume of solution to electrode area ratio of 25 (cm<sup>3</sup>/cm<sup>2</sup>) should be adopted. The degradation results should be compared as a function of pollutant and COD removal percentage, ACE, energy consumption (in kWh/kg<sub>pollutant</sub> and kWh/kg<sub>COD</sub>), and degradation time. The proposed procedure is summarized in a flowchart (Figure 9).

Ideally, a standard or normalized procedure should be elaborated, bringing the scientific community and manufacturers together to discuss and reach a consensus on the best practices to evaluate and compare the electrooxidation performance of a BDD electrode, independently of their origin. The creation of such consensual standard would enable faster developments and a straightforward transition of in-house BDD electrodes to

commercial production with consequent effective large-scale application in water treatment plants.

## Author contributions

Conceptualization: FO and PB; investigation: PB; writing-original draft preparation: PB; writing-review and editing: AG; supervision: FO and JT; project administration: FO and RS; funding acquisition: RS. All authors have read and agreed to the published version of the manuscript.

## Funding

This work was developed within the scope of the project CICECO-Aveiro Institute of Materials, UIDB/50011/2020, UIDP/50011/2020, and LA/P/0006/2020, financed by national funds through the FCT/MEC (PIDDAC). This work is also funded by national funds (OE) through FCT—Fundação para a Ciência e a Tecnologia, I.P., in the scope of the framework contract foreseen in the numbers 4, 5, and 6 of the article 23, of the Decree-Law 57/2016, of 29 August changed by Law 57/2017, of 19 July.

## Acknowledgments

The authors wish to thank the University of Aveiro and CICECO—Aveiro Institute of Materials for their contributions to this work, as well as the organizations responsible for funding the project: European Regional Development Fund (FEDER) and Fundação para a Ciência e a Tecnologia (FCT).

## Conflict of interest

The authors declare that the research was conducted in the absence of any commercial or financial relationships that could be construed as a potential conflict of interest.

## Publisher's note

All claims expressed in this article are solely those of the authors and do not necessarily represent those of their affiliated organizations, or those of the publisher, the editors and the reviewers. Any product that may be evaluated in this article, or claim that may be made by its manufacturer, is not guaranteed or endorsed by the publisher.

## Supplementary material

The Supplementary Material for this article can be found online at: <https://www.frontiersin.org/articles/10.3389/fmats.2023.1020649/full#supplementary-material>

## References

- Alvarez Pugliese, C. E., Martínez Hernández, L., Imbachi Ordoñez, S., Marriaga Cabrales, N., and Machuca Martínez, F. (2016). Pilot scale anodic oxidation of pretreated vinasse using boron doped diamond electrodes. *CT&F - Cienc. Tecnol. Futuro* 6 (4), 67–77. doi:10.29047/01225383.04
- Araújo, C. A. Á. d. (2006). Bibliometria: Evolução histórica e questões atuais. *Em Questão* 12 (1), 11–32.
- Azevedo, A. F., Baldan, M. R., and Ferreira, N. G. (2013). Doping level influence on chemical surface of diamond electrodes. *J. Phys. Chem. Solids* 74 (4), 599–604. doi:10.1016/j.jpcs.2012.12.013
- Ballutaud, D., Jomard, F., Kociniewski, T., Rzepka, E., Girard, H., and Saada, S. (2008). Sp<sup>3</sup>/sp<sup>2</sup> character of the carbon and hydrogen configuration in micro- and nanocrystalline diamond. *Diam. Relat. Mater.* 17 (4–5), 451–456. doi:10.1016/j.diamond.2007.10.004
- Baluchová, S., Taylor, A., Mortet, V., Sedláková, S., Klimša, L., Kopeček, J., et al. (2019). Porous boron doped diamond for dopamine sensing: Effect of boron doping level on morphology and electrochemical performance. *Electrochimica Acta* 327, 135025. doi:10.1016/j.electacta.2019.135025
- Bard, A. J. (2010). Inner-sphere heterogeneous electrode reactions. Electrocatalysis and photocatalysis: The challenge. *J. Am. Chem. Soc.* 132 (22), 7559–7567. doi:10.1021/ja101578m
- Belhadj Tahar, N., and Savall, A. (2019). Mechanistic aspects of phenol electrochemical degradation by oxidation on a Ta/PbO<sub>2</sub> anode. *J. Electrochem. Soc.* 145 (10), 3427–3434. doi:10.1149/1.1838822
- Bennett, J. A., Wang, J., Show, Y., and Swain, G. M. (2004). Effect of sp<sup>2</sup>-bonded nondiamond carbon impurity on the response of boron-doped polycrystalline diamond thin-film electrodes. *J. Electrochem. Soc.* 151 (9), E306–E313. doi:10.1149/1.1780111
- Bergmann, M. E. H., Iourtchouk, T., Schmidt, W., Hartmann, J., Fischer, M., Nüsske, G., et al. (2015). Laboratory- and technical-scale comparison of chlorate and perchlorate formation during drinking water electrolysis: A field study. *J. Appl. Electrochem.* 45 (7), 765–778. doi:10.1007/s10800-015-0826-z
- Bernard, M., Deneuville, A., and Muret, P. (2004). Non-destructive determination of the boron concentration of heavily doped metallic diamond thin films from Raman spectroscopy. *Diam. Relat. Mater.* 13 (2), 282–286. doi:10.1016/j.diamond.2003.10.051
- Bogdanowicz, R., and Ryl, J. (2022). Structural and electrochemical heterogeneities of boron-doped diamond surfaces. *Curr. Opin. Electrochem.* 31, 100876. doi:10.1016/j.coelec.2021.100876
- Braga, N. A., Cairo, C. A. A., Matsushima, J. T., Baldan, M. R., and Ferreira, N. G. (2009). Diamond/porous titanium three-dimensional hybrid electrodes. *J. Solid State Electrochem.* 14 (2), 313–321. doi:10.1007/s10008-009-0855-9
- Brillas, E., Boye, B., Sirés, I., Garrido, J. A., Rodn'guez, R. M. a., Arias, C., et al. (2004). Electrochemical destruction of chlorophenoxy herbicides by anodic oxidation and electro-Fenton using a boron-doped diamond electrode. *Electrochimica Acta* 49 (25), 4487–4496. doi:10.1016/j.electacta.2004.05.006
- Brillas, E., and Casado, J. (2002). Aniline degradation by Electro-Fenton<sup>®</sup> and peroxi-coagulation processes using a flow reactor for wastewater treatment. *Chemosphere* 47 (3), 241–248. doi:10.1016/s0045-6535(01)00221-1
- Brillas, E. (2014). Electro-fenton, uva photoelectro-fenton and solar photoelectro-fenton treatments of organics in waters using a boron-doped diamond anode: A review. *J. Mexican Chem. Soc.* 58 (3), 239–255. doi:10.29356/jmcs.v58i3.131
- Brillas, E., Garrido, J. A., Rodríguez, R. M., Arias, C., Cabot, P. L., and Centellas, F. (2008). Wastewaters by electrochemical advanced oxidation processes using a BDD anode and electrogenerated H<sub>2</sub>O<sub>2</sub> with Fe(II) and UVA light as catalysts. *Port. Electrochimica Acta* 26 (1), 15–46. doi:10.4152/pea.200801015
- Brillas, E., and Martínez-Huitle, C. A. (2011). *Synthetic diamond films: Preparation, electrochemistry, characterization, and applications*. New York, United States: Wiley.
- Brillas, E., Sires, I., Arias, C., Cabot, P. L., Centellas, F., Rodríguez, R. M., et al. (2005). Mineralization of paracetamol in aqueous medium by anodic oxidation with a boron-doped diamond electrode. *Chemosphere* 58 (4), 399–406. doi:10.1016/j.chemosphere.2004.09.028
- Brito, C. N., Ferreira, M. B., de, O., Marcionilio, S. M. L., de Moura Santos, E. C. M., Léon, J. J. L., et al. (2018). Electrochemical oxidation of acid violet 7 dye by using Si/BDD and Nb/BDD electrodes. *J. Electrochem. Soc.* 165 (5), E250–E255. doi:10.1149/2.1111805jes
- Bushuev, E. V., Yurov, V. Y., Bolshakov, A. P., Ralchenko, V. G., Khomich, A. A., Antonova, I. A., et al. (2017). Express *in situ* measurement of epitaxial CVD diamond film growth kinetics. *Diam. Relat. Mater.* 72, 61–70. doi:10.1016/j.diamond.2016.12.021
- Cano, A., Barrera, C., Cotillas, S., Llanos, J., Cañizares, P., and Rodrigo, M. A. (2016). Use of DiaCell modules for the electro-disinfection of secondary-treated wastewater with diamond anodes. *Chem. Eng. J.* 306, 433–440. doi:10.1016/j.cej.2016.07.090
- Cano, A., Cañizares, P., Barrera, C., Sáez, C., and Rodrigo, M. A. (2011). Use of low current densities in electrolyses with conductive-diamond electrochemical — oxidation to disinfect treated wastewaters for reuse. *Electrochem. Commun.* 13 (11), 1268–1270. doi:10.1016/j.elecom.2011.08.027
- Chang, M., Gao, C., and Jiang, J. (2009). Electrochemical oxidation of organic compounds using boron-doped diamond electrode. *J. Electrochem. Soc.* 156 (2), E50–E54. doi:10.1149/1.3042220
- Chaplin, B. P. (2014). Critical review of electrochemical advanced oxidation processes for water treatment applications. *Environ. Sci. Process Impacts* 16 (6), 1182–1203. doi:10.1039/c3em00679d
- Chaplin, B. P., Wyle, I., Zeng, H., Carlisle, J. A., and Farrell, J. (2011). Characterization of the performance and failure mechanisms of boron-doped ultrananocrystalline diamond electrodes. *J. Appl. Electrochem.* 41 (11), 1329–1340. doi:10.1007/s10800-011-0351-7
- Chaudhuri, S., Hall, S. J., Klein, B. P., Walker, M., Logsdail, A. J., Macpherson, J. V., et al. (2022). Coexistence of carbonyl and ether groups on oxygen-terminated (110)-oriented diamond surfaces. *Commun. Mater.* 3 (1), 6. doi:10.1038/s43246-022-00228-4
- Chen, G. (2004). Electrochemical technologies in wastewater treatment. *Sep. Purif. Technol.* 38 (1), 11–41. doi:10.1016/j.seppur.2003.10.006
- Chen, P., Mu, Y., Chen, Y., Tian, L., Jiang, X. H., Zou, J. P., et al. (2022). Shifts of surface-bound \*OH to homogeneous \*OH in BDD electrochemical system via UV irradiation for enhanced degradation of hydrophilic aromatic compounds. *Chemosphere* 291, 132817. doi:10.1016/j.chemosphere.2021.132817
- Chen, T.-S., Chen, P.-H., and Huang, K.-L. (2014). Electrochemical degradation of N,N-diethyl-m-toluidine on a boron-doped diamond electrode. *J. Taiwan Inst. Chem. Eng.* 45 (5), 2615–2621. doi:10.1016/j.jtice.2014.06.020
- Chen, X., and Chen, G. (2004). Proper hot filament CVD conditions for fabrication of Ti-boron doped diamond electrodes. *J. Electrochem. Soc.* 151 (4), B214–B219. doi:10.1149/1.1651529
- Chen, X., Gao, F., and Chen, G. (2005). Comparison of Ti/BDD and Ti/SnO<sub>2</sub>? Sb<sub>2</sub>O<sub>5</sub> electrodes for pollutant oxidation. *J. Appl. Electrochem.* 35 (2), 185–191. doi:10.1007/s10800-004-6068-0
- Choi, Y. S., Lee, Y. K., Kim, J. Y., Kim, K. M., and Lee, Y. K. (2017). Influence of manufacturing conditions for the life time of the boron-doped diamond electrode in wastewater treatment. *Korean J. Mater. Res.* 27 (3), 137–143. doi:10.3740/Mrsk.2017.27.3.137
- Cifre, J., Puigdollers, J., Polo, M. C., and Esteve, J. (1994). Trimethylboron doping of CVD diamond thin films. *Diam. Relat. Mater.* 3 (4–6), 628–631. doi:10.1016/0925-9635(94)90238-0
- Clematis, D., Cerisola, G., and Panizza, M. (2017). Electrochemical oxidation of a synthetic dye using a BDD anode with a solid polymer electrolyte. *Electrochem. Commun.* 75, 21–24. doi:10.1016/j.elecom.2016.12.008
- Clematis, D., and Panizza, M. (2021a). Application of boron-doped diamond electrodes for electrochemical oxidation of real wastewaters. *Curr. Opin. Electrochem.* 30, 100844. ARTN 100844. doi:10.1016/j.coelec.2021.100844
- Clematis, D., and Panizza, M. (2021b). Electrochemical oxidation of organic pollutants in low conductive solutions. *Curr. Opin. Electrochem.* 26, 100665. doi:10.1016/j.coelec.2020.100665
- Cobb, S. J., Ayres, Z. J., and Macpherson, J. V. (2018). “Boron doped diamond: A designer electrode material for the twenty-first century,” in *Annual review of analytical chemistry* (San Mateo, California: Annual Reviews).
- Comninellis, C., Kapalka, A., Malato, S., Parsons, S. A., Poullos, I., and Mantzavinos, D. (2008). Advanced oxidation processes for water treatment: Advances and trends for R&D. *J. Chem. Technol. Biotechnol.* 83 (6), 769–776. doi:10.1002/jctb.1873
- Comninellis, C., and Pulgarin, C. (1991). Anodic oxidation of phenol for waste water treatment. *J. Appl. Electrochem.* 21 (8), 703–708. doi:10.1007/bf01034049
- Cornejo, O. M., Murrieta, M. F., Castañeda, L. F., and Nava, J. L. (2020). Characterization of the reaction environment in flow reactors fitted with BDD electrodes for use in electrochemical advanced oxidation processes: A critical review. *Electrochimica Acta* 331, 135373. doi:10.1016/j.electacta.2019.135373
- Cornejo, O. M., Murrieta, M. F., Castañeda, L. F., and Nava, J. L. (2021). Electrochemical reactors equipped with BDD electrodes: Geometrical aspects and applications in water treatment. *Curr. Opin. Solid State Mater. Sci.* 25 (4), 100935. doi:10.1016/j.cossms.2021.100935
- Cotillas, S., de Vidales, M. J., Llanos, J., Saez, C., Canizares, P., and Rodrigo, M. A. (2016). Electrolytic and electro-irradiated processes with diamond anodes for the oxidation of persistent pollutants and disinfection of urban treated wastewater. *J. Hazard Mater* 319, 93–101. doi:10.1016/j.jhazmat.2016.01.050
- Crispim, A. C., da Silva Mendonça de Paiva, S., de Araújo, D. M., Souza, F. L., and Dos Santos, E. V. (2022). Ultrasound and UV technologies for wastewater treatment using boron-doped diamond anodes. *Curr. Opin. Electrochem.* 33, 100935. doi:10.1016/j.coelec.2021.100935
- da Silva, S. W., Navarro, E. M. O., Rodrigues, M. A. S., Bernardes, A. M., and Perez-Herranz, V. (2018). The role of the anode material and water matrix in the electrochemical oxidation of norfloxacin. *Chemosphere* 210, 615–623. doi:10.1016/j.chemosphere.2018.07.057



- Daskalaki, V. M., Fulgione, I., Frontistis, Z., Rizzo, L., and Mantzavinos, D. (2013). Solar light-induced photoelectrocatalytic degradation of bisphenol-A on TiO<sub>2</sub>/ITO film anode and BDD cathode. *Catal. Today* 209, 74–78. doi:10.1016/j.cattod.2012.07.026
- De Luna, Y., and Bensalah, N. (2022). Review on the electrochemical oxidation of endocrine-disrupting chemicals using BDD anodes. *Curr. Opin. Electrochem.* 32, 100900. doi:10.1016/j.coelec.2021.100900
- de Queiroz, J. L. A., da Silva, A. R. L., de Moura, D. C., da Silva, D. R., and Martínez-Huitle, C. A. (2017). Electrochemical study of carboxylic acids with Nb-supported boron doped diamond anode. Part 1: Potentiodynamic measurements and bulk oxidations. *J. Electroanal. Chem.* 794, 204–211. doi:10.1016/j.jelechem.2017.04.006
- de Souza, R. B. A., and Ruotolo, L. A. M. (2013). Phenol electrooxidation in different supporting electrolytes using boron-doped diamond anodes. *Int. J. Electrochem. Sci.* 8 (1), 643–657.
- Denisenko, A., Pietzka, C., Romanyuk, A., El-Hajj, H., and Kohn, E. (2008). The electronic surface barrier of boron-doped diamond by anodic oxidation. *J. Appl. Phys.* 103 (1), 014904. doi:10.1063/1.2827481
- Detlaff, A., Sobaszek, M., Klimczuk, T., and Bogdanowicz, R. (2021). Enhanced electrochemical kinetics of highly-oriented (111)-textured boron-doped diamond electrodes induced by deuterium plasma chemistry. *Carbon* 174, 594–604. doi:10.1016/j.carbon.2020.11.096
- Donthu, N., Kumar, S., Mukherjee, D., Pandey, N., and Lim, W. M. (2021). How to conduct a bibliometric analysis: An overview and guidelines. *J. Bus. Res.* 133, 285–296. doi:10.1016/j.jbusres.2021.04.070
- Durán, F. E., de Araújo, D. M., do Nascimento Brito, C., Santos, E. V., Ganiyu, S. O., and Martínez-Huitle, C. A. (2018). Electrochemical technology for the treatment of real washing machine effluent at pre-pilot plant scale by using active and non-active anodes. *J. Electroanal. Chem.* 818, 216–222. doi:10.1016/j.jelechem.2018.04.029
- Dychalska, A., Popielarski, P., Franków, W., Fabisiak, K., Paprocki, K., and Szybowicz, M. (2015). Study of CVD diamond layers with amorphous carbon admixture by Raman scattering spectroscopy. *Mater. Pol.* 33 (4), 799–805. doi:10.1515/msp-2015-0067
- Einaga, Y. (2018). Development of electrochemical applications of boron-doped diamond electrodes. *Bull. Chem. Soc. Jpn.* 91 (12), 1752–1762. doi:10.1246/bcsj.20180268
- Einaga, Y., Foord, J. S., and Swain, G. M. (2014). Diamond electrodes: Diversity and maturity. *MRS Bull.* 39 (6), 525–532. doi:10.1557/mrs.2014.94
- Enache, T. A., Chiorcea-Paquim, A.-M., Fatibello-Filho, O., and Oliveira-Brett, A. M. (2009). Hydroxyl radicals electrochemically generated *in situ* on a boron-doped diamond electrode. *Electrochem. Commun.* 11 (7), 1342–1345. doi:10.1016/j.elecom.2009.04.017
- Espinoza, L. C., Aranda, M., Contreras, D., Henríquez, A., and Salazar, R. (2019). Effect of the sp<sup>3</sup>/sp<sup>2</sup> ratio in boron-doped diamond electrodes on the degradation pathway of aniline by anodic oxidation. *ChemElectroChem* 6 (18), 4801–4810. doi:10.1002/celc.201901218
- Espinoza-Montero, P. J., Vasquez-Medrano, R., Ibanez, J. G., and Frontana-Urbe, B. A. (2013). Efficient anodic degradation of phenol paired to improved cathodic production of H<sub>2</sub>O<sub>2</sub> at BDD electrodes. *J. Electrochem. Soc.* 160 (7), G3171–G3177. doi:10.1149/2.027307jes
- Fabianska, A., Bialk-Bielinska, A., Stepnowski, P., Stolte, S., and Siedlecka, E. M. (2014). Electrochemical degradation of sulfonamides at BDD electrode: Kinetics, reaction pathway and eco-toxicity evaluation. *J. Hazard Mater.* 280, 579–587. doi:10.1016/j.jhazmat.2014.08.050
- Ferrari, A. C., and Robertson, J. (2004). Raman spectroscopy of amorphous, nanostructured, diamond-like carbon, and nanodiamond. *Philos. Trans. A Math. Phys. Eng. Sci.* 362 (1824), 2477–2512. doi:10.1098/rsta.2004.1452
- Flox, C., Garrido, J. A., Rodríguez, R. M., Cabot, P.-L., Centellas, F., Arias, C., et al. (2007). Mineralization of herbicide mecoprop by photoelectro-Fenton with UVA and solar light. *Catal. Today* 129 (1–2), 29–36. doi:10.1016/j.cattod.2007.06.049
- Freitas, J. M., Oliveira, T. D. C., Munoz, R. A. A., and Richter, E. M. (2019). Boron doped diamond electrodes in flow-based systems. *Front. Chem.* 7 (APR), 190. doi:10.3389/fchem.2019.00190
- Fryda, M., Herrmann, D., Schafer, L., Klages, C. P., Perret, A., Haenni, W., et al. (1999). Properties of diamond electrodes for wastewater treatment. *New Diam. Front. Carbon Technol.* 9 (3), 229–240.
- Ganiyu, S. O., and Martínez-Huitle, C. A. (2019). Nature, mechanisms and reactivity of electrogenerated reactive species at thin-film boron-doped diamond (BDD) electrodes during electrochemical wastewater treatment. *ChemElectroChem* 6 (9), 2379–2392. doi:10.1002/celc.201900159
- Gerger, I., and Haubner, R. (2008). The behaviour of Ti-substrates during deposition of boron doped diamond. *Int. J. Refract. Metals Hard Mater.* 26 (5), 438–443. doi:10.1016/j.jrmhm.2007.10.002
- Gheeraert, E., Gonon, P., Deneuille, A., Abello, L., and Lucazeau, G. (1993). Effect of boron incorporation on the “quality” of MPCVD diamond films. *Diam. Relat. Mater.* 2 (5–7), 742–745. doi:10.1016/0925-9635(93)90215-n
- Gomez-Ruiz, B., Diban, N., and Uriaga, A. (2019). Comparison of microcrystalline and ultrananocrystalline boron doped diamond anodes: Influence on perfluorooctanoic acid electrolysis. *Sep. Purif. Technol.* 208, 169–177. doi:10.1016/j.seppur.2018.03.044
- Gracio, J. J., Fan, Q. H., and Madaleno, J. C. (2010). Diamond growth by chemical vapour deposition. *J. Phys. D Appl. Phys.* 43 (37), 374017. doi:10.1088/0022-3727/43/37/374017
- Griesser, M., Stinger, G., Grasserbauer, M., Baumann, H., Link, F., Wurzing, P., et al. (1994). Characterization of tantalum impurities in hot-filament diamond layers. *Diam. Relat. Mater.* 3 (4–6), 638–644. doi:10.1016/0925-9635(94)90240-2
- Groenen Serrano, K., Savall, A., Latapie, L., Racaud, C., Rondet, P., and Bertrand, N. (2015). Performance of Ti/Pt and Nb/BDD anodes for dechlorination of nitric acid and regeneration of silver(II) in a tubular reactor for the treatment of solid wastes in nuclear industry. *J. Appl. Electrochem.* 45 (7), 779–786. doi:10.1007/s10800-015-0830-3
- Guedes, V. L. S., and Borschiver, S. I. (2005). “Bibliometria: uma ferramenta estatística para a gestão da informação e do conhecimento em sistemas de informação, de comunicação e de avaliação científica e tecnológica,” in *Encontro Nacional de Ciência da Informação*, 1–18. Salvador, Brazil: VI CINFORM Encontro Nacional de Ciência da Informação.
- Guimaraes, G. A. A., Lacerda, J. N., Xing, Y., Ponzio, E. A., Pacheco, W. F., Semaan, F. S., et al. (2020). Development and application of electrochemical sensor of boron-doped diamond (BDD) modified by drop casting with tin hexacyanoferrate. *J. Solid State Electrochem.* 24 (8), 1769–1779. doi:10.1007/s10008-020-04558-6
- Guo, L., and Chen, G. (2007). Long-term stable Ti/BDD electrode fabricated with HF/CVD method using two-stage substrate temperature. *J. Electrochem. Soc.* 154 (12), D657–D661. doi:10.1149/1.2790798
- Haenni, W., Rychen, P., Fryda, M., and Comninellis, C. (2004). “Chapter 5 Industrial applications of diamond electrodes,” in *Thin-film diamond II*. Editors C. E. Nebel and J. Ristein (Amsterdam, Netherlands: Elsevier), 149–196.
- Hangarter, C. M., O’Grady, W. E., Stoner, B. R., and Natishan, P. M. (2015). Electrochemical oxidation of phenol using boron-doped diamond electrodes. *ECS Trans.* 64 (46), 1–9. doi:10.1149/06446.0001ecst
- He, Y., Huang, W., Chen, R., Zhang, W., and Lin, H. (2015). Improved electrochemical performance of boron-doped diamond electrode depending on the structure of titanium substrate. *J. Electroanal. Chem.* 758, 170–177. doi:10.1016/j.jelechem.2015.08.017
- He, Y., Lin, H., Guo, Z., Zhang, W., Li, H., and Huang, W. (2019). Recent developments and advances in boron-doped diamond electrodes for electrochemical oxidation of organic pollutants. *Sep. Purif. Technol.* 212, 802–821. doi:10.1016/j.seppur.2018.11.056
- He, Y., Wang, X., Huang, W., Chen, R., Lin, H., and Li, H. (2016). Application of porous boron-doped diamond electrode towards electrochemical mineralization of triphenylmethane dye. *J. Electroanal. Chem.* 775, 292–298. doi:10.1016/j.jelechem.2016.06.023
- He, Y., Zhao, D., Lin, H., Huang, H., Li, H., and Guo, Z. (2022). Design of diamond anodes in electrochemical degradation of organic pollutants. *Curr. Opin. Electrochem.* 32, 100878. doi:10.1016/j.coelec.2021.100878
- Huang, K.-L., Chao, P.-J., Kuo, Y.-M., Chi, K.-Y., Cheng, H. M., Wu, R.-Z., et al. (2021). Response surface methodology-based fabrication of boron-doped diamond electrodes for electrochemical degradation of guaifenesin in aqueous solutions. *J. Taiwan Inst. Chem. Eng.* 123, 124–133. doi:10.1016/j.jtice.2021.05.035
- Huang, Y. H., Chen, C. C., Huang, G. H., and Chou, S. S. (2001). Comparison of a novel electro-Fenton method with Fenton’s reagent in treating a highly contaminated wastewater. *Water Sci. Technol.* 43 (2), 17–24. doi:10.2166/wst.2001.0068
- Hurwitz, G., Hoek, E. M. V., Liu, K., Fan, L., and Roddick, F. A. (2014). Photo-assisted electrochemical treatment of municipal wastewater reverse osmosis concentrate. *Chem. Eng. J.* 249, 180–188. doi:10.1016/j.cej.2014.03.084
- Hutton, L. A., Iacobini, J. G., Bitziou, E., Channon, R. B., Newton, M. E., and Macpherson, J. V. (2013). Examination of the factors affecting the electrochemical performance of oxygen-terminated polycrystalline boron-doped diamond electrodes. *Anal. Chem.* 85 (15), 7230–7240. doi:10.1021/ac401042t
- Iniesta, J. (2001). Electrochemical oxidation of phenol at boron-doped diamond electrode. *Electrochimica Acta* 46 (23), 3573–3578. doi:10.1016/s0013-4686(01)00630-2
- Isshiki, H., Yoshida, M., Tobita, R., Shigeeda, T., Kinoshita, M., Matsushima, K., et al. (2012). Enhancement of diamond nucleation by atomic silicon microaddition. *Jpn. J. Appl. Phys.* 51 (9), 090108. doi:10.1143/jjap.51.090108
- Jagannadham, K., Lance, M. J., and Butler, J. E. (2010). Laser annealing of neutron irradiated boron-10 isotope doped diamond. *J. Mater. Sci.* 46 (8), 2518–2528. doi:10.1007/s10853-010-5102-3
- Jia, F.-C., Bai, Y.-z., Qu, F., Sun, J., Zhao, J.-j., and Jiang, X. (2010). The influence of gas pressure and bias current on the crystallinity of highly boron-doped diamond films. *New Carbon Mater.* 25 (5), 357–362. doi:10.1016/s1872-5805(09)60039-1
- Jian, Z., Heide, M., Yang, N., Engelhard, C., and Jiang, X. (2021). Diamond fibers for efficient electrocatalytic degradation of environmental pollutants. *Carbon* 175, 36–42. doi:10.1016/j.carbon.2020.12.066

- Jiang, J., Chang, M., and Pan, P. (2008). Simultaneous hydrogen production and electrochemical oxidation of organics using boron-doped diamond electrodes. *Environ. Sci. Technol.* 42 (8), 3059–3063. doi:10.1021/es702466k
- Kapalka, A., Lanova, B., Baltruschat, H., Föti, G. r., and Comninellis, C. (2009). A DEMS study of methanol and formic acid oxidation on boron-doped diamond electrode. *J. Electrochem. Soc.* 156 (11), E149–E153. doi:10.1149/1.3207009
- Karim, A. V., Nidheesh, P. V., and Oturan, M. A. (2021). Boron-doped diamond electrodes for the mineralization of organic pollutants in the real wastewater. *Curr. Opin. Electrochem.* 30, 100855. doi:10.1016/j.coelec.2021.100855
- Kondo, T., Ito, H., Kusakabe, K., Ohkawa, K., Einaga, Y., Fujishima, A., et al. (2007). Plasma etching treatment for surface modification of boron-doped diamond electrodes. *Electrochimica Acta* 52 (11), 3841–3848. doi:10.1016/j.electacta.2006.11.001
- Kornienko, G. V., Chaenko, N. V., Maksimov, N. G., Kornienko, V. L., and Varnin, V. P. (2011). Electrochemical oxidation of phenol on boron-doped diamond electrode. *Russ. J. Electrochem.* 47 (2), 225–229. doi:10.1134/s102319351102011x
- Kowalska, M., Paprocki, K., Szybowski, M., Wrzyszczyński, A., Łoś, S., and Fabisiak, K. (2020). Electrochemical sensitivity of undoped CVD diamond films as function of their crystalline quality. *J. Electroanal. Chem.* 859, 113811. doi:10.1016/j.jelechem.2019.113811
- Kuchtová, G., Chýlková, J., Váňa, J., Vojs, M., and Dušek, L. (2020). Electro-oxidative decolorization and treatment of model wastewater containing Acid Blue 80 on boron doped diamond and platinum anodes. *J. Electroanal. Chem.* 863, 114036. doi:10.1016/j.jelechem.2020.114036
- Kwon, J.-I., You, M., Kim, S., and Keun, S. P. (2019). Performance of BDD electrodes prepared on various substrates for wastewater treatment. *J. Korean Inst. Surf. Eng.* 52 (2), 53–57. doi:10.5695/JKISE.2019.52.2.53
- Lacasa, E., Tsalaki, E., Sbokou, Z., Rodrigo, M. A., Mantzavinos, D., and Diamadopoulos, E. (2013). Electrochemical disinfection of simulated ballast water on conductive diamond electrodes. *Chem. Eng. J.* 223, 516–523. doi:10.1016/j.cej.2013.03.003
- Lagrange, J. P., Deneuville, A., and Gheeraert, E. (1998). Activation energy in low compensated homoepitaxial boron-doped diamond films. *Diam. Relat. Mater.* 7 (9), 1390–1393. doi:10.1016/s0925-9635(98)00225-8
- Larsson, K. (2020). “Simulation of diamond surface chemistry: Reactivity and properties,” in *Some aspects of diamonds in scientific research and high technology*. Editor E. Lipatov (London: IntechOpen).
- Lee, C.-H., Lee, E.-S., Lim, Y.-K., Park, K.-H., Park, H.-D., and Lim, D.-S. (2017). Enhanced electrochemical oxidation of phenol by boron-doped diamond nanowire electrode. *RSC Adv.* 7 (11), 6229–6235. doi:10.1039/c6ra26287b
- Lee, K. H., Seong, W. K., and Ruoff, R. S. (2022). CVD diamond growth: Replacing the hot metallic filament with a hot graphite plate. *Carbon* 187, 396–403. doi:10.1016/j.carbon.2021.11.032
- Lévy-Clément, C., Ndao, N. A., Katty, A., Bernard, M., Deneuville, A., Comninellis, C., et al. (2003). Boron doped diamond electrodes for nitrate elimination in concentrated wastewater. *Diam. Relat. Mater.* 12 (3–7), 606–612. doi:10.1016/s0925-9635(02)00368-0
- Li, H., Yu, Q., Yang, B., Li, Z., and Lei, L. (2015). Electro-catalytic oxidation of artificial human urine by using BDD and IrO<sub>2</sub> electrodes. *J. Electroanal. Chem.* 738, 14–19. doi:10.1016/j.jelechem.2014.11.018
- Li, H., Yu, Q., Yang, B., Li, Z., and Lei, L. (2014). Electrochemical treatment of artificial humidity condensate by large-scale boron doped diamond electrode. *Sep. Purif. Technol.* 138, 13–20. doi:10.1016/j.seppur.2014.10.004
- Li, W., Liu, G., Miao, D., Li, Z., Chen, Y., Gao, X., et al. (2020). Electrochemical oxidation of Reactive Blue 19 on boron-doped diamond anode with different supporting electrolyte. *J. Environ. Chem. Eng.* 8 (4), 103997. doi:10.1016/j.jece.2020.103997
- Li, X., Li, H., Li, M., Li, C., Sun, D., Lei, Y., et al. (2018). Preparation of a porous boron-doped diamond/Ta electrode for the electrocatalytic degradation of organic pollutants. *Carbon* 129, 543–551. doi:10.1016/j.carbon.2017.12.052
- Lim, P. Y., Lin, F. Y., Shih, H. C., Ralchenko, V. G., Varnin, V. P., Pleskov, Y. V., et al. (2008). Improved stability of titanium based boron-doped chemical vapor deposited diamond thin-film electrode by modifying titanium substrate surface. *Thin Solid Films* 516 (18), 6125–6132. doi:10.1016/j.tsf.2007.11.016
- Liu, F. B., Wang, J. D., Liu, B., Li, X. M., and Chen, D. R. (2007). Effect of electronic structures on electrochemical behaviors of surface-terminated boron-doped diamond film electrodes. *Diam. Relat. Mater.* 16 (3), 454–460. doi:10.1016/j.diamond.2006.08.016
- Liu, Z., Li, H., Li, M., Li, C., Qian, L., Su, L., et al. (2018). Preparation of polycrystalline BDD/Ta electrodes for electrochemical oxidation of organic matter. *Electrochimica Acta* 290, 109–117. doi:10.1016/j.electacta.2018.09.058
- Lourencao, B. C., Brocenschi, R. F., Medeiros, R. A., Fatibello-Filho, O., and Rocha-Filho, R. C. (2020). Analytical applications of electrochemically pretreated boron-doped diamond electrodes. *ChemElectroChem* 7 (6), 1291–1311. doi:10.1002/celec.202000050
- Lu, X.-R., Ding, M.-H., Zhang, C., and Tang, W.-Z. (2019a). Comparative study on stability of boron doped diamond coated titanium and niobium electrodes. *Diam. Relat. Mater.* 93, 26–33. doi:10.1016/j.diamond.2019.01.010
- Lu, X. R., Ding, M. H., Zhang, C., and Tang, W. Z. (2018). Investigation on microstructure evolution and failure mechanism of boron doped diamond coated titanium electrode during accelerated life test. *Thin Solid Films* 660, 306–313. doi:10.1016/j.tsf.2018.06.039
- Lu, X. R., Ding, M. H., Zhang, L., Yang, Z. L., Lu, Y., and Tang, W. Z. (2019b). Optimizing the microstructure and corrosion resistance of BDD coating to improve the service life of Ti/BDD coated electrode. *Materials* 12 (19), 3188. doi:10.3390/ma12193188
- Lu, Y.-G., Turner, S., Verbeeck, J., Janssens, S. D., Wagner, P., Haenen, K., et al. (2012). Direct visualization of boron dopant distribution and coordination in individual chemical vapor deposition nanocrystalline B-doped diamond grains. *Appl. Phys. Lett.* 101 (4), 041907. doi:10.1063/1.4738885
- Luong, J. H., Male, K. B., and Glennon, J. D. (2009). Boron-doped diamond electrode: Synthesis, characterization, functionalization and analytical applications. *Analyst* 134 (10), 1965–1979. doi:10.1039/b910206j
- Ma, P., Ma, H., Sabatino, S., Galia, A., and Scialdone, O. (2018). Electrochemical treatment of real wastewater. Part I: Effluents with low conductivity. *Chem. Eng. J.* 336, 133–140. doi:10.1016/j.cej.2017.11.046
- Machini, W. B. S., Enache, T. A., Jorge, S. M. A., and Oliveira-Brett, A. M. (2016). Isotretinoin oxidation and electroanalysis in a pharmaceutical drug using a boron-doped diamond electrode. *Electroanalysis* 28 (11), 2709–2715. doi:10.1002/elan.201600206
- Mackulák, T., Medvecká, E., Vojs Staňová, A., Brandeburová, P., Grabic, R., Golovko, O., et al. (2020). Boron doped diamond electrode – the elimination of psychoactive drugs and resistant bacteria from wastewater. *Vacuum* 171, 108957. doi:10.1016/j.vacuum.2019.108957
- Macpherson, J. V. (2015). A practical guide to using boron doped diamond in electrochemical research. *Phys. Chem. Chem. Phys.* 17 (5), 2935–2949. doi:10.1039/c4cp04022h
- Maldonado, V. Y., Becker, M. F., Nickelsen, M. G., and Witt, S. E. (2021). Laboratory and semi-pilot scale study on the electrochemical treatment of perfluoroalkyl acids from ion exchange still bottoms. *Water* 13 (20), 2873. doi:10.3390/w13202873
- Martin, H. B., Argoitia, A., Landau, U., Anderson, A. B., and Angus, J. C. (2019). Hydrogen and oxygen evolution on boron-doped diamond electrodes. *J. Electrochem. Soc.* 143 (6), L133–L136. doi:10.1149/1.1836901
- May, P. W., Ludlow, W. J., Hannaway, M., Smith, J. A., Rosser, K. N., and Heard, P. J. (2011). Boron doping of microcrystalline and nanocrystalline diamond films: Where is the boron going? *MRS Proc.* 1039, doi:10.1557/proc-1039-p17-03
- McBeath, S. T., Wilkinson, D. P., and Graham, N. J. D. (2019). Application of boron-doped diamond electrodes for the anodic oxidation of pesticide micropollutants in a water treatment process: A critical review. *Environ. Sci. Water Res. Technol.* 5 (12), 2090–2107. doi:10.1039/c9ew00589g
- McLaughlin, M. H. S., Corcoran, E., Pakpour-Tabrizi, A. C., de Faria, D. C., and Jackman, R. B. (2020). Influence of temperature on the electrochemical window of boron doped diamond: A comparison of commercially available electrodes. *Sci. Rep.* 10 (1), 15707. doi:10.1038/s41598-020-72910-x
- McNamara, K. M., Gleason, K. K., Vestyck, D. J., and Butler, J. E. (1992). Evaluation of diamond films by nuclear magnetic resonance and Raman spectroscopy. *Diam. Relat. Mater.* 1 (12), 1145–1155. doi:10.1016/0925-9635(92)90088-6
- Medeiros de Araújo, D., Cañizares, P., Martínez-Huitle, C. A., and Rodrigo, M. A. (2014). Electrochemical conversion/combustion of a model organic pollutant on BDD anode: Role of sp<sup>3</sup>/sp<sup>2</sup> ratio. *Electrochem. Commun.* 47, 37–40. doi:10.1016/j.elecom.2014.07.017
- Mehedi, H. A., Achard, J., Rats, D., Brinza, O., Tallaire, A., Mille, V., et al. (2014). Low temperature and large area deposition of nanocrystalline diamond films with distributed antenna array microwave-plasma reactor. *Diam. Relat. Mater.* 47, 58–65. doi:10.1016/j.diamond.2014.05.004
- Mehta Menon, P., Edwards, A., Feigerle, C. S., Shaw, R. W., Coffey, D. W., Heatherly, L., et al. (1999). Filament metal contamination and Raman spectra of hot filament chemical vapor deposited diamond films. *Diam. Relat. Mater.* 8 (1), 101–109. doi:10.1016/s0925-9635(98)00444-0
- Miao, D., Li, Z., Chen, Y., Liu, G., Deng, Z., Yu, Y., et al. (2022). Preparation of macro-porous 3D boron-doped diamond electrode with surface micro structure regulation to enhance electrochemical degradation performance. *Chem. Eng. J.* 429, 132366. doi:10.1016/j.cej.2021.132366
- Miao, D., Liu, T., Yu, Y., Li, S., Liu, G., Chen, Y., et al. (2020). Study on degradation performance and stability of high temperature etching boron-doped diamond electrode. *Appl. Surf. Sci.* 514, 146091. doi:10.1016/j.apsusc.2020.146091
- Migliorini, F. L., Steter, J. R., Rocha, R. S., Lanza, M. R. V., Baldan, M. R., and Ferreira, N. G. (2016). Efficiency study and mechanistic aspects in the Brilliant Green dye degradation using BDD/Ti electrodes. *Diam. Relat. Mater.* 65, 5–12. doi:10.1016/j.diamond.2015.12.013
- Mitadera, M., Spataru, N., and Fujishima, A. (2004). Electrochemical oxidation of aniline at boron-doped diamond electrodes. *J. Appl. Electrochem.* 34 (3), 249–254. doi:10.1023/b:jach.0000015623.63462.60

- Mitra, P., Chattopadhyay, K. K., Chaudhuri, S., and Pal, A. K. (1994). Electrical properties of boron-doped diamond films prepared by dc plasma decomposition of CO<sub>2</sub> + H<sub>2</sub>. *Mater. Lett.* 21 (1), 95–99. doi:10.1016/0167-577x(94)90130-9
- Moelle, C., Klose, S., Szücs, F., Fecht, H. J., Johnston, C., Chalker, P. R., et al. (1997). Measurement and calculation of the thermal expansion coefficient of diamond. *Diam. Relat. Mater.* 6 (5–7), 839–842. doi:10.1016/s0925-9635(96)00674-7
- Monteil, H., Pechaud, Y., Oturan, N., Trelu, C., and Oturan, M. A. (2021). Pilot scale continuous reactor for water treatment by electrochemical advanced oxidation processes: Development of a new hydrodynamic/reactive combined model. *Chem. Eng. J.* 404, 127048. doi:10.1016/j.cej.2020.127048
- Moreira, F. C., Boaventura, R. A. R., Brillas, E., and Vilar, V. J. P. (2017). Electrochemical advanced oxidation processes: A review on their application to synthetic and real wastewaters. *Appl. Catal. B Environ.* 202, 217–261. doi:10.1016/j.apcatb.2016.08.037
- Mousavi, M. P. S., Dittmer, A. J., Wilson, B. E., Hu, J., Stein, A., and Bühlmann, P. (2015). Unbiased quantification of the electrochemical stability limits of electrolytes and ionic liquids. *J. Electrochem. Soc.* 162 (12), A2250–A2258. doi:10.1149/2.0271512jes
- Mousset, E. (2022). Interest of micro-reactors for the implementation of advanced electrocatalytic oxidation with boron-doped diamond anode for wastewater treatment. *Curr. Opin. Electrochem.* 32, 100897. doi:10.1016/j.coelec.2021.100897
- Murugananthan, M., Latha, S. S., Bhaskar Raju, G., and Yoshihara, S. (2011). Role of electrolyte on anodic mineralization of atenolol at boron doped diamond and Pt electrodes. *Sep. Purif. Technol.* 79 (1), 56–62. doi:10.1016/j.seppur.2011.03.011
- Murugananthan, M., Yoshihara, S., Rakuma, T., Uehara, N., and Shirakashi, T. (2007). Electrochemical degradation of 17 $\beta$ -estradiol (E2) at boron-doped diamond (Si/BDD) thin film electrode. *Electrochimica Acta* 52 (9), 3242–3249. doi:10.1016/j.electacta.2006.09.073
- Naji, T., Dirany, A., Carabin, A., and Drogui, P. (2017). Large-scale disinfection of real swimming pool water by electro-oxidation. *Environ. Chem. Lett.* 16 (2), 545–551. doi:10.1007/s10311-017-0687-2
- Neto, M. A., Pato, G., Bundaleski, N., Teodoro, O. M. N. D., Fernandes, A. J. S., Oliveira, F. J., et al. (2016). Surface modifications on as-grown boron doped CVD diamond films induced by the B2O<sub>3</sub>-ethanol-Ar system. *Diam. Relat. Mater.* 64, 89–96. doi:10.1016/j.diamond.2016.02.001
- Neto, M. A., Silva, E. L., Ghumman, C. A., Teodoro, O. M., Fernandes, A. J. S., Oliveira, F. J., et al. (2012). Composition profiles and adhesion evaluation of conductive diamond coatings on dielectric ceramics. *Thin Solid Films* 520 (16), 5260–5266. doi:10.1016/j.tsf.2012.03.049
- Nidheesh, P. V., Divyapriya, G., Oturan, N., Trelu, C., and Oturan, M. A. (2019). Environmental applications of boron-doped diamond electrodes: 1. Applications in water and wastewater treatment. *ChemElectroChem* 6 (8), 2124–2142. doi:10.1002/celec.201801876
- Notsu, H., Fukazawa, T., Tatsuma, T., Tryk, D. A., and Fujishima, A. (2001). Hydroxyl groups on boron-doped diamond electrodes and their modification with a silane coupling agent. *Electrochem. Solid-State Lett.* 4 (3), H1–H3. doi:10.1149/1.1346556
- Oliveira, T. M. B. F., Ribeiro, F. W. P., Moraes, S., de Lima-Neto, P., and Correia, A. N. (2022). Removal and sensing of emerging pollutants released from (micro)plastic degradation: Strategies based on boron-doped diamond electrodes. *Curr. Opin. Electrochem.* 31, 100866. doi:10.1016/j.coelec.2021.100866
- Olson, E. J., and Bühlmann, P. (2012). Unbiased assessment of electrochemical windows: Minimizing mass transfer effects on the evaluation of anodic and cathodic limits. *J. Electrochem. Soc.* 160 (2), A320–A323. doi:10.1149/2.068302jes
- Oturan, M. A., Sirés, I., Oturan, N., Pérocheau, S., Laborde, J.-L., and Trévin, S. (2008). Sono-electro-fenton process: A novel hybrid technique for the destruction of organic pollutants in water. *J. Electroanal. Chem.* 624 (1–2), 329–332. doi:10.1016/j.jelechem.2008.08.005
- Pacheco, M. J., Morão, A., Lopes, A., Ciriaco, L., and Gonçalves, I. (2007). Degradation of phenols using boron-doped diamond electrodes: A method for quantifying the extent of combustion. *Electrochimica Acta* 53 (2), 629–636. doi:10.1016/j.electacta.2007.07.024
- Panizza, M., and Cerisola, G. (2009). Direct and mediated anodic oxidation of organic pollutants. *Chem. Rev.* 109 (12), 6541–6569. doi:10.1021/cr9001319
- Panizza, M., Michaud, P. A., Cerisola, G., and Comninellis, C. (2001). Anodic oxidation of 2-naphthol at boron-doped diamond electrodes. *J. Electroanal. Chem.* 507 (1–2), 206–214. doi:10.1016/s0022-0728(01)00398-9
- Parikh, R. P., and Adomaitis, R. A. (2006). An overview of gallium nitride growth chemistry and its effect on reactor design: Application to a planetary radial-flow CVD system. *J. Cryst. Growth* 286 (2), 259–278. doi:10.1016/j.jcrysgro.2005.09.050
- Paritoshrolovitz, D. J., Battaile, C. C., Li, X., and Butler, J. E. (1999). Simulation of faceted film growth in two-dimensions: Microstructure, morphology and texture. *Acta Mater.* 47 (7), 2269–2281. doi:10.1016/s1359-6454(99)00086-5
- Patel, A. N., Tan, S. Y., Miller, T. S., Macpherson, J. V., and Unwin, P. R. (2013). Comparison and reappraisal of carbon electrodes for the voltammetric detection of dopamine. *Anal. Chem.* 85 (24), 11755–11764. doi:10.1021/ac401969q
- Patel, K., Hashimoto, K., and Fujishima, A. (1992). Application of boron-doped CVD-diamond film to photoelectrode. *Denki Kagaku oyobi Kogyo Butsuri Kagaku* 60 (7), 659–661. doi:10.5796/electrochemistry.60.659
- Pelskov, Y. V., Sakharova, A. Y., Krotova, M. D., Bouilov, L. L., and Spitsyn, B. V. (1987). Photoelectrochemical properties of semiconductor diamond. *J. Electroanal. Chem. Interfacial Electrochem.* 228 (1–2), 19–27. doi:10.1016/0022-0728(87)80093-1
- Pleskov, Y. (2011). “Electrochemistry of diamond,” in *Synthetic diamond films*. Editors E. Brillas and C. A. Martínez-Huitle, 77–108. Hoboken, New Jersey, United States: John Wiley & Sons, Inc.
- Prawer, S., and Nemanich, R. J. (2004). Raman spectroscopy of diamond and doped diamond. *Philos. Trans. A Math. Phys. Eng. Sci.* 362 (1824), 2537–2565. doi:10.1098/rsta.2004.1451
- Pujol, A. A., León, I., Cárdenas, J., Sepúlveda-Guzmán, S., Manríquez, J., Sirés, I., et al. (2020). Degradation of phenols by heterogeneous electro-Fenton with a Fe<sub>3</sub>O<sub>4</sub>-chitosan composite and a boron-doped diamond anode. *Electrochimica Acta* 337, 135784. doi:10.1016/j.electacta.2020.135784
- Railkar, T. A., Kang, W. P., Windischmann, H., Malshe, A. P., Naseem, H. A., Davidson, J. L., et al. (2000). A critical review of chemical vapor-deposited (CVD) diamond for electronic applications. *Crit. Rev. Solid State Mater. Sci.* 25 (3), 163–277. doi:10.1080/10408430008951119
- Ramesham, R., and Rose, M. F. (1997). Electrochemical characterization of doped and undoped CVD diamond deposited by microwave plasma. *Diam. Relat. Mater.* 6 (1), 17–26. doi:10.1016/s0925-9635(96)00593-6
- Read, T. L., and Macpherson, J. V. (2016). Assessment of boron doped diamond electrode quality and application to *in situ* modification of local pH by water electrolysis. *J. Vis. Exp.* 107, 53484. doi:10.3791/53484
- Rivera, F. F., León, C. P. d., Walsh, F. C., and Nava, J. L. (2015). The reaction environment in a filter-press laboratory reactor: The FM01-LC flow cell. *Electrochimica Acta* 161, 436–452. doi:10.1016/j.electacta.2015.02.161
- Roccamante, M., Salmerón, I., Ruiz, A., Oller, I., and Malato, S. (2020). New approaches to solar Advanced Oxidation Processes for elimination of priority substances based on electrooxidation and ozonation at pilot plant scale. *Catal. Today* 355, 844–850. doi:10.1016/j.cattod.2019.04.014
- Rohatgi, A. (2019). *WebPlotDigitizer*. San Francisco, California, USA. Available: <https://automeris.io/WebPlotDigitizer> (Accessed 12 15, 2021).
- Rubí-Juárez, H., Cotillas, S., Sáez, C., Cañizares, P., Barrera-Díaz, C., and Rodrigo, M. A. (2016). Use of conductive diamond photo-electrochemical oxidation for the removal of pesticide glyphosate. *Sep. Purif. Technol.* 167, 127–135. doi:10.1016/j.seppur.2016.04.048
- Ryl, J., Burczyk, L., Bogdanowicz, R., Sobaszek, M., and Darowicki, K. (2016). Study on surface termination of boron-doped diamond electrodes under anodic polarization in H<sub>2</sub>SO<sub>4</sub> by means of dynamic impedance technique. *Carbon* 96, 1093–1105. doi:10.1016/j.carbon.2015.10.064
- Ryl, J., Burczyk, L., Zielinski, A., Ficek, M., Franczak, A., Bogdanowicz, R., et al. (2019). Heterogeneous oxidation of highly boron-doped diamond electrodes and its influence on the surface distribution of electrochemical activity. *Electrochimica Acta* 297, 1018–1027. doi:10.1016/j.electacta.2018.12.050
- Salazar-Banda, G. R., Andrade, L. S., Nascente, P. A. P., Pizani, P. S., Rocha-Filho, R. C., and Avaca, L. A. (2006). On the changing electrochemical behaviour of boron-doped diamond surfaces with time after cathodic pre-treatments. *Electrochimica Acta* 51 (22), 4612–4619. doi:10.1016/j.electacta.2005.12.039
- Salazar-Banda, G. R., de Carvalho, A. E., Andrade, L. S., Rocha-Filho, R. C., and Avaca, L. A. (2010). On the activation and physical degradation of boron-doped diamond surfaces brought on by cathodic pretreatments. *J. Appl. Electrochem.* 40 (10), 1817–1827. doi:10.1007/s10800-010-0139-1
- Salgueiredo, E., Amaral, M., Neto, M. A., Fernandes, A. J. S., Oliveira, F. J., and Silva, R. F. (2011). HFCVD diamond deposition parameters optimized by a Taguchi Matrix. *Vacuum* 85 (6), 701–704. doi:10.1016/j.vacuum.2010.10.010
- Salmeron, I., Oller, I., Plakas, K. V., and Malato, S. (2021). Carbon-based cathodes degradation during electro-Fenton treatment at pilot scale: Changes in H<sub>2</sub>O<sub>2</sub> electrogeneration. *Chemosphere* 275, 129962. doi:10.1016/j.chemosphere.2021.129962
- Salmerón, I., Plakas, K. V., Sirés, I., Oller, I., Maldonado, M. I., Karabelas, A. J., et al. (2019). Optimization of electrocatalytic H<sub>2</sub>O<sub>2</sub> production at pilot plant scale for solar-assisted water treatment. *Appl. Catal. B Environ.* 242, 327–336. doi:10.1016/j.apcatb.2018.09.045
- Schwander, M., and Partes, K. (2011). A review of diamond synthesis by CVD processes. *Diam. Relat. Mater.* 20 (9), 1287–1301. doi:10.1016/j.diamond.2011.08.005
- Sein, H., Ahmed, W., Jackson, M., and Polini, R. (2006). *Growth of polycrystalline diamond on titanium nitride on silicon substrates using negative bias assisted CVD*. Materials Park: Asm International.
- Sharma, D. K., Giro, A. V., Chapon, P., Neto, M. A., Oliveira, F. J., and Silva, R. F. (2022). Advances in RF glow discharge optical emission spectrometry characterization of intrinsic and boron-doped diamond coatings. *ACS Appl. Mater. Interfaces* 14 (5), 7405–7416. doi:10.1021/acami.1c20785



- Shaw, J., Jones, A. N., Monk, P. M. S., and Rego, C. A. (2002). Electrochemical behaviour of graphite- and molybdenum electrodes modified with thin-film diamond. *Diam. Relat. Mater.* 11 (9), 1690–1696. doi:10.1016/s0925-9635(02)00139-5
- Shroder, R. E., Nemanich, R. J., and Glass, J. T. (1990). Analysis of the composite structures in diamond thin films by Raman spectroscopy. *Phys. Rev. B Condens Matter* 41 (6), 3738–3745. doi:10.1103/physrevb.41.3738
- Sires, I., Brillas, E., Oturan, M. A., Rodrigo, M. A., and Panizza, M. (2014). Electrochemical advanced oxidation processes: Today and tomorrow. A review. *Environ. Sci. Pollut. Res. Int.* 21 (14), 8336–8367. doi:10.1007/s11356-014-2783-1
- Souza, F., Sáez, C., Lanza, M., Cañizares, P., and Rodrigo, M. A. (2016). Towards the scale-up of electrolysis with diamond anodes: Effect of stacking on the electrochemical oxidation of 2,4 D. *J. Chem. Technol. Biotechnol.* 91 (3), 742–747. doi:10.1002/jctb.4639
- Spitsyn, B. V., Bouilov, L. L., and Derjaguin, B. V. (1981). Vapor growth of diamond on diamond and other surfaces. *J. Cryst. Growth* 52, 219–226. doi:10.1016/0022-0248(81)90197-4
- Srikanth, V. V. S. S., and Jiang, X. (2011). “Synthesis of diamond films,” in *Synthetic diamond films*, 21–55. Hoboken, New Jersey, United States: John Wiley & Sons, Inc.
- Stanković, D. M., and Kalcher, K. (2016). Amperometric quantification of the pesticide azirac at boron doped diamond electrodes using flow injection analysis. *Sensors Actuators B Chem.* 233, 144–147. doi:10.1016/j.snb.2016.04.069
- Štenclová, P., Vyskočil, V., Szabó, O., Izák, T., Potocký, Š., and Kromka, A. (2019). Structured and graphitized boron doped diamond electrodes: Impact on electrochemical detection of Cd<sup>2+</sup> and Pb<sup>2+</sup> ions. *Vacuum* 170, 108953. doi:10.1016/j.vacuum.2019.108953
- Sun, J., Lu, H., Lin, H., Huang, W., Li, H., Lu, J., et al. (2012). Boron doped diamond electrodes based on porous Ti substrates. *Mater. Lett.* 83, 112–114. doi:10.1016/j.matlet.2012.05.044
- Swain, G. M., Anderson, A. B., and Angus, J. C. (2013). Applications of diamond thin films in electrochemistry. *MRS Bull.* 23 (9), 56–60. doi:10.1557/s0883769400029389
- Swain, G. M., and Ramesham, R. (2002). The electrochemical activity of boron-doped polycrystalline diamond thin film electrodes. *Anal. Chem.* 65 (4), 345–351. doi:10.1021/ac00052a007
- Swain, G. M. (2019). The susceptibility to surface corrosion in acidic fluoride media: A comparison of diamond, HOPG, and glassy carbon electrodes. *J. Electrochem. Soc.* 141 (12), 3382–3393. doi:10.1149/1.2059343
- Swain, G. M. (1994). The use of CVD diamond thin films in electrochemical systems. *Adv. Mater.* 6 (5), 388–392. doi:10.1002/adma.19940060511
- Tamor, M. A., and Everson, M. P. (2011). On the role of penetration twins in the morphological development of vapor-grown diamond films. *J. Mater. Res.* 9 (7), 1839–1849. doi:10.1557/jmr.1994.1839
- Tang, C. J., Fernandes, A. J. S., Costa, F., and Pinto, J. L. (2011). Effect of microwave power and nitrogen addition on the formation of {100} faceted diamond from microcrystalline to nanocrystalline. *Vacuum* 85 (12), 1130–1134. doi:10.1016/j.vacuum.2011.01.024
- Tawabini, B. S., Plakas, K. V., Fraim, M., Safi, E., Oyehan, T., and Karabelas, A. J. (2020). Assessing the efficiency of a pilot-scale GDE/BDD electrochemical system in removing phenol from high salinity waters. *Chemosphere* 239, 124714. doi:10.1016/j.chemosphere.2019.124714
- Teraji, T., Yamamoto, T., Watanabe, K., Koide, Y., Isoya, J., Onoda, S., et al. (2015). Homoepitaxial diamond film growth: High purity, high crystalline quality, isotopic enrichment, and single color center formation. *Phys. status solidi (a)* 212 (11), 2365–2384. doi:10.1002/pssa.201532449
- Trellu, C., Chakraborty, S., Nidheesh, P. V., and Oturan, M. A. (2019). Environmental applications of boron-doped diamond electrodes: 2. Soil remediation and sensing applications. *ChemElectroChem* 6 (8), 2143–2156. doi:10.1002/celec.201801877
- Triana, Y., Tomisaki, M., and Einaga, Y. (2020). Oxidation reaction of dissolved hydrogen sulfide using boron doped diamond. *J. Electroanal. Chem.* 873, 114411. doi:10.1016/j.jelechem.2020.114411
- Tryk, D. A., Tsunozaki, K., Rao, T. N., and Fujishima, A. (2001). Relationships between surface character and electrochemical processes on diamond electrodes: Dual roles of surface termination and near-surface hydrogen. *Diam. Relat. Mater.* 10 (9–10), 1804–1809. doi:10.1016/s0925-9635(01)00453-8
- Ueda, A., Kato, D., Sekioka, N., Hirono, S., and Niwa, O. (2009). Local imaging of an electrochemical active/inactive region on a conductive carbon surface by using scanning electrochemical microscopy. *Anal. Sci.* 25 (5), 645–651. doi:10.2116/analsci.25.645
- van der Drift, A. (1967). Evolutionary selection: A principle governing growth orientation in vapour deposited layers. *Philips Res. Rep.* 22, 267–288.
- van Eck, N. J., and Waltman, L. (2010). Software survey: VOSviewer, a computer program for bibliometric mapping. *Scientometrics* 84 (2), 523–538. doi:10.1007/s11192-009-0146-3
- Vanhove, E., de Sanoit, J., Arnault, J. C., Saada, S., Mer, C., Mailley, P., et al. (2007). Stability of H-terminated BDD electrodes: An insight into the influence of the surface preparation. *Phys. status solidi (a)* 204 (9), 2931–2939. doi:10.1002/pssa.200776340
- Vernasqui, L. G., Sardinha, A. F., Oishi, S. S., and Ferreira, N. G. (2021). Nanoscale control of high-quality boron-doped ultrananodiamond on dioxide titanium nanotubes as a porous composite. *J. Mater. Res. Technol.* 12, 597–612. doi:10.1016/j.jmrt.2021.02.099
- Vidales, M. J. M. d., Barba, S., Sáez, C., Cañizares, P., and Rodrigo, M. A. (2014). Coupling ultraviolet light and ultrasound irradiation with Conductive-Diamond Electrochemical Oxidation for the removal of progesterone. *Electrochimica Acta* 140, 20–26. doi:10.1016/j.electacta.2014.02.118
- Vieira Dos Santos, E., Saez, C., Canizares, P., Martinez-Huitle, C. A., and Rodrigo, M. A. (2017). Treating soil-washing fluids polluted with oxyfluorben by sono-electrolysis with diamond anodes. *Ultrason. Sonochem.* 34, 115–122. doi:10.1016/j.ultsonch.2016.05.029
- Vorlíček, V., Rosa, J., Vaněček, M., Nesládek, M., and Stals, L. M. (1997). Quantitative study of Raman scattering and defect optical absorption in CVD diamond films. *Diam. Relat. Mater.* 6 (5–7), 704–707. doi:10.1016/s0925-9635(96)00630-9
- Wang, X. H., Ma, G. H. M., Zhu, W., Glass, J. T., Bergman, L., Turner, K. F., et al. (1992). Effects of boron doping on the surface morphology and structural imperfections of diamond films. *Diam. Relat. Mater.* 1 (7), 828–835. doi:10.1016/0925-9635(92)90109-2
- Wang, Z., Liu, S., and Zhao, G. (2022). *In situ* electrochemical spectroscopy for boron-doped diamond electrode reactions: Recent progress and perspectives. *Curr. Opin. Electrochem.* 32, 100892. doi:10.1016/j.coelec.2021.100892
- Wei, C., and Chen, C.-H. (2008). The effect of thermal and plastic mismatch on stress distribution in diamond like carbon film under different interlayer/substrate system. *Diam. Relat. Mater.* 17 (7–10), 1534–1540. doi:10.1016/j.diamond.2008.03.004
- Wei, J.-j., Zhu, X.-p., Lü, F.-x., and Ni, J.-r. (2011). Comparative study of oxidation ability between boron-doped diamond (BDD) and lead oxide (PbO<sub>2</sub>) electrodes. *Int. J. Minerals, Metallurgy, Mater.* 18 (5), 589–593. doi:10.1007/s12613-011-0482-1
- Wild, C., Herres, N., and Koidl, P. (1990). Texture formation in polycrystalline diamond films. *J. Appl. Phys.* 68 (3), 973–978. doi:10.1063/1.346663
- Wild, C., Kohl, R., Herres, N., Müller-Sebert, W., and Koidl, P. (1994). Oriented CVD diamond films: Twin formation, structure and morphology. *Diam. Relat. Mater.* 3 (4–6), 373–381. doi:10.1016/0925-9635(94)90188-0
- Williams, O. A. (2011). Nanocrystalline diamond. *Diam. Relat. Mater.* 20 (5–6), 621–640. doi:10.1016/j.diamond.2011.02.015
- Witek, M. A., and Swain, G. M. (2001). Aliphatic polyamine oxidation response variability and stability at boron-doped diamond thin-film electrodes as studied by flow-injection analysis. *Anal. Chim. Acta* 440 (2), 119–129. doi:10.1016/s0003-2670(01)01055-8
- Wu, H., Xu, F., Liu, Z., Zhou, C., Lu, W., and Zuo, D. (2015). Preparation of large-scale double BDD electrodes and their electrochemical performances. *Trans. Nanjing Univ. Aeronautics Astronautics* 32 (6), 674–680.
- Xiang-Liu, J., Fang-Qing, Z., Jiang-Qi, L., Bin, Y., and Guang-Hua, C. (1991). “Systematic studies on transition layers of carbides between CVD diamond films and substrates of strong carbide-forming elements,” in *SPIE proceedings*. San Diego, CA, United States: Proceedings Volume 1534, Diamond Optics IV. doi:10.1117/12.48293
- Xu, S. G. (2016). Modeling and experimental study of electrochemical oxidation of organics on boron-doped diamond anode. *CNL Nucl. Rev.*, 1–15. doi:10.12943/cnr.2016.00018
- Yagi, I., Notsu, H., Kondo, T., Tryk, D. A., and Fujishima, A. (1999). Electrochemical selectivity for redox systems at oxygen-terminated diamond electrodes. *J. Electroanal. Chem.* 473 (1–2), 173–178. doi:10.1016/s0022-0728(99)00027-3
- Yamaguchi, C., Natsui, K., Iizuka, S., Tateyama, Y., and Einaga, Y. (2019). Electrochemical properties of fluorinated boron-doped diamond electrodes via fluorine-containing plasma treatment. *Phys. Chem. Chem. Phys.* 21 (25), 13788–13794. doi:10.1039/c8cp07402j
- Yang, N., Yu, S., Macpherson, J. V., Einaga, Y., Zhao, H., Zhao, G., et al. (2019). Conductive diamond: Synthesis, properties, and electrochemical applications. *Chem. Soc. Rev.* 48 (1), 157–204. doi:10.1039/c7cs00757d
- Yang, W., Tan, J., Chen, Y., Li, Z., Liu, F., Long, H., et al. (2022). Relationship between substrate type and BDD electrode structure, performance and antibiotic tetracycline mineralization. *J. Alloys Compd.* 890, 161760. doi:10.1016/j.jallcom.2021.161760
- Yano, T., Popa, E., Tryk, D. A., Hashimoto, K., and Fujishima, A. (2019a). Electrochemical behavior of highly conductive boron-doped diamond electrodes for oxygen reduction in acid solution. *J. Electrochem. Soc.* 146 (3), 1081–1087. doi:10.1149/1.1391724
- Yano, T., Tryk, D. A., Hashimoto, K., and Fujishima, A. (2019b). Electrochemical behavior of highly conductive boron-doped diamond electrodes for oxygen reduction in alkaline solution. *J. Electrochem. Soc.* 145 (6), 1870–1876. doi:10.1149/1.1838569
- Yoon, J.-H., Shim, Y.-B., Lee, B.-S., Choi, S.-Y., and Won, M.-S. (2012). Electrochemical degradation of phenol and 2-chlorophenol using Pt/Ti and boron-doped diamond electrodes. *Bull. Korean Chem. Soc.* 33 (7), 2274–2278. doi:10.5012/bkcs.2012.33.7.2274



- Yu, X., Zhou, M., Hu, Y., Groenen Serrano, K., and Yu, F. (2014). Recent updates on electrochemical degradation of bio-refractory organic pollutants using BDD anode: A mini review. *Environ. Sci. Pollut. Res. Int.* 21 (14), 8417–8431. doi:10.1007/s11356-014-2820-0
- Yuan, S., Guo, X., Li, P., Mao, Q., Lu, M., Jin, Z., et al. (2021). Insights into the surface oxidation modification mechanism of nano-diamond: An atomistic understanding from ReaxFF simulations. *Appl. Surf. Sci.* 540, 148321. doi:10.1016/j.apsusc.2020.148321
- Zanin, H., May, P. W., Fermin, D. J., Plana, D., Vieira, S. M., Milne, W. I., et al. (2014). Porous boron-doped diamond/carbon nanotube electrodes. *ACS Appl. Mater. Interfaces* 6 (2), 990–995. doi:10.1021/am4044344
- Zhang, C., Lu, X., Lu, Y., Ding, M., and Tang, W. (2019a). Titanium-boron doped diamond composite: A new anode material. *Diam. Relat. Mater.* 98, 107490. doi:10.1016/j.diamond.2019.107490
- Zhang, C., Xian, J., Liu, M., and Fu, D. (2018). Formation of brominated oligomers during phenol degradation on boron-doped diamond electrode. *J. Hazard Mater* 344, 123–135. doi:10.1016/j.jhazmat.2017.10.010
- Zhang, J., Yu, X., Zhang, Z.-Q., and Zhao, Z.-Y. (2020). Preparation of boron-doped diamond foam film for supercapacitor applications. *Appl. Surf. Sci.* 506, 144645. doi:10.1016/j.apsusc.2019.144645
- Zhang, J., Yu, X., Zhao, Z.-y., Zhang, Z., and Li, J. (2019b). Influence of pore size of Ti substrate on structural and capacitive properties of Ti/boron doped diamond electrode. *J. Alloys Compd.* 777, 84–93. doi:10.1016/j.jallcom.2018.10.120
- Zhou, M., Liu, L., Jiao, Y., Wang, Q., and Tan, Q. (2011a). Treatment of high-salinity reverse osmosis concentrate by electrochemical oxidation on BDD and DSA electrodes. *Desalination* 277 (1-3), 201–206. doi:10.1016/j.desal.2011.04.030
- Zhou, M., Särkkä, H., and Sillanpää, M. (2011b). A comparative experimental study on methyl orange degradation by electrochemical oxidation on BDD and MMO electrodes. *Sep. Purif. Technol.* 78 (3), 290–297. doi:10.1016/j.seppur.2011.02.013
- Zhu, C., Jiang, C., Chen, S., Mei, R., Wang, X., Cao, J., et al. (2018). Ultrasound enhanced electrochemical oxidation of Alizarin Red S on boron doped diamond(BDD) anode:Effect of degradation process parameters. *Chemosphere* 209, 685–695. doi:10.1016/j.chemosphere.2018.06.137
- Zhu, J. Z., Yang, S. Z., Zhu, P. L., Zhang, X. K., Zhang, G. X., Xu, C. F., et al. (1995a). Electrochemical behaviors of boron-doped diamond film electrodes grown selectively. *Chin. Chem. Lett.* 6 (8), 707–710.
- Zhu, P., Zhu, J., Yang, S., Zhang, X., and Zhang, G. (1995b). Electrochemical characterization of boron-doped polycrystalline diamond thin-film electrodes. *Fresenius' J. Anal. Chem.* 353 (2), 171–173. doi:10.1007/bf00322953

## Glossary

**ACE** average current efficiency

**AFM** atomic force microscopy

**AO** anodic oxidation

**BDD** boron-doped diamond

**C<sub>diamond</sub>** purity of chemically vapor deposited diamond

**C<sub>dl</sub>** double-layer capacitance

**COD** chemical oxygen demand

**CTE** coefficient of thermal expansion

**CVD** chemical vapor deposition

**EAOP** electrochemical advanced oxidation processes

**EC** energy consumption

**EELS** electron energy-loss spectroscopy

**EF** electro-fenton

**EIS** electrochemical impedance spectroscopy

**FWHM** full width at half maximum

**GDOES** pulsed radio frequency glow discharge optical emission spectroscopy

**HER** hydrogen evolution reaction

**HFCVD** hot-filament chemical vapor deposition

**HPLC** high-performance liquid chromatography

**HTHP** high pressure-high temperature

**ICE** instantaneous current efficiency

**J<sub>appl</sub>** applied current density

**J<sub>cut-off</sub>** arbitrary current density cut-off

**J<sub>limit</sub>** limiting current density

**MCD** microcrystalline diamond

**MCE** mineralization current efficiency

**MPCVD** microwave plasma chemical vapor deposition

**NCD** nanocrystalline diamond

**NDC** non-diamond carbon

**NDP** neutron depth profile

**OEP** oxygen evolution potential

**OER** oxygen evolution reaction

**PEF** photoelectro-Fenton

**Q'** average charge required for pollutant degradation

**Q'** average charge

**RF** radio frequency

**RFCVD** radio frequency plasma chemical vapor deposition

**SEF** sonoelectro-fenton

**SEM** scanning electron microscopy

**SHE** standard hydrogen electrode

**SIMS** secondary ion mass spectrometry

**SLR** systematic literature review

**SPEF** solar photoelectro-fenton

**TOC** total organic carbon

**UNCD** ultra-nanocrystalline diamond

**UV** ultraviolet

**XPS** x-ray photoelectron spectroscopy

**β** figure-of-merit or the Raman quality fraction

**η<sub>c</sub>** combustion efficiency

# Frontiers in Materials

Investigates the discovery and design of materials  
for future application

A multidisciplinary journal that explores the  
breadth of materials science, engineering and  
mechanics - from carbon-based materials to  
smart materials.

## Discover the latest Research Topics

See more →

### Frontiers

Avenue du Tribunal-Fédéral 34  
1005 Lausanne, Switzerland  
[frontiersin.org](https://frontiersin.org)

### Contact us

+41 (0)21 510 17 00  
[frontiersin.org/about/contact](https://frontiersin.org/about/contact)

